AUSROCK
CONFERENCE 2022

AN ISRM REGIONAL SYMPOSIUM

Conference Proceedings

AUSROCK CONFERENCE 2022

The Australasian Ground Control Conference & An ISRM Regional Symposium

29 NOVEMBER – 1 DECEMBER 2022
MELBOURNE, AUSTRALIA

ORGANISING COMMITTEE

Prof Serkan Saydam
FAusIMM
Conference Co-Chair

Prof Ismet Canbulat
FAusIMM
Conference Co-Chair

Jorge Andres Calderón

Diana Carroll
MAusIMM

Peter Craig
MAusIMM

Dr Sevda Dehkhoda
MAusIMM

Lesley Munsamy
MAusIMM(CP)

Joung Oh
MAusIMM

Patrycja Sheffield
MAusIMM

Baotang Shen

Sarah Webster
MAusIMM(CP)

Dr Chengguo Zhang
MAusIMM

AUSIMM

Julie Allen
Head of Events

Fiona Geoghegan
Manager, Events

Samara Brown
Conference Program Manager

REVIEWERS

We would like to thank the following people for their contribution towards enhancing the quality of the papers included in this volume:

Dr Sela Akdag

Jorge Calderón

Alex Campbell

Diana Carroll

Riaan Carstens

Nathan Chembe

Peter Craig

Dr Sevda Dehkhoda

Marc Elmouttie

Lesley Munsamy

Joung Oh

Patrycja Sheffield

Baotang Shen

Linda Snyman

Claire Stuart

Robyn Teet

Sarah Webster

Dr Chengguo Zhang

Qianbing Zhang

Jian Zhao

FOREWORD

On behalf of the Organising Committee, we welcome you to AusRock 2022: The Australasian Ground Control in Mining Conference, hosted by the AusIMM and UNSW Sydney.

This year's conference is hosted as the Regional Symposium of the International Society for Rock Mechanics and Rock Engineering (ISRM) and its affiliates in Australasia, the Australian Geomechanics Society, the New Zealand Geotechnical Society and the Eastern Australia Ground Control Group. The conference organisers thank these learned societies for their active support of the conference.

The conference follows on from earlier conferences that have successfully covered the various aspects of geotechnical engineering servicing the mining industry and, in so doing, shared best practices and experience. The conference targets all persons interested in the investigation, design and implementation of stable excavations, which is at the core of mining operations and contributes to a safe work environment.

In particular, the conference should be of interest to mine site operators, technical support staff, geotechnical engineers, mining engineers, consultants and researchers in the field of mining geomechanics and ground control.

It will provide an update to all mining industry geotechnical personnel on best practices in both Australasia and overseas. It is also intended to act as an information exchange vehicle between the coal and metalliferous sectors of the industry, focusing on new technologies and developments, industry needs and mine site problem solving and practical case studies.

At this conference, there is a good balance of papers covering all mining sectors, focusing on new technologies and innovations, industry needs and problem-solving and practical case studies, slope stability, geotechnical risk management and numerical modelling, and dynamic failures related to ground control in mining. There is an enormous potential for information exchange, technology transfer and collaborative technology developments – not to mention simply sharing common problems and establishing new networks – if the various sectors of our industry and profession can get together nationally on a regular basis.

All papers in this conference proceedings were independently peer-reviewed and edited to ensure the highest quality.

The conference has distinguished keynote speakers from Australia, Norway and the USA who, between them, cover issues and recent developments in ground control.

We hope that you will find this conference both valuable and stimulating and that the contacts made during the conference will be of great benefit to all.

Yours faithfully,

Ismet Canbulat FAusIMM & Serkan Saydam FAusIMM

AusRock Conference 2022 Organising Committee Co-Chairs

SPONSORS

Major Conference Sponsor

Platinum Sponsor

Gold Sponsor

Gold Partner

Silver Sponsor

Conference App Sponsor

Name Badge and Lanyard Sponsor

Poster Session Sponsor

Destination Partner

Supporting Partners

CONTENTS

Geotechnical design methodologies

Geotechnical education and training

Geotechnical instrumentation

Geotechnical instrumentation, monitoring and data management

Geotechnical risk management

Ground control and support

Interdisciplinary

Mine design – geotechnical considerations

Rock mass characterisation techniques and practice

Rock mechanics in mining, civil and petroleum engineering

Slope stability

Structure stability

Poster submission

Best practice case studies

Assessment of main factors contributing to the height of fracturing above longwall panels – a review and case-based numerical study

M W Chen[1], I Canbulat[2], S Saydam[3] and C G Zhang[4]

1. School of Minerals and Energy Resources Engineering, University of New South Wales, Sydney NSW 2052. Email: mingwei.chen@unsw.edu.au
2. School of Minerals and Energy Resources Engineering, University of New South Wales, Sydney NSW 2052. Email: i.canbulat@unsw.edu.au
3. School of Minerals and Energy Resources Engineering, University of New South Wales, Sydney NSW 2052. Email: s.saydam@unsw.edu.au
4. School of Minerals and Energy Resources Engineering, University of New South Wales, Sydney NSW 2052. Email: chengguo.zhang@usnw.edu.au

ABSTRACT

The height of fracturing (HoF) measures the propagation distance of continuous fracturing from the mining horizon and is also termed the height of cracking (Hebblewhite, 2020; Khanal *et al*, 2019) or hydrologically the height of groundwater drainage (Tammetta, 2013). In longwall practice, HoF is an important predictive indicator for assessing the dewatering effect of panel extraction on the shallow aquifer and surface flows.

The HoF determination is basically dependent on field measurement works, typically using surface extensometer, borehole televiewer imaging, piezometer monitoring, packer testing, borehole breakout logging, and isotopic tracer monitoring (Brown and Walsh, 2022; Corbett, 2022; Hebblewhite, 2020; Holla and Armstrong, 1986; Mills and O'Grady, 1998; Walsh *et al*, 2022a, 2022b). These methods or tools have been widely applied to observe rock fracturing and groundwater responses to longwalls at Australian coalmines, for example, Dendrobium Mine (Brown and Walsh, 2022; Walsh *et al*, 2022b), Appin Mine (Walsh *et al*, 2022a), and Springvale Mine (Corbett, 2022). In Chinese mines, borehole televiewer imaging and packer testing are more frequently used due to convenient instrumentation, quick testing, and not requiring long-term maintenance of the instrumentation boreholes. The HoF determination also involves further raw data interpretations, for which specialist software for data extraction and quantitative criteria for bounding the fracture transition and termination are necessary.

By combining the measured fracture distribution and longwall parameters regarding panel geometry and geological settings, several HoF models have been developed for conceptualising the understanding of strata depressurisation and providing mine engineers fast calculation tools for HoF prediction. The Mackie model considered the height of fracturing as the upper bound of fractured zone and revealed that within the fractured zone there are highly connected fractures and accordingly porosity enhancement and groundwater depressurisation, where the fracture network can be less transmissive from the mining horizon up (Hebblewhite, 2020). The fractured zone shares similar fracturing regime but different heights in varying models: HoF is 30 to 58 times of the mining height (*t*) based on Australian, Soviet and UK experience (Kendorski, 1993, 2006), and 21 to 33 *t* according to the field measurements in NSW Central Coast, Australia (Galvin, 2016). Some Australian longwall mines adopt Ditton model (Ditton and Merrick, 2014) (Equations 1.1 and 1.2 in Table 1) sourcing from NSW coalfield experience for HoF prediction, while Liu model (Liu, 1981) (Equations 2.1 to 2.4 in Table 1) developed from 27 coalmines in China is frequently used by Chinese coalmines.

TABLE 1

Two models of HoF prediction.

Equations		Applicability
$HoF = 2.215 \times w'^{0.357} \times D^{0.271} \times t^{0.372}$	Eq. 1.1	No strong strata
$HoF = 1.52 \times w'^{0.401} \times D^{0.535} \times t^{0.464} \times t'^{-0.4}$	Eq. 1.2	Strong strata
$H = 100t/(1.2t + 2.0) \pm 8.9$	Eq. 2.1	Competent strata
$H = 100t/(1.6t + 3.6) \pm 5.6$	Eq. 2.2	Medium competent strata
$H = 100t/(3.1t + 5.0) \pm 4.0$	Eq. 2.3	Soft strata
$H = 100t/(5.0t + 8.0) \pm 3.0$	Eq. 2.4	Weathered soft strata

Where t, w, and D are respectively the mining height, panel width, and depth of cover, in m; w' and t' are respectively effective panel width and thickness of competent rock units, in m.

The paper collects 24 data sets (He *et al*, 2020) including HoF measurement and correspondingly the mining height, panel width, depth of cover, and overburden lithology from 14 coalmines in China and further verifies that Ditton model conforms better to the field measurement. This comparison implies that incorporating more contributing factors into the model can help improve the overall performance in HoF prediction. In this context, the paper establishes an HoF database that incorporates about 200 HoF data sets collected from Chinese longwall mines. Statistical analysis is conducted for studying the correlation of HoF versus the mining height, panel width, depth of cover, ratio of panel width to depth of cover (*w/D*), and overburden strength and reveals that:

- HoF has a positive correlation to panel geometry, of which the mining height parameter is comparatively dominant.

- HoF has a positive correlation to *D* and *w/D*; the critical extraction threshold is 1.1 *w/D*, different than the 1.4 *w/D* from the UK experience (Li *et al*, 2022).

- HoF has a positive correlation to overburden strength, implying that low-strength rock masses can help constrain the continuous fracturing.

A discontinuum-based numerical model was then established using Voronoi tessellation to obtain a fundamental understanding of the continuous fracturing responses to varying longwall parameters. The model is verified using a ground subsidence profile measured in situ. Analysing the angle of fractures reveals that above the extracted panels (i) high-angle (45 to 90 degrees) fractures concentrate in the vicinity of goafs and chain pillars, and (ii) low-angle (0 to 45 degrees) fractures mainly concentrate along bedding planes and ground surface.

A fracture aperture gradient is then identified by interpreting borehole televiewer data, by which the modelled fractures are classified into different groups according to the normal displacement between two fracture surfaces. The fracture network has the following characteristics:

- The fracture aperture distribution is approximately symmetrical along the panel centreline and can be very different from the centreline outwards to pillar.

- In shallow longwall conditions the constrained zone in classical four- and five-zone HoF concepts can be relatively narrowed due to the through-going fracturing.

- The height of fracturing responses to varying panel geometries and coal measure geology conforms to the general understanding obtained via field measurement.

- Panel interaction can increase HoF and fracture aperture in narrow pillar settings, and the aperture enlargement is more pronounced by both sides of the pillar.

The research assesses the contribution of varying mining parameters to the height of fracturing above longwall panels, further consolidating the basis for further understanding groundwater depressurisation due to longwall mining.

REFERENCES

Brown, S and Walsh, R, 2022. The height of connected fracturing above a longwall coal mine: a field and isotopic investigation, *Proceedings of the 11th Conference on Mine Subsidence*, pp. 135–140.

Corbett, P, 2022. Groundwater system response to longwall mining at Springvale Mine, *Proceedings of the 11th Conference on Mine Subsidence*, pp. 153–170.

Ditton, S and Merrick, N P, 2014. A new sub-surface fracture height prediction model for longwall mines in the NSW coalfields, *Proceedings of Sydney Basin Symposium*, pp. 135–136.

Galvin, J M, 2016. *Ground Engineering – Principles and Practices for Underground Coal Mining*, Cham: Springer International Publishing AG, 683 p.

He, X, Zhao, Y, Zhang, C and Han, P, 2020. A model to estimate the height of the water-conducting fracture zone for longwall panels in Western China, *Mine Water and the Environment*, 39(4):823–838.

Hebblewhite, B, 2020. Fracturing, caving propagation and influence of mining on groundwater above longwall panels – a review of predictive models, *International Journal of Mining Science and Technology*, 30(1):49–54.

Holla, L and Armstrong, M, 1986. Measurement of sub-surface strata movement by multi-wire borehole instrumentation, *Bulletin of Proceedings of the Australasian Institute of Mining and Metallurgy*, 291(7):65–72.

Kendorski, F S, 1993. Effect of high-extraction coal mining on surface and ground waters, *Proceedings of the 12th Conference on Ground Control in Mining*, pp. 412–425.

Kendorski, F S, 2006. Effect of full-extraction underground mining on ground and surface waters: a 25-year retrospective, *Proceedings of the 25th International Conference on Ground Control in Mining*, pp. 1–6.

Khanal, M, Guo, H and Adhikary, D, 2019. 3D numerical study of underground coal mining induced strata deformation and subsequent permeability change, *Geotechnical and Geological Engineering*, 37(1):235–249.

Li, G, Paquet, R, Steuary, P, Ramage, R and Perceval, J, 2022. An introduction to the standardised subsidence information management system, *Proceedings of the 11th Conference on Mine Subsidence*, pp. 39–56.

Liu, T, 1981. *Surface movements, overburden failure and its application*, Coal Industry Press, 369 p.

Mills, K W and O'Grady, P, 1998. Impact of longwall width on overburden behaviour, *Proceedings of the 1998 Coal Operators' Conference*, pp. 147–155.

Tammetta, P, 2013. Estimation of the height of complete groundwater drainage above mined longwall panels, *Groundwater*, 52(5):723–734.

Walsh, R, Barbato, J, Leventhal, A and Swarbrick, G, 2022a. Managing far-field subsidence at Harris Creek cliff line, *Proceedings of the 11th Conference on Mine Subsidence*, pp. 309–325.

Walsh, R, Brown, S, Mills, K and Heritage, R, 2022b. Geological and hydrological characteristics of the Elouera Fault and the impacts of mining, *Proceedings of the 11th Conference on Mine Subsidence,* pp. 121–133.

Development of new performance prediction models for a raise boring machine based on indentation tests

A Sheterpour-Mamaghani[1], H Copur[2], C Balci[3], D Tumac[4], E Dogan[5], E Altintas[6], A Kocbay[7], T Erdogan[8] and A Gumus[9]

1. PhD Candidate, Mining Engineering Department, Istanbul Technical University, Istanbul, Turkey. Email: mamaghani@itu.edu.tr
2. Professor, Mining Engineering Department, Istanbul Technical University, Istanbul, Turkey. Email: copurh@itu.edu.tr
3. Professor, Mining Engineering Department, Istanbul Technical University, Istanbul, Turkey. Email: cemalb@itu.edu.tr
4. Professor, Mining Engineering Department, Istanbul Technical University, Istanbul, Turkey. Email: tumacde@itu.edu.tr
5. Senior Mining Engineer, Istanbul, Turkey. Email: engin3458dogan@gmail.com
6. Mine Manager, Efemcukuru Gold Mine, Izmir, Turkey. Email: erguna@efemcukuru.com
7. Head of Geotechnical Services and Groundwater Department, General Directorate of State Hydraulic Works, Ankara, Turkey. Email: ayhankocbay@gmail.com
8. Projects Coordinator, Sargin Construction and Machinery Industry Trade Inc., Ankara, Turkey. Email: tayfun.erdogan@sargininsaat.com
9. MSc Student, Mining Engineering Department, Istanbul Technical University, Istanbul, Turkey. Email: gumusar@itu.edu.tr

ABSTRACT

Excavation of vertical and/or inclined shafts in the underground structures requiring careful design and planning. Raise Boring Machines (RBMs) are commonly used for excavation of shafts for different purposes such as ventilation, orepass, and human-material transportation. Proper selection and accurate performance prediction of RBMs are two main parameters affecting the cost estimation and planning/scheduling. Indentation test is one of the most preferred methods that can be used to predict advance rate of RBMs. This study aims at suggestion of new prediction model for instantaneous penetration rate of RBMs based on indentation tests. Different rock (core) samples (with different geological origins) are obtained from the raise boring application projects in Turkey; then, the indentation tests are carried out on them by using a real-life insert (button), which is used in reamerhead cutters investigated in this study. Finally, the statistical relationships between the field performance and the indentation indices are investigated. The study indicates that the brittleness index (the ratio of maximum applied force to corresponding penetration) can be used to predict instantaneous penetration rate of RBMs used in the vertical raise bored shafts excavating rocks having uniaxial compressive strength lower than 100 MPa.

INTRODUCTION

Predicting performance of RBMs and the skills of the operator are two important factors causing remarkable uncertainty on the construction of shafts. RBM performance depends on a number of factors. Geological/geotechnical parameter is one of these factors that directly affects success of shaft excavation operation. RBM related mechanical features, operational parameters (available thrust and torque, reamerhead rotational speed) and technical-environmental parameters are other factors affecting the performance of RBMs.

Indentation (punch or stamp) hardness test is one of the laboratory approaches used for predicting penetration rates of Tunnel Boring Machines (TBMs) and RBMs. The indentation test is a nonstandard laboratory experiment originally designed to predict the normal force acting on button and disc cutters used on mechanical miners (Dollinger, Handewith and Breeds, 1998). The main approach is to predict forces, which would act on an actual cutter, by curve fitting of the force-penetration data obtained from indentation tests.

In this study, the operational-performance parameters of the RBMs are recorded/calculated during the field visits of different raise bored shaft projects in Turkey. Then, core samples are obtained from the shaft areas to perform indentation tests (by an insert tip with a diameter of 22.2 mm and width of

11 mm and define some important physical-mechanical properties. Finally, brittleness index obtained from the indentation tests is used as input parameter to suggest new empirical models for predicting unit penetration rate of RBMs for vertical (90°) raise bored shafts.

FIELD AND LABORATORY STUDIES

Different raise boring project sites in mining and construction industries (Balya Lead-Zinc Underground Mine, Yusufeli Dam and HEPP, and Efemcukuru Gold Mine) in Turkey were visited along six years (between 2014–2019). Reaming diameter was 2.44 m in all of the excavated shafts, and the lengths of the shafts varied between 50.6 and 198.9 m. Sandvik (Rhino 1088 DC) RBM was used in all of the investigated fields. Sandvik RBM is a hydraulically driven rig with maximum 4000 kN operating thrust. The machine is capable of operating at a torque of 300 kNm in pilot hole drilling and 160 kNm in reaming operation. In addition, it is capable of operating at a rotational speed of 60 rev/min in pilot hole drilling and 21 rev/min in reaming operation. The detailed information about the visited fields and the RBM are mentioned in Shaterpour-Mamaghani and Copur (2021).

Ten totally different rock samples representing different geological origins and lithological units were collected from the investigated projects. The samples were obtained from the core boxes of the boreholes drilled in the sites being cored mostly very close to the shafts. The measured values of operational parameters from the data acquisition system of the RBM included rotational speed, net pulling force of reaming, and consumed reamerhead torque. In addition, the calculated values of performance parameters included instantaneous penetration rate, unit penetration rate, and field specific energy. All values were recorded in the field for each drill string (rod).

The suggested method by the International Society of Rock Mechanics (ISRM, 2007) is applied to determine the uniaxial compressive strength (UCS) of rock samples. Moreover, the rock samples with the diameter of 54 or 63 mm are used in the indentation tests (the length to diameter ratio is kept as ~1.5; the top and bottom surfaces of the cores are sawn flat). The steel tube with an inner diameter of 110 mm, outer diameter of 126 mm and length of 100 mm are used in the indentation test. The indentation test equipment consists of a stiff press that pushes an indenter fixed to the upper platen of the load cell of the stiff press to the centre of a core sample surface pre-cast with hydrostone in a steel tube, after the data acquisition system is activated. The indenter is penetrated into the sample at a constant rate of 0.0254 mm/s until 5 mm displacement is reached. Data sampling rate is 20 Hz. Finally, the brittleness index given by Yagiz (2009) is calculated as in Equation 1:

$$BI_m = \frac{F_{max}}{p} \tag{1}$$

BI_m (in kN/mm) is estimated from maximum applied force (F_{max}) and corresponding penetration value (p) at this force. The results of field and laboratory studies are summarised in Table 1.

TABLE 1

Results of field measurements for vertical shafts and laboratory studies on the rock samples.

Project	Lithology	F_{thrust} (kN)	p (mm/rev)	IPR (m/h)	UCS (MPa)	BI_m (kN/mm)
Balya (Shaft 3)	Dacite	607	11	2.0	71.8	54.68
Balya (Shaft 3)	Limestone	1108	6	1.4	43.6	75.10
Balya (Shaft 3)	Andesite	1141	9	2.1	114.1	55.19
Balya (Shaft 4)	Dacite	1000	2	0.5	94.6	98.76
Balya (Shaft 4)	Metasedimentary	974	3	0.7	79.2	138.26
Balya (Shaft 4)	Andesite	909	2	0.4	116.6	29.33
Balya (Shaft 4)	Limestone*	880	4	0.9	-	-
Yusufeli (Shaft 2)	Diabase	937	2	0.5	53.3	141.72
Yusufeli (Shaft 2)	Granodiorite	1074	2	0.4	90.4	133.93
Efemcukuru (Shaft 1)	Phyllite	718	11	2.3	80.1	37.73
Efemcukuru (Shaft 2)	Hornfels	1145	3	0.6	83.7	62.54

* No testing could be performed on this rock sample (Limestone), since no rock sample could be obtained. However, reaming performance data is available for this rock.

F_{thrust}: net thrust (pulling force) of reamerhead, p: unit penetration rate, IPR: instantaneous penetration rate, UCS: uniaxial compressive strength, BI_m brittleness index.

RELATIONSHIP BETWEEN IPR AND BIM

The obtained brittleness index (BI_m) from the indentation test can be used to predict instantaneous penetration rate (IPR) of mechanical excavation machines such as TBM and RBM. Dollinger, Handewith and Breeds (1998) obtained strong correlation (R^2 of 89 per cent) between predicted and measured instantaneous penetration rates of 22 raise boring projects. In this study, BI_m values varied between 25 and 150 kN/mm. Moreover, net thrust (pulling force) of reamerhead (F_{thrust}) ranging from 607 to 1145 kN. Correlations between BI_m of the rock samples and F_{thrust} normalised by the unit penetration rate (p), instantaneous penetration rate (IPR), and unit penetration rate are seen in Figure 1, after discarding the outlier data of andesite with 116.6 MPa uniaxial compressive strength value. General and meaningful correlations are observed, although there is some scatter. However, it should be kept in mind that the correlations introduced in this study are limited with the data content as well as the upper and lower boundaries of the data should be considered in the prediction of performance parameters.
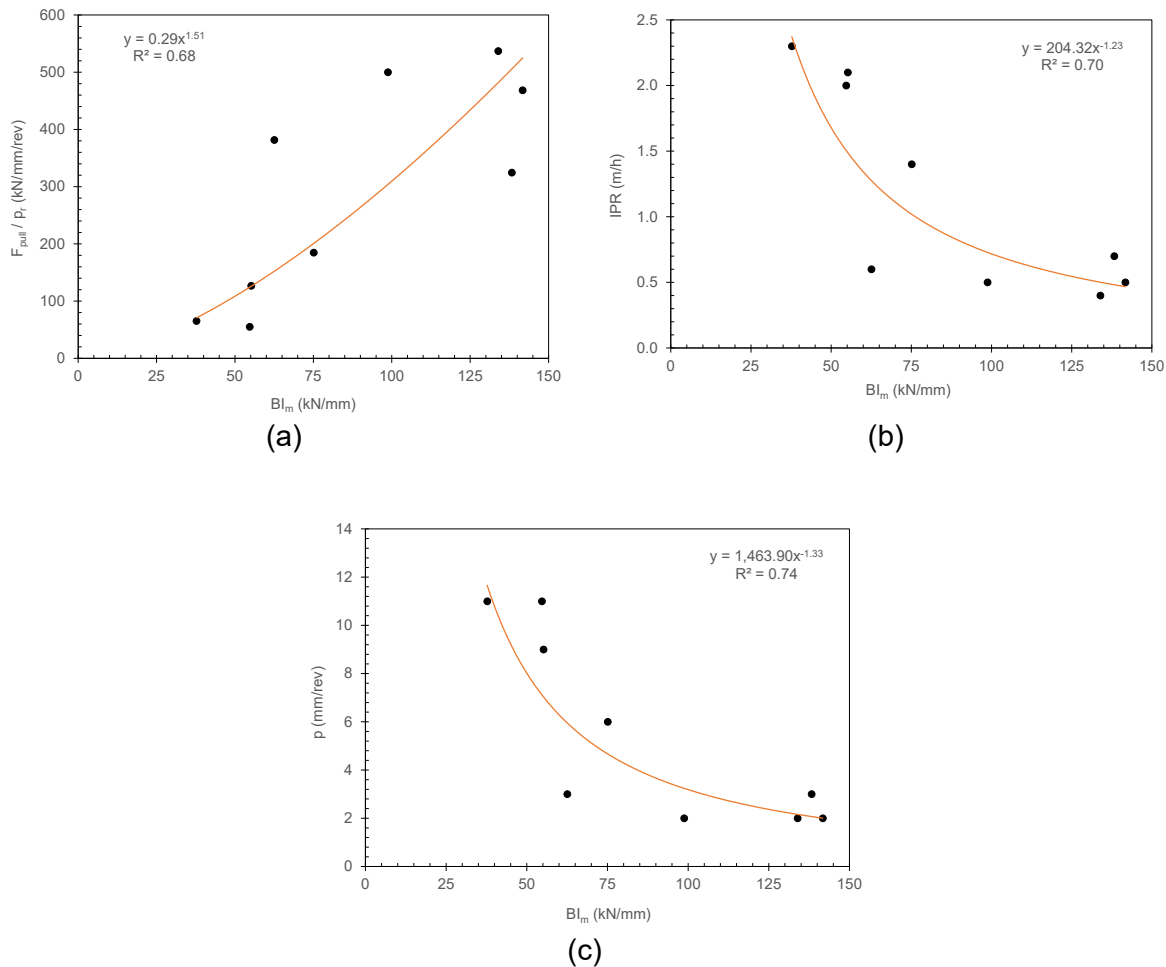
FIG 1 – Relationships between brittleness index (BI_m) and (a) ratio of net thrust (pulling) force to unit penetration rate, (b) instantaneous penetration rate, and (c) unit penetration rate.

CONCLUSIONS

It is difficult to collect long time operational data in raise boring operations, as well as performing indentation test on rock samples for performance prediction purpose. Therefore, there should be a simpler method to estimate the performance parameters of raise boring machines for saving time and budget in the feasibility stage of mining and tunnelling projects. Although the rock samples tested in this study show a wide range of characteristics varying from weak to very hard rocks with different geological origins, the proposed model in this study have some limitations including number of the data, intact and mass parameters of rocks, and field performance data. This study is an attempt to link the brittleness index with the instantaneous penetration rate of raise boring machines excavating vertical shafts. It is shown that the brittleness index can be used to predict instantaneous penetration rate, unit penetration rate, and normalised thrust force of RBMs.

ACKNOWLEDGEMENTS

REFERENCES

Dollinger, G L, Handewith, H J and Breeds, C D, 1998. Use of the punch test for estimating TBM performance, *Tunnelling and Underground Space Technology*, 13(4):403–408.

ISRM, 2007. The complete ISRM suggested methods for rock characterization, testing and monitoring: 1974–2006, in R Ulusay and J A Hudson (eds), *Suggested methods prepared by the ISRM commission on testing methods, compilation arranged by the ISRM Turkish National Group*, Kozan Ofset, Ankara, p 628.

Shaterpour-Mamaghani, A and Copur, H, 2021. Empirical prediction of reaming performance of raise boring machines based on pilot hole drilling performance, raise Inclination and rock properties, *Rock Mechanics and Rock Engineering*, 54:1707–1730.

Yagiz, S, 2009. Assessment of brittleness using rock strength and density with punch penetration test, *Tunnelling and Underground Space Technology*, 24:66–74.

Data management

Underground rock bolt detection

S Saydam[1], B Liu[2], B Li[3], S Saydam[4] and W J Zhang[5]

1. Digital Development Engineer, DSI Underground Group, Newcastle NSW 2290.
   Email: sarp.saydam@dsiunderground.com
2. Postdoc fellow, Minerals and Energy Resources at UNSW Sydney, Sydney NSW 2052.
   Email: boge.liu@unsw.edu.au
3. Senior Lecturer, Minerals and Energy Resources at UNSW Sydney, Sydney NSW 2052.
   Email: binghao.li@unsw.edu.au
4. Professor, Minerals and Energy Resources at UNSW Sydney, Sydney NSW 2052.
   Email: s.saydam@unsw.edu.au
5. Professor, Computer Science and Engineering at UNSW Sydney, Sydney NSW 2052.
   Email: wenjie.jane@gmail.com

INTRODUCTION

Rock bolts are commonly used to reinforce ground in underground mining and civil tunnel environments. Rock bolts serve two main functions: i) they suspend large, loose blocks of ground, and ii) provide a protective pressure arch to restrain the deformation in an excavated void. Automated and precise tracking of rock bolt positions can assist with the operational success of ground support by reducing the amount of labour required in current manual practices. A point cloud is a large list of x, y and z coordinates in three-dimensional space, that when visualised, show a precise 3D representation of a physical environment. Point cloud data can be collected using accurate LiDAR scanners. These scanners can be mounted on a stationary tripod or on a moving vehicle.

A key way point cloud data is used is in the bolt detection project being completed in conjunction with UNSW Sydney, which aims to provide an automated location of underground rock bolts from LiDAR scans. The immediate challenge with identifying rock bolts is that they constitute a very small portion of the data set amounting to approximately 0.01 per cent of some of the collected civil tunnel data. The process of detecting rock bolts from point clouds therefore requires a quick elimination of large background data while still preserving the bolt data. A further challenge is that the geometry of underground environments can often be very complex and non-uniform. To overcome these challenges, a two-step coarse to fine deep learning approach is taken. The first step is a coarse background elimination step aimed at removing as much of the background data as possible. The second step is a finer classification method, which uses deep learning to further segment the bolts from the remaining background. Additionally, a computer vision module is being implemented, which is expected to increase the detection rate by adding another dimension to the training data set.

METHODOLOGY

The bolt detection process involves collecting underground LiDAR scans containing exposed rock bolts, followed by the two-step, coarse to fine approach. This approach has been tested in both civil tunnel and underground hard rock environments.

Data set

The civil tunnel data was collected from a civil tunnelling project site in Sydney, New South Wales, Australia. The data set was obtained using a terrestrial LiDAR scanner, with the resolution of 6.3 mm at 10 m. A total of 84 scans of 2–6 m tunnel sections were captured, comprising of 10–20 bolts per scan.

The hard rock mine data was collected using the same LiDAR scanner at a resolution of 12.5 mm at 10 m of a total of 270 m of underground drives at an underground hard rock mine in NSW, Australia. A sample of this data set is shown in Figure 1.
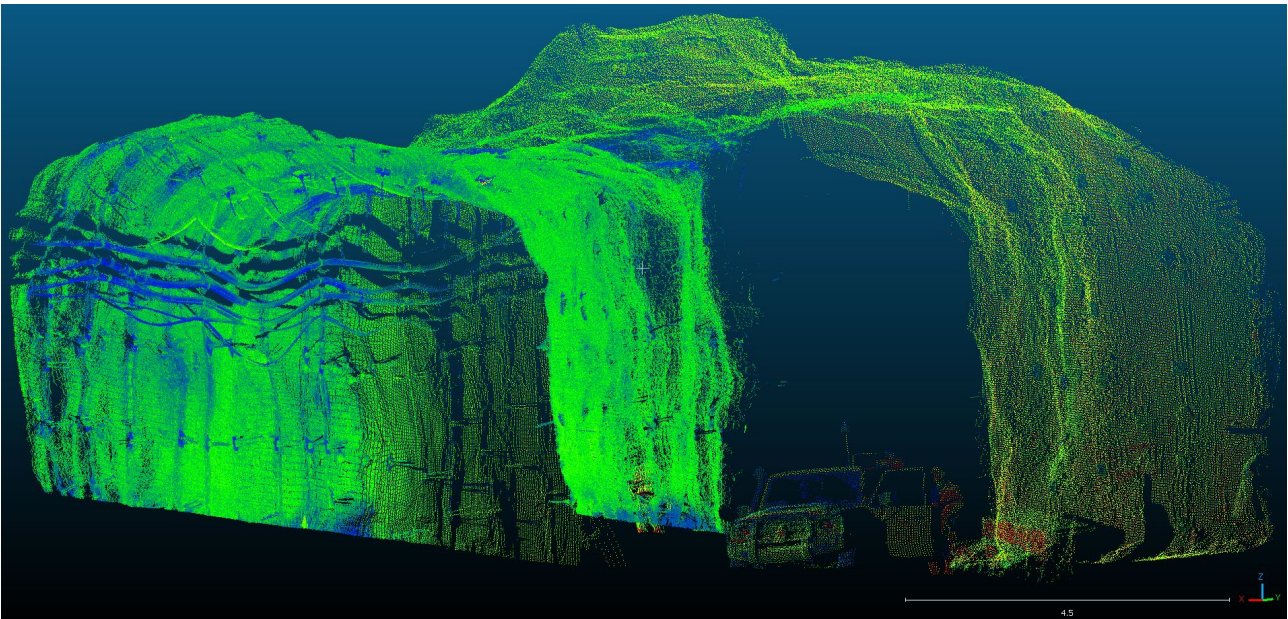
FIG 1 – Hard rock data sample.

Coarse to fine detection

As shown in Figure 2, The bolt detection method begins with a linear discriminant analysis with proportion of variance. This step statistically determines the local structure or geometry information for each point, based on the training data. In essence, it is an initial rough pass-through, aimed to filter out as much of the background data as possible. The results are then pruned to a confidence threshold determined by the previous step. Next, a clustering algorithm is used to discriminate between bolts and a fixed radius is extracted around the centre points of each cluster to nominate candidate bolts. The aim is to conserve as much bolt information as possible whilst simultaneously remove as much of the background data as possible. Notably, at this stage, the bolt candidates still form part of the background, but very few of the bolt candidates are left behind. The target is to produce zero false negatives whilst tolerating some false positives, which aim to be filtered out in the subsequent stage. The bolt candidates then feed into a three-part deep neural network, for further classification which ultimately produces the end detection result.
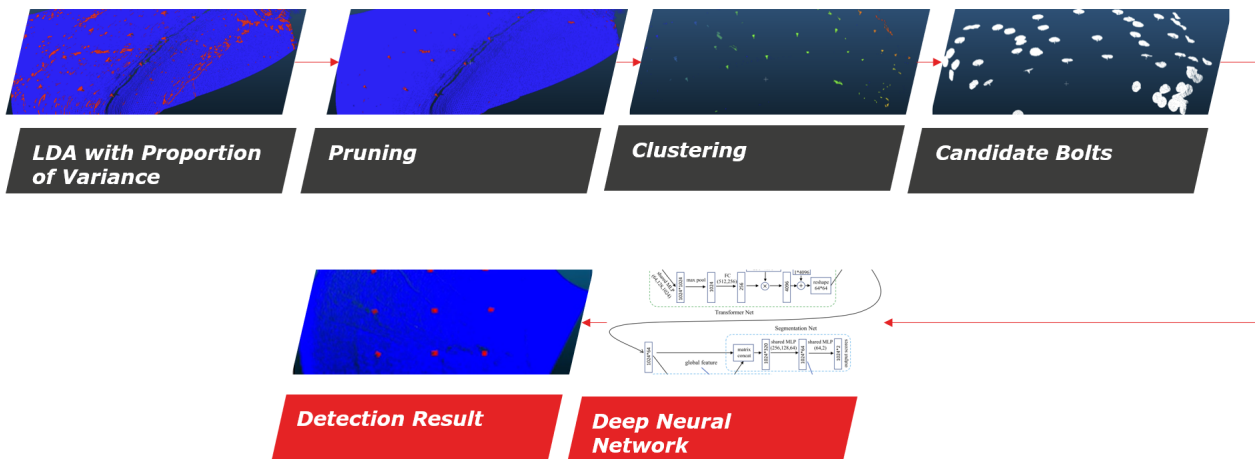
FIG 2 – Coarse to fine, deep learning overview.

Further improvements to the current method are in progress and include the incorporation of an additional 1000+ bolts worth of training data recently acquired from the underground hard rock mine. The supplementary training data is to be added to the 200 bolts that have already been trained. Additionally, a computer vision module is being implemented which aims to increase the reliability of the process even further. The purpose of these developments is to improve the hard rock bolt

detection results and to lead to accurately identifying the differences between single strand cable bolts, twin strand cable bolts, friction bolts and resin bolts.

RESULTS AND DISCUSSION

Thus far, significant breakthroughs have been made with civil tunnel data, producing a 97 per cent bolt classification rate with over 1000 bolts used for training data. Progress has also been made in the underground hard rock mine, obtaining a roughly 70–80 per cent detection rate using only 200 bolts for training, showing potential for comparable results when more data is used for training. The high classification rate purports to the potential for practical applications of the rock bolt detection method in improving ground support information systems.

This method can be foreseeably applied to help automate the rock bolt detection process, enabling for faster bolting audits, quick location of issues with installation of resin bolts through finding the tail end lengths, mapping stresses by identifying the angle of installation and allowing for better informed decisions about bolt spacing. In the long-term, there is further potential for integration into a much larger system of our sensors, communicating with each other in real time. This could ultimately assist in working towards a digital twin platform that can map and visualise data to reliably assess ground conditions and the performance of ground support. The automated rock bolt detection method simultaneously posits the potential to reduce the requirement of people underground, thus increasing safety whilst also improving the utilisation of labour.

Dynamic events and managing large deformations

Automated omission-free geotechnical deformation monitoring – a new method deployable by non-specialists

J Franke[1] and C Gonzalez[2]

1. Freelance mining consultant, Beaconsfield WA 6162. Email: jochen.franke@optusnet.com.au
2. CEO, Caroni Geospatial Pty Ltd, Mt Pleasant WA 6153. Email: carlos.gonzalez@caroni.com.au

INTRODUCTION

One of the regular tasks of geotechnical and mining engineers is the measurement and management of deformation in underground excavations. Although several methods are used to do so, the incumbent methodologies for monitoring deformation and ground support serviceability are limited to the use of visual observations or measurements at discrete points, resulting in a qualitative assessment only.

The introduction of LiDAR technology allows a quantitative assessment across the entire excavation volume and its rock surface, by collecting a full three-dimensional image of the entirety of an excavation such as an underground drive, decline, or a tunnel. Comparisons between epochs of complete 3D data coverage allows for change detection over time that doesn't feature otherwise typical omissions. The implementation of regular scanning has shown to be highly advantageous for mines with swelling or squeezing ground, but also at mines with rapid deformation.

Despite the LiDAR potential, its adoption has been slow. A key reason for that is that working with point clouds is foreign to most geotechnical engineers. Point clouds have long been the realm of surveyors, but to fully adopt their use in geomechanics requires retraining, upskilling, and devotion by the individuals and the company. Sites are already stretched, so often there are insufficient resources to be applied to bringing the new technology into use.

The solution to this hurdle is to partner with subject matter experts to achieve the desired high-quality outcomes without the commitment of time by geotechnical personnel. This paper presents a new solution of fully automated raw LiDAR point cloud data processing that not only enables geotechnical engineers to avoid having to learn unrelated skills by allowing for deformation monitoring without associated training or expertise, but it also provides instant reporting results as well as a sophisticated database with features otherwise not available. All data processing time and effort is completely replaced by an automated process which at the same time opens up the opportunity to monitor many more excavation volumes at a higher frequency than is possible with conventional tools and methodology.

3D POINT CLOUD DATA PREPARATION

The current workflow of converting raw 3D LiDAR point cloud data into meaningful deliverables is cumbersome and time consuming because it involves a number of manual data processing steps that require specialist data processing software. As a rule of thumb, every one hour of LiDAR data collection in an underground void requires up to ten hours of manual data post-processing, which illustrates the hurdle to technology uptake this presents to already stretched geotechnical engineers on-site. The most time-consuming incumbent manual processing steps include:

- Manual registration and manual georeferencing.

- Manual data cleaning.

- Manual comparison of two surveys for deformation analysis.

- Manual creation of specific analysis data such as profiles.

- Manual extraction of support features such as rock bolts.

- Manual comparison and/or analysis of rock bolts.

Data cleaning using manual selection and deletion tools in third party editing software is particularly tedious, repetitive and slow but unavoidable because if left out or completed with insufficient rigour then deformation reporting will be erroneous and unreliable. Figure 1 shows an example of

ventilation objects that needed to be removed from raw scan data. Other such objects include stationary or moving personnel, vehicles, or mobile equipment, pipes, or any other feature that is not part of the actual void surface to be monitored.
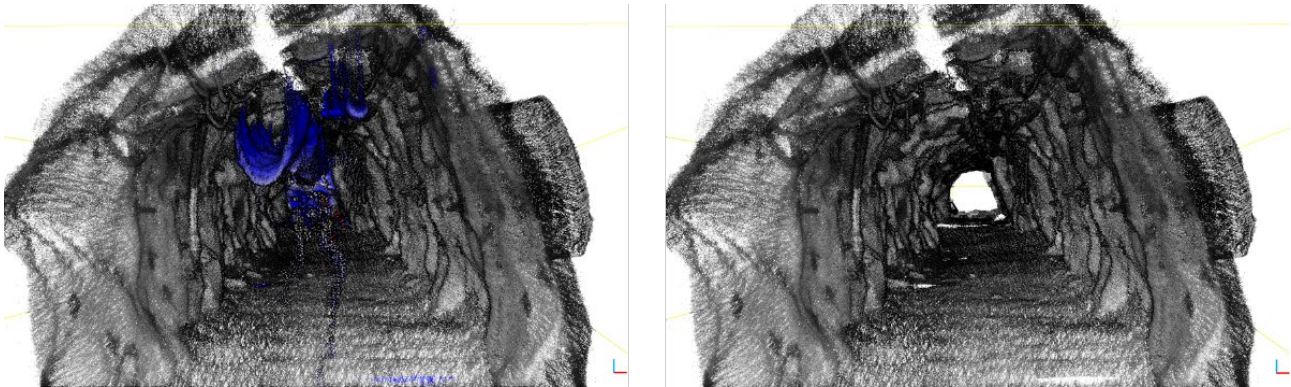
FIG 1 – Original point cloud with superfluous ventilation objects highlighted in blue (left), and cleaned point cloud with superfluous objects removed for further data processing (right).

This manual 3D point cloud data cleaning preparation step can now be completed fully automatically by using a state-of-the-art feature extraction algorithm based on semantic segmentation. This involves the collection of an initial sample database of the voids in question and their obstructing superfluous features and subsequent training of the segmentation model. As subsequent monitoring epochs are added to the database data cleaning becomes more and more robust.

ANALYSIS AND REPORTING

Whilst a useful visual tool, raw 3D LiDAR point clouds are only a means to an end for the purposes of underground void change detection. They come into their own once two epochs are compared to each other such that any deformations can be highlighted and importantly quantified for analysis and subsequent management action to facilitate safe underground access by personnel and machinery. As for data preparation, the extraction of relevant and meaningful information even from a cleaned data set is currently undertaken manually through a series of cumbersome, repetitive and altogether slow series of steps, once again in third party editing software.

Broadly speaking there are two key indicators to analyse any underground void deformation:

1. Changes in void surfaces.
2. Changes in rock bolt distances.

High density LiDAR scan clouds are supremely fit for purpose to analyse void surfaces because unlike other survey methods they cover the entire surface and will never miss any deformations. On the other hand it is important to facilitate easy interpretation of results by not overloading end users with too much information, which is best achieved through intuitive heat map type displays of the differential surface of two survey epochs. These type of heat maps as shown in Figure 2 can now be fully automatically generated, viewed and rotated in full 3D or automatically output as 2D views in reports without the need for manual processing and the associated expertise or investment in time and effort.
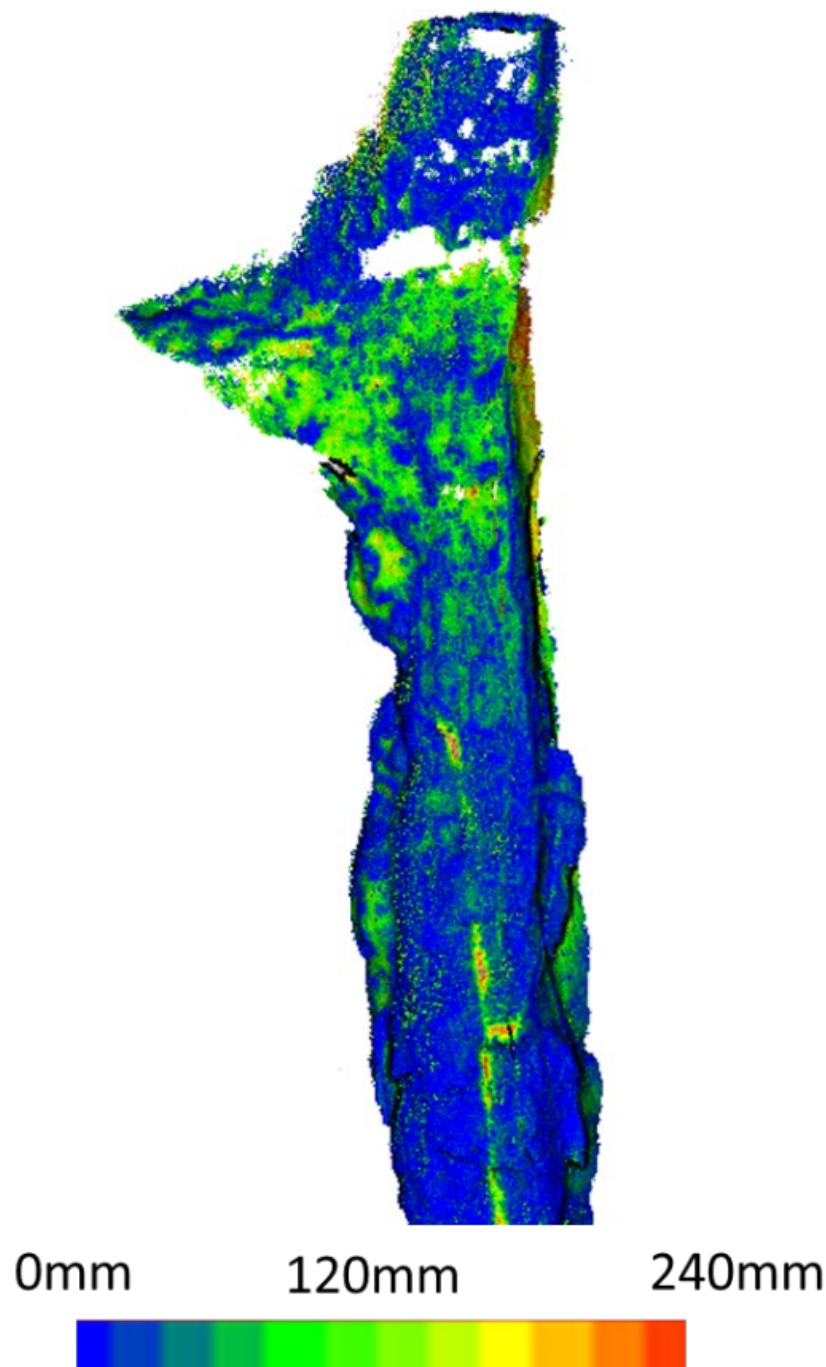
FIG 2 – Top view comparison of an original underground drive scan with a subsequent epoch coloured by deformation distance. Blue areas indicate no or small deformation, green up to red hues indicate larger deformations of up to 240 mm.

What's more, key rock bolt information highly important to geotechnical engineers can now be automatically extracted from raw scan clouds through a Machine Learning (ML) algorithm similar to the one utilised for data cleaning. In this case the algorithm is trained to:

- Detect rock bolts in the scan cloud.

- Extract the centre position of the bolt head and if applicable its direction as embedded in the void surface.

- Calculate, intuitively display and report on distances between bolt heads.

- Display and report on any bolt head position or directional deformations between epochs.

Caving characteristics and support loading of longwalls in massive strata

I Gray[1] and T R Gibbons[2]

1. Managing Director, Sigra Pty Ltd, Acacia Ridge Qld 4110. Email: ian@sigra.com.au
2. Principal Mining Engineer, Sigra Pty Ltd, Acacia Ridge Qld 4110. Email: timg@sigra.com.au

INTRODUCTION

Geotechnically massive strata may lead to a host of problems during longwall mining. These include windblast on initial goaf fall, sudden loadings on powered supports, periodic weightings, fractures that may propagate to surface, and extreme subsidence problems. It is essential to identify these problems prior to mining and to appropriately deal with them.

The problem is essentially that the rock mass does not breakup evenly and when it does so it tends to produce large blocks which may suddenly move. The rock types that produce these problems tend to be massive sandstones, massive siltstones and sometimes igneous sills. The fundamental problem with these is that they do not breakup readily. This is because the ratio of stress they are subject to compared to their strength is low. Thus, the shallower mines with lower stresses are more subject to this problem than deep highly stressed ones with similar strength rock.

GROUND BEHAVIOUR AROUND A LONGWALL

After goaf formation

Figure 1 shows the stresses and modes of failure around a longwall once the goaf has started to form. In this some massive strata has not yet failed and is projecting beyond the powered supports.
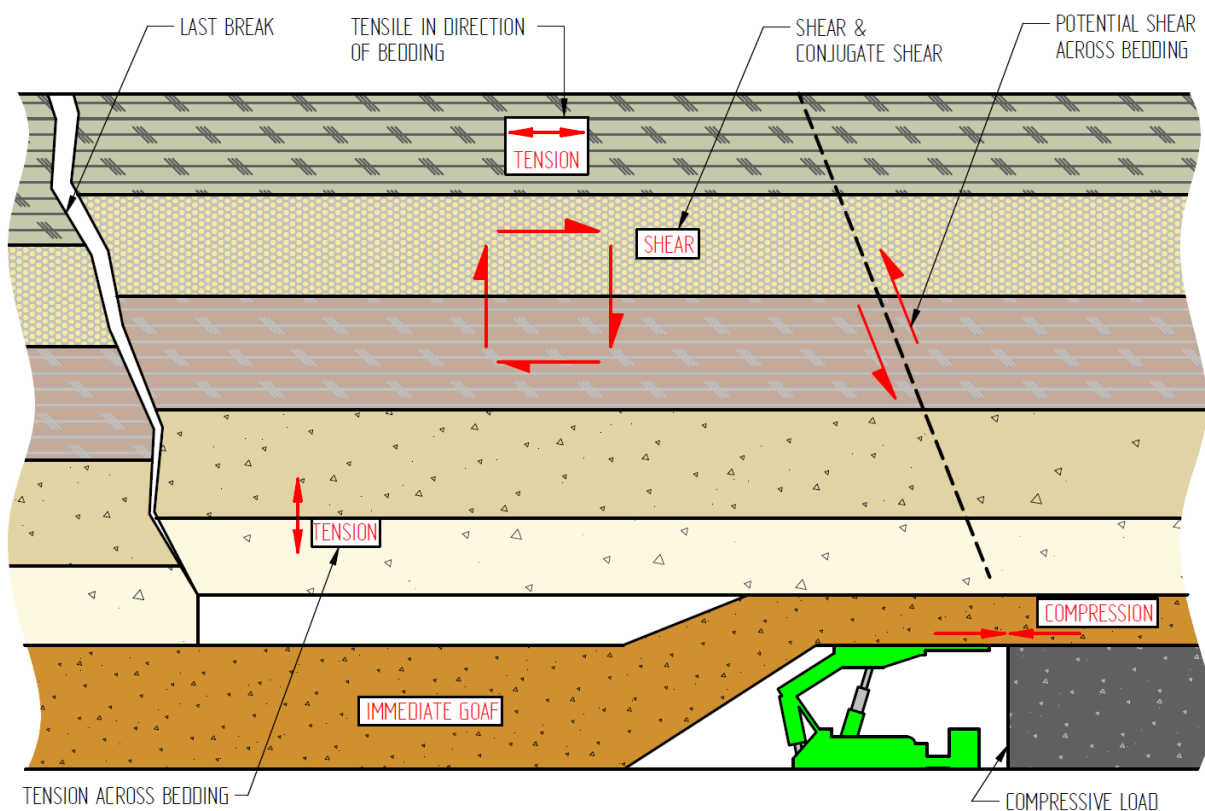
FIG 1 – The stresses in rocks and failure around a longwall face.

In Figure 1 the immediate goaf is weak and has failed. Above it the beds may separate in tension by the action of gravity. If the bedding planes are weak this will occur readily. At the top of the overhanging cantilever the rock is in horizontal tension. The tensile strength of the rock in this

direction is therefore very important as it is likely to control the overhang before failure. The bottom of the cantilever is subject to compressive stress but it is unlikely to fail. Shear failure is also a possibility. Two modes of shear may be considered. The first is shear across bedding while the second is shear on bedding due to the action of the conjugate shear stress. As the bedding planes frequently have far lower a shear strength than that existing across the strata this may be the limitation on the extent of the overhang. Indeed, in weak highly bedded shales, the strata may be seen to deform over the back of the powered supports in a similar manner to a soft backed book that is being bent. Here bedding plane shear dominates.

Initial goaf formation

If we consider the case of an initial goaf formation massive strata may frequently be considered to be of the form of a series of plates that are under compression from lateral stress and gravitational load. With mining the gravitational stress is relieved from below. The massive strata plate is quite likely to have become separated from the layer of strata above by vertical movement. Its failure mode is then likely to be by tensile stress at the top of the plate edge. It may also be by compression at the bottom of the plate edge, though this is less likely unless the pre-existing lateral stress is high. If the plate is massive it is assumed that it does not contain weak bedding planes that will shear.

Once the first goaf fall has taken place the situation changes dramatically and reverts more to the case shown in Figure 1. This is because the stress is relieved in at least one direction. In subsequent longwall panels the stress may have been relieved in both directions. This loss of stress leads to higher tensile stress at the top of cantilevering strata.

INDUCING GOAF FORMATION

How the goaf is induced to form will depend on the rock and in particular the stress that exists within it. If the fortunate situation exists that the minimum stress is vertical it may be possible to hydrofracture the strata prior to mining and induce horizontal fractures which thins the rock plate or cantilever and greatly weakens it. This stress situation may not exist prior to mining and vertical hydrofractures that traverse the face are unlikely to assist goaf formation.

Horizontal fractures are however possible to create once the coal has been removed. This means drilling out and fracturing over the goaf. Another option is to drill into the roof in what will be a tensile stress zone parallel to the face. The boreholes may induce a sufficient stress concentration that tensile failure then occurs or the holes may need to be fractured multiple times to induce failure. Both techniques that require the use of hydrofracturing in this manner are just in time approaches which become difficult to manage in an operational mine.

Drilling and blasting to induce failure is practised in some countries but the risk of inducing a gas explosion generally precludes its operation in Australia.

CONCLUSIONS

The critical factors for goaf formation are therefore the tensile strength of the rock both across and in the direction of bedding and the strength to shear along bedding. These are seldom measured. Proper tensile tests are required for both tensile failure modes. It is quite possible that a sandstone containing mica which lies in the bedding plane has a tensile strength of 0.2 MPa across the bedding and one of 7 MPa in the direction of the bedding. In addition, the cohesive strength term in the Mohr–Coulomb failure criterion may be 0.4 MPa along the bedding and 4 MPa across it. The anisotropic behaviour of the rock is therefore critical to failure. The increasing use geophysical interpretation for geotechnical purposes fails to take account of anisotropy.

The other factor that is a key to initial goaf formation is the state of stress in the rock. This is likely to vary through the rock layers with their stiffness and needs to be measured.

Finally, the use of plate and beam analysis is very useful.

Tight slot blasting for routine fault-slip seismicity control at Mt Charlotte Mine

P Mikula[1], R Carlton[2], M Ferguson[3], R Geranmayeh[4] and R Whiting[5]

1. FAusIMM(CP), Director, Mikula Geotechnics, Kalgoorlie WA 6430.
   Email: pm@MikulaGeotechnics.com
2. Senior Geotechnical Engineer, Bellevue Gold Limited, Kalgoorlie WA 6430.
   Email: rcarlton@bellevuegold.com.au
3. Senior Geotechnical Engineer, Mincor Resources, Kambalda WA 6442.
   Email: m.ferguson@mincor.com.au
4. MAusIMM, Geotechnical Engineer, Northern Star Resources Limited, Kalgoorlie WA 6430.
   Email: rgeranmayeh@nsrltd.com
5. MAusIMM(CP), Director, Rowland Technical Services Pty Ltd, Kalgoorlie WA 6430.
   Email: rwhiting@iinet.net.au

ABSTRACT

The concept of using specially designed slot blasts to mine through stress abutments that intersect faults, while controlling fault-slip seismicity, has come of age at Mt Charlotte Mine. Due to the high and adverse stress field and the presence of major faults, the mine is vulnerable to significant fault-slip seismicity. As mining proceeded, advancing stress abutments around various mined areas encroached on several major subvertical faults. If the sequence formed a diminishing pillar between stope and fault, the removal or failure of that pillar daylighted the fault, and often resulted in significant fault-slip seismicity.

A new strategy called 'Tight Slot Blasting' (TSB) was developed to restrain or dampen this style of fault-slip movement. The TSB has geometric similarities to a conventional cut-off slot used to create stress shadows, but its function is different. Its objective is to trigger and control a sudden shift of the stress state on a fault from an initial stable state, through an unstable transition, to a second stable state.

A TSB firing advances a long tall narrow slot through a stressed abutment between a stope void and a nearby fault, using a rapid blast with a low swell ratio, so that the slot substantially and rapidly fills with blasted rock fragments. During the blast process, the stressed rock is rapidly removed and transformed into the fragmented rock fill in the slot. The strategy deliberately allows a fault-slip episode to manifest at a chosen time and place. The tight-packed broken rock in the slot performs an essential shock-absorbing function by controlling the slip amount and rate on the fault, while at the same time the fill becomes compacted by the movement. This controls the dissipation of fault-slip energy, and greatly reduces the seismic response in time and space. A small closure across the slot occurs, with consequent relaxation and destressing of the adjacent rock mass.

Stress monitoring data shows that slot creation lowers the abutment stress in the nearby rock mass, while the newly placed fragmented rock fill acts as a shock absorber, providing considerable resistance to substantial fault-slip movement that otherwise could deliver a significant seismic event.

First used in 2007, the strategy has been refined to become a routine specialised practice for management of seismically hazardous situations at Mt Charlotte, with 12 successful TSBs conducted to date. Despite mining through multiple high stress abutments, seismic reactions have not exceeded ML 2.1 with any TSB firing, all remaining below the site tolerable maximum of ML 2.3. This paper presents an overview of the strategy, and five case examples of the strategy in critical stressed areas in July 2016, Sept 2017, Dec 2017 and two in Oct 2020. The strategy has successfully managed the seismicity and is expected to remain an essential part of the seismic management plan at Mt Charlotte Mine.

INTRODUCTION

Mt Charlotte Gold Mine is one of many operating in a seismically hazardous environment, due to the adverse interactions of the stress field, the major geological faults and structures, and the mining voids. In the period 1970 to 1998 the mine experienced 17 seismic events over ML 2.5. A ML 3.5

event in 1998 triggered a shift in mining strategies (as described by Mikula and Lee, 2002) to proactively manage large, damaging seismic events and ensure safe operation. The strategies included waste rock backfilling to avoid forming any large open stope voids, and avoiding the creation of diminishing pillars.

One important strategy was to design mining sequences retreating away from subvertical faults rather than towards them. However, that was impossible in geometrical situations with multiple faults, as retreating away from one fault would mean advancing towards another. To overcome that problem, a new mining strategy was crafted, namely the Tight Slot Blast (TSB). The TSB strategy is to rapidly create a tightly packed zone of broken rock cutting through a final stress abutment between stope void and fault. It was designed to rapidly destress the rock mass, together with controlled dampened shearing on faults.

There have been 12 TSBs conducted at Mt Charlotte, all successful. Five TSB case examples in critical high stress areas adjacent to a major mine-scale structure called Reward Fault are presented. These examples reflect the issues encountered, the operational improvements, and the increasing understanding of the function of this strategy.

GEOMECHANICAL ENVIRONMENT

The TSB case history examples are on 15 Level at 480 m, 16 Level at 505 m and 17 Level at 558 m depth. Event Local Magnitude (ML) is estimated from the IMS seismic monitoring system, and is considered approximately equal to Richter Magnitude. Orientations are relative to the Mine Grid, and Mine North is 38° west of True North. All depths are stated as Mine Depths, which increase downwards and are 32 m greater than true depths.

Mt Charlotte geomechanical data can be found in Mikula and Lee (2000). In brief, the Mt Charlotte orebody contains two major reverse fault sets, which divide the rock mass and the ore into large blocks. The older set dips moderately to the west (Neptune, Beta, Flanagan and Shea Faults). The other subvertical set – the TSB target set – dips steeply to the north-west (Charlotte, Reward and Maritana Faults). The infill of the fault sets varies, but generally comprises thick clayey gouge where weathered near surface, ranging to very thin non-clayey gouge at depth. Continuous structures subparallel to the main faults are common.

The most adverse structures for significant seismicity and for overbreak of large underground openings are those that dip moderately to the west. Typical dip/dip direction orientations of the faults in the case studies are: Reward Fault 80°/311°, Flanagan Fault 50°/288°, Beta Fault 45°/262°.

The Mt Charlotte deposits are hosting in the Golden Mile Dolerite rock mass which is stiff and strong. Laboratory test averages on 50 mm diameter specimens are Elastic Modulus 65 GPa and Unconfined Compressive Strength 175 MPa. Gold is associated with quartz veins through the dolerite and wide alteration halos around the veins. The rock mass comprises well-interlocked blocks with Rock Quality Designation close to 100 per cent. Joints are rough/irregular, undulating and may have thin chlorite infill. Typically, two plus random joint orientation sets are developed in any area.

Pre-mining stresses have been measured on numerous levels (Lee, Pascoe and Mikula, 2001). At the 16 Level the principal stress component magnitudes and orientations are considered to be 45 MPa North–South, 28 MPa East–West, and 14 MPa subvertical.

The stress field is adversely oriented with respect to both sets of the major faults, such that in some positions near to excavations the faults are loaded close to their in situ shear strength. This finding was based on results of several sets of HI stress overcoring measurements, made in the vicinity of faults during development while still remote from stoping. Resolution of measured stress components into the plane of structures indicated high shear stresses on the faults. It was apparent that small reductions in normal stress or increases in shear stress could potentially initiate seismic fault-slip shearing (Mikula and Lee, 2002).

A mine wide seismic system was initially installed in 1994, and has been updated over the years. The mine's seismic record since 1994 includes 85 events exceeding ML 2.0. The mean S:P Energy Ratio is high at 12 which indicates dominant (but not exclusive) fault-slip mechanisms for events.

THE TSB CONCEPT

Numerous legacy void configurations comprising of stressed pillar abutments left behind against subvertical faults have been formed over the 55-year life of the mine. The difficulty is that in an environment comprising multiple slip-vulnerable faults, it is not possible to retreat away from all of them and at the same time not form a diminishing or shrinking pillar (ie a stressed pillar formed between two stopes, or between a stope and a fault when a stope advances towards a fault). When the last section of a major pillar adjacent to a stressed fault is mined, removing the restraining abutment, the stresses may drive significant seismic slip on the fault. Certain Mt Charlotte faults are critically oriented to the stress field, and will shear if physical restraint is removed. Numerous fault-slip events larger than ML 2 occurred historically at the mine for this reason.

To solve that conundrum, a new strategy was devised to control the slip dynamics by triggering that seismic slip, and providing a shock absorbing restraint to dampen the intensity of the slip. That shock absorber was in the form of a large mass of broken rock, and was the basis for what became known as the TSB strategy.

This strategy was built on the understanding of seismicity gained at Mt Charlotte over many years (Mikula and Lee, 2002) and modelling work assisted by AMC Consultants (Mikula *et al,* 2005; Kempin *et al,* 2007).

The TSB is an active seismic management strategy. A TSB firing advances through a stressed abutment between a stope void and a nearby fault. It is designed to deliberately allow a potentially significant fault-slip episode to manifest, at a chosen time and place, but to substantially limit its magnitude to within an acceptable range.

The TSB creates a slot in such a way that the slot void is mostly filled with broken rock during the blast itself (Figure 1). The sudden removal of the pillar abutment allows the previously strained rock mass to attempt to initiate a seismic fault-slip movement. However that movement is rapidly terminated because the rock-filled void is the new restraining device, replacing the abutment pillar.
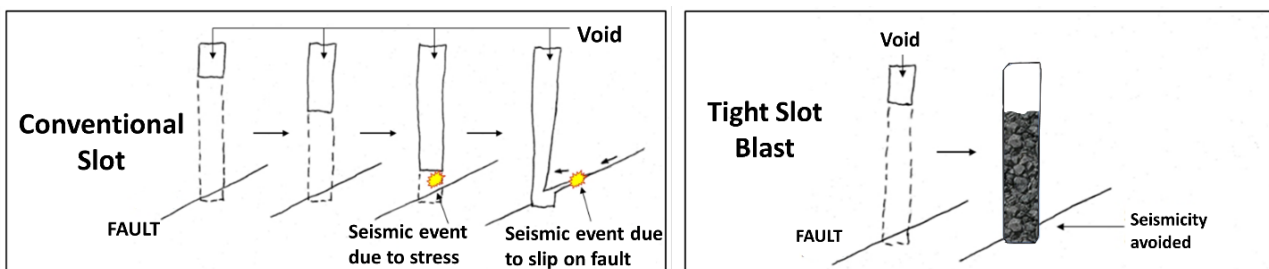
FIG 1 – The TSB blast concept in comparison to a conventional slot in high stress field. The TSB strategy avoids two forms of enhanced seismic reaction.

Differences with cut-off slots: The TSB has geometric similarities to a conventional cut-off slot used to create stress shadows, but its function is different. Its objective is to trigger and control a sudden shift of the stress state on a fault from an initial stable state, through an unstable transition, to a second stable state. The TSB does result in destressing in parts of the adjacent rock mass (and permits later activities to operate in a reduced stress environment), but that is not the primary goal of the strategy.

Differences with preconditioning: The TSB technique is different from preconditioning or destressing as it does not weaken a fault or a rock mass zone. Those techniques are conducted in confined conditions, and intended to weaken a fault or rock mass zone so that stress will be gradually dissipated and seismic risk reduced over time as mining advances. Mikula, Lee and Guilfoyle (1995) describe preconditioning trials at Mt Charlotte. Key differences of TSB from preconditioning are:

- The TSB is a conventional high-speed blast, designed to fragment the rock mass into pieces that become packed tightly into the newly formed blast slot void.

- The TSB slot geometry is designed to mine through a final pillar abutment to a fault and intersect the fault. This geometry permits significant shear slip to occur on the fault at the time of the blast. The geometric change, not the blast, induces the fault slip.

- The tight-packed broken rock fragments in the slot provide the essential shock-absorbing function that controls the slip amount and rate on the fault, while at the same time the fill becomes compacted by the movement. This controls the dissipation of fault-slip energy, and greatly reduces the seismic response in time and space. A small closure across the slot occurs, with consequent relaxation and destressing of the adjacent rock mass. The TSB does not need to fully destress the rock mass, as even small amounts of stress reduction are beneficial.

Differences with SLC blasting: The TSB blast itself differs from the semi-confined blasting conditions of Sub Level Caving (SLC) mining, because the TSB requires more void:

- The tight slots are narrow, the void available at the face by crush firing is less than SLC, and progressively less void is available to each successive ring as it is consumed while the TSB retreats.

- The TSB drive becomes occupied by uncompacted material falling under gravity during the initial period of the blast before rapid firing begins. This consumes some of the void at a greater rate than for the rapid-firing rings.

- The tonnages are much greater than single ring SLC, so proportionately more space is required to satisfy the void needs.

Key engineering requirements: Precise blast designs and accurate implementation is vital to achieve the required rapid destressing:

- Tight firing: The void ratio for the blast was about 18 per cent in early TSB work but that was found to be too small, and it was increased to 26 to 30 per cent in later applications. The void ratio is low so that the void becomes substantially packed with broken rock. This obstructs the free movement of the surrounding rock mass – and the fault – more and more as the broken rock fill becomes more and more compressed. It brings the fault slip movement to a halt without a dynamic shock. The broken rock does not need to fill 100 per cent of the void in order to function as a shock absorber.

- Fragmentation: The blast design must ensure small sizing of the rock fragments, such as 1 m maximum dimension of any particle.

- Rapid firing: Electronic detonation must be used to mine the slot rapidly, in about 1 or 2 seconds. This is necessary to ensure that the slot void is filled with broken rock faster than the surrounding rock mass can move substantially towards a new equilibrium. The quicker the slot is fired, the sooner the surrounding rock mass has to exert work on the blasted product as it mobilises. The firing duration is a balance between slow enough to allow time for blast movement of rock, yet fast enough to reduce the likelihood of a large seismic event occurring before the blast is completed. Rapid firing also improves detonation and reduces confinement effects such as dead-pressing.

Historically, in those instances when significant seismicity occurred with blasts at Mt Charlotte, the seismicity was observed to initiate usually 1 to 3 seconds after commencement of the blast, while in only three instances the delay was very short at about 0.1 second. This suggests the slot blast must be completed quickly. This is perhaps the ultimate in 'just-in-time' rock fill placement into the slot.

Limitation: If multiple intersecting faults are present, the TSB strategy may not significantly reduce seismicity on all the faults. The strategy relies on the ability to rapidly treat a substantial final diminishing pillar between stope and fault. Before the TSB blast, the pillar to the fault must be large enough to be stable under stress and prevent any fault-slip. This implies that:

- The TSB slot advance direction should be perpendicular to or at a substantial angle to the fault strike direction.

- The TSB blast volume must be able to break fully through to the fault.

The angle between the slot advance direction and the strike of the fault is critical. As the angle reduces (ie slot becomes subparallel to the fault strike), the diminishing pillar is less stable, and the TSB strategy loses effectiveness. This was the case for the 17 Level TSB case histories. While Reward fault was successfully destressed on that level, the slots were subparallel to Beta and

Flanagan faults strike. It was correctly hypothesised at the time that the Beta and Flanagan faults would be less effectively managed by the TSB strategy, and this opinion was proved correct.

TSB PERFORMANCE INDICATORS

The following performance indicators have been developed to measure the success of a Mt Charlotte TSB firing:

Indicator 1: Surface vibration from blasting and associated seismicity less than 10 mm/s. As Mt Charlotte is located adjacent to the city of Kalgoorlie-Boulder, there is a requirement for low surface vibrations resulting from mining activities. The target 10 mm/s was set externally for blasting, not for seismicity, but was adopted for TSB.

Indicator 2: Largest seismic event following within 30 days of the TSB firing not exceeding ML 2.3. This limit was set in 2006 for blasts in relation to acceptable surface vibration for mining in the ROB5 stope block at 777 m BD. While acknowledging that seismic event vibrations are less predictable than blast vibrations, the ML 2.3 figure was adopted as the target limiting magnitude.

Indicator 3: TSB slot fragmented rock fill can be mobilised by bogging but with effort. The rock in the slot after the TSB firing is adequately broken so that it can be mobilised, meaning that the packed broken rock is offering resistance to movement.

Indicator 4: TSB volume adequately fragmented. The blast design results in adequate fragmentation throughout the blast volume, without forming any bridges of 'frozen' rock.

Indicator 5: Substantially reduced seismicity during further stoping in the stress shadow of the TSB zone. Subsequent mining in the volume of influence of the TSB must not have much attendant seismicity, defined by an event rate less than two per day and all events less than ML 0.0. This is considered as confirmation that sufficient destressing was achieved.

A peculiar aspect is that good TSB outcomes may be attributed to factors other than the TSB. The temptation is to suggest that if the performance indicators are met, the TSB was not needed. It is not possible to recreate the mining without the TSB to see what would have happened in those circumstances. However historical experience at Mt Charlotte over previous years without TSB gives adequate realistic guidance as to likely adverse outcomes.

TSB MINING HISTORY

The history of TSB at Mt Charlotte is listed in Table 1, including a summary of the observed stress changes and seismic response experienced.

The historical mining method until 1998 was top down open stoping with subsequent introduced loose waste rock backfill. An open stope was first mined, leaving barrier rib and sill pillars to adjacent previously mined and filled stopes. Then those pillars were mass fired, allowing waste rock fill from those previous stopes to fill the new void. Replacement rock fill was placed via a surface location.

A long-section view of the major stoping blocks is shown in Figure 2. The original COB orebody was stoped out from 1971 to 1992, but large blocks of low-grade ore were left between the COB stopes and Reward fault, these being uneconomic to recover at the time, as well as presenting higher seismic hazard (Mikula and Lee, 2000).

Meanwhile, from 1992 to 1995, the separate large ROB5 orebody was substantially mined as a single open stope, except for a remnant left below the floor of the original stope. This remnant stope was initially considered too hazardous to recover, having defeated the first two mining attempts in 1995 and 1997. However, analysis of the experience with that stope led to the formulation in 2003 of the TSB strategy, which was first applied to the ROB5 in 2007. The strategy was successful (with largest event ML 2.2 compared to the Performance Indicator target of under ML 2.3) even though at the time the procedure was novel and untested (Kempin *et al*, 2007).

<div align="center">

TABLE 1

Summary of TSB applications and outcomes 2007 to 2020. TSB slot length is about 30 per cent greater than actual standoff from the fault since the slots were not oriented perpendicular to the fault.

</div>

TSB	Level	Stope	Date fired	TSB slot length (m)	Stress change measurements with TSB blast	Largest two seismic events within 30 days after firing
2515	25	ROB5_2	12 Jan 2007	20	15 MPa fall	ML 2.2 and 0.7
2515	25	ROB5_2	28 Mar 2007	16	15 MPa fall; 14 MPa rise	ML 1.8 and 0.7
2515	25	ROB5_2	9 Nov 2007	20	No data	ML 2.2 and 0.1
1467	14	COB_S4	17 Apr 2015	20	7 MPa fall	ML -0.2 and -0.5
1565	15	COB_S4_2	1 Jul 2016	27	2 MPa fall; 1 MPa rise	ML 2.1 and 0.2
1671#1	16	COB_S4_3	29 Sept 2017	15	1 MPa fall	ML 0.6 and 0.3
1671#2	16	COB_S4_3	9 Dec 2017	19	1 MPa fall	ML 0.7 and 0.1
1650#2A	16	COB_S4	25 Sept 2018	15	4 MPa fall	ML -0.1 and -0.1
1650#2B	16	COB_S4	19 Oct 2018	12	1 MPa fall	ML 2.0 and 0.8
1650TSC	16	COB_S4	7 Nov 2018	17	2 MPa fall; 1 MPa rise	ML 2.0 and 1.2
1728#1	17	COB_S4	2 Oct 2020	15	1 MPa fall	ML 1.9 and 0.5
1728#2	17	COB_S4	11 Oct 2020	21	5 MPa fall	ML 0.5 and 0.3
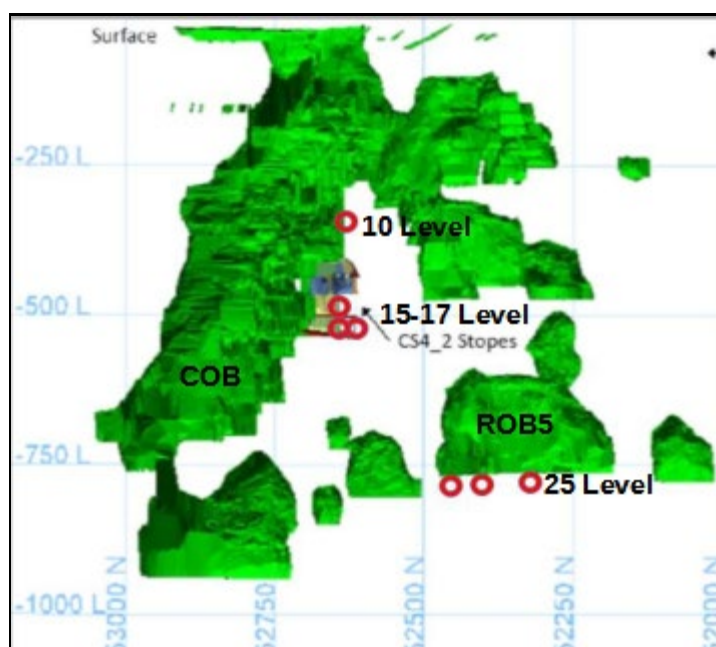
FIG 2 – Long-section looking east showing the major stope blocks and the locations of the TSB firings.

Following the ROB5 success, the TSB was considered to be a possible means of destressing the COB remnant abutment blocks near Reward Fault. Accordingly, in order to test the implementation, trial TSB work was conducted on 10 Level in an area that was not highly seismic.

The 14 Level had indicators of enhanced seismic hazard related to Reward Fault, including large events (ML 2.3 and 2.6) during previous mining. Detailed studies including numerical modelling (Mining One Pty Ltd, 2013) were conducted to guide the selection of mining method and sequence of the COB S4 mining block from the 14 to 17 Levels. The numerical modelling, using Map3D elastic simulation software and Excess Shear Stress analysis, used the same input parameters as had been calibrated to the ROB5 area during similar analysis in 2007. The overall sequence selected was to mine the abutment pillar, progressing southwards and downwards using the TSB strategy. The modelling suggested that the largest events could be as listed in Table 2. But the forecasts were quite inaccurate since the models could not simulate the shock-absorbing function of the TSB.

TABLE 2

Largest seismic event forecasts for faults from numerical analysis, and actual outcomes within 30 days after TSB firings within 20 m of the respective fault, or for the stress abutments, events more than 20 m from a fault.

	TSB 1565	**TSB 1671#1 and 1671#2**	**TSB 1680**
Reward Fault	Forecast ML 0.4 Actual ML -0.7	Forecast ML 1.4 Actual ML 0.7	Forecast ML 0.5 Actual ML 2.0
Flanagan Fault	Forecast ML 0.0 Actual ML -1.2	Forecast ML -0.5 Actual ML 0.2	No forecast made Actual: nil
Beta Fault	Forecast ML 0.2 Actual ML -1.2	Not forecast to be seismic Actual ML 0.3	Forecast ML 0.7 Actual ML 0.8
Stress abutment	No forecast made Actual ML 2.1	No forecast made Actual ML -0.7	No forecast made Actual ML -0.6
Angle TSB slot to fault	Reward 55°	Reward 45°	Reward 50° Flanagan 20° Beta 0°

CASE HISTORY – 15 LEVEL TSB

Design: On 15 Level a zone between the existing COB stope and the Reward Fault was to be mined (Figure 3). The design comprised first a stepped advance ring-by-ring up to a standoff distance of 20 m from Reward fault, and then TSB firing for the remaining section. The TSB firing length was 27 m in order to meet the 20 m standoff as the TSB drive was not perpendicular to the fault. The TSB had maximum width 15 m, and height 32 m (solid interval to overlying level).

Firing: The 15 Level TSB blast design pattern is shown in Figure 4. The design comprised 21 rings of 2 to 6 holes per ring. The drill pattern had two large non-charged reamer holes in every second row to locally improve fragmentation. This was considered to be successful, and large reamers are regarded as essential elements of the blast design. Blast design elements for this and other TSBs are shown in Table 3.

A problem with slumping of emulsion blast product occurred during charging of the TSB, likely due to wet conditions in some of the blastholes. However the blast was fired as scheduled and performed well. Guidance for future TSB blasts is to ensure explosives potency in wet conditions.

Fragmentation outcome: Two zones of bridged rock remained in the 15 Level TSB void after firing. Several small drilling campaigns were undertaken to remove a 12 m high bridge successfully. A second upper bridge was found in an area that had had explosive charging issues (slumping of emulsion in the holes). Probe holes were drilled into the bridge and encountered broken ground, showing that the firing had fractured and displaced the rock, but that the broken rock was still partly interlocked and self-supporting assisted by closure of the sides of the void.
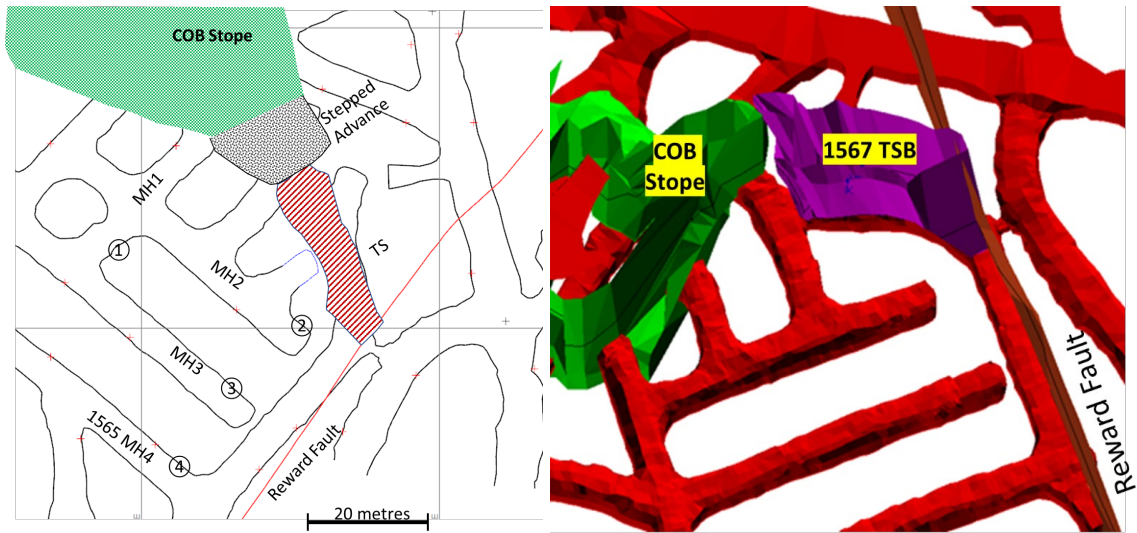
FIG 3 – (left) 15 Level plan showing COB stope void, stepped advance section up to 20 m of Reward Fault, and TSB section to advance the remaining distance through the abutment pillar to the Reward Fault. The local east–west stress component becomes concentrated in the gap between stope and fault, with orientation becoming more acute to the fault in the TSB vicinity. The numbered circles show the position of stress monitoring cells 1 to 4. (right) Perspective view of a 20 m-thick slice of 15 Level COB stope stepped advance, TSB and Reward fault. The view direction is towards NE and down, parallel to Reward Fault.
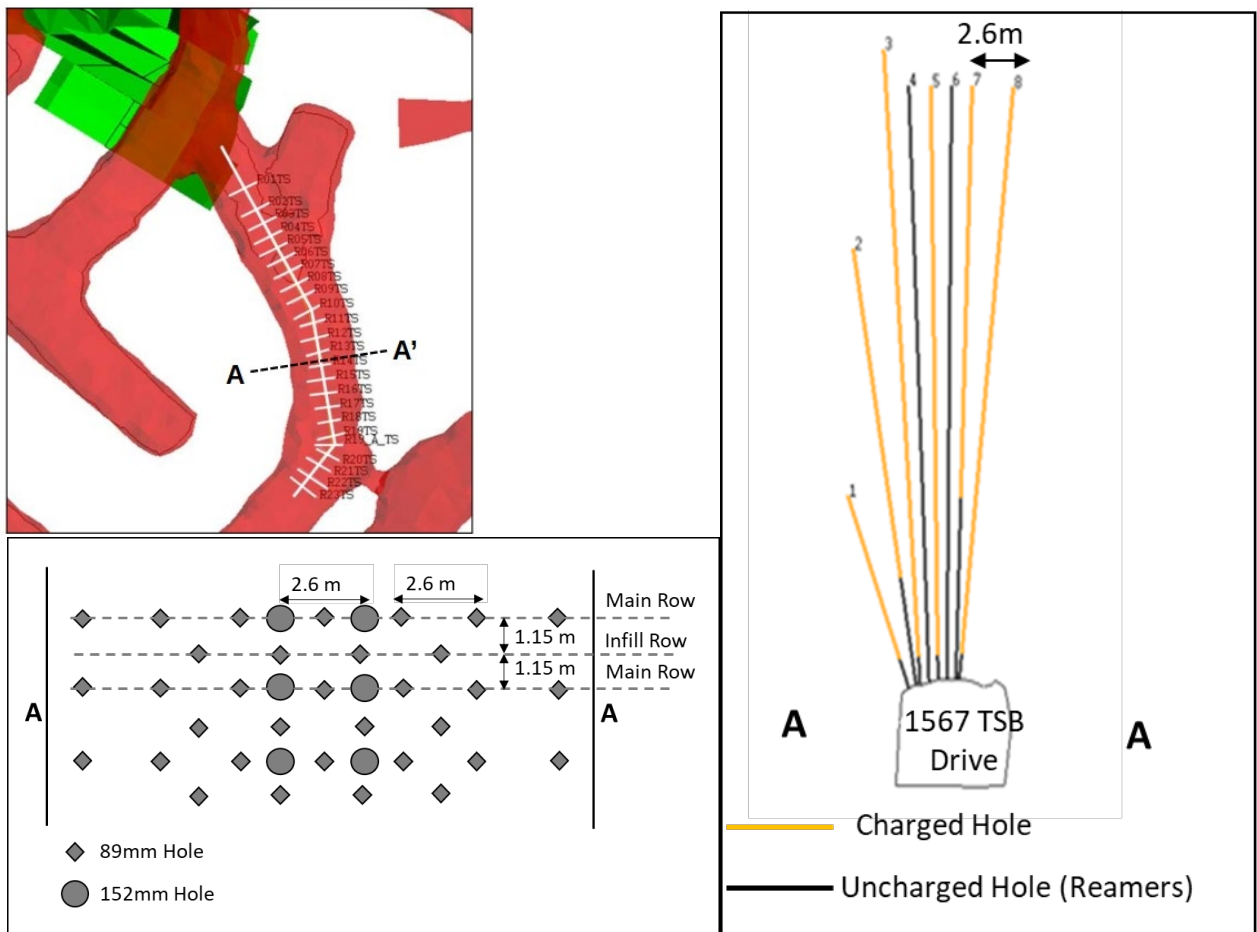
FIG 4 – (top left) Location of the rings within the 15 Level TSB. (lower left) Plan view sketch of a six row section of the 15 Level TSB blasthole design detail. Every second row has two non-charged reamers. Holes are shown as toe positions (maximum spacings). (right) Cross-section looking North showing 15 Level TSB blasthole design.

TABLE 3

Drill and Blast design parameters for TSB case histories.

Design element	15 Level	16 Level #1	16 Level #2	17 Level #1	17 Level #2
Fired volume	5650 m³	3240 m³	3930 m³	1280 m³	1940 m³
Material broken (tonnes)	16 600	13 990	12 000	3800	5700
Powder factor (kg/t)	0.98	0.84	1.08	1.33	1.24
Explosive type	Emulsion Subtek Velcro, Anfo Amex 500	Anfo Amex 500	Anfo Amex 500	Anfo Amex 500	Emulsion Subtek Velcro
Total explosive charge	16 200 kg	11 800 kg	12 300 kg	4900 kg	7100 kg
Total drill distance	3577 m	3052 m	2973 m	803 m	1019 m
Maximum hole length	34 m	34 m	34 m	24 m	27 m
Number of charged holes (89 mm dia)	109	119	119	44	54
Number of reamers (152 mm dia)	20	8	10	0	0
Rise diameter	N/A	1.1 m	1.1 m	1.1 m	1.1 m
Rise length	N/A	23 m	23 m	17 m	17 m
Average swell factor	18%	28%	26%	30%	28%
Number of explosive primers and detonators	280	269	260	88	127
Duration of TSB portion of blast	996 ms	1710 ms	1545 ms	920 ms	1180 ms
Design burden	1.15 m	2.3 m	2.3 m	2 m	2 m
Design maximum toe spacing	2.6 m	2.5 m	2.5 m	2.5 m	2.5 m

The interpretation of these observations was that the 18 per cent average swell factor for this TSB allowed only about 20 m vertical height of rock mass to be fully mobilised during the blast, while about 12 m of rock mass was fractured but still interlocked. The 18 per cent factor was therefore too low and a 30 per cent factor was calculated as more suitable for full mobilisation of the broken rock mass.

Blast vibration outcome: A number of surface vibration monitors are located around the mine, and these indicated that the blast vibration peak (resultant of all channels) on surface was 6 mm/s. However a ML 2.1 seismic event occurred 2.3 sec after the start of the TSB firing with peak vibration 12.5 mm/s (Figure 5).

Seismicity and damage outcome: Seismic activity after the TSB was elevated for about seven days. Events on Reward Fault were few and small, the largest being ML -0.7 immediately after the firing, and ML -1.1 one day later (Figure 6). The interpretation was that the TSB firing successfully reduced the hazard of fault-slip on this fault.

However the largest event after the TSB was ML 2.1 located 26 m north of and below the TSB, at the south edge of COB where stress would have increased after the TSB. It was the largest seismic event in the mine since 2008. It was distant from any major faults, and source parameters indicated a stress-driven crush failure mode. This indicated that the TSB caused significant shift in the stress field around the south end of the COB in this area.

The observed damage was located to only two areas, both of which were no-access areas to personnel. The first area experienced a 100 t shakedown of the backs in the 1507 old disused drive. The ground support in the drive was known to be corroded and the fall may have been due to the TSB blast itself rather than the seismicity. The second damage area was in another unused drive in the abutment below the TSB (Figure 7). The ML 2.1 event located about 10 m from this area and is considered to be the cause.
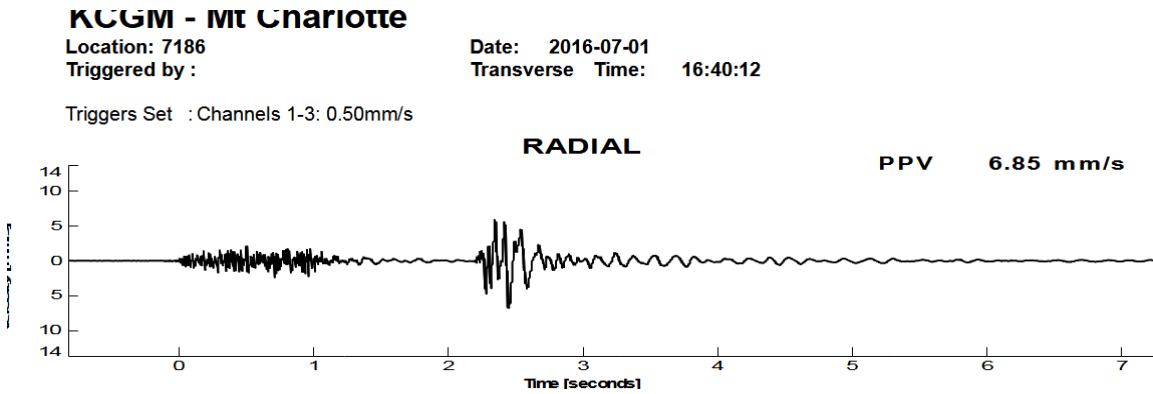
FIG 5 – An example of one channel of the surface triaxial vibration records showing the 15 Level TSB blast commencing at time 0 sec and the significant seismic event following at 2.3 sec.
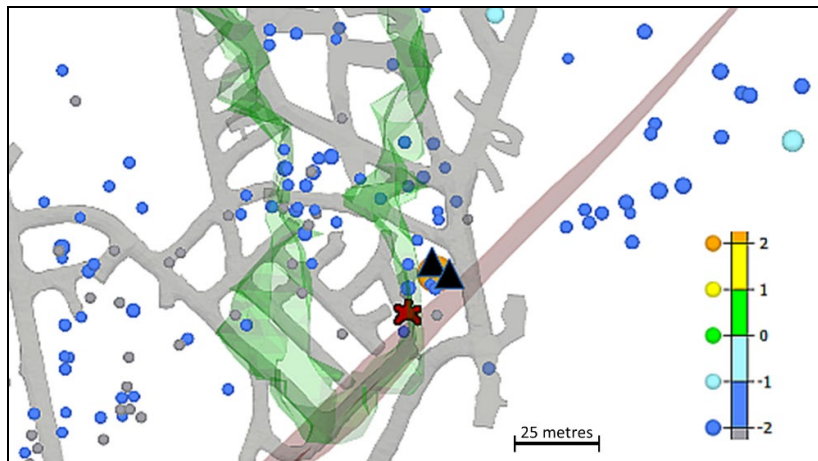
FIG 6 – View of seismic events on 15 Level over 30 days following the TSB firing. TSB initiation point shown by red blast symbol, damage locations by black triangles, Reward fault in pink, final stope void in green. Drawn in mXrap software (Harris and Wesseloo, 2015).

FIG 7 – Crush damage to pillar nose in the disused 1606, due to the ML 2.1 event immediately after the 15 Level TSB firing. Damage included two snapped Posimix bolts, torn mesh, and 80 t rock displaced.

Stress change analysis: Stress change data around the 15 Level TSB was obtained from a group of hydraulic stress meter monitoring cells installed in the vicinity (Figure 3) and oriented to monitor changes in the east–west stress component (being the locally highest stress component through the abutment pillar that was to be destressed).

Four stress cells were installed 86 days prior to the TSB blast, in boreholes about 3.5 m above the backs of the drive. Frequent measurements were taken to establish a baseline for the cells prior to the blast. Underground personnel were given training on how to read the gauges and record readings every time they entered the area. The underground operators appreciated this interaction and there was never a shortage of readings, indicating their understanding of the importance of this data.

Figure 8 shows the computed stress changes relative to zero at the time of the TSB blast, using a calibration factor of 1.4 based on the numerical modelling simulation of the action of the stress meter undertaken by McNabb (1997). Stress cell #2 in the immediate shadow of the TSB showed a 2 MPa stress drop with the TSB blast. All three cells near the TSB showed gradual stress drops over the next seven months, reaching 3 to 7 MPa falls.
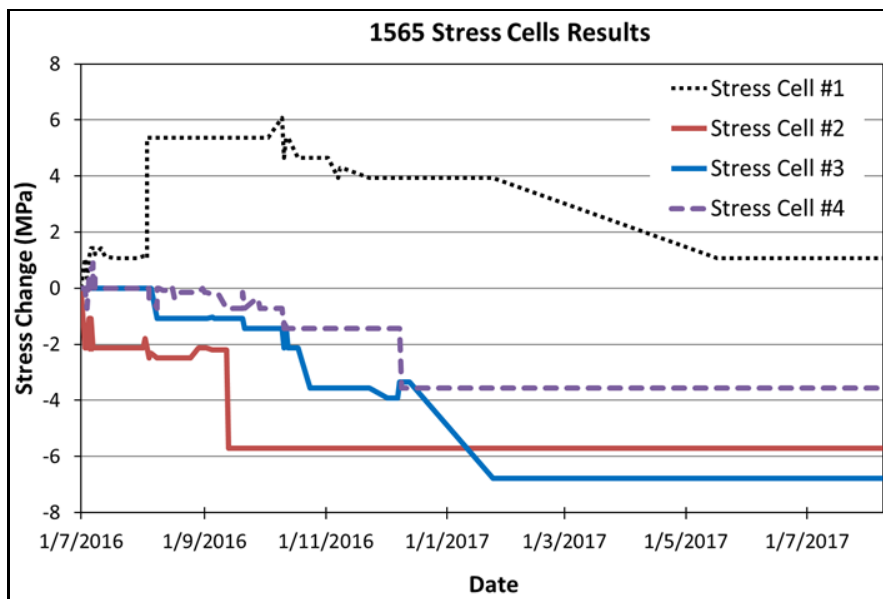
FIG 8 – Stress cell data showing monitored changes, starting from the time of the 15 Level TSB firing on 1 July 2016.

The fourth cell recorded a 4 MPa rise on day 34, in a stress abutment area distant from any fault. However it coincided with the firing of a rise at another location 225 m south of the TSB area. That rise intersected Flanagan fault which is also near the TSB area. This observation supports the site understanding that the major faults are adversely loaded in the stress field and are prone to movement in some circumstances.

CASE HISTORY – 16 LEVEL TSB#1 AND TSB#2

Design: On this level the design for the remaining abutment pillar between COB void and Reward Fault (Figure 9) allowed for single-ring advance for 10 m, up to a standoff of 24 m from the fault, followed by two separate TSB firings (15 m long and 19 m long respectively) to cover the remaining distance to the fault. Both TSBs were width 9.5 m and height 26 m. Based on lessons from the 15 Level TSB, to improve blast performance, two changes were made on this level:

- Two TSB firings were designed (rather than one as for 15 Level) to increase the swell factor.

- A free face was provided at both ends of the TSBs allowing the firings to progress in both directions concurrently. This was achieved by installing boxhole rises, of width 1.1 m and height 23 m, with blastholes designed to break out the boxholes into a 2.5 m strike and 9.5 m wide slot, leading into the rapid-firing portion of the TSB firing.
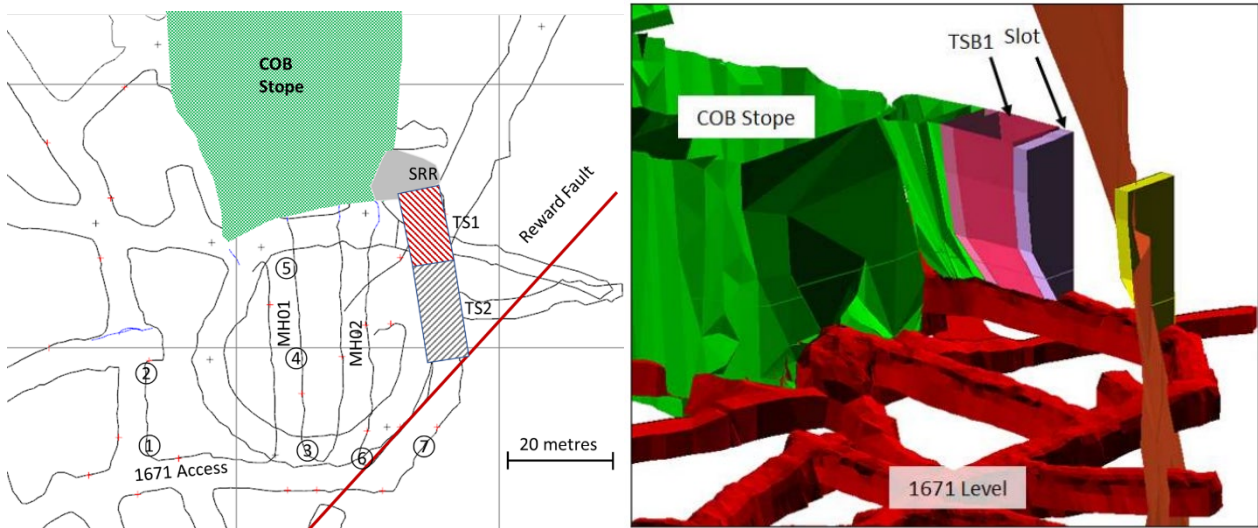
FIG 9 – (left) Plan for 16 Level TSBs showing COB and ROB3 stope voids, short stepped stope advance, and the two TSB firings to advance the final distance through the abutment pillar to the Reward Fault. The numbered circles show the position of stress monitoring cells 1 to 7. (right) Perspective view of a 20 m-thick slice of the COB stope, TSB#1, Slot#1, Slot#2, and Reward Fault. The TSB#2 shape is omitted for clarity.

Firing: The 16 Level TSB#1 design comprised 15 rings of 4 to 15 holes per ring, with parameters shown in Table 3. The blast design pattern used was the same as for 15 Level. The rapid-firing portion of TSB#1 was 1710 ms. For TSB#2, a similar sequence was used, and the rapid firing blast portion was 1545 ms. These were slower than the 15 Level TSB speed, but resulted in significantly better fragmentation.

Fragmentation outcome: The initial fired material from TSB#1 rilled out a distance of 25 m from the designed stope brow, and tightly filled the drive for the first 10 m of this distance (Figure 10). The rill slope angle was quite flat at 17°. This behaviour was attributed to the gases created from the firing which carried the fired material 25 m along the drive. The blasted material had a large portion of fines and fragments less than 300 mm in size, due to the high powder factor and rapid firing used.

FIG 10 – (left) Cross-section looking west of the COB stope and 16 Level TSB#1. The material expelled by the blast is highlighted yellow. The first 10 m of the rill was tight filled to the backs, and the rest rilled at an angle of 17° to a total distance of 25 m from the designed stope brow. (right) View in 1671 drive looking north, taken from about 15 m from the TSB#1 brow. Fired material is packed to almost the backs of the drive.

The fired material from the TSB#2 did not rill out as far as from TSB#1, and the fired material was noted to have a slightly larger fragmentation compared to TSB#1.

Blast vibration outcome: The surface vibration monitors recorded a surface vibration of 3.7 mm/s with the 16 Level TSB#1 firing, and 6.2 mm/s with the TSB#2 firing. The seismic monitoring system

also recorded the TSB#1 blast, and Figure 11 shows the waveform from an underground triaxial sensor at 48 m from the blast.
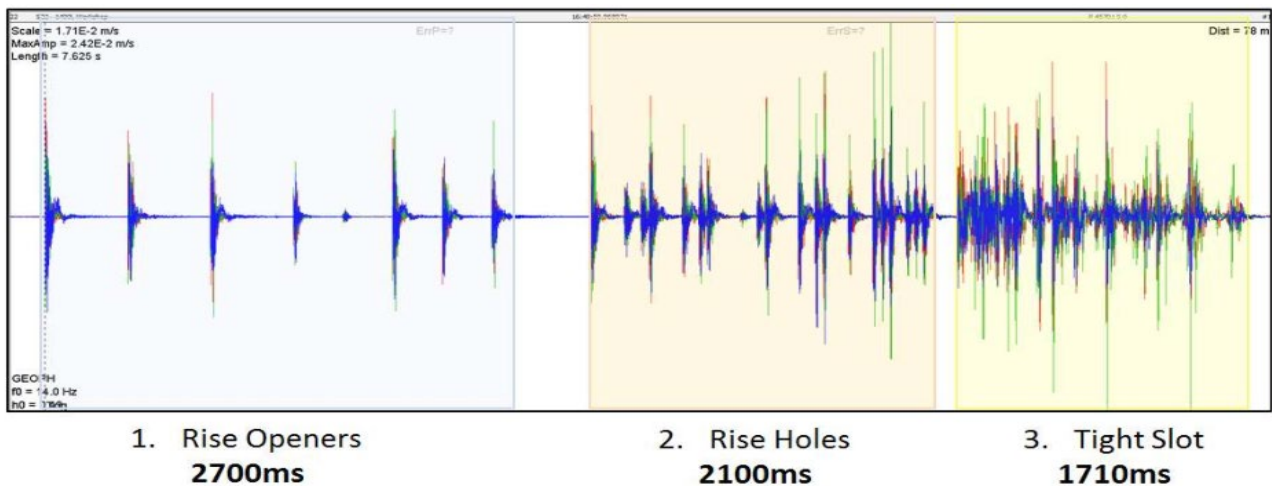
FIG 11 – Seismogram trace at 78 m distant of the 1671 TSB#1 firing showing the progression and timing of the rise opening, then the rise holes, and lastly the rapid TSB itself in the final 1710 ms.

Seismicity and damage outcome: After the 16 Level TSB #1 the largest event on or near Reward Fault was ML 0.6 and the events were clustered quite tightly in the TSB region. Overall, seismic response was subdued, as might be expected since this TSB#1 only covered half the distance to Reward Fault. Away from the faults, the largest event was ML -0.7. The worst damage from TSB#1 was shakedown of walls in the 1650 old Decline and 1670 intersection a short distance below the TSB area.

The Institute of Mine Seismology conducted an analysis of the seismicity following this TSB#1 (Meyer, 2017). They found events indicating a trend of increasing stress in the abutment zone on the southern side of the TSB#1 firing location, ie in the TSB#2 zone, and observed that if the zone were to become completely destressed due to mining, it could be expected that the Reward Fault would become hazardous. These findings agree with site expectations, supporting the requirement that pillar destressing in such situations only be conducted using the TSB strategy.

After TSB#2 the largest event was ML 0.7 on Reward Fault adjacent the TSB, with most events clustering in the Reward Fault zone east of the TSB. Overall, the seismic response was restrained similar to that of the 1671 TSB#1 firing. Damage from TSB#2 was minor, comprising shakedown of slabs from the walls below the mesh line, and bagging of mesh in the backs along the 1671 TSB access drive.

Stress change analysis: Seven hydraulic stress monitoring cells were installed in the vicinity of the 16 Level TSB area (Figure 9). These cells were oriented to monitor changes in the local East–West stress component. The cells were installed seven months prior to the TSB#1 blast, however some were damaged by equipment and had to be replaced only a few weeks before the blast.

Figure 12 shows the stress change data relative to zero at the time of the TSB#1 blast (29 Sept 2017). The TSB#2 blast occurred on day 71 (9 Dec 2017). The data for the surviving stress cells showed generally greater changes nearer to the TSB sites, with maximum change of about 6 MPa. Only some of the cells showed changes as would be expected from the shifts in stress abutment and shadow zones due to the TSB firings.
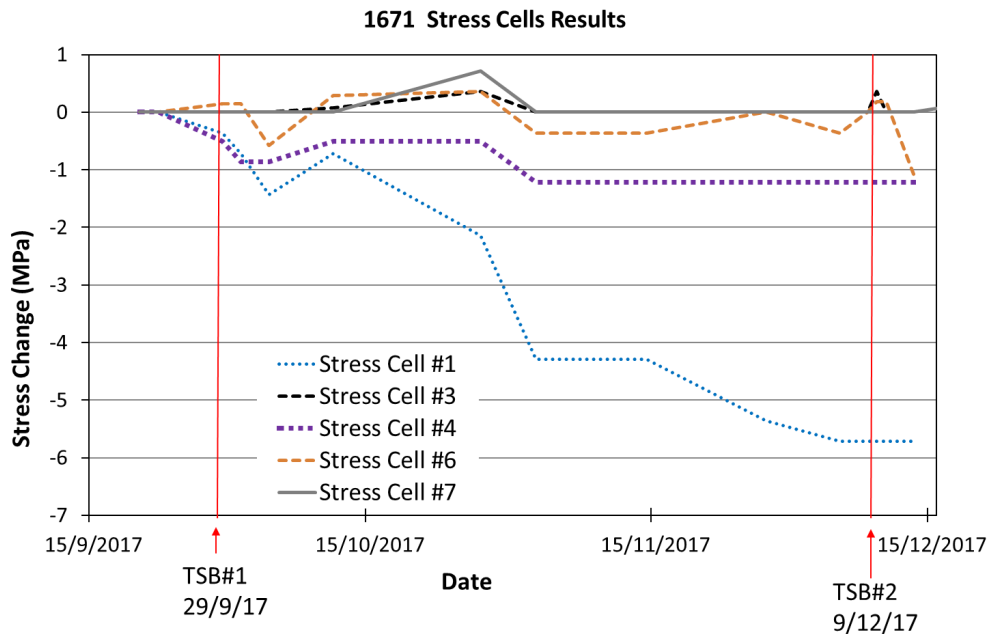
FIG 12 – Stress changes for the 1671 TSB#1 and TSB#2 firings, for the five surviving stress cells. Cell #1 was erratic. The remaining cells showed oscillating change after TSB#1, and falls after TSB#2. Cell #6 showed an unexplained sharp increase several days after the TSB#2 firing, then resumed a falling trend.

CASE HISTORY – 17 LEVEL TSB#1 AND TSB#2

Design: The 17 Level TSB zone design was similar to the 16 Level. The TSBs were 15 m and 21 m long respectively, of width 5 m and height 26 m (Figure 13). Again two boxhole rises were installed to ensure free faces for firing with improved swell factor allowance. The abutment pillar between the Reward Fault and the COB Stope was quite wide, so single-ring retreat of the TSB drive was done first to approach up to a standoff of 28 m from the fault.
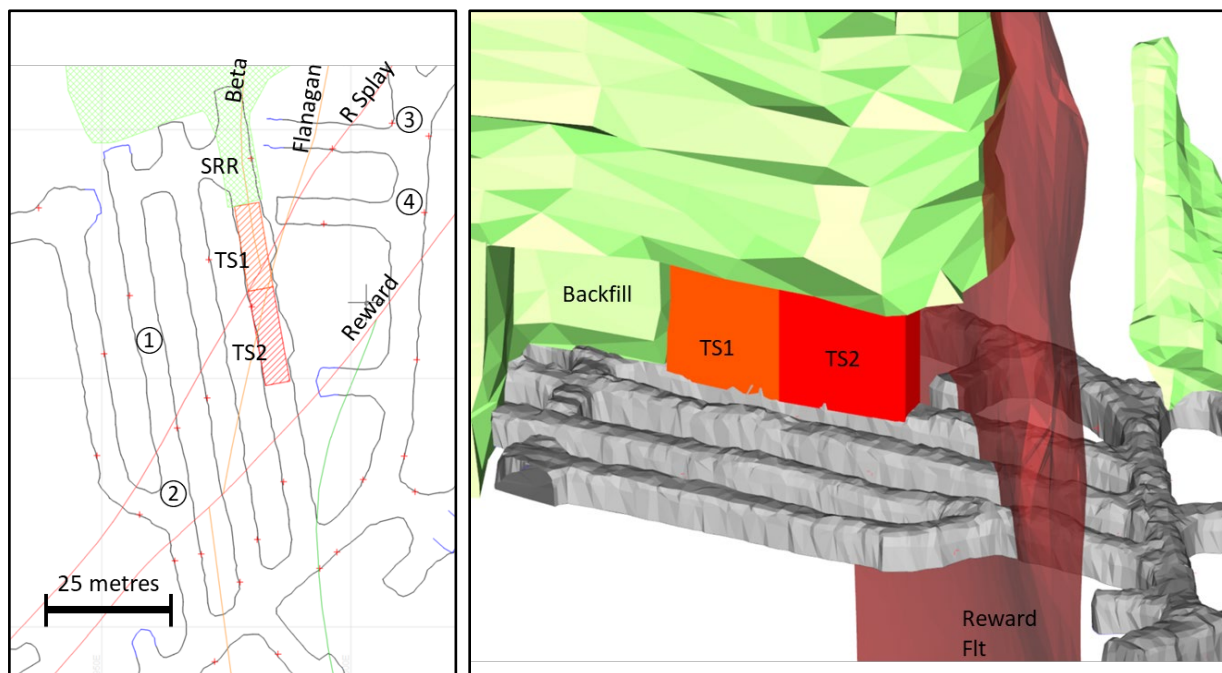
FIG 13 – (Left) Plan (North to top) of 1728 TSB#1 and #2 showing location of single ring retreat (SRR) along the drive, TS#1, TS#2, and major faults. The numbered circles show the position of stress monitoring cells 1 to 4. TS#1 advanced to intersect Reward Splay, and TS#2 continued the advance to reach a sheared zone adjacent to Reward Fault. (Right) oblique view looking NE of Tight Slot firings retreating away from backfilled void toward Reward Fault.

The 17 Level TSBs were the first to be conducted in an intersecting fault environment. Previous TSBs were designed to manage the approach to subvertical faults. But the 17 Level TSB zone encountered two more faults, namely west-dipping Beta and Flanagan Faults aligned oblique to the zone. It was considered that they would be less effectively managed by the TSB strategy, and this opinion was proved correct.

In the 15 and 16 Level designs, the millhole (or drawpoint) development on the west side of the TSB zone was not done until after TSB firings on that level, to prevent damage which may have resulted from the TSB firings. This allowed for the millholes to be developed later in the stress shadow of the TS drive.

However on 17 Level, the three adjacent millholes were mined before the TSB blasts, and the 19 Level millholes below were also nearing the final stages of development. One day before the TSB#1 firing, a ML 0.8 event occurred with a development cut on the 19 Level. This development was advancing along Beta Fault in the high stressed abutment at the south end of the COB Stope. The event confirmed the seismic vulnerability of these faults and the need for the TSB strategy.

Firings: Both TSB#1 and TSB#2 blast designs utilised a main row and infill row. Rings comprised 2 or 3 holes only, with additional holes around the box rises. Unlike previous TSBs, no reamer holes were included due to the narrower width of the slots, and the use of box hole rises positioned near the centre, not at the end, of each TSB zone. TSB#1 was charged with ANFO, however TSB#2 was charged with Emulsion due to the presence of groundwater close to the fault.

During the blast, the rise in the centre of the TSB was opened up slowly first over 6.5 sec, and then the remaining volume was rapid-fired within 920 ms for TSB#1 and 1180 ms for TSB#2.

Fragmentation outcome: The 17 Level TSBs fragmentation mimicked the behaviour of the 16 Level, with TSB#1 creating very well fragmented material with a rill of 16° out to 17 m from the brow, and TSB#2 with slightly larger fragmentation but less progression of the rill.

Blast vibration outcome: The surface vibration monitors recorded minimal vibration for both blasts with a maximum surface vibration of 2.7 mm/s for TSB#1 and 3.2 mm/s for TSB#2.

Seismicity and damage outcome: The largest event directly after the TSB#1 firing was ML 0.0, located 10 m west of the TSB at the south edge abutment of the COB Stope. Seismicity was scattered around the southern end of the COB Stope and around Beta and Flanagan Faults (largest being ML -0.2 on Flanagan Fault).

Only minor seismicity occurred on Reward Fault. This was confirmed by plotting a proxy for the cumulative displacement (cube root of Seismic Moment for each event, distributed onto the fault grid plane according to the event source radius) on the Reward fault plane (Figure 14). As shown, displacement increased on this fault following TSB#2. This indicates the fault displaced – presumably pushing into the broken rock fill in the slot – but without a major seismic event. This confirms the success of the TSB strategy.

Minor damage occurred in development close to the TS drive. Multiple bolts in the shoulder/wall of the TS drive were seen to be under significant load. Damage was confined to a large zone between Reward Fault and Flanagan Fault, showing the dominant influence of these faults. Three days after TSB#1, a large ML 1.9 event occurred during firing of the next development cut on 19 Level. The event was a fault-slip movement on oblique Beta Fault and resulted in significant bulking along the exposed Beta Fault in nearby development, and shakedown where ground support was inadequate.

A small seismic response occurred after the TSB#2 with the largest event being a ML -0.5 occurring 30 seconds after firing on Flanagan Fault. It was considered that the ML 1.9 event after TSB#1 had significantly reduced the shear loading on all the faults in this area, and therefore reduced the seismic response from TSB#2.

Stress change analysis: Four hydraulic stress monitoring cells were installed on the 17 Level around the TSB zone. These cells were oriented to monitor changes in the local East–West stress component (Figure 15). The cells were installed several months prior to the TSB#1 blast, however one was damaged prior to the first TSB firing and a second one prior to the TSB#2 firing. The three operational stress cells recorded a drop after TSB#1. One cell had a 5 MPa stress drop after TSB#2.
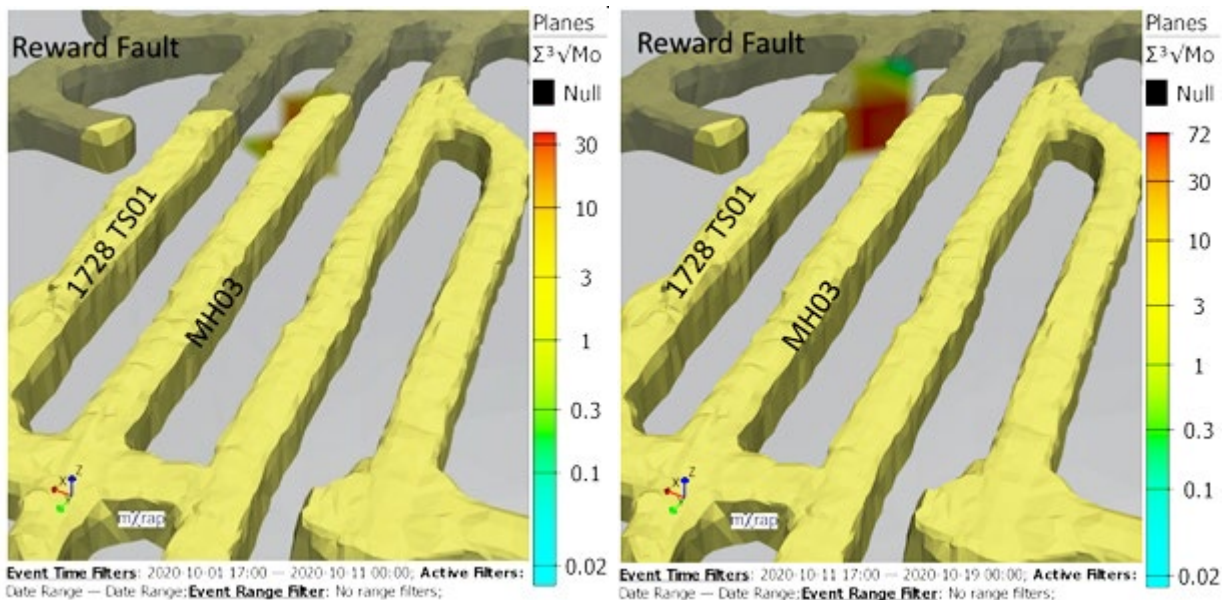
FIG 14 – Oblique view looking towards SE, showing a display of cube root of Seismic Moment as a scalar proxy for cumulative displacement plotted on the Reward fault plane which intersects the TS01 drive as well as adjacent drives. Numbers are relative only. (Left) Contours for events after TSB#01 firing up to just before TSB#2. The TSB#1 slot terminated some distance away from the fault and had very little effect on the fault stress conditions. (Right) Display for events after TSB#02 firing, showing significant fault slip despite no major seismic events – a clear validation of the TSB strategy. Drawn in mXrap software (Harris and Wesseloo, 2015).
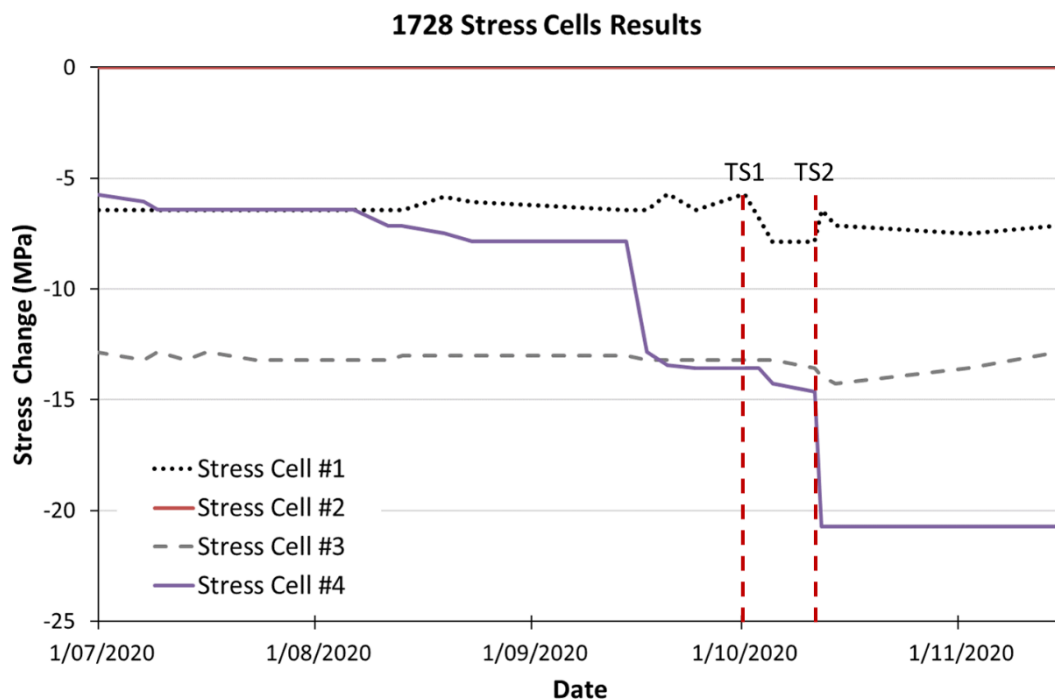
FIG 15 – Stress change in response to 1728 TSB #1 and #2. Measurements are relative values and cumulative since instrument installation.

EVALUATION OF TSB PERFORMANCE

The performance indicators for the five TSB blasts were evaluated as shown in Table 4, indicating that TSB performance was generally acceptable, and the successive improvements made to the TSB methodology have led to improved outcomes.

TABLE 4

Performance indicators for TSB cases.

	15 Level TSB	16 Level TSB#1	16 Level TSB#2	17 Level TSB#1	17 Level TSB#2
Indicator 1: Surface vibration < 10 mm/s	FAIL: 12.5 mm/s	PASS: 3.7 mm/s	PASS: 6.3 mm/s	PASS: 2.7 mm/s	PASS: 3.2 mm/s
Indicator 2: Largest seismic event < ML 2.3	PASS: ML 2.1	PASS: ML 0.6	PASS: ML 0.7	PASS: ML 1.9	PASS: ML 0.5
Indicator 3: TSB slot rock mobilised but with effort	FAIL: Additional drill and blast required	PASS: Successfully bombed down	PASS: Successfully bombed down	PASS: Successfully bombed down	FAIL: Additional drill and blast required
Indicator 4: TSB rock well fragmented	FAIL: A bridge required redrilling and slash firing	PASS: Blasted material size <0.3 m; fines present; tight filled the drive	PASS: Blasted material size variable, fines present	PASS: Blasted material size <0.3 m; fines present	PASS: Blasted material size variable, with fines
Indicator 5: Minor seismicity during stoping in TSB shadow: event rate < 2/day; all < ML 0.0	PASS: Event rate 0.4/day, all < ML -1.3	PASS: Event rate 1.2/day, all < ML -1.3	PASS: Event rate 1.0/day, all < ML -0.7	N/A (the next TSB firing followed within days)	PASS: Event rate 1.4/day, all < ML -0.1

CONCLUSIONS

Practicable and reasonable steps have been taken to limit fault-slip seismicity during stoping at Mt Charlotte. The mine has experienced greatly reduced seismicity since 1998, but significant events still occur as documented in the historical record.

The TSB strategy was engineered to deal with stressed abutment pillars adjacent to subvertical faults susceptible to slip. The strategy was tested in lower hazard environments before being applied to critical situations. Several performance indicators were developed for evaluation of strategy outcomes and to provide guidance for strategy improvements.

The TSB outcomes to date show that fault-slip seismicity on subvertical faults is adequately managed by this TSB process, with the largest event on Reward Fault being an acceptable ML 0.7, and with these Reward Fault events occurring within seconds of the blast. Both magnitude and timing are controlled.

While Reward Fault seismicity is managed, significant seismicity of up to ML 2.1 has occurred in the new stress abutments formed after TSB blasts.

If multiple intersecting faults are present, the TSB strategy may not significantly reduce seismicity on all the faults. The strategy relies on the TSB slot advance direction being perpendicular to or at a substantial angle to the fault strike direction. The 17 Level case histories showed that while Reward fault was successfully destressed on that level, the non-optimum Beta and Flanagan faults were less effectively managed by the TSB strategy, with events up to ML 1.9 occurring.

TSB slot lengths of 15 m to 27 m were used, corresponding to standoff distances of 11 m to 20 m from Reward Fault. Experience to date suggests that a 20 m standoff is adequate and shorter standoffs may be acceptable for Mt Charlotte conditions.

Stress change instrumentation data indicated significant stress falls of up to 2.2 MPa following TSB blasts, that confirmed the expected pattern of destressing.

Refinements under consideration for future TSB applications include:

- Review of explosives products to ensure the selection of the product most suited to the blast requirements.

- Maintain blast swell factor in the 25 per cent to 30 per cent range and/or add additional reamer holes.

- Inclusion of extensometer instrumentation to quantify fault movements.

- Expansion of instrumentation into areas expected to become new stress abutments as a result of the TSB firing.

- Maintain the ability to install replacement stress meter cells in case of damage.

Overall, the TSB strategy has successfully managed the seismicity on Reward Fault and is expected to remain an essential part of the seismic management plan at Mt Charlotte mine.

ACKNOWLEDGEMENTS

FIG 16 – The start of the TSB concept – a simple sketch on the back of an envelope in 2003.

REFERENCES

Harris, P H and Wesseloo, J, 2015. mXrap software, version 5, Australian Centre for Geomechanics, The University of Western Australia, Perth, Western Australia, https://mxrap.com/

Kempin, M, Sprague, A, Narendranathan, S, Mikula, P A and Lee, M, 2007. Destressing the ROB5 Remnant using Tight Slot Blasting at Mt Charlotte Mine, in *4th International Seminar on Deep and High Stress Mining* (Australian Centre for Geomechanics: Perth).

Lee, M F, Pascoe, M J and Mikula, P A, 2001. Virgin rock stresses vs. rock mass strength in Western Australia's Yilgarn Greenstones, in *Ground Control in Mines Workshop,* The Chamber of Minerals and Energy of WA.

McNabb, K E, 1997. Hydraulic Stressmeter, Final Report AMIRA Project P396, Mincad Systems Pty Ltd.

Meyer, S, 2017. Mount Charlotte Mine: Analysis of seismicity following 1671 destress firing, *Institute of Mining Seismology*, Internal report for KCGM.

Mikula, P A and Lee, M F, 2000. Bulk low-grade mining at Mt Charlotte Mine, in *Proceedings of MassMin 2000*, pp 623–635 (The Australasian Institute of Mining and Metallurgy: Melbourne).

Mikula, P A and Lee, M F, 2002. Forecasting and controlling pillar instability at Mt Charlotte Mine, in *Deep and High Stress Mining – First International Seminar* (Australian Centre for Geomechanics: Perth).

Mikula, P A, Lee, M F and Guilfoyle, K, 1995. Preconditioning a large pillar at Mt Charlotte Mine, in *Underground Operators Conference*, pp 265–272 (The Australasian Institute of Mining and Metallurgy: Melbourne).

Mikula, P A, Sharrock, G, Lee, M F and Kinnersly, E, 2005. Seismicity Management Using Tight Slot Blasting for Stress Control at Mt Charlotte Mine, in *Proceedings of the Sixth International Symposium on Rockburst and Seismicity in Mines (RaSiM6)*, (Australian Centre for Geomechanics: Perth).

Mining One Pty Ltd, 2013. Mt Charlotte Underground Projects: Geotechnical Evaluation of the CS4_2 Mining Strategy, Report for Kalgoorlie Consolidated Gold Mines, Job No 1533_G, 57 p.

Geotechnical challenges in extreme mining environments

Dynamic fracture mechanism of thermally degraded brittle rock under impact load

S Akdag[1,2], M Karakus[3], G D Nguyen[4] and A Taheri[5]

1. Postdoctoral Research Associate, The University of Adelaide, Adelaide SA 5005.
   Email: selahattin.akdag@adelaide.edu.au
2. Currently, Postdoctoral Research Fellow, The University of New South Wales, Kensington NSW 2052. Email: s.akdag@unsw.edu.au
3. Associate Professor, The University of Adelaide, Adelaide SA 5005.
   Email: murat.karakus@adelaide.edu.au
4. Associate Professor, The University of Adelaide, Adelaide SA 5005.
   Email: g.nguyen@adelaide.edu.au
5. Associate Professor, Queen's University, Kingston Ontario, Canada.
   Email: abbas.taheri@queensu.ca

ABSTRACT

During underground mining operations, rock masses are highly subjected to dynamic disturbance caused by blasting, mechanical drilling and earthquakes resulting in strain burst, slabbing and spalling. The dynamic fracture is a significant manifestation of rock failure in deep underground engineering, and it is of great importance to assess the dynamic fracture behaviour of the rock mass under elevated temperature conditions. The correlation between temperature – and loading rate-dependent dynamic fracture mechanism of strain burst is yet to be established. A good understanding of the dynamic fracture behaviour of brittle rock subjected to high-temperature under dynamic loading is required for the prediction of the damage extent during strain burst, and proper design as well as control of the underground rock structures. In this study, dynamic mode I fracture toughness tests are carried out on cracked chevron notched semicircular (CCNSCB) granite specimens to reveal the dynamic fracture characteristics of the brittle rock. For this purpose, a Split Hopkinson Pressure Bar (SHPB) apparatus is utilised to conduct the dynamic tests with various striker velocities on thermally degraded granite. The dynamic mechanical behaviour of granite after high-temperature treatment is examined and discussed. The dynamic fracture toughness is determined and compared for the specimens exposed to different temperatures at various dynamic impacts. The fracturing processes are recorded by a high-speed camera (HSC), and the crack propagation speeds are estimated by HSC image analysis. In addition, the dynamic fracture process and the coupled effects of temperature and loading rate on the dynamic fracture modes are identified by HSC image analysis. Energy partition characteristics in dynamic fracture of granite are quantitatively investigated.

INTRODUCTION

The ground control in highly stressed rock masses is a very challenging task due to dynamic loads which may lead to an increasing number of dynamic failures, eg rock bursts, spalling and slabbing (Gao *et al*, 2019). As mining and tunnelling progress to greater depths, the number of strain bursts encountered dramatically increased, resulting in significant operational and safety risks (Akdag *et al*, 2021; He *et al*, 2021). Rock bursts can not only be induced by excavation, but also can be induced or triggered by dynamic disturbance. The dynamic fracture is a significant manifestation of rock failure in underground engineering, and it is of paramount significance to assess the dynamic fracture behaviour of the deep rock mass. Therefore, a thorough understanding of rock fracture behaviour under dynamic loading conditions can benefit to apply mitigating measures for rock burst damage.

To study the progressive dynamic failure of thermally treated granite, dynamic three-point bending loading was applied on CCNSCB granite specimens by a SHPB and images of the entire fracture events were recorded with a high-speed camera (Phantom V2511–200 000 fps). The dynamic fracturing characteristics and crack propagation speeds were measured by the HSC. The dynamic fracturing process and the effects of thermal damage on the dynamic fracture modes were identified by detailed image analysis (Figure 1). The images were processed by an open-source code Ncorr to calculate the strain/displacement field of the measured surface (Blaber *et al*, 2015). Cracks

initiated from the tip of the notch and propagated along with the impact loading, and then the tensile failure along the dynamic loading direction dominated the failure. Subsequently, the sample splits into two halves almost along the force axis, and it is observed that a number of small fragments also ejected out from the specimen. This phenomenon represents the rock failure process during a rock burst induced by dynamic disturbances around underground openings (Kaiser and Cai, 2012). When the impact velocity was high, the impact of the loading rate on dynamic rock strength became more remarkable, and it increased under all temperatures. Along with the impact velocity, the failure mode of the pre-heated Australian granite changed from tensile splitting to pulverisation or breaking into many small pieces in which the excess strain energy pulverised the specimens. Under the same dynamic load, an increase in the treatment temperature weakened the interaction force between the particles and aggravated the fragmentation degree of the granite. This experimental observation agrees with the existing literature (Yao *et al*, 2017; Yin *et al*, 2018; Zhang and Zhao, 2013).
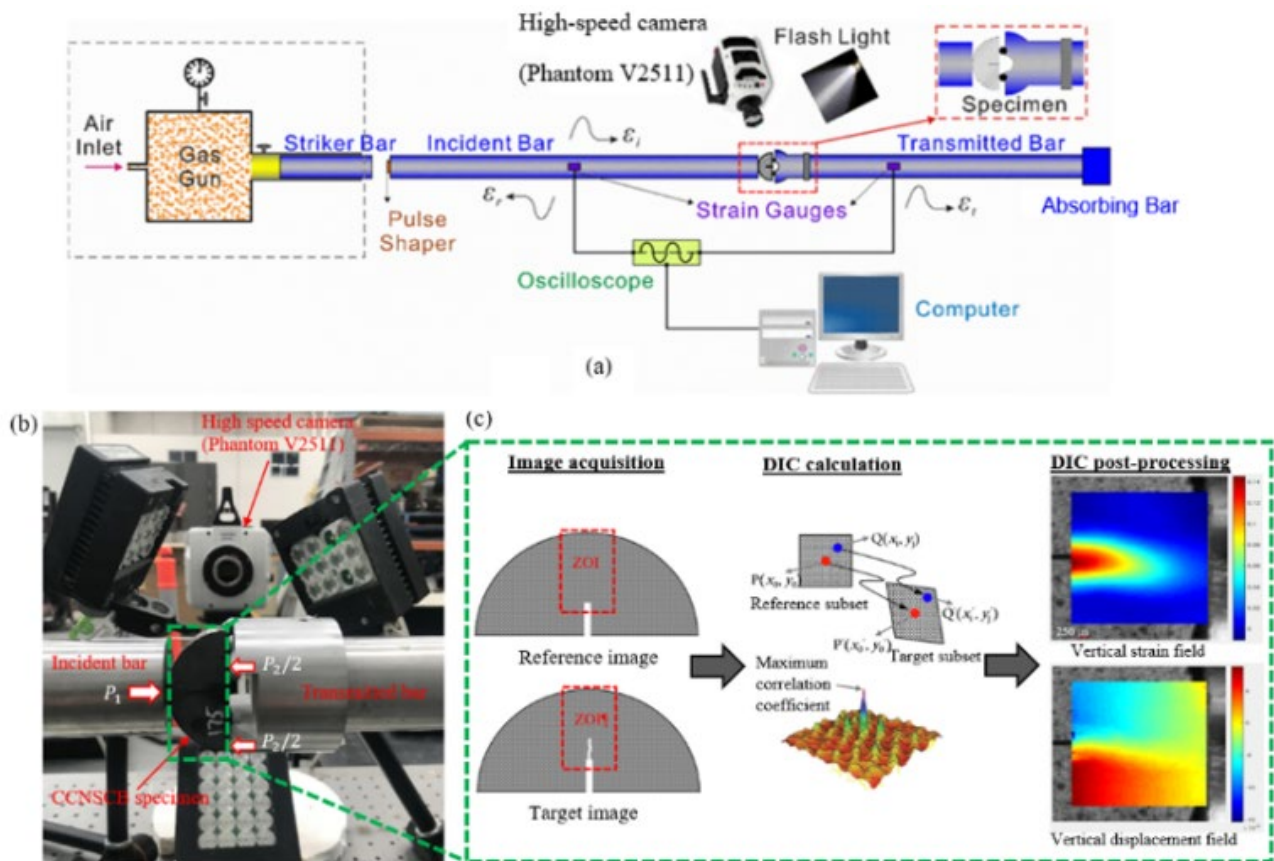
FIG 1 – (a) Schematics of the split Hopkinson pressure bar (SHPB) system (ε denotes strain and the subscripts In, Re and Tr refer to the incident, reflected and transmitted waves, respectively); (b) close-up view of the partial SHPB bars and CCNSCB specimen; (c) digital image correlation method.

In Figure 2, the curves have undergone into three stages: elastic deformation, yielding and failure. In the elastic deformation stage, the rate of increase in the stress decreased more slowly compared with that in the initial loading. Meanwhile, the micro-cracks within the rock began to increase in size under the action of the dynamic loading, resulting in a decrease in the curve slope. In the yielding stage, the rate of increase in the stress was lower than that in the elastic stage, mainly due to the rapid expansion of the micro-cracks within the specimen under the stress wave. When the curve reached the peak strength, the maximum load-bearing capacity was reached, which would lead to macroscopic damage and then failure. After failure, the rock demonstrated a strain-softening behaviour. At a given loading rate or impact velocity, the value of dynamic strength of the granite tended to decrease as the pre-heating temperature rose over the range from room temperature (25°C) to 250°C due to degradation influence of thermal damage on the overall rock strength in which high temperature aggravated the cumulative damage of the rock (Akdag *et al*, 2018). Similar results were observed by Yin *et al* (2018). In order to investigate the coupling effects of loading rate

and thermal damage on the dynamic fracture toughness of granite, a regression method was utilised, and the fitting of each group was obtained. Figure 2 presents the rate dependency of the dynamic fracture toughness of thermally-treated granite. It was found that the dynamic fracture toughness of granite showed an increasing trend with the rise of impact velocity under all heat-treatment temperatures. This may be due to multiple cracks formed by transgranular fractures around the crack tip and their interaction with the main crack tip delayed the onset of crack initiation. It is to be noted that temperature variation affects the dynamic fracture toughness of brittle rocks to a limited extent at lower loading rates, whereas it becomes more significant with higher dynamic impact loads. Based on the first law of thermodynamics, the energy consumed during dynamic fracturing in SHPB test can be quantified (Zhang *et al*, 2000). The energy dissipation is mainly for the evolution of rock from microscopic damage to macroscopic fracture, and the effective energy dissipation for rock breakage is much lower than the input energy. It is believed that as the loading rate increased when fragmentation becoming more severe, the growth of absorbed energy distributes to both dissipated and kinetic energy but more to the latter one.
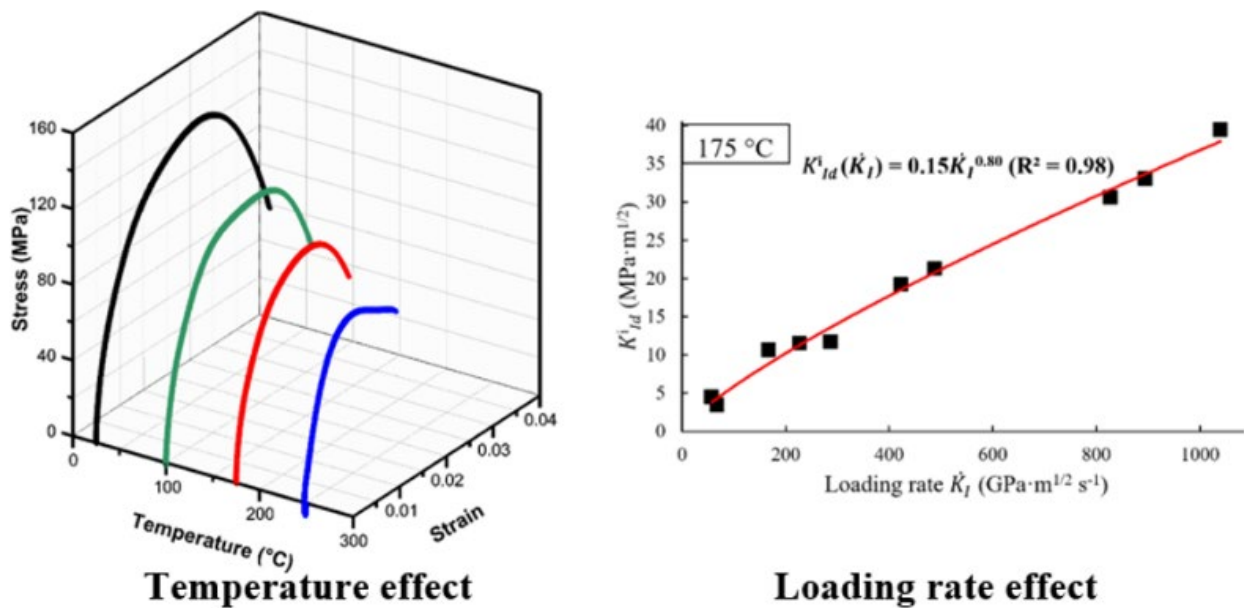
FIG 2 – Dynamic stress-strain behaviour and fracture toughness at different temperatures and impact velocities.

CONCLUSION

The dynamic deformation and fracture properties of thermally-treated granite under dynamic loading have been studied by SHPB system. The results show that along with the high impact velocity, the failure mode of the pre-heated granite changed from tensile splitting to pulverisation or breaking into many small pieces in which the excess energy pulverised the specimens. Under the same dynamic impact, an increase in the temperature weakened the interaction force between particles and aggravated the fragmentation degree of granite. The dynamic fracture toughness of the granite underwent ascending trends with increasing impact velocity and decreased with increasing temperature. That is to say, temperature variation influences the dynamic fracture toughness of granite to a limited extent at lower loading rates, whereas it becomes more remarkable with higher impact loads. To limit rock burst damage in the field, the energy absorption capacity of the ground support system should consider the energy-absorption of rock materials under dynamic loads.

REFERENCES

Akdag, S, Karakus, M, Nguyen, G D, Taheri, A and Bruning, T, 2021. Evaluation of the propensity of strain burst in brittle granite based on post-peak energy analysis, *Undergr Sp*, 6(1):1–11.

Akdag, S, Karakus, M, Taheri, A, Nguyen, G D and Manchao, H, 2018. Effects of thermal damage on strain burst mechanism for brittle rocks under true-triaxial loading conditions, *Rock Mech Rock Eng*, 51:1657–1682.

Blaber, J, Adair, B and Antoniou, A, 2015. Ncorr: open-source 2D digital image correlation Matlab software, *Exp Mech*, 55:1105–1122.

Gao, F, Kaiser, P, Stead, D, Eberhardt, E and Elmo, D, 2019. Strainburst phenomena and numerical simulation of self-initiated brittle rock failure, *Int J Rock Mech Min Sci*, 116:52–63.

He, M C, Ren, F, Liu, D and Zhang, S, 2021. Experimental study on strain burst characteristics of sandstone under true triaxial loading and double faces unloading in one direction, *Rock Mech Rock Eng*, 54:149–171.

Kaiser, P K and Cai, M, 2012. Design of rock support system under rock burst condition, *Int J Rock Mech Geotech Eng*, 3:215–227.

Yao, W, Xu, Y, Liu, H and Xia, K, 2017. Quantification of thermally induced damage and its effect on dynamic fracture toughness of two mortars, *Eng Fract Mech*, 169:74–88.

Yin, T, Bai, L, Li, X, Li, X and Zhang, S, 2018. Effect of thermal treatment on the mode I fracture toughness of granite under dynamic and static coupling load, *Eng Fract Mech*, 199:143–158.

Zhang, Q and Zhao, J, 2013. Effect of loading rate on fracture toughness and failure micromechanisms in marble, *Eng Fract Mech*, 102:288–309.

Zhang, Z, Kou, S, Liang, L and Lindqvist, P A, 2000. Effects of loading rate on rock fracture: fracture characteristics and energy partitioning, *Int J Rock Mech Min Sci*, 37:745–762.

Some considerations on rock dynamics issues in Mars

Ö Aydan[1]

1. Emeritus Professor, University of the Ryukyus, Okinawa, Japan.
   Email: aydan@tec.u-ryukyu.ac.jp

ABSTRACT

Rock dynamics is one of the most important topics in the field of rock mechanics and rock engineering. The spectrum of rock dynamics is very wide and it includes the failure of rocks, rock masses and rock engineering structures such as rock bursting, spalling, popping, collapse, toppling, sliding, blasting, non-destructive testing, geophysical explorations, science and engineering of rocks, earthquakes, and impacts. Undoubtedly, the rock dynamics issues in Mars would remain to be the same. Although mankind has no direct access to Mars yet, the Mars exploration rovers (Opportunity, Sprit, Curiosity and Perseverance), Mars Reconnaissance Orbiter and InSight Lander provided very valuable data so that some rock dynamics issues can be recognised. The author reports his considerations on rock dynamics issues in Mars from very careful examination of images and data provided from MERs and MRO and discusses their implications.

INTRODUCTION

Rock dynamics is recognised as one of the most important topics in the field of rock mechanics and rock engineering (Aydan, 2017a, 2020a, 2020b, 2022). The failure of rocks, rock masses and rock engineering structures such as rock bursting, spalling, popping, collapse, toppling, sliding, blasting, non-destructive testing, geophysical explorations, science, and engineering of rocks as well as earthquakes and impacts are some of topics in Rock Dynamics. Although the mankind has not been on Mars yet, the Mars exploration rovers (MER: Opportunity, Sprit, Curiosity and Perseverance), Mars Reconnaissance Orbiter (MRO) and InSight Lander provided tremendous data on various aspects of Mars, some of which have direct relations to rock dynamics issues (Figure 1).
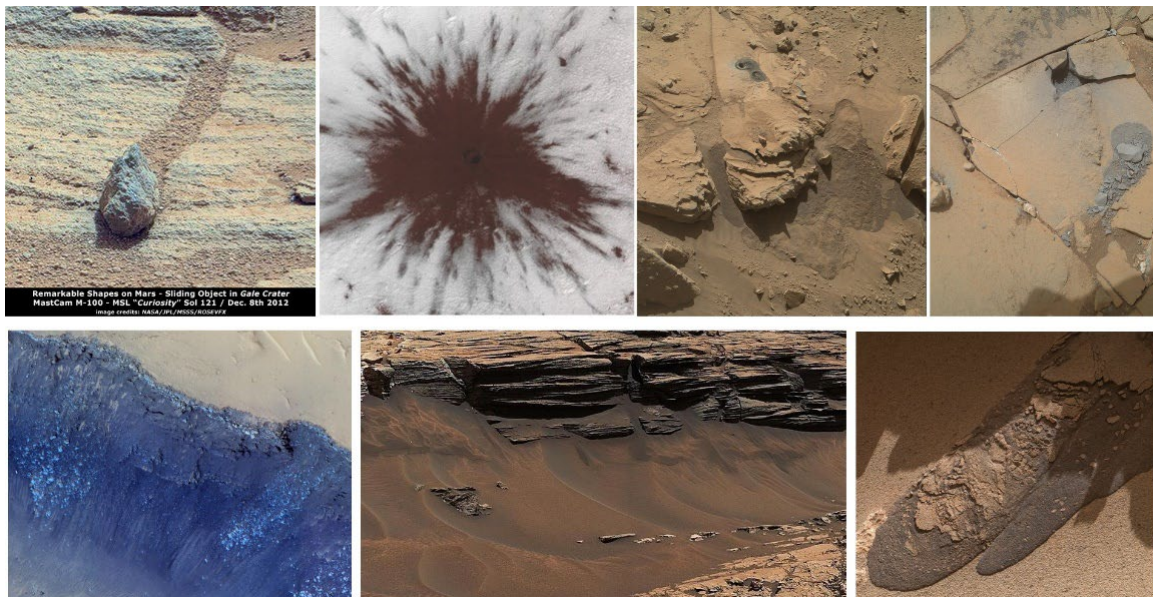
FIG 1 – Some examples of rock dynamics issues in Mars.

Mars Reconnaissance Orbiter has provided images of recent dynamic events such as impacts by meteorites, mass movements and rockfalls. InSight Lander has provided data on vibrations induced by seismic events named as Marsquakes and/or by meteorite impacts in addition to other sources. Mars Explorer Rovers (eg Opportunity, Sprit, Curiosity and Perseverance) have provided some direct data through drilling, grinding. chemical analyses, and imaging on outcrops of rocks on the surface of Mars. Unfortunately, Opportunity and Sprit lost their power units due to prolonging dust storms in Mars and they are no longer functioning. On the other hand, Curiosity has been currently

roving more than 28 km (July 2022) and has provided tremendous valuable data on the rocks of Mars in Gale Crater. Perseverance has been also providing similar data in addition to data from onboard seismic sensors (NASA, 2022).

In this study, the author presents some of his considerations and thoughts on various rock dynamics issues inferred on the bases of the images and data Mars exploration rovers, Mars Reconnaissance Orbiter (MRO) and InSight Lander with some references to similar events and phenomena on Earth. The issues involve vibrations caused by Marsquake and meteorite impacts, drilling and grinding of bits and metal wheels during roving over a rough terrain, mass movements and rockfalls. Particularly the metal wheels during roving cause some vibrations on soft or hard ground and they deserve great interest in relation to propagation and amplification of amplitudes of induced waves. The thoughts of the author on various rock dynamics issues in Mars come from very careful examinations of images and data provided from MERs and MRO with the considerations of similar situations on Earth and the author discusses their implications.

MARSQUAKES

The InSight Lander touched down on Mars on November 27, 2018 and recorded the first seismic event on April 24, 2019, which confirmed quakes of Mars. As there are evidences of moonquakes from Apollo program of NASA (2008), there was no doubt that Mars quakes should also occur (Aydan, 2017a). Aydan (2017a) stated the possible causes of Mars quakes could be due to:

- impacts by meteorites
- thermal contraction and expansion
- volcanic activity
- large scale mass movements
- plate-tectonic type movements
- daily rotation and annual solar motion.

The first vibration record obtained from a Marsquake by InSight lander was quite longer than those observed on Earth and shorter than those on Moon as seen in Figure 2. The seismic monitoring would improve the understanding of the seismicity and the interior structure of Mars and provide essential data on the necessity of quakeproof design of structures to be built in Mars. However, more similar instruments and instrumental data are necessary for decisive conclusions.
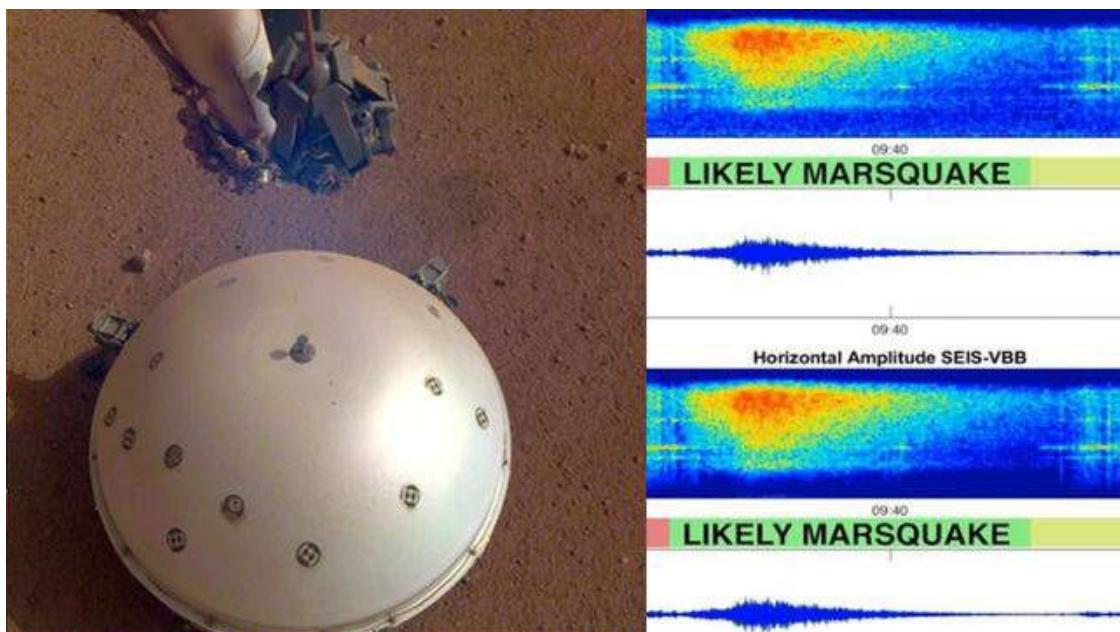
FIG 2 – A seismic record by the seismometer of the INSIGHT Mars module of likely Marsquake occurred on April 24, 2019.

METEORITE IMPACTS

Including Earth, meteorites of various sizes bombard planets and moon from time to time. These events result in shock waves and vibrations. Figure 3 show several examples of recent impacts on Mars. The vibrations caused by meteorite impacts depend upon the velocity, size and mechanical properties of impact object and ground. Figure 4 show some examples of accelerations induced by an impact object hitting various rock samples. The impact velocity and weight of the impact object was varied during measurements. In addition, the attenuation of vibrations occurs as a function of distance from the source area. Figures 5 and 6 show two such examples obtained on a limestone construction site and asphalt pavement over the embankment of a runway. At the limestone construction site, the impacts were induced by a shovel of a backhoe hitting ground. The vibrations shown in Figure 6 were caused by the drop of a sand-bag of 1 tonf (10 kN) on an asphalt pavement from a height of 1 m and 2 m.
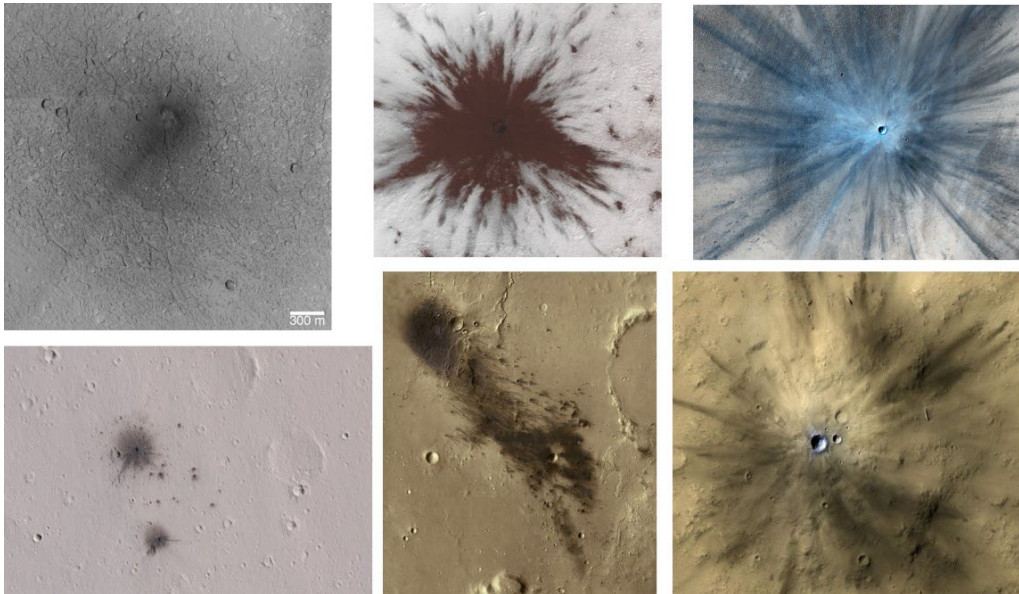
FIG 3 – Some recent meteorite impacts in Mars.
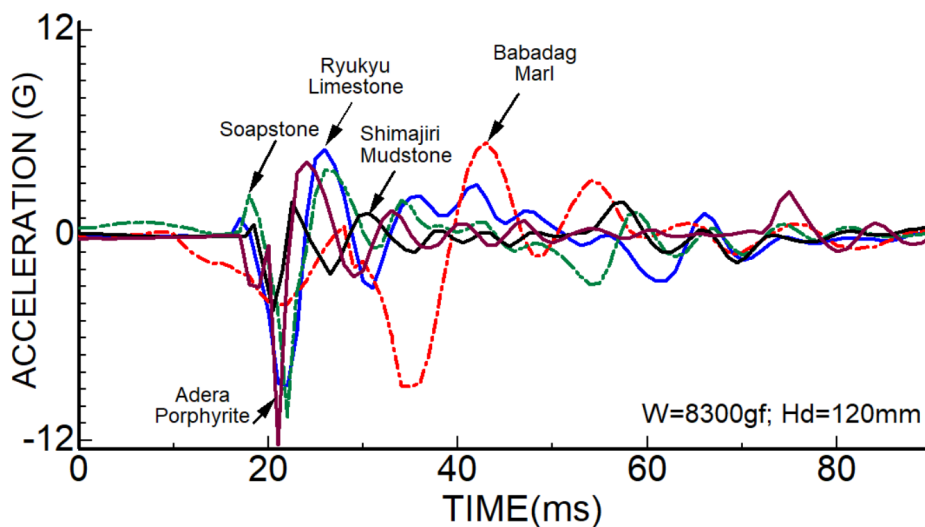
FIG 4 – Some examples of accelerations induced by an impact object hitting various rock samples.
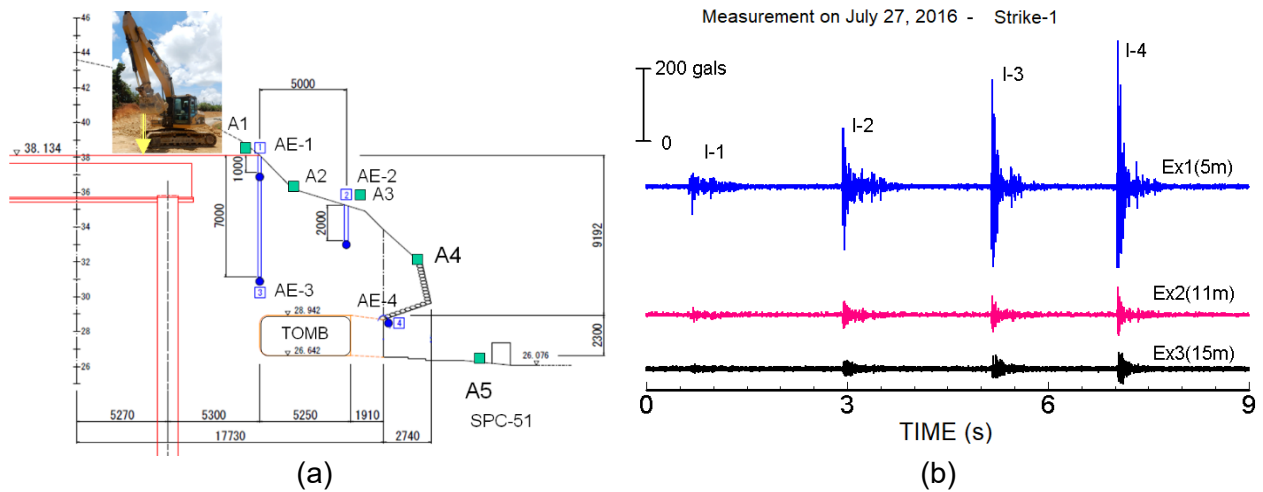
FIG 5 – Impact monitoring at a limestone construction site: (a) Impact location and position of sensors, and (b) recorded accelerations (from Aydan, 2017b).
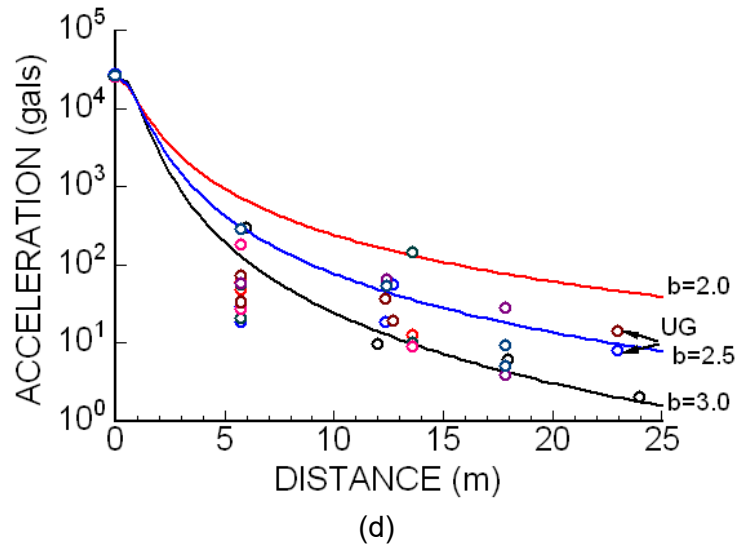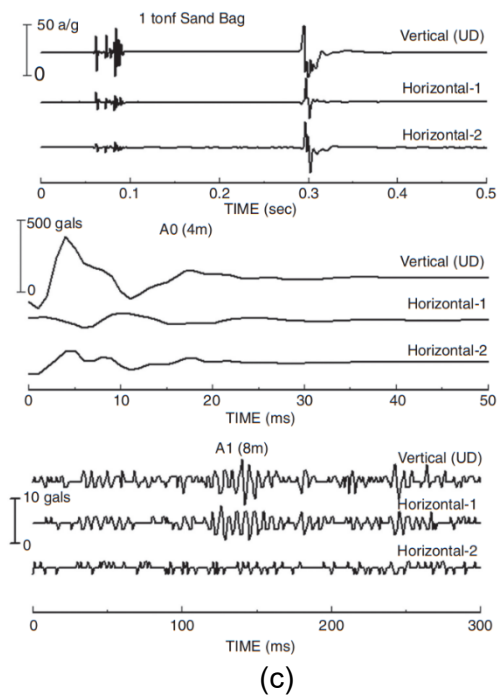
FIG 6 – Vibrations measurements on (a) the asphalt paved embankment of a runway and nearby (b) underground facility (from Aydan, 2017b). (c) Measured vibrations, (d) attenuation of maximum acceleration.

VIBRATIONS DUE TO WHEELS OF ROVERS AND THEIR EFFECTS

When one closely examines the images from the MERs, one can easily notice the effects of vibrations induced by their metallic wheels as seen in some of images released by NASA (2022). The recent video released about the sounds caused by the perseverance exploration rover clearly indicated some shock-like vibrations when the rovers pass over rock fragments. The effects of the vibrations caused by the metallic wheels are quite high on the hilly ground and overhanging rock blocks and layers and some surficial sliding and block sliding/falls occurred. Figure 7 shows some such examples. It seems that the vibrations caused by metal wheels of MERs during roving are probably amplified. Figures 8 and 9 show the amplification of motions on the top of model slopes with/without toe erosion subjected to base acceleration during sweeping tests in shaking table tests. The vibrations may be amplified up to 4–5 times that at the base.

FIG 7 – Sliding or fall of rock blocks and surficial sliding.
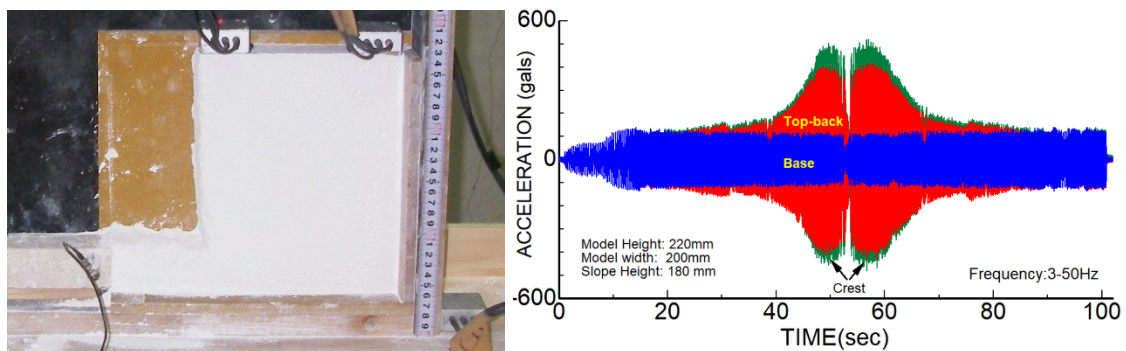
FIG 8 – A view of a steep model slope without toe erosion and its sweeping response.
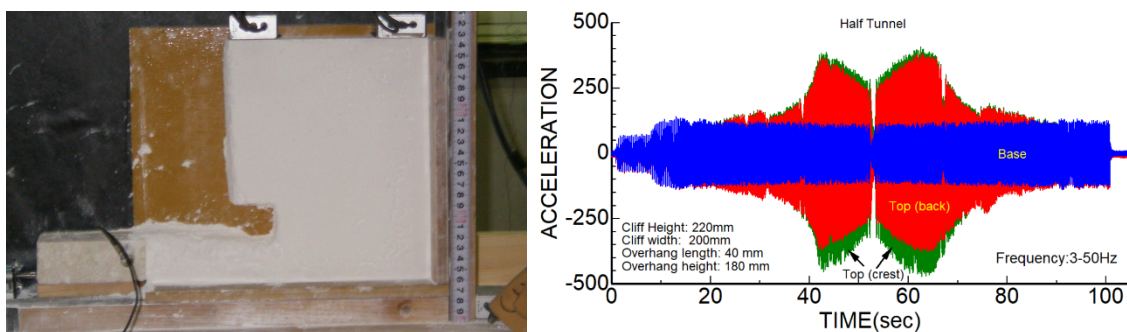
FIG 9 – A view of a steep model slope with toe erosion and its sweeping response.

DRILLING AND GRINDING INDUCED VIBRATIONS AND THEIR EFFECTS

The MERs are equipped with drilling and grinding tools for investigating rock surfaces and rock blocks. During operations, the drilling and grinding processes induce some vibrations and they cause

either fracturing and/or displacing rock blocks. The soil deposits on the target rock block surfaces are also displaced or sink along existing rock fractures. Figure 10 shows such effects of the vibrations induced during drilling/grinding operations. In addition, the weight of the MERs caused some fracturing of thin platy or elongated rock pieces due to bending stresses.

FIG 10 – The effects of drilling/grinding operations on target rocks and their surroundings.

Basalt of vesicular type are commonly observed on various parts of Mars. Although basalt is known to be very high strength rock, its porous structure causes the overall reduction of the strength. The samples from Mt. Fuji from Japan, Aswan from Egypt and Wanda Mines near Iguassu Falls in Argentina were utilised for measuring the vibrations caused during drilling and grinding (Figure 11). As examples, vibration measurements on vesicular basalt samples from Mt. Fuji were selected and some vibrations measurements grinding/drilling operations were recorded. Figures 12 and 13 show some acceleration records obtained from the stand-alone type QV3-OAM-SYN accelerometer during grinding/drilling operations. The surface was vertical and accelerations were measured parallel and perpendicular to the surface of grinding/drilling and vertical direction of the block. Regarding grinding operation, the largest acceleration occurred perpendicular to the grinding surface and it can be up to 2200 gals while the other components were about 1500 gals. As for drilling operations, the maximum accelerations were less than 900 gals and the largest acceleration occurred perpendicular to the drilling surface.

FIG 11 – Views of samples and mounted bits.
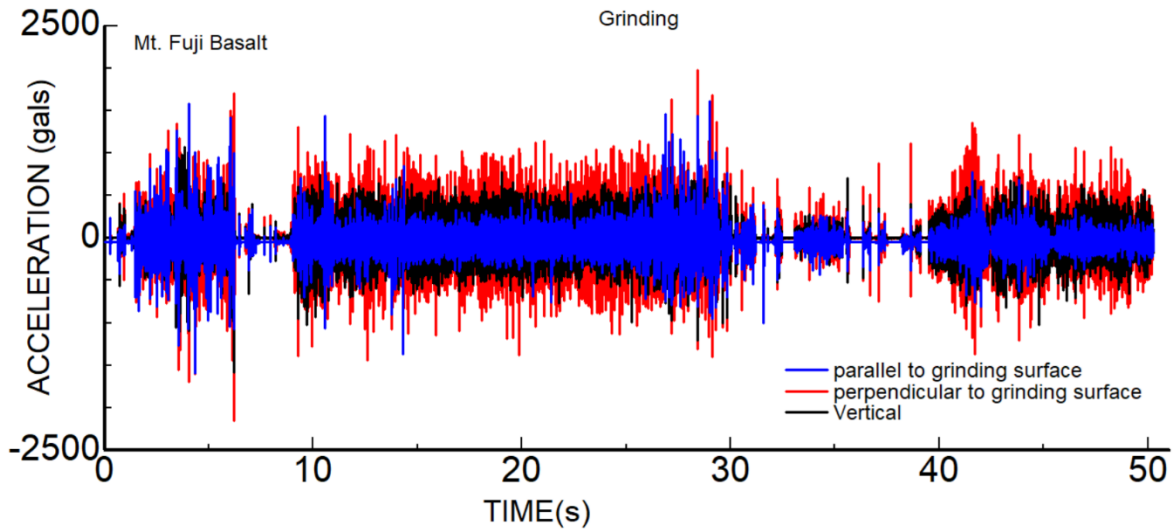
FIG 12 – Records of accelerations induced during grinding operation.
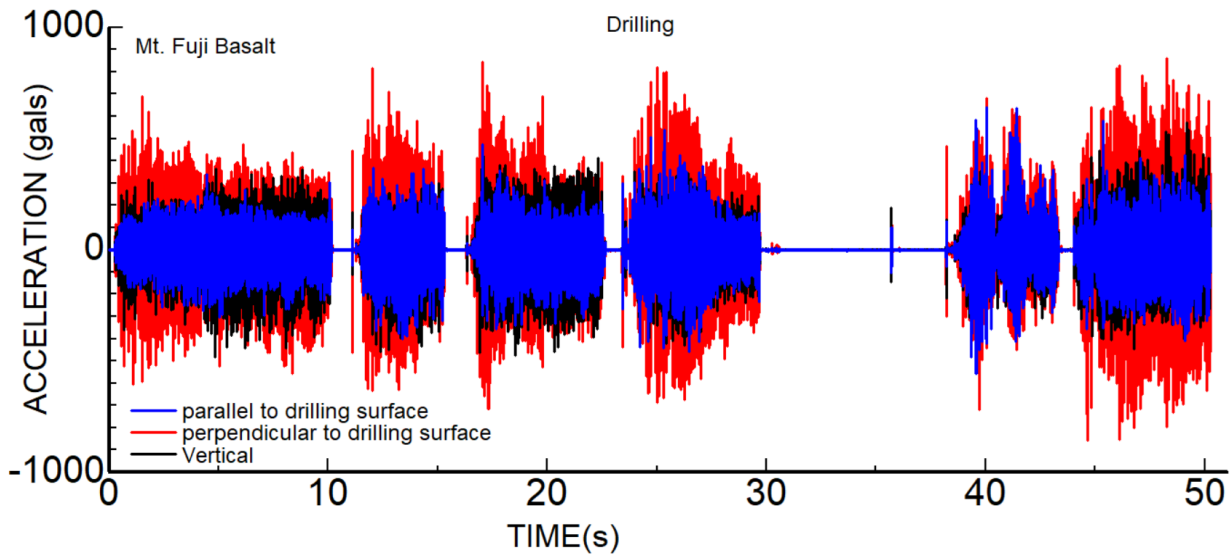
FIG 13 – Records of accelerations induced during drilling operation.

BLOCK MOVEMENTS

Images from the MERs also revealed displaced blocks probably due to vibrations resulting from impacts of meteorites and/or Marsquakes. In order to have an insight into the mechanism of block movements, some experiments reported by Aydan (2017b, 2020a, 2022) are referred herein. Sliding experiments on Ryukyu limestone blocks having a size of 100 × 80 × 40 mm were carried out by changing the inclination of base plate, which is also made of Ryukyu limestone. The inclination of base plate was 30 and 60 degrees. Figure 14a shows a schematic drawing of the test set-up. The motion of the block was restrained and the accelerations are continuously measured throughout the experiment. Figure 14b shows the acceleration records. As noted from the figure, the acceleration acting on the block is closely related to the excessive sliding force, which is given below:

$$a_s = g(\sin\alpha - \cos\alpha \tan\phi) \qquad (1)$$

Where ϕ is friction angle of the plane inclined at an angle α .

The acceleration of the block, which can be inferred from Equation 1, remains the same during sliding and it has the maximum value when the block hits the restraining wall. In other words, the acceleration is small and constant if the sliding velocity is constant. However, the acceleration is quite high when the block movement was restrained and it is more than six times the gravitational acceleration.
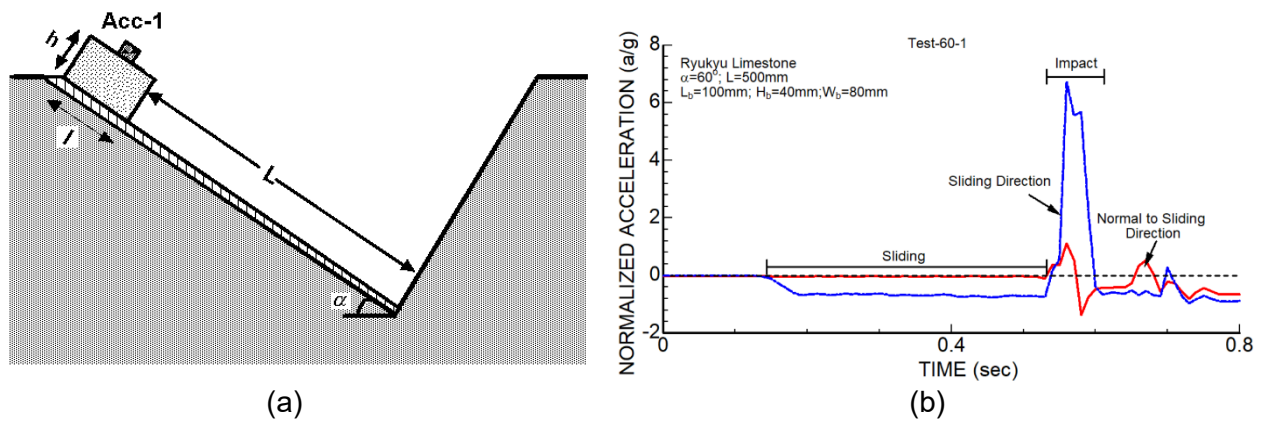
FIG 14 – Sliding and impact response of ryukyu limestone block (100 × 80 × 40 mm) on Ryukyu limestone base block (500 × 100 × 20 mm) (modified from Aydan, 2017b).

A rock block displaced on Mars shown in Figure 15a is considered and the conditions for its motion are analysed herein. The travel path length was 675 cm and the inclination of the path was almost 23.5 degrees. As rocks at the site were inferred to be basaltic, the result of a dynamic friction experiment on a saw-cut discontinuity of basalt from Mt. Fuji was utilised (Aydan, 2022). The simple mechanical considerations shown in Figure 15b yielded that the maximum acceleration and velocity to displacement of the rock block as given below:

Maximum Acceleration: 42.13 cm/s2

Maximum Velocity: 238.5 cm/s
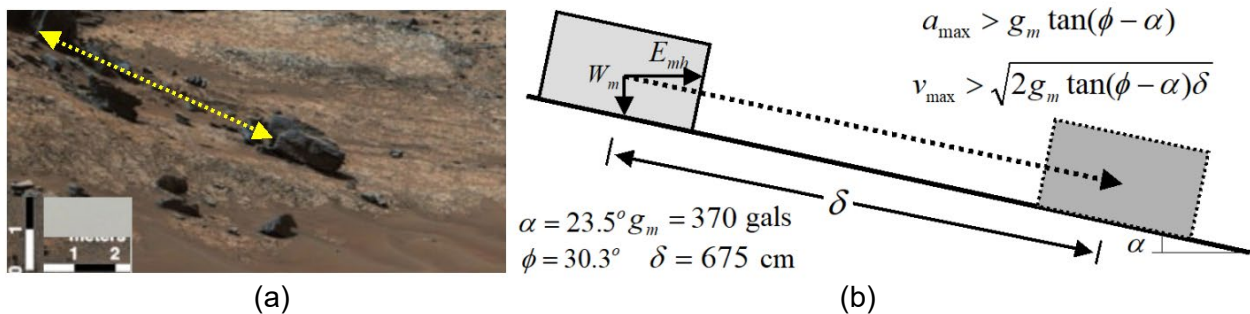
FIG 15 – (a) A view of displaced block on Mars and (b) a mechanical model of rock block subjected to gravity and impact forces.

The magnitude of the earthquake for this maximum ground acceleration value could be estimated to be about 3.8–3.9 using some empirical relations developed for earthquakes on Earth (Aydan, 2012). This class Marsquake is a very likely situation as NASA reported a Marsquake with a magnitude of 5 on May 4, 2022. As understood from this simple example, rock dynamics would be necessary for the assessment of various rock mechanics and rock engineering issues in Mars and other planets.

CONCLUSIONS

The rock mechanics aspects of Mars are fundamentally similar to those of the Earth and the differences result from gravitational acceleration, climatic conditions (temperature, humidity, winds), thickness of atmosphere and none or limited amount of groundwater. The rock dynamics issues in Mars are also likely to be quite similar to those on Earth. Although it is quite difficult to cover all aspects of rock dynamics, this study provides some insight to the rock dynamics issues of Mars to be encountered by mankind. Some of major conclusions are as follow:

- Vibrations caused by some of Marsquakes and meteorite impacts are one of the major rock dynamic issues in Mars and their effects can be evaluated using the principles and methods developed for those on Earth.

- The MERs induce very high vibrations due to their metallic wheels in rough rocky paths and they cause the movement of some sand deposits and rock blocks even small-scale rock slopes failures due to amplifications of the accelerations. More quantitative data on the vibrations caused by MERs in the environment of Mars would be quite useful for further investigations.

- Grinding/drilling operations induce some vibrations, which also cause some fracturing of rock of Mars and displacing of soil deposits. Particularly grinding operation may induce high acceleration compared to drilling operations.

- Block movements due to vibrations caused by Marsquakes and meteorite impacts in Mars can be evaluated using the methodology developed for those on earth with appropriate considerations of gravitational acceleration differences.

ACKNOWLEDGEMENTS

REFERENCES

Aydan, Ö, 2012. Ground motions and deformations associated with earthquake faulting and their effects on the safety of engineering structures, *Encyclopedia of Sustainability Science and Technology*, R Meyers (ed.), pp 3233–3253, Springer.

Aydan, Ö, 2017a. Some Thoughts About Rock Mechanics Aspects of Mars, UNSW, *3rd Off Earth Mining Forum – 2017OEMF*.

Aydan, Ö, 2017b. *Rock Dynamics*, CRC Press, 457 p.

Aydan, Ö, 2020a. *Rock Mechanics and Roc Engineering: Fundamentals,* CRC Press, 406 p.

Aydan, Ö, 2020b. *Rock Mechanics and Roc Engineering: Applications*, CRC Press, 410 p.

Aydan, Ö, 2022. Some thoughts on rock slope stability issues in Mars. *EUROCK2022*, 10 p.

NASA, 2008. Exploration: NASA's plans to explore the moon, mars and beyond. http://www.nasa.gov/

NASA, 2022. Images. https://mars.nasa.gov/mer/gallery/images.html

Lunar sub-surface temperatures

N Barnett[1], T Warren[2], A Dempster[3], J Oh[4] and S Saydam[5]

1. PhD candidate, Minerals and Energy Resources Engineering, UNSW Sydney NSW 2052. Email: nicholas.barnett@student.unsw.edu.au
2. Postdoctoral Research Assistant, Atmospheric, Oceanic and Planetary Physics, University of Oxford, UK. Email: tristram.warren@physics.ox.ac.uk
3. Professor, Electrical Engineering and Telecommunications, UNSW Sydney NSW 2052. Email: a.dempster@unsw.edu.au
4. Associate Professor, Minerals and Energy Resources Engineering, UNSW Sydney NSW 2052. Email: joung.oh@unsw.edu.au
5. Professor, Minerals and Energy Resources Engineering, UNSW Sydney NSW 2052. Email: s.saydam@unsw.edu.au

INTRODUCTION

The influence of the insulating properties of lunar regolith was shown in the sub-surface temperature tests performed by the Apollo missions, with no significant temperature fluctuations occurring below 80 cm from the lunar surface even if surface temperatures fluctuated >200 K between lunar days and nights (Heiken *et al*, 1991). Key to the thermal insulation of the regolith is its low density near the surface having the greatest insulative effect with the lunar regolith becomes denser with depth. As the regolith becomes denser, the thermal conductivity of the regolith increases (Hayne *et al*, 2017).

Thermal modelling software, Oxford 3D Thermal Model, which mapped the lunar surface temperatures effect on the thermal influence at the lunar south pole sub-surface over a lunar year found areas with brief illumination with surface temperatures >120 K could have sub-surface temperatures <112 K that can sustain long-term stable water ice at depths of <30 cm (Paige *et al*, 1992; King *et al*, 2020). Further to this, the observation of water molecules or other hydroxyls by the NASA/DLR Stratospheric Observatory for Infrared Astronomy (SOFIA) in non-permanently shadowed regions (PSRs) on the Moon, indicated that water could be present beyond PSRs (Honniball *et al*, 2021).

Using the Oxford 3D Thermal Model in selected regions in the lunar south pole, can provide insights into the location and depth of cold traps that could sustain water ice.

OXFORD 3D THERMAL MODEL

Oxford 3D Thermal Model (O3DTM) is able to determine the lunar surface temperature profile at high latitudes and subsequent sub-surface thermal profile by combining the one-dimensional sub-surface heat flow Hayne model and 3D shadowing and scattering effects (King *et al*, 2020). O3DTM models the sub-surface temperature profile through a three-part simulation:

1. Calculates the thermal energy flux at any given location through the lunar year.

2. Determines the error of the calculated surface temperature with Diviner satellite surface temperature data.

3. Determines the sub-surface temperature profile over the lunar year.

For the surface thermal modelling of the selected region, the Vasavada-Hayne density profile of the regolith was consistent throughout the lunar surface (Figure 1), used a grid spacing frequency of 16 ppd (pixels per degree). For each grid-point the sub-surface is logarithmically mapped using 26 distinct layers, as the thermal insulative influence of the regolith decreases with depth, to a maximum depth of 2.65 m. The thermal mapping was performed throughout a full lunar year to capture the seasonal cycles at a frequency between each time stamp of <2.5 hrs.
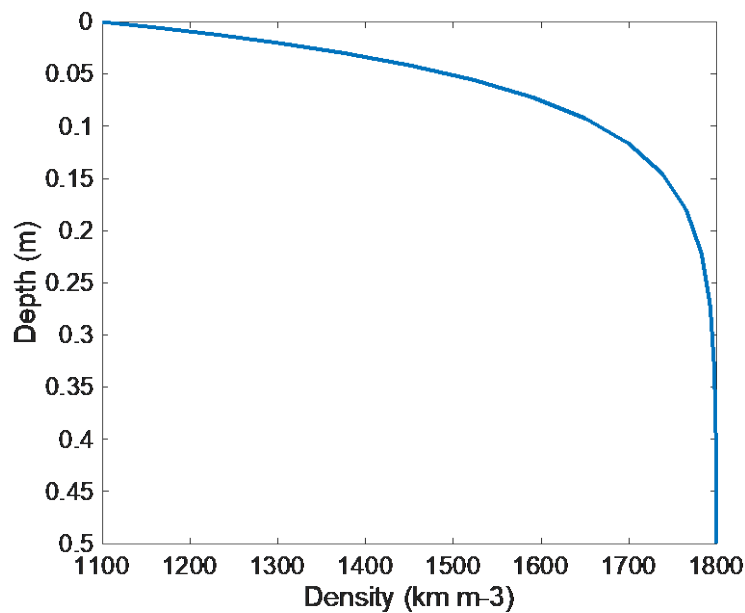
FIG 1 – Regolith density profile using Vasavada sub-surface density profile equation (Vasavada *et al*, 2012) using p_s = 1100 kg/m^3, p_d = 1800 kg/m^3 and H = 0.06 m (Hayne *et al*, 2017).

RESULTS AND DISCUSSION

Results from Oxford 3DTM indicate regions that have cold traps which could contain water ice can reside below lunar regions that have surface temperatures greater than 200 K over the period of a lunar year. Three sites were analysed around the modelled region, two with maximum surface temperatures (Sites #1 and #2) above 180 K and a third site located within a permanently shadowed region (Site #3) (see Table 1). The model determined that all three locations have the ability to sustain cold traps that are colder than 112 K at depths greater than 20 cm through to the maximum modelled depth of 2.65 m.

TABLE 1

Location of the three sites.

Site	Latitude (°)	Longitude (°)
1	-73.91	251.66
2	-79.09	244.91
3	-78.97	252.47

The minimum and maximum sub-surface temperature profile provides an analysis as to the temperature extremes at each depth throughout the entire lunar year (Figure 2). Sites #1 and #2 are located inside the northern rim of craters, with Site #1 experiencing maximum surface temperatures above 230 K during the lunar summer and Site #2 reaching maximum surface temperatures above 180 K. Site #3 is located inside a permanently shadowed region with maximum surface temperatures not reaching above 80 K throughout the lunar year. At depths >20 cm through to the modelled depth of 2.65 m, all three locations have sub-surface temperatures less than 112 K.
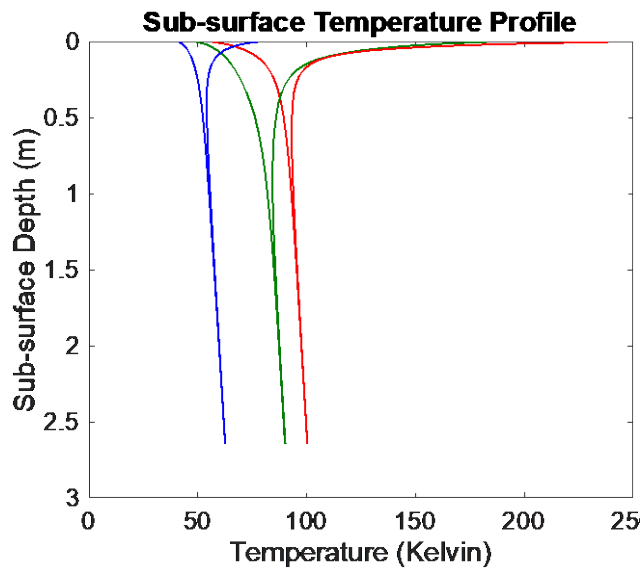
FIG 2 – The minimum and maximum cross-sectional sub-surface temperature profile from surface to 2.65 m deep for the three selected sites: Site #1 (red), Site #2 (green) and Site #3 (blue).

Figure 3 shows the surface temperature across the region (a) and the cross-sectional temperature profile across the region (b) shows two PSRs located at approximately -79°S and 252–255°E. The remaining mapped region has a maximum surface temperature >150 K. At 0.6 m below surface, the maximum temperature through the entire lunar year across the band between 79°S and 80°S remains <120 K, with two traps colder than 112 K located between 246.5°–255.5°E and 242.5°–247.5°.
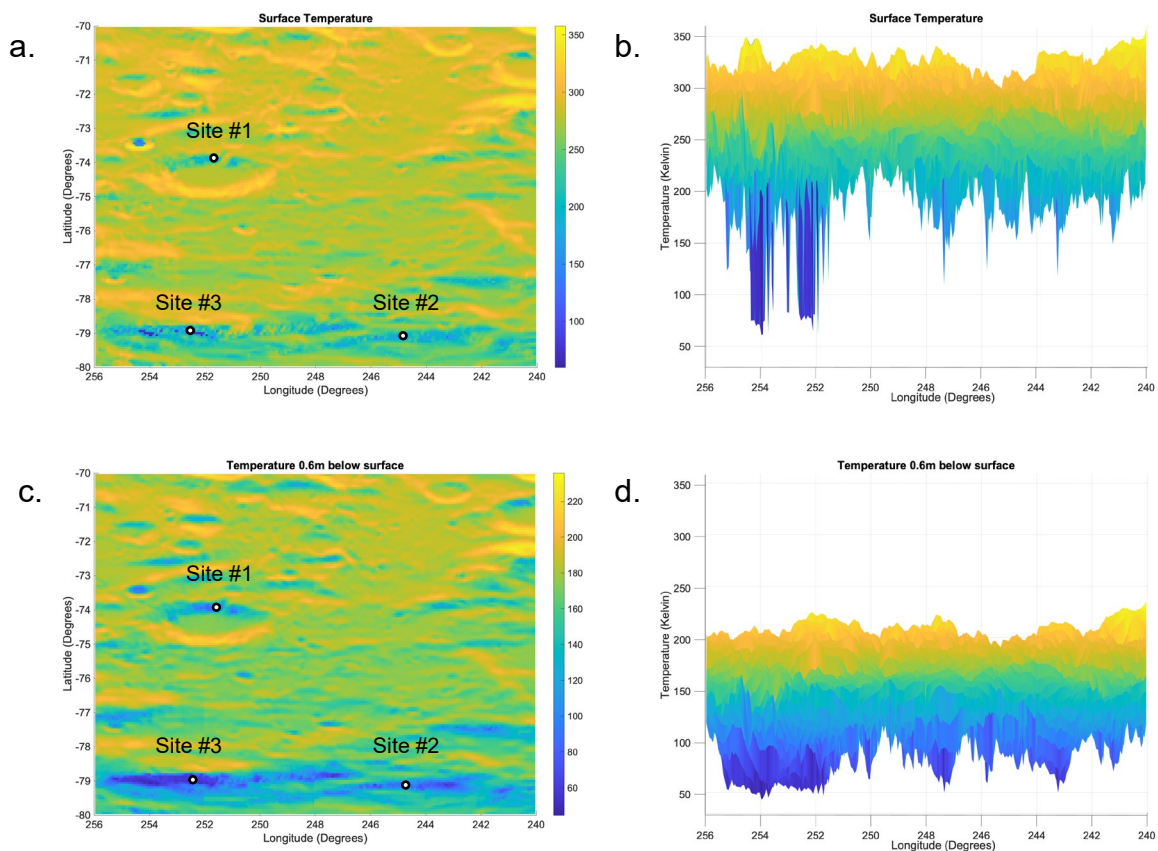
FIG 3 – O3DTM modelled maximum surface temperature (a, b) and the maximum temperature at 0.6 m below surface (c, d) across the region for an entire lunar year. (a) and (c) provide a top view of the maximum temperatures over the mapped region, and (b) and (d) are a cross-sectional view of the mapped region, displaying the maximum temperatures at surface and 0.6 m below surface.

Further analysis of the results is required to determine the exact location, size and depth of each cold trap within the region.

MODEL ACCURACY

There is currently no reference temperature profile for the lunar south pole region, so the surface temperature profile is compared with the measurements from the Lunar Reconnaissance Orbiter's Diviner Lunar Radiometer instrument (Diviner). Due to the resolution of the LOLA attitude data, O3DTM could have up to 30 K difference between the model and Diviner temperatures at higher latitudes, as seen by the example at Site #1 (Figure 4).
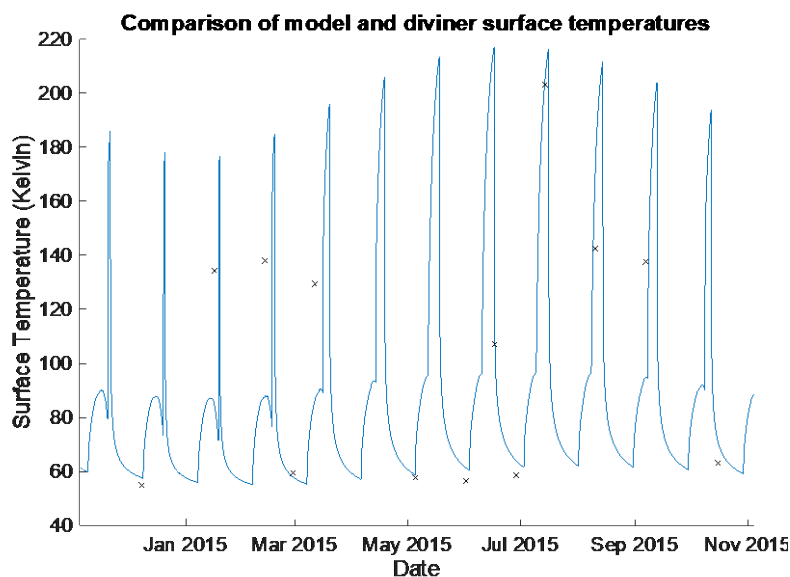
FIG 4 – O3DTM calculated surface temperatures (blue line) are mapped against recorded surface temperatures by Diviner (block crosses) at Site #1.

CONCLUSION

The thermal results of the mapped region using O3DTM provides an understanding of the thermal behaviour of the lunar sub-surface throughout the lunar year. These results indicate that the surface thermal influence results in thermal fluctuations down to depths of 1.5 m below the surface. Such thermal fluctuations of the lunar regolith could result in the thermal expansion and contraction of the regolith, that can lead to the presence of a dynamic *in situ* stress environment which varies throughout the lunar year.

The O3DTM sub-surface thermal map can provide temperature profile within the lunar regolith that can be used as heat sinks, thermal insulation and/or maintaining thermal stability for infrastructure and services.

Based on the modelling using Oxford 3DTM, cold traps that can sustain ice water (<112 K) are able to exist beyond permanently shadowed regions, with some regions sustaining a buried cold trap when maximum annual surface temperatures exceed 200 K. The depth of the cold traps can be <60 cm below the surface and they are able to be continuously connected and quite large: 10's km in length and >3 km wide.

ACKNOWLEDGEMENTS

REFERENCES

Hayne, P B J, Siegler, M, Vasavada, A, Ghent, R, Williams, J, Greenhagen, B, Aharonson, O, Elder, C, Lucey, P, Paige, D, 2017. Global regolith thermophysical properties of the Moon from the Diviner Lunar Radiometer Experiment, *Journal of Geophysical Research: Planets*, pp. 2371–2400. 10.1002/2017JE005387

Heiken, G H, Vaniman, D T and French, B M, (eds.), 1991. *Lunar Sourcebook: A User's Guide to the Moon*, Cambridge University Press.

Honniball, C, Lucey, P, Li, S, Shenoy, S, Orlando, T, Hibbitts, C, Hurley, D and Farrell, W, 2021. Molecular water detected on the sunlit Moon by SOFIA, *Nature Astronomy*, 5:1-7. 10.1038/s41550-020-01222-x

King, O, Warren, T, Bowles, N, Sefton-Nash, E, Fisackerly, R and Trautner, R, 2020. The Oxford 3D thermophysical model with application to PROSPECT/Luna 27 study landing sites, *Planetary and Space Science,* 182(March):104790. https://doi.org/10.1016/j.pss.2019.104790.

Paige, D A, Wood, S E and Vasavada, AR, 1992. The thermal stability of water ice at the poles of mercury, *Science*, 258(5082):643-646.

Vasavada, A, Bandfield, J, Greenhagen, B, Hayne, P, Siegler, M, Williams, J-P, Paige, D and Williams, J-P, 2012. Lunar equatorial surface temperatures and regolith properties from the Diviner Lunar Radiometer Experiment, *Journal of Geophysical Research*, 117. 10.1029/2011JE003987.

A quantitative risk assessment tool for geothermal outbursts at Lihir Gold Mine

D Bringemeier[1,6], Y Zhang[2], M Zoorabadi[3], N Kerr[4] and S Nicoll[5]

1. Technical Principal – Hydrogeology, SMEC, Brisbane Qld 4006.
   Email: detlef.bringemeier@smec.com
2. Hydrogeologist, WSP Golder, Brisbane Qld 4006. Email: ying.zhang@wsp.com
3. Technical Principal – Geotechnics and Tunnels, SMEC, Melbourne Vic 3004.
   Email: mahdi.zoorabadi@smec.com
4. Principal – Hot Ground Mining, Newcrest Mining Limited, Melbourne Vic 3004.
   Email: nicholas.kerr@newcrest.com.au
5. Senior Specialist – Geotech/Geothermal/Hydro, Newcrest Mining Limited, Brisbane Qld 4006.
   Email: sam.nicoll@newcrest.com.au
6. Adjunct Professor, University of Queensland, Geotechnical Engineering Centre, St Lucia Qld 4072.

INTRODUCTION

Lihir operations of Newcrest Mining Limited (NML) are on Lihir Island (PNG) which is located approximately 900 km north-north-east of the national capital Port Moresby. The mine is located within the Luise Caldera of the Luise Volcano which is located on the east coast of the island. The caldera is an extinct volcanic crater that is geothermally active. Volcanic activity on Lihir Island is limited to remnant hydrothermal venting in the Luise Caldera in the form of hot springs and fumaroles. Steam and gas (including H_2S) naturally discharge within the pit area and along the Kapit beach and near shore region. The hydrothermal reservoir temperatures can reach 100°C at the water table and exceed 200°C at depth. Newcrest maintains a Geo-hazard Management Plan to identify and manage the various geotechnical and geothermal hazards on-site. The major geothermal hazard to mining at Lihir is the occurrence of geothermal outbursts, which have occurred in the past with varying intensities and caused two 'near misses', production delays and material losses.

GEOTHERMAL OUTBURST MECHANISM

Eruptions in hydrothermal systems are violent phenomena, which result in an explosive release of energy generated by the mechanical work of expanding fluids. The main cause of these explosive events is the presence of hot and pressurised water at near surface conditions and its expansion as gas phase or liquid flashing to steam is driving these events. Hydrothermal eruptions specifically involve water close to its boiling temperature. These types of eruptions are generated in the near-surface, and result from the (rapid) formation of steam following a (sudden) pressure decrease. Highly permeable rock mass systems are likely to efficiently release steam generated during these changes, thus largely preventing pressure build-up and explosive events. However, if such a system is capped and trapped by low-permeability layers, steam may not escape efficiently, and pressurisation of the groundwater or geothermal system can result. Sufficient pressurisation may cause rupture of the capping layers, initiating rapid depressurisation and thus an explosive event.

Two endmember mechanism are proposed for historical outbursts at Lihir mine:

- Type I outbursts are understood to be driven by gas/vapor-filled voids of any form and are typically of relatively low energy, however, occur more frequently (Figure 1a).

- Type II outbursts involves higher energy events and seem to have a tectonically controlled component including larger network of fissures with connections to deeper parts of the hydrothermal system (Figure 1b and 1c).

Trigger mechanisms for both type of outburst can be quite similar. The main difference lies in the characteristics of the reservoir that is involved in the outburst event. The main trigger is the reduction of pressure at the outburst site. This can happen due to mining, or landslides (eg after heavy rainfalls or as a result of earthquakes).
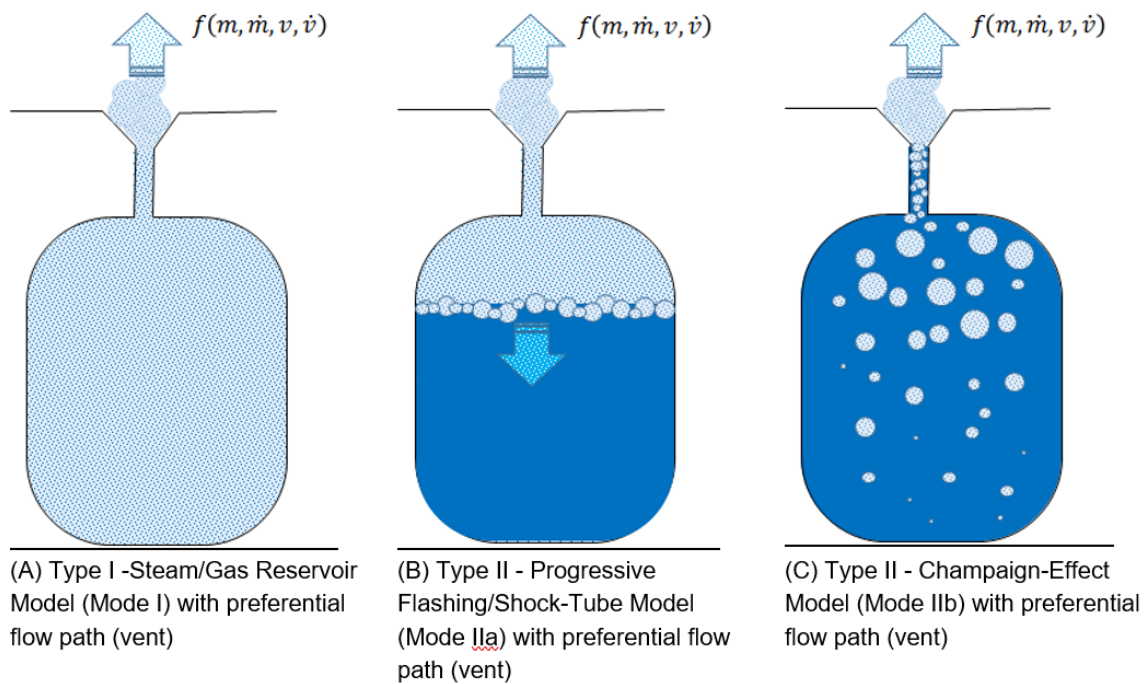
FIG 1 – Conceptual models of hydrothermal outbursts.

LIHIR OUTBURST RISK ASSESSMENT TOOL

Considering the limitation of the complex thermo-hydro-mechanical numerical modelling for large scale simulations, a quantitative, location specific outburst risk assessment model has been developed for Lihir mine. This model, coded in Matlab and compiled to a computer supported tool, is referred to as Lihir Outburst Risk Assessment Tool (LORAT). The development of LORAT follows a practical approach:

- Select simple models, such as approximating analytical expressions and empirical correlations that describe dynamic of hydrothermal eruptions.

- Combine simple models to simulate the possible evolution of an outburst, from the time of initiation to the vertical jetting phase.

LORAT estimates the minimum depth of cover and the amount of fluid released as a consequence of an assumed outburst. This estimate requires the knowledge of the type of cap rock concealing superheated fluid from the atmosphere, the rock containing the fluid (the reservoir) and the thermodynamic conditions of the reservoir. These properties are obtained from data files containing UniServices geothermal modelling results and stored in the LORAT database and are available for interrogation through the LORAT GUI and for the outburst risk analysis calculations. The thermodynamic conditions of the reservoir (typically pressure, temperature and phase saturation within matrix and fracture cells of the geothermal model) highly influence the outcome of outburst initiation and physical effect simulation. In particular, a fluid may occur as a compressed gas and/or vapour or pressurised superheated liquid water.

This software is specifically intended to assist the Lihir Mine Geothermal Team in the risk assessment of geothermal hazards. More specifically, LORAT is designed to implement the calculation of the following physical effects of an outburst:

- steam flux

- kinetic steam energy

- venting steam velocity

- rock fragment velocity

- impact velocity.

In addition, LORAT incorporates a qualitative risk assessment tool, which combines for every mining block the potential for an outburst to occur with the outburst consequence which itself is derived from physical effects estimated with LORAT.

As a preliminarily test, LORAT has been validated using historical Lihir outburst records from 2016. Calculations with LORAT show mining blocks with elevated (medium) outburst potential match well with locations of 2016 outbursts (Figure 2). Further validation would be required to improve the confidence in the predictive capability once more data become available.
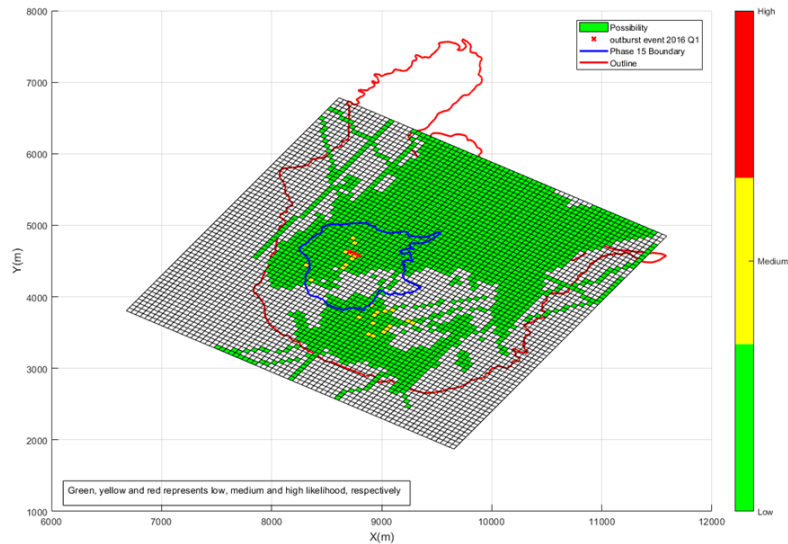
FIG 2 – Outburst potential for 50 × 50 × 12 m mining blocks calculated with LORAT and Lihir outburst locations for 2016.

OUTLOOK

The site team are concentrating on measuring shallow pressure environment via packer testing, and other sensors. Depressurisation efforts in the form of vertical and horizontal relief drilling have been the main control to relieve zones of high pressure. As mining moves north into the main geothermal upflow domain, direct measurement of the shallow pressure environment will be an important verification control. Site engineers are currently investigating the suitable application of high temperature packer technology for use in 12–48 m drill holes, within the active mining bench. This data set will help correlate the shallow temperate/pressure relationship and validate the effectiveness of depressurisation via relief drilling.

Design, implementation and field performance of a face destress blasting method for mine development

C Drover[1], E Villaescusa[2] and I Onederra[3]

1. Principal Engineer, Beck Engineering, Sydney NSW 2067. Email: cdrover@beck.engineering
2. Professor, Curtin University, Kalgoorlie WA 6430. Email: E.Villaescusa@curtin.edu.au
3. Associate Professor, University of Queensland, St Lucia Qld 4067.
   Email: i.onederra@uq.edu.au

ABSTRACT

Development face destress blasting is a construction technique in deep mining, which aims to prevent, reduce the frequency, or manipulate the timing of violent, stress-driven rock mass instability at the face. This paper presents a destress blasting design concept that was optimised for the specific rock mass conditions of a deep mine using the Hybrid Stress Blasting Model (HSBM) software. The design was then implemented in an area of the mine where stress-driven instability of the face regularly occurred during development. An adjacent tunnel was constructed in parallel without destressing, within the same rock mass conditions, as a control. The rock mass response to each excavation was quantitatively compared using high-resolution local seismic monitoring. Visual observations of the fractures created by destress blasting were also made. The analysis indicated that destressing reduced both seismicity and the rock mass stiffness ahead of the face. This was inferred from the spatial broadening of the development seismogenic zone and the typically significant reduction in the spatial density of seismic events. Seismic source mechanism analysis also indicated that destress blasting generated a much wider variety of failure modes than conventional blasting. Most seismic source mechanisms following destressing were associated with natural joint structures. A relatively small portion were consistent with newly created blast-induced fractures. The greater diversity of rock mass failure modes associated with destressing implied a lower potential for stain-energy accumulation within the rock mass at the face, and thus a lower risk of hazardous instability. Observations of visible rock fracturing indicated that the major principal stress influenced the damage intensity on natural geological structures within the destressed zone, and that numerical predictions of radial fracturing limits made by HSBM analysis were realistic representations of the real blasting performance.

INTRODUCTION

High stress concentrations at the mine development tunnel face may result in large volumes of rock being dynamically ejected into the work area (Figure 1). This poses a significant hazard to the construction workforce. Face destress blasting seeks to reduce this risk by using controlled detonations of explosives to manipulate the rock mass behaviour. Effective face destressing is difficult to verify in practice, due to the complex rock mass conditions and the difficulty in accurately quantifying the mechanical response to the creation of the destressed excavation. However, as mine development advances to greater depths, and tunnel face instability becomes more difficult to manage safely, the need for a validated engineering approach to face destressing blast design and implementation is becoming increasingly important. Ideally, destressing designs should be optimised on a case-by-case basis, considering the specific conditions of rock strength, induced stress and geological structure where the design is to be implemented. These factors play a major role in defining the extent of blast-induced fracturing, the rock mass response to mining and ultimately the destressing performance (Drover *et al*, 2018).

FIG 1 – Violent stress-driven instability of a development face with a significant ejection distance.

DESIGN

Examples of standard face destressing charge patterns have been described by Carr *et al* (1999) and O'Donnell (1999). Such designs have been applied in deep mines for many years and they are geometrically very similar. They commonly consist of a rectangular pattern of charges, with two to four central face holes parallel to the tunnel axis, and four or more charges angled into the tunnel perimeter through both the right and left hand side shoulder and lower wall. These designs have a large spacing between the charges. Results of HSBM numerical analysis (Figure 2) indicate that the length of blast-induced radial fracturing deceases as the stress increases. Given that rock mass destressing occurs primarily via shear on fractures (Saharan and Mitri, 2011), these numerical results suggest that standard blasting patterns may not be optimised for high stress conditions.

$\sigma_1 = 0$ MPa $\sigma_3 = 0$ MPa $\sigma_1 = 25$ MPa $\sigma_3 = 12$ MPa $\sigma_1 = 54$ MPa $\sigma_3 = 27$ MPa

Radial fracture interaction
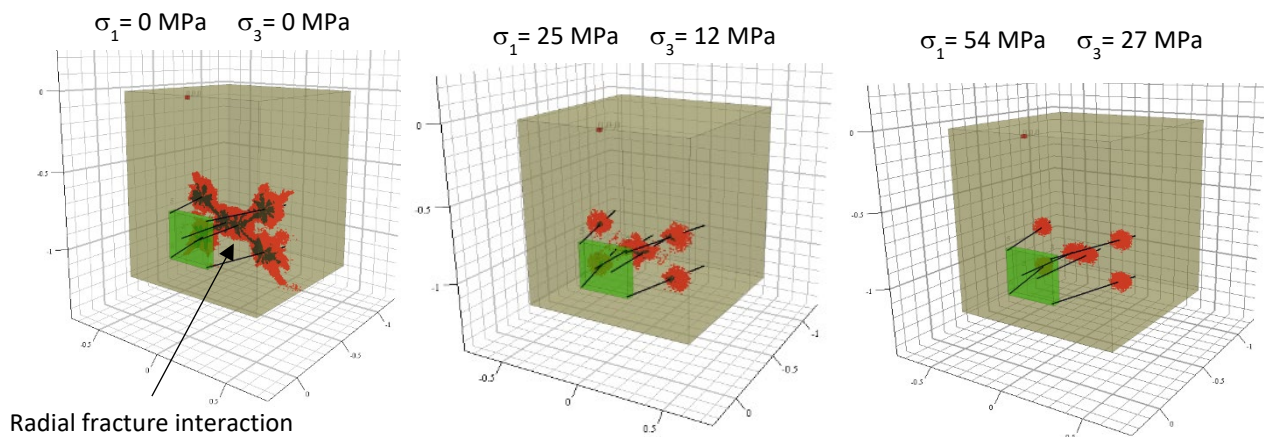
FIG 2 – HSBM numerical models of a standard face destress blasting pattern showing decreasing fracture interactions between the explosive charges as the induced stress increases.

An alternative face destress blasting design concept is illustrated in Figure 3 (Drover *et al*, 2018). The design consists of several parallel rows of destressing charges which are oriented subparallel, yet almost oblique to the major principal stress. The inter-row spacing of the charges was optimised for the specific rock mass conditions of a deep mine site, with fracture interaction desired between the charges. Each row of destressing charges was intended to create a plane of shear failure, with minimal deformation, ahead of the face, such that strain energy would be dissipated from the rock

mass. Shear was desired on not only the newly created radial fractures, but also the pre-existing natural geological structures. The important blast design parameters were as follows:

b   the destressing charge row burden (m).

s   the destressing charge inter-row spacing (m).

ϕ the destressing charge diameter (mm).

l_d the destressing charge length (m).

l_{rf} the maximum length of radial fracturing or joint dilation (m).

σ_1 the major principal stress (MPa).

σ_3 the minor principal stress (MPa).

$\Theta\sigma_1$ plunge of the major principal stress (degrees).

$\Theta\sigma_3$ plunge of the minor principal stress (degrees).

Θ_r the angle formed between the horizontal plane and rows of destressing charges and/or the continuous fracture plane.

Θ_f the angle formed between the horizontal plane and the imaginary line joining the opposite ends of the radial fracture tips of adjacent rows of destressing charges.

Θ_{rf} maximum angle of incidence between the plunge of the major principal stress and the angular limit of blasting induced fracturing.
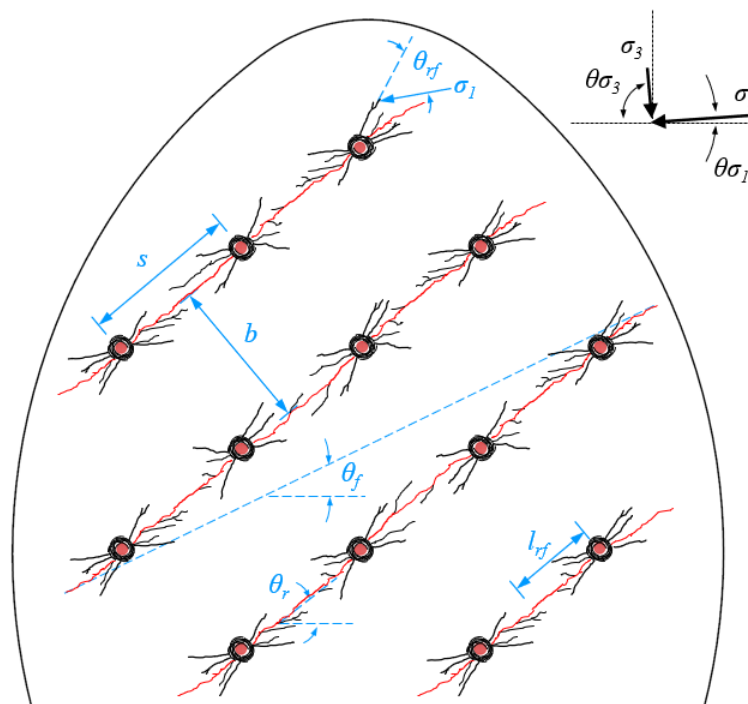
FIG 3 – Development face destress blasting concept diagram illustrating important design parameters and the conceptual relationship between the mining-induced stress, charge pattern layout and expected blast-induced radial fracture patterns (Drover *et al*, 2018).

Considering the observations of Jung *et al* (2001), the interaction of fractures from adjacent destressing charges was not expected in orientations subperpendicular to σ_1, ie across the burden. Therefore, the inter-row spacing between charges was the design parameter of greater importance when assessing crack interaction. The spacing dictates the amount of explosive work required for in-row fracture interaction between the destressing charges, with fracture interaction more likely for tighter spacing. For fracture interaction to occur reliably, $l_{rf} > s/2$, where l_{rf} may be estimated empirically or, preferably, via numerical blast modelling and field validation. The principal stresses were also critical considerations for the design. The magnitude of the main principal stress

component perpendicular to the tunnel axis (usually σ_1) controls fracture confinement, whereas its plunge guided the optimal angle (Θ_r) of the rows of destressing charges. In terms of the geometric design of the destressing rows, Θ_f was greater than $\Theta\sigma_1$ by a sufficient angle, in order to facilitate shear. Similarly, Θ_r differed from $\Theta\sigma_1$ by 30–40°, in order to promote shear deformation across the fracture planes. The parameter Θ_{rf} may vary, depending upon rock mass strength properties, the explosive energy of the destress charge, the prevailing stress conditions and orientations of any pre-existing geological discontinuities. In general, fracture interaction between explosive charges would be expected to occur only where $\Theta_r \leq \Theta\sigma_1 + \Theta_{rf}$.

This destressing blast design concept was numerically analysed in the HSBM software, in order to optimise the design parameters prior to a field trial. Numerical results of velocity attenuation for six detonation time steps at 10–4 second intervals post-firing are presented in Figure 4. The view is a cross-section at the mid-point of the charge column looking parallel to the longitudinal axis of the tunnel. The velocity attenuations are indicated by the colour scale. An index of incipient damage of 1000 mm/s was adopted and used to display the extent of potential disturbed zones, as well as interaction caused by the simultaneous initiation of destressing charges (Onederra *et al*, 2013). Black dot markers denote the locations of dislocated nodes (ie fractures) in the model. Given the realistic model inputs of σ_1 and σ_3, radial fracture interactions were only observed to span the spacing. The variability in velocity attenuation and damage for 1.5 m and 1.65 m charge spacings are illustrated in plan view in Figure 5. It is evident that the closer spacing of 1.5 m in the central destressing row of four holes (Figure 5a) produced a longer and more intense zone of interacting fractures than a 1.65 m borehole spacing (Figure 5b). In both cases, the zone of greatest fracture interaction is located at the toe of the charge. Based on these model results, an optimised charge spacing of 1.5 m was implemented during the destress blasting field trials.
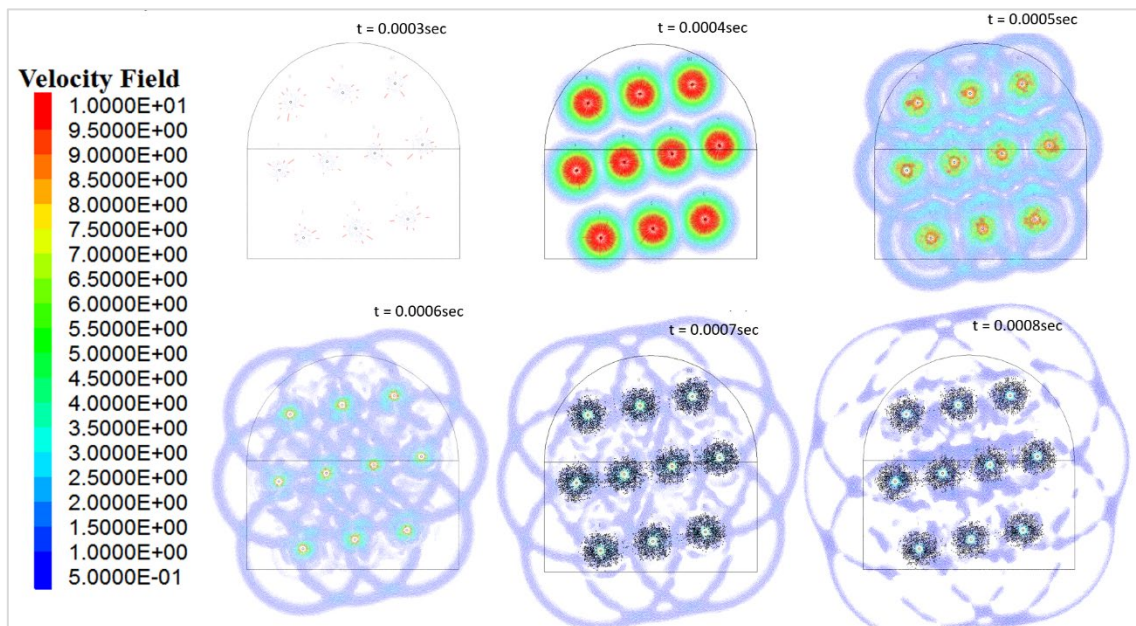
FIG 4 – Modelled velocity attenuation for several time steps post-initiation, showing propagation of the various wavefronts and simulated zones of blast-induced micro-fractures.
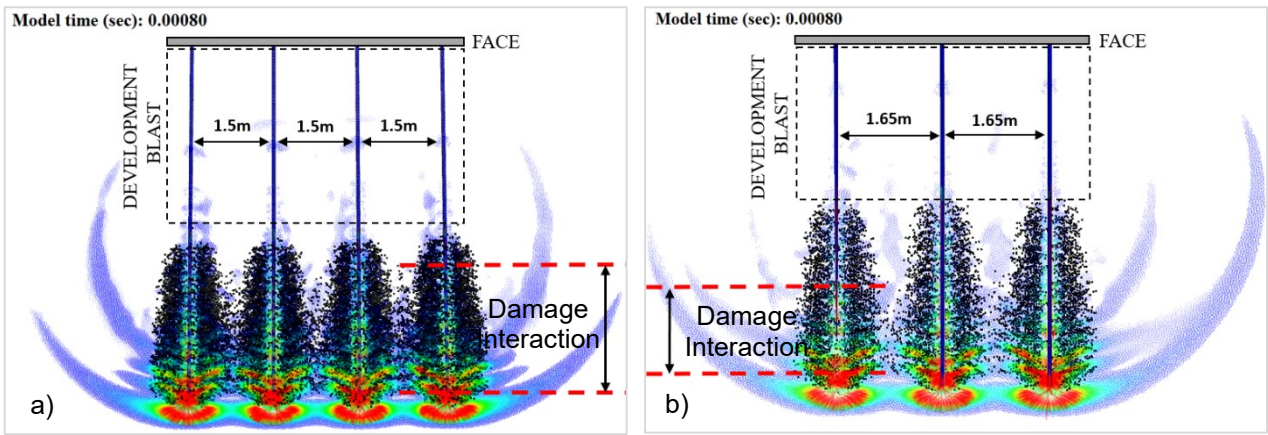
FIG 5 – Plan views of modelled velocity attenuation and rock mass damage zones for a row of destressing charges with 1.5 m and 1.65 m inter-row spacing.

IMPLEMENTATION

In order to quantitatively compare the rock mass response to both conventional and face destress blasting techniques, two tunnels were constructed in parallel. The tunnels were constructed within a single geotechnical domain, such that the conditions of rock strength, stress and structural geology were as close to identical in both tunnels as was realistically achievable. As indicated in Figure 6, the tunnels were developed simultaneously, and at the same rate, so as to minimise potential for one excavation to alter the stress conditions at the face of the other. Conventional development blasting was implemented in the southern excavation. Face destress blasting consistent with the aforementioned design concept was implemented in the north. Further detail on the tunnel construction and blast design in each tunnel is discussed by Drover and Villaescusa (2019).
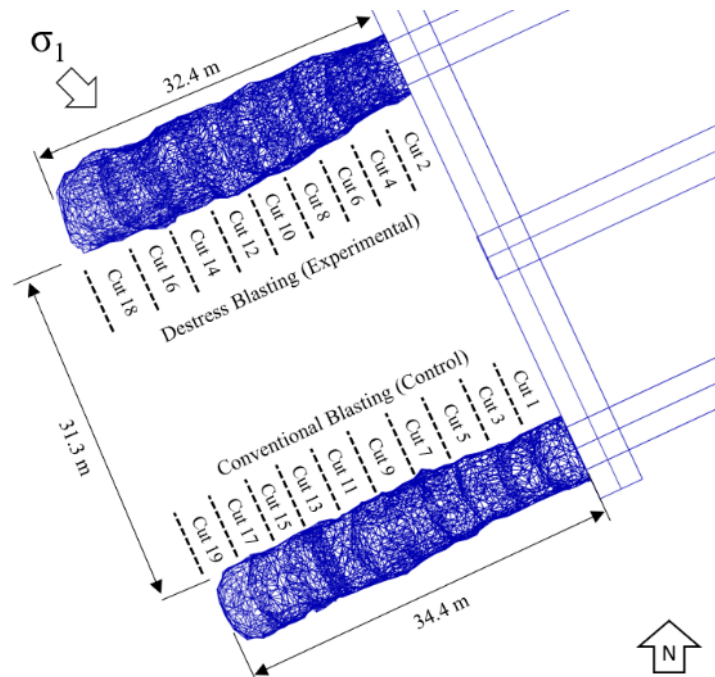
FIG 6 – Layout of the control and experimental excavations used to compare the rock mass response to conventional and face destressing development blasting techniques.

A sketch of the development blasting with face destressing charge arrangement in the northern tunnel is illustrated in Figure 7. The length of the standard development round was 3.8 m. Each development face charge consisted of a 3.2 m long, toe primed, fully coupled, blown ANFO load in a 45 mm diameter borehole, which was not stemmed. Cartridge wall control product was used for the perimeter charges. Each destressing charge consisted of a 2.9 m long, collar primed, fully coupled, blown ANFO load in a 63 mm diameter borehole. Collar priming was applied to the

destressing loads so that the detonation front propagated away from the excavation, which HSBM modelling indicated would increase blast-induced damage ahead of the face for destressing effect. Collar priming also directed the detonation front away from the explosives of the main development round. The destressing charges were fully confined using at least 1.0 m of tamped clay stemming packs, thus avoiding rifling of the explosive to the borehole collar and, more importantly, to maximise gas pressure in the destressing zone. High gas pressures were deemed necessary to maximise the likelihood of radial fracture interaction between adjacent charges, given the high confinement of the rock mass. High gas pressure was also deemed advantageous in order to dilate any pre-existing geological structures that intersected the charges.
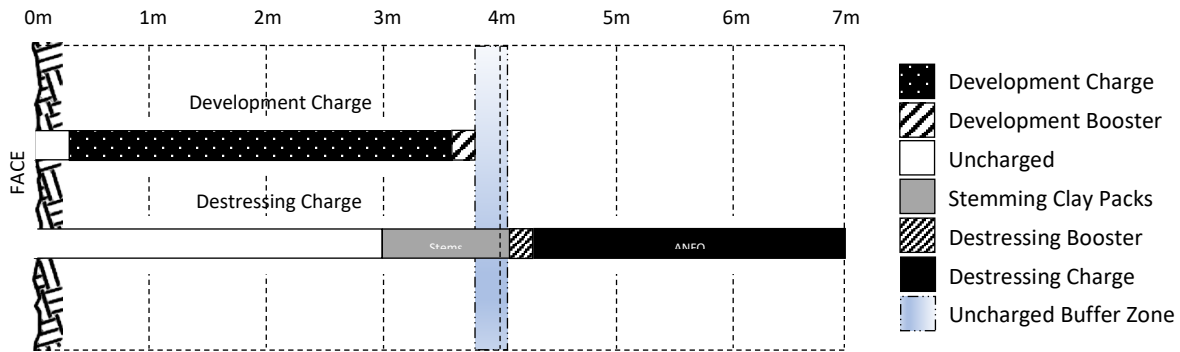
FIG 7 – Long-section sketch of the borehole explosive arrangement showing both the development and destressing charges and their relative position.

The destressing charges were initiated such that those in the same row were all detonated on the same delay. This was intended to further maximise the likelihood that adjacent charges would generate interacting and continuous planes of radial fracturing for shear and destressing effect. Non-Electronic detonators were used throughout, which likely introduced some scatter into the initiation sequence. Programmable electronic detonators would result in greater control over the detonation timing of the destressing charges, reducing scatter and thereby maximising cross-borehole damage interaction, but they were not available to the trial.

The destressing charges were all initiated prior to the first hole of the main development round's burn cut. This prevented the destressing charges from causing cratering of the face. It also created an opportunity to damage asperities of the pre-existing geological structures in the destressing zone, via gas migration into those joints, without inducing significant deformation along the structures. Inducing damage to the natural joints, causing strain energy dissipation along the joint surface with minimal deformation, was considered a key objective of the destressing process.

In terms of the relative loading position of the development and destressing charges, a 0.3 m wide uncharged buffer zone was maintained between the toe of the development charges and collar of the destressing charges. This buffer was implemented in order to avoid the potential for the destressing loads to cause sympathetic detonations in the main development round as they were initiated. The 3.2 m length to which the destressing charges extended beyond the toe of the development charges was determined based on experience, as this was anticipated to be the width of the zone of elevated stress concentration immediately ahead of the face.

COMPARISON OF THE SEISMIC RESPONSE

A sequence of long sections of the typical spatial characteristics of the seismogenic zones associated with conventional and face destressing development advance are shown in Figure 8. The modal location accuracy for the population of events recorded by the 3D sensor array surrounding the tunnels was 0.3 metres, or 0.8 per cent of the average hypocentral distance. The seismic data from the southern excavation without destressing reveals that the seismogenic zone was highly consistent in its basic shape. It always formed a crescent shape enveloping the zone of high stress concentration ahead of the face. There was some distribution of seismicity into the roof of the excavation, although this did not extend beyond the unsupported ground of the recently fired blast. During the latter blasts, the seismogenic zone below the floor of the tunnel was observed to extend several cuts back from the face. This was consistent with concentration of the subhorizontal stress.

The absence of any such seismic response in the roof at that time may be indicative of the effective stabilising action of the ground support scheme. The characteristics of the seismogenic zones associated with face destressing development were significantly more diverse. Generally, the seismogenic zone following destressing was larger and of a less uniform shape when compared to that of the conventionally blasted control tunnel. The seismicity also extended considerably further into the roof and floor of the tunnel where destressing was applied, with small-magnitude seismicity often induced behind the supported surfaces of the excavation. Destressing also generated some clustering of events further ahead of the face than was observed ahead of the conventional drill and blast tunnel.
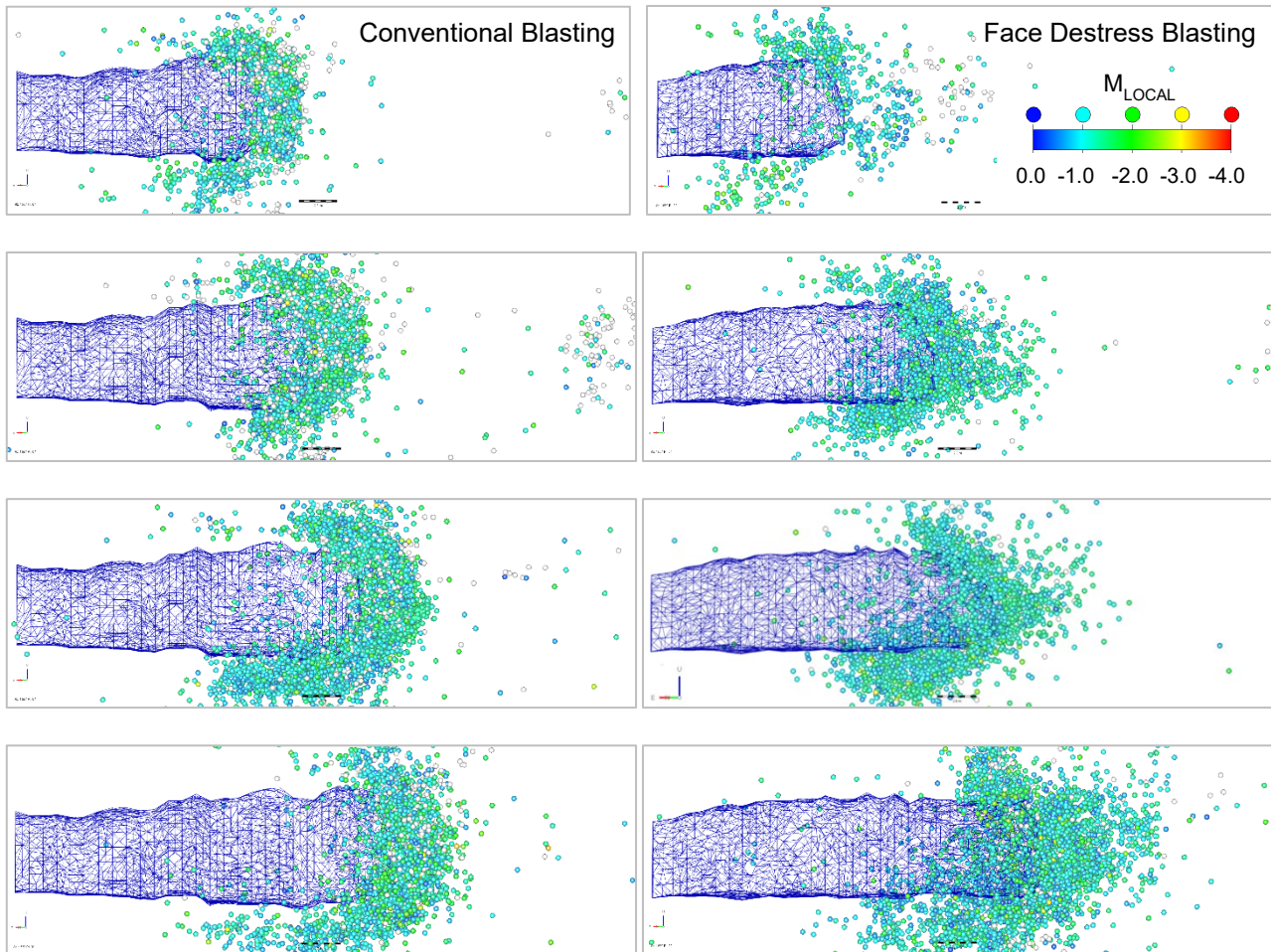
FIG 8 – Longitudinal section views of the seismic response to both conventional and face destressing drill and blast development advance.

When viewed in cross-section, the seismic data for a single development cycle in the conventional tunnel (Figure 9a) reveals minimal instability in the sidewalls. There was sometimes also an absence of seismicity in the left-hand side of the face. Furthermore, the seismicity in the roof and floor were very locally confined to the centre of these surfaces where the maximum stress concentration of the subhorizontal σ_1 occurred. In contrast, the seismicity following a face destressing blast (Figure 9b) typically extended deeper into the sidewalls, indicating that stress redistribution occurred over a much greater percentage of the excavation perimeter.

a) Conventional Blasting   b) Face Destress Blasting
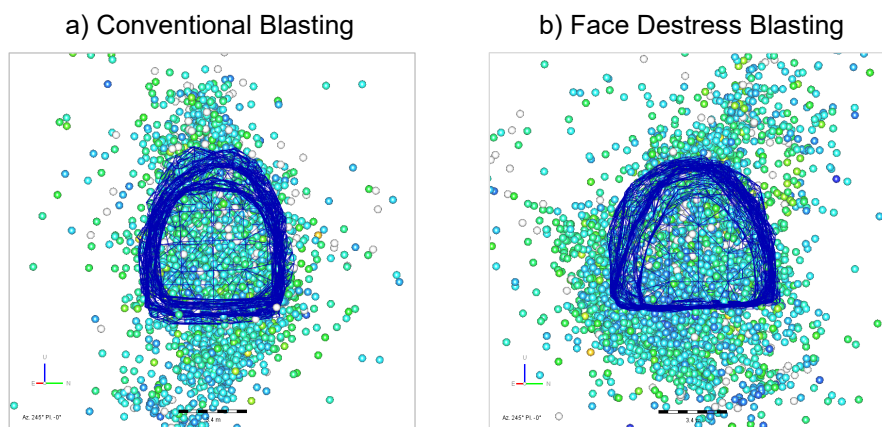
FIG 9 – Transverse sections of the typical spatial extents of the seismogenic zone surrounding the conventional and face destressing development excavations.

A chart of the total number of seismic events adjacent each excavation (Figure 10) indicates that most events occurred ahead of the face in both tunnels. In the destressing tunnel there were 32 per cent fewer events ahead of the face, 7 per cent fewer events in the floor and 48 per cent fewer events in the excavation roof over the entire duration of construction. The sidewalls recorded a 68 per cent increase in the number of events following face destressing, although the total number of events there was relatively low. These observations are consistent with the face being the excavation surface with the widest unsupported span and potentially highest or equal highest stress concentration, as it was subparallel to the major principal stress. Similarly, the roof and floor of each tunnel were also highly stressed by the σ_1 concentration. However, their smaller unsupported span did not generate the same instability. The data indicated that the walls were considerably more stable than the roof and floor of the tunnel. This was consistent with the minor principal stress being the subvertical component.
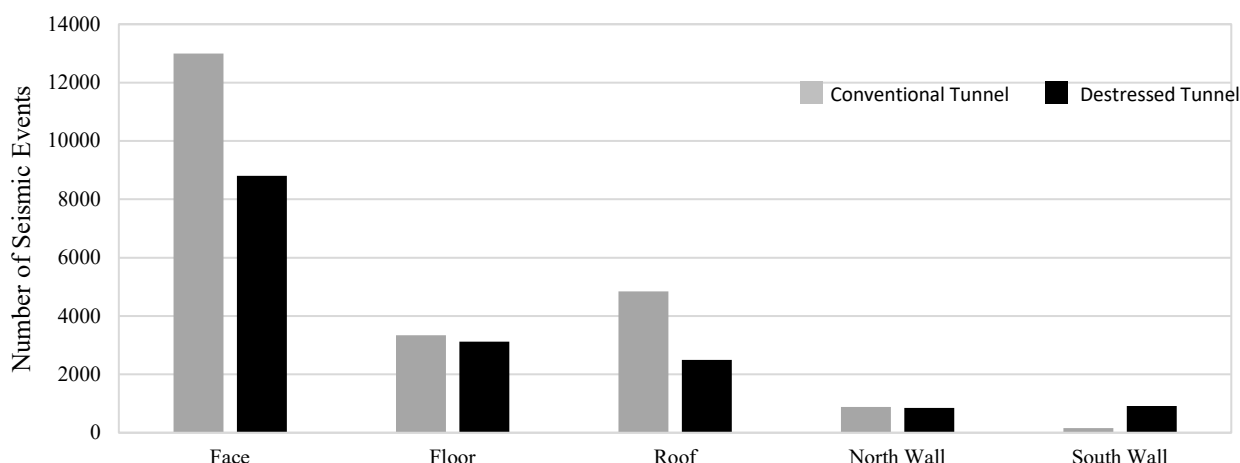
FIG 10 – The distribution of seismicity across the excavation surfaces.

A high-resolution spatial analysis of the seismic data was conducted for both the conventional and destressed development. The intent of this analysis was to characterise the seismic response at the face in high detail, establishing what effect destress blasting had on the location and intensity of the seismogenic zone. Figure 11 presents a plot of the average number of seismic events occurring during each development cycle, as a function of distance from the face position created after the development blast (Drover and Villaescusa, 2019). The characteristic seismic response to conventional development can be described as a relatively small number of seismic events adjacent the supported surfaces of the excavation. The number of seismic events then increased exponentially adjacent the unsupported ground, continuing to a peak between +0.9 m and +1.8 m ahead of the face. The number of events in the seismogenic zone then decayed rapidly to +3.0 m ahead of the face. This was indicative of a high strain gradient within the rock mass. Very little

seismicity was recorded more than 3.6 m ahead of the face. This seismic data indicated that the zone requiring destressing extended between 3.0 m to 3.6 m ahead of the face, which validated the destress blasting design in the northern tunnel.
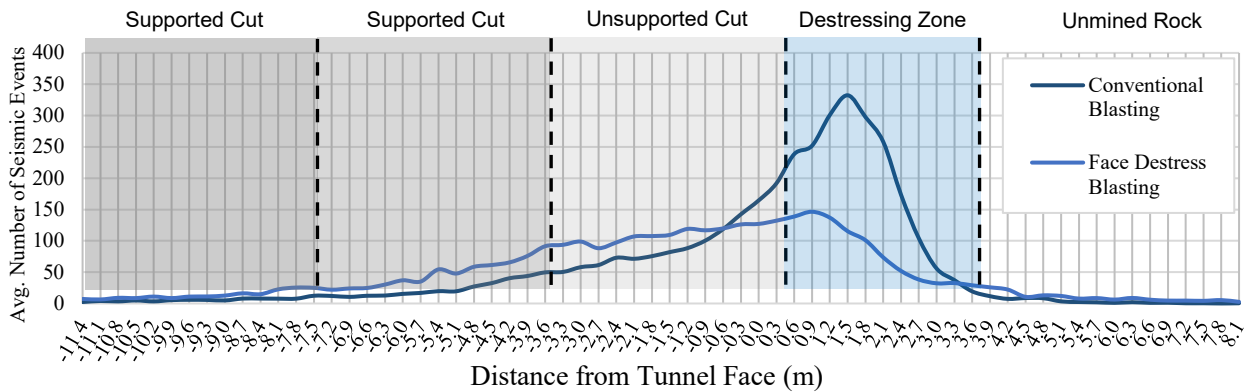
FIG 11 – The average number of seismic events occurring per development cycle at specific distances from the face location, for both conventional and face destressing development.

The characteristic response to face destressing in the north tunnel was a broader spatial distribution of seismic activity about the face position, but significantly lower overall event count when compared to the conventional development. A sharp increase in the event count leading to a high peak in the seismogenic zone ahead of the face was not observed in the destressing development, as it was in the conventional tunnel. Where destressing was applied there was a relatively even spatial distribution of the number of events throughout both the unsupported ground of the recent cut and the first 1.8 m of the destressed zone immediately ahead of the face. This was indicated by the relatively flat profile of the average event count curve over the distance range of -3.8 m to +1.8 m.

The steep increase and decay gradients in the average event count curve for the conventional development suggested that relatively high strain gradients existed within the rock mass adjacent and immediately ahead of the face position in that excavation. By contrast, the much flatter average event count curve and gradual decays around the destressed face strongly suggest that the strain gradients there were significantly lower. The much more broadly spatially distributed seismogenic zone was interpreted to be a result of a reduced rock mass stiffness adjacent the destressing development. The shape of the seismogenic zone was also more erratic around the destressed face. These observations in the seismic data implied a lower rock mass stiffness existed through the destressed zone with reduced strain energy release ahead of the face in particular. Overall, this response to destressing indicated that the strain conditions adjacent the excavation were less conducive to violent face ejection, when compared to conventional blasting.

The P-axes of the seismic event moment tensors for both tunnels are illustrated in Figure 12 (Drover and Villaescusa, 2019). The plan view (Figure 12a) and cross-section (Figure 12b) of the conventionally blasted tunnel indicate that the vast majority of the principal strain axes were subhorizontal and also subparallel to the tunnel face, major principal stress and dominant face-forming joint set (Dip/DipDir of 82/083) that was mapped in the area. A small minority of the events displayed P-axis solutions which were moderately inclined or subvertical. These were mostly located adjacent the excavation walls, floor or roof, where highly localised rotations of the stress field occurred as a result of the excavation. The P-axis orientations directly ahead of the face were very consistent. In contrast to the conventional tunnel, the P-axes of the moment tensor solutions in the northern tunnel with face destressing (Figure 12a and 12c) varied substantially in both orientation and plunge. Subhorizontal, moderately steeply dipping and subvertical P-Axis orientations were recorded both ahead of the face and adjacent the permanent excavation walls. This indicated that face destress blasting triggered a more diverse range of failure plane orientations surrounding the destressed tunnel and ahead of the face in particular.
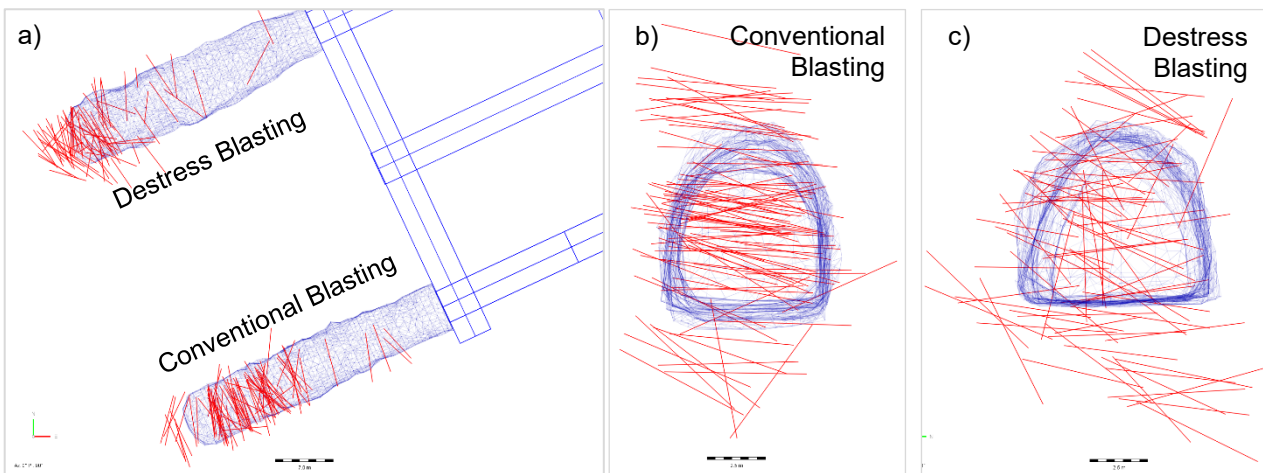
FIG 12 – Comparison of the P-axis of the moment tensors for conventional and face destressing development-induced seismicity.

A ternary diagram of the source mechanisms of events around both the conventional tunnel and destressing tunnel is shown in Figure 13. The data for the conventional tunnel development indicated that the dominant failure mechanism was strike-slip rupture, which was most likely along the aforementioned face-forming joint set. This set was approximately north–south striking with very steep dip. This mode of strike-slip failure was controlled by the major principal stress oriented subparallel to this joint set. The source mechanism data also indicated that there was some distribution of failure mechanisms consisting of oblique reverse and reverse joint rupture. These mechanisms may have been associated with rupture of structures in other discontinuity families. There was also one observation of vertical dip slip and another of normal rupture, but these mechanisms were a very small percentage of the total population.
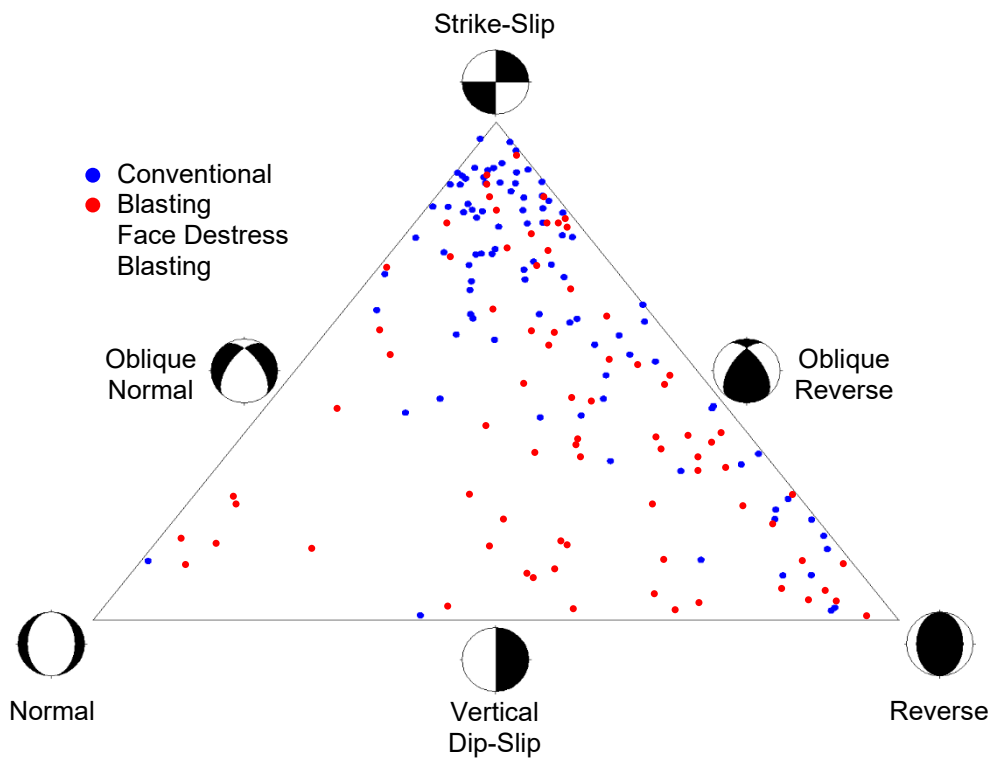
FIG 13 – Ternary diagram of the seismic source mechanisms associated with conventional and face destressing development.

In contrast to the conventional development, the face destressing excavation experienced a much broader dispersion of failure mechanisms. As indicated in Figure 13, the destressing tunnel

generated a much larger population of reverse, oblique reverse and vertical dip-slip style rupture events, in addition to strike slip sources. There were also a number of events with normal and oblique normal source characteristics. The much larger population of events with subvertical and moderately inclined deformation mechanics around this tunnel indicated that destress blasting damaged all joint sets to the point whereby the minor principal stress also became an important control on stability. This consequence of destress blasting is suggested to be a favourable one. Joint weakening to facilitate a greater diversity of failure modes effectively reduced the rock mass strength. This in turn was interpreted to have reduced the likelihood of high strain energy accumulation, which might culminate in a single large instability causing ground support damage or violent ejection of the face while personnel were working nearby (Drover and Villaescusa, 2019).

A photograph illustrating the angular range of fracturing generated by a destressing charge is presented in Figure 14. The visible fractures are identified in the image by white dotted lines. The upper and lower angular limits of those fractures with respect to the horizontal plane are indicated by the white dashed lines. The observations indicated that fracturing occurred within the range of 170 to 570 above horizontal (ie 130 to 530 inclined with respect to σ_1). Most of the visibly dilated fractures, but not all, were pre-existing natural joints aligned subparallel to the rows of destressing charges. There was no obvious fracturing perfectly parallel or subperpendicular to σ_1, either through intact rock or along geological structures. This indicated that gas penetration into favourably oriented geological structures was the dominant mechanism of face destressing.
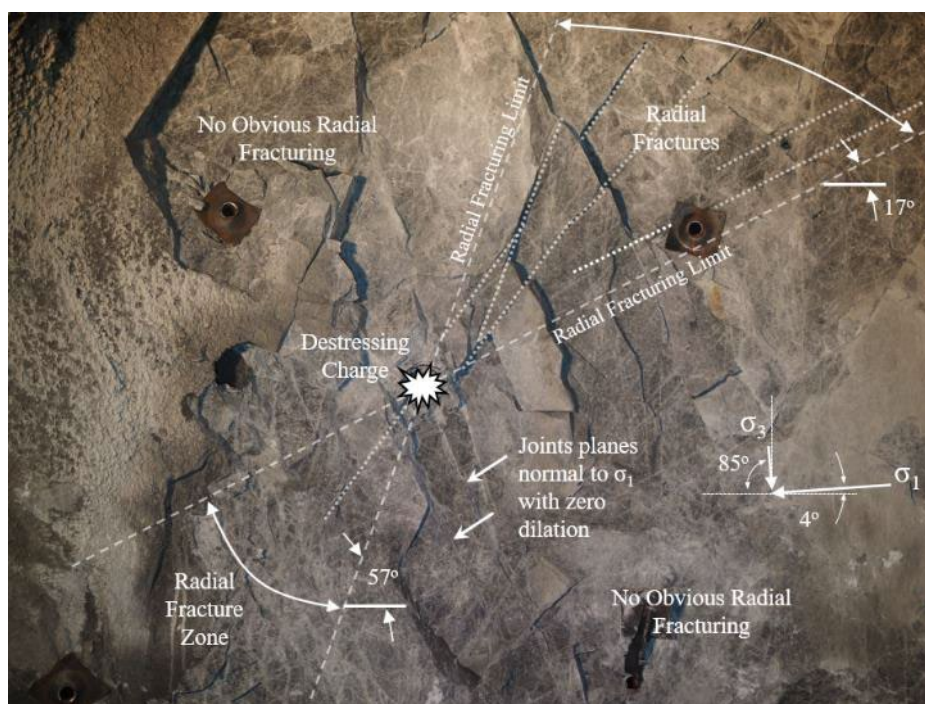
FIG 14 – Angular limits to the visible destress blasting-induced radial fracturing.

Evidence of radial fracture interaction across the spacing of the destressing charges is shown in Figure 15. In this case, one continuous dilated fracture was generated between two adjacent destressing charges separated by a distance of 1.8 m. Evidence of gas penetration was visible in the form of ANFO residue on the entire fracture surface. The residue was a combination of oil, moisture and rock dust which is visible as the darker coloured zones in the image. Explosive residue within the entire crack was the only clear evidence of fracture interaction between destressing charges, and it was only observed to align subparallel to the major principal stress.
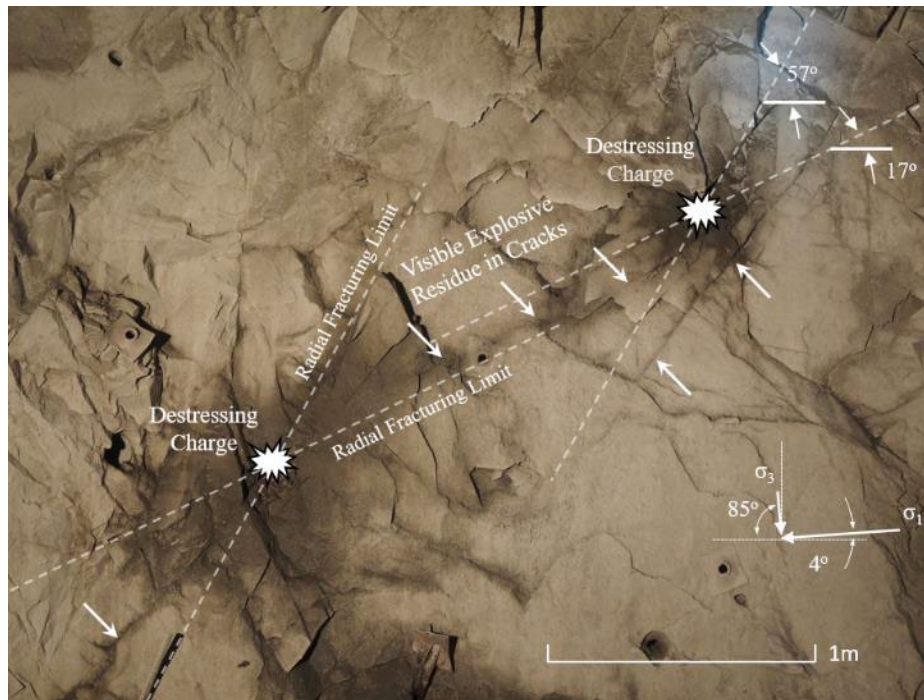
FIG 15 – Visible explosive residue within a continuous fracture spanning the charge spacing.

It was not obvious if this particular fracture was continuous across more than two boreholes. Nonetheless, this was a physical example of the desired mechanism of fracturing, which was intended to facilitate shear deformation of the face subparallel to the major principal stress. This observation validated the HSBM modelling of the destressing charge pattern, which indicated that significant fracture interactions would occur across a 1.6 m spacing. In this case, the fracture connecting the two destressing charges appeared to be formed through a combination of joint dilation, primarily, with some intact rock rupture. Numerous natural discontinuities in close proximity to each borehole were also dilated and hence may have also played a role in assisting the path of the blast gases.

CONCLUSIONS

A novel development face destressing blast design concept was developed and field tested in deep and high stress mining conditions. The blast design positioned several rows of destressing charges ahead of the face. Each row of explosives was subparallel, yet almost oblique to the major principal stress. Charge rows were also positioned to maximise explosive gas injection through favourably oriented natural geological structures. When detonated, the charges were intended to create a series of parallel shear fractures that assist in dissipation of stored strain energy from the rock mass. In order to increase the likelihood of achieving this objective during field trials, the key parameters of the blast design were optimised using the HSBM software and input data from a rock mass characterisation of the mining environment. The destressing approach was implemented in a development field trial and the rock mass response to the development was compared to a conventionally blasted excavation which did not utilise destressing methods. High resolution seismic monitoring data indicated that without destressing, the zone of elevated seismic activity extended up to 3.6 m ahead of the face. Where destressing was applied, the spatial density of events ahead of the face decreased significantly, with a slight increase in the number of events adjacent the unsupported walls. The rate of change of the spatial density of seismic events in the destressed excavation indicated a lower rock mass stiffness than was present in the conventionally blasted tunnel. This outcome was also indicated by the much wider variety of seismic source mechanisms in the destressed rock mass. Destress blasting-induced rock mass damage was primarily created along small scale, pre-existing geological structures. This was inferred from both source mechanism analysis of the recorded seismicity as well as visual observations of blast-induced fracturing at the tunnel face exposures. There was also evidence of gas interaction spanning the spacing of adjacent destressing charges, causing dilation of pre-existing joint structures. These observations validated the numerical optimisations of the blast design using the HSBM software.

ACKNOWLEDGEMENTS

REFERENCES

Carr, C, Rankin, D and Fuykschot, J, 1999. Development of advanced blasting practices at Forrestania Nickel Mines. *Proceedings of EXPLO '99*, pp 239–246 (The Australasian Institute of Mining and Metallurgy: Melbourne).

Drover, C and Villaescusa, E, 2019. A comparison of seismic response to conventional and face destress blasting during deep tunnel development. *Journal of Rock Mechanics and Geotechnical Engineering*, 11(5):965–978.

Drover, C, Villaescusa, E and Onederra, I, 2018. Face destressing blast design for hard rock tunnelling at great depth. *Tunnelling and Underground Space Technology*, 80(2018):257–268.

Jung, W-J, Utagawa, M, Ogata, Y, Seto, M, Katsuyama, K, Miyake, A and Ogawa, T, 2001. Effects of rock pressure on crack generation during tunnel blasting. *Kayaku Gakkaishi/Journal of the Japan Explosives Society*, 62:138–146.

O'Donnell, J, 1999. *The development and application of destressing techniques in the mines of INCO Limited, Sudbury, Ontario*, MSc Thesis: Laurentian University, Sudbury, Canada.

Onederra, I, Catalan, A and Chitombo, G, 2013. Modelling fracturing, disturbed and interaction zones around fully confined detonating charges. *Mining Technology*, 122(1):20–32.

Saharan, M and Mitri, H, 2011. Destress blasting as a mines safety tool: some fundamental challenges for successful applications. *First International Symposium on Mine Safety Science and Engineering*, pp 37–47.

Longwall face floor failure assessment using a semi quantitative risk rating methodology

J Emery[1], S Grimsey[2] and E Janetzki[3]

1. Geotechnical Engineer, Optimum Geotechnics, Yeppoon Qld 4703.
   Email: optimumgeotechnics@gmail.com
2. Geotechnical Superintendent, Kestrel Coal Resources, Emerald Qld 4720.
   Email: samantha.grimsey@kestrelcoal.com
3. Geotechnical Engineer, Kestrel Coal Resources, Emerald Qld 4720.
   Email: emily.janetzki@kestrelcoal.com

ABSTRACT

Floor failure on the longwall face is a complex problem due to the dynamic interaction between the surrounding strata and powered roof supports involving multiple variables. It can also be highly problematic and costly when not well understood as there are significantly less remedies available post event. This was the early experience at the case study mine where significant lost time was incurred due to unplanned delays in the first two panels. To detect and prevent such occurrences is clearly the best approach, hence a tool to predict both floor failure occurrence and magnitude prior to mining was developed. Several parameters were determined as the key drivers for the failure events that had been experienced at this site. These parameters were, in list of influence from highest to lowest, material strength, retreat rate and the presence of water. The parameters were evaluated using a semi quantitative risk rating system 'Heave Risk' and given a weighting per their apparent influence. This 'expert system' methodology was selected as the use of risk rating systems in underground coal mining is well established. The heave risk model was first applied to previously mined panels. It accurately identified all areas of known major floor heave, with clearly defined areas of low and high risk apparent. The heave risk model was then used prior to mining and evaluated post mining based on observed conditions. It was found to also be highly accurate for prediction. The variability of each parameter and its influence on the overall risk rating is illustrated and discussed.

INTRODUCTION

This paper describes a semi quantitative risk assessment method applied to estimate the relative level of risk to operations from floor instability along the face at an underground longwall mine. The objective of the research was to develop the following:

- A validated model for predicting areas of increased risk of floor instability on the longwall face.

- Improved understanding of the floor failure mechanisms.

Ultimately predicting both floor heave occurrence and magnitude decreases the uncertainty around these events with uncertainty essentially translating to risk (Galvin, 2016). Communicating this uncertainty (risk) to operations well in advance of mining would minimise any mine worker exposure to injury or lost productivity. Inadequate prediction of high risk areas and poor management may lead to conditions that are increasingly difficult to control, as depicted in Figure 1.

FIG 1 – Roof failure at the longwall face following severe floor heave event.

PARAMETER SELECTION

There are several parameters that must be considered when determining the risk associated with floor heave at the longwall face. Listed below are floor failure mechanisms likely to be encountered in underground coalmines according to Nemcik (2003):

- Puncture of longwall pontoons into the floor.

- Buckling of floor due to excessive coal seam displacement towards the goaf.

- Compressive floor failure due to sliding blocks within the floor.

- Floor heave adjacent to the goaf areas (ie maingate or tailgate roadways).

Understanding the dominant failure mechanism at this operation was the first step in defining the key parameters for the risk rating.

Historical review

Historical production data was reviewed to understand where delays had been encountered due to floor instability within the first three longwall panels. Within the areas identified the geological and geotechnical data set was analysed in detail. Two locations of severe floor failure impacting operation of the longwall were identified. These two locations are shown as blue points in Figure 2. At both locations, the uniaxial compressive strength (UCS) of the 1.0–2.0 m floor horizon had decreased to 5–10 MPa or lower. Due to the immediate 1 m of floor being consistently weak this was an important finding.
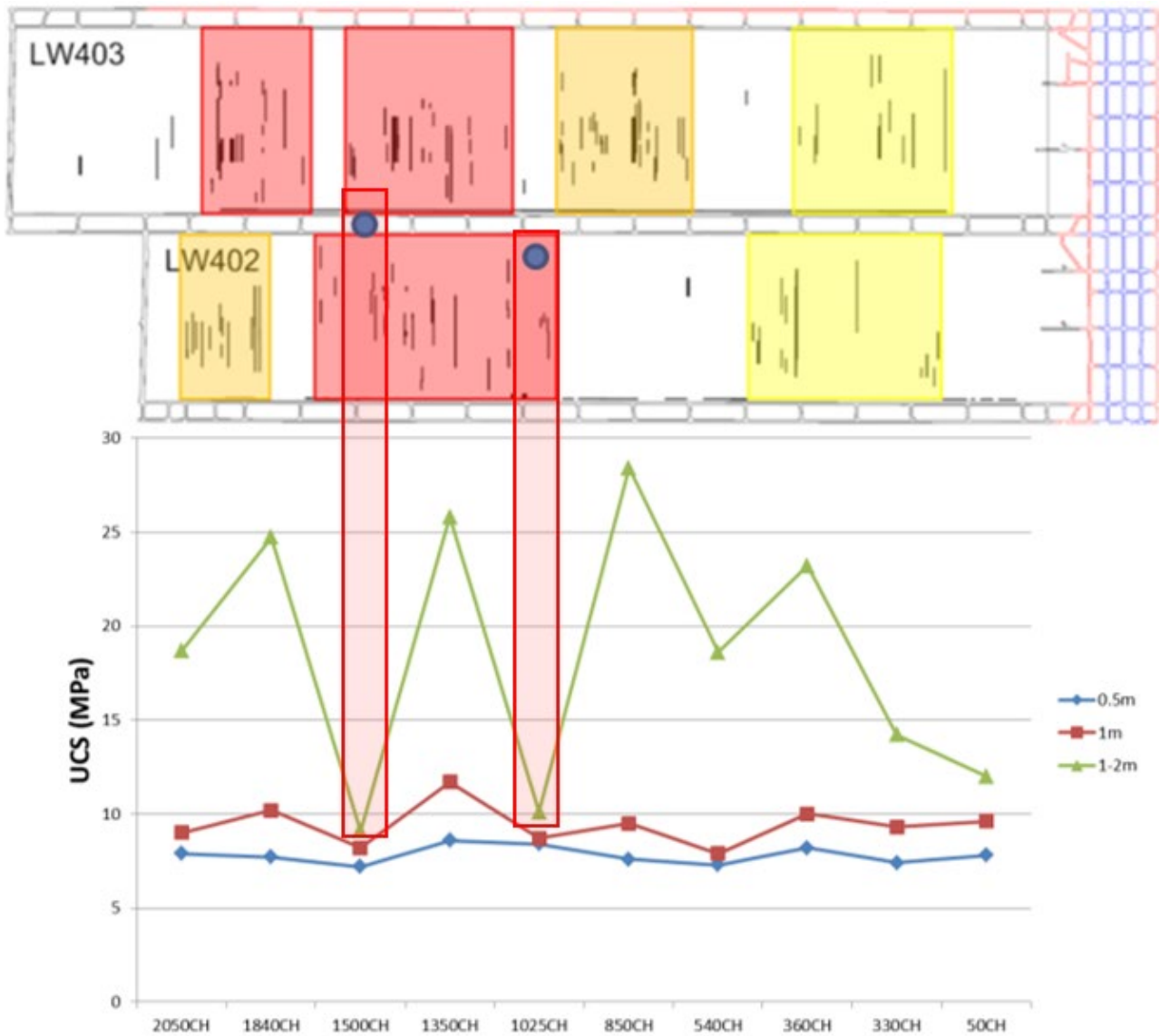
FIG 2 – Locations of severe floor heave impacting longwall operations and UCS of the 1.0–2.0 m floor horizon.

SEMI QUANTITATIVE RISK RATING SYSTEM (SQRR)

The SQRR included three parameters: floor strength index (FSI) 1–2 m, retreat rate and water make. All parameters have three possible subparameters with corresponding likelihood scores of 1, 5 or 10. Each parameter also has a weighting. Calculation of both a likelihood and consequence score is then completed at 100 m intervals along the length of a panel, to create a risk plot. Figure 3 is an example heave risk plot generated for one longwall block with each point representing the likelihood and consequence scores from a 100 m section.
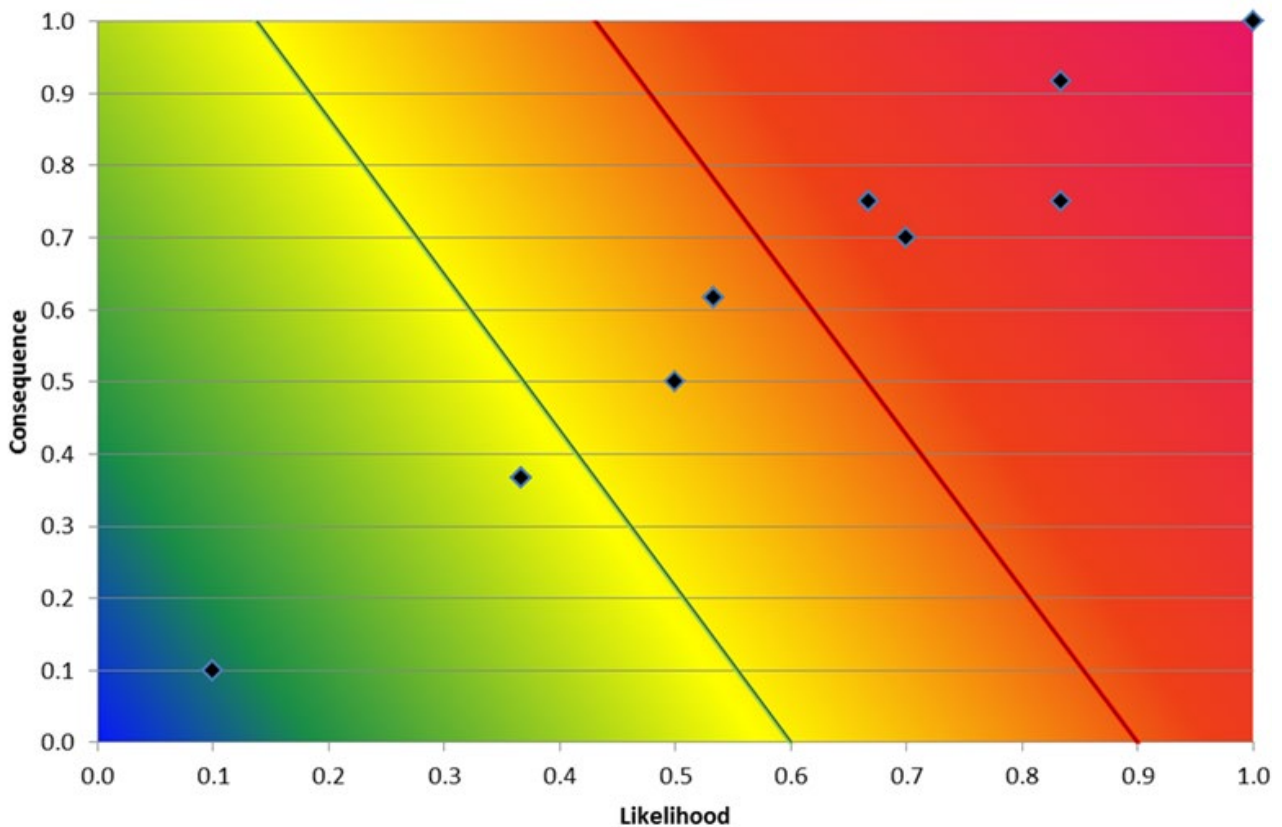
FIG 3 – Example heave risk plot.

Predicted risk rating

Heave risk was calculated for the first eight longwall panels, with four of them being extracted at the time of the initial study in 2017 as shown in Figure 4. When conducting a review of predicted floor heave risk zones against actual performance in 2019, no major floor heave events occured in any areas of moderate or high risk up to and including the seventh panel. This review allowed for revised or calibrated risk ratings for both the seventh and eighth panels based on the most recent retreat rates (Figure 5). This was required as the mine had achieved a significant and sustained uplift in productivity. The revised heave risk rating (Figure 5) for the seventh panel significantly reduced the percentage of the panel rated as high risk compared to th original (Figure 4). The calibration appeared valid with no major events reported during operation. Within LW408, the eighth panel, the portion of high risk areas remained relatively unchanged after calibration. This prompted the operator to implement several proactive strategies including water management, additional secondary roof and rib support, and minimisation of production stoppages. While moderate heave events were recorded within the high heave risk areas, overall, the LW408 panel was managed successfully. There were no major impacts to production and a reduced schedule forecast in line with the consistent, though reduced, level of productivity.
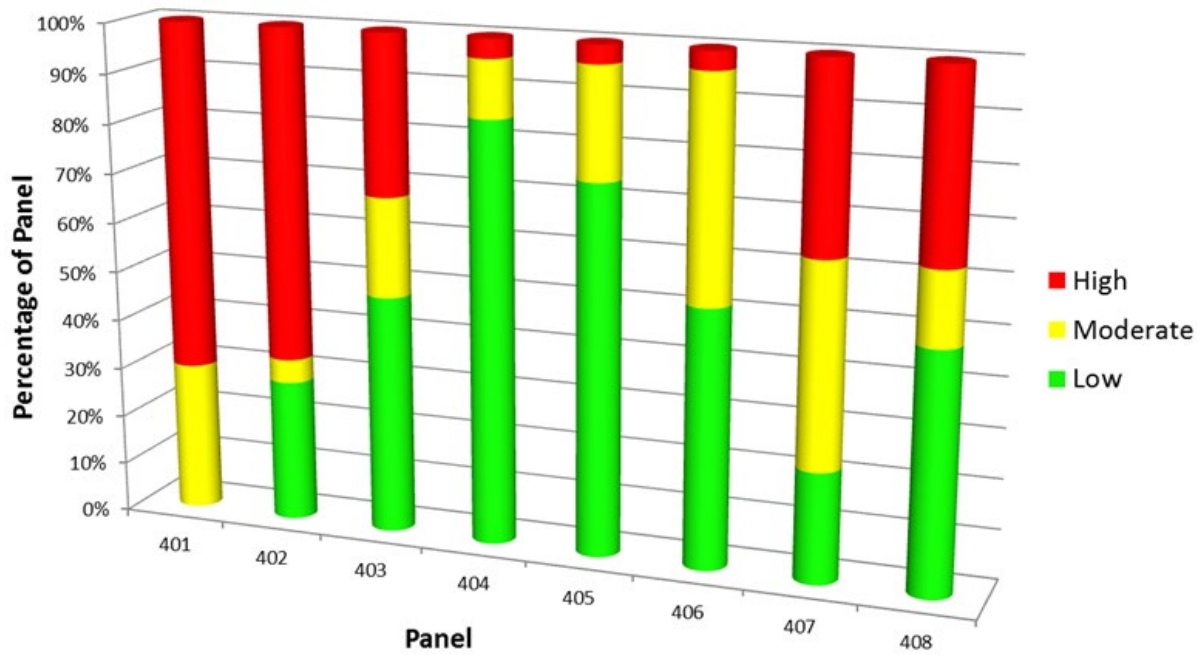
FIG 4 – Heave risk by panel (original).
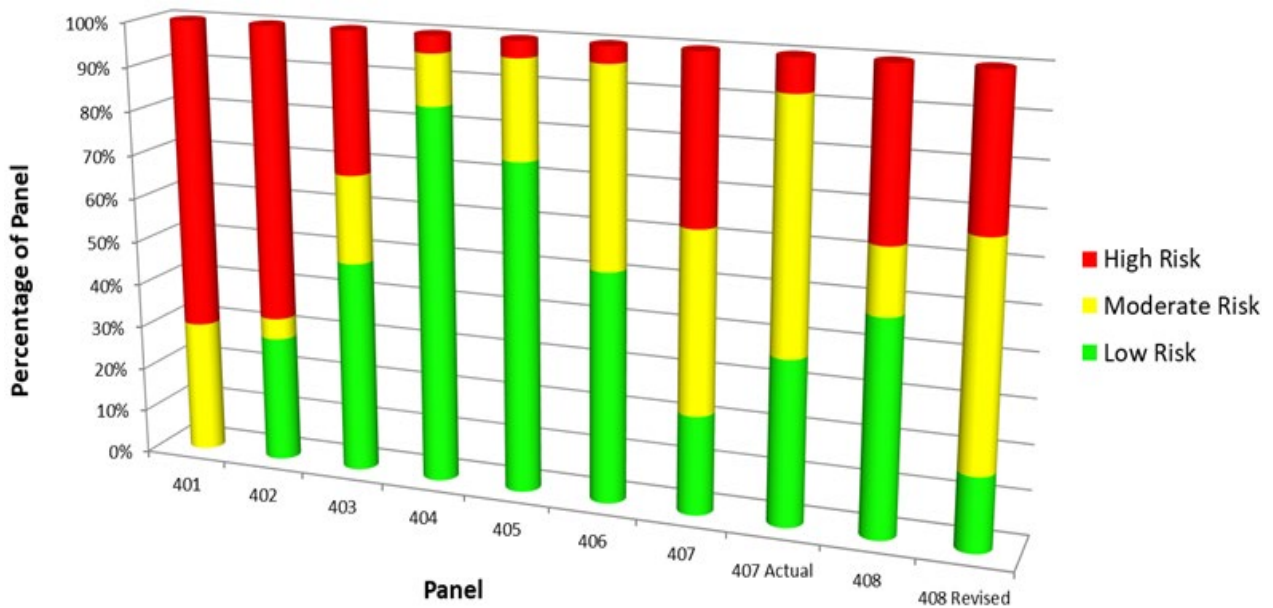
FIG 5 – Heave risk by panel (calibrated).

CONCLUSIONS

The SQRR described, 'heave risk', rated all areas of known major longwall face floor instability as high risk when run both pre and post mining in the panels described. Conversely, all areas with minimal floor instability were rated as low risk. This increased understanding was instrumental in minimising potential for an adverse outcome in LW408 panel, clearly articulating the change in risk profile between and within panels. Accurate forecasting of conditions allowed for timely and measured derating of the production schedule which improved the forecast of saleable product, in turn maintaining status as a reliable producer. The SQRR method described can be readily applied to many geotechnical challenges at underground coalmines, provided it is judiciously utilised with the appropriate level of engineering judgement. The results suggest the heave risk model has met this criteria, with its ongoing use at the mine site. Finally it is noted that significant bodies of work have been conducted in recent times (Saydam *et al*, 2020) on floor assessment for underground coalmines. As this research was published more recently than when this study occured they are not included in the literature review, though certainly should be for future work.

ACKNOWLEDGEMENTS

REFERENCES

Galvin, J, 2016. *Ground Engineering – Principles and Practices for Underground Coal Mining*, Springer International Publishing, Switzerland.

Nemcik, J, 2003. *Floor failure mechanisms at underground longwall face*, Doctor of Philosophy thesis, University of Wollongong, Faculty of Engineering, http://ro.uow.edu.au/theses/1826/.

Saydam, S, Masoumi, H and Timms, W, 2020. Floor stability – a comprehensive investigation into failure mechanism and controlling factors, ACARP Project C26064, Australian Coal Association Research Program.

Outbursts, coal bursts and rock bursts

I Gray[1] and J H Wood[2]

1. Managing Director, Sigra Pty Ltd, Acacia Ridge Qld 4110. Email: ian@sigra.com.au
2. Principal Geologist, Sigra Pty Ltd, Tarrawanna NSW 2518. Email: jeff@sigra.com.au

INTRODUCTION

This paper examines the occurrence of outbursts, coal bursts and rock bursts in underground mining. It then examines them from the viewpoint of the failure mechanism and velocity of particles. The presence of gas is extremely important as it can both act as the fluid pressure component of effective stress leading to failure, and as a substantial energy source in projecting material during a burst. For gas to drive a dynamic event it must be present as free gas held in voids within the rock or coal mass. This can pre-exist the burst event or be released from desorbing gas during it. The latter is typically part of a multi-stage outburst event which can reach very large proportions. Rock and coal bursts are driven by strain energy release and can vary in form. These tend to be single events associated with failure and strain energy release. It is also possible to conceptually have hybrid events where the failure of the mass and the energy release are due to both stress and expanding gas.

BURSTS DRIVEN BY STRAIN ENERGY

Rock bursts and coal bursts are strain energy driven events that occur following the sudden failure of the mass. The maximum velocity of expulsion due to the stress in the rock or coal mass and that directly surrounding it is given by relations of the form of Equation 1.

$$u = \sigma \sqrt{\frac{2(1-v)}{\rho E}} \tag{1}$$

Where:

u is the velocity of ejection

E is the Young's modulus

ρ is the density of the rock or coal

σ is the equal biaxial stress at the face – limited by rock strength

v is Poisson's ratio

The actual ejection velocity will be lower than this value depending on a number of other factors such as the actual stress at failure, the nature of the failure surface and how quickly the cohesive component of stress is lost with failure.

Where there are external energy sources the ejection velocity may be higher. External energy may come from elastic rebound of the roof and floor on pillar failure causing them to expand outward. It may also come from seismic sources separate from the opening, though these may only act to raise the stress level to that where failure occurs.

Such rock and coal burst failures are extremely high speed events that take of the order of one millisecond for the rock to reach peak velocity. In coals the velocities are of the order of 5 m/s while in very hard rocks they may approach 20 m/s.

BURSTS DRIVEN BY GAS – OUTBURSTS

Gassy rock, and particularly coal, can be prone to outbursts. In these free gas expands and drives the broken fragments outwards. Equation 2 describes the potential velocity that might be achieved by adiabatically expanding gas working on the fragmented material.

$$u = \sqrt{\frac{2P_1 \emptyset}{\rho(\gamma-1)}\left(1 - \left(\frac{P_1}{P_2}\right)^{\left(\frac{1-\gamma}{\gamma}\right)}\right)} \tag{2}$$

Where:

P_1	is the initial pressure
P_2	is the final pressure (atmospheric)
u	is the final velocity
ρ	is the density of the coal or rock
$\emptyset$	is the porosity of void space ratio of the coal or rock
γ	is the adiabatic index of the gas (1.3)

In this the pressure of the gas contained in the rock or coal and the porosity, which may be fractures within the mass, are the critical factors.

If a porous rock, which contains gas in the pore space, fails due to the effective stress within it, then the gas may impart its energy to the fragments. This occurs over a short distance over a period of milliseconds. Such outbursts may occur from sandstones or from salt deposits. In this event it may be possible to combine the contribution of energy from strain and expanding gas to provide an estimate of the velocity of expulsion.

If the available porosity of the mass is very low, such as in a coal seam, then the velocity of a burst is predicted to be low. It is however well known that outbursts do occur in coal which can expel fragments for some considerable distance. In a cleated or jointed coal the mechanism is considered to be one of failure of the mass followed by dilation, diffusion and pressurisation prior to expulsion. This is controlled by a time factor which is dependent on the characteristic diffusive behaviour of the coal, or other organic rock, and the dimension of the fragments that may form. Outbursts of this form do occur and tend to involve larger lump sizes where the larger lumps tend to travel further than the smaller ones which are slowed more rapidly by drag.

Where fine fault gouge material is involved the mechanism of transport is completely different. Rather than the gas expanding and pushing the fragments outwards, fines are entrained in a gas stream. Such outbursts frequently occur in a series of events. Figure 1 shows diagrammatically what is considered to happen. Here a continuous miner is shown intersecting a zone of gouge which then erodes. The outlet then blocks and the volume behind the blockage pressurises until the blockage is discharged. Erosion then continues until further blockage occurs. This type of outburst event occurs over a significant period. They can expel thousands of tonnes of coal and rock and expel a million cubic metres of gas. Nozzles may form on erosion may lead to gas velocities approaching Mach 1. In outbursts of this nature the fine particles carry much further than the larger ones. This distance may reach several hundred metres.
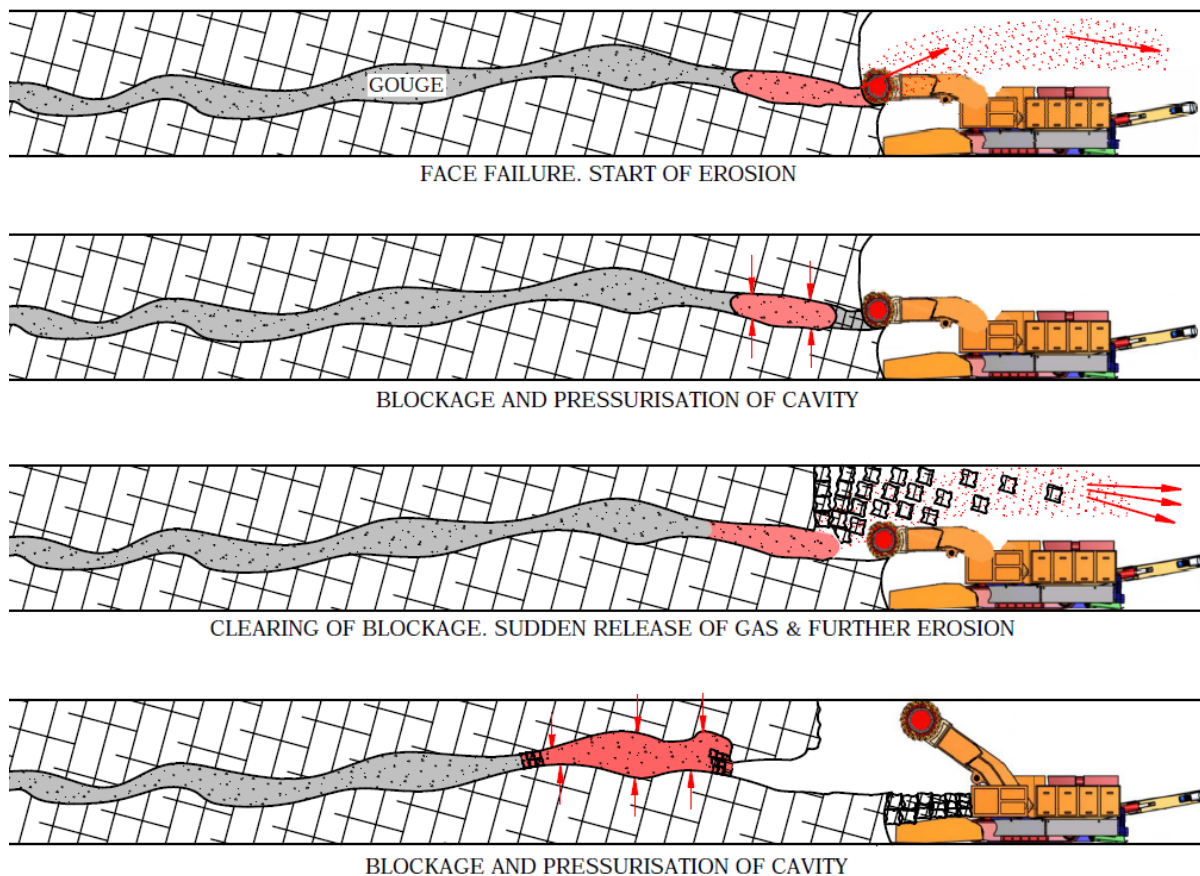
FIG 1 – Outburst involving erosion, blockage, pressurisation and ejection.

CONCLUSION

In the case of strain driven bursts and blocky outbursts it is possible to put an estimate on the expulsion velocity and hence the distance that particles fly, bounce and roll. It may be possible to mine safety from beyond this distance and if necessary take measures to reduce the distance. The dangers posed by gassy fine gouge material are too extreme and avoidance or degassing becomes essential.

Analysis of horizontal opening stability in lunar regolith

T Pelech[1], M Dello-Iacovo[2], N Barnett[2], J Oh[2] and S Saydam[2]

1. School of Minerals and Energy Resources Engineering, UNSW Sydney, NSW 2052, Australia. Email: t.pelech@unsw.edu.au
2. School of Minerals and Energy Resources Engineering, UNSW Sydney, NSW 2052, Australia.

ABSTRACT

In-Situ Resource Utilisation and Off-Earth mining require the application of horizontal drilling. The stability of such openings is challenging when excavating in the lunar regolith. Excavations on the Moon will encounter unconventional operational conditions such as different material properties, low gravity, and a moonquake. Micro-tunnelling or drilling to support lunar exploration and development of infrastructure on the Moon requires stability analysis to ensure its desired performance. The discrete element method (DEM) modelling technique has been utilised to investigate the optimum opening sizes on the lunar soil. From the literature, the mechanical properties of the lunar regolith have been reviewed and used for numerical model development. The model has been calibrated by simulating numerical triaxial tests with the Mohr–Coulomb failure criterion. Then, detailed parametric studies have been performed to investigate the influence of confinement, opening dimensions and moonquakes on the stability of openings. The findings have led to the development of a simple stability chart of the relationship between unsupported opening sizes and lunar regolith properties at different depths.

INTRODUCTION

In-Situ Resource Utilisation (ISRU) and Off-Earth mining require novel methods and models to test capabilities at a low cost before committing to expensive on-site experiments. In supporting NASA's Artemis Moon to Mars program, excavation and drilling of the lunar surface will be necessary. This research aims to determine the stability of horizontal openings in lunar regolith and conditions using the capability of numerical simulations. Various numerical modelling techniques have been employed to investigate rock/soil response under stress. Zheng, Kemeny and Cook (1989) employed the boundary element method (BEM) combined with the Mohr–Coulomb criterion to investigate the progressive spalling of rock flakes at the borehole surface under plane strain conditions. Many early studies also adopted the finite element method (FEM) (Vardoulakis and Papanastasiou, 1988; Cheatham, 1993; Ito, Kurosawa and Hayashi, 1998; Cai *et al*, 2014). However, due to the rock detachment characteristics of the tunnel collapse phenomenon, continuum methods cannot fully reproduce the fracture propagation process. As a result, the discrete element method (DEM) has been increasingly employed to overcome that limitation. Bond-particle model (BPM) is one of the simplest and most common forms of DEM. Unlike continuum models, BPM is constructed by a set of particles that can be independently bonded or debonded at contacts, which provides the capability to reproduce fracture initiation and propagation microscopically and macroscopically (Cundall and Strack, 1979; Potyondy and Cundall, 2004). Several programs and codes are available for implementing the Discrete Element Method, including Itasca PFC, EDEM and YADE. The open-source YADE program will be used for the experiments in this paper. The lunar regolith samples will be calibrated and validated using published data and simulated triaxial testing.

METHODOLOGY

Carrier III, Olhoeft and Mendell (1991) reported the bulk density and porosity of lunar regolith, as shown in Table 1. The porosity for lunar regolith shallower than 60 cm in-depth was reported to be in the range of 42 to 54 per cent. In order to estimate the porosity as greater depth, the calculation was made using Equations 1 and 2.

TABLE 1

In situ stress and porosity values for simulations.

Depth (m)	Modelled bulk density (kg/m³)	Calculated porosity (%)	Column density (kg/m³)	Applied vertical stress (Pa)	Expected horizontal stress (Pa)
0.6	1777	43%	1777	1727	1209
1.2	1839	41%	1819	3535	2475
2	1869	40%	1845	5978	4185
3	1885	39%	1863	9053	6337
4	1893	39%	1874	12144	8501

$$Bulk\ density = particle\ density \times (1 - porosity) \tag{1}$$

$$Bulk\ Density = 1.92\ \frac{z+12.2}{z+18} \tag{2}$$

The Column Density is a weighted average of the Modelled Bulk Density for each incremental depth in the column. For the Applied Vertical Stress at the respective depth lunar gravity (1.62 m/s²) to a 1 m² column of regolith is applied. The Expected Horizontal Stress is calculated based on previously measured *in situ* value (ie $K_0 = 0.7$) (Colwell *et al*, 2007). Table 2 shows physical parameters of lunar regolith used in DEM simulations.

TABLE 2

Physical parameters of lunar regolith used in DEM simulations.

Particle density	3100 kg/m³
Cohesion	3000 Pa
Friction angle	54°
Young's modulus	90 MPa
Poisson's ratio	0.25
Lunar Gravity	1.62 m²/s

Model calibration has been made using triaxial tests with Mohr–Coulomb failure criterion. The parameters calibrated include, mean particle radius, damping factor, friction angle and cohesion. Table 3 shows the sample calibration results.

TABLE 3

Calibration sensitivity to particle radius.

Mean particle radius (mm)	Damping coefficient	Input (micro DEM parameters)		Output (macro test results)		Cohesion error (Pa)
		Cohesion (Pa)	Friction angle (°)	Cohesion (Pa)	Friction angle (°)	
2.5	0.25	3000	54	3000	54	0
5	0.2	3000	50	3000	54	0
10	0.2	3000	54	5000	58	2000
12.5	0.2	3000	54	8000	56	5000
25	0.3	3000	54	20 000	56	17 000

The tunnel stability experimental procedure is summarised in Figure 1 (Pelech *et al*, 2022). The procedure has been divided into three parts, where the end of each part results in a saved sample and data outputs. After sample set-up stage, stability analysis was conducted by calculating total kinetic energy (KE) and visual collapse. The largest diameter stable tunnel is further tested for seismic stability analysis.
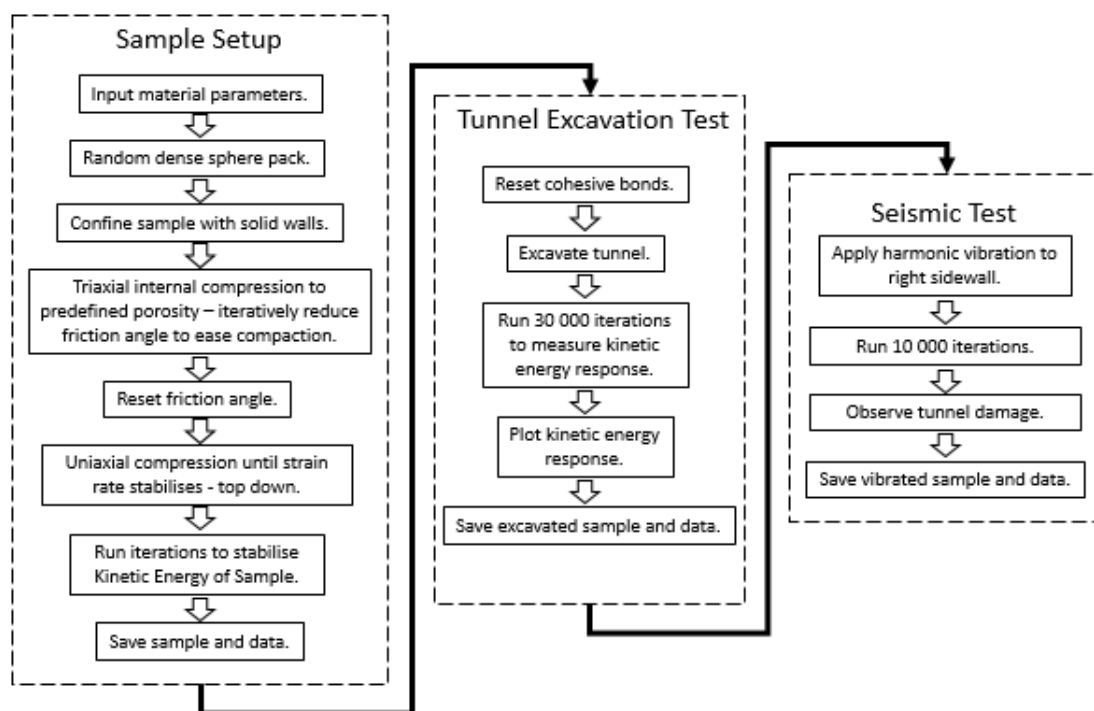
FIG 1 – Tunnel stability experimental procedure (Pelech *et al*, 2022).

RESULTS AND CONCLUSIONS

Table 4 shows the simulation results for different tunnel diameters and confinements. The samples have been labelled with an index that can be used for the Tunnel Stability Chart as shown in Figure 2.

TABLE 4

Tunnel stability experiments qualitative results (Pelech *et al*, 2022).

Index	Tunnel Diameter (mm)	Confinement (Pa)	6R sample – Failure?	3R sample – Failure?
E	50	1727	N	No Data
	50	3535	No Data	No Data
	50	5978	N	No Data
	50	9053	N	No Data
	50	12144	No Data	No Data
F	100	1727	Partial	Partial
	100	3535	Y	N
	100	5978	Y	N
B	100	9053	No Data	N
C	100	12144	Partial	N
	160	1727	No Data	Y
	160	3535	Partial	No Data
	160	5978	No Data	Y

	160	9053	Y	Y
D	160	12144	N	N
	250	1727	Y	No Data
	250	3535	Y	Y
	250	5978	Y	Y
	250	9053	Y	Partial
	250	12144	Y	N
	300	1727	Y	Y
A	300	3535	Y	Y
	300	5978	Y	Y
	300	9053	Y	Y
	300	12144	Y	Y
	400	1727	Y	Y
	400	3535	No Data	Y
	400	5978	Y	Y
	400	9053	Y	Y
	400	12144	Y	No Data
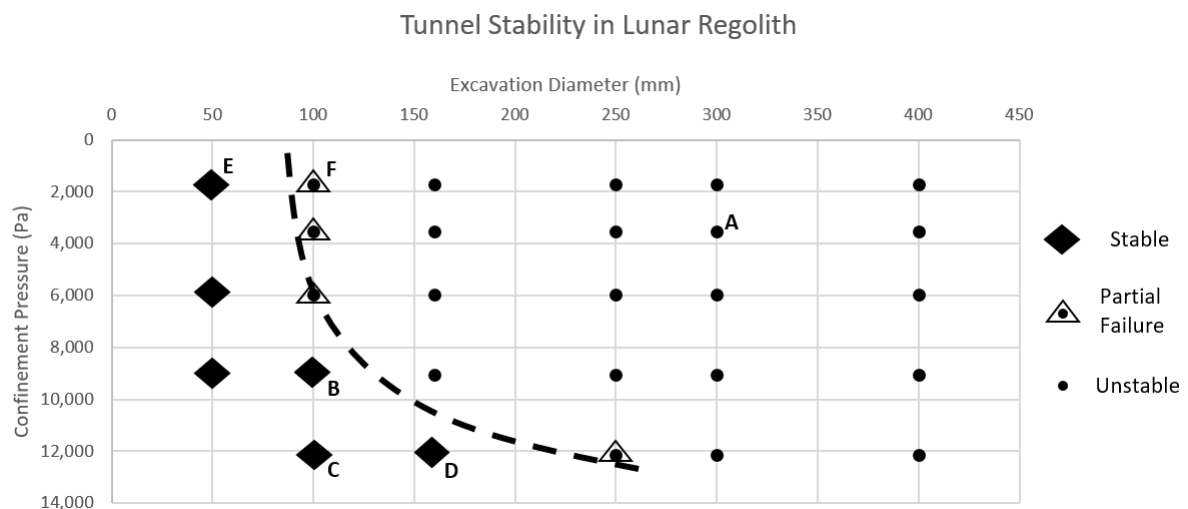
FIG 2 – Tunnel stability graph for lunar regolith (Pelech *et al,* 2022).

The results indicate that tunnel stability increases with confinement pressure (or depth) and decreases with an increase in its diameter. Figure 2 also shows that maximum possibly opening size would be 160 mm at depth of about 4 m. Further investigation has been made for this stable tunnel under seismicity loading which is 2 mm-amplitude and 10 Hz – frequency based on the reported lunar seismicity by Lammlein (1977). Stability of openings is decreased under given seismic conditions which may be induced by not only moonquake, also by vibrations from machine excavations or nearby rockets.

REFERENCES

Cai, M, Kaiser, P K, Morioka, H, Minami, M, Maejima, T, Tasaka, Y and Kurose, H, 2014. FLAC/PFC coupled numerical simulation of AE in large-scale underground excavations, *Int J Rock Mech Min Sci,* 44:550–564.

Carrier III, W D, Olhoeft, G R and Mendell, W, 1991. Chapter 9: Physical Properties of The Lunar Surface, in G H Heiken, D T Vaniman and B M French (eds.), *Lunar Sourcebook*, Cambridge University Press, 1991.

Cheatham, J B, 1993. A new hypothesis to explain stability of borehole breakouts, *Int J Rock Mech Min Sci Geomech Abstr*, 30:1095–1101.

Colwell, J E, Batiste, S, Horányi, M, Robertson, S and Sture, S, 2007. Lunar surface: Dust dynamics and regolith mechanics, *Reviews of Geophysics*, 45(2).

Cundall, P A and Strack, O D, 1979. A discrete numerical model for granular assemblies, *Geotechnique*, 29:47–65.

Ito, T, Kurosawa, K and Hayashi, K, 1998. Stress Concentration at the Bottom of a Borehole and its Effect on Borehole Breakout Formation, *Rock Mech Rock Eng,* 31:153–168.

Lammlein, D R, 1977. Lunar seismicity and tectonics, *Physics of the Earth and Planetary Interiors*, 14(3):224–273.

Pelech, T, Barnett, N, Dello-Iacovo, M, Oh, J and Saydam, S, 2022. Analysis of the stability of micro-tunnels in lunar regolith with the Discrete Element Method, *Acta Astronautica,* 196:1–12.

Potyondy, D O and Cundall, P A, 2004. A bonded-particle model for rock, *Int J Rock Mech Min Sci*, 41:1329–1364.

Vardoulakis, I G and Papanastasiou, P C, 1988. Bifurcation analysis of deep boreholes: I, Surface instabilities, *Int J Numer Anal Methods Geomech,* 12:379–399.

Zheng, Z, Kemeny, J and Cook, N G W, 1989. Analysis of borehole breakouts, *J Geophys Res Solid Earth*, 94:7171–7182.

Investigation of the internal mechanical structure of Mars based on geometrical patterns of faults

Y Tsukurimichi[1], T Takemura[2], D Asahina[3] and T Endo[4]

1. Master's student, Nihon University, Tokyo, Japan, 156–8550.
   Email: chyu22005@g.nihon-u.ac.jp
2. Professor, Nihon University, Tokyo, Japan, 156–8550. Email: takemura.takato@nihon-u.ac.jp
3. Senior Scientist, Geological Survey of Japan, AIST, Ibaraki, Japan, 305–8567.
   Email: d-asahina@aist.go.jp
4. Master's student, Nihon University, Tokyo, Japan, 156–8550.
   Email: chtk22001@g.nihon-u.ac.jp

INTRODUCTION

Scientific knowledge of Mars' surface morphology and internal geological structure has been accumulated through satellite imagery and numerical topographic data using remote sensing technology, as well as seismic surveys by the on-site lander. Recent studies show that Marsquakes could be caused by the release of strain energy generated by the contraction of Mars. In particular, Marsquakes occur around the graben where many faults are existed and formed regularly spaced patterns. This implies that Marsquakes occur when the stress field of the Martian crust is an extension condition, and normal faults appear on the surface.

We focus on the linear relationship between the fault spacing and the thickness of the mechanical layer as an approach to studying the internal structure from satellite images. Mechanical layer is a layer that composes of the same mechanical properties and is mainly bounded by lithology (Narr, 1991; Gross, 1993). The linear relationship between the thickness of the mechanical layer and the joint spacing has been studied and its slope is called the Fracture-Spacing Index (FSI) (Narr and Suppe, 1991). Soliva, Benedicto and Maerten (2006) showed that the stress drop zone (stress shadow) due to the fault activities affects the fault spacing. Figure 1 shows the approach used to estimate the thickness of the mechanical layer from the fault spacing on Mars.

This paper aims to better understand the internal mechanical structure of Mars estimated by the geometrical pattern of faults on the Martian surface. We report the initial studies of this work. The lab-scale physical experiments and numerical experiments were presented to demonstrate the relationship between the thickness of the mechanical layer and the geometric pattern of fractures formed in an extension field.
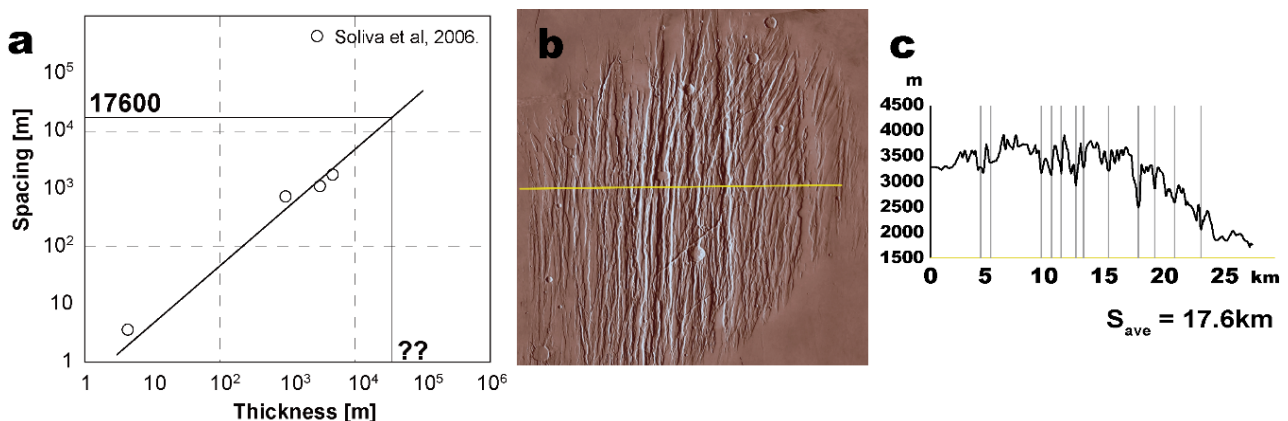
FIG 1 – An approach to estimate the mechanical layer of Mars based on the fault spacing. (a) Relationship between fault spacing and mechanical layer thickness (Soliva, Benedicto and Maerten, 2006), (b) Illustration of faults in the Olympica Fossae with the yellow scan line (Mars Trek (https://trek.nasa.gov/mars/)), (c) Elevation differences on the scan line in (b).

EXPERIMENTAL STUDY

Figure 2a shows a photograph of the equipment used for the experiment (300 mm × 500 mm × 250 mm high with a 10 mm thick acrylic sheet). An acrylic box was filled with dried kaolin, and the tensile stress field was reproduced by pulling the rubber sheet at the bottom of the box. The fracture spacing, recorded by the attached camera, was measured for different thicknesses of the kaolin layers (Figure 2b). The test duration was 5 minutes and the torque was kept constant at 4.32 Nm, and the maximum horizontal displacement at the edge of the kaolin layer was about 30 mm. We semi-automated the process to measure the fracture spacing as follows. First, the morphological operation was conducted to remove uneven illumination in the captured photo images, and they were binarised. Thereafter, the 100 scan lines were equally aligned in the tensile direction of the kaolin layer (ie perpendicular to the fracture), and the distances between neighbouring points on the fracture was measured and averaged.
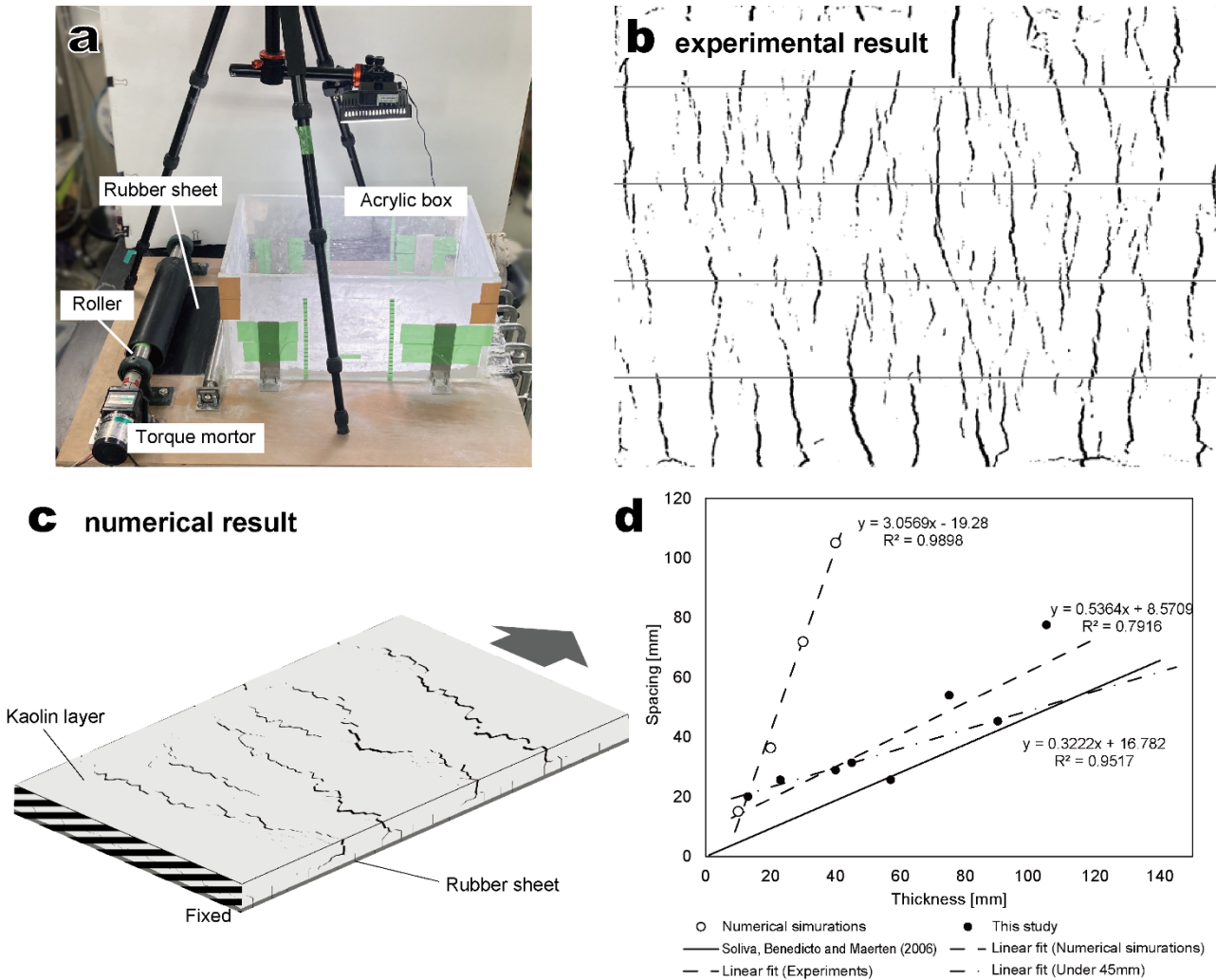
FIG 2 – Procedure and results of experiment and numerical simulates. (a) The photograph of the experimental set-up, (b) Binary image of the experimental results. In this figure, only four scan lines out of 100 are drawn. (c) Numerical results. Arrows indicate the tensile direction. (d) Experimental and numerical results. Solid line shows $S_{ave} = 0.45T^{1.01}$ (Soliva, Benedicto and Maerten, 2006).

NUMERICAL SIMURATIONS

The above experiments are simulated using the lattice models to demonstrate their basic fracture characteristics (Figure 2c). Lattice models are used to represent elastic continua and fracture development. The approach considered here is based on the Rigid-Body-Spring concept of Kawai (1978). Details regarding the lattice model are given elsewhere (Asahina *et al*, 2018). The computational domain is the same as the experiments discussed above, and the model is discretised with nodes, corresponding to the number of Voronoi cells. Two physical properties were assumed:

the rubber sheet and the kaolin layer. The horizontal displacements (maximum 30 mm) of the lattice node for the bottom rubber sheet are prescribed as the boundary conditions. Young's modulus of kaolin was set to 15.23 GPa (Vanorio, Prasad and Nur, 2003) and the tensile strength to 0.06 MPa (Pembele, Gui and Stirling, 2019). The simulation was conducted ten times with different domain discretisation for each layer thickness, and the average fracture spacing was measured.

RESULTS AND CONCLUSION

Figure 2d shows the results of experiments and simulations. The linear relationship between the thickness and the spacing has a high correlation, $R^2 = 0.9517$, under conditions with kaolin thicknesses of less than 45 mm. However, the correlation is low, $R^2 = 0.7916$, for data containing kaolin with a thickness of 45 mm or more. This difference suggests that crack spacing is governed by the boundary conditions of the equipment in this study for thicknesses greater than 45 mm.

On the other hand, the results of numerical simulation show that the relationship between the fracture spacing and thickness is linear, whereas its slope is larger than that of the experiment and the results of Soliva, Benedicto and Maerten (2006). At this stage of model development, it is not clear what the slope and intercept depend on. A subsequent study will investigate the proper assignment of physical parameters and fracture representation of the kaolin layer. We will use this approach to estimate the thickness of the mechanical layer of Mars based on the satellite imagery of the fault spacing.

REFERENCES

Asahina, D, Pan, P, Tsusaka, K, Takeda, M and Bolander, J E, 2018.2018. Simulating hydraulic fracturing processes in laboratory-scale geological media using three-dimensional TOUGH-RBSN, *Journal of Rock Mechanics and Geotechnical Engineering*, 10(6):1102–1111. doi: 10.1016/j.jrmge.2018.09.001.

Gross, M R, 1993. The origin and spacing of cross joints: examples from the Monterey Formation, Santa Barbara Coastline, California, *Journal of Structural Geology*, 15(6):737–751. doi: 10.1016/0191–8141(93)90059-J.

Kawai, T, 1978. New discrete models and their application to seismic response analysis of structures, *Nuclear Engineering and Design*, 48(1):207–229. doi: 10.1016/0029–5493(78)90217–0.

Narr, W and Suppe, J, 1991. Joint spacing in sedimentary rocks, *Journal of Structural Geology*, 13(9):1037–1048. doi: 10.1016/0191–8141(91)90055-N.

Narr, W, 1991. Fracture density in the deep subsurface: techniques with application to Point Arguello oil field, *American Association of Petroleum Geologists Bulletin*, 75(8):1300–1323. doi: 10.1306/0c9b2939–1710–11d7–8645000102c1865d.

Pembele, W, Gui, Y and Stirling, R, 2019. Laboratory tensile strength testing of clay soils using direct measurement, *7th Asia-Pacific Conference on Unsaturated Soils, AP-UNSAT 2019*, pp 198–204. doi: 10.3208/jgssp.v07.030.

Soliva, R, Benedicto, A and Maerten, L, 2006. Spacing and linkage of confined normal faults: Importance of mechanical thickness, *Journal of Geophysical Research: Solid Earth*, 111(1):1–17. doi: 10.1029/2004JB003507.

Vanorio, T, Prasad, M and Nur, A, 2003. Elastic properties of dry clay mineral aggregates, suspensions and sandstones, *Geophysical Journal International*, 155(1):319–326. doi: 10.1046/j.1365–246X.2003.02046.x.

Geotechnical design methodologies

Analysis and Design of Faceroad Roof Support (ADFRS)

M Colwell[1]

1. Director, Geotechnical Software Services Pty Ltd, Caloundra Qld 4551.
   Email: markcolwell@bigpond.com

ABSTRACT

This paper summarises the results of a research project whose goal was to provide the Australian coal industry with a longwall installation roadway (faceroad) design methodology that could be utilised by suitably qualified colliery personnel. This goal was achieved in 2012 and the design methodology (and software package) is referred to as Analysis and Design of Faceroad Roof Support (ADFRS). The intended benefits to underground operations, in the provision of this information and resource, are a safer and more productive workplace.

ADFRS filled the gaping void that existed with respect to the geotechnical design and management of Australian faceroads. In addition to the standard two-pass widening section of the faceroad, ADFRS deals with all other aspects of faceroad roof support design, including intersections, stables and adjacent maingate and tailgate intersections. In subsequent years further research and data collection were undertaken so that in addition to faceroads, ADFRS can be readily used for all forms of wide-roadway roof support design, such as belt chambers and tripper drives.

ADFRS is based on a sound mechanistic understanding of the roadway development and widening process and the design equations (with very strong correlations) are fully consistent with measured roof behaviour. To the best of the author's knowledge, ADFRS is the only systematic wide-roadway design technique to be developed for any country's underground coal industry.

INTRODUCTION

As a result of Australian Coal Association Research Program (ACARP) project C19008, the Analysis and Design of Faceroad Roof Support (ADFRS) design methodology was developed (Colwell and Frith, 2012). The intent of the research was to develop a roof support design methodology for wide-roadways. Based on past and current coal mining regulations, a wide-roadway is generally considered to be greater than 5.5 m wide and in most cases is the result of widening an existing roadway.

The research project focused on faceroads so that the design methodology would encompass all aspects of their formation, including the standard two-pass widening, faceroad intersections, stables and adjacent maingate and tailgate intersections. In subsequent years further research and data collection were undertaken so that in addition to faceroads, ADFRS can be readily used for all forms of wide-roadway roof support design and has been the dominant wide-roadway roof support design technique in Australia for the last 10 years.

To assist mine site geotechnical engineers effectively utilise ADFRS, a windows-based software program was developed so that calculations could be undertaken without mathematical error and technical support is available via an extensive Help facility. The software package is licensed/used by over 70 per cent of Australian longwall mines for wide-roadway roof support design.

BACKGROUND

Prior to ADFRS, faceroad performance associated with Australian collieries had been quite problematic. By way of example; of the 207 cases associated with the two-pass data set, 40 resulted in an unsatisfactory outcome involving the use of standing support, PUR injection and/or high levels of remedial tendon support with two faceroads 'lost' and having to be re-driven due to major roof falls in the two years prior to the study commencing.

Several other faceroads were abandoned in previous years due to major roof falls, however due to a lack of information they could not be included in the database. Nonetheless, a failure rate of around 20 per cent was simply unacceptable to Australian collieries and why the industry (via ACARP) funded the project.

In relation to other strata control issues, such as coalmine pillar and roof support design for standard roadway widths (ie typically between 4.5 to 5.5 m), there had been comparatively very little research undertaken in relation to the geotechnical design and management of faceroads. In fact there was a dearth of publications and prior research in relation to wide-roadway formation.

Due to the lack of reference material and to assist in achieving the goal of developing a roof support design methodology for faceroads that could be effectively utilised at all collieries, a comprehensive review of the existing, as well historical, practices associated with the design/management of Australian faceroads was undertaken. This also greatly assisted in an improved understanding of the reasons behind such a high failure rate. Learning from the past, both in terms of one's own as well as other's successes and mistakes, is crucial to individual and humankind's advancement and a basic process if we are not to continue repeating past mistakes.

Prior to ADFRS, Thomas' (2010) findings essentially represented Australian collieries' state of empirical knowledge with respect to faceroad roof support design and included the only published relationships relating roof support levels to some measure of the roof strength and stress acting. Figure 1 compares/plots the Reinforcement Density and Secondary Reinforcement Density Indices (RDI and SRDI) to an index referred to as the Stress Strength Ratio (SSR) and relates to Thomas' (2010) non-stress relieved wide-roadway database, which he defined as a roadway which is widened without the aid of a stress-relief or sacrificial roadway. This definition applies to the majority of faceroads formed in Australia.

(a) RDI v's SSR   (b) SRDI v's SSR
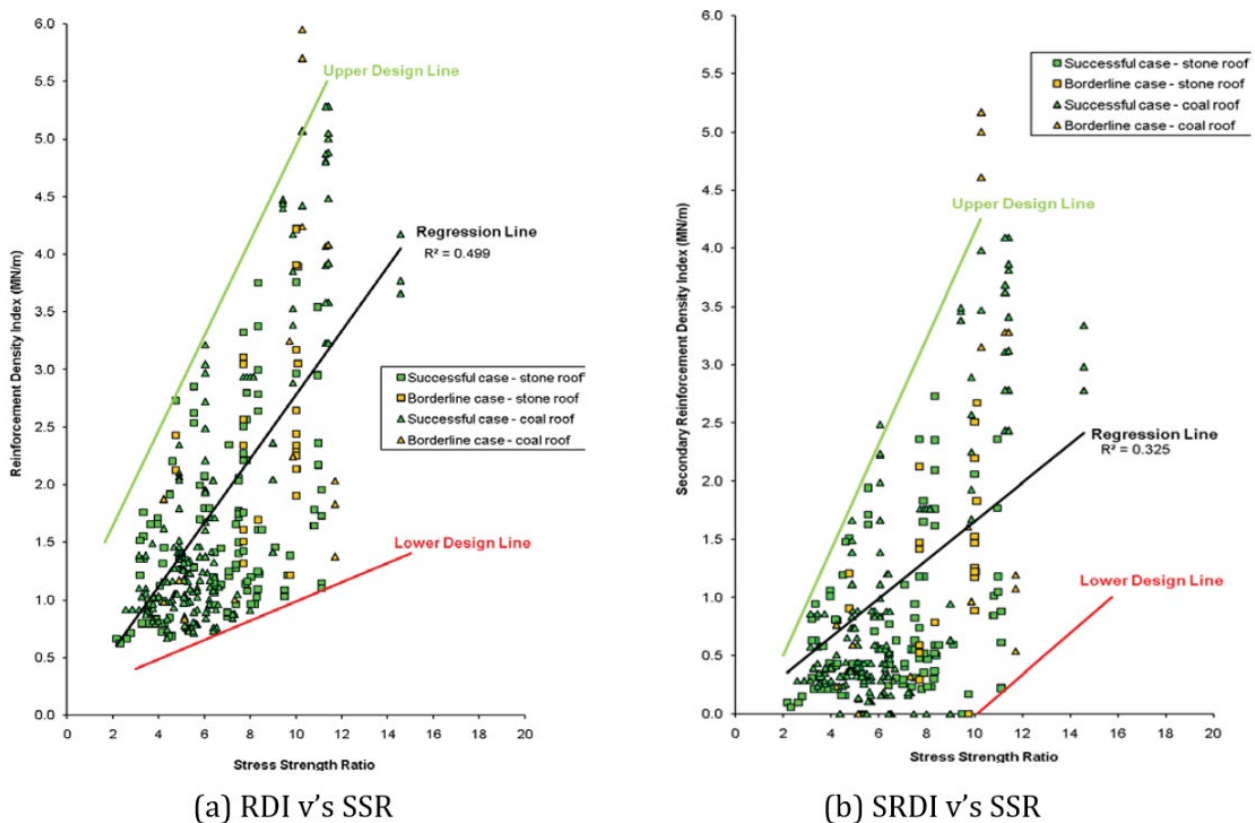
FIG 1 – Reinforcement Density Indices (RDI) and Secondary Reinforcement Density Indices (SRDI) versus Stress Strength Ratio (SSR) (after Thomas, 2010).

The RDI is reported in MN/m of roadway length and includes all roof bolts and longer tendons in its calculation with respect to the fully widened roadway; while the SRDI only relates to the longer cables that are installed within the roof. A significant point of note (which will be the subject of further discussion), is that both the RDI and SRDI include the actual length of the longer tendons within the roof as a part of their calculation.

Thomas (2010) states, *'roof behaviour is largely a function (assuming all other factors are equal) of the competency of the roof and the magnitude of the horizontal stress'* and *'in order to provide some form of measure of the roof's propensity to buckle'* he proposed the use of the SSR, where

the SSR is the depth of cover (H, m) divided by the Coal Mine Roof Rating (CMRR). The author totally agrees with the first quote, however further discussion concerning the use of the SSR is required as there are four basic problems:

1. By using depth of cover, the measure for stress that is utilised in calculating the SSR is essentially the vertical stress, which is <u>independent</u> of the drivage direction. However, the stress that is acting to cause failure within the roof is the resultant horizontal stress acting across the roof, which is <u>dependent</u> on the drivage direction. Across a coalfield there can typically be a moderate to strong relationship between horizontal and vertical stress and therefore, to a degree, vertical stress can be used as a 'surrogate' for horizontal stress in some analyses where *in situ* stress measurements are unavailable. This is typically not the case in Australia, where collieries routinely carry out *in situ* stress measurements such that the data is generally available.

   In terms of any empirical/analytical/numerical roof stability analyses, using the actual major and minor horizontal stress levels (acting within roof units of varying modulus) and computing the resultant horizontal stress acting perpendicular to the drivage direction is far superior to simply using vertical stress. Furthermore, the use of vertical stress is in direct conflict with Thomas' (2010) own statement, ie *'roof behaviour is largely a function (assuming all other factors are equal) of the competency of the roof and the magnitude of the horizontal stress'.*

2. The SSR combines measures of stress and roof 'strength' together as a single index for assessing roof support levels. From a structural engineering viewpoint, it is far better that the two indices remain separate and therefore understood/assessed individually before bringing them together (but still as two distinct indices) in terms of the outcome being analysed; whether the outcome is a Factor of Safety (FOS) or a required level of roof support.

3. The use of the SSR in this manner results in the application of simple linear regression (as illustrated in Figure 1), where only one explanatory/independent variable (ie SSR) is utilised to predict a continuous outcome (the dependent variables RDI or SRDI), as opposed to the use of multiple regression, with both stress and a measure of roof strength as independent variables, which would be far more appropriate.

4. The SSR calculation specifically relates to the CMRR and in-turn the CMRR relates directly to the primary bolted interval, which in terms of the ADFRS database ranged from 1.8 to 2.4 m. As demonstrated by research conducted in Australia and the United States (US), this is more than reasonable for a standard width roadway, however as will be discussed, for a widened roadway further distances into the roof need to be considered when evaluating roof stability and therefore roof support levels.

In relation to Figure 1 Thomas (2010) explains,

> *'the term 'successful' refers to those cases which exhibited controlled decelerations in displacement rate and/or low rates of on-going movement following widening and the term 'borderline' refers to those cases which exhibited creep rates of >2 mm/week following widening and/or required the use of PUR injection and/or standing support to control the roof.'*

When interviewing colliery personnel, it was found that the vast majority recognised that the use of polyurethane resin (PUR) injection and/or standing support to prevent a roof fall is an unacceptable (and therefore an unsuccessful not 'borderline') outcome. Furthermore, there are serious safety considerations for those who are called upon to install standing support and/or inject PUR under an unstable roof.

In addition, where a roof fall is considered imminent; stabilising the roof cannot usually be initially achieved with cables due to the time period required to install such support and the capacities needed to control 'dead weight roof loads' in a wide-roadway and therefore standing support is typically utilised. However, the standing support employed will need to be removed prior to installing the longwall shields, hence significant other remedial support measures (eg cable slings, long tendons and strata consolidation via resins/grouts ie PUR injection) will be required before the standing support can be removed.

The strength of the relationships displayed on Figure 1, would for geotechnical design be considered weak with R^2 values of 0.499 and 0.325 respectively. With only weak relationships and a large variance between upper and lower 'design' lines, it was necessary that intensive monitoring and reacting to the monitoring was a critical component of Thomas' (2010) faceroad design strategy.

This 'design strategy' of Thomas (2010) came to be known in Australia as the *'minimum support, monitor and react strategy'*, which because faceroads are formed up on the critical path for the start-up of the next longwall panel appealed to some collieries. It was believed that a colliery could compensate for an inadequate roof support design via monitoring and react in time with remedial tendon support to stabilise the roof, however in many instances this proved not to be the case.

The *'minimum support, monitor and react strategy'* is now fully recognised as an unacceptable design/management approach and does not comply with (and is contradictory to) the legislative environment under which Australian collieries are compelled to operate and manage risk, requiring the use of both effective pre-mining geotechnical design and a formal operational Strata Management Plan (SMP).

As a result of this background, it is not surprising that faceroad performance associated with Australian collieries had been quite problematic. The principal reason for such a failure rate was the clear absence of suitable design equations that can accurately assess the required levels/type of roof support as a function of some valid measure of the competency of the roof and the horizontal stress acting across the roadway. Therefore the goal of the study was clear; that being to develop such equations around which a credible design methodology could be formulated.

FACEROADS – PRACTICE AND OUTCOMES

Faceroads in Australia are developed in two or more passes in order to form the final excavation width. For the majority of a faceroad's length, it would be usual to drive the 1st pass at the standard roadway width used at the mine (typically between 4.8 and 5.4 m) and then 'strip' out on either side of the roadway to form the final roadway width of approximately 7.5 to 12 m, depending upon the size of the longwall face equipment.

The major advantage of forming up wide-roadways in two or more passes is that it allows the full range of roof conditions along the roadway to be exposed at a standard roadway width prior to widening. Therefore the actual condition of the roof and the need for secondary cable support prior to widening can be reviewed on a more informed basis.

In reviewing faceroad formation practice, creating/analysing the database and subsequently developing a credible design methodology, some measure or statement of acceptable or unacceptable outcomes needs to be available. Furthermore, in addressing/assessing the issue of success/failure; it is necessary to consider the operational context in which the safety of mine-workers is taken as a mandatory requirement.

The general design requirement is for a suitably conservative level of roof support along the faceroad while no more than is prudent from a risk-based perspective. Both optimistic under-support (eg *'minimum support'*) and highly cautious over-support carry significant business risks in the context of minimising the production outages between successive longwall panels. In technical/operational terms, success or failure with respect to roof support design will be related to a roof stability outcome, accepting that this will have a consequent effect on mining operations.

In terms of a satisfactory outcome, ostensibly there really is only one definition; namely that the faceroad roof behaves in such a way that the Trigger Action Response Plan (TARP) is not triggered to the extent that there is a requirement to undertake remedial roof support measures in order to maintain its serviceability up to the time of longwall shield installation.

This does not mean that the roof does not move or that time dependent creep effects do not occur following widening, simply that the measured outcomes are tolerable in the context of the faceroad requirements. Furthermore with respect to roof movement, there are many instances where only the first level of the TARP is triggered and this generally requires greater observation/more frequent monitoring to ensure a load-balance within the roof re-establishes (ie the reinforced roof

'settles down' and is still self-supporting) rather than the immediate introduction of remedial support.

The need for remedial ground support is of course <u>never</u> desirable and in some instances cannot be tolerated. For example, with respect to belt roads; the installation of any type of remedial (tendon or standing) support about the conveyor belt is even more difficult (as compared to a faceroad/travel road/tailgate), will inevitably cause production stoppages and is essentially unacceptable, whereas in other instances, remedial action is more tolerable as the safety/productivity risk is lower.

The critical issue is that remedial support, if required, is installed to further reinforce and control a reinforced roof that is still self-supporting and that the roof has not softened to an extent where a roof fall is potentially imminent endangering worker safety. Therefore the use of standing support and PUR along a faceroad or remedial cables to 'suspend' a softened roof would be an unacceptable outcome in terms of a <u>proactive</u> design methodology.

Based on the preceding background/discussion, the faceroad roof condition (or section thereof) was assessed both subsequent to 1st pass drivage and after the faceroad was fully widened utilising the following three criteria based categories:

1. **Satisfactory** – is where faceroad development went according to plan and while there may be a low level or infrequent triggering of the TARP, essentially no remedial roof support was required.

2. **Manageable** – is where the TARP is being triggered on a more frequent basis and/or there is a need for low to isolated moderate levels of remedial tendon roof support.

3. **Unsatisfactory** – is where a roof fall or faceroad abandonment has occurred, where PUR or standing support is required and/or where significant levels of remedial tendon roof support is required to suspend a softened roof.

THE INDUSTRY REVIEW

The aim of the industry review was to:

1. Construct both a contemporary and historical database of faceroad performance.

2. Utilise this information to determine the significant predictors of that performance.

Information was collected from 26 longwall operations involving all the major Australian coalfields, with 162 faceroads reviewed in terms of completeness and accuracy for inclusion in the final database. Based on the quality and completeness of the information provided, this resulted in 123 case studies suitable for inclusion in the database. These 123 case studies generated:

- 169 standard widening cases ranging in width from 7.5 to 9.5 m.

- 160 stables (ie shearer, maingate and tailgate stables) ranging in width from 7.7 to 12 m.

- 30 faceroad intersections.

- 64 maingate/tailgate intersections adjacent to the faceroad.

A standard widening case is where after development of the 1st pass of the faceroad there is only one further drivage/stripping sequence, being referred to as the 2nd pass. The standard widening will account for the vast portion of the faceroad. There were instances where the roof properties along the faceroad differed sufficiently resulting in noticeably variable roof behaviour and/or requiring variable levels of roof support generating two or more standard widening cases for the one case study.

With respect to the stables, it was not uncommon that their formation involved three and even up to four passes. In terms of the shearer stables; where a shearer stable was removed from the influence of the maingate/tailgate intersections (ie it is not a maingate or tailgate stable) 38 of these 54 cases were formed by a 1st and 2nd pass sequence. Therefore these 38 shearer stable cases could be readily combined with the 169 standard widening cases in terms of the statistical analyses as they are formed on simply a two-pass basis, resulting in 207 two-pass cases.

During the site inspections, information collected included geometric details, *in situ* stress measurements, roof/floor/rib material properties (including structural discontinuity information) and ground support patterns which included the type, placement, timing and quantity of roof/rib support installed (including remedial support where required). All available monitoring information as well as TARP/SMP related documentation was also collected. Where stress-relief roadways were utilised, this was noted and the effect on faceroad performance was assessed.

In addition, discussions were held with colliery personnel to ascertain how current faceroad performance compared to past experience. On most occasions this resulted in additional cases for inclusion in the database as well as a detailed description of the gradual development of the faceroad ground support/monitoring/TARP systems currently employed at the colliery. This allowed for a greater appreciation of some of the historical difficulties encountered by the collieries in satisfactorily managing faceroad behaviour. The collection of this information also allowed for a thorough understanding of the faceroad design techniques employed by Australian collieries.

Rock Mass Classification (RMC) systems

The study tested all RMC systems typically utilised by Australian collieries for roof support design. By far the most commonly used RMC index is the CMRR, which is assessed and calculated specifically in relation to the primary bolted interval. Via the various Analysis of Longwall Tailgate Serviceability (ALTS) research projects (Colwell and Frith, 2009), it has been amply demonstrated that the CMRR can be successfully used for roof support design purposes at all Australian collieries.

In addition to the CMRR, at several collieries the average Uniaxial Compressive Strength (Average UCS, MPa) of the roof (over various distances above the roofline) is contoured and at some collieries the Average UCS had been utilised to specify roof support levels. The Average UCS was typically derived from borehole sonic velocity logs, where sonic velocity had been correlated with laboratory UCS values.

Another RMC index sometimes utilised was the Roof Strength Index (RSI), which is also calculated over various distances above the roofline and is the Average UCS divided by the vertical stress (ie $RSI = $ Average UCS/σ_V) and therefore is essentially the reverse of the SSR (ie $RSI = $ strength/stress as opposed to SSR = stress/strength). As yet no industry-wide roof design tool/methodology has been developed using Average UCS or RSI.

When commencing the study, an alternative RMC index had been proposed, namely the Geophysical Strata Rating (GSR). Hatherly *et al* (2009) suggested that the GSR delivers results that are commensurate with CMRR values, or more to the point the individual Unit Rating (UR) values, which are essentially the 'basic building blocks' of the CMRR (refer Mark and Molinda, 2007). It should be noted that a GSR value is actually calculated every 5 to 10 cm (dependent on the geophysical logs) along the section of the borehole under review, therefore once the rock unit has been identified an Average GSR for the unit is calculated and consequently is more akin to the UR than CMRR, as the CMRR includes various adjustments in its final calculation.

Medhurst *et al* (2010) explained the GSR had been extended to allow for the assessment of coal units, with this being an extremely important consideration for its inclusion in the study. With respect to Australian collieries, currently and historically there is an abundance of coal roofs or mine roofs with a significant percentage of coal. In terms of coal as a roof/rock unit, it comprises approximately 40 per cent of all the rock types associated with the ALTS/ADFRS databases.

If the GSR could find the same widespread application and acceptance, as for example the CMRR has; then collieries could take full advantage of all available borehole information (ie geotechnical/geophysical logging and geomechanical testing of the core) for geotechnical design and evaluation purposes. Also the real test of any RMC index when used for ground support design is the strength of the correlations with respect to ground support levels. This can only be truly ascertained if the index is tested via an industry-wide database and the GSR was yet to be tested in this manner.

STATISTICAL ANALYSES

The statistical techniques of linear and logistic regression were utilised in examining the ADFRS database. Linear (including simple and multiple) regression techniques are routinely used where the outcome is continuous rather than categorical. Multiple regression is a statistical technique that uses several explanatory/independent variables to predict the outcome.

The ALTS research demonstrated that the principal geotechnical drivers which, in combination, essentially dictate the level of roof support required to maintain a stable roof both on development and during longwall extraction are the structural integrity of the immediate roof (as measured by the CMRR) and the resultant horizontal stress acting across the roof (σ_R, MPa) with its calculation based on the use of the Tectonic Stress Factor (TSF) model, which includes both a gravity and tectonic component as described by Nemcik, Gale and Mills (2005).

The Primary Roof Support (PRSUP) rating is a measure of the tendon capacity (kN/m^2) along the roadway normalised to the primary bolted interval (ie over which the CMRR is calculated) and includes all bolt/cable roof support that is installed off the continuous miner during roadway development. It is common in Australia to install longer cables off the miner for improved roof stability subsequent to development.

The Ground Support (GRSUP) rating incorporates all bolt and longer tendon roof support installed within the roof into a single rating, regardless of when the roof support is installed. GRSUP is calculated in a similar manner to that of the PRSUP; in fact if no additional support is installed within the roof subsequent to that installed off the continuous miner, then GRSUP will equal PRSUP.

The term 'normalised' means; that where a tendon/cable length is greater than the primary bolt length, it is the primary bolt length and not the cable's actual length which is utilised in conjunction with the cable's Ultimate Tensile Strength (UTS, kN) and support density to calculate the cable's contribution to the overall PRSUP/GRSUP ratings. By: (1) normalising PRSUP/GRSUP to the primary bolted interval, as well as (2) calculating σ_R over the same roof interval; a direct/valid comparison to the CMRR can be made. For further information in calculating PRSUP/GRSUP and σ_R, the interested reader is referred to Colwell and Frith (2012).

Based on the ALTS research and the use of multiple regression; Figure 2 illustrates the required level of primary roof support (designated as $PRSUP_{Dev}$) to maintain satisfactory roof stability subsequent to development, while prior to the roadway being subject to either: (1) adjacent longwall extraction, or (2) roadway widening; where $PRSUP_{Dev}$ is a function of the CMRR and the resultant horizontal stress acting normal to the development direction, designated as σ_R-Dev (MPa).
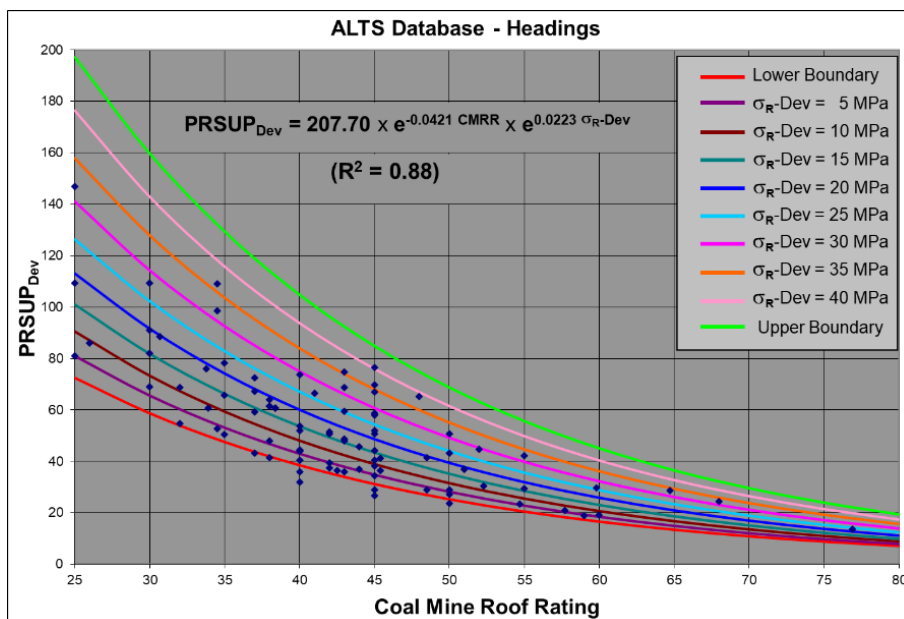
FIG 2 – $PRSUP_{Dev}$ versus CMRR and σ_R-Dev.

The relationship depicted makes perfect mechanistic sense and also illustrates that the PRSUP$_{Dev}$ versus CMRR relationships for varying stress levels acting across the roof (σ_R-Dev) fit seamlessly within the upper and lower boundaries. The extraordinarily high correlation (ie R^2 value) of 0.88 essentially means that 88 per cent of the reason(s) as to why Australian collieries select primary roof support levels to maintain satisfactory roadway conditions to an Australian 'standard', is a function of the CMRR and σ_R-Dev. In relation to the 12 per cent not accounted for directly by the relationship, this would include a number factors other than purely geotechnical considerations; a perfect example being the variability in the quality and timing of bolt/cable installation across the industry (ie operational/human factors).

The ALTS research confirmed what one would intuitively expect; if the actual cable length was utilised in calculating PRSUP$_{Dev}$ this had a significant negative impact on the resultant correlations. This being a contributing factor as to the weak correlations associated with Figure 1. It is critical that σ_R-Dev and PRSUP directly relate to the primary bolted interval so a direct/<u>valid</u> comparison to the CMRR can be made.

Cable length selection should be based on factors such as the anticipated Height of Softening (HOS, m), required anchorage length and the competency of the roof unit into which the cables are anchoring and therefore using roof support indices such as RDI and SRDI, which can wrongly influence cable length selection, is inappropriate.

In relation to the ALTS research; dependent on the roadway under consideration for design, the inclusion/exclusion of case types varied. Similar analyses were conducted in relation to the various faceroad data sets combining the satisfactory and manageable cases.

Linear regression analyses – two-pass data set

Due to space constraints associated with a conference paper it is only the two-pass data set analyses that are presented herein. The interested reader is referred to Colwell and Frith (2012) for a full description of all database analyses.

The two-pass faceroad data set comprises 207 cases; with 134 considered satisfactory, 33 manageable and 40 assessed as unsatisfactory. With respect to the linear (simple and multiple) regression analyses the satisfactory/manageable cases were combined (ie 167 cases) in terms of assessing appropriate levels of roof support. Based on the definition of a manageable case, it is reasonable to include such cases as the outcome will represent an appropriate level of roof support where a TARP is in place, which is a legislative requirement for all Australian collieries.

The initial series of multiple regression analyses reviewed total roof support levels (GRSUP Total) associated with the fully widened section of faceroad, in terms of the CMRR and σ_R-Dev resulting in a very strong correlation. With respect to the database, the primary bolt length ranged from 1.8 to 2.4 m with an average length of 2.0 m. However, it was recognised that for a fully widened faceroad (as compared to a standard width roadway) a greater distance into the roof should be reviewed. Therefore in addition to assessing the CMRR; for the subsequent series of multiple regression analyses set distances of 2 to 8 m at 1 m intervals into roof were also reviewed using average (ie weighted) values for UR, UCS, RSI and GSR.

σ_R-Dev was also re-calculated in terms of the distance and rock types within the section of roof under review. In keeping with the rationale of normalising the calculation of the GRSUP to the bolted interval (ie the distance over which the CMRR is calculated); for the set distances of 2 to 8 m (at 1 m intervals), any tendon roof support longer than the set distance under review was normalised to that distance. Therefore for a set distance of say 5 m, GRSUP Total, Average UR and σ_R-Dev were denoted as, GRSUP Total$_{5\,m}$, Average UR$_{5\,m}$ and σ_R-Dev$_{5\,m}$.

The multiple regression analyses (in combination with the logistic regression analyses, to be discussed) strongly indicated it was beneficial to utilise a roof section greater than the primary bolted interval in assessing the GRSUP Total required to maintain satisfactory/manageable faceroad behaviour subsequent to widening. It was found that there was no material benefit in terms of the correlations, beyond a distance of 5 m above the roofline (designated as the **5 m Roof Section**); nonetheless, it is <u>strongly</u> recommended that roof units up to 10 m above the roofline are reviewed to ensure the longer cables are anchoring in competent material.

In assessing GRSUP Total$_{5\,m}$; it was found that Average UR$_{5\,m}$ (as compared to UCS, RSI and GSR) was by far the superior RMC index. Based on the multiple regression analyses the following relationship for the 5 m Roof Section was found, which is also illustrated in Figure 3:

$$\text{GRSUP Total}_{5\,m} = 490.37 \times e^{-0.0427\ \text{Average UR}_{5}\,m} \times e^{0.0345\ \sigma_R\text{-Dev}_5\,m} \quad (R^2 = 0.75) \tag{1}$$
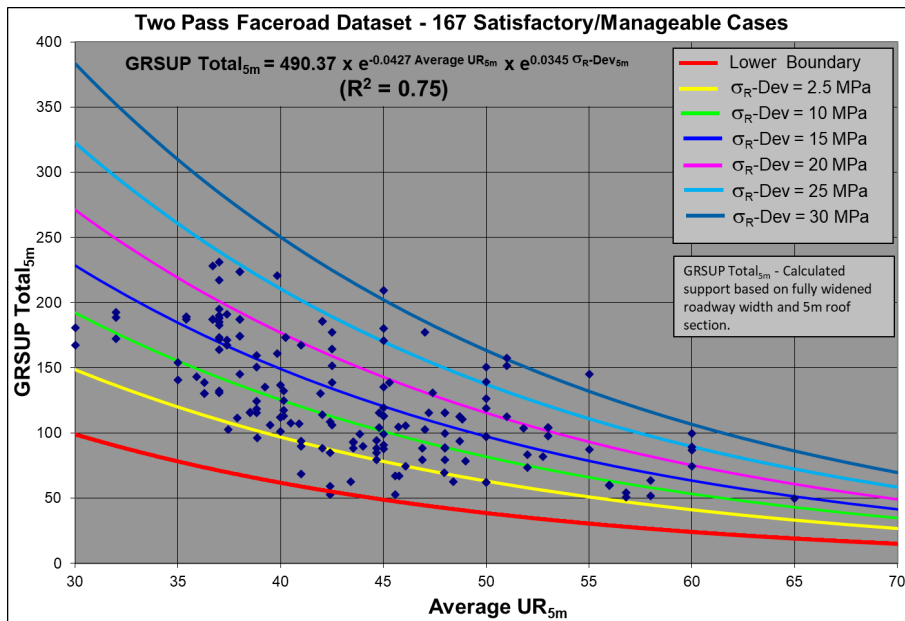
FIG 3 – GRSUP Total$_{5\,m}$ versus Average UR$_{5\,m}$ and σ_R-Dev$_{5\,m}$.

Another critically important aspect in relation to faceroad roof support design is to determine the appropriate level of roof support to install within the 1st pass prior to widening. Figure 4 plots the 1st pass GRSUP calculated over the 5 m Roof Section in terms of the fully widened roadway width (designated as GRSUP 1st Pass*$_{5\,m}$) with respect to GRSUP Total$_{5\,m}$. Figure 4 clearly indicates that approximately 65 per cent of the total roof support capacity installed within the fully widened faceroad is installed within the 1st pass prior to widening to achieve a satisfactory/manageable outcome.
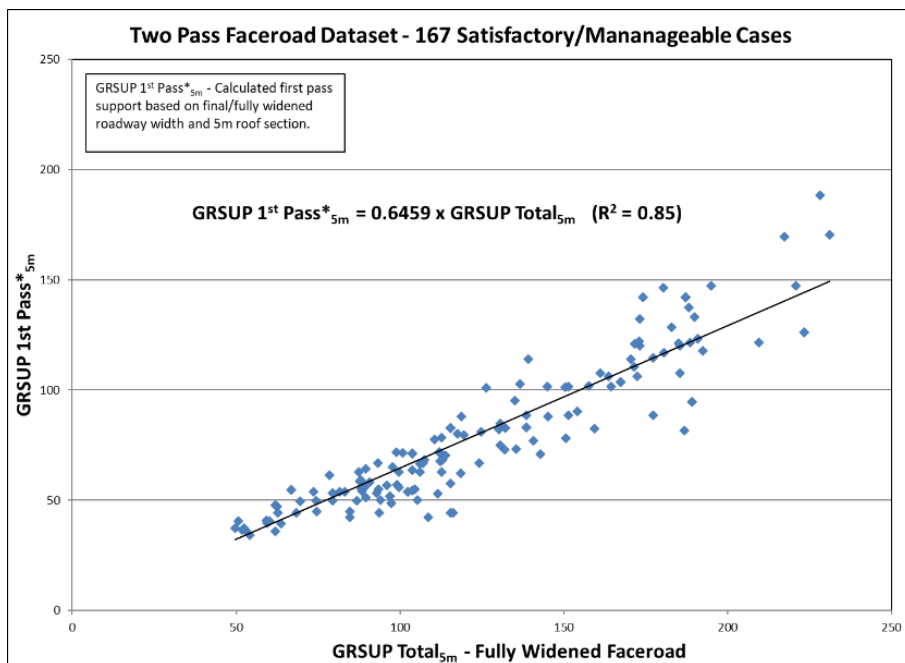
FIG 4 – GRSUP 1st Pass*$_{5\,m}$ versus GRSUP Total$_{5\,m}$.

On further examination it was found that on average 64.5 per cent of GRSUP Total$_{5\,m}$ was installed within the 1st pass with respect to the satisfactory cases, 61.9 per cent in terms of the manageable cases, while there was a significant drop to 54.2 per cent in relation to the unsatisfactory cases. Empirically and mechanistically the interpretation is that 1st pass stability is paramount to a successful widening and as will be discussed, the logistic regression analyses confirmed this interpretation.

Comparing average UR, UCS, RSI and GSR analyses

When utilising Average UCS, RSI and GSR over the 5 m Roof Section the correlations (ie R^2 values) were significantly lower being 0.54, 0.32 and 0.41 respectively as compared to 0.75 for Average UR$_{5\,m}$ with reference to Equation 1 and as illustrated in Figure 3. It is worth noting that by far the lowest correlation is that associated with the RSI, which is essentially the inverse of the SSR, thereby further demonstrating that both mechanistically and empirically, indices associated with roof strength and stress should be kept separate and only combined when the outcome is an FOS. This being another contributing factor as to the weak correlations associated with Figure 1.

It was extremely disappointing that the GSR returned such a weak correlation, however it was not totally unexpected as sonic velocity has approximately a 70 per cent impact on the GSR calculation or as Medhurst *et al* (2010) state, *'sonic velocity is the main driver of the GSR'*.

Like sonic velocity, the GSR is not able to satisfactorily assess the impact of bedding and laminations with respect to the lateral load-bearing capacity of a rock/coal unit where delamination occurs when subject to elevated horizontal stress conditions and/or roof sag. Sonic velocity, sonic-derived UCS, laboratory UCS and GSR are indices measured normal to the bedding/laminae, unlike the Discontinuity Rating associated with the UR/CMRR calculation, which directly relates to the bedding/laminae's impact on a roof unit's behaviour/stability where delamination occurs. The following explanation illustrates why the CMRR (and the individual UR's) is a far superior RMC system for coalmine roof strata.

As Galvin (2016) states,

> *'In coal mines, the immediate roof and floor strata are usually bedded due to the sedimentary origin of coal deposits. Bedding planes are characterised by low to zero tensile strength normal to the bedding planes and low shear strength relative to that of intact rock. Hence, bedding planes constitute potential slippage planes and can effectively divide the roof strata into an assembly of thin rock beams.'*

With respect to US collieries, Mark and Molinda (2007) state, *'Bedding was the factor that was most consistently cited as causing roof problems in coal mines. The two most common examples were weak laminations in shale and thinly interbedded sandstone and shale.'* They go on to explain that the issue of bedding (or grain alignment) is further complicated because some rock types may appear massive, but are actually highly laminated. For this reason, they emphasised the need for testing of the rock material to determine bedding plane/laminae strength even when the bedding is not readily visible, with the diametral point load test being the most appropriate in this regard.

Therefore in terms of horizontally bedded roof, the major structural feature is typically the bedding and/or laminae along which delamination occurs resulting in thinner (or slender) beams, which can buckle under sufficient horizontal stress with ensuing shear/tensile failure. Figure 5a is photo of a roof fall cavity associated with a Queensland colliery and clearly illustrates the formation of slender beams, their thickness dictated by the spacing of the carbonaceous laminae.

The rock type associated with the roof fall cavity is sandstone with abundant carbonaceous laminae as illustrated in Figure 5b, extending some 5 m above the roofline, which correlated directly with the height of the fall. Irrespective of the type of laminae, such laminated roof/rock units (with a varying intensity of laminae/bedding) as well as highly laminated coal units are extremely common roof/floor units with respect to Australian collieries.

(a) Roof Fall Cavity   (b) Roof core adjacent to roof fall site   (c) Sonic Velocity/GSR Interpretation
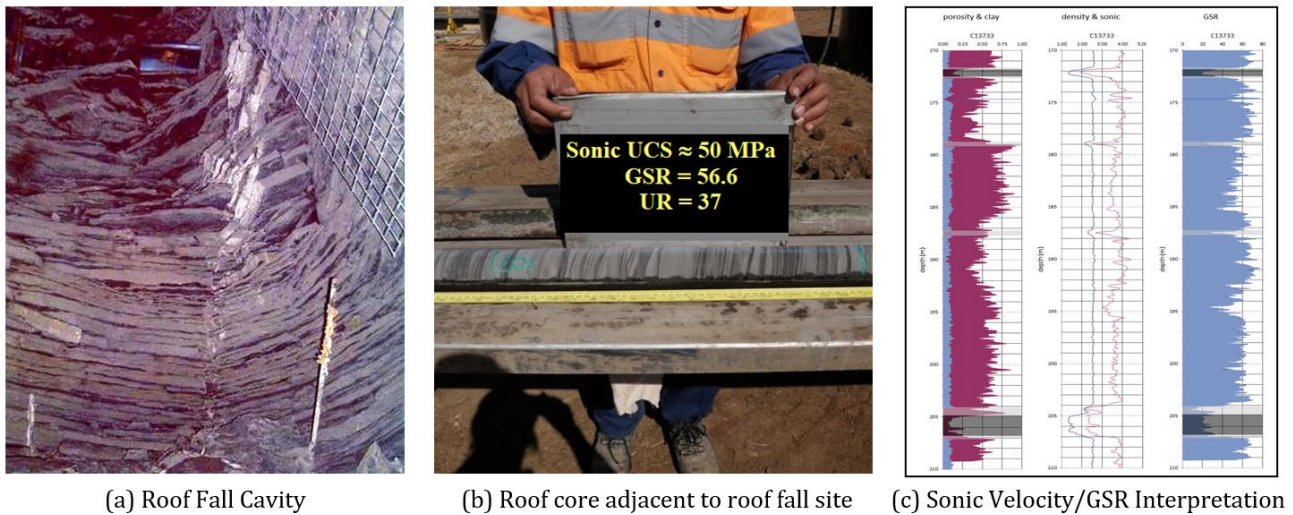
FIG 5 – CMRR, GSR and sonic velocity analyses associated with a roof fall.

The borehole/roof core was located only 10 m away from the roof fall location and was included within the ADFRS database. The GSR interpretations associated with the ADFRS database was undertaken by Dr Peter Hatherly (refer Figure 5c), while the author undertook the UR/CMRR assessments.

As illustrated in Figure 5b, the sonic-derived UCS is approximately 50 MPa and the Average GSR is 56.6, which in terms of these two roof strength indices are relatively high and would therefore be interpreted as relatively strong coalmine roof. However, when utilising the CMRR underground method to rate the laminae (associated with Figure 5b); the laminae was assessed to be planar with a spacing <6 cm and a persistence >3 m and based on diametral point load testing, the cohesion of the laminae was assessed as weak to very weak. In combination with a UCS of approximately 50 MPa, the resultant UR is approximately 37, which would be considered a weak (to very weak) unit.

It is important to note that a sonic-derived UCS is typically based on a 20 cm sonic transit time trace resulting in an average sonic velocity, which is calculated (and continuously re-calculated) over that vertical 20 cm distance. Therefore when there is an abundance of closely spaced laminae, the sonic velocity trace cannot adequately differentiate between the rock matrix and laminae material as it can between the overlying rock unit and coal seam (as illustrated in Figure 5c) and it simply produces an average sonic velocity over that 20 cm distance. This inability to satisfactorily differentiate between the rock matrix and laminae material applies equally to the GSR and explains why in comparison to the CMRR/UR, the UCS, RSI and GSR correlations were significantly weaker.

Logistic regression analyses – two-pass data set

A limitation of ordinary linear regression is the requirement that the outcome is continuous rather than categorical. But many interesting dependent variables/outcomes are categorical, eg patients may live or die, faceroad performance is satisfactory or unsatisfactory and so on. A range of statistical techniques have been developed for analysing data with categorical dependent variables such as logistic regression.

Logistic regression allows for the classification of cases or observations into two (or more) populations based on an outcome, which as previously indicated is referred to as the dependent variable. Logistic regression is able to distinguish which parameters (ie the independent variables) are significant predictors of a particular outcome and to then rank and quantify the relative importance of these independent variables on said outcome.

Furthermore, logistic regression can determine the most appropriate equation (in relation to those independent variables analysed) to act as a boundary of separation between the two populations in terms of the outcome. Within this study that equation is referred to as the *Discriminant Equation*, which can then be used to predict the outcome based on the significant predictors.

To undertake binomial logistic regression with a multinominal outcome (ie satisfactory, manageable and unsatisfactory), it was decided to eliminate the 33 manageable cases and compare the 134 satisfactory cases to the 40 unsatisfactory cases, thereby providing a dichotomous outcome. Therefore the resultant *Discriminant Equation* would potentially represent a design equation approximating a manageable outcome, while being effectively a *boundary of separation* between the satisfactory/unsatisfactory populations.

The uneven nature of the outcome (ie 134 satisfactory cases versus 40 unsatisfactory cases) limits the ability of most statistical techniques to discern an unbiased result and a greater weighting would be given to the satisfactory cases in terms of the resultant *Discriminant Equation*, which could potentially result in a design equation or methodology that does not adequately address the more difficult conditions. Therefore it was decided to weight the unsatisfactory cases by a factor of three. This results in a simulated database (for analysis) of 134 satisfactory and 120 unsatisfactory cases. Numerous analyses were performed and the interested reader is referred to Table 7.2 of Colwell and Frith (2012) which details the various parameters assessed, their range as well as the mean and standard deviation.

The best predictors of the final widening outcome were the Analytical Model for Coal Mine Roof Reinforcement (AMCMRR) FOS values calculated in relation to the 1st pass against both buckling failure and compressive yielding of the roof material over the 5 m Roof Section. The AMCMRR FOS values are a measure of 1st pass roof stability, with their calculation (including a detailed mine site example) explained by Colwell and Frith (2012).

From a predictive point of view there was essentially no difference in relation to which FOS value was utilised. However, from a geotechnical point of view the FOS calculated in relation to compressive yielding of the roof material ($FOS_{5\ m\text{-yield}}$) is considered more appropriate, as in terms of the load-balance calculation, it limits the mechanical advantage reinforcement component (associated with the longer pre-tensioned cables) by the yield strength of the rock units within the 5 m Roof Section. The resultant *Discriminant Equation* incorporating $FOS_{5\ m\text{-yield}}$ is:

$$z = 3.339\ FOS_{5\ m\text{-yield}} - 4.745 \tag{2}$$

The value z is referred to as the predicted log odds value. When z is less than zero one would predict/classify the case as unsatisfactory and when greater than zero the case would be predicted as satisfactory. Equation 2 successfully classified 105 of 120 weighted unsatisfactory cases (therefore 35 of 40 unsatisfactory cases or 87.5 per cent correct) and 107 of the 134 satisfactory cases (79.9 per cent correct) for an overall classification success rate of 81.6 per cent. Equation 2 can be rearranged so that the design variable $FOS_{5\ m\text{-yield}}$ relating to a manageable outcome can be calculated, ie $FOS_{5\ m\text{-yield}} = 4.745/3.339 = 1.421$.

The above findings indicate that if the 1st pass $FOS_{5\ m\text{-yield}} > 1.421$, then it is more likely that the faceroad will be manageable following widening (provided GRSUP Total$_{5\ m}$ is sufficient), however when $FOS_{5\ m\text{-yield}} = 1.421$ this also means there is 50:50 chance of the outcome (ie fully widened roadway performance) being satisfactory or unsatisfactory.

It is extremely important to recognise that in this way $FOS_{5\ m\text{-yield}}$ associated with the 1st pass is being used as a predictor of the eventual outcome and not as a Factor of Safety. To emphasise this point; in developing the ADFRS design methodology $FOS_{5\ m\text{-yield}}$ is not referred to as an FOS, it is referred to as the 1st Pass Reinforcement Index or $RF_{5\ m\text{-yield}}$.

The logistic regression analyses provided further confirmation that 1st pass stability is paramount to a successful widening and most importantly from an engineering/design perspective, reinforcement indices are provided (ie PRSUP$_{Dev}$, GRSUP Total$_{5\ m}$, GRSUP 1st Pass*$_{5\ m}$ and $RF_{5\ m\text{-yield}}$), which therefore not only quantify the total roof support level required for the fully widened roadway, but also the timing of installation as well as positioning of the bolts and cables across both the 1st and 2nd passes.

Development of a Faceroad TARP

In order to develop a TARP for faceroad formation using roof monitoring data, a basic roof behavioural model is required. Figure 6 provides a general representation of such a model for a two-pass formation along with three key roof displacement/behavioural/measured outcomes being;

Total Roof Displacement (TRD, mm), the Widening Surge (Surge, mm) and long-term creep (Creep Rate, typically reported as mm/day or mm/week) that can be linked to the ADFRS database. The Surge is defined as the initial increase in vertical roof displacement post-widening, with the Creep Rate being defined as the vertical roof displacement rate subsequent to the initial Surge.
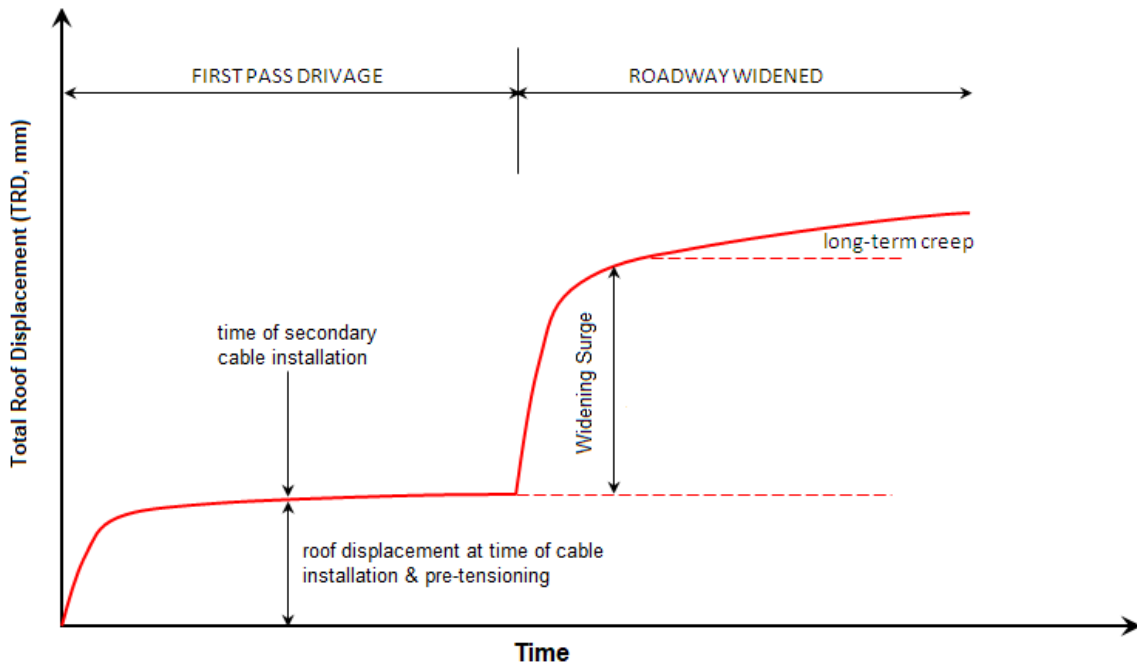
FIG 6 – General representation of faceroad roof displacement behavioural model.

Further analyses were undertaken relating $RF_{5\,m\text{-yield}}$ to these roof performance/extensometry outcomes/measurements as well as other roof performance indices such as HOS. For example Figure 7 plots the Surge and Creep Rate against $RF_{5\,m\text{-yield}}$.

(a) Surge (mm) v's $RF_{5m\text{-yield}}$

(a) Creep Rate (mm/day) v's $RF_{5m\text{-yield}}$
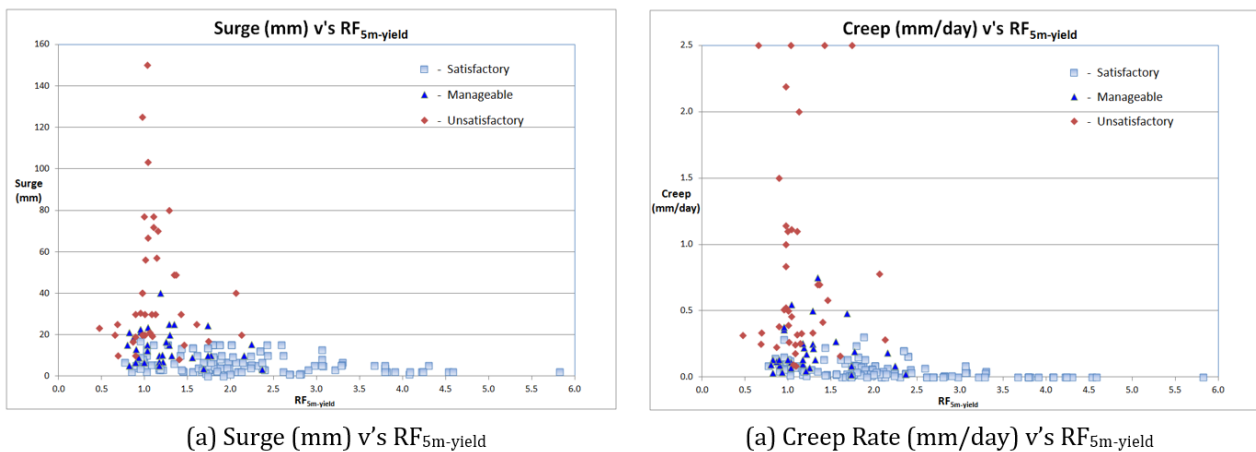
FIG 7 – Surge and Creep Rate versus $RF_{5\,m\text{-yield}}$.

With respect to Figure 7b it should be noted that in relation to the unsatisfactory cases there were two instances of roof falls and as such the Creep Rate was extremely high! In addition there were two other cases where Creep Rates of 8.33 and 18.44 mm/day were recorded requiring the use of standing support to avert a roof fall. So as not to overly increase the y-axis (and lose the visual detail for Creep Rates of <0.5 mm/day), these four cases have been given a nominal Creep Rate of 2.5 mm/day.

Figure 7 is quite emphatic in that all satisfactory cases (irrespective of their $RF_{5\,m\text{-yield}}$ value) surged no more than 20 mm upon widening and that the Creep Rate is less than 0.3 mm/day (approximately 2 mm/week) being virtually the same as that suggested by Thomas (2010) when

differentiating his borderline from successful cases. As a result of these and similar analyses, ADFRS was the first ground support design methodology that made specific recommendations with respect to a variety of TARP trigger levels and therefore as a methodology, ADFRS incorporates both design and management.

CONCLUSIONS

In relation to other strata control issues, such as pillar and roof support design for standard roadway widths (ie ≤ 5.5 m wide), there had been comparatively very little research undertaken prior to 2012 in relation to the geotechnical design/management of faceroads. As a result, in terms of a satisfactory outcome, faceroad behaviour associated with Australian collieries had been quite problematic and by way of example; of the 207 cases associated with the two-pass data set, 40 resulted in an unsatisfactory outcome involving the use of standing support, PUR injection and/or high levels of remedial tendon support with two faceroads 'lost' and having to be re-driven due to major roof falls in the two years prior to the study commencing.

A failure rate of approximately 20 per cent was unacceptable to Australian collieries. The principal reason for such a failure rate was the clear absence of suitable design equations that: (1) can accurately assess the required levels/type of roof support as a function of some valid measure of the competency of the roof and the horizontal stress acting across the roadway, and (2) were developed via an industry-wide database, which therefore intrinsically represented a tolerable/manageable level of risk to an Australian 'standard'.

The strength of the relationship between GRSUP $Total_{5\,m}$ as a function of the Average $UR_{5\,m}$ and σ_R-$Dev_{5\,m}$ would be considered strong to very strong with a correlation (ie R^2 value) of 0.75. In addition, the extraordinarily strong relationships (ie R^2 values approximately equal to 0.9) that already existed within ALTS for standard width roadway conditions (ie the 1st pass), in combination with this study's analyses, indicated that a robust design methodology could be developed and this proved to be the case.

Additionally, the logistic regression analyses in conjunction with the simpler mean and standard deviation calculations, as well as plotting $RF_{5\,m\text{-yield}}$ against various roof performance indices, demonstrated that $RF_{5\,m\text{-yield}}$ can be effectively utilised as a part of the design process.

In empirical/correlation terms (eg R^2 values and predictive success rate); this study essentially resulted in our faceroad roof support design knowledge going from weak R^2 values of 0.325 to 0.499 (Thomas, 2010) to very strong R^2 values 0.75 to 0.88 and a predictive capability in excess of 80 per cent and in this regard of particular importance, is that $RF_{5\,m\text{-yield}}$ correctly predicted 87.5 per cent of the unsatisfactory cases. As a result, credible roof support designs were available that could then be implemented and readily managed by the collieries.

Furthermore, this study significantly advanced our mechanistic understanding of the impact of roadway widening on roof behaviour, while confirming that 1st pass roof stability is paramount to a successful widening. However, more importantly from a design/engineering point of view, the analyses quantified the required roof support levels at all stages of the faceroad formation process. Finally, in terms of practical mining considerations, the study made a unique contribution, being the first ground support design methodology that made comprehensive recommendations with respect to TARP trigger levels associated with extensometry measurements.

The faceroad design methodology and software package emanating from this study is called Analysis and Design of Faceroad Roof Support (ADFRS), which was formulated to complement the mine site risk management approach to strata control/management employed by Australian collieries. In subsequent years further research and data collection were undertaken so that in addition to faceroads, ADFRS can be readily used for all forms of wide-roadway roof support design, such as belt chambers and tripper drives and has been the dominant wide-roadway roof support design technique utilised by Australian collieries for the last 10 years.

REFERENCES

Colwell, M and Frith, R, 2009. ALTS 2009 – A ten year journey, in *Proceedings of the 2009 Underground Coal Operator's Conference*, (ed: N Aziz and J Nemcik), pp 37–53 (The Australasian Institute of Mining and Metallurgy: Illawarra Branch).

Colwell, M and Frith, R, 2012. Analysis and Design of Faceroad Roof Support (ADFRS) – A roof support design methodology for longwall installation roadways, ACARP report C19008.

Galvin, J M, 2016. *Ground Engineering – Principles and Practices for Underground Coal Mining*, 684 p (Springer International: Switzerland).

Hatherly, P, Zhou, B, Peters, T and Urosevic, M, 2009. Detailed Geological Characterisation from Seismic Data, ACARP report C15018.

Mark, C and Molinda, G M, 2007. Development and application of the coal mine roof rating (CMRR), in *Proceedings of the International Workshop on Rock Mass Classification in Underground Mining*, pp 95–109 (NIOSH Information Circular 9453).

Medhurst, T, Hatherly, P, Zhou, B and Ye, G, 2010. Application of the Geophysical Strata Rating in Production Settings, ACARP report C17009.

Nemcik, J, Gale, W and Mills, K, 2005. Statistical analysis of underground stress measurements in Australian coal mines, in *Proceedings of the Bowen Basin Symposium 2005* (ed: J W Beeston), pp 117–122 (Geological Society of Australia, Coal Geology Group and Bowen Basin Geologists Group).

Thomas, R, 2010. The design and management of wide roadways in Australian coal mines, in *Proceedings of the 29th Conference on Ground Control in Mining*, pp 283–293 (West Virginia University).

Geotechnical education and training

The emerging role of the operational geotechnical engineer

C G Sweeney[1]

1. MAusIMM(CP), Design Manager, GeoStabilization NZ Ltd., Auckland 0630, New Zealand. Email: charles.sweeney@gsinz.nz

ABSTRACT

The underground mining industry is seeing unprecedented shortages in skilled labour. Migration to Australia being at an all-time low is a leading concern, with pandemic-induced border closures and lockdowns only exacerbating the skills shortage, not causing it. The skills shortage is forecast to peak in 2023 and remain high beyond 2025.

With this skills shortage in mind, mining companies throughout Australia are trying to deal with stricter protocols around Health and Safety (H&S) legislation, as well as more stringent controls on quality assurance, particularly as underground mines are reaching greater depths and extending into 'unchartered territory'. The cumulation of this is proving to be a major hurdle in 'effective' operational geotechnical management.

The drive for automation in mining is bringing another level of complexity. However, 'once automation is up and running, it presents the opportunity to access talent pools that may not normally be available. There is also a change in skillset that will be required to drive automation. 'The top two emerging roles that will be critical for the future of the mining industry are artificial intelligence and machine learning (AI/ML) specialists, and process-automation specialists' (Writer, 2021).

If anything positive has come from the pandemic, it has shown that remote working can be effective and that the drive for automation and critical evaluation of skills required on-site should be given greater priority. UQ acknowledges that the industry is changing, and that digital technology is required to be offered in mining related disciplines. Industry and academia need to do more to promote geotechnical engineering in mining and balance the curriculum to suit the future of mining and make it more enticing.

The average cost of a geotechnical failure is about $5 million in coalmines and can be into the hundreds of millions of dollars if production is affected (Cartledge Mining and Geotechnics, 2020). The cost of a good geotechnical design far outweighs the potential losses if a failure were to occur. This alludes to the growing importance of experienced geotechnical consultancies playing a pivotal role in managing mine site geotechnical hazards, while the industry is developing the next generation of geotechnical engineers.

INTRODUCTION

The mining industry in Australia is seeing unprecedented shortages in skilled labour. Migration to Australia being at an all-time low is a leading concern, with pandemic-induced border closures and lockdowns only exacerbating the skills shortage, not necessarily causing it. There are many potential causes, including the pull of mining professionals to civil infrastructure projects in major cities, the fact that there is no clear pathway for mining geotechnical engineers in higher education and the ever-changing mining environment and skills required of operational geotechnical engineers to effectively perform the role. The draw of geotechnical engineers to remote mine sites, in particular, is of concern due to the increasingly labour-intensive environment and rigorous work schedules being employed.

This coupled with the boom-and-bust cycle of mining, environmental concerns of prospective students entering higher education, as well as work-life-balance being at the forefront of peoples mind post-COVID, is further exacerbating the talent pool.

This has given rise to the emergence of experienced geotechnical consultancies taking on the reigns of operational geotechnical management, whilst the industry, and academia, look to promote and encourage geotechnical engineering in mining.

SKILLS SHORTAGE

The skills shortage spans all states in Australia and all professions. The industry, as a whole, is struggling to attract and retain quality workers. However, states such as Western Australia (WA) and those on the east coast (Queensland and New South Wales) are driving a salary imbalance – with the little talent that exists being poached leading to soaring salaries.

Over 250 000 people are employed across the mining value chain, making it one of the largest employment industries in Australia. Underemployment has been moving higher for several decades within most industries in Australia, although mining is by and large the lowest (Figure 1). This trend indicates that the mining talent pool is currently at peak capacity.
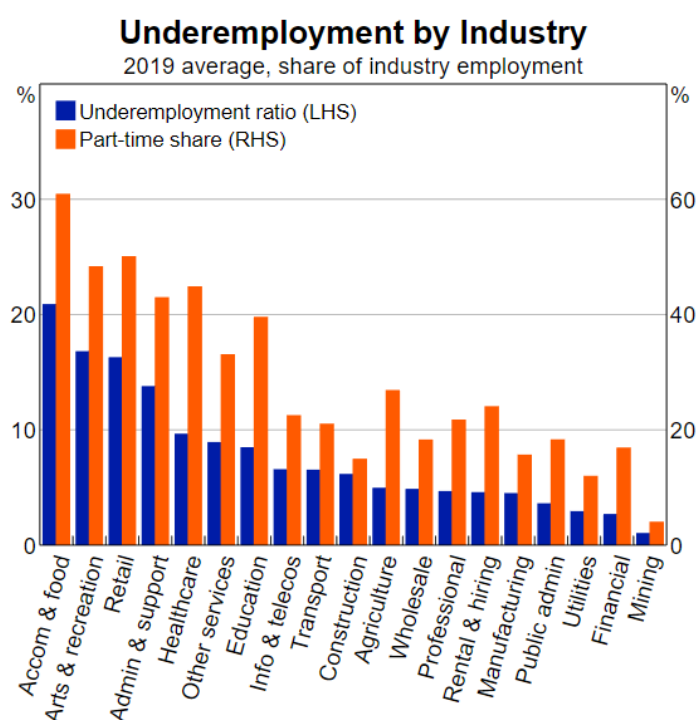
FIG 1 – Underemployment by Industry (Chambers, Chapman and Rogerson, 2021).

Even with the onset of COVID-19, employment in the resources sector grew by 8.5 per cent between February 2020 and November 2020 (Zakharia, 2021). This is largely on the back of unprecedented stimulus measures in China, as well as increased demand for commodities. This skills shortage affects project schedules and budgets, as well as investment decisions due to a skills dilution in the workforce. At a Mineral Sands Conference in Perth, Peter Dyball, managing director of Pit Crew Consulting Services Pty Ltd, indicated that 'with a 10 per cent drop in workforce productivity, this is worth at least $15 to $20 million in capital cost' and 'with the unemployment in WA at just 4.1 per cent, just about everyone who is qualified and experienced can be considered to be employed' (Barich, 2021). The skills shortage is forecast to peak in 2023 and remain high beyond 2025.

With the recent government spending on infrastructure projects, this has contributed to geotechnical engineers, who might have previously remained in the mining industry, finding employment within the civil construction sector, typically in major capital cities. This is creating a war of talent per se between the civil and mining industries. Engineers within the civil construction industry can work on large projects, in major cities, with all that they have to offer younger professionals, as well as offering career progression in a relatively stable industry. With each boom-and-bust cycle, the mining industry faces the same challenges of attrition and loss of interest. The industries short-term thinking can lead not only to a lack of skilled professionals, but also to soaring salaries, which ultimately costs companies more than an investment in talent development (Goetsch, 2020).

MINING'S CONTRIBUTION TO THE AUSTRALIAN ECOMONY

When the mining industry is booming, all Australians benefit – with the WA resources sector alone contributing $100 billion directly to the national economy in the financial year 2021–2022 (Gleeson, 2022). Australia's 'Australian Department of industry, Science, Energy and Resources' calculated that during the 2018–2019 financial year, resource and energy exports accounted for nearly 60 per cent of the country's export earnings, with mining sector revenue reaching a record $279 billion. Even with a looming skills shortage, a look at the bigger picture shows untold potential and a host of new opportunities as development progresses over the longer term in Asia, Africa and South America. Mining's contribution to Australian Society, indicates the necessity of building and maintaining a strong pipeline of talent, and understanding which skills will be needed in the rapidly changing industry (Goetsch, 2020).

ACADEMIA, INDUSTRY AND MINING RELATED HIGHER EDUCATION

For geotechnical engineers wanting to get into the mining industry, there is no current clear academic pathway. Civil Engineering courses don't generally cover the basics of mining and the career pathway to become a mining geotechnical engineer is often not explained or even heard about prior to entering higher education. It is typically geologists and mining engineers who undertake further study in geotechnical engineering to progress along this career pathway, even though this career path is not necessarily promoted. How can people entering higher education, pick a career path that they do not know exists? The 2018 Minerals Tertiary Education Council (MTEC) report, published by the MCA, highlighted a significant decline in enrolment numbers in most higher education disciplines related to mining and metals since 2012. For example, in 2018, only six students enrolled in mining engineering at the University of New South Wales (UNSW), compared to 120 enrolments four years earlier (McHugh, 2019).

Research suggests industry and education institutions must work together to address the looming skills shortage in the resources sector. Collaboration between academia and industry has proven effective in the past. In October 2018, Rio Tinto announced a $2 million investment in WA to forge a new curriculum designed to prepare local students to take on jobs in the mining industry. Similarly in 2017, Northern Star Resources announced that they were investing $50 million over ten years to support the development of an underground mining centre of excellence in Kalgoorlie (Goetsch, 2020). Is this type of collaboration and investment the 'most persuasive factor' to students to follow mining-related engineering programs at universities?

In the Swann Group 2020 survey, unsurprisingly, continued and increased support for such initiatives was repeatedly referenced in responses as a way of attracting students and encouraging them to continue in mining-related disciplines (Goetsch, 2020). Industry-support scholarships for mining-related disciplines were also referenced as being integral to the success of mining programs and their retention of students (Goetsch, 2020). Undoubtedly, funding research contributes to the development of new technology, techniques and knowledge that will benefit the future of the industry. Long-term industry investment in research and teachers represents an underutilised and impactful approach to improving mining education, tackling the skills deficit, and benefitting industry.

THE FUTURE OF MINING AND GEOTECHNICAL ENGINEERING

The drive for automation in mining, is bringing another level of complexity and exacerbating the current labour effort. However, 'once automation is up and running, it presents the opportunity to access talent pools that may not normally be available for, or interested in, FIFO work, or those specifically experienced in mining' says Accenture head of resources David Burns (Zakharia, 2021). There is also a change in skillset that will be required to drive automation. 'The WEF 2020 jobs report found that 67 per cent of repetitive and manual tasks, such as information and data processing, and about 60 per cent of tasks involving physical labour will be automated – where on the other hand the report said that the top two emerging roles that will be critical for the future of the mining industry are artificial intelligence and machine learning (AI/ML) specialists and process-automation specialists' (Writer, 2021). With this shift in skillset becoming more technology focused, it is paramount that the curriculum for mining and geotechnical engineering at university level shifts with it. 'The companies that succeed will be those that make the necessary changes quickly', says Burns (Zakharia, 2021).

Minerals Council of Australia (MCA) chief executive officer, Tania Constable, says that the 'Australian minerals industry already has a highly-skilled, highly-paid workforce that is well trained, however the combination of technology adoption, industry and learner exceptions and skills availability pressures will test how tradespeople are trained and inducted into the mining industry' (Zakharia, 2021). If anything positive has come from the pandemic, it has shown that remote working can be effective and that the drive for automation and critical evaluation of skills required on-site should be given greater priority. Mr Lind, general manager of Workforce Skills, Health and Safety at MCA, indicated that 'the pool of engineers is becoming problematic because we can't rely on the short-term bringing in of international expertise' (Barker, 2021). This, coupled with a shortage of university students studying mining related degrees, emphasizes the need for change.

A 2020 study by the University of Queensland (UQ) predicted that Australia would produce less than half of the required graduates in 2021. Mr Lind said that the minerals council was working with several universities on adapting curriculums. UQ acknowledges that the industry is changing, and that digital technology is required to be offered in mining related disciplines. In addition, head of engineering professor at UQ, Peter Knights, says that 'we have found that students generally want broader career options', which is why the UQ mining engineering course has become part of the mechanical, civil and mechatronics degree (Barker, 2020).

The environmental impact of mining is also of concern to new students, and this needs to be properly addressed. Knowledge that the mining industry is an essential industry for a transformation to clean energy needs to be advertised and addressed at school level to entice the next generation to want to be part of the solution.

MINING BENEFITS AND DISBENEFITS

With most mines being in a remote location, this adds another complexity to attracting quality talent. There appears to be a reluctance for young professionals to work in challenging environments, such as the underground coal industry, particularly in remote parts of Australia, and to such rigorous schedules. Where mines have traditionally only offered residential positions, the likes of Glencore in Mt Isa have seen that with over 200 job vacancies across the board, many of them engineers, companies are having to be flexible in their offerings. COVID-19 has had a lot of people assessing work life balance and the importance of family (Gleeson, 2022). Glencore's Queensland Metals chief operating officer Matt O'Neill says that 'we saw last year a lot of people able to do flexible working arrangements like working remotely or where they are only on-site one week out of four. This is becoming the norm in the mining industry to try and attract people' (Barker, 2021). The fact that a lot of the data processing and automation activities can be performed remotely, will go a long way in attracting more skilled labour to the underground mining industry.

With this skills shortage in mind, mining companies throughout Australia are also trying to deal with stricter protocols around Health and Safety (H&S) legislation, as well as more stringent controls on quality assurance, particularly as underground mines are reaching greater depths and extending into 'unchartered territory'. The cumulation of this is proving to be a major hurdle in 'effective' operational geotechnical management. Mining legislation ensures that mine managers and operators adequately risk assess ground stability concerns and take appropriate action to make the workplace as safe as reasonably practicable. To do this, allot of emphasis is placed on the operational geotechnical engineer to cover all bases. As such, operational geotechnical engineering is becoming more labour intensive.

EMERGENCE OF MINING CONSULTANCIES TO FILL THE GAP

With the growing complexity of keeping operational geotechnical management 'in-house', outsourcing to geotechnical consultancies is becoming a common occurrence. Geotechnical designs cost money, but the cost of a good geotechnical design often outweighs the potential losses if a failure were to occur. The average cost of a geotechnical failure is about $5 million in coalmines and can range up to $40 million. Total losses can be in the hundreds of millions of dollars if production is affected, (Mining Technology, 2020). Mine operators are aware that there is significant value in expert geotechnical inspections and design, as a way of ensuring that mining operations remain safe, while potentially staving off millions in losses in the long run. This alludes to the growing importance of experienced geotechnical consultancies playing a pivotal role in keeping mines safe

from geotechnical hazards, while the industry is developing the next generation of geotechnical engineers. This large step increase in the growing presence of consultants on operational mine sites – in most cases only periodically on-site, will require significant adaption and management in itself. Of particular importance is the day-to-day geotechnical hazard management, along with satisfactory record keeping. It is paramount to retain as much knowledge on-site of the relevant seam or orebody, and associated geotechnical hazards, to be able to effectively manage these risks.

CONCLUSIONS

Despite best efforts from industry, more needs to be done as the sting of the skills shortage will be felt strongly in Australia where mining plays a critical economic and social role. Industry and academia must work together to clearly promote the role of the mining geotechnical engineer, and benefits of mining to society in general, as well as adapt the curriculum to the future of mining – AI and automation. The emerging role of the operational geotechnical engineer is fast becoming more IT and AI focused. With the current skills shortage, work life balance requirements are also largely at the forefront of potential employees' minds and some semblance of remote working is fast becoming the norm. This is paving the way for experienced geotechnical consultancies to step in and fill the gap, whilst industry and academia look to encourage the development of the next generation of geotechnical engineers.

REFERENCES

Barich, A, 2021. West Australian mining skills shortage to peak in 2023 amid ongoing tightness, *S&P Global*. https://www.spglobal.com/marketintelligence/en/news-insights/latest-news-headlines/west-australian-mining-skills-shortage-to-peak-in-2023-amid-ongoing-tightness-67709968 [Accessed: 11 January 2022].

Barker, E, 2021. Mining engineer shortage sees competition for skilled workers ramp-up amid pandemic, *ABC News*. https://www.abc.net.au/news/2021–02–22/competition-for-mining-engineers-ramps-up-under-skills-shortage/13173582 [Accessed: 11 January 2022].

Barker, E, 2020. Mining companies employ international engineers as Australian enrolments decline, *ABC News*. https://www.abc.net.au/news/2020–12–16/mining-companies-hire-international-engineers-in-skills-shortage/12986650 [Accessed: 11 January 2022].

Cartledge Mining and Geotechnics, 2020. Proactive geotechnical advice can save mine operators millions, *Mining Technology*, https://www.mining-technology.com/contractors/project-management-and-consultancy/cartledge-mining-and-geotechnics/pressreleases/proactive-geotechnical-advice/

Chambers, M, Chapman, B and Rogerson, E, 2021. Underemployment in the Australian Labour Market, *Reserve Bank of Australia*. https://www.rba.gov.au/publications/bulletin/2021/jun/underemployment-in-the-australian-labour-market.html [Accessed: 13 September 2022].

Gleeson, D, 2022. Australian skills shortage on the agenda at IMARC, *International Mining*. https://im-mining.com/2022/09/01/australian-skills-shortage-on-the-agenda-at-imarc/ [Accessed: 14 September 2022].

Goetsch, E, 2020. Closing the skills gap in Australian mining, *AusIMM Bulletin*. https://www.ausimm.com/bulletin/bulletin-articles/closing-the-skills-gap-in-australian-mining/ [Accessed: 14 September 2022].

McHugh, A, 2019. Tackling the skills shortage in Australia's mining sector, *Cormac Consulting*. https://cormacconsulting.com.au/2019/05/tackling-the-skills-shortage-in-australias-mining-sector/ [Accessed: 14 September 2022].

Writer, S, 2021. How mining can adapt to the skills shortage, *Australian resources and investment*. https://www.australianresourcesandinvestment.com.au/2021/09/27/how-mining-can-adapt-to-the-skills-shortage/ [Accessed: 11 January 2022].

Zakharia, N, 2021. Is a mining skills shortage looming, *Australian Mining*. https://www.australianmining.com.au/features/is-a-mining-skills-shortage-looming/ [Accessed: 11 January 2022].

Geotechnical instrumentation

Measuring the influence of a sublevel cave on open stoping at Telfer

M J Woods[1], M P Sandy[2] and J Maxlow[3]

1. MAusIMM, Superintendent Geotechnical Engineering, Newcrest Telfer Operation, Perth WA 6000. Email: matthew.woods@newcrest.com.au
2. FAusIMM(CP), Principal Geotechnical Engineer, AMC Consultants, Perth, WA, 6005. Email: msandy@amcconsultants.com
3. Geotechnical Technician, Newcrest Telfer Operation, Perth WA 6000. Email: Jason.maxlow@newcrest.com.au

INTRODUCTION

The Newcrest Mining Limited Telfer operation comprises both open pit and underground operations producing gold and copper. The underground operation is made up of three production areas, the sublevel cave (SLC), M Reefs narrow vein open stoping and Western longhole open stoping areas.

With stoping situated on the abutments of a mature and active sublevel cave, the interaction between mining areas is often complex. This is particularly evident in the M Reefs orebodies with high levels of extraction in all four reefs, and reliance on pillars to maintain local and global stability. A key concern was the potential for a cascading pillar failure to develop and rapidly progress through the M Reefs stoping area.

The monitoring plan needed to capture any change in overall stability and identify if deformation was caused by pillar failure within the M Reefs and hanging wall closure, or shear on the reefs caused by SLC influence.

MINE DESIGN

Geology

The underground operation is within the Main Dome formation, a large, oval shaped open anticlinal fold consisting of a sedimentary stratigraphic sequence. The M Reefs are located on the eastern limb of the anticline in the upper Malu member of this formation, which has undergone moderate to intense sericite and silica metasomatism, resulting in very high intact rock strengths. However mechanical deformation during formation has resulted in interbedded weaker units.

Mine design

M Reefs stoping targets four shallow east dipping reefs using longhole open stoping and systematic pillars. Stoping occurs between 200 m and 500 m below surface, with a strike length of 750 m and is located to the east of the SLC and beneath the Main Dome open pit. Stoping retreats to internal declines or level accesses located off the main decline, all situated in the centre of the M Reefs orebody (Figure 1).

Since the start of M Reef mining several different stope and pillar designs have been used to provide locally and globally stable conditions. The two main pillar systems used are discrete sill pillars spaced systematically along the drives to provide local hanging wall stability, with larger down dip rib pillars to provide overall stability, and more recently the use of continuous sill pillars for operational reasons.

The main decline is located at the centre of the M Reefs and crosses the orebody at 90 degrees in multiple locations bracketed by large regional pillars.
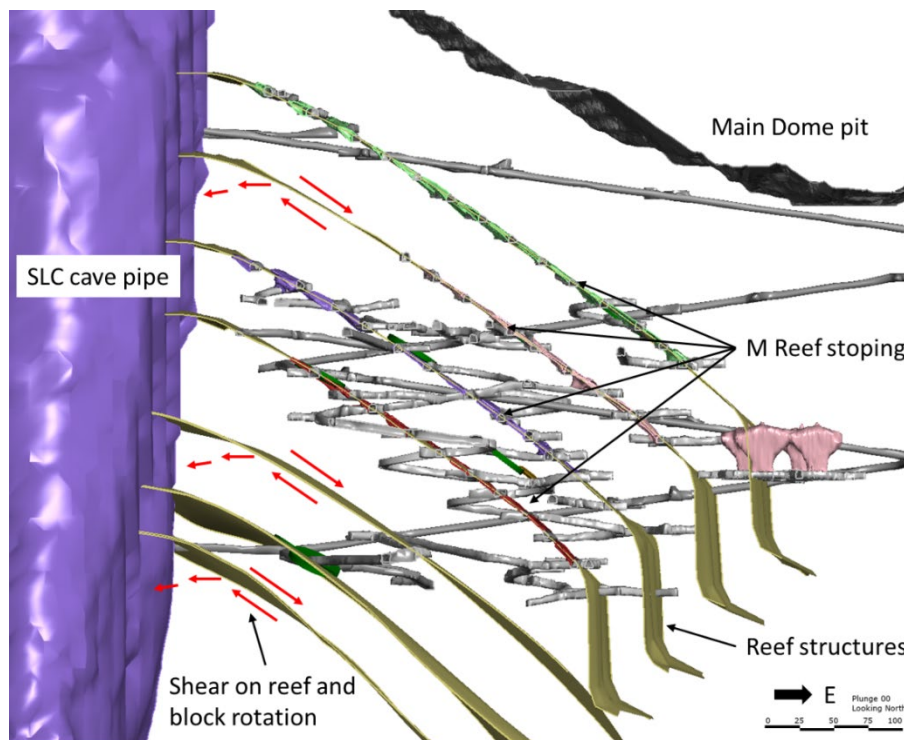
FIG 1 – Section through the M Reefs area looking north and mechanism of reef shear and block rotation.

MONITORING

When shear along reefs was identified in underground workings, two mechanisms were identified as potential drivers. Failure of M Reef pillars within stoped out areas reducing shear strength across the reefs or the influence of the SLC draw, cave growth and subsidence.

Due to the extent of the M Reefs stoping and high extraction, locations to directly monitor pillar and hanging wall stability were limited. A monitoring system consisting of externally purchased instruments and in-house designed and constructed shear monitors was developed to measure displacement and identify mechanisms occurring.

To test for potential pillar failure and global stability several externally purchased multi point borehole extensometers (MPBX) were installed into stope hanging walls from the overlaying development to measure closure where accessible locations permitted.

To test for the influence of SLC draw, in-house built shear monitors were developed and installed to measure deformation and direction of shear. Main decline access perpendicular to the M Reefs provided locations to measure shear movement on multiple reefs.

The shear monitors were constructed of two solid steel bars so the monitor can be secured to the hanging wall and footwall either side of the reef, two pieces of DIN rail with a section of tape measure attached to the underside piece and a slot cut in the top piece allowing them to slide past each other in both directions (Figure 2a). The location and set-up of each monitor was recorded to determine shear direction.

Measured shear direction on all reefs was hanging wall down, footwall up, indicating a toppling and rotational type mechanisms of the reefs and blocks between (Figure 1 and Figure 2a). Measured reef shear was also plotted against SLC draw (Figure 2b) with some correlation of reef shear to SLC draw rate, particularly for the shear monitors located closest to the cave pipe. Most notably as the SLC draw slowed and stopped as a new level was established, the shear rate also reduced.

The monitoring system above is used in conjunction with the mine wide seismic monitoring system and underground observations.
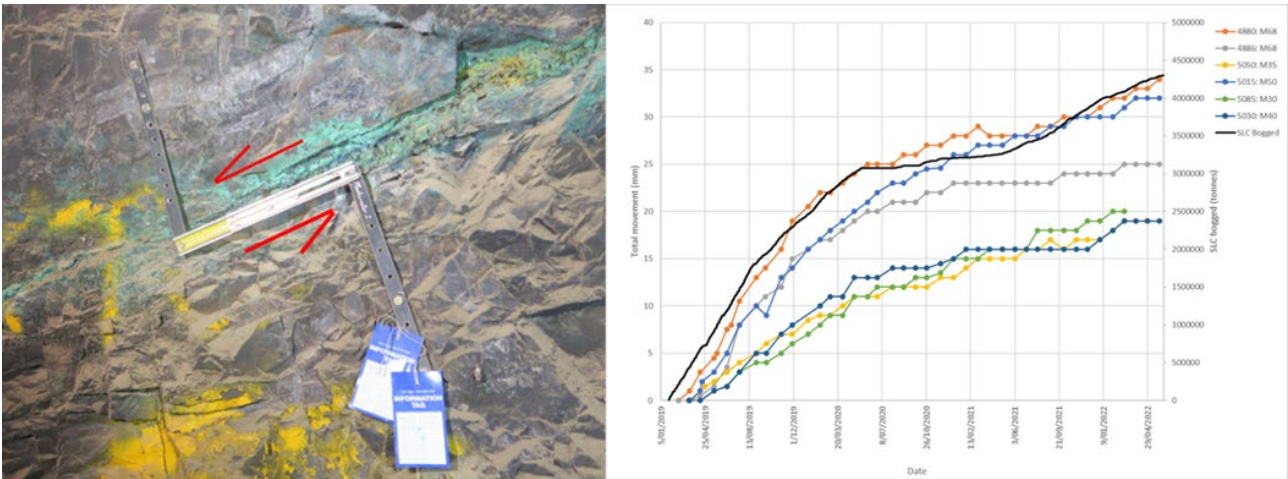
FIG 2 – (a) Shear monitor installed over reef, with arrows indicating direction of movement measured (left); (b) shows shear displacements and SLC draw plotted over time (right). The shear monitors closest to the cave show the greatest response.

CONCLUSIONS

With the complexity of multiple expansive mining areas in proximity and a mature active cave, interaction is inevitable and single cause or driver is rarely evident. But if a sound understanding of a basic hypothesis is applied, along with a clear understanding of what needs to be measured, a simple solution can provide significant insight.

In conjunction with a mine-wide seismic monitoring network and observation, the displacement-monitoring scheme is a key tool in monitoring the regional response and in providing management with confidence that there are no developing trends to progressive deterioration in regional stability.

ACKNOWLEDGEMENTS

Geotechnical instrumentation, monitoring and data management

Slope radar monitoring – a partnership and infrastructure case study of scalability, reliability and availability

R Dixon[1], L Tovey[2] and E Shilov[3]

1. Principal Geotechnical Engineer, BHP, Perth WA 6000. Email: rebecca.dixon@bhp.com
2. Senior Project Manager Technology, BHP, Perth WA 6000. Email: lincoln.tovey@bhp.com
3. Principal Support Engineer, IDS GeoRadar, Hendra Qld 4011.
   Email: evgeny.shilov@hexagon.com

ABSTRACT

BHP Western Australian Iron Ore (WAIO) operations use a suite of slope monitoring systems which are deployed to operational areas based on the ground control risk. Slope Radars are one system used within WAIO, having recently deployed and integrated a network of 22 radar systems across the operations. The integration required the development of supporting network architecture, infrastructure, virtualised hosting, security protocols and a technology support model. This has enabled data transfer between the physical radar systems located in open pits, to on-site offices, a vendor supported remote control room in Indonesia and the WAIO Integrated Remote Operations Centre for data analysis and monitoring of system and displacement alarms 24/7. The typical technical skillset of a Geotechnical Engineer does not include the knowledge and capability to understand and develop the supporting IT infrastructure required for establishing an integrated radar monitoring network. This paper will provide a discussion of the technology considerations for integrating radar systems and highlight the importance of the developed partnerships between internal geotechnical and technology teams and the external vendor team to ensure a reliable, robust and scalable slope monitoring solution.

INTRODUCTION

BHP Western Australian Iron Ore (WAIO) open pit operations are located in the Pilbara region of Western Australia, comprising five mines and four processing hubs connected to port facilities by more than 1000 km of railway (Figure 1). This integrated network means that multiple pits and pushback areas are active at any one time, with 80 active pits across WAIO in FY22. WAIO operations use a suite of slope monitoring systems to manage ground control risks, including slope radars deployed to monitor pit slope displacements. Recently integrating 22 slope radars to the WAIO monitoring network has involved the development of supporting network architecture, infrastructure, virtualised hosting, security protocols and a technology support model.

FIG 1 – BHP WAIO operations, Pilbara region of Western Australia.

DEFINING WAIO SLOPE RADAR REQUIREMENTS

Risk informed method

BHP's Our Requirements for Safety outline the minimum safety standard WAIO operations must meet, including the requirement to assess and implement further controls to manage identified risks via the hierarchy of control. Company-wide safety risks include geotechnical, fall or ground, risks with the requirement to manage all geotechnical risks and to 'separate and protect personnel from ground, excavations, waste dumps and stockpiles with the potential to: slip, fall or collapse' (BHP, 2021).

Wessels and Dixon (2019) described the 'Pilbara challenge' of multi-pit, geographically spread, structurally complex, and below water table iron ore operations in the Pilbara. These factors make it challenging for Geotechnical Engineers (Geotechs) to monitor changes in risk level and allocate monitoring resources appropriately to priority areas. WAIO Geotechs use a Pit Risk Ranking method to assess the ground control risk for active and planned mining areas. The risk assessment considers multiple factors including the mining plan, the current and ultimate pit depth, potential failure modes, stability assessment results and existing controls in place including slope monitoring coverage.

The outcome of the risk assessment informs a slope monitoring plan which defines the further controls required to manage identified ground control risks. Slope Monitoring is part of the verification component of the design-implementation-verification geotechnical cycle and is used to verify design assumptions associated with the geotechnical model and reconcile slope performance via slope displacement measurement (Sharon and Stacey, 2020). It is essential that a well-designed slope monitoring plan include early detection of developing instability, ability to analyse current and predicted conditions, communication of alarms and confirmation of expected slope performance (de Graaf and Wessels, 2013). For WAIO pit slopes with higher risk, known hazards, areas of previous

instability or where there is limited prism monitoring coverage, Slope Radars are deployed to monitor slope displacements.

Slope radar benefits

Ground based Slope Radar monitoring methods such as Real Aperture Radar (RAR) have been used in open pit mining applications since the early 2000s, and this monitoring method is now considered standard application to provide early warning of developing instability and for safety critical monitoring. Escobar *et al* (2013) describe the benefits of slope radars to provide broad area, georeferenced short and long-term near-real time deformation data sets. Today, ground based Synthetic Aperture Radars (SAR) provide high resolution imagery, 10 million pixels at full resolution scan in a short acquisition time, 20 second scan time for 180°, or 40s for 360° scan (IDS Georadar, 2022). With a scan range of up to 5 km, slope radars allow for monitoring from pit crests, away from active mining areas and can obtain longer term data sets for comparison with prisms monitoring data (Figure 2).

FIG 2 – WAIO Slope Radar monitoring system.

In late 2020, the WAIO Geotech team defined that a further 20 slope radars were required to be deployed across operations over the upcoming five years. In addition to the number of systems, other requirements for the WAIO radar monitoring solution were defined, including:

- Must be an integrated solution to provide 24 hours a day, 7 days a week monitoring coverage and response to radar alarms generated on-site in the Pilbara.

- Data communication requirements as described by de Graaf *et al* (2020), including the acquisition of the data, communicating data from the radar to local mine network and to WAIO's Integrated Remote Operations Centre (IROC).

- Centralised management of radar systems across WAIO.

- A fully supported solution. WAIO's Geotechs did not have the resources or expertise to troubleshoot technology and network issues.

- Failover and redundancy in the implemented solution, ie IT outages or disaster scenarios.

- A data management framework and archiving solution for historical radar data, to deal with the significant volume of data generated by the systems.

- Ability to integrate and analyse radar data with other monitoring instrumentation data.

- Potential for expansion of the solution in the future as additional systems are required to manage operational ground control risks.

- A documented approach, that could be followed by Project Management teams for future procurements.

To successfully procure and integrate the additional slope radar systems in 2021, it was clear that expertise outside of the Geotech team would be required via a partnership project with BHP Technology and the Slope Radar vendor.

DATA FLOW OF IDS RADAR

The operation logic of the radar can be described with the following steps:

1. Acquisition – acquiring radar data and creating RAW data files.

2. Filtering – applying a set of filters and reducing the file size.

3. Transmission – transmitting preprocessed data from the field to processing environment (physical or virtual).

4. Processing – applying atmospheric correction algorithms and advanced processing techniques to achieve the best result.

5. Alarming – alerting Geotechnical engineers on detected slope movement.

Steps 1 and 2 are performed in vendor application layer, while steps 3–5 are part of the solution design (Figure 3).
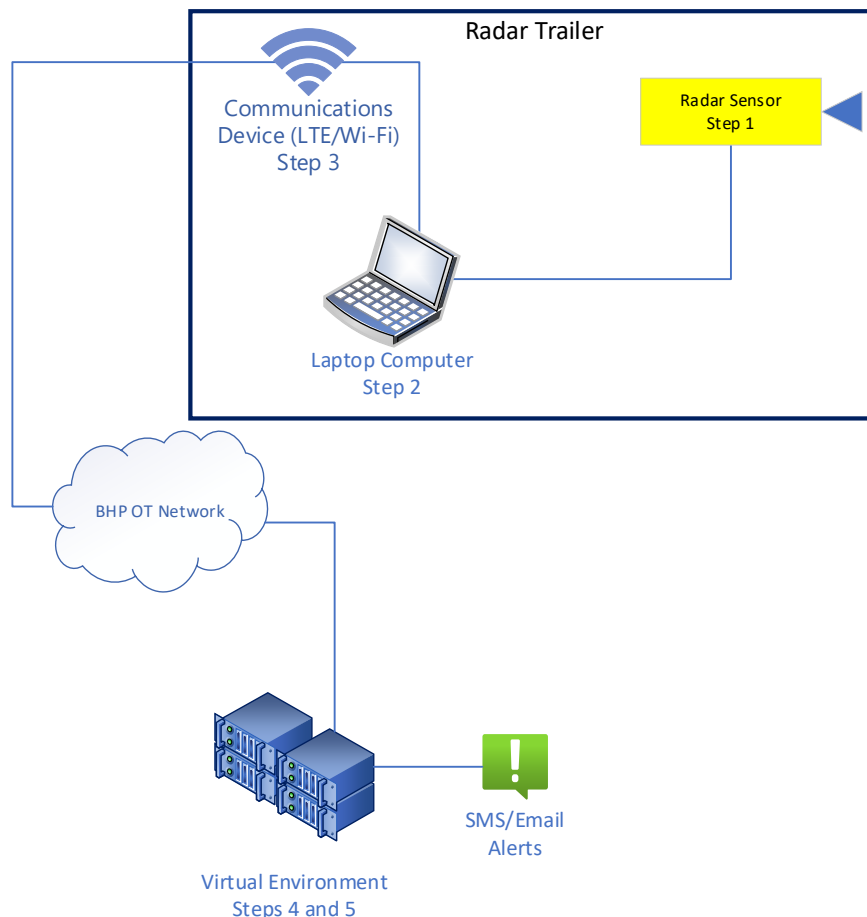
FIG 3 – Data flow for IDS Radar.

SOLUTION HISTORY

The first two slope monitoring radars from this vendor were purchased in 2013 and 2014. These were initially deployed outside of the supported BHP network, using the publicly available Telstra network. Each radar had a dedicated physical PC to process data and produce alarms. Following this there were several project teams assigned and projects opened between 2013 and 2021, but

each of these stopped for one reason or another. In 2021 additional radar systems were purchased and a Technology project team was assigned to the project. Close collaboration between the vendor, BHP Technology and Geotech teams in deploying the increased number of monitoring instruments can be attributed to the successful completion of this project.

The BHP Slope Monitoring solution including radar scanning capabilities, additional in-field devices, monitoring teams, and process flows is conceptualised below in Figure 4.
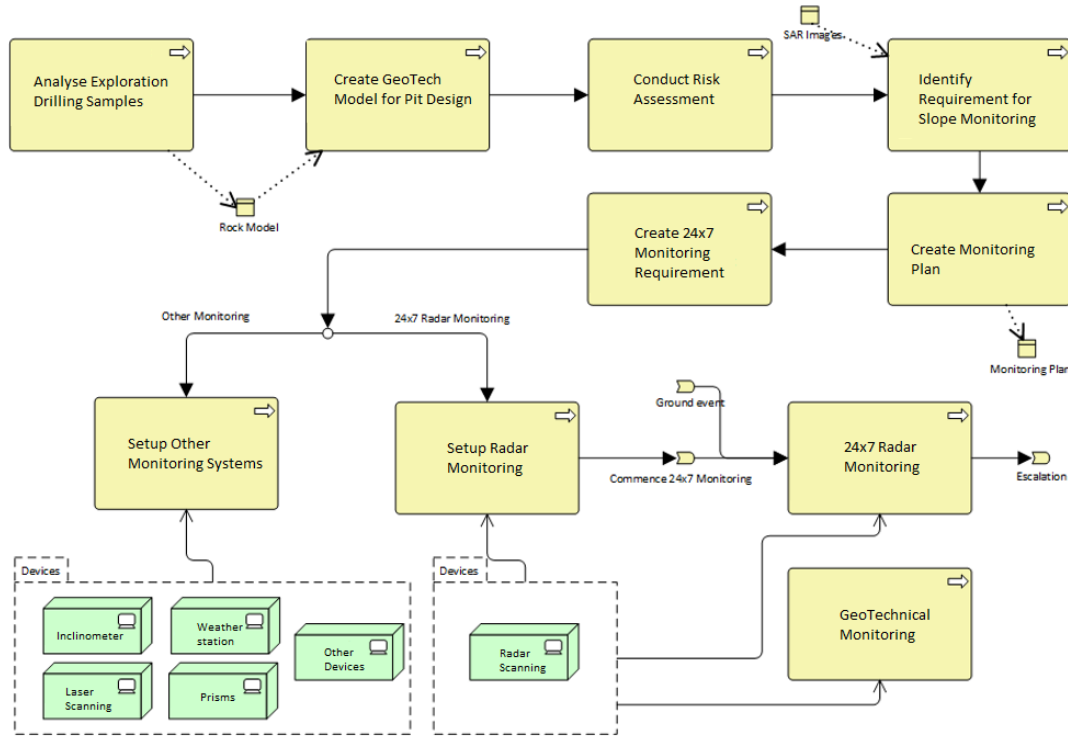
FIG 4 – Conceptual slope monitoring model.

INFRASTRUCTURE ANALYSIS AND DESIGN

Consideration of physical versus virtual infrastructure for the radar solution is determined by a series of key decision points around performance, accessibility, availability, survivability, supportability, cost, and scalability. Providing a fully physical computer environment reaps benefits to a point, yet the solution becomes difficult and costly to maintain and manage beyond a certain scale.

As detailed previously the initial two radars were each commissioned with a dedicated desktop PC hosting the Geotech monitoring and analysis software, located in specific mine site offices. The basic requirements for desktop computer resources are initially cheaper to provision than a fully racked server cluster, provides excellent performance gains for the initial investment, and are easy for site operations to locally manage and configure to meet requirements. Software installations are performed locally, and all data is collated on internal hard drives, leading to excellent application performance and data processing throughput.

When you consider introducing a complex server-to-multiclient application model, across multiple business operations, requiring highly available up-time for critical monitoring, a centrally managed support model (including patching, updating, and incident response management), and scalability required to meet growing business requirements, then a virtualised infrastructure deployment becomes essential.

Provisioning a computer cluster, either dedicated to the solution or shared across other business services, should be sized according to a 5-year business growth plan with full failover redundancy across physical locations. The modelling must include hosting all critical application and licensing workloads distributed across multiple locations in the event of disaster. Figure 5 depicts hardware deployment in WAIO across two physical locations (Data Halls A and B) with six available computer nodes and shared network storage (thick eager zeroed to ensure pre-allocated capacity is retained).
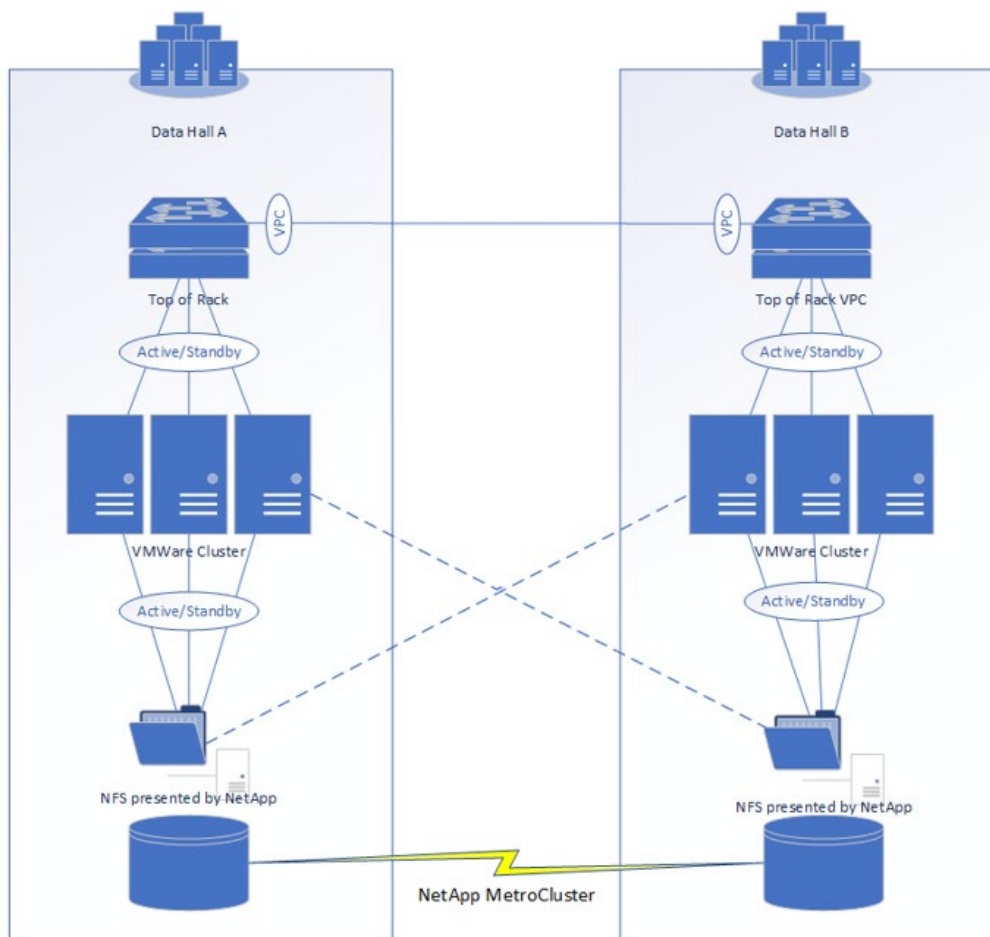
FIG 5 – Data hall topology.

To accommodate full failover, critical virtual loads should only be provisioned within a maximum of 50 per cent capacity across the physical servers, enabling zero-downtime live migration of workloads from one server to another via vMotion (VMware vSphere vMotion, 2022). By doing so, all service continuity aspects are covered, from routine quarterly OS patching and general IT maintenance, through to significant disaster involving complete loss of a single datacentre.

It is key to understand during the design phase which elements of the solution form the critical data and licensing pipeline, thus requirements for disaster and service continuity planning. In its most basic form, the radar collects raw scan data and partially processes the data onboard a locally hosted laptop. The partially processed data is sent across the network to a Data Master (virtual application server) with data processing subsequently completed before synchronising the final version of the data with a Data Server. Each Data Server is both a shared resource for all radars at a particular mine site and an application license service host for that sites' radars. Generated alerts are sent from the Data Master to the Data Server, and in turn passed to the Dispatch alerting client for remote operations monitoring at IROC, as described in Figure 6.
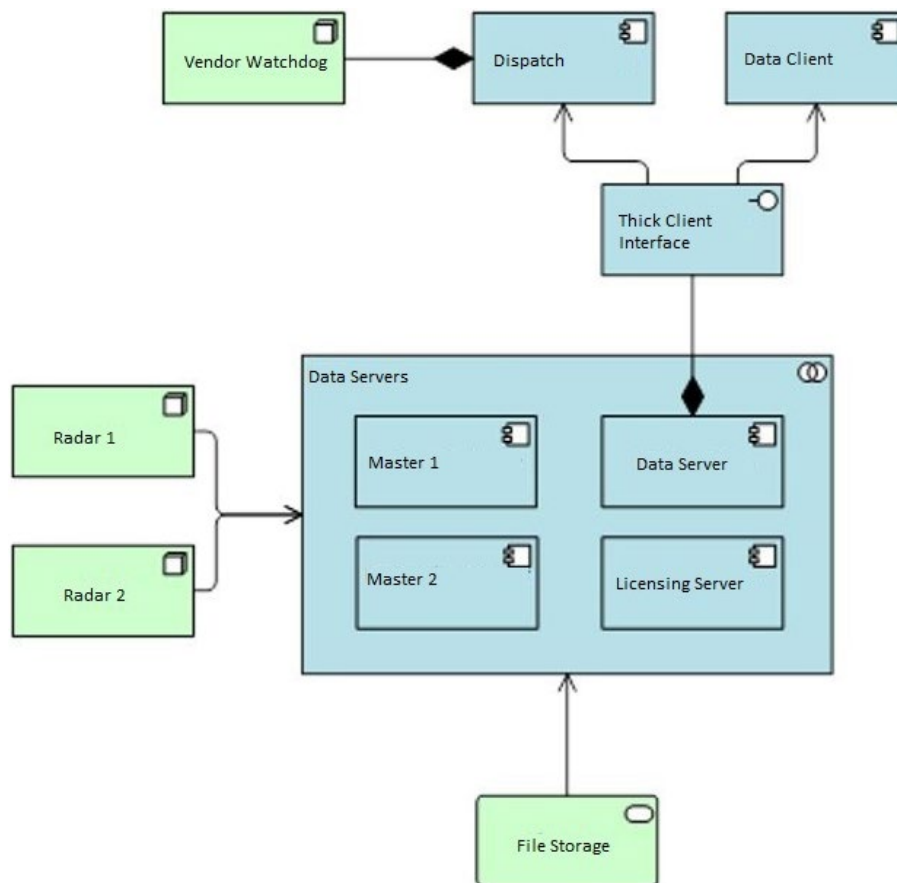
FIG 6 – Device and computer model.

In the event of a significant disaster there are discrete rules configured on the VMWare cluster for prioritisation of virtual servers to be brought back online to maintain basic operability. Whilst this solution depicted above provides Data Clients for current project and historical data analysis, these servers do not form part of the critical data pipeline and are not determined to be priority for disaster recovery.

When calculating overall growth capacity, careful consideration needs to be given equally to CPU, RAM, and GPU. The Slope Monitoring program at BHP deployed a GPU-intensive application suite, thus each server node is built with high-end nVidia graphics cards in line with Vendor recommendations.

SOLUTION DEPLOYMENT

Whilst general cluster computer capacity in BHP Data Centres in both the Pilbara and Perth was readily available for standard hosting solutions, there was limited availability of GPU-enabled computer resources to meet the project requirements. As such, a fit-for-purpose cluster was designed and deployed to meet not only current program deployment, but to exceed all 5 Year Plan for radars and other slope monitoring devices.

Physical infrastructure

The physical infrastructure deployed for the Slope Radar solution included six nodes, each with dual 48 GB nVidia graphics cards, 768 GB RAM, and 36 quad cores (144 available CPUs). These were deployed across twin data halls to accommodate full computer redundancy, as shown in Table 1. The decision to co-locate this cluster at the nearest centre of operation in the Pilbara, and not in a Perth data centre, was made with a view to both minimise network latency and reduce risks associated with WAN outages.

TABLE 1

Cluster resources.

Physical Host	Location	GPU (GB)	CPUs	RAM (GB)
ESX 1	DC 'A'	96	144	768
ESX 2	DC 'A'	96	144	768
ESX 3	DC 'A'	96	144	768
ESX 4	DC 'B'	96	144	768
ESX 5	DC 'B'	96	144	768
ESX 6	DC 'B'	96	144	768
TOTAL		576	864	4608

Virtual machines

The slope monitoring cluster hosts all virtual servers required to support 22 radars (including Masters, Data Servers, Clients, QA/Test, remote session hosts) distributed equally across the six nodes, with capacity to deploy future radars and additional slope monitoring devices. Each Master and Data Server has been provisioned with 500 GB local storage for radar project data and Client servers share a 17 TB pool of network storage, with resource allocations summarised in Table 2. Resource configurations for each virtual server is determined by function, with final allocations tuned via comprehensive workload testing and vendor recommendations. All VM workloads can be vMotioned between physical nodes and data hall locations with no application stunning.

TABLE 2

Virtual server configurations.

Group	App	Unit count	GPU (GB)	CPUs	RAM (GB)	Local storage (GB)	Shared storage (GB)
Radar	Master	22	2	6	16	500	0
Radar	Client	22	2	4	32	0	17000
Site	Data Server	4	0	4	8	500	0
Analytics	Historical Projects	2	2	6	16	1000	0
Access	Multi-Client Session Host	2	0	4	16	0	0
TOTAL			92	256	1152	15 000	17 000

Licensing

Software license provisioning was designed with the same underlying principle as the computer resources, to accommodate continuity in the event of a disaster and provide normal service continuity across both planned and unplanned outages. License services are co-located on each sites' Data Server, with Primary and Secondary (failover) license dongles interleaved in AnywhereUSB hubs mounted at the two data halls (Figure 7). In the event of a total outage at one data hall, support teams can remotely failover the licensing services to collect the application keys from the respective Secondary dongle. Fully redundant, highly available nVidia virtual GPU software license servers are also available to the cluster subnet and are used to serve a pool of floating licenses required to utilise the GPU capabilities.
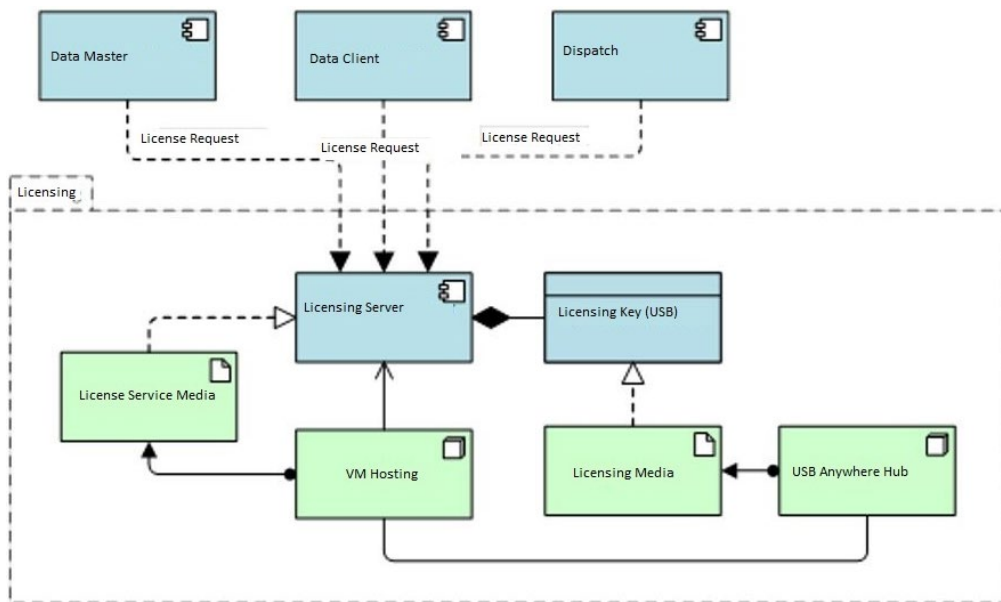
FIG 7 – Licensing model.

Connectivity

BHP sites operate with either private LTE (Long-Term Evolution) wireless or WTS (Wireless Telemetry System) wi-fi networks, providing challenges for any mobile equipment deployment. To accommodate full site-mobility, each radar trailer is provisioned with both LTE and WTS connectivity, via dual hardware installations. The access points are installed with physical network switches enabling mutually exclusive access to either the BHP LTE or WTS networks respectively, as described in Figure 8.
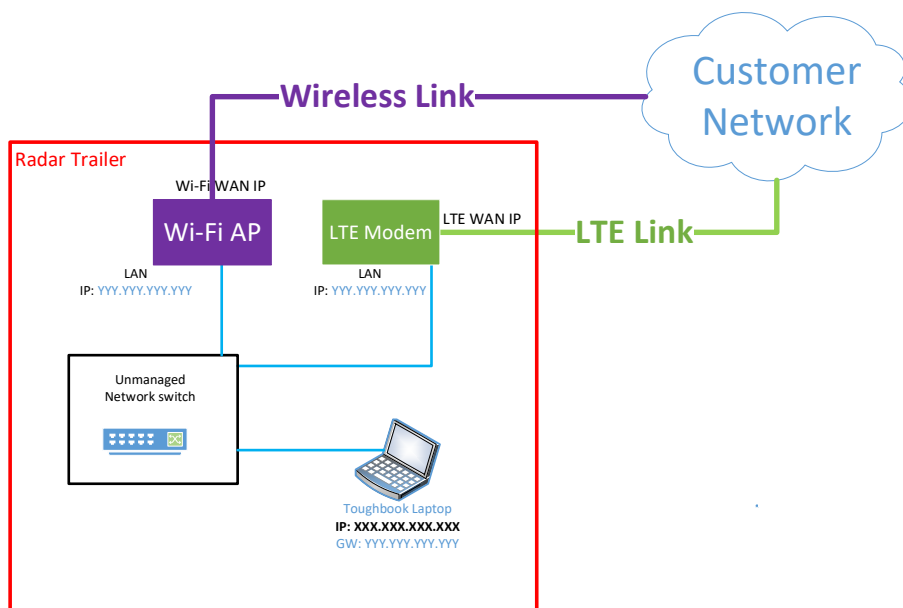
FIG 8 – Dual communications enablement.

Access control

To provision multi-user (concurrent), multi-session access for site based Geotechs, external monitoring teams, and IT support teams, an additional application layer via Citrix was deployed. This user access model is designed to accommodate Geotechs in the field and 24/7 remote monitoring operations support teams located in Perth and Indonesia. To provide additional access controls to the Dispatch alerting environment, monitored by the remote operations specialist team, a 'consented access' model was deployed via remote shadow requests. Some elements of the solution are provisioned within the standard IT (Information Technology) environment, which is where users

access the corporate network through their standard laptop hardware. The main technical elements of the slope radar solution, including all virtual servers, applications, and data are hosted within the OT (Operational Technology) network. A DMZ (Demilitarised Zone) facilitates discrete OT authentication for users to gain access into the OT network via an access gateway (Figure 9).
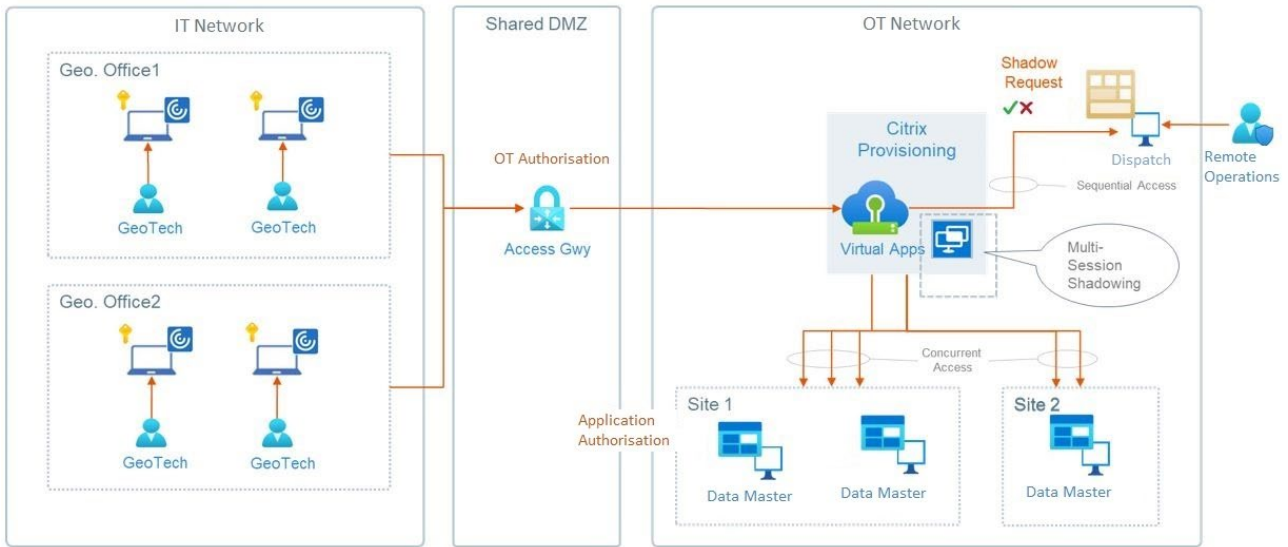
FIG 9 – Concurrent user access and authentication controls.

Monitoring technologies

Each layer of the solution is supported by various monitoring technologies and teams, including both vendor and enterprise monitoring solutions, described in Figure 10. Typical enterprise monitoring of the hosting environment includes disk space, application process and license services health, and VM accessibility, supported by dashboard displays and automated email alerts to relevant stakeholder groups.
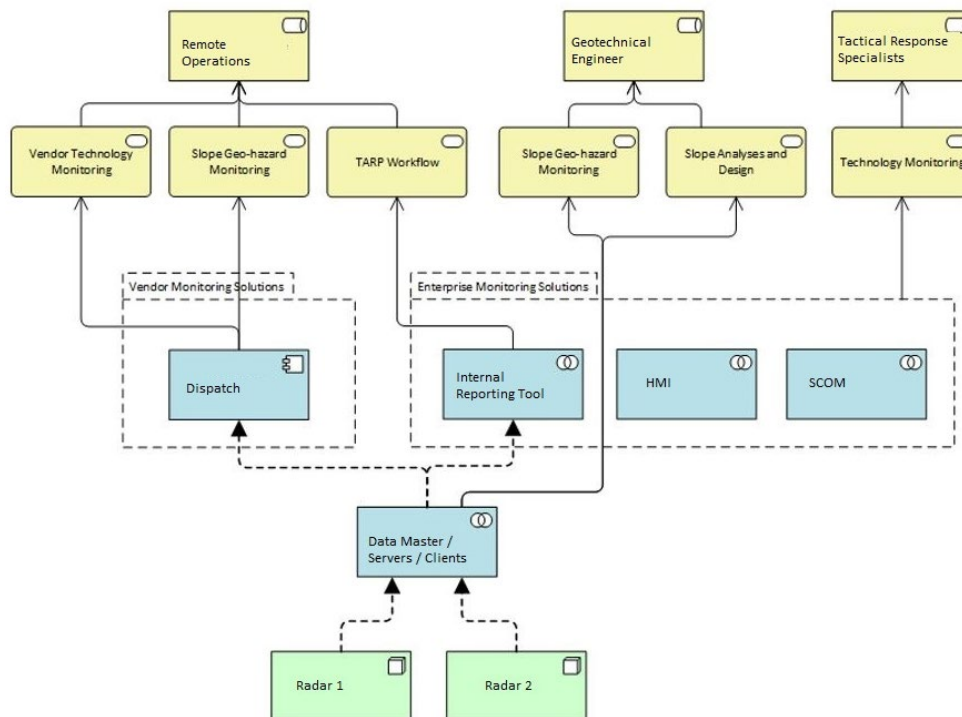
FIG 10 – Remote monitoring solution design.

Slope radar alerts

Slope Radar analysis applications include alarming functionality, with alerts presented to various teams when slope movement thresholds are exceeded, connection (network) errors, or other hardware faults occur. Figure 11 further details the types of vendor alarms that are monitored. WAIO operates under a model where Slope Radar alarms are triggered to:

1. The Geotechs on-site.

2. An offshore vendor support, remote monitoring control room in Indonesia providing 24 hours a day, 7 days a week analysis and response to alarms.

3. IROC remote operations for response by a centralised Mine Control team using the Dispatch application.

Central to the alarming process is a Slope Radar Trigger, Alarm, Response Plan (TARP) that covers the required responses by Geotechs, offshore vendor support, remote operations and Mine Production teams, to slope displacement (Geotech Hazard Map and Hazard Time Series) and various hardware level alarms.
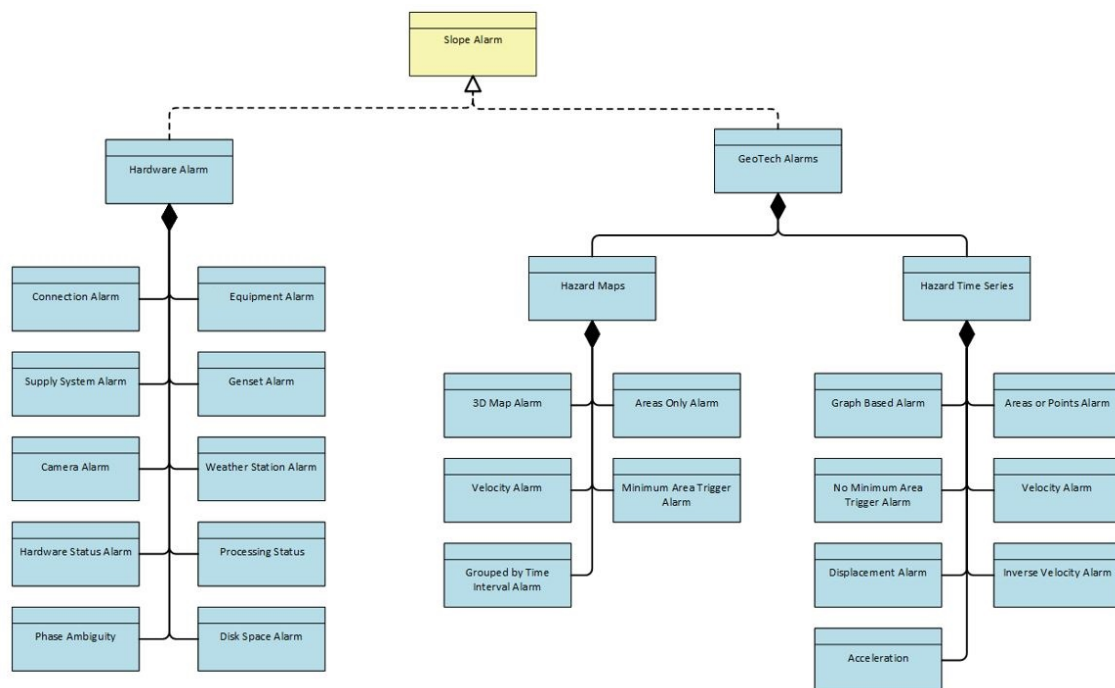
FIG 11 – Vendor alarm overview.

Other layers of technology used to support this solution, include automated messaging services targeted to key business stakeholders in the event of alarms for escalation. Alongside the technical teams monitoring alarms within the application suite and Dispatch, there is an SMS and SMTP relay service delivering text messages, phone calls, and email messages to specific groups depending on event severity, as shown in Figure 12.
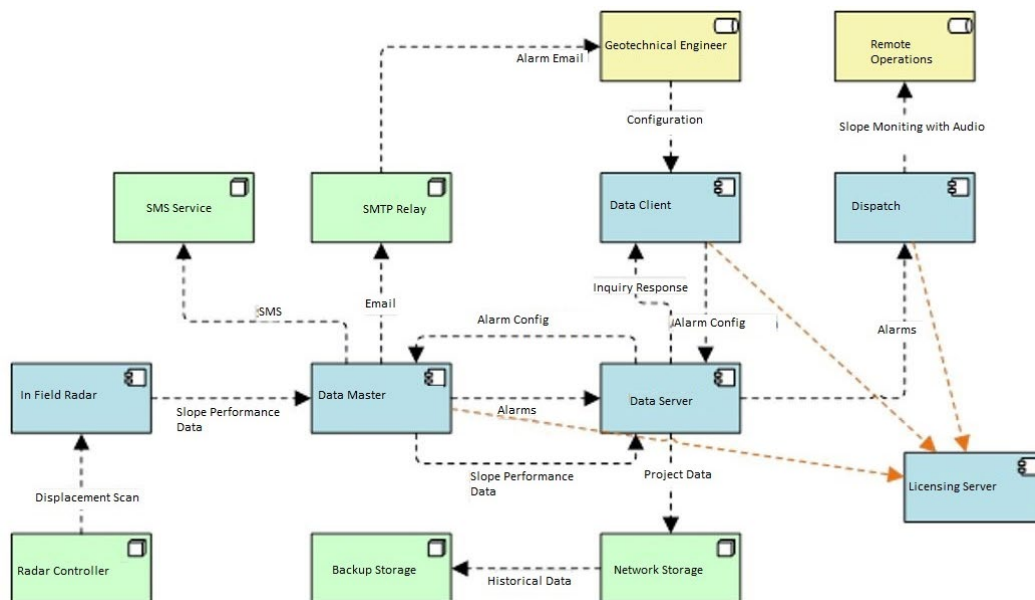
FIG 12 – Application cooperation design.

Data storage

In conjunction with active project storage provisioning (Table 2), additional storage was provided to accommodate near-line access to all recently closed projects and perpetual storage of any project exhibiting slope movement or failure. To facilitate a business requirement to have ready access to all projects closed within a 2-year time frame, 17 TB of low cost, low I/O 'Tier-S' storage was provisioned, with Geotechs able to self-serve transfer of data across the network via in-house scripts.

To meet standard governance requirements, any project with observable slope movement or failure is retained in perpetuity. A low-cost storage solution, hosted in the IT domain, was chosen to host this data with an automated managed file transfer protocol created to manage archiving into the IT network, and retrieval of data back into the OT network when required. Figure 13 shows the high-level data flows and storage provisioning required to meet these requirements.
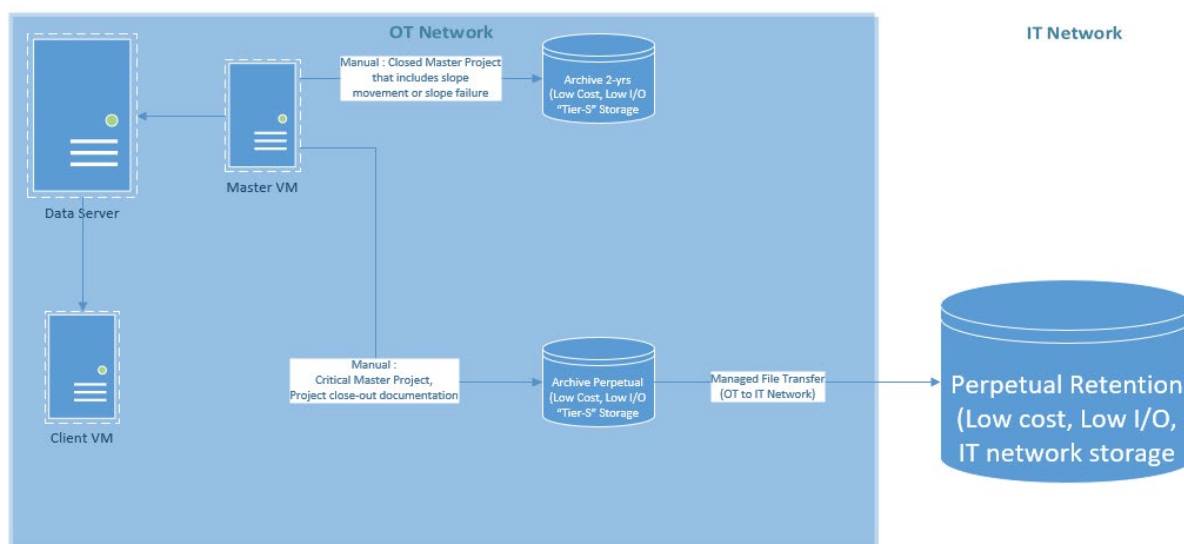
FIG 13 – Project archiving data flow and storage.

BUSINESS REPLICATION

Underpinning the framework of this project are a repository of document artefacts, describing the solution at both a conceptual and detailed design level, which can be leveraged for deployments across other parts of BHP. Guided by a comprehensive high-level design, each of the critical disciplines have been captured in both low-level designs and as-built documentation. This includes

design documentation across Hosting, Networking, Security and Firewall, Application, and Citrix Delivery disciplines.

Rigorous Transition to Operations (TTO) processes were followed during the project delivery, with the team documenting Disaster Recovery, Service Design, and Service Continuity Plans, plus specialist work instructions, and general support knowledge base articles and wiki pages for centralised information capture. Additional business processes were formulated in partnership with key stakeholder groups, including end-to-end support models (IT and Vendor) and TARPs.

Another key artefact for this project was the development of a new radar implementation plan. This is a visual guide, depicting swim-lanes covering all aspects including pre-radar procurement decisions and engagements (vendor contracts, RF studies), OT Hosting checklists (network, bandwidth, computer and storage availability), periphery monitoring decisions (internal monitoring applications, xMatters, remotely monitored OT Safety Dashboards), links to all relevant work instructions and shared documents, plus engagement with maintenance planning teams.

Finally, a key consideration for solution replication is the lessons learned from upscaling the original desktop solution to an enterprise environment. Replication of this solution is currently underway across other BHP Business Units and Functions, including Nickel West, BHP Coal, and Tailings Management teams.

CONCLUSION

This case study has demonstrated that when defining slope radar monitoring requirements, the number of systems is only one consideration. The solution developed needed to enable radar data transfer between the physical radar systems located in open pits, to on-site offices, a vendor supported remote control rooms for data analysis and monitoring alarms 24/7. When defining radar monitoring requirements consideration must also be given to the supporting infrastructure design including physical and virtual infrastructure, licencing, connectivity, access control, transmission of system alerts and radar data storage. Geotechnical Engineers typically do not hold expertise in developing the supporting IT infrastructure and the deployment of a network of 22 slope radars in WAIO was only possible via the partnership formed between BHP Geotechnical Engineering and Technology teams and the Slope Radar vendor, each team bringing their expertise to the solution.

ACKNOWLEDGEMENTS

REFERENCES

BHP, 2021. Safety Our Requirements, Available from: https://www.bhp.com/-/media/documents/ourapproach/governance/180529_safety.pdf.

de Graaf, P and Wessels, F, 2013. Slope monitoring and data visualisation state-of-the-art-advancing Rio Tinto Iron Ore's Mine of the Future™, in *Proceedings of the 2013 International Symposium on Slope Stability in Open Pit Mining and Civil Engineering* (ed: P M Dight), pp 803–814 (Australian Centre for Geomechanics: Perth).

de Graaf, P, Eberhardt, E, Neuwirt, A and Wessels, F, 2020. Data Acquisition, Transmittal, Validation and Management, in *Guidelines for Slope Performance Monitoring* (ed: R Sharon and E Eberhardt), pp 159–186 (CSIRO Publishing).

Escobar, A E E, Farina, P, Leoni, L, Iasio, C and Coli, N, 2013. Innovative use of slope monitoring radar as a support to geotechnical modelling of slopes in open pit mines in *Proceedings of the 2013 International Symposium on Slope Stability in Open Pit Mining and Civil Engineering* (ed: P M Dight), pp 793–802 (Australian Centre for Geomechanics: Perth).

IDS Georadar, 2022. IBIS-ArcSAR Lite/Performance, The world's most trusted slope monitoring radar, Available from: https://idsgeoradar.com/products/interferometric-radar/ibis-arcsar-lite-or--performance

Sharon, R and Stacey, P, 2020. Scope and Introduction, in *Guidelines for Slope Performance Monitoring* (ed: R Sharon and E Eberhardt), pp 1–5 (CSIRO Publishing).

VMware vSphere vMotion, 2022. Available from: https://www.vmware.com/au/products/vsphere/vmotion.html

Wessels, F and Dixon, R, 2019. Managing geotechnical risk in multi-pit operations, in *Proceedings of Mining Geotechnical Risk 2019* (ed: J Wesseloo), pp 311–322 (Australian Centre for Geomechanics: Perth).

Developments in the measurement of stress in rock

I Gray[1]

1. Managing Director, Sigra Pty Ltd, Acacia Ridge Qld 4110. Email: ian@sigra.com.au

INTRODUCTION

Other than being reasonably certain of the average vertical stress being lithostatic, there can be little certainty about stress in the ground. The stresses and strains in rock are a function of gravitational effects, external load, thermal changes, diagenesis and their mechanical properties including elastic, creep and post failure behaviours. It is highly desirable to measure stress where mining is going to take place, even if the virgin stress condition has already been changed by mining. The concept of some far field stress value that is more or less constant is usually invalid and can be dangerous to use in mine design.

Measuring stress is not simple. The basic processes are broken into two categories, one where the rock will not fail around the borehole in which the stress is being measured and one where the rock has failed or will fail. Because of the complexity and cost in obtaining a single, precise stress measurement it is highly desirable to have some system to be able to obtain an idea of the uniformity, or otherwise of the stress situation between precise measurements.

Table 1 shows the methods for measuring stress. The first five methods work on the basis of some fairly direct measurement of mechanical rock behaviour while the last three are attempts to get some idea of stress out of core long after it is removed from the host rock. While these latter methods appear to tick all the boxes for applicability there is a great deal of uncertainty in the results that they deliver. This paper reviews the methods for measuring stress and presents two new methods. These are a three dimensional overcore system to provide precise stress measurements in rocks that will not fail around the borehole and a core ovality system. The latter can be used to provide information on the stress difference orthogonal to the core. It is particularly useful because it can be used every metre of core length.

TABLE 1

Some methods of rock stress determination.

	No borehole wall failure	Borehole wall failure	Fractured rock mass
More direct stress measurement systems			
Hydrofracture	X	X	-
Hydrojacking	-	-	X
Overcoring	X	-	-
Borehole breakout	-	X	-
Core ovality (DCDA)	X	X	?
Highly indirect stress measurement systems			
Kaiser effect	X	X	X
Deformation rate analysis	X	X	X
Anelastic strain recovery	X	X	X

Overcoring is a prime method for measuring stress in rock where failure will not occur.

A new development in this area is a narrow angle cone cell which is locked into a pilot hole drilled ahead of the cone. It permits the measurement of three dimensional stress in any orientation HQ borehole. The cell is a glue in device which means that time must be allowed for the adhesive to set.

Logically this means installing the cell and then leaving it for a shift while the glue sets. The adhesive may be used under water and even in bentonite based drilling fluids. The cell has provided stress measurement that are consistent with two dimensional overcore systems that have been used down deep holes for many years.

The system has now been used successfully in sandstones and igneous rock. It is shown in Figure 1.
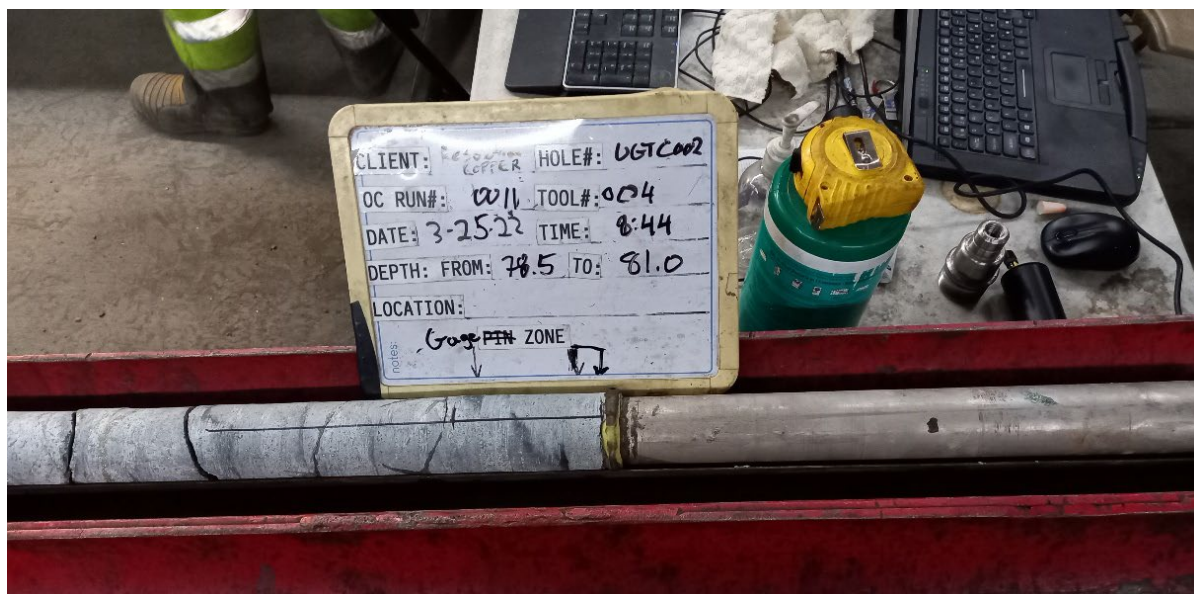
FIG 1 – 3D Overcore system for use in HQ core holes.

Core Ovality, which is also referred to as Diametrical Core Deformation Analysis (DCDA) involves the measurement of core diameter. It works on the basis that the core will expand elastically after it is cut and that this expansion may be used to gain a measurement of the stress difference orthogonal to the borehole. The key to making this system work is that the drill bit should not regrind the core and remove this expansion prior to the core reaching the inner barrel. This can be accomplished by providing the drill bit with an internal relief taper. This taper need not be great, but it should not wear out during drilling.

The recent development is the use of a semi-automated core ovality measurement system. In this any piece of core up to 1 m in length may be placed on the bed of the device and be rotated while measuring its diameter. This is done at 20° increments. Five or six such measurements are made and averaged. The average difference in diameter is a useful measurement in its own right. When combined with Young's modulus and Poisson's ratio the stress difference may be calculated. Figure 2 shows this device along with the results of diameter measurements. The system has been tested on overcore specimens and found to provide very similar values of stress differences.
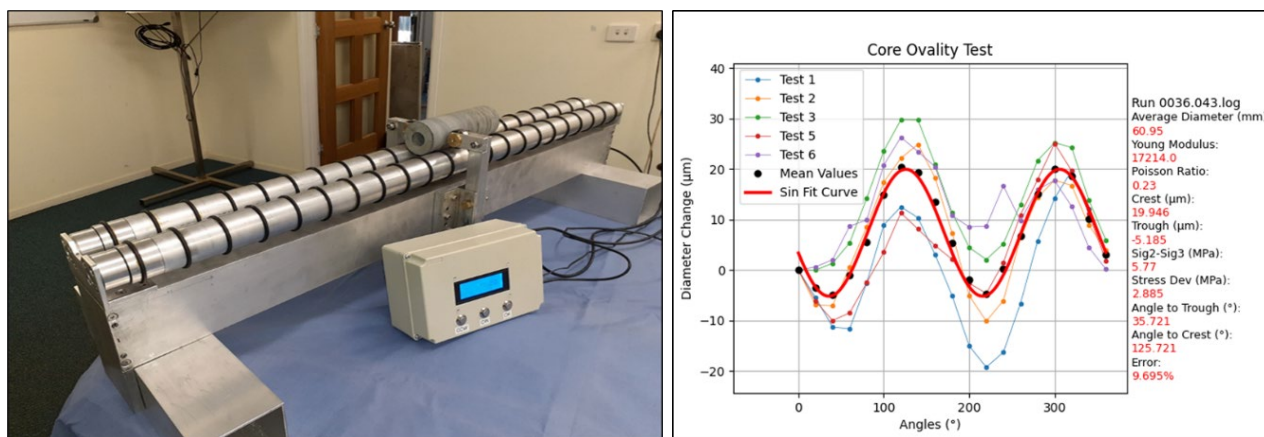
FIG 2 – Core ovality test equipment on left and traces in *µm* from core testing on the right.

COMBINATIONS OF STRESS MEASUREMENT METHODS

The use of core ovality enables a near continuous determination of the stress difference of the rock encountered in a core hole. It can be used as an indicator of stress change in a rock mass. If used on the drill site it can be used to help make a decision as to when a more precise measurement of stress should be made. This may be by overcoring or hydrofracture.

If borehole breakout occurs in the hole then core ovality may be used with the width of the breakout to arrive at an estimate of the full stress distribution orthogonal to the borehole. This requires information on the compressive strength of the rock orthogonal to the borehole and its Young's modulus and Poisson's ratio.

Core ovality may also be used in combination with the minimum stress derived from hydrofracture to arrive at a much better estimate of the major stress than can be derived from hydrofracture reopening alone.

Characterising coalmine roof using measurement-while-drilling technology

M Khanal[1], B Shen[2], J Qin[3], Y Duan[4] and X Luo[5]

1. Senior Research Engineer, Commonwealth Scientific and Industrial Research Organization, Pullenvale Qld 4300. Email: Manoj.Khanal@csiro.au
2. Senior Principal Research Engineer, Commonwealth Scientific and Industrial Research Organization, Pullenvale Qld 4300. Email: Baotang.Shen@csiro.au
3. Research Engineer, Commonwealth Scientific and Industrial Research Organization, Pullenvale Qld 4300. Email: Johnny.Qin@csiro.au
4. Senior Project Officer, Commonwealth Scientific and Industrial Research Organization, Pullenvale Qld 4300. Email: Joey.Duan@csiro.au
5. Senior Principal Research Scientist, Commonwealth Scientific and Industrial Research Organization, Pullenvale Qld 4300. Email: Xun.Luo@csiro.au

ABSTRACT

Gaining confidence in interpreting rock and strata properties of the coalmine roof is necessary for design, maintenance, modelling and optimisation of roadways supports. One of the key causes of roadway instabilities experienced in underground coalmines is an extreme variable nature (thickness, competence, discontinuities etc) of the coalmine roof. Normally, the thickness and strength of the roof are characterised with the geotechnical and geological data gathered from exploration boreholes, which are drilled often at considerable distances apart. This limited data cannot capture localised geological variations in the coalmine roof. With this background, this paper explores feasibility of using measurement while drilling concept to perform geotechnical characterisation of the coalmine roof.

The parameters, for example, penetration rate, rotary speed, torque, sound, vibration, obtained during the drilling process can provide valuable insights into geotechnical properties. The paper describes the progress of the experimental work conducted at the laboratory on synthesized concrete samples representing various rock strata using a field-scale drilling machine. The samples with and without interfaces have been tested to replicate various underground roof strata. The signals returned from the drill machine, as the drill bit passes through the layers, have been analysed and interpreted to characterise whether the drill response data can differentiate various strengths associated with the rock layers.

The initial laboratory results are promising as they show distinct responses of the various sample blocks in a controlled environment. The drilling data can differentiate the synthesized rock samples and detect 'signatures' of the roof strength variability and delineation of lithological interfaces (transitions). The weight and torque on the bit vary and show dependency on the strength of the blocks.

INTRODUCTION

One of the key causes of roadway instabilities experienced in underground mines is an extreme variable nature (thickness, competence, discontinuities etc) of the coalmine roof. It is necessary to gain confidence in interpreting rock and strata properties for design, maintenance, modelling and optimisation of roadways supports in the mine.

Normally, geological and geotechnical data are gathered from the exploration boreholes during mine planning. Due to the nature of these exploration boreholes, which are drilled at considerable distances apart, localised strength variations present in the geology may not be captured. The strength uncertainties associated with the localised geological variations may compromise rock mass competency and may pose challenges to effectively implementing various operational and design parameters to achieve stable and functional designs of the roadways.

One of the methods to capture the localised variations in the geology is to gather and analyse the drill returned signals during drilling at a local level. This method can be commonly referred as the Measurement While Drilling (MWD). The drill returned signals can provide different response while

drill bit passes through various drilled materials. Such information can be used to estimate competency of the local rock mass and gain confidence in design and implementation of the ground support systems. MWD can also provide information to identify discontinuities and joints in local scale drilling.

The research on application of MWD in the stratified layers, representing coalmine roof, and to detect top of the coal in surface mining, has been conducted in laboratory and field scale by various researchers (Bahrampour *et al*, 2015; Finfinger *et al*, 2000; Kahraman *et al*, 2016; Khanal *et al*, 2020; Leung and Scheding, 2015; Li *et al*, 2014; Partridge, 2019; Rostami *et al*, 2015; Segui and Higgins, 2002; Teale, 1965). MWD in underground coal mining environment has the potential to assist on real time design of roof support and reinforcement systems. It also allows early detection and response to localised geotechnical hazards that might have been overlooked due to the large scale nature of the exploration boreholes, for example, thinning roof coal layer, weak lithology, seam splits, discontinuities, voids. In surface mining, identification of top coal can help to efficiently utilise the energy during blasting and fragmentation.

Kahraman *et al* (2016) listed four instrumented systems for roof bolt drill developed by various researchers and organisations and highlighted their current status. In addition, there are other products, for example, ROCKMA (Rockma, 2020), iSURE (Sandvik, 2022) and Yabbigeosensing (Coal bed consultant, personal communication, 2022) that are on the market. However, as per authors' understanding, none of the Australian mines have a fully functional MWD system.

There are some challenges, for example, identification of inter-penetration of geological layers, voids, pinching on/off various layers, accuracy in analysing and interpreting the measurement data reliable classification between slightly different geological layers, deriving absolute rock properties, clearly delineating orebody and ore boundaries in metal mines, real time analysis and interpretation of huge number of data gathered during drilling process in developing fully reliable and functional MWD. A fully functional MWD can help to generate digital twin of the geological model. That can be assistance in achieving digital transformation in mining.

Rock geotechnical properties can be reflected in the drill returned signals that are generated while drill rod passes through the rock. The rate of penetration, rotary speed, torque, sound, vibration etc are different for various rock types, which are influenced by the rock properties. Therefore, a close analysis of these drill returned parameters can relatively provide valuable insights into the rock geotechnical properties. However, interpretation of the drill returned parameters to characterise the absolute rock properties is an extremely challenging task. The high noise to signal ratio in the drill returned signals that generates during drilling experiments, and separation of noise from the actual signal is an extremely challenging task. However, a comparative analysis is commonly provided using the derivation from the drilled returned signals. Nevertheless, interpretation of relative rock properties for various layers is still valuable in designing and reinforcing support systems. The most commonly derived parameter is the specific energy of drilling (Teale, 1965), which still cannot provide reliability and confidence in interpreting the absolute properties of rock.

This paper explores feasibility of using measurement while drilling concept to perform geotechnical characterisation of the coalmine roof. The parameters, for example, penetration rate, rotary speed, torque, obtained during the drilling process are analysed to characterise the drilled strata. The paper describes the progress of the experimental work conducted at the laboratory on synthesized concrete samples representing various rock strata using a field-scale drilling machine. The samples with and without interfaces have also been tested to replicate various underground roof strata.

SAMPLE PREPARATION AND EXPERIMENTAL RIG

A fundamental approach has been adopted to prepare synthetic rock samples of varying strength and thickness. These samples are prepared to resemble the variable nature of a typical coalmine roof. A general purpose cement and construction sand are chosen for experiments. For the samples without interface layers, three classes of geo-materials representing low, medium and high strength blocks are prepared representing various strengths of the strata that can be encountered in the coalmine roof. Each sample is of 0.4 m square area with 0.3 m height. For the interface samples, two blocks representing low and medium strength geo-materials are prepared. Each sample is of 0.4 m square area with 0.2 m height. In addition, a foam board has been used as an interface

between the blocks. Figure 1 shows the prepared samples at the laboratory. Once the individual samples are prepared, they are assembled in a 3 × 4 matrix type set-up, shown in the figure in order to represent a conceptual lithological units of various strength observed in a geomechanical set-up. These samples are cased in a large concrete structure as shown in right figure. This outer casing is needed to confine the samples during drilling process.

FIG 1 – Prepared samples. Left: without interface sample; Centre: with interface sample; and Right: example of the sample ready for drilling experiments.

Field scale drill rig equipped with various sensors, such as, displacement, torque, load on bit, has been selected for the experiment. The drill returned signals are analysed to extract various rock physical responses to the sensors which can be used to characterise the synthesized rock. The experimental drill rig and the sample placement for drilling is shown in Figure 2.

FIG 2 – Experimental set-up.

RESULTS AND DISCUSSION

For the sample without interface, three concrete blocks are stacked on top of each other without any material between the blocks. Figure 3 (left) shows a representative relationship between torque and thrust with respect to the displacement of the drill bit in the sample. The thrust and torque are directly related, as the thrust increases the torque also increases. The thrust and torque on the top block are lower than the other two blocks, suggesting top block is weaker than the remaining two blocks. The middle and bottom blocks show similar magnitudes of torque and thrust, suggesting they are of similar strength. The figure also shows the demarcation between the blocks. For the sample without interface, a representative specific energy for drilling (Teale, 1965) is also shown in the figure (Figure 3, right). The graphs are similar in nature with the force and torque relationships that distinguish various blocks of the samples. The middle and bottom blocks are almost similar in properties compared to the top block. The energy required to drill the weaker block is less compared to the other two blocks. During sample preparation stage, it was planned to prepare three different

strengths of the concrete blocks. However, from the drill data, it has been observed that bottom two are almost similar in strength, which has been verified by the laboratory tests for uniaxial compressive strength of the samples. Figure 4 shows a relationship between the laboratory measured uniaxial compressive strength and the derived specific energy for a number of drilled samples. From the figure, it can be noted that, it is a challenging task to relate the specific energy of drilling to UCS of the drilled medium.
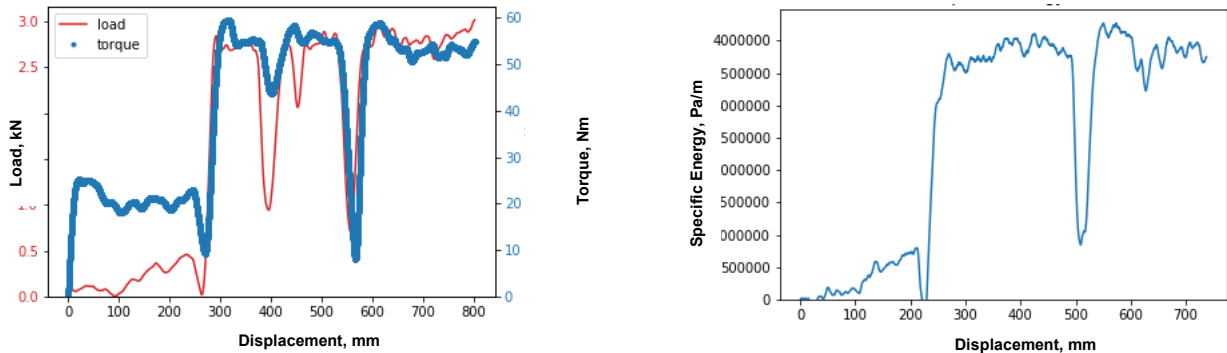
FIG 3 – (left) Monitored Thrust, Displacement, Torque for experiments without interfaces. (right) Calculated Specific Energy for experiments without interface samples.
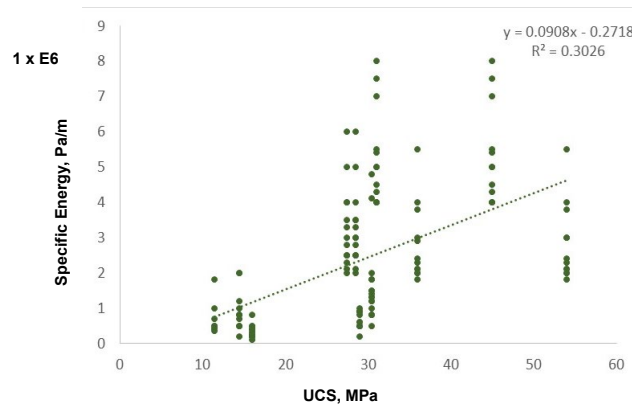
FIG 4 – Specific Energy versus measured UCS (Left: actual UCS; Right: Averaged UCS): Linear correlation.

For the sample with interface, two synthesized concrete blocks are separated by a relatively weaker 5 cm material. Figure 5 shows a representative relationship among torque and thrust with respect to the displacement of the drill bit for the interface samples. Similar to the above observations noted with the samples without interface, the thrust and torque are directly related. The figures clearly show the location of interfaces within the sample blocks. The figure also shows the derived representative specific energy of drilling with respect to the penetration depth of the drill bit. From the figures, it can be noted that the top block is weaker than the bottom block; and have a clear demarcation between the two concrete blocks and an interface layer, which is sandwiched between the concrete blocks.
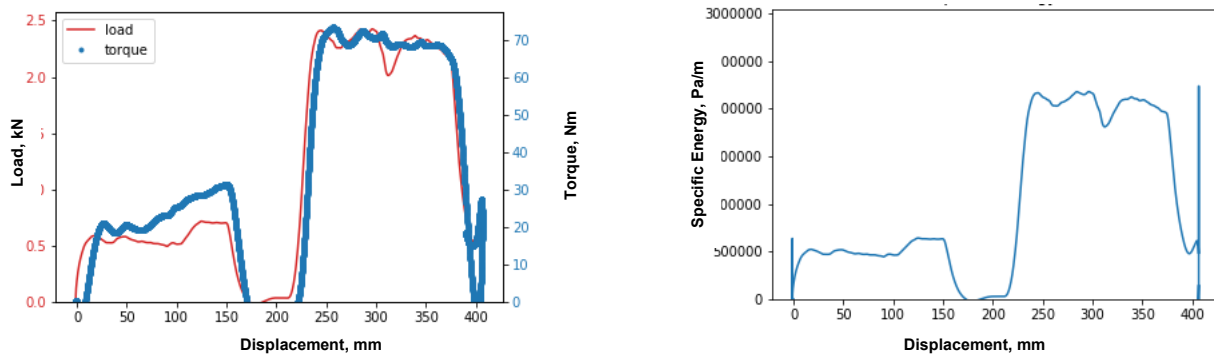
FIG 5 – (left) Monitored Thrust, Displacement, Torque for experiments with interface while drilling; (right) Calculated Specific Energy for experiments with interface samples.

CONCLUSIONS

From the drilling experiments conducted under controlled laboratory environment, it has been noted that the parameters, for example, penetration rate, rotary speed, torque obtained during the drilling process can provide valuable insights into rock response during drilling. It has been observed that the synthesized rock blocks that are separated by the strength of the material can be identified during MWD. The drilling data can differentiate the synthesized rock samples and detect 'signatures' of the roof strength variability and delineation of lithological interfaces (transitions). The weight and torque on the bit vary and show dependency on the strength of the blocks. However, it has also been noted that the identification of the absolute properties of the rock, for example, uniaxial compressive strength is a challenging task.

ACKNOWLEDGEMENT

REFERENCES

Bahrampour, S, Rostami, J, Ray, A, Naeimipour, A and Collins, C, 2015. Ground characterization and roof mapping: Online sensor signal-based change detection, *International Journal of Mining Science and Technology,* 25:905–913.

Finfinger, G L, Wilson, G, Peng, S and Thomas, B, 2000. Mining Publication: An Approach to Identifying Geological Properties from Roof Bolter Drilling Parameters, in *19th International Conference on Ground Control in Mining,* West Virginia University, pp 1–11.

Kahraman, S, Rostami, J and Naeimipour, A, 2016. Review of Ground Characterization by Using Instrumented Drills for Underground Mining and Construction, *Rock Mech Rock Eng*, 49:585–602.

Khanal, M, Qin, J, Shen, B and Dlamini, B, 2020. Preliminary Investigation into Measurement While Drilling as a Means to Characterize the Coalmine Roof, *Resources*, 9:10.

Leung, R and Scheding, S, 2015. Automated coal seam detection using a modulated specific energy measure in a monitor-while-drilling context, *International Journal of Rock Mechanics and Mining Sciences*, 75:196–209.

Li, Z, Itakura, K-I and Ma, Y, 2014. Survey of measurement-while-drilling technology for small-diameter drilling machines, *The Electronic Journal of Geotechnical Engineering*, 19:10267–10282.

Partridge, J, 2019. Measure while drilling: a case study at Daunia Coal Mine, *Proceedings of the Mining Geology 2019 Conference*, p 7280 (The Australasian Institute of Mining and Metallurgy: Melbourne).

Rockma, 2020. Rockma.

Rostami, J, Kahraman, S, Naeimipour, A and Collins, C, 2015. Rock characterization while drilling and application of roof bolter drilling data for evaluation of ground conditions, *Journal of Rock Mechanics and Geotechnical Engineering*, 7:273–281.

Sandvik, 2022. iSURE.

Segui, J B and Higgins, M, 2002. Blast Design Using Measurement While Drilling Parameters, *Fragblast 6*, pp 287–299.

Teale, R, 1965. The concept of specific energy in rock drilling, *International Journal of Rock Mechanics and Mining Sciences & Geomechanics Abstracts*, 2:57–73.

Geotechnical risk management

Underground mining subsidence in mine planning and risk assessment for cave mining

P M Cepuritis[1]

1. Geotechnical Manager – Underground, Mining One, Brisbane Qld 4000.
   Email: pcepuritis@miningone.com.au

INTRODUCTION

In hard rock mining, large-scale bulk mining methods such as block or panel caving (BC/PC) and sublevel caving (SLC) typically generate significant surface deformations such as subsidence. Surface deformations need to be considered in the project evaluation and planning stages of cave mines, for example, planning and location of critical underground mine planning infrastructure such as portals, haulage and vent shafts, access roads, or potential damage to existing infrastructure, changes to surface water management, waste dump, stockpile and tailings dam stability, and environmental impacts. Assessing the impact and risks associated with subsidence is a key component in robust mine planning and operations management.

PLANNING AROUND SUBSIDENCE

Subsidence assessment can be especially important factor in the evaluation of mining operations transitioning from open pit mining to underground cave methods. For example, at Palabora uncertainty of cave propagation and subsidence on interaction with the existing open pit, including size and timing of pit wall failures was identified as a key risk for the operation (Moss *et al*, 2006). Typically, open pit mine surface infrastructure is located close to final pit limits. This may include mills, administration buildings workshops, waste dumps and tailings dams. Some infrastructure can be easily relocated (such as administration buildings, pipelines, electrical transmission, workshops), albeit an additional capital cost. Other infrastructure, such as mills or tailings dams may involve significant capital costs or project risks such that their relocation is impractical. In this case, critical deformations produced by subsidence need to be established to ensure continuing function of infrastructure and these constraints may drive underground project planning.

MODELLING CAVE GEOMETRY

Defining the growth and extents of subsidence over the life of a cave mine is a fundamental task in cave mine planning. Surface subsidence is generally restricted to above the mining footprint within a subsidence angle between 35 to 80 degrees (Woo *et al,* 2009). However, the size, shape and magnitude of subsidence is related to cave growth and depends on a number of factors such as surface topography, rock mass quality, in situ stresses, influence of large-scale geological structures and rock fabric, footprint geometry and extraction rate and sequence. Subsidence is a therefore complex system, with potential uncertainty in the underlying mechanisms.

Several methods are available to geomechanics practitioners to assess likely cave formation, propagation, interaction with the surface over time to evaluate subsidence-based risks. The level of sophistication and reliability of these methods needs to be commensurate with aims and stage of project evaluation or operations and availability of data. For example:

- Conceptual to Prefeasibility studies: Empirical estimates of extents of various caving deformation zones (see Figure 1). For example, this can be used to establish personal safety and staging of restricted access limits, limits/catchment area of potential surface water ingress into the cave, identify the continuous zone, for infrastructure placement where moderate deformations may be tolerated.

- Prefeasibility: 2D or 3D linear elastic or elasto-plastic finite element modelling. For example, this approach can be used for first-pass assessment of the magnitudes of horizontal and vertical displacements in the continuous zone.

- Feasibility studies: Non-linear finite element or discrete element numerical modelling (Vyazmensky *et al,* 2010). For example, define potential variations of cave geometry and propagation directions based on-site conditions to better confine exclusion zones.

- Operations: Coupled non-linear finite/discrete element numerical modelling with flow (Beck *et al,* 2011; Kothari *et al,* 2020). Capable of modelling growth of various deformation zones with mining, more precise magnitudes of performance criteria, seismicity, groundwater ingress and mine abandonment evaluations.
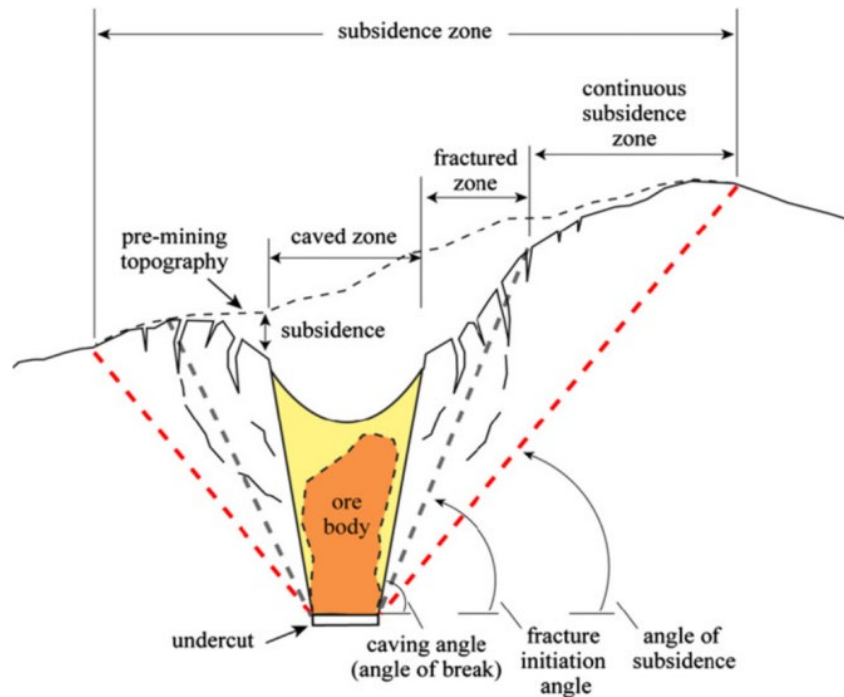
FIG 1 – Caving subsidence zones (Woo *et al,* 2009).

SUBSIDENCE RISK ASSESSMENT

Geomechanics specialists are largely in charge of assessing likely deformation extents and magnitudes over the mining life cycle, however, they are not necessarily informed nor understand how to evaluate all subsidence-based risks which requires interaction with other disciplines, for example structural, tailings dam and environmental engineering. Engagement with key stakeholders is essential to effectively communicate the evolution of surface deformation its impact on subsidence related risk evaluations.

Many approaches to subsidence risk assessment exist, such as bow-tie analyses, qualitative methods and land usage risk-decision approaches, as well as semi-quantitative and quantitative risk management approaches. Study and operations managers need to be aware of and incorporate various tools in evaluating and manage subsidence risks for mine planning and operations. The strategy for subsidence risk management should include:

1. Project and management team including all key subsidence risk stakeholders.

2. Identify and develop a register of perceived hazards, key risks and vulnerabilities.

3. Understand site specific subsidence and failure mechanisms, contributing factors and likely ranges of input values. Where uncertainty in the underlying mechanisms is high and the potential consequences are likely to be high, various plausible risk scenarios need to be considered and addressed (Li, 2004).

4. Establish critical performance criteria, locations and threshold values for each risk. Performance criteria may include: vertical/horizontals displacements, shear strains, angular distortion, pore pressure changes, differential consolidation, etc.

5. Design the subsidence evaluation analyses, with input from key stakeholders, to predict the performance criteria at required locations over the planned mine life cycle, capturing uncertainty where possible (see Figure 2).

6. Evaluate each of the subsidence related risks over the mining cycle, identifying key points/periods which may constrain or guide the mine plan.

7. Design and implement an instrumentation and monitoring plan to measure subsidence and performance compared to predicted performance to provide early warning of deviations, take necessary corrective actions, validate and calibrate the numerical modelling predictions and/or improve understanding of mechanisms.

8. Develop trigger action response plans (TARP's) for each identified risk from monitoring programs, incorporating uncertainty in threshold levels.

9. Re-assess mechanisms and design assumptions, adjust mine designs/remediation and mitigation measures, reforecast performance, update monitoring plans if required.
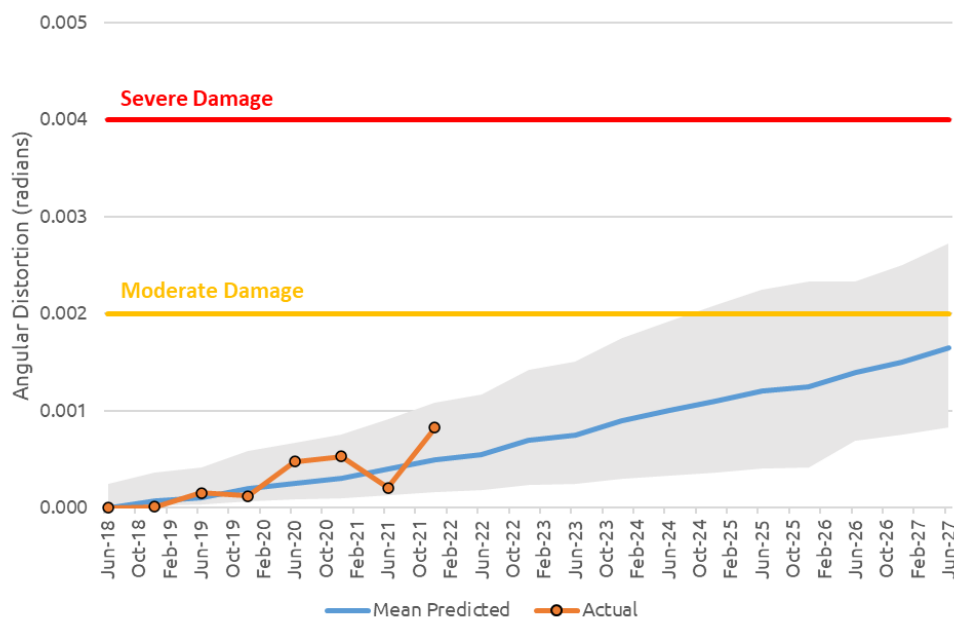
FIG 2 – Example building damage evaluation using subsidence modelling results showing upper bound, lower bound and mean angular distortion with actual performance.

CONCLUSIONS

Due to the complex and uncertain mechanisms inherent in subsidence assessment, study and operations managers are advised to develop flexible and responsive subsidence risk management strategies. Comprehensive subsidence risk evaluation also requires a collaborative interaction between practitioners responsible for predicted surface displacements and those responsible for defining critical infrastructure, performance criteria and capacity limits, and event consequences.

REFERENCES

Beck, D A, Sharrock, G and Capes, G, 2011. A Coupled DFE-Newtonian Cellular Automata Scheme for Simulation of Cave Initiation, Propagation and Induced Seismicity, *Proceedings of the 45th US Rock Mechanics/Geomechanics Symposium* (American Rock Mechanics Association: Alexandria).

Kothari, U, Sinaga, F and Nguz Tshisens, J, 2020. Understanding surface subsidence from a block cave by comparing InSAR data with 3D numerical modelling, in R Castro, F Báez, K Suzuki, R Castro, F Báez and K Suzuki (Eds.), *Proceedings of The Eighth International Conference and Exhibition on Mass Mining,* University of Chile, pp 318–326.

Li, G, 2004. Risk management of subsidence uncertainties, *Proceedings of the Sixth Triennial Conference on Coal Mine Subsidence – Subsidence Management Issues,* Mine Subsidence Technological Society, pp 161–172.

Moss, A, Diachenko, S and Townsend, P, 2006. Interaction between the Block Cave and the Pit Slopes at Palabora Mine, *Proceedings of the International Symposium on Stability of Rock Slopes in Open Pit Mining and Civil Engineering*, pp 399–410.

Vyazmensky, A, Elmo, D and Stead, D, 2010. Role of rock mass fabric and faulting in the development of block caving induced surface subsidence, *Rock Mechanics and Rock Engineering*, 43:533–556.

Woo, K, Eberhardt, E and van As, A, 2009. Characterization and Empirical Analysis of Block Caving Induced Surface Subsidence and Macro Deformations, *ROCKENG09: Proceedings of the 3rd CANUS Rock Mechanics Symposium*, Toronto.

Study of prevention methods for stress corrosion cracking in underground coalmines

H Chen[1], H L Ramandi[2], A Crosky[3] and S Saydam[4]

1. Postdoctoral Fellow, UNSW Sydney, Sydney NSW 1466. Email: honghao.chen@unsw.edu.au
2. Senior Lecturer, UNSW Sydney, Sydney NSW 1466. Email: h.lameiramandi@unsw.edu.au
3. Emeritus Professor, UNSW Sydney, Sydney NSW 1466. Email: a.crosky@unsw.edu.au
4. Professor, UNSW Sydney, Sydney NSW 1466. Email: s.saydam@unsw.edu.au

INTRODUCTION

Cable bolts and rock bolts are used as primary and secondary anchoring systems in many underground mines. Reports on the premature failure of cable bolts and rock bolts due to stress corrosion cracking (SCC) in underground coalmines have been increasing in the past two decades. The previous studies found that the SCC in both rock bolts and cable bolts occur as a consequence of atomic hydrogen diffusion into the material, which is known as hydrogen-induced stress corrosion cracking, HISCC (Craig *et al*, 2016; Wu *et al*, 2018b). While research to understand the process of SCC occurrence in underground mines is still required, finding a prevention solution to protect the bolts from HISCC is crucial.

In this study, we analyse a variety of commercially available coatings for steel corrosion prevention, including barrier coating (ie epoxy, polyester TGIC) and sacrificial coating (hot-dip galvanising). We test the coating on coupons manufactured from rock bolts and cable bolts used in the coal mining industry.

MATERIALS AND METHODS

We create an accelerated environment to reproduce the SCC similar to those observed from in-service failed bolts. All coupons are loaded near the material's yield stress during the test. The design of the testing coupons is according to our previously developed three-point bending (Wu *et al*, 2018b). We deform cable bolts king wires and rock bolts by inserting a loading pin into a section of slotted bolts. Two 150 mm king-wires with a pair of locking rings installed 75 mm apart towards each end make the cable bolt coupons. A 6 mm loading pin made from the same material (king-wire) is inserted between the two locking rings at the centre. The loading pin produces a load of approximately 1600 MPa, equivalent to 94 per cent of the yield strength at the centre of both wires (Wu *et al*, 2018b). The rock bolt coupons are 300 mm in length with a 15 mm wide slot cut along the centreline for a length of 100 mm in the centre of the coupon. A 30 mm diameter loading pin, made from the same material as HSAC 840 rock bolt, is then inserted at the specimen's centre. The pin produces a load of approximately 600 MPa (equivalent to the yield strength) on the centre of the coupon (Craig *et al*, 2016).

Both cable bolts and rock bolts coupons are coated by thermosetting polymer (epoxy and polyester TGIC) and hot dip galvanising. After the coating process, the test solution that is proven to create the HISCC is prepared using NaCl, Na_2S, and acetic acid (Wu *et al*, 2018a) for the immersion test (pH 2.4). All coated coupons and uncoated control coupons are fully immersed in the test solution for 120 hours. The solution is refreshed every 24 hours to maintain the H_2S concentration. Each coupon is immersed individually in a 1 L solution to ensure the chemistry of the solution is not affected by the chemical reaction between acetic acid and bolts.

RESULTS AND DISCUSSION

The test results of uncoated and galvanised coupons are shown in Figures 1 and 2. The results demonstrate that both uncoated and coated coupons crack during the test. On both rock bolt and cable bolt coupons, there are more corrosion products formed on uncoated coupons than galvanised ones, which means the galvanised coupons had less exposure time to the corrosive environment than uncoated coupons. However, the galvanising method can only delay the HISCC failure of rock bolt and cable bolt rather than preventing the failure.
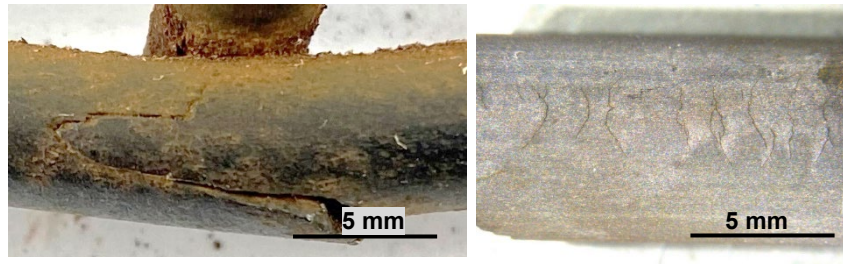
FIG 1 – Cracks on cable bolt coupons (left: uncoated, right: hot-dip galvanised).
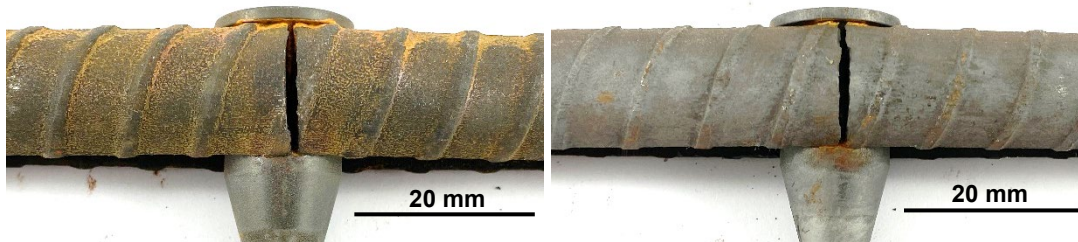
FIG 2 – Cracks on rock bolt coupons (left: uncoated, right: hot-dip galvanised).

For the epoxy and polyester TGIC coated coupons, the coating remains in good condition after the immersion test. The coupons are examined by Leica M205 A stereo microscope and no crack is observed on the surface.

The test results show the epoxy and polyester TGIC have successfully prevented the HISCC failure of rock bolt and cable bolt coupons. The galvanised coating undergoes dissolution in the test solution, allowing the corrosive environment access to the steel surface and subsequently resulting in failure.

CONCLUSIONS

We create a highly aggressive environment to accelerate HISCC. In such an aggressive condition, the sacrificial coating can no longer protect the bolts from HISCC occurrence. We show that the coating made from thermosetting material can prevent HISCC in the aggressive environment. Thus, thermosetting coatings have a great potential to overcome the HISCC problem in the mining industry.

ACKNOWLEDGEMENTS:

REFERENCES

Craig, P, Serkan, S, Hagan, P, Hebblewhite, B, Vandermaat, D, Crosky, A and Elias, E, 2016. Investigations into the corrosive environments contributing to premature failure of Australian coal mine rock bolts, *International Journal of Mining Science and Technology,* 26:59–64.

Wu, S, Chen, H, Craig, P, Ramandi, H L, Timms, W, Hagan, P C, Crosky, A, Hebblewhite, B and Saydam, S, 2018a. An experimental framework for simulating stress corrosion cracking in cable bolts, *Tunnelling and Underground Space Technology,* 76, 121–132.

Wu, S, Chen, H, Ramandi, H L, Hagan, P C, Crosky, A and Saydam, S, 2018b. Effects of environmental factors on stress corrosion cracking of cold-drawn high-carbon steel wires, *Corrosion Science*.

Characteristics of seismicity in the vicinity of a major dyke in a longwall coalmine

Y Duan[1,2], G Si[3], I Canbulat[4] and X Luo[5]

1. Senior Project Research Officer, CSIRO Mineral Resources, Brisbane Qld 4069. Email: yi.duan@csiro.au
2. PhD candidate, UNSW Minerals and Energy Resources Engineering, Sydney NSW 2052. Email: yi.duan@student.unsw.edu.au
3. Senior Lecturer, UNSW Minerals and Energy Resources Engineering, Sydney NSW 2052. Email: g.si@unsw.edu.au
4. Professor and Head of School, UNSW Minerals and Energy Resources Engineering, Sydney NSW 2052. Email: i.canbulat@unsw.edu.au
5. Senior Principal Research Scientist, CSIRO Mineral Resources, Brisbane Qld 4069. Email: xun.luo@csiro.au

ABSTRACT

The presence of unfavourable geological structures such as faults and dykes often can contribute to coal burst risk. Seismic events associated with rock fractures tend to cluster around these structures and it is important to understand the characteristics of seismicity for coal burst risk management. In an Australian underground longwall coalmine, two clusters of seismic activities close to the longwall face and within a section of the maingate roadway which was intersected by a major dyke were respectively identified. The induced seismicity in the dyke-roadway area was closely related to the longwall mining. These seismic events were located and the distribution of seismic events shows that more fractures were distributed on the inbye side of the dyke. The spatial-temporal changes of the seismic event locations delineate the fracture propagation as the longwall mined through the dyke. The frequency-magnitude relationship of seismicity was analysed and it was found that it changed significantly when the longwall was mining towards, through and past the dyke. The monitoring results demonstrate that because of the stiff dyke, the seismicity was intensified in the roadway section. It proves that the dyke promoted stress re-distribution and seismicity in its vicinity. More fractures were induced in the hanging wall of the dyke, whereas less strain energy was accumulated and released in the footwall of the dyke.

INTRODUCTION

Major geological discontinuities can induce abnormal stress re-distribution and seismicity during the mining process. Characterisation of seismicity near these geological features have been widely studied for dynamic risk assessment. van Aswegen and Meijer (1994) defined a specific group of seismic events occurred at the Tanton fault in the Welkom goldfield, whereas another group of seismic events close to stopes being mined were also recorded. The stress state around the fault was higher than that around the stope. The seismicity exhibited higher Es/Ep ratio, indicating dominant shear failure mechanisms. Joughin (1966) found that at the Harmony Mine, Free State Goldfields (South Africa), seismic events were not only located in the reef plane but also along the dykes. van Aswegen (2013) showcased two seismic events associated with a rock burst in a dyke at the Klerksdorp Goldfield, South Africa. They had high Es/Ep ratios with small seismic energy but still caused major damage. Urbancic *et al* (1992) investigated the space-time correlation of *b*-values (Gutenberg and Richter, 1956) with stress status. They found that spatial variations of decreasing *b*-values were well correlated with increasing stress release. Although time variations of *b*-value did not show clear correlations with the stress conditions. Kijko and Funk (1996) conducted a cross-correlation analysis on the clustered seismicity in a South African gold mine. They concluded that the clustered seismic activity rates and radiated energy were clearly related and the level of interaction between clusters decreases as distance increases. Liu *et al* (2013) introduced a forecasting approach incorporating cumulative apparent volume, energy index, spatial correlation length, fractal dimension and *b*-value to predict significant failures at a deep copper mine in China. The results showed that the seismic parameters responded differently prior to large failures and multi-parameter analysis can improve the reliability of forecasting. Lu *et al* (2015) evaluated daily maximum energy and seismic event number, fault total area, *b*-value, Z value, dominant frequency

and associated energy ratio to investigate the precursors to rock burst at a longwall mine. Abnormal clustering of seismic events and increasing of high-energy events close to the longwall face were regarded as a precursor to rock burst.

In this research, the space-time characteristics of seismicity near a major dyke in an underground longwall coalmine are investigated to understand the failure mechanisms related to this intrusive structure. The results demonstrated that the dyke promoted seismicity and stress re-distribution during the mining period. The rock mass behaviour at the inbye and outbye sides of the dyke are different and the microseismic signatures are presented.

PROJECT BACKGROUND

The monitoring project was carried out at an underground coalmine in 2017 and the targeted longwall panel has a width and length of 400 m and 3000 m, respectively. A section of the roadway of this panel is intersected by a stiff dyke of which the thickness ranged from 0.5 m to 3 m. The dyke has an approximate dipping angle of 75°–80° towards the North. During roadway development, a number of pressure bumps occurred near the dyke. The dyke-roadway intersected area was regarded by the mine as a coal burst prone area (Figure 1). The terms 'inbye' and 'outbye' refer to the two sides of the dyke towards the North and South, respectively.
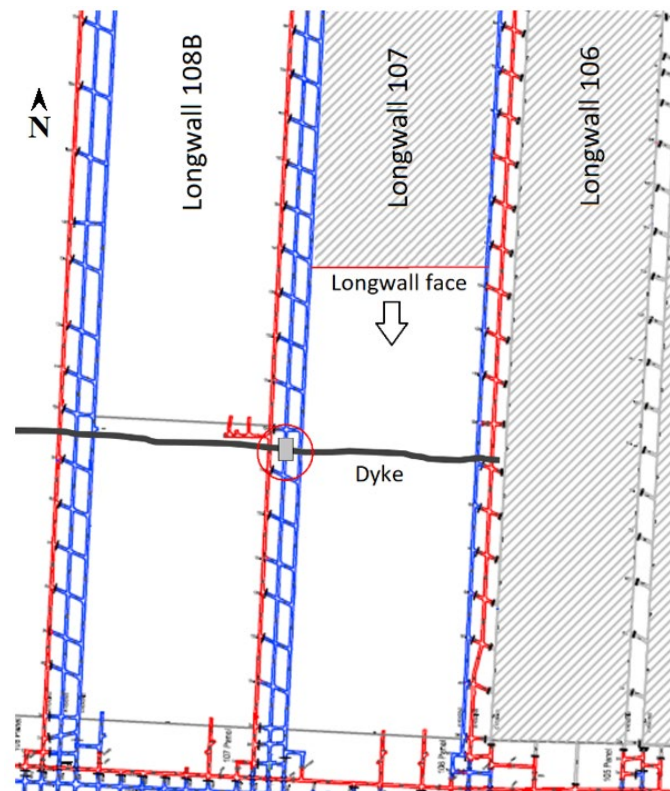
FIG 1 – Planview of the monitored longwall panel. The grey rectangle indicates where the monitoring network was installed. The coal burst prone area is indicated by the red circle.

To assess the seismic risks in the vicinity of the dyke, a seismic monitoring network consisting of four triaxial geophones is installed. At both inbye and outbye sides of the dyke, one horizontal geophone is placed 5 m into the rib first. The distance between this geophone and the dyke is 10 m. Then a second geophone is located with another 10 m away from the first geophone and is installed 10 m into the roof. All geophones are cemented to ensure good coupling. The seismic data logger is positioned on the ground surface and the geophone cables are deployed to the geophones via a deep borehole. The detailed geophone locations respect to the dyke are shown in Figure 2.
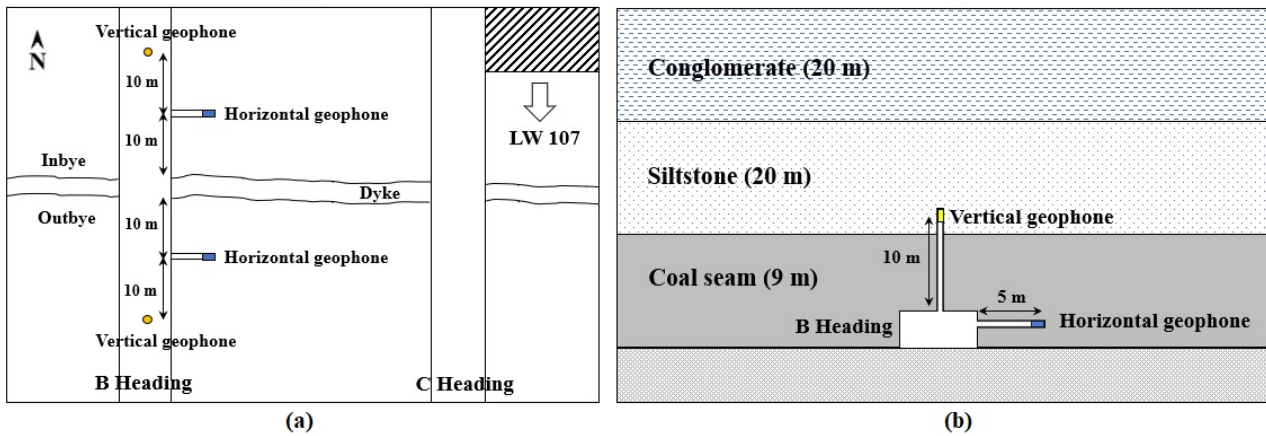
FIG 2 – Geophones locations with respect to the dyke in (a) plan-view, (b) cross-section (modified from Shen *et al,* 2020).

SEISMIC CHARACTERISTICS

The seismic data recorded from 26 November 2017 to 23 March 2018 is processed. Two major groups of seismic events are recorded during this project (Duan *et al,* 2021a). The first group is located around the longwall face. The second group is distributed close to the dyke. The seismic events near the dyke are analysed to characterise the seismicity near the dyke.

Seismicity

The daily and cumulative seismicity around the dyke is shown in Figure 3. In general, four stages are defined. Distinguishable seismic activities are observed during different mining stages. The rock fractures initiated around the dyke during the first stage. The longwall mined about 350 m during this period. The seismicity began to intensify when the longwall face was 100 m ahead of the dyke. During the second stage, the longwall started to mine the vicinity of the dyke and the seismicity reached 1000 events per day. The longwall mined through the dyke in the third stage and the seismicity was intensified after the longwall production was restored after one week of maintenance. In the final stage, the seismicity significantly decreased after the longwall passed the dyke 50 m. No geophones were damaged during the monitoring period. The locations of the longwall face associated with these four stages are shown in Figure 4.
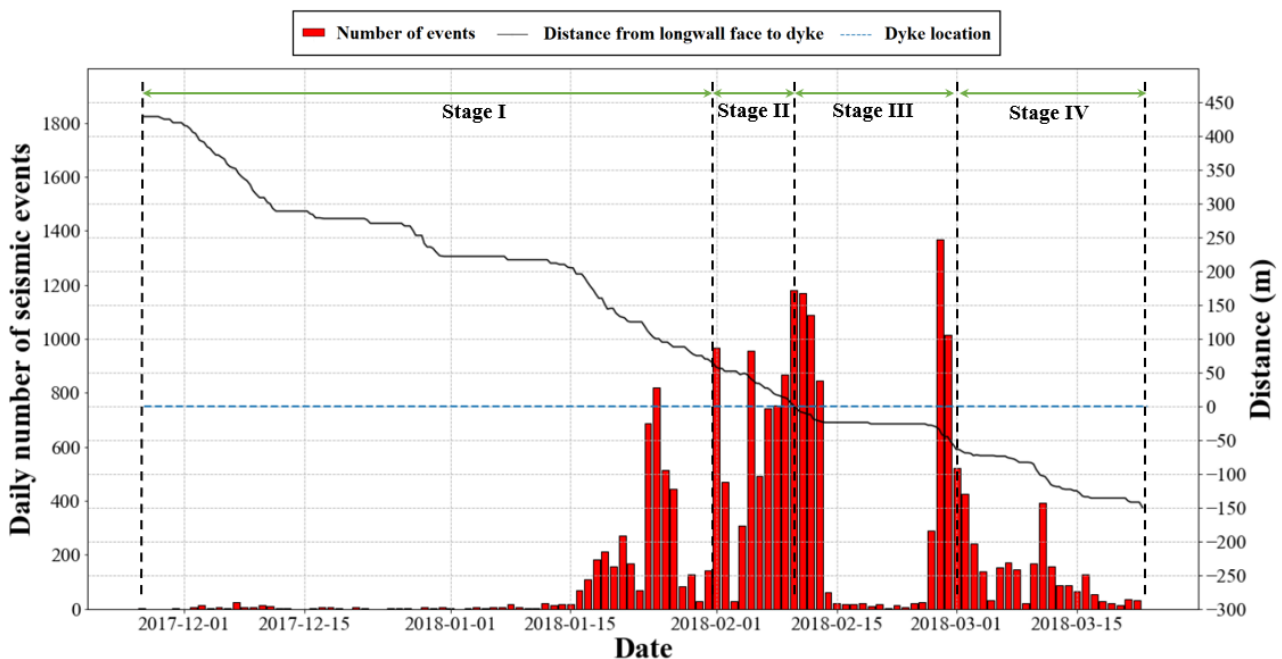
FIG 3 – Daily number of seismic events occurred near the dyke and the changes in the distance between the longwall face and dyke.
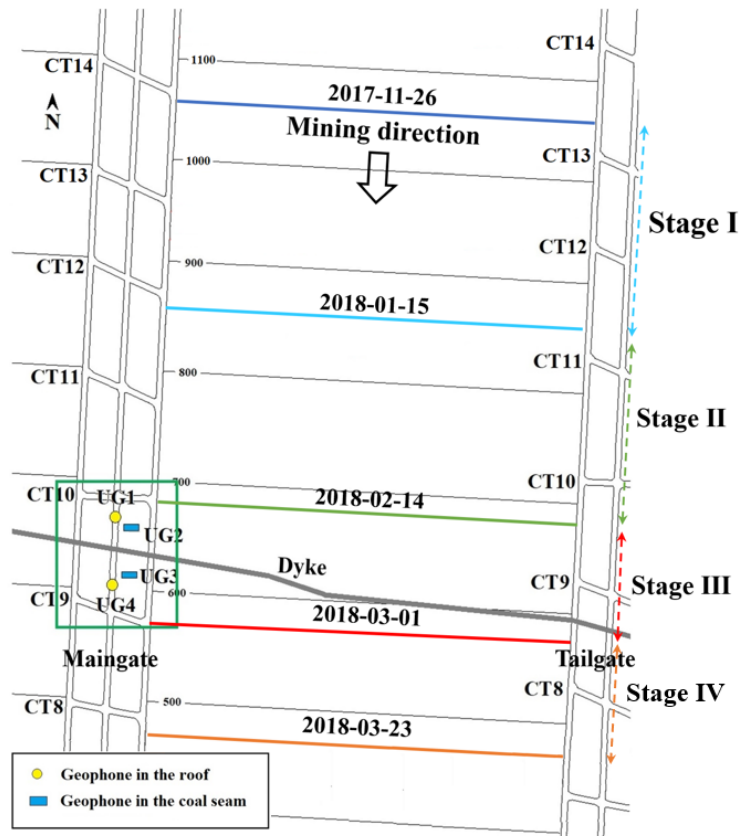
FIG 4 – The longwall mining progress related to four seismic stages. The locations of longwall face of Stage I to IV are indicated by lines in blue, green, red and orange, respectively.

Event locations

A total number of 4047 seismic events are located (Duan *et al*, 2021b). The evolution of the rock fractures near the dyke is shown in Figure 5. During the first two stages, the seismic events are mainly distributed at the inbye side of the dyke. In cross-section, they are in the immediate roof and conglomerate layer. As the longwall mined to the outbye side of the dyke in the third stage, the fractures propagated to the outbye side. However, seismic events are mainly in the coal seam and immediate roof, indicating more stress transfer to the outbye of the dyke. The fractures are clustered in the coal pillars, which suggests that the stress is more concentrated and re-distributed in the more confined rock mass. Additionally, more fractures are located between heading B and C, which should be related to the abutment stress induced by the longwall excavation.

(a)
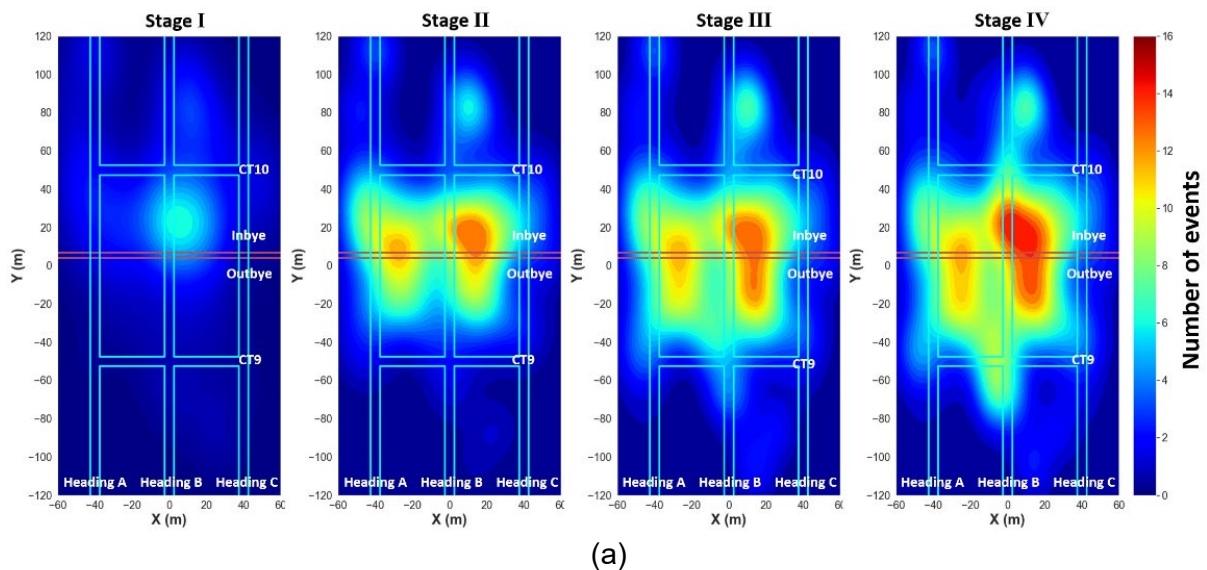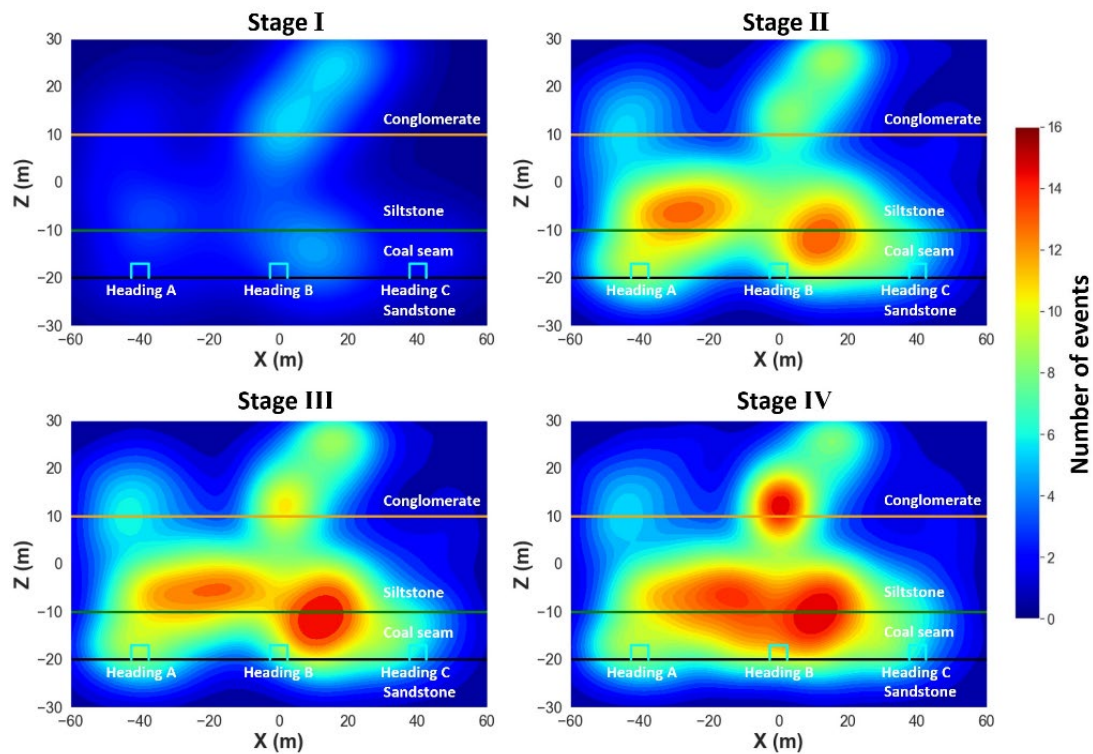
(b)
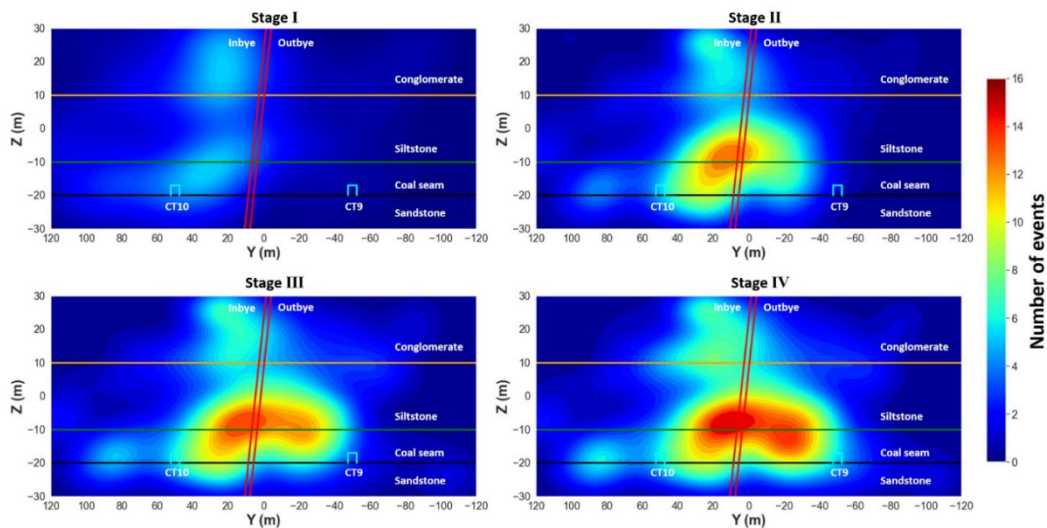
(c)

FIG 5 – The distribution of seismic events near the dyke. (a) plan-view; (b) cross-section, looking towards the north; (c) cross-section, looking towards the east. The inbye and outbye refers to the north and south of the dyke, respectively.

Frequency-magnitude distributions

The cumulative number and magnitudes of the seismic events near the dyke follows a log-linear relationship. As the inbye side of the dyke is subjected to more stress concentration and rock fractures, the correlation between the *b*-value (Gutenberg and Richter, 1956) and the vertical stress at the inbye side of the dyke is further explored to investigate if any seismic anomaly can be identified. The seismic events located at the inbye side of the dyke are selected. As suggested by Nava *et al,* (2017), to reduce the bias with the *b*-value estimation, a time window of 500 seismic events and a rolling window of 200 events are applied to calculate the *b*-values. The temporal changes of *b*-value (Figure 6) shows that the *b*-value gradually decreased when the longwall was mining towards to the dyke, indicating more frequent occurrence of significant seismic events and intensive seismic energy release. When the longwall was mining through the dyke, the b-value

remained stable. After the longwall mined past the dyke, more fractures propagated to the outbye side of the dyke. The energy of seismic events occurred at the inbye side of the dyke decreases, leading to gradual increasing of the *b*-value. No clear correlation between the *b*-value and the vertical stress is identified. It indicates that variation analysis of the *b*-value can provide more sensitive information for seismic risk assessment.
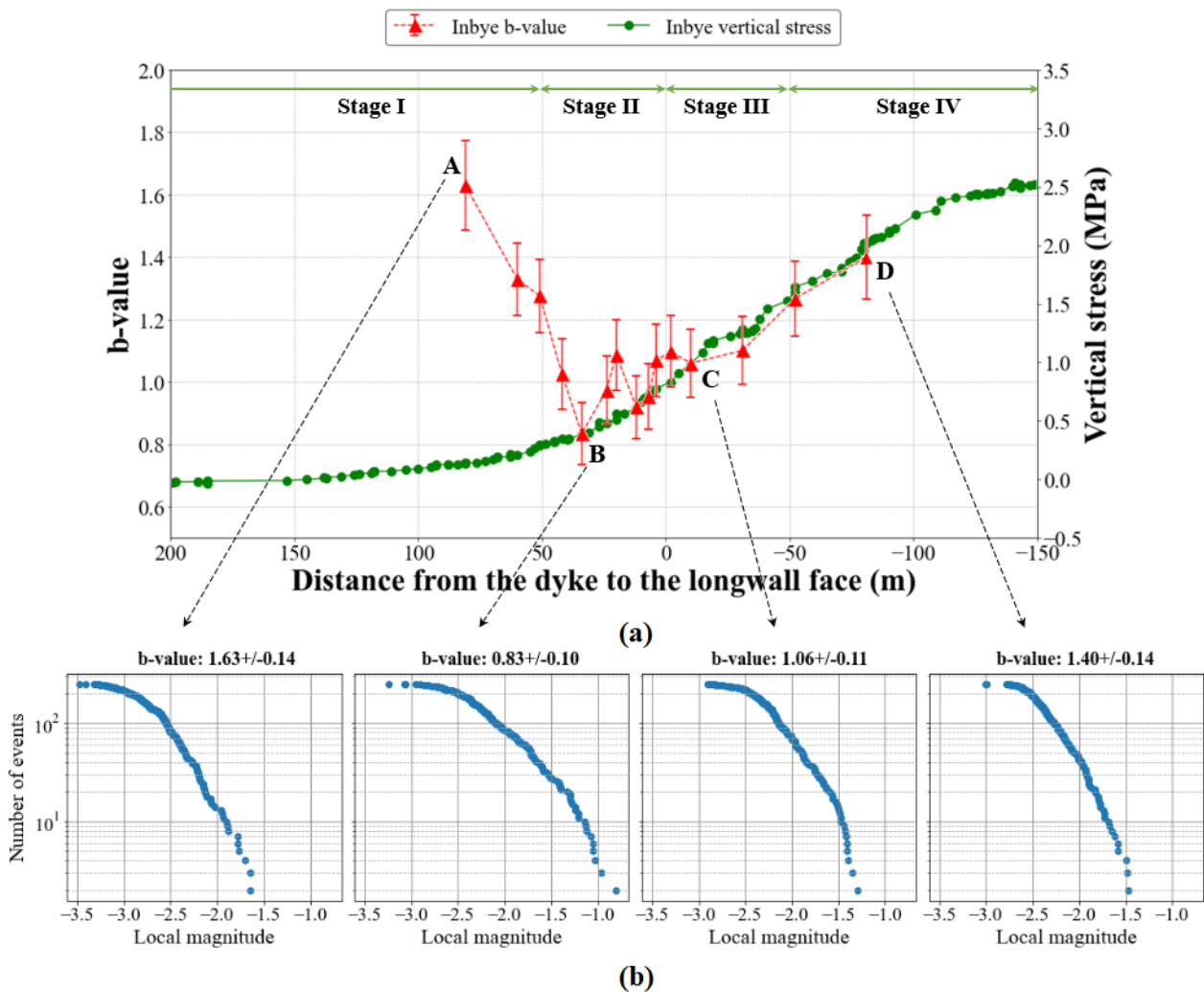
FIG 6 – (a) Variations of *b*-value and vertical stress at the inbye side of the dyke; (b) Frequency-magnitude distributions in four specific time windows for estimating the *b*-values in four stages.

CONCLUSIONS

The time-space variations of seismic characteristics near a major dyke at an underground longwall coalmine are presented in this research. The results demonstrate that the dyke intensifies the seismicity in the roadway section, inducing more seismic risks to mine personnel and facilities. The rock mass at the inbye and outbye sides of the dyke responds differently to the longwall mining. More fractures are located at the inbye side of the dyke before the longwall mined through the dyke, whereas the fractures propagated to the outbye side of the dyke after the longwall mined past the dyke. The temporal changes of *b*-value at the inbye side of the dyke were estimated using empirical parameters. The variations of *b*-value indicate more frequent and intensive seismic energy release when the longwall was mining towards the dyke. The sensitivity of the results subjected to the selected parameters can be further investigated to explore how to optimise the event sampling and provide more reliable indication prior to significant seismic energy release.

ACKNOWLEDGEMENTS

gratefully acknowledged. Sincere thanks to Binzhong Zhou and Jane Hodgkinson for their valuable comments and suggestions.

REFERENCES

van Aswegen, G, 2013. Forensic rock mechanics, Ortlepp shears and other mining induced structures, in A Malovichko and D Malovichko (eds), *8th International Symposium on Rockbursts and Seismicity in Mines*, Saint-Petersburg, pp. 1–19.

van Aswegen, G and Meijer, O, 1994. The mechanisms of seismic events around faults in mines, *Rock Mechanics in Petroleum Engineering*, (August 1994), pp 605–613. doi: 10.2118/28103-MS.

Duan, Y, Shen, Y, Canbulat, I, Luo, X and Si, G, 2021a. Classification of clustered microseismic events in a coal mine using machine learning, *Journal of Rock Mechanics and Geotechnical Engineering*, p 12. doi: 10.1016/j.jrmge.2021.09.002.

Duan, Y, Luo, X, Si, G and Canbulat, I, 2021b. Seismic source location using the shortest path method based on boundary discretisation scheme for microseismic monitoring in underground mines, *International Journal of Rock Mechanics and Mining Sciences*, 149(May 2021):104982. doi: 10.1016/j.ijrmms.2021.104982.

Gutenberg, B and Richter, C F, 1956. Magnitude and energy of earthquakes, *Annals of Geophysics*, 9(1):7–12. doi: 10.4401/ag-5590.

Joughin, W, 1966. *The measurement and analysis of earth motion resulting from underground rock failure,* University of Witwatersrand, Johannesburg, South Africa.

Kijko, A and Funk, C W, 1996. Space-time interaction amongst clusters of mining induced seismicity, *Pure and Applied Geophysics*, 147(2):277–288. doi: 10.1007/bf00877483.

Liu, J P, Feng, X, Li, Y, Xu, S and Sheng, Y, 2013. Studies on temporal and spatial variation of microseismic activities in a deep metal mine, *International Journal of Rock Mechanics and Mining Sciences*, 60:171–179. doi: 10.1016/j.ijrmms.2012.12.022.

Lu, C P, Liu, G, Liu, Y, Zhang, N, Xue, J and Zhang, L, 2015. Microseismic multi-parameter characteristics of rockburst hazard induced by hard roof fall and high stress concentration, *International Journal of Rock Mechanics and Mining Sciences*, 76:18–32. doi: 10.1016/j.ijrmms.2015.02.005.

Nava, F A, Márquez-Ramírez, V H, Zúñiga, F R, Ávila-Barrientos, L and Quinteros, C B, 2017. Gutenberg-Richter b-value maximum likelihood estimation and sample size, *Journal of Seismology*, 21(1):127–135. doi: 10.1007/s10950–016–9589–1.

Shen, B, Duan, Y, Luo, X, van de Werken, M, Dlamini, B, Chen, L, Vardar, O and Canbulat, I, 2020. Monitoring stress state near major geological structures in an underground coal mine for coal burst assessment, *International Journal of Rock Mechanics and Mining Sciences*, 129:104294, doi: 10.1016/j.ijrmms.2020.104294.

Urbancic, T I, Trifu, C I, Long, J M and Young, R P, 1992. Space-time correlations of b values with stress release, *Pure and Applied Geophysics*, 139(3–4):449–462. doi: 10.1007/BF00879946.

3D limit equilibrium and finite element model development for coalmine slopes

G Guy[1] and J Summerville[2]

1. Principal Geotechnical Engineer, Encompass Mining, Brisbane Qld 4000.
   Email: glen.guy@encompassmining.com
2. Principal Geotechnical Engineer, BHP, Brisbane Qld 4000.
   Email: Jayson.summerville2@bhp.com

ABSTRACT

Over the past five years in coalmine slope evaluation the application of 3D modelling has increased significantly as software has become more user friendly but also areas requiring evaluation have become increasingly complex. Often simplistic 2D Limit Equilibrium modelling and analysis has been poorly used to solve slope stability issues by back analysis and subsequent forward predictive analysis. A plane strain condition with slope movement perpendicular to the slope strike is assumed where in reality the problem is more complex. This often leads to a misinterpretation of the failure mechanism because the failure mechanism being modelled in 2D does not generally represent the actual failure mechanism observed in the pit, with 2D modelling often oversimplifying a slope.

This paper presents a case study where the initial slope assessment and remedial design evaluation was undertaken as a 2D Limit Equilibrium model which led to an overly conservative and costly remedial solution being implemented. Subsequent modelling of the slope using both 3D Limit Equilibrium and Finite Element methods were able to provide a better understanding of the structural complexities associated and correlate well with slope monitoring data to create a more realistic outcome.

INTRODUCTION

Traditionally geotechnical design assessments for both excavated and dumped slopes in open cut coal mining have been undertaken using simple 2D limit equilibrium (LE) models, that assume a basic hydrogeological assumption and generic shear strength properties. This was satisfactory in simplistic strip mining of the past where excavation depths were limited and continuity in geotechnical conditions could be assumed outside of a 2D section line.

As open cut coal mining has progressed deeper and conditions have become more complex due to increasing stress, geological structure, and consequently the groundwater regime this 2D LE approach has shown to be limited often leading oversimplification of a slope model or the manipulation of conditional assumptions to meet an expected outcome. These assumptions made can often lead to misrepresenting a potential failure mechanism and over engineering a solution to mitigate instability concerns that may not be justified, or conversely, missing a potential failure mechanism that exists outside a predetermined 2D plane.

Over the past five years in open cut coal mining slope evaluation, the application of 3D modelling has increased significantly as software has become more user friendly but also areas requiring evaluation have become increasingly complex. Often simplistic 2D LE modelling and analysis has been poorly used to solve slope stability issues by back analysis and then subsequently applied these conditions forward predictive analysis where a plane strain condition, with slope movement perpendicular to the slope strike is assumed, where in reality the problem is more complex.

This paper presents two recent case studies where the initial slope assessment was undertaken as a 2D LE model which led to either an overly conservative and costly remedial solution being implemented or underestimation of the potential slope failure. Subsequent modelling of the slope using both 3D LE and Finite Element (FE) methods were able to provide a better understanding of the structural complexities associated and correlate well with slope monitoring data to create a more realistic outcome.

CASE STUDY A – *IN SITU* ENDWALL BUTTRESS

Case study A is located in coal bearing sediments of Queensland's Bowen Basin where one to two economic coal seams are targeted using a combination of dragline and excavator overburden removal mining methods. Dragline mining typically targets long strikes or strips of gentle to moderately dipping coal seams with mining advancing down dip, an active dragline and truck waste dump is formed up dip and an advancing in situ highwall down dip. Often strips are confined by faulting which will be part of an *in situ* endwall, these walls are often only exposed for a limited period of time before the advancing dump covers them as waste is returned in-pit.

Case study A involves an endwall that was adjacent to a major infrastructure corridor that was also bounded by known and interpolated faulting. As part of routine inspections potential instability triggers were noted including cracking and displacement of the rock mass and a change in groundwater conditions. An initial assessment of the slope stability was undertaken using 2D LE modelling with a representative section cut through the assumed affected area and the underlying geological structure. Rock mass shear strength and groundwater conditions were manipulated until failure conditions (Factor of Safety less than 1.0) were obtained. Assumptions were made around the strength and continuity of a bedding parallel shear, groundwater levels, fault location and shear strength with the rock mass assessed as an isotropic medium with generic strengths. Based on these results remedial measures in the form of a significant waste rock buttress was installed at the completion of each strip to mitigate any potential mass movement.

The assumed 2D back analysis conditions that were derived were then utilised to undertake further 2D LE and FE forward analysis for the end wall further down the strip to replicate the same conditions. Representative sections were developed perpendicular to the slope and analysis run however the identified failure mechanism in the initial slope could not be adequately replicated and assessed in 2D (see Figure 1). This was concluded largely due to the cross dip of the bedding allowing a block to fail subperpendicular, the interplay of intersecting faults and confinement of the installed buttress.
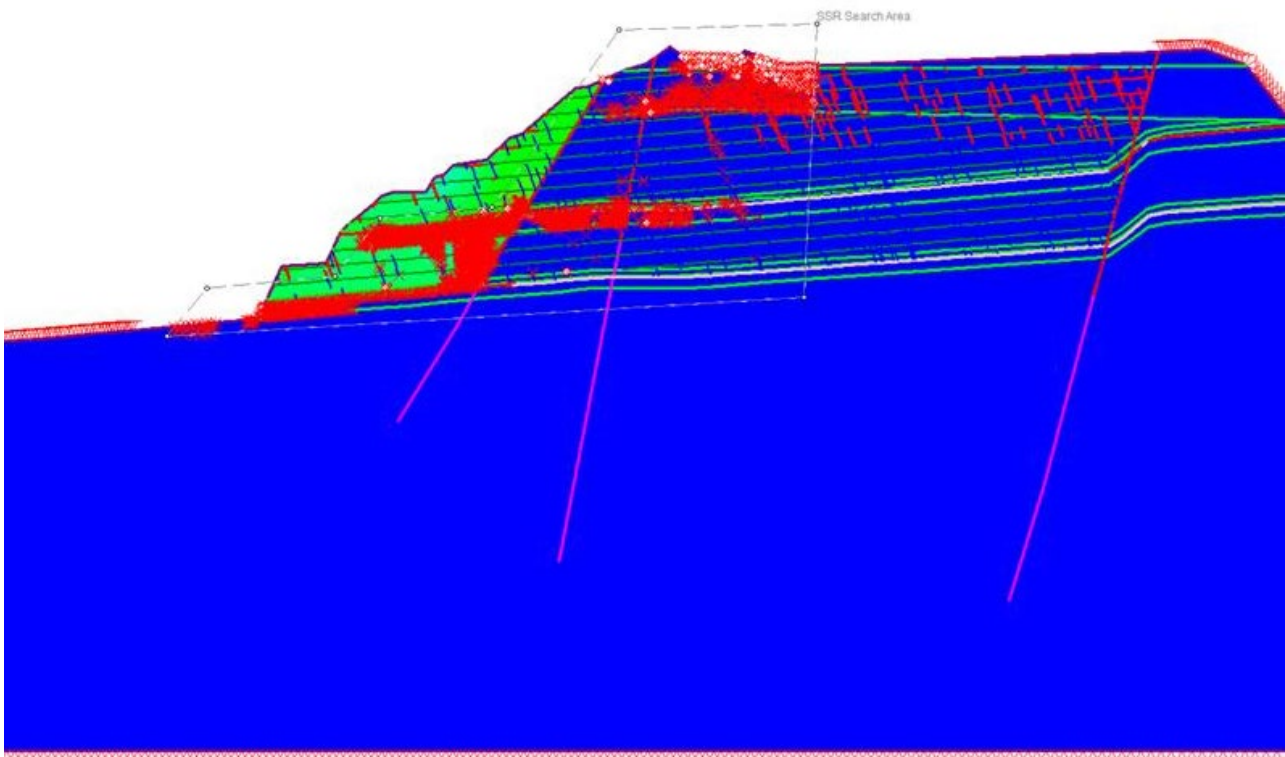
FIG 1 – 2D FE output for endwall stability assessment.

The initial 2D analysis had also made several assumptions on the slope model conditions during the slope assessment to replicate the potential failure conditions. These conditions were then assumed to be ubiquitous within the geological environment. The conditions assumed included a prevalent

weak layer or elevated piezometric level within the rock mass but should require validation through drill hole and geophysics analysis or the installation and monitoring of piezometers.

Following further data collection to validate the initial slope failure assumptions slope models were developed using the proposed slope design, the geological structure wireframes for coal surfaces and major faulting in both 3D LE and FE analytical software.

Analytical iterations were run initially in 3D LE to validate the slope model before 3D FE to determine the magnitude and location of potential slope deformation. Modelling indicated that:

- Ubiquitous low strength bedding parallel surfaces throughout an in situ wall are unlikely to be present. Weak layers may be present and reduce in strength due to unloading near the excavated face.

- Groundwater affects are localised due to features such as faulting and bedding dip.

- Rock mass strength is anisotropic with the orientation of defects playing a major part in stability.

- Intact rock shear strength will vary depending on the stress it has been placed under, this is shown to be different in a 3D analysis compared to a cross-sectional assessment.
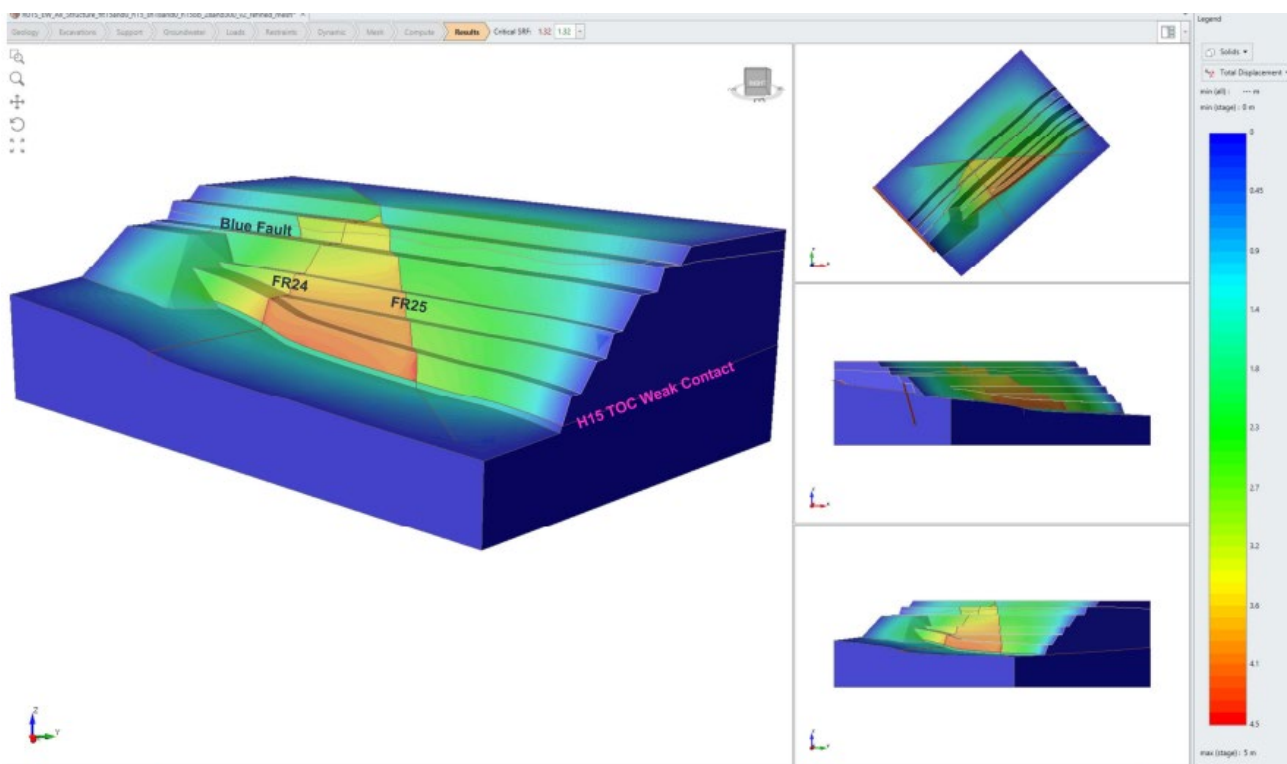
FIG 2 – 3D LEM output for endwall assessment.

On completion of the 3D analysis, slope mitigation measures—in the form of an earth buttress— were then reassessed and were able to be reduced, and eventually phased out as the conditions originally assumed were shown to not be as prevalent or exist within the slope.

CASE STUDY B – IN SITU HIGHWALL STRUCTURAL FAILURE

Case study B is situated in the multi-seam Permian aged sediments of the Sydney basin in an open cut truck and shovel mining environment. In situ excavated walls are often exposed for extended periods until covered by an in-pit waste rock dump following the extraction of coal.

The highwall in question was initially modelled using 2D LE as part of the life-of-mine (LOM) pit design assessment. A single representative cross-section was cut through the slope design and the underlying geological model, including a cross-cutting fault trace, for analysis. This comprised the strata bedding and major rock mass structure such as faulting and intrusions with the apparent dips being represented in the sectional geotechnical model. The section cut through an area was

intersected by a main fault and locally affected bedding orientation where it dipped locally out of the slope. Isotropic material strengths, with no allowance for defects or rock mass degradation, were applied to the geotechnical domains identified.

Analysis was run using a Cuckoo search methodology to determine the factor of safety of the slope with results indicating a stable slope with a preferred failure envelop incorporating a multi-bench failure scenario.

As the slope was further developed when deeper seems were extracted and interburden removed with blasting and excavation precursors to instability were noted during routine inspection. After further evaluation by sectional analysis mitigation measures in the form of separation and bunding applied. The slope ultimately collapsed with a failed volume larger than that expected and allowed for (see Figure 3) as well as a mechanism that wasn't anticipated from slope modelling.

FIG 3 – Highwall rock mass failure.

As part of the slope failure investigation a back analysis of the slope was undertaken using 3D LE and FE modelling software to fully capture the role of the geological structure such as bedding variation and faulting orientation in the failure. It was also found that rock mass jointing fabric and localised variation in saturation may have also played a role in the wall collapse and weren't able to accurately account for in cross-section.

Modelling in 3D LE was able to replicate the location and extent of the rock mass failure that had occurred and show that the failure was intensely related to three dimensional effects such as structural orientation for both rock mass jointing and faulting, local variations in bedding dip and changes in rock mass condition from blasting.

The discrete 2D plane that was modelled to initially assess the slope would have not been able to truly represent these conditions without applying unreasonable assumptions to the model to simulate failure conditions.

DISCUSSION

The stability of a rock slope is always an interaction between the excavated design profile and the underlying geology and structure. This relates to both the shape of the excavation with regard to the orientation of excavated wall, the dip of slopes on an individual or overall slope basis and the interplay with the orientation of faults, strength anisotropy in the rock mass and spatial distribution of

weaker zones. Complexities such as groundwater regimes, particularly around faulted ground or associated with other aquifers or aquicludes can also play a big part in slope stability.

2D analysis will infer plain strain conditions where any out of the plain effects such as strain or confinement can't be considered in analysis. The slope stability interaction of excavation and geology is also directional and therefore best represented in 3D rather than an apparent or estimated parameter produced in a 2D model. 2D cross-sections developed can often be bias due to the modellers best estimate of slope failure direction, this is often perpendicular to the slope face but may not always be the case.

Although 2D has been reliable when coalmine development was in a simplistic geotechnical environment, namely the continuity of conditions away from the sectional plane, as conditions have become more complex within the underlying geotechnical model 2D analysis has been difficult to represent actual conditions without compromising assumptions. It should be recognised that all geology, structural, and groundwater models are created in 3D, often with interpolators far coarser than a 3D analysis. All good mine planning is undertaken in a variety of 3D packages and based on an excepted geological model, geotechnical engineers will collect data in 3D, such as defect and groundwater data, however slope analysis is often reduced to a simplified 2D plane often with generic strengths and groundwater assumptions.

As coal mining moves away from a simplistic strip mining environment to a more geotechnical complex environment that can be modelled and designed in 3D it makes sense to be able to represent that in a slope stability assessment model.

ACKNOWLEDGEMENTS

Some considerations on rock slope stability issues in Afghanistan with an emphasis on Kandahar Region

A B Jahed[1], T Ito[2] and Ö Aydan[3]

1. University of the Ryukyus, Okinawa 903-0213, Japan. Email: bari.jahed@gmail.com; k218654@cs.u-ryukyu.ac.jp
2. University of the Ryukyus, Okinawa 903-0213, Japan. Email: takito@tec.u-ryukyu.ac.jp
3. University of the Ryukyus, Okinawa 903-0213, Japan. Email: aydan@tec.u-ryukyu.ac.jp

ABSTRACT

In this study, the authors compiled some case history data and present some typical examples of rock slope stability issues in Afghanistan with a special emphasis on Kandahar region and categorise rock slope failures according to the principles of modern rock slope engineering. The slopes considered involve rock-cut, natural rock slopes mainly. The effect of structural geology and discontinuous nature of rock mass on both slope-cuts and natural rock slopes is taken into account and some preliminary assessments on the stable and unstable rock slopes are presented. Furthermore, the seismic effect on their stability is also considered. It is also pointed out that similar issues could be observed in open pit mines, which may be exploited in years to come.

INTRODUCTION

Afghanistan is a land-lock country and the northern part of Afghanistan is highly mountainous and Hindu-Kush mountains shape her landscape (Figure 1a). The region along the Chaman fault constitutes a plate boundary between Indo-Australian plate and Euro-Asian plate, which is tectonically deformed so that folded sedimentary formations as well as basaltic intrusions and dykes are abundant within this tectonic boundary (Figure 1b). The southern part of Afghanistan is known as Chagai Arc and it is also highly deformed due to the subduction of Arabian plate beneath Euroasian plate along the Makran zone. The west side of Afghanistan is also highly deformed by dextral strike-slip faulting along Sistan Suture Zone. The region bounded by these tectonic features is named as Helmand Block. Kandahar is located at the north-east corner of Helmand block and it is about 100 km away from the Chaman Fault.

(a)   (b)
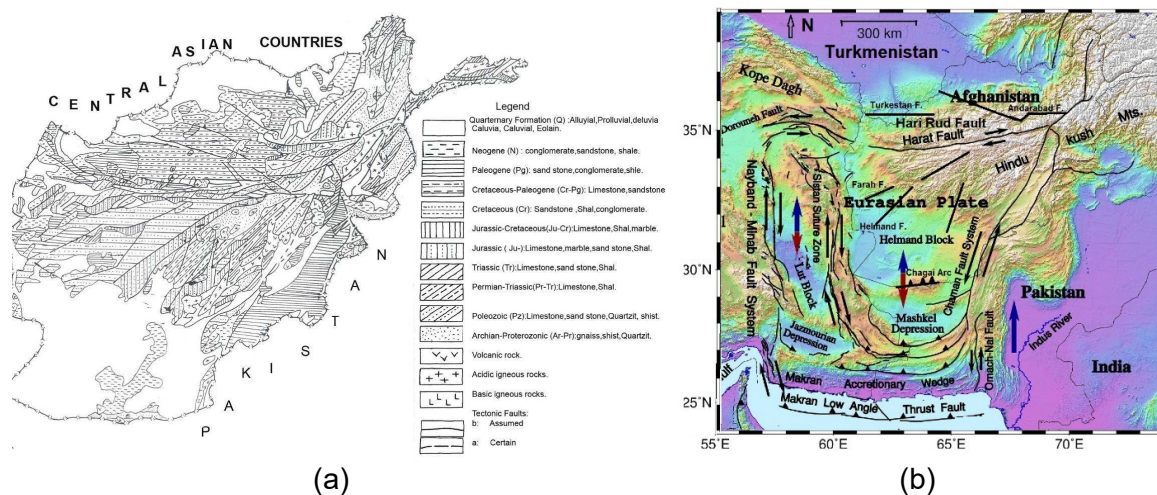
FIG 1 – (a) Simplified Geology of Afghanistan and (b) Tectonics of Afghanistan and neighbouring countries (modified from Nemati, 2018).

The large-scale rock slope stability issues are common in Afghanistan and there are also very large deep-seated slope failures and such an event recently occurred in Badakshan Province in 2014. However, there is almost no study on rock slope stability issues in Afghanistan. One of reasons could be the internal instability and invasions of Afghanistan by the former Soviets Union and the United States of America, which hindered both academic studies and the education of scientists and

engineers of Afghanistan. Therefore, this study undertaken by the authors could be one of the pioneering studies for Afghanistan.

The authors compiled some case history data on rock slope failures in Afghanistan with an emphasis on Kandahar Region. The rock slope failures can be broadly categorised as planar/wedge sliding, flexural/columnar toppling and deep-seated circular failures in view of modern rock slope engineering. In addition, huge boulders exist on slopes and they may topple and fall over the transportation routes as well as settlement areas. In addition, open pit mines to be exploited in years to come may also have the rock slope stability issues. The slopes of reservoirs of existing dams and those to be built in future would present similar issues. Besides gravitational and climatic effects, the seismic effects must be also considered when rock slope stability is assessed as Afghanistan is a seismically active country.

In this study, the authors present some typical examples of rock slope stability issues in Afghanistan with an emphasis on Kandahar Region and categorise rock slope failures according to the principles of modern rock slope engineering. The effect of structural geology and discontinuous nature of rock mass on both slope-cuts and natural rock slopes are taken into account and some preliminary assessments on the stable and unstable rock slopes are presented. Furthermore, the seismic effect on their stability is also discussed.

GEOLOGY, SEISMO-TECTONICS AND SEISMICITY

Afghanistan is underlain by Precambrian metamorphic rocks, which form high regions in the centre of the country and in the Hindu Kush (Figure 1a). The Central Afghanistan between Herat and Panjab is the northernmost structural high, encompassing metamorphic rocks. The part is connected to the Hindu Kush by Precambrian rocks in Koh-i-Baba. Precambrian rocks outcrop locally west of Jalalabad, close to Kabul and Khost, and are likely present in the Safed Koh Range. The Precambrian rocks of Afghanistan include phyllite, greenschist, garnet-mica schist and partially melted gneiss that experienced anataxis. Highly folded sedimentary formations are seen along tectonic boundaries and the South Turkestan suture zone in the northern part of Afghanistan.

Kandahar region constitute the south-east part of Afghanistan and its geology consists of sedimentary rocks such as conglomerate, sandstone and limestone and igneous rocks. The igneous rocks are mainly of extrusive type and consists of basalt. However ultramafic intrusions consisting of dunite, peridotite and serpentinite are also observed. The strike of folded layers, extrusive and intrusive intrusions is NE-SW.

Afghanistan is in Eurasian orogenic belt and one of the seismically active belts in the world. Modern fault movements, deformations, and earthquakes in Afghanistan are driven by the northward subduction of Indian and Arabian plates beneath Eurasia plate (Figure 1b). The subduction of Arabian plate along Makran subduction zone and the intrusion of Indian plate into Eurasian plate resulted in some major tectonic structures in the region. The Chaman Fault System is said to be accommodating 200 km relative slip and caused some earthquakes greater than 7. The most recent event was 1935 Quetta earthquake. The subduction Arabian plate beneath Eurasian plate causes a relative slip between the Lut block in Iran and the Helmand/Sistan block of Afghanistan, and it is called Sistan Suture zone. The seismo-tectonics of Kanadahar region is greatly affected by the relative slip along Chaman fault between Eurasian and Indo-Australian plate and this slip is probably the main cause of folding and intrusions in the region.

The active faults within Afghanistan can be divided into five fault systems; namely, Chaman, Hari-rud (Herat) and Central Badakhshan fault systems and Helmand internal fault system and South Turkestan fault system (Figure 1b). In the south-eastern Afghanistan and adjacent Pakistan, the Chaman fault system accommodates much of the differential movements between the Indian and Eurasian plates. The fault system has a reported slip rate of 2–20 mm/a and higher where it enters western Pakistan. The Indian plate has a 20–40 mm/a velocity where it comes close to a 300–400 km segment of Chaman fault between (31°N–33.5°N), suggesting that M>7.0 could occur at 200 years interval in this location. In central Afghanistan, the Hari Rud (Herat) fault having dextral sense extends from north of Kabul westward to Iran border with a slip rate of 2 mm/a, but evidence for active faulting remain controversial. In north-east Afghanistan, Badakshan and Dawraz-Karakul faults extends into in Pamir and Hindu Kush Mountains. Further north next to Turkmenistan and

Uzbekistan, there are some faults such as Turkestan fault zone and Andarabad fault. Hindukush region of Afghanistan is seismically very active (Malistan *et al,* 2016a, 2016b; Nasiry, 2020). The next seismically active regions are located along Chaman fault in east, Chagai Arc and Makran region in south and Sistan Suture Zone along Iran and Afghanistan Border in west. The north Afghanistan is also known to be very seismically active with earthquakes greater than M7.

SLOPE FAILURES AND SOME EXAMPLES FROM AFGHANISTAN

Slope failures

The slope failures induce tremendous damage to infrastructures as well as to residential areas, and they involve not only cut slopes but also natural rock slopes. Compared to the scale of soil slope failures, the scale and the impact of rock slope failures are very large and the form of failure differs depending upon the geological structures of rock masses of slopes (Aydan, 1989, 2007, 2017; Aydan *et al,* 1989, 2011, 2012). The slope stabilities may be categorised into three classes. The first category involves the failure of intact material under shearing, tensile or compressive stresses and the failure modes are shear or bending failure. The second category failures involve the failure of intact rock in shear or tension and slip or separation of discontinuities. The failure modes are combined shearing and sliding, buckling and flexural toppling failures. The third category is associated with the slip or separation of discontinuities and failure modes are planar or wedge sliding, toppling and/or block buckling failure. Furthermore, the failure of the rock slope failures may involve both active and passive modes under dynamic conditions such as earthquakes. However, the passive modes are generally observed when the ground shaking is quite large.

Examples of slope failures in Afghanistan

A survey of available digital images from various parts of Afghanistan with an emphasis on Kandahar region related to the issues of this study was implemented. The pictures are trimmed for the purpose of this study and re-arranged. Figures 2–7 show the failures according to the classifications given in previous subsection. As noted from Figures 2–7, the failures of rock slopes obey to those known in Rock Slope Engineering. They clearly indicate that the slope cuts must be evaluated according to the well-known principles and techniques developed and utilised in Rock Slope Engineering. The natural rock slopes are much more difficult as the information would be quite limited and it must be borne in mind that earthquakes and time-dependent weathering and degradation are another important parameters. Some guidelines would be presented for this purpose (Aydan, 2017, 2020).

FIG 2 – Some slope failures belonging to Category I involving shearing.
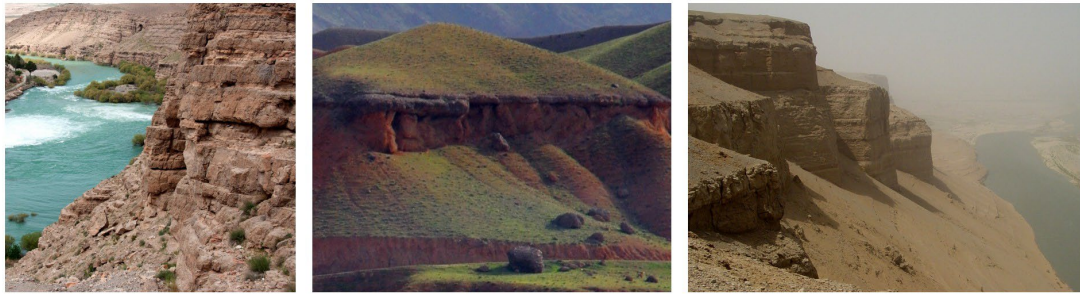
FIG 3 – Slope failures belonging to Category I involving bending as a result of differential weathering.

FIG 4 – Slope failures belonging to Category II involving combined shearing and sliding or flexural toppling.

FIG 5 – Slope failures belonging to Category III involving planar or wedge sliding.

FIG 6 – Slope failures belonging to Category III involving columnar toppling.

FIG 7 – Slope failures belonging to Category III involving rockfalls.

STRONG MOTION ESTIMATION FOR KANDAHAR

The strong motion estimation is done for some hypothetical earthquakes along Chaman fault with an emphasis on Kandahar Region. The Chaman Faults pass Kandahar City at a distance of 100 km. An earthquake along this fault occurred in 1935 with an estimated magnitude of 7.7–7.8. The fault parameters given in Table 1 were used to estimate ground motions at the epicentre and Kandahar City for a rocky ground. The estimated AMAX and VMAX are 77 gals and 26 kines. However, for soft ground these values would be 240 gals and 36 kines for soft ground as shown in Figure 8, which shows the AMAX and VMAX contours estimated to according to Aydan's method (Aydan, 2007, 2012). Although the estimation was based on an hypothetical earthquake on the Chaman fault, other possibilities such as the earthquakes on the faults in the close vicinity should be also taken into account.

TABLE 1

Characteristics of anticipated earthquake.

Length (km)	Mw	Slip (cm)	Duration (s)
168	7.7	600	40
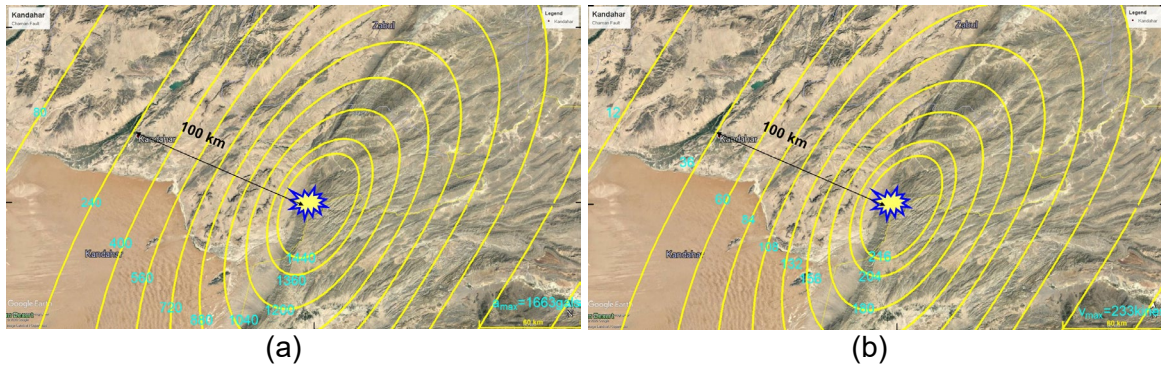
FIG 8 – Estimated (a) AMAX and (b) VMAX contours for M7.7 earthquake on Chaman fault.

GUIDELINES FOR ASSESSING THE STABILITY OF SLOPES

The stability assessment of rock slopes should consider by classifying slopes as soil slopes and rock slopes. Soil slopes can be generally analysed using limiting equilibrium methods based on circular sliding method with several variations. Although numerical analyses based on FEM or FDM may also be used, it is not common to do so. As said before, the scale of soil slope failures is small while the scale and the impact of rock slope failures are very large and the form of failure differs depending upon the geological structures of rock mass of slopes (Aydan, 1989; Aydan *et al*, 1989, 1991, 2011). Aydan (1989, 2017, 2020) and Aydan *et al* (1989, 1991) proposed an approach combining several methods based on the limiting equilibrium approach. This approach can be utilised for any slope of rock including soil slopes also. The readers are recommended to refer quoted references to determine the limiting stable slope angle under the given seismic, geometrical and physical conditions.

Figure 9 shows a plot of the slope angle of various rock slopes versus the inclination of the thoroughgoing discontinuity set, whose strike is parallel or nearly parallel to the axis of the slope. The plotted data include the data on stable and unstable natural rock slopes as well as man-made stable and man-made unstable rock slopes. Plotted data cover Afghanistan together an emphasis on Kandahar region. The plots for Kandahar region are distinguished. In the plots, the stability charts of a slope with a ratio of *t/H:1/75* for cross continuous and intermittent patterns (ξ=26.5°) for η=0.0 are also included to have a qualitative insight rather than a quantitative comparison. The chosen value of t/H is arbitrary and may not correspond to the ratios of slopes plotted in the figure. It is also interesting to note there is almost no failed slopes when the slope angle is less than 25–30° and most of the failed slopes have a slope angle greater than 25–30°. This is in accordance with the conclusion of Keefer (1984). Nevertheless, it is also noted that there are a great number of stable slopes having slope angle greater than 25–30°. This implies that the angle and the height of slopes cannot be only parameters determining the overall stability of natural rock slopes. Therefore, their geometrical orientations of discontinuities with respect to slope geometry and their mechanical properties and loading conditions must also play a great role in determining the stable angles of natural rock slopes. The results shown may serve as guidelines for a quick assessment of the stability of natural rock slopes and how to select the slope-cutting angle in actual constructions involving rock slopes.
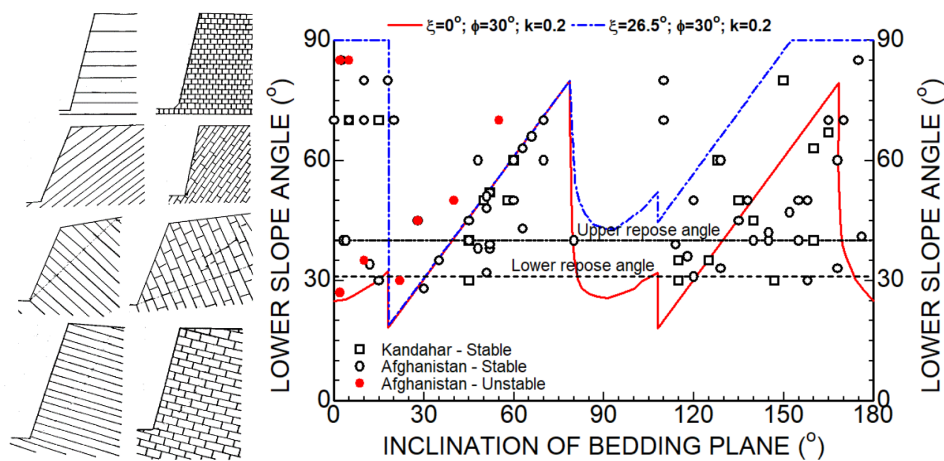
FIG 9 – The relation between slope angle and bedding plane angle for stable and failed case histories in Afghanistan.

For practical purpose to assess the stability of slopes, Keefer (1984) studied slope failures induced by earthquakes and he proposed some empirical bounds for slope failures, which are classified as disrupted or coherent. However, the empirical bounds of Keefer are not specifically given as formula. Aydan *et al* (2009, 2012) and Aydan (2007, 2017) also compiled slope failures caused by recent worldwide earthquakes according to Keefer's classifications and proposed an empirical equation for the maximum hypocentral distance of disrupted and coherent slope failures as a function of earthquake magnitude and fault orientation as shown in Figure 10. This approach can also be used for practical purposes to assess the stability of rock slopes subjected to earthquakes in the region.
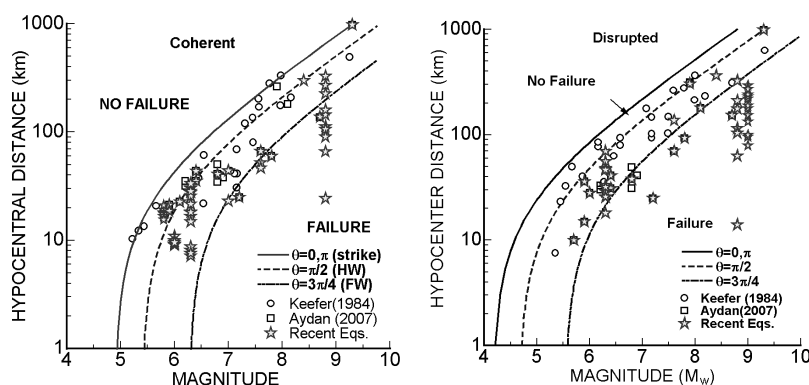
FIG 10 – Comparison of empirical relations with observations.

CONCLUSIONS

Some possible rock slope stability issues in Afghanistan with a special emphasis on Kandahar region have been considered in this study based on information gathered from available sources of documents and photos in the lights of principles of Rock Mechanics and Rock Engineering, Engineering Geology, and modern Rock Slope Engineering. It is clarified that the slope failures observed in Afghanistan are quite similar to those observed in other regions of the world. Therefore, when the slopes are to be cut in relation to new construction, the well-known principles of modern Rock Slope Engineering. Furthermore, the stability of natural rock slopes would be necessary and their stability condition must be evaluated by considering likely earthquake motions as well as rock mass conditions. There may be some rock slope stability issues during the construction of new transportation structures, existing and planned dams and open pit mines and the current static and seismic design of slopes can be adopted.

REFERENCES

Aydan, Ö, 1989. *The stabilization of rock engineering structures by rockbolts,* Doctorate Thesis, Nagoya University, 204 p.

Aydan, Ö, 2007. The inference of seismic and strong motion characteristics of earthquakes from faults with a particular emphasis on Turkish earthquakes, *The 6th National Earthquake Engineering Conference of Turkey*, Istanbul, pp 563–574.

Aydan, Ö, 2012. Ground motions and deformations associated with earthquake faulting and their effects on the safety of engineering structures, *Encyclopedia of Sustainability Science and Technology*, R Meyers (ed.), pp 3233–3253.

Aydan, Ö, 2017. *Rock Dynamics*, CRC Press, 462 p.

Aydan, Ö, 2020. *Rock Mechanics and Rock Engineering: Volume 2: Applications*. CRC Press, 383 p.

Aydan, Ö, Shimizu, Y and Ichikawa, Y, 1989. The Effective Failure Modes and Stability of Slopes in Rock Mass with Two Discontinuity Sets, *Rock Mechanics and Rock Engineering*, 22(3):163–188.

Aydan, Ö, Ichikawa, Y, Shimizu, Y and Murata, K, 1991. An integrated system for the stability of rock slopes, *The 5th Int Conf on Computer Methods and Advances in Geomechanics,* pp 469–465.

Aydan, Ö, Ohta, S and Hamada, M, 2009. Geotechnical evaluation of slope and ground failures during the 8 October 2005 Muzaffarabad Earthquake, Pakistan, *Journal of Seismology*, 13(3):399–413.

Aydan, Ö, Ohta, Y, Daido, M, Kumsar, H, Genis, M, Tokashiki, N, Ito, T and Amini, M, 2011. Chapter 15: Earthquakes as a rock dynamic problem and their effects on rock engineering structures, *Advances in Rock Dynamics and Applications*, Y Zhou and J Zhao (eds.), CRC Press, pp 341–422.

Aydan, Ö, Ulusay, R, Hamada, M and Beetham, D, 2012. Geotechnical aspects of the 2010 Darfield and 2011 Christchurch earthquakes of New Zealand and geotechnical damage to structures and lifelines, *Bulletin of Engineering Geology and Environment*, 71(4):637–662.

Keefer, D K, 1984. Slope failures caused by earthquakes, *Geological Society of American Bulletin*, 95:406–421

Nemati, M, 2018. Seismotectonic and seismicity of Makran, a bimodal subduction zone, SE Iran, *Journal of Asian Earth Sciences,* 169:139–161.

Multi-factor integrated data analytics and data-driven decision-making for ground control management

R Liang[1], C Huang[2], C Zhang[3], I Canbulat[4], L Munsamy[5], R Carstens[6] and L Prinsloo[7]

1. PhD student, School of Minerals and Energy Resources Engineering, The University of New South Wales, Sydney NSW 2032. Email: ruiyu.liang@unsw.edu.au
2. Postdoctoral fellow, School of Minerals and Energy Resources Engineering, The University of New South Wales, Sydney NSW 2032. Email: chaoran.huang@unsw.edu.au
3. Senior Lecturer, School of Minerals and Energy Resources Engineering, The University of New South Wales, Sydney NSW 2032. Email: chengguo.zhang@unsw.edu.au
4. Professor, School of Minerals and Energy Resources Engineering, The University of New South Wales, Sydney NSW 2032. Email: i.canbulat@unsw.edu.au
5. Head of Geotechnical, Anglo American, Brisbane Qld 4000.
   Email: lesley.munsamy@angloamerican.com
6. Principal Rock Engineer, Anglo American, Brisbane Qld 4000.
   Email: riaan.carstens@angloamerican.com
7. Chief Rock Engineer, Anglo American, Brisbane Qld 4000.
   Email: Lizelle.prinsloo@angloamerican.com

ABSTRACT

With recent advances in machine learning, data-based automated decision-making has been proven successful with promising outcomes in many industries. Its application in the mining sector can be ground-breaking; particularly the data-driven analytics that can support decision-making in the mine and consequently enhance mine safety, efficiency and sustainability. However, the current data science applications in the mining industry are mostly noncomprehensive, especially inadequate in evaluations, thus often requiring further study to be potentially beneficial to operations. Furthermore, it was found that existing literature paid limited attention to understanding the role of such techniques. Hence, in this paper we aim to build an end-to-end machine learning powered data-driven framework for intelligent geo-hazard analytics to support decision-making for underground mining data management, where multiple types of data are managed in an integrated database to support the unified machine-learning model. Here we present the framework as data-driven workflow processes, including data gathering, data preparation, data processing and data presentation. In addition, we present an application scenario of the proposed framework, where falls of ground (FoG) is managed with the historical FoG investigation reports, related panel hazard ratings, compliance data and rock mass characteristics. A demonstration can be dynamic forecasting of high-risk areas for FoG based on both spatial and temporal factors, including a 3D data visualisation. Such a scenario shows the potential of the proposed framework to establish connections among various data fields across a diverse category of data. Furthermore, the results offer important insights for ground instability management and can potentially optimise the underground operation flow.

INTRODUCTION

One of the most critical concerns in deep underground mining is the fall of ground (FoG) phenomenon (Kelly and Jager, 1996; Donnelly, 2018). A FoG is a failure caused by complex geological, geotechnical and mining factors. To reveal and regulate the geological hazard, several scholars have comprehensively researched the production data, hazard signs, and ground control plans in underground mining (Ma *et al*, 2020; Donnelly, 2018). However, extensive research is still needed to fully understand the mechanisms and causes of this complicated phenomenon (Ma *et al*, 2020). According to the review, previous work did not fully consider human factors and geological survey outcomes, while human factors are vital in data analytics. The feedback of the geological surveys reveal the potential mechanism of hazard occurrence. Therefore, this paper conducted the analytics with data from various monitoring in a case study mine, specifically referring to FoG investigation reports, regular compliance surveys of panels, and regular panel hazard rating reports. Finally, with the guidance of contributing factor coefficients and prediction outcomes, the model of FoG discrimination and prediction is completed.

DATA RESOURCES AND DATA STRUCTURE

Data resource

In this study, FoG is systematically analysed and integrated with compliance data and panel hazard rating reports. Firstly, the FoG report records basic information on the event's features, including physical design, support design, filtered FoG contributors, etc. The index count reaches around 396 columns. Then the compliance data, covers more than 70 indexes which reflect the status of safety and production concerning issues. It mainly focuses on checking whether the support and geological maintenance work are completed to standard. Besides surface condition, structure and rock mass classification (including GSI index) are recorded. The panel hazard rating data set contain four sections according to the mining workings it refers to: development, stopping, vamping, and ledging. According to the most frequently FoG occurrence, development and stoping data are the focus in this study. Of note is that there are also other data sets available, eg seismicity, which has not been fully used in this analysis.

Data structure and collection

Lack of data standardisation is the most general issue in mine digitalisation among all mine sites. To maximise data value in data analytics, we propose a data standard (an example is shown in Figure 1) and related data templates by considering the case study mine data status. Coordinates and timestamps are essential items required for further data fusion. Workplaces and reference numbers are required based on the mine data collection principles, which would contribute to refining coordinates matching.
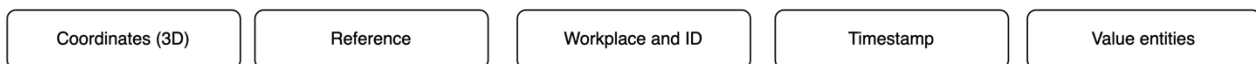
FIG 1 – Data structure for case study mine.

As each data set is from an individual procedure and managed by a separate department, one of the main data cleaning processes is to find out the internal connections among various data sets. Spatial-temporal analytics is the trend of big data analytics. In order to clean raw data into standard, preliminary data, mainly includes four steps: workplace unification, workplace-coordinate matching, timestamp extraction, and final data fusion, which are shown in Figure 2.
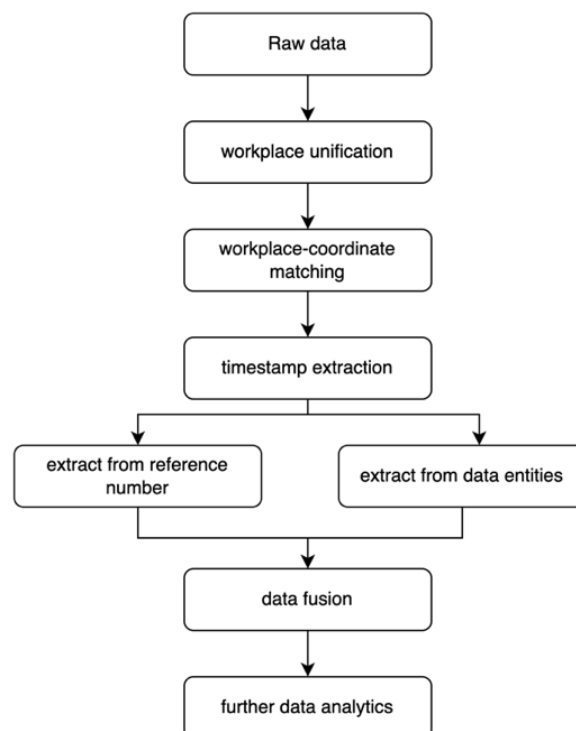
FIG 2 – Data cleaning workflow.

DATA ANALYTICS

There are various factors that contribute to a FoG event; this study started with the compliance and panel hazard rating data analytics. There are a wide range of indexes being covered, such as geological status, geological support, rock mass rating (GSI, RMR, or Q rating), and completion of safety concern workings etc. At the beginning of the data analytics, the key is identifying what index could contribute to discriminating a FoG event from compliance and panel hazard rating surveys. For example, the top ten contributing factors are listed in Table 1.

TABLE 1

Top ten contributing factors in each survey.

Num	FoG	PHR_Stopping	Compliance
1	Were any issues related to this incident captured prior to the accident in IRM.net? [FoGM-4]	MEASURING MONTH @ GSI (as per latest RED report)	Percentage of working places that complied
2	Contributing_Factor: Was additional support required? [Support]	PLANNING MONTH @ Prominent geological structure expected to be intersected? (fault, dyke, pothole, low angle joint)	Offset from Highway Line correct:
3	Any other features in the area? [Geology]	PLANNING MONTH @Any seismic event larger than MI 0.5 during the last three months within one panel length? (Check Seismic Quaterty Report)	GSI Value
4	To_Standard?: In stope tendons [Support]	MEASURING MONTH @ Siding depth	Barring adequate:
5	Was barring done properly? [FoGM-3]	PLANNING MONTH @ Structure orientation relevent to the mining face?	ABS-P declaration correct:
6	Were people able to hear any warning sounds? [FoGM-3]	MEASURING MONTH @ Face Shape correct?	Rock Mass Class
7	To_Standard?: Cable anchors [Support]	MEASURING MONTH @ What is the in-stope pillar cutting compliance?	Surface condition
8	Were the features appropriately treated/supported? [Geology]	MEASURING MONTH @ Strike dimension	Face safety net installed to standard (attachment…)
9	Did the team/individual diligently carry out every day routine responsibilities as required and perform to acceptable norms? [FoGM-3]	PLANNING MONTH @ Changing mining direction?	Risk Ranking
10	To_Standard?: Stope pillars [Support]	MEASURING MONTH @ Effect of Merensky pillar on IJG2	Siding support within standard:

OUTCOME OF MACHINE LEARNING MODEL

Based on the contributing factor analytics, a FoG prediction model was developed. Considering the panel hazard rating survey, k-NN and Support Vector Machine with Linear Kernel classifier are compared in this study (sampled within three months of hazard occurrence and same section). The result shows in Table 2.

TABLE 2

Comparison of FoG prediction model result.

Comparison		*k*-NN(k=5)	Support Vector Machine with Linear Kernel
Panel hazard rating data-based FoG prediction model result (cross-validation run five times)	Avg	0.82134	0.81695
	Max	0.88679	0.91837
	Min	0.73077	0.62264
Compliance data-based FoG prediction model result (cross-validation run three times)	Avg	0.71795	0.813675
	Max	0.79487	0.923077
	Min	0.64103	0.666667

Referring to the analytics result, all survey entity coefficients are ranked by weight using different algorithms. Then, after fusion comparison, we developed a multi-factor integrated FoG event prediction model. Merit to the real-time capability of the data management platform, with the regular survey data input, a prediction could be directly revealed in a 3D virtual model. Then, the mine site could rely on the guidance and the completion of the geological index and decide on how to prevent the hazard through strengthening and finalising support or related geological workings.

CONCLUSIONS

This study focuses on FoG hazard forecasting based on multi-factor integrated data analytics. We started with the individual analytics of all FoG event reports, compliance surveys, and panel hazard rating reports. Contributing factors are analysed and return coefficient weight ratings using different ML algorithms, which could be utilised in the final decision-making process. Then, considering the spatial-temporal connections of all indexes, data fusion analytics was completed. This model is the initial attempt on multi-factor fusion data analytics in hazard prediction. Since underground geohazards is caused by various contributing factors and mechanisms, more data sets would be involved in further research including the real-time visualisation of data.

REFERENCES

Donnelly, L, 2018. *Mining Hazards,* Springer International Publishing.

Kelly, A M and Jager, A J, 1996. Critically evaluate techniques for the in situ testing of steel tendon grouting effectiveness as a basis for reducing fall of ground injuries and fatalities, *Safety in Mines Research Advisory Committee*, GAP 205, October, pp 1–108.

Ma, C, Li, T and Zhang, H, 2020. Microseismic and precursor analysis of high-stress hazards in tunnels: A case comparison of rockburst and fall of ground, *Engineering Geology,* 265:105435.

The necessity of 3D analysis in open pit, rock slope, stability analysis – in theory and practice

A McQuillan[1] and N Bar[2]

1. Director, Rocscience, Inc, Southport Qld 4215. Email: alison.mcquillan@rocscience.com
2. Principal Geotechnical Engineer, Gecko Geotechnics, Mt Sheridan Qld 4868. Email: neil@geckogeotech.com

INTRODUCTION

Geotechnical models developed during the open pit mine planning stage are generally three-dimensional (3D) in component to capture the spatial variation in geological, structural, hydrogeological and geomechanical conditions. Yet when geotechnical analysis is completed, often the 3D geological, hydrogeological and structural models are simplified to two-dimensions (2D). This paper demonstrates this simplification, through referenced case studies, can lead to the wrong failure mechanism being analysed and/or a conservative Factor of Safety (FOS), or Strength Reduction Factor (SRF), being calculated, leading to a false sense of stability.

There exists a paradigm that the FOS calculated using 2D limit equilibrium (LE), or the Strength Reduction Factor (SRF) calculated using 2D finite element (FE), modelling methods is generally conservative, ie lower, than the true FOS. However, this assumption that 3D FOS, or 3D SRF, is always higher than 2D FOS, or 2D SRF, is not always correct (Chen and Chameau, 1983; Bromhead and Martin, 2004; Herza *et al,* 2017; Pyke, 2017; Dana *et al,* 2018).

3D MODELLING FOR SLOPE STABILITY ANALYSIS

Congress *et al* (2021) summarises several cases where the 3D FOS has been calculated as greater than the 2D FOS. Anagnosti (1969), Cavounidis (1987), Gens, Hutchinson and Cavounidis (1988), Mowen *et al* (2011), Lu *et al* (2013), Ho (2014), Domingos (2016), Stark and Ruffing (2017), Azizi *et al* (2020) further report cases where the 3D FOS is up to 50 per cent greater than the 2D FOS. Across all these studies there is not a single general rule that represents a consistent percentage increase between 2D and 3D FOS (Fredlund *et al,* 2017). However, it can be generally accepted that the difference between 2D and 3D FOS will be lower for homogeneous slopes (with isotropic material strengths), and higher for heterogenous slopes (with anisotropic, or directionally dependent material strengths) (Bahsan and Fakhriyyanti, 2018). Stark and Eid (1998) also note that the variance in FOS is less pronounced in slopes with a rotational failure mode, which usually occurs in homogeneous materials. Also, of importance in the 3D modelling process is that model is not constrained laterally. 3D models that are highly laterally constrained will produce a higher FOS than longer, laterally unconstrained 3D models. Examples of this phenomena are given by McQuillan *et al* (2021) and Hammah and Awuku-Asabere (2021), and described by Ugai and Leshchinsky (1995) and Griffiths and Marquez (2007).

There are also scenarios in which the 3D FOS is lower than 2D FOS. Such scenarios typically have highly varying geology, which results in the 3D case having higher shear stresses than the 2D section generally cut through the deepest part of the 3D slip surface (Bromhead and Martin, 2004).

The only way to assertively determine the 3D FOS is to analyse the scenario in true 3D, not apply a rule of thumb or general increase to 2D FOS. Results of LE (2D or 3D) should be validated with a fundamentally different type of analysis (eg finite element, finite difference etc), where similarity in results between methods should increase confidence in results of either analysis method (Ugai and Leshchinsky, 1995; Kainthola *et al,* 2013).

Results of 3D modelling should also be validated against the known performance of slopes. Examples of 3D analysis to back analyse excavated complex slopes are presented by Bar *et al* (2019, 2020, 2021), McQuillan *et al* (2020), Bar and Dixon (2021) and Figueiredo *et al* (2021).

If the slope under investigation includes any of the following conditions, 3D stability analysis should be included in the geotechnical design review process:

- Non-linear slope geometry.

- Spatially or laterally varying geological and hydrogeological conditions.

- Spatially varying material strengths, including anisotropic material behaviour in the same unit.

- Persistent structures, striking and intersecting up to 50° from the slope orientation (McQuillan *et al,* 2018).

- Highly variable 2D results within close spatial proximity to each other (Bahsan and Fakhriyyanti, 2018; Chakraborty and Goswami, 2021).

The recommendation of 3D analysis is not limited to 3D LE and 3D numerical analysis. Empirical methods that consider the 3D geometry of slope stability can be just as valuable (Romana, 1993; McQuillan *et al,* 2018).

DISCUSSION

One of the primary functions of a geotechnical engineers is to determine the risk of an excavation (surface or underground) or dumped, or constructed slope. Risk is quantified by determining a likelihood and consequence of failure. More often 'risk' is assessed by calculating a FOS and comparing this value against design acceptance criteria (DAC). Higher DAC should be implemented for designs based on levels of:

- data uncertainty (eg limited data)

- natural variability in model inputs

- consequence of failure or unacceptable performance

- limitations of the analysis method applied (Herza *et al,* 2017)

- ability to manage safety risks associated with ground failure.

Typically, minimum FOS are based on decades of back analysis of observed failures (Hezra *et al,* 2017; Stark and Ruffing, 2017). DAC, including minimum FOS, commonly applied to mining slopes are summarised by Read and Stacey (2008), and although not explicitly stated, are interpreted to apply to 2D stability analysis.

Where industry is increasingly calculating slope stability in 3D, the authors pose the question, should the minimum FOS DAC be higher for 3D stability analysis, compared to 2D analysis?

This question is raised where, if the industry accepted minimum 2D FOS of 1.2 is based on the premise that the 3D FOS is always higher than 2D analysis, ie 2D analysis will always result in a more conservative FOS, then the minimum acceptable FOS for 3D analysis should be greater than 1.2 to align to this paradigm. For example, a minimum FOS of 1.4 to 1.5 should be applied to align to an assumption that the 3D FOS is approximately 20 to 30 per cent greater than the 2D FOS.

In the authors' opinion, where 3D FOS calculations are based on the same principle mechanics as 2D FOS calculations, ie at FOS = 1.0 in 2D and 3D, shear resistance equals destabilising forces and moments, or in simpler terms the capacity of the system equals the demand, a minimum FOS of 1.2 remains applicable.

This is assuming:

- 3D analysis is representative of true slope stability in that it removes the inherent 2D simplifications

- the 20 per cent capacity in design, associated with a FOS = 1.2, is within acceptable risk limits, considering the uncertainty, variability, consequence of failure and limitations of the analysis method applied. If higher uncertainty, variability and consequence of failure is associated with the design then a higher FOS should be applied, regardless of modelling in 2D or 3D

- 3D back-analysed material strengths have been applied in the analysis.

CONCLUSIONS

The calculation of FOS is engrained in geotechnical design review and acceptance criteria. To adequately calculate FOS geotechnical engineers need to representatively model slope geometry,

geology, material strength, groundwater conditions and structural conditions, all of which inherently vary in 3D.

REFERENCES

Anagnosti, P, 1969. Three dimensional stability of fill dams, *Proceedings: 7th International Conference on Soil Mechanics and Foundation Engineering*, pp. 275–280.

Azizi, M, Marwanza, I, Ghifari, M and Anugrahadi, A, 2020. Three dimensional slope stability analysis of open pit mine, *IntechOpen*.

Bahsan, E and Fakhriyyanti, R, 2018. Comparison of 2D and 3D stability analyses for natural slope, *International Journal of Engineering and Technology*, 7(4.35):662–667.

Bar, N and Dixon, R, 2021. Unveiling unknowns: Practical application of InSAR for slope performance monitoring and risk management across multiple surface mines, *Engineering Geology*, 293(4):12.

Bar, N, Arrieta, M, Espino, A, Diaz, C, Mosquea, L A, Mojica, B, McQuillan, A, Baldeon, G and Falorni, G, 2021. Back-analysis of ductile slope failure mechanisms and validation with aerial photogrammetry, InSAR and GbRAR to proactively manage economic risks to protect the mine plan, *RIC2021 Conference Proceedings*, Toronto, Canada.

Bar, N, Kostadinovski, M, Tucker, M, Byng, G, Rachmatullah, R, Maldonado, A, Pötsch, M, Gaich, A, McQuillan, A and Yacoub, T, 2020. Pit slope failure evaluation in near real time using UAV photogrammetry and 3D limit equilibrium analysis, *Australian Geomechanics*, 55(2):33–47.

Bar, N, Ryan, C, Yacoub, T, McQuillan, A, Coli, N, Leoni, L, Harries, N, Bu, J, Rea, S and Pano, K, 2019. Integration of 3D limit equilibrium models with live deformation monitoring from interferometric radar to identify and manage slope hazards, *14th Int ISRM Congress on Rock Mech and Rock Eng*, Foz do Iguassu, Brazil.

Bromhead, E and Martin, P, 2004. Three-dimensional limit equilibrium analysis of the Taren landslide, *Advances in Geotechnical Engineering Skempton Conference*, 2:789–802, London.

Cavounidis, S, 1987. On the ratio of Factor of Safety in Slope Stability Analyses, *Geotechnique*, 37(2):207–210.

Chakraborty, A and Goswami, D, 2021. Three-dimensional (3) slope stability analysis using stability charts, *International Journal of Geotechnical Engineering*, 15(5):624–649. DOI: 10.1080/19386362.2018.1465743

Chen, R and Chameau, J, 1983. Three-dimensional limit equilibrium analysis of slopes, *Geotechnique*, 33(1):31–40.

Congress, S, Kumar, P, Gajurel, A, Patil, U and Puppala, A, 2021. Two- and three-dimensional slope stability analyses of rock cut using unmanned aerial photogrammetry data, *International Foundations Congress and Equipment Expo*. https://doi.org/10.1061/9780784483435.004

Dana, H, Kakaie, K, Rafiee, R and Bafghi, A, 2018. Effects of geometrical and geomechanical properties on slope stability of open-pit mines using 2D and 3D finite difference methods, *Journal of Mining & Environment*, 9(4):941–957.

Domingos, V, 2016. *Three-dimensional slope stability using the limit equilibrium method*, M.Sc dissertation, Federal University of Goias, Goiania, Brazil.

Figueiredo, L, Barros, M, Hammah, R, Santos, Y, Souza, T and Nogueira, C, 2021. Case study: open pit three-dimensional slope stability back-analysis for an anisotropic iron ore rock mass, *Proceedings: SSIM2021*, pp. 107–120. doi:10.36487/ACG_repo/2135_04

Fredlund, M, Fredlund, D and Zhang, L, 2017. Moving from 2D to a 3D unsaturated slope stability analysis, *Proceedings: Second Pan-American Conference on Unsaturated Soils.* https://doi.org/10.1061/9780784481691.014

Gens, A, Hutchinson, J and Cavounidis, S, 1988. Three-dimensional analysis of slides in cohesive soils, *Geotechnique*, 38(1):1–23.

Griffiths, D and Marques, R, 2007. Three-dimensional slope stability analysis by elasto-plastic finite elements, *Geotechnique*, 57(6):537–546. doi: 10.1680/geot.2007.57.6.537

Hammah, R and Awuku-Asabere, F, 2021. Does 3D slope stability analysis always produce higher factors of safety than 2D?, Online: https://www.rocscience.com/learning/does-3d-slope-stability-analysis-always-produce-higher-factors-of-safety-than-2d

Herza, J, Ashley, M and Thorp, J, 2017. Factor of Safety? Do we use it correctly?, *Proceedings ANCOLD 2017 Conference*.

Ho, I, 2014. Parametric studies of slope stability analyses using three-dimensional finite element technique: Geometric effect, *Journal of GeoEngineering*, 8(1):33–43.

Kainthola, A, Verma, D, Thareja, R and Singh, T, 2013. A review on numerical slope stability analysis, *International Journal of Science, Engineering and technology Research*, 2(6):1315–1320.

Lu, H, Fredlund, M and Fredlund, D, 2013. Three-dimensional limit equilibrium analysis of open pits, *Proceedings: Slope Stability 2013*, pp. 541–554.

McQuillan, A, Bar, N and Yacoub, T, 2021. On the comparison of 2D and 3D stability analyses of an anisotropic slope, *Proceedings: Rocscience International Conference*.

McQuillan, A, Canbulat, I, Payne, D and Oh, J, 2018. New risk assessment methodology for coal mine excavated slopes, *International Journal of Mining Science and Technology*, https://doi.org/10.1016/j.ijmst.2018.07.001

McQuillan, A, Yacoub, T, Bar, N, Coli, N, Leoni, L, Rea, S and Bu, J, 2020. 3D slope stability modelling and its interoperability with interferometric radar data to improve geotechnical design, *Proceedings: 2020 International Symposium on Slope Stability in Open Pit Mining and Civil Engineering*.

Mowen, X, Zengfu, W, Xiangyu, L and Bo, X, 2011. Three-dimensional critical slip surface locating and slope stability assessment for Lava Lobe of Unzen Volcano, *Journal of Rock Mechanics and Geotechnical Engineering*, 3(1):82–89.

Pyke, R, 2017. How great are 3D effects in slope stability analysis?, LinkedIn article.

Read, J and Stacey, P, 2008. *Guidelines for Open Pit Slope Design*, CSIRO Publishing, Victoria.

Romana, M, 1993. *A Geomechanical Classification for Slopes: Slope Mass Rating, Comprehensive Rock Engineering: Principles, Practice and Projects*. Pergamon Press Ltd, Oxford.

Stark, T and Eid, H, 1998. Performance of three-dimensional slope stability methods in practice, *J. Geotech. Eng Division, ASCE*, 124(11):1049–1060.

Stark, T and Ruffing, D, 2017. Selecting minimum Factors of Safety for 3D Slope Stability Analysis, *Proceedings: Geo-Risk 2017: Reliability-Based De-sign and Code Developments*, pp. 259–266.

Ugai, K and Leshchinsky, D, 1995. Three-dimensional limit equilibrium and finite element analyses: a comparison of results, *Soils and Foundations*, 35(4):1–7.

30 years of seismic system design, implementation and interpretation

J Player[1], S Webber[2], E Jones[3] and G Sweby[4]

1. MAusIMM(CP), Principal Engineer, MineGeoTech Pty Ltd, Perth WA 6000.
   Email: johnplayer@minegeotech.com.au
2. Geotechincal Superintendent – Mungari Operations, Evolution Mining, Kalgoorlie WA 6430.
   Email: Stephen.Webber@evolutionmining.com
3. MAusIMM(CP), Principal Study Manager – Geotechnical, MineGeoTech Pty Ltd, Perth WA 6000. Email: emmajones@minegeotech.com.au
4. Principal Consulting Geotechnical Engineer, MineGeoTech Pty Ltd, Perth WA 6000.
   Email: gordonswseby@minegeotech.com.au

ABSTRACT

Seismic systems are a tool for the monitoring and forecasting the rock mass response to excavation. Common issues encountered at mine site audits and reviews are: how to design an effective seismic system, implementation of the design, interpretation of seismic source results and understanding the reliability of the seismic source. These issues are often a function of several items including:

- Experience of site personnel in undertaking seismic system design.

- Personnel not envisioning multiple phases of system expansion to understand system robustness issues.

- System design/expansion occurring in response to damaging seismic activity rather than planned expansion of a system

- The mine access development is often localised in comparison to the total orebody being mined hence, planning sensors in longholes in advance of development rather than in short holes close to development will improve the three-dimensional aspect of the network.

- Limited site processing of the seismic event data, hence engineers do not see the uncertainty associated with event location, size, source and system layout.

Mine site users require a framework to appreciate the challenges and limitations in locating large events. For example, event locations are given as precise measurements (to the nearest centimetre) whereas the volume of deformation resulting in the event often has dimensions of tens of metres or more (as defined by the source radius). A stronger awareness of the uncertainty of rock mass yield within large seismic sources will assist site users in the interpretation of rock mass damage.

The encountered design and implementation errors are reviewed and discussed with a practical set of rules presented to provide a robust seismic system that provides consistent results and increases the user's understanding of uncertainty in source location and size.

The authors' experience across multiple mine sites, seismic systems and damaging seismic events over a 30 year period has been summarised into practical rules for site personnel of all experience levels.

SEISIMIC SYSTEMS AND ROCK MASS RESPONSE MONITORING

These general rules come from the combined experience of the authors across multiple mines and are presented to help mining/geotechnical engineers and their managers that have limited seismic system knowledge. The rules are based on the authors experiences with:

- The design, installation, maintenance and improvements in the seismic system.

- Experience processing of tens of thousands of events when processing of seismic events was done on-site and not outsourced. Hence site engineers learnt to understand how well a seismic system functioned, difficultly in picking arrival times from wave forms, which sensors had noise, and which sensors were regularly rejected with errors and ground truthing these to the rock mass response.

- The investigation of over 100 dynamic rock failures (rock bursts).

Effective seismic systems are a balance of sufficient sensors to monitor the expected rock mass response and the cost and practicality of achieving this. Seismic sources do not emit simple radiating waveforms but rather complex three-dimensional waveforms where the actual recorded waveform is located relative to the type of source.

The general rules can be considered in the following sections:

- Array design
- Sensor type
- Sensor installation
- Sensor cable
- Seismic enclosure
- Audit system
- System accuracy
- Blast calibration.

Some of the rules may seem basic or obvious but are stated as they have been identified by the authors as problems on mines with operating seismic systems.

Array design

The purpose of a seismic array is to monitor rock mass failure and to facilitate the interpretation of seismic sources. This is best achieved when the sensor array surrounds the seismic source (ie the source is within a volume of rock defined by the sensors as opposed to all sensors being on one side of the source) as this provides the most accurate location and seismic source parameters. Errors in location also result in errors in the source parameters.

The ideal robust array design uses the following principles:

- Use the life-of-mine plan to plan the array with timing of expansion as the mine void increases.

- Balance of near and far sensors (Near sensors increase sensitivity to small events but have overlap between the P and S wave energy windows and hence it is harder to define the source correctly. Distant sensors are less sensitive to small events but allow better recording of moderate to large events as there is a separate of the P and S wave components by the time they arrive at the sensor). Waveforms recorded by distant sensors have a greater low frequency content thus improving the quality of the location and source parameters of large events.

- Three-dimensional rather than planar (use longholes to achieve this, possibly using exploration holes). It is common for seismic arrays to be relatively planar as a result of a lack of development on both sides of the orebody.

- Robust in terms of maintaining sensitivity and accuracy when individual sensors are offline.

- Consider how mine voids are going to influence the ray path and travel time between source and sensor.

- Consider the impact of different lithological units, major faults, rock mass damage due to stress which will influence the different P and S wave velocity. A sensitivity analysis should be undertaken to assess the effect of velocity variation on seismic source location.

Array design can be tested by undertaking sensitivity and accuracy modelling.

Sensitivity

Sensitivity of an array is defined by the minimum magnitude of above which all events are recorded. It is represented by the lower departure from a straight line on a Gutenberg-Richter plot, Figure 1. This can be represented by an isosurface in mine space.

Remembering magnitude is a log scale and a change of 0.3 is doubling or halving of sensitivity of the array.

Figure C 12 Log Cumulative Frequency vs ML graph for cluster 1

Figure C 9 Log Cumulative Frequency vs ML graph for cluster 8

Figure C 1 Log Cumulative Frequency vs ML graph for cluster 0
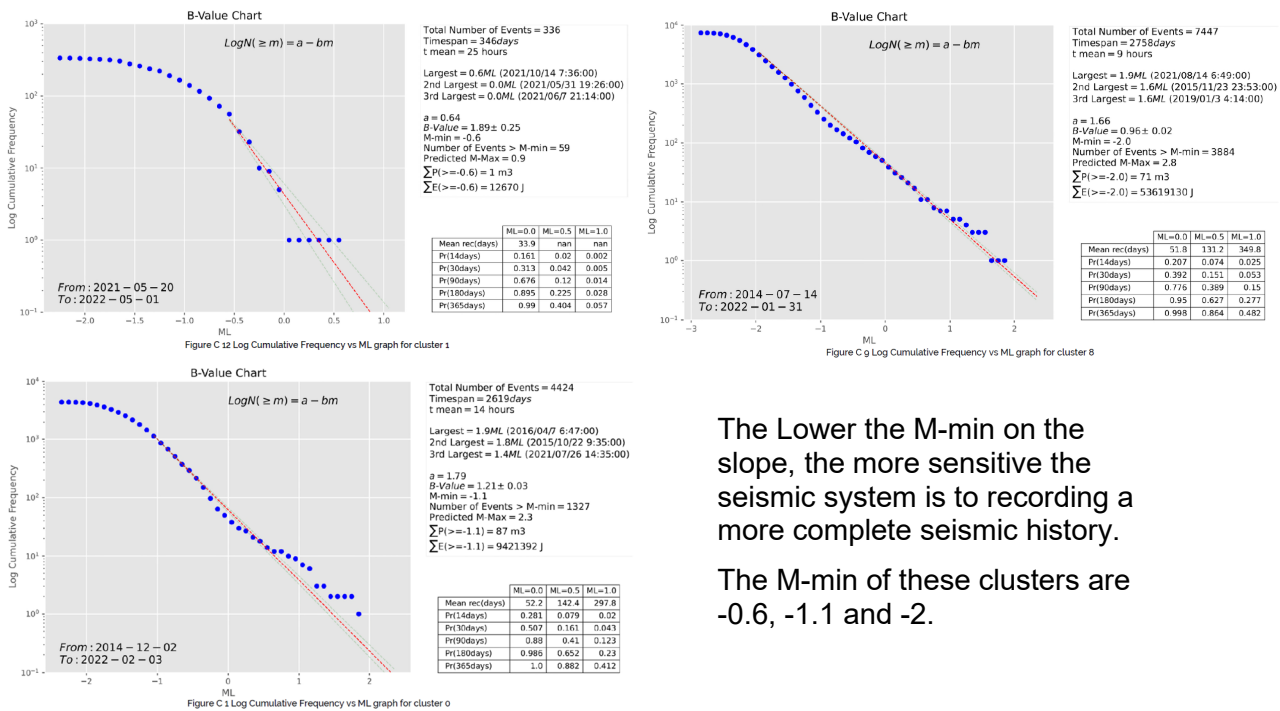
The Lower the M-min on the slope, the more sensitive the seismic system is to recording a more complete seismic history.

The M-min of these clusters are -0.6, -1.1 and -2.

FIG 1 – Example Gutenberg-Richter plots with a difference in sensitivity of 32 times.

Accuracy

Accuracy can be defined by three-dimension error or in a specific direction and be represented by an isosurface. An example is shown in Figure 2. This is typically done for accuracy of a -0.5 Local Magnitude event. The accuracy of the of the events is likely to be different in terms of easting, northing and elevation particularly if the arrays is designed with a non-uniform distribution of sensors and this should be reviewed.
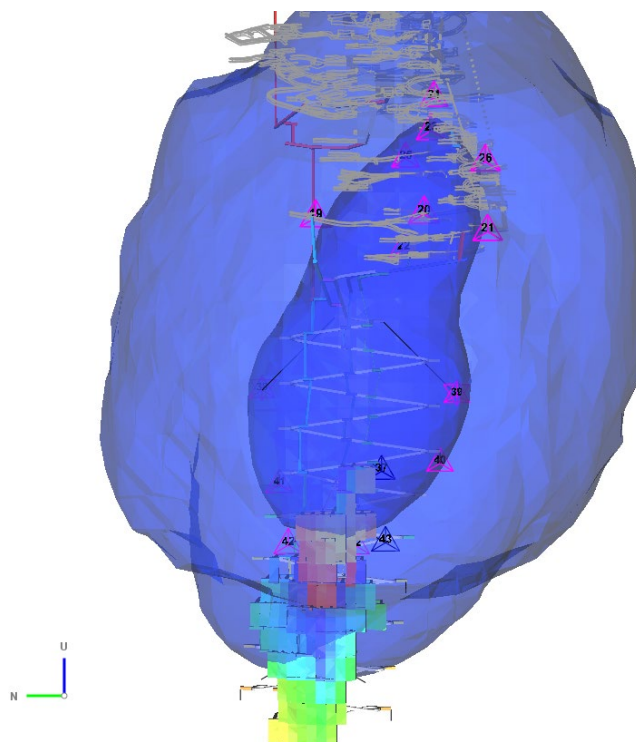
FIG 2 – Isosurface for accuracy of an expanded for 20 m and 50 m error in location.

Design criteria

Our minimum design standard for Australian operations should be to a sensitivity of -1.0 Local Magnitude and 20 m accuracy for a -0.5 Local Magnitude event. A robust system would allow additional sensors to be installed to easily increase sensitivity in areas that require the additional monitoring as mining progresses.

The main advantage of isosurfaces is that they can be viewed in three dimensions in the mine visualisation software or seismic software. This permits personnel to assess and understand the system limitations with regards to where people are working or seismic clusters.

Two case examples are presented; case one has sensors only located near a single spiral decline (Figures 3 and 4), case two has a multiple deposits with sensors located on both the footwall and hanging wall of the deposits (Figures 5 to 7). The impact of clustered sensor arrays compared to well distributed sensors arrays is clearly observed with regards to accuracy and sensitivity on the mine working areas.
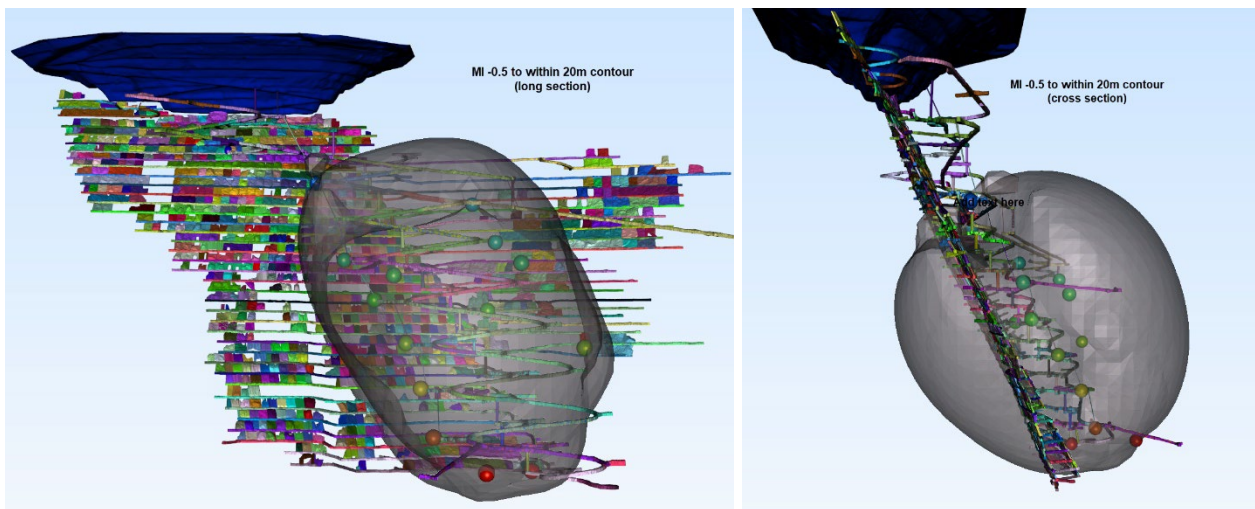
FIG 3 – Accuracy of seismic system to locate a Ml -0.5 event when sensors are only on the decline.
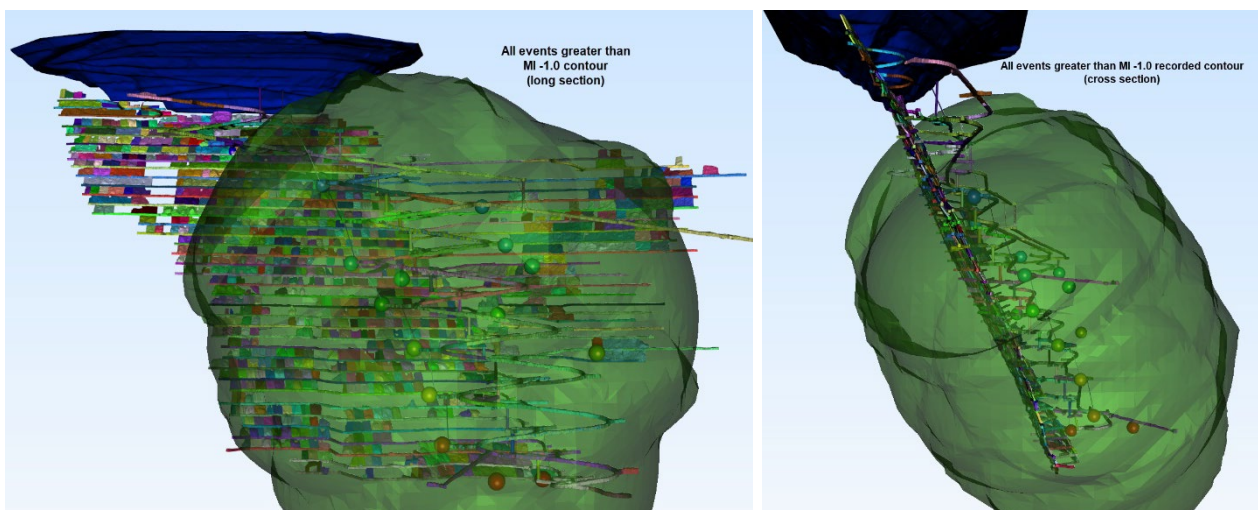
FIG 4 – Sensitivity of a seismic system to record all events greater than Ml -1.0 when sensors are only on the decline.
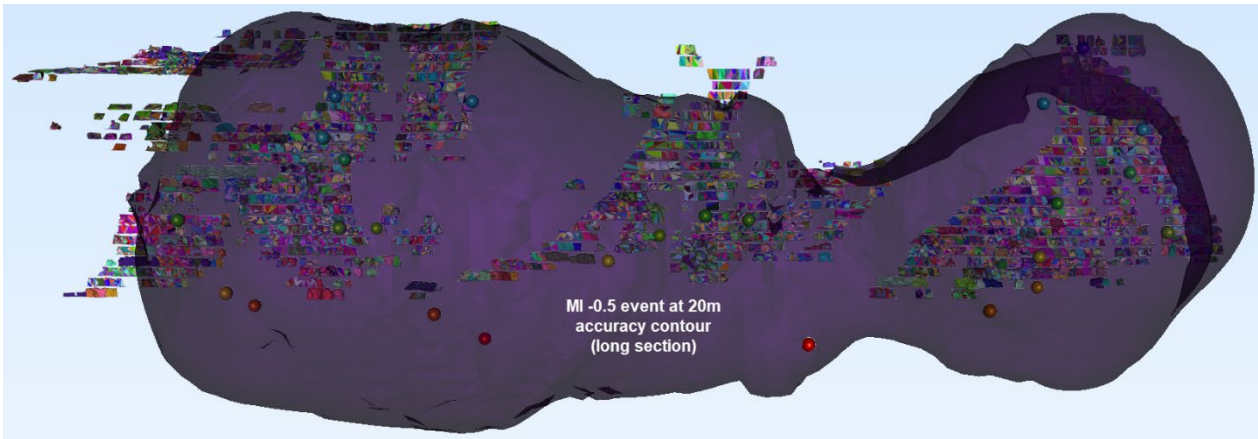
FIG 5 – Accuracy of seismic system to locate a MI -0.5 event when sensors are both sides and along the strike of the orebody.
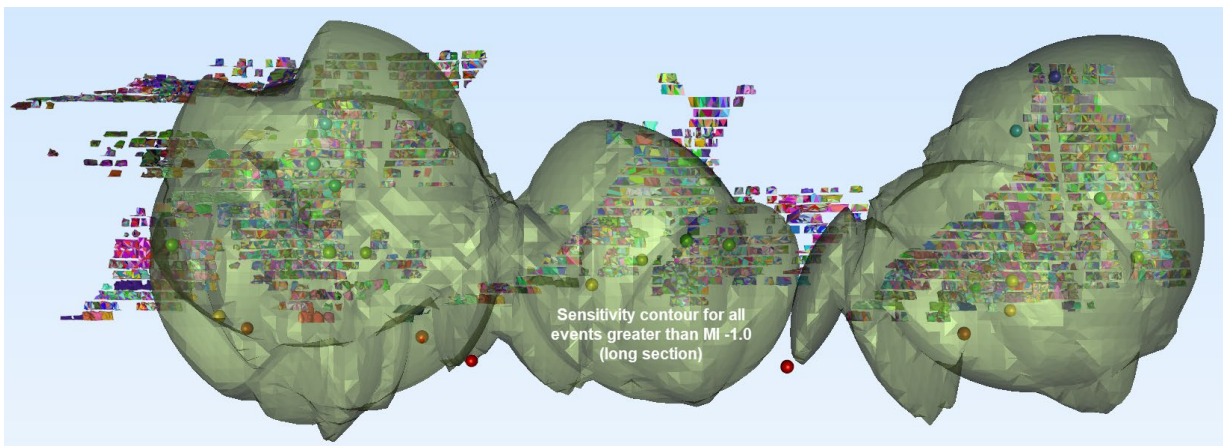
FIG 6 – Sensitivity of a seismic system to record all events greater than MI -1.0 when sensors are both sides and along the strike of the orebody.
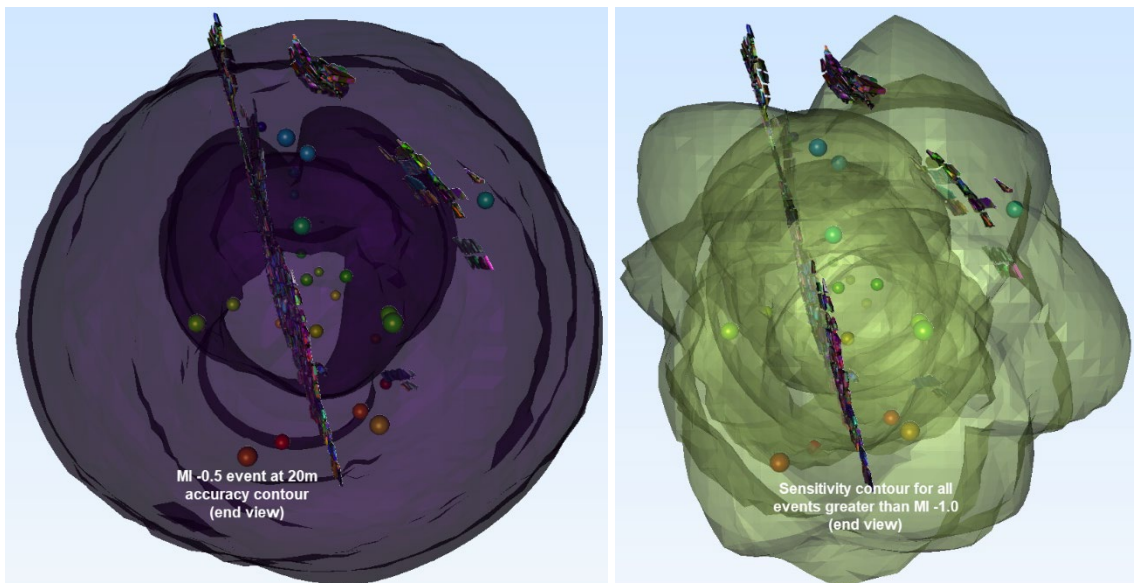
FIG 7 – Accuracy and sensitivity contours from an end view for a well distributed seismic sensor array.

Sensor type

Geophones (magnetic core on springs in a coil making an electrical pulse when excited by ground vibration) are the most common sensor type used due to frequency range and durability, also

available as uniaxial or triaxial components. A triaxial sensor will record the full waveform from seismic source whereas a uniaxial sensor will only record the parts of the waveform that will cause the magnet to move.

Geophones are defined by a 'natural frequency'. In the mining environment, 4.5 Hz and 14 Hz geophones are most commonly used. The natural frequency is the frequency below which, the content of the waveform will not be completely recorded. This will lead to the moment and thus magnitude being underestimated. Examples are shown in Figures 8 and 9. The low frequency component has not been completely captured by the 14 Hz geophones so the corner frequency determined from these spectra would be too high and these the moment and magnitude would underestimated. If the frequencies are fully captured the results is a clear low frequency plateau (similar to the dotted best fit line in the S wave plot) would be observed. But these clear plateau's are not observed, particularly on the P-wave.
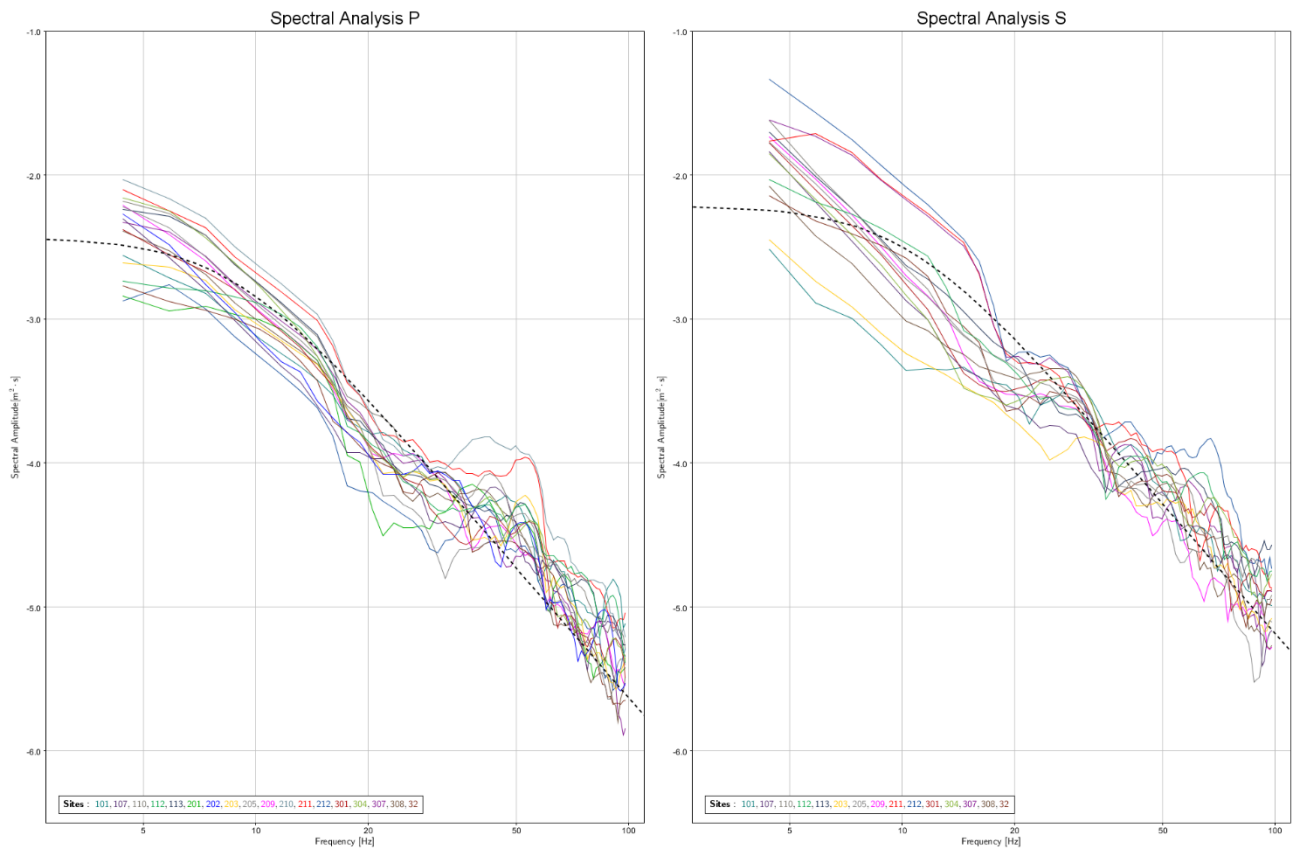
FIG 8 – ML = 2.9 (Mw = 3.0) a distant event where the low frequency plateau is not clear.
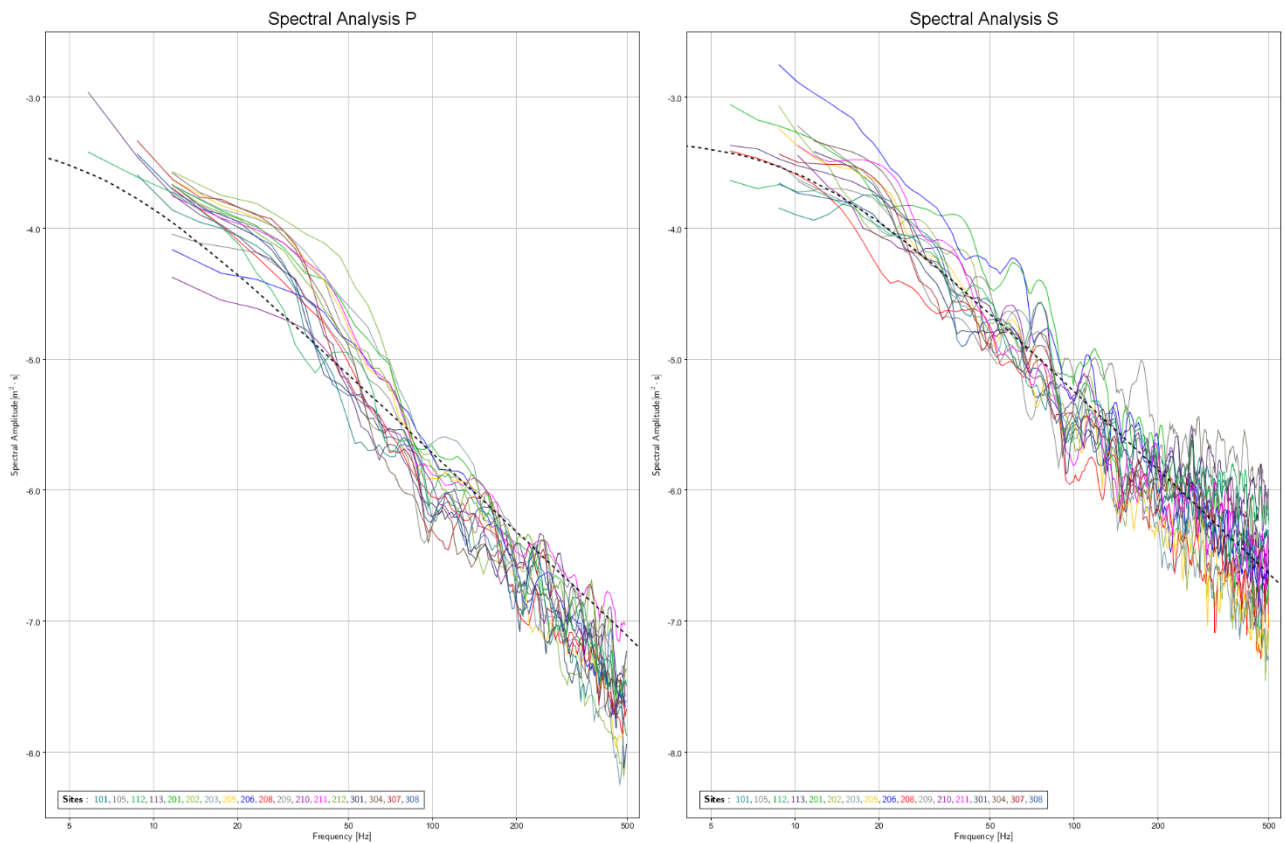
FIG 9 – ML = 2.1 (Mw = 2.3) a near event where the low frequency plateau is not clear.

Low frequency sensors have a narrow range of installation angles compared to higher frequency sensors, Table 1.

TABLE 1

Geophone limitations.

Sensor	Tilt sensitivity	Maximum magnitude
4.5Hz	2 degrees	2.9
8Hz	15 degrees	2.3
14Hz omni	Any orientation	1.9

Maximum magnitude (in Table 1) is calculated for a static stress drop of 0.5 MPa, S-wave velocity of 3500 m/s and corner frequency equal to the natural frequency of the geophone. In reality, these parameters will vary so the maximum magnitude is a guide rather than a strict rule. The seismic system vendor will assist in the selection of the most appropriate sensors. Typically, the maximum expected magnitude and corner frequency would be estimated and sensors selected with natural frequency with one half to one third of the corner frequency.

However, consideration to the casing size of the sensor and the hole diameters that can be drilled is required. Small casing sensor options are available. Use sensors that have orientation accelerometers (smart sensors) that allow the actual orientation of the sensor to be measured post installation.

Sensors come with user specified cable length so order what you need to locate the sensors where it is required.

Sensor installation (underground)

The sensors for clean waveforms need to be located away from excavations particularly outside of damaged rock mass and so that they are also don't have changes in the high frequency content of the wave due to interference from the excavation. Low frequency sensors can be located 10–12 m away as they are less sensitive to the high frequency change. High frequency sensors should be installed in holes a minimum of 20 m long. This is important because poor quality waveforms make it harder to define the P and S arrival picks which increases location error and source parameter determination.

The sensor location accuracy is required to be known to within 1 m so drill holes need to have downhole surveys on them when and drill hole deviation occurs in addition to a collar pickup and collar survey.

Other requirements and tips before and during the installation process are detailed here.

Collar location

- Locate the collar of the hole in niche or cuddy or back of unused stockpile to protect the cable. The site should be in a low vehicular traffic area so as to minimise the likelihood of damage.

Grouting

- Downholes are preferred because they are easier to grout, however, keep the sensor 1 m from the bottom of the hole to be clear of mud.

- Thick mix grout is not needed because grout shrinkage will be from the collar towards the sensor. In upholes grout shrinkage can expose the sensor.

- Grout thickness can be thinner than conventional cable bolting but not as thin as what most diamond driller use for grouting.

- Grout can be GP or Low Heat (the latter provides more work time) and use additives like methocel to improve fluidity during pumping and reduce shrinkage.

- If highly shearing ground is being used, decoupling the sensor cable by running it with conduit should be considered but this can lead to vibration in the cable. This can introduce noise so should only be considered if it is likely to happen.

- Depth markers on the cable or conduit so you know the depth of installation.

Records

- Clearly label all seismic holes (paint or reflective signs) using the same ID as what is in the seismic system to make it easier to trouble shoot later.

- Have a sensor installation card/history that records and confirms:

  o sensor serial ID and site ID

  o where the sensor is the mine

  o grouting success or issues with grouting/placing of the sensor

  o depth downhole

  o date of grouting

  o the cable pairs used on the connecting cable to seismic enclosure

  o that is surveyed, the survey data and the calculated sensor location

  o the sensor location used in the seismic system (at least 50 per cent of the systems we have worked on have had errors in the sensor location from typing into the computer)

  o have the actual sensor holes and sensor location in 3D visualisation software as a double check

  o date sensor is commissioned and decommissioned.

Sensor run cable

The sensor run cable is the extra length of cable from the sensor cable that is supplied to the seismic monitoring enclosure. The cost of low impedance cable which has better transmission of the electrical pulses from the geophone to the analogue to digital convertor, has reduced significantly so that it is only a relatively small additional cost in the total system cost compared to using the 0.5 mm^2 DEKRON instrumentation cable alternative. The low impedance cable can also come with the same colour coding as the cable on the sensor reducing error potential of mixing axis components.

The cable run should consider:

- Individually and overall shielded.

- Four pairs for a triaxial, two pairs for a uniaxial.

- Consider Steel Wire Armoured (SWA) Cable is cable needs to be in high traffic area where equipment damage is likely or there is rough handling during installation. This will also require special glands on the enclosure.

- Limit the number of joints, ideally only at the sensor and the enclosure.

- No larger than 0.5 mm^2 core (larger diameter core introduced frequency notching).

The cable run should:

- Be planned with the head electrician on-site.

- Be more than 1 m from high voltage cable to minimise electrical noise.

- Perpendicularly cross high voltage cables to minimise electrical noise (the influence of which is shown in Figure 10.

- Have a loop of 1–2 m, every 200 m to allow repair to cables if broken.

- Maximum run lengths of 500 m and only if electrically quiet, preference is to be under 300 m.

- Use 'pig tail hangers' to speed up the handing of the cable or a 'cable tie gun'.

- Label the cable when it gets to the enclosure area. Particularly when there are multiple geophones using the same type cable to ensure no errors.

Record the cable run on paper level mine plans and in 3D to allow visualisation and trouble shooting. Damage to cable runs is, in the authors experience, the major cause of poor system performance. As such, it is important, that cable runs are documented in detail so that damage sites can be quickly located and rapidly repaired.
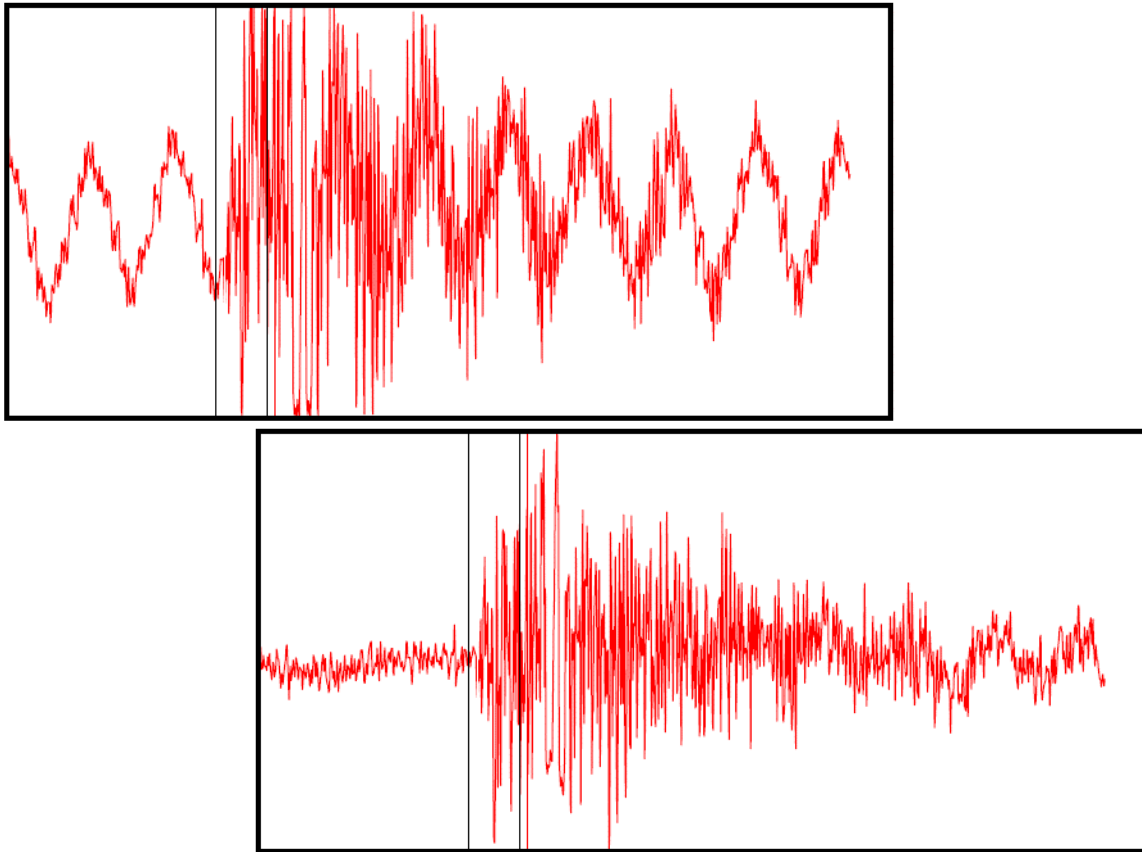
FIG 10 – Example seismogram with significant 50 Hz electrical that has been successfully removed by a notch filter.

Seismic enclosure

The internal layout of seismic enclosures and the hardware used within them has improved considerably over the last 15 years and now are less complicated for site practitioners to set-up and diagnosis issues.

The main consideration is now site specific rules regarding access to 240 V power enclosures. The standard enclosure design is for 240 V internally in the enclosure.

Other considerations are:

- Maintain a durable label on the cable for future trouble shooting (Figure 11).

- Data transmission underground – is it over fibre optics or copper and where is it located?

- Where is the nearest ethernet switch (limit of 100 m) or should it be included within the enclosure (allows options for additional non-seismic monitoring and control).

- Additional battery/UPS in the enclosure sized to suit the power draw and expected duration of underground power outages.

- Have a schematic inside the enclosure that shows the wiring details and sensor locations.

FIG 11 – Well labelled cables but poorly terminated into the enclosure.

Audit system

The following are critical when undertaking an audit of a seismic system:

- Cables are correctly labelled and are on the correct termination bars in the enclosure.

- Unlabelled cables can best traced and tested by doing Test Triggers, Figure 12.

- Each wire of each pair has a specific wiring position for correct polarity.

- Check sensor locations are the actual, not the design.

- Check there is no typographic errors in the sensor coordinate.

- Plot system sensor coordinates in 3D space against drill holes, check, do they match?

- Are all components of all sensors recording successful triggers (daily check).

- Review the P and S wave velocities. Has there been a blast calibration completed?

- Document software upgrades and changes.
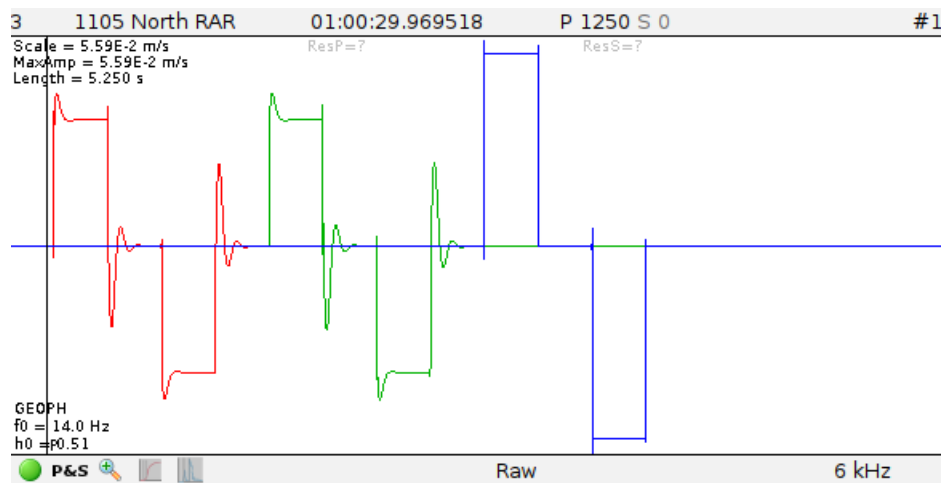
FIG 12 – Example Geophone with blue axis not functioning to a test trigger.

Blast calibration

A calibration blast program needs to cover a sufficient spatial volume of the monitored rock mass so that rock mass variability is addressed. A good example is:

- A completed ore drive/footwall drive prior to production starting or a hanging wall exploration drive.

- Jumbo drilled holes maximum 50 m apart at 30–45° down at 0.5 m off the toe as deep as you can go.

- Survey the holes.

- 700 mm long by 32 mm diameter plug explosive and fill hole with water (larger sites will need more explosive).

- Holes to be timed to have at least 1 second between holes and separate to normal blasting.

- The more test shots you fire the more understanding of the rock mass velocity variance will be gained and hence variability in seismic source location.

System accuracy

The following items are significant to understand the reported seismic source location:

- The accuracy of the event location reported in the seismic processing software is not the real error, it is a report of the precision of the solution, hence you can be precisely wrong for events with a low number of triggers.

- The hypocentre is the origin of the event and is not necessarily in the middle of the source volume.

- The hypocentre is a mathematical solution and makes no judgement on whether it is physically meaningful.

- The hypocentre for events over local magnitude 0.5 become increasingly less useful with increasing size as they are a volume as opposed to a point.

- The hypocentral distance is the distance from the hypocentre of the event to the sensor.

- The source volume is volume over which the accumulated strain energy is dissipated, Table 2 (Mendecki, Lynch and Malovichko, 2010). Always think of large events involving large volumes of rock even through the resultant damage can be considerably less than the source volume.

TABLE 2

Events size and source size.

Moment Magnitude	1	0.5	0	-0.5	-1	-1.5
Source Size 0.5MPa stress drop (m)	65	35	20	12	6	4
Source size 0.1MPa stress drop (m)	110	64	35	20	12	6

CONCLUSIONS

The rules cover eight common issues the authors have observed with seismic system design, maintenance and monitoring. They are meant to increase awareness, aid the knowledge and development of engineers and managers that have not worked with seismic systems before or have not planned a seismic system upgrade before. By doing these items well, the challenge of interpretation of the seismic data will have a better foundation.

ACKNOWLEDGEMENTS

Thanks to the geotechnical site engineers and mining engineers that have worked us with over the decades on mines with seismic issues and to seismic system suppliers for discussing their improvements to their systems and taking onboard our concerns when they are identified.

REFERENCE

Mendecki, A J, Lynch, R A and Malovichko, D A, 2010. Routine Micro-Seismic Monitoring in Mines, *Australian Earthquake Engineering Society 2010 Conference*, https://aees.org.au/wp-content/uploads/2013/11/56-RichardLynch.pdf

Consideration of asymmetric drive geometry and conditions on the loading capacity of pastefill barricades

D Sainsbury[1], B Sainsbury[2] and M Revell[3]

1. Director and Principal Geotechnical Engineer, Geotechnica, Melbourne Vic 3182.
   Email: david.sainsbury@geotechnica.com.au
2. Professor, Deakin University, Waurn Ponds Vic 3216.
   Email: breanne.sainsbury@deakin.edu.au
3. Principal Minefill Engineer, MineFill Services, Terrigal NSW 2260. Email: mat@minefill.com

ABSTRACT

This paper extends the existing knowledge associated with the design and placement of prefabricated pastefill barricades through a consideration of asymmetric drive geometry and conditions. The load capacity of prefabricated barricades and their failure modes are considered in relation to abutment geology and barricade geometry that includes curvature and span and drive geometry that includes abutment angles, haunch angles and misalignment. Design charts are provided for typical barricade sizes to provide general guidance for design capacities and optimising location placement based on asymmetric drive geometry. A recent barricade failure is considered in relation to the drive geometry and the potential impact it had on the installed capacity.

INTRODUCTION

Pastefill is used in underground mining operations to provide passive support to the surrounding rock mass during adjacent excavation. Pastefill is used in preference to hydraulic fill due to its non-segregating nature during placement (Dalcé, Li and Yang, 2019).

Cemented pastefill is mixed in a backfill-plant on the surface and transported underground through pipelines (Sivakugan, Veenstra and Naguleswaran, 2015). Pastefill is contained within the stope typically by impermeable bulkheads. This compares to historical permeable barricades employed to contain draining hydraulic fill within stopes. It is highlighted that in industry many operations refer to the paste containing structures as barricades. Upon hydration of the cement within the pastefill mass, stress arching of the fill into the stope and drive walls reduces the active pressure applied to bulkheads at the base of a stope (Fahey, Helinski and Fourie, 2009).

The typical geometry of a paste bulkhead and its placement in relation to a backfilled stope is presented in Figure 1.
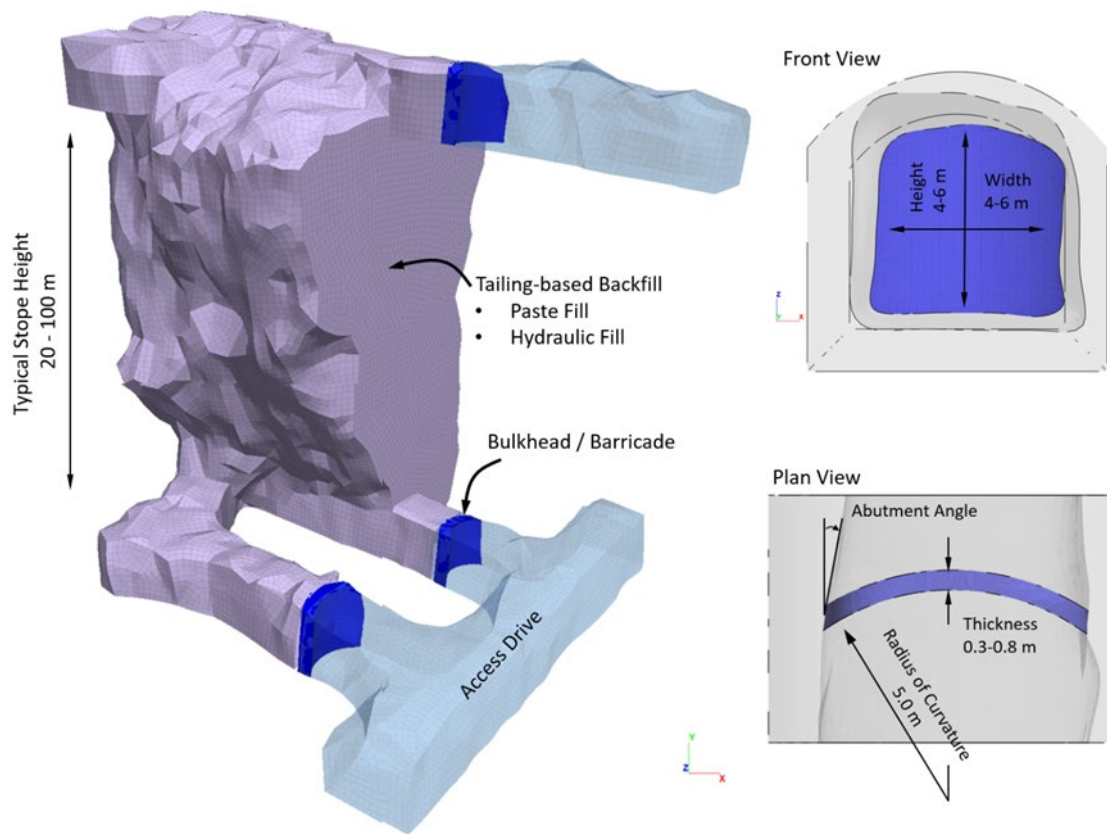
FIG 1 – Typical paste-fill stope profile and location of bulkhead in extraction drives/cross-cuts.

In Australia paste bulkheads are typically constructed using prefabricated arched shaped frames. After erecting the frame, a layer of mesh is attached to the downstream side of the frame which is then covered with hessian and sprayed with approximately 200–400 mm fibrecrete. Figure 2 presents the typical stages of construction for a fibrecrete bulkhead. It is important to note that the prefabricated frames play no role in the bulkhead capacity. They are simply a fast way to erect a backing structure to spray the fibrecrete and they also ensure the arch profile is maintained.

FIG 2 – Formwork and steps of construction of fibrecrete bulkheads (a) pre-fabricated arch placement (b) placement of the mesh and hessian over the arch (c) sprayed fibrecrete.

The cost of erecting a fibrecrete bulkhead in Australian mines is approximately $8000–$12 000. The total construction time is approximately one to two shifts. The bulkhead is usually constructed 'just-in-time' prior to filling the stope. The location of the bulkhead is pre-determined based on operational conditions and standard work procedures (Helinski *et al*, 2011) which are site specific.

RISK OF FAILURE

Bulkhead/barricade failure and the subsequent inrush of paste or hydraulic fill into the underground mining environment is a core risk associated with any hydraulic or paste backfill. Causes of

bulkhead/barricade failure have previously been discussed by Grice (1998), Revell and Sainsbury (2007a) and Sheshpari (2015). Contributory causes usually include complex stope geometry, non-ideal filling procedures and lack of real-time data to assess the evolving conditions.

'In October 2019, two workers at an underground mine were approaching a paste retaining wall during pastefilling, when the wall catastrophically failed. An inrush of fluidised paste entered the drive inundating the workers…'. An investigation into the incident found that the 'wall failed due to excessive hydraulic pressure being exerted from the pastefill' (Department of Mines, 2020). A photograph of the failed barricade is presented in Figure 3.

FIG 3 – Drive side of failed paste wall with fill pipe through wall (after Department of Mines, 2020).

Contributory causes of the failure included (a) no effective means of pressure relief in place (b) the pressure of the paste mass exceeded the wall's capacity (c) the paste behind the barricade was quite fresh meaning it flowed further than expected once uncontained (Department of Mines, 2020).

Actions recommended to mines using fibrecrete bulkheads for pastefill containment included:

- Conducting a detailed engineering and risk assessment (site investigation) for individual stopes. This is especially important to determine when there are variations to standard layouts and processes.

- Use remote monitoring devices to remove workers from potential danger zones associated with the barricades and enforce exclusion zones during the stope filling process.

Based on the recommendations for a stope-based site-investigation, it can also be suggested that the geometry of the drive may have contributed to the failure. This research addresses the important aspect of drive geometry on the as-built capacity of bulkheads and shows how such failures may occur even under ideal filling conditions.

BARRICADE DESIGN CONSIDERATIONS

Design methodology

The design of pastefill bulkheads has historically relied upon analytical solutions (eg Smith and Mitchell, 1982; Li, Aubertin and Belem, 2005; Li and Aubertin, 2009a, 2009b) and numerical methodologies (Grabinsky, Cheung and Bentz, 2014; Cui and Fall, 2017; Helinski, Fahey and Fourie, 2010) that are limited by the necessary simplification of geometry, the properties of the bulkhead materials and the representation of the wall-bulkhead interface.

A calibrated 3D numerical modelling approach has been proposed as the most appropriate method of bulkhead design (Bridges, 2003) and FLAC3D has been used to accurately model the non-linear

loading behaviour of shotcrete barricade structures since 2007 (Sainsbury and Revell, 2007). The FLAC3D methodology, and its validation, has been described in detail in Sainsbury and Revell (2007) and allows the specification of complex strain-softening material models to simulate the brittle shotcrete behaviour, together with sliding interfaces to represent the shotcrete–wall rock interface. The explicit large-strain formulation allows the full failure mechanism of a bulkhead to be analysed.

However, since the original models that considered rigid drive sidewalls (Sainsbury and Revell, 2007) the modelling methodology has been updated to reflect deformable (not rigid) sidewalls. Grabinsky, Cheung and Bentz (2014) show through a sensitivity study that assuming fully rigid boundary conditions can provide bulkhead results that may overestimate the strength and underestimate of ductility. Within the modelling procedure, the sidewalls are represented with an elastic material model. Based on the results of Grabinsky, Cheung and Bentz (2014) the inclusion of deformable sidewalls may impact the predicted capacity of the bulkhead by 150 per cent.

It is also important to note that the consideration of reinforcing bars and weld wire mesh as identified by (Grabinsky, Cheung and Bentz, 2014) has not been considered with the numerical modelling technique. Although significant advances have been made to explicitly simulate the behaviour of wire mesh, (Karampinos, Baek and Hadjigeorgiou, 2018) the inclusion of this in the bulkhead model is not considered necessary. It is not necessary since the wire mesh is not considered as a structural element in the bulkhead – it is included as formwork to hang the mesh and spray the shotcrete onto. In addition, the mesh is not installed on the free face of the bulkhead, and the additional tensile capacity at the submerged faced is unlikely to prevent failure. From the observed bulkhead failure photos (Figure 3) it is evident that the mesh does not prevent the failure.

Asymmetric drive geometry

Previous research conducted by Revell and Sainsbury (2007b) was able to show that the construction of arch-shape bulkheads significantly increases the ultimate failure pressure (up to 300 per cent) – when compared to flat bulkheads. This outcome is also confirmed by Cheung (2012) who showed that even with only a moderate curvature, arch bulkheads provide a doubling in loading capacity. This increased loading capacity is a direct result of the arched bulkhead shape being able to remain in compression (eg no tensile failure) and a greater thrust/normal force being generated at the wall abutment as shown in Figure 4.
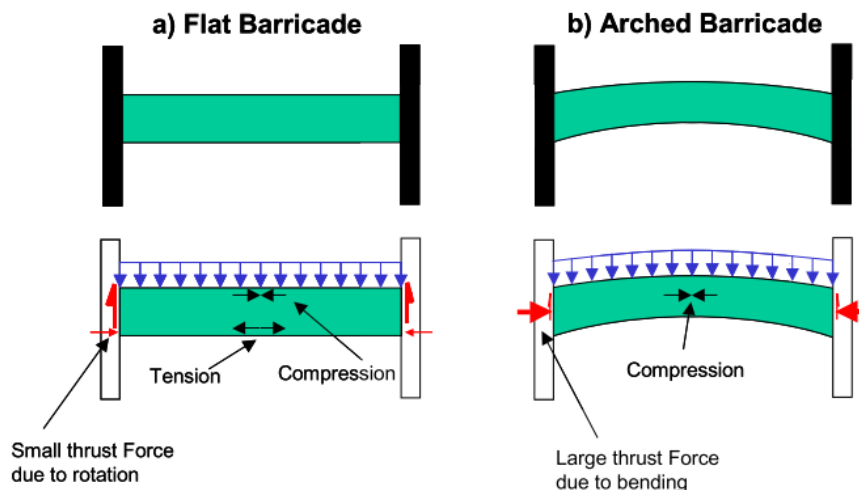
FIG 4 – Forces within a flat and arched bulkhead (after Revell and Sainsbury, 2007b).

An example of an arched and flat bulkhead failure mode is presented in Figure 5.
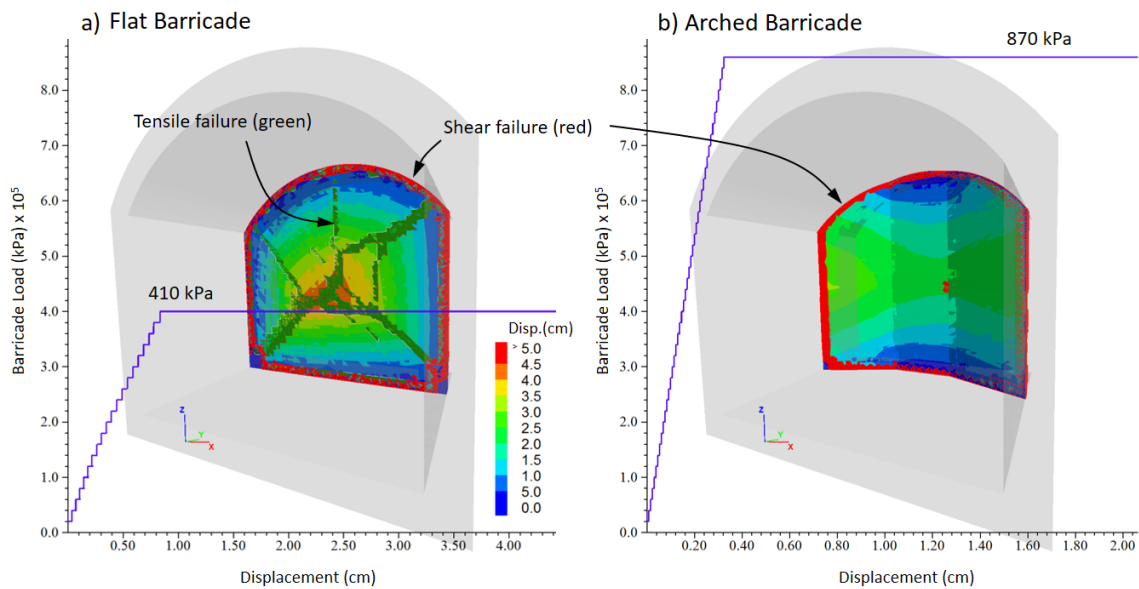
FIG 5 – Comparison of arched and flat bulkhead failure mechanism.

As such, it is usual to design and construct bulkheads with an arched shape. However, numerical models used to do this, up to this point (eg Helinski *et al*, 2011; Revell and Sainsbury, 2007b) have only considered that the drive walls are parallel or symmetric in nature. This is rarely the case. To study the effect of asymmetric drive geometry a series of simulations have been conducted that consider asymmetry in the sidewalls and back, together and separately. Figure 6 presents the results of a drive geometry that is telescopic on one side only and the back (drive roof).
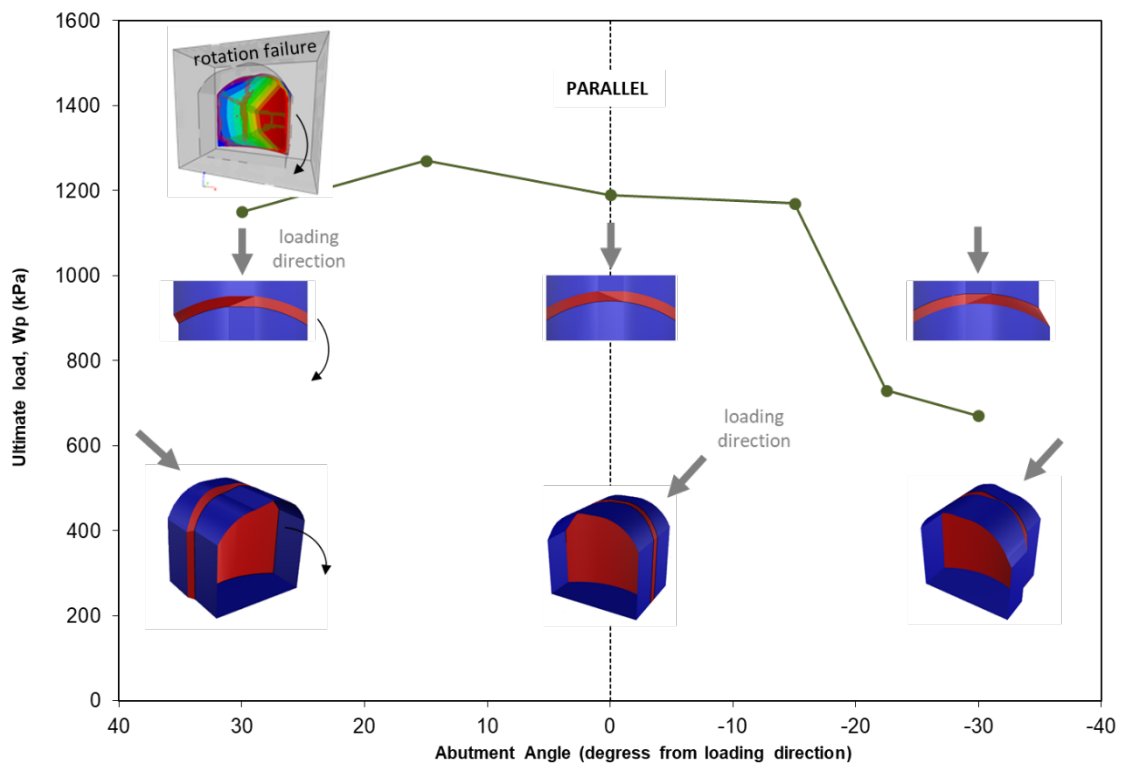
FIG 6 – Consideration of positive and negative sidewall abutment geometry on one sidewall only including the back of the drive.

A significant reduction in capacity is observed (40 per cent reduction) when one-sidewall/back has a negative abutment angle. However, the capacity is little changed when one-sidewall/back has a positive abutment angle. The mode of failure in this case is rotation/shear along the 'straight' sidewall

geometry – the positive sidewall abutment is 'locked-in'. When the drive back is not considered in the asymmetry of the drive, the simulation results presented in Figure 7 are observed.
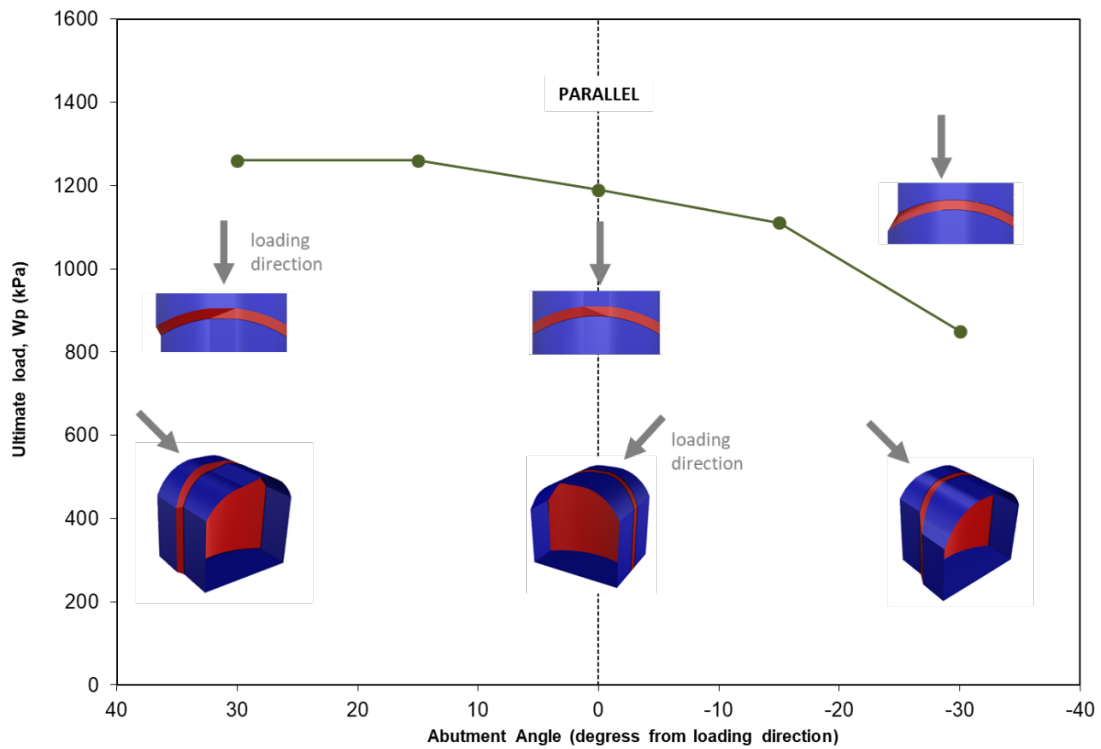
FIG 7 – Consideration of positive and negative sidewall abutment geometry on one side only.

In comparison to Figure 6, the results are less impacted, in relation to the reduction in strength, since the back of the drive provides additional resistance to moving since it can 'lock-in' the barricade.

When the back of the drive is considered only in relation to positive and negative abutment angles (Figure 8) a significant decrease is capacity is observed for the 30° negative abutment angle case.
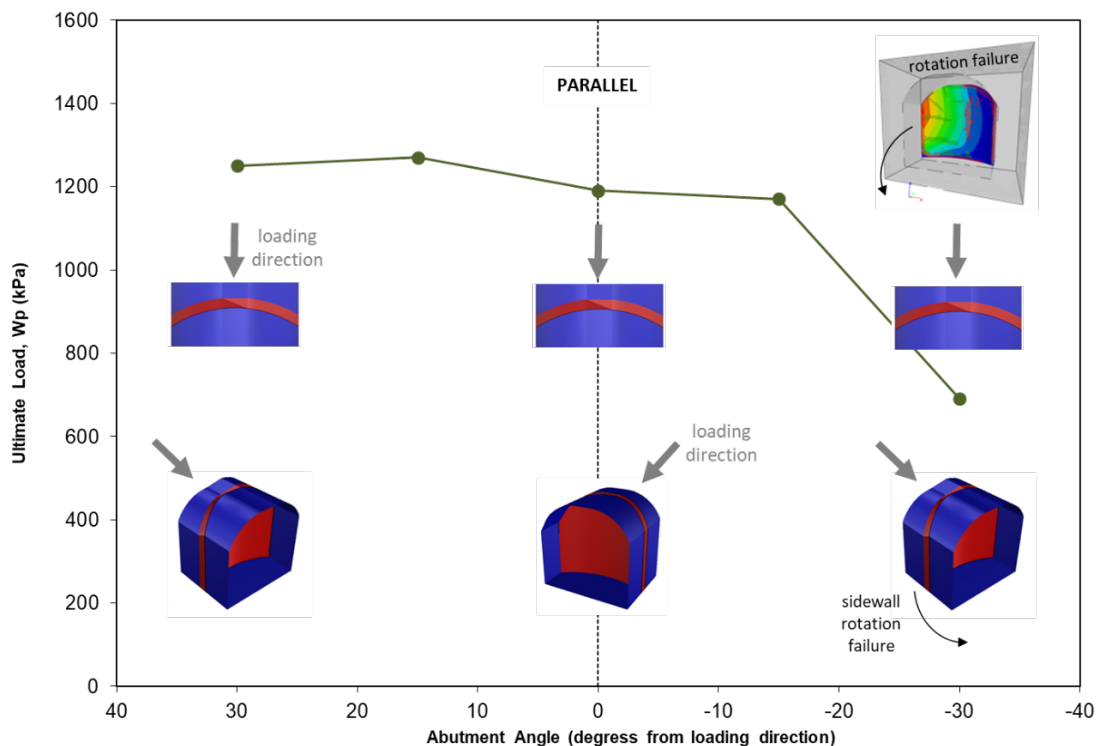
FIG 8 – Consideration of positive and negative back abutment geometry.

This result is similar to the results in Figure 6 which suggests that a negative abutment angle in the back of the drive has the most significant impact on reducing the performance capacity of the barricade.

BARRICADE DESIGN APPLICATION

The design charts provided in Figures 6, 7 and 8 are applied for a case the considers the as-built geometry of the drive. Through the consideration of the sidewall and back angles an optimum barricade location can be selected (Figure 9).
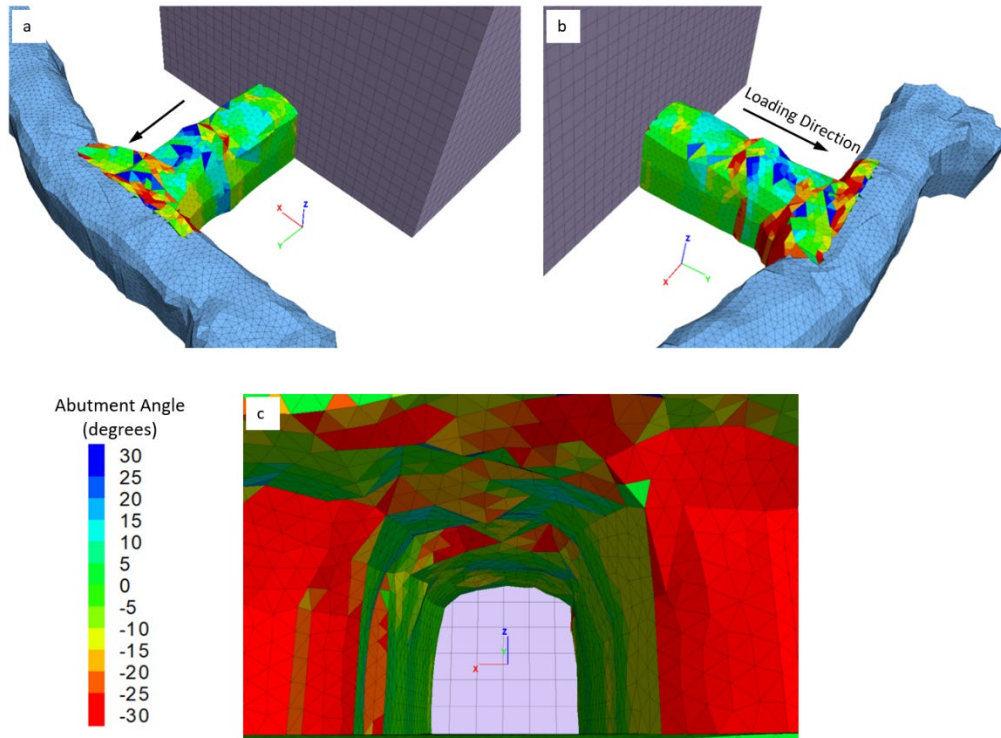
FIG 9 – Consideration of a negative abutment angle at the location of the barricade failure.

Once the location is selected, it can be accurately located by survey to ensure capacity is achieved. A review of the geometry of the drive in Figure 3 after the barricade failure suggests that a negative abutment angle is observed on the side of the barricade that failed. It is highlighted in red in Figure 10.

FIG 10 – Consideration of a negative abutment angle at the location of the barricade failure.

SUMMARY AND CONCLUSIONS

Design charts are provided based on a validated numerical modelling methodology to consider the ultimate capacity of prefabricated barricades installed in asymmetric drive geometries. It has been shown that capacity of the fibrecrete barricades can decrease by up to 50 per cent when negative abutment angles are encountered. A review of a recent barricade failure suggests that negative abutment angles may have impacted the ultimate capacity of the installed barricade leading to the failure. Based on the results the modelling the following guidelines are suggested for mining operations using prefabricated barricades:

- Barricade design must consider the location in relation to the as-built drive sidewall and back angles.

- Barricade must be relocated if any quadrant exceeds a negative (outward) angle greater than 30 degrees.

- Increase barricade thickness (capacity) if any quadrant has a negative (outward) angle between 15 and 30 degrees.

- Increase barricade thickness (capacity) if any quadrant has a positive (inward) angle greater than 30 degrees.

REFERENCES

Bridges, M, 2003. *A New Era of Fill-Retaining Barricades.*

Cheung, A, 2012. Arched and Flat Cemented Paste Backfill Barricade Walls, Thesis, Department of Civil Engineering, University of Toronto.

Cui, L and Fall, M, 2017. Modeling of pressure on retaining structures for underground fill mass, *Tunnelling and Underground Space Technology*, 69:94–107, doi: 10.1016/j.tust.2017.06.010.

Dalcé, J B, Li, L and Yang, P, 2019. Experimental study of uniaxial compressive strength (UCS) distribution of hydraulic backfill associated with segregation, *Minerals*, 9(3), doi: 10.3390/min9030147.

Department of Mines, 2020. Significant Incident Report No. 279: Paste Wall Failure.

Fahey, M, Helinski, M and Fourie, A, 2009. Some aspects of the mechanics of arching in backfilled stopes, *Canadian Geotechnical Journal*, 46:1322–1336, doi: doi:10.1139/T09–063.

Grabinsky, M W, Cheung, D and Bentz, E, 2014. Advanced structural analysis of reinforced shotcrete barricades, in *MineFill 2014, Proceeding of the 11th International Symposium on Mining with Backfill* (Australian Centre for Geomechanics: Perth).

Grice, T, 1998. Stability of Hydraulic Backfill Barricades, in *Sixth International Symposium on Mining with Backfill*, pp 1–5 (The Australasian Institute of Mining and Metallurgy: Melbourne).

Helinski, M, Wines, D, Revell, M and Sainsbury, D, 2011. Critical factors influencing the capacity of arched fibrecrete bulkheads and waste rock barricades, in *Minefill 2011, International Conference on Mining with Backfill*, pp 1–12 (The Southern African Institute of Mining and Metallurgy).

Helinski, M, Fahey, M and Fourie, A, 2010. Coupled two-dimensional finite element modelling of mine backfilling with cemented tailings, *Canadian Geotechnical Journal*, 47(11):1187–1200, doi: https://doi.org/10.1139/T10–020.

Karampinos, E, Baek, B and Hadjigeorgiou, J, 2018. Discrete element modelling of a laboratory static test on welded wire mesh, *Proceedings of the Fourth International Symposium on Block and Sublevel Caving, Caving 2018*, pp 735–746, doi: https://doi.org/10.36487/ACG_rep/1815_57_Hadjigeorgiou.

Li, L and Aubertin, M, 2009a. Horizontal pressure on barricades for backfilled stopes, Part I: Fully drained conditions, *Canadian Geotechnical Journal*, 46(1):37–46, doi: https://doi.org/10.1139/T08–104.

Li, L and Aubertin, M, 2009b. Horizontal pressure on barricades for backfilled stopes, Part II: Submerged conditions, *Canadian Geotechnical Journal*, 46(1):47–56, doi: https://doi.org/10.1139/T08–105.

Li, L, Aubertin, M and Belem, T, 2005. Formulation of a three dimensional analytical solution to evaluate stresses in backfilled vertical narrow openings, *Canadian Geotechnical Journal*, 42(6):1705–1717, doi: 10.1139/t05–084.

Revell, M and Sainsbury, D P, 2007a. Paste bulkhead failures, in *Minefill 2007* (Canadian Institute of Mining: Montreal).

Revell, M B and Sainsbury, D P, 2007b. Advancing Pastefill Bulkhead Design Using Numerical Modeling, in *Minefill 2007* (Canadian Institute of Mining: Montreal).

Sainsbury, D and Revell, M, 2007. Advancing pastefill bulkhead design using numerical modelling, *CIM*, 100(25).

Sheshpari, M, 2015. Failures in backfilled stopes and barricades in underground mines, *Electronic Journal of Geotechnical Engineering*, 20(1):191–212.

Sivakugan, N, Veenstra, R and Naguleswaran, N, 2015. Underground Mine Backfilling in Australia Using Pastefills and Hydraulic Fills, *International Journal of Geosynthetics and Ground Engineering*, 1(2):1–7, doi: 10.1007/s40891–015–0020–8.

Smith, J and Mitchell, R, 1982. Design and control of large hydraulic backfill pours, *CIM Bulletin*, 75(838).

Vivien Mine modelling back analysis to forecast ground conditions and ground support

G Sweby[1], P Mikula[2] and J Player[3]

1. Principal Consulting Geotechnical Engineer, MineGeoTech Pty Ltd, Perth WA 6000.
   Email: GordonSweby@minegeotech.com.au
2. Director, Mikula Geotechnics Pty Ltd, Kalgoorlie WA 6430. Email: pm@MikulaGeotechnics.com
3. Principal Engineer, MineGeoTech Pty Ltd, Perth WA 6000.
   Email: JohnPlayer@minegeotech.com.au

ABSTRACT

A numerical modelling back-analysis exercise was carried out at a WA gold mine at which early signs of seismicity (rock noise, scatts from active faces) were becoming apparent as depth of mining increased towards the 500 m mark. Some strain bursting had occurred and it was necessary to discover what the implications of this were for greater depth. The aim of the modelling was to:

1. Establish a correlation between observed ground conditions and model predicted damage, in overstressed areas of the mine.

2. Use this correlation to forecast rock mass damage and ground control requirements for proposed future stoping panels at greater depth.

Good correlation has been achieved between observed rock mass damage, and a 3D Finite-Element RS3 model, run in elastic mode. Two candidate stress field orientations were modelled. The model parameter best fitting the observations was the Strength Factor (SF), the ratio of strength/stress. The good match (correlation coefficient of 0.7) between observed and modelled suggests that the elastic approach is justified for the depth range and rock mass properties analysed. The correlation also enabled a link between observed damage and installed ground support performance.

Using the linear best-fit between observed and modelled, a forecasting exercise was carried out using the same RS3 model, modified to include future stoping. The resulting damage and ground support categories were obtained from the modelled SF for each proposed stoping level.

Also, a series of generic geometries was assessed to investigate the impact of varying stope face lead/lag distance, sill pillar height and stope pillar size, on ground conditions. The key finding of the generic geometries were:

- Ground support schemes have been defined for the expected conditions.

- All ore drives are expected to have significant damage in the backs and rehabilitation.

- Lead/lag distance not to exceed 10 m.

- Sill pillar/level intervals of less than 20 m require an increase in ground support scheme.

- Pillar sizes for maintaining footwall and hanging wall stability should be at least 10 m × 5 m.

INTRODUCTION

A numerical modelling exercise was carried out for Vivien Gold Mine, Ramelius Resources Ltd. The aim was to:

1. Establish a correlation between observed ground conditions and model predicted damage, in overstressed areas of the mine.

2. Use this correlation to forecast rock mass damage and ground control requirements for proposed future stoping panels at greater depth.

The damage forecast was then used to make adjustments to ground support schemes and recommendations for sequencing and layouts.

Stoping had progressed from the 380 level down to the 140 level (140 m below surface to 380 m below surface). The mining method, targeting the ~5 m wide, steeply dipping mineralised qua rtz

vein, is longhole open stoping with pillars. Limited floor benching and flatback stoping have been used also. The current void model is as shown in Figure 1.

Proposed future stoping is planned from the 120 level to the 980 level using similar mining methods (Figure 1).
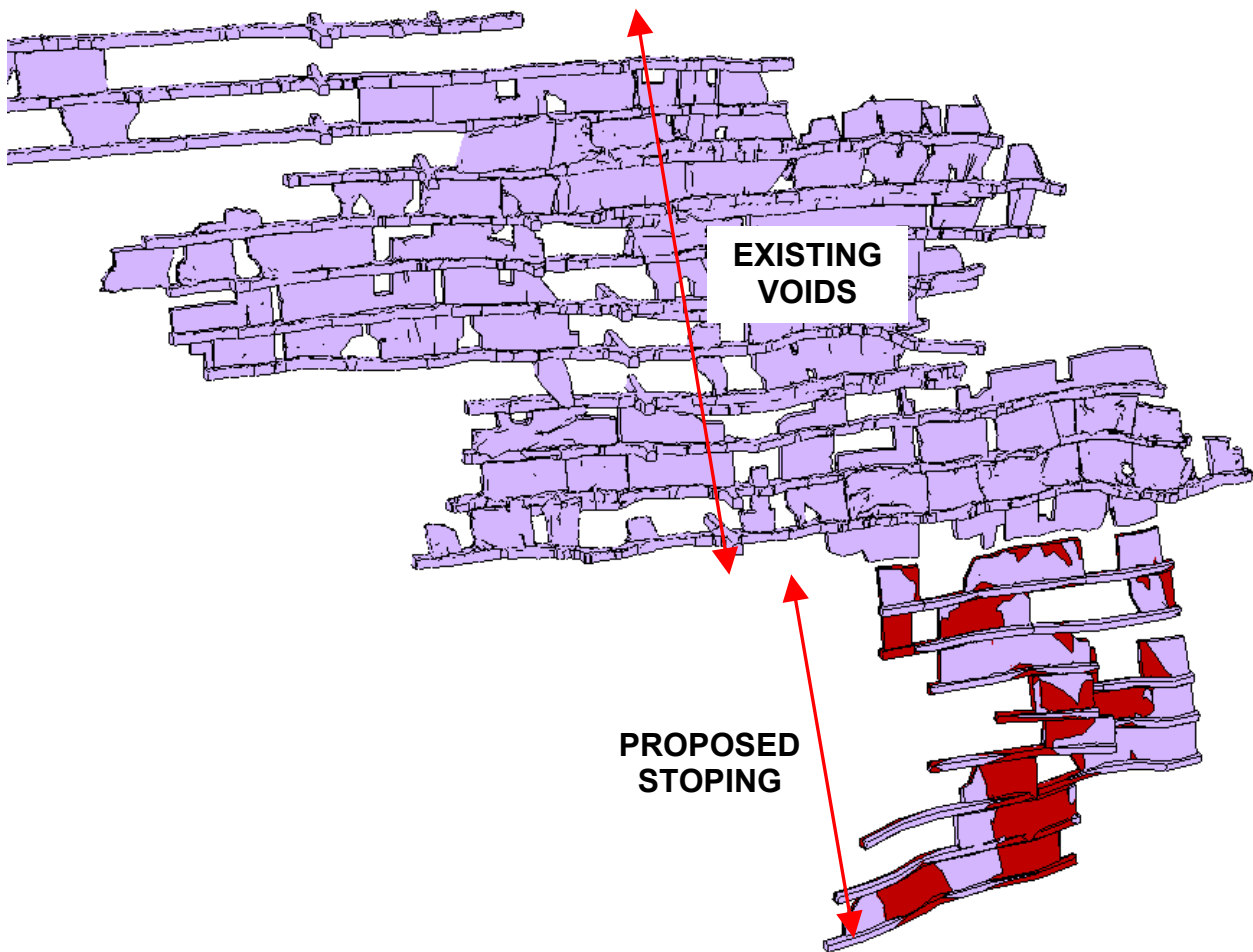
FIG 1 – Existing void model and proposed future stoping.

BACKGROUND

Geology

The geology applicable to this study consisted of a dolerite hosted quartz vein orebody, sheared in some areas but this was not captured in the model.

The dip of the orebody is steep, averaging 75° to the East (local mine grid). Maximum strike length is ~400 m. The orebody width ranges from ~1.5 m to ~5 m.

No significant geological faults occur in the region of interest and thus no discontinuities were included in the model.

Mining method and design

The mining method is primarily mechanised open stoping with upholes, from ore drives developed from centrally located access cross-cuts off a spiral decline in the footwall. The mine is accessed from a portal cut in the existing open pit void, Figure 2.

FIG 2 – Mine entrance portal in the existing Vivien Pit (courtesy of Ramelius Resources).

Ore drives are 4.5 m wide by 4.8 m high (asbuilt) with a level spacing of 20 m (floor-to-floor).

Semi-systematic island, rib and sill pillars and in some areas Cement Rock Fill (CRF) sill and rib pillars have been used to control hanging wall conditions, and all but final stopes are rock filled or CRF filled.

GEOTECHNICAL DATA

Rock mass quality

For the purposes of this study, the rock mass quality for both the host dolerite and the quartz vein has been assumed as Geological Strength Index (GSI) of 80 (Table 1), based on underground observations and core data.

TABLE 1

Rock Mass Strength and Elastic Parameters.

Lithology	GSI	UCS	Rock mass Modulus (GPa)[1]	Rock mass Poisson's ratio[2]	Density (t/m^3)
Dolerite Host	80	240	74	0.2	2.9
Quartz Vein	80	100	33	0.2	2.6

[1] Determined using Generalised Hoek Diederichs (Hoek and Diederichs, 2006) method, which is based on the UCS and GSI.

[2] Determined using Hoek *et al* (1995) method.

Intact rock strength

The uniaxial compressive strength of the vein (100 MPa) is significantly lower than the host dolerite (240 MPa), as documented in Table 1. This was captured in the model by means of the geologically interpreted solid used for mine design.

In situ stress

No stress measurements have been carried out on-site, so two stress assumptions were tested as part of the analysis (Tables 2 and 3), as follows.

TABLE 2

Base case stress field: maximum principal stress **oblique** to strike.

Principal stress	k-ratio	Azimuth	Dip
Maximum	2	050	00
Intermediate	1.5	140	00
Minimum	-	000	90

TABLE 3

Alternate stress field: maximum principal stress **parallel** to strike.

Principal stress	k-ratio	Azimuth	Dip
Maximum	2	000	00
Intermediate	1.5	090	00
Minimum	-	000	90

GROUND BEHAVIOUR – OBSERVATIONS

A series of 49 underground observations were documented, to categorise ground response and rock mass damage according to the damage scale given in Table 4. The numeric damage categories are allocated to allow numerical model calibration. As an example, the extent of damage described as Category 3 is shown in Figure 3.

TABLE 4

Damage Rating Scale.

Damage category	Description of damage
0	No distress
1	Minimal distress/perhaps rock noise, but no scats
1.5	Fractures producing a few small, isolated scats
2	Fractures producing more scats, but not bagged, quartz snow/dusting
3	Bagging up to 0.1 m in mesh/or loose to 0.5 m where no support/first distress in bolts (clamped, shearing)/quartz spitting with rock noise
4	Bagging up to 0.3 m in mesh/or loose to 1.5 m where no support or during rehab/bolts showing load/loss of a few bolt plates and rings/much spitting and cracking
5	Bagging up to 1 m in mesh/or falls/bolts heavily loaded/rehab definitely required

The timing of the observations was recorded at each observation point, so that a sequenced model could be set-up such that each observation was temporally as well as physically located in the model.
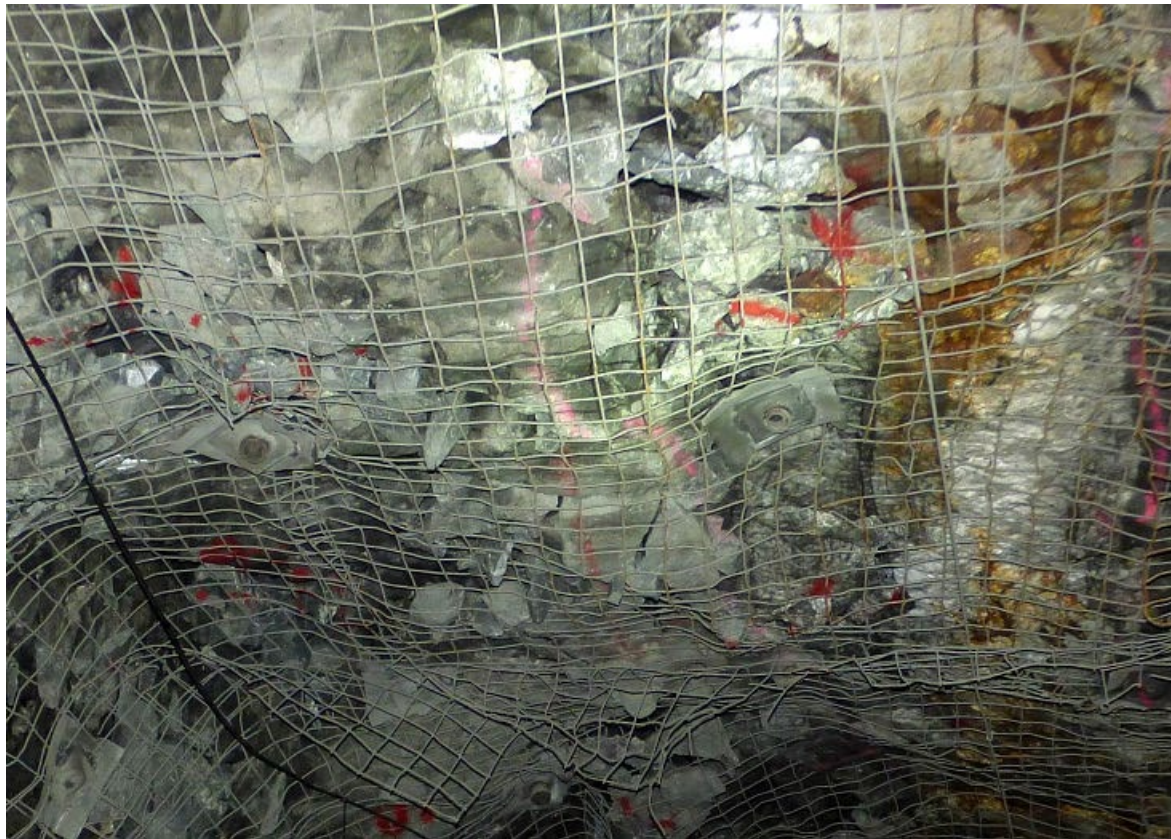
FIG 3 – Damage Category 3.

The observation points used in the correlation study are located as shown in Figure 4.
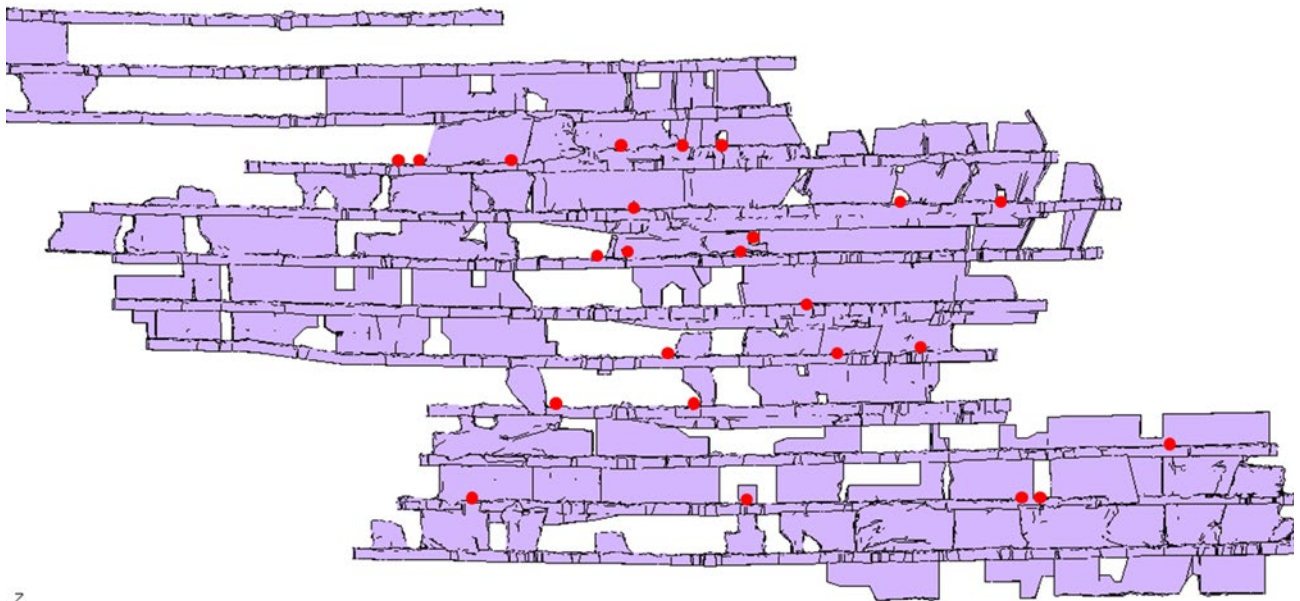
FIG 4 – Location of rock mass damage observation points used in model correlation.

NUMERICAL MODELLING – BACK-ANALYSIS

Key parameters and assumptions

The numerical model was built using the 3D finite-element software RS3 (Rocscience, 2020), based on the development and stoping voids provided by Ramelius Resources Ltd (Figure 1).

For the purposes of this assessment, it was assumed that the rock mass behaves linear elastically, with parameters given in Table 1. (This assumption would not be valid if it were a requirement to determine strains or displacements).

Evaluation criterion

To develop a correlation between damage rating observations and model results, several model outputs were tested, namely:

- strength factor (strength/stress)
- minimum principal stress
- elastic volumetric strain
- inelastic volumetric strain.

It was found that the most reliable correlation was obtained between damage rating and Strength Factor (SF). This factor can be equated to a Factor-of-Safety (FoS) against overstressing. A SF of <1.0 generally indicates failure, and values >1.0 indicate stability. A typical plot of SF at a stope brow is shown in Figure 5.
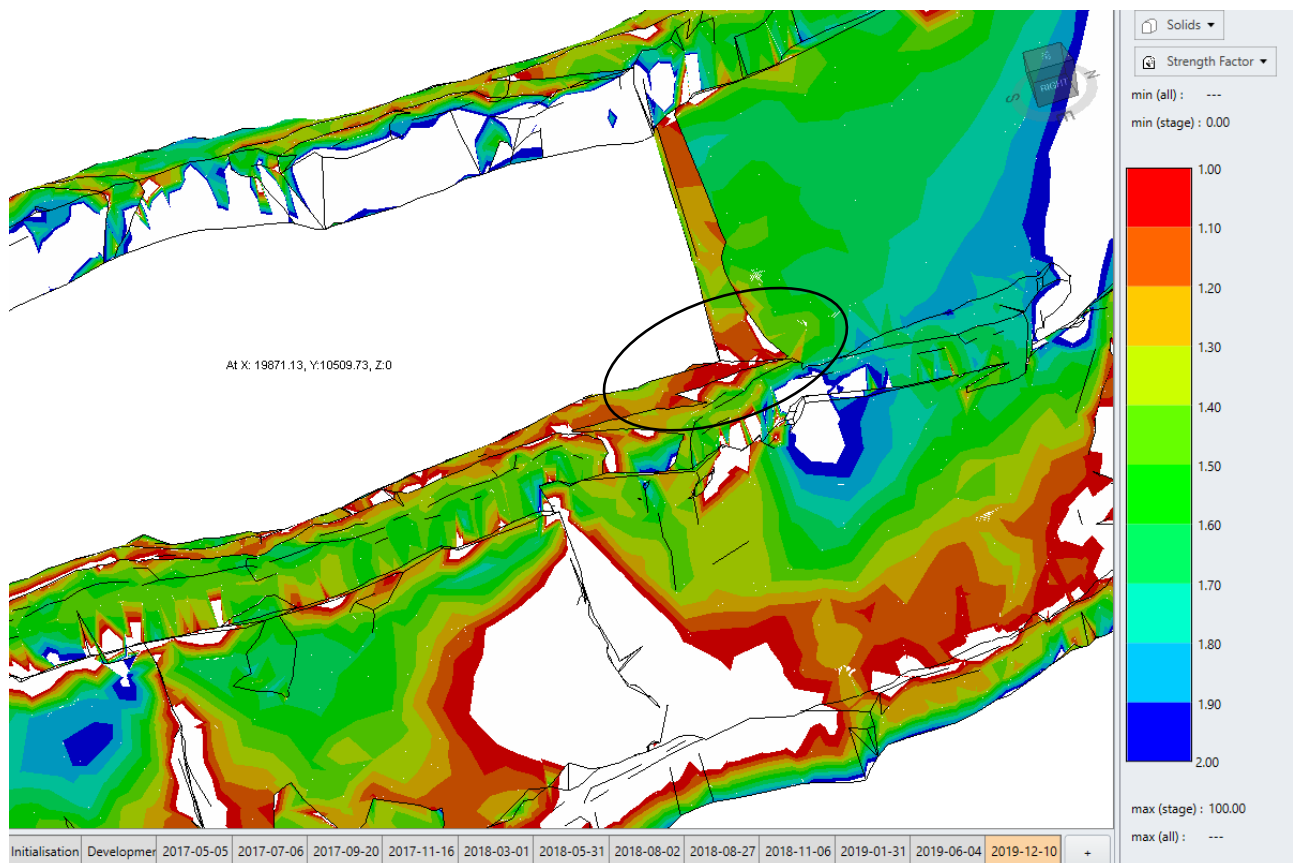
FIG 5 – Strength factor surface contours at a stope brow/ore drive intersection (ringed). Contour colours range from red (1.0) to blue (2.0), outside this range is shown in white (transparent).

Back analysis results

For the purposes of this back-analysis, the actual value of SF is less important than the **relationship** between SF and damage rating. From Figure 6 it can be seen that a good correlation exists between SF and damage rating for the base case stress field, with lower SF indicating higher damage, as would be anticipated. The correlation is slightly less (Figure 7) for the strike parallel stress field. The oblique stress field is thus adopted for the purposes of forecasting.
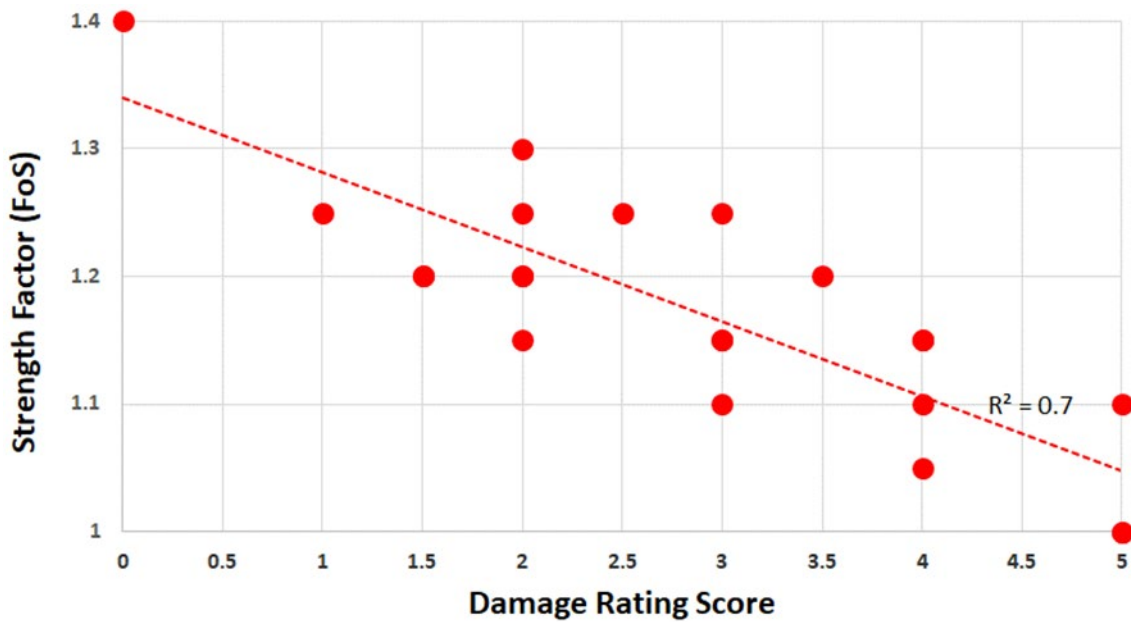
FIG 6 – Correlation between Strength Factor and Damage Rating for an oblique Stress Field.
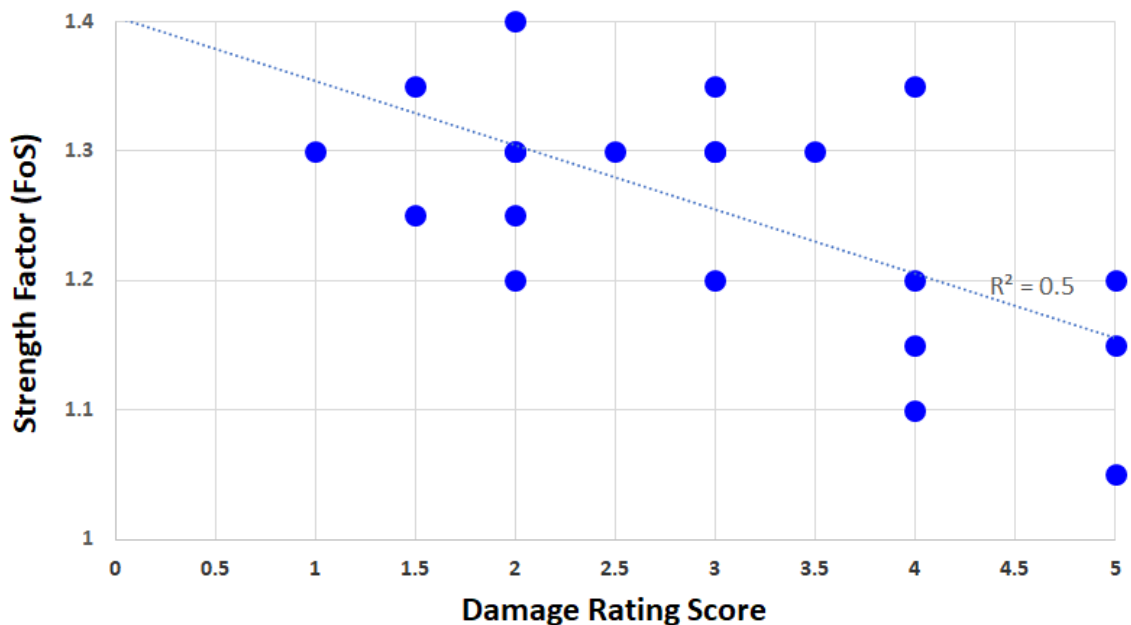
FIG 7 – Correlation between Strength Factor and Damage Rating for a strike parallel Stress Field.

DESIGN SPECIFICATIONS

Ground support

Based on the back-analysis correlation between damage rating and Strength Factor, forward analysis was carried out on a proposed 30-stope mining sequence. Each stope was a separate step in the model. Strength factors have been calculated along the ore drive and brow positions for each stope in the sequence, and the resulting predicted damage rating determined.

The ground control requirements required for each damage level (Table 1) was proposed based on the existing performance and experience in similar ground conditions.

Layout and sequencing

The model forecast the rock mass conditions in the ore drive, as capital development was not part of the project. All stoping voids were captured in the model. The final modelled stoping sequencing

to complete extraction followed that proposed by site, with guidance on the sequence provided from generic case modelling.

NUMERICAL MODELLING – GENERIC CASES FOR LAYOUT DESIGN

The establishment of a rock mass damage criteria allows a series of generic stope and pillar geometries to be tested to provide input into an improved mine planning process:

- stope brow lead/lag distances, 0–40 m tested
- sill pillar dimensions, 10–25 m tested
- stope pillar dimensions, 5 × 5 m to 15 × 10 m.

CONCLUSIONS

Good correlation has been achieved between observed rock mass damage, and a 3D Finite-Element RS3 model, run in elastic mode. The model parameter best fitting the observations was the Strength Factor (SF), the ratio of strength/stress. The good correlation (0.7) between observed and modelled suggests that the elastic approach is justified for the depth range analysed.

Using the linear best-fit between observed and modelled, a forecasting exercise was carried out using the same RS3 model, modified to include future stoping. The resulting damage and support categories were obtained from the modelled SF obtained for each proposed stoping level.

The forecast for the extraction has matched in a broad sense the actual rock mass response allowing for changes in the stoping sequence with ground conditions not as poor as the model suggested but the pattern of area that would be damaged matched.

The limitations of the work were the inputs to the model–stress gradient and orientation and rock mass strength.

The work in this paper highlights the use of observational rock mass damage and ground support scheme loading, compared to forecasts from three dimensional finite element modelling. The results were used to successfully provide extraction sequencing and ground support scheme upgrades for stoping at Vivien Gold Mine.

ACKNOWLEDGEMENTS

Thank you to Paul Marlow of Ramelius Resources for allowing the publication of this paper.

The full version of this paper is available from the MineGeoTech website.

REFERENCES

Hoek, E and Diederichs, M S, 2006. Empirical estimation of rock mass modulus, *International Journal of Rock Mechanics and Mining Sciences*, 43:203–215.

Hoek, E, Kaiser, P K and Bawden, W F, 1995. *Support of underground excavations in hard rock*, Rotterdam: Balkema.

RocScience, 2020. RS3 Version 4.003 – 3D Finite Element Analysis for Rock and Soil, www.rocscience.com, Toronto, Ontario, Canada.

Generation of 3D planar failure hazard maps for pit slope management

D E Tennant[1]

1. Principal Geotechnical Engineer, Newcrest Mining, Melbourne Vic 3004.
Email: david.tennant@newcrest.com.au

ABSTRACT

In the fields of geotechnical engineering and slope management, various software packages are used to assess the behaviour or propensity for a slope to fail. Traditional kinematic analysis calculates the probability of failure of design sectors with respect to dominant structural set orientations. A novel methodology is provided here to view potential hazardous slope behaviour in 3D, allowing engineers to make informed decisions regarding various pit slope geometries. Apparent dips are calculated for every point in space with respect to every slope orientation of the entire pit surface/design, specifically in reference to bench and inter-ramp planar failure mechanisms. Implementing a proactive approach to slope design will not only lead to early mitigation of risk but can also add direct value by enhancing or improving upon slope angles for earlier access to ore. From a safety perspective, identification of unfavourably oriented slope geometries can be dealt with before failure occurs. This methodology relies on a strong understanding of the existing rock mass anisotropy, particularly behind the face, thereby removing some of the uncertainty surrounding pit design as well as presenting engineers with an additional means to manage risk.

INTRODUCTION

Traditionally, 2D cross-section analyses are conducted to assess the kinematic behaviour of any given slope. Unfortunately, most input data are projected onto a 2D plane where apparent thicknesses of lithological units and apparent angles of faults can be misleading and inaccurate.

The objective of assessing structural and modelled data against any pit surface, whether it be a pit design or pushback, is to proactively assess pit slopes and their kinematic behaviours prior to mining, especially with regards to the most dominant failure mechanisms observed. Similar methodologies have been attempted (Bester *et al*, 2015; Basson *et al*, 2016), however the methodology presented here builds on and focuses primarily on planar failure in 3D, thereby improving upon the traditional 2D kinematic analysis.

METHODOLOGY

When attempting to create a 3D hazard map, all structures and structural orientations need to be considered. The first step involves collating mapped surface structures as well as structures that may have been logged behind the face to further understand the orientation of non-daylighting structures. Creating a continuous fabric that extends beyond and behind the pit face/design allows the user to assess angles in all directions that may not otherwise be considered (Figure 1).
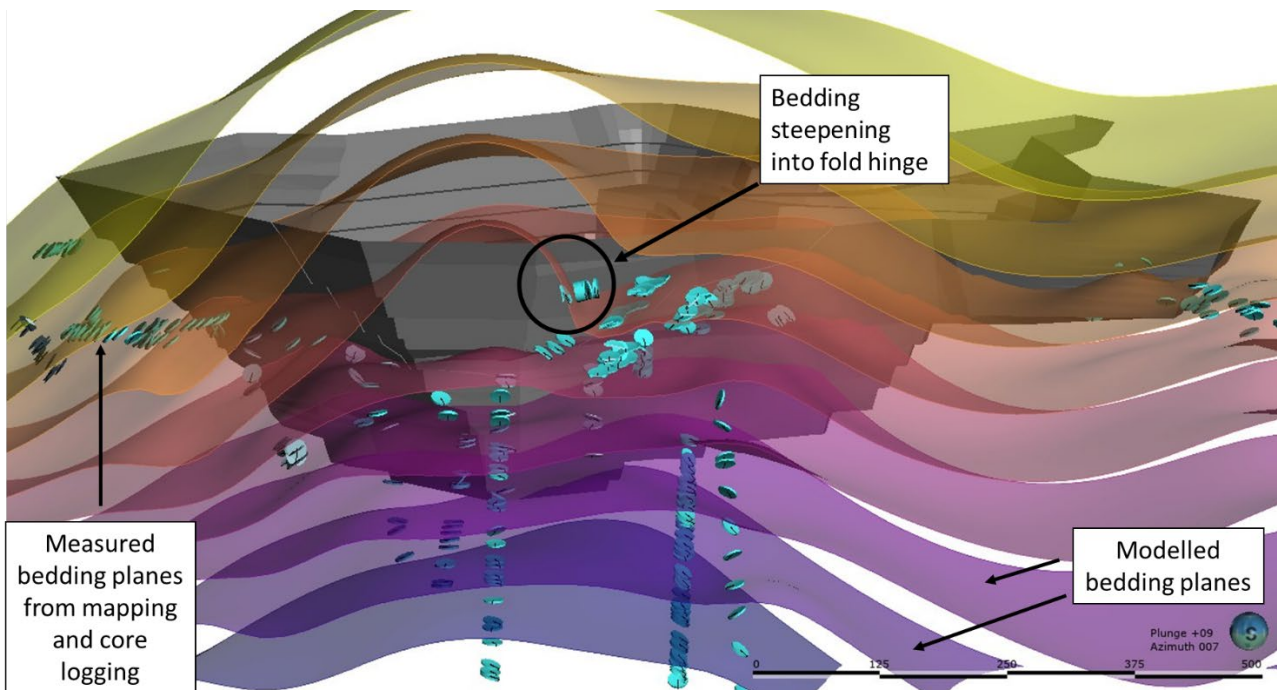
FIG 1 – Form interpolant of bedding planes making use of surface mapping and drill hole logging data. A pit design shell is shown in relation to the modelled planes.

Secondly, it is important to consider the trigonometry of planar failure mechanisms which forms the basis of this methodology. An apparent dip for every structure with respect to every point on a pit surface needs to be calculated. This is represented in 2D with the following formula:

$$\alpha = Tanx^{-1} \left(sin\ \beta \cdot tan\ \delta \right) \tag{1}$$

where:

α   is the apparent dip angle

β   is the difference in dip direction

δ   is the true dip of the measured structural feature (ie vein, joint, fault etc)

Equation 1 presents a problem where data cannot be displayed in 3D. This is largely due to the fact that the 'lesser/smaller' angle between two oriented planes needs to be calculated first, and the *sine* of that angle would only render a positive result, meaning planes can only dip out of the face. While this is not true in nature, the cosine of the angle is needed to render negative values in Equation 2:

$$\alpha = Tanx^{-1} \left(cosine\ \beta \cdot tan\ \delta \right) \tag{2}$$

There is another consideration that needs to be made before producing the most accurate result and this involves contouring. Usually, interpolators are used to contour single parameters (eg elevation in digital elevation models). Seeing as the concern is with unfavourable apparent dip angles behind the face, a radial basis function interpolator needs to be used to interpolate two parameters (ie apparent dip and elevation) at any given location in X and Y coordinates (Leapfrog Geo provides this capability). The result from such an interpolation can be seen in Figure 2. When various rock mass properties for the structural feature in question are included, colours can be assigned. For example, if defect surfaces are assumed to be cohesionless with a friction angle of 33°, then everything greater than the friction angle and less than the slope angle is contoured in 'red' (Figure 2). This provides the mechanism for planar failure to occur and can now be viewed in 3D.
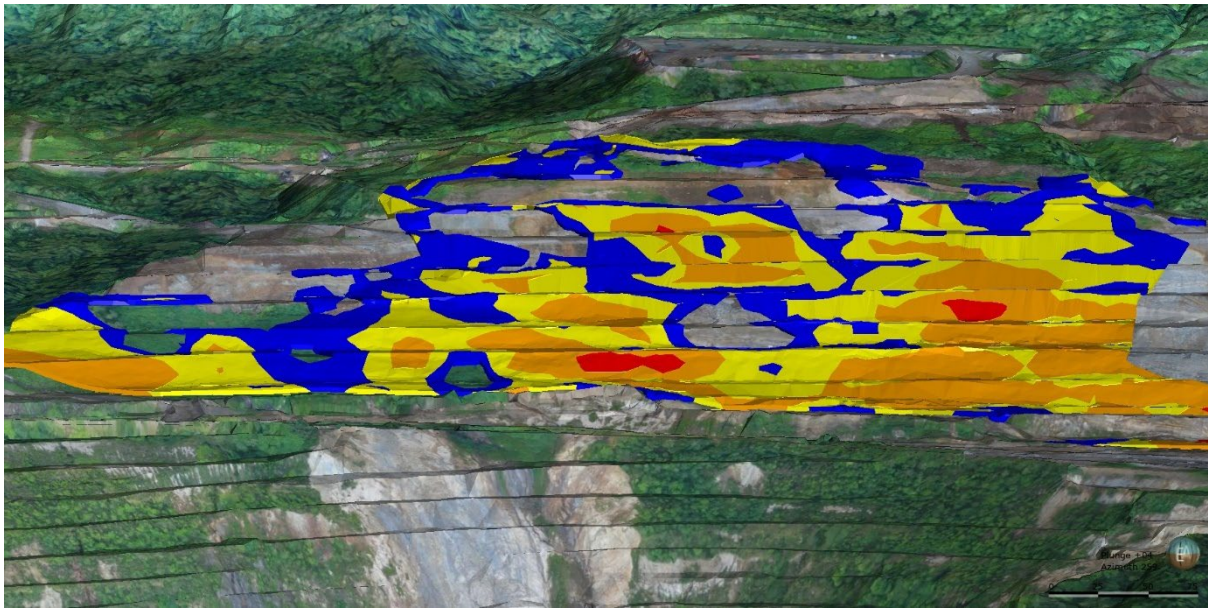
FIG 2 – A 3D interpolant of apparent dip angles evaluated on a lithology that has experienced historical planar failures. All benches in red have the propensity for planar failure.

This methodology can also be used as a back analysis or calibration tool. If you can replicate historical failures and more importantly, the exact position of historical failures, then it's safe to assume that the methodology can be used for forward analysis. Having this information prior to mining can significantly enhance slope performance. Additionally, if large sectors have favourably oriented structural sets and anisotropies, steepening the slope angle can improve upon the waste to ore ratio thus adding direct value to production.

It is important to note that this methodology does not replace the full suite of kinematic analyses. However, if planar failure is the dominant failure mechanism, zones of unfavourably oriented structural sets can be 'flagged', and any pit surface/design can be quickly divided into geotechnical design sectors.

CONCLUSION

This methodology represents an alternative means towards targeting zones of unfavourable kinematics in open pit environments. Engineers are often reactive to damaging events and 'fighting fires' is a common practice. Early identification of unfavourable structural sets can also assist in the modification of slope angles as well as provide justification for future slope optimisation. The understanding of rock mass anisotropy, particularly behind the face, and its interaction with unfavourable slope geometries has been problematic for geotechnical engineers for some time. This methodology removes some of the uncertainty surrounding non-daylighting structures and is an important tool for pit slope management and even pit slope design.

REFERENCES

Basson, I, Creus, P, Gabanakgosi, K, Mogorosi, O and Bester, M, 2016. Defining geotechnical design sectors: Apparent dip analysis at Jwaneng Mine, Botswana, *Proceedings of the First South African Geotechnical Conference*, pp 93–98.

Bester, M, Basson, I and Koegelenberg, C, 2015. A practical methodology to define geotechnical design sectors in structurally-controlled anisotropic environments, *Slope Stability 2015 Conference*, The South African Institute of Mining and Metallurgy.

Integrated geotechnical audits and benchmarking for mining operations

J J Van Wijk[1] and A R Penney[2]

1. General Manager, AMC Consultants Pty Ltd, Adelaide SA 5000.
   Email: jvanwijk@amcconsultants.com
2. Technical Manager/Director, AMC Mining Consultants (Singapore) Pte Ltd, Singapore 018937.
   Email: apenney@amcconsultants.com

ABSTRACT

Successful management of geotechnical risk at a mining operation is more than just having a good ground control management plan or using advanced numerical modelling and the latest monitoring technologies. The fundamental requirements for effective geotechnical risk management include identification of potential failure modes, identifying and implementing appropriate controls, and demonstrating the effectiveness of those controls.

Effective geotechnical risk management requires an integrated approach by confirming that appropriate risk management systems have been identified and implemented (management plans, procedures etc), and that these systems are executed consistently in the field across all working areas.

Development of a thorough integrated auditing process executed by an experienced team of technical subject matter experts with substantial operational knowledge, provides a more complete picture of catastrophic hazard management. Following consistent evaluation criteria allows benchmarking of systems and implementation compliance between the sites being audited, and the results can then be ranked against other operations in an industry database.

INTRODUCTION

Geotechnical risk management requires a holistic approach. Implementing the latest technologies such as advanced numerical modelling, hi-tech rock mass classification systems such as acoustic scanners, or state-of-the-art monitoring is no longer sufficient to manage the risk.

Fundamental to the holistic approach is the identification of the hazards, understanding the geotechnical characteristics and failure modes, identifying and implementing effective controls, and using a verification and reporting process that provides for identification of ineffective controls and continuous improvement to improve control effectiveness.

GEOTECHNICAL RISK

The focus of geotechnical risk management is often on identifying failure modes that can result in a fatality or multiple fatalities. The process of fatal and catastrophic hazard management and assurance is shown in Figure 1, and summarised below.

FIG 1 – Conceptual approach to assurance for fatal and catastrophic hazard management.

When reviewing the effectiveness of the risk assessment process, it is necessary to consider the range of inputs and systems which formed the basis of the risk assessment. Inputs often include regulations, standards, corporate guidance, ICMM (International Council of Mining and Metals)

guidelines, discussions with key stakeholders, and evaluating whether appropriate technology has been implemented.

Various systems are used to outline the processes of managing and communicating the risks. These systems take the form of hazard management plans, design guidelines, procedures, training content, and verification procedures. Only once the inputs are clearly defined, and systems have been developed and implemented, can their effectiveness in managing geotechnical hazards and mitigating the risk be measured.

The primary focus of the geotechnical auditing process is to provide assurance that failure modes and their related hazards have been identified, justified, and are controlled, with appropriate controls in place to prevent failure, and mitigate potential consequences.

There are nine key aspects to geotechnical risk management (the nine 'S's'):

1. Stress/strain – is the *in situ* stress state well understood and is the knowledge used to support design decisions?

2. Structure – have geological structures been identified, analysed, and characterised?

3. Strength – have the material properties and failure criteria been determined for the rock mass?

4. Size – has the balance between reducing the size of access ways and mining fronts for stability, with mining fleet and optimised production targets been adequately considered?

5. Sequence – optimal extraction sequence is key to managing geotechnical hazards.

6. Support – design, installation, testing, and monitoring of ground support are key to reducing geotechnical risk.

7. Surveillance – geotechnical instrumentation, inspections, damage mapping, QA/QC testing, internal and external auditing and review etc, are essential for conducting back analysis, assessing effectiveness, and refining designs.

8. Staff – experienced and skilled geotechnical teams and good documentation and processes make for safe operations.

9. Studies – pre-feasibility and feasibility studies are critical to justify a mine, but investigations (including analyses and data interpretation), reconciliation, and optimisation studies must continue throughout the mine life.

AUDITING AND VERIFICATION

Using subject matter experts who are independent from the operation with relevant experience in geotechnical engineering operations and studies is critical. Independence from the site allows an unbiased view of the performance. Numerous examples of audits completed by people following a set process with no knowledge of operations and studies exist, with many not providing the value necessary for real improvements at the operations.

Ensuring consistency in a geotechnical operational audit is key. As audits and verifications typically look at operational safety and performance, AMC Consultants has defined topics with questions to test each topic. This process not only looks at the nine key aspects outlined above, but the processes used in the updating of this knowledge, the communication of the design requirements to key staff, and the operational influences that affect the design recommendations. The key focus of this process is to ensure that the process outlined in the system documents can be demonstrated and verified via an in-field integrated audit.

The topics include:

- Geological/geotechnical knowledge.

- Development and maintenance of a geotechnical model.

- Mine planning and design.

- Mining operations.

- Operational performance monitoring and reporting.

- Ground support.

- Hazard management processes.

- Drill and blast.

- Back analysis and reconciliation.

- Training and competency.

- Backfill and inrush.

Assessments of compliance are often graded as yes or no responses. However, this approach does not allow for items which are applied in principle, but lack clear guidelines or documentation, or where the in-field practices mismatch the procedures. Using a three-tier system allows better definition of full compliance, partial compliance (where small gaps or opportunities for improvement are observed, but the intent of the audit item is largely being met), and non-compliance. Table 1 shows results from an audit completed on an underground operation. The results also include simple charts for the overall site performance (Figure 2). A detailed breakdown of compliance grades is also provided on each section showing the overall system and implementation compliance, results per category, and details of findings/recommendations for urgent, moderate, and minor attention (Figure 3).

TABLE 1

Summary of auditing and verification process

Section	Compliant	Partly Compliant	Non-Compliant	Compliant Only	Compliant and Partly Compliant
1 – Mine Planning and Design	18	3	0	86%	100%
2 – Geotechnical Knowledge and Model	8	2	3	62%	77%
3 – Operations (Control)	11	3	0	80%	100%
4 – Operations Performance Monitoring	13	4	0	78%	100%
5 – Ground Support	15	6	2	67%	92%
6 – Management of unstable rock	3	4	1	38%	88%
7 – Operations (Drill and Blast)	9	1	0	90%	100%
8 – Design Confirmation and Back Analysis	3	5	0	38%	100%
9 – Training and Competency	3	2	0	60%	100%
10 – Backfill	24	4	4	75%	88%
11 – Inrush	10	2	4	67%	78%
Summary	117	36	14	71%	92%
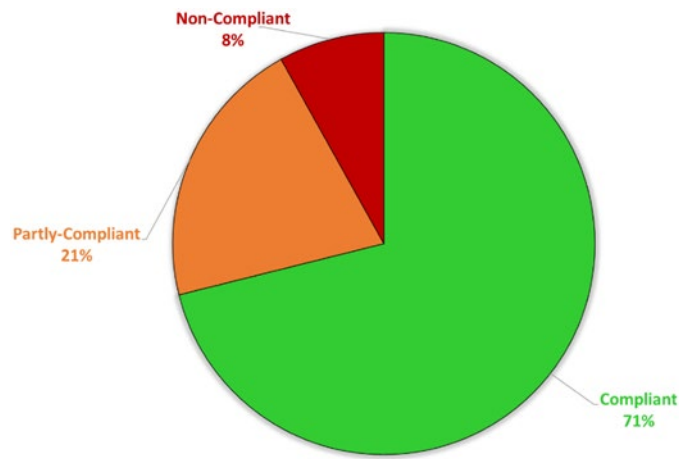
FIG 2 – Pie chart illustrating overall audit result.

FIG 3 – Breakdown of individual sections and score.

With any line item identified as partly compliant, or non-compliant, it is essential that the team completing the audit outlines the reasoning and provide an agreed solution and time frame to help bring items into full compliance.

A key aspect of demonstrating the overall compliance against others in the industry is demonstrated in Figure 4. AMC maintains records of geotechnical audits to show how the performance compares to other sites globally. The benchmark database maintains confidentiality of each mine site – however, in some cases where a mining company has requested multiple sites be audited, AMC can show the comparisons between the sites to management groups.
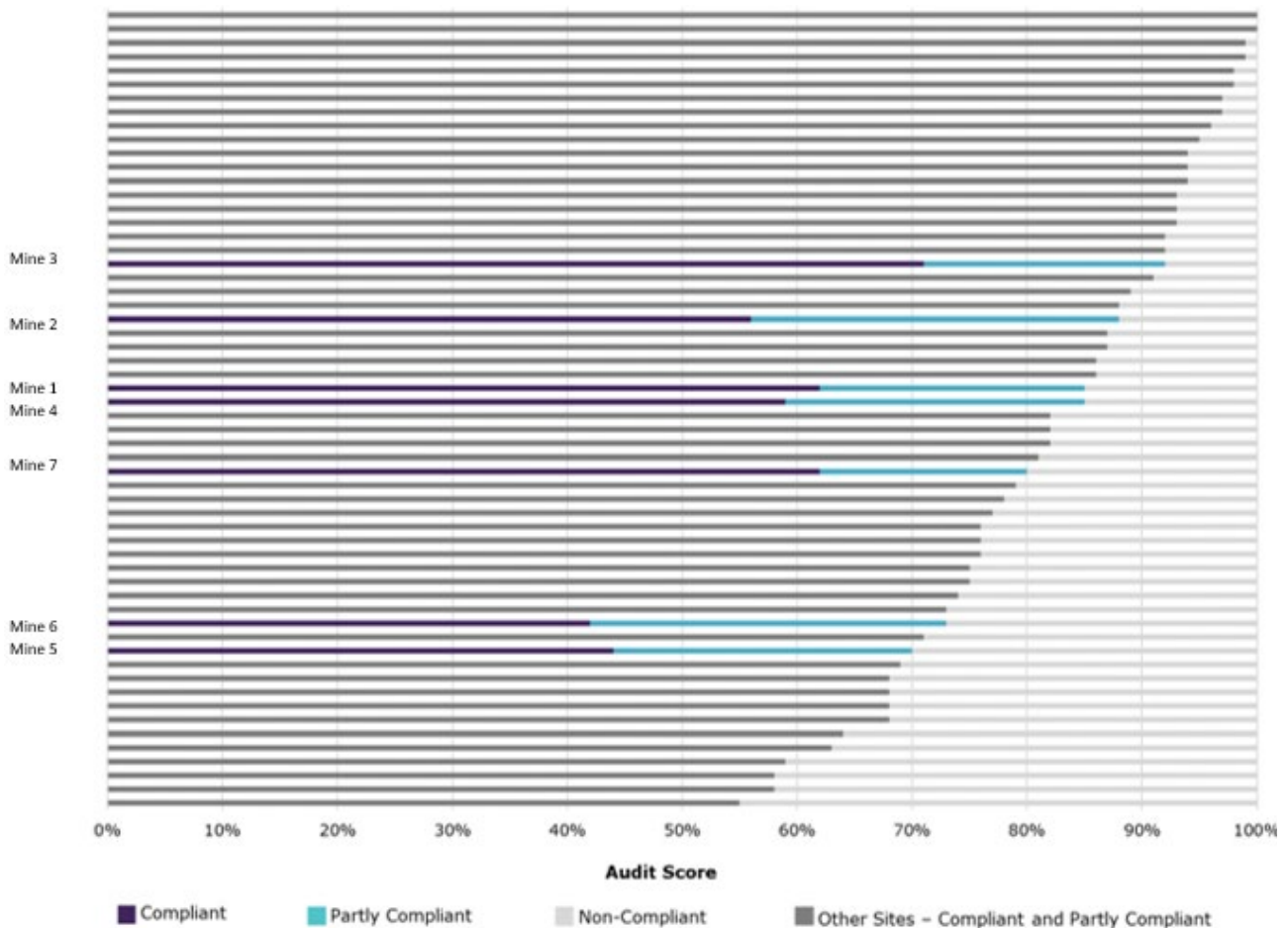
FIG 4 – Example of benchmarking audit results.

CONCLUSIONS

Using subject matter experts who are independent from the operation with relevant experience in geotechnical engineering operations and studies is critical. Independence from the site allows an unbiased view of the performance.

The nine 'S's' provide a useful basis for understanding and managing geotechnical hazards. If the items contained in the nine 'S's' are not well understood, it is likely to result in an inadequate understanding of the rock mass, the relevant failure modes, and ultimately how to manage the hazards.

Adopting appropriate risk management processes, and identifying appropriate controls that are specific, measurable, and auditable is a key component for effective risk management. The ICMM provides a relatively straightforward process to follow.

Using a consistent, comprehensive auditing process to verify effectiveness of the hazard management strategy enables audit results to be compared across different operations and jurisdictions.

In addition to the outcome of the audit, an audit report should include the agreed steps to rectify or improve deficiencies that were identified during the audit, with a proposed time frame for the improvements to be implemented.

ACKNOWLEDGEMENTS

BIBLIOGRAPHY

Government of Western Australia, Department of Mines, Industry Regulation and Safety. *Geotechnical Considerations Underground – Audit Guide*. Available from: www.dmp.wa.gov.au.

International Council on Mining and Metals (ICMM). *Critical Control Management Implementation Guide*. ISBN:978-1-909434-21-9. Available from: ICMM, www.icmm.com

International Organization for Standardization (ISO), 2018. *ISO 31000:2018 Risk Management Guidelines*. Available from: ISO, www.iso.org.

Photogrammetry-based mapping techniques in slope stability management

D Wang[1] and T Wang[2]

1. MAusIMM(CP), RPEQ, Principal Geotechnical Engineer, Inspiration Seven Pty Ltd, Brisbane Qld 4000. Email: support@inspirationseven.com
2. Data Analysis Engineer, Inspiration Seven Pty Ltd, Brisbane Qld 4000. Email: inspirationsevenau@gmail.com

ABSTRACT

Photogrammetry-based techniques supported by traditional mapping tools are more frequently used for open pit geotechnical mapping. It fundamentally involves the collection of geological, structural and rock mass data from pit batters when safe to do so. These are essential components for refining and implementing continuous improvements to geotechnical models. The geotechnical model is used to review bench performance, optimise geotechnical design parameters, interpretation and analysis of pit slope stability. This paper is a case study of implementing different pit mapping methods at Mount Carlton gold mine, North Queensland. It critically reviews the tools required, including the Brunton compass, mobile application Clino, geotechnical data mapping software CloudCompare (2015) and Sirovision software. The review compares the image precision, structural measurements and data analysis. The review also underlines mine site management philosophy for safe geotechnical data collection to identify in-pit geotechnical hazards and the mitigation of potential slope instability.

Sirovision is a remote sensing system for site geology mapping and interpreting geotechnical characteristics of exposed mining faces. The system utilises off-the-shelf digital SLR cameras to capture stereo photographs of the rock face and uses the latest image processing technology to generate accurate 3D models. These 3D models are digitally analysed using computational geometry to extract unbiased and accurate geological and geotechnical data.

CloudCompare processes high accuracy 3D dense cloud rock surfaces reconstructed with photogrammetry software to extract the geological planes using the FACET or Compass plugins. The major discontinuity sets can be observed and the orientation (dip/dip direction) obtained from the algorithm is accurate and reliable for geotechnical assessment, including kinematic and rock slope stability analysis.

INTRODUCTION

The Mt Carlton operation (MCO) is located in Northern Queensland Australia, and has run as an open pit mine since commencing in 2012. The mine is approximately 150 km south-south-east of Townsville. The current V2 open pit has been designed and mined in stages. Stages 1, 2, 3 and 4 are approved for open pit mining under the current Environmental Authority (EA).

Pit geology model comprising lithology, alteration and structural geology data. The geology model is integrated with geotechnical and hydrogeological data to develop geotechnical domains and geotechnical model for slope stability analysis and the mine design parameters. Previous geological mapping and interpretation from James Cook University (JCU) summarised the deformational history as follows: D1: High-angle normal faulting in response to E-W extension; D2: Normal faulting along low-angle (ie partly layer-parallel) detachment faults and high-angle antithetic normal faults, in response to E-W extension; D3: High-angle normal faulting in response to N-S extension; D4: Strike-slip faulting along dyke margins; D5: Emplacement of WNW trending dykes (felsic). The V2 pit lithological domains are tectonic-lithological blocks controlled by the shallow east dipping D2 faults and sequence from the base upwards.

The geotechnical hazards associated with operation adjacent to slope faces typically include rockfalls and structurally controlled instabilities such as wedge, planar slip, and toppling failures. Detailed information and knowledge of batter/slope face rock mass conditions and geological structure features are essential and critical to validate slope design parameters and assess the stability of pit slope.

THE IMPORTANCE OF PIT MAPPING

Following mine faces exposure, pit wall systematic mapping to obtain discontinuities' orientation, spacing and length of planes, is the main method to determine the sizes, shape and orientations of daylighted structures. Based on the mapping data, kinematic analysis will identify the modes of failure and provide the possibility for the mine to establish appropriate mine controls to mitigate the hazards that may result from these modes of failure.

Rock mass behaviour and discontinuity characterisation are the primary objectives of data acquisition for rock mechanics engineering. An ongoing review of the geotechnical database through mapping of geological and geotechnical features is critical to support building geological and geotechnical modelling and further facilitating mine design and planning and operations. Mapping provides important data to assess the suitability of the current mine design and the general stability of the mine slope, which influence slope excavation and the productivity of mining.

PIT MAPPING METHODS AND TARGETS

Field measurements for slope discontinuities present in rock mass play a pre-eminent role to evaluate the properties of the rock mass. Face mapping (line scan and window mapping), photogrammetry (Sirovision, Adamtech or CloudCompare) or laser scanning systems (I site scan etc), are the principal methods used in the mining industry for the collection of in situ data for verification of geotechnical parameters and the as-built slope configuration.

The face mapping, photogrammetry or laser scanning systems shall demonstrate the following requirements to help geotechnical engineers identify and report (escalation) of changes to stratigraphy/structural models and pit configurations that are deemed to be safety and/or slope stability:

- The scope and requirement of data collection shall be focused on the geotechnical design parameters which can influence the potential slope stability and failure mechanisms.

- Routine data collection, analysis and reporting shall be compatible with the development rate of the slope and suitable to identify and respond to the development of potential failure mechanisms.

- Selection of data collection technique shall satisfy the accuracy and precision for capturing the required level of detail of the geotechnical characteristics material to slope stability.

- Targeted data collection shall also be conducted if anomalous or unexpected slope performance is detected or slope failure occurs.

Brunton compass and mobile APP FieldMove Clino

These two methods are adopted by the site for application in areas:

1. Batters are free from rockfall and other hazards, which is suitable for a closer standoff distance to conduct face mapping. Discontinuities are in bench scale persistence. These two methods mostly apply to wall sign-off and quick kinematic analysis for bench faces.

2. Scanline mapping and window mapping have been used in mining and civil engineering for many years, which involves measuring and recording the attributes of all the structures that intersect a given sampling line or collecting all the structural data above a given cut-off size from within a specified area of a rock face.

Petex (2016) has developed a digital compass-clinometer application (FieldMove Clino) for field geologists to gather geological data on smartphones, which has the following features:

- Digital compass clinometer for data capture on your smartphone.

- User defined list of rock units or stratigraphy.

- Digital notebook and camera within the app.

- Import your basemap to work offline, or use online map services.

- Automatic positioning using the GPS in your device or manual over-ride.

- Easy editing of data and projects.

- Export your data as MOVE or CSV files to other applications such as MOVETM.

- Expanded library of symbols for planar and linear data.

- Stereonet display of geological data.

Site mapping data comparisons (refer to Table 1) between the two methods indicate the difference in Dip and Dip direction is within five degrees.

TABLE 1

Mapping comparison between compass and APP Clino.

Temporary Southern Wall	56 / 194	Design = 60/194				
RL: 476mRL						
Mapping Point		Compass		Clino App		
Foliation	Dip	Dip Direction	Dip	Dip Direction	Dip Difference	Dip Direction Difference
F1	44	276	48	272	-4	4
F2	50	272	54	269	-4	3
F3	58	276	63	274	-5	2
F4	46	277	51	275	-5	2
F5	76	258	73	259	3	-1
F6	66	258	67	259	-1	-1
F7	58	274	62	277	-4	-3
F8	54	272	59	277	-5	-5
F9	40	328	45	332	-5	-4
Joints	Dip	Dip Direction	Dip	Dip Direction		
J1	88	152	84	149	4	3
J2	82	154	83	152	-1	2
J3	88	157	90	155	-2	2
J4		174	80	170		4
J5	78	162	80	160	-2	2
J6	44	114	47	110	-3	4
J7	54	358	49	358	5	0
J8	67	147	68	150	-1	-3
J9	84	192	80	190	4	2
Shear	Dip	Dip Direction	Dip	Dip Direction		
	63	357	63	358	0	-1

Photogrammetry mapping (Sirovision and CloudCompare)

Traditional approaches used for mapping require measuring near bench faces found in open pit mines. Such methods present numerous issues, such as safe access often does not exist to the rock faces to carry out geological mapping. Meanwhile, it is difficult to measure the orientation and geometry of large geological structures. Furthermore, mapping with a compass at the base of the slope exposes people to risks from rockfalls.

Requirement for a solution to measure and map features of interest from a safe distance makes more techniques to be considered to satisfy such requirements. Photogrammetry mapping through using photogrammetric image processing particularly helps cater to the geotechnical characterisation of rock slopes.

Sirovision is a geological/geotechnical mapping and analysis system that generates accurate, scaled 3D images of rock faces from stereo photographs taken in either open pit or underground environments. It allows for the remote and safe capture of geological and geotechnical features. Further analysis tools for wedge detection and slope stability provide valuable inputs to geotechnical support designs and for identifying safety hazards in open pits and underground environments.

Sirovision photogrammetry procedure

Site operation utilises Sirovision for geological mapping of structures in the walls as they are exposed. The photos are routinely taken following batter scaling and washing down of all new walls. It provides us with a valuable tool allowing for 3D images to be taken and processed promptly.

Select the area of the wall to be photographed, then mark up a series of control points on the wall or at the pit crest. Selecting the lens you will use and determine the location of your two camera positions based on the area that you are trying to photograph. Taking pairs of photos from baseline

positions till all required photos have been taken. These sets of images will be processed in the office to produce geo-referenced 3D images. Based on the processed images, geotechnical mapping can be conducted to identify structures.

The camera offset (baseline) is established by taking the distance to the face and dividing by seven. The distance to the wall is found by sighting the wall with the disto.

CloudCompare

Over the past decade, Unmanned Aerial Vehicle (UAV) borne remote sensing methods using photogrammetry and LiDAR have been used in mining operations, such as surveying, monitoring stockpile volumes, tracking equipment and simplistic mapping of deposit sites. Exploration geologists are interested in the use of UAVs to access remote areas for mapping mineral deposits.

Agisoft PhotoScan (2022) is an advanced image-based 3D modelling solution aimed at creating professional quality 3D content from still images. Generally the final goal of photographs processing with PhotoScan is to build a 3D surface, orthomosaic and Digital Elevation Model (DEM). The processing procedure includes four main stages:

1. Camera alignment.

2. Generating dense point cloud.

3. Generation of a surface: Mesh and/or DEM.

4. After the surface is reconstructed, it can be textured (relevant for mesh model only) or an orthomosaic can be generated.

With photogrammetry software, dense point cloud, digital surface model (DSM) and orthophotos can be generated. 3D dense clouds reconstructed in the setting of high accuracy, with millions of points of a rock surface, can be imported into CloudCompare to extract the geological planes using the FACET/Compass plugin. The major discontinuity sets can be observed and the orientation (dip/dip direction) of the discontinuity sets obtained from the algorithm is accurate and reliable for future geotechnical work such as rock slope stability analysis.

CloudCompare is a 3D point cloud (and triangular mesh) editing and processing software. Originally, it has been designed to perform direct comparisons between dense 3D point clouds. It relies on a specific octree structure that enables great performance when performing this kind of task.

Moreover, as most point clouds were acquired by terrestrial laser scanners, CloudCompare was meant to deal with huge point clouds on a standard laptop – typically more than 10 million points. Soon after, a comparison between a point cloud and a triangular mesh has been supported.

Afterwards, many other point cloud processing algorithms have followed (registration, re-sampling, colour/normal vectors/scalar fields management, statistics computation, sensor management, interactive or automatic segmentation etc) as well as display enhancement tools (custom colour ramps, colour and normal vectors handling, calibrated pictures handling, OpenGL shaders, plugins etc).

There are two methods of extracting the discontinuities: The Kd-Tree (KD) approach and the Fast Marching (FM) approach with both methods implementing a least square fitting algorithm.

Kd-tree approach divides the 3D point cloud recursively into small planar patches until the points fit the best-fitting plane given the Root Mean Square (RMS) threshold. These planar patches are then back clustered into bigger facets according to a co-planarity criterion.

FM approach divides the 3D point cloud systematically into smaller patches and subsequently regroups them. Hence, all the patches will have a similar size. After the meshes or facets are extracted, they can be classified by orientation (dip/dip direction) into single planes and plane families. A stereogram can be produced which is useful for rock slope stability analysis. Query can be done on the stereogram. Figure 1 presents the general workflow.

The facets data can be exported as Comma-Separated-Variable (CSV) ASCII file or shapefiles for further analysis in other software.

General workflow

Processing of images with PhotoScan includes the following main steps:

- loading photos into PhotoScan;
- inspecting loaded images, removing unnecessary images;
- aligning photos;
- building dense point cloud;
- building mesh (3D polygonal model);
- generating texture;
- building tiled model;
- building digital elevation model;
- building orthomosaic;
- exporting results.

FIG 1 – General workflow for Agisoft PhotoScan and drone image mapping.

Compass plugin is used to extract the discontinuities present in the rock mass, which can extract geological planes accurately based on its algorithm and export results in CVS or other forms. Figure 2 shows the extracted data.
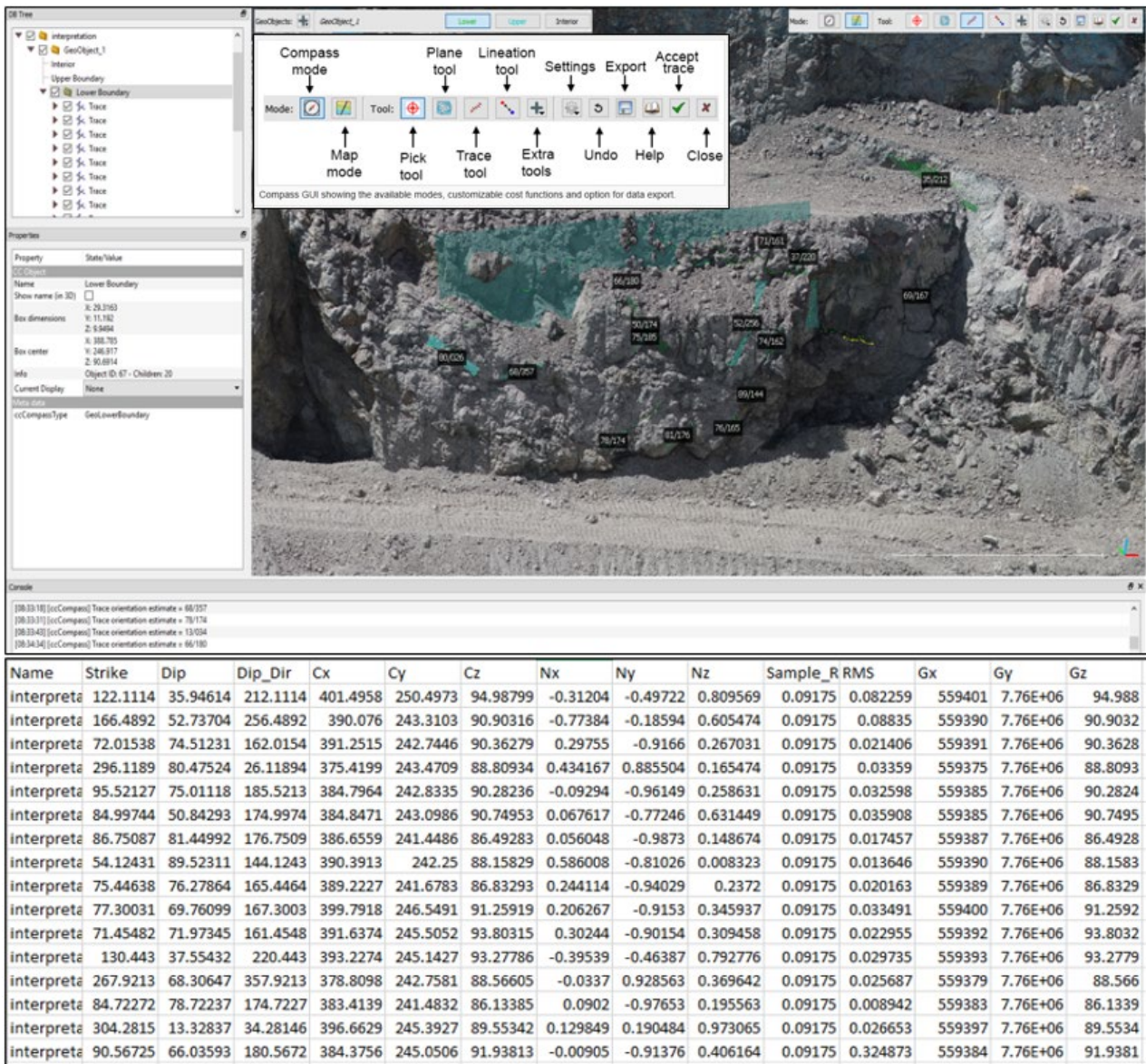
FIG 2 – Extraction of geological planes on-site.

CASE STUDY – SLOPE STABILITY ANALYSIS AND MONITORING

The rockfall occurred approximately 3:00 am on 29/10/2019, with a total estimated amount of 150 tons. The instability event is mainly triggered by structure and persistent groundwater saturation.

The site adopts drone mapping to obtain 3D images. As indicated in Figure 3, blue squares depict the camera positions and orientations. The numbered flags indicate the positions of the Ground Control Points (GCP) used for bundle adjustment.

Geotechnical mapping was conducted timely based on obtained 3D images and related structures were identified for assessing the mechanism of instability.

Two cross-sections are analysed to determine the orientations of shear plane 1, shear plane 2, and shear plane 3, together with their influence on the designed pit shell and current as-built slope geometry. Among which shear plane 1 is the dominant discontinuity and its persistence and extension intersection are critical to assess the stability impact on coming benches. It is important to figure out the development of the shear plane whether it pinches somewhere below or continue to extend to lower levels and determine within acceptable levels of confidence the possibility of large scale wedge instability.
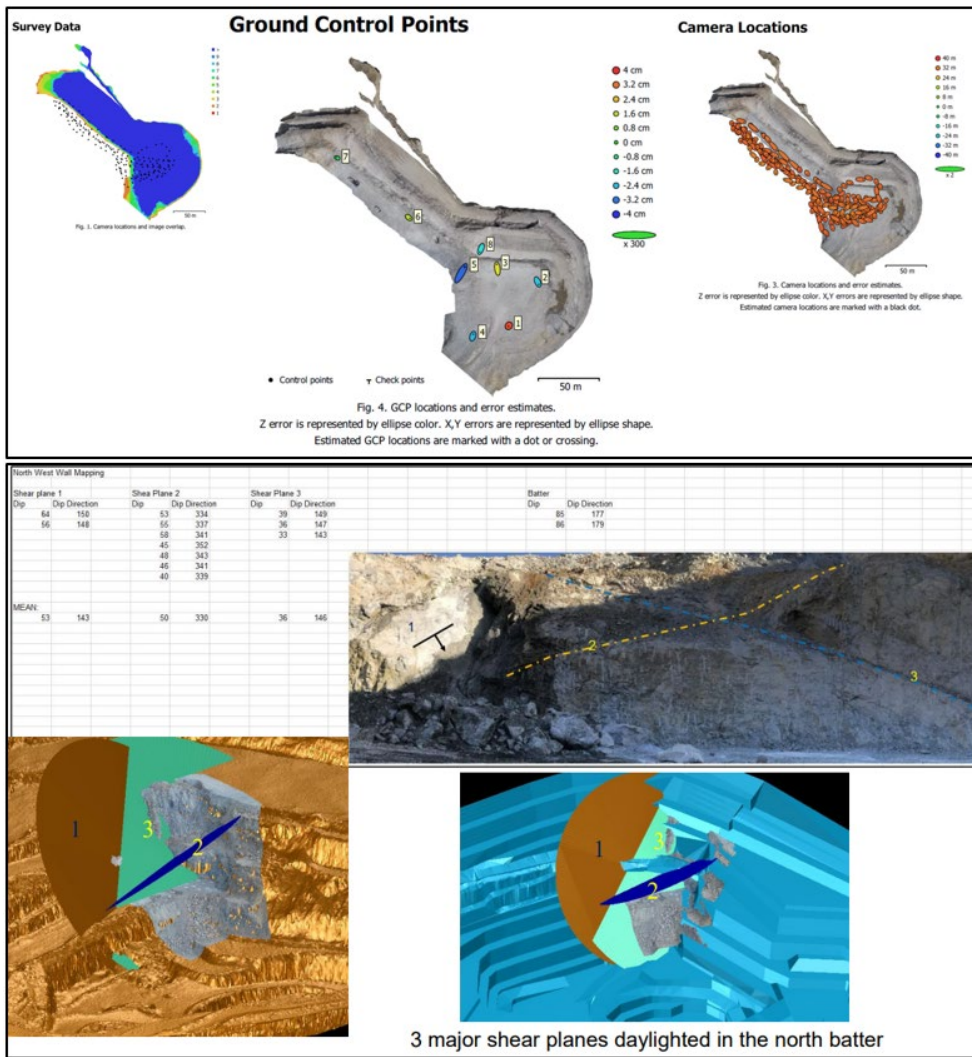
FIG 3 – Mapped three major shear planes in North Slope.

Adjacent drill hole HC19DD1318 core logging data indicates there is no obvious major shear plane in-depth range 65 m ~ 85 m that may intersect the drill hole. Daylighted shear plane 1 is highly unlikely to extend further down to 25RL bench level, as presents in Figure 4.
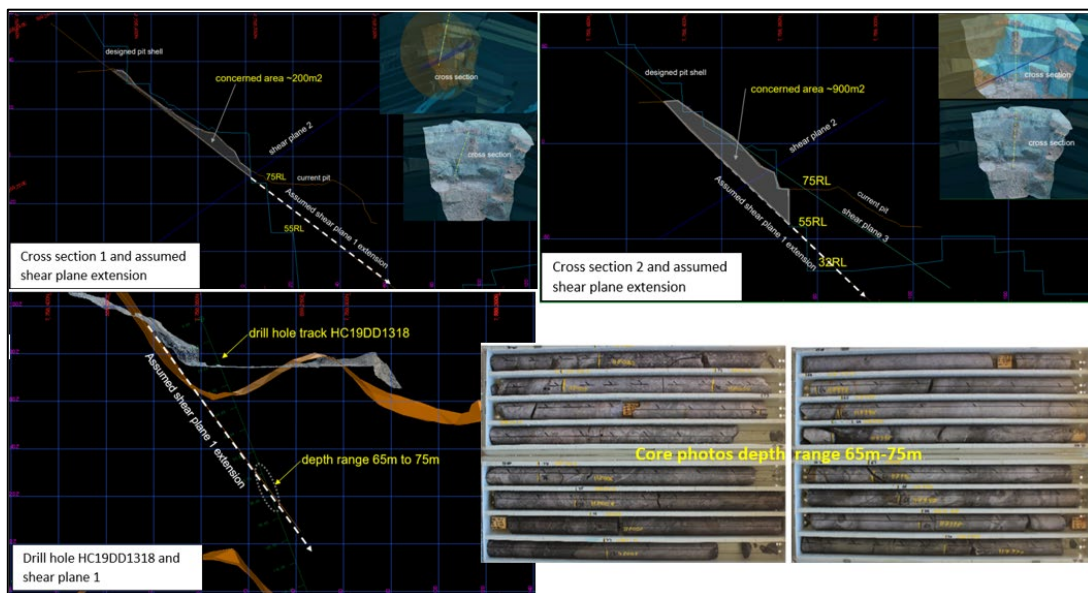
FIG 4 – Shear planes and assumed extensions.

Further analysis conducted for the two scenarios: shear plane 1 followed the contact of lower rhyodacite extend to the next flitch or shear plane 1 will be terminated at approximately 60RL at the base of lower rhyodacite. Swedge analysis indicates the probability of wedge failure contributed by shear plane 1 and shear plan 2 is low and the probability of wedge failure caused by shear plane 1, plane 2 and plane 3 is also low (refer to Figure 5).
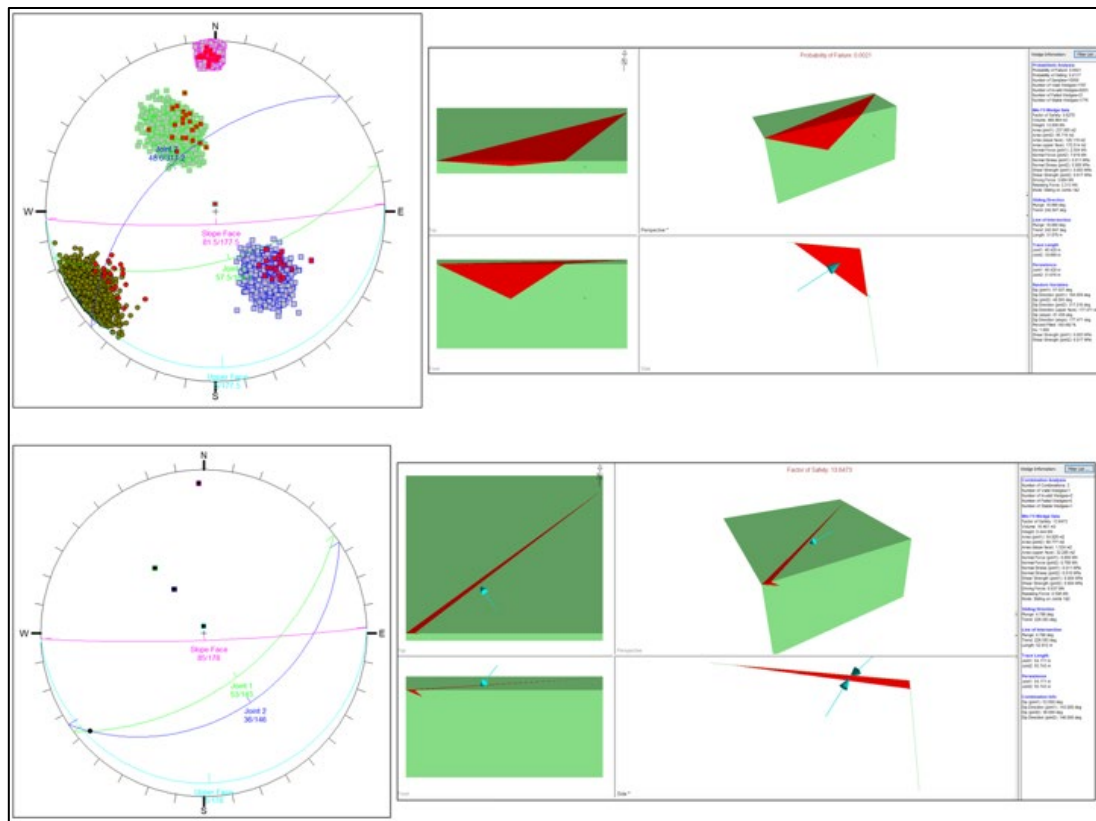
FIG 5 – Probability of further wedge failure is low.

Based on the available geology, structure and mapping data, failure mechanism is analysed and appropriate mine controls require to mitigate the hazards are assessed:

- The instability reported on 29/10/2019 is a sliding failure other than wedge failure, triggered by water saturated rock mass sliding down following contact plane.

- There will be a low possibility for large scale wedge failure in the area as per the Swedge analysis.

- Critical shear plane 1 highly possibly terminated at RL60, following the base of lower rhyodacite.

- Fault_second1_clip presented in previous report October 2019 (Wang, 2019) requires further work to confirm the geological model validity.

- Groundwater from pit north requires diverting or pumping out for mitigating the impact on slope stability.

- Requires manage ongoing blasting vibration to mitigate impact to the north wall.

- Re-assessment is required as mining progress down to pit bottom.

Three recommended options for mining engineers:

Option 1

- Rehab the failure and shift 10 m from current pit shell design to mitigate the shear plane impact to current as built pit shell stability.

Option 2

- Cut back or conduct slope support to eliminate the shear plane induced instability.

Option 3

- Rehab the failure and implement radar to close monitor the movement in the concerned area, counter actions will be deployed as per batters displacement trend.

CONCLUSIONS

Face mapping (line scan and window mapping), photogrammetry (Sirovision, Adamtech or CloudCompare) or laser scanning systems (I site scan etc), are the principal methods used in the mining industry to validate the design model through geotechnical mapping and evaluating slope performance. Structural data are a key input for kinematic, limit equilibrium and numerical slope design analyses. At Mt Carlton mine, traditional and 3D digital photogrammetric mapping methods were utilised to obtain various scales of mapping data remotely from bench to inter-ramp to overall pit scale and analysis the ground conditions and potential failure mechanism to manage slope stability to mitigate mining related hazards. There are some constraints for digital imaging systems such as they still cannot be used to determine the physical features of the structures without ground proofing, particularly surface roughness and nature of any infillings. Meanwhile, their ability to accurately define flat-lying and vertically inclined structures are also questionable. However, with a well-planned ground proofing and sampling program, these disadvantages can be minimised.

ACKNOWLEDGEMENTS

REFERENCES

Agisoft, 2022. Agisoft Metashape User Manual Standard Edition (previously known as Agisoft PhotoScan), ver 1.8, pp. 12–44. Available from: https://agisoft.com/downloads/user-manuals/ [Accessed: 17 September 2022].

CloudCompare, 2015. CloudCompare Version 2.6.1 – User Manual, Available from: https://www.danielgm.net/cc/ [Accessed: 17 September 2022].

Department of Minerals and Energy, Western Australia, 1999. Guideline Geotechnical Considerations in Open Pit Mines, August 1999, p. 11.

Tannant, D, 2015. Review of Photogrammetry Based Techniques for Character and Hazard Assessment of Rock Faces, *International Journal of Geohazards and Environment*, pp. 76–77.

Wang, D and Nuttall M, 2018. Ground Control Management Plan, Mt Carlton Mine, pp. 1–39.

Wang, D, 2019. Northwest Batter RL85 Geotechnical Review, Mt Carlton Mine, pp. 1–15.

Petex, 2016. FieldMove Clino – user manual, Available from: https://www.petex.com/media/fieldmove clino [Accessed: 17 September 2022].

Thiele, S and Samsu, A, 2017. Rapid, semi-automatic fracture and contact mapping for point clouds, images and geophysical data, *Solid Earth*, 8, pp. 1241–1253.

Read, J and Stacey, P, 2009. Guidelines for Open Pit Design, pp. 19–21, pp. 329–349 (CSIRO Publishing: Melbourne).

A case study in managing a high consequence geotechnical risk in a Queensland coalmine

K Young[1], M Martin[2] and D Payne[3]

1. Geotechnical Superintendent, BMA, Brisbane Qld 4000. Email: kathryn.young@bhp.com
2. Principal Geotech, BMA, Brisbane Qld 4000. Email: mike.martin@bhp.com
3. Geotechnical Manager, BMA, Brisbane Qld 4000. Email: dan.payne@bhp.com

ABSTRACT

This paper outlines the evolution of managing high consequence risk scenarios in BHP Coal, with particular focus on managing the stability of an endwall that is adjacent to a public infrastructure corridor running through a Central Queensland coalmine.

BHP Coal developed a Geotechnical Consequence Register after industry failures identified shortcomings in traditional risk assessment practices. Traditional risk assessments consider the consequence and likelihood of a geotechnical event occurring under normal operational conditions. As such, the risk rating for a high consequence, low likelihood failure may fall within the acceptable range, even where a lack of meaningful geological data exists due to the area being off lease or outside of mining reserves. The Geotechnical Consequence Register lists all geotechnical failure scenarios of high consequence, identifies if current controls are adequate, and highlights if specific Geotechnical Management Plans are required.

This case study reviews a failure scenario that was identified through the geotechnical consequence register. The scenario had previously been considered low likelihood and subsequently driving a low risk; however, the likelihood ranking was impacted by a lack of geological data outside of the mining lease and predominately informed by an acceptable historical slope behaviour. Additional exploration identified previously unmapped faulting which increased the risk rating. The requirement to develop a specific management plan resulted in an increase in the required factor of safety, design changes, the implementation of additional monitoring and a corresponding monitoring Trigger Action Response Plans (TARP).

In the case study area, the initiation of a geotechnical instability was identified early through the increased monitoring program. The instability was successfully managed and any impact to the infrastructure corridor off lease was prevented.

BHP Coal has used the Geotechnical Consequence Register for several years to identify and assess high consequence geotechnical failure scenarios. In some areas this has justified additional exploration, more stringent design acceptance criteria and an increased level of geotechnical monitoring. The process has been successful in ensuring that geotechnical risk is controlled in areas that often receive less attention than active production areas.

INTRODUCTION

BHP considers fall of ground (geotechnical failure) to be a principal hazard at its open cut coalmines in the Bowen Basin. A principal hazard has the potential to cause multiple fatalities (Office of the Queensland Parliamentary Council, 1999). Many controls are implemented, from the design stage through to actual excavation, to ensure that geotechnical risk is managed to an acceptable level and aligned with the business's risk appetite.

Some well-publicised failures in the mining industry prompted internal reviews of where geotechnical failure scenarios could have outsized impacts (ie a high consequence) on a mine's operation, public infrastructure, or social license to operate. For some cases it was identified that although the likelihood of an event was perceived to be very low, the consequence of a failure was so great that the inherent risk was not acceptable to the business. Over the last five years BHP coal has put an emphasis on identifying these high consequence scenarios, assessing their risks, and implementing appropriate controls.

This paper outlines the evolution of geotechnical risk management pertaining to high consequence failure scenarios. A case study is used to demonstrate the successful identification of a scenario, the

implementation of additional controls, and the response when monitoring flagged potential movement in the area.

GEOTECHNICAL RISK MANAGEMENT

Risk identification and assessment

Risk assessments are used in the mining industry to help identify, analyse and evaluate potential events, typically in accordance with the International Organization for Standardization – Risk Management Guidelines 31000 (2018). Hadjigeorgiou (2019) and Hebblewhite (2019) have documented some of the limitations associated with various risk assessment tools. This paper builds on these findings by further addressing two specific issues: having insufficient granularity in a risk assessment, or having a low residual risk rating that gives a false sense of acceptability.

The first deficiency commonly occurs when risk assessments are too high-level and only evaluate a site-wide risk (eg geotechnical failure of highwalls and endwalls). These generic assessments fail to highlight specific areas where the consequence of a failure could be significantly higher (eg a highwall failure that can be controlled with only a minor impact on production versus a highwall failure affecting infrastructure and negatively impacting long-term production).

The second problem often encountered is when the likelihood of an event is rated low enough to cause the overall risk rating (regardless of consequence) to drop to an acceptable level within a company's semi-quantitative risk framework. In these cases, there is a tendency to say that nothing further needs to be done, which can be problematic with low frequency, high severity events (Francis and Robertson, 2021).

An event may be incorrectly perceived as unlikely due to an insufficient range of experiences within the risk assessment participants (especially when historical performance of the area in question has been acceptable); at other times it may be due to a limited amount of geological data that has failed to identify any adverse conditions (giving a false impression that the area is structurally benign). Even for risks correctly assessed as having a very low likelihood of occurring, the resultant low risk rating can still mask that for some events additional controls are required to eliminate or further reduce the risk, as the consequence of failure is so great that the event cannot be allowed to occur.

It is also worth stating that after recent tailings dam failures, community and shareholder appetite for mining failures off lease or into the public domain has decreased.

Geotechnical consequence register

A geotechnical consequence register was developed by BHP Coal to address some of the shortcomings of existing risk identification and assessment practices. The consequence register lists all specific potential high consequence geotechnical failure scenarios that have impacts both within and outside of operational areas but are not appropriately captured in routine mining risk assessments and procedures. These include geotechnical instabilities that may:

- Extend past the mining lease with potential impacts to public infrastructure (eg roads, railways and power lines).
- Impact critical mine infrastructure (eg power lines and water networks).
- Create major environmental issues (eg impacts on creeks and creek diversions).
- Cause major inrush events (eg failures impacting dams, levees and water retention bridges).

For each scenario, the impact type is reviewed to determine whether it is primarily a health and safety, environmental, community, reputation, legal or financial risk. The maximum foreseeable loss is estimated for the scenario assuming no controls are in place. The register then considers current preventative and mitigating controls, which includes a review of the current state of confidence in geological, structural and hydrogeology models in the area. A severity level is assigned based on effective existing mitigating controls, with a likelihood of occurrence considered separately based on effective existing preventative controls. The severity and likelihood values selected are used to determine a residual risk rating.

The maximum foreseeable loss and residual risk ratings are filtered to identify scenarios that require the development of a specific geotechnical management plan (ie separate from the sites general principal hazard or ground control management plan). If the maximum foreseeable loss is above a certain threshold, the scenario is flagged for additional controls as the event cannot be allowed to occur regardless of likelihood. Similarly, a residual risk rating above a certain threshold indicates the current controls are inadequate.

Risk treatment

Management plans for specific scenarios must identify the controls required to prevent the scenario from occurring and usually require a high confidence geological model, an appropriate geotechnical design, good operational practices, and a robust slope monitoring program to validate stability.

Geological exploration is completed to develop a geotechnical model, but this is often without sufficient data to support a true assessment of the confidence levels. When an absence of adequate information is identified, a decision must be made to conduct additional exploration to improve confidence (which is often difficult due to the presence of infrastructure or off lease approvals), implement a conservative design to account for worst case conditions, or accept the risk of failure and rely on mitigating controls to manage any hazards.

A separate risk assessment is used to review the geological confidence in upcoming mining areas. The geologist indicates the current geological confidence around areas of geotechnical significance (ie areas where the geotechnical model input parameters have a major impact on the calculated stability). Geological models are considered high confidence where there is a high density and reliability of data with ongoing pit mapping and drilling during operations to refine the geological database and three-dimensional (3D) model (Read and Stacey, 2009). The geotechnical engineer highlights where high consequence areas require an increased level of confidence so the geologist can develop a plan to obtain this information and ensure that exploration is adequate to support mine design requirements.

Geotechnical analyses are then completed to determine the factor of safety, which is a ratio of the forces resisting failure to the forces driving failure. Based on the geotechnical model created, a typical pit design is completed to meet a minimum factor of safety requirement of 1.2, which means there are 20 per cent more resisting forces than driving forces. Empirically, a factor of safety of 1.2 equates to a probability of failure of 10–15 per cent (Read and Stacey, 2009).

Operational TARPs are used on-site to identify and manage geotechnical hazards that occur during the mining process. Operational TARPs do not prevent hazards from occurring and usually only identify them once they have already initiated (eg an instability has developed or is actively progressing). While operational TARPs can help to ensure a safe working environment, they manage hazards reactively and do not always indicate the immediacy of remediation measures required.

Instrumentation and monitoring plans are used to verify that an area is stable or to provide early detection of movement that could lead to an instability developing. Effective monitoring can also provide insight into the mechanism of failure and the extent and sequence of deformation, which can assist with both the selection of an appropriate remediation option and the measurement of its impact (eg on the rate and extent of slope movement).

CASE STUDY – BHP QUEENSLAND COALMINE HIGH CONSEQUENCE SCENARIO

Scenario identification

In the early stages of developing the consequence register, a significant failure scenario was identified at one of BHP's Queensland coal operations. The operation is bisected by an infrastructure corridor, with pit walls and open voids on either side (Figure 1). The corridor contains a public road, a rail line (servicing multiple BHP mines and other external operations), communication infrastructure and power lines. If the worst-case failure scenario occurred, the maximum foreseeable loss was estimated at being hundreds of millions of dollars. This is primarily attributable to damaging the rail line and interrupting the transport of coal to the port. Significant damage to public infrastructure would also have a detrimental effect on the company's social license to operate.
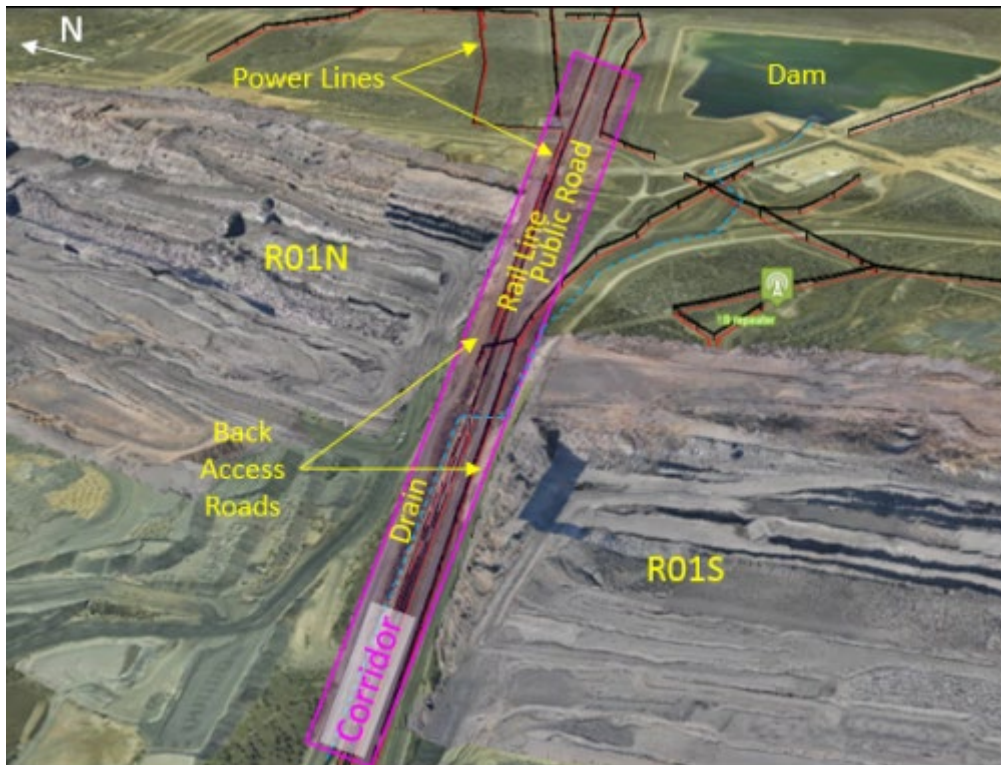
FIG 1 – Aerial image of the infrastructure corridor.

The likelihood of a failure scenario of this magnitude occurring had always been considered highly unlikely, as the geological conditions within the corridor were not thought to be adverse. In accordance with BHP's risk matrix, a risk with a likelihood rating of 'highly unlikely' returns a residual risk rating that is in the acceptable range regardless of the severity level of the event (Figure 2). Historically this may have resulted in the area receiving no further attention, as the current controls were thought to be adequate. However, the new process utilising the consequence register flagged the area for additional review due to the severity level.

Likelihood	Severity Level				
	1	**2**	**3**	**4**	**5**
Highly Likely	30	90	300	900	3000
Likely	10	30	100	300	1000
Possible	3	9	30	90	300
Unlikely	1	3	10	30	100
Highly Unlikely	0.3	0.9	3	9	30

FIG 2 – Residual risk rating table (green cells (RRR<90) indicate risk is within appetite).

Geological confidence

As part of the review process, further investigation into the geological modelling was undertaken. Since the area was off lease and contained critical infrastructure, exploration drilling had been inhibited and there was initially very limited geological data. It became apparent that the absence of adverse geological structure in the model was due to the lack of information to identify its presence, rather than the actual absence of structure. Similar situations occur when a mining area boundary is purposely selected to terminate against known areas of structural complexity to avoid operational complications. Once an area is excluded from mineable reserves, no further exploration is usually carried out and any later stage drilling program is likely to be impacted by a lack of access.

A high level of confidence in the geological model was required to ensure that a robust geotechnical design could be completed to proactively design out geotechnical hazards. This required a shift in the exploration approach as drilling density needed to be sufficient to both better define known structure as well as prove the absence of adverse structure.

The exploration of the infrastructure corridor was an iterative process. An initial drilling program was undertaken in 2018 with the aim of providing a better understanding of the environment. The program provided additional evidence that major structures were present within the corridor but did not provide sufficient information to inform the geotechnical design or achieve confidence in the model to the level required. The program was hampered by limited access and resultant wide spacing between drill holes.

Designs were updated with worst-case assumptions from the drill program findings to ensure that the risk was sufficiently managed. The impact of this design change was a significant loss of coal which justified additional exploration. The next stage of drilling was more targeted and successfully increased the resolution of known structures, as well as disproving the presence of adverse structures in other areas. This greatly improved the confidence in the structural model and the subsequent geotechnical design.

Further reviews were completed over the following years including a major structural review in 2021 which incorporated the results of a large-scale 3D seismic program, additional drilling with optical and acoustic televiewer (OTV/ATV) results and available face mapping data. Face mapping proved to be particularly challenging as blasted batters had been excavated in some areas (usually in the weathered horizons) while blasted material had been dumped against the wall as a buttress in others. This meant that the *in situ* wall was not visible in some sections.

A step change in the 2021 review was providing an interpretation of confidence of the geological data. Confidence in the data was determined by the level in which the data was inferred; high confidence was adopted where intersections/mapping confirmed the data while low confidence was adopted where the faults were projected from a distance greater than 60 m from the closest data point.

The resultant model included a large normal fault that crossed the corridor road and intersected the endwalls on both the southern and the northern side of the corridor with multiple smaller scale faults also present (Figure 3). The main fault has a persistence of 2300 m and like most large faults, is not a single plane but a broken zone approximately 0.2 m in width. The pitward dipping coal seams on the southern side of the corridor, along with known clay bands within the seams that are susceptible to degradation upon contact with water, meant that significant design changes had to be made to ensure the area met the factor of safety requirement. Figures 4 and 5 are cross-sections through the northern and southern side of the corridor road showing faults, base of tertiary and weathering and coal seams.
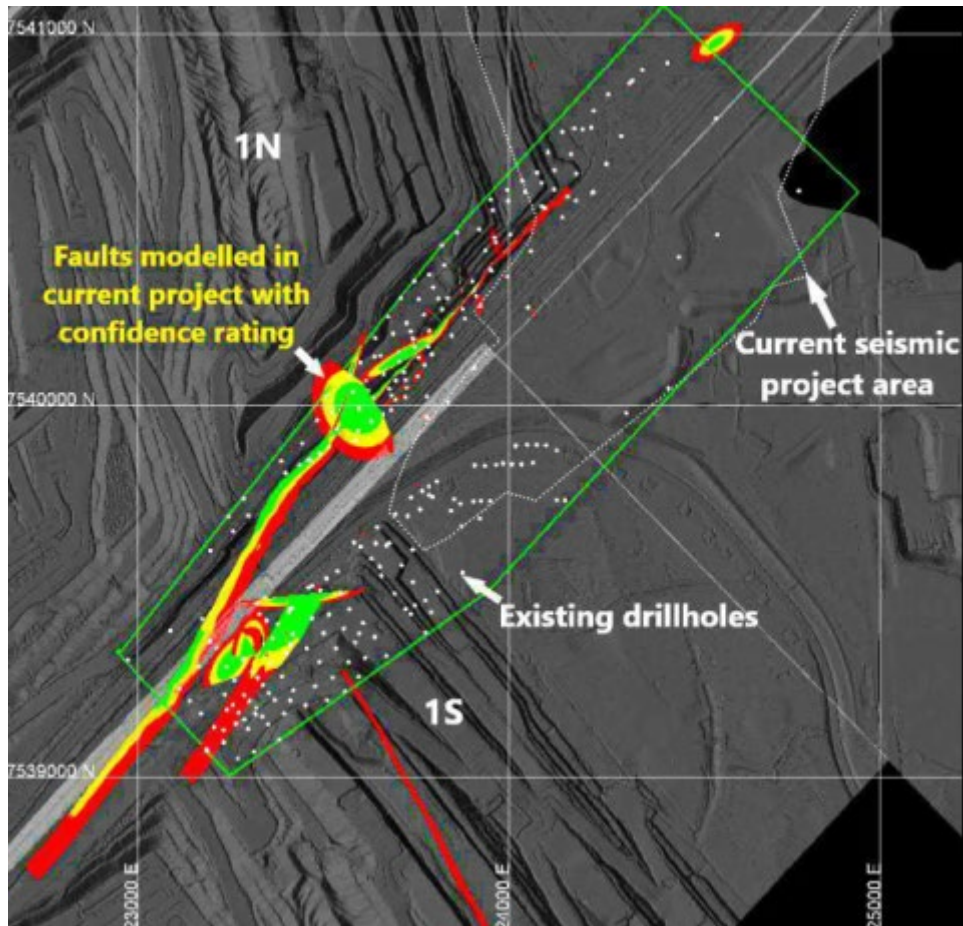
FIG 3 – Corridor fault model.
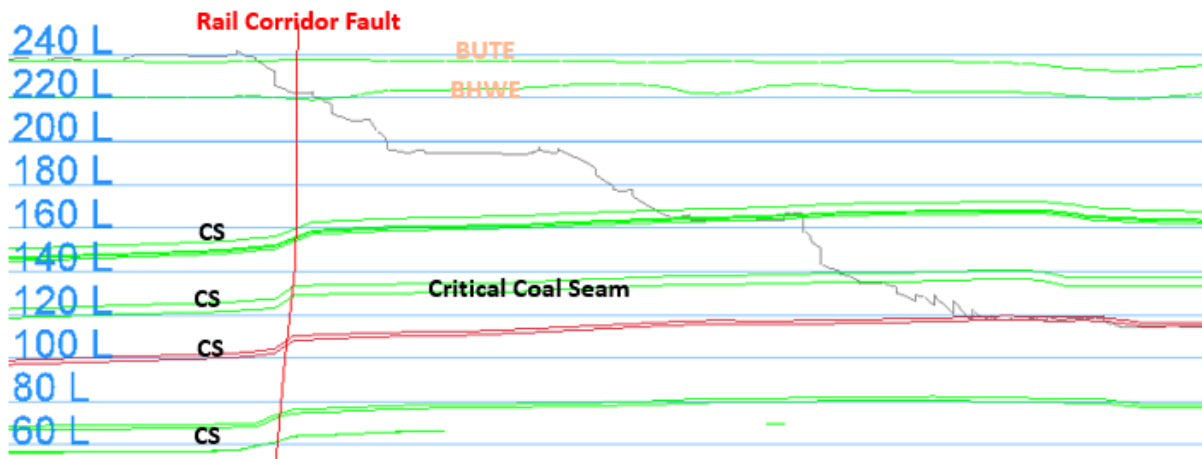
FIG 4 – Cross-section through the Endwall on the northern side of the corridor showing coal seams (CS) and fault intercepts.
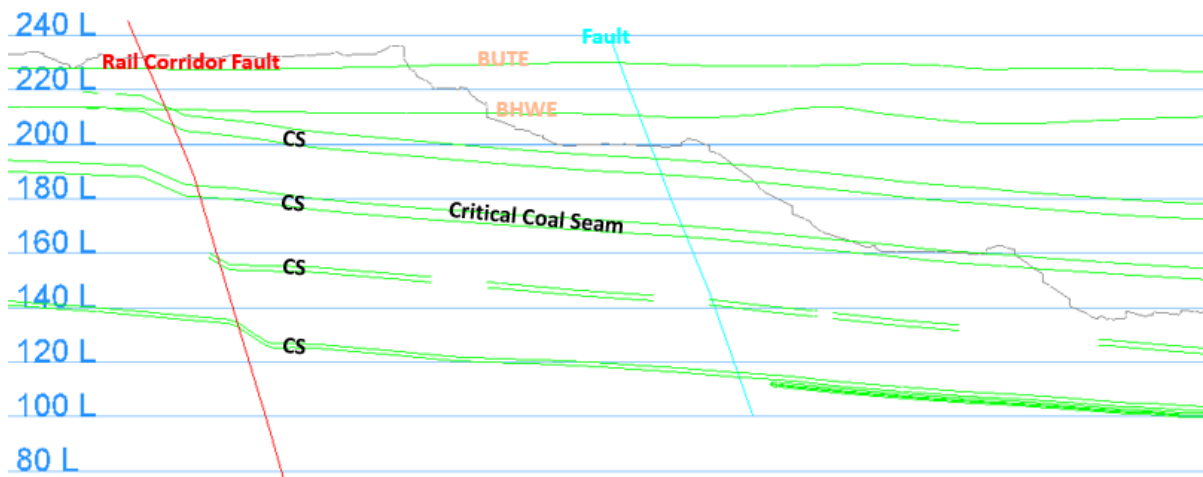
FIG 5 – Cross-section through the Endwall on the southern side of the corridor showing coal seams (CS) and fault intercepts.

Design acceptance criteria

The existing endwalls in the area achieved a factor of safety of 1.2, which had been considered acceptable for the operational mine environment. This factor of safety was deemed insufficient for areas identified to have a high consequence of failure. A factor of safety of 1.5 was adopted to lower the probability of failure and provide an additional margin for error against uncertainty in the geological data and modelling processes. The target factor of safety of 1.5 is based on industry practice and considered guidelines provided in Western Australia's Department of Minerals and Energy's *Geotechnical Considerations in Open Pit Mines Guideline* (1999), as well as the Guidelines for Open Pit Slope Design (Read and Stacey, 2009).

In addition to the higher factor of safety, conservative design assumptions were still required given there was insufficient geological confidence in the area in 2018. As mentioned previously, designs were updated using worst-case assumptions from the initial drill program findings. This resulted in significant coal loss which justified further exploration. Each stage of the drilling program increased confidence in the geological model and allowed for design optimisation with less conservatism.

Previously there were not any limits in place to maintain a minimum offset between the two open pit voids on either side of the corridor (ie to minimise the length of corridor unconfined on both sides simultaneously). Traditional 2D stability analyses are not suitable for this type of problem, so 3D analyses were investigated to help improve the understanding of the rock mass behaviour and the influence of confinement. A minimum offset between the two open pit voids was determined and put in place as a control.

3D models were created in Rocscience RS3 after a significant review of the structural geology of the area was completed at the end of 2021. Material parameters were a combination of derived parameters and generic material parameters used across BHP Coal. Overburden Fresh Permian parameters were derived from the UCS taken from validated lab test data and the GSI from visual slope interpretation. The cohesion of coal was increased based on lower bound triaxial test results. Defect strengths including bedding, joints and top of coal contact was taken from validated direct shear test results across BHP Coal.

Consistent persistent weak tuff or shear were not identified in the critical coal seam, however, there were weak contacts at inconsistent horizons observable within the coal core. Therefore, a weak top of coal contact was included in the geotechnical models.

No elevated water table was identified within the area of interest and the model had been adjusted accordingly. The slope is largely dewatered despite the presence of the drain behind the crest of the southern endwall due to large open pit voids on either side of the infrastructure corridor. This was confirmed based on interpretation of piezometer data and dipped production bores which were drilled on the endwall.

Table 1 shows the results and failure mechanism identified.

TABLE 1
3D modelling of the infrastructure corridor faulting.
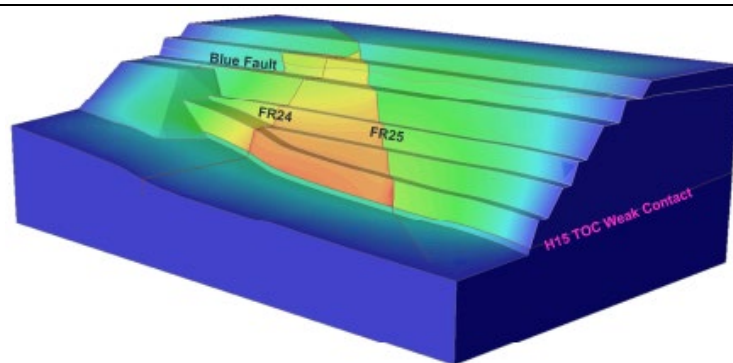
	Critical SRF = 1.32 Failure mechanism is an inverted wedge sliding on coal roof. Failure Backscarp limited by 'Blue Fault' and unlikely to impact critical infrastructure.
	Critical SRF = 1.55 Failure mechanism is an inverted wedge sliding on coal roof. Buttressing the coal seam reduces the likelihood of instability for the inverted wedge mechanism and achieves acceptance criteria.
	Critical SRF = 1.54 Case for east of fault intersection. No other faults identified. Failure mechanism is sliding on coal seam weak contact. Strata dip decreases significantly east of fault intersection. Acceptance criteria is met without buttressing.
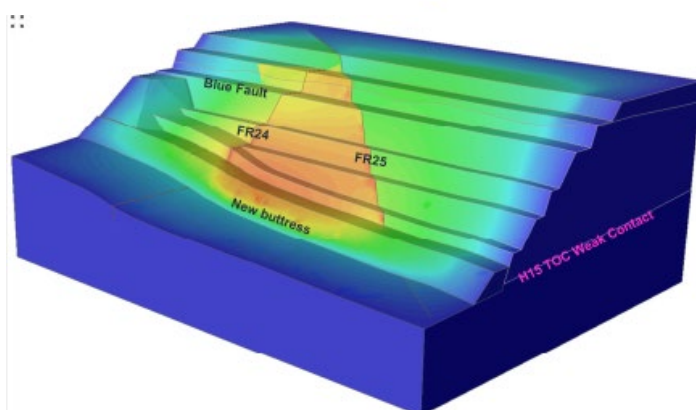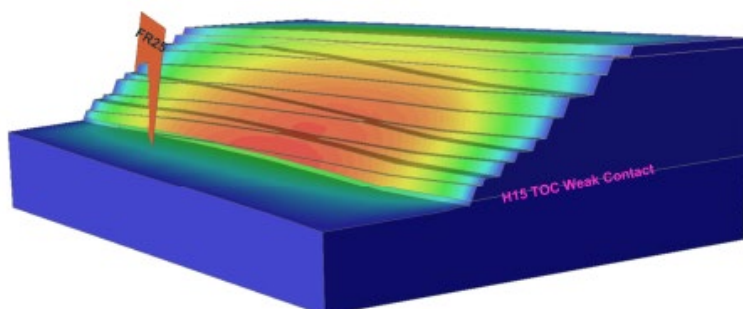
A theoretical option would be to accept the cost of failure and not complete any remediation (ie not increasing geological confidence or the target factor of safety). This could only occur if the potential safety risk can be adequately controlled in the field and may involve implementing additional controls such as proactive monitoring and extended standoffs. However, accepting failure in this high consequence scenario was not within the business's risk appetite given the potential financial and reputational impacts.

BHP Coal has developed a cost calculator tool to estimate the potential financial cost of failures as this was previously not well understood (Young *et al*, 2020, 2021). A simple cost-benefit analysis comparing exploration costs, conservative design costs and the cost of an instability is usually enough to identify the benefits of additional exploration and the requirement for higher confidence models, as was the case in this scenario. If any changes occur in the future (eg exploration program is cancelled/delayed, a new fault structure is identified, a mining area is brought forward in the schedule etc) it is essential to complete change management and ensure the implications are fully understood and communicated to all stakeholders.

Geotechnical monitoring

A robust monitoring plan was required for the corridor to show that it was stable and provide early detection of changes that could indicate a developing instability (historically there was no permanent monitoring conducted in this area). The monitoring plan developed for the corridor was designed to provide insight into the mechanism of any potential instability and the location, extent and sequence of deformation. Additionally, the monitoring plan was later revised to also confirm key model assumptions, in particular the water table, so that deviations from initial model inputs could be identified and managed.

To create a comprehensive monitoring system, different types of instrumentation were installed to accurately capture and ensure reliability in the data (Table 2). For example, LIDAR/UAV was used to provide short to medium term indications of movement at low accuracy, while InSAR data was used for very accurate long-term monitoring (with the advantage of an available historic data set), each of which were only valid if there was no surface disruption within the period of interest. As another example, slope stability radars were used to validate movement seen on downhole TDRs, if the surface ravelling was not excessive.

Multiple instruments were also installed to ensure sufficient redundancy in the system in the event some became damaged or broke-down. Additional instruments are being installed to keep pace with the advancing mining front (Figure 6).

TABLE 2
Types of monitoring used on the infrastructure corridor.

Instrument	Purpose
Time Domain Reflectometry (TDR)	TDRs indicate the depth of movement down a borehole and can be correlated against a geological model to identify failure planes. Monitoring checks are focused at the depth of the critical coal seams identified in the stability assessment.
GNSS (Global Navigation Satellite System Units)	GNSS ground based units position themselves by satellite tracking, generally giving a very accurate measurement for their fixed location. Multiple GNSS units are fixed along the corridor road with additional units installed as the mining footprint has progressed east. GNSS units show the direction of movement and the velocity can be calculated and correlated against TARPs.
Extensometers	Extensometers provide distance measurements between two adjacent fixed points and can be used to provide estimates of movement across a crack. Several extensometers are installed on the endwall to track natural surface crack propagation.
Vibrating Wire Piezometers (VWPs)	VWPs are used to interpret standing water levels from pressures measured at the installation depth down a borehole. The water table was also confirmed by drilling and dipping additional production holes. Future TARPs will be set-up to trigger when the measured water level exceeds what was assumed in the stability modelling.
LIDAR (Light Detection and Ranging) and UAV (Unmanned Aerial Vehicle) Scans	Successive LIDAR and UAV scans of the ground surface can be compared (by subtraction of differences) to indicate the location and magnitude of movement. Usability is limited by the accuracy of the scanning equipment. LIDAR scans are completed at least monthly. When completing a LIDAR subtraction, both differences between the current and previous month as well as the current month and previous year are considered.
InSAR (Interferometric Synthetic Aperture Radar)	InSAR uses microwave scans from a satellite to measure movement of the ground surface, with the advantage of being able to access historical data sets to gain greater understanding of long-term movements. There are some challenges using the data in locations where pit progression has disturbed the area or the surface has been regraded; however, confidence in the data is high in areas with permanent infrastructure and low disturbance.
Blast Monitoring	Vibration monitors use geophones to measure the peak particle velocity at the point of installation and can be used to calibrate models of blast energy attenuation with distance. Vibration limits are in place for blasts adjacent to the infrastructure corridor.
Slope Stability Radar (SSR)	Slope stability radars measure changes in distance between the wall and the radar, providing an indication of the magnitude of slope movement in near real time. The installation of slope stability radars is triggered by the monitoring TARP and is used to validate other monitoring sources.
Visual Inspections	Visual inspections are important for identifying ground deformation and understanding the 3D relationship between a range of observations. Regular inspections are completed of the buttress performance, coal seam exposure within the endwall, endwall deformation as well as the endwall strata.

FIG 6 – Monitoring installed in the infrastructure corridor.

Management plan

A geotechnical management plan was developed to outline the requirements for managing the risk of an endwall failure that could impact the infrastructure corridor containing the road and rail line. The management plan is tailored to this specific scenario and describes the required design and monitoring controls, as well as the roles and responsibilities of site personnel to manage the risk.

Design controls consist of the required slope design criteria to ensure that any potential failure surfaces that could impact the infrastructure corridor meet a minimum factor of safety of 1.5. These requirements are regularly reassessed as mining progresses and new walls are exposed for mapping, as additional exploration drilling is completed, and as monitoring instrumentation detects changes.

There are also constraints on blast designs to ensure that vibrations are kept within allowable limits to prevent permanent damage to the ground. Any blasts above the specified thresholds require approval by the site Geotechnical Engineer and risk owner. Strategies to reduce blast vibration include using lower density explosives, deck charging to redistribute loads as well as changing initiation point, sequence and delay timing. Blast vibration monitoring results must be continually reviewed/reconciled and the site parameters updated to improve future vibration predictions. The vibration limit on the southern side of the corridor was subsequently further reduced based on a couple of larger blasts that triggered movement in the slope (as detected by some of the GNSS units).

Monitoring controls consider that each type of instrument has its own strengths and weaknesses and that an integrated system is required to provide a comprehensive understanding of the movement in the area. Deformation and velocity trigger thresholds for different instruments were developed based on assessing the baseline data over a period of approximately 6 months, as well as determining levels of movement that are above those expected from typical slope relaxation. Some types of instrumentation have automated alarms that send a text message to the site Geotechnical Engineers if a trigger level is breached.

The management plan includes an area-specific Trigger Action Response Plan (TARP) that includes these monitoring triggers as well as requirements for notification and reporting. The TARP outlines predetermined actions to mitigate the effects of a developing instability and to re-establish control in

the area. Response levels are determined by changes that could impact corridor stability, with three response levels above normal conditions

- Normal Response: In control.

- Moderate Response: Increase awareness, monitor, investigate.

- Major Response: Increase monitoring, implement additional controls, prepare contingencies.

- Critical Response: Controls (potentially) breached, stop normal operations, treat problem directly, implement business continuity plan if required).

In the event a critical response is required (ie a geotechnical failure impacts the public road, rail or power utilities), the objective is to ensure actions can be quickly implemented to manage the safety risk to company personnel and the public. A more detailed business continuity plan, tailored to the specific circumstances, would be developed post-event to mitigate the risks associated with a disruption to operations.

The management plan is reviewed and approved annually by the Site Senior Executive (SSE). The purpose of the review is to assess continued relevance, adjust controls based on recent information and developments, consider newly identified risks, and ensure the risk is being managed within acceptable levels.

Hazard response

After a large blast adjacent to the corridor road in 2019, new cracking was observed on the natural surface in a projection approximately following that of a known fault. The two GNSS units closest to the southern intersection of the fault with the endwall showed an increased rate of movement on the endwall and some lipping was visible in pit on clay bands within the coal seam. InSAR data (Figure 7) now shows areas where there was increased movement, although this was not known at the time of the event since the InSAR data was only processed at the end of the month.
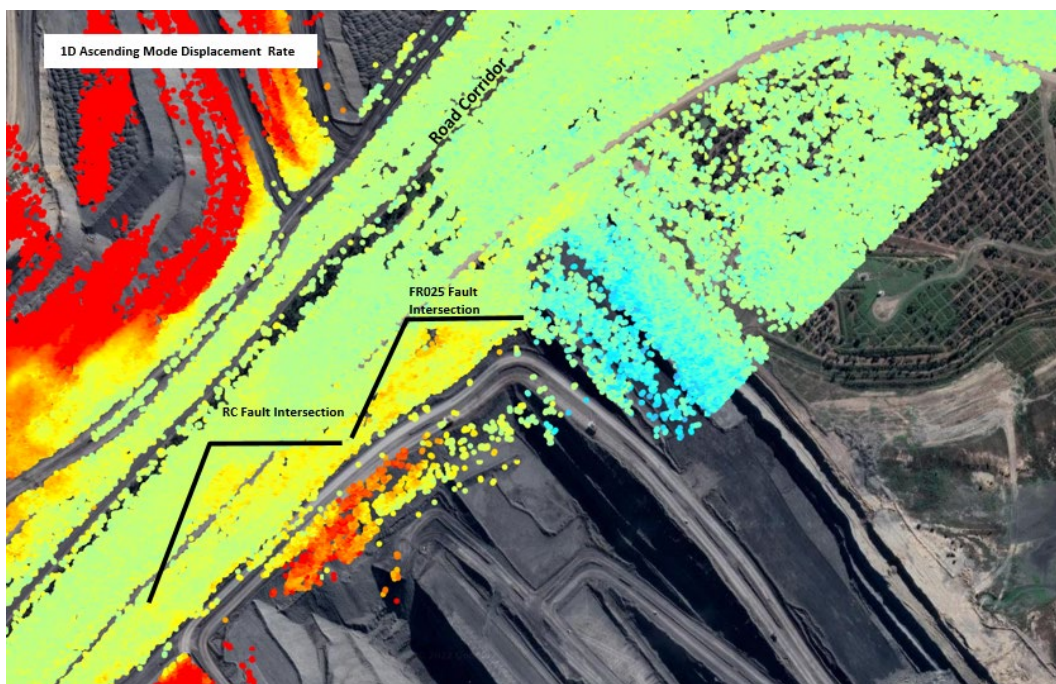
FIG 7 – InSAR data showing locations of potential movement.

Back-analysis of the area showed that significant degradation of the clay bands within the coal must have occurred along with water pressure build-up in the fault. The GNSS units clearly showed an acceleration in movement after blasting, indicating it was a contributing factor. TDR and slope stability radar data did not detect any signs of movement, although due to pit progression the placement of the slope stability radar may not have been in line with the direction of movement.

Remediation/stabilisation works were completed in the area displaying some signs of localised instability. This was accomplished by accelerating progression of the waste dump to act as a buttress and realigning the haul road against the bounding pit endwalls. After the buttress was installed on the critical seam horizon, a significant decrease in the rate of movement was observed on the GNSS units. The area on natural surface was also re-graded to manage drainage away from the fault plane; no further cracking was identified after the re-grade.

Blast vibration limits on the southern side of the corridor road were also reduced, as the blast which likely initiated the movement was within the previous limits but caused higher vibrations than previously recorded in the area.

It is unknown whether the event would have progressed to have a significant impact on the overall stability of the infrastructure corridor without any additional actions; however, the monitoring, management plan and TARP that were in place enabled the issue to be identified and responded to in a timely manner before a significant issue developed. There was also a clear plan to escalate the issue and put additional controls in place.

CONCLUSION

Over the last several years BHP Coal has reviewed its mine sites to identify specific high consequence geotechnical stability scenarios. A consequence register was developed to assist with the assessment of these scenarios and overcome some shortcomings of traditional risk assessment practices. The register is also used to identify scenarios that require a specific geotechnical management plan.

This case study clearly demonstrated that having a low confidence geological model (as well as historic good slope performance) led to the likelihood of failure being considered artificially low, as adverse structure simply had not been identified. Later identification of this structure was problematic due to the loss of real estate through mining and infrastructure development, had significantly impacted the ability to drill sufficient exploration holes to develop a high confidence geological model. To enable a robust design, areas that could impact stability must be included in exploration even if they are not part of the mining reserves.

The low confidence also impacted the ability to produce a design appropriate for the level of risk, and the subsequent investment in exploration was quite minimal compared to the coal loss and other implications of a conservative design. The response to a potential hazard developing in the case study area further highlighted the importance of continuing ongoing exploration, sufficiently in advance of mining, to allow for identification of adverse geology and development of a high confidence geological model to permit the required timely design optimisation.

A specific geotechnical management plan was developed for the case study scenario. The management plan outlined the required controls to prevent the scenario from occurring and manage the risk to an acceptable level. This included a high confidence geological model, an appropriate geotechnical design, good operational practices, and a robust slope monitoring program.

ACKNOWLEDGEMENTS

REFERENCES

Department of Minerals and Energy Western Australia, 1999. *Geotechnical Considerations in Open Pit Mines Guideline*.

Francis, G and Robertson, R, 2021. Criminal Manslaughter & How Not to Do It, A Practical Guide for Directors, How to Demonstrate Due Diligence, R2A Pty Ltd Consulting Engineers.

Hadjigeorgiou, J, 2019. Understanding, managing and communicating geomechanical risk, in J Wesseloo (ed.), *Mining Geomechanical Risk 2019*, pp. 3–20 (Australian Centre for Geomechanics: Perth).

Hebblewhite, B K, 2019. Geotechnical risk in mining methods and practice: critical issues and pitfalls of risk management, in J Wesseloo (ed.), *Mining Geomechanical Risk 2019*, pp. 299–307 (Australian Centre for Geomechanics: Perth).

International Organization for Standardization, 2018. *Risk Management Guidelines 31000*.

Office of the Queensland Parliamentary Council, 1999. *Queensland Coal Mining Safety and Health Act*.

Read, J and Stacey, P, 2009. *Guidelines for Open Pit Slope Design*, CSIRO, Collingwood.

Young, K, Robotham, A and Virk, G, 2021. Structural instabilities and their economic consequence in open cut coal mines, *Bowen Basin Symposium 2021*.

Young, K, Robotham, A and Virk, G, 2020. Economic consequences of geotechnical instabilities in open cut coal mines, in PM Dight (ed.), *Slope Stability 2020: Proceedings of the 2020 International Symposium on Slope Stability in Open it Mining and Civil Engineering*, pp. 145–154 (Australian Centre for Geomechanics: Perth).

Ground control and support

An empirical system for primary and secondary support in US coalmines

Z Agioutantis[1] and C Mark[2]

1. Professor and Chair, Department of Mining Engineering, University of Kentucky, Lexington KY 40502, USA. Email: zach.agioutantis@uky.edu
2. Principal Roof Control Specialist, Technical Support, Mine Safety and Health Administration (MSHA), Pittsburgh PA 15217, USA. Email: mark.christopher@dol.gov

ABSTRACT

This paper presents an empirical design methodology that is based on successful US roof support systems using both primary and secondary support in coal mining entries and intersections. The recent nationwide dramatic reduction of roof fall rates, especially in areas with weaker roof, can be directly correlated to the effectiveness of the roof support systems.

A large database of roof fall histories at several mines is used to define the approximate boundaries of three modes of roof support with respect to roof strength as classified by the Coal Mine Roof Rating (CMRR) and in situ vertical stress as indicated by the depth of cover. These roof support classifications are:

- Suspension, where roof bolts mainly provide skin control for strong roof.

- Beam building or reinforcement, where a roof of moderate strength can be supported by roof bolts only.

- Supplemental (secondary) support, where the primary support by roof bolts may be augmented by several secondary support systems, eg cable bolts, trusses, additional roof bolts or standing supports.

The Primary Support Rating index (PSUP) captures the capacity of the primary roof bolt system as a function of the actually implemented roof control plan, ie roof bolt length, roof bolt density, and roof bolt capacity, while it does not consider the type of bolt. The actual PSUP value is compared against a suggested PSUP value derived from statistical analysis of US case histories. Where secondary support is indicated, the expected rock load determines the necessary capacity of the secondary support system. A new (free) software package, Analysis of Mine Roof Support (AMRS), implements the design methodology and also allows comparison with other international indices such as the Reinforcement Density Index (RDI), the PRSUP, etc.

INTRODUCTION

Roof falls involve a collapse of a portion of a mine entry that extends to or above the anchorage zone of the roof bolts. Each roof fall, therefore, represents a failure of the roof support system. In recent years, the roof fall rate in US coalmines has decreased from about 2.3 per 200 000 underground hours worked to about 0.7. This remarkable decrease occurred mainly between 2005 and 2013, which coincides with the period where cable bolt usage increased from approximately one million to more than four million units annually, while underground coal production remained essentially constant.

Mark and Stephan (2019) presented a 'rock load' methodology for designing cable bolt support systems. The 'rock load' corresponds to the weight of the rock that needs to be supported by primary or secondary support systems. Rock load can be calculated for entries or intersections using the entry width or intersection span, the thickness of roof to be supported, and the 'roof fall angle', which can be obtained from roof fall profiles. The number or spacing of the cable bolts is then matched to the calculated rock load.

Mark *et al* (2001) proposed the Analysis of Roof Bolt Systems (ARBS) methodology for designing primary support systems. ARBS was based on a roof fall database which was obtained from 37 coalmines located in all the major US coalfields. ARBS suggested a level of primary roof support based on the depth of cover and the immediate roof quality (strength). However, ARBS was

developed before cable bolts came into wide use, and the database did not include many weak roof/high stress applications. As such the ARBS recommended support levels are also out of date.

This paper describes the updated roof fall case history database, and how it has been used to derive updated recommendations for primary support design. It then shows how these recommendations dovetail with the cable bolt design methodology to create a comprehensive approach to roof support design called Analysis of Mine Roof Support (AMRS).

ROOF SUPPORT MECHANICS

Roof support design begins with an understanding of how roof bolts support the ground. As illustrated in Figure 1, roof bolts work in several different modes depending on: (1) the strength of the roof; and (2) the magnitude of the vertical stress at the mine (Mark, 2000; Gale *et al*, 1992).
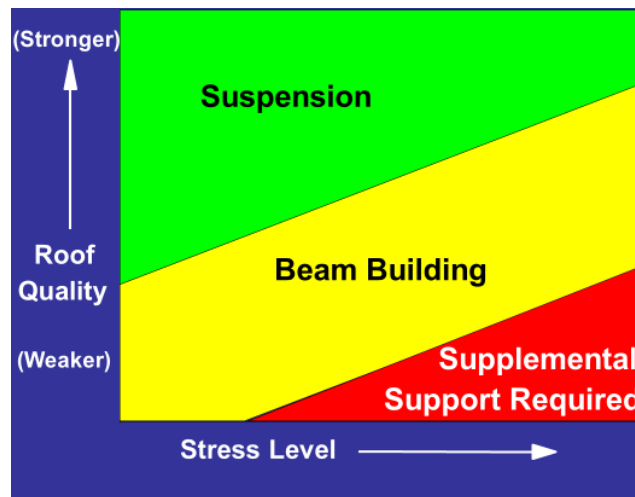
FIG 1 – Roof support mechanisms determined by stress level and roof quality (after Mark, 2000).

When the immediate roof is a thick, competent formation (ie sandstone or limestone), roof falls above the bolt anchorage are very rare. Under these conditions, roof bolts still serve the essential purpose of preventing 'skin' failures involving thin slabs or blocks of loose rock. Roof bolts also work in suspension when a thin, weak, immediate roof can be suspended from an overlying strong unit.

When no strong, stable unit is available, the bolts reinforce the immediate roof to create a 'beam.' The bolts reinforce the rock by maintaining friction on bedding planes, keying together blocks of fractured rock and controlling the dilation of failed roof layers. Stronger, stiffer beams are built with longer bolts, larger diameter bolts, and increased grout length. The density of the support system can also be increased by adding additional bolts to the pattern or by reducing the row spacing.

Secondary support is required where the roof is so weak, relative to the ground stresses, that roof bolts alone are not able to prevent roof failure from progressing above the anchorage horizon. In these cases, cable bolts, cable trusses, or standing support carry the dead-weight load of the broken roof, and the roof bolts act primarily to prevent unravelling of the immediate roof.

The AMRS methodology builds on this basic framework. First, it quantifies the boundaries between the three support regimes shown in Figure 1. Then guidelines for support selection are derived for each regime. Throughout, the method is based on the actual experience of US coalmines.

PRIMARY SUPPORT ROOF FALL DATABASE AND STATISTICAL ANALYSIS

The original ARBS database was based on underground surveys that covered more than 1500 miles (2400 km) of drivage and included 900 roof falls (Molinda *et al*, 2000). The data yielded more than 100 'case histories', each one of which was a portion of a mine defined by its unique geology, depth, roof span, and roof support. NIOSH expanded the database during the 2000s to include another 800 miles (1300 km) of mining drivage and 600 roof falls from another 12 mines known for weak roof conditions. The database was limited to cases where: (1) there were no effects from retreat or multiple seam mining; and (2) the roof was supported by primary roof bolts only (no cable bolts or other supplemental support).

Data collected for each case history included:

1. The stress level.

2. The rock quality represented by the Coal Mine Roof Rating (CMRR); the CMRR was developed in 1994 to quantify geologic descriptions of coal measure rocks into a single strength rating (Mark and Molinda, 2005).

3. The roof span (entry or intersection spans).

4. The roof support density which captures the capacity of the roof bolt system, and was measured using the Primary Support Rating index (PSUP) (Mark *et al,* 2020).

Note that PSUP is a rough measure of the amount of steel installed in the roof. It does not consider the type of bolt (ie fully grouted versus point anchor, tensioned versus non-tensioned etc), because it is difficult to show that one bolt type is superior to another.

The data were analysed using statistics. The first goal of the analysis was to help quantify the boundaries between the three roof support regimes shown on Figure 1. Logistic regression (LR) was used to model the data, because it is the technique of choice when the outcome is binary (like 'successful' and 'unsuccessful'). The LR model that best fit the data was used to derive Equation 1.

$$LnCMRR20 = 0.277 * Ln(H) + 1.64 \qquad (1)$$

where lnCMRR20 is the natural logarithm of the actual CMRR value minus 20 (Mark, 2016), and H is the overburden depth (ft).

Equation 1 is shown on Figure 2 as the 'Discriminant'. It minimises the likelihood of misclassifications, meaning in this case that a successes and failures are approximately equally likely to be misclassified.
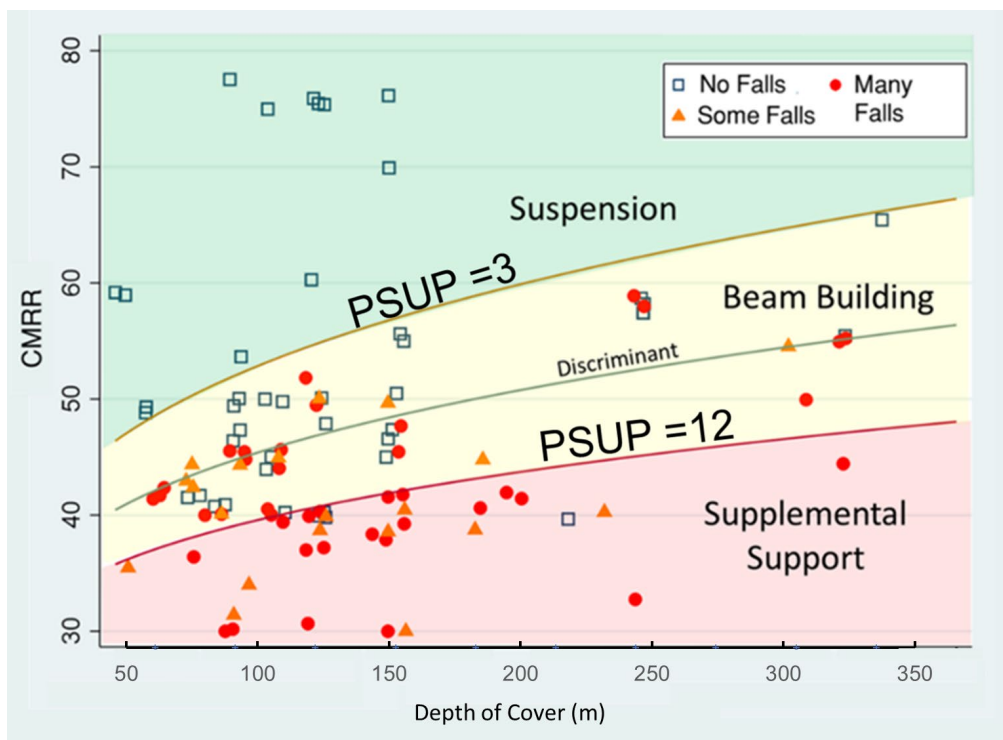
FIG 2 – The roof bolt support case histories, showing the discriminant equation and the estimated boundaries between the three roof support regimes. The 'no falls' category includes all the 'successful' cases with less than two falls per thousand four-way intersections, 'many falls' includes cases with more than ten falls per thousand intersections, and 'some falls' are cases with rates between the two extremes.

As discussed by Mark *et al* (2020), an equation was derived to predict the suggested PSUP at any depth. The final AMRS equation that suggest the appropriate level of primary support is a function of the actual sum of diagonals, the predicted sum of diagonals (which is a function of roof rock

quality), the overburden depth and LnCMRR20 which represents the quality of the roof rock. Once the suggested level of primary support is determined (PSUPs), then mine personnel can try to match that with an appropriate design of the support system. In other words, the suggested PSUPs which is a function of depth, geology and span dimensions should be matched the installed roof support capacity (actual PSUP).

Figure 2 shows that when the suggested PSUP exceeds 12, primary support alone is unlikely to be successful, and supplemental support is recommended. The AMRS method for calculating the rock load for supplemental support design is described by Mark *et al* (2020).

ANALYSIS OF MINE ROOF SUPPORT (AMRS) SOFTWARE

A new software package, Analysis of Mine Roof Support Systems (AMRS), implements the design methodology described in this paper. The AMRS users can select 'Primary Support: Roof Bolts' (for entries) (Figure 3) and/or 'Secondary Support' (for both entries and intersections). In addition, secondary support calculations have been implemented for four support systems: cable bolts, truss bolts, roof bolts and standing supports (Figure 4). 'Primary Support' calculations are performed using the statistical model described above. 'Secondary Support' calculations are performed using the rock load concept. The user also enters the basic input parameters, which are the CMRR, the depth of cover, and the spans (entry width and sum of diagonals) on the Input/Project Parameters/General screen.

The program allows for both Imperial and Metric units and it also allows the user to specify yield or ultimate strength for roof bolts (Figures 5 and 6).
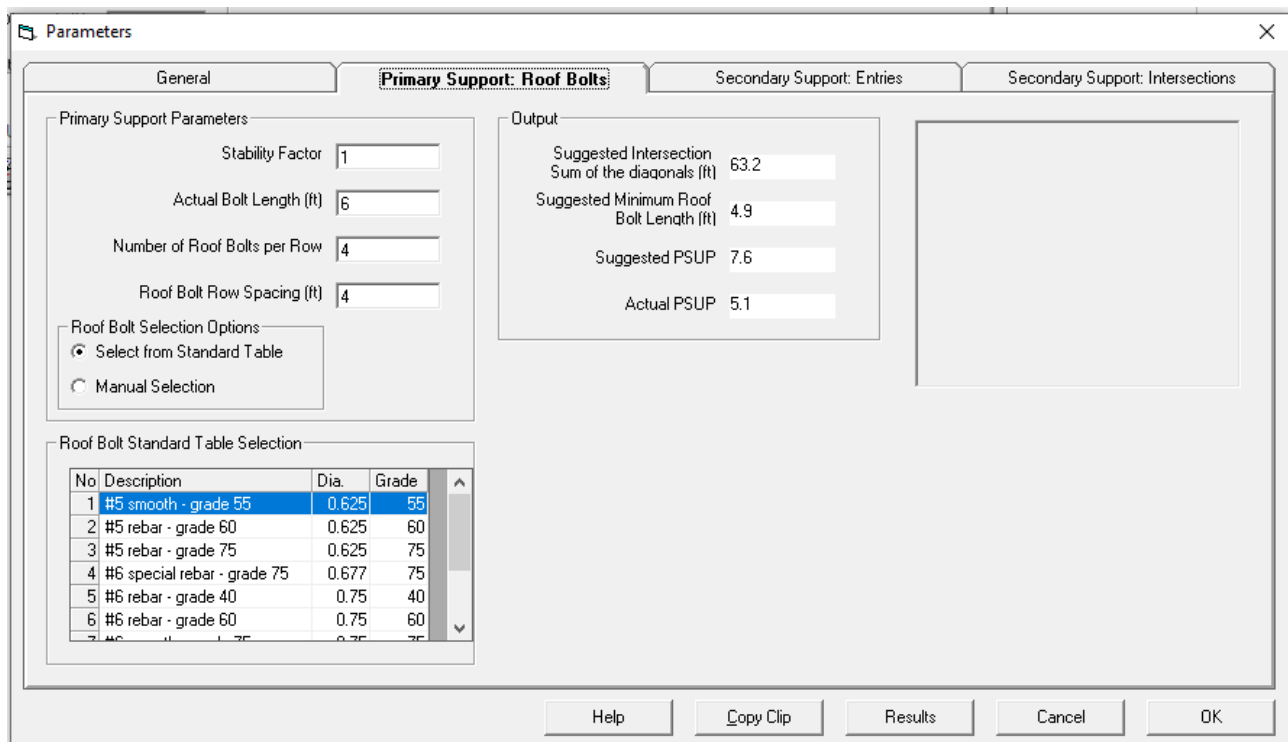
FIG 3 – Primary support options in Imperial units using US bolt specifications; diameter is specified in inches and grade is in thousand psi (ksi) and corresponds to the yield strength of steel.
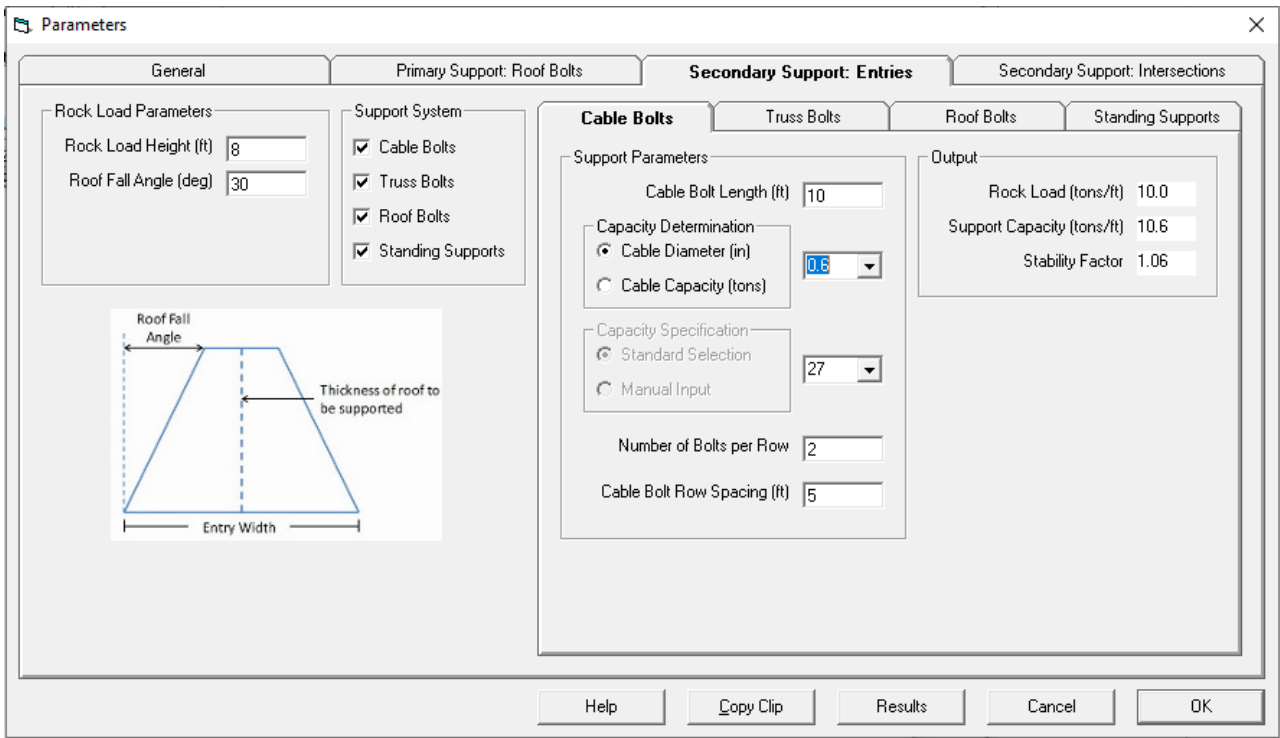
FIG 4 – Secondary support options for cable bolts; cable diameter is specified in inches and bolt capacity in US tons.
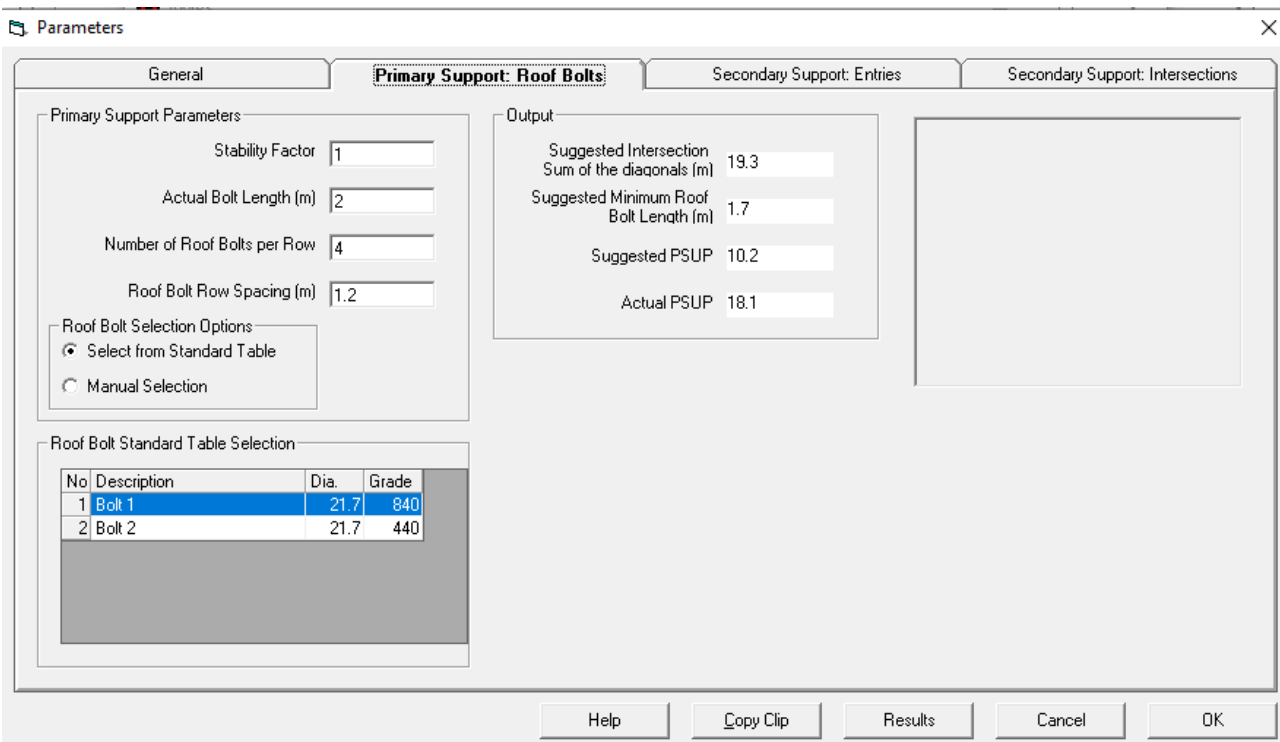
FIG 5 – Primary support options in metric units using AUS bolt specifications; diameter is specified in millimetres and grade is in MPa and corresponds to the ultimate strength of steel.
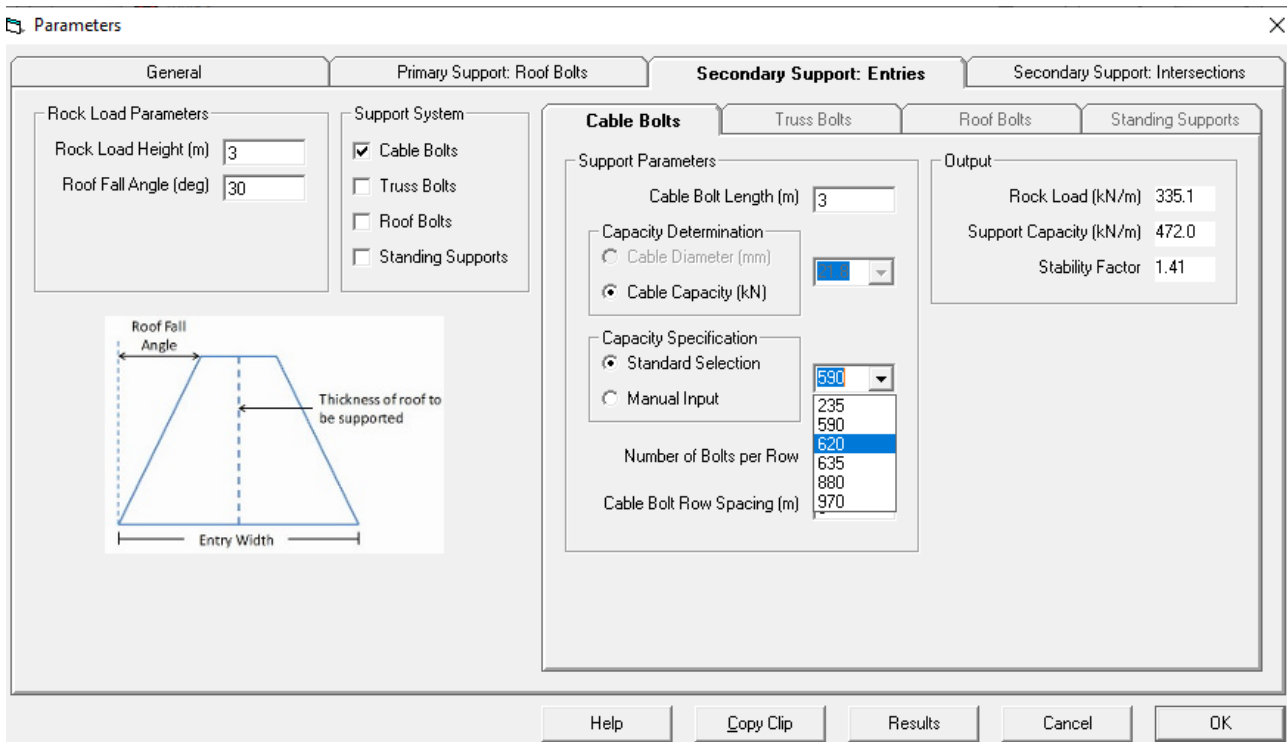
FIG 6 – Cable bolt capacity specification in metric units (kN); rock load and support capacity are specified in kN/m.

AMRS also reports the Reinforcement Density Index (RDI) and PRSUP, two parameters that are used extensively for roof support design in Australia (Thomas, 2010; Molinda *et al*, 2000; Colwell and Frith, 2009) (Figure 7).
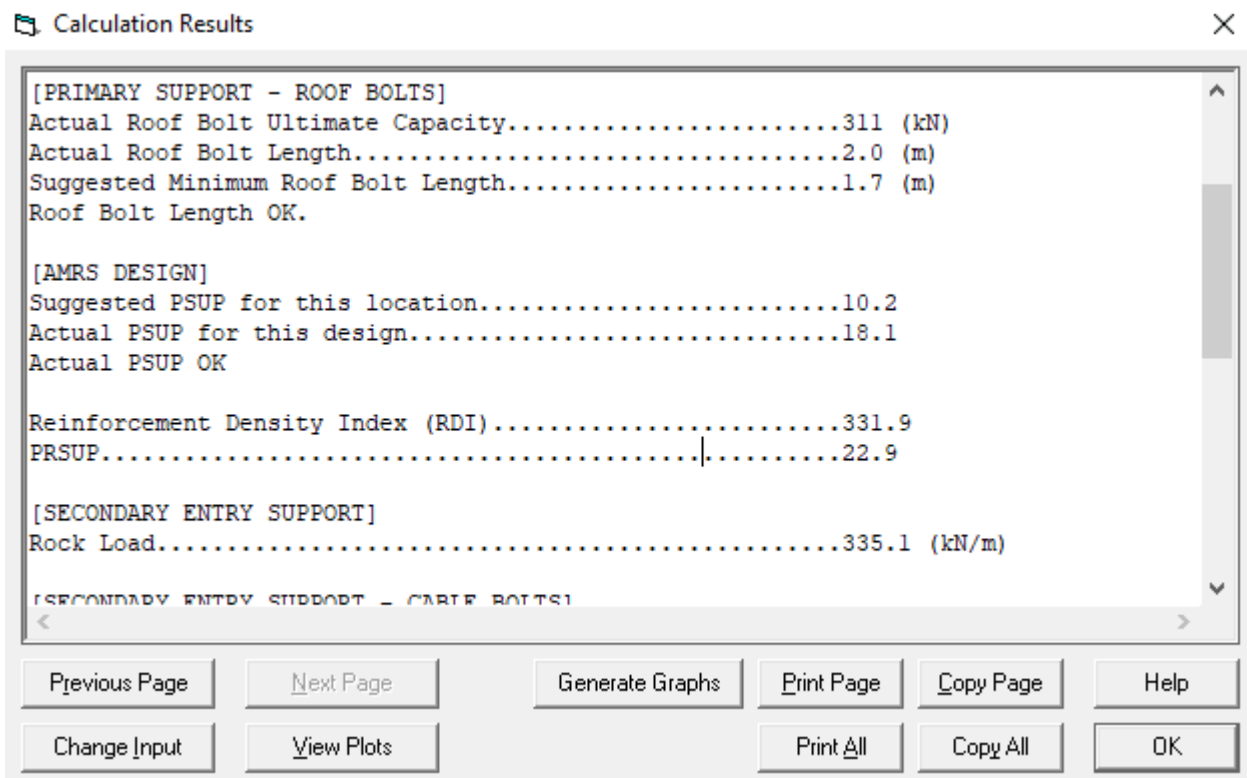
FIG 7 – Calculation results in metric units; in addition to PSUP, the Reinforcement Density Index (RDI) and PRSUP are calculated and displayed. Ultimate bolt capacity is also shown.

The RDI and PRSUP values are calculated using the following equations:

$$RDI = 14.5 * (Lb * Nb * CU)/(Sb * We) \text{ -- (Imperial units)} \tag{2}$$

$$RDI = (Lb * Nb * CU)/(Sb * We) \text{ -- (Metric units)} \tag{3}$$

$$PRSUP = (Lb * Nb * CU)/(Sb * We) \text{ -- (Imperial units)} \tag{4}$$

$$PRSUP = (Lb * Nb * CU)/(14.5 * Sb * We) \text{ -- (Metric units)} \tag{5}$$

where:

CU = the ultimate (tensile) capacity of the bolt (kips or kN)

Lb = the length of the bolt (ft or m)

Nb = the number of bolts per row

Sb = the spacing between rows of bolts (ft or m)

We = the entry width (ft or m)

If the user enters the bolt grade (GR) in Imperial units (ksi), AMRS converts it to the ultimate tensile strength of the bolt steel (UTS (ksi)) using the following logic (based on the minimum values provided in Table 3 of ASTM F432 (2019)):

$$UTS \text{ (ksi)} = (GR * 0.9) + 35 \tag{6}$$

AMRS uses the following equation to convert the ultimate strength of the bolt steel (CU) in Imperial units to the yield strength or bolt grade (GR):

$$GR \text{ (ksi)} = (UTS - 35)/0.9 \tag{7}$$

For cable bolts, the Secondary RDI (SRDI) is given by the equations:

$$SRDI = 14.5 ((Lcb-1)*Ncb*CUcb)/(Scb*We) \text{ -- (Imperial units)} \tag{8}$$

$$SRDI = ((Lcb-0.33)*Ncb*CUcb)/(Scb*We) \text{ -- (Metric units)} \tag{9}$$

Where 0.33 m or 1 ft is subtracted from the length of the cable bolt for the 'tail'.

The secondary PRSUP for cable bolts is given by the equations:

$$PRSUPcb = (Lb * Ncb * CUcb)/(Scb * We) \text{ -- (Imperial units)} \tag{10}$$

$$PRSUPcb = (Lb * Ncb * CUcb)/(14.5 * Scb * We) \text{ -- (Metric units)} \tag{11}$$

The secondary PRSUP uses the primary roof bolt length, rather than the length of the cable bolts, in the calculation. In addition, Ncb = the number of bolts per row, Scb = the spacing between rows of cable bolts (ft or m), CUcb = the ultimate (tensile) capacity of the cable bolt (kips or kN), and We = the entry width (ft or m).

The dimensions of RDI, SRDI and PRSUP are kN/(1000 m).

SUMMARY AND CONCLUSION

During the past two decades, US roof fall rates have fallen dramatically. More robust roof support systems have driven the improvement. A key factor has been an increased reliance on secondary supports, particularly cable bolts, where traditional roof bolting systems are insufficient.

This paper presents an empirical design methodology that builds on and quantifies the basic roof support concepts that have been successful in the US. It defines three modes of roof support, based on the roof strength relative to the stress level, and uses real world data to provide the boundaries between these regimes. It also presents simple guidelines for the design of primary roof bolt and supplemental roof support systems. The new computer package, 'Analysis of Mine Roof Support (AMRS)', implements the design methodology. AMRS is provided free of charge and can be downloaded from http://www.minegroundcontrol.com/roof-support/.

ACKNOWLEDGEMENTS

REFERENCES

American Society for Testing and Materials, 2019. ASTM F432, Standard Specification for Roof and Rock Bolts and Accessories, American Society for Testing and Materials, West Conshohocken, PA, 19428–2959 USA.

Colwell, M and Frith, R, 2009. ALTS 2009 – A Ten Year Journey, *Proceedings of the 2009 Coal Operators' Conference,* Wollongong, NSW, pp 37–53.

Gale, J, Fabjanczyk, M W, Tarrant, G C and Guy, R J, 1992. Optimisation of reinforcement design of coal mine roadways, *Proceedings of the 11th International Conference on Ground Control in Mining*, Wollongong, NSW, pp 272–279.

Mark, C and Molinda, G M, 2005. The Coal Mine Roof Rating (CMRR)—a decade of experience, *International Journal of Coal Geology*, 64(1–2):85–103. https://doi.org/10.1016/j.coal.2005.03.007.

Mark, C and Stephan, R, 2019. Preventing Roof Falls in Weak Ground, *Proceedings 38th International Conference on Ground Control in Mining*, Morgantown, WV, pp 296–300.

Mark, C, 2000. Design of Roof Bolt Systems, NIOSH IC 9453: Proceedings of the NIOSH Open Industry Briefing, New Technology for Coal Mine Roof Support, pp 111–132.

Mark, C, 2016. The Science of Empirical Design in Mining Rock Mechanics, *International Journal of Mining Science and Technology*, 26:461–470.

Mark, C, Molinda, G M and Dolinar, D R, 2001. Analysis of Roof Bolt Systems, *Proceedings 20th International Conference on Ground Control in Mines*, Morgantown, WV, pp 218–225.

Mark, C, Stephan, R and Agioutantis, Z, 2020. Analysis of Mine Roof Support (AMRS) for US Coal Mines, *Mining, Metallurgy and Exploration*, 37:1899–1910. https://dx.doi.org/10.1007/s42461–020–00301-x

Molinda, G M, Mark, C and Dolinar, D R, 2000. Assessing Coal Mine Roof Stability Through Roof Fall Analysis, NIOSH IC 9453: Proceedings of the NIOSH Open Industry Briefing, New Technology for Coal Mine Roof Support, pp 53–72.

Thomas, R, 2010. The Design and Management of Wide Roadways in Australian Coal Mines, *Proceedings 29th International Conference on Ground Control in Mining*, Morgantown, WV, pp 283–293.

Development of a damage/failure mechanisms database for Kazakhstan underground mining industry

M Akhmedya[1] and A Mortazavi[2]

1. School of Mining and Geosciences, Nazarbayev University, Nur-Sultan 010000 Kazakhstan. Email: madyar.akhmedya@nu.edu.kz
2. School of Mining and Geosciences, Nazarbayev University, Nur-Sultan 010000 Kazakhstan. Email: ali.mortazavi@nu.edu.kz

ABSTRACT

Mining is recognised as being one of the most dangerous industries in the world due to the difficult working conditions. Working in such hazardous circumstances in an underground mine often results in a variety of accidents. The working conditions at Kazakhstan's underground mines have deteriorated owing to a lack of a risk-reduction plan and methodology. This paper evaluates different underground mines in Kazakhstan and demonstrates the employed mining method and the observed failure modes. Risk assessment has long been recognised as a valuable technique for preventing accidents. In the underground mining sector, risk assessment tools play an important role in avoiding work-related accidents. However, geotechnical uncertainty is a significant source of severe incidents like stress-induced roof collapse, wedge failure, seismicity etc, which result in human and financial losses. A geotechnical risk assessment performed early in the mine design process might assist justify a different mine design component, such as different support systems for a dangerous location within the mine openings during mining. The goal of this research is to create a damage/failure database aiming at the development of a geomechanical risk assessment methodology. This work identifies a thematic structure linked to risk assessment and management for the examined Kazakhstan mining sector. As part of the developed database, the dominant modes of failure within the Kazakhstan underground mining conditions were investigated. The study will provide opportunities to establish future research objectives for Kazakhstan's mining industry where there are significant gaps between state-of-the-art research and mining operations in practice.

INTRODUCTION

Risk assessment in mines has grown critical not just for establishing a safe working environment, but also because it is now required by law. Because unrecognised hazards can lead to unknown and uncontrollable risks, the competency of a risk assessment process is dependent on the hazard identification phase. As a result, it is critical to identify all potential dangers to control mining risks. The objective of this work was to identify the safety dangers that exist in underground mines in Kazakhstan and to create a preliminary database of such hazards. Accident data from mining firms and open sources was examined to identify potential safety issues that might contribute to accidents. After analysing and assessing the safety risks of identified hazards, the database can be used by the mine managements in making better decisions.

The dominant failure mechanisms that cause instability, need further investigations. An unanticipated shift in failure propagation might considerably delay mining operations and have an impact on both surface and underground infrastructure. Thus, it is important to create a database which eventually can provide miners with some trends of rock mass behaviour. Studies of the failure processes involved, as well as the effect of collapsed rock masses, are major steps to achieve this goal. The aim of this research was to create a damage classification database that enables the identification of the most common failure mechanisms within the Kazakhstan underground mining industry. This was accomplished by comprehensive data collecting from field mapping and analyses of the extent of damaged observed underground.

Overview of the methodology

Collecting reliable data is the most important step in the development of a damage classification database. In this work, a major portion of the data was compiled from the technical reports prepared by the mines geotechnical departments. The presented data had already gone through verifications, statistical analyses, and compared against observations in field. Accordingly, the data was used as

input had reasonable accuracy. This approach was more cost-effective in a sense that we used data that already existed within the investigated mine geotechnical databases, as opposed to direct measurement of data which is very time consuming. In the next phase of this work, it is intended to visit various mine sites across the country and document the observations and dominant failure modes in a more systematic and unified manner.

LITERATURE REVIEW

For all research fields and initiatives, previous, relevant literature must be taken into account. When reading an article, the author starts by discussing past research to map and analyse the research area, inspire the study's goal, and explain the research question and hypotheses, regardless of discipline.

Commonly used underground mining methods

After an orebody has been explored and defined, and enough data has been gathered to support further research, the crucial task of determining the best mining technique or procedures may begin. The decision is merely preliminary at this point, and it will serve as the foundation for a project plan and feasibility assessment. Details may need to be revised later, but the core concepts for mineral extraction should be included in the final plan. In terms of the underlying concepts, just a few mining methods are utilised today. Variations in each of these methods are almost unlimited due to the uniqueness of each mineral deposit (Hustrulid *et al*, 2001). Commonly used underground mining methods are the Room and Pillar method, Stoping methods, and Cut and Fill methods. The room and pillar method is typically used for flat-bedded deposits with modest thickness. In open stopes, this system is used to recover resources. The method leaves pillars to support the hanging wall; miners strive to leave the fewest pillars feasible to retrieve the most ore. There are three types of room-and-pillar mining methods: Classic room-and-pillar, Post room-and-pillar, and Step room-and-pillar. In the stoping methods, the ore is recovered in open stopes that are generally backfilled after mining. Stopes are often huge mine openings that are mined by various configurations and sequences. In the Cut-and-fill method, the ore is extracted in horizontal slices, beginning at the bottom undercut and progressing upward. Muck is loaded and removed from the stope, and ore is drilled and blasted. Mined-out cuts are filled with backfill or waste rock which acts as both a support for the stope walls and a working platform for mining of the upper cuts. Figure 1 illustrates the geometry of the commonly used underground mining methods as outlined above.
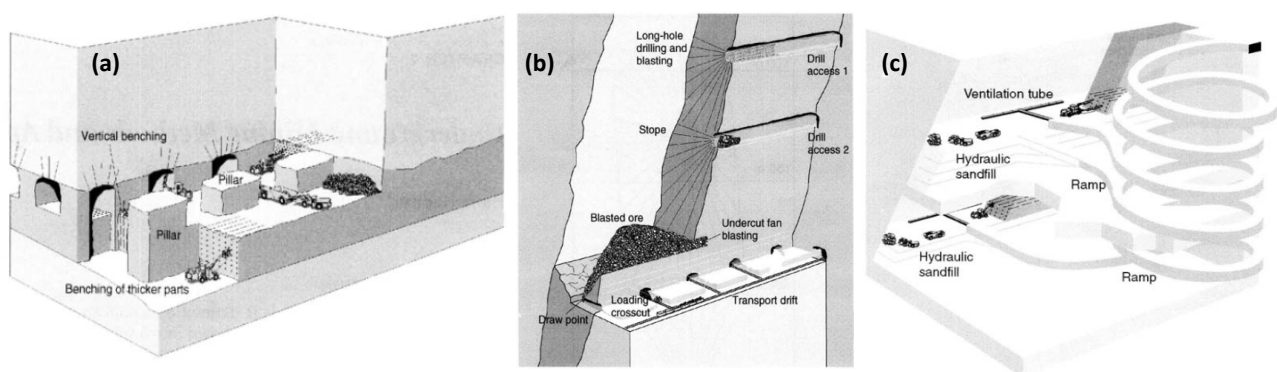
FIG 1 – Commonly used underground mining methods: a) Classic room-and-pillar method, b) Sublevel Open Stoping method, C) Cut-and-fill Method (Hustrulid *et al,* 2001).

Significance of failure modes in geomechanics design

The development of underground mine openings is associated with challenges in terms of ground management and excavation stability. The rock strength is increased as a function of confinement and depth, but it is reduced significantly due to mining leading to extensive failures. Ground failures can occur at microscale, such as development of microcracks in rocks, to the macro scale, in the form of massive falls of ground, dynamic bursting, and wedge failures. Mining at great depth poses geotechnical problems such as rapid collapse and substantial deformation in rock mass structures. Therefore, the recognition and classification of dominant modes of failure are necessary. The

geotechnical problems in underground excavations may be assessed by gathering rock engineering data, considering site-specific variables, and calculating parameter uncertainty. Underground engineering projects need the use of proper mining processes, sequential excavation, and ground support systems (Morissette *et al*, 2014). Estimating rock engineering characteristics, particularly in seismically active mines at high depths, is complicated and unpredictable due to a broad variety of factors in rock mass compositions, ground behaviour modes, failure mechanisms, and in situ stresses. Visualisation, interpretation, and evaluation of the true orientation and geometry of rock mass formations are challenging to achieve during the design process. A complicated failure mechanism, such as rapid failure and substantial deformation, as well as insufficient and incorrect ground support systems, might result in engineering catastrophes during the building stage. To solve the challenges in mining operations, ground control and management techniques should be implemented in line with knowledge, experience, and management.

Failure modes are associated with an abnormal structure or material behaviour. Failure mechanisms are linked to abnormal physical conditions or states. A failure mode is caused by a failure mechanism. In practice, this is reduced to three or four frequent causes of failure due to design flaws, stress concentrations, or other *in situ* and environmental factors. The result of a failure is referred to as a failure mode. To detect the dominant failure modes, the deformational mechanisms of the problem must be known. The governing boundary conditions control the behaviour of underground structures. The underground mine systems have geometric complexities, and material behaviour non-linearities and, thus, require advanced analysis methods to predict the failure mechanisms. Potential failure modes may be detected using advanced numerical methods. The commonly observed failure modes observed in underground mining environments are wedge and planar failures, stress-induced failures, water pressure-induced failures, blast-induced failures and damages, etc.

Review of existing rock damage classification databases

Case no I

Li *et al* (2020) considered the database which comprises records with fields corresponding to seven parameters that characterise the stress state and other geological elements, as well as the support used, seismic parameters related to the rock burst event, and the accompanying damage scale, for each case history. According to the authors, a rock burst is a dynamic failure caused by a sudden and violent release of elastic energy accumulated in rock and coal masses, which can result in fatalities, failure of underground working spaces, deformation of supporting structures, damage to construction machines, and construction delays, among other things. Unlike routine geomechanics issues like slope stability and fracture propagation, which have received a lot of attention, the rock burst phenomena still need more study. As the demand for natural resources grows, the complexity and depth of future underground mines will need better empirical methodologies and innovative multidisciplinary approaches to anticipate and mitigate the risk. The authors discussed five main parameters – buried depth of the tunnel, H; maximum tangential stress of the surrounding rock, MTS; uniaxial compressive strength, UCS; uniaxial tensile strength, UTS; elastic energy index, or their combination in their paper for long-term rock burst prediction (Zhou *et al*, 2016). Those factors, on the other hand, are most often chosen because of their availability early in a project and their effect on rock burst propensity – thus being primarily relevant for long-term forecast – and they may be insufficient for short-term prediction (Li *et al*, 2018). In other words, a short-term rock burst often happens when the superposition of static and dynamic loads exceeds the surrounding rock's capabilities, hence, short-term assessments should include extra information on the development of dynamic stresses.

Case no II

Heal (2010), gathered reports of rock burst incidents in 13 Australian and Canadian deep rock mines, and for the prediction study, he created a database with 254 rock burst case histories of varying strength resulting from 83 recorded seismic events. The database comprises records with fields corresponding to 15 parameters that characterise the stress state and other geological elements, as well as the support used, seismic parameters related to the rock burst event, and the accompanying

damage scale, for each case history. There are seven parameters employed for our analysis of rock burst prediction along with the proposed damage scale (Table 1).

TABLE 1

Descriptive statistics of the input parameters for the selected database (Heal, 2010).

Parameter	Min	Max	Mean	Standard Deviation (SD)
$\sigma 1$/UCS (P1)	18	95	54.51	17.81
Support condition (P2)	2	25	7.88	4.22
Excavation span [m] (P3)	2	30	7.24	3.01
Geological condition (P4)	0.5	1.5	0.90	0.26
Seismic events magnitude (P5)	-0.3	3.5	1.88	0.81
PPV [m/s] (P6)	0.12	7.87	1.66	1.31
Rock density [kg/m^3] (P7)	2700	4300	2966.77	444.78

Selected parameters are stress condition (P1), support condition (P2), excavation environment (P3), geological condition (P4), seismicity (P5, P6), and rock density (P7). Also, the authors introduced the rock burst damage scale (RDS). Based on this scale in this study, rock burst damage is categorised into five tiers. The amount of rock expelled when a rock burst occurs determines the scale's categorisation (Figure 2).
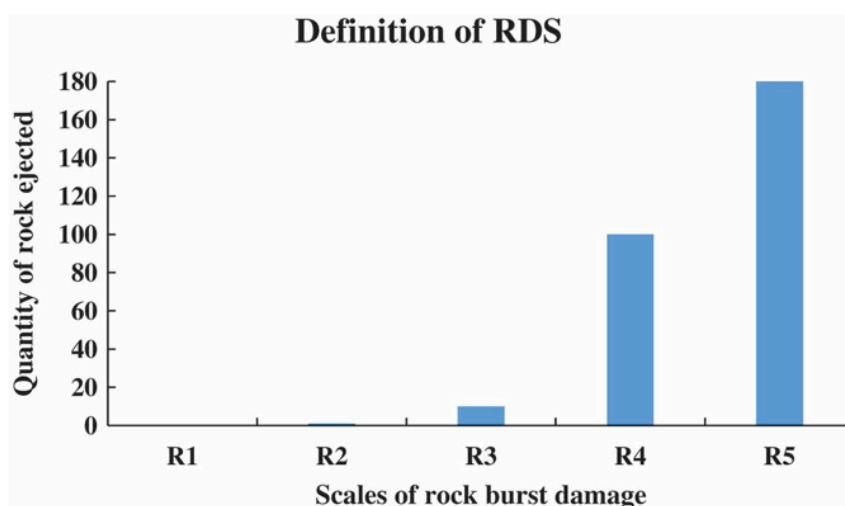
FIG 2 – Schematic diagram of RDS.

The five levels considered are:

R1: no damage or minor displacements in rock mass.

R2: less than 1 ton of rock displaced with minor damage.

R3: 1 to 10 ton of rock displaced.

R4: 10 ton to 100 ton of rock displaced.

R5: above 100 ton of rock displaced.

The discrete values examined for each parameter are summarised in Table 2. P1, P3, P5, P6, and P7 are continuous variables among the specified parameters, while P2 and P4 are discrete variables. The geological and support condition parameters (P2 and P4) were discretised using the reference values proposed by Heal (2010), based on descriptions of those parameters from site reports of rock burst damage; whereas the other parameters were discretised using the software WEKA (a workbench with visualisation tools and algorithms for data analyses and predictive modelling). We

use WEKA's equal frequency binning approach, which divides the data into intervals with about the same number of instances (Holmes *et al,* 1994).

TABLE 2

Classification and discretisation values for all parameters.

Parameters	Classification and discretisation values				
Stress condition $\sigma 1$/UCS	<39.2	39.2–48.65	48.65–58.95	58.95–70.65	>70.65
Normalised value	0	0.25	0.5	0.75	1
Support condition	Dynamic support with pattern reinforcement	Mesh or fibrecrete support with pattern bolting and cable bolts	Mesh or fibrecrete support with pattern bolting and second bolting	Mesh or fibrecrete support with pattern bolting	No surface support with spot bolting reinforcement
Normalised value	0	0.25	0.5	0.75	1
Excavation span (m)	<5.15	5.15–5.95	5.95–7.05	7.05–9.45	>9.45
Normalised value	0	0.25	0.5	0.75	1
Geological factor	No major structures like faults, folds, only minor blast related structures	No major structures like faults, folds, but the discontinuity and unstable rock block in rock mass may promote rock failure		No major structures like faults, folds, that could induce the rock burst occurrence	
Normalised value	0	0.5		1	
Seismic event magnitude	<1.25	1.25–1.65	1.65–2.05	2.05–2.6	>2.6
Normalised value	0	0.25	0.5	0.75	1
Particle peak velocity (PPV) [m/s]	<0.575	0.575–1.02	1.02–1.71	1.71–2.71	>2.71
Normalised value	0	0.25	0.5	0.75	1
Rock mass density [kg/m³]	<2800	2800–2900	2900–3000	3000–3100	>3100
Normalised value	0	0.2	0.4	0.6	1

Case no III – Failure modes and effect analysis (FMEA)

Islam and Chakraborty (2021) considered the working conditions of Barapukuria Coal Mine (BCM) which is an underground mine at the North-western side of Bangladesh. According to authors, this mine has grown insecure because of lack of a risk-reduction plan and methodology in place. As a result, the goal of this study was to use the failure modes and effect analysis (FMEA) approach in BCM to identify possible risks. FMEA is a quality management technique that calculates a risk priority number (RPN) using severity, occurrence, and detection scores to identify likely failure modes. The estimate of RPN to prioritise failure modes is an important part of FMEA. A quality point scale (1–10) is commonly used at this step to assess the three aspects of a failure mode's dangers, with the higher the score, the greater the risk of accidents.

They looked at some accident statistics in BCM and discovered that roof falls are more dangerous than other types of accidents. The authors examined the causes and consequences of accidents using the FMEA approach, and then advised steps to decrease dangers. As a result, an integrated strategy that can forecast risk before actual catastrophes is essential, and the FMEA can be a useful tool in this scenario since it is a strong method for detecting multi-horizon risks and reducing threats that can be enhanced further. They analysed several mishaps that happened during BCM production stages, including their causes, impacts, and controls. This is normally accomplished by a careful investigation of the mine region by a geologist or geotechnical engineer. Authors have made a table with hazard, potential causes, consequences, and actions which should be taken to prevent those issues (Table 3).

TABLE 3

Major hazards identified in BCM with Failures and Controls (Islam and Chakraborty, 2021).

Hazards	Potential causes	Potential consequences	Action Recommended
Roof fall	Geological setting and geotechnical status, Inadequate support system, Collapse of pillar.	Collapsed roadway, Damage machineries and personnel's, Death workers.	Proper supporting systems, Monitoring strata pressure regularly through EED, systematic support rule (SSR) formulated and imposed.
Subsidence	Underlying goaf and barriers, Longwall mining method, Working depth in mine, Nature of roof.	Goaf area originated, Collapse of mine, Disrupt groundwater table, Damage agricultural land, houses and factories	Improving mine design using longwall retreating mining method, Applying Hydraulic Sand Stowing (HSS) filling method, Regular subsidence monitoring and treatment
Water inrush	Adjacent UDT aquifer sources, Water seepage into mine, Faults in the mining area	Shutdown of production, Water seeping into mine workings, Loss of men and equipment	Controlled by regular pumping, Monitoring fissures and faults, Timely reporting by hydrogeology section, Water volume monitors using pre-set alarm.
Mechanical	Installed heavy equipment, Brakes fail, Unawareness driving, Defective equipment	Increased temperature in mine, Equipment jams, Collapse roadway.	Equipment and brake maintenance, Aware of the mine working, Regular maintenance
Spontaneous combustion	Intrinsic and Extrinsic properties of coal.	Production operations sealed off, Endangering lives and properties, Polluted mine environment.	Worked out panels sealed properly, R&D efforts initiated in the mine level, Storage height not more than 7 m, Avoiding fire occurrence using proactive energization
Electrical	Wet working conditions, Defective equipment, Earthing system damaged.	Electric shock and/or burn, Fire arising from electric defects, Ignition of firedamp or coal dust.	Inspect equipment regularly, Checking earthing point regularly, Use of Personal Protective Equipment.
Poisonous gas emissions	Spontaneous combustion, Poorly controlled Ventilation system, Mine fires.	Failing of cooling system, Oxygen deficiency, CO and CH4 emissions.	Sealed goaf area, Heat control procedure, Airborne respirable dust (ARD) monitoring, Developing borehole gas survey.
Temperature and humidity	Geothermic gradient, Mining equipment, Auto-oxidation of coal and carbonaceous matter, Mine water thermal influx, High temperature of surface air.	Heat stroke, Ventilation system damaged, shutdown production.	Heat Reduction, Allowing optimum quantity of air in longwall panels, Channelised water percolated intake airways, Air cooling system installed in the panels.

DATABASE DEVELOPMENT FOR KAZAKHSTAN UNDERGROUND MINES

General database format

When building a database system, the most critical aspect to consider, is the data that needs to be gathered. Once the key parameters are selected, the following considerations must be made:

- Which data are required for quantitative back-analysis?

- What contextual information is critical?

- What information is necessary to collect?

Data collected via observation (such as damage mapping) should be maintained separate from data collected through measurement (such as seismic events). Correlations between the two may be made afterwards; however, it is critical not to contaminate observational data with assumptions regarding the cause of the harm. Each damage mapping report must have some basic information. This comprises the following:

- The date and time of the observation.

- The person who makes the observation.

- Short summary of the observation.

It is also critical to record the period since the last observation for failures. This enables the definition of a time frame within which a potentially harmful event may have happened (instead of assuming that the damaging event was the most recent). Multiple inspections of the same place as part of a normal ground-condition auditing procedure may also assist in determining whether damage was genuinely caused by a failure, illustrating the need of a systematic documenting strategy. However, in this research we used only secondary data collection method. In future works, systematic visits from the mining sites will be carried out to collect primary data. The compiled data consists of general information of the mine, mining method, rock mass characteristics, observed failures, values of measured RMR and RQD, and lithology.

Database design

The data presented in the tables were derived from the technical reports provided by the mine geotechnical department and prepared by SRK consulting for the mines. It consists of six main parameters mentioned above. Based on these reports, it is concluded that the increased structural and tectonic disturbance of the rock mass, intense fracturing, shearing of rocks, and the presence of a significant amount of chlorite and sericite in them cause low natural strength and stability of ores and host rocks with the classification of the deposit as complex in terms of engineering and geological conditions for industrial development. Schistosity has a significant impact during the development of workings along the strike, when, due to its opening under pressure, swelling and exfoliation of rocks appear, especially in the central and eastern parts of the field. Table 4 represents the main geomechanical and geological parameters of the Tishinsky mine, which is located 15 km south of Ridder and uses the sublevel open stoping mining method. It is reported that the increased structural and tectonic disturbance of the rock mass, intense fracturing, and rock shearing has led to a very low *in situ* rock mass strength and stability. In terms of RMR rating indicators, the Tishinky mine rock mass is characterised as medium to poor quality.

TABLE 4

Geomechanical data reported for Tishinsky mine (SRK Consulting, 2018a).

Rock mass characteristics	Observed Failures	Horizon, Rock type, (RMR)	Rock type (RQD%)	Lithology
* A large zone of hydrothermal alteration of volcanic-sedimentary rocks with pyrite-polymetallic veinlet-disseminated mineralisation. * Overlain by Quaternary formations up to 40 m thick	Risk of destruction of the walls of the pumping chamber	* -290 siltstones (46) * -290 shales (44) * -270 siltstones (61) * -310 shales (50) * -270 quartz-chlorite seritised schists (41) * -250 quartz-chlorite seritised schists (55) * -250 shales (49) * -250 chlorite-sericite-quartz rocks (35)	* Siltstones and shales (36) *Albitophyres (54) * Ore (43)	Siltstones Micro Quartzites Quartz albitophyres Chlorite-sericite-quartz schists Solid sulfide polymetallic ores Solid sulfur-pyrite ore Backfill intervals

Similarly, the Dolinny deposit is characterised by complex morphology of orebodies, a variety of geological and structural conditions of occurrence, and is characterised by high variability in the stability of rocks. Table 5 represents the compiled data about the main geomechanical and geological parameters of the Dolinny mine which is located 3 km east of Ridder outskirts and uses the sublevel open stoping mining method. The geomechanical parameters of all lithological differences were determined and the average values are given in the table above.

TABLE 5

Geomechanical data reported for Dolinny mine (SRK Consulting, 2018b).

Rock mass characteristics	Rock type, (RMR)	Rock type (RQD%)	Lithology
* Complex morphology of orebodies * A variety of geological and structural conditions of occurrence * Variability in the stability of rocks.	* quartz albitophyres (70) * tuff gravelstones (70) * siliceous aleuropelites (69) *seritised breeds (66) * microquartzites (65) * hanging wall aleuropelites (70) * red-green tuffs (70)	* quartz albitophyres (93) * tuff gravelstones (92) * siliceous aleuropelites (85) * seritised breeds (78) * microquartzites (74) * hanging wall aleuropelites (89) * red-green tuffs (88)	* Lithological types of hanging wall rocks: hanging wall aleuropelites, tuffs, tuffites, gravelstones * Ore zone: quartzites, microquartzites, siliceous-calcareous aleuropelites, silty sandstones, grey-green albitophyres, the lower member is represented by volcanomictic and tuffaceous gravelstones * Dykes occur in the ore zone: diabases, diabase porphyries; interlayers of sericite-argillaceous, sericite-carbonate rocks appear on ore-rock contacts.

Table 6 represents the compiled data about the main geomechanical and geological parameters of the Ridder-Sokolny mine which is located 3 km from the Ridder downtown. In terms of mining method, this mine has a combination of sublevel open stoping, sublevel caving, and narrow vein drift and fill to selectively mine individual or small clusters of veins with high gold grades. In the process of performing the work, the available data on the physical and mechanical properties and parameters of the fractured massif rocks were considered. The hardest rocks of the deposit can be considered microquartzites, agglomerate tuffites, and the weakest rocks are sericite-chlorite-quartz rocks and shales.

TABLE 6

Geomechanical data reported for Ridder-Sokolny mine (SRK Consulting, 2018c).

Rock mass characteristics	Observed Failures	Rock type, (RMR)	Rock type (RQD%)	Lithology
*Upper ore zone: a cluster of subhorizontal VMS-style lens-shaped bodies associated with a carbonaceous unit adjacent to a vertical fault structure * The lenticular VMS-style mineralisation is underlain by a steeply dipping to subvertical polymetallic Cu-rich stringer – stockwork ore zone. Structurally controlled gold-bearing	Risk of flooding of mine workings by surface water: 1 – groundwater breakthrough from Quaternary deposits 2 – water breakthrough from existing collapse craters 3 – water breakthrough from existing flooded	* calcareous aleuropelites + quartz albitophyres + red-green tuffs + hanging side aleuropelites + ores – (58) * microquartzites + sericite microquartzites (68) * sericite-argillaceous shales (54) * sericite-carbonate rocks (60) * sericite-chlorite-quartz rocks agglomerate tuffs (60)	*calcareous aleuropelites + quartz albitophyres + red-green tuffs + hanging side aleuropelites + ores (61) * microquartzites + sericite microquartzites (58) * sericite-argillaceous shales (34) * sericite-carbonate rocks (62) * sericite-chlorite-quartz rocks (71) * agglomerate tuffs + felsite porphyries + porphyrites (74)	* Calcareous aleuropelites * Quartz albitophyres * Red-green tuffs * Hanging wall aleuropelites * Quartz-barite rocks * Quartzites * Sericite microquartzites * Sericite-carbonate rocks * Sericite-chlorite-quartz rocks * Agglomerate tuffs, quartz-sericite rocks, gravelstones silty tuffs * Quartz albitophyres * Diabases, diabase porphyries (dykes) * Plagioclase porphyries

Based on reported data, the dominant failure modes for Tishinsky and Ridder-Sokolny mine were determined and compared against one another. The failure modes were plotted against recorded RMR and RQD distributions for both mines. The average values of RMR and RQD were calculated, and the failure modes were derived from actual observations reported for each mine site.

Figure 3 represents the correlation between RMR values and observed failure modes. It can be seen from this figure, that at the average RMR value of 47.6 the destruction or failure of the walls of the pumping chamber was observed for the Tishinsky mine. Moreover, for the Ridder-Sokolny mine at an RMR value of 60, the risk of flooding of mine workings by surface water was observed. As can be seen, the failures occurred mostly for the rock masses having an RMR rating between 45 and 60 which corresponds to a fair rock mass. Figure 4 shows the average values of RQD at which failures were observed. The average value of RQD for the Tishinsky mine where the failure of the walls of the pumping chamber was observed equals 44.3. For the Ridder-Sokony mine, the risk of flooding of mine workings by surface water was recorded at an average RQD value of 59.5. It can be seen

that failures mostly occur where the rock mass RQD was between 40 and 60 which represents poor to fair rock masses.
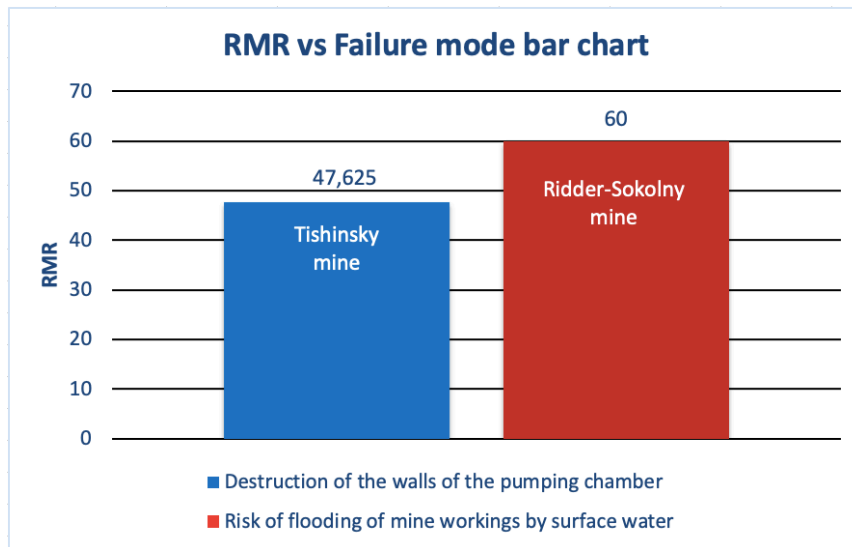
FIG 3 – The calculated distribution of failure modes for Tishinsky and Ridder-Sokolny mines as a function of recorded RMR.
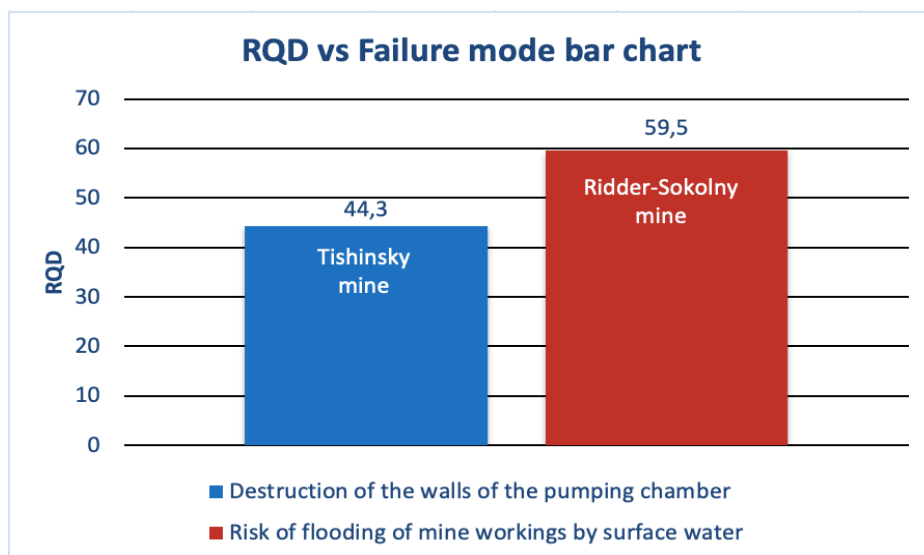
FIG 4 – The calculated distribution of failure modes for Tishinsky and Ridder-Sokolny mines as a function of recorded RQD.

A similar analysis was carried out for Belousov mine which is located at East of Kazakhstan. The mining method of this mine is a combination of sublevel stoping, both with and without pillars, cut-and-fill stoping and sublevel caving. The available geomechanical data are summarised in Table 7 which was obtained through personal communication with mine geotechnical department. The presented data shows the complexity of the engineering and geological conditions of the mine.

TABLE 7

A summary of available geomechanical data reported for Belousov mine.

Classifications of rocks and ores of the deposit, parameters of rock properties	Fracture density (joints/m)	Fracture modulus (joints/m)	Compressive strength (MPa)	Tensile strength, (MPa)	The strength coefficient according to Protodyakonov	Assessment of the complexity of engineering and geological conditions of the field development
Dense monolithic rocks, porphyry, porphyry, siliceous siltstones, quarried sandstones, siltstones, quartzites, gravelites, gravelly sandstones, ore, marble.	1	<5	>90	>15	6.3	Very simple engineering and geological conditions of mining. The occurrence of dangerous phenomena is unlikely.
Porphyry, porphyry, sandstones, siltstones, siliceous siltstones, gravelites, gravelly sandstones, chloritised epidotised sandstones, calcareous sandstones-siltstones, marbles.	2	5–10	90–60	15–10	5–6.3	Simple engineering and geological conditions. In most cases, the workings will be stable. There may be stabs, detachments, dislocations.
Shale: porphyry, sandstones, siltstones, sandstones, aleurope sandstones, gravelites sandstones, chlorite-quartz shales, chlorite-sericite-quartz shales, carbonate-quartz-chlorite shales, epidote-chlorite-quartz shale.	3	10–15	60–30	10–6	5–6.3	Rather complex engineering and geological conditions. The most likely are stabs, detachments, rockfalls.
Intensely shale, fractured sandstones, siltstones, tectonic shales, chlorite-sericite-quartz shales, chlorite-quartz shales, carbonate-quartz-chlorite shales, epidote-chlorite-quartz shales.	4	>15	<30	<6	<5	Very difficult engineering and geological conditions. Collapses and rockfalls are most likely.

Based on the conducted assessment, the entire geological array of the deposit was divided into four classes of potential rock instability. The 1st class of potential instability of rocks in the deposit is formed by low-power, unstressed areas in terms of falls of ground. The 2nd class of potential instability of rocks at the deposit is widespread (40–60 per cent). It is represented by both brittle failure and large deformations in rock units such as marbled limestones, siltstones, etc. The 3rd class of potential instability of rocks is widespread in melange bodies and crushed zones, confined to the steep part of the South Grebenshinskaya tectonic plate. This class of potential instability is presented by intensely fractured brittle rocks and intensely dissected fragmented crushed plastic rocks. The 4th class of potential instability includes crushed zones and shear zones at orebody contacts. Petrographically it is represented by tectonic shales, fragmented siltstones, sandstones, and marbled limestones, with low strength properties.

CONCLUSION

In this research several underground mines of Kazakhstan, demonstrating the mining technology used and failure mechanisms were evaluated. The failure classification database was developed for three main mines, namely Tishinksy, Ridder-Sokolny and Dolinny. It can be seen from the derived charts that failures mostly occur at zones of poor to fair rock masses. In the presented work data was compiled from previous geomechanical analyses conducted within the mines geotechnical departments. All geotechnical data were compiled within the Microsoft Excel environment and analysed. The developed database is work in progress and the next step of the project is conduct *in situ* and direct measurement of key geotechnical data with regard to the observed failure modes. Another challenge in the development of the database is the confidentiality of some data, in

particular, the ones that led to accidents. The final goal of this research is to develop a failure and damage classification chart for Kazakhstan underground mining industry which can be used in geomechanical risk assessment of new and developing underground mines.

ACKNOWLEDGEMENT

REFERENCES

Heal, D, 2010. Observations and Analysis of Incidences of Rockburst Damage in Underground Mines, School of Civil and Resource Engineering, University of Western Australia, Perth.

Holmes, G, Donkin, A and Witten I H, 1994. WEKA: A machine learning workbench, *Proceedings of ANZIIS '94 -Australian New Zealand Intelligent Information Systems Conference*, pp 357–361.

Hustrulid, W A, Bullock, R C and Bullock, R L, 2001. Underground mining methods: Engineering fundamentals and international case studies, SME.

Islam, M Z and Chakraborty, P, 2021. Importance of failure modes and effect analysis application for risk analysis in Barapukuria Coal Mine, Bangeladesh, *Complexity*, 8(5).

Li, N, Zare Naghadehi, M and Jimenez, R, 2020. Evaluating short-term rock burst damage in underground mines using a systems approach, *International Journal of Mining, Reclamation and Environment*, 34(8):531–561.

Li, N, Zare, M and Jimenez, R, 2018. Evaluating the importance of factors affecting short-term rock burst damage using rock engineering systems, *Proceedings of the 2018 European Rock Mechanics Symposium*, vol 2.

Morissette, P, Hadjigeorgiou, J, Punkkinen, A R and Chinnasane, D R, 2014. The influence of change in mining and ground support practice on the frequency and severity of rockbursts, *Proceedings of the 7th International Conference on Deep and High Stress Mining*.

SRK Consulting, 2018a. Geomechanical state of the mountain range on Tishinsky mine, Report prepared for KAZZINK LLP.

SRK Consulting, 2018b. Geomechanical state of the mountain range on Dolinny mine, Report prepared for KAZZINK LLP.

SRK Consulting, 2018c. Geomechanical state of the mountain range on Ridder-Sokolny mine, Report prepared for KAZZINK LLP.

Zhou, J, Li, X B and Mitri, H S, 2016. Classification of rockburst in underground projects: comparison of ten supervised learning methods, *Journal of Computing in Civil Engineering*, 30(95):04016003 1–13, doi:10.1061/(ASCE)CP.1943–5487.0000553.

Ground support systems at Rampura Agucha Underground Mine

B Banerjee[1], S Parihar[2] and N Kumar[3]

1. Deputy Head Geotechnical, RAM, Hindustan Zinc Ltd., Vedanta, Bhilwara, Rajasthan, 311022, India. Email: binayak.banerjee@vedanta.co.in
2. Deputy Manager Geotechnical, RAM, Hindustan Zinc Ltd., Vedanta, Bhilwara, Rajasthan, 311022, India. Email: sunil.parihar@vedanta.co.in
3. Head Technical Services, RAM, Hindustan Zinc Ltd., Vedanta, Bhilwara, Rajasthan, 311022, India. Email: nirmalendu.kumar@vedanta.co.in

INTRODUCTION

Rampura Agucha Pb-Zn Mine (RAM) is located about 200 km to the south-west of Jaipur in the state of Rajasthan, India. Open pit mining operations commenced in 1988 and continued to 2018. RAM open pit footprint is the largest in India with length of 2000 m, width 1500 m and depth of 400 m. Development of an underground mine under the operating pit commenced in 2013, through trial mining longhole open stoping with cemented backfill was established as a preferred mining method. Nine years in operations underground mine has reached the production capacity of 4.5 MT, which represent more than 70 per cent of the ore volume mined by the pit. RAM is currently the world second largest underground Pb-Zn mine. The isometric view of the complete mine is shown in Figure 1.
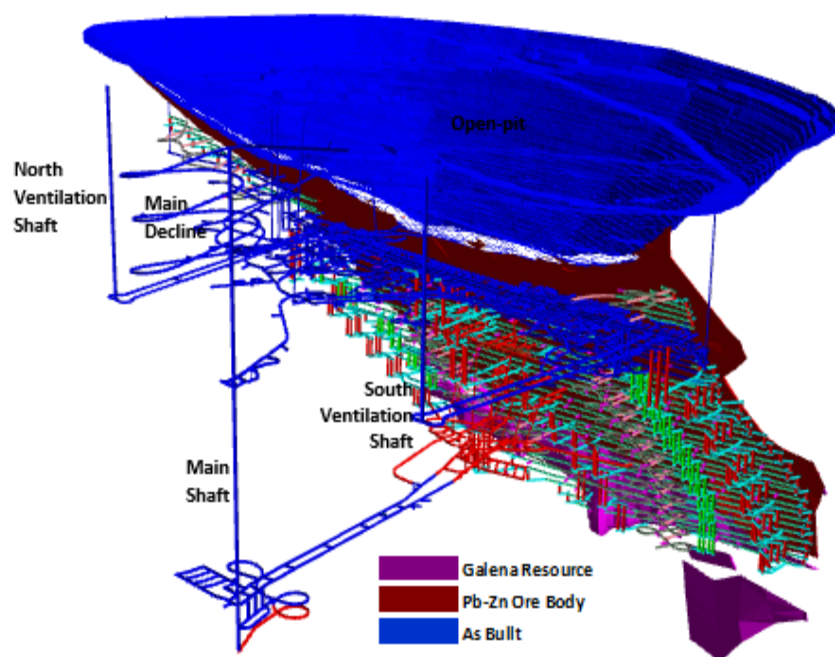
FIG 1 – Isometric view of RAM mining layout.

Geotechnical conditions at RAM are diverse and challenging, which require special consideration for stope mining and underground development. This paper discusses ground support regime adopted at the mine.

GEOTECHNICAL CONDITIONS

Current mining horizons are at a depth 500–700 m below surface. The *in situ* stress regime can be characterised as following: σ_1 is horizontal and runs approximately parallel to the orebody (Messy Private Ltd, 2011). The ratio of vertical and horizontal stress is about 1.2.

There are three geotechnical domains (HZL RAM Internal Report, 2022):

1. Foliated Schist/Gneiss.

2. Psammitic Bands and Intrusions.

3. Ore Zone.

Intact rock properties (CIMFR, 2022) and Q' values for these domains are presented in Table 1.

TABLE 1

Geotechnical domains.

Domain	Sub domain	UCS (MPa)	Young's modulus E (GPa)	Q'
Foliated Schist/Gneiss	GBSS/GBSG	45	11.36	7.8
	GBG	70	14.49	13.2
Psammitic Bands and Intrusions	QTZ/QBG	70	22.39	13.1
	PEG	80	17.36	6.1
	AMP	90	18.5	25.6
Ore Zone	Ore	60	20.75	6.0
	OSZ	10		0.9

The anisotropic nature of the major geotechnical domain is illustrated in Figure 2.
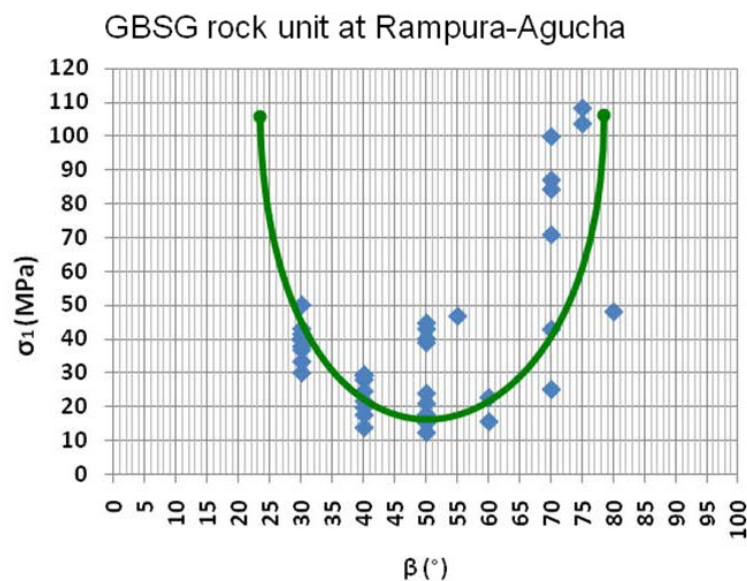
FIG 2 – Intact strength anisotropy – GBSG.

All new excavations are regularly mapped. The mine has developed a comprehensive three-dimensional litho-structural model using Leap Frog software, which is regularly updated and is being utilised for mine planning and geotechnical assessments. The transverse view of the mine has been provided in Figure 3 to visualise the orientation of the footwall rock units with respect to the open pit and the ore body.
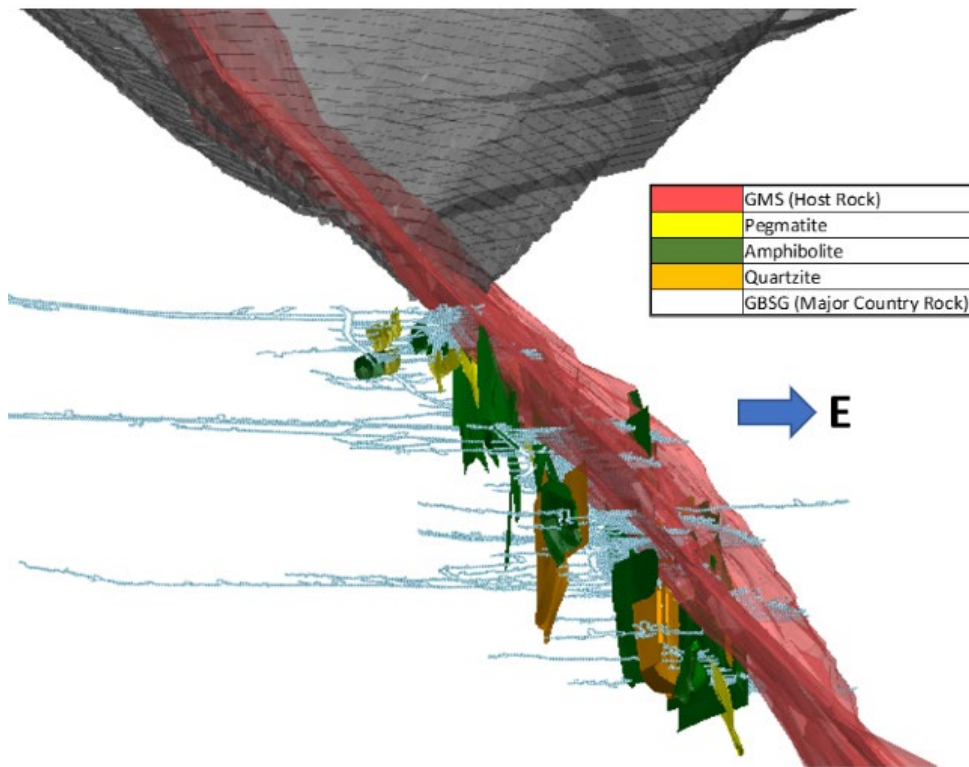
FIG 3 – Litho-model of RAM UG mine.

GROUND SUPPORT SYSTEMS

The mine develops more than 30 km of tunnels annually, typical dimensions are 5.3 m × 5.6 m for declines and footwall drives and 4.8 m × 4.8 m for ore access drives. A typical ore access layout is shown in Figure 4.
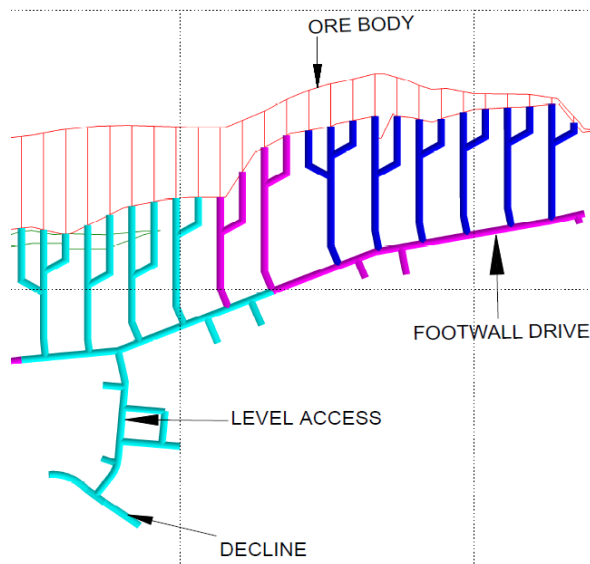
FIG 4 – Ore access layout at -580 mRL.

It is worth noting that more than 70 per cent of development is situated in a weak foliated gneiss (GBSG). This lithological unit tends to rapidly deteriorate when exposed to humid conditions, hence all development is shotcreted floor to floor, as shown in Figure 5.

FIG 5 – Footwall drive at -380 mRL.

Development drives in GBSG, which are oriented at less than 40 degrees to the trend (N10°E) of foliation, are experiencing squeezing deformations. A typical mechanism of development deterioration is shown in Figure 6.
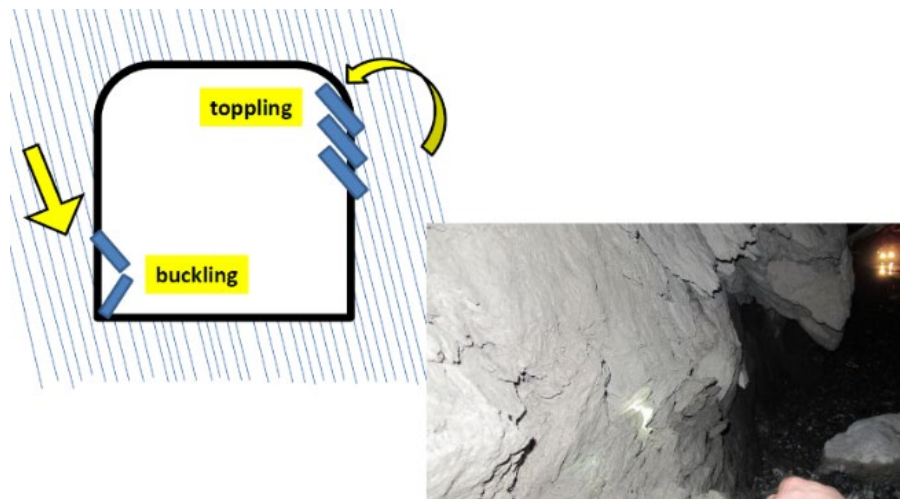
FIG 6 – Deterioration of footwall drive at -205 mRL.

In the early stages of underground mining under the operating pit, development in mining areas subparallel to foliation experienced closure of more than 300 mm and had to be continuously rehabilitated to maintain safe access. This led to a review of the ground support regime – surface support was strengthened, and cable anchors were added to redistribute support load deeper into the rock mass. Support system utilised for development subparallel to foliation in proximity of open stoping areas is shown in Figure 7. Upgradation of support systems allowed to maintain safe access and reduced rehabilitation requirements by more than 80 per cent.
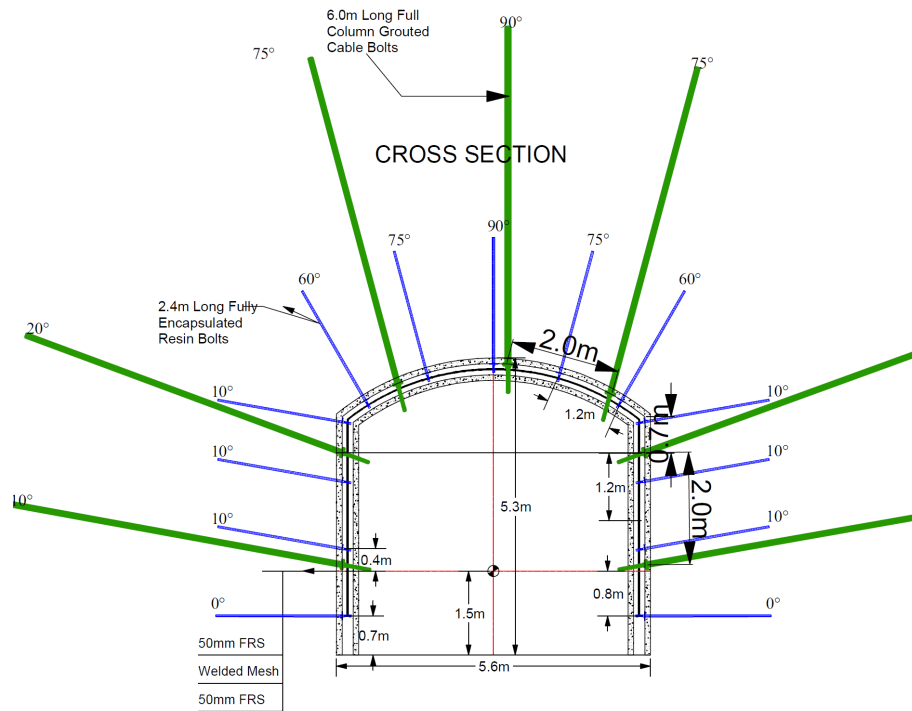
FIG 7 – Ground support for development subparallel to foliation close to stoping areas.

In declines and mine infrastructure development located at a distance more than 200 m from mining areas squeezing is mild, with tunnel closure less than 100 mm, support system used in these areas is shown in Figure 8.
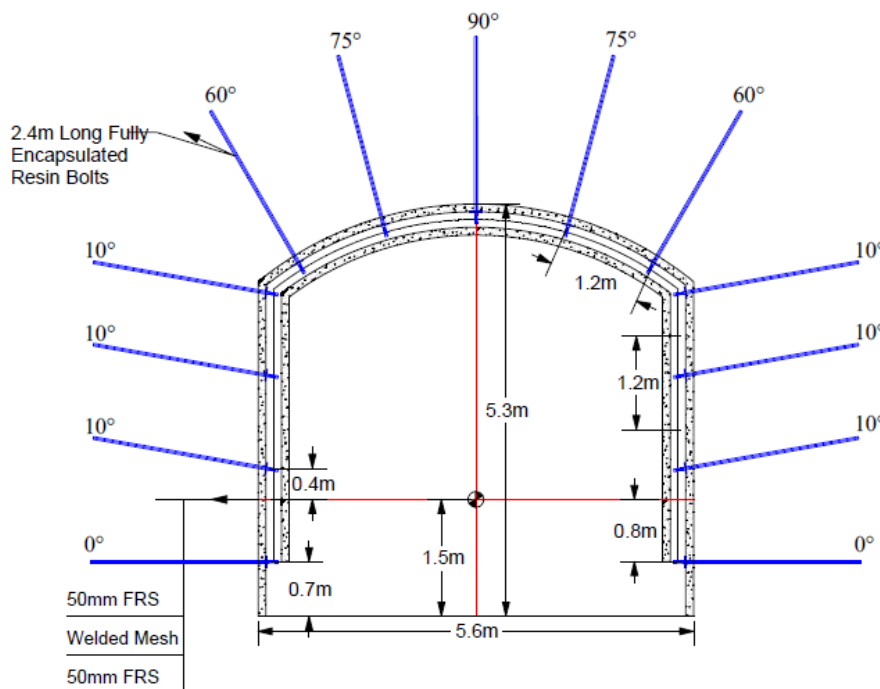
FIG 8 – Ground support for declines about 200 m away from stoping areas.

Another important aspect is ground support for development of cross-cuts through ore. More than 60 per cent of such development is in a very weak, soil like, shear zone. RAM utilises grouted SDA's and significant surface support (as shown in Figure 9) to develop through this challenging ground. Performance of this support system has been very reliable.
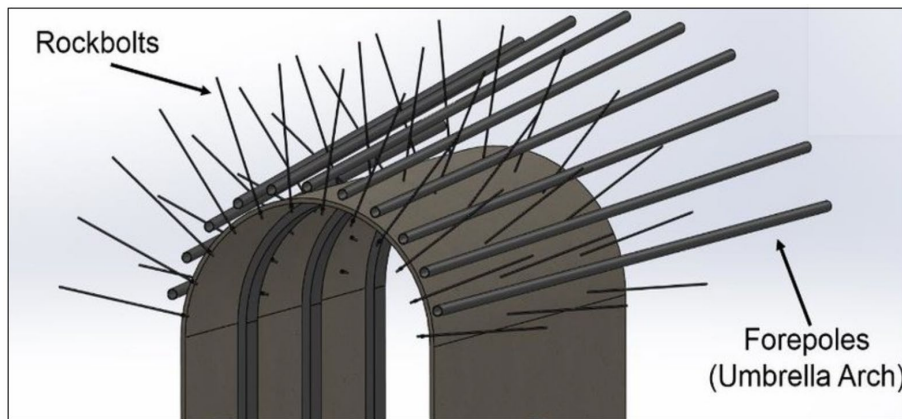
FIG 9 – Section of drive showing installed fore poles and rock bolts within shear zone.

GROUND SUPPORT REVIEW

LOM ground support modelling

RAM has carried out a Life-of-mine ground support study to assess the ground support requirements as mining fronts move to depths 1000 m below surface (Beck Engineering, 2020). It provides a general guide for anticipated support performance.

Three dimensional numerical simulations of LOM stoping sequence were carried out to determine suitable ground support for future development considering the impact of mining induced. This includes footwall drives, declines, ore drives and development through paste. To evaluate excavation stability and support elements sufficiency, the following criteria have been reviewed:

- bolt loads and strains

- depth of damage to assess embedment

- displacements and damage to assess the potential for instability

- factor of safety for stable areas by comparing the capacity of support elements to actual loads.

The model assessment identified several key phenomena for stress, drive closure, depth and proximity to the barrier pillar (as shown in Figure 10) which impacts the ground support requirement and model forecasts. The most interesting fact which was not basically apparent before the study is that the developments closer to the pillars separating the mining fronts attracted excess stress and the development within the pillar zones will become a major challenge.
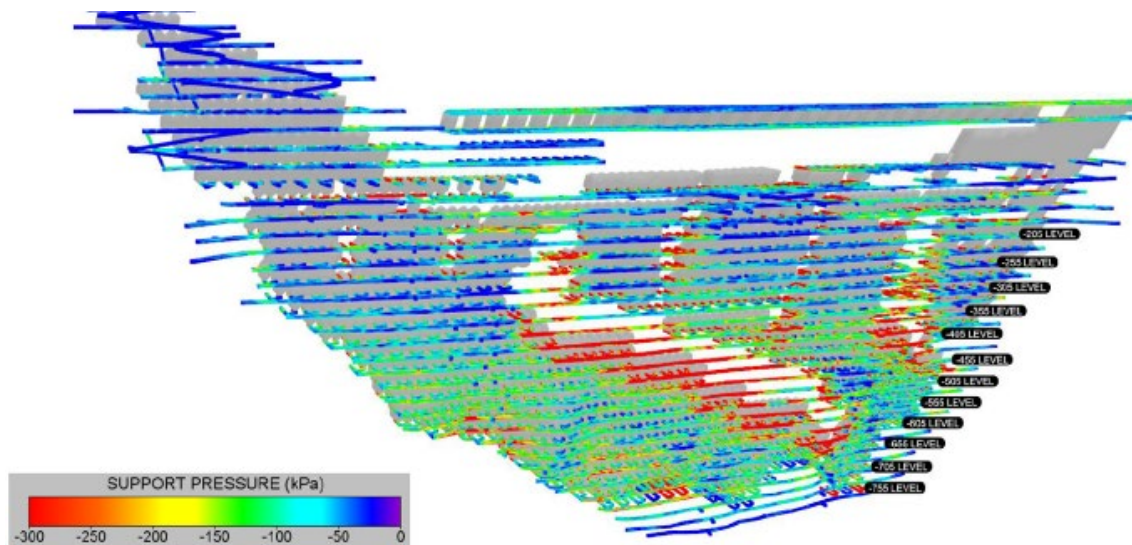
FIG 10 – Support pressure at late stage of mining (~2040).

Based on the modelling study, key points which drive the support requirement of any area are:

- Drive closure increases with depth, due to increasing load, however the correlation is low due to the impact of the distance to the regional pillar.

- Drive closure is significantly higher in proximity to the regional pillar due to stress concentration and loading on drives. Model forecasts show a step changing the cable bolting requirements will be necessary to maintain long-term access on the footwall drives, particularly in the GBSG below the 700 m depth. We note the onset of deformation will begin slowly during the initial stages of stoping on the level and increase rapidly with progressive nearby stoping on the level.

- Cable bolting with Osro Straps of pillar noses in the waste cross-cuts should be undertaken below 700 m depth due to increasing deformation.

Benchmarking with other mines

Overall, the forecast rock mass conditions at RAM are similar to the ones at Agnew Mine, George Fisher Mine, sections of Perseverance Mine and N3500 at Mt Isa Mine. The LOM ground support approach developed at RAM has some similarities with the approaches adopted at these operations.

Ground support review process

Underground development in proximity to mining areas is instrumented with tape extensometers, multipoint borehole extensometers and stress-meters.

Geotechnical engineers are analysing the data collected from visual inspections and geotechnical instruments, to assess ground support performance and rehabilitation requirements. This data set is also important for calibration of numerical models which are utilised to guide stope scheduling.

A comprehensive visual inspection program for all development is in place to assess drive damage against set criteria, as shown in Figure 11.

The monitoring information is utilised to continuously reassess the ground support requirements. The ground support design is evolving during and after construction, to ensure that the actual installed support is adequate for the conditions.

Damage Level	General Description	Rock Mass/ Tunnel Damage	Example
S0	No Visible Damage (Low Stress Condition)	Description: No stress-induced damage visible Depth of Damage (m): 0m indicated depth of damage Tape Extensometer Reading (mm): 0-5mm (cumulative) Area of Damage (% of drive profile): <1% of drive profile affected Ground Control: Easily controlled with minimal support eg check scaling and spot bolting.	
S1	Minor Damage (Spalling)	Description: Superficial damage only, easily visible crack on shotcrete. Depth of Damage (m): 0m to 0.2m indicated depth of damage Tape Extensometer Reading (mm): 5-15mm (cumulative) Area of Damage (% of drive profile): <10% of drive profile affected Ground Control: Easily controlled with minimal support eg spot bolting and shotcrete if required.	
S2	Moderate damage (or spalling)	Description: Spalling clearly developed and more widespread in shoulder and walls, start of shotcrete fall and sagging of wire-mesh. Depth of Damage (m): Indications of damage/loosening up to 0.5m depth into walls or backs (10%-15% of shoulder and wall*) Tape Extensometer Reading (mm): 15-25mm (cumulative) Area of Damage (% of drive profile): 10% to 25% of profile affected Ground Control Rehabilitation required in excavations(F/W drives) and to be ensured on monthly basis as per stoping plan.	
S3	Significant damage to excavations.	Description: Damage evident in all excavation surfaces. High 'sagging' in the mesh clearly developed; Shearing on foliation/bedding clearly indicated, Plate bending observed. Depth of Damage (m): Indications of damage/loosening to a depth up to 1.5m-2.0m (40% of shoulder or wall *) Tape Extensometer Reading (mm): >25mm (cumulative) Area of Damage (% of profile): >25% of profile affected Ground Control: Immediate rehabilitation effort required to maintain safe access.(cable bolts requires below -255mRL)	

FIG 11 – Excavation damage criteria utilised at RAM.

CONCLUSION

At RAM ground support designs are based on an average set of expected conditions with a factor of safety to account for unknowns. The mine has a long-term outlook on support evolution through the LOM cycle.

Ground support philosophy is routed in the observational method. As the mining progresses, the actual conditions are revealed, and specific vulnerabilities are targeted. This sometimes permit rationalisation of the heaviest support categories or even trigger a change to the design if conditions are worse than expected.

Adopted approach allowed to maintain safe working environment under challenging geology and significant mining induced stress.

ACKNOWLEDGEMENT

REFERENCES

Beck Engineering, 2020. 'Life of Mine Ground Support Strategy for Rampura Agucha Mine'.

CIMFR, 2022. 'Study to estimate geotechnical properties of rock core samples from Rampura Agucha Mine, HZL, Rajasthan'

HZL RAM Internal Report, 2022. 'Ground Control Management Plan – Revision 7'.

Messy Private Ltd., 2011. 'HZL, Rampura Agucha Mine Project – Hydraulic and HF Test'.

A global review of geotechnical challenges and ground support practices in sublevel caving mines

A D Campbell[1]

1. Principal Engineer, Beck Engineering, Brisbane Qld.
   Email: acampbell@beckengineering.com.au

ABSTRACT

Sublevel caving (SLC) is a mining method adopted in a wide range of mining depths and ground conditions with various layouts adopted to suit orebody geometry. Sublevel caving offers more flexibility and versatility compared to other cave mining methods and is a low cost alternative to open stoping. SLC also has the advantage that stopes are not required to remain stable during production, and no backfill is required. This flexibility combined with increasing pressure on mines to target deeper and lower grade mineralisation has led to increased uptake of the method. The implementation of SLC mining methods across a wide range of mining depths and rock mass conditions has led to ground control practices which vary globally from mine to mine. To date, there has been limited documentation of ground control practices in SLC mining and few benchmarks available in the literature.

This paper describes the main findings from a global benchmark of sublevel cave mines conducted over three years as part of the Caving 2040 research consortium. The purpose of the project was to document and compare operational practices, technical aspects and hazard management techniques across SLC mines around the world. The review included 21 mines spread over four continents and 17 different mining companies. This paper provides an overview of geotechnical conditions, challenges and ground control practices at each of the benchmarked SLC mines. Mine design and sequencing practices adopted for ground control purposes and hazard mitigation are provided with case studies. The impact of depth and rock mass conditions on mining productivity and development rates is also described.

INTRODUCTION

Sublevel caving (SLC) is a top-down mining method that relies on gravity flow of ore that is fragmented by blasting (Kvapil, 1965). Blasted ore is extracted in accordance with a prescribed tonnage or grade shutoff. As the ore is extracted, the overlying waste material caves naturally as mining progresses. The SLC mining method is a safe, low capital and early production mining alternative to other mass mining methods such as block caving. The method is amenable to a high degree of automation and has been successfully used in a wide range of geotechnical conditions, commodities and orebody geometries. Therefore, SLC mining will likely continue to be adopted as a technically and economically viable mining method for orebodies with lower grade and increasing depth.

Current and planned mining now exceeds depths of 1 km for various modern SLC mines. The benchmarking study found a trend of increasing ground control challenges due to a combination of increased mining scale, increased depth and implementation of the method in more difficult ground conditions. Many of the benchmarked mines face challenges associated with drive stability and convergence, brow control, seismicity and rock bursting as well as production delays for rehabilitation and/or redrilling in areas impacted by ground deformation.

Modern SLC mines adopt a range of hazard management strategies for ground control, which are outlined in this paper. These practices include mine design, sequencing, ground support, re-entry protocols and procedures. Hazard management and ground support practices are provided for each of the benchmarked mines, as well as details of the geotechnical conditions at each mine.

GLOBAL BENCHMARK OF SLC MINES

The global benchmark of SLC mines and operational review was carried out from 2019 to 2022 as part of the Cave Mining 2040 research consortium. The objective of the project was to:

- Document current state of SLC mines around the world including technical and operational practices, hazard management, and current challenges at each mine.

- Benchmark and compare mines in a wide range of operating conditions, countries, commodities, mining depths and adaptations of the SLC mining method.

- Document advances in technology and operating practices over the past 10–20 years.

- Benchmark mines with unique conditions and challenges, for the benefit of future mines.

- Develop an extensive document to serve as a manual of operational practices around the world and identify the current state-of-the-art for each aspect of SLC mining.

A total of 21 mines spread over four continents participated in the review and additional three mines which have ceased operations were benchmarked from the literature. The majority of SLC mines are located in Australia and South Africa as shown in Figure 1. Four (known) large scale SLC mines were not included in the benchmark due to access limitations and other constraints. The author acknowledges that there are other SLC mines around the world that were not included in the project as shown in Figure 1.
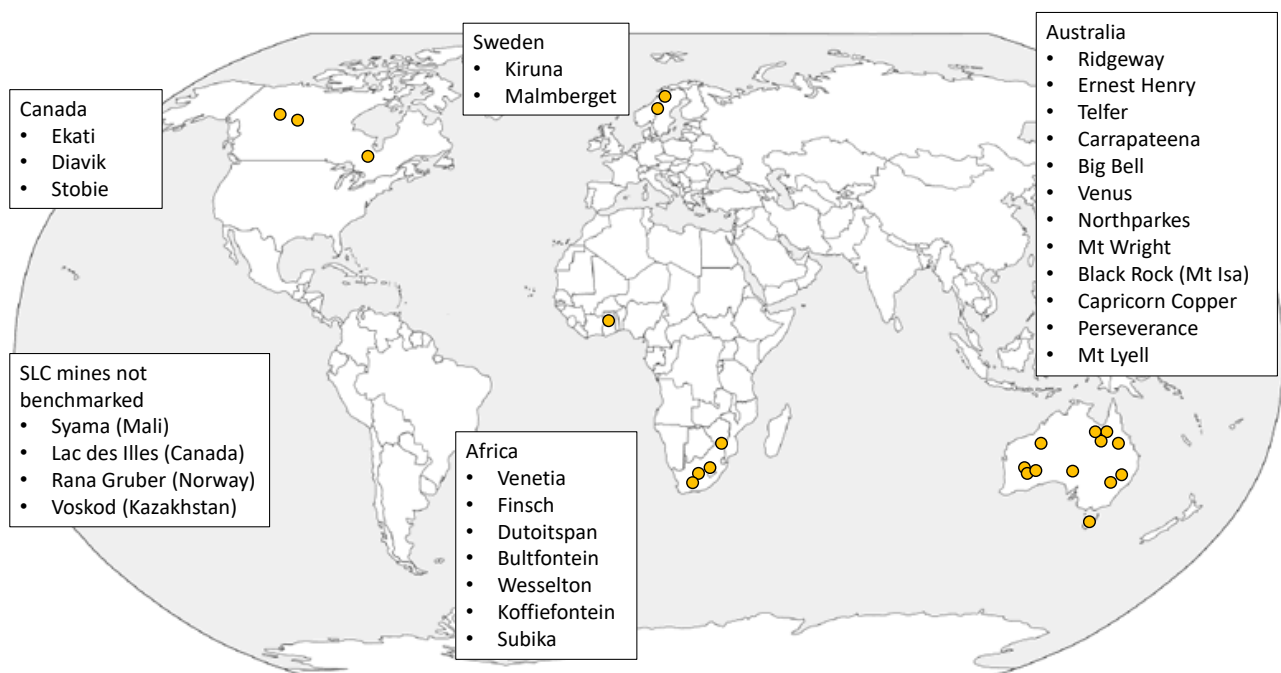
FIG 1 – The location of sublevel caving mines included in the global review.

The project included a site visit and underground tour for most of the mines. Each mine provided access to technical and operational information, mine plans, procedures, and management plans to enable a review of current practices. A total of 120 parameters were recorded for each mine ranging from production, development, equipment fleet, infrastructure, drill and blast and recovery. The information provided by each mine was used to write a report for each mine, including details of geology, mine design and planning, mine operations, drill and blast, geotechnical, infrastructure and material handling, and hazard management practice. The document provided context for the comparisons made in the benchmarking metrics and charts, as each of the mines has similarities and differences to the other mines. The reports also outline practices at each mine, and act as a reference source and guideline for the reader.

The benchmarked mines and corresponding production rates, commodity type and mine design parameters are summarised in Table 1.

TABLE 1

Mining parameters for each of the benchmarked mines.

Mine	Peak production rate (Mt/pa)	Commodity	Level layout	Sublevel spacing (m)	Cross-cut spacing (m)	Drive width (m)
Ernest Henry	6.825	Copper Gold	Transverse	25	15	6
Telfer	5.6	Gold	Transverse	25	14	5
Northparkes	1	Copper Gold	Transverse	25	15	5
Mt Wright	1.4	Gold	Both	25	12	5.5
Koffiefontein	1.1	Diamond	Transverse	23	19	4
Bultfontein SLC	0.5	Diamond	Transverse	20	19	4
Dutoitspan NWC SLC	0.2	Diamond	Longitudinal	15	18	4
Finsch	3.2	Diamond	Both	25	21	4.5
Carrapateena	4.25	Copper Gold	Transverse	25	15	6
Ridgeway	6	Gold	Transverse	25 and 30	14	6
Perseverance	1.5	Nickel	Transverse	25	14.5	5
Stobie	1.825	Nickel	Transverse	21.5 and 30.5	12.2	6.1
Kiruna	27	Iron Ore	Transverse	28.5	24.75	7
Malmberget	17	Iron Ore	Both	25	22.5	6.5
Mt Lyell	2.5	Copper Gold	Both	20 and 25	15	4.5
Big Bell	1.55	Gold	Longitudinal	25	15	5
Ekati (Koala SLC)	1	Diamond	Transverse	20	14.5	5
Ekati (Panda SLR)	1.2	Diamond	Transverse	20	14.5	5
Diavik (A154S Pipe)	0.5	Diamond	Transverse	25	15	5
Diavik (A418 Pipe)	1.1	Diamond	Transverse	20 and 25	15	5
Black Rock (Mt Isa)	0.4	Copper	Longitudinal	20 and 25	15	5
Capricorn Copper	1	Copper	Both	25	15	5
Venetia K01	4.5	Diamond	Transverse	25	17.5	5
Venetia K02	1.5	Diamond	Transverse	25	17.5	5
Venus	0.7	Nickel	Transverse	25/30/35	20	4.5
Subika	2.5	Gold	Transverse	25	15	5

Geotechnical conditions

The benchmarked SLC mines operate in a wide range of ground conditions from highly competent volcanics to altered ultramafics, and from leached shales to various types of kimberlite. Geology and rock mass conditions within some of the individual mines is also highly variable, particular in the kimberlite mines which typically have multiple types of kimberlite, which vary in strength and rock mass response. The geotechnical conditions for each mine are summarised in Table 2, including the current operating depth, *in situ* stress regime and UCS and RMR of the orebody and host rock. A complete description of the geology and geotechnical conditions at each mine is detailed as part of the project reports, but is not possible to provide within this paper. Examples of rock mass response to mining at Perseverance, Stobie and Ridgeway SLCs are illustrated in Figure 2. As expected, the range of rock mass response to mining is as varied as the ground conditions previously described. Mines with squeezing and bursting conditions are specified in Table 2.

TABLE 2

Geotechnical characteristics and major hazards at each mine.

	Current mining depth	Major/intermediate/min or principal stress at 1 km (MPa)	Major principal stress orientation	Orebody UCS (MPa)	Orebody RMR	Host rock UCS (MPa)	Host rock RMR	Far-field stress/orebody strength	Squeezing ground	Rock bursting or damaging seismicity
Ernest Henry	810	51/35/22	Horizontal	115	60	120	60	0.36	No	Moderate to Severe
Telfer	1085	52/32/19	Horizontal	150	55	220	60	0.38	No	Moderate to Severe
Northparkes	645	55/35/24	Horizontal	145	55	100	55	0.24	No	Minor
Mt Wright	700	26/13/10	Horizontal	75	48	180	75	0.24	Minor	No
Koffiefontein	600	30/22/15	Vertical	40	38	187.5	62	0.45*	Moderate to severe	No
Bultfontein	885	30/26/18	Vertical	57	45	180	85	0.47*	Minor	No
Dutoitspan	755	30/26/18	Vertical	45	45	160	85	0.5*	Minor	No
Finsch	780	30/22/15	Vertical	95	45	250	60	0.46*	Minor to moderate	No
Carrapateena	600	50/37/29	Horizontal	180	65	80	60	0.17	No	Minor
Ridgeway	980	52/35/25	Horizontal	120	65	110	65	0.42	No	Moderate
Perseverance	1100	60/34/23	Horizontal	90	45	150	55	0.73	Moderate to Severe	Moderate to Severe
Perseverance (talc UM)	1100	60/34/23	Horizontal	45	40	150	55	1.47	Severe to Extreme	Minor
Kiruna	1000	37/29/28	Horizontal	150	70	200	65	0.25	No	Moderate to Severe
Malmberget	900	36/26/17	Horizontal	155	65	180	65	0.21	No	Moderate
Mt Lyell	1085	51/37/26	Horizontal	120	50	180	60	0.46	Moderate	Moderate
Big Bell	650	70/41/27	Horizontal	110	61	145	65	0.42	Minor	Moderate to Severe
Ekati (Koala SLC)	580	25/20/18	Vertical	40	40	150	70	0.36*	Minor	No
Ekati (Panda SLR)	480	25/20/18	Vertical	40	40	150	70	0.30*	Minor	No
Diavik (A154S Pipe)	500	26/21/18	Vertical	45	50	95	90	0.29*	Minor	No
Diavik (A418 Pipe)	525	26/21/18	Vertical	15	50	95	90	0.68*	Minor	No
Black Rock (Mt Isa)	185	37/29/25	Vertical	35	40	10	30	0.20*	Minor to moderate	No
Capricorn Copper	475	55/31/23	Horizontal	50	50	100	55	0.52	Minor	No
Venetia K01	450	34/24/14	Vertical	95	65	150	65	0.15*	No	NA
Venetia K02	435	34/24/14	Vertical	55	65	150	65	0.25*	No	NA
Venus	675	63/40/27	Horizontal	102	45	160	60	0.42	Minor to moderate	Minor
Subika	500	55/35/27	Horizontal	154	70	200	65	0.18	No	NA

*kimberlite mines typically have low overburden stress due to the cave drawdown and competent host rock, and the stress to strength ratio is much lower than calculated here.

FIG 2 – Various ground conditions and rock mass response in SLC mines. Clockwise from the left, squeezing conditions at the Perseverance mine (after Struthers et al, 2000), jointed rock mass prone to wedge failure at Stobie (after Power and Just, 2008) and favourable rock mass conditions without major ground control problems at the Ridgeway SLC (after Power and Just, 2008).

The range of operating depths for the benchmarked mines is illustrated in Figure 3. Some SLC mines operate close to surface, particularly sublevel retreat (SLR) mines which start production directly below a previously mined open pit. SLR mines include Black Rock, Ekati, Diavik, Venetia K01 and Koffiefontein. The deepest SLC mines are Perseverance, which had a final mining depth of 1100 m, and the Mt Lyell and Telfer mines with final mining depths of 1085 m below surface. Kiruna and Malmberget in Sweden currently have mining depths of 1000 m and 900 m respectively, but have plans for future mining depths of up to 1380 m below surface and studies for additional depth extensions.
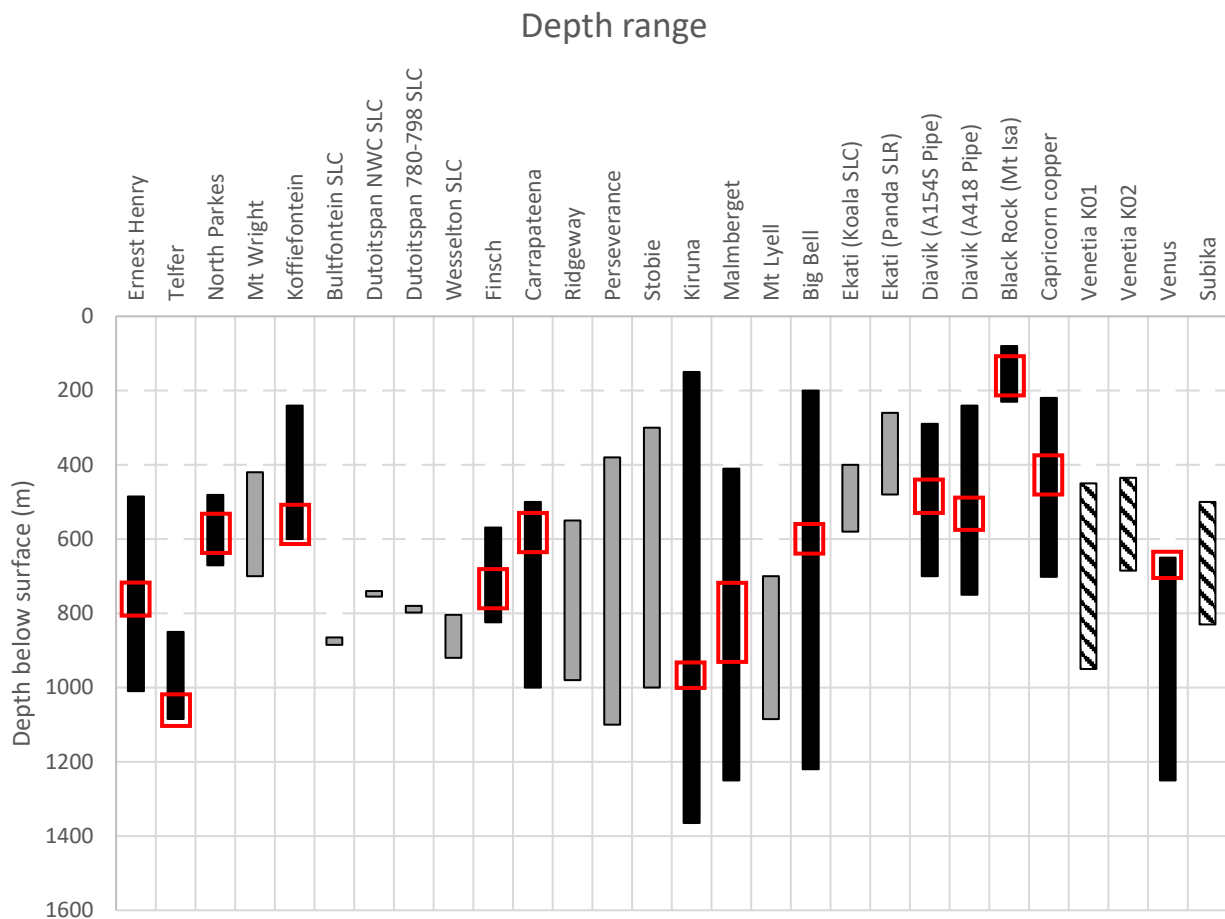
FIG 3 – Depth range for each of the benchmarked mines. Dark bars indicate mines currently in operation, light bars indicate mines that have ceased SLC mining and the hatched bars are mines that are yet to start production. The red box indicates the depth of operating production levels at the time of the benchmark.

The SLC mining method has historically been reserved for near vertical orebodies with strong ore and a weak hanging wall host rock (Bull and Page, 2000). The global benchmark found the SLC mining method is being increasingly adopted in conditions outside of normal convention, such as weak and variable orebodies and deposits with strong hanging wall host rock. The development of the sublevel shrinkage (SLS) mining method was a response to mitigating airgap formation in sublevel caving mines with strong host rock that would not readily cave. These mines include Subika and Mt Wright. Other mines with strong host rock in the hanging wall include Telfer, Ernest Henry, Malmberget and Kiruna, all of which have been successful SLC mines that are outside the range of typical rock mass conditions in historic literature and textbook conventions. The wide range of rock mass conditions is demonstrated by the figures provided in Table 2.

Many of the benchmarked mines have ground control problems related to squeezing ground, or damaging levels of seismicity. These hazards typically govern ground control procedures and ground support design at each mine. The mine operating procedures and mine productivity are impacted by geotechnical hazards and ground control problems. This is discussed in more detail in the following sections. The mines with squeezing conditions are typically the kimberlite mines due to the weak nature of some kimberlite facies, as well as the metalliferous mines with weak rock mass and high stress conditions. The Perseverance mine is perhaps one of the most extreme case studies of squeezing in a SLC mine, particularly in the weak altered ultramafics, which experienced very high rates of wall closure of up to 250 mm per week (Struthers *et al*, 2000).

The ratio of major principal stress to UCS of a specific rock type has been used as an empirical relationship for indicating potential for rock bursting (Martin *et al*, 1999; Hoek and Brown, 1980). Other empirical methods that use the maximum tangential stress (ie the induced stress) such as Hou

et al (1992) and Russenes (1974) forecast weak rock bursting at a stress to strength ratio above 0.4 and strong rock bursting if the maximum tangential stress to strength ratio is above ~0.55. It is acknowledged that the mining induced stress in proximity to faults and underground excavations is a more accurate proxy for seismic potential compared to the far-field *in situ* stress regime. However, it was not possible to source this information for each mine and not possible to detail the complex stress paths that evolve for each individual mine during SLC production. Nonetheless, the comparison of UCS and far-field stress for the benchmarked mines identified some interesting findings. The orebody UCS and far field stress conditions at each mine are plotted in Figure 4. This plot identifies two distinct groups of mines. One group which is characterised by locally weak conditions (mostly kimberlite mines), and the group of mines being deeper metalliferous mines in strong rock masses. The first group of mines are most commonly impacted by ground control problems associated with weak rock masses that deform and unravel close to the cave front, squeezing conditions and drill and blast problems causes by hole cut-offs. The second group of mines are subject to higher stress conditions which typically causes the mine to be seismically active. Many of these mines have experienced potentially damaging levels of seismicity or have a history of bursting conditions. The Perseverance mine has both squeezing conditions in the weak ultramafics and seismic and bursting conditions in the more brittle felsics and olivine ultramafics. The benchmark also illustrated that orebody RMR versus stress is a more reliable indicator of squeezing potential compared to rock strength.
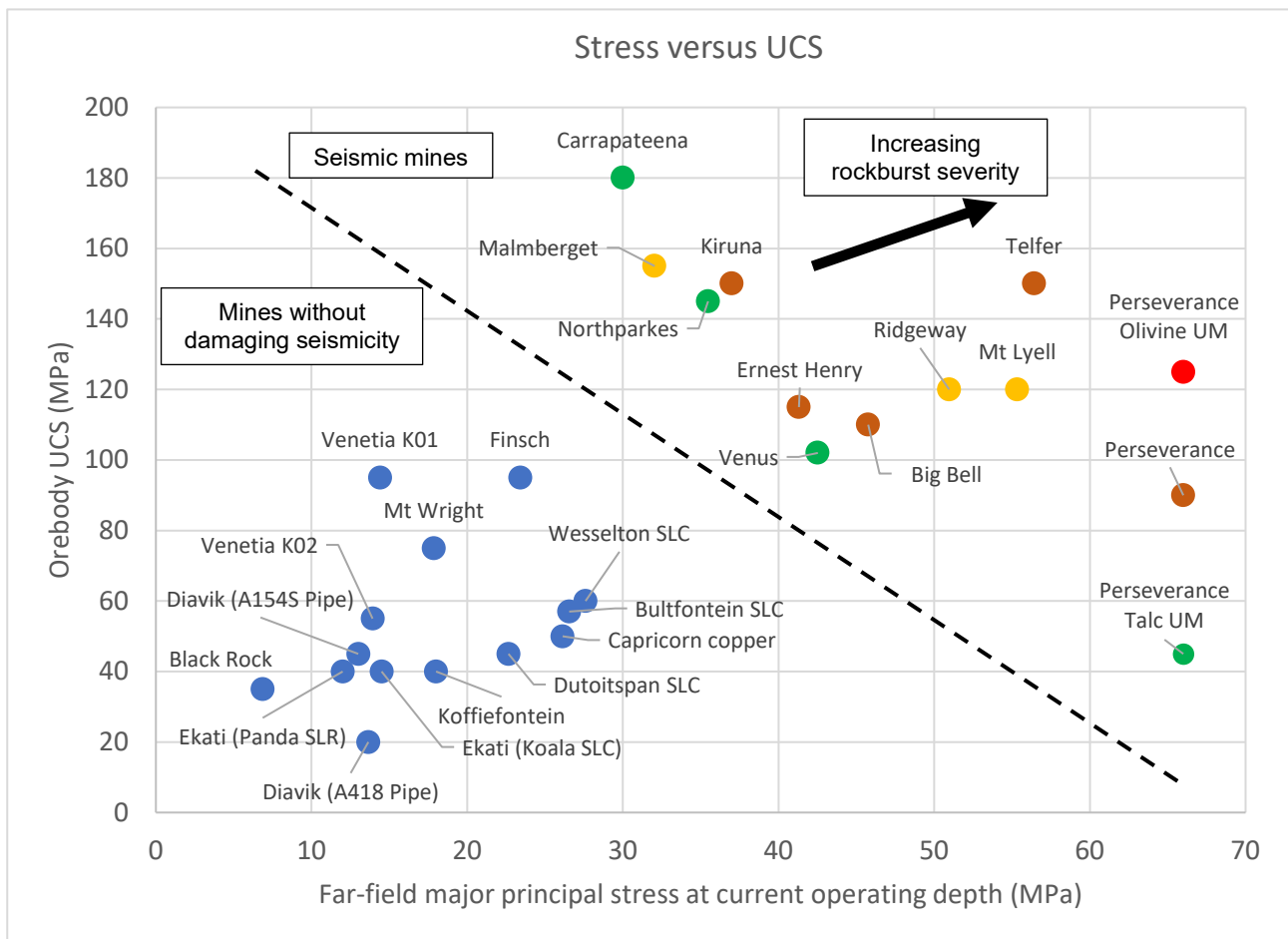
FIG 4 – UCS versus *in situ* stress with the markers coloured by observed bursting hazards.

Ground support practices

Ground support at each mine has been classified into classes, or tiers, ranging from very light to very heavy as it would not be practical to list all of the ground support standards employed at each mine. These support classes are defined by the type and amount of surface support and reinforcement elements in the support standards in each mine. Examples of each ground support tier are:

- Very light – Either weld mesh or 50 mm fibrecrete with friction stabilisers (ie split sets).

- Light – Weld mesh with resin bolts.

- Moderate – Fibrecrete and weld mesh with resin bolts. Fibrecrete is typically applied first and the mesh installed during resin bolting. Meshing may be from shoulder to shoulder, or from grade to grade.

- Heavy – Fibrecrete and weld mesh (both to grade line) with resin bolts. Pattern cablebolting undertaken generally on a campaign basis and cablebolt rings generally designed to be between production blast rings. Cablebolting varies from backs and walls, to backs only, and single and twin strand cables are used.

- Very heavy – Same as 'heavy support, with the addition of straps made of mesh, expanded steel or osro type straps. A second layer of fibrecrete is also typically used (ie F/C – mesh – F/C layers).

The ground support classes adopted at each of the benchmarked mines is summarised in Table 3. It is noted that some mines install brow straps without cablebolts. This type of support has been also denoted as 'heavy' support as part of this benchmark. Mines that use dynamic ground support are also listed in Table 3, as are mines the mesh development faces.

TABLE 3

Ground support practices for each of the benchmarked mines.

Mine	Class of ground support in orebody	Class of ground support in non-production areas	Face meshing	Dynamic support
Ernest Henry	Moderate to very heavy	Light to moderate	Yes	Yes
Telfer	Moderate to heavy	Moderate	Yes	Yes
Northparkes	Light to moderate	Light	No	No
Mt Wright	Light to moderate	Light	No	No
Koffiefontein	Heavy to very heavy	Light to moderate	No	No
Bultfontein SLC	Light to moderate	Light to moderate	No	No
Dutoitspan NWC SLC	Light to moderate	Light to moderate	No	No
Finsch	Moderate to heavy	Light to moderate	No	No
Carrapateena	Light to moderate	Light to moderate	Yes	No
Ridgeway	Moderate to heavy	Light to moderate	No	No
Perseverance	Moderate to very heavy	Moderate to heavy	Yes	Yes
Stobie	Moderate to heavy	Light to moderate	No	No
Kiruna	Light to moderate	Light to moderate	Yes	Yes
Malmberget	Light to moderate	Light to moderate	Yes	Yes
Mt Lyell	Moderate to heavy	Light to moderate	No	Yes
Big Bell	Moderate to heavy	Moderate	Yes	Yes
Ekati	Light to moderate	Light	No	No
Diavik	Light to moderate	Light	No	No
Black Rock (Mt Isa)	Moderate to heavy	Moderate	No	No
Capricorn Copper	Light to moderate	Light	No	No
Venetia K01	Light to moderate	Light	No	No
Venetia K02	Light to moderate	Light	No	No
Venus	Moderate to heavy	Moderate	Yes	Yes
Subika	Light to moderate	Light	No	No

Resin bolts are the most common form of rock reinforcement used by SLC mines. Mines that use friction stabiliser bolts (ie split sets) are typically those with weak rock mass conditions where resin bolt installation is not possible. Mines using friction stabilisers such as split sets include Capricorn Copper and Mt Wright. Inflatable Swellex type bolts are used at Diavik and Ekati, and cone bolts were trialled at the Perseverance mine for a short period of time. Some mines have adopted hybrid bolts such as the MD and Kinlock bolts, including Carrapateena and Telfer. The Telfer mine used hybrid bolts for ground support upgrades on the lower production levels as seismic hazard potential increased with progressive mining at depth.

Dynamic ground support adopted at the benchmarked mines includes debonded resin bolts, yielding bolts, hybrid bolts and debonded cablebolts. Surface support for the used in dynamic ground support standards is typically weld mesh with some form of steel strap. High-capacity chain link mesh and cable-lacing is not used at any of the benchmarked SLC mines.

The strength to stress ratio has been used to develop an empirical guide for rock mass response, bursting potential and difficulty to support (Martin *et al*, 1999; Hoek and Brown, 1980). The strength to stress ratio for each of the benchmarked mines in provided in Table 2, and the orebody strength and far field major principal stress values from Figure 4 are plotted on the Martin *et al* (1999) chart in Figure 5. Mines such as Perseverance fall into the 'extremely difficult to support' category, which is expected given the observations and operating conditions in the ore drives as shown in Figure 2. Seismic mines such as Ernest Henry, Big Bell, Mt Lyell and Telfer also fall into the empirical range for seismic conditions with a stress to strength ratio of greater than 0.35 to 0.5.
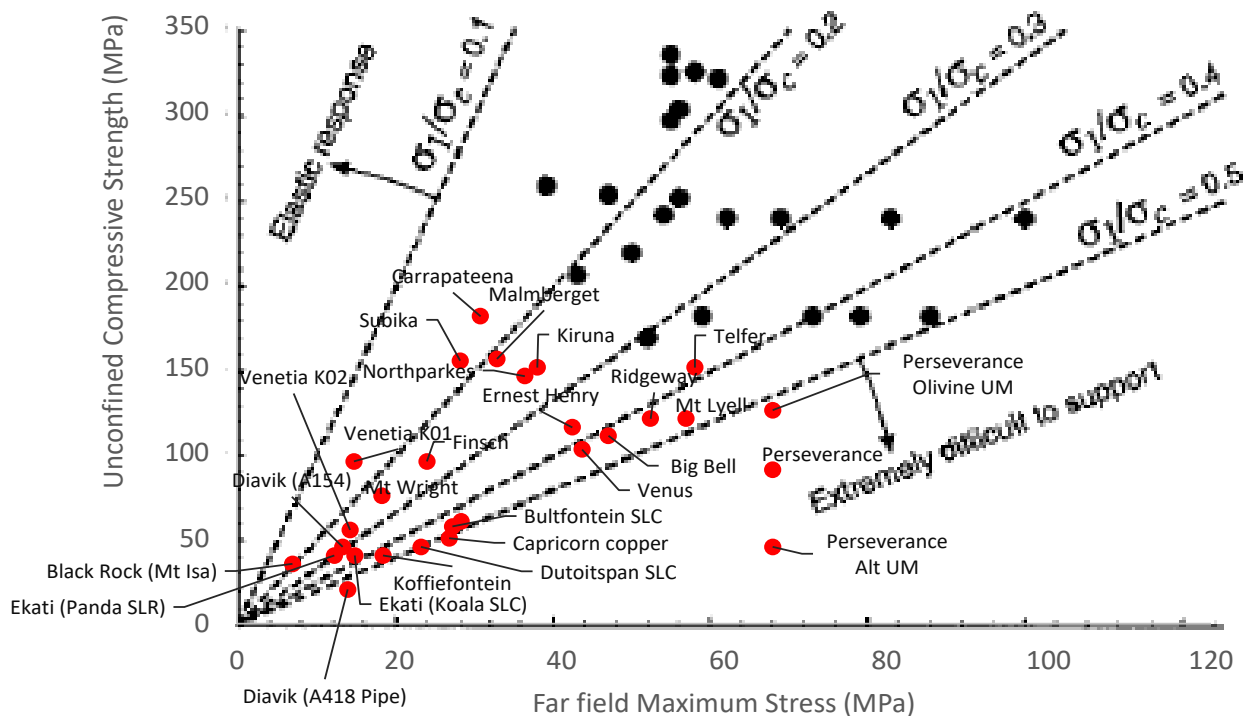
FIG 5 – Orebody strength and far field stress for the benchmarked SLCs overlaid on the chart by Martin *et al* (1999).

Additional brow support is installed at the mines with elevated deformation in proximity to the cave front (common in weak, jointed rock masses) and mines with poor ground conditions that are subject to significant back-break from blasting. Brow support typically consist of either resin bolts or cablebolts with a W-strap or Osro strap that is installed between the production rings. This helps to prevent back-break from one production ring impacting the next production ring, which would prevent access to the hole collars for hooking up the next blast ring. Examples of light, moderate and heavy ground support at SLC brows are provided in Figures 6 to 8 (respectively).

FIG 6 – 'Light' ground support at a SLC brow region, consisting of resin bolts and weld mesh.

FIG 7 – 'Heavy' ground support at a SLC brow region, consisting of fibrecrete to floor, weld mesh to 3.5 m from the floor iwith resin bolts, and a second pass of ground support including W straps and hybrid bolts.

FIG 8 – 'Very heavy' ground support at a SLC brow region, consisting of fibrecrete to floor, weld mesh to 1 m from the floor installed with resin bolts, and a second pass of ground support including mesh straps, hybrid bolts and cablebolts.

Hazard management

The most common controls for managing ground control problems at the benchmarked mines are provided below. This list is prioritised from the most effective controls to those that are regarded as less effective or have higher potential to expose personnel to ground control hazards. For the most part, feedback of the most effective ground control measures adopted at each mine roughly corresponds with the classic hierarchy of controls breakdown for control effectiveness. The most common geotechnical hazard control measures were:

- Appropriate cross-cut spacing, pillar size and drive dimensions. Pillars must be sufficiently large to maintain stability and prevent yielding through the pillar cores which can result in severe deformation and ground control problems. Smaller drives are inherently more stable and large production drives (wider than 5.5 m) only adopted at mines with strong competent rock mass.

- Mine layout with consideration of major and intermediate scale structures and the orientation of the major principal stress. Mines with strong rock masses generally consider structure to be more critical, while stress orientation tended to rank more highly as a mine planning consideration in the mines with weak rock mass conditions.

- Production sequence, including the orientation of the cave front, cave front length and lead-lags between neighbouring cross-cuts and sublevels. It is noted that mines with fewer operational problems are those that operate with a high degree of discipline, including maintaining a lead-lag of two to three production rings between neighbouring cross-cuts.

- Minimising blast damage to drive boundaries during development and brows during production blasting to minimise ground control problems, rehabilitation, rockfall potential and lost access to production ring collars.

- Drive profile and geometry. Flat backs in SLC drives (theoretically) increases recovery due to wider draw compared to drives with an arched profile (Bull and Page, 2000), however arched backs provide significant improvement in stability, and this may be a necessary trade-off to

ensure safe production in some circumstances. Mines with high stress and/or severe ground control problems may also consider a horse-shoe shaped profile which has proven to be successful at the Ernest Henry operation (Esterhuizen, 2018).

- Ground support, which varies significantly from mine to mine depending on the local rock mass conditions and expected rock mass response. SLC mines typically adopt heavier ground support standards compared to stoping mines at similar depths and rock mass conditions, based on the authors experience. This is mostly due to the constant retreating drawpoint position in each production drive, as well as high mining induced stresses and the complex stress path of increasing stress as the cave front approaches followed by decreasing stress and low confinement in proximity to brows and below previously mined levels. Many of the highly seismic mines use dynamic ground support, with debonded rock bolts and/or cablebolts or hybrid bolts being the most common dynamic ground support types.

- Increased support at production brows, which may be installed as part of the primary ground support regime, or installed in a second pass. Expanded steel W-straps or Osro type straps installed with either rock bolts or cablebolts between production blast rings are a highly effective method for preventing brow loss and excess backbreak or wear at the benchmarked mines.

- Face meshing is used on many of the benchmarked SLCs with seismic conditions to reduce risk of rockfalls or slabbing from development faces during charging.

- Procedures for delayed re-entry times after blasting to mitigate personnel exposure during the most seismically active areas of the mine are in place at most of the seismically active mines.

- Most of the SLC mines have some form of Trigger Action Response Plan (TARP) for reacting to geotechnical hazards such as large seismic events, specific seismic trends, certain levels of squeezing or drive close, and other hazards such as airgap formation and mudrush.

Geotechnical impacts on mine operations

Geotechnical requirements governed tactical and strategic decision-making at the mines with significant ground control challenges such as Perseverance, Stobie, Koffifontien and Black Rock. The majority of the other mines were also found to have multiple geotechnical requirements for mine planning. These operational requirements commonly include specification of interlevel sequence and offsets between cave fronts on neighbouring sublevels, cave front length and direction, maximum lead-lag between neighbouring ore drives, the maximum number of production blasts at end of shift firing and spacing between production blasts.

Geotechnical aspects of the mine design such as ore drive spacing and level spacing impact mine stability, mining costs and ore recovery. Although sufficiently large pillars between ore drives are required to maintain mine stability, some mines are hesitant to increase pillar sizing due to the perceived impact on ore recovery. Findings from the benchmark identified that minor changes in cross-cut spacing and/or ore drive width had no significant impact on recovery or dilution. These findings are published in Campbell (2022).

The benchmark found that mines with stronger rock mass conditions in the orebody (higher UCS and high RMR) has a moderate correlation with increased productivity in terms of the average production tonnes per drawpoint, per day. The tonnes/day/drawpoint is a useful measure for comparing productivity of SLC mines, particularly during mining studies when determining an appropriate production rate for a potential SLC mines (Power, 2021). Mines with favourable ground conditions generally achieve 300 to 400 tones/day/drawpoint, and mines in unfavourable ground conditions typically achieve lower rates in the order of 200 to 250 t/day/drawpoint.

The deepest SLCs in the world currently operate at 1000 m to 1100 m below surface. Kiruna currently has plans to expend mine production to 1380 m, and potentially deeper. The original all SLC mine design for Carrapateena extended to a final depth of ~1600 m prior to the lower half of the SLC being redesigned to be a block cave (OzMinerals, 2020). Ernest Henry and Malmberget are also planning depth extensions that will potentially see the depth of mining extend below 1250 to 1500 m respectively. The benchmark noted significant ground control challenges, mostly related to seismicity for mines extending below a depth of around 700 to 800 m. Those mines at 1 km or deeper

have particularly challenging geotechnical conditions. Based on the benchmark and experience at each of the mines around the world, it seems possible for the SLC mining method to be viable at mining depths of 1500 m with favourable conditions and a high degree of geotechnical controls and operational discipline. Although the practical depth limit for any mine is based on the local stress regime and rock mass conditions, it is the authors opinion that the SLC mining method is potentially limited to a maximum mining depth in the order of 2.0 km, unless step change innovations in mining operational techniques and applied technologies are able to be developed and adopted.

CONCLUSIONS

Sublevel caving (SLC) is a mining method that continues to be adopted in a wide range of mining ground conditions and increasing mining depths. The global benchmarking study found a trend of increasing ground control challenges in modern SLC mines due to a combination of increased mining scale, increased depth and implementation of the method in adverse ground conditions. Many of the benchmarked mines face challenges associated with drive stability, seismicity and rock bursting as well as production delays for rehabilitation and redrilling in areas impacted by ground deformation.

Many of the benchmarked mines have ground control problems related to either squeezing ground, or damaging levels of seismicity. These hazards typically govern ground control procedures and ground support design at each mine. This paper provides an overview of geotechnical conditions, challenges and ground control practices at each of benchmarked of SLC mines, including mine design and sequencing practices adopted for ground control purposes and hazard mitigation.

The global benchmark found that the SLC mining method is being increasingly adopted in rock mass conditions outside of textbook conventions, including in weak orebodies and deposits with strong host rock in the hanging wall. This is due to mining companies attempting to economically mine lower grade deposits at increasing operating depths, which typically require low cost mass mining methods such as SLC and block caving. Modern SLC mines currently operate at depths up to 1100 m, with some current operations planning depth extensions to 1500 m. The review and benchmark of the global SLC mining industry demonstrated that achieving mining depths of 1500 m is likely to be possible with favourable conditions and a high degree of geotechnical controls and operational discipline. Though it is noted that large scale SLC mining is potentially limited to a maximum mining depth in the order of 2.0 to 2.5 km, unless step change innovations in mining, operational techniques and applied technologies are able to be developed and adopted.

ACKNOWLEDGEMENTS

- Kiruna and Malmberget mines (LKAB) – Gurmeet Shekhar, Yunus Hazar, Matthias Wimmer, Steve Belohlawek.

- Mt Wright (Resolute) – Stuart Long.

- Northparkes (CMOC) – Ellie Hawkins, Sarah Webster, Zecheng Li.

- Subika (Newmont) – Frans Basson.

- Telfer and Ridgeway (Newcrest) – Paul Kline, Otto Richter, Lino Manca, Robbie Lowther.

- Venetia (DeBeers and Anglo American) – Freddie Breed, Denver D'Angelo, Tshepo Mokele.

- Venus (BHP) – Michael Hopkins, Rigo Rimmelin.

REFERENCES

Bull, G and Page, C H, 2000. Sublevel caving–today's dependable low-cost 'ore factory', in G Chitombo (ed.), *MassMin 2000*, pp 537–556.

Campbell, A D, 2022. A global review of recovery, dilution and draw control in sublevel caving mines, *Proceedings of the Fifth International Conference on Block and Sublevel Caving, Caving 2022* (Australian Centre for Geomechanics, Perth).

Esterhuizen, H C J, 2018. Controlling the effects of stress and seismicity in a sublevel caving operation, in Y Potvin and J Jakubec (eds), *Proceedings of the Fourth International Symposium on Block and Sublevel Caving, Caving 2018,* pp 607–622 (Australian Centre for Geomechanics, Perth).

Hoek, E and Brown, E T, 1980. *Underground excavations in rock*, London: Institution of Mining and Metallurgy.

Hou, F, Liu, X and Wang, M, 1992. Discussion on rockburst origin and degree, *Proceedings of the 3rd Academic Conference of National Rock Dynamics*, Wuhan, pp 448–457.

Kvapil, R, 1965. Gravity flow of granular materials in hoppers and bins – Part 2 Coarse material, *International Journal of Rock Mechanics and Mining Sciences*, 2(3):277–292.

Martin, C D, Kaiser, P K and McCreath, D R, 1999. Hoek-Brown parameters for predicting the depth of brittle failure around tunnels, *Canadian Geotechnical Journal*, 36(1):136–151.

OzMinerals, 2020. OZ Minerals' Carrapateena Life of Province Plan Scoping Study, available online www.ozminerals.com/ArticleDocuments/364/200623_OZ_Minerals_Carrapateena_Life_of_Province_Plan_Scoping_Study.pdf

Power, G R, 2021. An analysis of productivity in sublevel cave mines, Underground Operators conference, Perth, 2021

Power, G R and Just, G, 2008. Mass Mining by Sublevel Caving, Internal report, Mass Mining Technology Research Group, University of Queensland.

Russenes, B F, 1974. *Analysis of rock spalling for tunnels in steep valley sides*. Norwegian Institute of Technology.

Struthers, M A, Turner, M H, McNabb, K and Jenkins, P A, 2000. Rock Mechanics Design and Practice for Squeezing Ground and High Stress Conditions at Perseverance Mine, *MassMin 2000*, pp 755–764.

Accurately defining failure geometries and their variability

K H B Chu[1] and E J Hancock[2]

1. Geotechnical Engineer, Engenex, Hobart Tas 7005. Email: Bernard.chu@engenex.com
2. Principal Geotechnical Engineer, Engenex, Hobart Tas 7005.
   Email: Eamonn.hancock@engenex.com

ABSTRACT

Failures within hard rock underground excavations have historically been defined by a depth of failure, estimated in the field or through individual measurements, with a simplified failure geometry; such as 1/3 span, cubic or paraboloid. This simplified shape, volume and mass of failure is typically used to estimate *in situ* demand as a simplified discrete point. However, the highly variable failure geometry indicates simplified methods to estimate the mass can be erroneous in comparison to high precision LiDAR scans.

Advances in technology have enabled the accurate capture of failure geometry and allow a far more accurate analysis of failures to be completed. This case study investigates a number of real-life failures to accurately define the failure geometry, the distribution of the failure parameters and compares this to traditional methodologies. This paper also outlines a suggested means of standardising failure geometry parameters whilst accounting for their variability.

INTRODUCTION

Static and dynamic falls of ground within hard rock excavations represent a catastrophic failure of an engineering control, they also provide vital information on circumstances leading to rock mass demand exceeding the capacity of the engineered ground control scheme (EGCS). EGCS are one of many controls used to protect people and equipment working underground and should be designed to avoid catastrophic failure. Accurately understanding the specific reasons why a failure has occurred and characterising the likely *in situ* demand, enables the engineering team to ensure future EGCS are designed to exceed the likely demand.

It is vital to understand: what caused the failure, what defined the geometry and size of the failure and how this influenced the volume of failure and subsequent imparted demand. Empirical methods have placed limited attention to the variability of these parameters, with values such as depth of failure and mass typically limited to a single point source measurement, or an estimate using simplified geometries. These simplified geometries typically lead to over estimation of the volume in the order of 50–100 per cent, inflating the mass imparted upon the EGCS.

LiDAR technology has enabled engineers to easily capture accurate measurements of underground excavations and detailed failure geometries. This data enables a far more accurate estimate of the volume, mass and associated distribution of demand using the exact failure geometry typically controlled by the *in situ* discontinuities. This approach, in most cases, dramatically reduces the back analysed mass imparted on the EGCS.

Using a large data set of back analysed failures, this paper outlines a method of determining an accurate representation of the failure geometry, the distributed depth of failure, volume, and area of failure. The results are then compared with empirical methods typically used throughout the industry. A suggested means of standardising the approach is also outlined to maintain consistency. The common terms are defined below:

- **Failure site (FS):** The location where the rockfall originated from.

- **Depth of failure (DoF):** Refers to the distribution of the depth(m) of failed material, either fallen or ejected but must be completely detached from the stable ground at the FS. The distribution is calculated over a 5 mm × 5 mm area perpendicular to the original face of the excavation.

- **Perimeter of failure (PoF):** Refers to the length(m) traced around the FS on the surface of the remaining excavation.

- **Area of failure (AoF):** Refers to the surface area defined by the PoF at the failure site.

- **Volume of failure (VoF):** Refers to the calculated value using LiDAR data to determine the volume of the void left behind at the FS.

- **Volume of failed material (VoFM):** Refers to the volume of the fallen, ejected or detached material in the position where it has come to rest.

- **Height of concealment (HoC):** Refers to the height at which the VoFM covers the failure site, this typically occurs with large failures from the lower wall.

- **Width of concealment (WoC):** Refers to the width at which the VoFM covers the failure site, this typically occurs with large failures from the lower wall.

METHODOLOGY

All information used to quantify the DoF has been determined using the methodology listed within this section. All data points are based on LiDAR scans captured using the Zeb Revo, with the generated point clouds processed using the software Cloud Compare.

Scan processing

Only good quality scans are used in this analysis to ensure the output values are consistent and errors are minimised as far a reasonably practical. Good quality point clouds are considered to be post failure scans free of any debris blocking the view of the FS. Unfortunately, some larger wall failures are omitted in this analysis, because the scans were taken with debris or fibre reinforced shotcrete (FRS) covering parts of the failure. It should be noted, the following data points are biased towards back and shoulder failures as they are more likely to be unobstructed by debris. The following primary steps are used to determine the VoF and DoF distribution:

1. Using software 'Cloud Compare', align post failure LiDAR scan to the pre-failure survey pick up.

2. Once the two scans are aligned, trim off parts of the scans that are not part of the failure. Use the tool 'segment' for this step.

3. Using function: Tools→ Volume→ Compute 2.5D Volume, generates a point cloud representing the volume (Figure 1).

4. Select the tool 'Show Histogram' and select the option 'Export histogram as csv.'
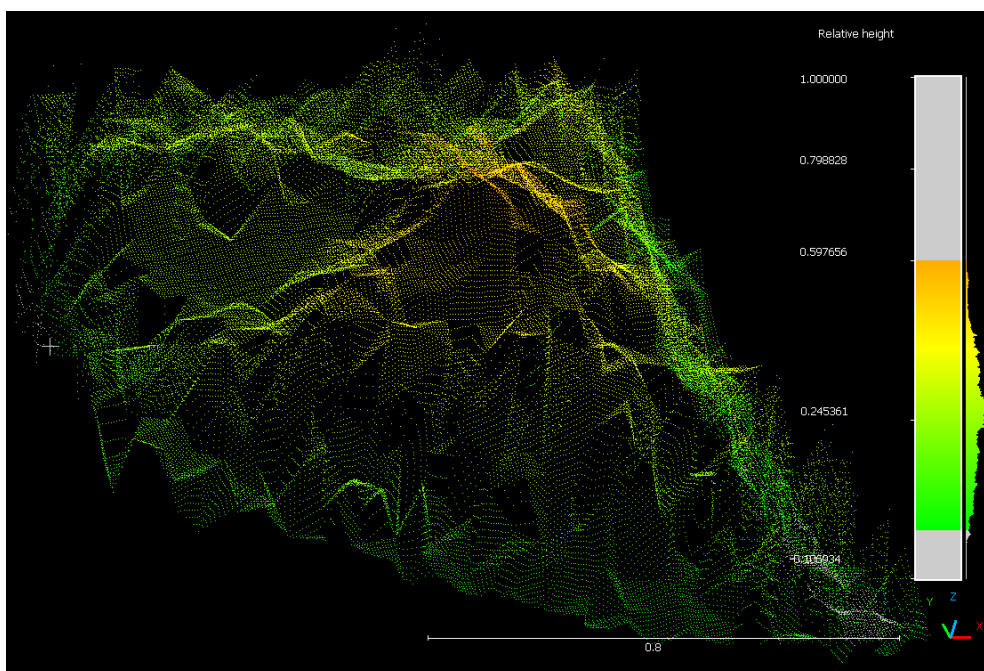
FIG 1 – Cloud Compare generated '2.5D' volume.

Depth of failure

The DoF distribution values can be plotted for visualisation purposes, as shown in Figure 2. This figure clearly shows the maximum DoF and the variability of DoF distribution for the individual FS.
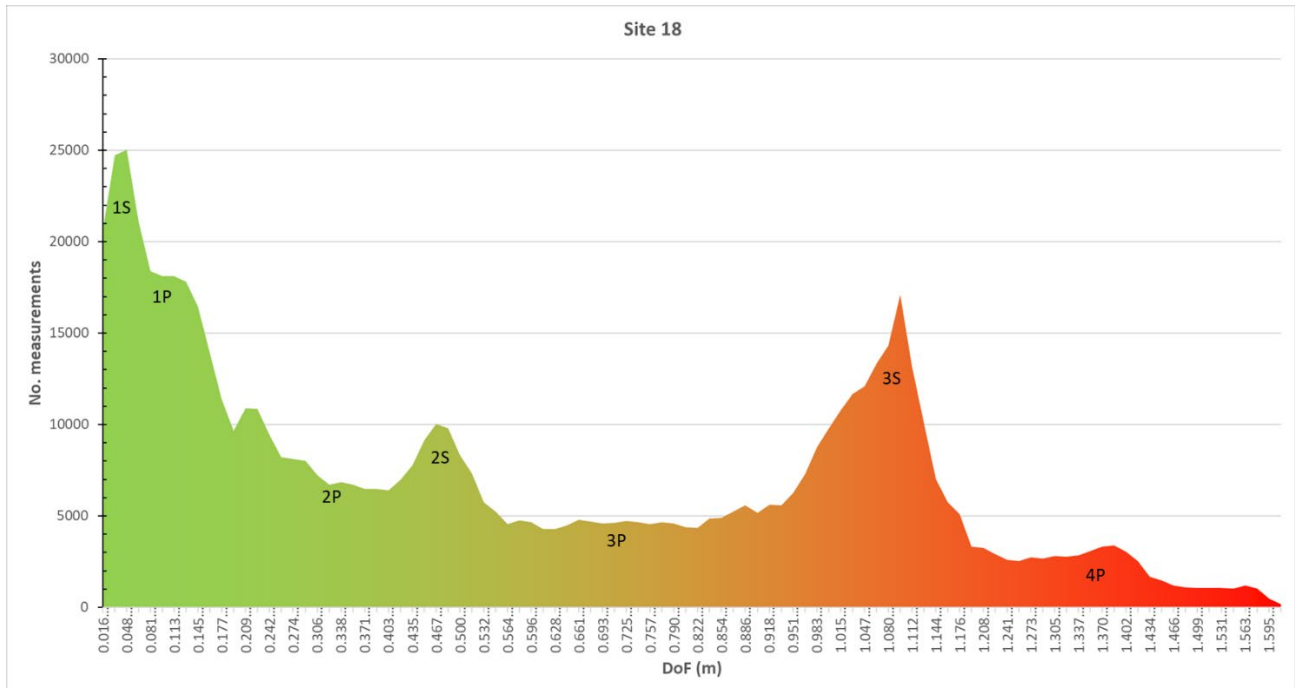
FIG 2 – DoF distribution of one failure site.

Area of failure

Using the generated point cloud (refer to Figure 1), the AoF can be obtained either by manually tracing a polygon around the failure scar or as part of step 3 above.

Volume of failure

Whilst processing the scan, step 3 above, the 'Results' window displays the calculated values, as shown in Figure 3. If processed correctly, the total VoF is defined as the 'Added volume' in this analysis.

The step size used within the calcuation influences the accuracey of the resutls, smaller step sizes result in an increased accuracy of the volume and surface area calcualtion. Both the matching cells (%) and average neighbours per cell (neighbours/8) are a measure of the the number of cells that have a matching cells in both point clouds. A higher percentage of matching cells or the avearge number of neighbours means more cells have matched. The acceptable minimum in this analysis is >70 per cent matching cells.
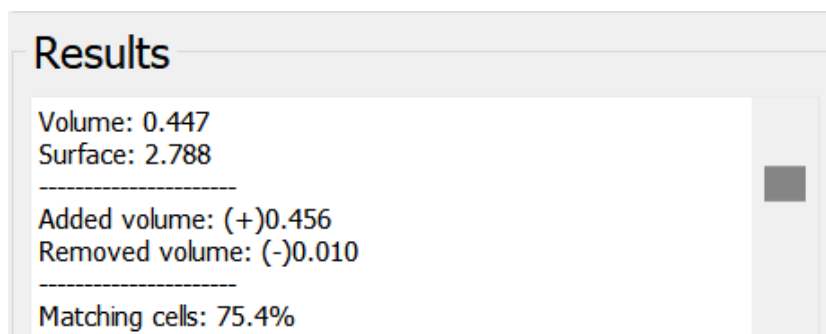
FIG 3 – Result window from function '2.5D Volume'.

DISCUSSION

Depth of failure

DoF values obtained from LiDAR scans are much more accurate than empirical techniques historically used within the industry. Generally, DoF can be inferred from observations or photos such as mine mesh squares and bolt length, as it can be unsafe to stand too close to the failure, as shown in Figure 4. In some cases, DoF is measured using a measuring tape or distance metre (disto). However, even tape measurements are limited to a handful of measurements which can only accurately measure DoF if the pre-failure excavation profile is still intact, as is the case in Figure 4.

FIG 4 – A failure site with an overhang.

In comparison, LiDAR derived DoF provides a high-resolution distribution of measurements, as shown in Figure 5. This method utilises the pre-failure excavation profile and the failure scar to accurately determine the volume of failed material and permits engineers to accurately calculate the likely mass and potential demand imposed on the EGCS. Detailed point clouds along with other information also allows an accurate portrayal of the likely failure mechanism (or mechanisms) which may have taken place.

Relative height (60223 values) [244 classes]

bin 199
< 95.115 %
val = 0.467711
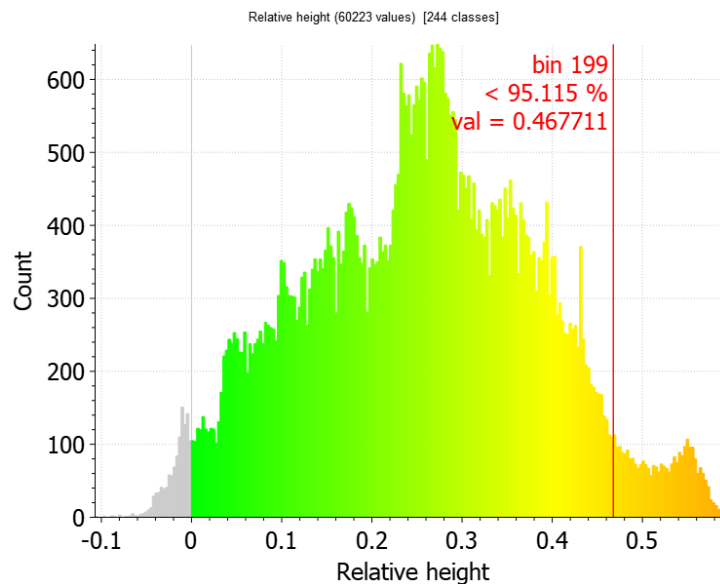
FIG 5 – DoF output from Cloud Compare (LiDAR).

As an example, the following characteristics can be deduced from Site 18 DoF within Figure 2 (moving from the PoF to the maximum DoF):

- **1S:** The initial high number of shallow measurements around the outer edge of the failure are expected, as the free face of the failure can create a chamfering effect within the FRS near the PoF.

- **1P:** The depth of FRS can be clearly seen at the inflection point before the first plateau, approximately 70 mm of depth, where the rock has not failed at the FRS-rock interface.

- **2P:** The second plateau (2P) before 2S corresponds to the start of the planar geometry within the failure void, shown within Figure 6. These planes appear to be random but as a collective dip in two groups diagonally opposed to each other at approximately between 40° and 55°.

- **2S:** The 2S spike corresponds to a rough, undulating geometry of a physical plateau within the failure scare, shown within Figure 6. The lower number of points, in comparison to 3S indicates the plateau is a smaller. The rounded shape of 2S indicates the plateau is also undulating. These characteristics indicate failure is likely to have occurred through smaller disordered defects within the intact rock. The actual failure geometry and the shallow DoF values suggest a spalling failure mechanism has controlled this part of the FS geometry.

- **3P:** The third, and much longer plateau within the DoF distribution represents the larger planar failure surfaces controlling the deeper failure geometry. Discontinuity surfaces are typically a plane of weakness within the rock mass and explain why the rock failed in this location and formed such a geometry.

- **3S:** The third spike, 3S, corresponds to the second major plateau within the failure geometry. A higher sharper peak within the distribution (Figure 2) indicates a physically larger and flatter plateau within the failure geometry (Figure 6).

- **4P:** The final plateau represents the deepest part of the physical failure, where opposing discontinuities are approaching each other. At this depth, stress imposed on the discontinuities is potentially at its highest and may represent the initial point of rupture. Only a handful of points were recorded at the maximum depth of failure of 1.61 m.
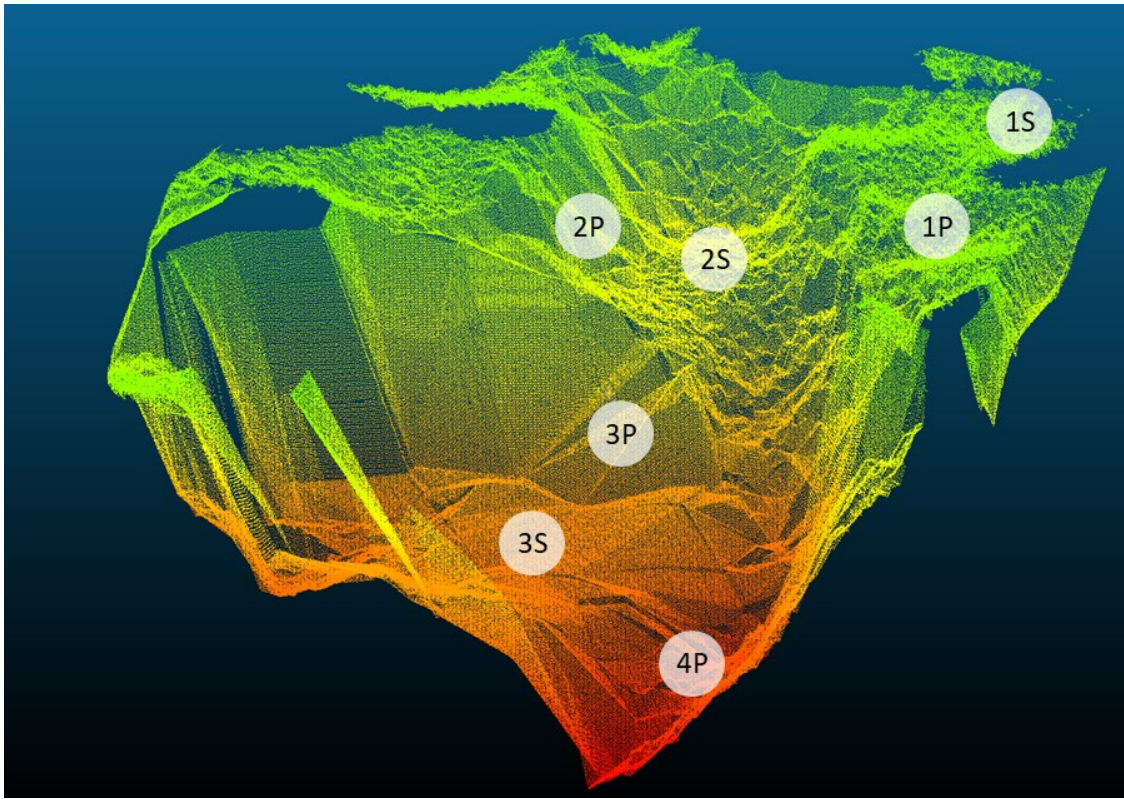
FIG 6 – Site 18 failure geometry.

The DoF distribution for multiple FS has been combined into a single graph (Figure 7) showing a combined distribution.

Three distinct failure populations are present within the combined DoF graph (Figure 7).

1. Spalling failure mechanism: 0 m to ~0.7 m DoF, this equates to approximately 75 per cent of all DoF values.

2. Drive scale discontinuities controlling the failure geometry: ~0.7 m to ~1.2 m DoF, ~20 per cent of all DoF values.

3. Large pillar or mine scale structures, eg faults or lithological contacts, controlling the failure geometry: >1.2 m DoF, this equates to approximately ~5 per cent of all DoF values.
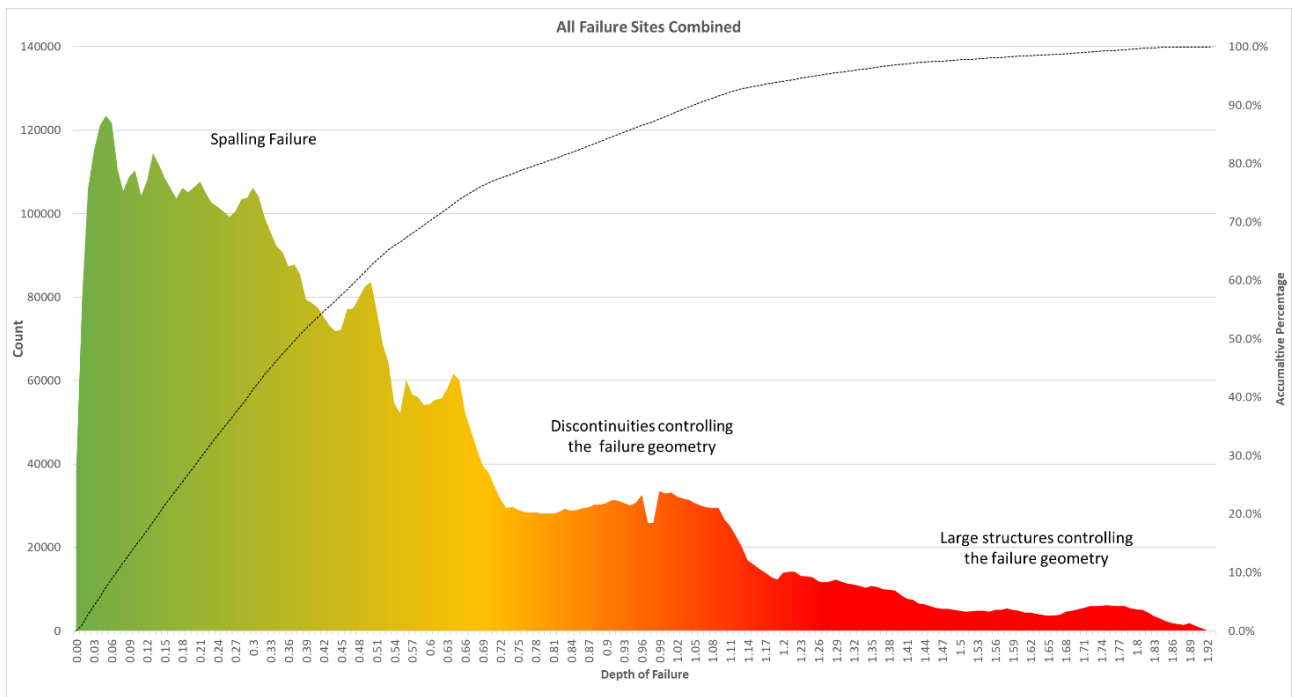
FIG 7 – Combination of all DoF from all failure sites.

Each population represents an individual failure mechanism; spalling, structurally controlled block ejection and fault slip. Spalling typically occurs along small defects within the intact rock, but may also intersect larger discontinuities with the rock mass, an illustration of this failure mechanism is shown in Figure 8. Spalling is defined as the development of visible extension fractures under compressive loading near the boundary of an excavation (Diederichs, Carter and Martin, 2010).
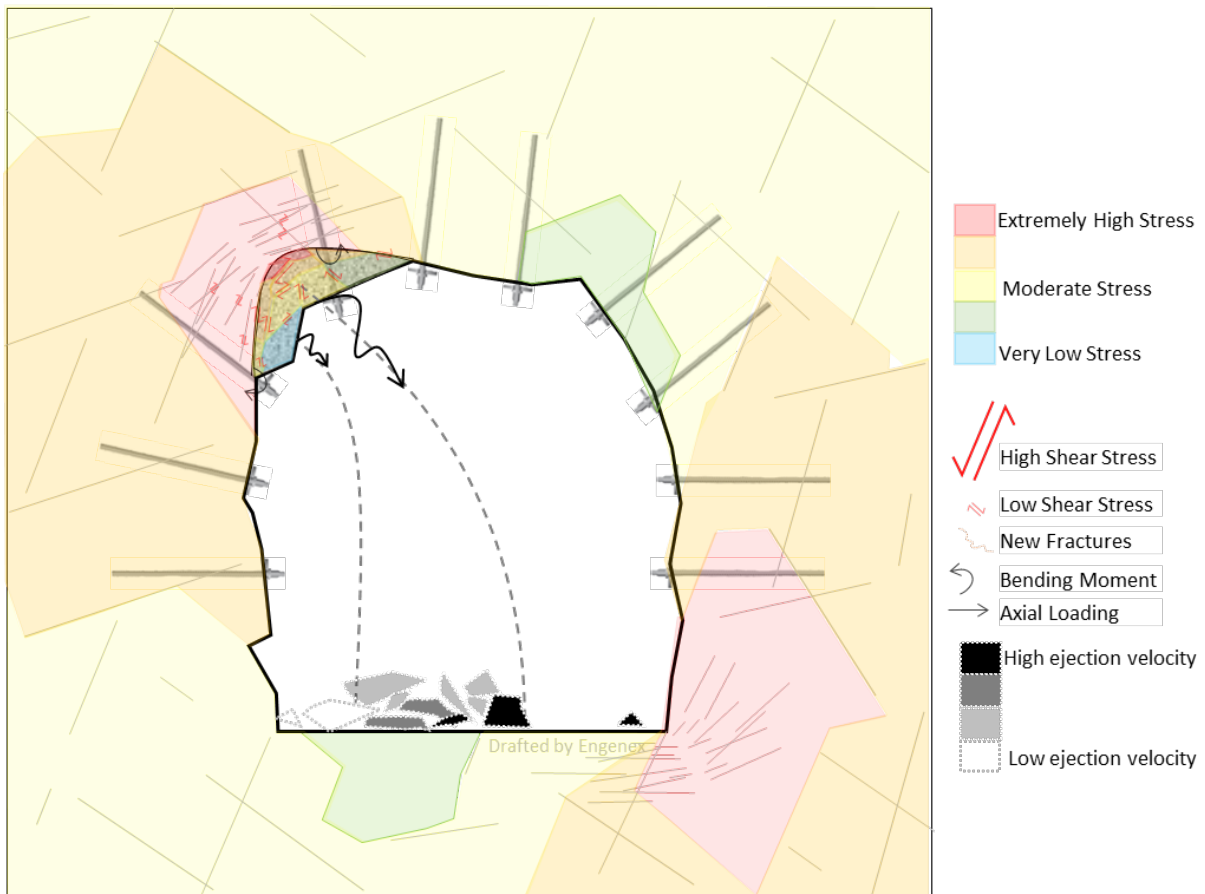
FIG 8 – Spalling failure mechanism.

It's shallow, localised and violent nature is typically associated with new development and unsupported excavations within high stress. The depth of failure is typically shallow, less than 0.7 m, but if left unsupported may progressively get deeper over time. Events are typically associated with localised seismic events ranging from -1.5 ML to 0 ML with an implosive crack closing signature. Dynamic failure and associated demand at the boundary of an excavation for both spalling or structurally controlled block ejection can only occur when all four factors required for dynamic failure are present within an excavation, as illustrated in Figure 9.

Brittle Rock Mass
Rock mass strength is influence by:
- Intact rock strength
- Discontinuity density and characteristics

High Stress
High stress conditions arise from:
- Creation of a void within the rock
- Heterogeneity within the rock mass

Dynamic Excavation Failure

Void
A volume which rock can fail into:
- Development excavation
- Vent rise
- Production void
- Drill hole

Trigger
Change in stress:
- Sudden change in void shape or size, e.g. development or production blast
- Slip of a structure
- A nearby failure, e.g., pillar shearing or crushing

FIG 9 – Factors required for dynamic failure within an excavation.

As the size of the FS increases, the likelihood of intersecting existing discontinuities also increases. Where failures occur within a blocky rock mass with a DoF greater than 0.5 m to 0.7 m, such as Site 18 in Figure 2, the geometry of failure will be likely governed by pre-existing discontinuities. The observed damage frequently consists of shear failure along structures, resulting in a sudden and violent ejection of large blocks (Villaescusa, Kusui and Drover, 2016). This sudden shear failure leading to violent block ejection occurs along the naturally forming blocks at the boundary of the excavation, as illustrated in Figure 10. This can occur either at or shortly after the spalling limit is reached depending on the brittle nature of the rock mass and may become more severe as the induced stress increases.
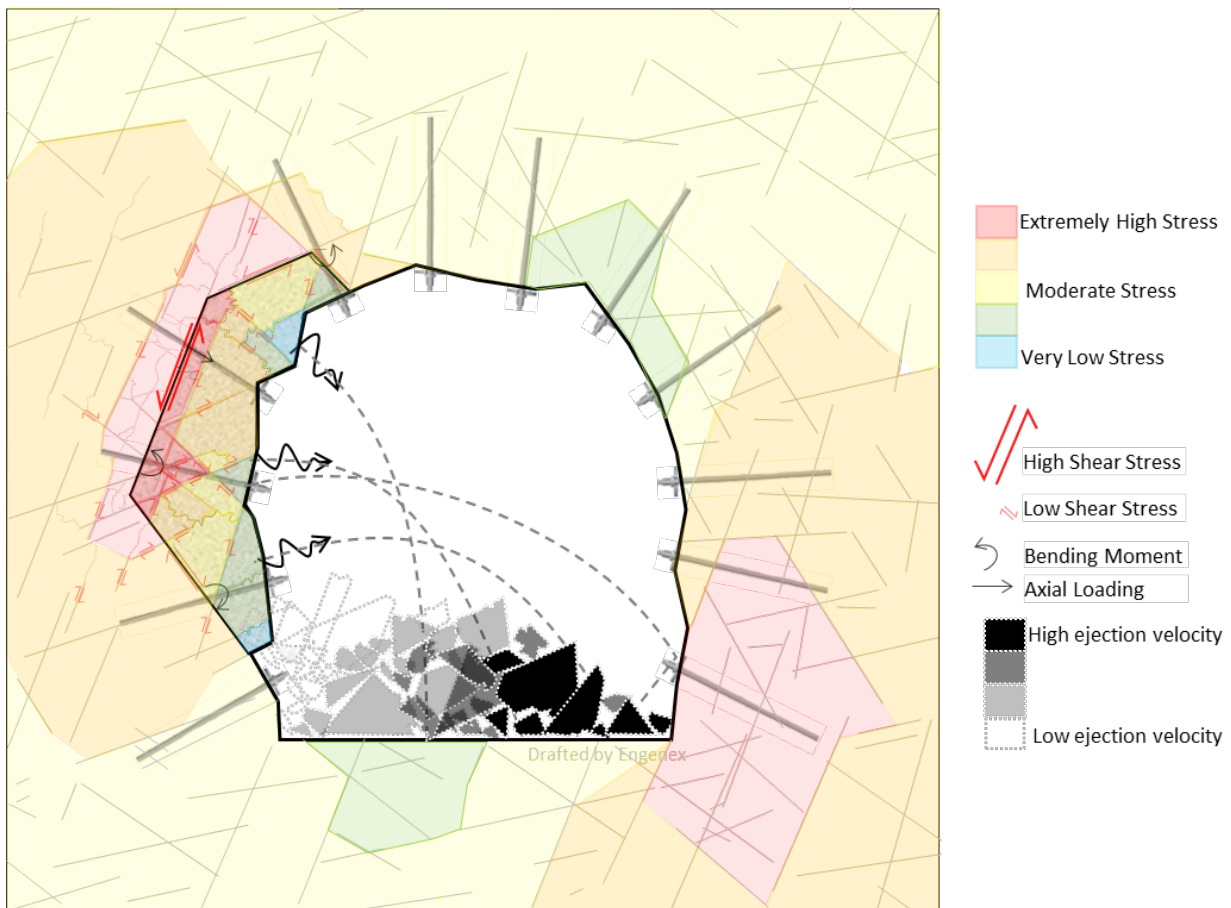
FIG 10 – Structurally controlled block ejection.

In situations where a major geological feature, such as a fault or lithological contact intersect the excavation, an increase to the DoF will likely occur. During a fault slip event, other discontinuities can also experience high shear forces near the boundary of the excavation, resulting in ejection and the potential rupturing of reinforcement elements and surface support, as illustrated in Figure 11.

If a fault slips across an excavation within a high stress abutment, shearing of the fault itself can be significant and most definitely cannot be stopped with rock reinforcement due to the extreme shear forces exceeding the capacity of the bolts. This highlights the importance of using a surface support with high energy and displacement capacity in excavations which intersect faults.

It is important to note that deeper failures may experience multiple failure mechanisms, such as Site 18 in Figure 2. In such cases, the mechanism with the higher demand (kJ/m^2) should govern the design.
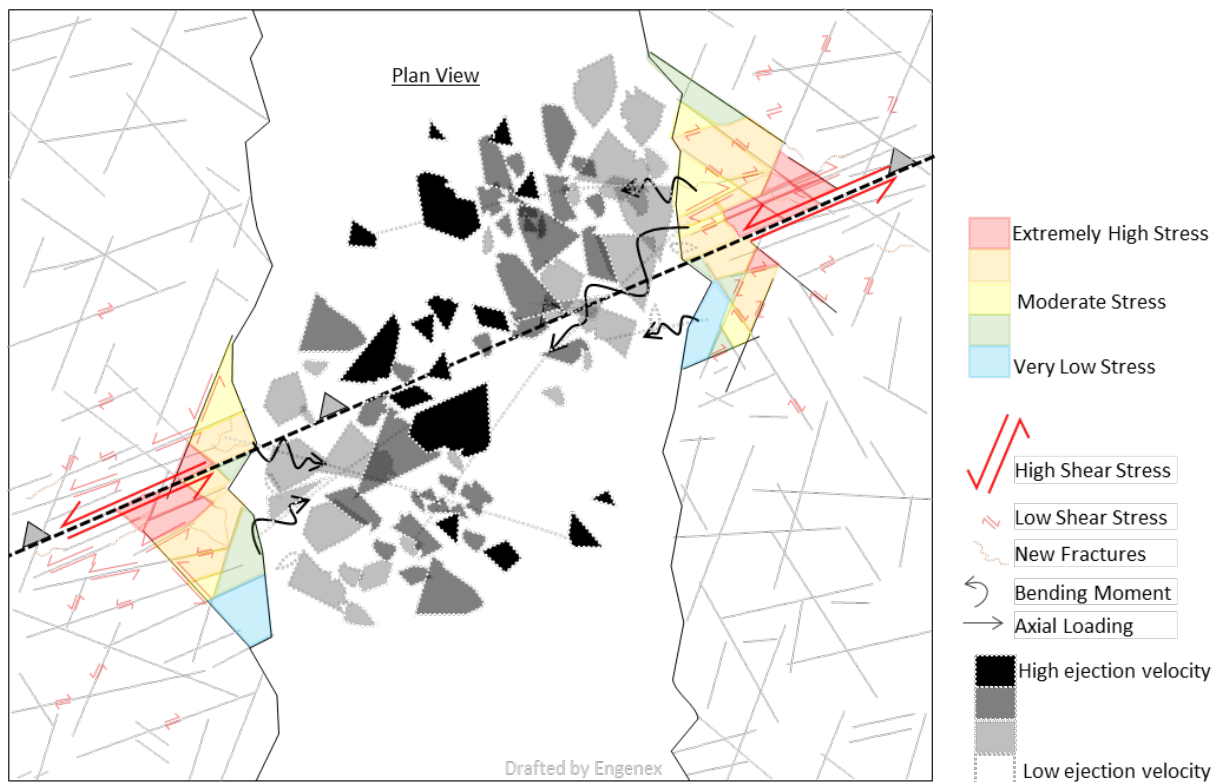
FIG 11 – Fault slip failure mechanism.

Volume of failure

The current industry standard for determining VoF is typically derived from DoF and span of the failure measurements. These values are used as inputs for various assumed geometric shapes, such as a paraboloid, to describe the failure scar within the excavation. The paraboloid volumes derived by Equation 1, are then used to estimate the demand on the EGCS.

$$Paraboloid\ Volume = \frac{\pi \times r^2 \times h}{2} = \frac{\pi \times (span/2)^2 \times DoF}{2} \tag{1}$$

The parabolic volumes of each FS have been determined using the maximum DoF and span of the failure. These are compared to actual volumes derived from Cloud Compare function '2.5D volume', as shown in Figure 12, to illustrate the size of each failure and variability in comparison to the paraboloid volume. Each FS has also been defined by the predominate failure mechanism.

The difference between the paraboloid derived volumes and the LiDAR derived volumes can be between -30 per cent to +200 per cent as shown in Figure 12. Smaller failures (<1 m^3) that failed due to spalling, are more likely to have a geometric volume represented by a paraboloid, due to the minimal influence from discontinuities. However, Figure 12 clearly illustrates failures with volumes over 2 m^3 are typically overestimated by Equation 1.
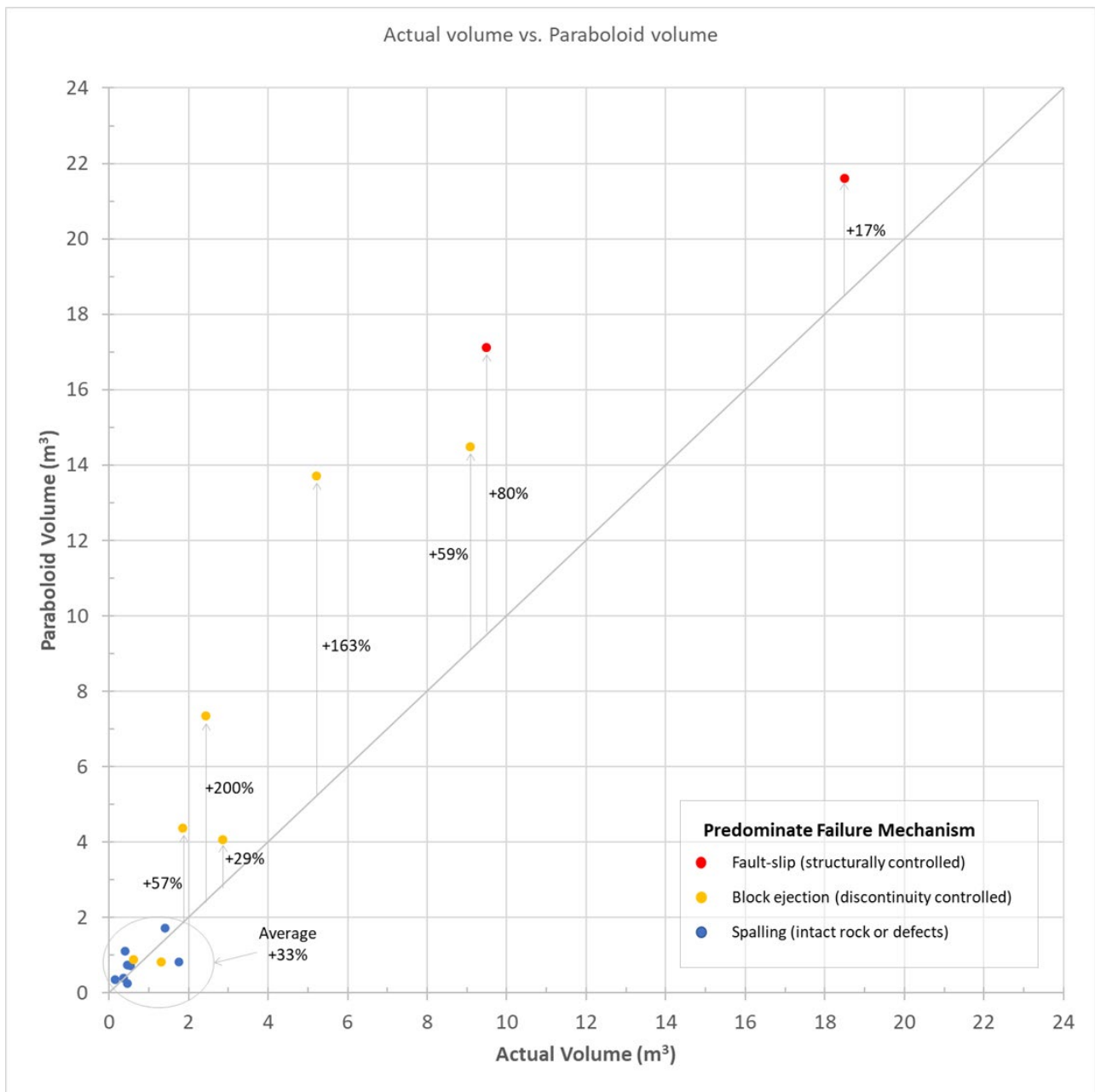
FIG 12 – Comparison of paraboloid volume and actual volume.

Discontinuity controlled failures

The orientations of discontinuities controlling the failure geometry can be extracted from the LiDAR scans by using functions within the Cloud Compare software. Once the scan is aligned to mine grid, the function RANSAC is used to fit planes onto the point cloud. Information such as dip and dip direction can be obtained from the fitted planes (Figure 13). Furthermore, dip and dip direction can be used for DoF back analysis to understand how structures and stress concentrations may influence DoF and VoF.
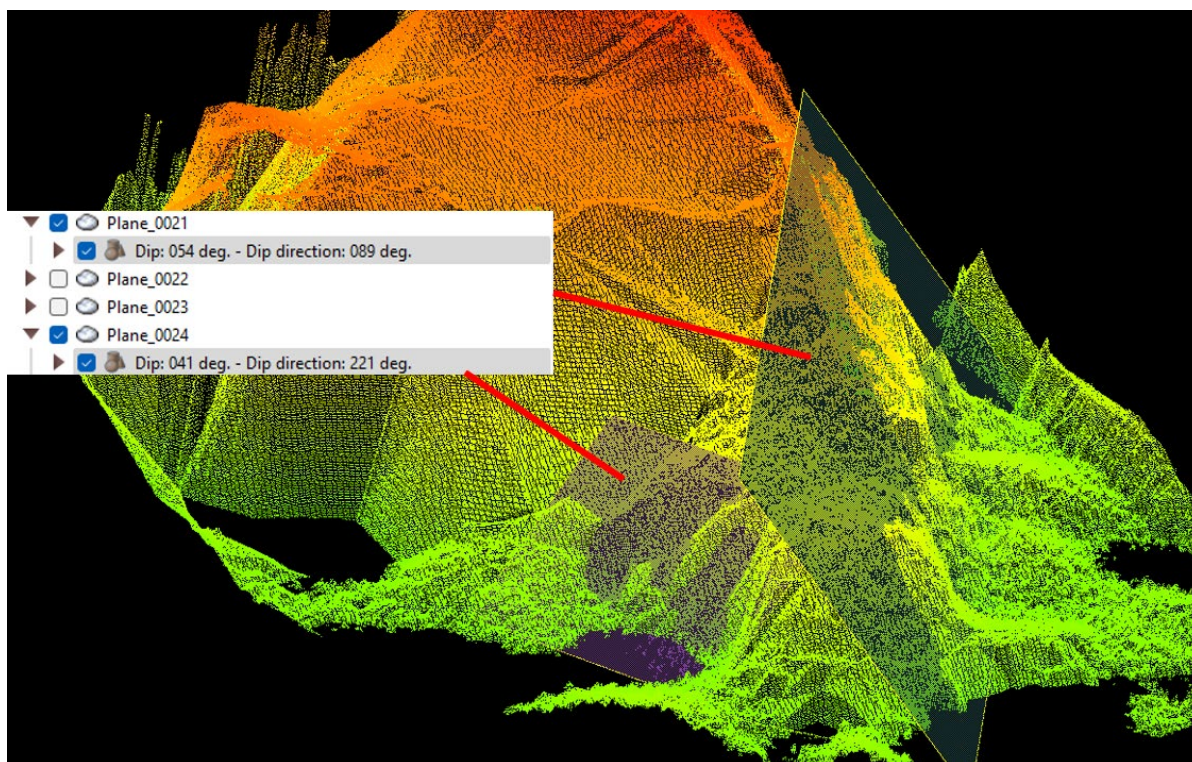
FIG 13 – Dip and dip direction from fitted planes.

CONCLUSION

Wherever possible, the FS should be scanned with LiDAR to obtain a point cloud which can be used to accurately define the DoF distribution. The DoF distribution can be further used to accurately calculate the mass and likely demand. This minimises the inconsistencies which come with visual estimates or single point measurements.

The database of FS clearly indicates that as the size of the failure increases, the geometry of the FS is more likely to be controlled by rock mass discontinuities. The discontinuities which defined the failure geometry should match any mapping completed prior. Combining information such as discontinuity dip and dip direction, failure geometry, DoF and other FS characteristics allows a better understanding of the failure mechanisms of catastrophic failures. Furthermore, the associated demand on the EGCS can be accurately estimated.

Figure 12 clearly illustrates that simplified geometries, such as paraboloids, consistently overestimate the failure volume, and consequently the calculated demand, by up to 200 per cent. For spalling failures, where the geometry is not controlled by discontinuities, then a simplified shape may give tolerable results but it is not recommended.

REFERENCES

Diederichs, M S, Carter, T and Martin, D, 2010. Practical Rock Spall Prediction in Tunnels. *International Tunneling Association*, pp. 1–8.

Villaescusa, E, Kusui, A and Drover, C, 2016. Ground Support Design for Sudden and Violent Failures in Hard Rock Tunnels, *Proceedings of the 9th Asian Rock Mechanics Symposium*, pp. 1–18, ARSM.

In situ dynamic testing of mesh straps and W-straps

B Darlington[1], J Graham[2], P Mikula[3] and P Young[4]

1. R&D Engineer, Sandvik Mining and Rock Technology, Newcastle NSW 2324.
   Email: bradley.darlington@sandvik.com
2. Geotechnical Engineering Superintendent, IGO Ltd, Perth WA 6151.
   Email: jason.graham@igo.com.au
3. Director, Mikula Geotechnics Pty Ltd, Kalgoorlie WA 6430. Email: pm@Mikulageotechnics.com
4. Global Product Line Manager, Sandvik Mining and Rock Technology, Brisbane Qld 4064.
   Email: peter.young@sandvik.com

ABSTRACT

In underground mines experiencing dynamic events, there is an ever-present challenge to design and maintain a capable ground support system. One key component of ground support systems is surface support, which serves the essential roles of retaining failed rock and transferring forces generated by surface displacement to rock bolts or other support elements. Observations underground show that in many instances, standard mesh panels alone do not provide sufficient dynamic support to retain substantial bulking failures imposing displacement onto mesh, and in such cases Mesh straps and W-straps may be employed.

Determining the performance of surface support elements proves to be difficult, with a multitude of variables at play in the underground environment. Quite comprehensive work has been completed on laboratory testing of surface support systems; however, very little work has been conducted on *in situ* dynamic testing of Mesh straps and W-straps.

In 2019 in Western Area's Flying Fox Mine, *in situ* dynamic testing was conducted on a series of Mesh straps and W-straps using Sandvik's *in situ* Dynamic Test Rig (DTR). The testing regime applied impact energies from 5.1 to 15.3 kJ to Mesh straps and W-straps. The performance of the straps that did not fail was a maximum absorbed energy of 9.3 kJ and 14.2 kJ for the Mesh straps and W-straps respectively.

The testing successfully demonstrated the ability of Sandvik's DTR to test not only rock bolts, but also surface support elements, creating new testing and research possibilities. The testing also provided important design guidance data that is not practicable to obtain using laboratory dynamic testing facilities.

INTRODUCTION

As mining progresses to deeper and more complex orebodies, the demand on ground support systems amplifies. These demands include static strength, controlling constant squeezing ground, and dynamic support capacity during seismic events. Selection of ground support elements is critical to ensure the product meets the requirements of specific excavation locations.

The difference between a static and dynamic ground support system can vary depending on ground support type. For instance, static bolts are typically very stiff and allow minimal deformation of ground, whereas dynamic bolts are designed to yield with moving ground, whilst still maintaining support of the rock.

When an excavation ages or becomes stressed, parts of the rock mass may fracture, allowing existing cracks and discontinuities to expand, causing areas or whole drives to deform, resulting in drive convergence. In these instances, rehabilitation is key to maintain the drive in a safe condition for both personnel and machinery. Many different forms of rehabilitation exist, and vary from site to site; however, a commonly used method involves installation of straps over specific locations showing signs of localised rock deformation or considered vulnerable to such deformation in the future.

There are several approaches to determine product specifications: workshop, or laboratory, testing and *in situ*, or underground, testing. Each testing approach has its own positives and drawbacks, which poses the question of which testing approach ground support companies can/should use. The

most common approach is workshop/laboratory testing, which allows ground support supply companies to test new or existing products quickly and easily. This approach also allows testing to focus on specific features of the product to be tested. However, a drawback of workshop/laboratory testing is that it can disassociate the product from the environment in which it will be ultimately used.

The other popular test approach is *in situ* or underground testing, which allows the tested ground support product to react to the environmental conditions in which it is actually used. This includes the way in which the product interacts with installation machines, how the product works with other ground support products, and possibly most importantly, how the product interacts with the rock mass and excavations. An example of this approach is the Sandvik in situ DTR device, which has been used since 2013 to undertake in situ dynamic loading of 280 bolts. An example of such testing is presented in Vallati, Weaver and Halling (2020). An *in situ* quasi-static testing program of conventional mesh sheets was reported by Whiting (2017).

One product group that has been tested using both approaches is rehabilitation straps, including 'Mesh-straps' and 'W-straps'. Examples of each are shown in Figure 1. Straps may be installed to enhance the performance of conventional modular mesh sheets, by increasing the stiffness of the surface support response, and reducing the hazard of separation of mesh sheet overlaps. Straps may be used in many situations, including stope brow support during blasting, and where seismic damage has occurred or is anticipated.

Straps can be tested for both static and dynamic capacity in both laboratory and *in situ* conditions.

FIG 1 – (left) Installed Mesh strap; (right) W-straps.

Sandvik was approached to work alongside Western Areas Limited to conduct a test regime at Flying Fox mine in Forrestania, Western Australia, focusing on the *in situ* dynamic performance of Mesh straps and W-straps. This was the first time that the Sandvik DTR method was utilised for dynamic

loading of Mesh straps and W-straps, and it may be a world first for this type of testing. The testing was conducted in February 2019, and considered two strap load application configurations, central and end loading. The central configuration tested the performance of the straps when loaded in the centre between two securing rock bolts. The end configuration highlighted the difference when testing nearer to the end of the strap. The testing regime applied a single dynamic impact between 5.1 kJ to 15.3 kJ on a series of samples of both Mesh straps and W-straps.

The aim of the testing program was to search for the maximum survivable energy and loading rate capacities that the straps could withstand without catastrophic failure.

TEST LOCATION

The testing regime took place at a depth in the mine of approximately 250 m below surface in Stockpile 16, which had sufficient access to the backs along with ample space for machinery to manoeuvre for both installation of the straps and the dynamic testing. The rock type at Stockpile 16 testing site consists of geomechanically competent Dolerite with an average Unconfined Compressive Strength (UCS) of 222 MPa, ensuring that bolt anchorage in the rock mass was adequate and would not affect the outcome of the test (ie the Mesh straps and W-strap were intended to fail prior to the bolt). There was no damage to the rock mass or the pre-existing ground support as a result of any of the Sandvik testing.

The straps were installed in rows as shown in Figure 2 and were tested in installation order as numbered.
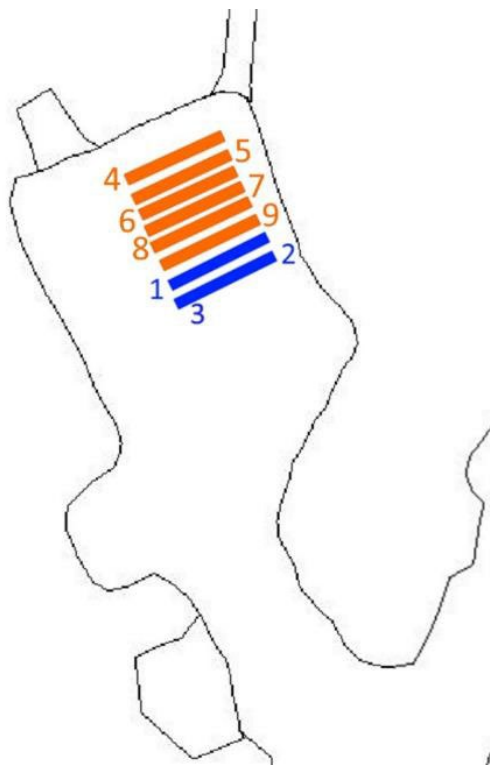
FIG 2 – Strap installation location – Stockpile 16 (blue: Mesh straps; red: W-straps, Mesh strap samples 2 and 3 were on opposite halves of the same Mesh strap.

TESTING CONFIGURATIONS

Dynamic testing was conducted with the use of Sandvik's *in situ* DTR, which utilises a 'direct impact' energy generation technique. In order to connect the DTR to each test strap, a circular steel load transfer plate, shown in Figure 3, was installed behind each sample, as shown in Figure 4. This plate design was selected to allow transfer of the energy from the DTR to the strap and also allow possible bending of the plate and strap under load. This bending is an approximation to strap bending that is anticipated during a dynamic disturbance underground.
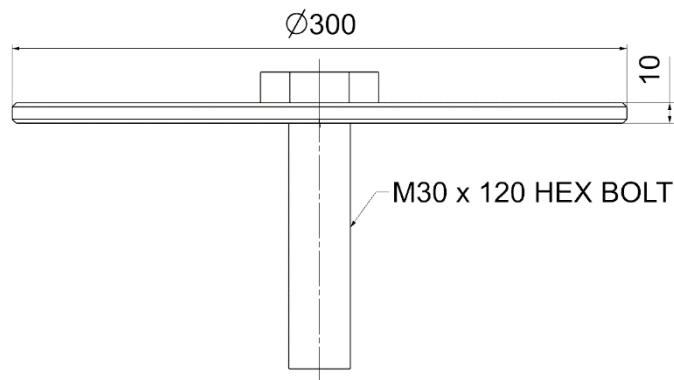
FIG 3 – Steel plate geometry (dimensions in mm).

FIG 4 – Steel load transfer plate installed behind Mesh strap (left) and behind W-strap (right), also showing the top of the DTR coupling unit attached to the plate in readiness for a test.

Two strap loading configurations were analysed: central loading and end loading. The central loading configuration positioned the load at the centre of the strap with two MD rock bolts positioned 1 m apart to secure the strap on either side of the load transfer plate, as shown in Figure 5.
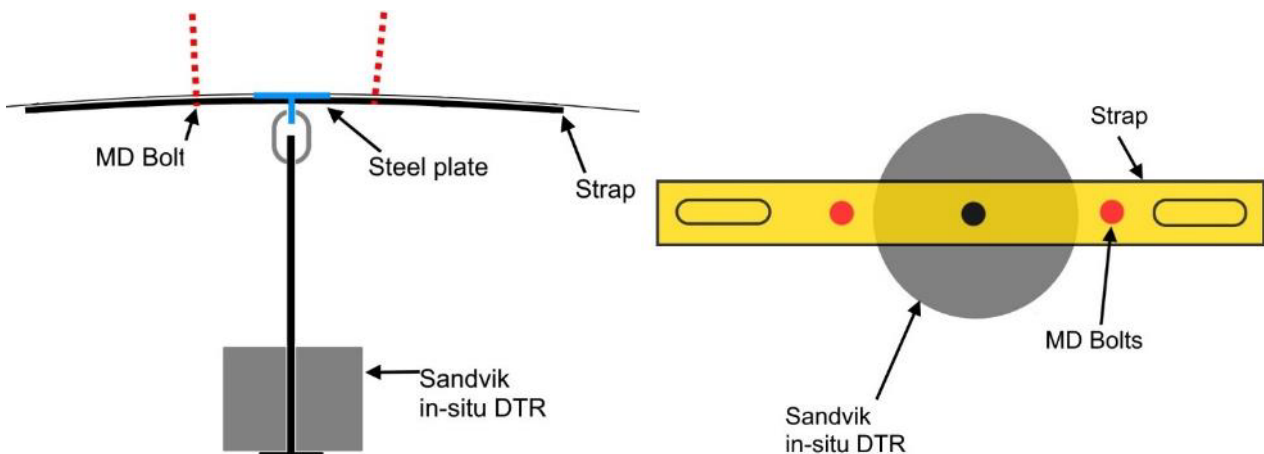
FIG 5 – Centre load configuration.

The end loading configuration was set-up with two MD bolts, one near the centre of the strap, and one between the load transfer plate and the end of the strap, as shown in Figure 6. In the case of the W-straps, the securing bolt was placed at the position in the slotted hole as close as possible to the end of the strap, and for the Mesh straps the bolt was placed in the third mesh aperture from the edge (three mesh wires between securing bolt and edge of Mesh strap). In all cases the two securing bolts were approximately 1 m to 1.5 m apart (dictated by bolt position within elongated slot).
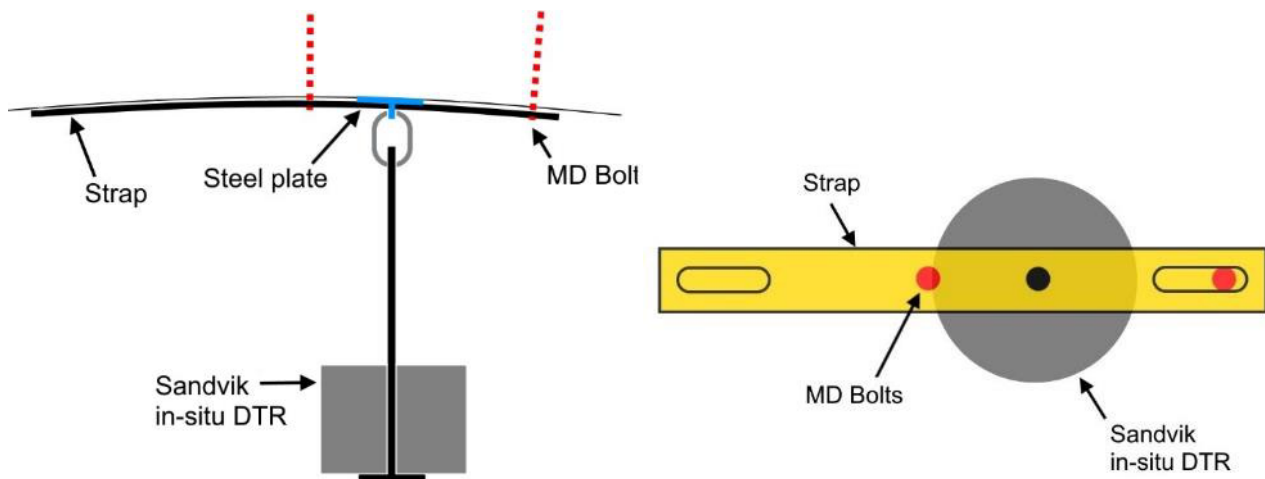
FIG 6 – End load configuration.

The Mesh straps used for this testing were Fero Weld Mesh straps FSSHDG4486004 (8 mm Gauge strand, 100 mm × 100 mm aperture) 6 m long and 400 mm wide. Based on published data, these products have a strand yield strength of 350 MPa and Ultimate Tensile Strength of 550 MPa, with a minimum weld shear strength of 23 kN.

The W-straps used were Fero straps FWS280–3600PG-S (Slot hole), which are a galvanised 3.6 m long, 280 mm wide strap utilising 1.9 mm steel. The holes are spaced approximately 500 mm apart with 500 mm long slotted holes at each end of the strap, terminating 200 mm from the end of the strap.

The MD bolt in each configuration was coupled with a Sandvik combi-plate (300 mm × 280 mm × 1.8 mm plate coupled with a 150 × 150 × 6 mm bearing plate) to replicate the typical installation practices of the straps. In no test did the plate or the securing bolt experience any failure – in all cases of failure, the strap tore off behind the bolt bearing plate.

A friction bolt was installed adjacent to the strap to assist with the dynamic testing, primarily to support the DTR weight prior to the test. This bolt was completely independent of the test samples.

The aim of the loading regime was to search for the maximum survivable energy and loading rate capacities that the strap can withstand without catastrophic failure. As such, the energy and/or loading rate levels were increased until failure occurred, then reduced to investigate survivable configurations. The configurations tested were:

- Three Mesh strap samples, two with end load configuration and one with centre load configuration.

- Six W-straps, three with centre load configuration and three with end load configuration.

The relatively small sample sizes were due to space availability in the test area and the time available on-site to conduct the test regime.

The monitoring data collected during the DTR test comprised:

- Load applied to the steel-plate, using a piezoelectric load sensor positioned within the claw component, recording at a rate of 25 kHz. The load sensor measures change in load, so it does not register the static weight of the rig prior to or after the test.

- The acceleration of the claw component, which is integrated twice to calculate the displacement of the steel plate as the test progresses.

- The final displacement of the steel plate, physically measured at the end of the test except if strap failure has occurred.

The load and displacement data are then used to calculate the energy transferred through the claw component during the test.

MESH STRAP TEST SPECIFICATIONS AND RESULTS

Specifications and summary results are shown in Table 1. The energy and loading rate progression for the Mesh straps started at 5.1 kJ (527 kg mass with 4.4 m/s impact velocity), which was applied to an end configuration test. The result from this test was a catastrophic failure of the Mesh strap, whereby the end of the strap pulled past the securing bolt.

The sample 2 test was conducted on another end configuration sample. In view of the failure of the first Mesh strap of that configuration, the energy was modified to 5.4 kJ, while the drop height was altered to decrease the impact velocity to 3.9 m/s This resulted in the test configuration arresting the dynamic disturbance without failure.

The sample 3 test was conducted on a centre configuration and was increased to 10.6 kJ (5.5 m/s impact velocity), based on the expectation that the centre configuration would provide a significant increase in dynamic capacity.

Acknowledging that only three tests were able to be conducted, the maximum supported load for the end configuration was found to be 5.4 kJ and for the centre configuration 10.6 kJ. The test parameters and results are shown in detail in Table 1 with further observations in Table 2.

TABLE 1

Mesh strap test parameters and results.

Sample number	Test configuration	Loading mass (kg)	Drop height (mm)	Theoretical impact velocity (m/s)	Theoretical input energy* (kJ)	Energy absorbed calculated (kJ)	Test duration (ms)	Peak input load (kN)	Load transfer plate displacement calculated (mm)	Load transfer plate displacement measured (mm)
1	End	527	990	4.4	5.1	6.1	370	61	482	250**
2	End	706	785	3.9	5.4	4.3	176	83	234	250
3	Centre	706	1525	5.5	10.6	9.3	146	101	300	320

* Input energy is the energy due to free falling mass until the point of contact with bottom of slide rod, it does not include the additional energy applied during strap deformation.

** Strap overloaded to catastrophic failure.

TABLE 2

Mesh strap failure notes.

Sample	Test configuration	Failures near Securing bolt	Failures near DTR load transfer plate
1	End	Three lateral wires failed (tensile failure at welds) around securing bolt (Figure 8)	Five lateral wires failed with a mix of tensile failure at welds and weld failure
2	End	Two lateral wires failed on central securing bolt (combination of tensile failure at welds and weld failure) (Figure 9)	Nil failed at steel plate interface
3	Centre	Three lateral wires failed at LH securing bolt, none at RH securing bolt (Figure 10)	Nil failed at steel plate interface

The Load displacement response of each Mesh strap is shown in Figure 7, which clearly shows a varied response for the end and centre configurations. Small portions of the measured load are slightly below zero due to the oscillatory nature of the response caused when wires fail, and video footage indicates that the claws/drop mass briefly enter free-fall.
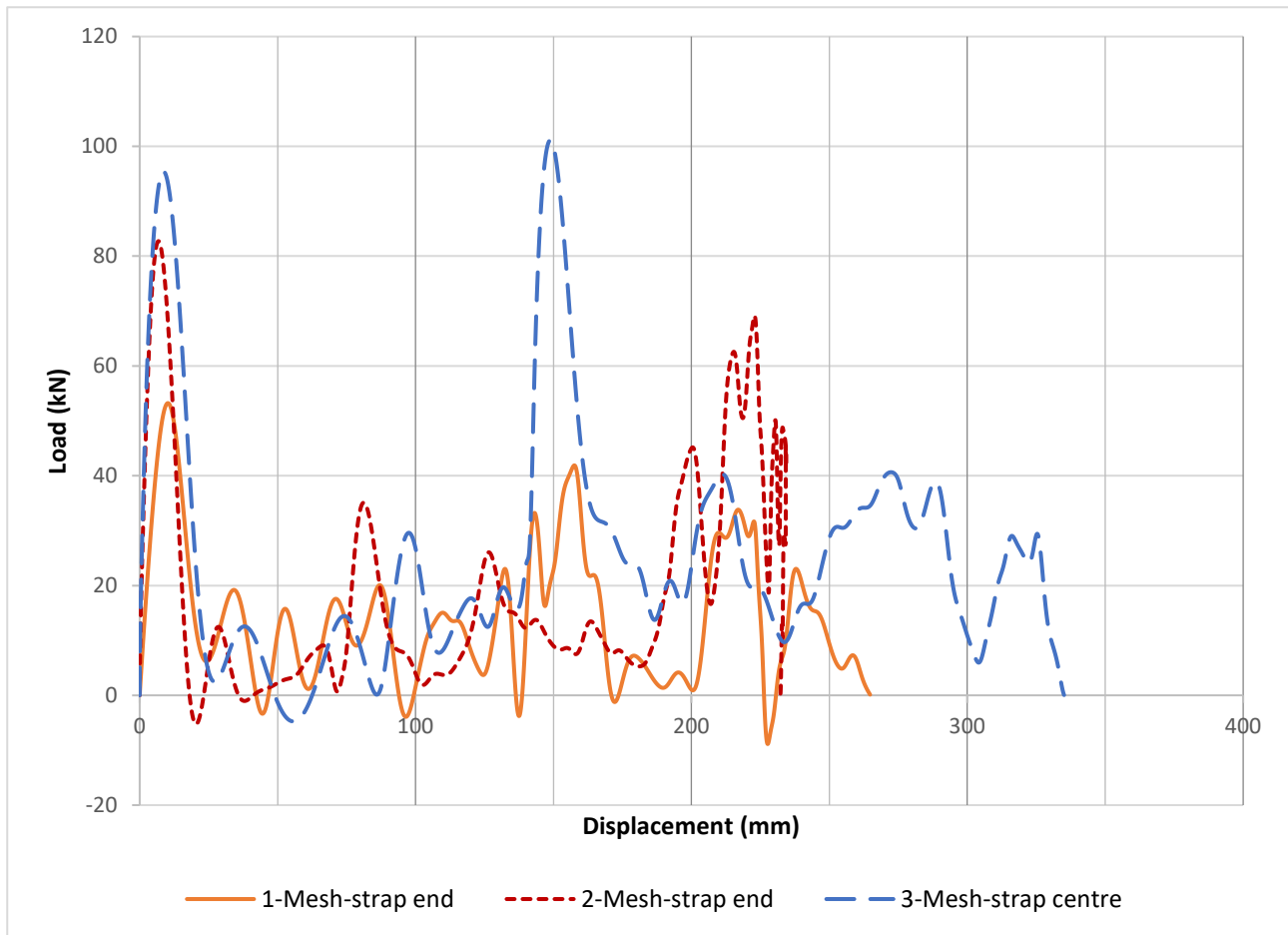
FIG 7 – Mesh strap load displacement responses. Sample 1 experienced catastrophic failure.

The two end configuration samples showed lower peak loads 61 kN and 83 kN compared to 101 kN for the centre configuration. The varied peak loads may be related to the way in which the strap longitudinal strands are able to develop and transfer dynamic tensile load along the strap to points distant from any failure zone. At the end of the strap, no tensile load can be transferred. Towards the centre of the strap, loads can be transferred beyond the zone that is experiencing failure. This behaviour is displayed in the failure mode of sample 1 (Figure 8) where the three cross strands of the Mesh strap pulled past the securing bolt to detach the Mesh strap from the securing bolt. Compared with the limited rupture of cross strands towards the centre of the strap of sample 2 (Figure 9) under lower impact velocity.
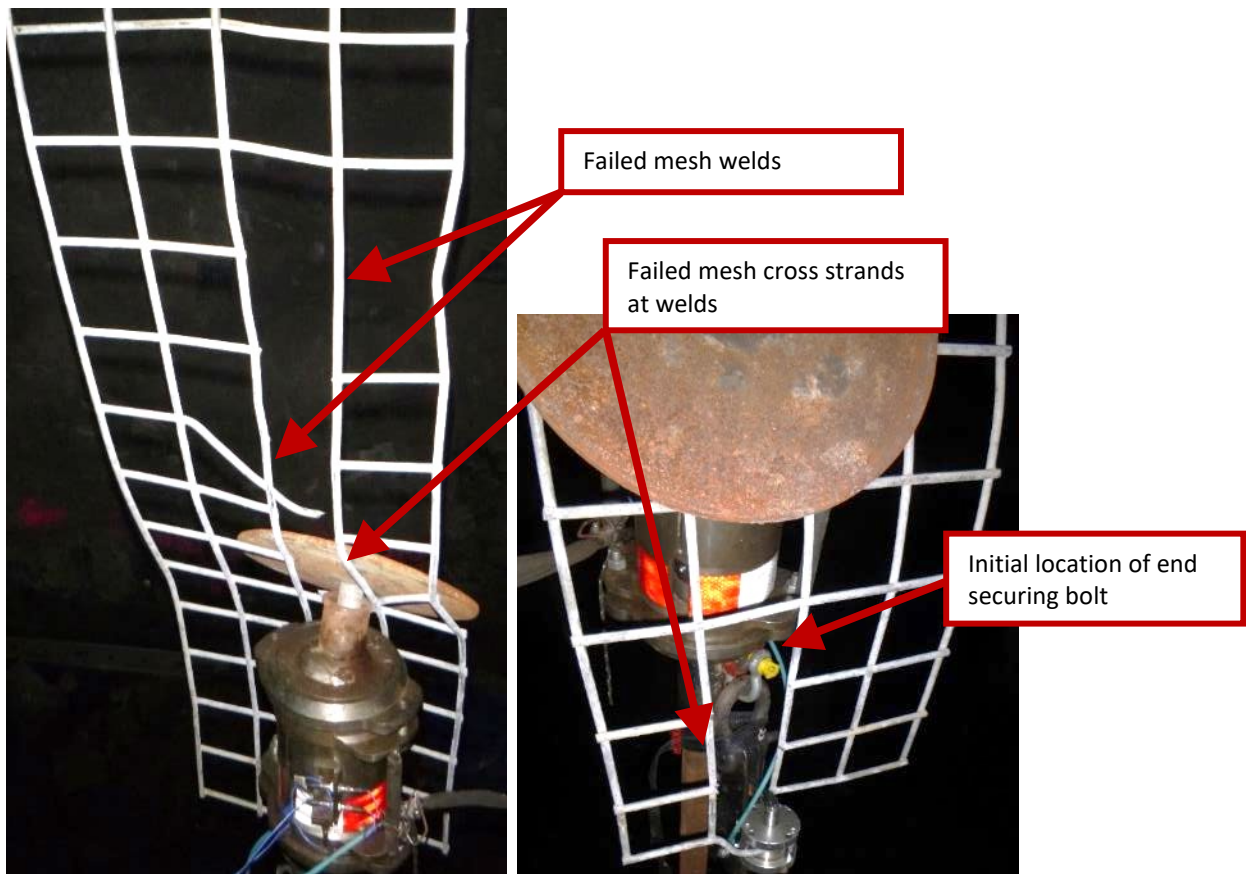
FIG 8 – Mesh strap end sample 1 failure mechanism.

FIG 9 – Mesh strap end sample 2 – 'LH' securing bolt failed wires.

The centre configuration test showed similar cross strand failure around the securing bolt (Figure 10). However, due to the location of the securing bolts, the higher dynamic energy was dissipated effectively due to the increased quantity of cross strands available, together with load transfer to the longitudinal strands.

FIG 10 – Mesh strap centre sample 3 'LH' securing bolt failed lateral wires.

The failure modes of the cross strands in the samples varied from rupture of the strand at the weld to overload of the welds as shown in Figure 11. Using the wire strand Ultimate Tensile Strength of 500 MPa and a diameter of 8 mm, the theoretical rupture strength of the strands (under static tensile load) is 25 kN.

FIG 11 – Mesh cross strap failure mode – left: sample 1 rupture; right: sample 3 weld failure.

W-STRAP TEST SPECIFICATIONS AND RESULTS

Specifications and summary results are shown in Table 3. Three samples were tested with each of centre and end configurations. This allowed for a spread of dynamic loads in each configuration, and as such a better understanding of the W-strap capacity was achieved. The test order was conducted to find the failure energy, then reduce dynamic energy to search for the maximum energy without failure as follows:

- Centre configuration: 10 kJ (sample 4) → 15 kJ (sample 6 – failure) → 12.4 kJ (sample 5).

- End configuration: 5 kJ (sample 8) → 10 kJ (sample 7 – failure) → 7.5 kJ (sample 9).

The peak energies survived by the W-straps in end and centre configurations were 7.5 kJ and 12.4 kJ respectively. These results mirror those of the Mesh straps, whereby the centre configuration has a higher dynamic energy capacity than the end configuration. The full test parameters and results are shown in Table 3, with further observations in Table 4, and the load displacement responses are shown in Figures 12 and 13. As was seen for Mesh straps, video footage indicated that portions of the load responses drop below zero when the strap yields suddenly allowing the drop mass and load transfer plate to briefly enter free-fall.

TABLE 3

W-strap test parameters and results.

Sample number	Test configuration	Loading mass (kg)	Drop height (mm)	Theoretical impact velocity (m/s)	Theoretical input energy (kJ) **	Energy absorbed calculated (kJ)	Test duration (ms)	Peak input load (kN)	Load transfer plate displacement calculated (mm)	Load transfer plate displacement measured (mm)
4	Centre	706	1505	5.4	10.4	9.3	139	95	289	310
5	Centre	1547	820	4.0	12.4	14.2	220	80	509	495
6	Centre	1547	1005	4.4	15.3	6.8	185	69	386	350*
7	End	706	1505	5.4	10.4	11.3	67	145	360	300*
8	End	706	785	3.9	5.4	4.0	150	44	434	355
9	End	706	1085	4.6	7.5	5.4	135	81	280	280

** Input energy is the energy due to free falling mass until the point of contact with bottom of slide rod, it does not include the additional energy applied during strap deformation.

* Strap overloaded to catastrophic failure.

TABLE 4

W-strap failure notes.

Sample	Test configuration	Failure observations
4	Centre	Slight tearing around the RH securing bolt approximately 200 mm (Figure 14 left), Nil at LH securing bolt
5	Centre	Severe tearing around LH securing bolt – approximately 500 mm (Figure 15), minimal tearing around RH securing bolt approximately 60 mm
6	Centre	Catastrophic strap failure (hole elongation approximately 300 mm followed by strap tensile failure) at LH securing bolt, followed by strap tensile failure at DTR steel plate
7	End	Catastrophic strap failure (tearing followed by tensile failure) at central securing bolt, then tearing around end securing bolt (Figure 14 right)
8	End	Hole elongation (tearing) on central securing bolt only, sliding to end of elongated hole at end securing bolt
9	End	No movement around central securing bolt, approximately 100 mm hole elongation (tearing) on end securing bolt
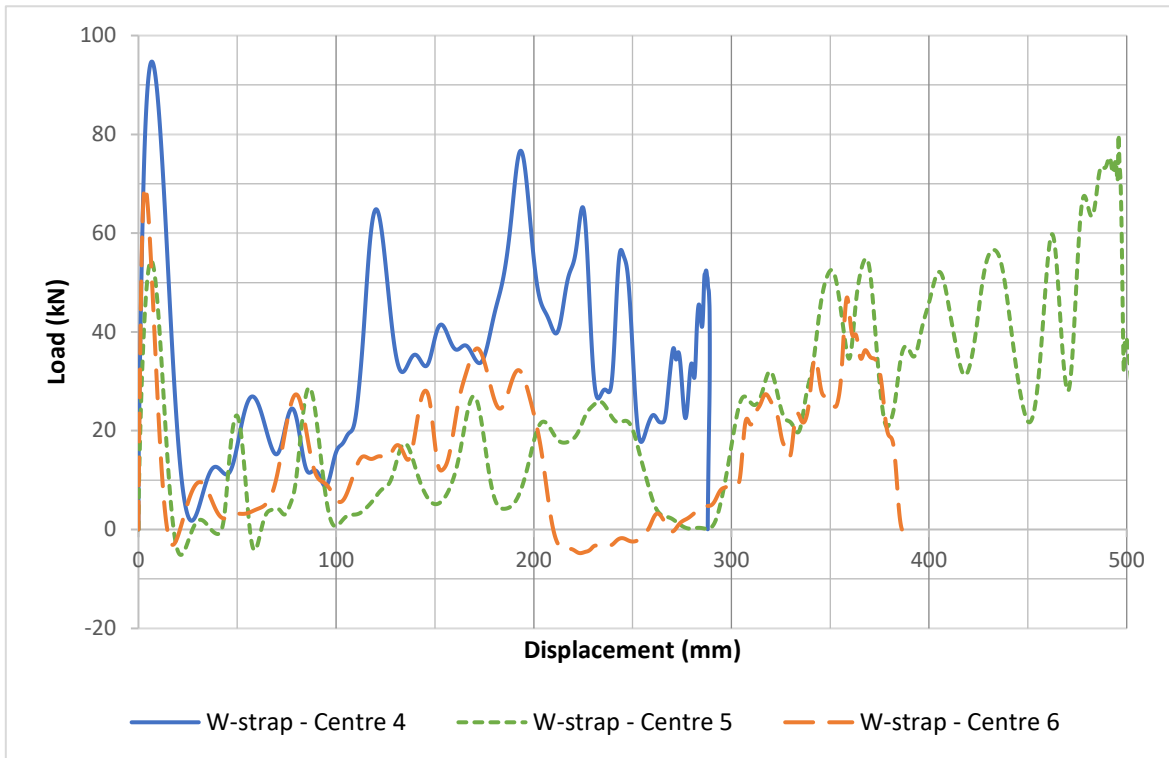
FIG 12 – W-strap load displacement response – centre test configuration, sample 6 experienced catastrophic failure.
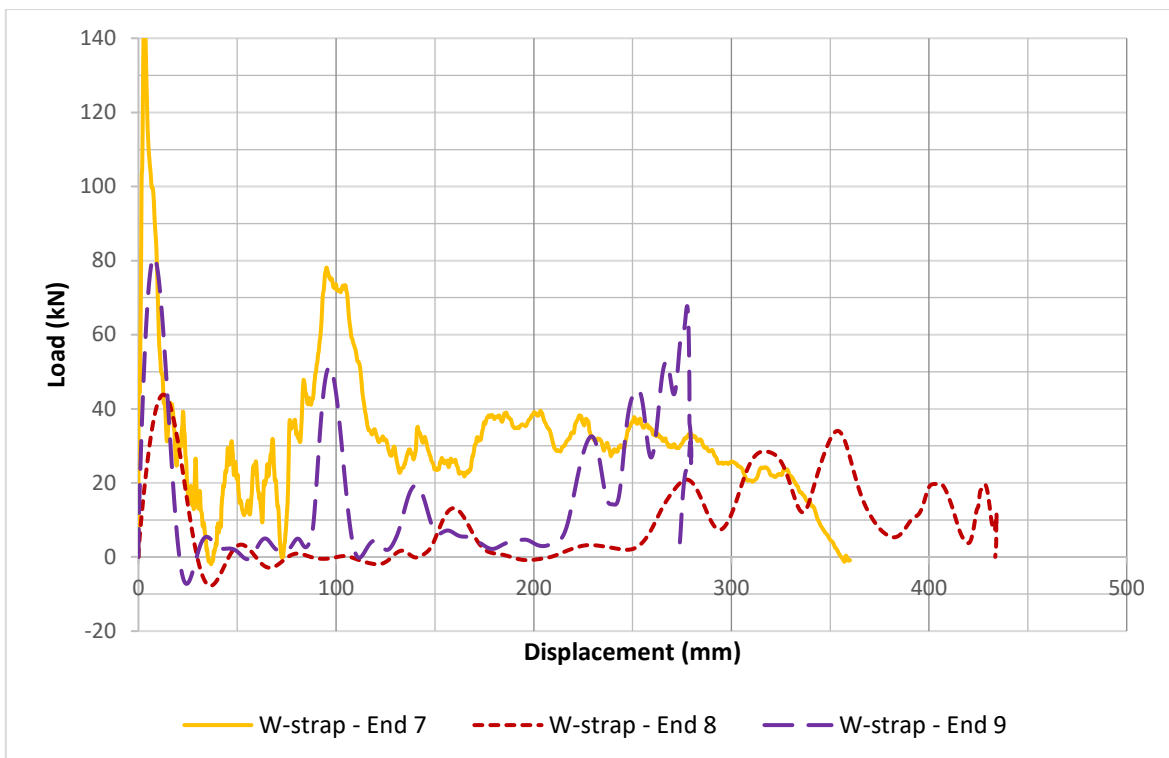
FIG 13 – W-strap load displacement response – end test configuration, sample 7 experienced cat-astrophic failure.

When comparing the different load displacement responses from Figures 12 and 13, all samples exhibited an initial peak load, which is a measure of the elastic resistance of the claw and the load transfer plate to deflection, until the initial friction between the W-strap, bearing plate and ground was overcome and lateral sliding movement of the strap commenced. The loads then varied greatly

between configurations and samples due to the inherent variabilities of installation conditions, the interactions of the straps with the securing bolts, and the frictional restraint acting on the W-straps.

W-strap samples 4, 5, 6 and 9 all showed similar hole tearing, which was the chief energy dissipation method. The tearing of the W-straps around the securing bolts occurred in the straps secured using both elongate slots and round holes, as shown in Figures 14 and 15.

The load transfer plate was bent about 50 mm during one W-strap test, which indicates a substantial load resistance existed in the W-strap at some point during the test.

FIG 14 – Tearing around securing bolts; left – sample 4 round hole that has become elongate as the strap pulled a considerable distance past the securing bolt; right – sample 7 elongate hole has torn through to the end of the strap disconnecting it from the securing bolt.

FIG 15 – Severe hole tearing – W-strap centre sample 5.

When a securing bolt was situated at the end of the plate and tearing occurred, in one case (sample 7) the strap failed to dissipate sufficient dynamic energy to avoid rupture. This is due in part to the limited solid material available between the end hole and the end of the strap to tear and absorb the dynamic energy. As a result, the maximum survivable load is lower than the centre configuration testing.

DISCUSSION AND CONCLUSIONS

The dynamic impact load applied to the Mesh strap or W-strap produced a rapid deflection of the strap, with deflection ranging 0.25 to 0.35 m for the Mesh straps, and 0.28 to 0.5 m for the W-straps. The strap has limited stiffness to resist bending in the impact load direction, which is nearly perpendicular to the strap. Load transfer caused a very high reaction load to be developed longitudinally in the strap as a response to the deflection. The reaction load was high enough to firstly initiate slippage of the strap behind the support bolt bearing plate, and secondly to develop high shear load at the point of contact to the support bolt.

For a typical test deflection of 0.35 m and with 1.0 m spacing of support bolts, and without catastrophic failure, the strap must slide about 0.2 m in total behind the support bolt bearing plate – and up to about 0.4 m of sliding if the deflection is 0.5 m. Thus, some rupture or tearing of mesh cross strands or W-strap metal is very likely to occur.

The mesh strap resistance to this sliding movement depends on the shear resistance of a cross strand in contact with a support bolt. If the cross strand ruptures, resistance becomes low until further sliding brings the next cross strand into contact with the bolt. Thus, the Mesh strap load chart (Figure 7) show substantial peaks and lower average loads between peaks.

The W-strap resistance to sliding occurs as the metal tears, but the tearing process is continuous and episodic, so those load charts (Figures 12 and 13) show pronounced peaks with lower average loads between peaks.

The load charts for all but one test reveal some intervals where strap deflection displacement was occurring at the same time as the registered load was zero or negative. This indicates that resistance to deflection displacement was lost for some intervals. Some such intervals were particularly pronounced:

- #1 Mesh strap end configuration: 270 to 330 mm (catastrophic failure followed).
- #6 W-strap centre configuration: 210 to 260 mm (catastrophic failure followed).
- #8 W-strap end configuration: 60 to 140 mm and again 170 to 210 mm.

Low resistance against deflection also means low resistance developed at the point contact of the strap with the support bolt. The weak link for Mesh straps was continued rupture of successive cross strands under shear loading. In no case did any longitudinal strands (under tensile load) rupture, so those were not the weakest link. Mesh is designed to spread tensile loads throughout the grid of strands, not to cope with a point shear load at one node or contact point to a support bolt. The distributed load along the length of the strap becomes concentrated into a point shear load at the contact to the supporting bolt.

The weak link for W-straps was continued longitudinal tearing of the strap metal as the strap was pulled past the securing bolt.

The performance of the straps that did not fail was a maximum absorbed energy of 9.3 kJ for the Mesh straps and 14.2 kJ for the W-straps.

The testing successfully demonstrated the ability of Sandvik's DTR to test these surface support elements. The testing also provided important design guidance data that is not practicable to obtain using laboratory dynamic testing facilities.

It is hoped that these observations and test data will enhance the understanding of the performance of these straps during dynamic disturbances, and will lead to improvements in strap design and use in underground mines.

ACKNOWLEDGEMENTS

REFERENCES

Vallati, O, Weaver, S and Halling, E, 2020. Dynamic testing of ground support: a comparison between in situ and laboratory testing, *Paper presented at the ISRM International Symposium – EUROCK 2020, physical event not held*, June 2020.

Whiting, R, 2017. In situ static performance assessment of mine mesh, in *Proceedings of the Eighth International Conference on Deep and High Stress Mining* (ed: J Wesseloo), pp 747–762 (Australian Centre for Geomechanics: Perth), https://doi.org/10.36487/ACG_rep/1704_51_Whiting.

A design and construction methodology for deep mine development

C Drover[1] and E Villaescusa[2]

1. Principal Engineer, Beck Engineering, Sydney NSW 2067. Email: cdrover@beck.engineering
2. Professor, Curtin University, Kalgoorlie WA 6430. Email: E.Villaescusa@curtin.edu.au

ABSTRACT

The stability of access tunnels is one of the main engineering challenges in deep underground mine construction. Many underground hard rock mining operations are now reaching depths where the induced stresses are such that sudden and violent failure of the excavations can occur very soon after construction. The loading conditions on the installed ground support schemes are often underestimated by conventional engineering design methods. Therefore, the actual loading conditions often exceed the installed ground support capacity. This can result in failure of the excavations and, in extreme cases, potentially closure of mining operations amounting to hundreds of millions of dollars in lost production. More frequently, violent excavation instability at great depth causes operational delays, costly and unplanned rehabilitation, as well as risks to worker safety. In order to address this challenge, this paper briefly summarises a modern, innovative approach to the design and construction of mine development at great depth. The process follows seven main steps. The first step is to characterise the rock mass strength, structure and stress. The second step is a stability assessment, which identifies the plausible modes of excavation failure, based on the rock mass characterisation. The third step is the definition of an excavation geometry which is harmonic to the high stress conditions. The fourth step is to prepare a site-specific face destressing drill and blast design which will reduce the potential for rock mass instability during the development construction cycle. The fifth step is to accurately quantify the expected loading conditions on the installed ground support. The method of doing so is uniquely analytical and probabilistic. It is based on the natural mechanical relationships between rock strength, structure, induced stress and the physical characteristics of the instability, including its mass and ejection velocity. The sixth step of the design process is to specify a ground support scheme arrangement with sufficient strength and displacement capacity to exceed the rock mass demand by a safe margin. The final stage is to install the complete ground support scheme using mechanised technologies which minimise the exposure of the equipment operators to unsupported ground at the tunnel face.

INTRODUCTION

Underground mass mining operations are widely viewed as the dominant mineral extraction methods of the future, given that the near surface resources are progressively being depleted. However, rock mass failures of a dynamic nature are threatening the ability of the mining industry to continue doing business at great depth. It is often the case that mass mining operations require advanced development access into deep and highly stressed work areas prior to the commencement of production. For example, deep block caving operations are a capital-intensive mining method which carry the risk of stress-driven failure of the access infrastructure very early in the project life cycle, especially during the development phase and the initiation of caving.

The trend to mine deeper orebodies results in increased loading demands on the excavations and installed ground support schemes, due to the increase in rock stress with depth. In many cases, this increase in demand is not met with the necessary increase in the energy dissipation and displacement capacity of the installed ground support schemes. Operational methodologies also frequently remain conventional. That is, aligned with historic practices more suited to low or medium rock stress environments. Such conventional practices include empirical ground support design methods, square excavation shapes non-harmonic to the induced stress field, development blasting practices and choice of mining equipment. Continuous improvements in design, construction and monitoring methodologies are required if deep hard rock tunnels are desired to be safely and economically constructed at great depth.

Rock mass characterisation

The first stage in the development design process is the rock mass characterisation. This process seeks to quantify the strength properties of the rock, the physical characteristics of the geological structures as well as the magnitude and orientation of the principal rock stresses. These factors are investigated and characterised for each and every distinctive geotechnical domain that is identified in the mining precinct.

Strength

The subsequent stages of the development design process, such as the tunnel stability assessment and ground support demand analysis, ideally require that high resolution spatial models of laboratory-derived measurements of the rock strength properties be developed as the input data. The resolution of those models is ideally at the same scale as the rock mass instability mechanisms that might be expected to occur and cause tangible impacts on the life-of-mine plan. Sufficient rock strength data may be collected directly from the locations of planned development infrastructure via diamond drill core sampling in advance of construction. For example, sample collection from pilot boreholes along the centreline of each extraction drift on a panel cave production level, and from other boreholes on approximately orthogonal orientations, would be an ideal data source to define the range and spatial variability of the rock strength values. Important properties for testing include the uniaxial and triaxial compressive strength, tensile strength, modulus and Poisson's ratio. Fracture toughness is also beneficial to collect and compare spatially to other factors, such as lithology and the presence of stress-induced disking of diamond core. Core disking has previously been correlated to dynamic, stress-induced development instability with major seismicity at several mining operations (Figure 1).
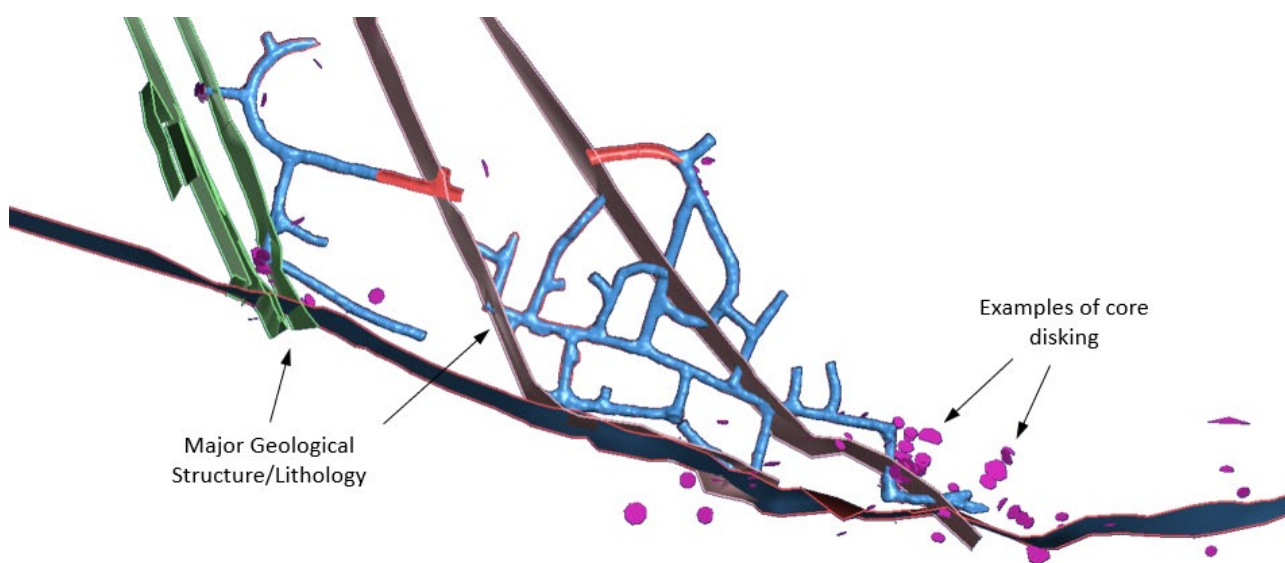
FIG 1 – Plan view of a deep mine level showing the development infrastructure, major lithological boundaries and the recorded locations of stress-induced diamond drill core disking.

Structure

The structural characterisation of the rock mass is multi-scaled, considering local geological structures at the scale of the individual excavations, as well as the larger mine-scale geological features such as major faults. The intent of characterising the local scale features is to define a concise structural model for each geotechnical domain, which identifies the number of distinct joint sets that are present, as well as their fundamental properties, such as orientation, trace length and spacing, as outlined in Table 1. The characterisation of the larger mine-scale geological features is preferentially focused on identifying their orientation and location with respect to the mine infrastructure, such that consideration for upgraded ground support capacity may be later given to these areas, where necessary, due to the potential for structures to generate large seismic events. Major geological structures may also determine the boundaries of distinct geotechnical domains which have unique small-scale structural characteristics.

TABLE 1

Example of a structural model for rock mass characterisation (Villaescusa *et al*, 2018).

Set	Dip (Deg)	Dip direction (Deg)	Fisher	Minimum trace length (m)	Avg. trace length (m)	Maximum trace length (m)	Minimum spacing (m)	Avg. spacing (m)
1	21	150	11.23	1.30	4.07	10.00	0.02	0.50
2	78	240	38.62	3.50	3.69	4.10	0.24	1.33
3	45	005	36.36	1.20	2.66	4.20	0.06	0.32
4	88	131	13.96	1.20	2.45	4.00	0.01	0.36

TABLE 2

Example of a structural model for rock mass characterisation (Villaescusa *et al*, 2018) (continued).

Set	Maximum spacing (m)	Cohesion (kPa)	Cohesion Std Dev. (kPa)	Friction angle (deg)	Friction angle Std Dev. (deg)
1	1.79	50.00	5.00	40.00	4.0
2	2.90	50.00	5.00	40.00	4.0
3	0.76	50.00	5.00	40.00	4.0
4	1.79	50.00	5.00	40.00	4.0

Stress

The characterisation of the *in situ* stress state both before and during active mining is critical to understanding the potential for exposure of mining operations to issues such as mining-induced seismicity, stress-driven excavation instability and dynamic ground support loading. Stress measurements can be performed well in advance of the commencement of mining using borehole stress measurement techniques, such as the WASM Acoustic Emission method (Villaescusa *et al*, 2002), and then later once the mine access excavations have been established, using methods such as the CSIRO HI Cell (Worotnicki and Walton, 1976). These data sets of stress measurements may be used to develop and/or calibrate high resolution 3D numerical models of mining-induced rock stress and strain conditions throughout the life of the mine plan. When combined with a rock mass strength model, models of numerically calculated rock stress provide a tool to conduct very detailed spatial analysis of the future development stability.

STABILITY AND FAILURE MECHANISM ANALYSIS

In the context of sudden, stress-induced instability of hard rock mine tunnels, with an associated violent release of strain energy at the tunnel boundary, it is considered that there are four generic mechanisms of excavation failure. These include superficial spalling, ejection of large structurally-controlled blocks, shear/crushing failure of pillars formed between adjacent excavations and rupture of significant geological structures (ie faults) which intersect the excavation. These mechanisms are illustrated in Figure 2. Scaled-down laboratory experiments by Kusui (2015) demonstrated that superficial spalling of excavations surfaces subjected to very high compressive stress occurs prior to the initiation of crushing or shear failure of the adjoining pillars. Furthermore, observational evidence of excavation failures at many underground mines indicates that ejection of large structurally-controlled blocks occurs as an intermediate mechanism, ie after spalling but before pillar failure. The observations indicate that where development precincts experience very high induced stresses in-cycle, the instability of large, structurally-defined blocks takes time to develop. This mechanism often occurs once the development face has advanced by 20 m or more beyond the affected area. By contrast, fault rupture may potentially occur at any time during the development cycle. This mechanism may occur over a large scale and is often controlled by factors such as global changes in mine extraction geometry and the associated stress field adjustments. The conceptual progression of dynamic, stress-driven excavation damage mechanisms is illustrated in Figure 3 as

a Load-Displacement plot, based on the experimental results of Kusui (2015) as well as recent observational evidence from underground mines.
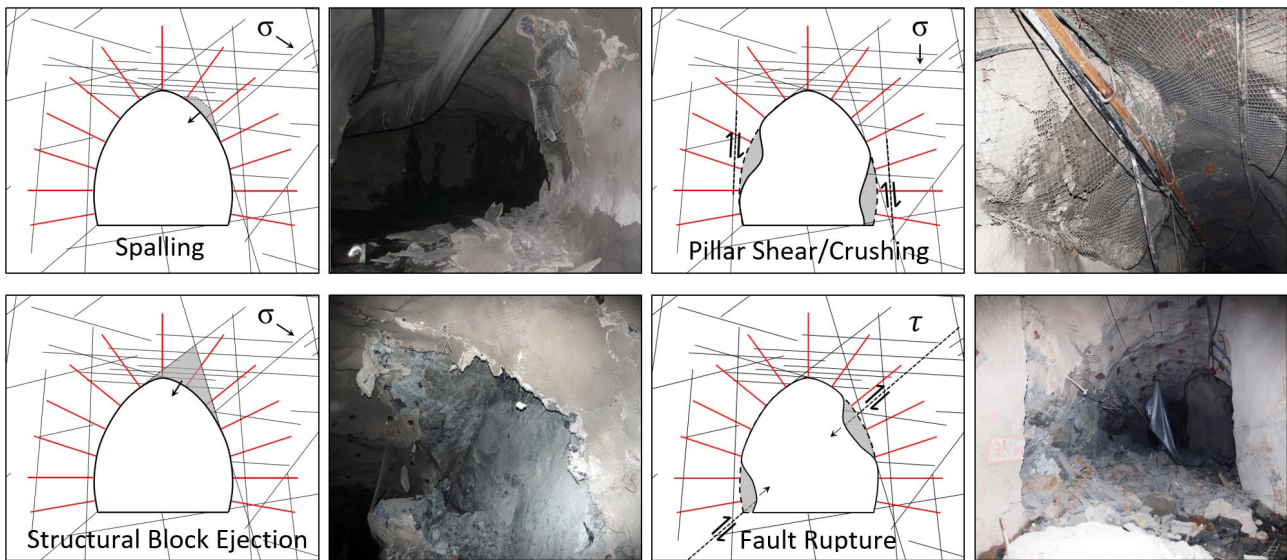
FIG 2 – Modes of tunnel failure involving violent strain energy release at the excavation boundary.
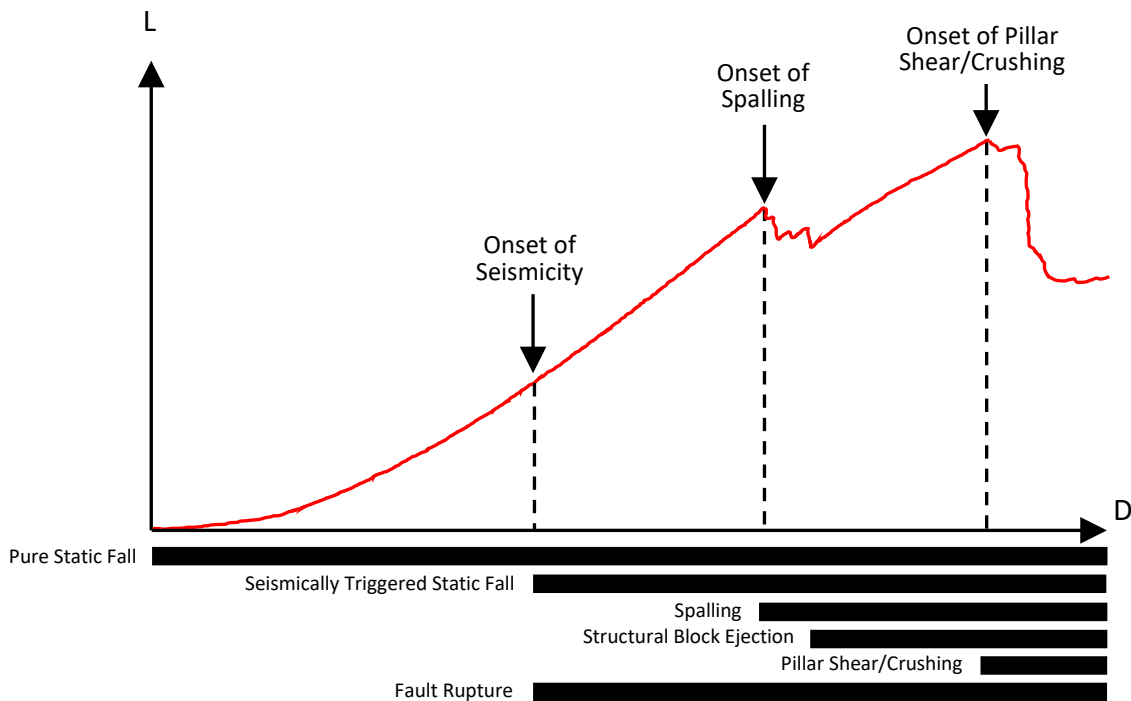
FIG 3 – Theoretical progression of rock mass failure modes at the excavation boundary.

Kusui (2015) also defined the ratios of UCS to maximum tangential stress (σ_c / σ_{max}), for instability of spatially isolated excavations (eg declines) and UCS to average pillar stress (σ_c / σ_{avg}), for excavations formed by thin pillars (eg drawpoints, cross-cuts), at which spalling and/or shear-crushing modes of excavation damage initiate. That analysis was performed across a wide range of rock strengths and it is important to note that the strength criterion value at the onset of failure changes as a function of UCS. It is not constant, as is often assumed. Those results have been used to develop several stability charts which, when applied to 3D models of the UCS parameter and mining-induced stress, provide a criterion by which to assess the likelihood of development instability. An example stability chart is presented in Figure 4. A related spatial analysis for shear/crushing failure of vertical pillars subjected to concentration of the major principal stress is illustrated in Figure 5.
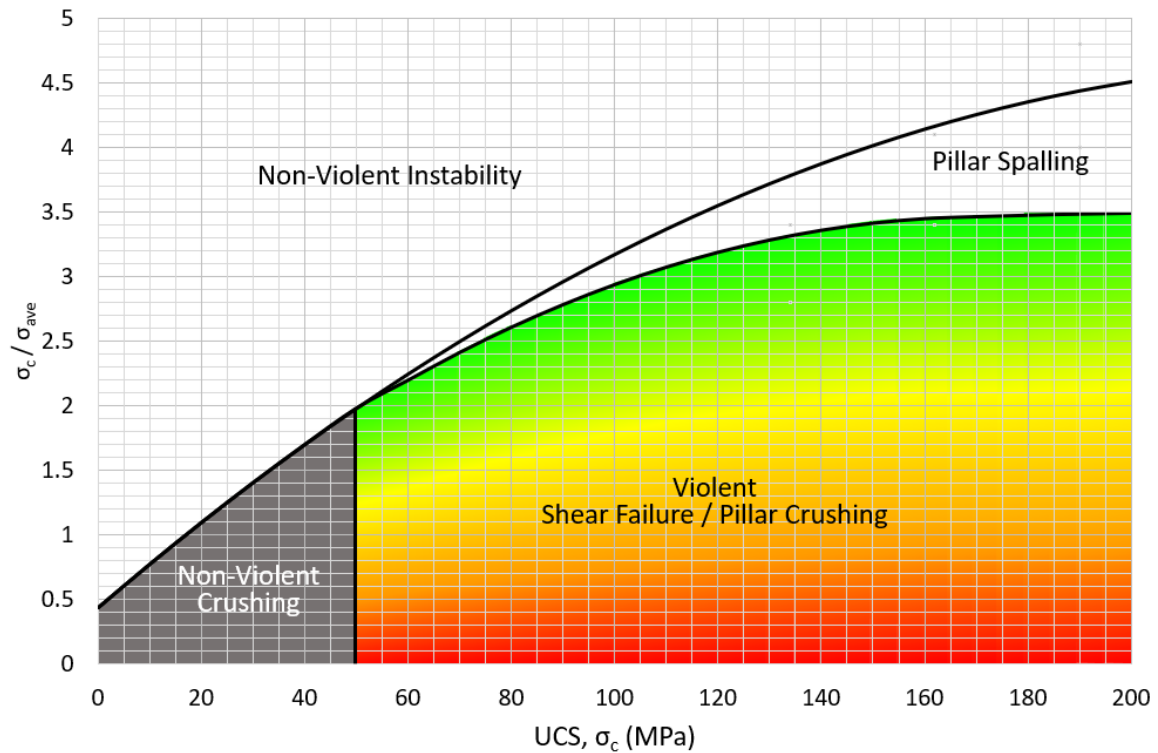
FIG 4 – Stability chart for excavations formed by thin pillars (modified after Kusui, 2015; Drover, 2018).
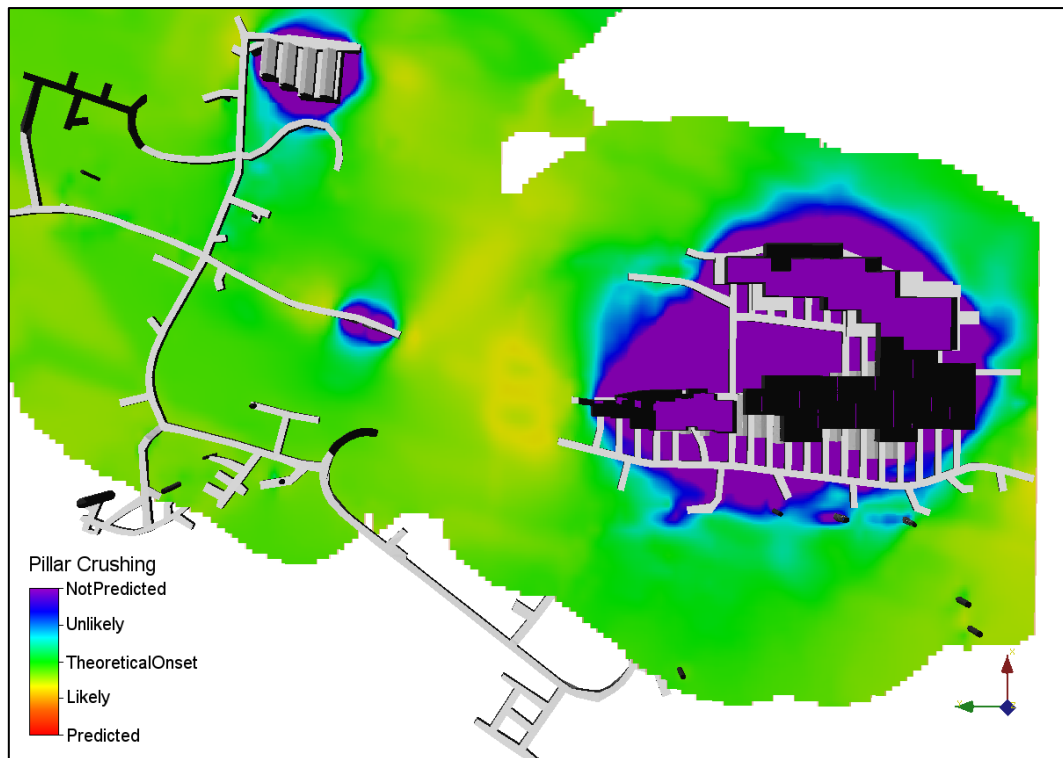
FIG 5 – Spatial map of predicted late-stage dynamic instability with pillar shear/crushing, specifically for vertical (ie interlevel) pillars experiencing high concentration of the subhorizontal major principal stress.

EXCAVATION GEOMETRY AND DEVELOPMENT DESTRESSING

As mining operations advance to greater depths or the existing development excavations become exposed to an advancing stress front, such as a caving abutment, it is likely that square development excavation shapes will eventually become unstable. Square development profiles are optimised for

mining equipment passage, ease of blasthole pattern drilling and to minimise waste rock removal costs, for example. However, as stress concentrations at the acute apexes between the walls, roof and floor increase, rock mass instability will occur, causing ground support loading. Vertical tunnel walls which experience high stress concentrations tangential to the excavation boundary almost immediately enter tensile loading. The result is frequently observed underground as surface support damage such as fractured shotcrete and bagging mesh, which requires costly and disruptive ground support rehabilitation campaigns, often very soon after the initial construction. Unplanned overbreak of such excavations prior to ground support installation has also been known to exceed 20 per cent.

Sustainable, safe and productive mining at great depth relies heavily on the inherent stability of the development excavations. For this reason, rounded development profiles are suggested to be more appropriate. These may include backfilled inverts to prevent dynamic floor heave, where appropriate. Such profiles not only provide a more stable long-term solution, but the initial excavation construction is also likely to be safer due to the reduced potential for rounded walls to experience instability in-cycle. Development face destress blasting, which seeks to create a shear-failure mode of strain energy dissipation in the rock mass ahead of the face (Saharan and Mitri, 2011; Drover *et al,* 2018), has also been shown to have significant positive effects in terms of reducing seismic activity and rock mass stiffness ahead of the advancing face (Drover, 2018). Destress blasting may also be implemented in the floor of the excavation, if needed, in order to reduce the potential for dynamic floor heave.

GROUND SUPPORT DESIGN

The most common ground support design methods of recent years have focused on the energy balance approach. That is, assessing the kinetic energy demand of the rock mass and factoring this against the energy dissipation capacity of the installed ground support scheme. This approach requires that a surplus energy dissipation capacity be available from the ground support scheme, in order to exceed the demand defined by some loading criteria. The ground support design process described here is fundamentally based upon the notion that the kinetic energy of the unstable rock mass is principally derived from the sudden and violent stress-driven release of strain energy from the rock mass at the immediate excavation boundary, ie within the reinforcement zone and perhaps extending some distance beyond it. The critical input variables defining the rock mass demand on the ground support are the mass of the instability and its initial velocity of ejection, which varies according to an approximately linear dependence on UCS (Kusui, 2015). The mass of instability is expressed in terms of tonnes per metre square (T/m^2) at the excavation surface where the failure occurs (Drover, 2018). This represents the mass of unstable rock that may be ejected via shallow spalling slabs or large blocks, for example.

For spalling modes of failure, the depth of instability is typically shallow and not more than 0.5 m, which for most rock types corresponds to a mass of instability of approximately 1.35 T/m^2 at the excavation surface. If failure mechanisms involve the ejection of structurally controlled blocks defined by small-scale joints with large intersecting trace length, the demand may be much greater. In order to define the mass of the instability for these mechanisms, the structural model for the relevant geotechnical design domain (see Table 1) are applied as inputs to the SAFEX software. This software package generates a probabilistic simulation of the plausible block-forming geometries, considering each of the identified joint sets in a particular rock mass and the natural dispersion of the orientation, spacing and trace length values within each set (Villaescusa *et al,* 2018). The mass of instability for ground support design typically accounts for all possible blocks up to the 90th percentile but may be adjusted to include more or less of the plausible blocks if additional evidence, such as underground observations, warrants. The initial velocity of rock mass ejection for all aforementioned failure mechanisms, excluding fault rupture, has been shown to be proportional to the uniaxial compressive strength of the intact rock by Kusui (2015). The linear increase in ejection velocity as UCS increases does exhibit some variability. This was possibly a result of the joint strength conditions influencing the ejection velocities, with weaker joints resulting in lower values.

A design chart for estimation of ground support demand in hard rock with strong joints is illustrated in Figure 6. This chart uses the probabilistically derived mass of instability and UCS at the tunnel boundary as inputs to derive a solution for dynamic rock mass demand. The various demand categories vary from Very Low (<5 kJ/m^2) to Extremely High (>45 kJ/m^2) as defined by Villaescusa

et al (2016b). These categories are shown to the right of the chart. Fourteen demand lines contained on the chart represent the kinetic energy equation solution for masses of instability ranging from 0.5 T/m^2 up to 3.5 T/m^2. The relevant demand value for ground support design can be read off the chart by noting where the host rock UCS intersects the demand line corresponding to the probabilistically derived mass of instability. For example, in a host rock mass with UCS of 150 MPa, where 90 per cent of all plausible block forming geometries have a mass of instability of 1.75 T/m^2 or less, the maximum demand on ground support is estimated to be 40 kJ/m^2. Rather than utilise a factor of safety approach, it is suggested that the ground support scheme capacity surplus should be in the order of 20 kJ/m^2 above the rock mass demand, for most conditions. A ground support scheme with an installed capacity of 60 kJ/m^2 would therefore be recommended for this example. It should be re-iterated that this chart pertains to hard rock with strong joints. Ground support design charts for massive rock and rock with moderately strong joints are not shown here. A key consideration in rock mass demand assessment for ground support design is to control the block forming geometries at the excavation boundary, thus avoiding potential progressive failure (unravelling) with a large depth of instability.
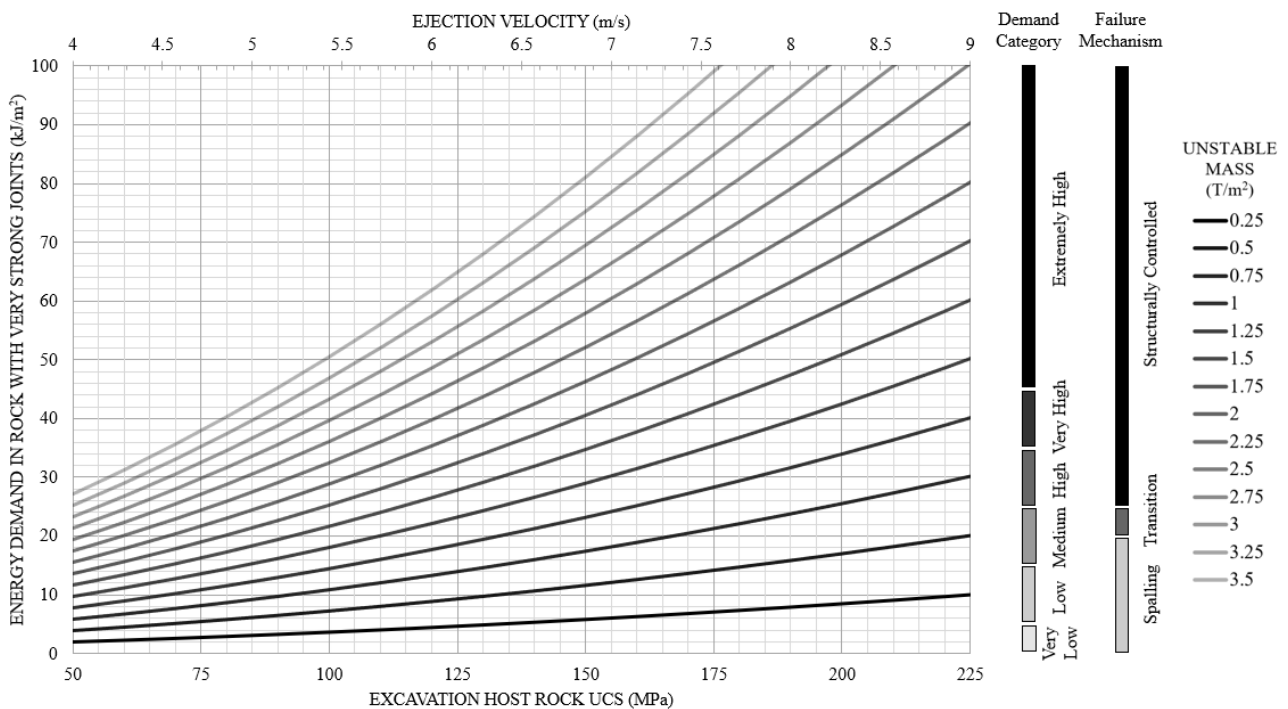
FIG 6 – Energy demand chart for ground support design in hard rock with strong joints (Drover, 2018).

If the ground support scheme energy dissipation capacity is to exceed the rock mass demand by a safe margin, then suitable reinforcement and surface support products must be selected. The role of the reinforcement is primarily to stabilise any significant structurally-controlled blocks that may become unstable at the tunnel perimeter, as well as provide retention of the surface support layer(s). Reinforcement element selection is made on the basis of the energy dissipation capacity of that element exceeding the rock mass demand over a range of displacement that is compatible with the capacity of the surface support system. The energy dissipation capacity versus displacement performance of various reinforcement elements and some combined reinforcement and surface support schemes have previously been published by Player (2012); Villaescusa *et al* (2014, 2016a). Continuously Mechanically Coupled (CMC) or Discretely Mechanically or Frictionally Coupled (DMFC) elements with a high energy dissipation capacity and displacement range of 300 mm or less are preferred. Examples include de-coupled resin-encapsulated PosiMix bolts as primary reinforcement and fully cement-grouted plain strand cable bolts as the secondary reinforcement. An example of a high energy dissipation capacity ground support scheme arrangement consisting of these elements is shown in Figure 7. The choice of reinforcement encapsulating medium is heavily dependent on ground conditions and the incycle development schedule requirements. In many cases the primary reinforcement elements can be efficiently installed using resin cartridges. However,

where complex rock structure or stress-fractured ground exists close to the excavation, installation of resin cartridges can be difficult and time-consuming. Reinforcement systems that employ innovative resin-pumping technologies may be more suitable in those conditions.
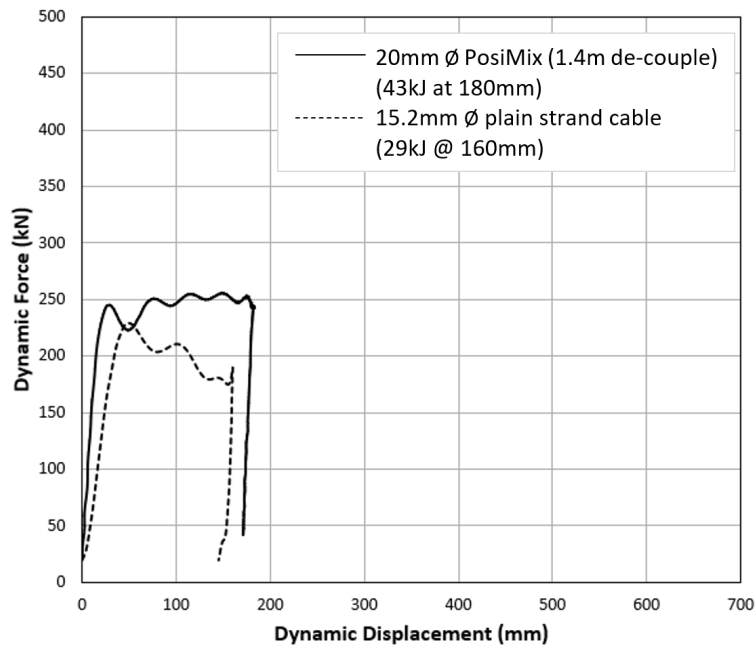
FIG 7 – Load displacement performance of a 20 mm diameter, resin-encapsulated PosiMix bolt with 1.4 m decouple and a 15.2 mm diameter, fully cement-grouted plain single-strand cable bolt.

The purpose of the surface support layer(s) is to provide spatially consistent areal retention capacity of the excavation surface, containing any rock mass instability that might form in between the spacing of the reinforcement elements. The surface support layer must also provide load transfer capacity from any unstable region of the excavation to the reinforcement elements located at the stable region. This is particularly critical where failure of some nearby reinforcement elements has occurred due to overloading or installation quality issues. In mine development likely to experience very high dynamic loading demand, the continuity of the load transfer and energy dissipation capacity of the surface support layer is crucial to minimising the potential points of weakness, such as overlaps, that may fail during loading. Integration of the surface support layer and reinforcement elements over a spatially continuous area spanning across any instabilities is key to this objective.

High tensile woven mesh rolls spanning from floor-to-floor are regarded as the superior product for this purpose. This is due to their extremely high capacity and the areal continuity of that high capacity, with far fewer overlaps to act as a point of weakness compared to conventional weld mesh. Embedding any form of mesh within a shotcrete layer will increase both the surface support total capacity as well as its stiffness response (Morton *et al,* 2009). Simultaneous activation and consumption of the energy dissipation capacity of both shotcrete and mesh is also optimised when shotcrete is internally reinforced by the mesh in a rigid manner. In many, if not most situations, a mesh layer exposed external to the shotcrete will typically tolerate up to 200–300 mm of displacement before achieving even 10 per cent of its load bearing capacity, by which time the shotcrete will have substantially fractured, often to the point of delamination and complete loss of load-bearing capacity. Laboratory strength testing of new products developed for high capacity surface support have recently been performed at the WA School of Mines and these are ongoing (Villaescusa, 2019).

An example of a multi-layered ground support scheme for extremely high energy dissipation in the order of 60 kJ/m^2 is illustrated in Figure 8. This scheme is a field-tested design for use in rock mass conditions where potentially large structurally-controlled blocks may be dynamically ejected from the excavation. The arrangement of the design consists of an initial 50 mm thick primary layer of plain shotcrete (no fibres). This is immediately followed by the installation of a high-tensile steel, woven chain-link mesh sheet (G80/4.6 or similar), which is integrated with a pattern of primary reinforcement elements, such as decoupled PosiMix bolts or fully cement-encapsulated rebar. The primary

reinforcement pattern is staggered in a so-called Dice-5 layout, and spacings between the individual elements are dictated by the anticipated maximum rock mass demand and the individual capacity of each element. This layer is installed in-cycle in order to manage early-stage failure mechanisms, such as spalling, which may occur during construction. It also includes a secondary overspray layer of plain shotcrete from floor-to-floor, the purpose of which is to mechanically bond the primary mesh and shotcrete layers together, to ensure a simultaneous loading response by both components. This primary layer is implemented for several consecutive development rounds, typically for up to 15–20 m of lateral advance, before a secondary ground support layer is installed (Figure 9).
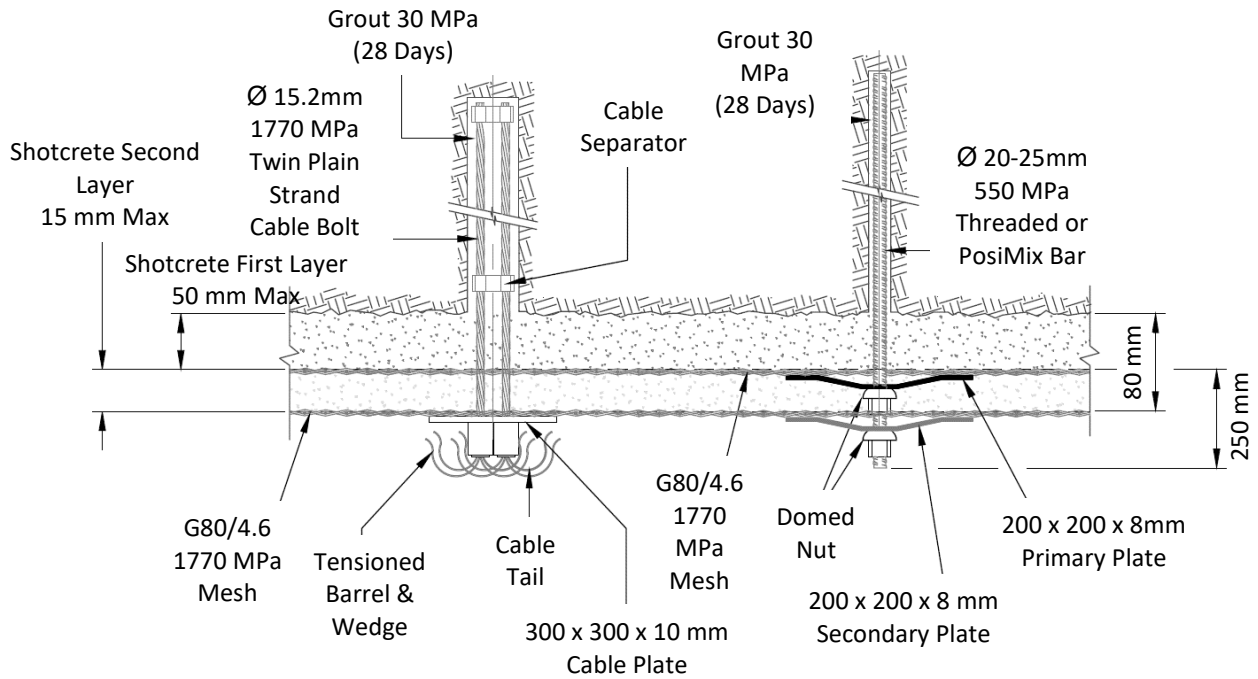
FIG 8 – Arrangement of reinforcement and surface support components in a ground support scheme for extremely high energy dissipation capacity >60 kJ/m^2 (Drover, 2018).
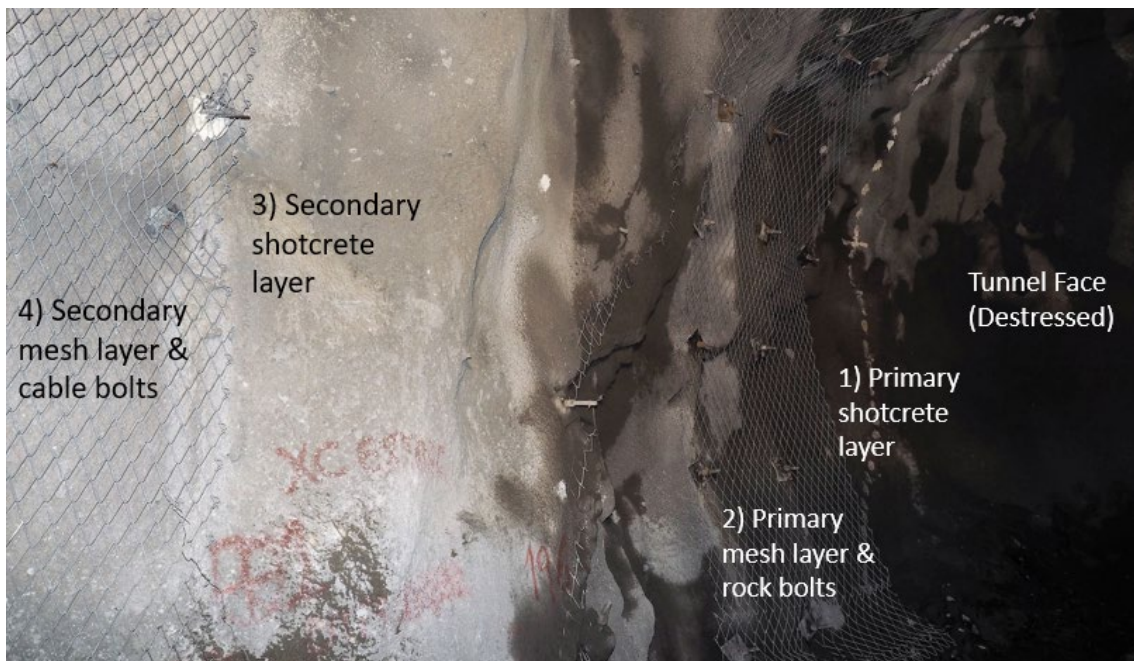
FIG 9 – A primary ground support layer to manage shallow spalling failure, with a secondary layer lagging by 3–4 development rounds, to manage structurally-controlled instability of large blocks (Villaescusa *et al*, 2016b).

The secondary ground support layer consists of another sheet of high tensile woven mesh from floor-to-floor, which remains permanently external to the mesh-reinforced shotcrete layer. The secondary mesh layer provides redundant retention capacity in the event that the primary layer is overloaded. The mesh overlaps of the second layer are offset from those in the first, minimising the risk of ejection through the overlaps. Wire lacing may also be used to secure all external mesh overlaps. This mesh layer coincides with an infill pattern of fully-cement grouted plain strand cable bolts for deep reinforcement, in either a twin or single strand configuration, depending on required capacity. Based on recent unpublished tests at the WA School of Mines, cement grouting of cables is preferred over resin injection grouting for dynamic capacity, due to higher yield loads being achieved at the strand-grout interface. The lag-time for installation of the secondary ground support layer must be limited, such that the deep reinforcement is installed before any structurally-controlled instability has time to develop.

This double-layered ground support scheme arrangement is arguably the most robust design that would be implemented in practice. It is reserved for those conditions where extremely high rock mass dynamic loading demands justify its implementation, for instance when development crosses seismically active major structures. Where the rock mass demand is anticipated to fall within the medium to very high range, ie 25–45 kJ/m^2 (Villaescusa *et al,* 2016b), and the additional capacity of the secondary mesh layer is not justified, it is omitted. For those demand conditions, a single mesh-reinforced shotcrete layer is installed, but with a similar arrangement of primary and secondary reinforcement elements, usually consisting of resin-encapsulated PosiMix bolts, of deliberately selected embedment and de-coupling lengths, together with single plain strand cement-grouted cable bolts in place of the higher capacity twin-strands. This single layer arrangement of ground support has proven to tolerate numerous large events in the order of +2.0 ML and above with minimal requirement for rehabilitation, despite very high rock mass demands being observed at the excavation boundary (Figure 10).

FIG 10 – Performance of a single-layered high energy dissipation ground support scheme following a +1.9 ML seismic event and associated dynamic loading. Rehabilitation was not required due to the remaining load-bearing capacity.

GROUND SUPPORT IMPLEMENTATION

In recent years, the conventional Australian approach to deep mine development construction is to use twin-boom jumbos for ground support installations. These jumbos have historically been employed to install weld mesh surface support, in addition to various types of reinforcement elements, including continuously mechanically coupled (CMC), continuously frictionally coupled (CFC) or discretely mechanically or frictionally coupled (DMFC) elements (Thompson *et al,* 2012).

More recently, as part of the Mine Development at Great Depth Research Project, Phase 2, the transition to routine installation of high tensile woven mesh has been successfully implemented in a number of mines that were previously experiencing elevated seismic activity and associated impacts to development stability. The transition to high energy dissipation capacity chain-link mesh and reinforcement elements such as resin-encapsulated, de-coupled PosiMix bolts has been made with no significant modification to the jumbo fleet being required, as illustrated below in Figure 11.

FIG 11 – Installation of high-tensile chain-link mesh surface support in deep mine development using a conventional twin-boom jumbo (Goldfields region, Western Australia).

CONCLUSIONS

Mining operations worldwide are reaching greater depths below the surface in search of the next generation of resource opportunities. In order to ensure safe and reliable production, advancements in the geotechnical design and construction of the access development are required to keep pace with the more challenging rock mass conditions. This paper has presented a short summary of the conceptual approach to mine development design and construction that has been progressively developed at the WA School of Mines over the last 20 years, with a particular focus on the latest Mine Development at Great Depth research program output from 2015–2020. The holistic approach to development design consists of seven main steps. The first step includes a characterisation of the conditions of rock strength, structure and stress and the variability of these factors throughout the mining environment. Specific focus is given to characterising the development precincts. The second step is a stability assessment to identify the potential modes of excavation damage and/or failure that must be managed by ground support. The third stage is to define a stable excavation geometry which is harmonic to the expected mining-induced stress conditions at depth. The fourth phase is to design a development destress blasting program for implementation which reduces the potential for sudden stress-driven instability of the advancing face whilst the construction workforce is present there. The fifth stage is to estimate the future rock mass demand on ground support based on a probabilistic analysis of the data previously collected during the rock mass characterisation. The sixth stage is to specify a ground support scheme arrangement with sufficient energy dissipation capacity to stabilise the excavation during any stress-driven rock mass instability, with sufficient surplus capacity available to ensure infrastructure reliability and minimal rehabilitation requirements, if any. The final stage is to implement the development design, including mechanised construction equipment and innovative ground support products for high energy dissipation capacity.

ACKNOWLEDGEMENTS

REFERENCES

Drover, C, 2018. *Design, construction and monitoring of hard rock tunnels at great depth*, PhD Thesis: Western Australian School of Mines, Curtin University, Kalgoorlie, Australia.

Drover, C, Villaescusa, E and Onederra, I, 2018. Face destressing blast design for hard rock tunnelling at great depth. *Tunnelling and Underground Space Technology*, 80:257–268.

Kusui, A, 2015. *Scaled down tunnel testing for comparison of surface support performance*, PhD Thesis: Western Australian School of Mines, Curtin University, Kalgoorlie, Australia.

Morton, E, Villaescusa, E and Thompson, A, 2009. Determination of Energy Absorption Capabilities of Large Scale Shotcrete Panels, *Proceedings of the 2009 ECI Conference on Shotcrete for Underground Support*, paper 6, 20 p.

Player, J, 2012. *Dynamic testing of rock reinforcement systems*, PhD Thesis: Western Australian School of Mines, Curtin University, Kalgoorlie, Australia.

Saharan, M and Mitri, H, 2011. Destress blasting as a mines safety tool: some fundamental challenges for successful applications. In: *First International Symposium on Mine Safety Science and Engineering*, pp 34–47.

Thompson, A, Villaescusa, E and Windsor, C, 2012. Ground Support Terminology and Classification: An Update, *Geotech & Geol Eng*, 30(3), pp 553–580.

Villaescusa, E, 2019. Ground Support for Tunnels at Great Depth, Technical presentation to the Chilean Rock Mechanics Society: April 11, 2019, Santiago, Chile.

Villaescusa, E, De Zoysa, A, Player, J and Thompson, A, 2016a. Dynamic testing of combined rock bolt and mesh schemes, *Proceedings of the Seventh International Conference and Exhibition on Mass Mining,* pp 789–798.

Villaescusa, E, Kusui, A and Drover, C, 2016b. Ground support design for sudden and violent failures in hard rock tunnels, *Proceedings of the 9th Asian Rock Mechanics Symposium*, Indonesia.

Villaescusa, E, Player, J and Thompson, A, 2014. A reinforcement design methodology for highly stressed rock masses, *8th Asian Rock Mechanics Symposium*, Japan.

Villaescusa, E, Seto, M and Baird, G, 2002. Stress measurements from oriented core, *Rock Mechanics and Mining Sciences*, 39:603–615.

Villaescusa, E, Thompson, A and Windsor, C, 2018. Probabilistic estimate of rock mass static and dynamic demands for underground excavation stabilisation, *Rock Mechanics and Geotechnical Engineering*, 11:481–493.

Worotnicki, G and Walton, R, 1976. Triaxial hollow inclusion gauges for determination of rock stresses in-situ, *Proc. ISRM Symp. on Investigation of Stress in Rock, Supplement*, pp 1–8. Instn Engrs.

Data analytics and machine learning methods applied to underground coalmine roof convergence data

J Emery[1], I Canbulat[2], L Yao[3] and C Zhang[4]

1. PhD Candidate, UNSW, Yeppoon Qld 4703. Email: optimumgeotechnics@gmail.com
2. Head of School, UNSW School of MERE, Sydney NSW. Email: i.canbulat@unsw.edu.au
3. Acting Associate Head of School, UNSW School of CSE, NSW. Email: lina.yao@unsw.edu.au
4. Senior Lecturer, UNSW School of MERE, NSW. Email: Email: chengguo.zhang@unsw.edu.au

ABSTRACT

This paper documents a process of data analytics and machine learning applied to coalmine roof convergence data. It follows a publication documenting the formation of the database. For each set of analyses Python scripts were utilised to extract data from an SQL database, with subsequent analyses also executed in Python, utilising open-source tools such as scikit-learn. Preliminary analyses with classic machine learning algorithms included multiple logistic regression, K-nearest neighbours, decision tree, random forest, support vector machine, kernel support vector machine, artificial neural network (ANN), naïve Bayes and multiple linear regression. Results indicated that relationships were complex and non-linear, with the artificial neural network most suitable. An ANN model was then refined through a standard process of hyperparameter optimisation and data augmentation to arrive at a final model. Due to the black box nature of the ANN further insight into how the parameters interacted was sought and found with Shapley additive explanations (SHAP values). SHAP values utilise Game Theory, where each input parameter or feature is a 'player' while the data set is the 'team'. The SHAP value is the impact of each player on the target value, essentially establishing the contribution of each input parameter. The results from all analyses are delivered in the paper, together with insights, applications, strengths, and limitations of the methodology.

INTRODUCTION

The prediction of ground support and ground behaviour in underground coalmines is a complex problem involving multiple variables. Due to these complexities multi-variate statistical methods have found widespread application. This has commonly included both multiple linear regression and multiple logistic regression, with the latter finding increased application with increasing number of independent variables (Mark, 2015).

The dependent variable in this study is total roof displacement (mm) as measured on mechanical 'tell-tale' extensometers (devices). The independent variables investigated include roof convergence (displacement in mm), coalmine roof rating (CMRR), depth of cover (m), bolt and cable lengths, support density (PRSUP), horizontal stress direction, roof lithology type, roadway orientation, roadway width and duration (time).

Coalmines are comprised of multiple excavation types that undergo multiple loading conditions. The underlying mechanics driving behaviour vary between and within each situation. To limit variation in the underlying mechanics the population was restricted to only instruments installed in gate roads with standard bord width, and data from the first 90 days post development. By creating this population subset, the loading condition should be confined to tributary area with consistent reorientation of the stress field in all directions.

METHODS

There are seldom examples of the application of machine learning or analysis of tell-tale data to understanding coalmine roof behaviour. One notable study was completed by Giese, Emery and Canbulat (2019), who effectively predicted roof convergence locally at a coalmine using a neural network model in the NeuralTools software. Giese *et al* (2019) did not consider model selection or evaluation however and included <200 case histories while this database included >5000 case histories. Although not involving ML, Corbett, Sheffield and Szwec (2014) incorporated extensometer data into a novel approach for successfully understanding geotechnical risk factors at a mine, though applied limited statistical analysis.

Analyses started with descriptive statistics for understanding the data set combined with Power BI dashboards for visualisation of relationships between variables. This then progressed to multivariate statistics, machine learning (ML) model evaluation, artificial neural network development and finally ANN model evaluation. This paper discusses from ML model evaluation onwards based on prediction of a binary outcome ie classification. The outcomes were categorised as either: $\leq$10 mm; or >10 mm total displacement. Creation of categories is a prerequisite of data sets with non-linear relationships between variables, as there is no continuous scale between them. Classification did however create some issues which needed to be addressed, such as data imbalance, with around 80 per cent belonging to category A ($\leq$10 mm).

Model selection

This section describes the results of analyses with conventional supervised learning ML algorithms (Table 1) in the Scikit-learn library, a Python Application Programming Interface (API). A summary of the supervised learning models in scikit-learn can be found here https://scikit-learn.org/stable/supervised_learning.html. In this case, the ANN appeared most suitable for the displacement prediction. Although, neural networks require higher computational time, it was easily the most suitable and accurate method for predicting displacement. This finding is in line with that generally reported where data volume increases, deep learning tends to outperform conventional ML (Aggarwal, 2018). The results did exhibit some variation and, surprisingly, model accuracy was lowest for the ANN, but it made up for this with improvements in recall, specificity and the F1 score. Overall, the ANN did a better job of defining the two categories, likely due to the complexity of the data set and absence of linear correlations between the input variables.

TABLE 1

ML model evaluation summary

Evaluation metric	Machine Learning Model (scikit-learn library)							
	ANN	Random forest	KNN	Decision tree	Naive bayes	Kernel SVM	SVM	Logistic regr.
Accuracy	74%	81%	79%	78%	75%	81%	80%	80%
Precision	60%	67%	63%	58%	54%	73%	70%	73%
Recall	75%	56%	57%	58%	53%	47%	42%	40%
Specificity	74%	90%	88%	85%	83%	93%	94%	95%
F1 Score	67%	61%	60%	58%	54%	57%	53%	52%

Artificial neural network

This section describes the development of the Artificial Neural Network (ANN) it's component features and the iterative refinement process. All coding was completed in Python using open-source API's including Pandas, Numpy, Tensorflow and Keras. All feature values were converted to numerical values as required in Python. This included creating categories for stress, depth and the angle between the roadway and the major principal stress. A basic ANN framework is illustrated in Figure 1 with each feature representing an input layer, and the output being total displacement. The input and output variables may also be described as the independent and dependent variables.
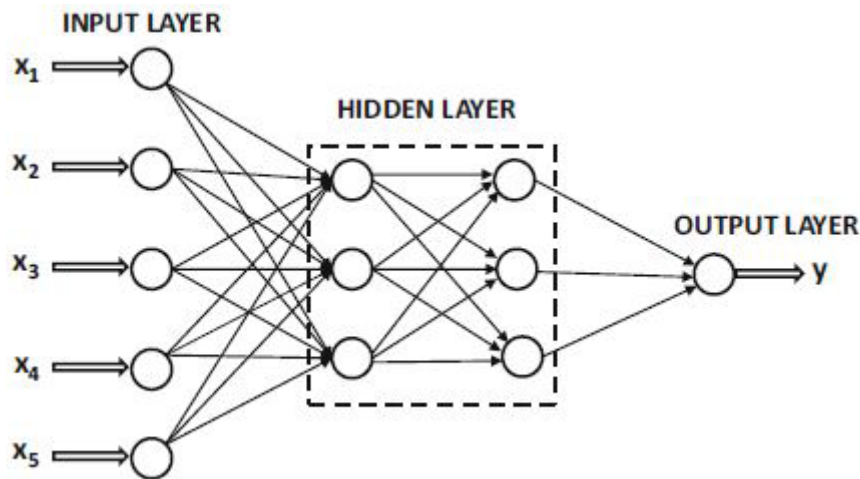
FIG 1 – ANN model layers (Aggarwal, 2018).

The features (or input variables) selected to generate this model have been assumed to be directly influencing the output variable, with the number of features significantly reduced compared to those mentioned in the introduction. These features are listed as follows:

- Roadway Type

- Coalmine Roof Rating (CMRR)

- Primary Roof Support Rating (PRSUP)

- Roof Type (Coal versus Stone)

- Depth (Shallow, Moderate, Deep)

- Roadway Angle to Major Principal Stress (Minor, Moderate, Major)

- Duration in days.

Roadway type includes headings, intersections and cut throughs (cross-cuts). The CMRR is calculated from bore-core with both the CMRR and Ln(CMRR-20) utilised. The PRSUP is derived from the roof support installed off the continuous miner per metre of advance and is a measure of support density. Depth is measured from the surface in metres, with <200 m defined as shallow depth, 200–400 m moderate depth and >400 m defining the deep category. The angle between the roadway and major principal horizontal stress (MPHS) direction is categorised as either minor, moderate, or major according to the divisions in the analysis of horizontal stress in mining method (Mark, 2003). Roadways oriented <30° to the MPHS defines the minor category, 30–60° moderate and >60–90° major.

As mentioned previously with >80 per cent of all data falling in category A, an imbalance existed which may limit model performance. To address this imbalance those mines with <20 per cent of devices in category B were augmented by multiplying existing category B values by 0.98 and adding these into the data set. This resulted in roughly equal amounts of data in each category. Loss and accuracy versus epochs plots during model training exhibited a much tighter trend with the augmented data set indicating improved learning. This was reinforced by a significant improvement in model performance in all confusion matrix parameters.

Optimisation of the learning functions, or hyperparameters, within the augmented model was undertaken. This included changes to the learning rate, epochs, number of hidden layers, units, and activation functions, with two optimisation methods employed. The first method relied on a python library Hyperas, within Keras, and the second a manual iterative process. The manual iterative process significantly outperformed Hyperas. The modifications included an additional hidden layer (from 2 to 3), changed the activation functions to TanH (2) and RELU (1), 128 units per layer, reduced batch size from 128 to 32 and increased epochs from 200 to 750. Model results for the stages described in this section are tabled below. Note that each time a model is run it gives slightly different results, therefore the mean of ten runs for each model is reported.

Shapley additive explanations

This augmented ANN model increased performance to $\geq$80 per cent for all metrics (Table 2). With performance now reasonable the problem of interpretability of the NN model remained. This is a known issue with the more complex or 'less interpretable' ML models (Figure 2). One way to bridge the problem of interpretability is with SHapley Additive exPlanations (https://shap.readthedocs.io/en/latest/index.html), otherwise known as SHAP values (Lundberg and Lee, 2017). SHAP unifies six common additive methods (including LIME and DeepLIFT), with a Game Theoretic approach to determine the influence of each parameter. In game theory each input parameter or feature is a 'player' while the data set is the 'team'. The resultant SHAP value is the impact of each player on the target value, essentially establishing the contribution of each feature to the output.

TABLE 2

ANN model evaluation summary.

Confusion matrix	Model results (%)			
	With duration	Without duration	Non-augmented	Augmented
Accuracy	79.0	80.0	81.0	83.0
Precision	64.55	65.26	61.12	79.47
Recall	59.75	66.87	70.42	84.89
Specificity	86.46	85.31	84.52	80.43
F1 Score	62.0	66.0	65.0	82.0
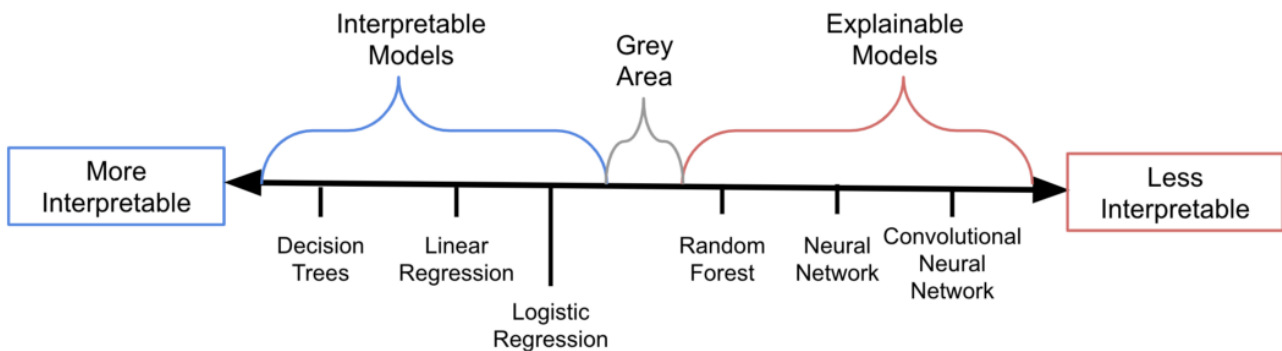
FIG 2 – ML model interpretability (O'Sullivan, 2020).

Multiple model variations were analysed with SHAP. Interpretation of SHAP was based on custom dependency, decision, and bee swarm plots. An example bee swarm plot is illustrated below (Figure 3). Features are ranked in importance from top to bottom on the left Y axis. The SHAP value is plotted on the x axis (positive or negative), while the feature value is shown on the colour scale. In this model Z=depth therefore the pink dots indicate the deepest locations, while the blue dots are shallower. Each of the plot types have their place, though the bee swarm plots proved highly beneficial for insightful model refinement. For example, in Figure 3 duration was noticeably evenly distributed across the range of SHAP values, and ranked second lowest in order of importance, therefore it was removed from the feature set. In the absence of duration (Figure 4), the distributions illustrated more distinct patterns, including higher CMRR associating with lower levels of roof movement (negative SHAP value). A similar pattern was evident with coal roof. While coal roof had the second lowest ranking there is a distinct negative trend between feature values and SHAP values.
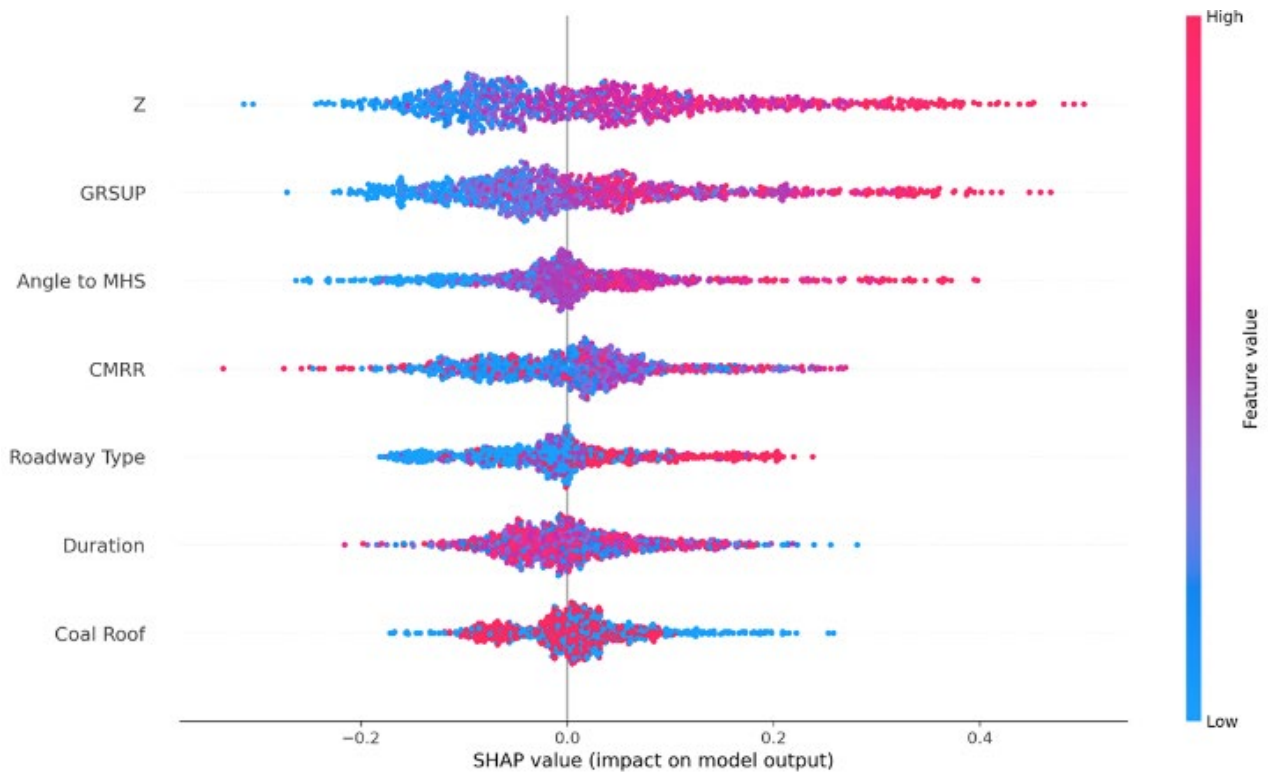
FIG 3 – SHAP bee swarm plot (with duration).
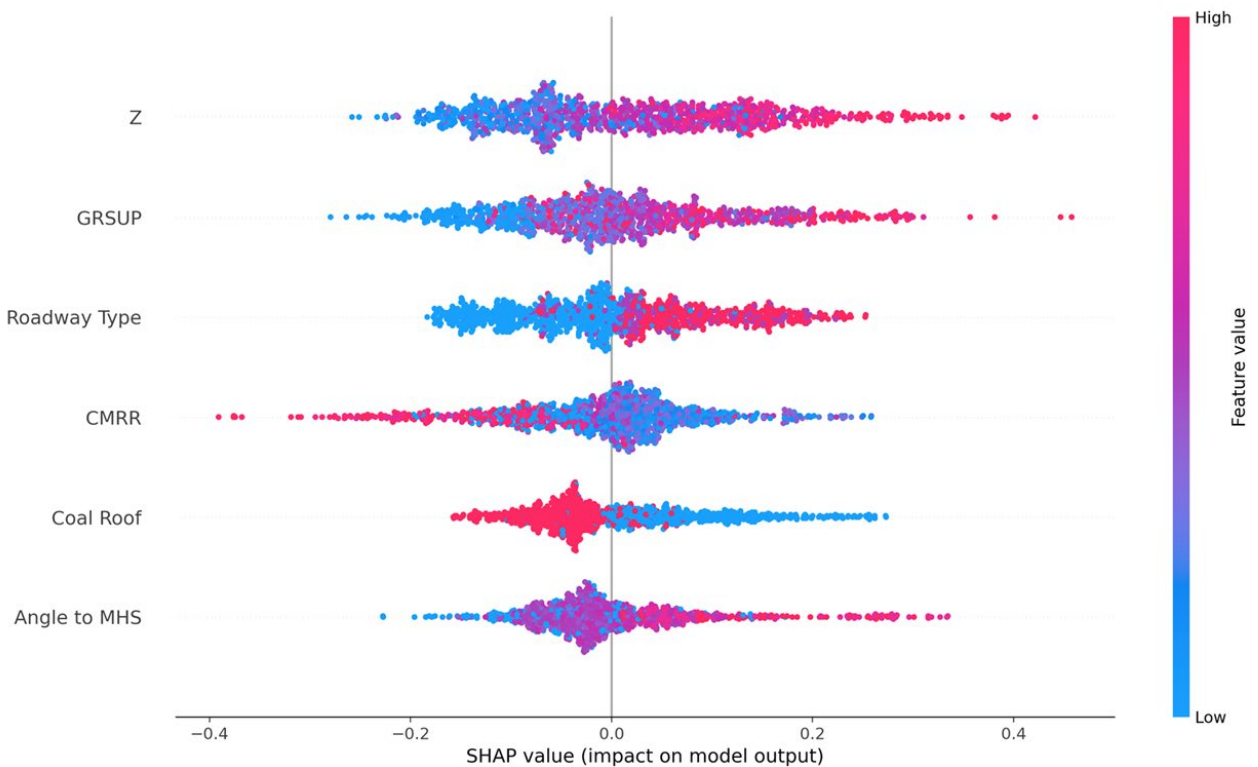
FIG 4 – SHAP bee swarm plot (without duration).

CONCLUSIONS

This paper briefly describes a program of data analytics applied to an industry wide database of roof extensometer data from underground coalmines. The artificial neural network was found to be the most appropriate ML algorithm for predicting the outcome variable (roof movement). A novel method for interpreting the influence of the features within the ANN was applied to the model, namely Shapley Additive Explanations. These SHAP values provided insight into what is otherwise typically

a black box solution, which proved remarkably valuable when combined with the knowledge of the underlying mechanics in each situation. This is an area for further research.

ACKNOWLEDGEMENTS

REFERENCES

Aggarwal, C, 2018. Neural Networks and Deep Learning, Springer Link publishing, Switzerland.

Corbett, P, Sheffield, P and Szwec, M, 2014. A New Tool for Extensometer Data Analysis and Improved Understanding of Geotechnical Risk Factors, *Proceedings of AusRock 2014: Third Australasian Ground Control in Mining Conference*, pp 217–231 (The Australasian Institute of Mining and Metallurgy: Melbourne).

Giese, S, Emery, J and Canbulat, I, 2019. Assessment of development roadway roof conditions at an operating underground coal mine using neural network analysis, *Coal 2019: Coal Operators' Conference*, University of Wollongong & the Australasian Institute of Mining and Metallurgy, 2019, pp 66–81.

Lundberg, S M and Lee, S, 2017. A unified approach to interpreting model predictions, *31st Conference on Neural Information Processing Systems (NIPS, 2017)*, CA, USA.

Mark, C, 2003. Analysis of Horizontal Stress Effects in Mining (AHSM), Pittsburgh, PA: U.S. Department of Health and Human Services, Public Health Service, Centers for Disease Control and Prevention, National Institute for Occupational Safety and Health, 2013 Aug.

Mark, C, 2015. The science of empirical design in mining rock mechanics, *Proceedings of the 34th International Conference on Ground Control in Mining*, Morgantown, West Virginia, pp 225–237.

O'Sullivan, C, 2020. Interpretability in Machine Learning, accessed 22/09/2022, https://towardsdatascience.com/interpretability-in-machine-learning-ab0cf2e66e1.

Data cross validation for a newly commissioned dynamic drop test facility

D W Evans[1]

1. Business Development and Strategic Projects Manager, DSI Underground, Bennetts Green NSW 2290. Email: david.evans@dsiunderground.com

ABSTRACT

Research into the dynamic properties of ground support elements continues to grow at a global level, given the increasing importance of this field of application within underground hard rock mining. Measuring the mechanical response of such elements under the rapid onset of simulated rock burst loads forms the basis for this experimental work, typically utilising gravitational drop testing methods. This field of research is fundamentally driven by an increasing need for dynamic performance data, given the constant evolution of rock bolting product designs, materials selection, combination testing and specific application needs based on ground types and loading scenarios.

A smaller number of globally recognised dynamic test facilities have predominantly lead research within this arena, typically in association with academic institutes, larger industry groups and government research institutes. However, due to the increasing requirement for dynamic performance data, additional facilities have now emerged in order to satisfy the overall demand for test work. These newer facilities are more typically associated with suppliers to the underground hard rock industry, with experimental designs looking to replicate, at least in part, the work of the primary facilities. For standardisation, repeatability and calibration purposes, the cross validation of test data between primary and secondary facilities becomes an obvious and important consideration across this field of research.

This paper outlines the development of a new dynamic drop test facility for testing rock bolts, including the structural design and associated high speed data capture system. Based on the utilisation of identical bolt types, material grades, anchoring systems and decoupled 'free-lengths', comparative data has been generated to provide cross validation of the new test facility against data generated by a globally recognised primary facility. The cross validation of data provides increasing confidence in the repeatability and accuracy of the new facility as activity continues towards the provision of further experimental test work.

INTRODUCTION

The requirement to develop internal capability for the dynamic testing of rock bolt elements has been driven by the increased demand for performance data that is directly related to the mechanical design, anchoring media and geotechnical application of the bolt element. This increasing demand for performance data directly aligns with the need to increase the speed of product development activity for dynamic rock bolt elements – without this critical performance feedback, product development cycles become constrained. Against this background, a project was commenced to develop a test rig design to provide provisional internal capability to test rock bolt elements under dynamic loading conditions.

Alignment with pre-existing test methods was seen as an important consideration in the positioning of this project. Two predominant methods are well documented – known as the 'momentum transfer method' (Villaescusa, Thompson and Player, 2015) and the 'direct impact method' (ASTM, 2008; Li *et al,* 2021). In both methods, the rock bolt specimen to be tested is installed within a test pipe housing, seeking to simulate the conditions of an underground bolt installation. Both methods utilise test masses falling through a pre-determined height to apply dynamic loads under gravitational acceleration and subsequent impact. Given the momentary time frames involved with the test, high speed data capture systems are also used, at varying degrees of complexity, to measure event parameters and ultimately permit energy calculations of the bolts performance.

For the momentum transfer method, the test pipe housing, test beam and test mass are structurally linked and are released as a combined assembly under gravity. The combined assembly falls until the test beam strikes impact buffers, with momentum from the test mass subsequently loading up

the test piece. For the direct impact method, the test pipe housing is held stationary and the test mass, upon release, falls along the length of the test element, striking impact plates attached to the base of the test element. A comprehensive reference for this method is provided by Li *et al* (2021), which details work on calibrating dynamic test rigs between laboratories and encourages effort towards the standardisation of test methods. While it is important to understand that the two test methods exist – and that there are structural differences between the two methods, it is not within the scope of this paper to provide a detailed evaluation of the two methods.

For data cross validation purposes, advantages were seen in aligning the design of the new test unit with the momentum transfer method and to also utilise the 'split pipe' technique. Fundamentally, greater potential existed to cross match test data in common with tests conducted by WASM, an important consideration for the project. Further to this, a new design concept arose that permitted the development of a simplified, flexible and cost-effective test rig, which also aligned with the momentum transfer method. WASM's recognition as a significant testing authority in this field of research further consolidated alignment decisions and this direction was subsequently taken for the project.

The overall goals of the project were to provide a drop test mechanism to enable dynamic loads to be placed onto a bolt specimen; to permit high speed data capture for both force and displacement; to permit captured energy to be calculated; to provide digital analysis and associated reporting of the test; to permit physical inspection of post-test specimens and to provide such facilities at a relatively flexible and low-cost capital solution. The new rig was to permit provisional testing for product development work, while maintaining test work relationships with third party test facilities.

NEW DYNAMIC TEST RIG DESIGN

Structural overview

The design for the new dynamic test rig is shown in Figure 1, with the entire assembly consisting of:

- An external structural frame, predominantly featuring four vertical columns and a base in the form of a circular annulus.

- The steel test pipe, which is grouted internally, cured and then drilled to house the installed rock bolt element. The steel wall of the test pipe is circumferentially cut around the mid-point, defining an upper test pipe and a lower test pipe. This circumferential cut simulates a geotechnical fault or discontinuity, where the mid-portion of the bolt will be subjected to dynamic loads during the test.

- The test mass, connected to the lower test pipe and with its profile guided under a generous clearance within vertical channels attached inside the external frame.

The entire structure is approximately 3.8 m in height, 1.9 m in diameter and weighs 2.1 t, excluding the weight of the test mass. On conducting a test, the entire assembly is raised vertically by the upper lift point to a pre-determined height above a levelled sand bed. The assembly is then released using an electronically triggered quick release mechanism and falls under gravitational acceleration. The annular base of the test frame impacts the sand bed, which buffers and arrests the fall, rapidly decelerating the test frame and upper test pipe. The lower test pipe takes loads under the continued forward momentum of the test mass. These opposed forces from the impact subsequently act at the mid-point discontinuity in the test pipe, bringing dynamic loads directly onto the installed rock bolt.

The structure has been designed to take test loads up to at least 500 kN, notionally 50 t. An FEA analysis was conducted of the structure under static loading scenarios at 500 kN – and the peak deflection of the structure was shown to be of the order 0.7 mm at this load. Rigidity or stiffness of the structure is certainly an important consideration, particularly given the high-speed force oscillations that will occur during dynamic impact. However, this static FEA analysis is a reasonable indicator of the load bearing performance of the test frame structure. It should also be noted that dynamic test loads for typical rock bolting elements are more of the order of 300 kN, so this adds further headroom within this loading and deflection scenario.
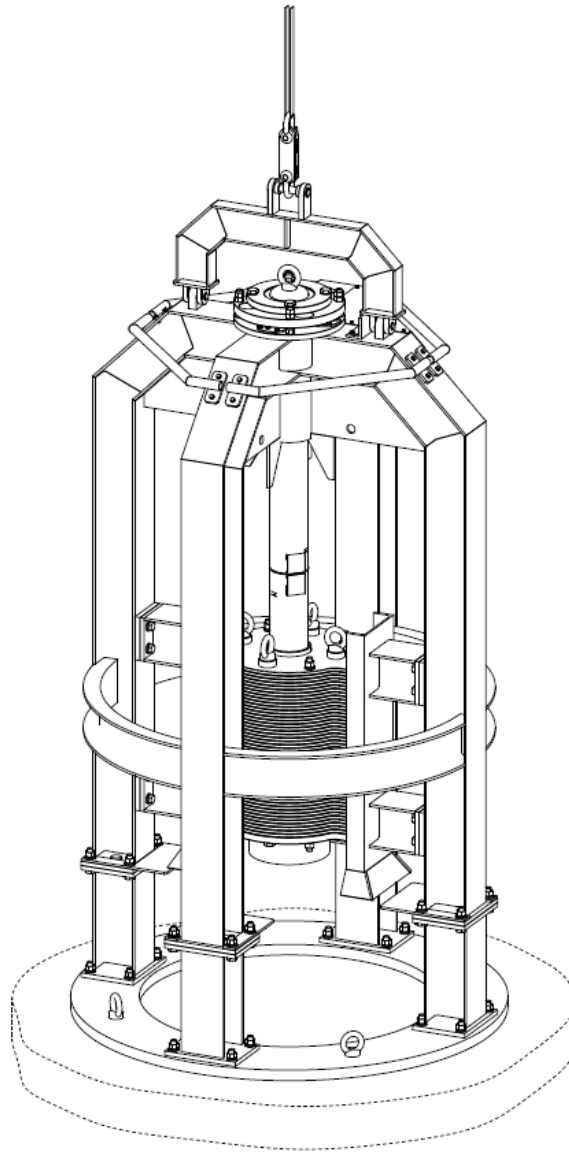
FIG 1 – A perspective view of the newly developed test rig design.

Test mass weight, drop height and impact velocities

The test mass weighs approximately 2003 kg, with the total weight being further amended to include the weight of the lower test pipe assembly. With the test mass being held constant, the selected drop height is used to vary the amount of input energy under gravity. The drop height is measured using a laser distance gauge, accurate to the order of 1 mm. Drop heights typically range between 2.0 m and 3.5 m, meaning that theoretical impact velocities vary between 6.3 ms^{-1} and 8.3 ms^{-1}. While impact velocities subsequently become a secondary variable, it is of worthwhile note that the linearity of test results does not appear to be affected by increasing energy input through increased drop height (refer to the data summary section of this paper).

Test mass total displacement and theoretical energy

The theoretical energy input is determined by the total displacement that the test mass moves through during the test. The total displacement is the sum of the drop height, plus the post-test gap at the test pipe discontinuity, plus the embedment depth of the test frame footing into the sandpit. The theoretical input energy is then simply calculated as E = m × g × h, where:

E = theoretical energy input (J)

m = mass (kg)

g = gravitational acceleartion (ms^{-2})

h = test mass total displacement (m)

High speed measurement, analysis and reporting system

Two primary parameters are measured during the dynamic test event:

1. The force acting on the rock bolt element (kN).

2. The associated displacement at the discontinuity in the pipe (mm).

Both force and displacement are measured in line with event time, recorded to an accuracy of 0.02 milliseconds (msec). Force is measured using a load cell array, which is positioned between the upper part of the test frame and the upper test pipe. Displacement is measured using a high-speed digital camera and image processor, digitally recording two targets that are positioned at the pipe discontinuity – above and below the split. From the test data, a force verses displacement curve is produced – this curve is subsequently utilised to calculate the captured energy (kJ), which equates to the area under the curve, or the integral of force with respect to displacement.

Rates of data capture are at 50 kHz for the load cells and at 7 kHz for the high-speed camera from which displacement measurement is provided. The load cell readings, being captured at higher rates, are then compiled into averaged data packets that meet the frequency of the camera speed – this correctly matches the force versus displacement data relative to the event time.

An example test curve from the new test facility is shown in Figure 2. Upon processing the captured data, two force versus displacement curves are produced – with the first curve showing the raw data set and the second curve charting a smoothed curve derived from the raw data set. The data smoothing 'moving average' is separately adjustable for both the force data set and the displacement data set. The moving average values remain associated against a common event time, before being brought together in a final smoothed force versus displacement curve. A third curve, for cumulative energy, is also produced using the trapezoidal method to progressively calculate the area under the smoothed force versus displacement data curve. The use of the smoothed data set here subsequently provides a slightly conservative calculated energy value. These three test curves are all mapped together, relative to the event time and in sequence with the high-speed video footage. Note that if the displacement reverses at the end of the test due to spring back of the bolt element, the energy calculation ends at the point of the reversal – any further data measurement is subsequently excluded from the energy result.

Force and Cumulative Energy

Bolt Type: 2.4m Posimix, 1.4m Debonding
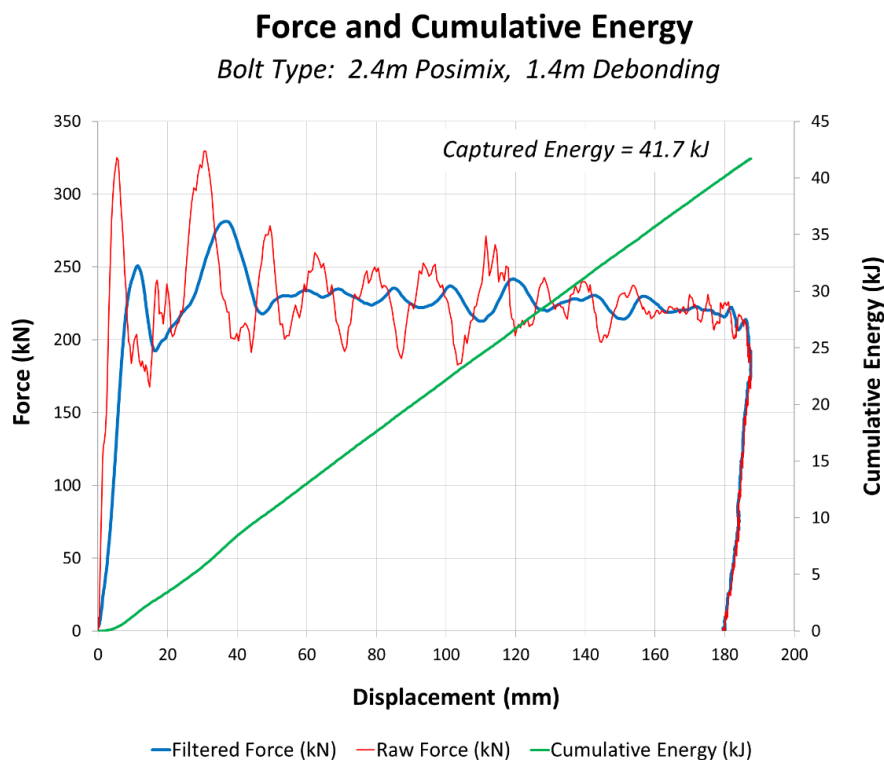
FIG 2 – An example test curve from the new drop test facility.

Energy capture and external losses

The test rig is currently capable of capturing up to 50 kJ of measured energy from the rock bolt element in a single test event. The captured energy from the test is then compared against the theoretical energy input, as a percentage energy capture efficiency. It is known that energy is lost out of the system during the test, in the form of vibration, noise and heat. However, it is highly complex to directly measure these losses and an intentional decision was made to exclude this aspect from the project scope. Of further note, the rock bolt element is typically pre-tensioned during installation into the test pipe, as per a standard underground rock bolt installation. Subsequently, a small portion of the energy capacity of the rock bolt element will be taken up under applied pretension.

Instrument calibration

Calibration checks of the system are conducted to ensure measurement accuracy is maintained. The load cell array is periodically cross-checked using a calibrated universal test machine to apply static compressive loads, ensuring that the load cell outputs remain both linear and accurate across their full rated capacity – within the history of this project there has been no observable drift. It is noted that discussion exists concerning the performance of load cell strain gauge technology versus piezoelectric technology, regarding high-speed signal processing (Li *et al*, 2021; ASTM, 2008). While acknowledging that different perspectives exist concerning this matter (Tacuna Systems, 2022), the strain gauge technology that is employed within the new test rig design appears to provide repeatable high speed data capture. A simple advantage of strain gauge technology is that static loads are witnessed and measured both before and after the dynamic test loads have been captured. Note that during free fall, the mechanical design of the new test rig permits the load cells to return to zero prior to impact.

The accuracy of displacement measurements from the high-speed video camera are of equal importance. The video system will capture around 1400 individual still images through the course of a typical test. In post event data processing, digital recognition software is used to identify the two displacement targets in each image, then further locate calibrated measurements that are embedded within the targets and use these calibrated measurements to determine the axial distance between the two targets. This digital recognition process is repeated in turn, image by image – identify, calibrate and measure – so that no single image can fall out of calibration and return an incorrect result. This digital recognition technique also negates any concerns with offset movement, bounce or vibration during the test, as every displacement measurement is based on a calibrated still image. The results returned via this digital method provide very fluid displacement versus time curves, a further indication of repeatability and accuracy.

Deceleration on impact (buffering)

The sand pit is used as the method of deceleration of the test frame on impact. While this may initially be perceived as a rudimentary method, a number of considerations are taken into account to ensure repeatability and adequate buffering response. The condition of the sand is kept dry and clean from any form of contaminant to ensure that the sand properties remain consistent and homogenous. The sand is also maintained to a constant depth within the pit and is levelled prior to every test – which further provides a levelled reference point from which to measure the drop height. The geometric shape and surface area of the base of the test frame is never modified or adjusted, so that immediate contact pressures between the frame footing and the sand buffer are consistent. Following each test, embedment depths of the frame footing into the sand are also measured to provide a physical check of repeatability, relative to the drop height.

While buffering pressures through the sand are not directly measurable, the associated response from the high-speed test data is readily captured and measured. The primary measurement relating to buffering performance is the time duration (msec), taken from the initial impact or onset of load, through to the first peak in force (kN) – and is measured from the force versus time test data. From test curves given in Li *et al* (2021), the time to first peak force is shown to be in the order of 5–10 msec. By comparison, the new rig and sand buffer has generated time to first peak values in the order of 4–9 msec. While methods and bolt types differ, the time to the first peak in force falls within a similar range. Based on the physical conditions that are maintained within the sand buffer, as well

as test data from the time to first peak in force, there is strong indication that the sand pit provides a suitable buffering response and time-based onset of load.

Rock bolt element mechanical response

A further reference measurement is the initial gradient (kN/mm) to the first peak in the force versus displacement test curve. This is an indicator of the stiffness of response of the bolt sample – and has been designated as the value 'K' (Li *et al,* 2021). K values are influenced by both the bolt type and installation conditions – for example, the embedment media used, applied pre-tension and any mechanical take up in the installation. Higher K values indicate a stiffer response or an increased onset of load with respect to displacement. Li *et al* (2021) report K values in the order of 11.4 to 22.0 MN/m across four different test rigs, using the same bar type and with each rig using the direct impact method. By comparison, the new drop test method into the sand buffer has returned K values in the order of 13.2 to 53.2 kN/mm, across a number of different rock bolt types. Note that MN/m as a unit of measurement directly equates to values reported in kN/mm. A comparison of reported K values across test rigs provides a good indication that the stiffness of onset of load provided by the sand buffer induces a mechanical response in the rock bolt element of a similar order.

DYNAMIC TEST RESULTS

Test work overview

Using the new test rig design, a substantive series of test work was conducted across three different rock bolt types:

1. A solid bolt design (*Dynamic Posimix*), installed using a polyester resin cartridge as the encapsulation media. The solid bolt was 2.4 m in length and had a 1.4 m long debonding tube. Five tests were conducted of this bolt design.

2. A hollow bolt design (*Dynamic SDA*), installed using a pumpable urea silicate resin as the encapsulation media. The hollow bolt was 2.4 m in length and had a 1.0 m long decoupled region. Six tests were conducted of this same bolt design.

3. A mechanical point anchored friction bolt (*Kinloc Indie*), with no encapsulation media. The point anchored friction bolt was 2.4 m in length. Twenty tests were conducted of this bolt design.

Being for internal test work purposes, the bolts were all supplied by DSI Underground Australia. Across all three product types, 31 tests were conducted in total. Note that it is not the intent of this paper to provide a detailed analysis of each individual bolt type, but to focus on the overall data summary associated with the performance of the new test rig.

Data summary – internal test work

Results from the 31 tests were graphically compiled into a summary chart, provided in Figure 3. This chart shows the relationship between the captured dynamic energy (kJ) of the rock bolt, relative to the peak displacement (mm) measured at the pipe discontinuity during the dynamic event. Subsequently, each individual test is represented as a single data point on this summary chart. The three different bolt types are denoted as different data series, overlayed together, as indicated in the chart legend. 'Stable' results are classified as tests where there was no failure or rupture of the bolt element or dislodgement of the anchoring system. The two 'bar rupture' results are classified as tests where the bolt installation anchored and loaded to the point of fracture of the steel bolt element – and in this instance, the captured energy and displacements are measured right at the point of bar rupture. Note that the captured energy is the energy measured by the high-speed data capture system – it is not simply the theoretical gravitational energy from the drop height.

A linear regression analysis was conducted across all 31 tests, returning an R^2 value of 93.89 per cent. This indicates a very strong statistical relationship between the individual test points and the calculated line of best fit – and fundamentally expresses a very strong linear trend in the test results. While this data set incorporates three different bolt types, it is of note that the steel grades used within these bolt types are each of similar base mechanical properties. In order to produce a linear trend of this nature, the instrumentation involved must return both repeatable and accurate

values. If force and displacement measurements are unreliable, this will produce a greater scatter and misalignment between comparison data. Subsequently, the data set indicates high levels of repeatability in both the bolt type, as well as the measurement capability of the new dynamic test rig design, providing high confidence in the measured results.

Dynamic Test Summary
(Compiled from DSI Underground Test Rig Data)

No. Tests = 31

$y = 0.2096x + 3.9716$
$R^2 = 0.9389$

Orange = Bar Rupture**

Blue & Green = Stable Test*

* Blue & Green results show the dynamic energy contained by the bolt, with a stable test outcome.

** Orange results show dynamic energy and displacement at the point of rupture of the internal bar.

Dynamic Energy (kJ) (y-axis)

Peak Displacement (mm) (x-axis)

▲ 2.4m Posimix
No. Tests = 5

● 2.4m Kinloc Indie
No. Tests = 20

◆ 2.4m Dynamic SDA
No. Tests = 6

FIG 3 – Summary of results from the newly developed test rig.

Corresponding WASM results

Dynamic test work for two rock bolt designs is held in common with WASM. The first is the solid bolt design referenced above (*Dynamic Posimix*), having a 2.4 m length, a 1.4 m debonding tube and anchored with a polyester resin cartridge, with three tests in total conducted by WASM of this specific bolt format. The second is the mechanical point anchored friction bolt (*Kinloc Indie*), having a 2.4 m length, with five tests in total being conducted by WASM of this specific bolt format. All rock bolt parameters are identical between the internal test program and WASM's test work, to ensure that the cross correlation of data provides a true and direct comparison.

Results from the eight WASM dynamic tests are compiled into a summary chart provided in Figure 4. This chart shows the relationship between the captured dynamic energy (kJ) of the rock bolt, relative to the peak displacement (mm) measured during the dynamic event, with each individual test being represented as a single data point on the chart. A linear regression analysis was conducted across the eight tests, returning an R^2 value of 87.11 per cent. While this is a smaller data set by comparison, the WASM data still exhibits a strong statistical relationship between the individual test points and the calculated line of best fit.

Dynamic Test Summary

(Compiled from WASM Data)

No. Tests = 8

$y = 0.2154x + 1.1615$
$R^2 = 0.8711$

Orange = Bar Rupture**

Brown & Purple = Stable Test*

* Brown & Purple results show the dynamic energy contained by the bolt, with a stable test outcome.

** Orange results show dynamic energy and displacement at the point of rupture of the internal bar.

△ 2.4m Posimix
No. Tests = 3

O 2.4m Kinloc Indie
No. Tests = 5
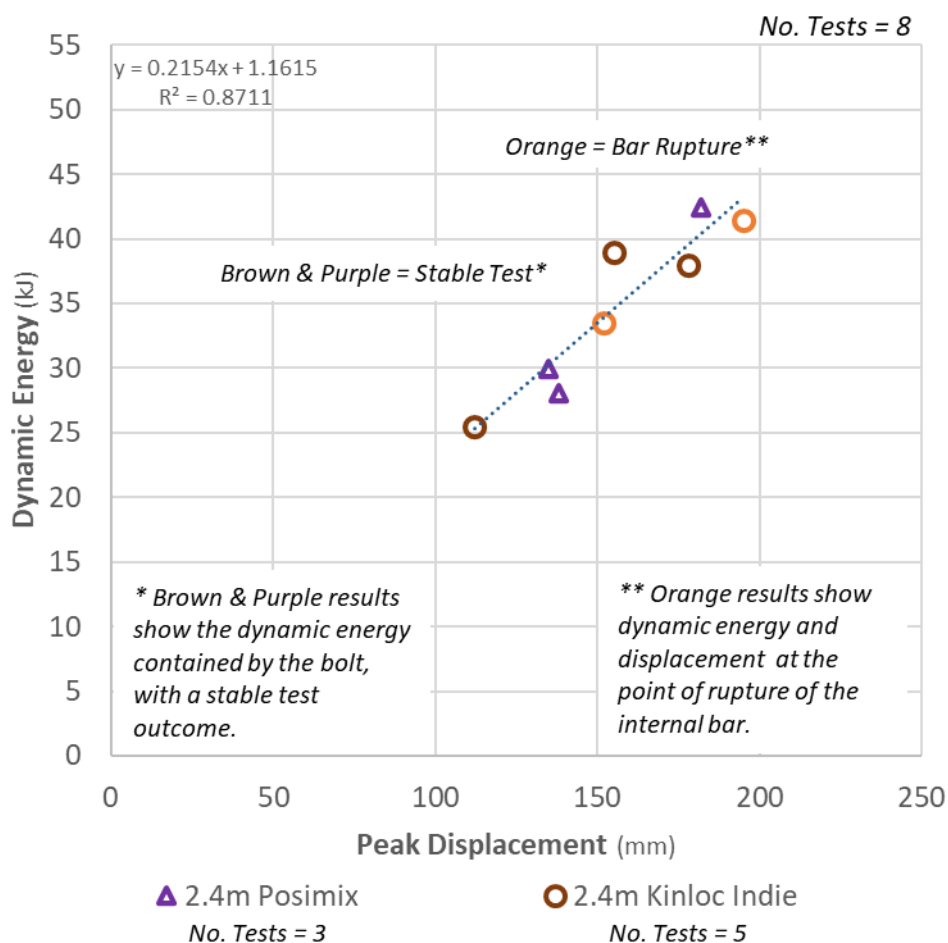
FIG 4 – Summary of corresponding results from WASM.

Data correlation – internal test results and WASM

Where a test comparison existed for identical bolt types, specifically for 2.4 m Posimix and 2.4 m Kinloc Indie, 25 dynamic test results from the internal test program were overlayed with eight dynamic test results from WASM testing – these are compiled into a final summary shown in Figure 5, with each of the 33 individual tests being represented as a single data point on this chart. A linear regression analysis was conducted across all 33 tests, returning an R^2 value of 93.13 per cent. While the internal test program represents the greater portion of the data set influencing the R^2 value, the WASM data remains statistically significant in this combined analysis. Within this context, the WASM test results correlate well with the internal test work – and a clear linear relationship is visibly shown between the two data sets.

Dynamic Test Summary
(Combined Overlay of DSI & WASM Data)

No. Tests (25 + 8) = 33

$y = 0.2105x + 3.2472$
$R^2 = 0.9313$

Orange = Bar Rupture**

Brown, Purple & Blue = Stable Test*

* Brown, Purple & Blue results show the dynamic energy contained by the bolt, with a stable test outcome.

** Orange results show dynamic energy and displacement at the point of rupture of the internal bar.

Dynamic Energy (kJ) — Peak Displacement (mm)

DSI Test Data
▲ 2.4m Posimix (n=5)
● 2.4m Kinloc Indie (n=20)

WASM Test Data
△ 2.4m Posimix (n=3)
○ 2.4m Kinloc Indie (n=5)
○

FIG 5 – Combined overlay of data from new test rig and WASM.

CONCLUSION

Across 31 tests and three different rock bolt designs, a statistical analysis of results strongly indicates that the new dynamic test rig design provides a highly repeatable method for the dynamic testing of rock bolts. Further to this, cross correlation of test data against an external source, conducted using eight available WASM data points associated with two of these rock bolt designs, provides a strong indicator of the accuracy of the new high-speed data capture system – for both force and displacement measurement, as well as final energy calculation methods. Subsequently, the new test rig design is increasingly seen to provide a valid method for provisional in-house dynamic testing of rock bolts, working in line with the methods of WASM, a globally recognised dynamic test facility.

REFERENCES

ASTM, 2008. D7401–08 – Standard test methods for laboratory determination of rock anchor capacities by pull and drop tests, February 2008.

Li, C C, Hadjigeorgiou, J, Mikula, P, Know, G, Darlington, B, Royer, R, Pytlik, A and Hosp, M, 2021. Performance of identical rockbolts tested on four dynamic testing rigs employing the direct impact method, *Journal of Rock Mechanics and Geotechnical Engineering*.

Tacuna Systems, 2022. Comparing Strain Gauges to Piezoelectric Sensors. 21 April, 2022. Available from: https://tacunasystems.com/knowledge-base/comparing-strain-gauges-to-piezoelectric-sensors/ [Accessed: 17 June 2022].

Villaescusa, E, Thompson, A and Player, J, 2015. *Dynamic testing of Ground Support Systems*. Perth: MERIWA.

Algebraic optimisation of excavation alignment using the stress tensor

P B Hills[1]

1. Senior Principal Geotechnical Engineer, Pitt & Sherry Operations, Hobart Tas 7000.
   Email: phills@pittsh.com.au

ABSTRACT

A simple algebraic method of aligning large scale underground excavations such as a crusher station or workshop or indeed any large cavern or mine layout to the optimal stress condition is outlined. The method uses the stress transformation law to determine how the component stresses vary as the stress tensor is rotated around its axis. The aim is to define the orientations at which the maximum and minimum horizontal stresses occur such that the excavation can be aligned with its long axis paralleling the trend of the maximum horizontal stress leading to the minimum potential for overstressing of the side walls.

The physical environment in which the stress field is acting is unchanged. At the design location, the trend and plunge of the major principal stress is unchanged. However, the coordinate system by which the location of the stress field is described is arbitrary and the stress transformation law allows that coordinate system to be rotated to a more convenient orientation and for the component stresses to be calculated within the alterative coordinate system. The stress field is typically described in terms of normal and shear stresses aligned to a north–south, east–west, vertical, coordinate system. In this scenario, there are two orientations in the 360° horizontal plane defined by the coordinate system where the horizontal normal stresses are equal, and at 45° to those orientations, two orientations where they diverge to the maximum extent. Those orientations of maximum divergence correspond to the trend of the maximum and minimum horizontal stresses, usually designated σ_H and σ_h, and that is what the algebraic manipulation seeks to determine.

This technique is a first pass assessment which relies on a knowledge of the full stress tensor. It is not a replacement for numerical modelling or detailed design, but a tool to guide planning.

THE STRESS TENSOR

The concept of stress acting at a point in the rock mass, and the components of the stress tensor are described in most fundamental geomechanics textbooks and reference papers relating to rock stress (eg Amadei and Stephansson, 1997; Hudson, Cornet and Christiansson, 2003; Brady and Brown, 2005). It is not the intention of this paper to reiterate those descriptions, but rather to outline how the components of the stress tensor can be manipulated algebraically to determine an optimum stress condition for a large underground opening. None-the-less, a summary is illustrative.

The cartoon in Figure 1a illustrates the components of the stress tensor and the standard nomenclature for those components. For convenience, the point at which the stress is acting is considered to be an infinitesimally small cube orientated within a mutually orthogonal coordinate system x, y, z, at which normal stresses σ_{xx}, σ_{yy} and σ_{zz} act perpendicular to the faces of the cube and shear stresses τ_{xy}, τ_{yx}, τ_{yz}, τ_{zy}, τ_{xz} and τ_{zx} act parallel to the faces of the cube. The stress tensor is then written in matrix form as:

$$\begin{bmatrix} \sigma_{xx} & \tau_{xy} & \tau_{zx} \\ \tau_{yx} & \sigma_{yy} & \tau_{yz} \\ \tau_{xz} & \tau_{zy} & \sigma_{zz} \end{bmatrix} \tag{1}$$

The shear components are complimentary in that $\tau_{xy} = \tau_{yx}$, $\tau_{yz} = \tau_{zy}$ and $\tau_{xz} = \tau_{zx}$. The stress tensor can be rotated in three-dimensional (3D) space and at a single 3D orientation the shear stresses cancel to zero. That is, $\tau_{xy} = \tau_{yx} = \tau_{yz} = \tau_{zy} = \tau_{xz} = \tau_{zx} = 0$. The normal stresses at that point are the principal stresses, and by definition σ_{xx} is the largest principal stress denoted σ_1, σ_{zz} is the smallest principal stress denoted σ_3, and acts perpendicular to σ_1, and σ_{yy} is the intermediate principal stress denoted σ_2, and acts perpendicular to both σ_1 and σ_3, it is not the arithmetic mean of the values of σ_1 and σ_3. At that orientation, the matrix can be written:

$$\begin{bmatrix} \sigma_1 & 0 & 0 \\ 0 & \sigma_2 & 0 \\ 0 & 0 & \sigma_3 \end{bmatrix} \qquad (2)$$

The special case of the principal stress is illustrated in Figure 1b.

FIG 1 – Cartoons illustrating the stress components at a point (a) and the special case of the principal stresses (b). After Hudson, Cornet and Christiansson (2003).

CARTESIAN COORDINATE SYSTEM

The notation for the stress tensor is arbitrary. To make use of it, it is converted into a cartesian coordinate system assigning directions *xx*, *yy* and *zz* to north–south, east–west and vertical, such that:

$$\begin{bmatrix} \sigma_{xx} & \tau_{xy} & \tau_{zx} \\ \tau_{yx} & \sigma_{yy} & \tau_{yz} \\ \tau_{xz} & \tau_{zy} & \sigma_{zz} \end{bmatrix} = \begin{bmatrix} \sigma_{NS} & \tau_{NS-EW} & \tau_{V-NS} \\ \tau_{EW-NS} & \sigma_{EW} & \tau_{EW-V} \\ \tau_{NS-V} & \tau_{V-EW} & \sigma_V \end{bmatrix} \qquad (3)$$

Each of the principal stresses may also be described in terms of magnitude in units of megapascals (MPa) and direction as trend and plunge in the units of degrees (°). This in total is the data that is typically provided to the geotechnical engineer when a stress measurement is undertaken. In Australia, at relatively shallow depth, the major and intermediate principal stresses are generally in or close to the horizontal plane with the minor principal stress close to vertical (*cf* stress orientations at extreme depth in South Africa). However, that is not always the case due to secondary influences such as geological structure, topography, or even pre-existing underground excavations. Table 1 presents an anonymous but real data example which will be manipulated throughout the paper. This data set was specifically chosen because, as a result of topography, all principal stresses have a moderate plunge, and therefore the orientations of σ_H and σ_h aren't immediately apparent.

TABLE 1
Stress measurement data.

σ_1			σ_2			σ_3		
Magnitude (MPa)	Trend (°)	Plunge (°)	Magnitude (MPa)	Trend (°)	Plunge (°)	Magnitude (MPa)	Trend (°)	Plunge (°)
34.58	274.53	49.04	30.92	144.05	29.40	22.08	038.28	25.74

σ_{NS} (MPa)	σ_{EW} (MPa)	σ_V (MPa)	τ_{NS-EW} (MPa)	τ_{EW-V} (MPa)	τ_{V-NS} (MPa)
26.51	29.73	31.34	-3.61	-3.95	-2.57

THE FAVOURABLE STRESS CONDITION

Leeman (1964) made the observation that 'it is possible to obtain qualitative information about the stresses in rock from observations of the fracturing of the sidewalls of horizontal and near-horizontal boreholes'. The breakout he observed occurred on opposite sides of a horizontal borehole due to compression normal to the direction of the breakout.

The phenomenon has since been used to determine the orientation and relative magnitude of horizontal stresses around vertical boreholes and is widely discussed in the literature (eg Read and Martin, 1996; Amadei and Stephansson, 1997). It is also fundamental to two-dimensional (2D) stress measurement using the hydraulic fracture technique. Typically, stresses signified σ_H and σ_h represent the maximum and minimum horizontal stresses acting on the borehole normal to one another. Although there are other factors at play, including rock strength and fabric, joint patterns and structure, the more deviatoric the magnitude of the stresses σ_H and σ_h, the greater the depth of breakout that can be expected.

Reflecting on these observations it is clear that the orientation of the proposed excavation is a key parameter in determining the impact that the stress regime will have upon it. This is the case irrespective of the magnitude of the stresses involved. It has been found that when large excavations are oriented parallel to the maximum horizontal stress, σ_H, and the minimum horizontal stress, σ_h, is perpendicular to the longwalls of the excavation, the degree of over-stressing in the walls is minimised. Therefore, the degree of potential spall is minimised. An early investigation of this phenomenon was summarised by Haimson, Lee and Huang (1986) who observed from experience that 'properly oriented tunnels in a high horizontal (stress) field are typically self-supporting'. The focus of those authors was the development of a hydroelectric cavern. Their modelling clearly demonstrated lesser over-stressing of the cavern walls when its long access was aligned to σ_H (Figure 2). Consequently, the focus of the remainder of their paper was the determination of the orientation and magnitude of σ_H and σ_h from the measured stress tensor.
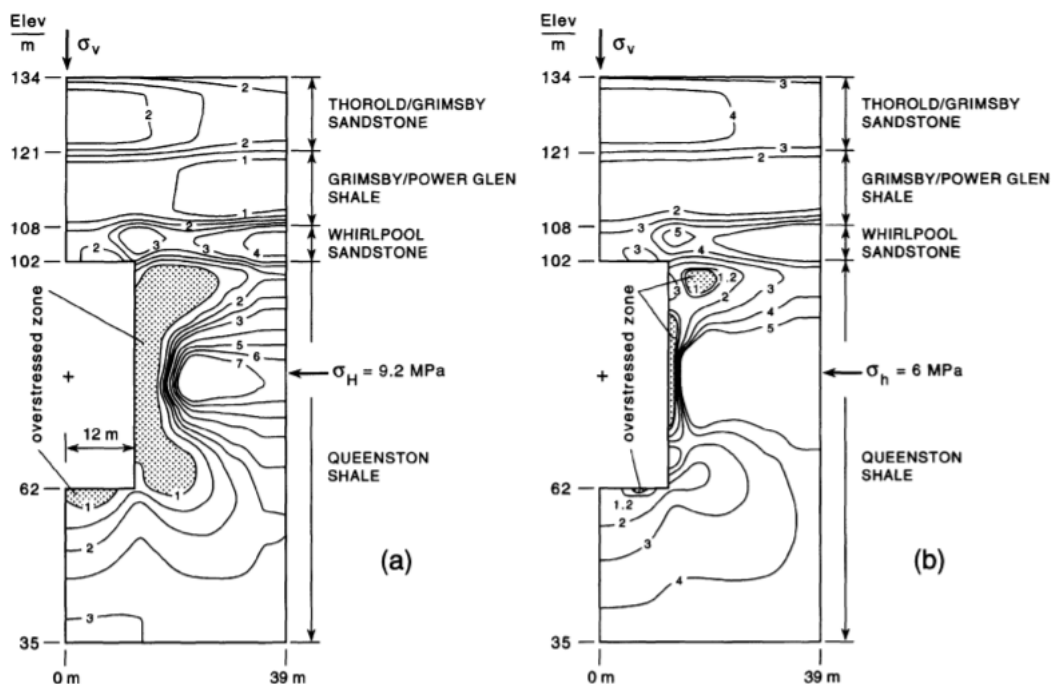
FIG 2 – Stress modelling illustrating the degree of over-stressing in the walls of a cavern with the long axis aligned to σ_h (a) or σ_H (b). After Haimson, Lee and Huang (1986) as reproduced by Amadei and Stephansson (1997).

STRESS TRANSFORMATION LAW

The stress transformation law describes the rotation of the coordinate system x, y, z, informing the stress tensor, to a new coordinate system x', y', z'. As described by Amadei and Stephansson (1997) and Brady and Brown (2005), the transformation matrix $[A]$ comprises direction cosines derived from

the rotation about point P between the two coordinate systems being considered through angles β and δ for which the trend and plunge of the principal stresses is unknown. However, [A] can also be defined from the trend and plunge of the principal stresses in the original coordinate system when the trend and plunge of the stresses in the revised coordinate system are known and it is the magnitude of the component stresses that is sought. Priest (1985) provides an explanation for the applicable case using the vector algebra method for decomposition of a force. In the case being illustrated, the trends and plunges are 00/000, 00/090 and 90/000 corresponding to σ_{NS}, σ_{EW} and σ_V respectively and the form of the direction cosines reflects this. Both scenarios, showing the known data in each case, are illustrated in Figure 3.
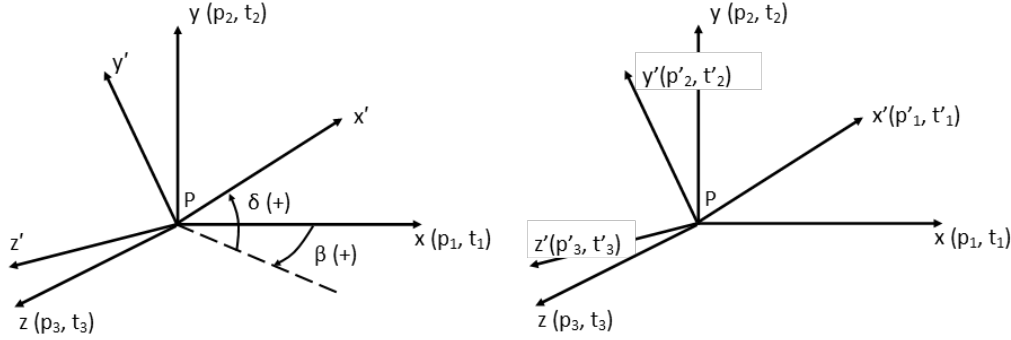
FIG 3 – Transformation between two coordinate systems were the angles of rotation are known (L) and where the trends and plunges in the new coordinate system are known (R).

The transformation which forms the crux of the analysis performed below is as follows:

$$[A] \times \begin{bmatrix} \sigma_x & \tau_{xy} & \tau_{zx} \\ \tau_{yx} & \sigma_y & \tau_{yz} \\ \tau_{xz} & \tau_{zy} & \sigma_z \end{bmatrix} \times [A]^{-1} = \begin{bmatrix} \sigma_{x'} & \tau_{x'y'} & \tau_{x'z'} \\ \tau_{y'x'} & \sigma_{y'} & \tau_{y'z'} \\ \tau_{z'x'} & \tau_{z'y'} & \sigma_{z'} \end{bmatrix} \tag{4}$$

and in the case being considered,

$$[A] = \begin{bmatrix} \cos p_1 \times \cos t_1 & \cos p_1 \times \sin t_1 & \sin p_1 \\ \cos p_2 \times \cos t_2 & \cos p_2 \times \sin t_2 & \sin p_2 \\ \cos p_3 \times \cos t_3 & \cos p_3 \times \sin t_3 & \sin p_3 \end{bmatrix} \tag{5}$$

and

$$[A]^{-1} = \begin{bmatrix} \cos p_1 \times \cos t_1 & \cos p_2 \times \cos t_2 & \cos p_3 \times \cos t_3 \\ \cos p_1 \times \sin t_1 & \cos p_2 \times \sin t_2 & \cos p_3 \times \sin t_3 \\ \sin p_1 & \sin p_2 & \sin p_3 \end{bmatrix} \tag{6}$$

ORIENTING THE UNDERGROUND EXCAVATION

From the original stress measurement, the orientation and magnitude of two perpendicular horizontal stresses, σ_{NS} and σ_{EW}, are already known. What is not known is whether the magnitudes of σ_{NS} and σ_{EW} as measured are the maximum and minimum horizontal stresses. As a matter of probability, they usually aren't. However, it is possible to incrementally adjust the trend of the principal stresses and recalculate σ_{NS} and σ_{EW}, allowing them to act as a proxy for σ_H and σ_h.

The methodology involves incrementally rotating the trend of principal stresses, at the magnitude and plunge determined by the stress measurement, through 360°. This is done by adding (say) 15° increments to the trend of each of the principal stresses and redetermining the component stresses at each increment using the stress transformation law. When this is done, σ_{NS} and σ_{EW} will vary progressively while σ_V will remain constant. Ensuring that the transformation remains valid can be ascertained using the three stress invariants I_1, I_2 and I_3 which are defined as follows:

$$I_1 = \sigma_{xx} + \sigma_{yy} + \sigma_{zz} = 87.58 \tag{7}$$

$$I_2 = \sigma_{yy}\sigma_{zz} + \sigma_{xx}\sigma_{zz} + \sigma_{xx}\sigma_{yy} - \tau_{yz}^2 - \tau_{xz}^2 - \tau_{xy}^2 = 2515.46 \tag{8}$$

$$I_3 = \sigma_{xx}\sigma_{yy}\sigma_{zz} + 2\tau_{yz}\tau_{xz}\tau_{xy} - \left(\sigma_{xx}\tau_{yz}^2 + \sigma_{yy}\tau_{xz}^2 + \sigma_{zz}\tau_{xy}^2\right) = 23608.67 \tag{9}$$

and must be satisfied at each step.

Taking the data from Table 1, the principal stress matrix is:

$$\begin{bmatrix} 34.58 & 0 & 0 \\ 0 & 30.92 & 0 \\ 0 & 0 & 22.08 \end{bmatrix} \tag{10}$$

and the component stress matrix is:

$$\begin{bmatrix} 26.51 & -3.61 & -2.57 \\ -3.61 & 29.73 & -3.95 \\ -2.57 & -3.95 & 31.34 \end{bmatrix}. \tag{11}$$

Working in an Excel spreadsheet, the trend and plunge of the principal stresses from Table 1 are converted to radians and entered into Equation 5 as follows. In the following example, the original stress tensor is regenerated algebraically.

The rotation matrix is:

$$\begin{bmatrix} (\cos(0.86) \times (\cos(4.79)) & (\cos(0.86)) \times (\sin(4.79)) & (\sin(0.86)) \\ (\cos(0.51)) \times (\cos(2.51)) & (\cos(0.51)) \times (\sin(2.51)) & (\sin(0.51)) \\ (\cos(0.45)) \times (\cos(0.69)) & (\cos(0.45)) \times (\sin(0.69)) & (\sin(0.45)) \end{bmatrix}$$

$$= \begin{bmatrix} 0.05 & -0.65 & 0.76 \\ -0.71 & 0.51 & 0.49 \\ 0.71 & 0.56 & 0.43 \end{bmatrix} \tag{12}$$

then the transposed rotation matrix is:

$$\begin{bmatrix} 0.05 & -0.71 & 0.71 \\ -0.65 & 0.51 & 0.56 \\ 0.76 & 0.49 & 0.43 \end{bmatrix} \tag{13}$$

and the stress transformation, ((10) × (12)) × (13) is:

$$\begin{bmatrix} \mathbf{26.51} & -3.61 & -2.57 \\ -3.61 & \mathbf{29.73} & -3.95 \\ -2.57 & -3.95 & 31.34 \end{bmatrix}. \tag{14}$$

This step provides a demonstration that the algebra is correct. That is, Equation 14 is equivalent to Equation 11. The key values in Equation 14, σ_{NS} and σ_{EW}, are highlighted in bold text. Whereas the calculations can be undertaken by any suitable means, they are most easily undertaken by writing the transposition equations into a spreadsheet, particularly so, as the calculations are sensitive to rounding errors; a spreadsheet to undertake the calculations is included in the Appendix.

It is then a matter of rotating the trend of the principal stresses incrementally through 360°, recalculating values for σ_{NS} and σ_{EW}, by repeating the above calculations and substituting those values in Equations 12 and 13. An increment of 15° is recommended. As an example, at 289.53°, the trend of each principal stress has been increased by 15°, such that the principal stresses are as defined in Table 2. Take note that the magnitude and plunge of the principal stresses remain unchanged.

TABLE 2
Example of rotated principal stresses.

	σ_1			σ_2			σ_3	
Magnitude (MPa)	Trend (°)	Plunge (°)	Magnitude (MPa)	Trend (°)	Plunge (°)	Magnitude (MPa)	Trend (°)	Plunge (°)
34.58	**289.53**	289.53	30.92	**159.05**	159.05	22.08	**053.28**	053.28

The stress tensor matrix at the revised orientation after performing the transformation analysis is:

$$\begin{bmatrix} \mathbf{28.53} & -3.93 & -1.46 \\ -3.93 & \mathbf{27.71} & -4.48 \\ -1.46 & -4.48 & 31.34 \end{bmatrix} \tag{15}$$

Because the rotation has only occurred in the horizontal plane, σ_v remains unchanged and the stress invariants remain unchanged at 87.58, 2515.46 and 23 608.67, even though all the components of the stress tensor with the exception of σ_v have changed.

The progressive results for σ_{NS} and σ_{EW} when the trend of the principal stresses is rotated at increments of 15° commencing from a revised trend of 285° are listed in Table 3.

TABLE 3

Recalculated values for σ_{NS} and σ_{EW}.

Trend	σ_{NS}	σ_{EW}	Trend	σ_{NS}	σ_{EW}
274.53	26.51	29.73	94.53	26.51	29.73
289.53	28.53	27.71	109.53	28.53	27.71
304.53	30.44	25.8	124.53	30.44	25.8
319.53	31.73	24.51	139.53	31.73	24.51
334.53	32.05	24.19	154.53	32.05	24.19
349.53	31.32	24.92	169.53	31.32	24.92
4.53	29.73	26.51	184.53	29.73	26.51
19.53	27.71	28.53	199.53	27.71	28.53
34.53	25.8	30.44	214.53	25.8	30.44
49.53	24.51	31.73	229.53	24.51	31.73
64.53	24.19	32.05	244.53	24.19	32.05
79.53	24.92	31.32	259.53	24.92	31.32

The recalculated values for σ_{NS} and σ_{EW} are each plotted against the rotated trend of σ_1 forming an out of phase sinusoidal pattern as illustrated in Figure 4. Every 90°, one or other parameter will be at the maximum magnitude while the other is at the minimum. Between those points, the two parameters will be equal. The critical orientations are listed in Table 4.
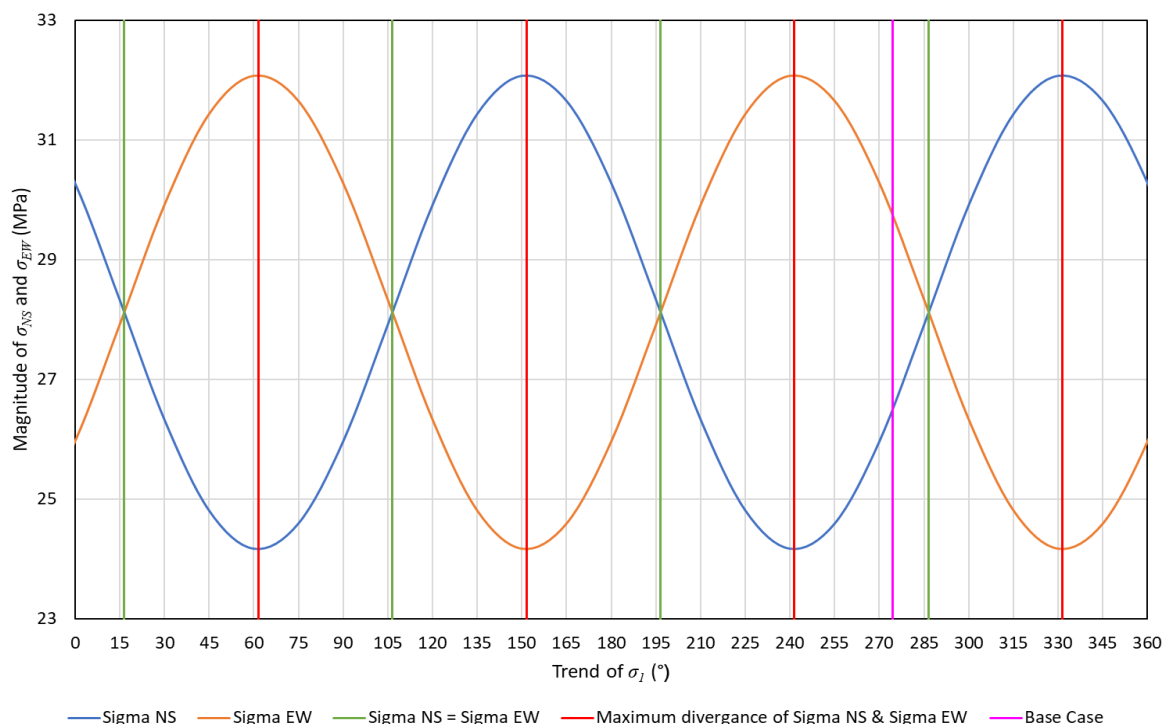
FIG 4 – Sinusoidal plot of σ_{NS} and σ_{EW} around 360°.

TABLE 4

Critical trend angles of σ_1.

Maximum Divergence	Equivalence
061.52°	016.52°
151.52°	106.52°
241.52°	196.52°
331.52°	286.52°

The orientations of maximum divergence are σ_H and σ_h. There are of course only two orientations, 061.52° – 241.52° and 151.52° – 331.52° and σ_H is expected to be close to the orientation of σ_1, ie 274.53°, whereas σ_h will be aligned normal to that. So, σ_H is aligned at 061.52° – 241.52°. The difference in trend between σ_H and σ_1 in this example is 33.01°, but it could be as much as 45°. Figure 5 illustrates the variation between the orientation of the principal stresses and that of the major and minor horizontal stresses.
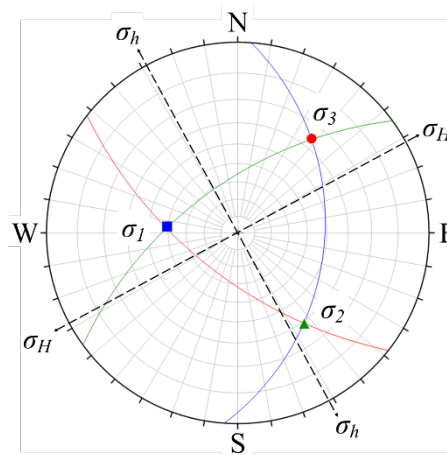
FIG 5 – Variation between the orientation of the principal stresses and that of the major and minor horizontal stresses σ_h and σ_H.

The sinusoidal plot also indicates the magnitudes of σ_H and σ_h to be of the order of 32 MPa and 24 MPa respectively. However, a more accurate estimate can be obtained by substituting the calculated orientation difference back into the transformation spreadsheet to determine that σ_H = 32.07 MPa and σ_h = 24.17 MPa. Throughout these calculations, σ_v remains unchanged at 29.16 MPa.

MODELLING THE UNDERGROUND EXCAVATION

To illustrate the value of the technique, consider an underground cavern for a workshop or crusher station of dimensions 45 m long × 8 m wide × 12 m high. The cavern is effectively a rectangular prism with a long axis in the horizontal plane. Results from simple finite element modelling in which the proposed excavation is established in an arbitrary rock mass subject to the example stress regime illustrates a significant difference in stress loading resulting from the orientation of the cavern (Figure 6). The form of the result is similar to that observed by Haimson, Lee and Huang (1986).
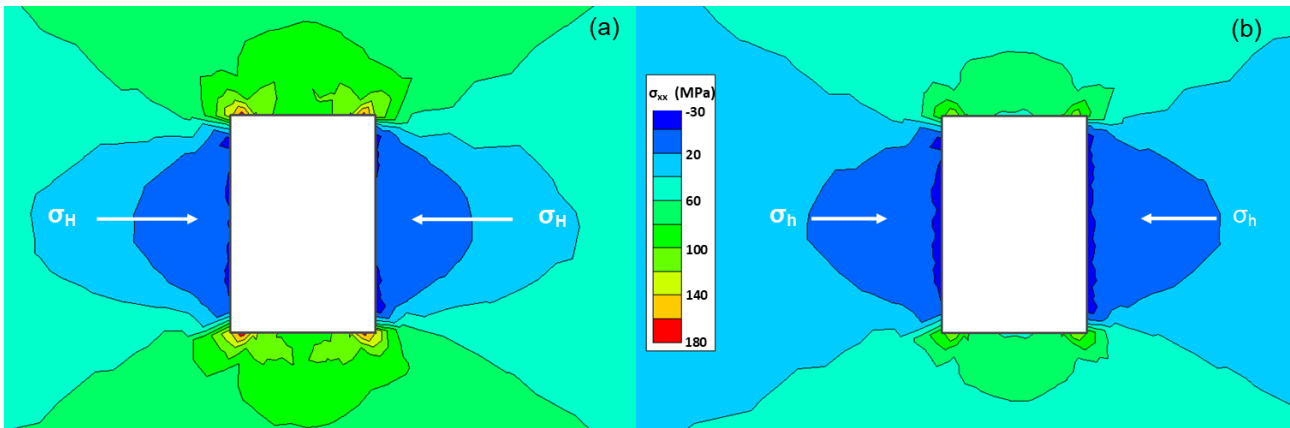
FIG 6 – Stress modelling illustrating stress contours around the cavern oriented with the long axis aligned to σ_h (a) or σ_H (b).

CONCLUSIONS

The impact of the orientation of the stress field with respect to underground excavations is well understood. In the usual case of an excavation in the near horizontal plane, it is the orientation of the major and minor horizontal stresses, rather than the principal stresses, which is of greater significance. In recent years, stress measurements in hard rock mines have typically used 3D techniques defining the full state of stress. However, that is not necessarily the information that is required for optimising the orientation of large openings.

This paper describes an algebraic method for determining the orientation and magnitude of the major and minor horizontal components of the stress field from existing 3D measurements.

REFERENCES

Amadei, B and Stephansson, O, 1997. *Rock Stress and its Measurement*, 490 p, Chapman & Hall: London.

Brady, B H G and Brown, E T, 2005. *Rock Mechanics for Underground Mines (3rd Edition)*, 628 p, Springer: New York.

Haimson, B C, Lee, C F and Huang, J H S, 1986. High horizontal stresses at Niagara Falls, their measurement, and the design of a new hydroelectric plant, in *Proceedings of the International Symposium on Rock Stress and Rock Stress Measurements*, pp 615–624, Centek: Luleå.

Hudson, J A, Cornet, F H and Christiansson, R, 2003. ISRM Suggested Methods for rock stress estimation – Part 1: Strategy for rock stress estimation, *International Journal of Rock Mechanics & Mining Sciences,* 40:991–998.

Leeman, E R, 1964. The measurement of stress in rock – Part 1 – The principles of rock stress measurements, *Journal of the South African Institute of Mining and Metallurgy*, 65(2):45–81.

Priest, S D, 1985. *Hemispherical projection methods in rock mechanics*, 124 p, George, Allen & Unwin: London.

Read, R S and Martin, C D, 1996. Technical Summary of AECL's Mine-by Experiment – Phase 1: Excavation Response, 170 p, Whiteshell Laboratories: Pinawa, Manitoba.

APPENDIX

Calculation spreadsheet:

	A	B	C	D	E	F
1	**Determination of σ_H and σ_h from the 3D Stress Tensor**					
2						
3	**Input**					
4						
5	**Principal Stresses**					
6						
7		**Magnitude**	**Trend**	**Plunge**		
8	σ₁	34.58	274.53	49.04	15	289.53
9	σ₂	30.92	144.05	29.40	15	159.05
10	σ₃	22.08	38.28	25.74	15	53.28
11						
12	**Component Stresses**					
13						
14	σ_NS	σ_EW	σ_V	τ_NS-EW	τ_EW-V	τ_V-NS
15	26.51	29.73	31.34	-3.61	-3.95	-2.57

Right side near rows 7–10:

Formulae for red cells
- =C8+E8
- =C9+E9
- =C10+E10

(1) Input in blue cells only
(2) For subsequent iterations copy the red cells F8, F9 & F10 and paste them as 'values' to cells C8, C9 & C10 repectively.

(1) Input in blue cells only (row 15)

	A	B	C	D	E	F
17	**Output**					
18						
19	**Stress Invariants**				Equation	
20						
21	I₁	87.58			{7}	
22	I₂	2515.46			{8}	
23	I₃	23608.67			{9}	
24						
25	**Principal Stress Matrix**					
26						
27	34.58	0	0		{10}	
28	0	30.92	0			
29	0	0	22.08			
30						
31	**Component Stress Matrix**					
32						
33	26.51	-3.61	-2.57		{11}	
34	-3.61	29.73	-3.95			
35	-2.57	-3.95	31.34			
36						
37	**Convert trend and plunge to radians**					
38						
39	Trend	Plunge				
40	4.79	0.86				
41	2.51	0.51				
42	0.67	0.45				
43						
44	**Stress Transformation**					
45						
46	**Rotation Matrix [A]**					
47						
48	0.05	-0.65	0.76		{12}	
49	-0.71	0.51	0.49			
50	0.71	0.56	0.43			
51						
52	**Transposed Rotation Matrix [A]⁻¹**					
53						
54	0.05	-0.71	0.71		{13}	
55	-0.65	0.51	0.56			
56	0.76	0.49	0.43			
57						
58	**Rotated Stress Tensor ={10}x{12}x{13}**					
59						
60	26.51	-3.61	-2.57		{14}	
61	-3.61	29.73	-3.95			
62	-2.57	-3.95	31.34			
63						
64	**Stress Invariants**					
65						
66	I₁	87.58	OK		{7}	
67	I₂	2515.46	OK		{8}	
68	I₃	23608.67	OK		{9}	
69						

Cell formulae

Stress Invariants
- =A15+B15+C15
- =A15*B15+B15*C15+C15*A15-D15^2-E15^2-F15^2
- =A15*B15*C15+2*D15*E15*F15-(A15*(E15^2)+B15*(F15^2)+C15*(D15^2))

Principal Stress Matrix
- =B8 | =0 | =0
- =0 | =B9 | =0
- =0 | =0 | =B10

Component Stress Matrix
- =A15 | =D15 | =F15
- =D15 | =B15 | =E15
- =F15 | =E15 | =C15

Convert trend and plunge to radians
- =RADIANS(C8) | =RADIANS(D8)
- =RADIANS(C9) | =RADIANS(D9)
- =RADIANS(C10) | =RADIANS(D10)

Transformation to new coordinate system

Rotation Matrix [A]
- =COS(B40)*COS(A40) | =COS(B40)*SIN(A40) | =SIN(B40)
- =COS(B41)*COS(A41) | =COS(B41)*SIN(A41) | =SIN(B41)
- =COS(B42)*COS(A42) | =COS(B42)*SIN(A42) | =SIN(B42)

Transposed Rotation Matrix [A]⁻¹
- =A48 | =A49 | =A50
- =B48 | =B49 | =B50
- =C48 | =C49 | =C50

Rotated Stress Tensor
- =MMULT(A54:C56,MMULT(A27:C29,A48:C50))

Stress Invariants
- =A60+B61+C62
- =A60*B61+B61*C62+C62*A60-B60^2-C61^2-C60^2
- =A60*B61*C62+2*B60*C61*C60-(A60*(C61^2)+B61*(C60^2)+C62*(B60^2))

Right side (Graphing):

Graphing

(3) Copy the **values** of cells C8, A60 & B61 into the following table for each iteration in turn.

Trend	σ_NS	σ_EW
274.53	26.51	29.73
289.53	28.53	27.71
304.53	30.44	25.80
319.53	31.73	24.51
334.53	32.05	24.19
349.53	31.32	24.92
4.53	29.73	26.51
19.53	27.71	28.53
34.53	25.80	30.44
49.53	24.51	31.73
64.53	24.19	32.05
79.53	24.92	31.32
94.53	26.51	29.73
109.53	28.53	27.71
124.53	30.44	25.80
139.53	31.73	24.51
154.53	32.05	24.19
169.53	31.32	24.92
184.53	29.73	26.51
199.53	27.71	28.53
214.53	25.80	30.44
229.53	24.51	31.73
244.53	24.19	32.05
259.53	24.92	31.32

(4) Sort data on "Trend" for plotting

Right side near rows 66–68:
- =IF(B66=B21,"OK","ERROR")
- =IF(B67=B22,"OK","ERROR")
- =IF(B68=B23,"OK","ERROR")

Rock stress measurements – a site geotechnical toolkit

P B Hills[1]

1. Senior Principal Geotechnical Engineer, Pitt & Sherry Operations, Hobart Tas 7000.
   Email: phills@pittsh.com.au

ABSTRACT

Increasingly over the past couple of decades, the importance of understanding the *in situ* stress regime in underground hard rock mines has become accepted by all. Providers have responded to this requirement and various techniques for undertaking the measurements have been honed while others have slipped from use. It is a simple, though not inexpensive task to engage a provider to undertake the require measurements, and a comprehensive report will ensue.

So, what has actually been obtained? What should the geotechnical engineer do next? What tools are necessary to do so?

Regardless of the method of measurement, the report will describe the location of the measurement site and describe the basis of the methodology used in undertaking the measurements and a log of the measurement program. Finally, it will include the results, which should incorporate the normal and shear stress components of the full stress tensor.

Ground control management plans (GCMP's) and stress summary reports and spreadsheets prepared by site geotechnical engineers always include the magnitude, trend and plunge of the principal stresses. Remarkably few site-based summaries include the full stress tensor. This is a significant gap as the full stress tensor is vital for any further data manipulation. However, without the algebraic tools to undertake those manipulations, their value is diminished.

This paper seeks to provide a checklist of ideas to be considered. It provides commentary on the options available to dissect the stress measurement report and ensure that the maximum possible value is derived from it. The manipulation and presentation of component stress data is also discussed. The various methods of stress measurement are not the focus of the paper but some of the strengths and weaknesses of them over which the site geotechnical engineer has some control, are highlighted.

INTRODUCTION

Rock stress is a basic parameter of the rock mass in any mine or underground civil excavation. However, although it is a parameter as fundamental as discontinuity orientation, intact rock mass properties, or the properties of joints and other discontinuities, it is a parameter that comes with significant challenges.

First and foremost is the cost of obtaining the data. It can cost as much as $100K to complete a set of stress measurements at a single site. There are less expensive options, but there are further potential challenges.

Secondly, there are challenges surrounding the representivity of the data however it is obtained. A single measurement measures a volume of rock about the size of the billiard ball. That measurement is then, typically, used to describe the stress tensor in a cubic kilometre of rock or more. A large mine might have 15 or 20 individual tests from no more than 5–10 measurement sites; a mere drop in the ocean when compared to the amount of joint orientation data that might be available.

Thirdly, the measurements may not be representative even at the local scale. Factors such as unknown voids, fault zones, localised alteration of the rock mass etc might be in play.

Finally, stress measurement can be considered a bit of a 'black box'. That is not to say that tests are not performed in a diligent manner. Nor is it to suggested that the reporting of those results is not equally professional. All service providers have their own codes for data manipulation, albeit that they necessarily conform to the mathematics of stress data manipulation. However, the detail is their commercial intellectual property, and is not provided as a consequence. Even though reports contain the basic data including, by way of example, strain changes obtained during overcoring in the case

of overcoring stress measurements or cumulative count plots in the case of stress memory measurements, the site geotechnical engineer does not have the mathematical tools to replicate the final results.

So, the geotechnical engineer is left with a small and expensive data set, which though it may truly reflecting the measurement sites themselves, might not be truly representative of site conditions. Putting this in context for a medium sized mine, the number of individual assays informing the mineral resource could number in the tens of thousands, there may several thousand measurements of rock structure, there could be a hundred or more rock property tests of one form or another, but if there are more than ten rock stress measurements, that's a significant database.

STRESS MEASUREMENT TECHNIQUES

It is not the intention of this paper to describe the full gamut of stress measurement techniques in current usage in any detail. The focus of the paper is the full stress tensor in hard rock mines, what the data means and what to do with it.

There are two direct measurement techniques in common use in Australia which involve overcoring an array of strain gauges epoxied to the rock mass. These are the Hollow Inclusion (HI) Cell and the Australia, New Zealand Inflatable (ANZI) Cell. Both are similar in their deployment and operation, and both are relatively robust. The advantage of these techniques is that they allow the measurement of the stress tensor now. The strain gauges are monitored while the cell is overcored to full strain relief. Knowing the magnitude of the strain relief for a minimum of six variously oriented strain gauges allows the stress tensor to be determined.

Alternatively, there are stress memory techniques. Again, there are two, Acoustic Emission (AE) and Deformation Rate Analysis (DRA). These measurements involve analysis of the Kaiser Effect on oriented cores shipped to a testing facility. These techniques are much less expensive, but they measure the immediately past highest stress to with the core has been subjected; that might not be the stress acting at the time that the core was taken.

SPATIAL INFORMATION

Your stress measurement report will undoubtedly contain spatial information regarding the grid coordinates of the measurement site and perhaps the orientation and location of the mine grid with respect to an established regional datum, the depth below surface, the proximity to other mine workings and the orientation of the measurement itself. The service provider requires this information to undertake the various calculations involved in deriving the result. However, this information always comes from the mine itself and so the geotechnical engineer has full control over it. Prior to providing the information to the service provider, the geotechnical engineer should ensure that it is correct by checking with the site surveyor. Then ensure that whatever information is provided back in the stress measurement report is correct, and that no transcription errors have crept in, as they may influence the results provided.

While there can be reasons for being selective in determining the orientation in which the measurement is undertaken, mathematically it makes no difference provided you know what it is. The essential information for the service provider is the dip and bearing of the drill hole at the location of the measurement regardless of the measurement technique.

Finally, it is important to specify whether the coordinates of the measurement are in a standard grid or local grid. If the latter, then the rotation from the local grid to the standard grid is essential knowledge if a comparison to other sites is to be considered. Survey 'common points' will allow an affine transformation to be undertaken to determine precise coordinates in a universal grid. They can be useful future reference and should be available from the site surveyors.

THE STRESS TENSOR

The concept of stress acting at a point in the rock mass, and the components of the stress tensor are described in most fundamental geomechanics textbooks and reference papers relating to rock stress (eg Amadei and Stephansson, 1997; Hudson, Cornet and Christiansson, 2003; Brady and Brown, 2005). It is not the intention of this paper to reiterate those descriptions, but rather to outline

how the components of the stress tensor can be manipulated algebraically to determine an optimum stress condition for a large underground opening. None-the-less, a summary is illustrative.

The cartoon in Figure 1(A) illustrates the components of the stress tensor and the standard nomenclature for those components. For convenience, the point at which the stress is acting is considered to be an infinitesimally small cube orientated within a mutually orthogonal coordinate system x, y, z, at which normal stresses σ_{xx}, σ_{yy} and σ_{zz} act perpendicular to the faces of the cube and shear stresses τ_{xy}, τ_{yx}, τ_{yz}, τ_{zy}, τ_{xz} and τ_{zx} act parallel to the faces of the cube. The stress tensor is then written in matrix form as

$$\begin{bmatrix} \sigma_{xx} & \tau_{xy} & \tau_{zx} \\ \tau_{yx} & \sigma_{yy} & \tau_{yz} \\ \tau_{xz} & \tau_{zy} & \sigma_{zz} \end{bmatrix}. \tag{1}$$

The shear components are complimentary in that $\tau_{xy} = \tau_{yx}$, $\tau_{yz} = \tau_{zy}$ and $\tau_{xz} = \tau_{zx}$. The stress tensor can be rotated in three-dimensional (3D) space and at a single 3D orientation the shear stresses cancel to zero. That is, $\tau_{xy} = \tau_{yx} = \tau_{yz} = \tau_{zy} = \tau_{xz} = \tau_{zx} = 0$. The normal stresses at that point are the principal stresses, and by definition σ_{xx} is the largest principal stress denoted σ_1, σ_{zz} is the smallest principal stress denoted σ_3, and acts perpendicular to σ_1, and σ_{yy} is the intermediate principal stress denoted σ_2, and acts perpendicular to both σ_1 and σ_3. It is not the arithmetic mean of the values of σ_1 and σ_3. At that orientation, the matrix can be written

$$\begin{bmatrix} \sigma_1 & 0 & 0 \\ 0 & \sigma_2 & 0 \\ 0 & 0 & \sigma_3 \end{bmatrix}. \tag{2}$$

The special case of the principal stress is illustrated in Figure 1(B).

FIG 1 – Cartoons illustrating the stress components at a point (L) and the special case of the principal stresses (R). After Hudson, Cornet and Christiansson (2003).

CARTESIAN COORDINATE SYSTEM

The notation for the stress tensor is arbitrary. To make use of it, it is converted into a cartesian coordinate system assigning directions xx, yy and zz to north–south, east–west and vertical, such that

$$\begin{bmatrix} \sigma_{xx} & \tau_{xy} & \tau_{zx} \\ \tau_{yx} & \sigma_{yy} & \tau_{yz} \\ \tau_{xz} & \tau_{zy} & \sigma_{zz} \end{bmatrix} = \begin{bmatrix} \sigma_{NS} & \tau_{NS-EW} & \tau_{V-NS} \\ \tau_{EW-NS} & \sigma_{EW} & \tau_{EW-V} \\ \tau_{NS-V} & \tau_{V-EW} & \sigma_{V} \end{bmatrix}. \tag{3}$$

Then, each of the principal stresses may also be described in terms of eigenvalues and eigenvectors as magnitude in units of megapascals (MPa) and direction as trend and plunge in the units of degrees (°). In total, the eigenvalues and eigenvectors for the principal stresses and the component normal

and shear stresses in a north–south, east–west and vertical coordinate system, is the data that is typically provided to the geotechnical engineer when a stress measurement is undertaken.

Some stress measurement reports refer to bearing and plunge, bearing and dip, or even dip direction and dip in reference to the direction of eigenvectors. While it is generally understood what is meant, these terms are not strictly correct because they describe planes rather than vectors. This distinction is important when selecting the 'global orientation format' to visualise the principal stress orientation using the RocScience program DIPS® as geotechnical engineers commonly do. This paper will refer to trend and plunge throughout.

STRESS MEASUREMENT DATA

The fundamental data in the stress measurement report is of course the measurement data. Regardless of the measurement technique, the data will include the magnitude of the principal stresses and the trend and plunge of each. Equally important are the component normal and shear stresses, presented in a north–south, east–west and vertical coordinate system. Table 1 presents a fabricated data set of two stress measurements at a single site which will be manipulated throughout the paper in worked examples.

TABLE 1

Stress measurement data.

Principal stresses	σ_1			σ_2			σ_3		
	Mag. (MPa)	Trend (°)	Plunge (°)	Mag. (MPa)	Trend (°)	Plunge (°)	Mag. (MPa)	Trend (°)	Plunge (°)
Test 1	50.50	063.75	13.82	18.58	161.99	30.23	7.10	312.24	56.13
Test 2	39.81	056.90	09.02	15.04	158.09	50.71	9.56	319.82	37.85

Component stresses	σ_{NS} (MPa)	σ_{EW} (MPa)	σ_V (MPa)	$\tau_{NS\text{-}EW}$ (MPa)	$\tau_{EW\text{-}V}$ (MPa)	$\tau_{V\text{-}NS}$ (MPa)
Test 1	23.78	44.63	12.77	15.59	11.62	0.22
Test 2	20.24	30.57	13.59	12.74	4.93	0.07

Typically, the orientation of the principal stresses will also be depicted in stereographic projection as illustrated in Figure 2, providing a quick check that they are mutually orthogonal. The same will be the case for the average stress condition. If they are not mutually orthogonal, then one or more of the trend and plunge values is wrong; if a transcription error hasn't occurred, it is necessary to check back with the service provider and see if there is a typographical error.
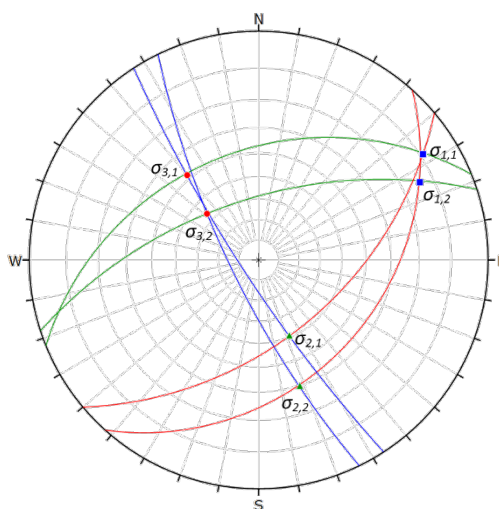
FIG 2 – Stereographic plot of principal stresses.

MANIPULATION OF STRESS MEASUREMENT DATA

Assessment of stress measurement data requires manipulation of the raw data received from the service provider to determine stress gradients, localised and general stress field orientations, or for comparison with results from elsewhere (locally or regionally). This can include determining basic site data for numerical modelling or input to empirical design tools.

The tools outlined below allow the geotechnical engineer to manipulate the stress measurement data received from the service provider to achieve a meaningful understanding of the stress regime at his/her site and how to determine its validity. Manipulation of the data is best undertaken through the creation of spreadsheets into which raw data can be input to reach a defined output. The various calculations are sensitive to rounding errors which will accumulate if each input step is rounded to (say) two significant figures using a pocket calculator. None-the-less, numbers presented in the discussion are truncated for clarity.

Determination of the stress invariants

The three stress invariants, I_1, I_2 and I_3, are so-called because they are invariant quantities associated with the stress tensor which are independent of the coordinate system in which the stress tensor is described. They take the form:

$$I_1 = \sigma_1 + \sigma_2 + \sigma_3 \tag{4}$$

$$I_2 = \sigma_y\sigma_z + \sigma_x\sigma_z + \sigma_x\sigma_y - \tau_{yz}^2 - \tau_{xz}^2 - \tau_{xy}^2 \tag{5}$$

$$I_3 = \sigma_x\sigma_y\sigma_z + 2\tau_{yz}\tau_{xz}\tau_{yz} - \left(\sigma_x\tau_{yz}^2 + \sigma_y\tau_{xz}^2 + \sigma_z\tau_{xy}^2\right) \tag{6}$$

The stress invariants provide a useful check on the various algebraic calculations that are demonstrated through the course of this paper. That is because for any valid stress tensor n, the stress invariants for any component stress matrix $\begin{bmatrix} \sigma_{xx}^n & \tau_{xy}^n & \tau_{xz}^n \\ \tau_{yx}^n & \sigma_{yy}^n & \tau_{yz}^n \\ \tau_{zx}^n & \tau_{zy}^n & \sigma_{zz}^n \end{bmatrix}$ including the principal stress matrix $\begin{bmatrix} \sigma_1 & 0 & 0 \\ 0 & \sigma_2 & 0 \\ 0 & 0 & \sigma_3 \end{bmatrix}$, are the same, ie they are invariant. If that is not the case in any calculation presented below, then quite simply, there is an error.

Averaging of stress measurements

Some service providers provide a 'site average' or 'combined' measurement where several separate measurements have been undertaken in close proximity. However, that is not always the case, particularly if the operation has a lot of old stress measurement reports which need to be considered. Averaging the stresses must be completed using the component stresses and then the average principal stress determined from the averaged components.

Averaging of the matrices is undertaken thus:

$$\left\{ \begin{bmatrix} \sigma_{xx}^A & \tau_{xy}^A & \tau_{xz}^A \\ \tau_{yx}^A & \sigma_{yy}^A & \tau_{yz}^A \\ \tau_{zx}^A & \tau_{zy}^A & \sigma_{zz}^A \end{bmatrix} + \begin{bmatrix} \sigma_{xx}^B & \tau_{xy}^B & \tau_{xz}^B \\ \tau_{yx}^B & \sigma_{yy}^B & \tau_{yz}^B \\ \tau_{zx}^B & \tau_{zy}^B & \sigma_{zz}^B \end{bmatrix} \right\}/2 = \left\{ \begin{bmatrix} \sigma_{xx}^{(A+B)} & \tau_{xy}^{(A+B)} & \tau_{xz}^{(A+B)} \\ \tau_{yx}^{(A+B)} & \sigma_{yy}^{(A+B)} & \tau_{yz}^{(A+B)} \\ \tau_{zx}^{(A+B)} & \tau_{zy}^{(A+B)} & \sigma_{zz}^{(A+B)} \end{bmatrix} \right\}/2 = \begin{bmatrix} \sigma_{xx}^C & \tau_{xy}^C & \tau_{xz}^C \\ \tau_{yx}^C & \sigma_{yy}^C & \tau_{yz}^C \\ \tau_{zx}^C & \tau_{zy}^C & \sigma_{zz}^C \end{bmatrix} \tag{7}$$

Substituting the component stresses for the two measurements gives:

$$\left\{ \begin{bmatrix} 23.78 + 20.24 & 15.59 + 12.74 & 0.22 + 0.07 \\ 15.59 + 12.74 & 44.63 + 30.57 & 11.62 + 4.93 \\ 0.22 + 0.07 & 11.62 + 4.93 & 12.77 + 13.59 \end{bmatrix} \right\}/2 = \begin{bmatrix} 22.01 & 14.16 & 0.14 \\ 14.16 & 37.60 & 8.27 \\ 0.14 & 8.27 & 13.18 \end{bmatrix} \tag{8}$$

which is the component matrix for the average stress condition. The average principal stresses can be calculated from this matrix. The stress invariants derived from this component stress matrix using Equations 4, 5 and 6 are $I_1 = 72.79$, $I_2 = 1344.32$ and $I_3 = 6791.51$.

Determination of principal stresses from component stresses

It is unlikely that the service provider will provide a report without including the principal stresses and their trend and plunge. However, if it is necessary to average two or more stress measurements then the eigenvalues and vectors of the principal stresses will need to be determined.

Firstly, from the component stress matrix in Equation 8, determine the average normal stress:

$$\sigma = \left(\sigma_{xx}^c + \sigma_{yy}^c + \sigma_{zz}^c\right)/3 = (22.01 + 37.60 + 13.18)/3 = 24.26 \tag{9}$$

and subtract the average from the normal stresses. That is:

$$\begin{bmatrix} 22.01 - 24.26 & 14.16 & 0.14 \\ 14.16 & 37.60 - 24.26 & 8.27 \\ 0.14 & 8.27 & 13.18 - 24.26 \end{bmatrix} = \begin{bmatrix} -2.25 & 14.16 & 0.14 \\ 14.16 & 13.34 & 8.27 \\ 0.14 & 8.27 & -11.08 \end{bmatrix}. \tag{10}$$

Determine the quasi-invariants of this matrix using Equations 4, 5 and 6.

$$J_1 = -2.25 + 13.34 + -11.08 = 0 \tag{11}$$

$$J_2 = -(-2.25 \times 13.34 + 13.34 \times -11.08 + -11.08 \times -2.25 - 8.27^2 - 0.14^2 - 14.16^2) = 421.81 \tag{12}$$

$$J_3 = (-2.25 \times 13.34 \times -11.08) + (2 \times 8.27 \times 0.14 \times 14.16)$$
$$-(-2.25 \times 8.27^2 + 13.34 \times 0.14^2 + -11.08 \times 14.16^2) = 2741.99 \tag{13}$$

$$\tau = \sqrt{(2 \times 421.81)/3} = 16.77 \tag{14}$$

$$3\theta = acos(\sqrt{2} \times 2741.23/16.77^3) = 0.61 \tag{15}$$

The principal stresses are calculated from these factors as follows:

$$\sigma_1 = \left(2/\sqrt{3}\right) \times \sqrt{421.81} \times \cos(0.61/3) + 24.26 = 47.50 \tag{16}$$

$$\sigma_2 = \left(2/\sqrt{3}\right) \times \sqrt{421.81} \times \cos(0.61/3 - 2 \times \pi/3) + 24.26 = 16.76 \tag{17}$$

$$\sigma_3 = \left(2/\sqrt{3}\right) \times \sqrt{421.81} \times \cos(0.61/3 + 2 \times \pi/3) + 24.26 = 8.53 \tag{18}$$

Thus the principal stress matrix with the same form as Equation 2 is:

$$\begin{bmatrix} 47.50 & 0 & 0 \\ 0 & 16.76 & 0 \\ 0 & 0 & 8.53 \end{bmatrix} \tag{19}$$

and the stress invariants derived from this principal stress matrix using Equations 4, 5 and 6 are I_1 = 72.79, I_2 = 1344.32 and I_3 = 6791.51, equivalent to those determined from the component stresses in the previous section, and thus confirming the accuracy of the calculation.

To determine the trend and plunge of the principal stresses, take the average component stress matrix from Equation 8 and subtract each principal stress from the normal stresses in turn. For σ_1:

$$\begin{bmatrix} 22.01 - 47.50 & 14.16 & 0.14 \\ 14.16 & 37.60 - 47.50 & 8.27 \\ 0.14 & 8.27 & 13.18 - 47.50 \end{bmatrix} = \begin{bmatrix} -25.49 & 14.16 & 0.14 \\ 14.16 & -9.90 & 8.27 \\ 0.14 & 8.27 & -34.32 \end{bmatrix} \tag{20}$$

Obtain the 2 × 2 matrix determinant in one of three combinations. For example choose:

$$\sigma_{yy} \times \sigma_{zz} - \tau_{zy} \times \tau_{yz} = (-9.90 \times -34.32) - (8.27 \times 8.27) = 271.26 \tag{21}$$

$$\tau_{zy} \times \tau_{zx} - \tau_{xy} \times \sigma_{zz} = (8.27 \times 0.14) - (14.16 \times -34.32) = 487.09 \tag{22}$$

$$\tau_{yx} \times \tau_{zy} - \sigma_{yy} \times \tau_{xz} = (14.16 \times 8.27) - (-9.90 \times 0.14) = 118.49 \tag{23}$$

Then:

$$\sqrt{271.26^2 + 487.09^2 + 118.49^2} = 569.99 \tag{24}$$

And:

$$271.26/569.66 = 0.48 \tag{25}$$

$$487.09/569.99 = 0.85 \tag{26}$$

$$118.49/569.99 = 0.21 \tag{27}$$

The other combinations are:

$$\tau_{yz} \times \tau_{xz} - \sigma_{zz} \times \tau_{xy} = 487.20$$

$$\sigma_{zz} \times \sigma_{xx} - \tau_{xz} \times \tau_{zx} = 874.63$$

$$\tau_{xz} \times \tau_{xy} - \tau_{yz} \times \sigma_{xx} = 212.80$$

And:

$$\tau_{xy} \times \tau_{yz} - \tau_{xz} \times \sigma_{yy} = 118.54$$

$$\tau_{xz} \times \tau_{xy} - \sigma_{xx} \times \tau_{zy} = 212.80$$

$$\sigma_{xx} \times \sigma_{yy} - \tau_{yx} \times \tau_{xy} = 51.78$$

It is necessary to follow the steps illustrated in Equations 20 to 27 for each of the other principal stresses to inform Table 2.

TABLE 2

Eigen values and vectors for the average stress condition.

Eigen values		Eigen vectors		
σ_1	47.50	0.48	0.85	0.21
σ_2	16.76	-0.75	0.27	0.60
σ_3	8.53	0.46	-0.44	0.77

Then:

$$\sigma_1 \, Plunge \, = \, atan\left(0.21 \div \sqrt{(0.48^2 + 0.85^2)}\right) = 12.00° \tag{28}$$

$$\sigma_1 \, Trend \, = \, atan(0.85/0.48) = 060.88° \tag{29}$$

$$\sigma_2 \, Plunge \, = \, atan\left(0.60 \div \sqrt{(-0.75^2 + 0.27^2)}\right) = 36.87° \tag{30}$$

$$\sigma_2 \, Trend \, = \, atan(0.27/-0.75) = -19.95° = 160.05° \text{ (corrected to positive)} \tag{31}$$

$$\sigma_3 \, Plunge \, = \, atan\left(0.77 \div \sqrt{(0.46^2 + -0.44^2)}\right) = 50.58° \tag{32}$$

$$\sigma_3 \, Trend \, = \, atan(-0.44/0.45) = -44.10° = 315.90° \text{ (corrected to positive)} \tag{33}$$

The data of the averaged stress condition is illustrated in Table 3 and the result is clear in stereographic projection as illustrated in Figure 3.

TABLE 3

Averaged stress measurement data.

Principal stresses	σ_1			σ_2			σ_3		
	Mag. (MPa)	Trend (°)	Plunge (°)	Mag. (MPa)	Trend (°)	Plunge (°)	Mag. (MPa)	Trend (°)	Plunge (°)
Average	47.50	060.88	12.00	16.76	160.05	36.87	8.53	315.90	50.58

Component stresses	σ_{NS} (MPa)	σ_{EW} (MPa)	σ_V (MPa)	$\tau_{NS\text{-}EW}$ (MPa)	$\tau_{EW\text{-}V}$ (MPa)	$\tau_{V\text{-}NS}$ (MPa)
Average	22.02	37.60	13.18	14.16	8.27	0.14

A spreadsheet for undertaking these calculations is included in the appendix.
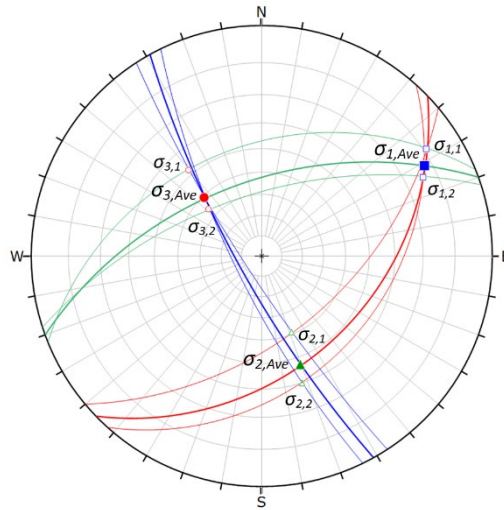
FIG 3 – Stereographic plot of principal stresses including average stress condition.

Determination of component stresses from principal stresses

In some stress measurement reports and summaries, eg ground control management plans (GCMP's) and site summaries, component stresses might not have been included. If this is the case, they can be calculated using the Stress Transformation Law because essentially all that is occurring is that the principal stress 'cube' illustrated in Figure 1(R), for which the principal stress matrix is known is being rotated to align with the cartesian coordinate system. This is a specific case of the Stress Transformation Law as outlined by Amadei and Stephansson (1997) and Brady and Brown (2005) although the transformation matrix is written slightly differently than in those texts because the trend and plunge of the axes of both the principal stress condition (see Table 3) and the component stress condition, being 00/000, 00/090 and 90/000, are known and the angle of rotation between the two conditions, angles β and δ as per Amadei and Stephenson (1997), are not known. Priest (1985) provides an explanation for the applicable case using the vector algebra method for decomposition of a force.

The principal stress matrix is:

$$
\begin{bmatrix} \sigma_{xx} & \tau_{xy} & \tau_{zx} \\ \tau_{yx} & \sigma_{yy} & \tau_{yz} \\ \tau_{xz} & \tau_{zy} & \sigma_{zz} \end{bmatrix} = \begin{bmatrix} 47.50 & 0 & 0 \\ 0 & 16.76 & 0 \\ 0 & 0 & 8.53 \end{bmatrix} \tag{34}
$$

and the component stress matrix is:

$$
\begin{bmatrix} \sigma_{xx'} & \tau_{x'y'} & \tau_{x'z'} \\ \tau_{y'x'} & \sigma_{yy'} & \tau_{y'z'} \\ \tau_{z'x'} & \tau_{z'y'} & \sigma_{zz'} \end{bmatrix}. \tag{35}
$$

The trend and plunge of the principal stresses from Table 3 are assigned terms t_1, p_1, t_2, p_2, t_3 and p_3 and entered into the rotation matrix [A] where:

$$
[A] = \begin{bmatrix} \cos p_1 \times \cos t_1 & \cos p_1 \times \sin t_1 & \sin p_1 \\ \cos p_2 \times \cos t_2 & \cos p_2 \times \sin t_2 & \sin p_2 \\ \cos p_3 \times \cos t_3 & \cos p_3 \times \sin t_3 & \sin p_3 \end{bmatrix} = \begin{bmatrix} 0.48 & 0.85 & 0.21 \\ -0.75 & 0.27 & 0.60 \\ 0.46 & -0.44 & 0.77 \end{bmatrix} \tag{36}
$$

and the transposition of that matrix:

$$
[A]^{-1} = \begin{bmatrix} 0.48 & -0.75 & 0.46 \\ 0.85 & 0.27 & -0.44 \\ 0.21 & 0.60 & 0.77 \end{bmatrix}. \tag{37}
$$

Then the component stress matrix is determined as follows:

$$
[A] \times \begin{bmatrix} \sigma_{xx} & \tau_{xy} & \tau_{zx} \\ \tau_{yx} & \sigma_{yy} & \tau_{yz} \\ \tau_{xz} & \tau_{zy} & \sigma_{zz} \end{bmatrix} \times [A]^{-1} = \begin{bmatrix} \sigma_{xx'} & \tau_{x'y'} & \tau_{x'z'} \\ \tau_{y'x'} & \sigma_{yy'} & \tau_{y'z'} \\ \tau_{z'x'} & \tau_{z'y'} & \sigma_{zz'} \end{bmatrix} = \begin{bmatrix} 22.01 & 14.16 & 0.14 \\ 14.16 & 37.60 & 8.27 \\ 0.14 & 8.27 & 13.18 \end{bmatrix}, \tag{38}
$$

which is the same as the result determined in Equation 8.

A spreadsheet for undertaking these calculations is also included in the appendix.

PRESENTATION OF DATA

There are two aspects to the graphical representation of the stress measurement data. The first is the stereographic representation of the orientation of the principal stresses which has already been discussed. The example used is for two measurements at a single site. It is common for a mine to have a number of stress measurements at a number of locations in 3D space, and the average site result for each should be plotted in a combined stereographic plot. This will allow a quick assessment of whether the orientation of the stress field is broadly consistent across the site, and if this is not the case, point to results which might be anomalous; that does not necessarily mean 'erroneous' as there could be a number of reasons for the anomaly such as a significant fault, topography, etc.

Data confidence for direct measurements

One of the challenges of direct measurement of the stress tensor using HI Cells or ANZI cell is obtaining a full suite of data from the overcored instrument. HI Cells have 12 strain gauges and ANZI cells 18, but robust results might not be obtained from all gauges due to gluing difficulties or faults, joints or voids etc in the rock mass. For a given site measurement, the service provider will usually identify these failures and indicate how many gauges were used in the calculation of the stresses. If a site result has been calculated, the number of accepted gauges will have been taken into account. If not and the site result is being determined from two or three (or more) individual measurements on-site, then the average component stresses for the site should be determined as outlined above ('averaging of stress measurements') with the individual component stresses weighted on the basis of the number of gauges used for each individual test. For example, if three individual HI Cells were used and they have (say) 10, 12 and 11 successful gauges respectively, then each of the components should be weighted accordingly. As an example:

$$\sigma_{xx}^{Ave} = \big((\sigma_{xx}^{Test\ 1} \times 10) + (\sigma_{xx}^{Test\ 2} \times 12) + (\sigma_{xx}^{Test\ 3} \times 11)\big)/33$$

and so on.

Lee (1997) proposed a system for rating the site measurement from HI Cells on the quality of the raw data. A weighting is assigned to the site measurement on the basis of that rating for the purposes of comparing it with site measurements from elsewhere in the mine. After discussion with Max Lee (pers. comm., 2021) his rating system has been expanded to incorporate ANZI Cells as illustrated in Table 4.

Data confidence for stress memory techniques

Measurements obtained from stress memory techniques such as AE and DRA are not rated using same system as direct measurements techniques. In part this is because the challenges that the rating system seeks to overcome do not apply as samples that are likely to result in a suboptimal result are not chosen. However, that doesn't make them superior, and there are a number of reasons why this might not be the case.

The risk in the use of stress memory techniques is knowing what has actually been measured. As an example, Villaescusa *et al* (2006) explain that AE uses the Kaiser effect to determine the *'maximum stress level … to which a sample had previously been subjected'*. The unknown in this explanation is whether or not the maximum stress to which the sample has been subjected is the stress condition acting now. For the site geotechnical engineer, it is most usually the latter that he or she wants to know. Consequently, it is strongly recommended that stress memory techniques are calibrated against direct measurements prior to sole reliance being placed upon them. Hadjigeorgiou, Dight and Potvin (2020) make a similar recommendation. While good correlation was found by Villaescusa *et al* (2006) in the Yilgarn Province of Western Australia and has been demonstrated elsewhere, there are other examples where satisfactory correlation of either orientation or magnitude, or both is not demonstrated as is the case with some measurements in the Gawler Province of South Australia leading to them not being considered by Hills, Raymond and Doyle (2015) at Challenger and questioned by Balog, Cox and Ormerod (2021) at Carrapateena.

TABLE 4

Confidence rating for direct stress measurements (after Lee, 1997).

Rating	Weighting	Comments
Excellent	8	• At least three good individual overcores of CSIRO HI Cells (≥ 33 strains), good rock property data for each, and no experimental difficulties. (Equivalent to two good ANZI Cells although three preferred). • Variable results between adjacent cells is not considered to be an issue, rather a characteristic of the local rock mass. • Good rock property data is required, ideally not significantly different between cells. • Data collection from two or more boreholes is considered to be better than from one borehole.
Good	6	• At least two good individual overcores (24 to 32 strains). • The third cell may have had gluing and/or electrical problems. • Significantly different rock properties between cells, and/or anisotropic or microcracked rock. • It is difficult for stress measurements using the borehole slotting or hydraulic fracturing techniques to be rated any higher than good. Two ANZI Cells are required.
Fair	3	• Only two overcores, and not complete due to some gluing and/or electrical problems (16 to 23 strains). (May be obtained with one good ANZI Cell with sufficient strains). • Technical difficulties with the overcoring, eg groundwater, glue bonding, discing problems, transient temperature effects, but with good rock property data. • Alternatively, poor rock property data and up to 24 good overcore strains.
Poor	1	• Poor data from two overcores and biaxial tests (<15 strains). (May be obtained with one poor – fair ANZI Cell with sufficient strains). • High variability between individual tests. Poor glue bonding.

Stereograph plots

Stereograph plots are usually used to present orientation data and they have already been used in this paper. As mentioned already it is essential that data is plotted as trend and plunge. It is also important that equal angle projection is used. It is tempting to also use the 'add set window' tool in DIPS to determine an average stress condition. This is erroneous as the average is undertaken on the principal stress eigenvectors rather that the component stresses and is algebraically incorrect. To illustrate this point, sets have been created on the data presented in Table 1 highlighting the difference between the algebraic average and 'sets average'. The difference is only small given two data points. Critically, the points, indicated by the stars in Figure 4, are not mutually orthogonal. The angles between the 'sets average' locations are 88.56°/91.44°, 90.42°/89.58° and 91.48°/88.52° for σ_1/σ_2, σ_2/σ_3 and σ_1/σ_3 respectively in this example, and the variance from 90°/90° can increase significantly with more data points.
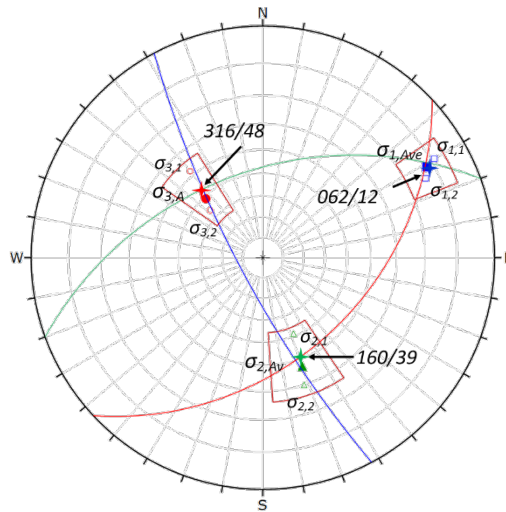
FIG 4 – Stereographic plot of principal stresses highlighting the difference using the 'add sets window' tool.

Gradient plots

Sites with a database of stress measurements over a number of levels typically produce a gradient plot showing the magnitude of the stresses as a function of depth. These plots are easily enough created in EXCEL® and a linear trend can be added. It is necessary that the equation for the linear trend be used to create a separate data set if it is intended to rotate the plot to have a descending depth on the y-axis and increasing magnitude on the x-axis. Adding a trend line to the rotated data will not give a correct solution. Data sets will need to be manipulated to create x as a function of y in this case, which is not a standard EXCEL output, but the resultant plot is more intuitive (Figure 5).
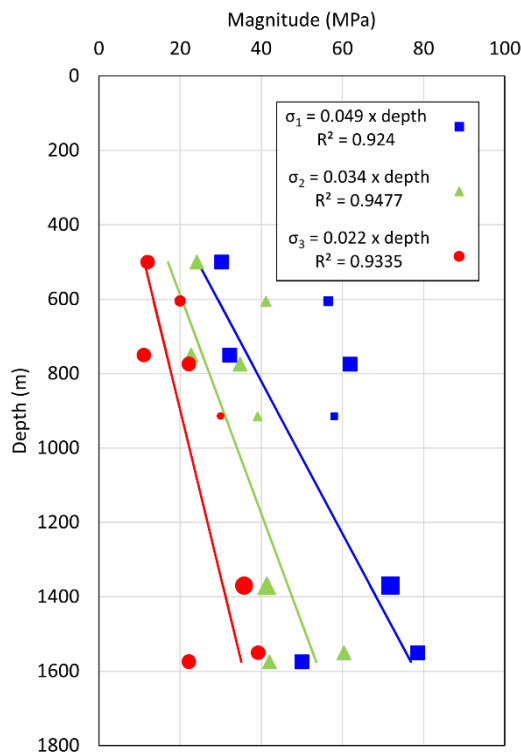
FIG 5 – Stress gradient plot. Symbol size reflects weighting.

Validation of stress measurements

Lee *et al* (2006) proposed that the typical scatter in plots of principal stresses against depth for stress measurements across the Yilgarn Province of Western Australia was significantly reduced when the principal stresses were plotted against the first stress invariant, I_1. This allowed for the establishment

of simple ratios between the principal stresses $\sigma_1 : \sigma_2 : \sigma_3$. The authors went on to demonstrate a similar relationship in Eastern Australia. Harrison, Hudson and Carter (2007) expanded on those findings with the addition of databases from Britain, Finland and Chile and determined that the overall relationships were a function of the mechanical properties of the rock mass and not a quirk of statistical analysis.

An invariant plot for the Figure 5 data is presented in Figure 6. The ratios of the principal stresses as indicated from the trend lines is 1.5: 1.5: 2.2 which is very similar to that indicated for Australia generally of 1.5: 1.5: 2.3 by Lee *et al* (2006). Subsequently, Lee *et al* (2010) defined six separate stress provinces across Australia and Hills (2020) added a seventh in Tasmania.
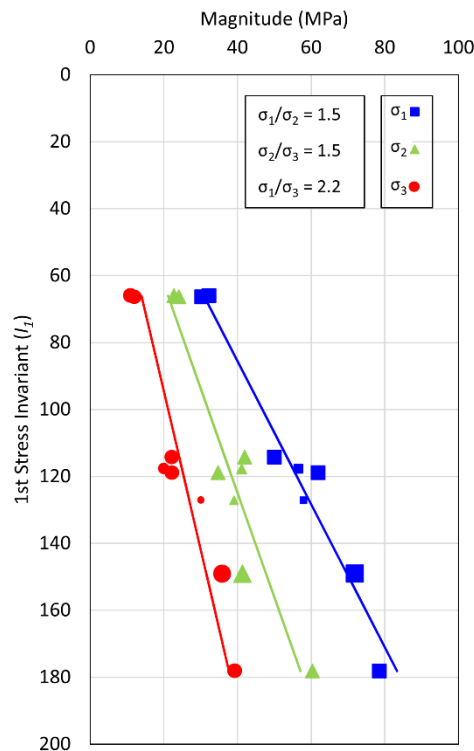
FIG 6 – Stress invariant plot of Figure 5 data.

WHAT DOES THE DATA MEAN?

The tools and procedures outlined herein provide a toolkit for managing stress measurement data. Some simple rules of thumb can be used to guide implementation.

- Unless the service provider has advised that a particular measurement has not been successful, don't discard it; there are never too many stress measurements.

- A successful measurement is a valid stress measurement. If it not what is expected, it may be influenced by factors such as structure, topography or mining, but it's not wrong.

- Interpretation of seismic data can aid interpretation. Likewise observations of stress damage in drill core or drill holes or underground such as borehole breakout in isolated shafts or damage in early development, but it is important not to use mining induced stress damage to inform the *in situ* virgin stress tensor.

- Plotting data in stereographic projection will rapidly illustrate the collective orientation of the stress tensor. As a general rule averaging all the site stress measurements, regardless of depth, will provide the best site estimate of orientation unless two or more distinct populations are apparent.

- Where distinct populations are apparent, consider why this might be. A distinct spatial, structural or depth influence is probably real. Particularly so if there are multiple orebodies of different orientation. Maloney, Kaiser and Vorauer (2006) proposed that there might be distinct stress populations at various depths.

If the procedures outlined above have been followed, the geotechnical engineer should be able to have confidence in the output. However, the numbers might still not be what is expected. Geological structures and topography can mean that the expected results are not always obtained. It is also possible that the data represents a mining induced rather than a virgin stress condition even though that is not what was sought. Hills (2020) described all these variations across the Tasmanian data set where, despite a regional pattern being established across the region, structure was found to define the stress regime at the Renison Mine, topography defined the stress regime at Hellyer Mine and the stress regime measured at the Mount Lyell Mine appeared to be dominated by past mining and in all likelihood did not represent virgin rock stress.

It is essential that rock stress data is ground truthed against observations of the rock mass itself. It is also valuable to compare the results from one site with another close by or across a particular geological province. Stress measurements, by whatever method, are expensive to undertake and no one site will every have too many, if indeed they have enough. Consequently, it make sense to share the data where mutual benefit can be gained.

CONCLUDING REMARKS

The purpose of this paper has been to provide a series of tools to allow site geotechnical engineers to interpret their stress measurement reports, fill in any blanks in the raw data, and analyse the output from a number of stress measurement programs holistically. It also discusses confidence in and presentation of the stress measurement data and validation of the results.

ACKNOWLEDGEMENTS

REFERENCES

Amadei, B and Stephansson, O, 1997. *Rock Stress and its Measurement*, 490 p, Chapman & Hall: London.

Balog, G, Cox, D and Ormerod, T, 2021. Carrapateena project to date – Geotechnical risks and management, in *Proceedings of the 14th Underground Operators Conference*, pp 63–70 (The Australasian Institute of Mining and Metallurgy: Melbourne).

Brady, B H G and Brown, E T, 2005. *Rock Mechanics for Underground Mines,* third edition, 628 p, Springer: New York.

Hadjigeorgiou, J, Dight, P M and Potvin, Y, 2020. Rock stress data, in Y Potvin and J Hadjigeorgiou (eds), *Ground Support for Underground Mines*, pp 117–138 (Australian Centre for Geomechanics: Perth).

Harrison, J P, Hudson, J A and Carter, J N, 2007. Is there a relation between the in-situ principal stress magnitudes in rock masses?, in E Eberhardt, D Stead and T Morrison (eds), *Proceedings of the 1st Canada-US Rock Mechanics Symposium*, 8 p, CRC Press: Boca Raton.

Hills, P B, 2020. Tasmanian rock stress, *Australian Geomechanics*, 55(1):77–111.

Hills, P B, Raymond, N and Doyle, M, 2015. Empirical ground support and reinforcement design at Challenger Gold Mine, in *Proceedings of the ACG International Seminar on Design Methods in Underground Mining*, pp 385–398 (Australian Centre for Geomechanics: Perth).

Hudson, J A, Cornet, F H and Christiansson, R, 2003. ISRM Suggested Method for rock stress estimation – Part 1: Strategy for rock stress estimation, *International Journal of Rock Mechanics & Mining Sciences*, 40:991–998.

Lee, M F, 1997. Confidence rating system for rock stress measurements, AMC Consultants: Melbourne.

Lee, M F, Mollison, L J, Mikula, P and Pascoe, M, 2006. In situ rock stress measurements in Western Australia's Yilgarn Craton, in *In-situ Rock Stress – Measurement, Interpretation and Application*, pp 35–42, Taylor & Francis: London.

Lee, M F, Mollison, L, Campbell, A and Litterbach, N, 2010. Rock stresses in the Australian Continental Plate – variability and controls, in C Y Chin, C I Massey, T J McMorran, G M Pinches and A L Williams (eds), *Proceedings of the 11th IAEG Congress – Geologically Active New Zealand*, 16 p, CRC Press: Boca Raton.

Maloney, S, Kaiser, P K and Vorauer, A, 2006. A Reassessment of insitu stresses in the Canadian Shield, in *Proceedings of the 41st US Rock Mechanics Symposium,* Golden, American Rock Mechanics Association.

Priest, S D, 1985. *Hemispherical projection methods in rock mechanics*, 124 p, George, Allen & Unwin: London.

Villaescusa, E, Li, J, Windsor, C R and Seto, M, 2006. A comparison of overcoring and AE stress profiles with depth in Western Australia, in *Proceedings of In situ Rock Stress*, pp 223–228.

APPENDIX

Calculation spreadsheets.

Determination of principal stresses from component stresses

	A	B	C	D	E	F		
1	Determination of Principal Stresses from Component Stresses							
2								
3	**Input**							
4								
5	**Component Stresses**							
6								
7	σ_{NS}	σ_{EW}	σ_V	τ_{NS-EW}	τ_{EW-V}	τ_{V-NS}		
8	**22.01**	**37.60**	**13.18**	**14.16**	**8.27**	**0.14**	*(1)* Input in blue cells only. Solution in red cells.	
9								
10	**Output**						*Cell formulae*	
11								
12	**Component Stress Matrix**					Equation	**Component Stress Matrix**	
13								
14	22.01	14.16	0.14			**{8}**	=A8 =D8 =F8	
15	14.16	37.60	8.27				=D8 =B8 =E8	
16	0.14	8.27	13.18				=F8 =E8 =C8	
17								
18	**Average Normal Stress**						**Average Normal Stress**	
19								
20	24.26					**{9}**	=(A14+B15+C15)/3	
21								
22	**Subtract Averge from Normal Stresses**						**Subtract Averge from Normal Stresses**	
23								
24	-2.25	14.16	0.14			**{10}**	=A14-A20 =B14 =C14	
25	14.16	13.34	8.27				=A15 =B15-A20 =C15	
26	0.14	8.27	-11.08				=A16 =B16 =C16-A20	
27								
28	**Determine quasi-invariants, τ & 3ϴ**						**Determine quasi-invariants, τ & 3ϴ**	
29								
30	$J_1 =$	0.00				**{11}**	=A24+B25+C26	
31	$J_2 =$	421.81				**{12}**	=A24*B25+B25*C26+C26*A24-B24^2-C25^2-C26^2	
32	$J_3 =$	2741.99				**{13}**	=A24*B25*C26+2*B24*C25*C26-(A24*(C25^2)+B25*(C24^2)+C26*(B24^2))	
33	$\tau =$	16.77				**{14}**	=SQRT((2*B31)/3)	
34	$3ϴ =$	0.61				**{15}**	=ACOS(((SQRT(2))*B32)/B33^3)	
35								
36	**Determine Principal Stresses**						**Determine Principal Stresses**	
37								
38	$\sigma_1 =$	47.50				**{16}**	=(2/(SQRT(3)))*(SQRT(S31))*COS(S34/3)+A20	
39	$\sigma_2 =$	16.76				**{17}**	=(2/SQRT(3))*(SQRT(B31))*(COS((B34/3)-(2*(PI()/3))))+A20	
40	$\sigma_3 =$	8.53				**{18}**	=(2/SQRT(3))*(SQRT(B31))*(COS((B34/3)+(2*(PI()/3))))+A20	
41								
42	**Principal Stress Matrix**						**Principal Stress Matrix**	
43								
44	47.50	0	0			**{19}**	=B38 =0 =0	
45	0	16.76	0				=0 =B39 =0	
46	0	0	8.53				=0 =0 =B40	
47								
48	**Stress Invariants**						**Stress Invariants**	
49								
50	I_1	72.79				**{4}**	=A44+B45+C46	
51	I_2	1344.32				**{5}**	=A44*B45+B45*C46+C44*A44-B44^2-C45^2-C44^2	
52	I_3	6791.51				**{6}**	=A44*B45*C46+2*B44*C45*C46-(A44*(C45^2)+B46*(C44^2)+C46*(B44^2))	
53								

Subtract Principals from Normal Stresses in turn

	A	B	C	D	E	F				
54	**Subtract Principals from Normal Stresses in turn**						**Subtract Principals from Normal Stresses in turn**			
55										
56	σ_1									
57										
58	-25.49	14.16	0.14			**{20}**	=A15-B39	=B15	=C15	
59	14.16	-9.90	8.27				=A16	=B16-B39	=C16	
60	0.14	8.27	-34.32				=A17	=B17	=C17-B39	
61										
62	σ_2									
63										
64	5.25	14.16	0.14			**{20}**	=A15-B40	=B15	=C15	
65	14.16	20.84	8.27				=A16	=B16-B40	=C16	
66	0.14	8.27	-3.58				=A17	=B17	=C16-SB0	
67										
68	σ_3									
69										
70	13.48	14.16	0.14			**{20}**	=A15-B41	=B15	=C15	
71	14.16	29.07	8.27				=A16	=B16-B41	=C16	
72	0.14	8.27	4.65				=A17	=B17	=C17-B41	
73										

Calculate 2 x 2 Matrix Determinant

	A	B	C	D	E	F			
74	**Calculate 2 x 2 Matrix Determinant**						**Calculate 2 x 2 Matrix Determinant**		
75									
76	σ_1		σ_2		σ_3		σ_1	σ_2	σ_3
77									
78	271.26		-143.04		66.77	**{21}**	=(B59*C60)-(B60*C59)	=(B65*C66)-(B66*C65)	=(B71*C72)-(B72*C71)
79	487.09		51.88		-64.68	**{22}**	=(B60*C58)-(B58*C60)	=(B66*C64)-(B64*C66)	=(B72*C70)-(B70*C72)
80	118.49		114.19		113.03	**{23}**	=(B58*C59)-(B59*C58)	=(B64*C65)-(B65*C64)	=(B70*C71)-(B71*C70)
81									
82	569.99		190.24		146.35	**{24}**	=SQRT(A78^2+A79^2+A80^2)	=SQRT(C78^2+C79^2+C80^2)	=SQRT(E78^2+E79^2+E80^2)
83									
84	0.48		-0.75		0.46	**{25}**	=A78/A82	=C78/C82	=E78/E82
85	0.85		0.27		-0.44	**{26}**	=A79/A82	=C79/C82	=E79/E82
86	0.21		0.60		0.77	**{27}**	=A80/A82	=C80/C82	=E80/E82
87									

Calculate Plunge and Trend and Correct to Positive

	A	B	C	D	E	F		
88	**Calculate Plunge and Trend and Correct to Positive**						**Calculate Plunge and Trend and Correct to Positive**	
89								
90	σ_1 Plunge		12.00		12.00	**{28}**	=DEGREES(ATAN(A86/SQRT((A84^2)+(A85^2))))	=C90
91	σ_1 Trend		060.89		60.89	**{29}**	=DEGREES(ATAN2(A84,A85))	=IF(C91<0, C91+360,C91)
92	σ_2 Plunge		36.89		36.89	**{30}**	=DEGREES(ATAN(C86/SQRT((C84^2)+(C85^2))))	=C92
93	σ_2 Trend		160.06		160.06	**{31}**	=DEGREES(ATAN2(C84,C85))	=IF(C93<0, C93+360,C93)
94	σ_3 Plunge		50.56		50.56	**{32}**	=DEGREES(ATAN(E86/SQRT((E84^2)+(E85^2))))	=C94
95	σ_3 Trend		-044.09		315.91	**{33}**	=DEGREES(ATAN2(E84,E85))	=IF(C95<0, C95+360,C95)
96								

Final Result

	A	B	C	D	E	F			
97	**Final Result**						**Final Result**		
98									
99		Mag.	Trend	Plunge					
100		(MPa)	(°)	(°)					
101	σ_1 =	47.50	060.89	12.00			=B39	=E91	=E90
102	σ_2 =	16.76	160.06	36.89			=B39	=E93	=E92
103	σ_3 =	8.53	315.91	50.56			=B40	=E95	=E94
104									

Determination of principal stresses from component stresses

	A	B	C	D	E	F
1	**Determination of Component Stresses from Principal Stresses**					
2						
3	**Input**					
4						
5	**Principal Stresses**					
6						
7		**Magnitude**	**Trend**	**Plunge**		
8	σ₁	47.50	60.89	12.00			*(1)* Input in blue cells only. Solution in red cells.
9	σ₂	16.76	160.06	36.89		
10	σ₃	8.53	315.91	50.56		
11						
12	**Principal Stress Matrix**						**Principal Stress Matrix**
13						
14	47.50	0	0			{34}
15	0	16.76	0			
16	0	0	8.53			
17						
18	**Convert trend and plunge to radians**						**Convert trend and plunge to radians**
19						
20	**Trend**	**Plunge**				
21	1.06	0.21				
22	2.79	0.64				
23	5.51	0.88				
24						
25	**Stress Transformation**						**Transformation to new coordinate system**
26						
27	**Rotation Matrix [A]**						**Rotation Matrix [A]**
28						
29	0.48	0.85	0.21			{36}
30	-0.75	0.27	0.60			
31	0.46	-0.44	0.77			
32						
33	**Transposed Rotation Matrix [A]⁻¹**						**Transposed Rotation Matrix [A]⁻¹**
34						
35	0.48	-0.75	0.46			{37}
36	0.85	0.27	-0.44			
37	0.21	0.60	0.77			
38						
39	**Component Stress Tensor ={10}x{12}x{13}**						**Rotated Stress Tensor**
40						
41	22.01	14.16	0.14			{38}
42	14.16	37.60	8.27			
43	0.14	8.27	13.18			
44						
45	**Stress Invariants**						**Stress Invariants**
46						
47	I₁	72.79				{4}
48	I₂	1344.32				{5}
49	I₃	6791.51				{6}
50						

Formulas (column H):

Principal Stress Matrix:
- Row 14: =B8   =0   =0
- Row 15: =0   =B9   =0
- Row 16: =0   =0   =B10

Convert trend and plunge to radians:
- Row 21: =RADIANS(C8)   =RADIANS(D8)
- Row 22: =RADIANS(C9)   =RADIANS(D9)
- Row 23: =RADIANS(C10)   =RADIANS(D10)

Rotation Matrix [A]:
- Row 29: =COS(B21)*COS(A21)   =COS(B21)*SIN(A21)   =SIN(B21)
- Row 30: =COS(B22)*COS(A22)   =COS(B22)*SIN(A22)   =SIN(B22)
- Row 31: =COS(B23)*COS(A23)   =COS(B23)*SIN(A23)   =SIN(B23)

Transposed Rotation Matrix [A]⁻¹:
- Row 35: =A29   =A30   =A31
- Row 36: =B29   =B30   =B31
- Row 37: =C29   =C30   =C31

Rotated Stress Tensor:
- Row 41: =MMULT(A35:C37,MMULT(A14:C16,A29:C31))

Stress Invariants:
- Row 47: =A41+B42+C43
- Row 48: =A41*B42+B42*C43+C41*A41-B41^2-C42^2-C41^2
- Row 49: =A41*B42*C43+2*B41*C42*C43-(A41*(C42^2)+B43*(C41^2)+C43*(B41^2))

A review of dynamic energy-absorbing cable bolts

M Holden[1], J Liu[2], S Akdag[3], D Foster[4], C Zhang[5], J Oh[6], H L Ramandi[7], P Craig[8] and S Saydam[9]

1. R&D Manager, Jennmar Australia, Sydney NSW 2567. Email: mholden@jennnmar.com.au
2. PhD candidate, Minerals and Energy Resources Engineering, UNSW Sydney NSW 2052. Email: jia.liu2@student.unsw.edu.au
3. Post-doctoral Researcher, Minerals and Energy Resources Engineering, UNSW Sydney NSW 2052. Email: s.akdag@unsw.edu.au
4. Research Engineer, Minerals and Energy Resources Engineering, UNSW Sydney NSW 2052. Email: daniel.foster@unsw.edu.au
5. Senior Lecturer, Minerals and Energy Resources Engineering, UNSW Sydney NSW 2052. Email: chengguo.zhang@unsw.edu.au
6. Associate Professor, Minerals and Energy Resources Engineering, UNSW Sydney NSW 2052. Email: joung.oh@unsw.edu.au
7. Senior Lecturer, Minerals and Energy Resources Engineering, UNSW Sydney NSW 2052. Email: h.lameiramandi@unsw.edu.au
8. National Manager, Jennmar Australia, Sydney NSW 2567. Email: pcraig@jennnmar.com.au
9. Professor, Minerals and Energy Resources Engineering, UNSW Sydney NSW 2052. Email: s.saydam@unsw.edu.au

INTRODUCTION

High stress in rock masses can cause significant instability problems such as squeezing deformation in soft rock and rock bursts in hard rock. The support system applied in burst-prone areas in high-stress conditions is required to be able to carry high load and accommodate large deformation of the rock mass without experiencing any serious damage. Yielding support systems are promising to provide support for both squeezing and burst-prone rock mass encountered in mining or tunnelling at depth. They are ideally strong and stiff initially and then ductile after yielding (Potvin and Hadjigeorgiou, 2020). With respect to support design, a ground support system has to create a safe working environment under both static and dynamic loading conditions by providing the functions of reinforcing, retaining, holding and connecting elements (Cai and Kasier, 2018).

Rigid rock bolts and cable bolts perform reinforcing and holding functions of a ground support system. In highly fractured ground or with large excavation spans (eg at roadway intersections or in caverns), unstable ground depth can exceed the length of typical rigid rock bolts (ie greater than ~3.0 m). In such cases, flexible cable bolts are needed to tie the reinforced and retained rock mass back to deeper and more stable rock. The flexibility of cable bolts allows anchor lengths greater than the tunnel opening that would otherwise restrict rigid bolts. Cable bolts also offer higher strength to weight ratio, with tensile strengths 2–3 times that of standard rebar bolts. This high strength comes at the cost of lower strain tolerance, typically around 5–7 per cent at break. Despite the lower strain tolerance, cable bolts are often used as dynamic support in demanding burst-prone ground conditions. The lower strain tolerance is compensated by allowing sufficient free length for stretching or incorporating a yielding device. There are a number of dynamic cable bolts available on the market and a number of testing campaigns have been undertaken to quantify the dynamic performance of these cable bolts. This paper reviews the existing range of dynamic cable bolts and discusses the potential areas for improvement and further research.

REVIEW OF DYNAMIC CABLE BOLTS

There are a number of dynamic cable bolts available on the market today and others that are currently in development. Similar to rigid rock bolts, these cables utilise one or a combination of mechanisms to dissipate excess energy in a rock burst event, including shank stretching, extrusion and localised structural deformation (Sharifzadeh et al, 2020).

Dynamic cable bolts that rely on stretching of the strand are the simplest and most cost-effective. These include debonded single or multi-strand cables in various sizes, most commonly 15.2 mm. Debonding is achieved with a plastic tube that partially covers the strand to decouple it from the ground. A recently cable bolt developed in China called the constant-resistance energy absorbing

cable (CREAC), uses a new grade of steel wire with higher elongation properties to improve energy-absorption properties (Wang *et al,* 2022). The resultant cable was shown to achieve 16 per cent elongation at break, which is ~2.5 times greater than a standard cable.

There are also a number of dynamic cable bolts that utilise an extrusion-type yielding device to dissipate energy. For instance, the Garford Dynamic Cable Bolt, which is a 15.2 mm debonded compact strand that includes a device which works by pulling the toe end of the cable through an anchor that generates a stick-slip behaviour to dissipate energy. The Garford cable can absorb up to 30 kJ of energy at 300 mm displacement (Garford, 2014). The CRLD (constant-resistance, large-elongation) cable anchor, developed by Manchao He and colleagues in China (He *et al,* 2021), is another cable bolt that incorporates an extrusion-type yielding device. The device works by pulling a wedge through a steel tube that generates stick-slip phenomena, similar to the Garford dynamic cable bolt. The issue with extrusion-type yielding devices is the inconsistent nature of the stick-slip mechanism, which results in high variation in energy absorption. In addition, the performance of this type of mechanism is highly dependent strain rate.

The Duracable, developed by Duraset in conjunction with SRK Consulting (Ortlepp *et al,* 2005), is a dynamic cable bolt that uses frictional sliding of the strand through a steel tube to dissipate energy. The steel tube is deformed into a sinusoidal wave shape after assembly on the cable. When installed, the cable is fully encapsulated in grout locking the shape tube. Any ground movement causes the cable to frictional slide through the 'wavy' tube, which dissipates energy as heat.

Majority of cable bolt designs utilise a barrel and wedge (B&W) end fitting to terminate the cable at the surface plate. Impact loading B&W's can cause it to failure prematurely. Bulbing near the collar or an adjacent compliant device, such as a yield tube (Jennmar, 2021; Roberts and Faulkner, 2019), can help prevent over-stressing the B&W under impulse loading.

AREAS OF IMPROVEMENT and FURTHER RESEARCH

The majority of laboratory-based dynamic testing has been completed on cable bolts up to 3.5 m in length (Villaescusa *et al,* 2010). However, cable bolts are commonly supplied and installed in lengths greater than 5.0 m. As a result, the dynamic performance of longer length cable bolts tends to be extrapolated from dynamic test conducted on shorter length versions or inferred from full-scale static tests that are simpler to perform. There could be benefit to upgrading or building a new dynamic test facility that can more confidently quantify the dynamic performance of longer length bolts.

Furthermore, there is a lack of dynamic testing data on a range of high-capacity solid and hollow cable bolts, with breaking strengths in excess of 70 t. Dynamic version of these cables could offer opportunities to improve development rates and reduce cost by either reducing bolting densities (that is, assuming a larger bolt spacing does not affect system integrity) or increasing installation speed. Mechanised installation of hollow cable bolts with a torque-tension end fitting, such as the 70T TEX cable bolt (Jennmar, 2022) has dramatically improved development times in coal mining. With further development, such cables could be adapted for hard rock applications and potentially offer similar development rate benefits as experienced in coal.

Sharifzadeh *et al* (2020) highlighted that currently available rock bolts struggle to meet the reaction pressure requirement for 'extremely high' dynamic demand (energy absorption: >35 kJ.m^{-2}, reaction pressure: >400 kPa, surface displacement: >300 mm) and suggested that cable bolt reinforcement might offer a solution. Continued development of dynamic cable bolts, particularly variation with higher tensile capacity, will be important as future mining operations progress to ever-greater depths, and rock burst conditions become more prevalent and demanding.

Furthermore, the torque-tension end fittings mentioned previously are more rigidly affixed to the cable, which can overcome shortcomings with standard B&W's. B&W's require sliding movement of the wedge within the barrel to effectively clamp onto the cable and engage the full capacity of the strand. Interruption of this sliding mechanism caused by corrosion (Hassel *et al,* 2006) and shock loading from dynamic impulses can lead to premature failure of the B&W. A rigidly affixed end fitting is not susceptible to same type of failure. However, there is currently no dynamic performance data on these types of fittings.

ACKNOWLEDGEMENTS

REFERENCES

Cai, M and Kaiser, P K, 2018. *Rockburst support reference book, Rockburst phenomenon and support characteristics,* MIRARCO—Mining Innovation, Laurentian University, Sudbury [Preprint].

De Zoysa, U and Manoj, H, 2018. Dynamic Tested Cement Encapsulated Cablebolt Systems, research report for Oyu Tolgoi LLC, Western Australian School of Mines, Kalgoorlie.

Garford, 2014. Garford Dynamic Cable Bolt, website http://www.garforduk.com/garford-dynamic-cable-bolts.html, accessed: 27 September 2022.

Hassel, R, Villaescusa, E and Thompson, A, 2006. Testing and evaluation of corrosion on cable bolt anchors, *Proceedings from 41st US Rock Mechanics Symposium, '50 Years of Rock Mechanics – Landmarks and Future Challenges'*, Golden, Colorado.

He, M, Wang, Q and Wu, Q, 2021. Innovation and future of mining rock mechanics, *Journal of Rock Mechanics and Geotechnical Engineering*, 13(1):1–21.

Hutchinson, D J and Diederichs, MS, 1996. *Cablebolting in Underground Mines*, Bi Tech Publishers, Richmond.

Jennmar, 2021. Product data sheet on yield tube, https://www.jennmar.com.au/assets/Uploads/Documents/Hard-Rock-Catalogue-Feb-2021/Hard-Rock-V9–48.pdf

Jennmar, 2022. Product data sheet on 31 mm 70T SUMO TEX cable, https://www.jennmar.com.au/assets/Uploads/Apr-2022-Coal-Product-Updates/31 mm-70T-SUMO-TEX-Cable.pdf

Ortlepp, W D, Human, L, Erasmus, P N and Dawe, S, 2005. Static and dynamic load displacement properties of a yielding cable anchor—determined in a novel testing device, *6th International Symposium on Rockburst and Seismicity in Mines*, Perth, Australia, pp. 529–534.

Potvin, Y and Hadjigeorgiou, J, 2020. *Ground support for underground mines*, Australian Centre for Geomechanics.

Roberts, T and Faulkner, D, 2019. Polyester resin injection of dynamic resin and cable bolting systems to improve development efficiency, in J Hadjigeorgiou and M Hudyma (eds), *Ground Support 2019: Proceedings of the Ninth International Symposium on Ground Support in Mining and Underground Construction*, Australian Centre for Geomechanics, Perth, pp. 505–518.

Sharifzadeh, M, Lou, J and Crompton, B, 2020. Dynamic performance of energy-absorbing rockbolts based on laboratory test results, Part I: evolution, deformation mechanisms, dynamic performance and classification, *Tunnell Underground Space Technol*, 105:103510.

Villaescusa, E, Thompson, A, Player, J and Morton, E, 2010. Dynamic testing of ground control systems, MERIWA report, no. 287, Project M349A, Minerals and Energy Research Institute of Western Australia, Perth.

Wang, Q, Xu, S, Xin, Z, He, M, Wei, H and Jiang, B, 2022. Mechanical properties and field application of constant resistance energy-absorbing anchor cable, *Tunnelling and Underground Space Technology,* 125:104526. 10.1016/j.tust.2022.104526.

Assessing corrosion of reinforcement on a large scale

E Jones[1], R Hassell[2] and N Power[3]

1. Principal Study Manager Geotechnical, MineGeoTech, Perth WA 6000.
   Email: emmajones@minegeotech.com.au
2. Manager Operations and Technical Services, Mining and Civil Integrity Testing, Albany WA
   6330. Email: Rhett.hassell@minecivilit.com.au
3. Engineering Geologist, MineGeoTech, Perth WA 6000.
   Email: nadiapower@minegeotech.com.au

ABSTRACT

Wiluna Mining Corporation are progressively re-entering the old Wiluna underground mining complex.

The existing underground was abandoned in 2013 by previous owners and left to flood with water levels reaching above the East Pit portal and Happy Jack Pit portal and up to 300 m below surface in the Bulletin underground. Re-entering the mine commenced in 2017 with dewatering of the Bulletin decline.

The underground development had been previously supported with friction bolts, with weld mesh in places. Until mid-2021 rehabilitation requirements were based on an external visual inspection of the installed ground support scheme. However, several incidents involving falls of ground due to corroded bolts have occurred during this time, showing that this approach was inadequate. The challenge the operation faced was should the entire decline be rehabilitated, the implication being not only a large rehabilitation cost but also the impact of severe delays to the mining schedule. The question was asked can the operation better understand the level of corrosion damage and potentially optimise rehabilitation requirements.

A proposal to use a systematic approach to assess corrosion by environmental condition mapping, visual external corrosion assessment, and internal corrosion assessment via borehole camera inspections was provided and accepted by Wiluna Mining Corporation.

The objective of this work was to produce a three-dimensional map showing the degree of corrosion on the reinforcement systems in the capital infrastructure, this would then be used to risk assess and prioritise rehabilitation requirements.

This paper summarises the approach, methodology and results that provided the Wiluna mine planning team with information to enable planning of resources and budget to justify priorities of rehabilitation.

INTRODUCTION

Wiluna Mining Corporation's (WMC) operation is located approximately 730 m north-east of Perth, Western Australia.

The operation has a reported Ore Reserve of 36.8 Mt at 1.2 g/t for 1.42 Moz contained gold (WMC, 2022). The operation has transitioned from a free-milling operation to a sulfide ore operation, producing gold in concentrate and dore from tailings retreatment.

The historic Wiluna mining area has been mined for over 150 years. Apex Minerals undertook completed underground mining from 2007 to 2013. When mining was abandoned in 2013, the underground excavations were flooded.

WMC purchased the Wiluna Gold Mine in January 2014. In 2016 the company completed a Feasibility study for the underground mine, commencing underground mining with the re-entering of the old workings in 2017.

GEOLOGICAL SETTING

The underground mine is dominated by tholeiitic basalts and dolerites, komatiitic basalts and high Mg basalts, and other minor felsic volcanics, sediments or intrusions. There are two styles of

mineralisation, free-milling reef gold and sulfide hosted deposits. The local geology is not thought to influence the ground support corrosion with no evidence of higher rate of corrosion due to alteration minerals such as sulfides. However, large-scale structures are observed to provide a conduit for groundwater flow into the underground excavations.

MECHANICS OF GROUND SUPPORT CORROSION

The ground support corrosion rate is generally caused by the local atmospheric or groundwater conditions. The Wiluna Gold Mine has an additional environmental criterion being previously submerged sections of the mine.

The main types of corrosion observed on underground reinforcement systems include uniform and localised corrosion in the form of pitting.

Uniform corrosion occurs when the anodic and cathodic areas of the metal surface change position continually, resulting in regular removal of the metal from the surface. Pitting corrosion is the highly selective attack of passive metals at defects in the passive oxide layer. The corrosion attack is in the form of pits, usually covered by corrosion products or remnants of the original protective layer. Pitting is considered more dangerous than uniform corrosion because it is difficult to detect, predict and design against.

BACKGROUND

In 2015, prior to commencing mining activities, accessible declines were inspected to visually assess the state of existing ground support scheme against rock mass condition. The work concluded that isolated areas required rehabilitation relating to deterioration (ground relaxation) and damp areas.

On 30 June 2020, a fall of ground occurred in the Bulletin Decline at the 1205 mRL level. The main causal factor was determined as corroded ground support. A recommendation from the investigation was to re-assess the entire decline against the current ground support scheme standards and prioritise rehabilitation based on advancement of corrosion and personnel exposure. Once all poor-quality areas have been rehabilitated the intervening portions would be re-bolted and meshed progressively (WMC, 2020).

In June 2021, a review of the corrosion rehabilitation work to date was completed by MineGeoTech. The review found that management of the ground support corrosion damage risk and subsequent rehabilitation had significant gaps. The previous rockfalls in the decline showed there was a high level of risk to personnel, and the mining plan if resources were taken away from orebody development and re-directed to decline rehabilitation. A more rigorous and systematic approach was required.

Location of the assessment

Nearly 6000 m of decline development was to be assessed. A balance is required to achieve a suitable data density but also complete the work in a time effective manner. The assessment was separated into two sections:

1. A detailed corrosion assessment in the Bulletin Decline (approximately 1000 m) that was not historically flooded but exposed to still, humid air. Individual corrosion assessment was completed every 5–10 m. Increased inspections where undertaken where changes in the corrosion damage profile were seen along the drive.

2. A less detailed corrosion assessment in the Golden Age Decline (approximately 4700 m). This development was underwater until dewatering commenced for re-entry by WMC. It tended to have a more homogeneous ground support corrosion damage. As such inspections were completed every 50–100 m of drive length.

The ground support scheme slightly varied throughout the decline. Most of the scheme comprised of 47 mm diameter friction bolts with lengths of 2.2 m and 2.4 m. These bolts have a nominal thickness of 3.2 mm and are particularly susceptible to corrosion damage. Some intersections had cable bolts in addition to this. No surface support was installed.

Areas of more recent rehabilitation comprised of 47 mm diameter friction bolts and galvanised weld mesh. This was only present in small sections, often in intersections.

CORROSION ASSESSMENT PROCESS

Corrosion of ground support systems in mines is not uncommon, however the effect on performance, residual capacity and lifespan is not well understood. Hassell *et al* (2004) and Hassell (2007) presented a process of what data can be collected and how to use this to identify severity of corrosion.

The process involves environmental condition mapping of the underground excavations in combination with qualitative and quantitative assessments of the condition of the reinforcement and support systems.

Corrosion inspection results

A total of 225 internal friction bolt inspections were completed. An example of how the corrosion classification results were collated is shown in Figure 1. They are coloured by the internal observed corrosion damage with reds being more highly corroded and blues have low corrosion. Table 1 is a summary of the internal assessment results.
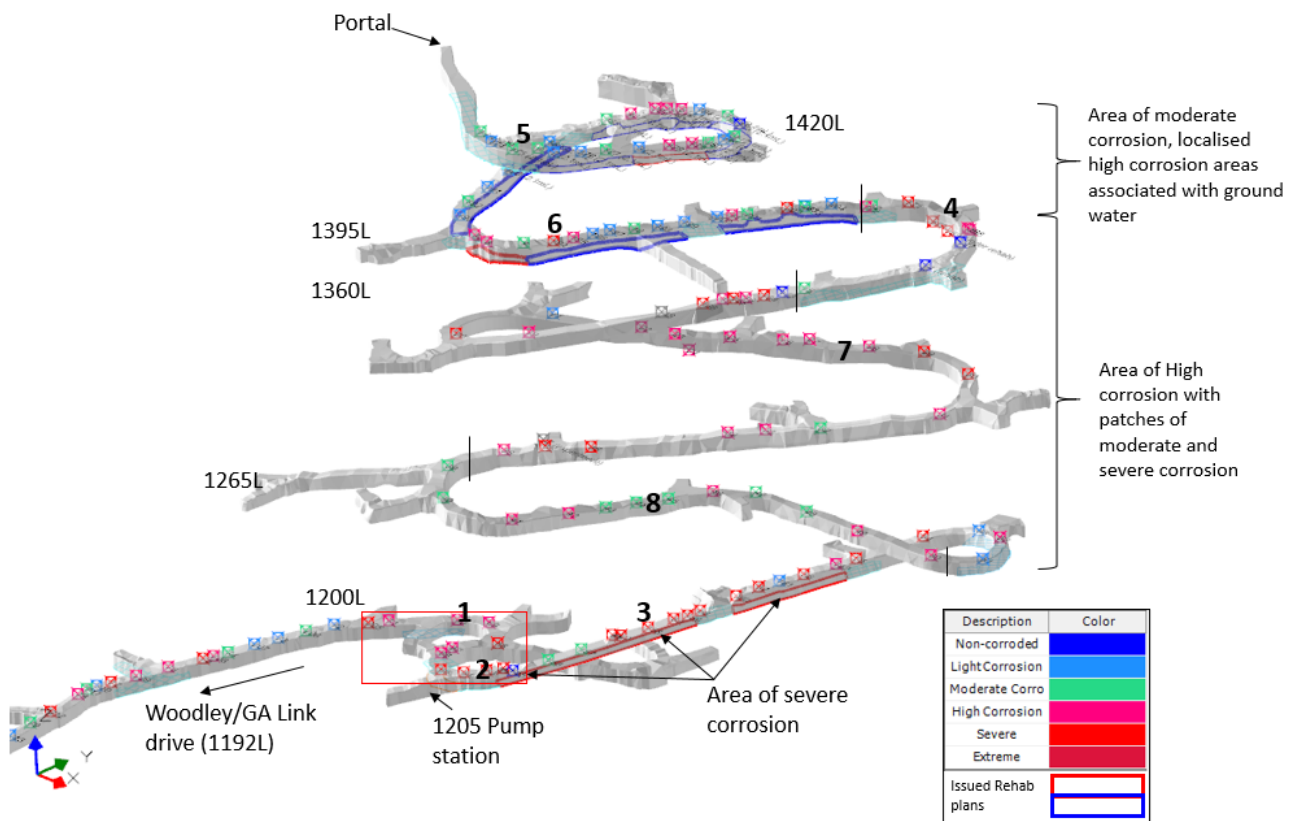

FIG 1 – Bulletin decline corrosion map, looking north-west.

TABLE 1

Summary of internal friction bolt corrosion assessment.

Decline	Number of bolts inspected	Number lightly corroded	Number of moderately corroded	Number of high to severely corroded
Bulletin Decline	122	29 (32%)	22 (18%)	61 (50%)
Bulletin-Woodley Link	54	27 (50%)	8 (15%)	19 (35%)
Golden Age	49	22 (45%)	8 (16%)	19 (29%)

Where mesh was present at a bolt test site, this was measured for average wire diameter. Fifty measurements were taken of which five (10 per cent) had an estimated remaining capacity less than 40 kN (40 kN is the assumed initial capacity).

Underground observations made during the exercise concluded:

- All bolts internally inspected had light corrosion or higher.

- The Bulletin decline has several major structures that intersect with associated presence of water which has produced unfavourable conditions and has potentially exacerbated corrosion levels.

- The Bulletin–Woodley and Calais-Golden Age decline link has been historically fully underwater but is presently predominantly dry. Corrosion mapping showed that there are fewer bolts that are high to severely corroded compared to the Bulletin decline.

- Considering the Golden Age decline was underwater most bolts and mesh are still serviceable apart from localised areas that have active water flow.

RISK ASSESSMENT PROCESS TO DETERMINE REHABILITATION

To apply the results of the corrosion assessment to rehabilitation requirements, the internal corrosion severity is used as a guide to determine the overall serviceability of the bolt, as this appears to be the main influence during failure at the mine. However, consideration to surface fixtures is incorporated where internal corrosion is zero to light.

To determine how corrosion influences friction bolt serviceability, two failure modes are considered: loss of frictional resistance and reduction in tensile capacity.

While the visual assessment has limitations, it can be used to guide friction bolt serviceability and rehabilitation requirements. The following was used to determine serviceability of the friction bolt at the mine (Hassell, 2021):

- **Non-corroded to light corrosion**: Corrosion damage causing premature bolt failure would not be expected.

- **Moderate corrosion**: Corrosion damage causing premature bolt failure is unlikely. However, there is an increased risk as corrosion products are more pronounced and they could be hiding deeper pitting corrosion.

- **High to Severe corrosion**: There would be concerns with corrosion damage causing premature bolt failure.

Where the corrosion classification was high to severe, the bolt was deemed to require rehabilitation at Wiluna.

Risk assessment to prioritise rehabilitation

To determine what level of corrosion required rehabilitation and then priority of rehabilitation, a risk assessment using the operation's risk matrix was utilised.

The corrosion maps were used to select areas where there were common corrosion level and environmental factors. These areas were then risk assessed. Table 2 is a summary of the results of this exercise.

TABLE 2

Corrosion and risk assessment summary.

Section ID	Mine	Level From	Level To	Meters of rehab	Internal bolt corrosion	Water presence	Structure presence	Risk matrix	Risk
1	Bulletin	1200	-	125	Severe	Damp	Yes	13 (H)	High
2	Bulletin	1200	1205	23	High	Damp	Yes	13 (H)	High
3	Bulletin	1205	1220	124	High	Damp	Yes	13 (H)	High
4	Bulletin	1415	1420	250	Moderate	Damp	Yes	9 (M)	Medium
5	Bulletin	1415	1375	224	High	Damp	Yes	9 (M)	Medium
6	Bulletin	1375	1364	54	Severe	No Flow	Yes	13 (H)	High
7	Bulletin	1357	1278	580	High	Damp	Yes	9 (M)	Medium
8	Bulletin	1278	1242	260	High	Damp	Yes	9 (M)	Medium
9	Bulletin	1200	1160	300	High	No Flow		9 (M)	Medium
10	Bulletin	1160	-	0	Light	No Flow		5 (L)	Low
11	Bulletin	1130	1115	175	High	No Flow		9 (M)	Medium
12	Golden Age	1094	1087	100	Severe	No Flow		8 (M)	Medium
13	Golden Age	1015	1005	130	Severe	No Flow		8 (M)	Medium
14	Golden Age	940	920	115	High	Wet		8 (M)	Medium
15	Golden Age	865	857	55	Severe	No Flow		8 (M)	Medium

The corrosion rehabilitaiton project successfully achieved its it objectives:

- Classify and map the levels of corrosion damage to the ground support in the decline.
- Quantify and justify the scale of rehabilitaiton and requirements for ongoing monitoring and thereby mitigating the risk of the mine plan.
- Risk assess to pritorise rehabilitation and monitoring.
- Develop procedures to support this work to ensure consistent approach with identification and classification.
- Increased the knowledge at the operation regarding the risk of corrosion thereby impoving mine safety to personnel.

ACKNOWLEDGEMENTS

REFERENCES

Hassell, R C, 2007. *Corrosion of rock reinforcement in underground excavations*, PhD thesis, Curtin University of Technology, Kalgoorlie.

Hassell, R C, 2021. Wiluna Mining Corrosion Report, Mining and Civil Integrity Testing (MCIT) External Consultant Report, 21 July 2021.

Hassell, R C, Villaescusa, E, Thomson, A G and Kinsella, B, 2004. Corrosion Assessment of ground support systems, in E Villaescusa and Y Potvin, *Proceedings of the Fifth International Symposium on Ground Support: Ground support in Mining and Underground Construction*, pp 990–1013 (A A Balkema: Rotterdam).

Wiluna Mining Corporation, 2020. Internal memorandum regarding outcomes of the Bulletin 1205L fall of ground.

Wiluna Mining Corporation, 2022. ASX Announcement 12 April 2022 Ore Reserves Update and Feasibility Progress Report, https://wilunamining.com.au/investors/announcements/

Support structure design for rock burst damage restraint initiated by a low-intensity seismic wave

E Kabwe[1] and M Karakus[2]

1. Senior Geomechanics Engineer, Beta-Hunt Underground Operations, Kambalda WA 6442. Email: kabweeugie@yahoo.com
2. Professor, University of Adelaide, Adelaide SA 5000. Email: murat.karakus@adelaide.edu.au

ABSTRACT

Deep hard rock underground mines tend to experience high stress as such drives exhibit dynamic responses attributed to a rock burst variant (strainburst). This dynamic behaviour is difficult to predict, and every effort is made to devise the appropriate dynamic support system for its associated failure restraint. This paper outlines the back analysis and the support scheme design for an underground decline that exhibited damage from a dynamic strainburst occurrence. It employs a decline section that experienced a dynamically loaded strainburst that initiated rock fragment ejections. The procedure involves a preliminary structural analysis, a seismic intensity measure, and a rock mass simulation to determine the static stress concentration and ground support system response. The numerical simulation is conducted in FLAC3D which employs the advanced strain-softening IMASS constitutive model governed by two Hoek–Brown (HB) bounding yield surfaces. To account for the post-peak brittleness response associated with strainburst the plastic strain multiplier (ε_{crit}) is adjusted to $0.0 < \varepsilon_{crit} < 1.0$. The back-analysis shows that the occurrence was initiated by a low-intensity seismic wave that superimposed an extra stress component to the initial static stress which triggered rock fragment ejections. Additionally, the appropriate support scheme comprised of Weldmesh, Fibrecrete, static (split set) and yieldable (Kinloc) reinforcements is recommended and implemented. Thereafter, the bolt's efficiency is evaluated based on the axial force and elongation capacities and then compared with the published bolt performance data. The evaluation results show that the maximum bolt axial force (0.1 per cent) and elongation (0.006 per cent) are below the designed capacity and rupture strain.

INTRODUCTION

Has surface mineral orebodies depleted mining has now shifted to deeper levels of underground mining at such depths major challenges attributed to rock burst-related occurrences are exhibited (Cai, 2017, 2019). Rock bursts and associated occurrences are usually exhibited in deep mines, as the mining depth increases, stress-induced rock fractures become a frequent occurrence in many cases coupled with violent rock ejection from tunnel faces. Such occurrence brings about production delays, due to rehabilitation plans, clean-ups, and a high possibility of tunnel collapse as well as fatalities. Hence, immediate dynamic support system installation in burst-prone tunnels is required to restrain its associated rock mass dilation. In most mines, empirical, analytical, and numerical tools are employed to predict rock burst and design the appropriate support system to restrain rock burst failure. However, these tools cannot predict the mechanism with sufficient accuracy in terms of its occurrence, location, and intensity. the most reliable way is through the Institute of Mine Seismology (IMS) system capable of capturing real-time seismic activity's intensity, time, and location of occurrence. Before dynamic support design and installation in tunnels, it is important to fully understand this dynamic mechanism. Several mining experts have gained knowledge and understanding through observation experience. A common dynamic support design procedure considers the energy dissipation capacity of a proposed tunnel support system relative to the falling rock kinetic energy demand. In addition to this, back analysis of a real case of violent excavation failure provides insight into both ejection velocity and depth of rock mass failure. The information attained from this analysis is then employed to calculate the energy demand on the proposed ground support system. Therefore, this study serves as an example of a back analysis of an underground mine that experienced a rock burst event. Firstly, the rock burst dynamic mechanism and its examples are reviewed with a complete focus on strain burst. Secondly, measures to capture the energy dissipated from a seismic-triggered event and restrain excavation damage are discussed. Lastly, the appropriate integrated support system to restrain excavation damage for the case study is determined and implemented.

Rock burst mechanism

A rock burst is defined as violent damage to an excavation that occurs suddenly with energy dissipation and is often associated with seismic events (Ghorbani *et al*, 2020; Li *et al*, 2019; Zhai *et al*, 2020). Cook's (1965) earlier encounter and observation associated rock burst with seismicity and defined it as a subset of seismic events that lead to severe excavation damage. He further stated that all rock bursts are a result of seismic events but not all seismic events result in rock bursts. Further on, it was investigated and concluded that energy less than 100 kJ did not result in excavation damage due to rock burst but higher than 1.5 GJ resulted in rock burst. Ortlepp and Stacey (1994) further defined rock bursts as excavation damage resulting from seismic events. Ghorbani *et al* (2020) elaborate on the occurrence of rock burst as a product of stress redistribution after excavation. A rock burst is classified as either a strainburst or fault-slip burst, where a strain burst is more associated with the static stress concentration and redistribution around the excavation boundary. Damage from this mechanism can be either from rock ejections or not and it is exclusively related to the strain energy accumulation closer to the excavation or energy from a far-field seismic event. Strain energy accumulation is more pronounced in stiff, strong, and brittle rock masses. In that the stiffer the rock masses the more strain energy accumulation. whereas brittle is the rapid release of that stored energy violently. If the rock mass strength is associated with a high stiffness matrix and is highly brittle raises the elastic strain energy accumulation before failure. The strain burst is also characterised by the simultaneous occurrence of a burst and seismicity. On the other hand, a fault-slip burst is characterised by rock ejections due to a seismic trigger from a remote or far-field seismic source. It is more powerful than a strain burst and causes more damage to excavations and underground structures. Kaiser *et al* (1996) defined a rock burst as an occurrence around an excavation in a violent manner and associated it with a seismic event. They later classified rock burst as a self-initiated mechanism that involves static stress concentration exceeding the rock mass strength leading to violent failure and/or remotely triggered by a large seismic event. Li *et al* (2019) state that rock burst is defined as a dynamic rock mass reaction involving energy transition from static strain to fracture and kinetic energies during burst occurrence. They define rock ejection intensity as mainly dependent on the static stress concentration (strain burst) and seismically triggered (fault slip/seismic burst). Therefore, in this study, we adopt the definition of a strainburst as a violent failure of a rock mass around an excavation boundary caused by excessive un-fractured and partially fractured, brittle rock mass straining. That tends to occur when the tangential stress and differential stress are at their peak induced by excavation advance or triggered by a dynamic stress pulse from seismic waves of a large remote seismic event. Strainbursts are more common in underground mines and are classed as self-initiated, mining-induced, and seismically triggered (Cai *et al*, 2019). During tunnel excavation, the static stress redistribution leads to an increase in the tangential stress which cannot be high enough to cause a rock mass failure. In this case, a small seismic event superimposes an extra stress magnitude on the static stress concentration, in turn, triggers a strainburst (Figure 1).
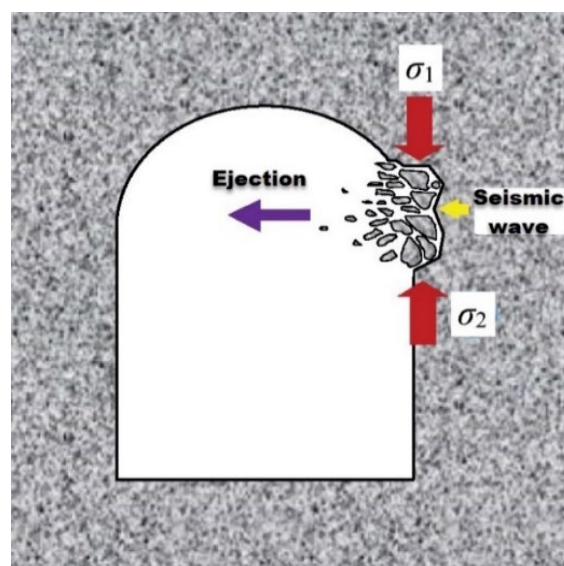

FIG 1 – Extra stress magnitude from a seismic wave.

However, its intensity is still dependent on the strain energy accumulation in the surrounding rock mass as such it is considered to belong to the strain burst category even though it is seismically triggered. Therefore, this paper's focus is on strainburst because of a remote seismic trigger from a recent seismic event and static stress concentration.

Ground control methods in the burst-prone excavations

An effort has been made to understand the rock burst mechanism to restrain it by employing the appropriate support structures (Li, 2017, 2021; Li *et al*, 2019). It has long been understood that the use of ductile reinforcements to restrain dynamic displacements due to rock burst is the most efficient one. Split set bolts were the first to be used for dynamic displacement restraint in South African mines in the early 1950s. However, these bolts cannot efficiently restrain the mechanism due to their low load-bearing capacity. Later, a fully encapsulated rebar bolt was also employed to restrain dynamic displacement but presented the same outcome (Li, 2021). After deduction of the limitations of these bolts, Cook and Ortlepp (1968) proposed a yieldable bolt hypothesis to help restrain damage from rock burst and the first yieldable rock bolt (cone bolt) was developed in the 1990s. It was a fully encapsulated bolt in a borehole with cementitious grout and was soon modified to use resin grout. Later a great number of energy-absorbing yieldable bolts were introduced: the Durabar (Ortlepp *et al*, 2001), the modified cone bolt (Simser, 2002), the Roofex yielding bolt (Charette and Plouffe, 2007; Galler *et al*, 2011), the Garford dynamic bolt (Varden *et al*, 2008), the Yield-Lok bolt (Wu and Oldsen, 2010), the D-bolt (Li, 2010) and the He bolt (He *et al*, 2014), to effectively control damage from rock burst these bolts need to be coupled with surface elements to form a firmly linked dynamic support system. Therefore, this section outlines the methodology employed to design the static and dynamic support systems for underground excavations. Cardinal aspects to consider in the design of minimum static or dynamic support standards for excavations are the support capacity and support demand. These aspects are associated with the loading mode, loading rate, load share in the integrated support system, support system displacement, and energy-absorbing capacity (Rahimi *et al*, 2020). The support capacity and demand are evaluated on the support element combination (integrated system), type of loads, displacements, and energy demand (dynamic loading conditions) (Kabwe *et al*, 2020c, 2020d). Rahimi *et al* (2020) presented a design procedure for the ground support system which caters to both static and dynamic rock mass conditions in underground mines.

The depth of failure and fracture, as well as support requirements under static and dynamic situations, were all important factors in this design. As well as a capacity assessment of the support system based on load, displacement, and energy absorption parameters. Underground mining, when the danger of seismic occurrences is low, uses ground support design based on static loading circumstances. Fibrecrete, rock bolts, and cable bolts are common ground support systems for static loading circumstances, whereas dynamic loading conditions include an absorbing kinetic energy component generated from seismic occurrences. Results from conducted drop-weight tests indicate that in hard rock mass about 25 per cent and 75 per cent of energy are absorbed by surface elements and reinforcements, respectively. Whereas in soft rock mass conditions the energy absorption by reinforcements and surface elements is 30 per cent and 70 per cent, respectively. In static ground conditions, distribution, and load transfer from the surface elements to reinforcements are not critical. However, in dynamic ground conditions, it is required to ensure the performance of ground support schemes. During the support design phase, all elements that impact the excavation's stability are scrutinised to comprehend the geotechnical environment and estimate the long-term stress changes that may occur within the rock mass around the excavation. Every effort is taken to comprehend and identify potential failure mechanisms, as well as to minimise them by correct design, mining sequencing, or alternate support methods and tactics. The factors that must be considered before any excavation design are as follows:

1. The design must be based on good geotechnical principles to preserve the stability of relevant excavations.

2. Identifying potential failure mechanisms along the excavation backs, sidewalls, and face.

3. The support system performance criteria consider the maximum loading capacity and energy absorption capacity.

4. The excavation's design life, as well as the detection of any actual or prospective rock burst/seismicity or static stress concentration.

When excavation sequencing is determined as critical for ground control, it must be specified as part of the design and cannot be changed unless approved. Furthermore, mining excavation techniques and processes must be planned to avoid uncontrolled instabilities, either locally or regionally, and large departures from design must be recorded throughout the mining. Any significant deviation from the original design must be re-evaluated to establish the impact on local or regional stability, and appropriate mitigations must be incorporated to manage this change.

THE CASE STUDY

The case study employs an Australian underground mine operating at a depth of 500 m, its operation is focused on a longhole open stopping (LHOS) method subjected to high stress. the operation consists of a pre-existing open pit and development extends up to the 1095 decline where the strainburst occurred (Figure 2). It is in a mining complex that contains several high-grade gold deposits from the Western Australian goldfields. Before the commencement of its underground mining operations, material extraction was conducted from two adjacent pits (Northern and Southern pits). The northern pit was mined out to a depth of 64 m while the southern pit was to a depth of 30 m. Later, the southern pit was backfilled with waste rock extracted from the northern pit.
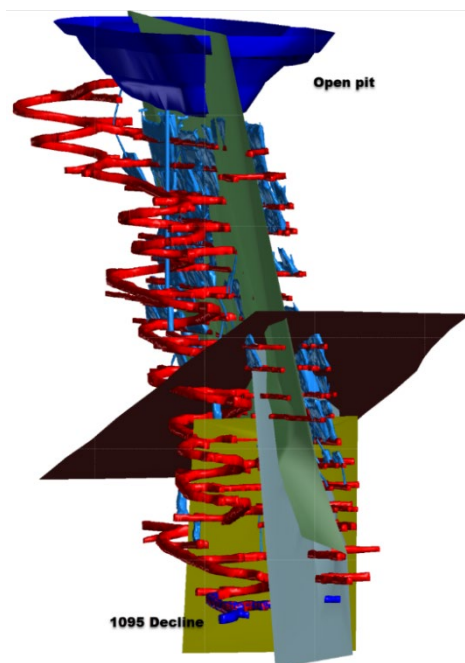
FIG 2 – Underground mine complex.

Geology of the mine deposit

The mine's deposit occurs within a banded-iron formation (BIF) sequence within greywackes on the western limb of an overturned antiform adjacent to the Bare hill shear. The sequence generally trends north–south and dips steeply at 72° towards the east. The gold mineralisation is mainly contained within two BIFs (east and west lodes) controlled by the intersection of the vertical to subvertical host 4 m wide BIF unit and a series of south plunging quartz ladder veins arrays, the intersection plunges approximately 30° to the south (Figure 3).
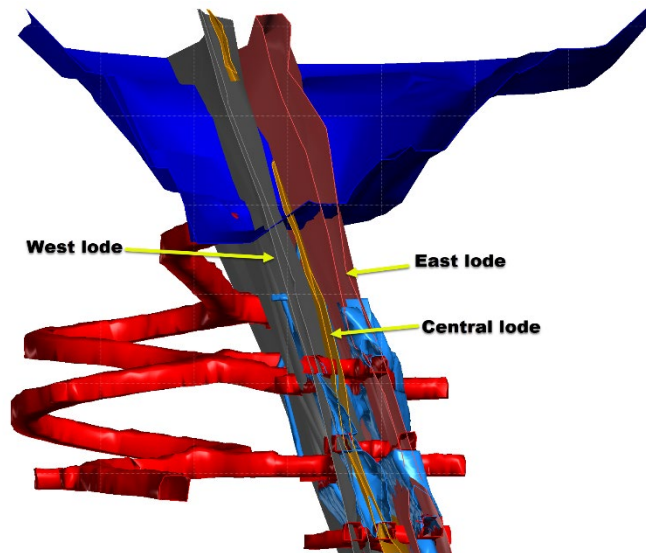
FIG 3 – East, central, and west lodes.

Several post-mineralising faults at various angles offset the BIF sequence and minor lodes occur within the footwall and hanging wall. given the limited amount of development completed at the underground operation, specific structural domains have been identified which include the access, companion, sharp, triple, and shallow faults. Whereas there are three major geotechnical domains namely the ore, footwall, and hanging wall. The ore domain is comprised of three BIF units separated by greywacke whilst the footwall and hanging wall are located to the west and east of the mineralised BIF units, respectively. Joint orientations appear to remain consistent across these 'domain' boundaries.

Rock mass properties

Laboratory-based rock strength testing was undertaken on representative core samples of the two major rock types (Table 1). The table shows that the UCS of greywacke is in the range 130 MPa – 280 MPa, and the mean 193 MPa is classified as a very strong rock. The BIF is also very strong although its average UCS is 130 MPa and appears to be relatively low compared to BIF rock strength. Triaxial tests have not been conducted on the site, reliance is on the additional tools from to determine the rock mass strength parameters which are presented in Table 2.

TABLE 1

Strength test results.

Rock type	UCS (MPa) A+C			UCS (MPa) Total		
	Mean	Std Dev	No samples	Mean	Std Dev	No samples
Greywacke	193	55	26	173	66	33
BIF	130	30	3	113	38	4

TABLE 2

Rock mass properties and strength parameters.

Rock type	σ_{ci} (MPa)	GSI	m_i	m_b	s	a	c (MPa)	θ (°)	σ_t (MPa)	E
BIF	130	81	20	10.15	0.12	0.50	5.91	55	1.4	37 753
Greywecke	193	71	18	6.39	0.04	0.50	5.93	54	1.1	45 477

Geological structures

The stability performance of the underground development is predominantly dominated by the occurrence of major geological structures are illustrated in Figure 4. However, the bulk of structural analysis is based on conducted mapping and geotechnical diamond core sample logging. The major

defects identified sets from the diamond drill core within the pit and their contour plot orientation is presented in Table 3 and Figure 5, respectively. Limited defect orientation collected from underground development headings is also presented and shows little variation from that attained from pit mapping and borehole logging.
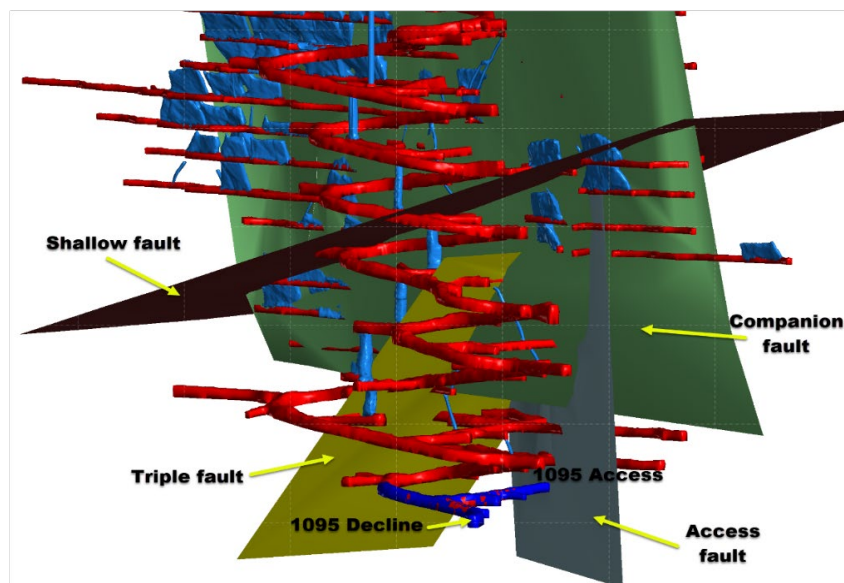

**FIG 4** – Major structures and mine excavation intersection.

TABLE 3

Major defect sets identified in the pit.

Defect set	Dip/ direction (°)	Type	Planarity	Roughness
1	69°→084	Foliation and subparallel joint set	Planar and undulating, minor stepped	Smooth (polished) to slightly rough; clean
2	86°→167	Well-developed joints	Planar and undulating (minor stepped)	Smooth (polished) to slightly rough; clean
3	07°→026	Well-developed joints	Planar, stepped and undulating	Rough and smooth; clean
4	31°→176	Moderately developed joints and veins	Planar, stepped and undulating	Rough and smooth; quartz filled, clean, and slightly oxidised
5	69°→028	Moderately developed joints	Planar and undulating	Smooth and rough; clean pyrite and quartz

It is worth noting that the above data is based on:

1. Assessments of the individual boreholes which indicate that it is highly unlikely all defect sets are present within the rock mass at any given location.

2. Some of the sets identified represented variations of a single feature/set.

3. These disparities occur because of faulting and variations in the reliability of core orientations.
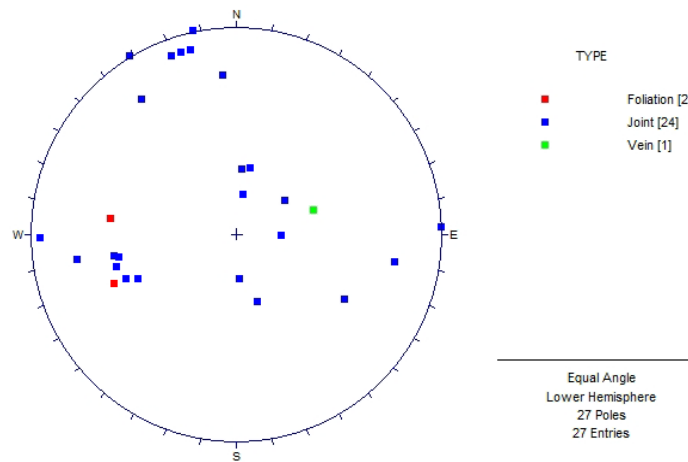
FIG 5 – Defect orientation plot.

The rock mass in the 1095 decline locality comprises greywacke, which is the dominant rock type with three main joint sets present (Table 4), the data set is also illustrated in a stereo plot (Figure 6). When compared to the data set collected from the open pit it was deduced that two main joint sets were common throughout, while the third set was anomalous as such can be compared to a more recent data set collected from the underground development.

TABLE 4

Joint sets and properties.

Set ID	Type	Dip/dip direction	Comment
1	Joint, vein	72°/103°	Strong set orthogonal to Set 2
2	Joint, vein	85°/169°	Strong set orthogonal to Set 1
3	Joint, vein	41°/349°	Widely spaced set
4	Joint	31°/070°	Weak, only two joints were observed in the immediate area
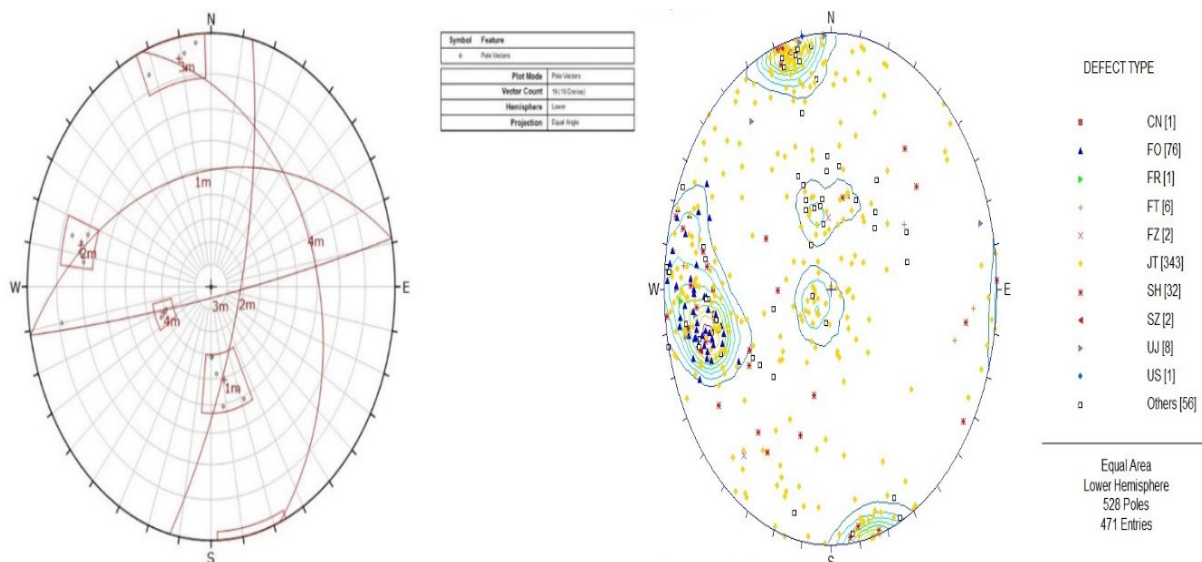
FIG 6 – Stereo plot for the underground joint sets.

The two dominant orthogonal joint sets are characteristic of the rock mass presented in the face. One of these sets strikes subparallel and dips steeply out of the face towards the work area. A prominent joint is evident at the top of the face dipping at 40°/354° and outlines a shallow wedge (Figure 7).
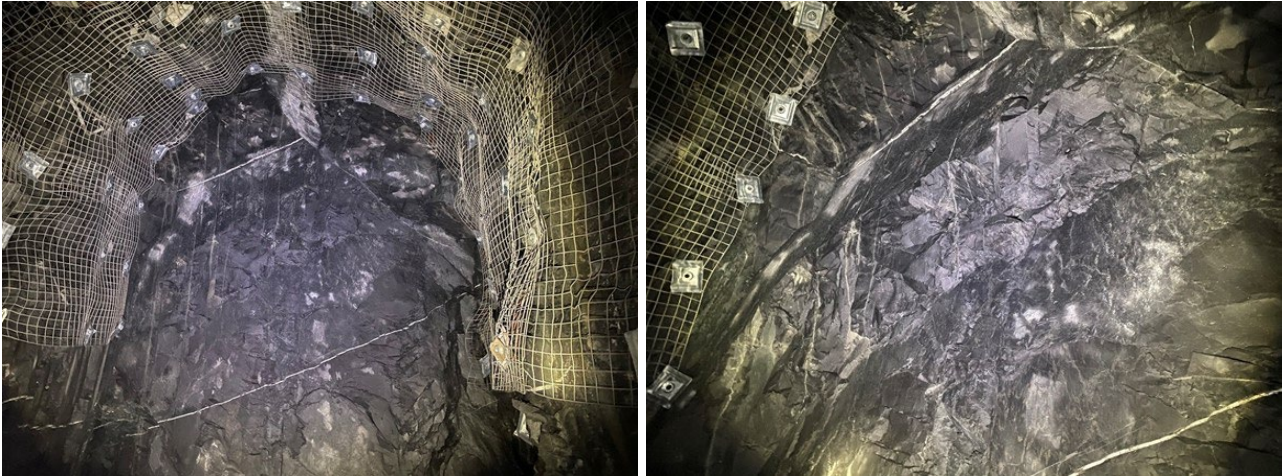
FIG 7 – Face with dominant orthogonal joint sets.

Two persistent shallow southerly dipping quartz-carbonate veins and 25 to 30 cm deep butts are evident in the face. However, no major faults intersected the 1095 decline coinciding with the location of the face from which the rock ejection occurred (Figure 4). The moderate northerly dipping structure is less prevalent in the adjacent decline than the two dominant (orthogonal) joint sets, though, appears to be persistent. A structure with a similar orientation is evident in the lower pillar of the 1095 Access which is part of a widely spaced moderate northerly dipping joint set susceptible to shearing. Block stability analysis of the 1095 decline face was conducted based on the joint sets observed below the 1095 Access. The analysis indicated that the largest wedges would be expected to occur in the westerly trending development anticipated mass of five tons. Faces in easterly trending development are expected to be more stable as the dominant steep easterly dipping joint set plunges into the face this limit sliding occurrence.

In situ stress regime

The *in situ* rock stresses have been measured using the HI Cell method at the nearby underground site (Table 5). Based on the typical Australian goldfields stress versus depth relationships it is expected that at the current depth the major principal stress magnitude will be 68 MPa.

TABLE 5

In situ stress components.

Principal stress component	Stress gradient (MPa)	Trend (°)	Plunge (°)
σ_1	0.073D + 6.16	150	05
σ_2	0.051D + 3.48	240	05
σ_3	0.028D + 0.62	330	80

## STRAIN BURST OCCURRENCE AND BACK ANALYSIS

Several rockfalls, rock popping, rock cracking, and other brittle-plastic-associated failures occurred before and during mining. The previous events appeared sporadic, were not associated with major geological structures, and were not extensive as the one that occurred in the 1095 decline on the 13 February 2021 referred to as a rock burst (Table 6) and before the occurrence, of the mine recorded a seismic event with an intensity of 0.45 M_L.

TABLE 6

Historical failures in the underground complex.

Date	Location	Description
20/01/2021	1095 Access	Face spitting and cracking – face meshed
12/12/2020	1110–01	Freshly scaled, re-bogged face, cracks, and rock ejection from the roof
13/08/2020	1125 Access	Loud bang/concussion in backs of current face
10/08/2020	1125 Access	Spalling backs and face popping and banging when scaled
25/01/2020	CEB Decline	Rock popping and unravelling – Shoulders and walls.

Therefore, in this section, back analysis of the violent rock ejection leading to damage that occurred in the 1095 decline is performed. It is noted that during the conducted inspection a crown pillar above one of the 1225 Level stopes failed, breaking into the 1240 Access. The timing of this failure is unknown and considered unlikely that is associated with the 1095 decline rock ejection because the events were 175 m apart (Figure 8).
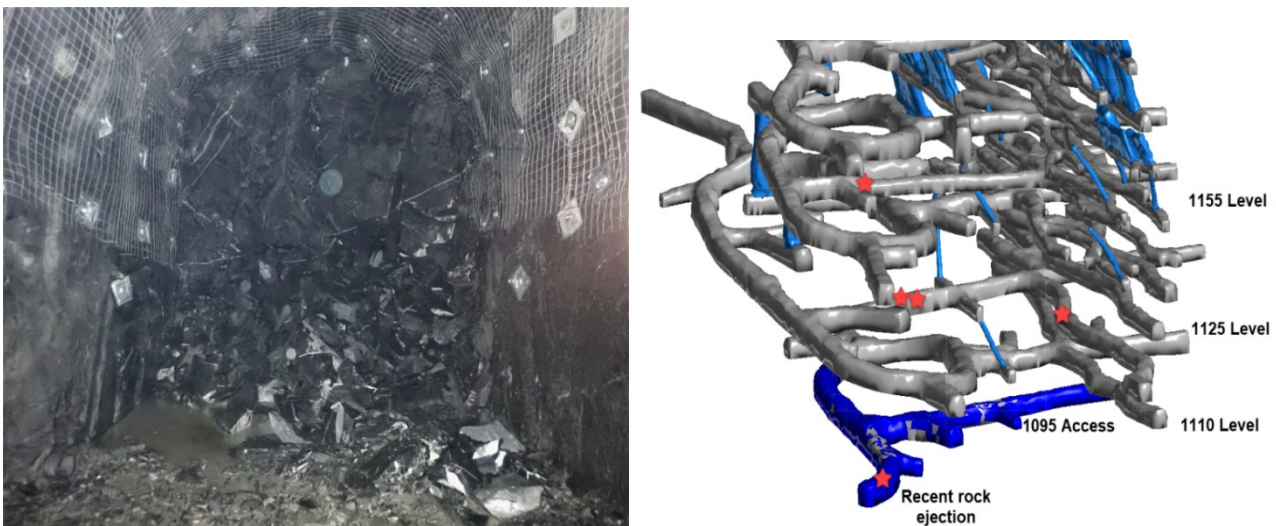
FIG 8 – Rock ejection from the 1095 decline and historical related failures.

The back analysis involved the Kinematic analysis to determine the rock mass structural setting, a seismic intensity reading and finally a numerical analysis to determine the static stress concentration and redistribution.

Numerical simulation and static stress concentration determination

Even though the empirical and analytical solutions can determine the extent of failure around excavations leading to rock burst. It must be emphasized that these tools cannot determine failure accurately by considering the interaction of the stress, geomechanics conditions, and dynamic nature of the rock mass. The solutions can employ rock mass characterisation and experimental data (Kabwe *et al*, 2020b, 2020a; Keneti and Sainsbury, 2018). However, this is not sufficient to determine and provide specific dynamic geomechanics predictions. Hence, numerical modelling comes into play as a solution to this limitation and provides prediction and mitigation to the seismic event before its occurrence. To model, a strain burst numerically certain attributes need to be considered which include:

1. Three-dimensional (3D) model meshing to account for the 3D stress state in the X-Y-Z space.

2. Fine mesh densification in areas of anticipated strainburst related failure such as tunnel-rock mass and stope-rock mass boundaries. This accounts for the heterogeneity and static stress concentration around the excavations.

3. Initial state of stress should be initialised by the displacement boundary conditions to account for the accurate rock mass loading history.

4. The choice of constitutive model that considers failure and replicates the rock mass yielding.

Constitutive model

In this case, the advanced strain-softening IMASS constitutive model is governed by two bounding yield surfaces (peak and residual) and Hoek–Brown (HB) peak strength envelope. The choice of this model is to determine the redistribution and concentration of the static stress around the excavations during face advance. The numerical model is constructed in a Finite Volume numerical code FLAC3D and comprises a block hosting underground stopes and drifts with an open pit representing the portal access (Figure 9). It is large enough to minimise boundary effects with far-field boundaries. Further densification into finer elements around the excavations to accurately capture the stress and strain distributions are provided by the Octree mesh function.
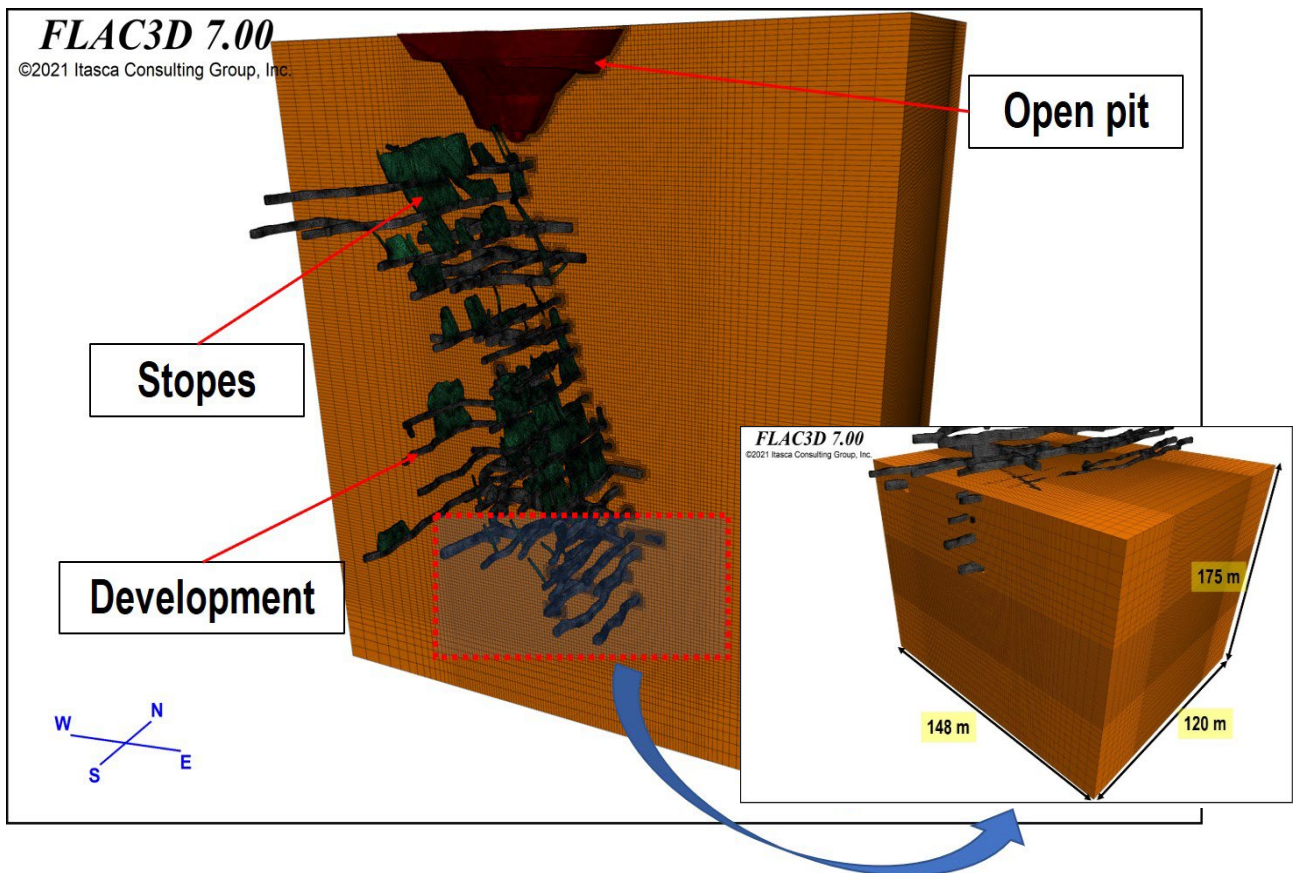
FIG 9 – Block hosting underground drifts and stopes.

The stress regime is imposed everywhere in the domain in the form of transformed 3D stress tensors presented in Table 7. The block is divided into two sections assigned different constitutive laws; the outer section exhibits elastic behaviour while the inner obeys the IMASS (Figure 10). To account for the rock mass brittleness behaviour associated with strainburst, the ε_{crit} for the rock mass matrix is adjusted to a value <1.0 (and above 0.0) (Ghazvinian *et al,* 2020a; Ghazvinian *et al,* 2020b; Kabwe, 2022a). The material properties and parameters employed in the advanced IMASS constitutive model are presented (Table 8). While the boundary conditions are set to restraint (velocity components (0,0,0)) for all sides, bottom and top.

TABLE 7

Transformed 3D stress tensors applied to the model.

σ_{xx}	σ_{yy}	σ_{zz}	σ_{xy}	σ_{yz}	σ_{xz}
-275	-170	-175	69	45	25
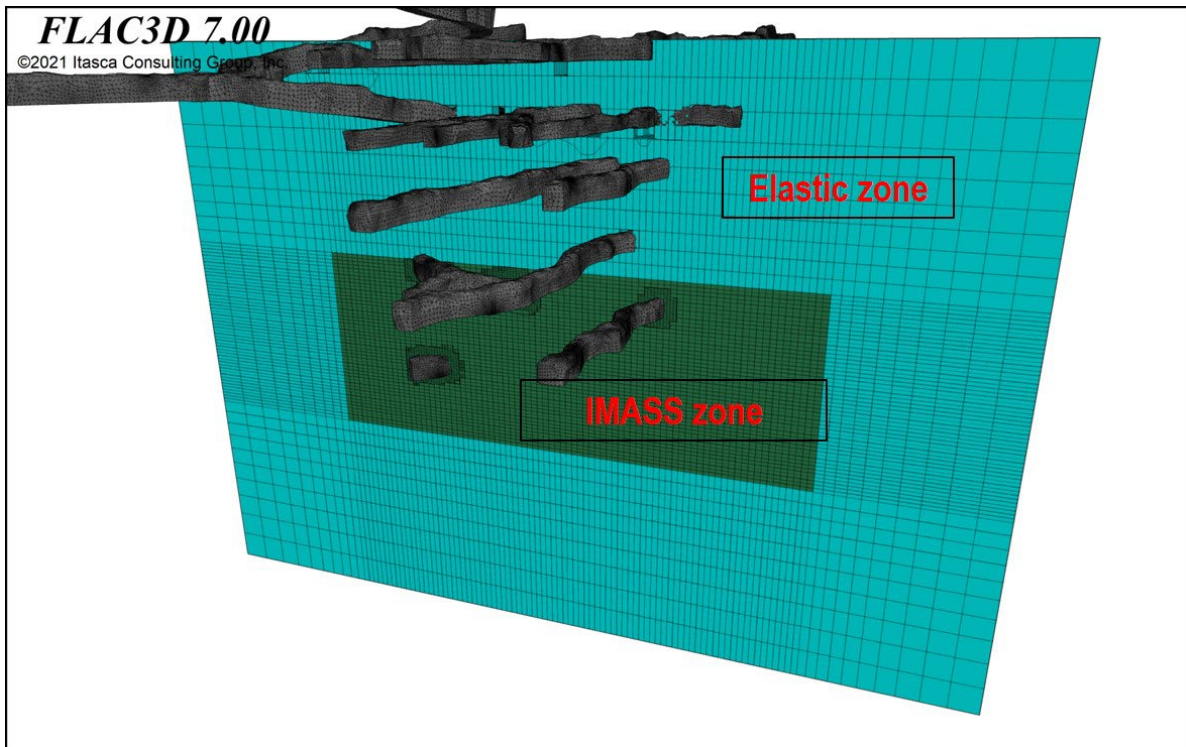
FIG 10 – Assigned elastic and IMASS constitutive laws.

TABLE 8

Rock mass properties and strength parameters.

Rock type/zone	σ_{ci} (MPa)	GSI	m_i	ε_{crit}	Density (kg/m³)	E (MPa)	Poisson ratio (ν)
Elastic					2800	72 000	0.25
BIF	130	81	20	0.4	2830	59 000	
Greywecke	193	71	18	0.1	2800	72 000	

Simulation results and static stress condition

The static stress concentration around an excavation boundary can lead to a strainburst damage potential. In that the larger the static stress the more prone to strainburst damage to an excavation. The intensity of the stress around an excavation can be a good indication of the additional stress components from a seismic wave required to cause excavation damage. This stress factor is based on tangential stress (σ_1) – Unified Compressive Strength (UCS) ratio (Heal, 2010). The instability of an excavation can be expected if this stress ratio (σ_R) is less than 5 and potential rock burst if it lies between 2–3 (Equation 1). It is postulated that the severity of a strainburst damage around an excavation is more when the confining stress value is closer to zero and higher deviatoric stress:

$$\sigma_R = \frac{UCS}{\sigma_1} \tag{1}$$

The numerical modelling determines the stress concentration around excavations although the stress factor is an empirical index. The results obtained show that the backs, shoulders, and walls of the 1095 decline exhibit higher total stress (140 MPa) and lower confining stress (60 MPa), signifying a very high deviatoric stress (80 MPa) (Figure 11). It is observed that the tangential stress redistribution is concentrated in the back and shoulder with a low σ_R ranging between 0–3 (Figure 12), it is further deduced that the current static stress value coupled with an extra stress component from a seismic wave would cause a strainburst occurrence.
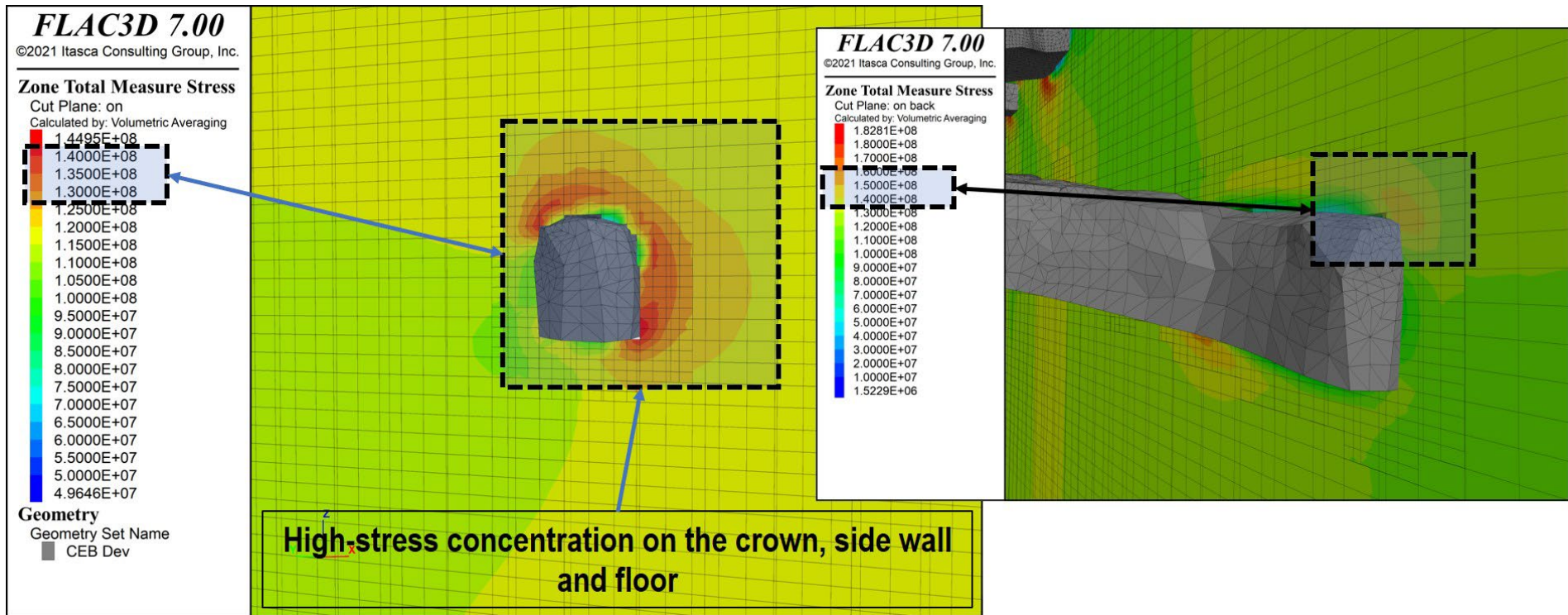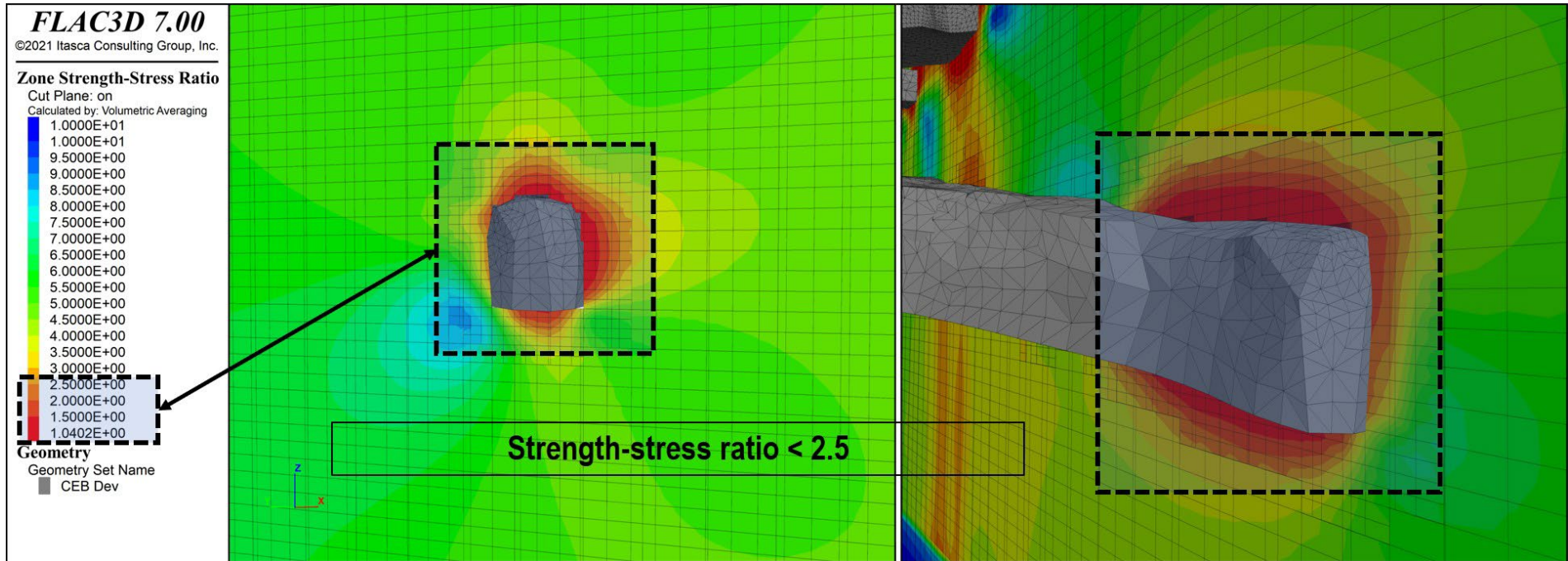
FIG 11 – Stress concentration around the decline section.

FIG 12 – Strength-Stress ratio distribution around the decline section.

MINIMUM SURFACE ELEMENTS AND REINFORCEMENT STANDARDS

In this section, we discuss the minimum ground support required for excavations at the underground mine. The life span of most of its excavations or drives is generally less than three years, although in some instances long-term is required to access additional orebodies. In this case, the support system design required to transform these to long-term includes reinforcing backs and sidewalls of all declines and development drives up to 0.5 m from the face as part of the normal mining cycle. The development face is supported in areas of high seismic risk where there are planned to intersect fault wireframe, airleg drive/sublevel/slot, or where development has reached the final design. The ground support design methodology employed for these excavations involves:

- an initial pass estimation of the preliminary support requirements using an empirical approach.

- kinematic analysis to characterise the structural features and the rock mass fabric.

- block stability analysis to identify potential failure, type of failure, and factor of safety (F_S).

- estimation of the yield zone or plastic flow extension around the tunnel using numerical solutions.

- assessment of the support system capacity, demand, and energy absorption requirements (anticipated seismicity).

The minimum ground support designs currently employed at the underground operations are presented in the proceeding section. The support systems are designed with a F_S (1.5) based on the current underground excavation support practice design and LOM.

Static ground support scheme

Ground support systems for excavation in areas that are not expected to be affected by seismicity/dynamic occurrences are determined by empirical, kinematic, and analytical block stability methods. The empirical method employs the support chart which compares the span of the excavation and the rock mass quality. The kinematic method determines the structural fabric of the rock mass which is used as input for the analytical block stability method to determine the mode and probability of rock mass failure. As stated earlier static ground support assessment and design require both empirical, kinematic, and analytical methods. In the determination of support demand (S_D) in static rock mass conditions equation (Equation 2) is used:

$$S_D = \rho g d_f \tag{2}$$

Where ρ is the rock density (t/m³), g is the gravity (m/s²) and d_f is the depth of failure (m), this depth under static conditions is attained by Equation 3:

$$d_f = 0.49(\pm 0.1) + 1.25\left(\frac{\sigma_{1max}}{\sigma_c}\right)a \tag{3}$$

Where a is the excavation radius (D-shaped drive, $a = w/\sqrt{2}$), σ_{1max} is the maximum tangential stress, σ_c is the UCS and 0.49 (± 0.1) is the calibration factor (C). The F_S for the support system is calculated as:

$$F_S = \frac{Loading\ capacity\ of\ the\ support\ members}{Total\ effective\ static\ loads\ on\ the\ surrounding\ rock\ mass} \tag{4}$$

Dynamic ground support scheme

In dynamic support system design, the most cardinal aspect which is unknown is the energy demand that is absorbed by the reinforcement and surface elements. In addition, the proportion of energy absorption between the reinforcement and surface elements in a composite support system. The dynamic capacity of a support system can be determined by two plausible methods which are the addition of reinforcement capacity to the surface element capacity, and the computation of the capacity of the weakest link in the dynamic support system which is usually the surface elements. Surface elements absorb a large proportion of energy and fail before the reinforcement capacity is fully solicited. The current dynamic support design is based on several historical seismicity-associated failures. Which was done by review of support requirements and developing a fit-for-

purpose dynamic ground support system that is implemented. In addition, ground support audits are conducted in areas that require dynamic support and upgrade, as necessary. At this mine, an increased number of seismic-associated ground failures has led to the dynamic support system requirement that has been assessed considering the following failure mechanism: remotely triggered strain burst. self-triggered strain burst and seismic shakedown (Table 9).

TABLE 9

Dynamic support of excavations near seismic sources.

Development	Specification
Development: 5.0 × (5.0–7.5) m	High seismic risk – 3.0 m Kinloc bolts and 5.6 mm weld mesh.
	Medium seismic risk – 2.4 m Kinloc bolts and 5.6 mm weld mesh.
	Low seismic risk – 3.0 m split sets, 2.4 m Kinloc bolts and 5.6 mm weld mesh.
Capital development: (4.8–5.0, 5.0–5.5) m	High seismic risk – 2.4 m split sets, 3.0 m Kinloc bolts and 5.6 mm weld mesh.
	Low seismic risk – 2.4 m split sets, 3.0 m Kinloc bolts and 5.6 mm weld mesh.

Note: High seismic risk = ≤12 m, Medium seismic risk = 12–21 m and Low seismic risk = >21 m distance from the source.

Ground support profile and analysis

In this section, we employ the analytical-based approach methods attributed to Kaiser *et al* (1996) to evaluate the dynamic support system. The approach involves static load demand determined from Equation 1 and dynamic load energy demand estimations the same design procedure is adopted with the energy demand consideration. The dynamic energy demand from the ejected rock due to dynamic ground response is expressed as Peak Particle Velocity (PPV) generated by a far-field event. The modified correlation (Potvin and Wesseloo, 2013) to determine the PPV at a distance (R) from a seismic source is expressed by:

$$ppv = \frac{C10^{\frac{1}{2}(m_L+1.5)}}{R+R_0} \tag{5}$$

Where C is a constant that lies between 0.2–0.3 for design purposes, R is the distance to the seismic source, $R_0 = \alpha 10^{1/3(m_L+1.5)}$, m_L is the event magnitude and α lies between 0.53–1.14. it was recommended that C lies between 0.2–0.3 corresponding with the 95 per cent confidence level of static stress drop of 1 MPa. While static stress drops above 1 MPa the values present a lower confidence level. On the other hand, the energy demand (E_D) is computed using Equation 6. With the assumption that an intact volume of rock having a mass (m) is ejected at a velocity (v) by a distance (d) while deforming the support structure under the influence of gravity (g) and q the gravity effect constant factor (1 for backs, 0 for walls and -1 for floor):

$$E_D = \frac{1}{2}mv^2 + qmgd \tag{6}$$

It must be emphasized that rock ejection velocity is usually different from the PPV due to effects on the seismic waves attributed to the reflection, refraction, and amplification. The presentation of Equation 7 for the estimation of damage extension only applies to static stress conditions. However, the depth of fracture extension due to seismicity requires the inclusion of the dynamic stress (σ_{max}) and its increment ($\Delta\sigma_{max}$). Hence, Kaiser and Cai (2012) provided a semi-empirical correlation between depth of failure associated with high stress and dead load computed as a function of stress level expressed by:

$$d_f = \left[1.25\left(\frac{\sigma_{max}+\Delta\sigma_{max}}{\sigma_c}\right) - C\right]w/\sqrt{2} \tag{7}$$

Where $\sigma_{max} = 3\sigma_1 - \sigma_3$, $\Delta\sigma_{max} = nC_S\rho ppv$ (MPa), n is the directional factor dependent on the incident angle of the dynamic wave and C_S is the propagation speed of the shear wave (S-wave) through the rock mass (m/s). To estimate and determine the efficacy of the dynamic support system, the support demand aspect associated with the energy dissipated by a seismic event is considered. In this

analysis, we adopt a seismic event (ML = 0.45) that occurred in the 1095 decline (Figure 13) results are employed as input parameters in the analysis for dynamic support demand computations of the suggested surface and reinforcement elements (Table 10).
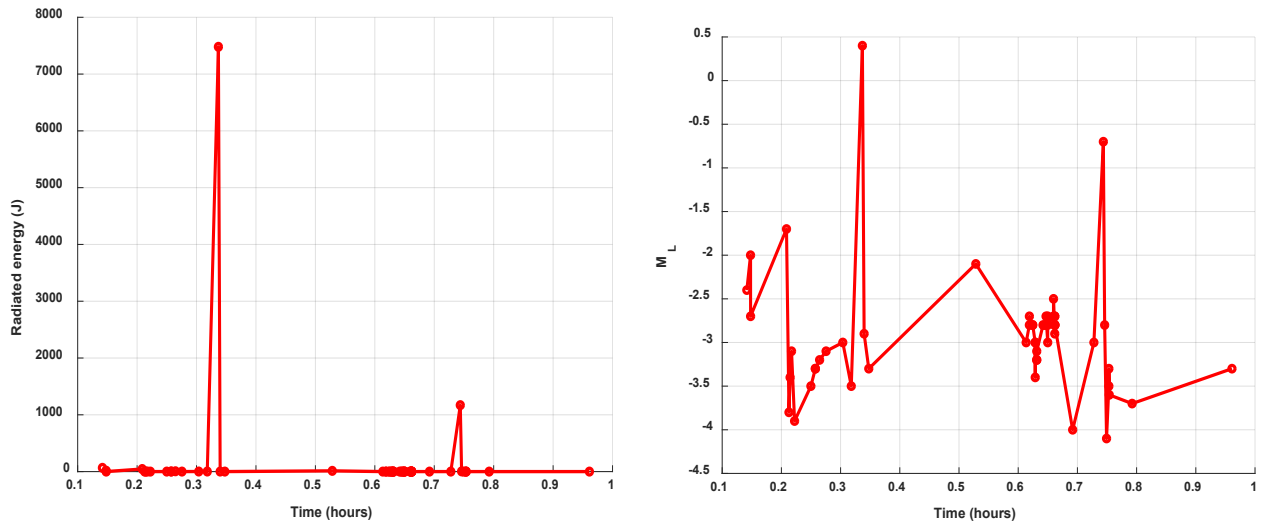

FIG 13 – Energy and Magnitude with time attained from the recent seismic activity.

TABLE 10

Dynamic support analysis.

Remote triggered strainburst				Input parameters		
1. Estimation of ppv				c^*, constant	0.25	m^2/s
ppv	1.00	m/s		R, distance from the source	10	m
2. Estimate $\Delta\sigma_{max}$				R_0, source radius	9.79	m
$\Delta\sigma_{max}$	37.3	MPa		M_{max} (local)	2.3	
3. Estimate change in failure depth, Δdf				n, incidence angle factor	4	
Δdf	1.02	m		ρ, density	2700	kg/m^3
4. Estimate volume change, $\Delta V_{failure}$				C_s, shear wave velocity	3440	m/s
$\Delta V_{failure}$	20.6	m^3		w, drive width	5.5	m
5. Richter conversion, $M_{L,R}$				Rock type	Greywacke	
$M_{L,R}$	0.45	from graph		UCS	177	MPa
E_s	2.00	MJ		L, potential failure length	5.5	m
6. Energy demand, $E_{support}$				η, energy efficiency	0.1	
$E_{support}$	9.9	kJ/m^2		F_S, factor of safety	1.5	
				σ_{max}, max tangential stress	96	MPa
Self-triggered strainburst				b_f, bulking factor	0.05	
1. Dynamic depth of failure, df				l, cut length	4	m
C	0.64			M_d, support element mult.	1.25	
df	0.15	m		n, ejection velocity ratio	1	
2. Volume of failed rock, V				g, gravity constant	9.81	m/s^2
V	0.7	m^3		C, stress fracture constant	0.64	
3. Energy release, E_s				s, strain burst surface factor	0.25	
$M_{L,R}$	0	from graph1		d_{ult}, ultimate deform of GS	0.15	m
E_s	1.00	MJ				
4. Energy demand, $E_{support}$				**Dynamic support summary**		
				Remote triggered strain burst	9.9	kJ/m^2
$E_{support}$	6.8	kJ/m^2		Self-triggered strain burst	6.8	kJ/m^2
				Seismic shakedown	5.1	t/m^2
Seismic shakedown				Displacement demand	59	mm
1. Estimation of ppv						
ppv	1.00	m/s		**Notes**		
2. Survival safety factor, $S_{Fsurvival}$				Green shade: Variable parameters		
$S_{Fsurvival}$	1.07			Grey shade: Constants		
S_{design}	1.61					
3. Depth of failure						
$\Delta\sigma$	37.3	MPa				
C	0.64					
df	1.17	m				
4. Static load demand, Ps						
Ps	5.1	t/m^2				
5. Displacement demand, D						
D	59	mm				

Support calculator						
Support element	**Bolt**	**Row**	**Bolt (m²)**	**Bolt Condition**	**Dynamic**	**Static**
2.4 m Split set	1.1	1.5	0.6	0%	5	9
0.3 m Fibrecrete	1	1	1.0	50%	5	1
2.4 m Kinloc	1.1	1.5	0.6	100%	20	18
Support (F_S)	**2.2**	**$E_{support}$**	**10 kJ/m²**	**Total support capacity**	**15 kJ/m²**	

It is drawn from Table 10 above that the suggested support system (Split set, Fibrecrete, and Kinloc) can restrain tunnel response associated with the dynamic dilation of the surrounding rock mass. the support design profile can efficiently restrain the dynamic response of the seismic-prone tunnels at the underground operations (Figure 14).
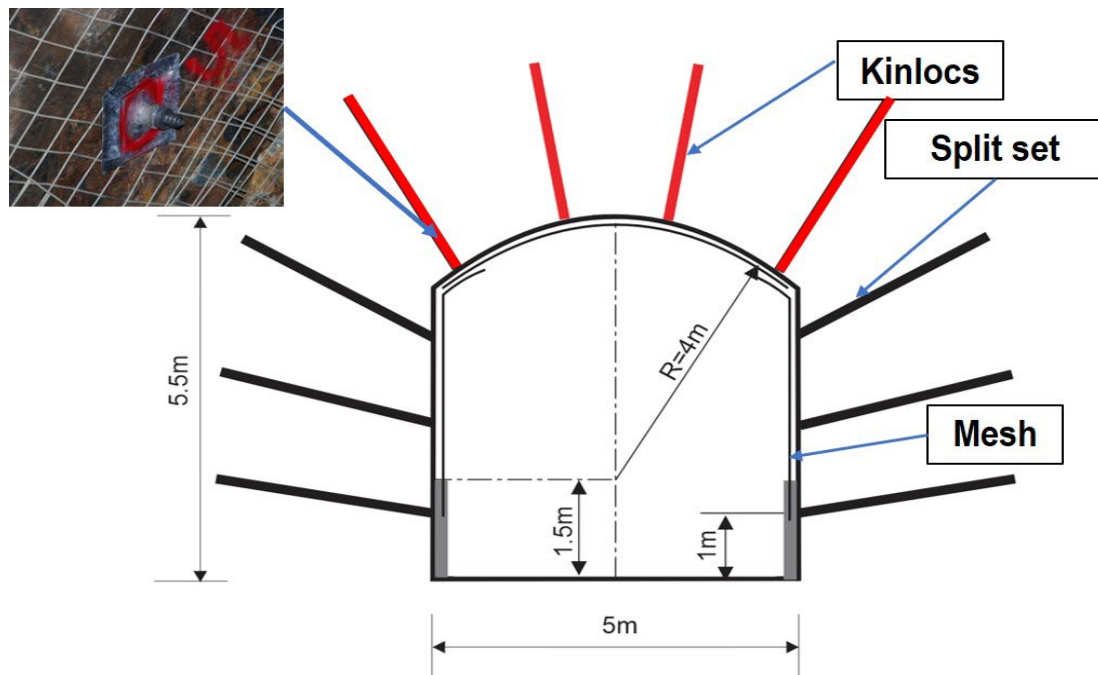
FIG 14 – Suggested support system profile.

In addition to the dynamic capacity, the load-bearing capacity is also determined, and below show examples of calculations from this data set (Table 11).

TABLE 11

Ground support demand versus capacity calculator.

Constants	Value	d_f (m)	E_D (KJ/m²)
g (m/s²)	9.81	0.8	10.32
ρ (t/m³)	2.8	1.0	12.90
v (m/s)	2	1.2	15.48
d (m)	0.2	1.4	18.06
q (Assumed for backs)	1	1.6	20.64

Note: in the above table the velocity of 2.0 m/s is purely for example purposes.

Note that there are practical limits to the ground support capacity and if demand exceeds this, then further assessment and use of alternative methods must be considered. Maximum demand capacity may vary depending on the failure mechanisms and ground support system employed to restrain failure. Kaiser *et al* (1996) suggests a maximum practical support limit of 50 kJ/m², the fractured zone extent (suggested 2 m upper limit), and/or tunnel closure exceeds 300 mm.

Suggested dynamic support system efficacy

In this section, the focus is on the rock bolts which is the first line of exposure to the dynamic response of a rock mass when an integrated dynamic support system is set-up. The performance of the support is based on the axial force and the elongation that it will exhibit. This is then compared with documented bolt capacities in the product technical data sheet to determine their performance. In this section, we adopt the 3D simulation to represent a replica of the 1095 decline and rate of excavation advance assumed to be 4 m/cut followed by three rows of reinforcements (Figure 15). Simulation of the installed support system performance in burst prone ground is performed in this section it employs bolts assigned as cable elements installed with plates to form a rigid tunnel boundary connectivity and neglects the stress relaxation effect (Kabwe, 2020) with their mechanical properties including Fibrecrete presented in Table 12. The stiff and yieldable bolt properties are attained from support element calibrations performed using the ITASCA calibration tool (Figure 16).
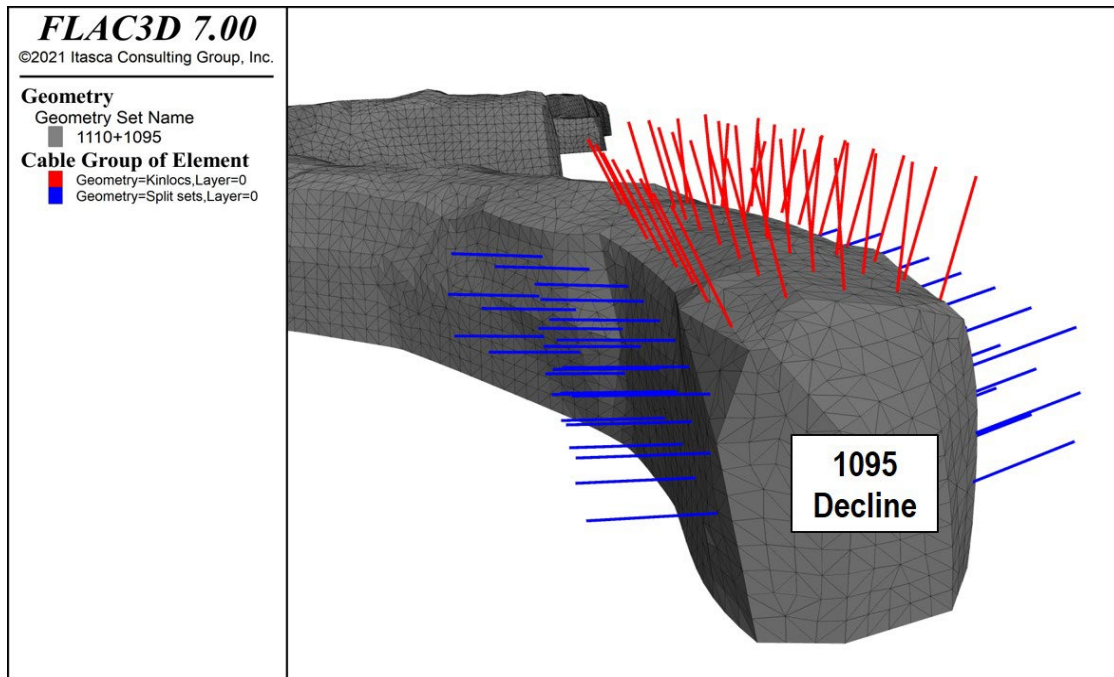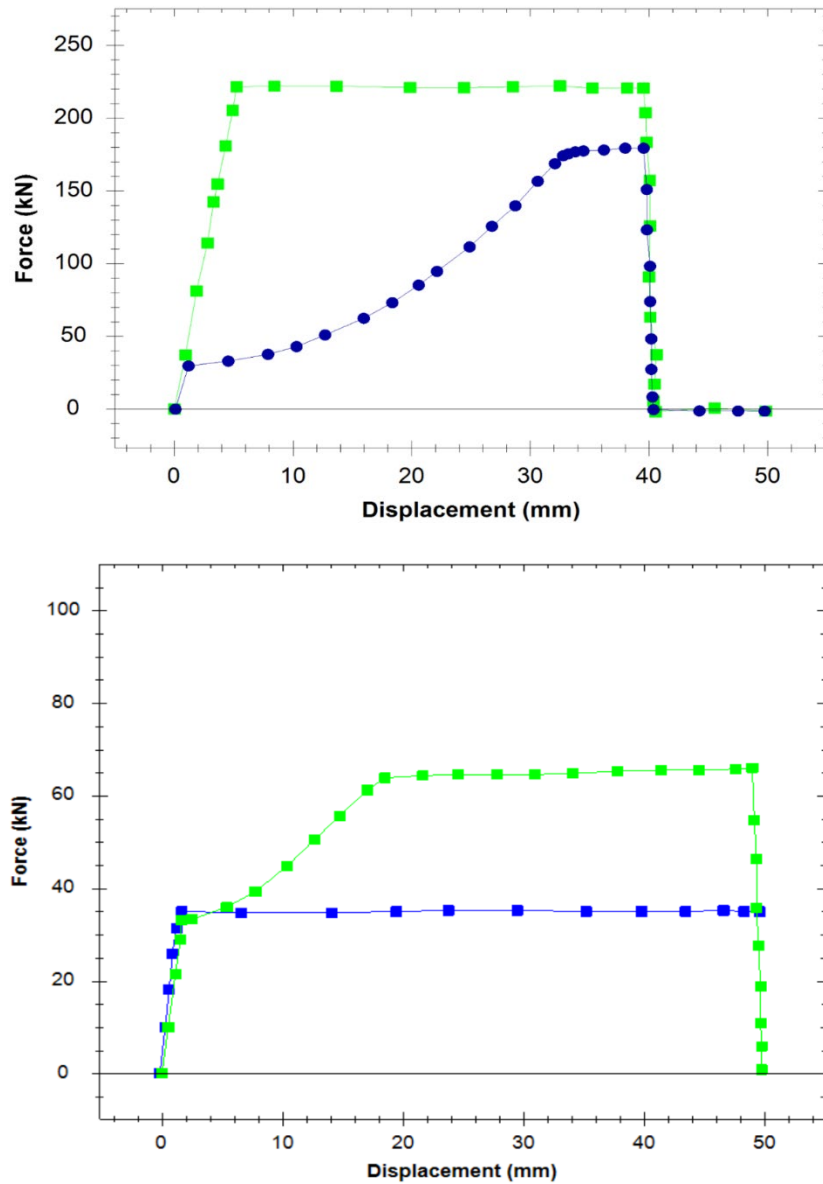
FIG 15 – Support design profile in FLAC3D.

TABLE 12

Liner and shell element properties.

Element	Yield strength (kN)	Tensile Strength (kN)	Diameter (mm)	Cross-Sectional Area (mm²)	E (GPa)
Kinloc	240	315	47	370	20
Split set	160	180	47	355	20.7
	Compressive strength (MPa)	Thickness (m)	v		
Fibrecrete	32	0.25	0.25		10

FIG 16 – Force-displacement characteristic: (a) Kinloc and (b) Split set bolts.

The simulations performed involved a stress relaxation of the unsupported excavation's peripheral until equilibrium. Thereafter, the simulation included the installation of rock bolts as cable elements with assigned mechanical properties (Figures 17 and 18). The reinforcement effects of the installed support elements on the excavation peripheral are determined by the strength-stress ratio distribution at various stages of this simulation.
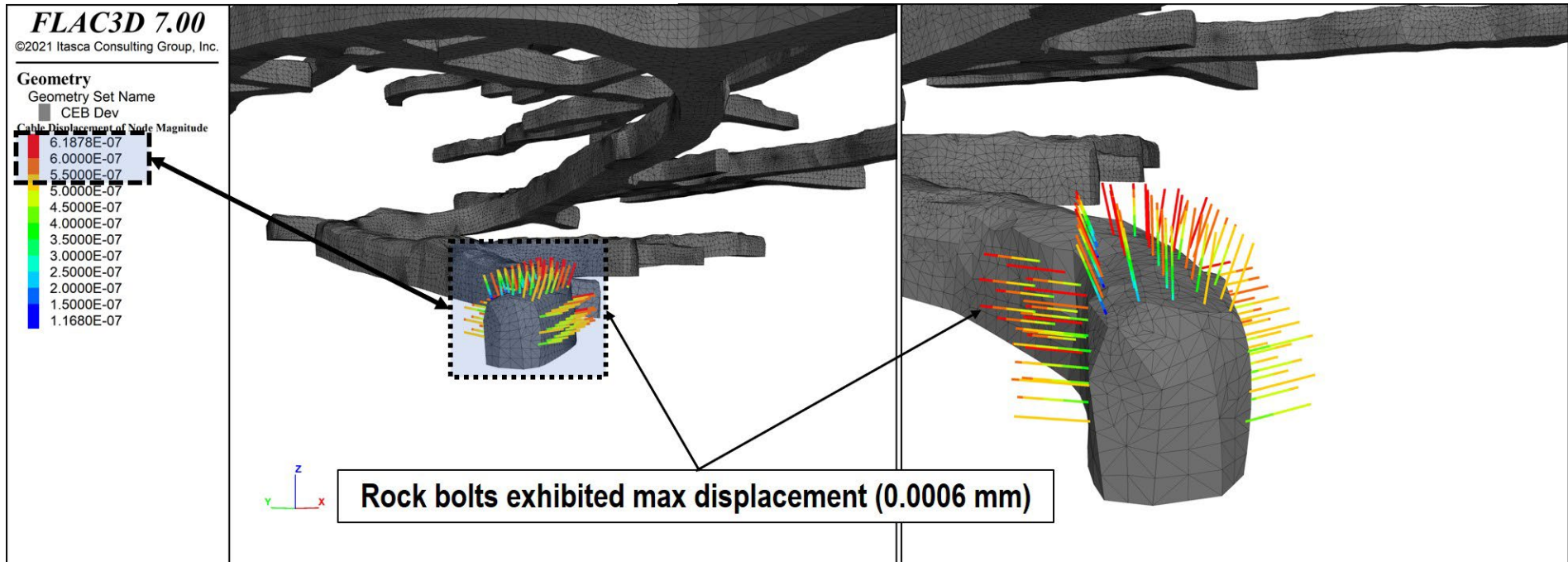
FIG 17 – Bolt's elongation performance.
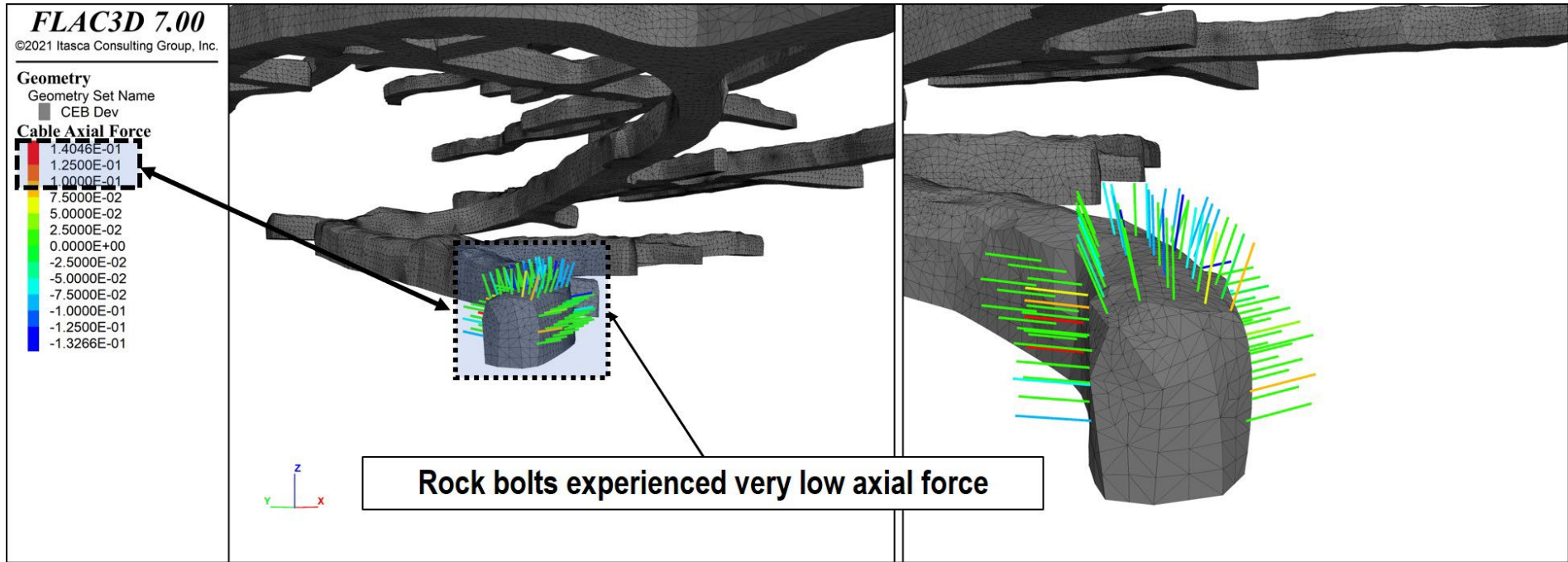
FIG 18 – Bolt's axial force performance.

On the bolt's performance, it is observed that the rock bolts handled the load with a maximum axial force of 0.14 kN which is below their ultimate capacity (Table 13). The bolts that exhibited more of this axial load are on the right wall of the decline section. The tangential stress in this decline section was elevated by its redistribution from the enhanced back confinement due to the installed rock bolts. The other factor considered in the bolt's performance is the bolt elongation and it's observed from the simulation that the maximum attained is 0.0006 mm (Table 14). It was also observed that the rate of bolt elongation was more in the Kinloc bolt as compared to the Split set bolt implying that they can handle more yielding (Figure 16).

TABLE 13

Bolt load capacity (Numerical versus Published data).

Support element	Length (m)	Load capacity (kN)	Axial force in the numerical model (kN)	% Change
Kinloc bolt	2.4	240	0.14	0.1%
Split set bolt	2.4	160	0.14	0.1%

TABLE 14

Bolt elongation capacity (Numerical versus Published data).

Support element	Length (m)	Max displacement (mm)	Max displacement in the numerical model (mm)	% Change
Kinloc bolt	2.4	360	0.0006	0.0016%
Split set bolt	2.4	-	0.0006	0.0016%

In the typical load-displacement curve the initial bolt response starts with linear behaviour associated with elasticity. A representation of the bolt stretches at the collar before yielding this determines the ultimate strength capacity of the bolt (Kabwe, 2022b). When an axial force is increased beyond the yielding point the ultimate bolt capacity is reached. Additional axial force beyond the bolt's ultimate limit results in a rapid bolt displacement which reduces its efficacy. In this study, the Kinloc bolt show large post-peak displacement before failure implying a large yielding capacity compared to the Split set bolt.

CONCLUSIONS

The use of a 3D modelling represents the geological conditions and the excavation sequence, this provided a good match between model results and captured strainburst damage. It is deduced that the strainburst occurrence was not influenced by fault slip associated with structural features. It was ascribed to a tangential stress component overlaid with a small-scale far-field seismic wave.

Decline development at the location of the strainburst damage trends west, and presented analysis indicates development in this orientation is more susceptible to instability. It is recommended that face mesh be installed on all westerly trending development. The numerical model results also proved the effectiveness of a dynamic support system in restraining burst damage. The appropriate dynamic support scheme comprised of static (split sets), and yieldable (Kinloc) bolts are recommended and implemented.

A 3D numerical model is an adequate tool to obtain reliable results and a good understanding of potential rock burst occurrence, tunnel stability and dynamic ground support performance. Additionally, the numerical approach assisted in the identification of the tangential stress concentration around the excavation. Its combination with the empirical approach provided an effective solution to the understanding of the strainburst associated rock fragment ejection mechanism and dynamic support system performance evaluation.

REFERENCES

Cai, M, 2017. Principles of rock support in burst-prone ground, *Tunnelling and Underground Space Technology*, 36(June 2013):46–56.

Cai, M, 2019. Rock support in strainburst-prone ground, *International Journal of Mining Science and Technology*, 29(4):529–534.

Cai, M, Champaigne, D, Coulombe, J G and Challagulla, K, 2019. Development of two new rockbolts for safe and rapid tunneling in burst-prone ground, *Tunnelling and Underground Space Technology*, 91(January), 103010.

Charette, F and Plouffe, M, 2007. Roofex-results of laboratory testing of a new concept of yieldable tendon, *Deep Mining,* 7:395–404.

Cook, N G W, 1965. A note on rockbursts considered as a problem of stability, *Journal of the Southern African Institute of Mining and Metallurgy*, 65(8):437–446.

Cook, N G W and Ortlepp, W D, 1968. A yielding rock bolt, Chamber of Mines of South Africa, Research Organization Bulletin, 14.

Galler, R, Gschwandtner, G G and Doucet, C, 2011. Roofex bolt and its application in tunnelling by dealing with high stress ground conditions, *ITA-AITES World Tunnel Congress*, Helsinki, Finland.

Ghazvinian, E, Fuenzalida, M, Orrego, C and Pierce, M, 2020a. Back analysis of cave propagation and subsidence at Cadia East Mine, pp 535–550.

Ghazvinian, E, Garza-Cruz, T, Bouzeran, L, Fuenzalida, M, Cheng, Z, Cancino Martínez, C and Pierce, M, 2020b. Theory and Implementation of the Itasca Constitutive Model for Advanced Strain Softening (IMASS), pp 451–461.

Ghorbani, M, Shahriar, K, Sharifzadeh, M and Masoudi, R, 2020. A critical review on the developments of rock support systems in high stress ground conditions, International Journal of Mining Science and Technology, 30(5):555–572.

He, M, Gong, W, Wang, J, Qi, P, Tao, Z, Du, S and Peng, Y, 2014. Development of a novel energy-absorbing bolt with extraordinarily large elongation and constant resistance, *International Journal of Rock Mechanics and Mining Sciences*, 67:29–42.

Heal, D, 2010. *Observations and analysis of incidences of rockburst damage in underground mines*, PhD thesis, The University of Western Australia, Perth.

Kabwe, E, 2020. Numerical Analysis of a Rock Bolt Load Indicator Washer Neglecting the Stress Relaxation Effect, *Mining, Metallurgy and Exploration*, 37(2). https://doi.org/10.1007/s42461–020–00187–9.

Kabwe, E, 2022a. Back analysis of a strainburst-rock fragments ejection initiated by a low-intensity seismic wave, *International Journal of Rock Mechanics and Mining Sciences*, Under review.

Kabwe, E, 2022b. Performance of Dynamic Reinforcements to Restrain Remote Triggered Strainburst Associated Failure, *International Journal of Rock Mechanics and Mining Sciences*, Under review.

Kabwe, E, Karakus, M and Chanda, E K, 2020a. Creep constitutive model considering the overstress theory with an associative viscoplastic flow rule, *Computers and Geotechnics*, 124, 103629.

Kabwe, E, Karakus, M and Chanda, E K, 2020b. Isotropic damage constitutive model for time-dependent behaviour of tunnels in squeezing ground, *Computers and Geotechnics*, 127, 103738.

Kabwe, E, Karakus, M and Chanda, E K, 2020c. Proposed solution for the ground reaction of non-circular tunnels in an elastic-perfectly plastic rock mass, *Computers and Geotechnics*, 119(November 2019), 103354.

Kabwe, E, Karakus, M and Chanda, E, 2020d. Time-Dependent Solution for Non-Circular Tunnels Considering the Elasto-viscoplastic Rockmass, *International Journal of Rock Mechanics and Mining Sciences*.

Kaiser, P K and Cai, M, 2012. Design of rock support system under rockburst condition, *Journal of Rock Mechanics and Geotechnical Engineering*, 4(3):215–227.

Kaiser, P K, McCreath, D R and Tannant, D D, 1996. *Canadian Rockburst Support Handbook*, Geomechanics Research Center.

Keneti, A and Sainsbury, B A, 2018. Review of published rockburst events and their contributing factors, *Engineering Geology*, 246(January):361–373.

Li, C C, 2010. A new energy-absorbing bolt for rock support in high stress rock masses, *International Journal of Rock Mechanics and Mining Sciences*, 47(3):396–404.

Li, C C, 2017. Principles of rockbolting design, *Journal of Rock Mechanics and Geotechnical Engineering*, 9(3):396–414.

Li, C C, 2021. Principles and methods of rock support for rockburst control, *Journal of Rock Mechanics and Geotechnical Engineering*, 13(1):46–59.

Li, C C, Mikula, P, Simser, B, Hebblewhite, B, Joughin, W, Feng, X and Xu, N, 2019. Discussions on rockburst and dynamic ground support in deep mines, *Journal of Rock Mechanics and Geotechnical Engineering*, 11(5):1110–1118. https://doi.org/10.1016/j.jrmge.2019.06.001

Ortlepp, W D and Stacey, T R, 1994. Rockburst mechanisms in tunnels and shafts, *Tunnelling and Underground Space Technology Incorporating Trenchless*, 9(1):59–65.

Ortlepp, W D, Bornman, J J and Erasmus, N, 2001. The Durabar–a yieldable support tendon–design rationale and laboratory results, *Rockbursts and Seismicity in Mines (RaSiM5)*, 263–266 (South African Inst of Mining and Metallurgy: Johannesburg).

Potvin, Y and Wesseloo, J, 2013. Towards an understanding of dynamic demand on ground support, in Y Potvin and B Brady (eds), *Ground Support 2013: Proceedings of the Seventh International Symposium on Ground Support in Mining and Underground Construction*, pp 287–304 (Australian Centre for Geomechanics: Perth). https://doi.org/10.36487/ACG_rep/1304_18_Potvin

Rahimi, B, Sharifzadeh, M and Feng, X T, 2020. Ground behaviour analysis, support system design and construction strategies in deep hard rock mining – Justified in Western Australian's mines, *Journal of Rock Mechanics and Geotechnical Engineering*, 12(1):1–20.

Simser, B, 2002. Modified cone bolt static and dynamic tests, Noranta Technology Centre Internal Report, Noranta Technology Centre, Quebec, Canada.

Varden, R, Lachenicht, R, Player, J R, Thompson, A G and Villaescusa, E, 2008. Development and Implementation of the Garford Dynamic Bolt at the Kanowna Belle Mine, *10th Underground Operators' Conference*, p 95 (The Australasian Institute of Mining and Metallurgy: Melbourne).

Wu, Y K and Oldsen, J, 2010. Development of a new yielding rock bolt-Yield-lok bolt, *44th US Rock Mechanics Symposium and 5th US-Canada Rock Mechanics Symposium.*

Zhai, S, Su, G, Yin, S, Zhao, B and Yan, L, 2020. Rockburst characteristics of several hard brittle rocks: A true triaxial experimental study, *Journal of Rock Mechanics and Geotechnical Engineering*, 12(2):279–296.

Roof characterisation for hazard planning at Oaky North mine using geophysical data

T Medhurst[1], B Vorster[2] and A Huey[3]

1. Director, Resource Geotechnical Pty Ltd, Cairns Qld 4870. Email: resgeotech@bigpond.com
2. Principal Geotechnical Engineer, Coal Assets Australia, Glencore, Singleton NSW 2330.
   Email: brian.vorster@glencore.com.au
3. Geotechnical Engineer, OSE Group Pty Ltd, Cairns Qld 4870.
   Email: adam.huey@osegroup.com.au

ABSTRACT

Roof conditions at Oaky North Mine can be prone to stress related damage and/or time dependent degradation. The ability to identify these areas prior to mining has proved challenging using traditional methods. To help alleviate this situation, a study was initiated to investigate methods for roof characterisation using geophysical logs. This involved the use of neutron log data to provide an indirect measure of the proportion of carbonaceous/micaceous laminae present in the immediate roof strata. Detailed analysis of the shale–porosity inter-relationships arising from this analysis provided a means to estimate the proportion of laminations for a given roof interval. This paper outlines the process and how it was used to improve the current GSR modelling and hazard mapping process.

INTRODUCTION

Oaky North Mine had experienced difficulties in predicting areas of poor roof conditions in some areas of the mine, which was having an impact on the application of TARPs, development rate and secondary support management process. The immediate sandstone roof is fine grained and finely bedded and mostly of good quality. However, there are areas commonly referred to as 'micaceous roof' that are prone to stress related damage and/or time dependent degradation. Carbonaceous banding which is often associated with micaceous layers in the immediate roof was known to be prevalent and suspected to have a role in this roof behaviour.

This prompted an initial study into the characteristics of micaceous roof at Oaky North. Roof cores were taken and sampled for geotechnical laboratory testing. The testing program included triaxial testing, shear testing, slake durability testing and measurement of moisture content from which porosity could be determined. In addition to the geotechnical testing, cores were taken for petrographic and XRD analysis.

A complementary investigation was also undertaken to examine the use of geophysical logs for strata characterisation using the Geophysical Strata Rating (GSR). The study showed that porosity, clay and GSR values obtained through the analysis of the geophysical logs were consistent with the results obtained by other geotechnical testing and characterisation methods. Lower values of GSR were also found in zones of poor roof. However only relatively small changes in GSR were identified when compared to the relatively large differences in roof behaviour that were observed. Presumably this was due partly to the increased presence of carbonaceous and micaceous material. But also, other factors such as timing/type of support installation and the location of overlying weaker units such as the Sandy Creek siltstone (SCST) needed to be considered.

Careful drilling and logging are often able to identify such zones, but this is often 'after the fact', and methods were needed to aid prediction. As part of previous research activities, a method for assessing the distribution of laminated clays within sandstones using porosity-clay cross-plots was identified (Hatherly and Medhurst, 2010) that could be applied in GSR analysis (Medhurst, 2017). It was therefore proposed to further develop this approach and determine whether it could be used to improve the current strata characterisation and hazard management planning process.

STRATA CHARACTERISATION

Clay – porosity models

The distribution of the clays within the various rock types can then be investigated by cross-plotting the clay content against the porosity for a given strata interval. Figure 1 shows an example of a histogram of cross-plotted data taken from two different boreholes (Hatherly *et al*, 2016). The histogram in Figure 1a shows that the clay content is independent of the porosity which is largely constant. In Figure 1b the clay content and the porosity are inversely related. As discussed by Katahara (1995), these differences are due to the clays in the first borehole being present as grains which don't affect the overall porosity estimate. Such clays constitute a structural clay model, in which the clays replace the grains. In the second case, the clays are present as tight laminated clays which have low porosity. Layers of laminated clays are interbedded with porous sandstone and form a laminated clay model.
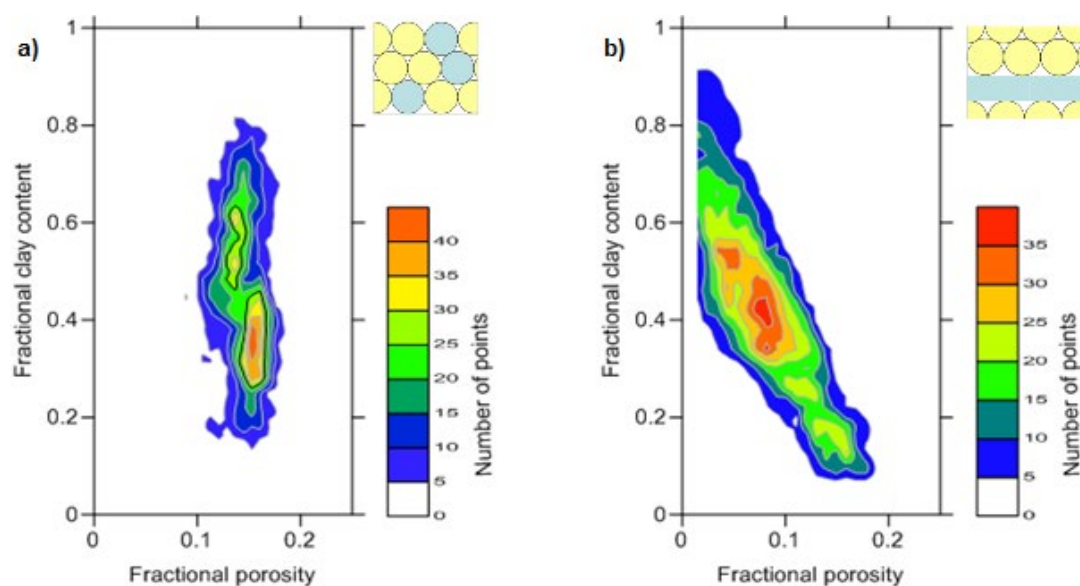
FIG 1 – Cross plots of clay content and porosity.

From a geotechnical perspective, it is useful to be aware of these differences. With laminated clays, separation along bedding planes is to be expected. This is a useful concept that could be applied at Oaky North, but it requires a reliable method for estimating both clay and porosity.

Gamma log versus neutron log clay analysis

Gamma logs record natural (passive) radioactive emissions, of which the main sources in borehole walls are potassium-bearing clay minerals. They are the standard method in Australia for geophysical lithological logging as they can be run in dry and even cased boreholes, making it useful for near surface layers and for lithologies above the water table. The disadvantages of gamma logs are that they have poor resolution and can be inaccurate when potassium bearing minerals occur as part of the shale (or clay) component of the rocks and as part of the matrix. For example, clean sandstones that contain potassium rich feldspars in their matrix can present as being clay rich. Conversely, if potassium deficient kaolinite and, to a lesser extent, the swelling clays are present, the log response for these shales is decreased.

An alternative, less-common method is neutron logging. The neutron log response is largely due to the amount of hydrogen present. The analysis of the neutron log in combination with the density log allows the effect of the hydrogen in the pore water to be removed, leaving only the response to the water that is bound in the clay minerals. There is generally a strong correlation between the amount of matrix-bound water present (as indicated by the X-ray diffraction analysis) and the shaleyness predicted by the neutron and density log analysis. In general terms, the neutron-density shale analysis can be more reliable than the gamma log.

Figure 2 shows an example of clay porosity analysis of the immediate roof interval from a typical hole at Oaky North. The plot on the left shows the analysis using the gamma log and the plot on the right shows the analysis using the neutron log. The corresponding cross-plots are shown.
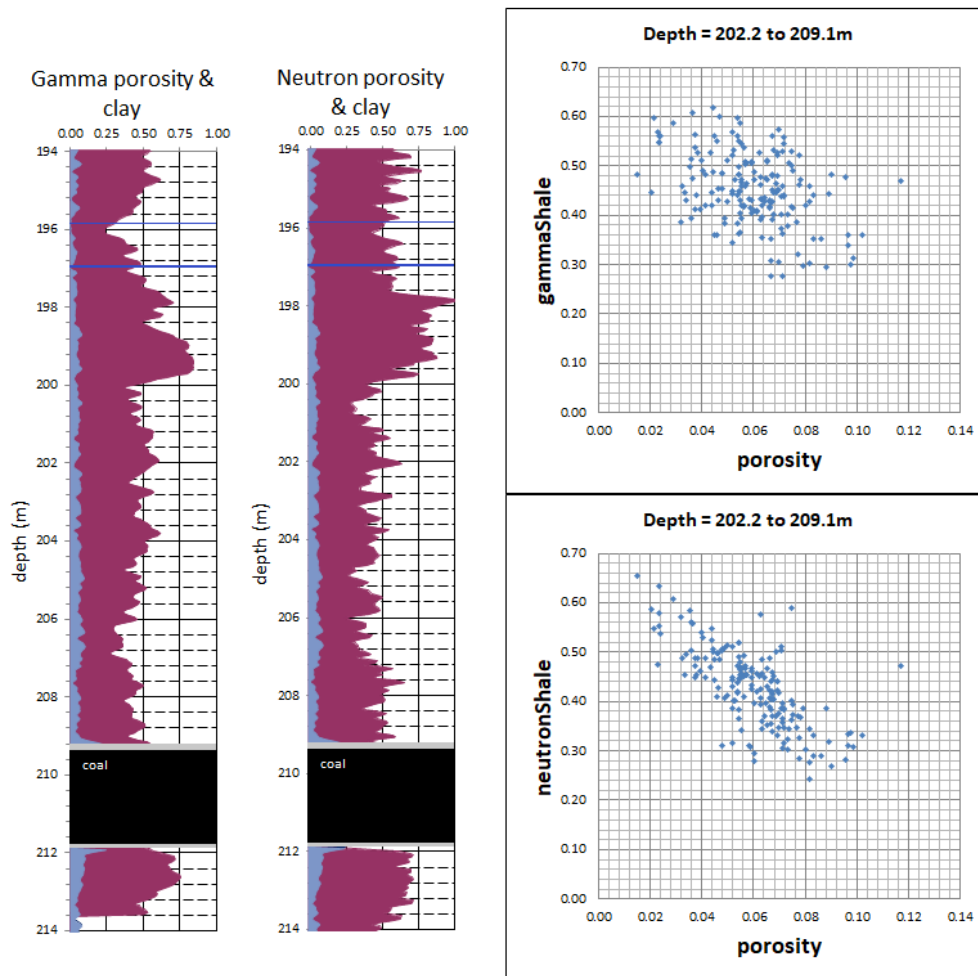

FIG 2 – Example of clay porosity relationship at Oaky North.

The neutron analysis shows a finer resolution for identifying individual beds in the immediate roof strata than that of the gamma analysis. With this higher resolution, a much stronger correlation with laminated strata is observed with the neutron-based analysis. It is noted that neutron logs are influenced by the presence of mica and iron rich minerals such as chlorite, which were identified in the mineralogical analysis. It was therefore concluded that the neutron-based analysis would better approximate the influence of laminated carbonaceous and/or micaceous material present in the strata and any clays that may be associated with time dependent degradation. In other words, this provides a potential measure of the degree of laminated roof strata.

Laminated strata

To investigate the ability to predict the presence of carbonaceous/micaceous strata, a series of locations around the mine were selected to assess the laminated clay-porosity model. Figure 3 shows an example of the analysis.
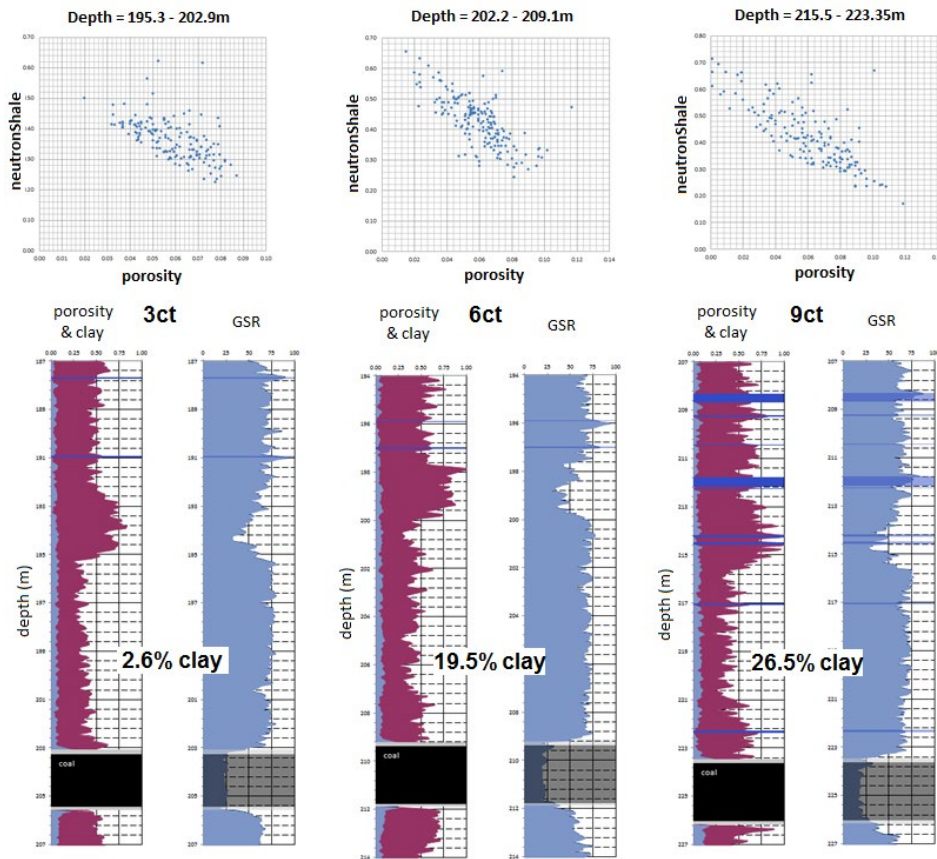
FIG 3 – Example of porosity, clay and GSR logs for roof strata along gate road.

The analysis shows GSR values are relatively constant whilst the neutron analysis shows the presence of laminated sandstones with increasing carb/shale and/or micaceous contents. The results indicate an increase from 2.6 per cent to 26.5 per cent in 'shales' over the 8 m roof horizon.

Based on the preceding analyses, it was determined that a measure of shale content taken from neutron log data would be a useful indicator of laminated roof conditions. However, the analysis also showed that the location of the carbonaceous/micaceous zones is an important influence on the roof behaviour. Further analysis was, therefore, undertaken on holes of unknown location and without prior knowledge of roof conditions (supplied by OCN) to test the hypothesis (shown in Figure 4).
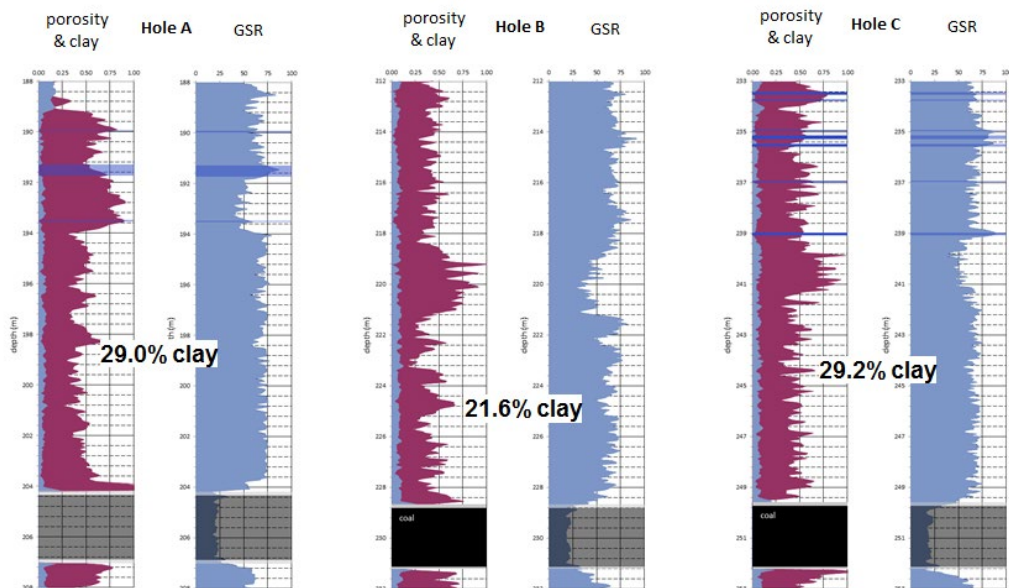
FIG 4 – Porosity, clay and GSR logs for test holes.

Estimated shale contents for the roof sandstone between the GC seam and the SCST from the cross-plots are also shown. An example of the test hole analysis is summarised in Table 1 along with description of conditions provided by OCN following the test.

TABLE 1

Example of test hole analysis.

Hole	Shale	Conditions	Comments
A	29.0%	Good ground conditions	Distance to SCST = 10 m, shales in upper 5 m
B	21.6%	Centreline cracking and bagging	Distance to SCST = 7 m, shales in lower 4 m
C	29.2%	Significant amounts of roof bagging and centreline cracking	Distance to SCST = 8 m, shales evenly distributed

The results suggested that poor roof conditions were more critical if the shales were in the lower part of the roof. In most cases at Oaky North, heights of softening in roadways are generally limited to the first 4 m to 5 m of roof. It was therefore proposed to examine shale contents in the 0.5 m to 4.5 m roof interval as means of assessing poor roof. The first 0.5 m of roof was excluded to eliminate any near seam effects from the data. The results are summarised in Table 2 and show a good correlation between estimated shale content and roof conditions.

TABLE 2

Test hole analysis in 0.5 m to 4.5 m roof interval.

Hole	Shale	Conditions
1	0.0%	Good ground conditions
2	31.7%	Transition to centreline cracking and bagging
3	33.3%	Centreline cracking and bagging
4	30.9%	Centreline cracking and bagging
5	59.3%	Very poor conditions
6	16.0%	Good ground conditions
7	29.6%	Centreline cracking and bagging
8	32.1%	Significant amounts of roof bagging and centreline cracking

GEOTECHNICAL ANALYSIS

Shale content

To develop a laminated roof model at Oaky North using neutron logs, a process was adopted for velocity matching that also preserved the matrix density values used in the previous gamma-based analysis. This was important to achieve consistency in the analysis. In most holes broad estimates of shale content were similar between gamma and neutron-based assessments, albeit that the frequency (fineness) of the resulting shale distributions in each log are different.

In some cases, significant variations between gamma and neutron-based estimates were present, which required further analysis. In these cases, the resulting log data were found to hover around, above and below the 50 per cent shale/sand threshold, making estimates of shale content over the interval very sensitive to the end points used. This is, however, an unavoidable outcome from the analysis simply due to the nature of the roof strata, being at the cusp of the sand/shale threshold.

Figure 5 shows the proportion of shales present in the roof at Oaky North from the neutron-based analysis. Based on the analysis outlined in Table 2, it was determined that areas with shale contents greater than 25 per cent (0.25) are most likely associated with carbonaceous/micaceous roof.
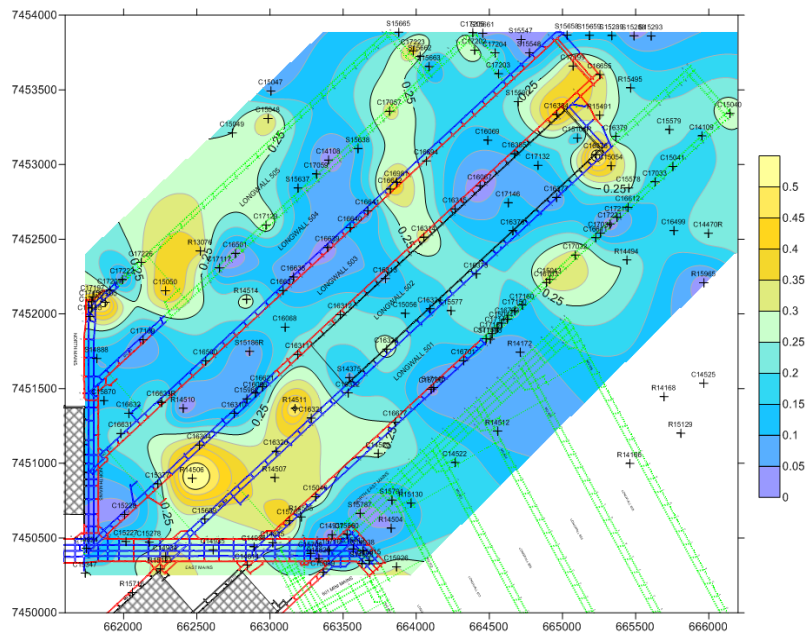
FIG 5 – Shale proportion in 0.5 m to 4.5 m roof horizon above the GC seam.

Roof conditions

Variations in roof quality, roof beam thickness and mining induced stress conditions will all affect roof conditions. The issue of roof quality is addressed via estimation of shale content. Experience also shows that the GC seam to SCST interburden thickness is an important parameter at Oaky North as it defines the maximum thickness of the potential roof beam, but also influences the performance and required anchorage length of the long tendon support.

Figure 6 shows the SCST-GC interburden thickness. Areas where the GC-SCST is less than about 10 m had also been found to correlate with areas of poor roof. This of course is also dependent on how weak or strong the roof beam is (lamination dependent) and the ability of the beam to resist the imposed stresses.
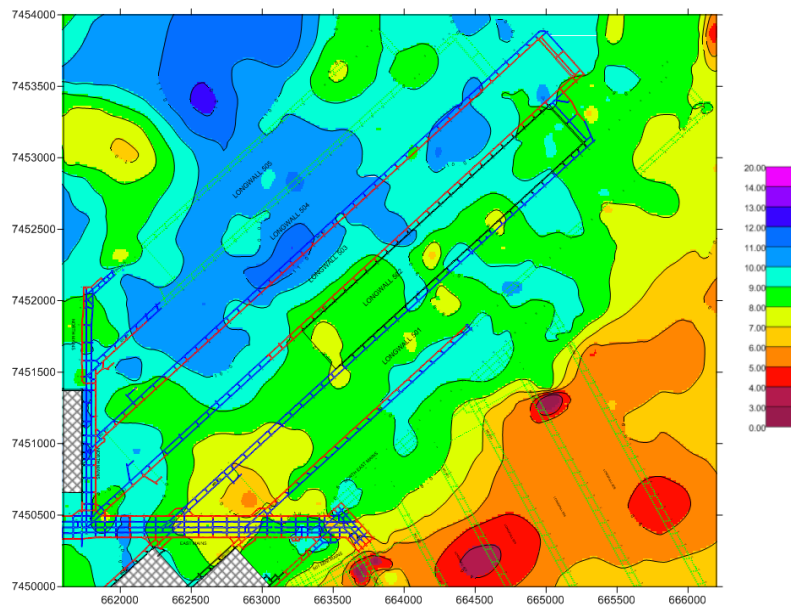
FIG 6 – GC to SCST interburden thickness.

Mining induced stresses

Failure of roof strata is dependent upon the strength to stress ratio of the strata. The estimation of mining induced stresses, however, is more problematic. Our experience suggests that development roadways in virgin mining areas might be subjected to stress concentration factor (SCF) ≈ 1.2 to 1.3.

However, in areas adjacent to longwall panels, geological structure or other mined out areas can have a significant effect on *in situ* stress conditions. From this perspective, the overall stress impact on roof support requirements needs to be considered on a case-by-case basis as part of the support design. Nevertheless, areas where roof quality and sensitivity to high stress conditions would be most prominent for hazard planning purposes.

In our experience, stress related impacts on roof behaviour start to develop when the GSR-to-horizontal-stress ratio GSR/σ_H < 4. And this exacerbates until complete loss of roof beam competency develops as the GSR/$\sigma_H \approx 1$. Areas of potentially poor roof were deemed to be associated with the combined influence of a weak and relatively thin roof beam. It was therefore proposed where the GC-SCST is less than about 10 m and the clay is greater than 0.25, this tends to be associated with poor roof conditions, shown in Figure 7.
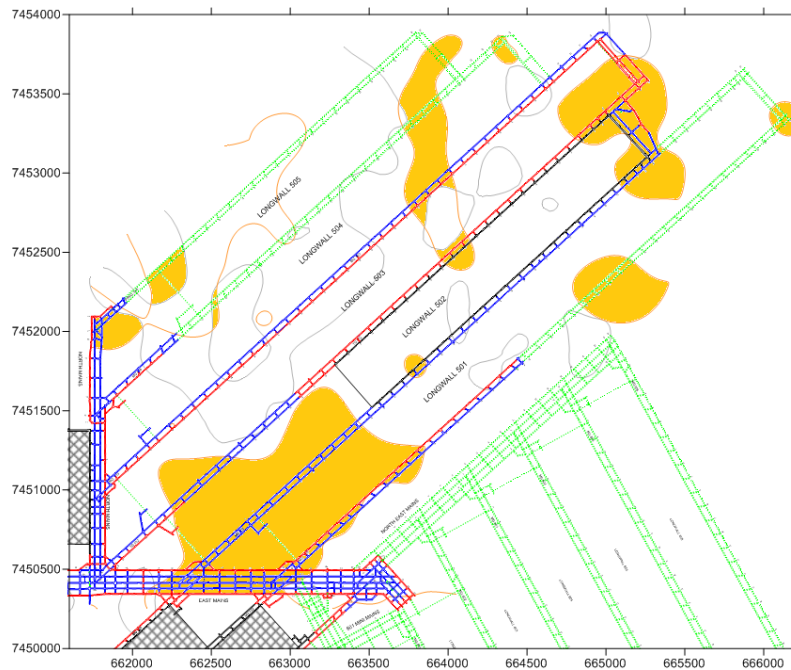
FIG 7 – Roof zones prone to stress related damage.

GSR in laminated strata

The general premise of the laminated clay model is the inverse correlation between porosity and clay content (VShale) arising from the neutron log analysis. The slope of this line defines the relationship between the proportion of clays between sand layers and porosity, ie the higher the porosity, the higher proportion of sand and vice versa. This also means that it provides a pseudo measure of the proportion of laminations as a function of the porosity. And, as such, if it can be established as a general relationship for a particular strata interval, then it could be used as a measure of laminated roof.

Figure 8 shows the neutron porosity relationship for the sandstone roof at Oaky North. This suggests a general relationship that can be applied to estimate GSR for laminated strata.
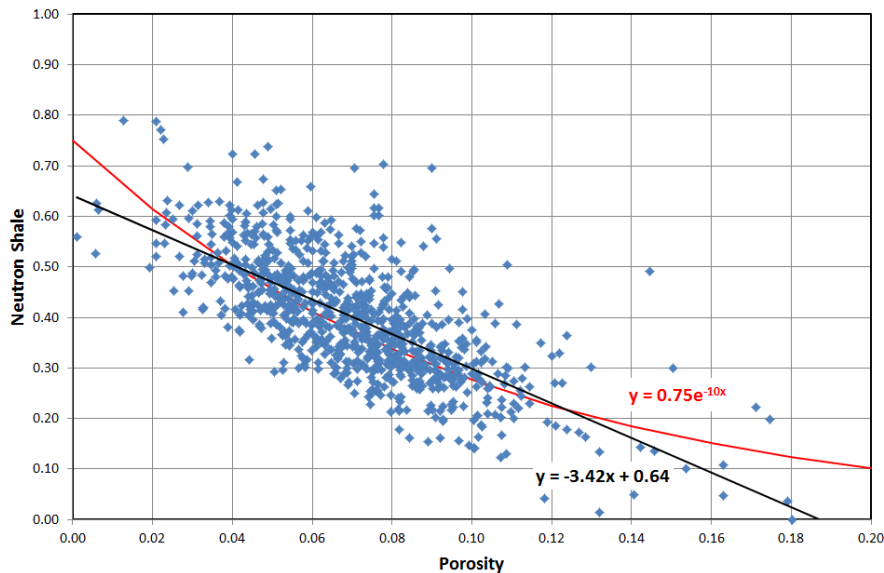
FIG 8 – Relationship between porosity and neutron shale in immediate roof.

Both the linear best fit and an exponential curve approximation is shown. From a mathematical perspective an exponential relationship is more useful in a GSR formulation as it avoids the effect of zero cut-offs, ie where porosity >0.18 if a linear correlation is used. It is, therefore, proposed that the value of the GSR could be decreased in accordance with the porosity (ϕ) versus shale relationship. A lamination factor is proposed as follows:

$$GSRL = GSR \times L$$

where L = 1 – 0.75e-10ϕ.

It should be noted that this relationship is specific to Oaky North where laminated sandstone roof can be identified according to the relationship shown in Figure 8. The resulting effect is a 50 per cent reduction in GSR for a typical value of ϕ = 0.05 for the laminated sandstones. The purpose of this reduction is to enable the use of GSR values in convergence-based support design (Medhurst, 2017), which includes measures such as GSR/σ_H ratio to incorporate mining induced stress influences into the analyses.

In related studies, a laminated roof reduction factor has been successfully applied to the GSR for carb/micaceous strata to assess support requirements and TARP triggers at Oaky North. For these roof conditions, this can reduce GSR values by approximately 50 per cent.

Depending upon the roof quality and by applying a threshold GSR/σ_H < 4 and the lamination factor, more detailed assessments can be made relative to the mining sequence. Stress direction is also important, eg roadways versus cut-throughs, and obviously these considerations need to be included in the context of roof quality and stress concentration effects.

CONCLUSIONS

The study identified that areas of poor roof occur where the sandstone beam is laminated, with roof stability being dependent upon the stresses imposed. A strata model was developed that used an estimate of shale content over the 0.5 m to 4.5 m roof interval as an identifier of carbonaceous/micaceous roof. Experience showed that the GC to SCST interburden thickness is an important parameter as it governs the effective thickness of the overlying roof beam, but also influences the performance and required anchorage length of the long tendon support. A composite plan was subsequently developed to represent areas of potentially poor roof conditions where the GC-SCST is less than 10 m and the clay is greater than 25 per cent (0.25). Work continues on refining the approach to account for mining induced stresses.

ACKNOWLEDGEMENTS

REFERENCES

Katahara, K W, 1995. Gamma ray log response in shaly sands, *Log Analyst*, 36(4).

Hatherly, P and Medhurst, T P, 2010. Additional opportunities for geophysical log analysis, *Proc Bowen Basin Symposium 2010*, pp 147–152 (GSA Coal Geology Group).

Hatherly, P, Medhurst, T and Zhou, B, 2016. Geotechnical evaluation of coal deposits based on the Geophysical Strata Rating, *Int J of Coal Geology*, 163:72–86.

Medhurst, T, 2017. *ACARP Project C24015 End of Grant Report: Convergence Based Roof Support Design*, PDR Engineers Pty Ltd Report No. 15080.

Admixture use in cemented rock fill

J O'Brien[1], B Roache[2] and M Gray[3]

1. Senior Geotechnical Engineer, Glencore, Mt Isa Qld 4825. Email: jake.obrien@glencore.com.au
2. Principal Geotechnical Engineer, Neboro, Melbourne Vic 3000. Email: broache@neboro.com.au
3. Manager – Underground Mining, New Century Resources, Melbourne Vic 3000. Email: mgray@newcenturyresources.com

ABSTRACT

Admixture use in cement products is commonplace in the construction and mining industries. Many Australian mines have an operational concrete batch plant and stock hydration control and water reducing admixtures. The benefits of admixture use, especially in shotcrete is understood and well documented.

Cemented rock fill (CRF) is used to fill stope voids and create stable vertical and undercut surfaces at some Australian mines. These mines generally mix rock fill with a slurry of cement and water without the use of admixtures. Recently published work on optimisation of CRF mixes has mainly focused on the strength increases associated with changes to the mix grading proportions by the addition of fines, but not focusing on the potential benefits of admixture use. Admixture use in CRF may be the simplest CRF optimisation method, as the admixtures will often be added by the push of a button at the batch plant.

A CRF testing program was undertaken to test the benefits of admixture use in terms of strength gain, using hydration control additives (HCA) and high range water reducer (HRWR) admixtures. Rock fill gradings were strictly controlled in the test process to allow clear definition of the difference admixtures provide in compression at 28 days. The testing results define admixture associated strength gains in a 6 per cent general purpose (GP) cement by dry weight CRF mix (131 kg of cement/m³). Costings have been developed to allow a mine operator to understand the cost benefits of admixture use in CRF due to reduced operating costs. Operational efficiency advances and a suggested admixture implementation plan for CRF optimisation is offered.

INTRODUCTION

CRF is a fill product that has widespread use worldwide, including at Australian underground mines where it is often favoured by small to mid-sized narrow vein operations due to relatively low implementation cost. Miners make use of concrete batch plants that are often already part of the mine infrastructure and mix rock fill with a slurry of cement and water to create CRF. Mixing generally occurs underground at mixing bays located near the stope tip point, where loaders mix the slurry with the rock fill and then deposit the CRF directly into the stope. There are some variations to this, such as surface CRF mixing, use of ejector trucks to dump CRF into the stope or even conveyor fill systems, however the process of batching a cement slurry on surface and agitator truck transport of the slurry to underground mixing sumps is commonly followed. Figure 1 shows a schematic representation of the typical CRF process.

Admixture use in CRF or cemented aggregate fill (CAF) mixes is commonplace in North American mines, but admixtures are not used with CRF in the majority of Australian underground mines that implement a CRF fill process. Admixture use in CRF may be the simplest CRF optimisation method, as the admixtures will often be at the mine site's concrete batch plant for use with shotcrete and other concrete products, ready to use and can often be added by the push of a button.

This paper describes a process that mines can follow to optimise their CRF mix, with the intent to reduce operating costs and increase backfilling rates, but not compromise the stability of the CRF exposures when mining. Admixture is added as a part of this optimisation process, to show the influence of both high range water reducers (HRWR) and hydration control additives (HCA), and a cost benefit assessment example is provided.
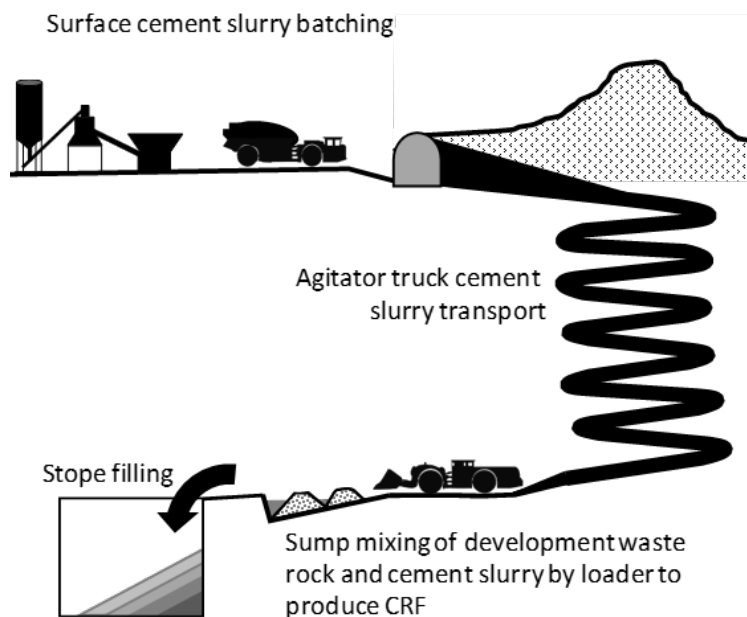
FIG 1 – Schematic representation of the typical CRF process.

BACKGROUND OF ADMIXTURE USE IN CRF

Some North American mines have a history of using admixtures in their CRF mixes. Stone (2007) discusses the widespread use of admixture in CRF at mines in Nevada and that HCA products increase hydration time and HRWR products make the fill more flowable. Stone also makes the connection between the high clay content of some waste rock sources at Nevada mines and the need to use admixtures to prevent the clays soaking up water and preventing significant reduction in water to cement (w:c) ratios.

Published test results documenting the potential benefits of admixture use in CRF are relatively limited. There are three key references that describe testing results of admixture use with CRF. All describe a clear relationship between CRF strength gain and admixture use.

Wang *et al* (2002) demonstrated gains in unconfined compressive strength (UCS) tests of 26 per cent and 30 per cent using two different HRWRs. A simple summary of the results showed that an admixture addition of 300 mL/100 kg cement, increased the CAF UCS by 26 per cent, while a UCS increase of 30 per cent at a dosage of 600 mL/100 kg cement was possible.

Farzam, Rispin and Karlson (1998) describe the use of HRWR to gain substantial improvements in cemented aggregate fill CRF compressive strengths at the Getchell Mine in Nevada. This had a flow on effect of improving the CRF UCS, while reducing cost by allowing reduction in cement use. A 14 per cent improvement in 28-day UCS test results was achieved with a 4 per cent cement CRF mix and more than 30 per cent improvement when using a 7 per cent mix.

Wang and Villaescusa (2001) discuss various factors that influence the strength of CAF. Admixture use is mentioned, and some strength gains are published. The admixture type is not stated, but Wang and Villaescusa state:

> The general trend from the experimental results is that a 0.3~0.4% admixture dosage is capable of increasing CAF strength by around 12%. The results also show that a dosage of 0.5% would indicate an adverse impact on the development of cemented aggregate fill strength.

They report significant strength gains when tailings were added to the CAF, in addition to the admixture, with strength gains of between 35 per cent and 55 per cent, depending on the admixture dosage rate.

Two common types of admixture products that are available at most mine site batch plants are HCA and HRWR products. Each has a specific role to perform and both products have seen significant development and improvement over time. The names of the admixture brands have not been used

in this paper, as most concrete admixture suppliers have products available, although each will have specific advantages and disadvantages.

HCAs have replaced set retarders in shotcreting and high-performance sprayed concrete (HPSC) applications in recent years and are the most common product stocked at a mine concrete or shotcrete batch plant. HCAs allow the user to control when the hydration process of the cement commences by varying the dosage of the product. Some key advantages of HCA products over traditional set retarders is that HCAs deliver improved slump retention performance, prevent generation of heat caused by hydration, have less sensitivity to placement conditions and temperature and critically, they are specifically formulated to be used with HRWRs and nozzle set-accelerators (SAs).

HRWRs are used to allow mix designs to be formulated to deliver performance improvements through lower w:c ratios which in turn delivers higher strength concrete. They can also be used to increase the workability or slump of the concrete without causing segregation, as well as improve pumpability and placement characteristics.

When cement is mixed with water, electrical charges on the surface of the cement particles cause them to attract to one another and during this process much of the mix water can become absorbed leading to loss of slump and workability. In basic terms, HRWRs work by neutralising the surface charges on the cement particles so that the amount of mix water absorbed is greatly reduced, and they also help to develop a repulsion force between particles in the mix leading to lower viscosity.

Water-reducing admixtures are typically divided into three main categories:

- Low-range – lignosulfates, hydroxylated carboxylic acids, carbohydrates.

- Mid-range – lignosulfates, polycarboxylates.

- (HRWRs) High-range – polycarboxylates (PCEs), sulfonated formaldehyde condensates (melamine/naphthalene-based), lignosulfates.

Most mine-site concrete/shotcrete batch plants will stock HRWRs, with PCEs being the newest technology and this is increasingly common due to their suitability to mining applications. The PCE HRWRs are synthetically produced allowing for very high performance at low dose rates.

## ADMIXTURE IN CRF – TEST WORK TO DEFINE POTENTIAL BENEFITS

Laboratory test work was conducted by adding admixture to CRF mixes and assessing the compressive strength change compared to a control sample of CRF. The selected admixtures were HCA and HRWR.

When HCA is omitted from the mix design, the cement will immediately commence the hydration process after water is added during batching of the cement slurry on the surface. By the time the cement slurry is mixed with development waste rock to produce the CRF and then tipped into the stope, the cement may have been undergoing hydration for more than one hour.

As cement hydration progresses, the cement produces bonds between the CRF fines (material less than 10 mm) and aggregates and develops strength. During this early part of the cement hydration process, these bonds are relatively weak and if the CRF is mechanically impacted or agitated these bonds will be damaged. This results in overall strength loss within the CRF.

This is the same reason concrete test cylinders, sprayed square test panels or round determinate panels (RDPs) should not be disturbed for approximately 12–24 hours after being produced. Cement bonds are preserved from damage caused by agitation, flexing, dropping or bumping the samples. This same concept applies with CRF. As each bucket of CRF is tipped into the stope, it will impact the CRF already in the stope with significant force. This impact damages the bonds forming in the CRF leading to overall strength reduction. By using HCA-dosed CRF the cement hydration process is significantly delayed improving overall CRF performance. By considering a standard CRF filling process involving cyclic tipping of CRF into the stope, HCA-treated CRF within the stope will be less sensitive to ongoing damage from CRF being tipped into the stope. Cement hydration will not commence until a controlled time, meaning that additional layers of CRF tipped into the stope will eventually protect and shield previously placed CRF from impact damage.

Similarly, as the CRF accumulates in the stope some consolidation may occur, which results in particles moving relative to each other and therefore breaking any cement bonds which may have started forming. HCA-dosed CRF will be less sensitive to strength loss caused by consolidation-induced damage to the cement bonds. The delayed hydration strength boosting effect is shown conceptually in Figure 2. It is also important to note that a significant risk in transporting grout in an agitator truck is that the grout can harden in the bowl if it is not discharged in a timely manner. This can occur due to breakdowns, emergencies, or delays and the risk is reduced if HCA is used as the rate of hardening of the slurry is controlled and can extended by adding more product.
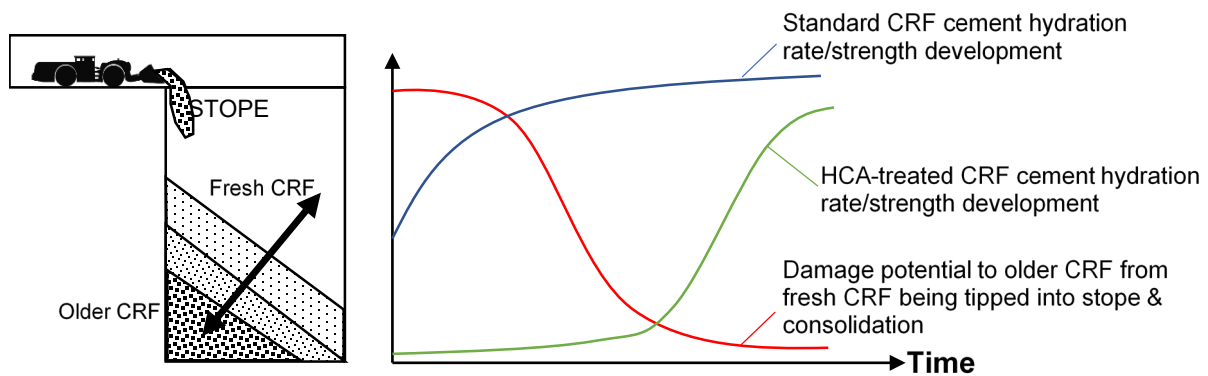
FIG 2 – Conceptual diagram and graph showing the interaction between older and freshly placed CRF, damage from tipping and consolidation and hydration time of standard CRF and HCA-dosed CRF for the first 24 hours after batching. HCA-dosed CRF delays the cement hydration which helps to avoid damage to the bonds leading to higher overall strength of the CRF.

HRWR is used in CRF primarily to either reduce the water required in the mix design to achieve higher strengths, or to achieve a UCS target using lower cement content as less water is needed to meet the workability/slump target.

Another application of HRWR is to enable modification of the cement slurry recipe. This has the flow on potential of HRWR being used to improve CRF productivity that is sometimes limited by agitator truck cycle times. In many Australian mines, the CRF is produced when an agitator truck is filled with cement slurry on the surface at the concrete batch plant, in a batch size typically of 5 m³ to 6 m³ and limited by the volume of the bowl. The cement slurry is transported underground in the agitator and delivered to a mixing sump close to the stope void being backfilled. A loader/bogger mixes the cement slurry with approximately 80 t development waste rock and trams CRF in its bucket to the tipping edge and tips the CRF into the stope void. Due to the time required to batch and transport each load from the agitator, the agitator cement slurry delivery rate is almost always the limiting factor in this overall process.

For mine sites that wish to decrease agitator cycle time to increase CRF production rates, HRWR can offer a solution. The solution involves modifying the batch plant cement slurry mix design, so that the agitator brings a concentrated cement slurry as high in cement content as possible, to the underground mixing sump. The concentrated cement slurry is then diluted back to normal cement slurry w:c ratio at the underground mixing sump via water addition, which can easily be controlled using a simple mechanical flow meter. HRWR is required in the concentrated cement slurry mix in order to be able to successfully batch and transport a very low w:c ratio cement slurry underground.

This results in the agitator spending more time transporting cement rather than water and CRF production rates can be significantly increased. For a practical example, consider a typical underground mine, described in Table 1 that demonstrates an increase in CRF production by 50 per cent.

TABLE 1

Comparison between standard and concentrated CRF batching.

CRF recipe	Standard	Concentrated approach
Agitator load size	6 m³	6 m³
Cement slurry at batch plant	6 m³	6 m³
Admixture usage	None	HCA + HRWR
UG water addition	None	3 m³
Total cement slurry produced per agitator trip to underground mixing bay	6 m³	9 m³
Total waste rock added	80 t	120 t
Total CRF produced per agitator trip	40 m³	60 m³

Laboratory test set up

The following factors were considered during the preparation for testing of CRF samples:

- Particle size distribution (PSD) of samples was standardised for the test program. PSD variability in run of mine waste can cause variability in the strength derived from UCS testing of CRF cylinders. An optimised Talbot grading with a maximum particle size of 40 mm was used to build consistent samples. The Talbot grading from Talbot and Richard (1923) is commonly used in the cement industry to form dense samples that are inherently stronger due to a lack of void space and increased density. The test sample gradings are shown in Figure 3. All mixes were created using readily available engineered sands, aggregates and cement from concrete ready-mix batch plants in order to ensure repeatability of testing and consistency of results, as shown in Figure 4. The test grading was achieved using the following process:

  o Step 1 – Determined an average PSD for a 'typical' mine development waste rock, limited to 40 mm top size (grey line in Figure 3).

  o Step 2 – Determined the Talbot grading for CRF limited to 40 mm top size (orange line in Figure 3).

  o Step 3 – Mixed a control rock fill as close as possible to the grey line using engineered sands and aggregates from batch plants (green line in Figure 3).

  o Step 4 – Attempted to use tailings addition (blue line in Figure 3) to the control mix (green line in Figure 3) to get the PSD of the control mix closer to the Talbot grading. The result was the finalised test sample grading (brown line in Figure 3).

- Cylinder size for test samples was selected as 150 mm diameter and 300 mm height. This was a functional size that reduced material handled in sample preparation, and easily fitted into the 2000 kN UCS machine. A maximum particle size of 40 mm, which is about a quarter of the test cylinder diameter is generally deemed at the limit of an acceptable ratio for testing a well graded rock fill, according to Penman (1971).

- A loading rate of 5 mm/minute was applied, with peak UCS recorded.

- Strength size effects when testing 150 mm diameter (6 inch) cement cylinders is a common issue that has been discussed by others, and well summarised by Warren *et al* (2018). Strength adjustments should be applied if attempting to relate 150 mm UCS test cylinders to real world strengths. In the case of this test program, only relative differences between samples was of interest, to establish a potential real-world improvement by using admixture, so therefore no strength adjustment was applied.

- The control CRF mix contained 6 per cent cement (dry weight). A more considered way of describing cement consumption is to use cement in kg/m³ of CRF produced. The control CRF mix contained 131 kg/m³ of general purpose (GP) cement. This prevents any confusion over

how the cement usage is calculated and is not influenced by moisture value measurement errors in the aggregates, which may be the case when defining cement content as a weight% of the dry solids in the mix. For example, a 6 per cent cement CRF mix could be used to describe the CRF cement quantity in terms of wet weight or dry weight and lacks the simplicity and precision of describing as cement used in kg/m^3.
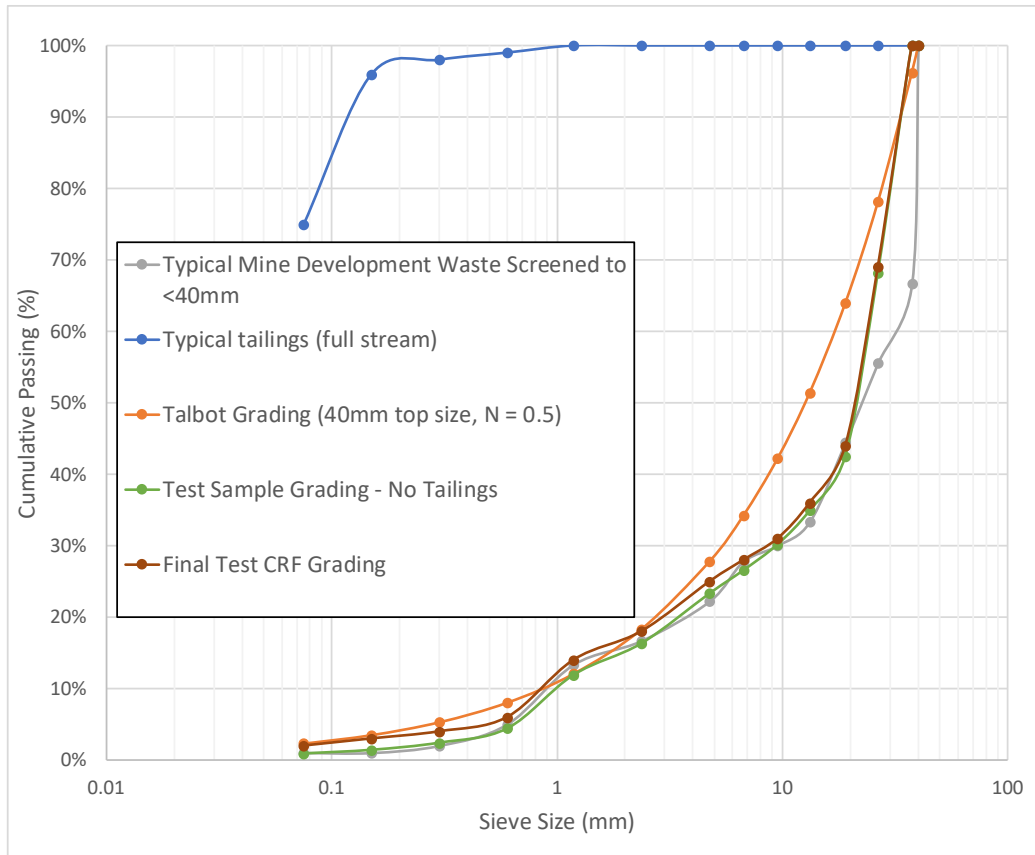

FIG 3 – PSD development of the test CRF.

FIG 4 – Laboratory CRF samples being prepared for UCS testing. Additional aggregates were used but are not visible in this photograph.

HCA testing program

To demonstrate the benefits of HCA usage in CRF, a testing program was devised. Two mixes were batched, one to replicate a CRF control mix and a second with HCA added at 240 mL/100 kg of GP. Three 150 mm diameter by 300 mm high cylinders were cast for each mix and were cured at 25°C in high humidity for 28 days before UCS testing. To mimic the damage to cement bonds of the already placed CRF in the stope during the initial curing period, the cylinders were tapped and agitated at 30 minutes and at 1.5, 2.5 and 3.5 hours after casting. Figure 5 shows the basic agitation and tapping method used.
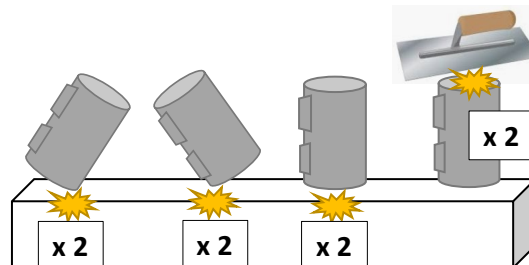
FIG 5 – Agitation and tapping method used for all HCA test cylinders.

The HCA treated CRF mix results demonstrated an increase in UCS of 33 per cent on average at 28 days, as shown in Figure 6. This testing result shows the importance of HCA when considering *in situ* CRF performance and raises the potential for cement reduction to achieve the design CRF strength in the stope.

HCA addition to the CRF mix enables reduced cement usage, while achieving the design CRF strength and resulting in significant cost reduction. The scale of cost reduction will depend on the mine production rate, but the saving due to reduced cement usage can easily be in the range of tens of thousands to hundreds of thousands of dollars in reduced expenditure.
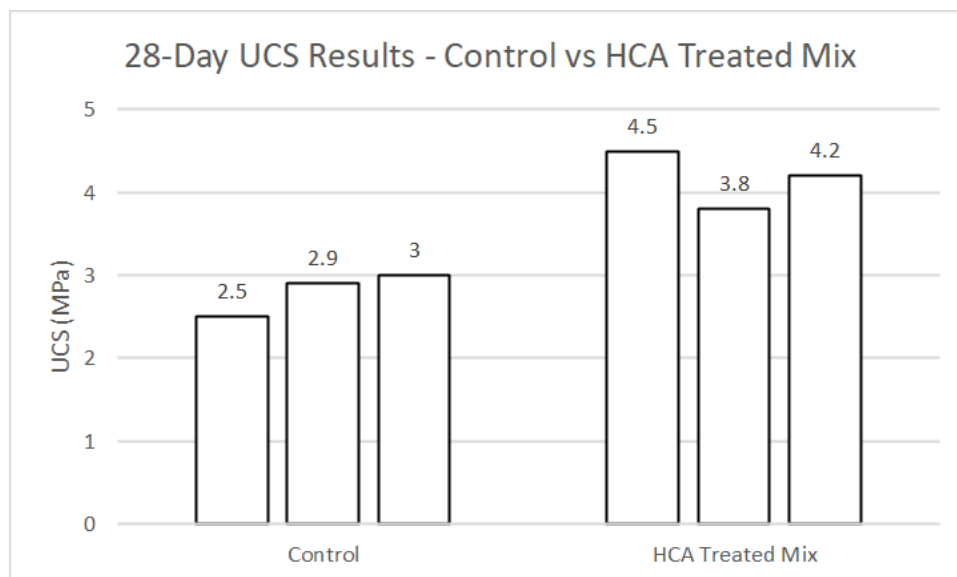
FIG 6 – 28-day UCS results of HCA treated CRF cylinders subjected to agitation after casting.

Removing the agitator truck bottleneck – using HCA and HRWR

A laboratory testing program was devised to demonstrate the concentrated cement slurry concept. As explained, earlier, if more cement can be taken underground by the agitator truck, stope void filling rates may be able to increase significantly. There are two main components involved with validating the concentrated cement slurry concept:

1. Confirm the concentrated cement slurry can be successfully batched and transported and discharged from an agitator truck in the mixing sump. A concentrated cement slurry recipe was tested and HRWR and HCA were added to achieve desired consistency – the aim was to

produce a flowable cement slurry mix that could be easily batched, transported and discharged.

2. Water is added to the concentrated cement slurry to produce standard cement slurry from which CRF is produced.

A potential issue with adding water to a concentrated cement slurry containing high levels of HRWR is that too much water addition may cause segregation of the cement slurry, which is detrimental to CRF performance and shown in Figures 7 and 8. The example of a segregated test cylinder shown in Figure 8 only achieved a UCS of 0.8 MPa after 28 days curing time due to lack of cementing of aggregates caused by segregation of the cement slurry. A series of trials were completed and involved batching various concentrated cement slurry mixes using HCA and HRWR and adding water until segregation occurred. It was found that best results were obtained when water addition produced 1.5 times the starting volume as a standard cement slurry mix (6 per cent cement by dry weight or, more correctly, 131 kg/m^3 cement per 1 m^3 of CRF produced), meaning a 50 per cent gain in cement slurry volume for each agitator truck cycle.

FIG 7 – CRF mix in concrete mixer showing segregation. Note the slurry is too runny and is not coating and clinging to the aggregates.

FIG 8 – Photograph of CRF cylinder showing clear segregation of the cement slurry from the aggregate. Note the colour change in the base of the cylinder, as well as the lack of slurry coating the large aggregate.

A series of concentrated cement slurry recipes were explored using a range of HCA and HRWR addition rates. For each mix, three 150 mm diameter × 300 mm height cylinders were cast and cured at 25°C, at high humidity. The cylinders were tested for UCS after 28 days curing time, with results summarised in Figure 9. The UCS test results demonstrate that the concentrated cement slurry concept can produce CRF compressive strength ranges typically required by mine operators when aiming for a 50 per cent increase in cement slurry volume per agitator trip. A typical concentrated cement grout CRF recipe for 50 per cent agitator cement slurry volume increase is presented in Table 2.

TABLE 2

A typical concentrated cement grout CRF recipe to deliver 50 per cent grout yield increase (6 m^3 of concentrated grout makes final volume of 9 m^3 of standard grout slurry)

1. Surface Batch Plant – 6 m^3 grout for Agitator	
Binder (dry) (kg)	8093
Added water (kg)	3227
w:c	0.40
HRWR dose (mL/100 kg of GP)	118
HCA dose (mL/100 kg of GP)	245
Estimated Air Content (%)	3.0%
Density (kg/m^3)	1892
2. Underground – water addition to make extra grout	
Water added (kg)	2912
3. Underground – final diluted grout recipe – 9 m^3	
Binder (dry) (kg)	8093
Total water (kg)	6139
w:c	0.76
HRWR dose (mL/100 kg of GP)	118
HCA dose (mL/100 kg of GP)	245
Estimated Air Content (%)	3.0%
Density (kg/m^3)	1585
4. Underground – development waste rock addition	
Waste rock addition (kg)	120 000
5. Final CRF produced	
Estimated Air Content (%) (includes porosity)	20.0%
Total Yield Estimate per agitator trip (m^3)	61.9
Density (kg/m^3)	2169
Binder usage (kg/m^3)	131
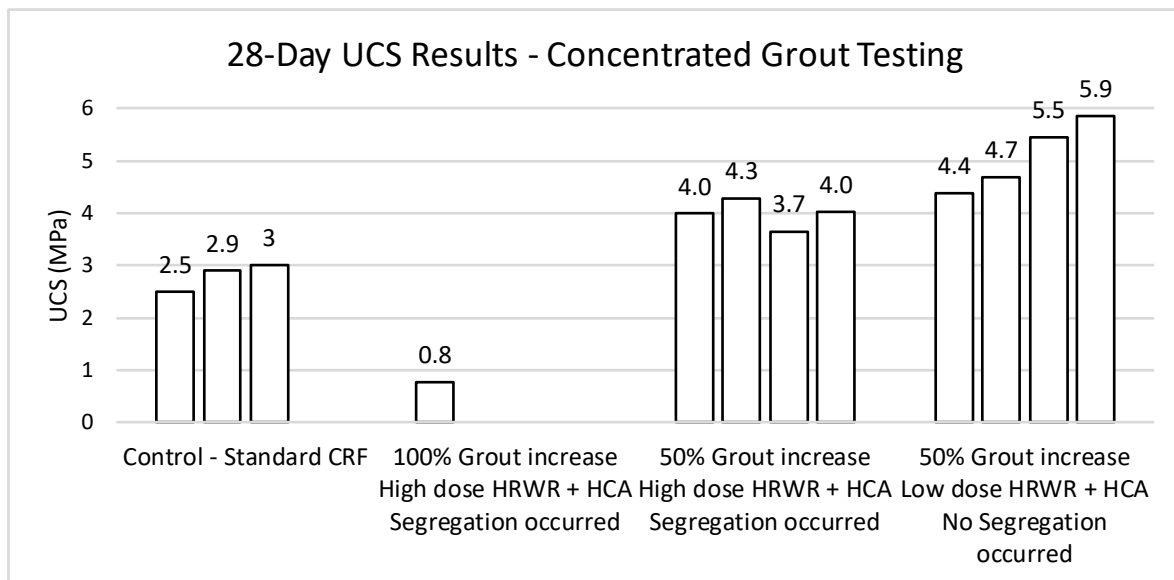
FIG 9 – 28 day UCS test results of the concentrated cement slurry mix designs. The 50 per cent cement slurry increase with low dose of HRWR and HCA provided the best strength results.

COST BENEFIT ASSESSMENT OF CRF WITH ADMIXTURE

A cost benefit assessment was carried out by an operating underground narrow-vein gold mine that uses CRF backfill, to determine if there is a benefit in utilising the concentrated grout CRF technique.

The assessment involved a simplified desktop analysis of operational data and consideration of practical aspects of the CRF process by comparing standard CRF practice to the concentrated grout CRF technique. It was found that the concentrated grout CRF technique offered a 20 per cent increase in the CRF production rate per shift, 50 per cent increase in the CRF produced per agitator trip underground, and a 4.4 per cent reduction in the total CRF cost per cubic metre placed. The results of the cost benefit assessment are presented below in Tables 3 and 4. Note that typical values were used for simplicity.

TABLE 3

Assessment results for CRF production rates – standard CRF compared to concentrated grout CRF technique.

CRF production rates		
CRF technique	**Standard CRF**	**Concentrated grout CRF**
Total agitator cycle time (mins) (includes batching, tramming and mixing)	96	116 (extra time waiting for LHD due to extra mixing and tipping, as the 9 m^3 of grout is mixed in two × 4.5 m^3 loads due to mixing bay size limit).
Total possible agitator cycles per shift (assume nine working hours per shift)	5	4
CRF produced per agitator cycle (m^3)	40	60 (Due to extra grout from underground water addition)
CRF produced per agitator cycle (t)	80	120
CRF volume produced per shift (m^3)	200	240
% increase in CRF production	0%	20%

TABLE 4

Assessment results for CRF production rates – standard CRF compared to concentrated grout CRF technique.

CRF Costs – per 1 m³ CRF placed		
CRF Technique	**Standard**	**Concentrated grout CRF**
Agitator cost ($) Includes machine, operator and fuel costs	$5.36	$2.88
GP binder cost ($) Assume 131 kg/m³ of GP and GP cost of $240/tonne	$31.37	$31.37
Admixture cost ($)	$ –	$1.58
LHD placement cost	$10.60	$9.40
Total CRF cost per 1 m³ placed	$47.33	$45.23
Cost reduction (%)	0%	4.4%

CRF OPTIMISATION PROCESS USING ADMIXTURE

A CRF optimisation process was developed with the aim of delivering a practical step by step guide for operators to improve their CRF operation. The optimisation steps include utilising available supplementary sources of aggregates and fines to improve the CRF grading, consideration of the suitability of these materials and the available binder products and finally using admixture technology. As with any optimisation process, a mine operation would focus on the items that they have available to them and are most attractive to easily implement.

Step 1 – Characterise what you have

For each material proposed to be used in the CRF mix design, it is recommended to test for some basic properties to determine their suitability for incorporation in the CRF mix. These properties have been extensively described by others, such as Wang and Villaescusa (2001), Stone (1993) and Saw and Villaescusa (2011). The basic parameters are summarised below.

Site water

The following parameters should be checked:

- pH – a value close to 7 is generally going to produce the best results with values between 6–8 advised.

- Salinity/conductivity – lower values are preferred as high salinity or conductivity can create issues with the binder and reaction with aggregates and fines used in the CRF mix.

- Presence of deleterious salts/compounds – some salts and other minerals may affect the setting time of the binder and the performance of any admixtures used. Water quality testing results should be checked with your admixture and binder suppliers to ensure water quality is within the desired range.

Aggregates and fines

The following parameters should be checked as a minimum:

- PSD – It is logistically difficult to send a samples of mine waste to a laboratory for testing the particle size distribution ranges, due to the amount of rock fill required and the difficulty in safely sieving large size fractions. As per AS 1289.3.6.1–2009, the maximum sieve size is 75 mm, which is not large enough for CRF waste which will usually be screened to have an upper size fraction of 300 mm to 400 mm. Rock fill material will have size fractions ranging from fines (defined as less than 10 mm for rock fill) to cobbles (+60 mm) and boulders (+200 mm) with the maximum size usually limited by grizzly screening, which makes the

conventional sieving process considerably difficult to conduct as well as being time consuming. Other methods can be used to speed up the process, such as utilising particle size distribution calculation from digital images.

- Mineralogy – X-ray analysis or similar method to determine key minerals/chemistry to highlight any potential red flags (such as high sulphide content which may cause reduced CRF performance). This check can be completed by environmental/soil testing providers and they usually require a small sample, although the information is often already available, and possibly contained in site environmental or geological reports. Some sites also include this information in their geotechnical ground control management plans (GCMPs).

- Basic strength data – A very weak aggregate may either strengthen or weaken the CRF as described by Wang and Villaescusa (2001). This is typically only able to be determined through UCS testing of proposed CRF mixes.

- Supply Cost – $/tonne typically used.

- Environmental/regulatory synergies – if the site has a surface stockpile of aggregate/waste rock/tailings that must be placed underground at some stage, it may be beneficial to consider using these materials in the CRF mix.

Binder

As a starting point the binder types and costs should be checked. Conduct UCS tests with various available binder types in CRF cylinder samples. Generally, OPC GP (Ordinary Portland Cement, General Purpose) is most commonly available at batch plants, however GGBFS (Ground Granulated Blast Furnace Slag, or more simply SLAG) or fly ash may also be available at competitive rates. Sometimes a switch in binder may be a relatively simple way to reduce costs, potentially without significant performance differences.

Step 2 – Optimise the PSD

Once the available CRF constituent materials have been characterised and confirmed fit for purpose, the next step is to optimise the PSD. This is achieved by producing blended aggregate gradings with the available materials until the target PSD is achieved. Many mines that use development waste as rock fill in CRF can benefit significantly by the addition of fines (material less than 10 mm), such as tailings sand. This is well documented in previous work such as by Stone (2007) that pursuing a Talbot grading with an N factor of approximately 0.5 is an ideal target for most CRF situations. Stone notes that the N factor can be varied to either produce flowable (N < 0.5) or stiff (N > 0.5) CRF depending on site requirements. The Talbot grading process is well described in numerous publications, but specifically for a mine fill project by Warren *et al* (2018) and this is a process that most mines can implement using the Talbot and Richard (1923) gradation equation:

$$P = 100 \, (\frac{u}{Umax})^N$$

where:

P   = percent passing

u   = particle size

U_{max} = maximum particle size

N   = distribution

Once there is an understanding of the rock fill grading at the mine, the maximum particle size is decided and the idealised grading curve for better CRF mix performance can be determined.

In order to produce a mix design that blends various available fines and aggregates to get as close as possible to the target PSD, a blended aggregate grading spreadsheet is required. These can be easily sourced from cement and aggregate suppliers or alternatively sourced from the internet. The exercise involves selecting proportions of each material to get to the right mix design and is somewhat trial and error.

The next step is to confirm the performance of the mix by visual assessment and UCS testing. Generally speaking, larger diameter cylinder testing is better, as segregation and water absorption are more readily seen at larger scale, and scale effects will have less influence on UCS results. Often mixing on the surface with a loader and viewing the performance of the mix is recommended, observing signs of excess or insufficient cement paste volume, bleeding and flowability performance. Compressive strength is confirmed by laboratory UCS testing.

By optimising the PSD using blended materials, a reduction in cement binder may be possible to meet the original strength target of the control mix whilst also achieving a cost reduction through reduced cement binder content.

Step 3 – Addition of admixture

The mine site admixture supplier can advise the admixture dose rates and offer suggestions on how to use the admixtures for benefit. The typical dosing range of each admixture will be dependent on the site conditions and the mix design and advice is typically required regarding admixture usage, implementation and batching procedures when using admixture for a new process such as use in CRF.

Admixture selection

Both HCA and HRWR admixture should be considered for use with CRF.

HCA incorporation into the mix design may lead to improved cement binder performance of the CRF product in the stope. Subsequently, it would be recommended to incrementally reduce cement content to deliver cost savings whilst ensuring the UCS strength targets are maintained.

Utilising both HCA and HRWR products may allow a concentrated grout mix design to be formulated, which could deliver both operational productivity gains and cost savings to a typical mine using CRF backfilling practices.

Desktop costing

Complete a desktop study to determine the likely cost benefits. This can be considered a stop point for internal discussion and approval, prior to proceeding. Seek advice from your mine site's admixture supplier for likely admixture usage rates, based on the site conditions and the proposed mix designs. Careful desktop/data analysis is critical to understand the true costs associated with changes to the CRF backfilling mix design and process. For example, in the previous Cost Benefit Assessment section, it was shown that a concentrated grout reduced the Agitator cycles per shift from five cycles down to four cycles, added $94 per tonne to the batching cost yet the concentrated grout allowed more total CRF production per shift at a lower cost per tonne placed. It is also recommended to consult closely with operational staff to ensure all aspects are considered when proposing a change to the CRF process.

Site trials and laboratory UCS testing

If there appears to be a cost justification, loader bucket trials on the surface can be used to produce a set of test samples. If results are favourable this can be followed by a full trial stope.

Uncertainty will remain to a certain extent when introducing a HCA product while reducing the cement content at the same time. The amount of cement that can be removed from a HCA-dosed CRF mix remains undefined and will vary between mine sites due to their own inherent differences. Attempting to replicate the process of damage to the CRF samples over time, in an attempt to match the amount of time to fill and cover the stope placed CRF, will provide a starting point for justification of cement reduction and the amount. This should then be followed up with observation of HCA-dosed CRF performance in a non-critical stope exposure.

Similarly, when adopting a concentrated grout CRF technique, careful attention to the quality and consistency of the cement slurry is required, followed up with observation of CRF performance in a non-critical stope exposure.

CONCLUSIONS

Admixture use in CRF offers significant benefits in terms of reduced costs to achieve equivalent compressive strength performance and greater efficiencies when transporting cement slurry by agitator truck. Improvements in performance of CRF was investigated by adding admixture during the preparation of controlled samples, and it was demonstrated that a HCA treated CRF mix has delivered an UCS increase of 33 per cent at 28 days. This testing result shows the importance of HCA when considering in-situ CRF performance and raises the potential for cement reduction to achieve the design CRF strength. HCA addition to the CRF mix enables reduced cement usage, while achieving the design CRF strength and resulting in significant cost reduction. The scale of cost reduction will depend on the mine production rate, but the saving due to reduced cement usage can easily be in the range of tens of thousands to hundreds of thousands of dollars in reduced expenditure.

Test results demonstrated that the concentrated cement slurry concept can be used to move greater quantities cement underground by agitator truck and more efficiently fill stopes. A simple costing example presented a 20 per cent increase in the CRF production rate per shift, 50 per cent increase in the CRF produced per agitator trip underground and a 4.4 per cent reduction in the total CRF cost per cubic metre placed.

A CRF optimisation process was developed with the aim of delivering a practical step by step guide for operators to improve their CRF operation. The optimisation steps include utilising available supplementary sources of aggregates and fines to improve the CRF grading, consideration of the suitability of these materials and the available cement binder products and finally using admixture technology.

REFERENCES

Farzam, H, Rispin, M and Karlson, R, 1998. The Use of Unique Admixture Technologies in Mine Backfill-Technology Description and Case Histories, in *Minefill 98: Proceedings Sixth International Symposium on Mining with Backfill*, pp 71–75 (The Australasian Institute of Mining and Metallurgy: Melbourne).

Penman, A, 1971. Rockfill Building Research Station, Department of the Environment, 10 p.

Saw, H and Villaescusa, E, 2011. Research on the mechanical properties of minefill: influences of material particle size, chemical and mineral composition, binder and mixing water, in *Minefill 2011, 10th International Symposium on Mining with Backfill* (The Southern African Institute of Mining and Metallurgy).

Stone, D, 1993. The Optimization of Mix Designs for Cemented Rockfill, in *Proceedings of the Fifth International Symposium on Mining with Backfill*, pp 249–53 (The Southern African Institute of Mining and Metallurgy).

Stone, D, 2007. Factors that affect cemented rockfill quality in Nevada Mines, *CIM Bulletin*, 100(1,103):1–6.

Talbot, A and Richard, F, 1923. The Strength of Concrete, its relation to the cement, aggregates and water, University of Illinois, Engineering Experiment Station Bulletin, No. 137.

Wang, C and Villaescusa, E, 2001. Factors influencing the strength of cemented aggregate fill, in *Minefill 2001: Proceedings of the Seventh International Symposium on Mining with Backfill*.

Wang, C, Tannant, D, Padrutt, A and Millette, D, 2002. Influence of admixtures on cemented backfill strength, *Mineral Resources Engineering*, 11(3,2002):261–270.

Warren, S, Raffaldi, M, Dehn, K, Seymour, J, Sandbak, L and Armstrong, J, 2018. Estimating the unconfined compressive strength (UCS) of emplaced cemented rockfill (CRF) from QA/QC cylinder strengths, in SME Annual Meeting, Minneapolis, Minnesota, 25–28 February 2018.

Friction bolt performance over the past ten years in Australian mines

D J Reardon[1], T M Nester[2], B J Barsanti[3] and A N Page[4]

1. Senior Geotechnical Engineer, Dynamic Geotechs, Lymington Tas 7109.
   Email: dynamicgeotechs@gmail.com
2. Director, Operational Geotechs, Keilor East Vic 3033.
   Email: trent@operationalgeotechs.com.au
3. Director, Operational Geotechs, Perth WA 6164. Email: ben@operationalgeotechs.com.au
4. Director, Geotechnical Mining Services, Trevallyn Tas 7250. Email: ash@gms.net.au

ABSTRACT

The load capacity of a friction bolt has long been regarded as 4 t/m of embedment for ground support design analysis and supported by *in situ* pull test results. In recent years, the authors have observed lower pull test results or inconsistent results which were rarely sighted in the early 2000s. The lower pull test results indicated in some cases that reliable friction bolt capacity (≥90 per cent of results) is closer to 3 t/m of embedment with some geotechnical engineers adjusting the ground support parameters in the design work accordingly.

This can be in contrast with other mines which reliably obtain 4 t/m (or greater) using the same suppliers bolt in similar ground conditions. This raised several questions:

- What is the effect of poor installation (bolt twist or bolt hole deviation)?

- Does the performance of friction bolts vary in different rock masses?

- Does bolt performance vary between suppliers?

- What effect does increased jumbo feed/percussion/rotation settings have?

- Have the bolt dimensions or steel strip width changed?

- Have the physical bolt properties changed?

- Have the steel properties changed?

This paper was aimed to answer as many of these questions as possible and discuss each variable in detail. This project included friction bolt trials at various mine sites across Australia, multiple friction bolt manufacturers, steel manufacturers and laboratory analysis. The paper also includes discussion on what the authors consider best practice for pull testing. It should be noted, the terms 'friction stabiliser' and 'split set' used in this paper are used in a generic manner and is not linked to any specific ground support supplier.

Whilst its acknowledged within the industry the term split set and friction stabiliser is used interchangeably, the authors acknowledge that the term split set is a trademark of Split Set Mining Systems and has been used in context in this paper.

INTRODUCTION

This paper represents results, observations and analysis derived over ten years of pull testing and metallurgical testing of 46–47 mm diameter C-shaped, friction stabilisers. The data includes five mine sites from across WA and the east coast of Australia in a range of commodities from gold, nickel and base metals. This paper also considers friction bolts from six different ground support suppliers, three different drill bit suppliers, five underground development contractors, and various owner-operator workforces using development drilling jumbos, which is summarised in Table 1.

TABLE 1

Summary of pull test results analysed over the last ten years.

Mine site	F	S	R	Bellevue	Tropicana
Commodity	Gold	Nickel	Base Metals	Gold	Gold
No. pull tests completed	439	161	124	300	922
Suppliers' bolts used	1, 2, 3, 4 & 5	1	1	5 & 6	5
Average rock types UCS range (MPa)	99–146	129–201	54–209	286–621	91–235
Stress conditions (σc/σ1) SRF Q System	Moderate to High	Moderate to High	High	Low	Low to Moderate
Development contractor or owner operator workforce	OO	OO, P, G, B	OO	G	M

This paper expands on pervious work completed by Scott (1977a), Davis (1979) and Tomory (1997) for C-shaped friction stabilisers and the factors affecting their anchorage capacity. Work completed by Scott (1977a) initially lists three main variables that dictate the anchorage of Split Set rock anchor:

1. The wall thickness of the split set; the thicker the wall the more anchorage attained.

2. The metallurgy of the steel; the higher the yield point, the more anchorage attained.

3. The size of the borehole into which the split set is thrust; the smaller the hole, the greater the anchorage.

These variables presented by Scott (1977a) are of particular note considering the past and ongoing optimisation efforts by some ground support suppliers and drill consumable suppliers in the Australian market over the last decade. Particularly, in the 'optimisation' of products while still producing reliable pull test anchorage loads in Australian underground mines. The term 'reliable' within this paper is defined as 90 per cent of pull test results meeting the minimum requirements set out in a site's Ground Control Management Plan (GCMP) or as set out in a site's geotechnical Principal Management Plan (PMP).

Tomory (1997) adds to the work completed by Scott (1977a) and also includes data for friction stabiliser anchorage varying with rock type, bolt installation drive time, slot closure, bit size, various diameter and length split sets and commentary on pull out strength development with time. Of particular note is the perception of 'improvement' in pull test results observed between initial installation and some weeks later in laminated rocks or highly stressed ground conditions, where 'movements along cracks or shearing planes which … intersect the bolt produce offsets which may lead to the bolt locking up' Tomory (1997). The authors have observed that this generally occurs at the start of the bolt near the excavation rather than at the end, or rarely uniformly along the length of the bolt. This is consistent with the rationale for installing a rock bolt in the first place, ie something loose or potentially unstable that needs to be retained to provide a safe work environment. The authors have observed in laminated, broken and/or high stress conditions (as shown in Figure 1) that a consistent level of pull test anchorage bias can be produced, particularly for bolts with increased age adjacent to nearby development or stoping activities. In contrast, the influence of 'rock mass lockup' or pull test bias was rarely observed in the data for mines with low stress environments and good to very good rock mass conditions.
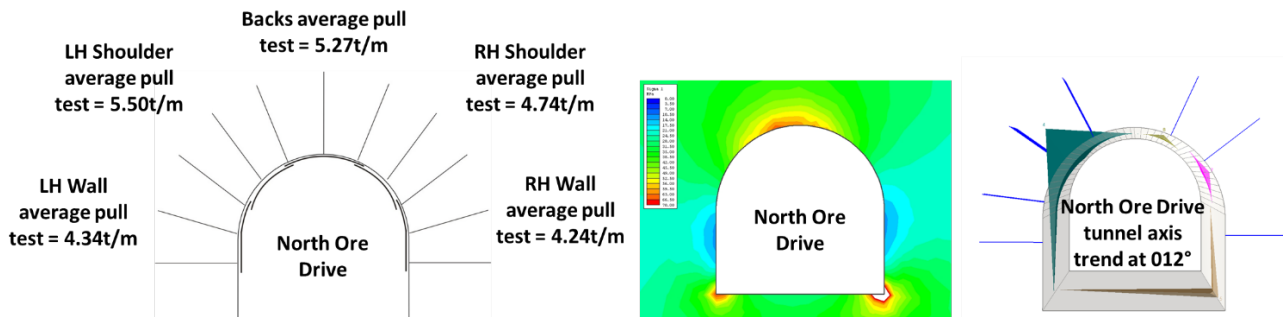
FIG 1 – Example of pull testing bias in laminated high stress conditions for 69 Friction stabiliser tests between 7850 and 7950 mRL at Mine site F. Friction bolts produced by Supplier 4, with Phase 2D and Unwedge models for the area shown for context.

To ensure that a site-based geotechnical practitioner can account for this bias in a data set and ground support designs it is recommended that pull collars are evenly distributed around the development profile by jumbo operators and that pull testing is completed on all available bolts, rather than pull collars that are easy to get to for the testing operator. The youngest aged development (last 5–10 cuts closest to the active development face) is of particular interest in monthly pull testing.

All pull test results used for the analysis in this paper were completed with a Geotechnical Engineer present in the integrated tool-carrier basket (IT basket) to confirm the initial slipping result obtained (to the nearest 0.5 t). Observations regarding ground conditions, friction bolt damage or twist, age since installation, hole sizes and bolt hole deviation were also recorded prior to testing each bolt. Most tests were completed to a maximum of 14 t regardless of bolt length in line with minimum friction stabiliser specifications for weld rings by suppliers. Pull testing was completed using annually calibrated 20 t or 30 t battery operated hydraulic jacks with digital or analogue gauges. All results are presented in metric tonnes (for 2.4 m bolts) or tonnes/meter where varying bolt lengths were considered.

The degree of bolt twist was estimated by a geotechnical engineer for each of the 1946 pull tests recorded to the nearest 45°, allowing correlation of bolt damage (twisting) to pull test results. When a large number of twisted bolts occur in a data set, a bolt twist curve can be plotted to distinguish between different failure mechanisms. This also allows different bolt suppliers or different bits to be compared in the same ground conditions even when bolts are damaged or twisted by jumbo operators.

An independent data set of metallurgical testing of friction bolts has been completed for 43 bolt samples, across six different bolt suppliers focusing on chemical analysis and material property testing. The material change in friction bolt stabiliser usage over the past ten years has been of particular interest, in particular the strip width feed material change from HA350 to AB0400 to HA400 by BlueScope. Results for international steel supply used in friction stabilisers manufactured by some suppliers is also considered with variable results presented.

The influence of individual jumbo operator bolting techniques during installation and this effect on friction stabiliser anchorage has also been tracked for 1946 pull test results. These have highlighted the negative influences of using rotation during installation and bolt indexing relative to the hole angle drilled. Experience has shown a positive increase in site pull test results when operators are individually tracked for friction stabiliser anchorage on a monthly interval, with results communicated back to each operator on a one-on-one basis. Anecdotally the authors have noticed better pull test results at mine sites when development contractors and owner-operator mines reward jumbo operators for positive pull test results in addition to other performance incentives, rather than performance incentives being based on development metres advanced alone.

The data set discussed within this paper considers friction stabilisers produced by DSI, Fero, Jennmar, Minova, Split Set Mining Systems and Tonry at various stages over the last decade. To ensure confidentiality of the ground support suppliers product performance, all defining references to each company have been removed from tables and figures discussed.

FRICTION BOLT DATA

Influence of steel and bolt metallurgy

Friction bolt metallurgy is complex, the product starts its life as hot rolled coil that is heated to a temperature above the steel's recrystallisation temperature. It is then uncoiled, slitted down and re-coiled into specific strip widths specified by the ground support supplier. From here the coil is unwound again and fed through a roll former that typically has 10–12 roll-forming dies to cold work the flat plate into the desired C-Shape. Once the desired length and shape is achieved the bolt is guillotined, a taper applied on the insertion end and a weld ring fixed at the driving end. The last step typically involves galvanising the product in a molten zinc bath typically >440°C before the bolts are allowed to dry and then packaged into bundles ready for transport.

Due to the multiple stages of bending and shaping, the parent steel coil goes through the slitting and roll-forming process, and an increase in yield and ultimate strength occurs in the steel used to make the friction stabiliser due to the influence of cold working (strain hardening). There are many methods for calculating the various levels of strain hardening for different steel alloys as described by Gao, Wu and Li (2019) but this falls outside the scope of this paper, with the authors instead focusing on testing data obtained for actual comparisons.

Previous industry knowledge of Australian steel products indicates that the galvanising process has a negligible increase in steel yield strength properties, with less than 1 per cent variation in yield strength for hot rolled steel products described by Robinson (2000). Due to the influence of steel strength on pull test results, some site geotechnical practitioners request an electronic copy of the parent steel heat certificate before bolt deliveries are made to site to track the quality of bolts delivered and calibrate monthly pull testing data distributions. Experience has shown that most reputable ground support suppliers can provide this data in a timely, transparent, and consistent manner when requested. The heat certificate produced by the steel mill at the time of coil manufacture is useful in determining the physical properties of the steel and the weldability of the product. A subset of 14 independent metallurgical and physical property tests were collated for bolt Suppliers 5 and 6 in 2021. The results of steel strength to Carbon Equivalent (CE) ratio are plotted below in Figure 2, with two distinct steel alloys present in the data.
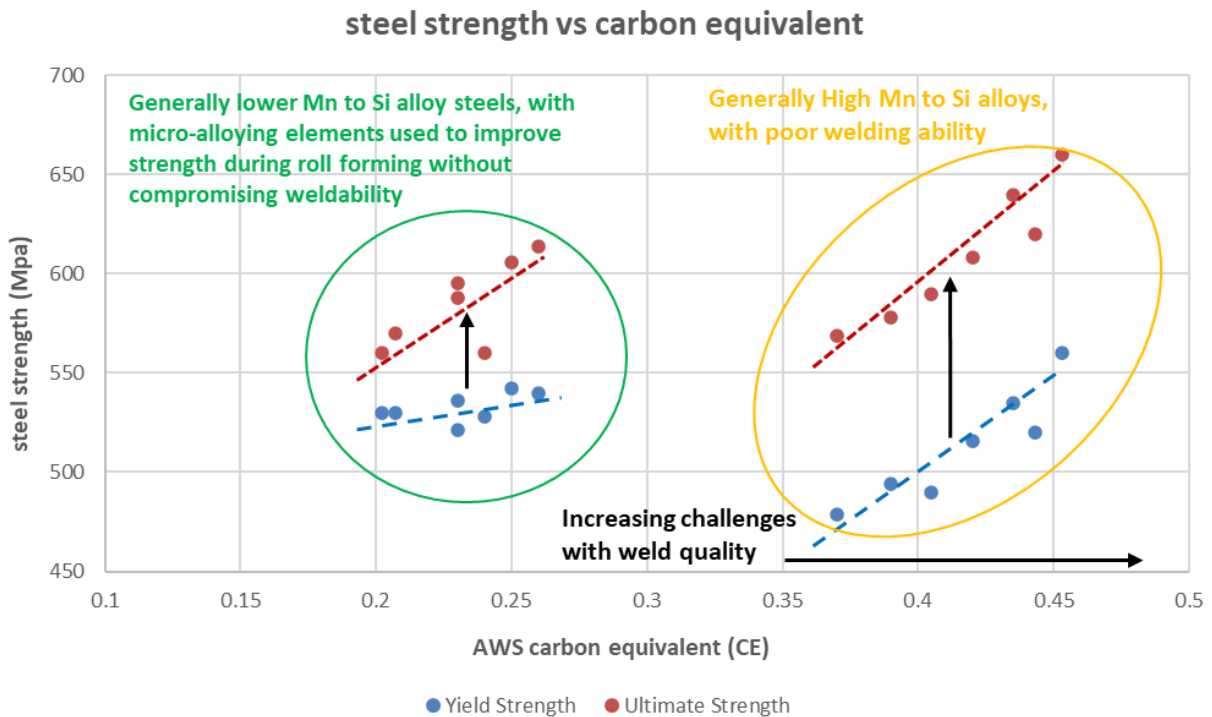
FIG 2 – 2021 independent friction stabiliser testing data for bolts produced by Suppliers 5 and 6, highlighting the variance in CE ratio relative to bolt strength properties and steel alloys.

CE ratio is a measure of weldability, particularly important for the transfer of load from the friction stabiliser to the weld ring and hence onto the plate and surface support for underground support systems. The authors have observed some sites having intermittent issues with weld ring quality over the last decade, particularly around the heat affected zone (HAZ) near the weld ring. This has at times led to an elevated risk of rockfall at some mines due to the ground support system not behaving as per geotechnical support calculations (eg weld ring failure at loads less than 10 t or 4 t/m).

For the purposes of this paper CE ratio is defined as per the American Welding Society formula whereby:

$$CE\ (AWS) = \%C + (\%Mn+\%Si)/6 + (\%Cr+\%Mo+\%V)/5 + (\%Cu+\%Ni)/15$$

Many different formulas for CE ratio exist based on a range of industrial applications and steel alloys. The authors (experienced site-based geotechnical engineers, not steel metallurgists) consider the AWS CE formula to provide a good correlation between bolt behaviour from underground workings and the steel alloys used in Australian friction stabiliser manufacture. In general, the authors have observed increasing numbers of failed weld rings for friction bolts made from a CE ratio greater than 0.4. Figure 2 graphically shows the variance in CE ratio between two different steel alloys used in friction stabiliser manufacture.

The variance between heat certificate yield strength and actual bolt yield strength post manufacture (after strain hardening/cold working) is displayed for the same 14 independent tests in Figure 3. The actual relationship is considered far more complex than the simplified relationship displayed on the graph. The authors consider this is an area where further work is required, particularly considering the variability caused by different steel alloys as described by Hashimoto (2006) and Panigrahi (2010). Figure 3 does indicate that the variation in yield strength caused by cold working the bolt into the desired C-shape can range from 20 to 12 per cent.
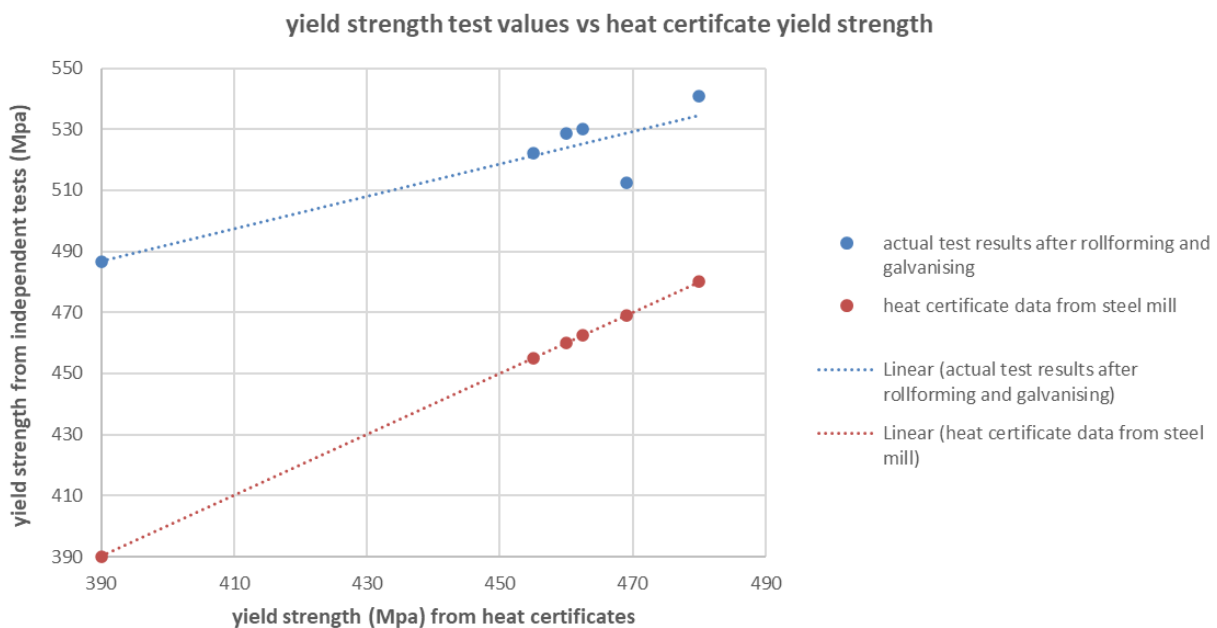
FIG 3 – 2021 independent friction stabiliser testing data for bolts produced by Suppliers 5 and 6, highlighting the variance in yield strength from steel mill heat certificate and yield strength post bolt manufacture.

Influence of friction stabiliser dimensions

C-shaped friction stabilisers start their life as a flat piece of coiled up plate, strip width is referred to as the starting width of the flat plate before being rolled into the desired C shape by the ground support supplier. The authors are aware of two main strip widths used in the Australian market over the last decade – 109 mm and 107.5 mm – with these widths supported by independent tests. There has been some suggestions by prominent industry representatives that the original Split Set produced by Ingersoll Rand in the 1970s utilised a 111 to 112 mm strip width. The authors are yet

to find documentation supporting this argument, but a decrease in the volume of steel used to make friction bolt dimensions remains.

A small data set of friction stabiliser dimensions from 2012 to 2014 showed that minimum strip thickness of 3.2 mm (1/8th of an inch) was achieved across many bolt suppliers. Repeating the same exercise in 2021 has shown that 3.2 mm thickness is no longer considered a minimum specification for thickness by many ground support suppliers, but rather a 'nominal' dimension. It is normal for ground support suppliers to update their specifications from time-to-time in line with market trends and optimising products for capacity or cost. Concerningly however, the term nominal in engineering or mathematical terms has no tangible statistical significance, as opposed to other transparent definitions such as minimum, average, mean, median or mode. Geotechnical practitioners should view ground support specifications referring to nominal or typical dimensions/specifications with caution, as there is no guarantee or legal requirement that a ground support supplier needs to produce a product to this standard.

Table 2 illustrates the change in strip width thickness of hot rolled coil over the last few years by some ground support suppliers and steel mills. Independent testing between years 2018 and 2021 indicates a 4 per cent drop in average steel thickness.

TABLE 2

Summary of C-shaped friction stabiliser thicknesses with time including data from two mines and four ground support suppliers.

Year of bolt surveys	Sample size	Average friction bolt thickness (mm)	St Dev thickness (mm)
2018	21	3.30	0.10
2021	8	3.17	0.04

Influence of steel grade and steel physical properties

During 2013 friction stabiliser feed material for many Australian ground support suppliers changed from HA350 to AB0400. The implication of this change to in 2013 was significant, with a sharp increase in pull test failure rates observed at mine site F (Figure 4) and numerous other mines. It took the authors and other industry partners over a year of part time investigation work and independent testing to confirm that the primary cause of this sudden rise in poor pull test results was indeed caused by the widespread adoption of an alternative steel product, AB0400, in friction stabiliser manufacture. AB0400 was then used extensively across most of the underground domestic friction stabiliser market for a period of four years. In 2017 BlueScope reverted to a steel blend similar to the superseded HA350 product now referred to as HA400. The authors understand that not all ground support suppliers swapped feed material from AB0400 to HA400 at this time and that some suppliers import various steel coils from overseas steel mills. Internal BlueScope data viewed by the authors shows that the superseded HA350 blend used prior to 2013 actually conformed closer to a 500N specification in AS/NZS 3678, which at the time was a superior blend for friction stabiliser material.

Number of pull tests completed each month with failure rate over time
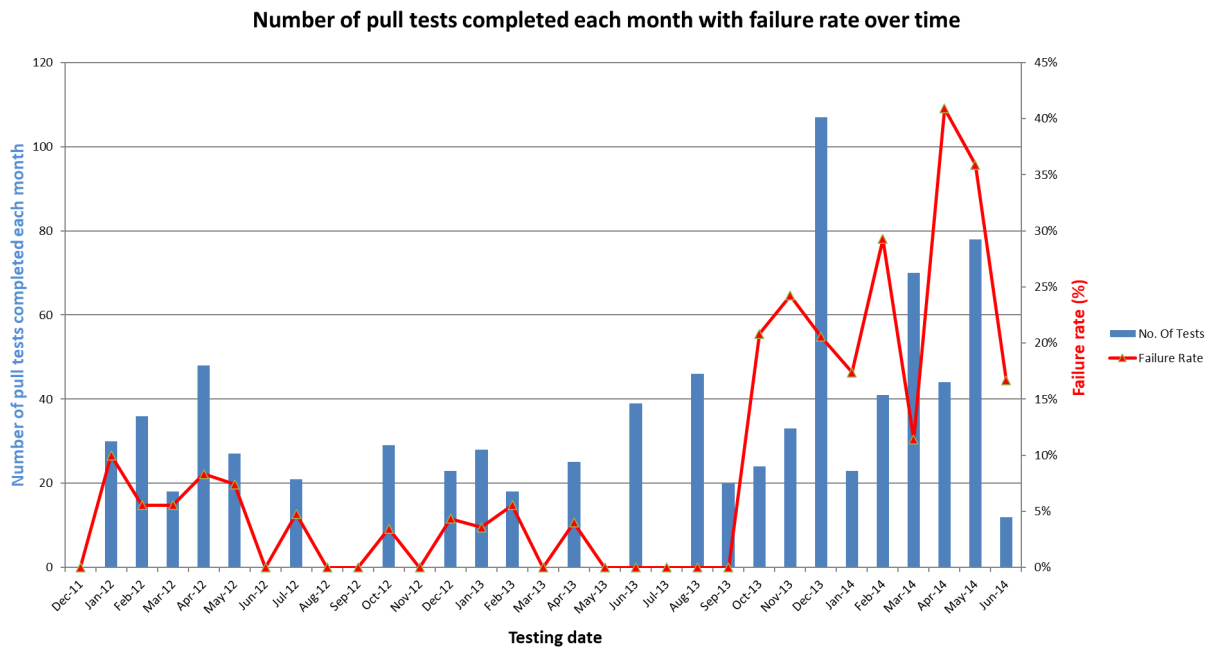
FIG 4 – 2012 to 2014 Monthly pull testing data from mine site F, displaying number of bolts tested and failure rate on pull testing for bolts not meeting the minimum GCMP requirement of 4 t/m.

In January 2021 Tropicana Gold Mine observed a sudden and uncharacteristic increase in the number of failed bolts in routine monthly pull testing (36 per cent failing to meet the site's minimum specification in its GCMP). As with most friction stabiliser investigations, bit sizes were checked, operators were spoken to, ground conditions were cross-checked against instances of poor pull test results and the bolts were inspected and measured to see if anything had changed.

A review of the suppliers QAQC heat certificates from the steel mill relating to the batches of bolts installed in the previous month (during December 2020) revealed that a ~20 per cent drop in yield strength had occurred from the steel mill used for bolt manufacture in the previous 3 months.

To confirm what actual yield strength steel was required for successful friction stabiliser performance at the Tropicana Gold Mine, a testing campaign of ten 390 MPa yield strength bolts and ten 490 MPa yield strength bolts was completed in the same drive, using the same bits, in the same ground conditions by the same jumbo operator and using the same jumbo. These results are presented in Figure 5 and show that there is on average a 2.1 t difference between the two grades of bolts produced by the same ground support supplier when other variables are isolated. The standard deviation for the 390 MPa bolts and the 490 MPa bolts is considered to be a function of operator alignment during installation and local ground conditions.
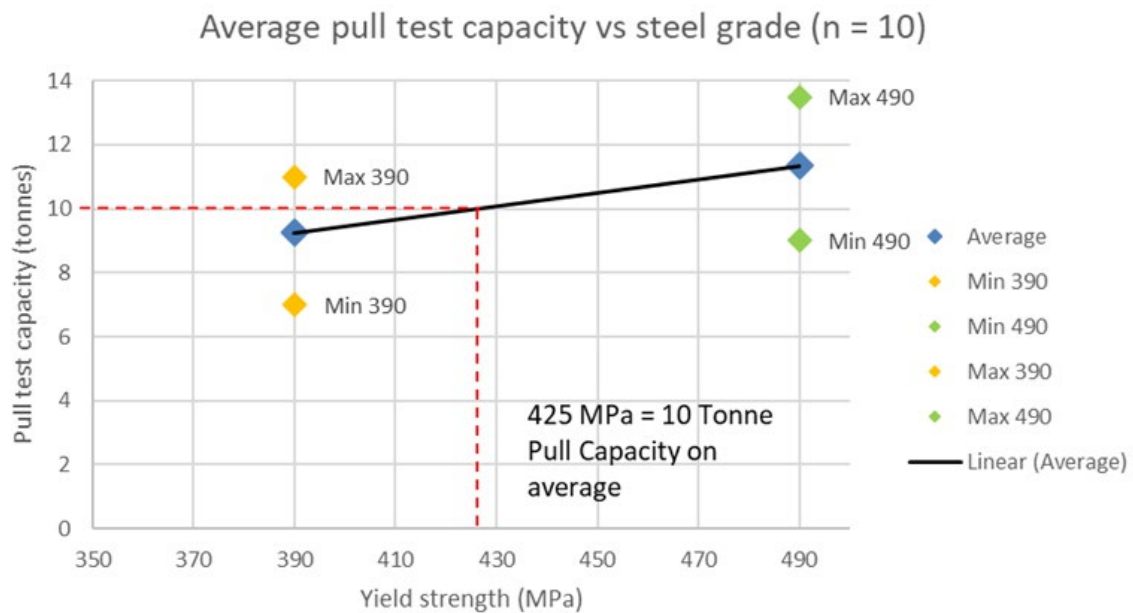
FIG 5 – Influence of parent steel yield strength on pull test anchorage at Tropicana Gold Mine.

Upon completion of this testing program the site's GCMP was updated to reflect the new minimum specifications (of 420 MPa yield strength) for friction stabilisers, allowing the mining development contractor to engaged with the ground support supplier to ensure supply of a fit for purpose product. It is important to note in this example that steel grade alone does not necessarily yield good pull test results – with the influence of operator installation being a critical component in achieving reliable pull test results at the Tropicana Gold mine.

Anecdotal evidence shows that the frequency of twisted bolts is more prevalent in bolts made from lower yield strength and/or thinner steel, in line with the reduced torsional rigidity of the friction stabiliser. The exact index angle applied by the jumbo operator when installing the bolt into the hole to generate various degrees of bolt damage (twisting) is an area that requires further work in trial conditions to accurately quantify the variables involved.

The steel grade lessons learned by the authors from the incidents in 2013 and 2021 highlight that the different specifications for friction stabiliser manufacture held by different ground support suppliers is not necessarily applicable for each site in achieving the required support capacity outlined in site geotechnical analysis for ground support designs. This is visibly displayed in Figure 6 below for 2021 heat certificate data for Suppliers 1, 3 and 5. The topic of individual standards across each of the ground support suppliers in the Australian market can present additional challenges (or opportunities) to site-based geotechnical engineers for support calculations and tender selection of ground support supplier, particularly when assessing the price per unit for ground support items.

The trend by some ground support suppliers changing their internal specifications for ground support products without written notice to the client or an effective change of management process highlighting risks to the consumer is of significant concern. Such an occurrence may place the ground support supplier company and its directors in a compromising position regarding the expectations outlined in some State and Territory Workplace Health and Safety regulations.

RAW STEEL DISTRIBUTIONS
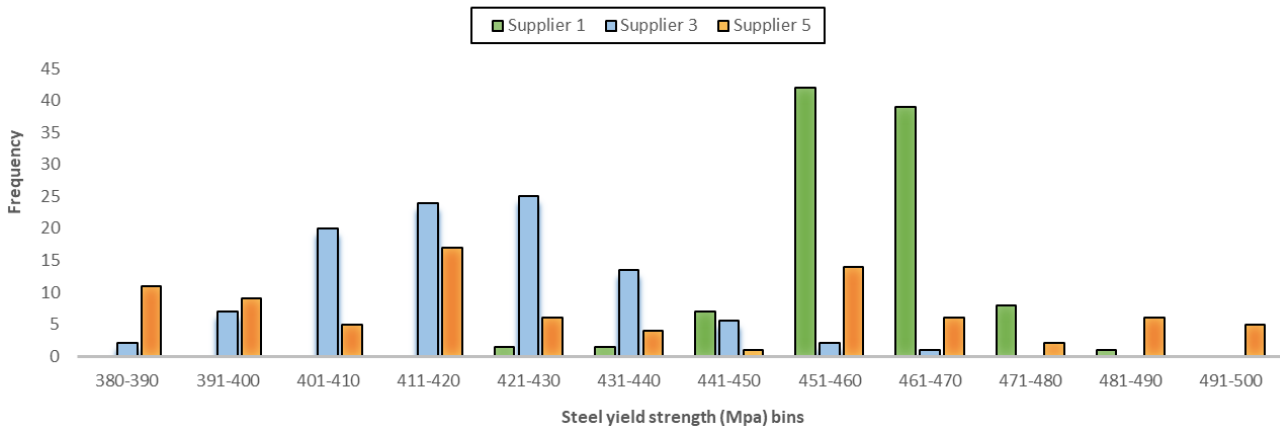
FIG 6 – Distribution of parent steel yield strength pre bolt manufacture for ground support Suppliers 1, 3 and 5 in 2021.

The authors consider it best practice for site-based geotechnical practitioners to send the relevant ground support supplier specification requirements used in geotechnical ground support designs (usually outlined in a site's GCMP or PMP), for acknowledgement to ensure that the ground support supplier can fulfill their legal requirements relating to Workplace health and Safety regulations for products supplied to the mine site.

Table 3 is an example of specifications included in some site's GCMP and PMP documents for minimum friction stabiliser specifications. The authors acknowledge that there are many different combinations of strip width, thickness, bolts shape and yield strength that can used by a ground support supplier to still arrive at a friction stabiliser with the same anchorage capacity.

TABLE 3

Example of minimum friction stabiliser specifications specified in some site's GCMP.

Tolerances on friction stabilisers	
Minimum yield strength of raw steel	≥420 MPa
Minimum strip width of	≥107.5 mm
Minimum gauge thickness of	3.2 mm ± 0.1 mm
Bolt length tolerance	±5 mm
Minimum galvanising thickness of	≥60 µm
Bolt diameter	±0.5 mm
AWS Carbon Equivalent (tube and ring)	<0.35

Influence of different bolt suppliers

As part of a ground support tender process at mine site F in 2014, a pack of friction stabilisers from each of the five ground support companies invited to tender were tested in the site's ground conditions to assess actual performance for the mine. At the time, two of the suppliers still used a 109 mm strip width while three suppliers used a 107.5 mm strip width. The results from a small-scale trial across the five brands of 2.4 m friction bolts indicated that bolt shape was a more of a critical component in determining pull test anchorage rather than strip width alone.

The variance in capacity between bolt manufacturers 3 and 4 was of particular note given that these two ground support suppliers both used a 109 mm strip width but recorded very different results in site pull testing. Unfortunately, the variable of steel grade yield strength was not considered as part of this testing campaign. The authors believe this would have helped explain the large variation in average bolt pull tests between suppliers. If the variance between manufacturers 3 and 4 was indeed due to bolt cross-sectional shape alone, then this variable would result in a 60 per cent reduction in

pull test anchorage for friction stabilisers when a poor C-shaped cross-section is adopted by a supplier. Previous work completed by Davis (1979) and Scott (1977b) suggests that maximum friction bolt performance occurs when C-shaped friction stabilisers are circular in nature and in contact with the borehole around the whole annulus of the bolt.

Cross-sectional samples installed into inside diameter (ID) 45 mm steel pipes from each of the five bolt suppliers compared to pull test results at mine site F suggests otherwise. In fact, frictional load generation along the length of a friction stabiliser is more complex than previously thought with bolt Supplier 4 having one of the least cross-sectional areas in contact with an ID 45 mm pipe, but recording the highest and most consistent pull test anchorage results in the trial as shown in Figure 7.
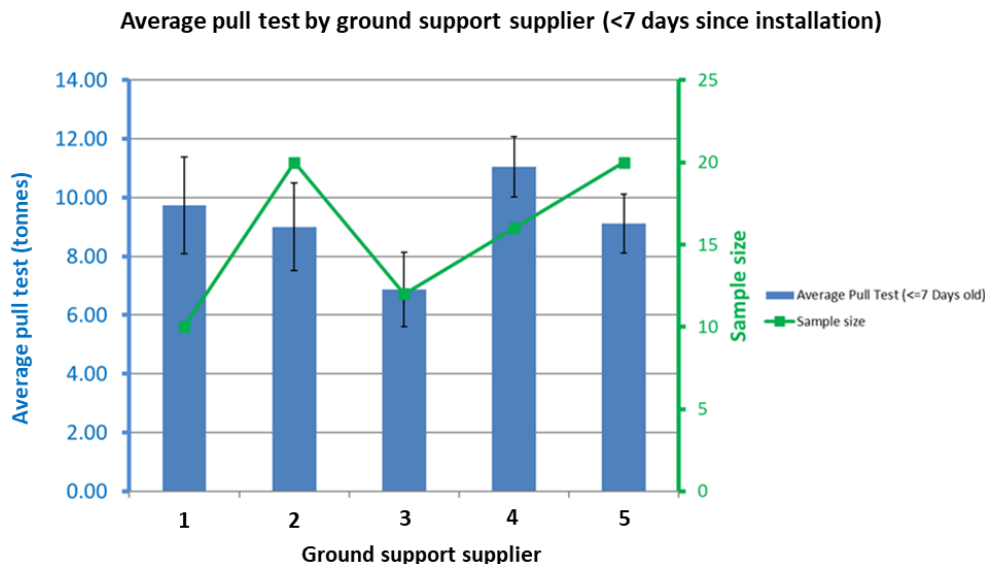
FIG 7 – 2014 pull tests for five different ground support suppliers at mine site F.

The results from the testing campaign at mine site F resulted in the award of the ground support tender to the supplier with the best bolts suited to this site's ground conditions and conforming to this site's minimum standards in the GCMP, rather than unit price. Before this change of ground support supplier, mine site F installed six No-Entry signs in active development headings in the previous 12 months due to substandard pull test results and conducted multiple rounds of rehab in fresh development to ensure a safe work environment. In the following 12 months after changing the ground support supplier, the number of No-Entry signs installed and rehab associated with poor pull tests was reduced to zero, significantly improving development rates, jumbo utilisation and safety at the mine.

The authors are concerned that there is a perception within the wider Australian mining community that all friction stabilisers within the (Australian and international) markets are made equal, and to the same specification between suppliers. Observations and testing form the authors over the last decade indicate this could not be further from the truth as observed in Figure 7. Binding contractual arrangements for ground support elements that are made without confirming that the products meet a site's GCMP or PMP specifications or are suited to the sites specific ground conditions are of a considerable concern, particularly when such decisions are made in a corporate office without the involvement of site-based geotechnical practitioners.

Influence of drill bit and hole sizes

Drill bit size has long been a critical factor for achieving successful split set anchorage in underground hard rock mines. Many occurrences of poor pull test results have been observed by the authors due to incorrect bits being used for the different company's friction stabilisers or a particular mine site's ground conditions. This paper includes 72 pull tests referenced to drill bit and internal hole size measurements, of note is the variance in pull tests observed between different mine sites using the same sized bit and bolt due to the ground conditions or level of intra-hole radial rifling observed. The results show that pull tests generally improve with a smaller bit size until the borehole becomes too small for the bolt and the C shaped friction stabiliser is forced to overlap on

itself greatly reducing frictional anchorage along the length of the bolt. This is in line with previous observations made by Scott (1977b) and Tomory (1997). The influence of bit size is shown graphically in Figure 8 for three different mine sites, of particular note is the variance in average pull test anchorage between the different sites using different sized drill bits, largely due to the influence of each site's individual ground conditions.
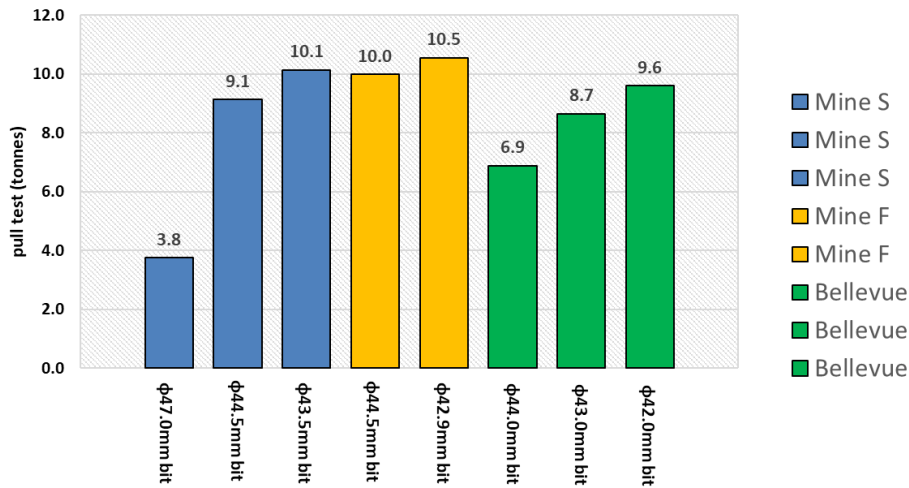
2.4m friction stabiliser tests relative to bit size at 3 mine sites

FIG 8 – Friction stabiliser pull test results for various mine sites varying with bit size.

The variance in ground conditions between mines can be significant, particularly when considering the degree of intra-hole radial rifiling observed along the borehole. This is discussed further in the section 'Influence of Jumbo feed, percussion, and rotation pressures'. Figure 9 shows the variability observed between mine site F and Bellevue Gold Mine when considering the level of intra-hole radial rifiling between starting bit size and average internal hole size from borehole micrometer results. There is potential that this effect has been observed in previous work completed by Player *et al* (2009) and may help to explain the large spread in pull testing data observed in some data sets. Traditionally many people within the mining industry have associated borehole overbreak to poor ground conditions and/or low UCS values. The authors consider this an area where further work is required, particularly considering other parameters such as jumbo drilling pressures, rock mass grain size, elastic modulus (E) and Poisson's ratio (v).
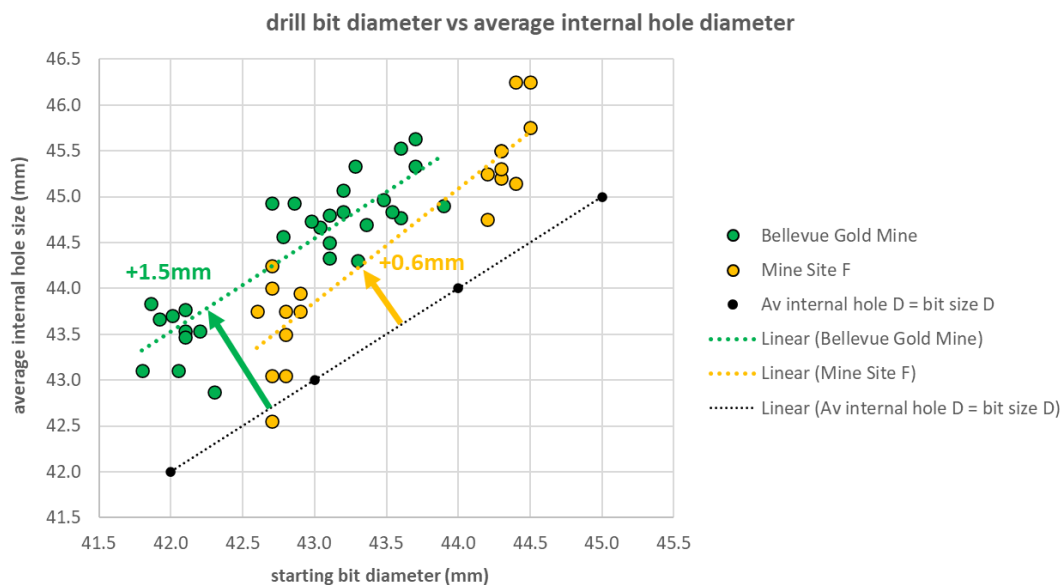
FIG 9 – Starting bit diameter before hole drilling and average internal hole size after drilling based off borehole micrometer results for mine sites F and Bellevue Gold Mine.

It is recommended, (particularly at the start of a new mining project) that geotechnical practitioners complete borehole micrometer testing to confirm what actual bit sizes are suitable for generating reliable loads in their actual ground conditions. It would also be advisable to complete such work before entering a long-term binding drill consumable and/or ground support supply contract to ensure that the planned products being used for executing the sites Ground Support Standards (GSS) are likely to be fit-for-purpose in providing a safe work environment for underground personnel.

A small data set has been recorded by the authors for the variance of new bit sizes over the last decade. The data recorded indicates a general trend of new 43 mm bits becoming larger in diameter for Suppliers S and E, providing greater bit life but at the potential detriment of friction stabiliser anchorage. Unlike development jumbo boring bits used in the face to bore the next cut in the development cycle, the primary role of a 43 mm bolting bit is to generate reliable loads for friction stabilisers to provide a safe work environment for underground personnel, rather than extended bit life or drill bit productivity.

In 2021, the authors randomly surveyed several 43 mm bolting bits across three suppliers with the following data shown in Table 4 for comparison.

TABLE 4

Starting bit diameter results for various bit suppliers, data recorded in 2021.

Drill bit supplier	Average new bit diameter (mm)	St Dev (mm)	Max bit diameter recorded (mm)	Sample size
D	43.8	0.13	44.0	15
E	44.5	0.23	44.8	10
S	44.3	0.17	44.5	10

Of particular note is that none out of the 35 new 43 mm diameter bits surveyed actually recorded a measurement of 43.0 mm.

Influence of jumbo feed, percussion, and rotation pressures

A smooth borehole allows a friction bolt to contact as much of the rock mass along the length of the hole as possible. A limited data set is available for the influence of different drilling pressures used in the drilling of bolt holes at mine site F and Bellevue Gold Mine. There is a complex relationship between the intra-hole roughness of a borehole and the jumbo drifter frequency, torque and drilling pressures associated with drilling the hole as shown in Figure 10. In particular, how these attributes contribute to drill bit balance in the hole during the drilling process to produce a smooth profiled hole.

Feed: 90 Bar, Percussion: 215 Bar
Average pull Test = 11.3t

Feed: 100 Bar, Percussion: 230 Bar
Average pull Test = 9.9t
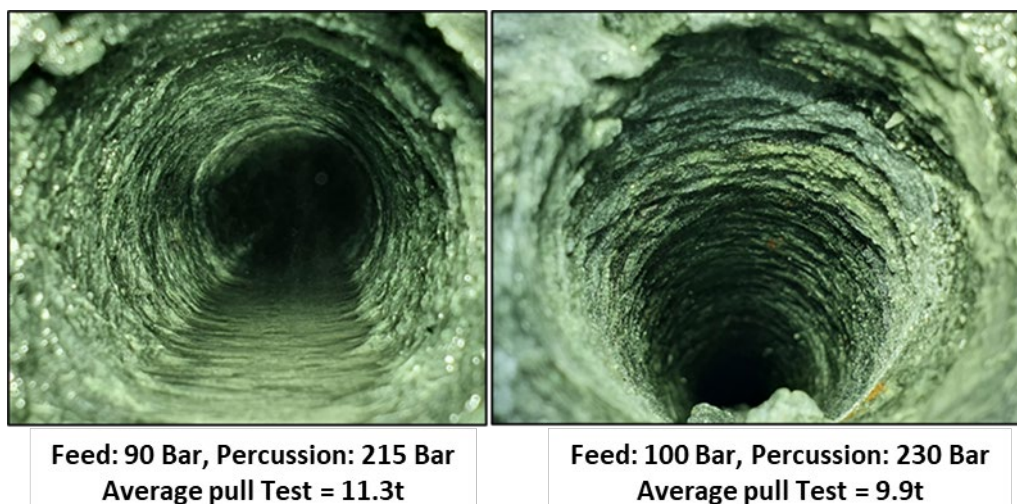
FIG 10 – Variance in intra-hole borehole roughness (or rifling) affecting pull test results at Bellevue Gold Mine relative to jumbo feed and percussion settings, sample size = 10 bolts for each setting.

Table 5 provides a summary of pull test results relative to jumbo feed and percussion settings for mine site F and Bellevue Gold Mine. The results suggest that there is a minor increase (10 to 15 per cent) in the pull test results obtained when slightly lower feed and percussion settings are used to drill each bolt hole. The exact cause for this and the increased level of intra-hole roughness for higher drilling pressures is not well understood and is an area where further work is required.

TABLE 5

Summary of pull test results relative to jumbo feed and percussion settings used.

Drilling pressures	Drifter model	Average pull test (tonnes)	St Dev (tonnes)	No. tests	Mine site
Mine F, Feed 90 Bar, Percussion 210 Bar	RD525	10.9	2.7	10	F
Mine F, Feed 90 Bar, Percussion 180 Bar	HLX5	11.2	2.5	11	F
Mine B, Feed 100 Bar, Percussion 230 Bar	RD525	9.9	3.0	9	Bellevue
Mine B, Feed 90 Bar, Percussion 215 Bar	RD525	11.3	2.2	8	Bellevue

Previous cost comparison discussions with mining development contractors have indicated an unfavourable cost relationship should a development contractor be requested to bore bolt holes at reduced pressures, hence increasing the time taken to bore each hole and in turn the time taken to support the cut. The current rationale for some mines is to leave the jumbo operator unconstrained with drilling pressures attempting to achieve maximum efficiency and pay for a higher capacity friction stabiliser to make up for the increased intra-hole roughness.

Influence of poor jumbo operator installation techniques

Observations and testing data over the last decade have shown that the rate of friction stabiliser damage or twisting has to become significantly more pronounced in pull testing results. The authors have not been able to identify a single cause for this in the data, but rather a combination of factors that may contribute to this occurrence:

- 'Optimisation' of split set dimensions by ground support suppliers to produce more cost-effective products that are less forgiving to poor installation techniques.

- The 'optimisation' by steel mill and ground support suppliers to produce steel that is quicker to roll through a roll-former at lower strength to produce a more cost-effective product that has a lower torsional rigidity.

- An overall skills shortage in the Australian underground labour market meaning operators move onto the development drilling jumbo in reduced time frames, with reduced experience and/or training.

- A reduced rate of jumbo operators that have had experience installing friction stabilisers with air-leg operated drills. Manual installation methods such as air-leg operated drills require correct bolt alignment for the successful installation, unlike modern mechanical methods using development drilling jumbos where the bolt can be forced into the hole at poor alignment angles.

- The increased power of high frequency development drilling jumbo drifters in the last decade, allowing curved or bent holes to be drilled and friction bolts to be installed at poor angles. (indexing).

Figure 11 shows examples of good and bad friction stabiliser bolt installation from borehole camera surveys:

- Bent bolt during installation, resulting in sections of the bolt no longer touching the borehole.

- Good bolt free from twisting with adequate hole closure.

- Twisted bolt due to bolt indexing relative to borehole orientation and/or using rotation during installation.

- High degree of slot closure due to small bit size, nearly resulting in both edges of the friction stabiliser touching.
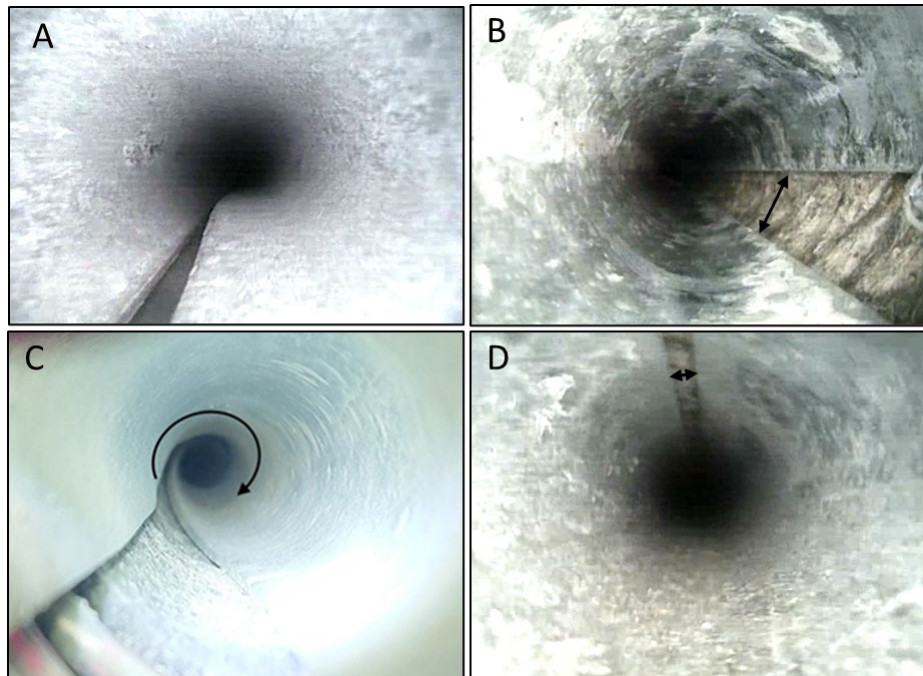
**FIG 11** – Examples of good and bad jumbo operator installation practises.

The practise of bolt indexing causing twisting of a friction stabiliser to occur is of particular note in this paper. The authors have observed that many poor pull test results have been caused by jumbo operators failing to line up the bolt correctly with the hole angle drilled as shown in Figure 12. Concerningly most of the bolt and meshing procedures reviewed by the authors over the last decade fail to discuss this or acknowledge its occurrence. This negative effect on friction bolt performance often reduces the pull test anchorage by 40–90 per cent when bolt twisting in excess of 90° occurs.
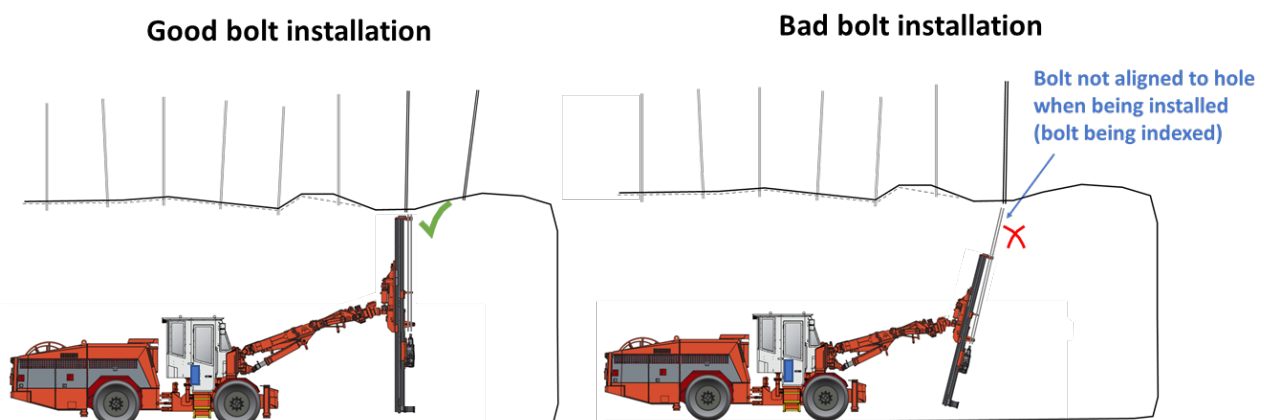
FIG 12 – Examples of good and bad jumbo operator installation practises, by bolt indexing.

The degree of bolt twist was estimated by a geotechnical engineer for each of the 1946 pull tests recorded to the nearest 45°, allowing correlation of bolt damage (twisting) to pull test results. When large numbers of twisted bolts occur in a data set, a bolt twist curve can be plotted to distinguish between different failure mechanisms as shown in Figure 13. This also allows different bolt suppliers

or different bits to be compared in the same ground conditions even when bolts are damaged or twisted by jumbo operators.
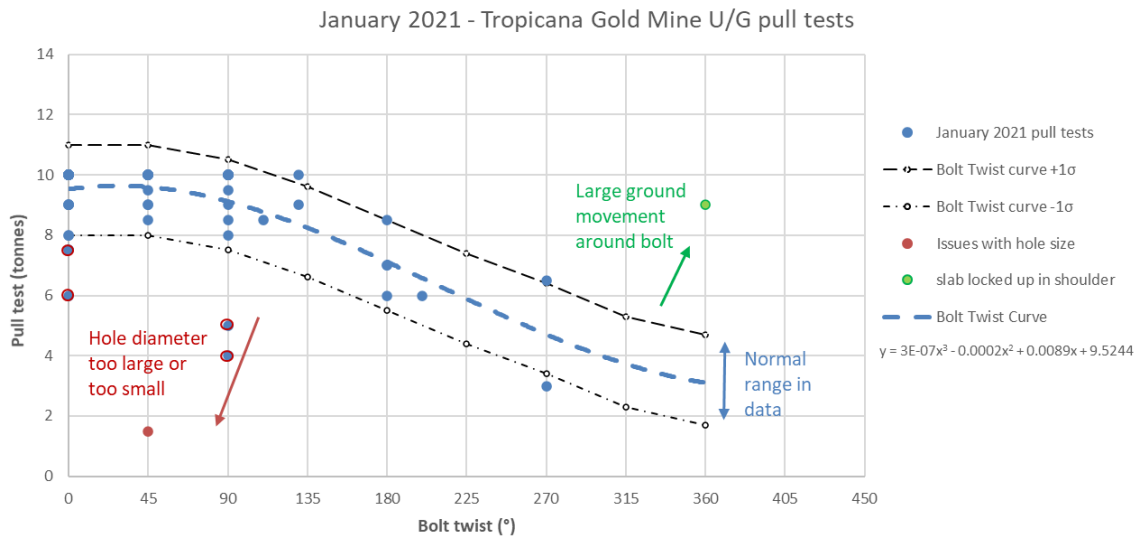
FIG 13 – Monthly pull testing data from Tropicana Gold Mine plotted on bolt twist graph.

In general, the data shows that once a bolt is twisted >90° there is a drop off in the pull test anchorage values obtained in line with the reduced area of the bolt that touches the inside of the borehole around the annulus. The exception to this occurs when localised ground movement increases the frictional resistance along the bolt near the start of the excavation. Considering a subset of 211, 2.4 m bolts tested at mine site F, the average pull test result for bolts with less than 90° of twist was 11.06 t, compared to bolts with bolt twist values in excess of 90° which was 7.87 t. This represents a 40 per cent reduction in the load capacity of a friction stabiliser due to poor jumbo operator installation methods. Bolts that were twisted >180° preformed even more poorly, with an average of 6.24 t representing a 77 per cent reduction in anchorage capacity.

Observations of pull test results that plot below the bolt twist curve generally occur due to the following four reasons:

1. Bolt was bent during installation as shown in Figure 11a.

2. Bolt hole was drilled with excessive feed pressures or inadequate collaring time causing the hole to visibly bend (or deviate) over its length – sometimes by as much as 0.6 m over a 2.4 m length causing the annulus of the bolt to no longer touch sections of the internal borehole.

3. The hole size was too large, either due to bit size used or localised ground conditions.

4. The drill bit was too small, causing the edges of the friction stabiliser to overlap, reducing the area of the bolt in contact with the borehole.

The authors have observed that the scatter surrounding the bolt twist curve is generally due to the ground support suppliers raw steel inputs, drill bits sizes used and the sites ground conditions. ie a tighter tolerance in raw steel yield strength across bolts delivered to site delivers a reduced standard deviation or 'band of data' along the twist curve, likewise with more consistent drill bits and ground conditions. This is discussed in further detail in the section 'Influence of steel grade and steel physical properties' where the historical yield strength for three different ground support suppliers is shown.

The influence of poor jumbo operator installation techniques is further highlighted in pull testing data from March 2020 at mine site S. This month's pull testing assessed friction stabiliser bolts installed by development crews OO, B and G in the same fresh development headings using the same suppliers bolts. Figure 14 shows the average pull test result for the month of March by individual operator and by mining contractor. At first glance the data indicated the following:

- Development group OO, monthly pull testing average = 11.7 t.

- Development Contractor B, monthly pull testing average = 9.4 t.

- Development Contractor G, monthly pull testing average = 9.8 t.

March average pull tests by development contractor
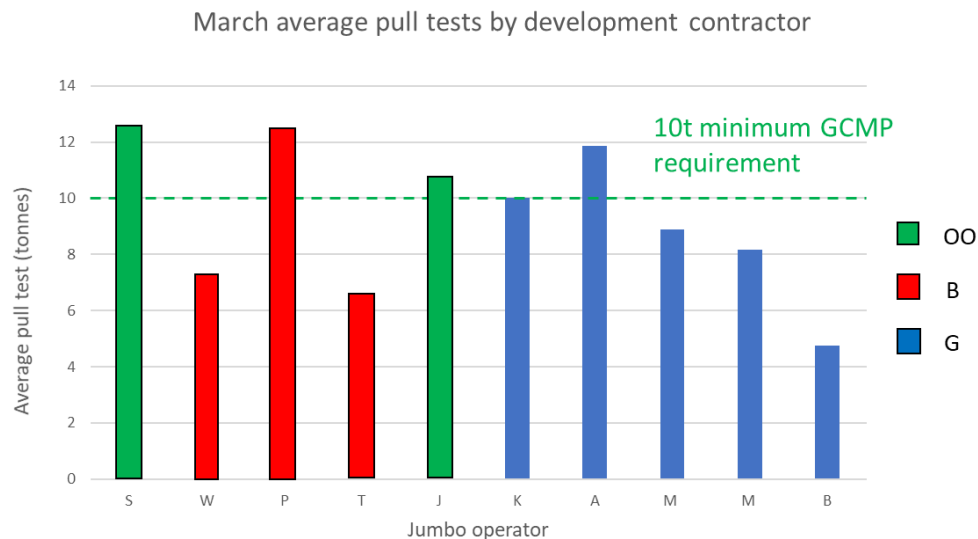
FIG 14 – March 2020 monthly pull testing data from mine site S plotted by mining contractor and individual operator.

Assessing the data by the development crew or mining contractor initially suggests that contractor B and G have installed poor quality ground support not meeting the sites minimum requirements in the GCMP for the month of March (eg 90 per cent of results ≥10 t). At mine site S, it was a site requirement for the jumbo operators to paint or write their initials on each plate or attach a cattle tag and name with each pull collar, this process allowed for further assessment of the pull testing data. When the results were split by an individual operator it was found that significant variation in the quality of ground support occurred for both contractor B and G. Operator 'B' and 'T' averaged less than 7 t for 2.4 m friction stabiliser installation during the month while other jumbo operators 'P' and 'S' averaged in excess of 12.5 t for the month as shown in Figure 14.

Many site-based geotechnical practitioners use 90 per cent of pull testing data meeting or exceeding 4 t/m (or similar) in monthly testing as a GCMP or PMP requirement for acceptable geotechnical risk limits. The authors have found that for an individual jumbo operator to comply with a site requirement such as 90 per cent of their bolts meeting or exceeding 10 t, an average of >11 t is usually required.

Recent individual monthly tracking and feedback of pull test results to individual operators at Tropicana Gold Mine in 2022 has shown that multiple operators are now capable of achieving a consistent 14 t pull testing average for 2.4 m friction stabilisers, representing a 20 to 50 per cent increase in individual pull test results over the previous 12 months. This improvement is significant to the mine site and may allow the geotechnical team at Tropicana to explore alternative bolt spacings in the future, should jumbo operator turnover/retention remain at manageable levels and monthly pull testing results remain consistent.

CONCLUSIONS

During the course of this investigation, the authors determined that:

- A direct relationship exists between the carbon equivalent of the parent steel used in friction bolt manufacture and the rate of torn pull rings observed in pull testing and rock mass loading conditions underground. This should be of particular interest in seismic conditions or mines with convergence.

- When other variables are isolated, a direct relationship exists between the yield strength of the steel used to make a friction stabiliser and the pull tests anchorage results obtained, in line with observations made by Scott (1977a) over 40 years ago.

- The effect of galvanising and roll-forming results in a positive improvement in bolt yield strength, this relationship is likely not to be linear and complex in nature due to the

microstructure compositions of alloyed steels, particularly in the transition of steel composition from Ferrite to Pearlite.

- The strip width and steel material properties have generally been 'optimised' over the last decade to produce a more cost-effective product, in line with Australian mines' increased focus on costs over the last decade. The data shows that these are generally less forgiving to poor jumbo operator installation techniques.

- Some bit suppliers have generally increased the size of new bolting bits over the last ten years to the stage where some new bolting bits are not fit-for-purpose in some ground conditions at some underground mines.

- The feed, percussion and rotation pressures used by jumbo development drills have increased over the last decade, generally resulting in a higher instance of friction stabiliser damage and decreased anchorage when bolt misalignment occurs by jumbo operators. The historical correlation of drive time to friction stabiliser anchorage has become less consistent due in part to the increase in drifter power and torque.

- A direct relationship exists between the degree of rock bolt twisting caused by bolt misalignment and the use of rotation and pull test results. Anecdotally pull testing trials have suggested that the bolt miss-alignment or 'bolt indexing' is considered the more critical variable in successful friction stabiliser installation and performance.

- The variance between individual jumbo operators in the quality of ground support installed can be significant. The tracking of individual operators by use of cattle tags secured to pull collar plates, or operator initials painted on pull collar plates allows individual feedback to be given to each operator on a monthly basis during routine pull testing for continuous improvement. Of particular note is the payment structure by some high-speed development contractors for their staff and the inclusion (or exclusion) of tangible QAQC metrics for the quality of ground support installed each month.

Future optimisation efforts by ground support suppliers, steel mills, drill consumables suppliers, underground development face drill suppliers and mining development operators, should consider relevant updated Work Health and Safety regulations, relating to legal obligations in providing a safe work environment in Australian underground mines. In particular, for those businesses operating in Australian States or Territories where recent legislation changes have levelled the liability between site management teams and industry suppliers during incident investigations by regulators.

The data presented in this paper acts as a series of snapshots in time over the last decade for issues encountered by the authors and as such does not necessarily reflect the quality of products produced by ground support suppliers or installation practises by mining development contractors at present. Any similarities to other Australian mine sites, operator names or suppliers when not fully named or referenced in this paper is coincidental.

The data discussed in this paper indicates that it would be prudent for site-based geotechnical practitioners to assess bolt performance in their actual ground conditions by testing to loads greater than 10 t, within fresh development to determine if the ground support calculations should consider 3 t/m, 3.5 t/m, 4 t/m or 5 t/m for reliable C shaped friction stabiliser performance.

ACKNOWLEDGEMENTS

REFERENCES

Davis, R L, 1979. Split-set rock bolt analysis, *International Journal of Rock Mechanics and Mining Sciences and Geomechanics Abstracts*, 16:1–10.

Gao, H, Wu, Y F and Li, C Q, 2019. Performance of normalization method for steel with different strain hardening levels and effective yield strengths, *International Journal of Engineering Fracture Mechanics,* 218(2019).

Hashimoto, S and Nakamura, M, 2006. Effects of microalloying elements on mechanical properties of reinforcing bars, *ISIJ International*, 46(10):1510–1515.

Panigrahi, B K, 2010. Microstructure-mechanical property relationships for Fe/Mn/Cr rock bolt reinforcing steel, *Journal of Materials Engineering and Performance*, 19:885–893.

Player, J R, Villaescusa, E and Thompson, A G, 2009. Dynamic testing of friction rock stabilisers, in M Diederichs and G Grasselli (eds), *ROCKENG09, Proceedings of the 3rd CANUS Rock Mechanics Symposium*, Toronto, 15 p.

Robinson, J C, 2000. Does Galvanising affect steel strength, *Corrosion Management Journal*, 9(2).

Scott, J J, 1977a. United States Patent No. 4 012 913 – Friction Rock Stabilisers.

Scott, J J, 1977b. Friction rock stabilisers – a new rock reinforcement method, a new rock reinforcement method, in W S Brown, S J Green and W A Hustrulid (eds), *Monograph on Rock Mechanics Applications in Mining*, pp 242–249, Society of Mining Engineers of the American Institute of Mining, Metallurgical and Petroleum Engineers, New York.

Tomory, P B, 1997. Analysis of split set bolt performance, Master of Applied Science Thesis, University of Toronto.

Dynamic drop testing of Sandvik's D47 and D39 MDX bolts at the Swerim's testing facility

O Vallati[1], B Darlington[2] and L Sandberg[3]

1. Research and Development Engineer, Sandvik Mining and Rock Technology, Heatherbrae NSW 2324. Email: osvaldo.vallati@sandvik.com
2. Research and Development Engineer, Sandvik Mining and Rock Technology, Heatherbrae NSW 2324. Email: bradley.darlington@sandvik.com
3. Project Manager, Swerim, Luleå Sweden 974 37. Email: lars.sandberg@swerim.se

ABSTRACT

The D47 and D39 Mechanical Dynamic Extra bolts (D47 MDX and D39 MDX) have been developed in response to the ever-increasing demand from the mining industry for rock bolts with high dynamic capacity. To prove such capacity, Sandvik has performed numerous *in situ* dynamic testing with the unique Dynamic Test Rig (DTR) (Darlington, Rataj and Roach, 2019; Roach, Rataj and Darlington, 2019).

To complement the collection of testing data, Sandvik, in collaboration with the Swedish Research Institute for Mining, Metallurgy and Materials (Swerim) have performed additional experiments in laboratory condition using Swerim's new drop test rig. This rig utilises a momentum transfer method to apply a dynamic load to the bolt. The sample falls together with the mass until the support beam impacts stationary dampers and the momentum energy is transferred to the bolt. Part of the charged energy is released by the dumpers while the remaining portion is absorbed by plastic deformation and/or displacement of the ground support element.

The D47 and D39 MDX bolts have been tested at Swerim's test facility with different levels of input energy. Six tests were performed at the specification energy of 36 kJ and six tests were carried out with the maximum allowable energy from the facility, ie 44 kJ. The bolts confirmed their dynamic performance absorbing the input energy without failure. The D47 MDX bolt absorbed up to 33 kJ with 150 mm displacement while the D39 MDX bolt absorbed up to 35 kJ with 162 mm displacement.

This work will present an overview of the drop test rig at Swerim's facility and a collection of results of the test performed on the D47 and D39 MDX bolts. The test method and results will be analysed and compared to the tests carried out with the *in situ* DTR.

INTRODUCTION

Dynamic support is utilised to cope with extreme loading conditions in underground mines. In addition to bearing the deadweight of the rocks, they also mitigate the effects of dynamic loading such as rock bursts and seismic events. To address such condition, Sandvik developed and introduced the Mechanical Dynamic Extra (MDX) bolts (Darlington, Rataj and Roach, 2019; Roach, Rataj and Darlington, 2019). These rock bolts have proven to be reliable, yieldable and can absorb the high energy developed by a dynamic event.

To quantify the energy absorption capability, or dynamic capacity, of the bolt, the industry has been relying on laboratory and *in situ* dynamic testing, of which there are currently two energy application methods. The momentum transfer method is utilised in the test rigs at Swerim, Luleå, Sweden (Vallati, Weaver and Halling, 2020) and Western Australia School of Mining in Kalgoorlie, Australia (Player and Villaescusa, 2004). The direct impact method is adopted by Sandvik's *in situ* testing rig (Darlington, Rataj and Roach, 2019), Canmet located in Ottawa, Canada (Plouffe, Anderson and Judge, 2008), Epiroc/New Concept Mining in South Africa (Knox, Crompton and Berghorts, 2018), and Central Mining Institute in Katowice, Poland (Pytlik, Prusek and Masny, 2016).

The theory of both methods is comprehensively described in literature, for example in the works of Player and Villaescusa (2004) and in Li and Doucet (2011). In both cases, the sample bolt is connected to the testing rig, and is loaded by a falling weight that, with its inertia, creates an impact loading. In the Momentum transfer method, the beam, rock bolt, and drop mass fall freely at the beginning of the test until the movement of the beam is halted with a pair of dampers, thereby transferring the kinetic energy of the mass to the rock bolt. In the direct impact method, the beam

and the sample holding the rock bolt are fixed in the test rig, while only the mass is falling freely. The mass stops abruptly by hitting the impact plate of the rock bolt (in continuous tube test) or of the sample holding the rock bolt (split tube test), thereby transferring the momentum of the mass to the rock bolt. In the momentum transfer method, a share of the charged energy is absorbed by the dampers. Therefore, to reach a specific energy to be absorbed by the rock bolt, the energy absorbed by the dampers must be compensated for by increasing the charged energy. Also, a share of the impact speed is absorbed when the test beam hits the dampers and may need to be compensated for by increased drop height. The test aims to reproduce a seismic event, the stiff beam connected to the upper part of the sample simulates the rock mass at the anchor point, which is not ejected during the seismic event, while the drop mass simulates the ejected rock.

In this context, this work intends to provide an overview of the newly developed drop test rig at the Swedish Research Institute for Mining, Metallurgy and Materials (Swerim) laboratory facility and a new collection of test results performed on the D47 and D39 Mechanical Dynamic Extra bolts (D47 MDX and D39 MDX). In this study, a total of 12 rock bolts were tested at different loading levels, six bolts were charged at the specification energy of 36 kJ and six tests were carried out with the maximum allowable energy from the facility, 44 kJ. The final part of the paper aims to explore the consistency of the test results comparing the laboratory testing at the Swerim facility to the test carried out *in situ*, underground, using Sandvik's drop test rig (DTR).

SWERIM DYANIMC TESTING FACILITY

Description

The dynamic drop test rig at Swerim facility, utilises a momentum transfer method to apply a dynamic load to the rock bolts.

Figure 1 shows the main components of the rig. The rock bolt is installed in a sample, simulating the targeted rock properties (1) that is fixed to the test beam (2). The load is determined by the applied weight package (3) and specified drop height. As the test beam (2) is released it accelerates to the impact speed given by the drop height and hits the dampers (4). The weight package (3) will continue downwards and thus applying a dynamic load on the rock bolt (5).

1. Parent capsule, holding test sample
2. Test beam
3. Weight package
4. Dampers
5. Rock bolt
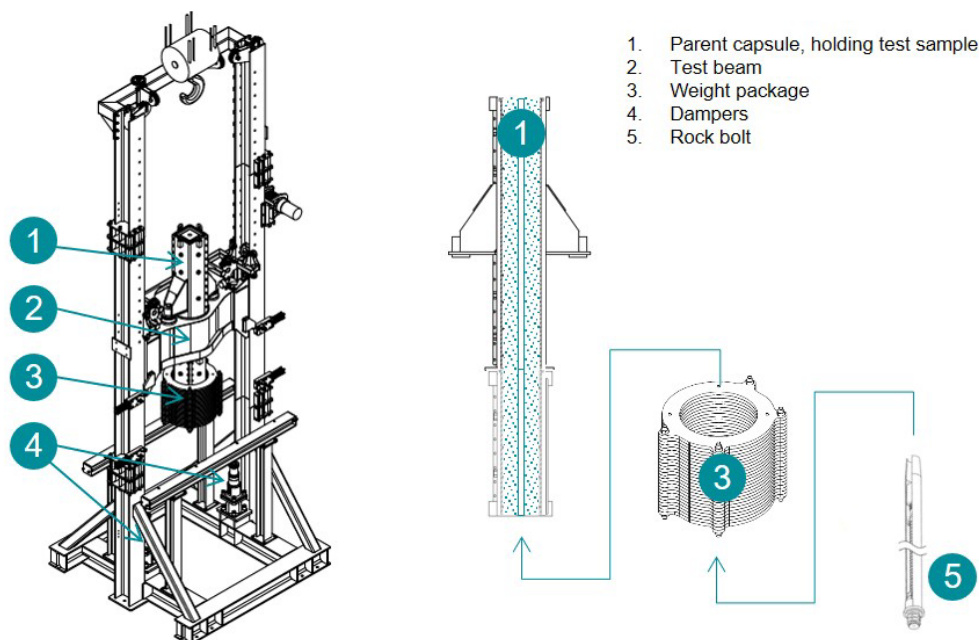
FIG 1 – Swerim drop test rig – components and working principle.

The rock bolts can be installed in two standard sample types; the large matrix type, as used for the tests and presented in this paper, and the simpler, less costly type, based on round steel tubes with a diameter of 60–80 mm. In the latter sample type, the bolts are grouted directly into the steel tubes,

or for mechanically anchored bolts and friction bolts, a hole is produced either by a removable core when grouting or a subsequent drilling operation.

Measuring system

The test sequence is captured by a Photron FASTCAM Mini AX100 Mono high-speed camera (Figure 2a). The displacement is determined by image analysis in Photron FASTCAM Analysis (PFA) using fiducial markers to track the movements (Figure 2b). To isolate the component of charged energy absorbed by the dampers and obtain the energy absorbed by the bolt, the relative movement between the test beam and weight package is calculated. The force acting on the bolt is measured using four PCB 215B piezo-electrical force rings mounted to an adaptor plate, which is placed between the washer on the bolt and the bottom plate of the weight package, (Figure 3). A photo-sensor triggers the high-speed camera prior to the test beam hitting the dampers and the trigger signal is logged together with the force-time data. This enables mapping of the displacement-time data from the camera with the force-time data from the force rings to obtain the desired force-displacement plots.

(a)   (b)
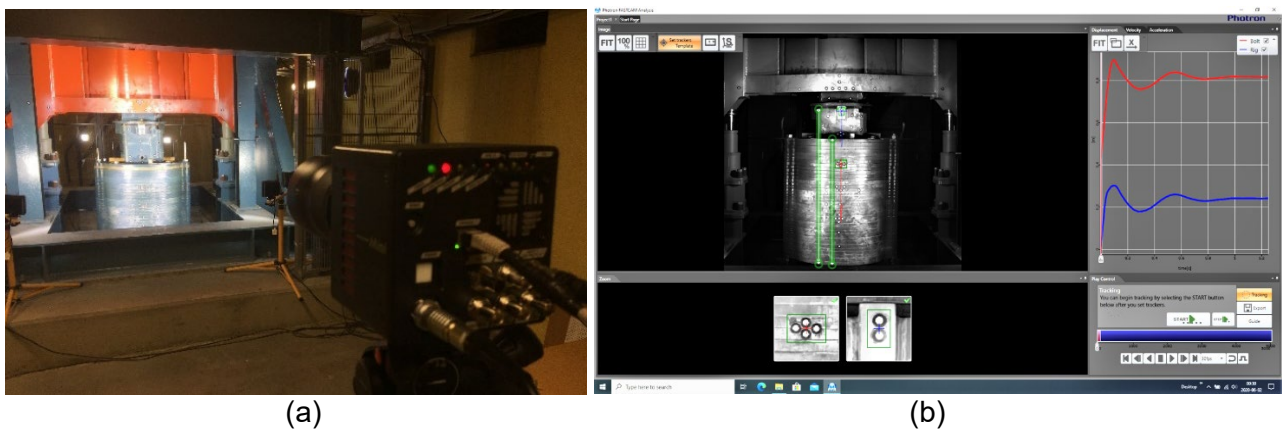
FIG 2 – Details of the instrumentation of drop testing rig at Swerim facility – displacement measurement; (a) high speed camera; (b) post-processing software.
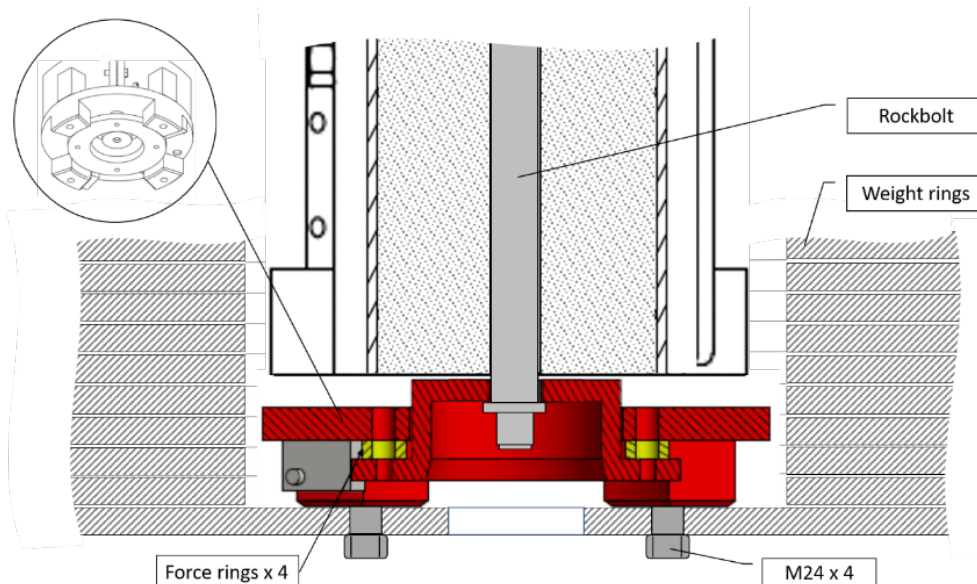
FIG 3 – Details of the instrumentation of drop testing rig at Swerim facility – load measurement.

DESCRIPTION OF THE SAMPLES

The MDX bolts

The MDX bolt from Sandvik is a rock bolt designed for variable ground conditions and has proven to be extremely efficient for areas with seismic activity. The bolt comes into two different sizes: the D47 MDX bolt with a nominal diameter of 47 mm and the D39 MDX, with a nominal diameter of 39 mm (Roach, Rataj and Darlington, 2019). While the D47 MDX bolt was designed to be installed with jumbos in Ø45 mm holes the D39 MDX was optimised for smaller holes and dedicated bolting equipment typically used in Canadian, North American and European markets.

The bolt features a split tube (47 mm or 39 mm diameter respectively) reinforced with a 20 mm bar through its centre. Once installed into the rock, the expanded wedge, activated by rotation of the 20 mm bar, anchors the bolt into the rock allowing a long free length of bar between the toe (wedges) and the head of the bolt. During a seismic event the entire free length of the bar can stretch, effectively absorbing the energy from the event. Figure 4 shows the main components of the bolt.

In this laboratory investigation, a total of twelve 2.4 m long bolts were tested, six D47 MDX and six D39 MDX.

FIG 4 – The MDX bolt.

Preparation of the sample for testing

The MDX bolts were installed in concrete filled square hollow tubes, to replicate rock during the dynamic testing. A full sample consisted of two tubes, 1 m and 2 m long, grouted individually, and assembled together in the parent capsule to create a 3 m long sample, Figure 5. This enables both split and continuous tube test configuration. For the MDX bolts, being mechanically anchored at the bolt toe, the performance is assumed to be independent on test configuration as the bolt absorbs the charged energy along its full length in both cases. However, for a split-tube load case, the MDX bolt can provide a minor portion of extra strength from friction between the outer tube surrounding the bar and the rock. For these tests, the decision was made to only test in continuous-tube configuration.
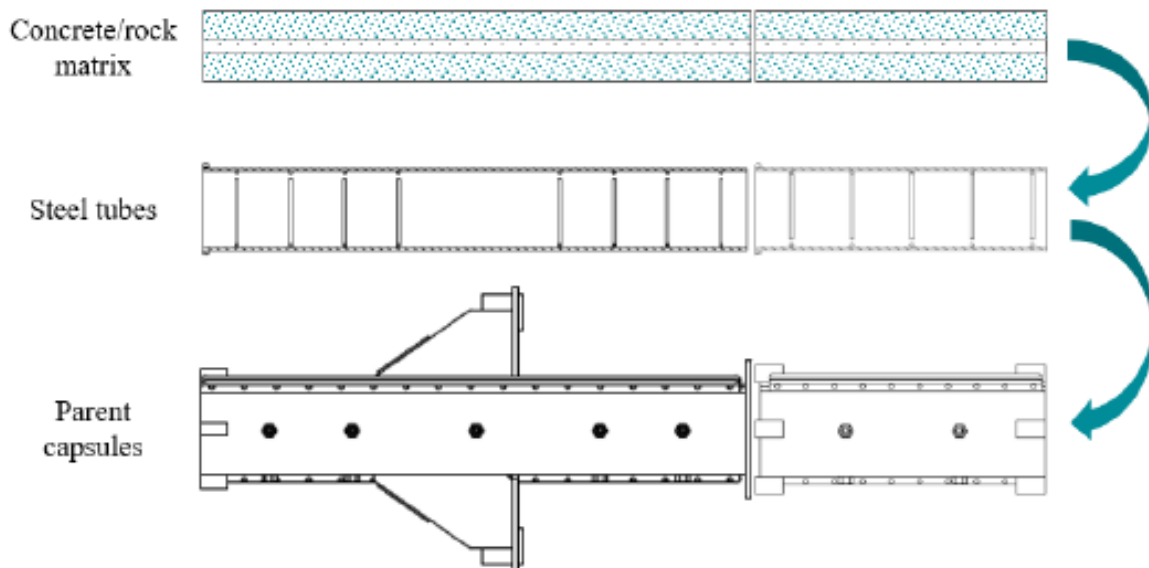
FIG 5 – Sample set-up for testing.

To cope with the high capacity of the bolt, and to simulate competent hard rock, high strength concrete and thick-walled steel tubes were selected for this application (Figure 6). This combination allowed the MDX wedge mechanism to expand during the installation of the bolt and during the dynamic impact. The tubes have a cross-section of 300 × 300 mm and a wall thickness of 10 mm. In addition, a welded stop flange on the upper end and welded internal rebars eliminate the risk of the tubes sliding in the parent capsule or the concrete sliding in the steel tubes. The parent capsules holding the grouted samples are manufactured from 15 mm steel with a yield strength of 700 MPa and together with the 10 mm thick steel tubes holding the concrete matrix, the samples are encapsulated by 25 mm steel giving a very solid installation condition.
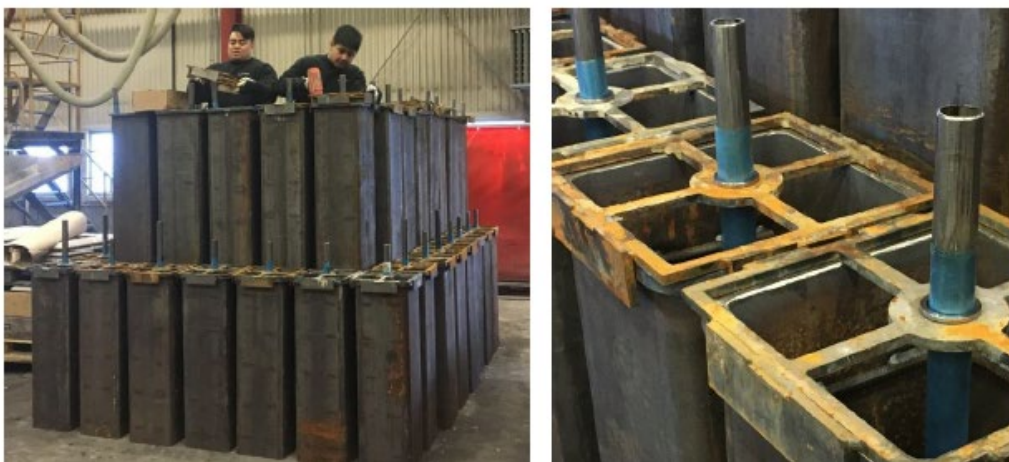
FIG 6 – Steel tubes with steel cores ready for concrete pour.

After 28 days of concrete curing, rock bolts were installed in the samples using an installation rig featuring a hydraulic hammer, which is mounted on a sled with guide rails and a feed screw. Installation is achieved by placing the parent capsules holding the samples in the installation rig, the rock bolts with toe entering the sample and head in the adaptor, which is then hammered in (Figure 7). Finally, a torque of 400 Nm was applied to engage the anchor according to the standard installation procedure (Sandvik, 2021).

FIG 7 – Bolt installation rig.

DROP TESTING

Two different tests level were investigated; for each load level three bolts of the same type were tested. Six tests were performed subjecting the bolt to a specification energy of approximately 25 kJ, while the remaining six samples were tested at high energy, up to 34 kJ, which was the maximum capacity of the test apparatus.

The test sequence involved raising the beam assembly, consisting of the drop beam, test sample and the selected weight, to a drop height of 2.16 m. Once released, the beam assembly free falls until impacting the dampers, at which point the momentum of the falling beam assembly is transferred to the bolt. The drop height for the two test levels were the same to keep the impact velocity constant, while the weight was adjusted to produce the desired charged energy levels. In this configuration, the dumpers were estimated to absorb approximately 20–25 per cent of the charged energy.

Test results

All bolts withstood the dynamic energy successfully dissipating the input energy, a summary of the tests and results are presented in Table 1.

TABLE 1

Test summary and results.

Sample ID	Drop mass (kg)	Drop height (mm)	Impact velocity (m/s)	Charged energy (kJ) [#1]	Bolt displacement (mm) [#2]	Peak load (kN)	Absorbed energy by the bolt (kJ) [#3]	Failure yes/no
D47 #1	1702	2160	6.51	36.1	129	236	27.1	no
D47 #2	1702	2160	6.51	36.1	114	255	26.1	no
D47 #3	1702	2160	6.51	36.1	129	236	27.2	no
D47 #4	1988	2160	6.51	42.1	152	244	33.4	no
D47 #5	1888	2160	6.51	40.0	128	242	29.2	no
D47 #6	1788	2160	6.51	37.9	123	240	27.5	no
D39 #1	1688	2160	6.51	35.8	151	248	29.2	no
D39 #2	1688	2160	6.51	35.8	136	242	28.0	no
D39 #3	1688	2160	6.51	35.8	122	243	26.2	no
D39 #4	1988	2160	6.51	42.1	162	240	34.9	no
D39 #5	2038	2160	6.51	43.2	157	238	33.7	no
D39 #6	2088	2160	6.51	44.2	162	237	34.5	no

Note [#1]: Input energy includes only the potential energy component (no extra bolt displacement or dampers).

Note [#2]: Static displacement taken at the end of the test.

Note [#3]: Absorbed energy calculated as the area under the load-displacement curve.

The load displacement curve for the six D47 MDX and the six D39 MDX samples is presented in Figures 8 and 9 respectively.

The plot shows an initial ramping load, typical for this type of mechanically anchored bolt. As the bar is loaded by the impacting mass, the wedge system engages and expands further into the concrete matrix. This is followed by the sustained load that ranges between 200–250 kN, at which stage, the bar is plastically deformed without failing until all the energy is absorbed and the maximum displacement is reached. The amplitude of the displacement experienced by the bar is dependent on the applied energy and consists of primarily plastic elongation of the rebar. Additional components of displacement occur as the wedges further engage in the anchor upon impact, along with the deformation of the washer (Figure 10). This latter component was insignificant in the case of the radiused washer adopted for the D39 MDX bolt.

The energy absorbed by the bolt can be calculated as the area under the load-displacement curve to the point of peak displacement. The energy absorbed ranged between 26.1 kJ and 34.5 kJ, confirming that a portion of the charged energy is absorbed by the dampers.
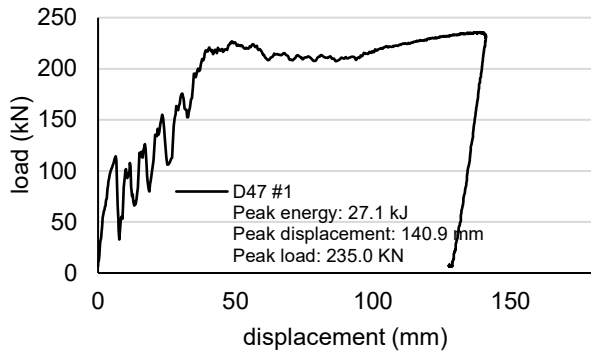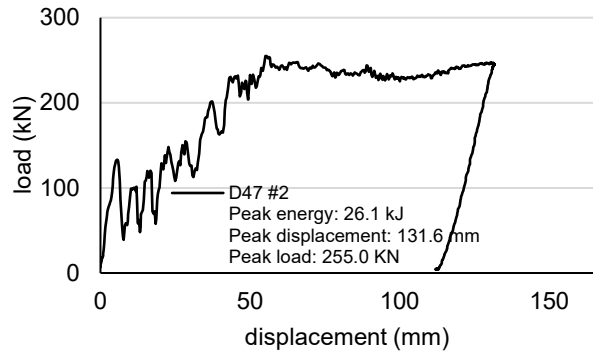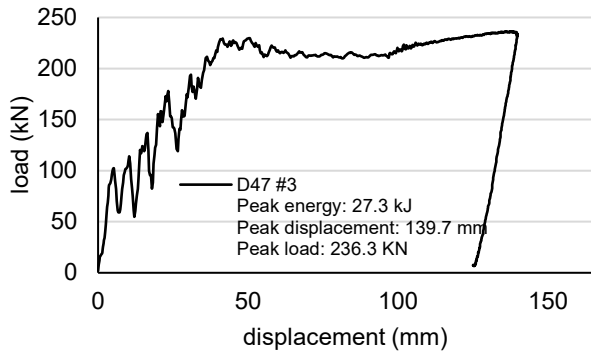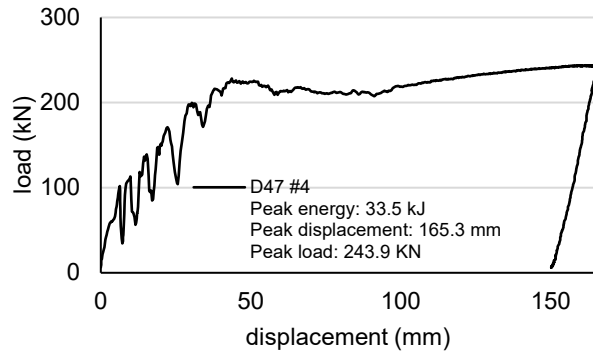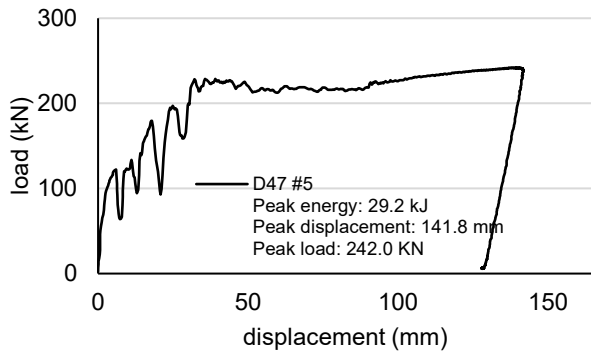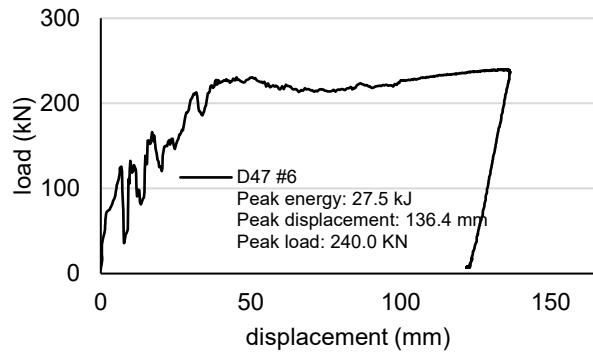
FIG 8 – Test results for D47 MDX bolts.
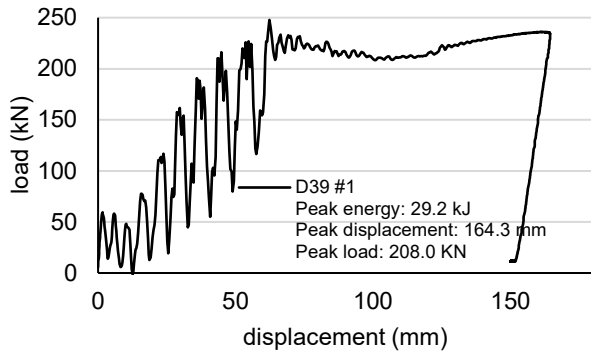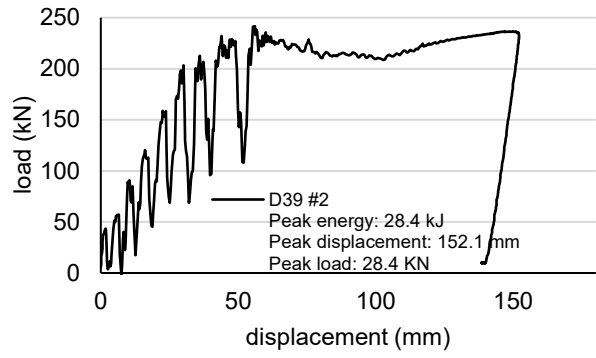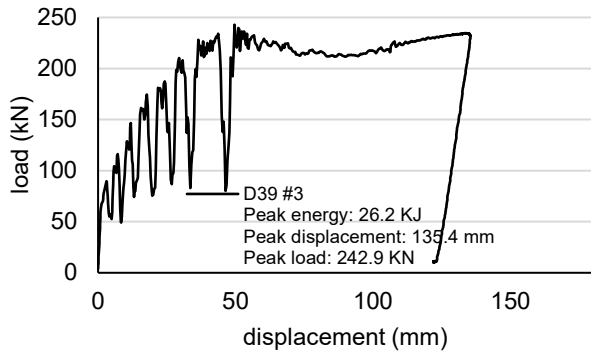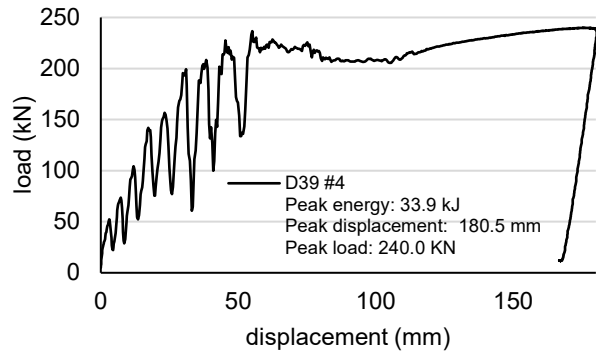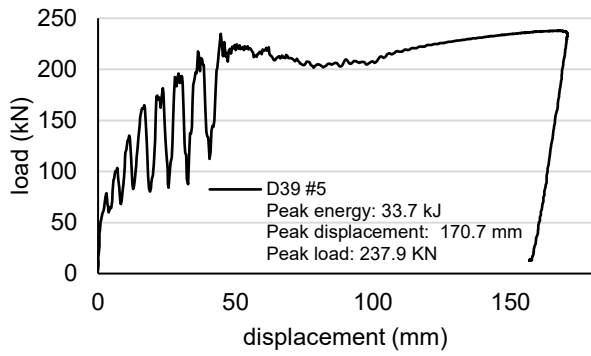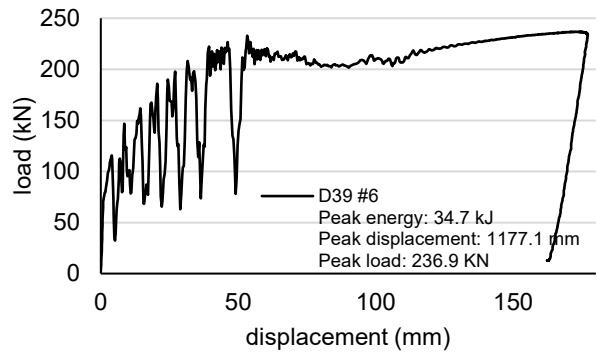
FIG 9 – Test results for D39 MDX bolts.

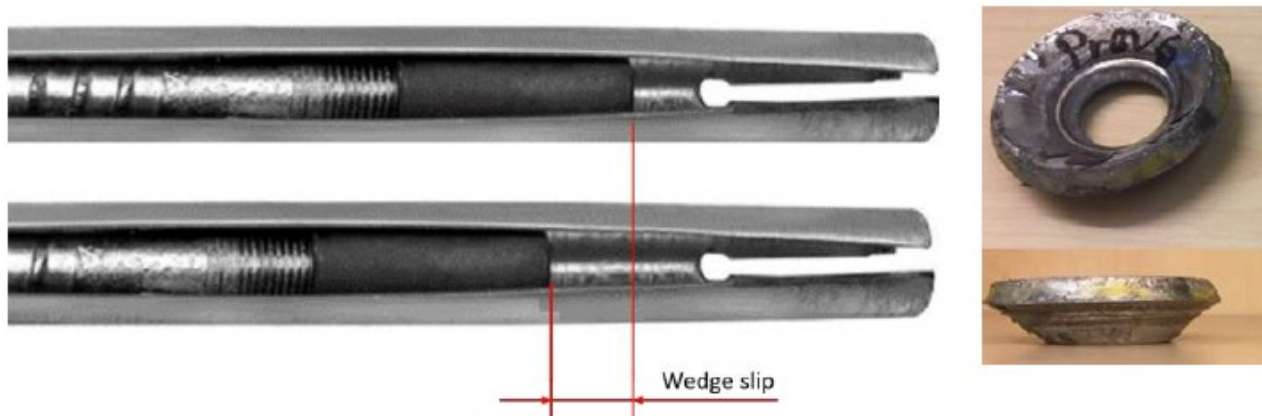**FIG 10** – Details of the sample after testing: (a) Extra wedge engagement after loading; (b) Typical deformation of the washer on the D47 MDX bolt.

After dynamic testing all bolts were examined, with the overall result that all bolts survived the testing without catastrophic failure. The plastic elongation obtained in the rod was distributed evenly over the length and no localised necking (reduction in cross-sectional area) was detected. No damage was observed to the nuts or threads after the test. All test samples behaved consistently, and in line with previous testing (Vallati, Weaver and Halling, 2020) with a residual displacement ranging between 114 mm to 162 mm.

Sample D39 #6, which was subjected to the maximum charged energy, was cut open after testing to study the status of the wedges and anchoring area. Small cracks and localised concrete crushing were observed in the area where the anchor engages to the concrete, in addition to a noticeable bulging of the steel tube. The high compressive forces from the anchor acting on the concrete were transferred to the surrounding steel shell, which caused a small elastic expansion of the steel shell. This expansion of the steel tube induced tensile stresses in the concrete resulting in cracks forming. A review of the test results, this phenomenon did not influence the response of the bolt or the test rig.

COMPARISON BETWEEN SWERIM FACILITY AND *IN SITU* DROP TESTING

To explore the consistency of MDX dynamic performance, a comparison is presented between the laboratory testing at Swerim facility and Sandvik's *in situ* drop test rig (DTR). The importance of a comparison between test methods was highlighted by recent research (Li *et al,* 2021) due to a fundamental lack of a standardised testing procedure. Test apparatus can differ by test methodologies, stiffness, proportion of energy lost during impact, impact loading time, measurement technologies and even test report are usually inconsistent between facilities.

The *in situ* DTR has been comprehensibly described in literature (Darlington, Rataj, Roach, 2019; Roach, Rataj and Darlington, 2019). The test is based on the direct impact method and, as for its name, it is carried out on a bolt installed into the rock mass, underground, at the mine. A slide rod is connected to the sample bolt head and is used as guide for the free-falling mass that impacts on the impact plate. The load is transferred to the bolt head through the slide rod and claw assembly. In the direct-impact method the energy input is defined by the kinetic energy at the point of impact, and in contrast to the moment transfer method, it is almost entirely absorbed by the bolt as there are no dampers.

A schematic of the two methods is presented in Figure 11.
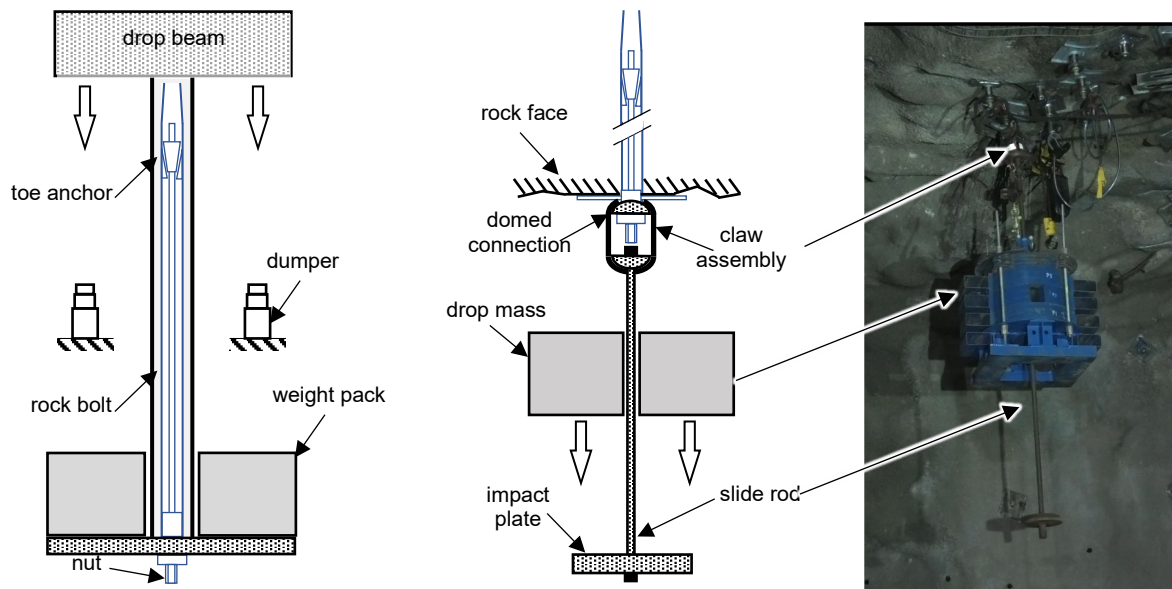
FIG 11 – Schematic of the momentum transfer method used at Swerim facility, and the direct impact method used in the *in situ* drop test method. (a) laboratory testing: momentum transfer (continuous tube configuration); (b) in situ testing: free-fall method (DTR).

The comparison between the two methods is based on the common output, which is the energy absorbed by the bolt. In both methodologies the energy absorbed by the bolt is calculated by integrating the load-displacement curve derived from the sensors installed on the rig. Both test methods measure the impact load with a piezoelectric loadcell(s) located near the nut of the bolt. The Swerim facility uses four loadcells in the impact plate, while the DTR uses one loadcell within the claw assembly. In the case of the Swerim facility, the displacement is directly measured by a high-speed camera, while for the DTR, the displacement is calculated by double integration of accelerometer data, or can be extrapolated from the loadcell measurements.

For this study, two tests are compared, which were carried out on the same bolt type (2.4 m D47 MDX). The Swerim test charged energy was 36.1 kJ; however, the DTR theoretical input energy produced by the falling mass was 27.1 kJ. The input energy, although different, produced similar effects on the bolts, which both absorbed approximately 27 kJ.

Comparing the load measurements from these two tests (Figure 12), it can be observed that the primary differences are the loading rate and impact time. The DTR loading impact shows a shorter loading time with a sharper response. This behaviour could be attributed to the stiffness of the rock in which the bolt in installed, which securely restrains the wedge anchor. The moment transfer method exhibits a gentler loading that could be caused by the low stiffness of the concrete matrix and the stiffness of the rig. In addition, for the momentum transfer method the impact is not direct and instantaneously applied to the bolt (as happens with the direct impact method), but rather, the mass has an initial velocity, and its momentum is applied to the bolt. The difference in loading rate produces higher peak loads but the bolt responses both have a similar maximum displacement (Figure 13). It was not in the scope of this preliminary study to address the differences in lading rate and impact duration, and more tests are needed to support this thesis.
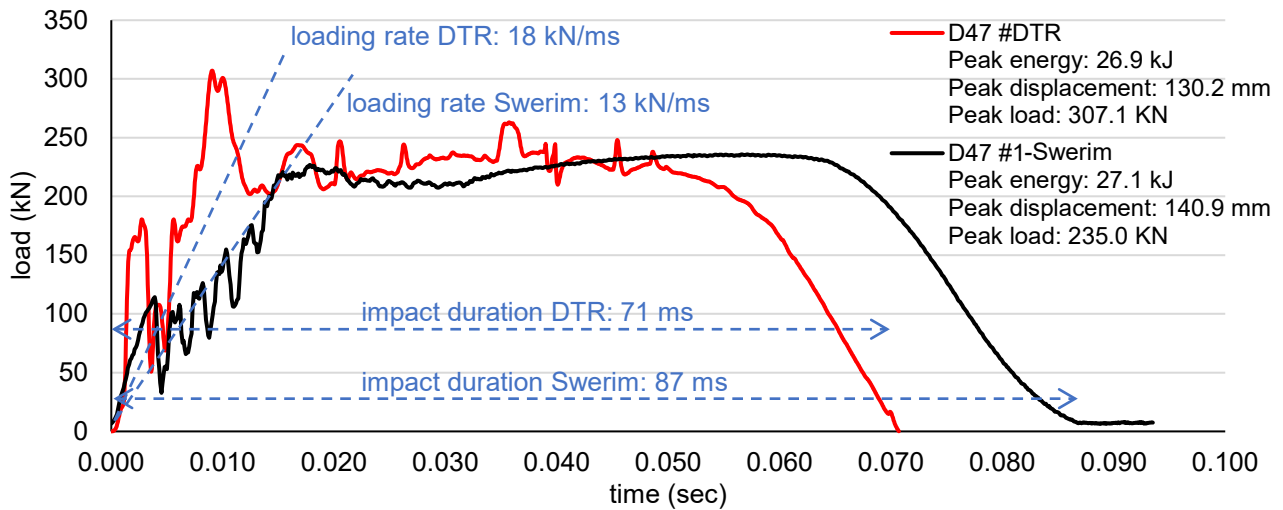
FIG 12 – Load versus time plot for the Swerim facility (momentum transfer method) and DTR (direct impact method).
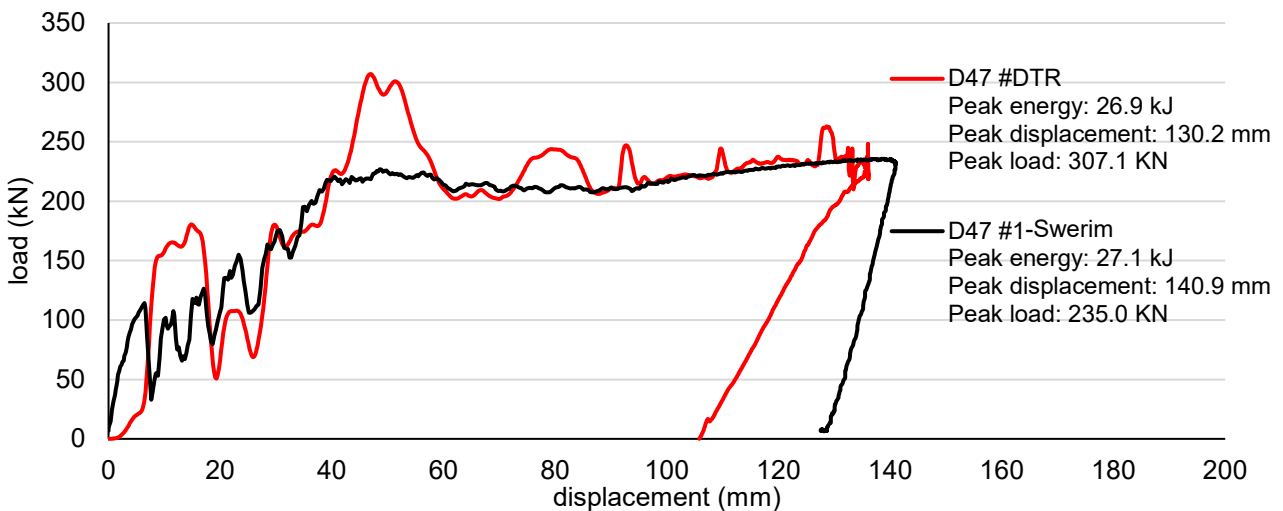
FIG 13 – Load versus displacement curve for the Swerim facility (momentum transfer method) and DTR (direct impact method).

CONCLUSION

Dynamic bolts are used to cope with the ever-increasing challenges in the mining industry, assisting to manage the high stresses generated by rock burst and seismic events. Their dynamic capacity is defined as the level of energy that the bolt can absorb and dissipate during a seismic event, which is best quantified by dynamic testing. Numerous test rigs have been developed in the past decade, which are based on two different energy application methods: momentum transfer and direct impact methods.

The newly developed rig at the Swedish Research Institute for Mining, Metallurgy and Materials (Swerim) lab facility in Luleå, utilises the momentum transfer method. Within this method, the rock bolt is installed in a thick-walled steel tube filled with a concrete matrix. A weight pack is attached to the lower part of the sample while a stiff beam is connected to the upper part. The components are lifted to the desired height and, and once realised, fall together until the beam impacts the dampers. The dampers arrest the downward motion of the beam connected to the upper part of the sample, whilst the momentum energy of the lower mass is applied and absorbed by deformation of the ground support element.

As part of this study, an experimental investigation was carried out on the D47 and the D39 Mechanical Dynamic Extra (MDX) bolts. These are dynamic ground support elements with extreme capacity, ideal for areas with seismic activity and variable ground conditions. During a seismic event,

the entire bolt is stretched, as the free length of the bar extends from the anchor to the bolt's head, making the bolt extremely efficient in responding to seismic loading.

Twelve 2.4 m long samples were tested at the Swerim facility, at two different loading levels. Three D47 MDX and three D39 MDX were tested at a charged energy of 36 kJ. Three D47 MDX and three D39 MDX were tested at a high energy between 38 kJ and 44 kJ. All bolts withstood the single impact test with an absorbed energy ranging between 26.1 kJ and 34.5 kJ. The energy was primarily absorbed by uniform plastic deformation of the bar, but also in a smaller portion, by further wedge engagement and deformation of the flat washer of the D47 MDX bolt.

Test results at the Swerim facility were comparable with previous test carried out with the Sandvik *in situ* drop test rig (DTR). This rig is based on the direct impact method and allows test to be carried out on bolts installed underground in the mine. The comparison showed that the two test methods produce a similar bolt response. In the DTR testing, the peak load is reached faster, and the total impact duration is shorter, while the Swerim rig produces a gentler loading.

REFERENCES

Darlington, B, Rataj, M and Roach, W, 2019. New method to evaluate dynamic bolts and development of a new dynamic rock bolt, in *Deep Mining 2019: Proceedings of the Ninth International Conference on Deep and High Stress Mining* (The Southern African Institute of Mining and Metallurgy: Johannesburg).

Knox, G, Crompton, B and Berghorts, A, 2018. The relationship between the magnitude of impact velocity per impulse and cumulative absorbed energy capacity of a rock bolt, in *Proceedings of The Fourth Australasian Ground Control in Mining Conference Proceedings*, pp 160–169 (The Australasian Institute of Mining and Metallurgy: Melbourne).

Li, C C and Doucet, C, 2011. Performance of D-Bolts under dynamic loading, in *Rock Mechanics and Rock Engineering,* 45:193–204.

Li, C C, Hadjigeorgiou, J, Mikula, P, Knox, G, Darlington, B, Royer, R, Pytlik, A and Hosp, P, 2021. Performance of identical rockbolts tested on four dynamic testing rigs employing the direct impact method, in *Journal of Rock Mechanics and Geotechnical Engineering*, 13(4):745–754.

Player, J R and Villaescusa, E, 2004. Dynamic testing of rock reinforcement using the momentum transfer concept, in *Fifth International Symposium on Ground Support*.

Plouffe, M, Anderson, T and Judge, K, 2008. Rock bolts testing under dynamic conditions at CANMET-MMSL. in T R Stacey and D F Malan (eds.): *6th Int. Symp. on Ground Support in Mining and Civil Engineering Construction*, pp 581–96 (SAMM symposium series S51: Cape Town).

Pytlik, A, Prusek, S and Masny, W, 2016. A methodology for laboratory testing of rockbolts used in underground mines under dynamic loading conditions, in *Journal of the Southern African Institute of Mining and Metallurgy*, 116(12):1101–1110.

Roach, W, Rataj, M and Darlington, B, 2019. Development of a new Sandvik 'little brother' dynamic rockbolt and the in situ dynamic evaluation of bolts, in *Ground Support 2019: Proceedings of the Ninth International Symposium on Ground Support in Mining and Underground Construction*, pp 201–212 (Australian Centre for Geomechanics: Perth).

Sandvik, 2021. Ground Support Brochure https://www.rocktechnology.sandvik/globalassets/products/rock-tools/pdf/ground-support-brochure-eng.pdf [Accessed: 14 September 2022].

Vallati, O, Weaver, S and Halling, E, 2020. Dynamic Testing of Ground Support: A Comparison Between In-Situ and Laboratory Testing, Paper presented at the ISRM International Symposium – EUROCK 2020, physical event not held.

Assessment of ground support requirements in coal burst-prone mines

C Wei[1], J Watson[2], C Zhang[3] and I Canbulat[4]

1. School of Minerals and Energy Resources Engineering, University of New South Wales, Sydney NSW 2052. Email: chunchen.wei@unsw.edu.au
2. School of Minerals and Energy Resources Engineering, University of New South Wales, Sydney NSW 2052. Email: elementaryjohn@hotmail.com
3. School of Minerals and Energy Resources Engineering, University of New South Wales, Sydney NSW 2052. Email: chengguo.zhang@unsw.edu.au
4. Professor, School of Minerals and Energy Resources Engineering, University of New South Wales, Sydney NSW 2052. Email: i.canbulat@unsw.edu.au

INTRODUCTION

Coal burst is defined as a dynamic release of energy within the rock or coal mass in underground coalmines that causes violent rock or coal ejection in the vicinity of mine excavations. It poses one of the highest safety and productivity risks in the mining industry as coal bursts have the potential to cause multiple fatalities. As Australian coalmines go deeper, the likelihood of coal burst increases. Thus, it is critical to assess the ground support requirements in coal burst-prone conditions. A previous study conducted by the authors (Wei *et al*, 2022) reviewed the support capacities of a wide range of ground support elements in laboratory tests. This study aims to examine the role and effects of the ground support elements and systems for Australian underground coalmines to minimise the damage caused by catastrophic dynamic failures (ie coal and rock burst) and enhance the safety of mine workers.

GROUND SUPPORT PRINCIPLES FOR BURST-PRONE AREAS

For a ground support system in burst-prone areas, three main principles are well-acknowledged: use yielding support elements (to increase energy absorption), address the weakest link, and establish an integrated support system (Cai and Kaiser, 2018; Potvin and Hadjigeorgiou, 2020; Wei *et al*, 2022).

Yielding support has been used worldwide in burst-prone areas to mitigate the rock burst risks. A yielding support system can accommodate a large amount of rock fracturing and absorb the associated dynamic energy (Cai and Kaiser, 2018). This function can be achieved by yielding support elements (eg yielding rock bolts and mesh) with large deformation capacity (Wei *et al*, 2022).

It is well recognised that the weakest link of a support system is often the surface retaining elements and the connection between bolt and plate (Kaiser and Cai, 2012; Potvin and Hadjigeorgiou, 2020). The weak link in the support system can be highly likely failed much before that the reinforcements reach their theoretical design capacity. Heal (2010) studied 254 rock burst cases and concluded that only 30 per cent of rock burst damage was due to failure of reinforcement elements. In comparison, the majority of rock burst damage was caused by the failure of either the surface elements or the connection between the surface support and the reinforcements, highlighting the weakest link in a support system (Wei *et al*, 2022).

In burst-prone areas, an integrated support system is effective when it can provide all the required support functions, ie reinforcement, retaining, holding and connection (Cai and Kaiser, 2018). In general, the most important aspect of an integrated support system is to ensure the deformation compatibility between each support element within the system. Then, the support system can reach the highest possible dynamic support capacity, instead of failing at the weakest link while the yielding rock bolts have not even reached their yielding state (Wei *et al*, 2022).

SUPPORT CAPACITIES OF GROUND SUPPORT ELEMENTS IN THE LABORATORY

The support capacities of yielding rock bolts, mesh, and integrated support systems obtained from laboratory loading tests are assessed in a previous study conducted by the authors (Wei *et al*, 2022).

According to the energy-absorbing mechanisms, the yielding rock bolts can be classified into two categories: stretching rock bolts, and ploughing or structural extrusion rock bolts. In recent decades, many yielding rock bolts can provide more than 300 mm of yielding displacement and load capacity greater than 100 kN, which was a critical requirement proposed by Kaiser *et al* (1996) for yielding bolts in burst-prone areas. Apart from the energy absorption and yielding deformation capacity, the initial stiffness and energy absorption rate are also critical factors when applying yielding rock bolts in practice. Stretching yielding rock bolts perform well for both the initial stiffness and energy absorption rate (Wei *et al*, 2022).

The chain-link mesh has greater energy absorption and deflection capacities than weldmesh, indicating that the chain-link mesh is more suitable in burst-prone areas. The TECCO mesh series demonstrated better energy absorption capacity than that of other mesh types (Wei *et al*, 2022).

The dynamic loading tests in South Africa showed that the support capacity of the mesh support system was approximately double by adding rope lace, and it was four times higher when adding mesh straps. The test results in WASM showed that all the support systems with chain link mesh and yielding rock bolts were classified as high support capacity, which has more than 15 kJ/m^2 of energy absorption capacity (Wei *et al*, 2022).

A COUPLED ANALYSIS OF BURSTS IN SUPPORTED AND UNSUPPORTED COALFACES

A coupled model was established to estimate the ejection velocity in supported and unsupported coalfaces. Gas environment within coal was also considered in the coupled analysis. Two burst scenarios were examined using the proposed coupled model: a burst in development heading of an unsupported face, and a ribside burst in a supported rib. Burst thickness of 1.0 m, 2.0 m and 3.0 m and depths of mining 250 m, 500 m and 750 m were considered. Released energy is computed by three-dimensional elastoplastic analysis using FLAC3D. The coupled model results clearly show the superiority of bolts with a capacity for greater plastic elongation. Conveniently from the design perspective, maximum mesh tension is governed entirely by bolt capacity and mesh rupture strain. It should not be forgotten that for the straps to carry load back from the mesh to the bolts, they must act as beams and therefore have sufficient bending moment capacity. For height of mining 3.0 m and three bolts per strap, the greatest bending moment is a minimum if the bolts are located 0.5 m, 1.5 m and 2.5 m above the floor.

This study advances the understanding of ground support requirements in coal burst-prone mines. The coupled model can estimate the ejection velocity in coalfaces considering support elements with given capacities. The coal burst hazard profile with a selected ground support system can then be quantitatively examined in various geological and geotechnical conditions.

REFERENCE

Cai, M and Kaiser, P, 2018. *Rockburst support reference book–volume I: rockburst phenomenon and support characteristics*, Laurentian University: Sudbury, Canada.

Heal, D, 2010. *Observations and analysis of incidences of rockburst damage in underground mines*, PhD Thesis, University of Western Australia.

Kaiser, P K and Cai, M, 2012. Design of rock support system under rockburst condition, *Journal of Rock Mechanics and Geotechnical Engineering*, 4(3):215–227.

Kaiser, P K, MacCreath, D R and Tannant, D D, 1996. *Canadian Rockburst Support Handbook*, Geomechanics Research Centre: Laurentian University, Sudbury, Ontario.

Potvin, Y and Hadjigeorgiou, J, 2020. *Ground Support for Underground Mines*, Australian Centre for Geomechanics: Perth.

Wei, C, Zhang, C, Canbulat, I, Song, Z and Dai, L, 2022. A review of investigations on ground support requirements in coal burst-prone mines, *International Journal of Coal Science and Technology*, 9(1):1–20.

Interdisciplinary

Fluid flow in discontinuous porous media with special reference to block caving of mines

M Vahab[1], A Jafari[2], P Broumand[3] and N Khalili[4]

1. Lecturer, UNSW Sydney, Kensington NSW 2052. Email: m.vahab@unsw.edu.au
2. PhD Candidate, UNSW Sydney, Kensington NSW 2052. Email: jafari@unsw.edu.au
3. Assistant Professor, Shiraz University, Shiraz, Iran. Email: pbroumand@shirazu.ac.ir
4. Scientia Professor, UNSW Sydney, Kensington NSW 2052. Email: n.khalili@unsw.edu.au

ABSTRACT

This paper presents the implementation of the eXtended Finite Element Method (XFEM) in the general-purpose commercial software package COMSOL Multiphysics for multi-field thermo-hydromechanical problems in discontinuous porous media. To this end, an exclusive enrichment strategy is proposed in compliance with the COMSOL modelling structure. COMSOL modules and physics interfaces are adopted to take account of the relevant physical processes involved in thermo-hydromechanical coupling analysis, namely: the mechanical deformation, fluid flow in porous media and heat transfer. The model preprocessing, level-set-updates, coupling of the relevant physics and postprocessing procedures are performed adopting a coherent utilisation of the COMSOL's built-in features along with the COMSOL's LiveLink for MATLAB functions. The capabilities and performance of the proposed approach are investigated by examining several multi-field thermo-hydro-mechanical simulations with reference to the block caving process in mines.

INTRODUCTION

The thermo-hydro-mechanical (THM) coupled processes due to fluid flow in deformable porous media, subject to natural discontinuities, has been a crucial area of interest for the prediction of the physical response in many engineering problems in geotechnics, mining, petroleum engineering, water resources, reservoir engineering and environmental engineering, to name a few (Khalili and Loret, 2001). Over the past decades, concurrent experimental, analytical and numerical efforts (see Zienkiewicz *et al,* 1999) were undertaken to develop predictive tools for the analysis of the role of discontinuities on the THM processes in deformable porous media (Gawin, Pesavento and Schrefler, 2006). With excellent inherent flexibility in tackling all types of discontinuities, computational superiority, and other algorithmic advantages (eg circumventing the need for remeshing, data transfer, and mesh refinement for high gradients), extended finite element method (XFEM) (Khoei *et al,* 2018; Vahab, Khoei and Khalili, 2019) has emerged as one of the most versatile tools for the study of discontinuities in deformable porous rock media. In this respect, XFEM has been extensively adopted for the development of hydro-mechanical (Jafari, Vahab and Khalili, 2021) and thermo-hydro-mechanical (Khoei and Bahmani, 2018) frameworks for the analysis of fluid flow within partially/fully saturated deformable porous media in the presence of discontinuities.

Block caving refers to a mass mining technique in which the extraction of ore depends largely on the action of gravity and *in situ* stresses (Mejia *et al,* 2022). Through fragmentation of a thin horizontal layer at the mining level of the ore column by means of hydro-fracturing, the vertical support of the ore above is removed, causing the ore to cave into the excavated void due to gravity (Van As and Jeffrey, 2000). Block caving is increasingly used worldwide as the mining technique of choice for the extraction of low-grade orebodies. Examples include: Northparkes mine (Australia), Palabora mine (South Africa), Questa mine (New Mexico), Henderson mine (Colorado) and Freeport mine (Indonesia), to name a few. Australia has, in particular, embraced block caving in several of the upcoming projects including: Olympic Dam copper-gold mine, Mount Keith nickel project, Telfer copper-gold mine, and Mount Lyell copper mine (Australian Mining, 2014).

In this work, underpinned by our recent developments on the implementation of XFEM for solid mechanics (Jafari, Vahab and Khalili, 2021), and by taking advantage of the exceptional flexibility of the COMSOL software in dealing with any arbitrary coupling processes, we present a thermo-hydro-mechanical framework for the XFEM analysis of fractures in deformable porous media. In this context, An exclusive XFEM framework for the study of THM coupling processes (see Figure 1) is proposed, which is compatible with the structure of COMSOL. The discontinuity interfaces are

tracked by means of level set functions introduced via external MATLAB functions, which accommodate the evolution of cracks prior to (ie at the preprocessing stage) and during the analysis. Moreover, by using internal functions and variables of the software, stress intensity factor calculation as well as numerical contact analysis are performed within the Multiphysics theme. The proposed framework enables robust and efficient tackling of block caving process with enhanced reliability in 3D settings.
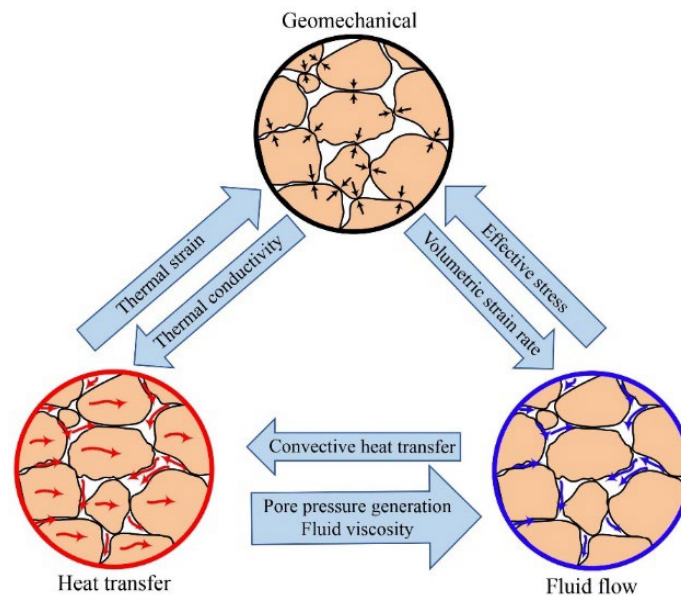
FIG 1 – Thermo-hydro-mechanical coupling flow chart.

IMPLEMENTATION IN COMSOL

COMSOL is a general-purpose multi-field program that renders sophisticated multiphysics modelling capabilities. In this software, a combination of available built-in physics interfaces can be incorporated in conjunction with user-defined physics to investigate formidable multiphysics problems (Jafari, Vahab and Khalili, 2021). The thermo-hydro-mechanical coupling analysis of fractured deformable porous media, considered here, involves three distinct physics that take account of the mechanical deformation, fluid flow and heat transfer. In COMSOL, the 'Solid Mechanics' physics interface facilitates the most general toolkit to perform continuum based structural analysis by solving the equations of motion endowed with suitable constitutive material behaviour (Jafari *et al*, 2022).

The fluid flow-through the porous domain can be simulated via the 'Porous Media and Subsurface Flow' module. In the case of low-velocity flows, which is commonly the case in geomechanics, the 'Darcy's Law' physics interface is employed to incorporate the flow-continuity equations within the porous medium. The 'Heat Transfer' module offers heat transfer analysis in the host domain. In this module, the 'Heat Transfer in Porous Media' physics interface is utilised to include the convection-diffusion equation through both solid matrix and pore fluid phases. Based on the XFEM approach, for which the theoretical background is presented in the previous section, one can circumvent the requirement of mesh alignment with the internal interfaces. Extending the recent work of the authors on the XFEM implementation of fracturing of solid formations in COMSOL, three distinct COMSOL interfaces are introduced, one for each of the physics involved (Jafari, Vahab and Khalili, 2021).

Several important features such as integration tools and analytical functions are inherently incorporated within COMSOL software. However, additional external functions are imperative to implement in order to successfully execute the various functionalities required for the XFEM simulation, such as the level-set analysis in the preprocessing stage. These additional functions/subroutines are developed in MATLAB and linked to the model through the COMSOL Live-link for MATLAB software extension.

FIG 2 – Three-dimensional thermo-hydro-mechanical simulation of a fault in porous media; problem geometry and boundary conditions.

(a)   (b)   (c)
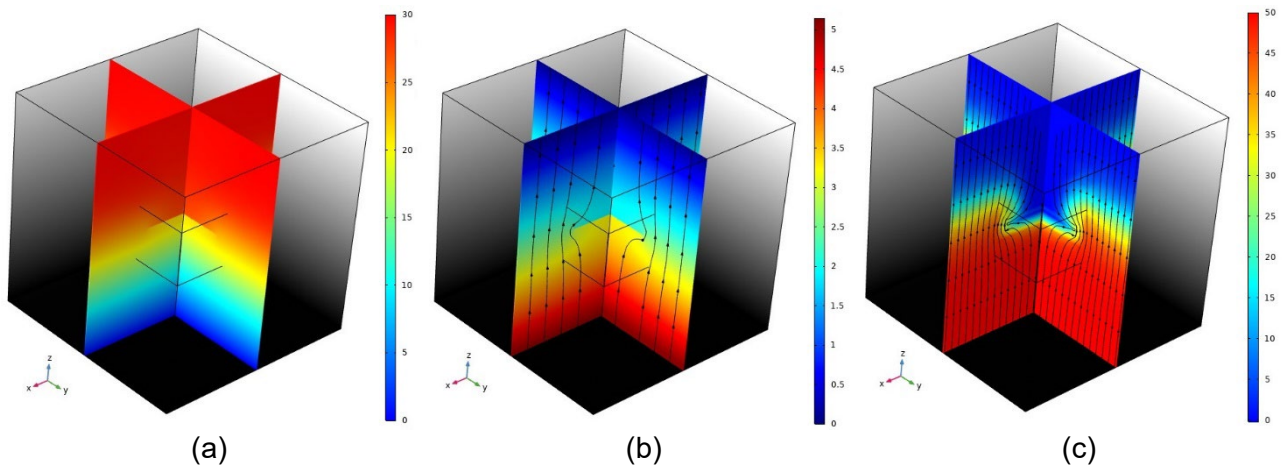
FIG 3 – 3D thermo-hydro-mechanical simulation results on two perpendicular planes; (a) distribution of vertical displacement u_z (mm), (b) pressure distribution (MPa) together with fluid flow streamlines, and (c) temperature distribution (°C) with heat flux streamlines.

NUMERICAL SIMULATION

Here an example is presented to show the application of the proposed thermo-hydro-mechanical XFEM framework to the study of three-dimensional problems in geomechanics. Suppose a cubic domain with a side length of 50 m that encompasses a penny-shaped impermeable discontinuity of diameter $2a_0$ = 20 m located at its centre. The problem definition and material properties of the bulk are given in Figure 2. The bottom surface is subjected to a prescribed temperature of 50°C and a constant inflow rate of 10^{-4} m/s, while both the pressure and temperature are assumed to vanish over the top surface (i.e, $p = 0$; $T = 0$). The remainder surfaces are undrained, with no fluid flow/heat flux. All faces of the domain are constrained in their corresponding normal directions, except the top surface, to emulate the *in situ* boundary conditions. The porous domain is discretised using 2312 brick elements, clustered in the vicinity of the internal discontinuity with an average element size of 1.5 m, in conjunction with 45 415 tetrahedral elements, elsewhere, that is simulated for the total duration of 3×10^5 s. Figure 3 illustrates the contours of vertical displacement u_z as well as pressure and temperature fields, over two cross-shaped planes perpendicular to the discontinuity. Clearly, the discontinuity induced by the penny-shaped inclusion can be observed in all three distribution contours. This is further elaborated by noting the flow and heat flux streamlines that are depicted in Figure 3b and 3c, where a diversion from the far-field vertical alignment can be observed adjacent to the discontinuity region. The promising results presented here showcase the flexibility of the implemented technique in dealing with intricate scenarios in the 3D thermo-hydro-mechanical analysis of porous media with discontinuities.

CONCLUSIONS

In this study, an XFEM implementation for modelling thermo-hydro-mechanical problems in COMSOL Multiphysics commercial software is presented. The framework is applied for multi-field fracture analysis in 3D settings. COMSOL's built-in features and external MATLAB functions are employed in the modelling procedures of preprocessing and level-set-updating, various coupling effects between the physics and postprocessing. Finally, a numerical simulation investigating the thermo-hydro-mechanical XFEM modelling of single discontinuities in 3D deformable porous media is presented. This, in turn, circumvents the comprehensive simulation of hydraulic fracturing preconditioning of mines. Showcasing the practicality of the inclusion of this process in practical applications in COMSOL Multiphysics is left to future studies.

REFERENCES

Australian Mining, 2014. The new building blocks of block mining, 21st February.

Gawin, D, Pesavento, F and Schrefler, B A, 2006. Hygro-thermo-chemo-mechanical modelling of concrete at early ages and beyond, Part I: hydration and hygro-thermal phenomena, *International Journal for Numerical Methods in Engineering*, 67(3):299–331.

Jafari, A, Broumand, P, Vahab, M and Khalili, N, 2022. An eXtended Finite Element Method Implementation in COMSOL Multiphysics: Solid Mechanics, *Finite Elements in Analysis and Design*, 202:103707.

Jafari, A, Vahab, M and Khalili, N, 2021. Fully coupled XFEM formulation for hydraulic fracturing simulation based on a generalized fluid leak-off model, *Computer Methods in Applied Mechanics and Engineering*, 373:113447.

Khalili, N and Loret, B, 2001. An elasto-plastic model for non-isothermal analysis of flow and deformation in unsaturated porous media: formulation, *International Journal of Solids and Structures*, 38(46–47):8305–8330.

Khoei, A R and Bahmani, B, 2018. Application of an enriched FEM technique in thermo-mechanical contact problems, *Computational Mechanics*, 62(5):1127–1154.

Khoei, A R, Vahab, M and Hirmand, M, 2018. An enriched–FEM technique for numerical simulation of interacting discontinuities in naturally fractured porous media, *Computer Methods in Applied Mechanics and Engineering*, 331:197–231.

Mejia, C, Azad, E, Roehl, D, Vallejos, J A and Rojas, E, 2022, August. Stress shadowing effects during hydraulic fracturing in block caving operations, *Proceedings Caving 2022: Fifth International Conference on Block and Sublevel Caving*, pp 1211–1226 (Australian Centre for Geomechanics: Perth).

Vahab, M, Khoei, A R and Khalili, N, 2019. An X-FEM technique in modeling hydro-fracture interaction with naturally-cemented faults, *Engineering Fracture Mechanics*, 212:269–290.

Van As, A and Jeffrey, R G, 2000, July. Caving induced by hydraulic fracturing at Northparkes mines, *4th North American Rock Mechanics Symposium*, OnePetro.

Zienkiewicz, O C, Chan, A H C, Pastor, M, Schrefler, B A and Shiomi, T, 1999. *Computational Geomechanics*, Chichester: Wiley.

Mine design – geotechnical considerations

Simulation of weathering impact on weak rock

H Zhai[1], K Yui[2], I Canbulat[3] and C Zhang[4]

1. Geotechnical Engineer, Evolution Mining, Bland NSW 2671.
   Email: hao.zhai@evolutionmining.com
2. Master Student, UNSW, Randwick NSW 1466. Email: z5087167@student.unsw.edu.au
3. Head of School, UNSW, Randwick NSW 1466. Email: i.canbulat@unsw.edu.au
4. Senior Lecturer, UNSW, Randwick NSW 1466. Email: chengguo.zhang@unsw.edu.au

ABSTRACT

Sedimentary rock is a lithology that is commonly encountered in mining practices. Their properties, especially the resistance against weathering, are often of critical importance to long-term engineering stability due to their ubiquitous existence on the earth's crust. The weathering of rocks is a complex process that involves physical degradation, chemical and biological erosions. In this study, the impact of physical weathering on four common sedimentary rocks, namely sandstone, siltstone, limestone and shale, are simulated in the laboratoryoratory environment taking into consideration the impact of preservation condition, temperature and time. In order to optimise the design of the experiment, Taguchi's design of experiment method is implemented based on the L16 orthogonal array and selected simulation conditions. The weight and dimension variation, fracture intensity, slake durability, and uniaxial strengths of specimens are then tested to quantify the impact of weathering under various conditions.

The results indicate that weathering significantly influences the strength of shale, siltstone and limestone but not sandstone. The impact of weathering on dimension variation is insignificant. For soft rocks, most physical weathering took place after second cycle of simulation, resulting in strength reduction up to 100 per cent (disintegration) but generally in a range from 28 per cent to 32 per cent. Additionally, time is the most important factor contributing to the physical weathering of weak rocks, followed by residual, preservation conditions and temperature. Last but not least, some shales, depending on the content of clay minerals, tend to develop significant fracturing or even disintegrate under the influence of weathering.

INTRODUCTION

The sedimentary rock is a lithology that is commonly encountered in mining practices. Acting as the weakest link in the rock mass, some soft sedimentary rocks have triggered or contributed to many instabilities in both open pit and underground workings, along with other critical factors such as water content, slope angle, mining practices, ground support, time etc. This study has been undertaken to further the understanding of the weak rock mass behaviour under the influence of repetitive water content and temperature changes and to aid the design of long-term stability for both slopes and underground workings.

From the engineering point of view, the weak rock mass is often defined based on physical properties such as rock mass with low inherent strength (eg R0-R2 according to ISRM, 2015) or high joint intensity (eg RQD <25 per cent). However, a definition based on the lithological origin helps understand why some rock mass degrades faster than others. Such a definition is provided by Santi (2006):

- Materials with high clay content, such as over-consolidated clays, cemented clay, shales, marls, and flysch.

- Young materials, such as Quaternary carbonates, Tertiary sediments, and Tertiary volcanic.

- Highly weathered materials, such as saprolites and weathered igneous and metamorphic rock.

- Metamorphosed materials, such as melange and metashale.

- Hardened soils, such as hardpan, caliche, and tropical duracrusts.

Regardless of whether a rock mass is 'born weak' due to a low degree of lithification or 'altered weak' as a result of weathering and/or technic disturbance, all weak rock masses can be subject to further

weathering once exposed by excavation. According to Watters (1995), weathering effect is a result of the alteration and breakdown of the rock mass by physical, chemical and biotic means near the earth's surface. All three processes commonly act together, though the individual contribution varies based on the climatic conditions and the distance to the excavation surface. In order to reduce the complexity, this study focused on the impact of physical weathering.

The physical breakdown of rock material generally characterises physical weathering into progressively smaller fragments without marked changes in the nature of the mineral content (Ollier, 1984; Selby, 1993). This degradation process produces an unaltered residual material with reduced physical properties. The main processes by which physical weathering occurs include differential thermal expansion and insulation, wet-dry expansion, freeze-thaw action, and crystallisation expansion. The latter two are rarely encountered in Australia and therefore are not considered in this study. While the first two factors can be considered as the impact of local temperature change and annual precipitation, in other words, the impact of temperature and water content.

A large number of tests still hinders the implementation of this study as a result of the combination of different factors and necessary repetition. In order to further reduce the complexity of this study, the design of experiment method developed by Taguchi and Konishi (1987) was adopted. With this method, the impact of temperature, water content, and the number of repetitions on four different rocks are captured with only 16 specimens. Compare to some other commonly used statistical methods (eg Response Surface Method); this method focuses on simplifying the experiment complexity rather than investigating the interaction of different factors.

METHODOLOGY

Design of experiment

The design of the experiment is undertaken following the methodology developed by Taguchi and Konishi (1987). This methodology comprises two steps: (1) selection of an orthogonal array (OA) to establish the experimental requirements and (2) performing analysis of variance (ANOVA) for test result analysis. An orthogonal array is a special matrix. In an OA, each factor and level should appear the same number of times, and the influence of each element and level is balanced. The selection of an orthogonal array is based on the required number of elements and levels defined by the scope. For this study, an L16 array is selected based on four factors and up to four levels as shown in Table 1.

TABLE 1

Selected factors and levels.

Factor	Rock type	Preserve condition	Temperature situation	Cycle times
Level 1	Limestone	Wet	50°C	0 cycles
Level 2	Siltstone			2 cycles
Level 3	Sandstone	Dried	20°C	4 cycles
Level 4	Shale			8 cycles

Four rock types (levels), namely Gambier Limestone, Hawkesbury Sandstone, siltstone and shale (supplied by Austral brick), are sourced from local quarries as the test material for this study. Specimens were drilled and cut from rock blocks and kept in two conditions (levels), wet conditions or oven dried (105°C), before the test to simulate the rainy and arid weather in the natural environment. Although the natural temperature in Australia varies in an extensive range from subzero to close to 50°C, the room temperature of the laboratory (20°C) and 50°C in a temperature-controlled oven are used to simulate the mild and extreme temperature conditions. The exposure time is also a contributing factor to the degree of weathering. In this study, the concept of cycles is defined as the number of fully saturated and dried repetitions a specimen has undergone. The number of cycles is used to account for the impact of time. The final L16 OA developed based on the selected factor is shown in Table 2.

TABLE 2

L16 OA adopted based on the selected factors and levels.

Reference	Rock type	Preserve condition	Temperature situation	Time
1	Limestone	Wet	50°C	0 cycles
2	Limestone	Wet	20°C	4 cycles
3	Limestone	Dried	20°C	2 cycles
4	Limestone	Dried	50°C	8 cycles
5	Siltstone	Dried	50°C	0 cycles
6	Siltstone	Wet	50°C	8 cycles
7	Siltstone	Dried	20°C	4 cycles
8	Siltstone	Wet	20°C	2 cycles
9	Sandstone	Wet	50°C	2 cycles
10	Sandstone	Wet	20°C	8 cycles
11	Sandstone	Dried	20°C	0 cycles
12	Sandstone	Dried	50°C	4 cycles
13	Shale	Wet	20°C	0 cycles
14	Shale	Wet	50°C	4 cycles
15	Shale	Dried	20°C	8 cycles
16	Shale	Dried	50°C	2 cycles

The experiment's output needs to be grouped to analyse the influence of each factor. For a factor, the average performance of one level can be calculated as follows.

$$\overline{A_k} = \frac{\sum_{i=1}^{n} Y_i}{n} \tag{1}$$

where $\overline{A_k}$ is the average performance of factor A at level k, n is the total number of responses at level k, and Y_i is the i th response at level k.

The significance and contribution of each factor can be quantified using ANOVA which is widely availaboratoryle in many software, including Microsoft Excel, Matlaboratory and R Studio. For this study, all analysis work was undertaken with R Studio.

Specimen preparation and simulation

All specimens were prepared in accordance with the ISRM standard (2015) with an average diameter of 41 mm and an aspect ratio of 2 as shown in Figure 1. It is worth noting that siltstone and shale can be mechanically damaged during the sample preparation stage and are potentially subject to sampling bias.

The following standard stimulation process was followed and repeated until the required number of cycles was reached.

1. Place specimen in the 50°C oven or shaded area of the laboratory (approximately 20°C) for 24 hrs depending on the required temperature condition of each test.

2. Take the specimens out of the oven and allow them to cool down for 1 hr.

3. Fully submerge specimens in a bucket of water (approximately 18°C) or place specimens in the shared area of the laboratory, depending on the required moisture content.

4. Repeat steps 1–3 until the required number of cycles is reached.

5. Perform laboratoryoratory tests to determine the physical properties of weak rocks.
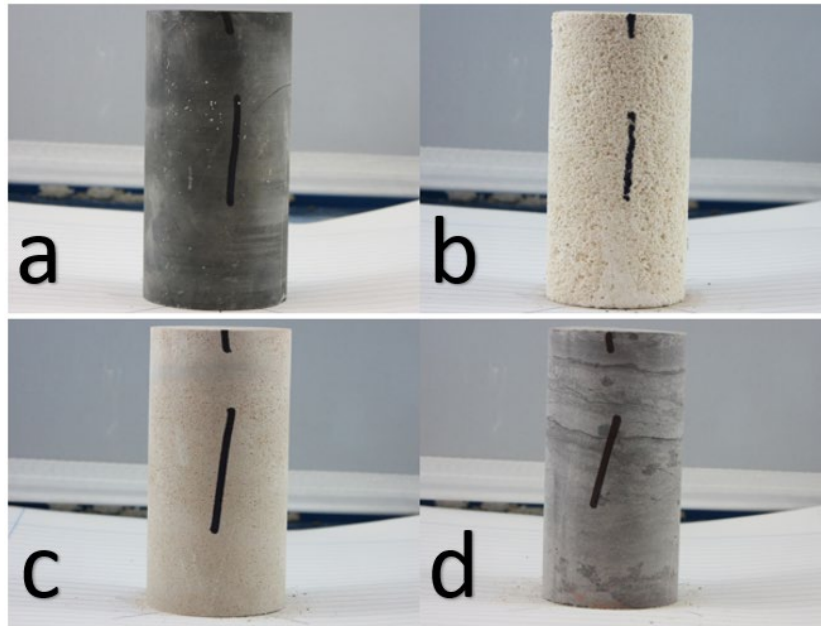
FIG 1 – Mudstone (a), limestone (b), sandstone (c) and shale (d) specimens.

Laboratory tests

A number of measurements and laboratoryoratory tests were performed to determine the physical properties of each specimen after weathering simulation. The detail of each measure and test are elaborated in the following subsections.

Weight and geometry

The weight and geometry of each specimen are measured before and after the required number of simulation cycles to determine the weight loss, a metric of weathering propensity and potential swelling.

The weight of the specimen was measured with a digital scale. The diameter and height of the specimens were measured three times with a digital calliper as recommended by ISRM (2015).

Uniaxial compressive strength

The standard uniaxial compression strength (UCS) tests were performed on the strength of specimens before and after weathering simulation following the ISRM (2015) recommended testing procedure. All UCS tests were performed on an MTS 815 test platform (shown in Figure 2).

The UCS of specimens were calculated with the following equation.

$$\sigma = \frac{P}{A_0} \tag{2}$$

Where σ is the UCS, P is the peak force, and A_0 is the average correctional area.
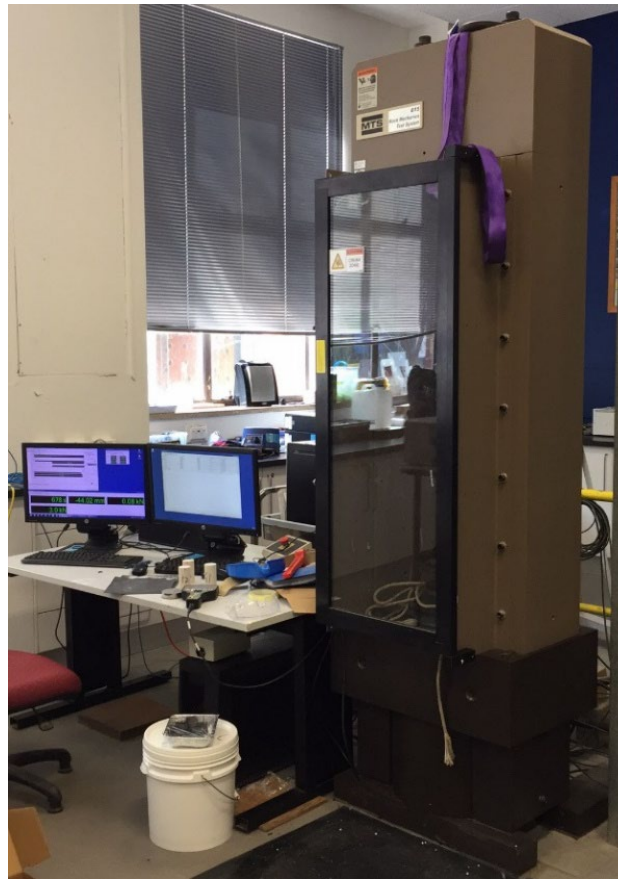
FIG 2 – MTS 815 test platform.

Fracture intensity

In addition to the mechanical tests, a photographic method was also used to measure the fracture intensity initiated by weathering simulation. This measurement was only performed on shale as there were no visible fractures on other weak rock specimens. Eight additional shale specimens were weather stimulated for this measurement.

According to Multi-Dimensional System of Fracture Abundance Measures, the fracture intensity in a 2D space (surface) can be defined as follows (Mauldon and Dershowitz, 2000).

$$P21 = \frac{Length\ of\ fracture\ traces}{Area\ of\ exposure} \tag{3}$$

After every weathering simulation cycle, the cylinder shale specimens were photographed from four angles at 90° intervals (Figure 3a). These four photos are then mosaiced with Adobe Photoshop to provide a panoramic view of the specimen (Figure 3b). The total length of all fracture traces in the panoramic photos is then measured using ImageJ.

(a)   (b)
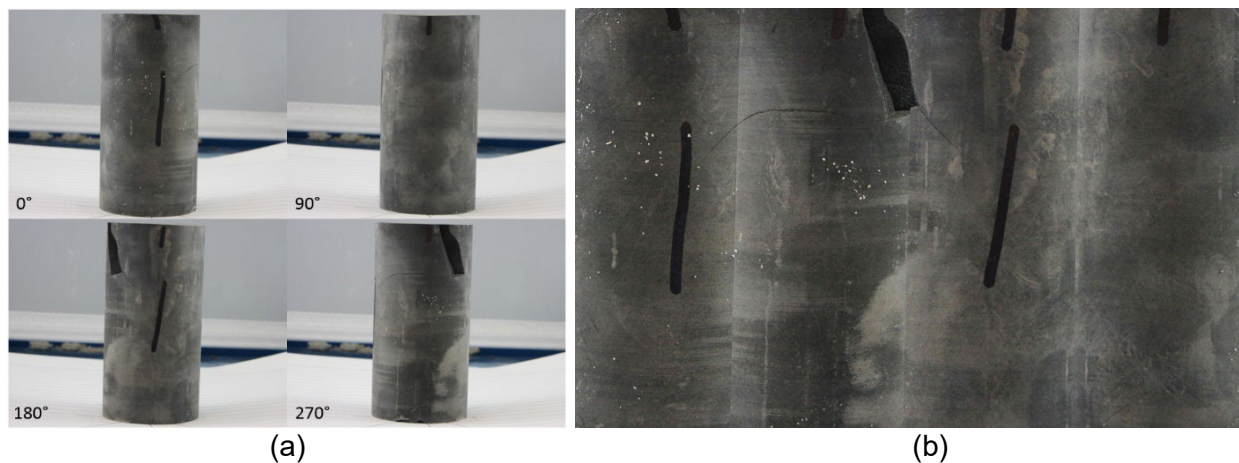
FIG 3 – (a) Shale specimen photographed from four different angles and (b) final mosaic.

RESULTS AND ANALYSIS

The entire test was completed in four weeks. Two simulation cycles were performed on specimens following the prescribed conditions (Table 1). The results were presented and discussed in the following subsections.

Weight and geometry variation

The weight and diameter variations of all 16 specimens are presented in Figures 4 and 5. The impact of physical weathering simulation is negligible to both the weight and diameter of all specimens. The actual weight and diameter vary in a small range from 1 per cent to 2 per cent. It is worth noting that Cycle 6 and 8 shale samples disintegrated in the simulation process resulting in no measurements.
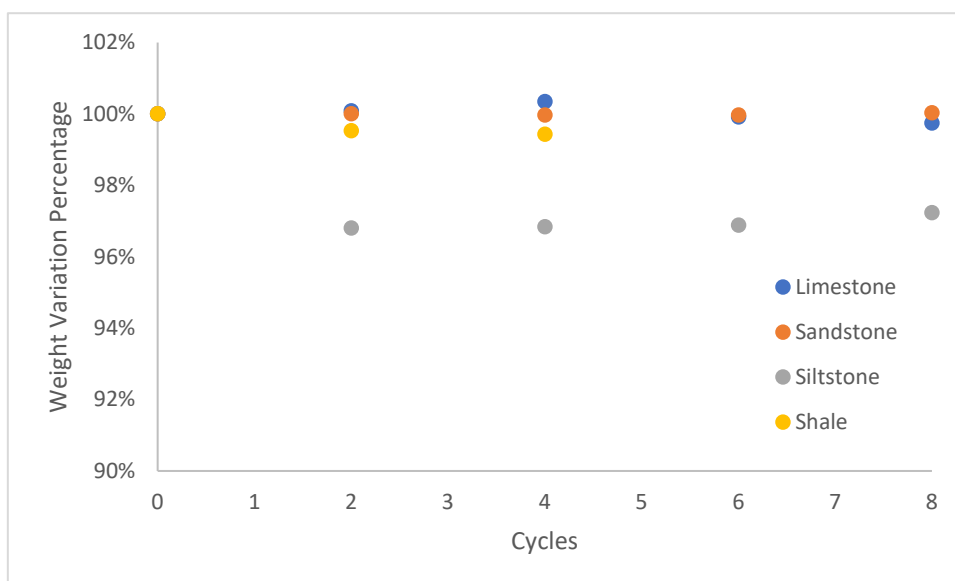

FIG 4 – Weathering simulation-related weight variation.
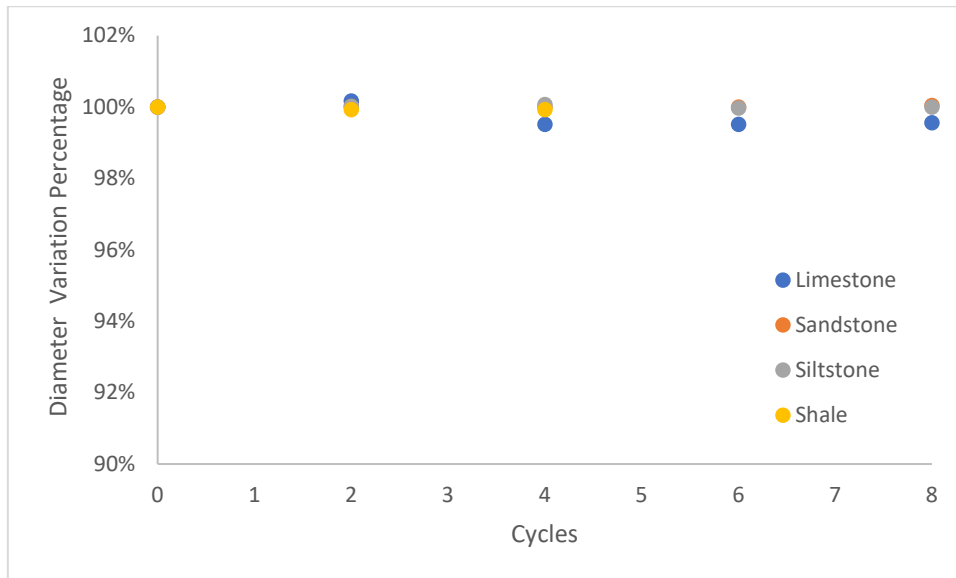
**FIG 5 –** Weathering simulation-related diameter variation.

Uniaxial compressive strength

The UCS of the specimen is a direct measurement of weathering-induced degradation. From the lithology point of view, the UCS of all four tested rock types decreased as the number of weather simulation cycles increased as shown in Figure 6. Compared to the sandstone with an average strength of 171 MPa, the influence of weathering on softer rocks, including limestone, shale, and siltstone is more significant, especially after the four simulation cycles. After eight simulation cycles, the final strength degradation varies from 9 per cent for sandstone to 100 per cent for shale (disintegrated after four cycles) but generally between 28 per cent to 32 per cent for the other two rock types. The UCS of the second cycle sandstone specimen was 124 MPa which was lower than the general strength range. The inspection of the specimen after the test reveals that the failure occurred on a natural defect (vein) and is invalid. This isolated test does not affect this general trend between sandstone and the number of weathering simulation cycles.
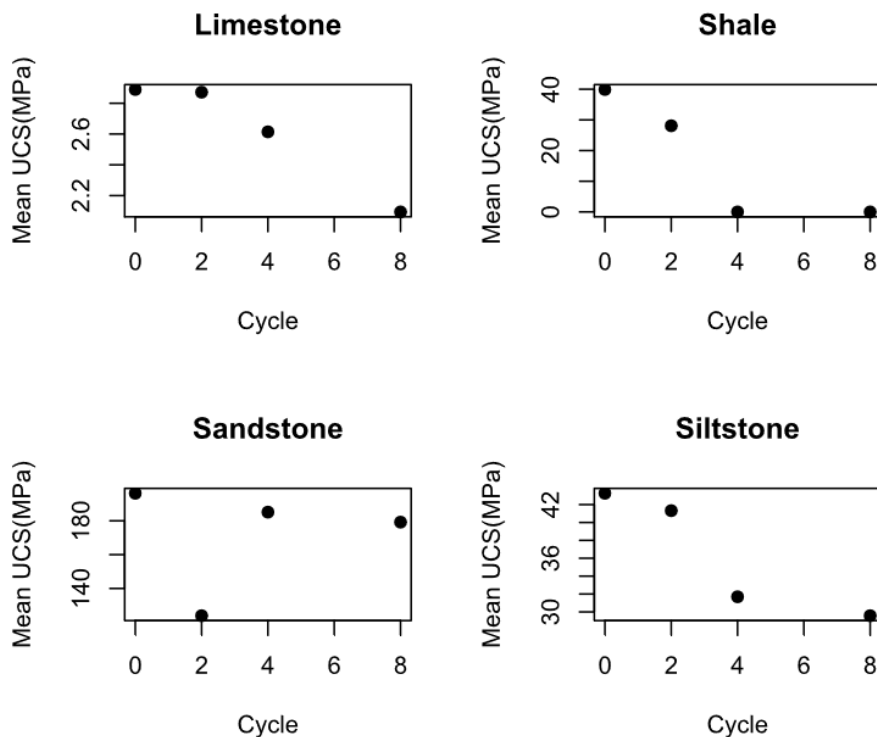
**FIG 6 –** Influence of weathering simulation on UCS of limestone, shale, sandstone and siltstone.

The influence of the other three controlled factors, namely preserve conditions, drying temperatures and number of cycles, on the UCS are shown in Figure 7. In terms of preserving conditions, the average UCS of oven-dried specimens is 5 MPa lower than the wet preserved contoured parts. Clay-rich rocks, including shale and siltstones, are known to be reactive to water and are the main contributor to this difference. The difference induced by different drying temperatures is insignificant. This finding suggests that the temperature variation within the normal range is unlikely to trigger/accelerate the weathering. However, temperature variation in the more extensive range may induce some additional mechanisms such as freeze and thaw, thermal expansion and contraction. Among all controlled factors, the number of cycles has been identified as the most significant factor in weathering. On average, the residual strength after eight cycles of weathering simulation is approximately 37 per cent of the original strength, and most strength reduction occurred after two cycles. The shale and siltstone influence this outcome, and the level of reduction may vary for other lithologies. It is also noted that sandstone is significantly stronger than the other three and is considered a reference lithology to moderate to high-strength rocks.
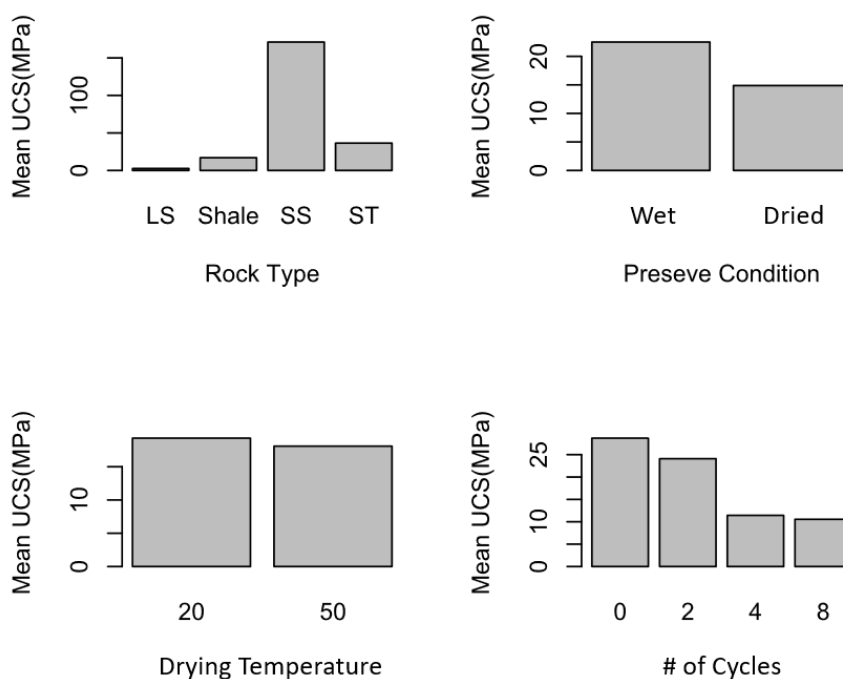
FIG 7 – Influence of rock type, moisture content, drying temperature, and the number of cycles in the weathering simulation.

Fracture intensity

The relationship between fracture intensity and the number of simulation cycles for four additional shale specimens is shown in Figure 8. Out of four specimens, only two survived eight weathering simulation cycles. The other two disintegrated on cycles four and six, similar to the shale specimens prepared for the UCS test. The general trend of fracture intensity increases with the number of simulation cycles from less than 0.1 mm/mm^3 to over 0.3 mm/mm^3. Higher increments have been found in both premature specimens. Interestingly, the inflection points of fracture intensity to the number of simulation cycles are 2 to 3, which aligns with the UCS to the number of simulation cycle relationships for shale, siltstone and limestone.
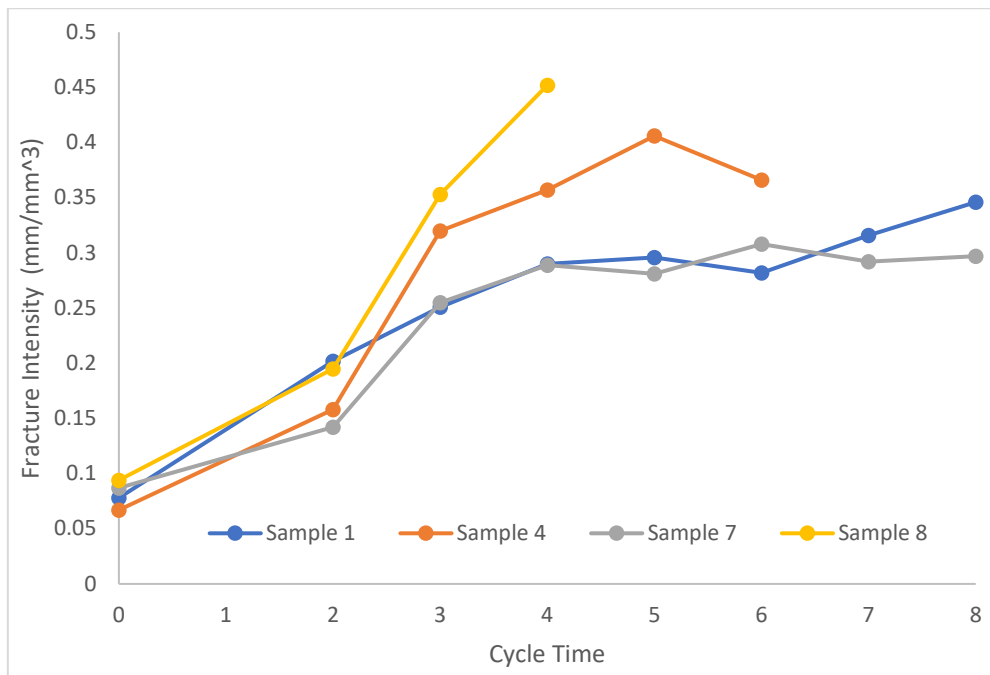
FIG 8 – Fracture intensity of four shale specimens.

ANOVA

ANOVA was undertaken to quantify the contribution of each factor and the result is presented in Table 3. The weighted contribution is the percentage of variances associated with each factor and is used to measure and compare the contribution of each factor. It is evident that the rock type (62.8 per cent) is the most influential factor, which dictates the behaviour/strength of the rock mass. Followed by the number of cycles (20.2 per cent), residual (12.1 per cent), preserve conditions (4.7 per cent) and drying temperature (0.1 per cent). This contribution weighting is in line with the test result and the general field experience. It is noted that the residual is rated as the third most important factor and it can be interpreted as the combination of inherent variances of rock mass and other uncontrolled factors, including chemical weathering. This study is limited to sedimentary rocks and the contribution of each factor may change for other lithologies.

TABLE 3

ANOVA analysis of the test result.

Parameters	Sum of squares	Degree of freedom	Mean square	Weighted contribution (%)
Model	3674.7	11	334.1	100
Rock type	2308.3	2	1154.1	62.8
Preserve condition	174.3	1	174.3	4.7
Drying temperature	4.3	1	4.4	0.1
Number of cycle	744.0	3	248.0	20.2
Residual	443.9	8	186.0	12.1

RESULTS AND ANALYSIS

This study is undertaken to simulate the influence of physical weathering on three soft sediment rocks, including siltstone, limestone and shale, and hard sandstone. The impact of the number of cycles, temperature and preservation conditions are simulated in this study. In order to optimise the design of the experiment, the Taguchi design of the experiment method is implemented based on the L16 orthogonal array. The weight and geometry

variation, fracture intensity and UCS of specimens are then tested to quantify the impact of weathering under various conditions.

The results indicate that weathering significantly influences the strength of shale, siltstone and limestone but not sandstone. The impact of weathering on dimension variation is insignificant. For soft rocks, most physical weathering took place after second cycle of simulation resulting in strength reduction up to 100 per cent (disintegration) but in a general range from 28 per cent to 32 per cent. Additionally, time is the most important factor that contributes to the physical weathering of weak rocks followed by residual, preservation conditions and temperature. Last but not least, some shales, depending on the content of clay minerals, tend to develop significant fracturing or even disintegrate under the influence of weathering.

ACKNOWLEDGEMENTS

REFERENCES

ISRM, 2015. *The ISRM suggested methods for rock characterisation, testing and monitoring: 2007–2014,* R Ulusay (ed.).

Mauldon, M and Dershowitz, W, 2000. A multi-dimensional system of fracture abundance measures, *Geological Society of America Abstracts with Programs*, 32(7):474.

Ollier, C D, 1984. *Weathering*, American Elsevier, New York, 304 p.

Santi, P M, 2006. Field methods for characterising weak rock for engineering, *Environmental and Engineering Geoscience*, 12(1):1–11.

Selby, M J, 1993. *Hillslope materials and Processes,* Oxford University Press.

Taguchi, G and Konishi, S, 1987. Taguchi methods orthogonal arrays and linear graphs: tools for quality engineering, American Supplier Institute.

Watters, R J, 1995. The effects of weathering on Rock Mass, Department of Geological Science, University of Nevada-Reno.

Rock mass characterisation techniques and practice

Formation of fracture zones under static and impact loading conditions and their characteristics

*Ö Aydan[1], S Kodate[2], J Tomiyama[3] and Y Suda[4]*

1. Emeritus Professor, University of the Ryukyus, Okinawa, Japan.
   Email: aydan@tec.u-ryukyu.ac.jp
2. Chubu Engineering Consultants Co. Ltd., Hiroshima, Japan.
   Email: shinya.koudate@cecnet.co.jp
3. Professor, University of the Ryukyus, Okinawa, Japan. Email: jun-t@tec.u-ryukyu.ac.jp
4. Associate Professor, University of the Ryukyus, Okinawa, Japan.
   Email: ysuda@tec.u-ryukyu.ac.jp

ABSTRACT

Fracture zones are commonly found in the Earth's crust. These zones may cause very severe engineering problems. Therefore, the formation and the assessment of the mechanical characteristics of these zones is of great concern for rock engineers. A new double shearing jig was used to study the formation of shear zones in rock under static and impact loading conditions using the device developed by the authors. A series of experiments were undertaken to investigate formation on the formation and characteristics of fracture zones in laboratory. Although actual fracture zones are more complicated, various tests give some insight view of the formation of fracture zones as well as some information on their mechanical behaviour under both dynamic conditions and static conditions. The authors report the outcomes of these experiments and discuss their implications in practice.

INTRODUCTION

Fault/shear zones are commonly found in the Earth's crust. These zones may cause very severe engineering problems such as heavy water inflow, squeezing, instability and they may be pathways for leakage of radio-active wastes to the environment. Therefore, the formation and the assessment of the hydro-mechanical and mechanical characteristics of these zones is of great concern for rock engineers. As well known, the fault/shear zones consist of intact rock blocks bounded by discontinuities with or without gouges and the intensity of fracturing in adjacent rock differs depending upon the amount of relative slip (Figure 1).

(a)   (b)   (c)
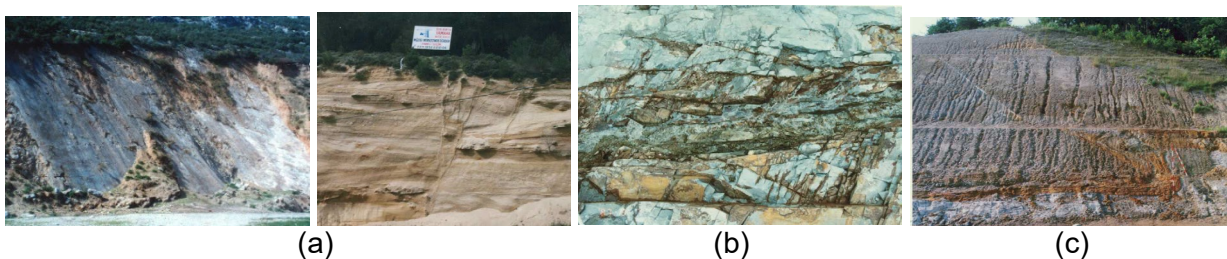
FIG 1 – Some examples of fault/shear zones in rock: (a) Normal fault (Efes, Mudanya); (b) Strik-slip (Okumino); (c) Thrust fault (Miyoshi).

In this study, the results of an experimental programs undertaken on the formation as well as mechanical and frictional characteristics of fault/shear zones are presented. The experimental program involves laboratory double shearing tests under both static and dynamic conditions. Although actual fracture zones are more complicated, various tests give some insight view of the formation of fracture zones as well as some information on their mechanical behaviour under both dynamic conditions and static conditions. The authors report the outcomes of these experiments and discuss their implications in practice.

EXPERIMENTAL SHEARING DEVICE AND SAMPLES

Double shear jig and samples

Double shearing device shown in Figure 2a was developed. The pre-designated normal load on the shear plane up to 10 kN can be applied and the normal load can be continuously monitored throughout static and dynamic tests. This enables us to obtain the cohesion or adhesion and friction angle of shear plane. The sample length is 100 mm or longer and the area of shearing can be up to 30 mm by 30 mm. The central part of the sample is 40 mm long. The both side of the sample, which is 30 mm or longer, is fixed by platens. The shearing force is applied onto the central part of the sample. The samples can be intact rock, containing two discontinuities parallel to shearing direction, and interface between grouting material and rock or steel, which can be useful for evaluating adhesion between grouting material and adjacent material such as rock or steel.
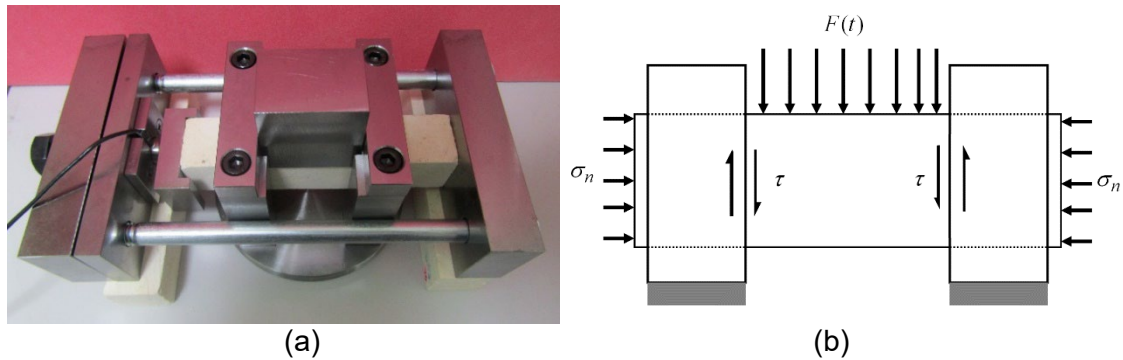

(a)   (b)

FIG 2 – Double-shearing jig (a) and an illustration of a sample subjected to double shearing (b).

Static and impact loading devices

Aydan *et al* (2019) developed an impact loading device as shown in Figure 3a. The nominal impact shearing velocity can be changed between 1401 and 3132 mm/s. Besides loading, strain of samples, the acceleration induced by impact loading can be measured using a sampling rate in the order of a nano-second. In most of the experiments, the sampling rate was fixed to 5 microseconds. The monitoring was done by using YOKOGAWA SL-1000 data acquisition system and recorded on to computers during impact tests.
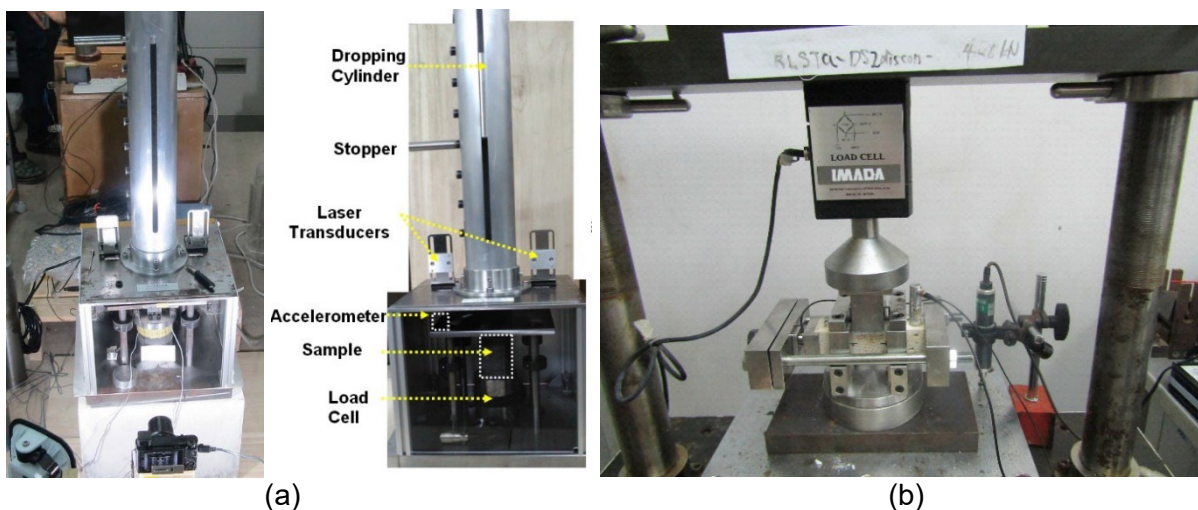

(a)   (b)

FIG 3 – Views of (a) impact shearing loading device and (b) static shearing loading device.

Static double shearing device with a capacity of 20 kN and adjustable displacement-controlled system was used. During static experiments, applied load, displacement, strain and acoustic emissions were measured simultaneously using YOKOGAWA SL-1000 data acquisition system and recorded on to computers.

DOUBLE SHEAR TESTS

Post-failure states of samples of coral Ryukyu limestone and Oya tuff subjected to impact loading are shown in Figure 4a while Figure 4b shows the post-failure states of intact and saw-cut discontinuities of sandy Ryukyu limestone (locally known as Awa-ishi) subjected to static loading. As noted from the figures, a fracture zone develops along the projected shearing planes. It is noted that the impact loading results in a much wider fracture zone as compared with that caused by static loading. This observation was also observed in uniaxial and Brazilian tensile testing (Aydan *et al* 2014a, 2014b). A new double shearing jig shown in Figure 2a was used to study the formation of shear zones in rock under static and impact loading conditions using the device developed by Aydan *et al* (2019). Figure 5 shows the shear zone formation in some rocks.
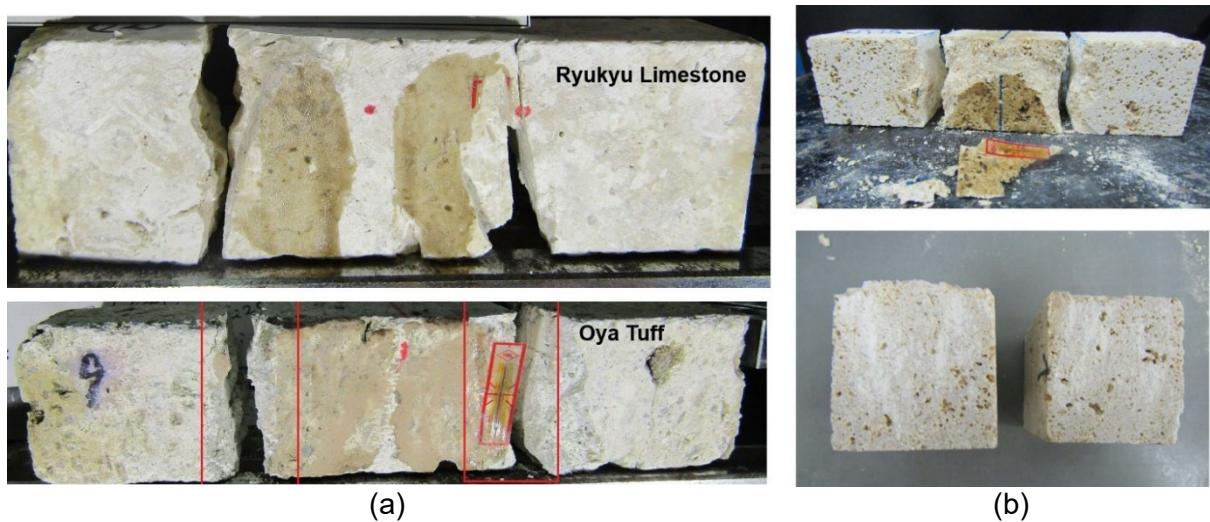
FIG 4 – Experimental set-up for double shear tests of tuff and coral limestone; impact loading (a); and sheared intact rock and saw-cut planes of sandy limestone; static loading (Awa-ishi) (b).
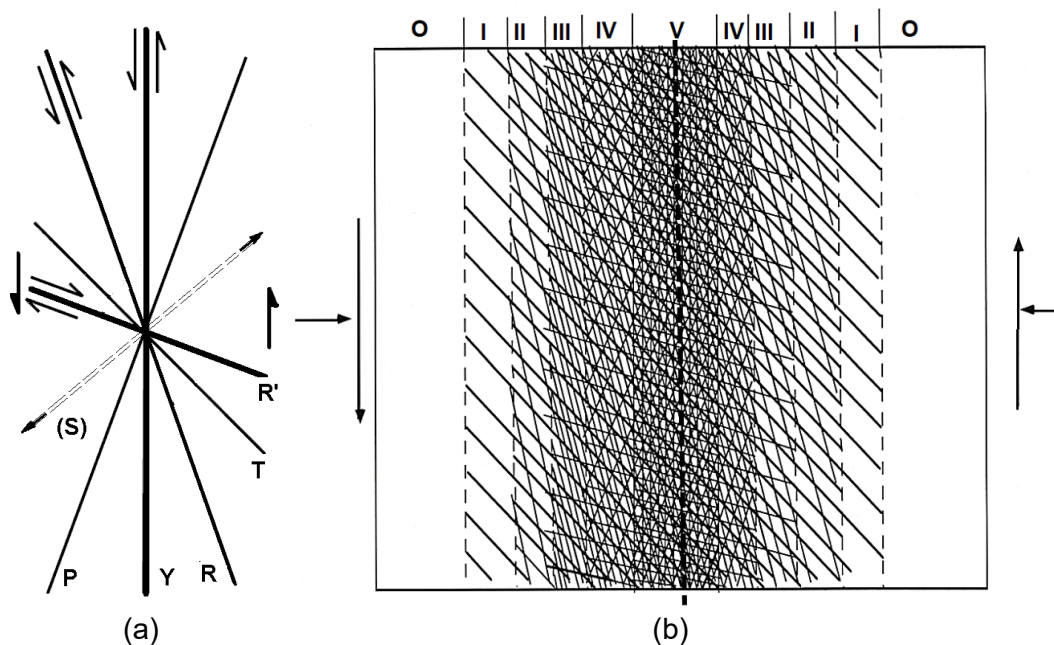
FIG 5 – Idealised fractures, and zones with different intensity of fracturing.

FRACTURES IN FRACTURE ZONES

The formation of the fracture systems within the shear zone under static and dynamic conditions resemble to each other while the thickness of the shear zone is larger under dynamic conditions. Fractures shown in Figure 5c are denoted by T, R, R', P, Y or D and S are interpreted as tension,

Riedel, Skempton and master shear fractures and cleavage. T (tension) fracture first occur in such zones and it is aligned parallel to the maximum compressive stress within the fracture zones. This fracture may be suppressed and R fracture inclined at angle of $\phi/2$ (ϕ: friction angle) occurs if normal compressive stress is high. Then fractures R' later P develop in order to accommodate deformation in the fracture/shear zone. Finally, relative slip is accommodated by the master shear fracture Y or D. R' fracture is inclined at angle of $90 - \phi/2$ to the shearing direction. All of the above fractures may not be observed in every fracture zone. Sometimes, they may be complementary of each other in relation to the amount. Depending upon the amount of relative slip, within a fault/shear zone it is likely to observe six different zones (0–V) as shown in Figure 5b:

- Zone 0: No fractures.

- Zone I: T fractures only.

- Zone II: T-R fractures.

- Zone III: T-R-R' fractures.

- Zone IV: T-R-R'-P fractures.

- Zone V: T-R-R'-P-Y(or D) fractures with gouge.

Within Zone V, almost all fractures would be observed together with gouges of different thickness depending upon the relative slip.

CHARACTERISATION OF FRACTURE ZONES

The characterisation of fault/shear zones is very important aspect in rock engineering and the methods may be different depending upon the purpose of the engineering works. Their mechanical behaviour may be important in many engineering problems while the seepage and diffusion characteristics could be quite important in nuclear waste disposal projects. In this section, the applicability of rock classifications and Needle Penetration Index (MPI) to characterise the fracture zones are given.

Applicability of needle penetration index (NPI)

Aydan *et al* (2014a) utilised the needle penetration tests at several fault/shear zones as shown in Figure 7. Figure 7 shows the variation of NPI at three different fault zones. As noted from the figure, the NPI values decrease drastically and it has a minimum value in the gouge zone of the faults. NPI values at such locations are around 0.5 and 1. Furthermore, NPI is generally lower on the hanging wall or mobile side of the fault. When adjacent rock is relatively hard, the utilisation of the NPI together with Schmidt hammer technique may be more practical for the characterisation of fault/fracture zones.

Applicability of rock mass classifications

The rock mass classifications addressing the fault/shear zones could be Q-system (Barton *et al,* 1974), Rock Mass Rating (RMR) (Bieniawski, 1989) and Rock Mass Quality Rating (RMQR) (Aydan *et al,* 2014b). The fault/shear zones depicted in Figure 5b may be rated according to rock mass classification systems may be as given in Table 1. Although these values may change depending upon actual circumstances, they may be some guidelines for engineering purposes. The zones IV and V may be interpreted as fault core while the zones I, II and III are interpreted a damage zone in a broad description of fracture/shear zones (Scholz *et al,* 1993).
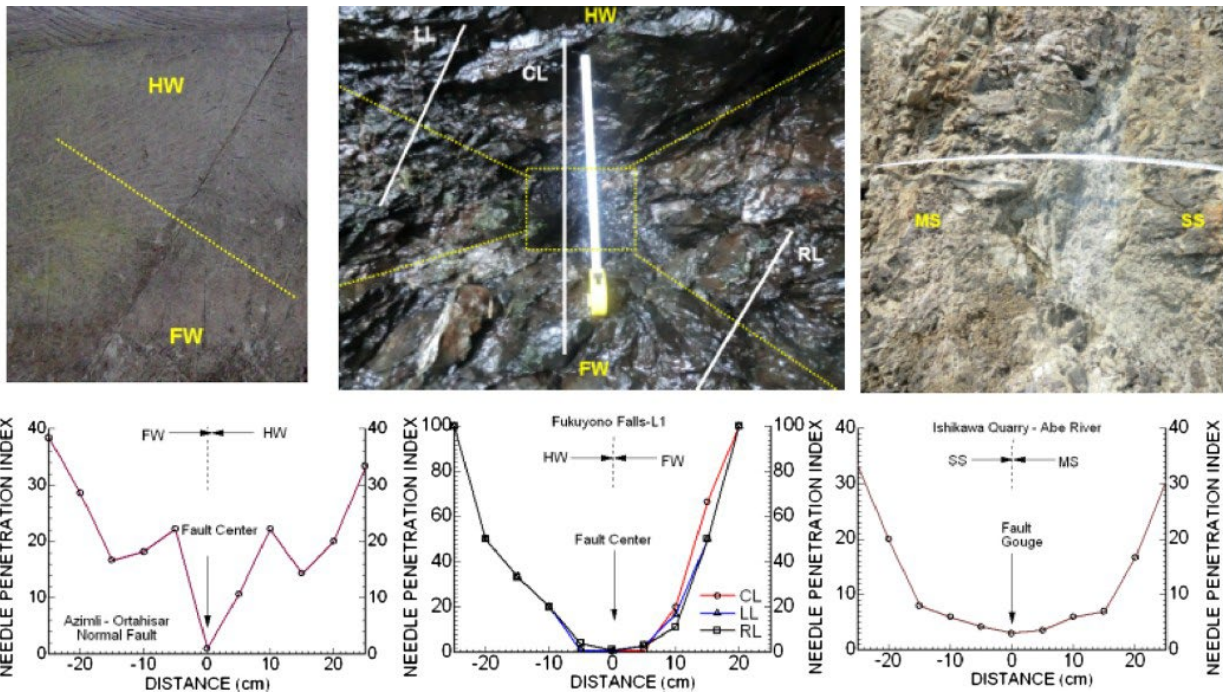
FIG 6 – Views of faults and measured NPI values with distance from the centre of the fault (NF normal fault, TF thrust fault, SSF strike-slip fault, HW hanging wall, FW footwall, MS mobile side, SS stationary side) (from Aydan *et al*, 2014a).
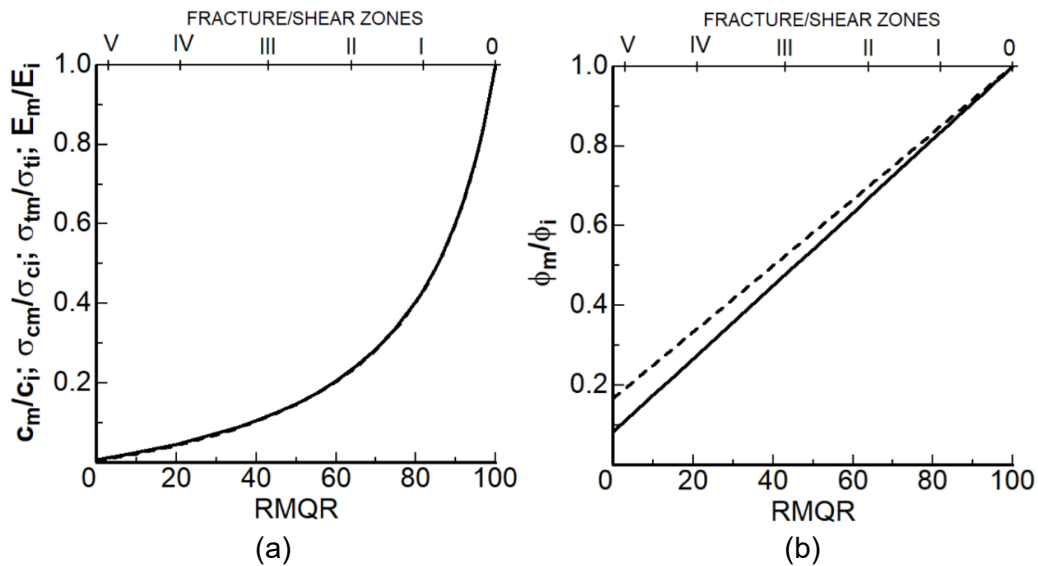
ESTIMATION OF PROPERTIES OF FRACTURE ZONES

Aydan *et al* (2014b) proposed the following empirical formula to estimate the mechanical properties (α) of rock mass normalised by those of intact rock.

$$\alpha = \alpha_0 - (\alpha_0 - \alpha_{100}) \frac{RMQR}{RMQR + \beta(100 - RMQR)}$$

(1)

Where α_0, α_{100} and β are empirical constants.

The values of these parameters are given in Table 4. When this equation is applied to fracture/shear zones, the properties of gouge may be utilised. Aydan *et al* (2022) reported some experimental results on the model and actual fault gouges. For example, Aydan *et al* (2022) reports the ratio of uniaxial compressive strength of fault gouge in shale to that of intact rock was ranges between 1/150 and 1/250. On the other hand, the friction angle of fault gouges may be reduced to 6 and 10 degrees and the ratio of the friction angle of fault gouges to that of intact rock could be 1/6 and 1/12. Figure 7 shows some estimations of normalised mechanical properties of fracture/shear zones for six different zones shown in Figure 5 using Tables 1 and 2 and Equation 1.

FIG 7 – Estimation of mechanical properties of zones of fracture/shear zones: (a) normalised strength parameters and (b) normalised friction angle.

TABLE 1

Rating of zones (0–V) according to various rock mass classifications.

Classification	0	I	II	III	IV	V
Q-Value	533	79.2	8.33	1.03	0.11	0.0033
RMR	100	89	71	52	31	8
RMQR	100	82	64	43	21	0–5

TABLE 2

Values of α_0, α_{100} and β for various properties.

Property (α)	α_0	α_{100}	β
Deformation modulus	0.0	1.0	6
Poisson's ratio	2.5	1.0	0.3
Uniaxial compressive strength	0.0	1.0	6
Tensile strength	0.0	1.0	6
Cohesion	0.0	1.0	6
Friction angle	0.3	1.0	1.0

CONCLUSIONS

A series of experiments were undertaken to investigate formation on the formation and characteristics of fault/shear zones in laboratory. Although actual fracture zones are more complicated, various tests give some insight view of the formation of fault/shear zones as well as some information on their mechanical behaviour. Methods based on rock classifications may also be applicable to such zones. Therefore, the actual geometry and constituents of fracture zones must be taken into account when their mechanical characteristics are assessed.

REFERENCES

Aydan, Ö, 2001. Modelling and analysis of fully coupled hydro-thermo-diffusion phenomena, *Int. Symp. On Clay Science for Engineering*, Balkema, IS-SHIZUOKA, pp 353–360.

Aydan, Ö, Ohta, Y, Daido, M, Kumsar, H, Genis, M, Tokashiki, N, Ito, T and Amini, M, 2011. Chapter 15: Earthquakes as a rock dynamic problem and their effects on rock engineering structures, Y Zhou and J Zhao (eds), *Advances in Rock Dynamics and Applications*, CRC Press, Taylor and Francis Group, pp 341–422.

Aydan, Ö, Sato, A and Yagi, M, 2014a. The Inference of Geo-Mechanical Properties of Soft Rocks and their Degradation from Needle Penetration Tests, *Rock Mechanics and Rock Engineering*, 47:1867–1890.

Aydan, Ö, Ito, T, Tokashiki, N and Kodate, S, 2019. Shock Tests and Some considerations, *Proceedings of ISRM 14th International Congress of Rock Mechanics*, Brazil, pp 1085–1092.

Aydan, Ö, Ulusay, R and Tokashiki, N, 2014b. A new rock mass quality rating system: Rock Mass Quality Rating (RMQR) and its application to the estimation of geomechanical characteristics of rock masses, *Rock Mech Rock Eng,* 47:1255–1276.

Aydan, Ö, Shimizu, Y, Akagi, T and Kawamoto, T, 1997. Tests for mechanical properties of model fracture zones, *The 1st Asian Rock Mechanics Symposium, ARMS'96*, pp 643–648.

Aydan, Ö, Kiyota, R, Iwata, N, Kumsar, H and Sakamoto, I, 2020. An experimental study on frictional properties of faults, *47th Japan Rock Mechanics Symposium*, JSCE, Tokyo, pp 197–202.

Barton, N R, Lien, R and Lunde, J, 1974. Engineering classification of rock masses for the design of tunnel support, *Rock Mech,* 6(4):189–239.

Bieniawski, Z T, 1989. *Engineering rock mass classifications,* New York: Wiley.

Scholz, C H, Dawers, N H, Yu, J Z and Anders, M H, 1993. Fault growth and fault scaling laws: preliminary results, *J Geophysical Research,* AGU 98(B12),21:951–921; 961.

The coalmine roof rating – an update in its calculation and mechanistically why it works

M Colwell[1]

1. Director, Geotechnical Software Services Pty Ltd, Caloundra Qld 4551.
   Email: markcolwell@bigpond.com

ABSTRACT

The Coal Mine Roof Rating (CMRR) is a rock (roof) mass classification (RMC) system/index that was originally developed by the United States Bureau of Mines (USBM) for aspects of underground coalmine geotechnical design and was first introduced to Australia as a part of the original Analysis of Longwall Tailgate Serviceability (ALTS) project conducted in 1997/1998.

In subsequent years further refinement to its calculation was undertaken, such that the CMRR is now an industry standard for quantifying the structural competence of the primary bolted roadway roof interval and has been routinely/widely used by Australian collieries over the last 25 years with great success for roof support/chain pillar design.

There have been many publications discussing the use and calculation of RMC systems and this paper also provides an important update and recommendations in how best to calculate the CMRR. However, it is rare to find an explanation as to why and how a RMC system/index satisfactorily takes account of the mechanics and rock mass behavioural issues associated with ground reinforcement. This paper provides such an explanation and insight with respect to the CMRR so it is: 1) better understood, 2) to allay any concerns, and therefore 3) will continue to be confidently used by and for the collieries' benefit.

INTRODUCTION

The CMRR was originally developed by the USBM in the early 1990s to quantify descriptive geological data used in coalmine design and roof support selection and was adapted from Bieniawski's (1973) rock mass rating (RMR).

As Mark and Molinda (2007) explain; the CMRR was developed because none of the existing RMC systems adequately provided for the layered geology and geologic structures typical of underground coalmines. They go on to state:

> It employs the familiar format of Bieniawki's RMR, summing the individual ratings to obtain a final CMRR on a 0–100 scale. It is also designed so that the CMRR/unsupported span/standup time relationship is roughly comparable to the one determined for the RMR.

The original calculation process/method was based solely on information obtained from underground/highwall exposures such as roof fall material and overcasts (ie the 'Underground Method'). In subsequent years the US National Institute of Occupational Safety and Health (NIOSH) continued to refine and made some modifications to the calculation of the CMRR. The most significant advancement was developing the process by which the CMRR could also be assessed from borehole core.

As discussed by Barton and Bieniawski (2008) as well as Mark and Molinda (2007); the historical and contemporary success of utilising RMC systems/indices for ground support design associated with underground coal/metalliferous mines as well as the tunnelling industry is undeniable.

Irrespective of this success, there are some rock mechanics/geotechnical practitioners (eg Palmström and Broch, 2006; Galvin, 2016) that are overly cautious (even quite dismissive) of their use and/or wish to pigeonhole the use of RMC systems/indices to the planning or feasibility stage of a project rather than during construction of the underground roadway/tunnel. It would appear the reason is that they consider RMC systems do not satisfactorily take account of the behavioural mechanisms and such reservations held by colleagues should be respected and addressed.

To allay such concerns, this paper explains mechanistically why the CMRR has been so successfully utilised for the last 25 years by Australian collieries for roof support/chain pillar design as a part of the original ALTS and current ALTS 2009 design methodology (Colwell and Frith, 2009) and for wide-roadway roof support design (eg longwall installation roadways) as a part of the Analysis and Design of Faceroad Roof Support (ADFRS) design methodology (Colwell and Frith, 2012).

CALCULATING THE CMRR

The CMRR is calculated over and is specific to the primary bolted interval employed at the colliery, which in Australia has ranged from 1.5 to 2.7 m with the vast majority of roof bolts used being 1.8 or 2.1 m in length. Like other RMC systems, the CMRR starts with the premise that the structural competence of coalmine roof is determined primarily by discontinuities that weaken the rock fabric, while noting; 1) it's specifically designed for bedded/laminated coal measure rocks, 2) it concentrates on the primary bolted interval and its ability to form a stable mine roof, 3) it's applicable to all coalmine roof types, and 4) it provides a methodology to guide data collection.

The CMRR consists of individual rock (stone/coal) Unit Ratings (UR's), which assess the structural competence of units within the primary bolted interval, and adjustments which consider the geotechnical competence of all the units in association with one-another.

The UR's are the basic building blocks of the CMRR, with units being defined as rock intervals with distinct structural characteristics. While units are also commonly distinct lithological types, it is stressed that the units are distinguished by geotechnical, not geological, characteristics. While the calculation of the CMRR is discussed in more detail by Mark and Molinda (2007), the following summary and current recommendations are provided for the purpose of this paper.

The UR is calculated based on the following borehole core information:

- The Uniaxial Compressive Strength (UCS, MPa), averaged over the unit thickness which is converted to a UCS Rating.

- Geotechnical logging of the core which results in the calculation of the Rock Quality Designation (RQD) index and Fracture Spacing (FS, mm), specifically with respect to the unit under consideration.

- The FS had been defined as the average spacing of actual core breaks or fractures within the geotechnical unit (eg if there are 8 pieces in a 1 m long section of core then the FS = 125 mm). However, as will be discussed, this definition has been modified to benefit this assessment.

- RQD and FS Ratings are then determined and the lower of the two is the resultant Discontinuity Spacing Rating (DSR).

- Diametral point load testing of the core resulting in the diametral point load test (Diametral PLT) strength index (Diametral $I_{s(50)}$, MPa), which is averaged over the unit thickness, such that the average Diametral $I_{s(50)}$ is then converted to the Diametral PLT Rating.

- The lower of the DSR and Diametral PLT Ratings is typically used as the Discontinuity Rating.

- An estimate of the unit's moisture sensitivity, which is converted to a Moisture Sensitivity Deduction (MSD) being a negative value.

Individual Unit Ratings are then determined based on the above where; UR = UCS Rating + Discontinuity Rating + MSD. The MSD is applied only if a unit is moisture sensitive and is exposed to a level of moisture that would cause structural deterioration of the unit.

Where these factors coincide (ie moisture sensitive roof units that are exposed to a level of moisture that would cause structural deterioration of the units), this can become a dominant mechanism leading to roof deformation; however, Australian collieries typically experience mostly dry roof conditions (with occasional 'drippers') and therefore while assessing the MSD is crucially important; it is generally not a major factor with respect to the UR/CMRR calculations associated with the ALTS/ADFRS databases.

The Thickness-Weighted Average of the UR's within the bolted interval (Roof Ratings Weighted – RR_w) is then adjusted for the effects of the Strong Bed, Unit Contacts, Groundwater and the

Surcharge to determine the CMRR, such that; CMRR = RR$_w$ + Strong Bed Adjustment + Unit Contact Adjustment + Groundwater Adjustment + Surcharge Adjustment.

Like the MSD; it is crucially important to properly assess these adjustments prior to calculating the CMRR; however, in terms of the Australian databases (as opposed to a specific colliery) the adjustments typically have a secondary impact on the CMRR calculation.

It is the UCS and discontinuities (and resultant UCS and Discontinuity Ratings) associated with the primary bolted interval which are the principal determinants with respect to the resultant UR/CMRR values associated with the ALTS/ADFRS databases and therefore it is their evaluation and mechanistic impact that are the primary focus of this paper.

UCS evaluation and UCS rating

When estimating the average UCS for a unit all available information should be utilised in that assessment, ie laboratory/field testing of the core and (if available) a site-specific sonic-derived UCS. Once the average UCS of the unit has been determined, it is converted to a UCS Rating as graphically illustrated in Figure 1 and ranges from a minimum of 5 points to a maximum of 30.
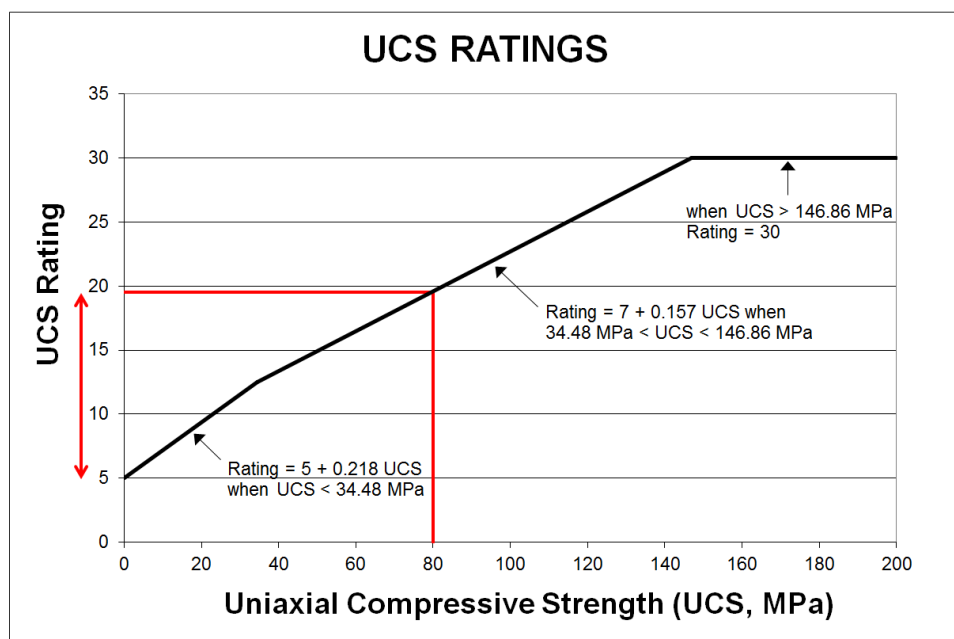

FIG 1 – UCS converted to UCS rating.

For coal measure roof units, the UCS will generally range between approximately 5 MPa (eg weak coal/carbonaceous units) to 80 MPa (eg strong sandstones). Therefore, in practical terms, there is typically a 14 point variation (as illustrated in Figure 1) such that for every 5 MPa increase there is approximately a 1 point linear increase in the UCS Rating. Mark and Molinda (2007) indicate that approximately one-third of the CMRR is determined by the UCS Rating.

Discontinuity rating

The Discontinuity Rating 'captures' the mechanistic effect of how a unit will delaminate due to horizontal stress and/or roof sag and has a possible range of between 18 (where the RQD = 0) and 60. Therefore the practical lower limit of the UR is 24 (ie 5 MPa rock with an RQD of 0, excluding an MSD). However, like the UCS Rating which is rarely greater than 20 (refer Figure 1); for the typical range of coalmine roof encountered in Australia the Discontinuity Rating is rarely greater than 45.

This explains why the typical CMRR range associated with the Australian databases is 30 to 65, with an absolute range of 25 to 77. So while the theoretical CMRR scale is 0–100, in practical terms this is not the case and needs to be appreciated in terms of its use and assessing the relative impact of the various ratings and adjustments on the final CMRR calculation.

Once the units have been identified, the RQD and FS are calculated for each unit based on the information recorded while the core is in the 'splits'. Following photographing, boxing of the core and the removal of any samples for laboratory testing; where the core allows then axial and diametral point load testing should be conducted to obtain representative average Axial $I_{s(50)}$ and average Diametral $I_{s(50)}$ values of the unit.

Axial point load testing of the core is important and provides additional/valuable information in assessing a unit's average UCS, however conducting a sufficient number of Diametral PLT's is crucial in terms of best estimating the unit's Discontinuity Rating.

Where the core allows, it is strongly recommended that a Diametral PLT be conducted at a maximum interval of 100 mm (ie a minimum of 10 tests/m) for <u>at least</u> the first 5 m above the intended roofline. For laminated rock types (eg sandstone with abundant carbonaceous laminae, refer Figure 2), it is more appropriate to 'target', or at least bias the testing to the bedding/laminae rather than a mixture of the bedding/laminae and the rock matrix that may occur with evenly spaced testing, as well as noting whether the test was conducted on the bedding/laminae or rock matrix.

FIG 2 – Photograph of roof core being sandstone with abundant carbonaceous laminae.

The unit's average Diametral $I_{s(50)}$ is an excellent index relating both to bedding plane/laminae strength and the resultant average beam thickness associated with a unit which undergoes delamination due to horizontal stress and/or roof sag.

For example as Galvin (2016) states:

> *In coal mines, the immediate roof and floor strata are usually bedded due to the sedimentary origin of coal deposits. Bedding planes are characterised by low to zero tensile strength normal to the bedding planes and low shear strength relative to that of intact rock. Hence, bedding planes constitute potential slippage planes and can effectively divide the roof strata into an assembly of thin rock beams.*

With respect to US collieries, Mark and Molinda (2007) state, 'Bedding was the factor that was most consistently cited as causing roof problems in coalmines. The two most common examples were weak laminations in shale and thinly interbedded sandstone and shale.' They go on to explain that the issue of bedding (or grain alignment) is further complicated because some rock types may appear massive, but are actually highly laminated and state, 'If the diametral test results show that the rock fabric or laminations are low-strength, it would be illogical to give the rock high marks for discontinuity spacing', ie a high DSR.

For these reasons, they emphasised the need for testing of the rock material to determine bedding plane/laminae strength even when the bedding is not readily visible, with the Diametral PLT being the most appropriate test in this regard.

The RQD, FS and average Diametral $I_{s(50)}$ are then converted to RQD, FS and Diametral PLT Ratings and the Discontinuity Rating is then determined as previously described.

Fracture spacing assessment – an update

To both emphasise the importance of the role of bedding/laminae and realistically account for its effect in assessing the FS, the author strongly recommends that for laminated rock types; if in the opinion of the geotechnical engineer insufficient Diametral PLT's have been conducted with respect to the bedding/laminae and/or it is assessed that the bedding/laminae are essentially weak contacts along which delamination will readily occur, then these bedding/laminae can be included as fractures within the unit and the FS should be recalculated accordingly. A textbook illustration as to why this recommendation has been made is shown in Figure 3, which displays a sandstone unit with substantial laminae.
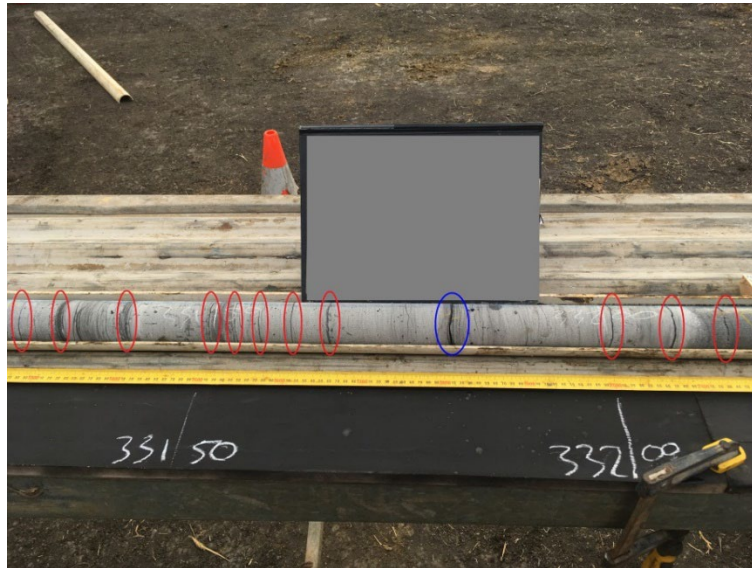
FIG 3 – Photograph of sandstone roof core with substantial laminae.

The only core break identified by the exploration geologist is circled in blue, however under sufficient horizontal load (and if there is an underlying void into which the strata can move) this unit would also readily delaminate along those laminations circled in red. Therefore specifically for this approximate 900 mm length of core shown in Figure 3, the FS would reduce from 450 mm to maximum of 69 mm and accordingly the FS Rating reduces from 40.3 to 29.7, where FS Rating = 5.64 ln (FS) + 5.8.

It is also very important to note; if there is a lack of Diametral PLT's targeting the bedding/laminae, then the original Discontinuity Rating tables associated with the Underground Method can also be used to rate the bedding/laminae to return a Discontinuity Rating.

In addition, while bedding/laminae typically dominate over subvertical jointing in terms of roof behaviour; if significant roof jointing is encountered or subsequently identified via mapping/inspection, then once again the Underground Method can be employed to reassess the CMRR for a section of roadway previously determined via borehole information. This being a clear example of how the CMRR can be used at: 1) the roadway roof support design stage based on borehole information, 2) during construction of the underground roadway, and 3) if required, re-evaluating planned roof support levels prior to longwall retreat or roadway widening.

The relative impact of the UCS and discontinuity ratings on the unit rating

While the FS is the actual value associated with the geotechnical logging of the core in the 'splits'; the unit's Effective Fracture Spacing (FS_{eff}, mm) closely approximates the resultant average beam thickness associated with a unit which undergoes delamination due to horizontal stress and/or roof sag and is a data output parameter associated with the UR calculation.

With respect to the 201 roof units (within approximately 10 m of the roofline) associated with the ADFRS database; the maximum FS_{eff} is 2750 mm, while 97 per cent have an $FS_{eff} \leq 1000$ mm.

Therefore, as illustrated by Figure 4, with respect the typical range associated with coalmine roof units, in practical terms there is a 27 point variation in the Discontinuity Rating (ie 18 to 45) as opposed to the typical 14 point variation associated with the UCS Rating (refer Figure 1).
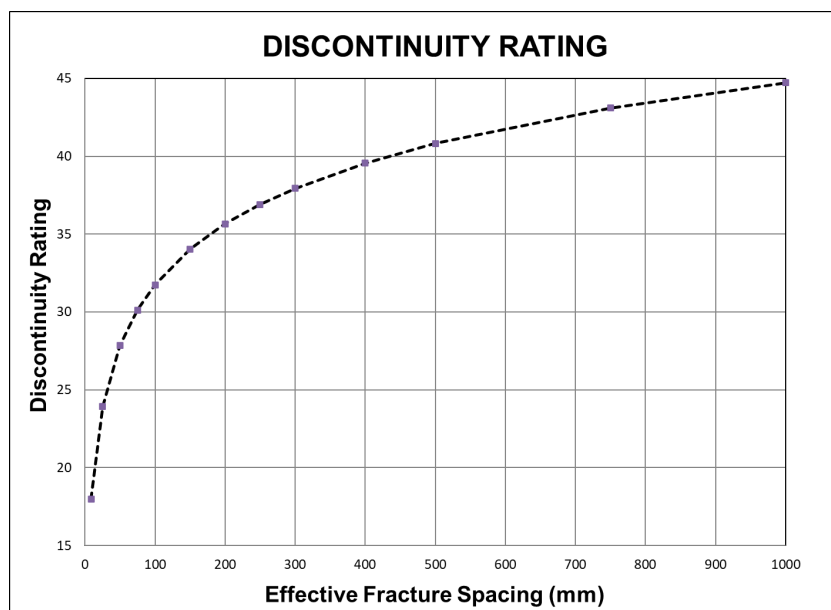
FIG 4 – Discontinuity rating versus effective fracture spacing.

As opposed to the UCS Rating, where there is essentially a linear increase of 1 point for every 5 MPa increase from 5 to 80 MPa; Figure 4 reveals a logarithmic relationship where there is rapid increase in the Discontinuity Rating, particularly over the initial 200 mm change in the FS_{eff}. Therefore for dry conditions (ie MSD = 0) and in terms of the typical ranges; the Discontinuity Rating has approximately a two-third impact on the UR calculation (ie 27/41), as opposed to the approximate one-third impact of the UCS Rating (ie 14/41). This being consistent with the Mark and Molinda (2007) assessment.

To further illustrate the relative impact of the UCS and Discontinuity Ratings on the UR; the average unit UCS and FS_{eff} (associated with the ADFRS database) are approximately 35 MPa and 164 mm, which return a UCS Rating of 12.5 and Discontinuity Rating of 34.5 resulting in a UR of 47. Remembering the minimum UCS and Discontinuity Ratings are respectively 5 and 18, the effective contribution of the UCS is 7.5 points (ie 12.5–5) and the FS_{eff} is 16.5 points (34.5–18) or respectively a 31 per cent (ie 7.5/24 × 100) and 69 per cent (ie 16.5/24 × 100) impact.

The preceding discussion reinforces that like most other RMC systems, the CMRR (representing the structural competence of coalmine roof) is determined primarily by discontinuities that weaken the rock fabric rather than its UCS.

## SLENDER BEAM BEHAVIOUR AND ROOF REINFORCEMENT MECHANISMS

Colwell and Frith (2021) demonstrated that slender beam behaviour is by far the dominant behavioural mechanism associated with coalmine roof leading to roof failure, which is a process (within the zone of softening) where; 1) delamination (or de-coupling) occurs forming slender/thin beams within the roof which 2) buckle as a consequence of axial loading resulting in 3) shear and tensile failure.

Salamon (1989) was emphatic that, '..field experiments are vital in the evaluation of the efficacy of the models' and further stated, 'I do not believe that the simplicity of the model is the problem. Measurements will soon support or reject an oversimplified attempt.'

Decades of roof/rib extensometer measurements overwhelmingly support slender beam/column behaviour as the dominant instability mechanism within a coalmine roof/rib subject to elevated horizontal/vertical stress conditions and therefore, <u>must</u> be representatively accounted for in any credible empirical, analytical, or numerical approach to coalmine roof/rib stability assessment and ground support design.

An example of a physical model of a coalmine roadway, faithfully representing slender beam behaviour, is illustrated in Figure 5, which is taken from Hoek and Brown (1980) where they state that this figure:

> ...illustrates the buckling of slabs in the roof and floor of an excavation in a high horizontal stress field. This type of failure was observed in model studies conducted by the Australian Coal Industry Research Laboratory (ACIRL) in an attempt to simulate the structural and stress conditions in the coalfields near Sydney, Australia.
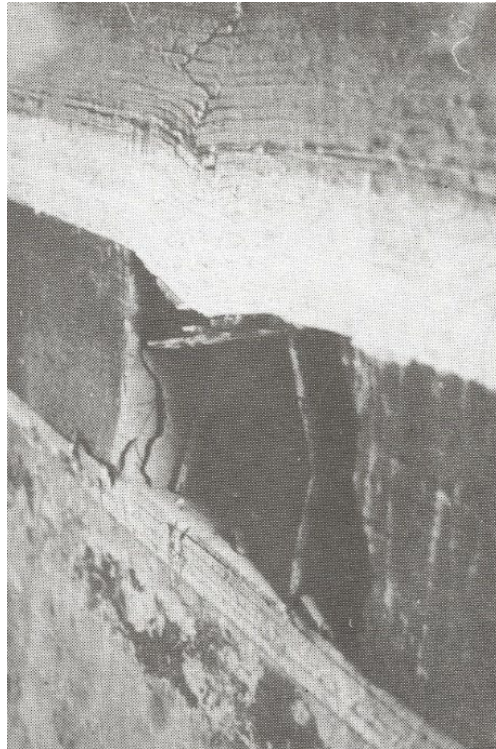
FIG 5 – ACIRL coalmine roadway physical model (after Hoek and Brown, 1980).

Hoek and Brown (1980) go on to state:

> In jointed or bedded rock masses, the presence of structural features parallel to the excavation surfaces will result in the formation of plates and slabs, Whatever the reason for the presence of these slabs, it takes little imagination to visualise that they are susceptible to buckling under axial stress.

Based on measured roof behaviour using extensometers; Figure 6 illustrates a commonly held model for the development/progression of roof softening. The main point of note is that roof softening progresses higher into the roof as a series of discrete 'steps' with such steps only occurring once certain levels of total roof displacement (TRD, mm) have been exceeded in the underlying roof strata.
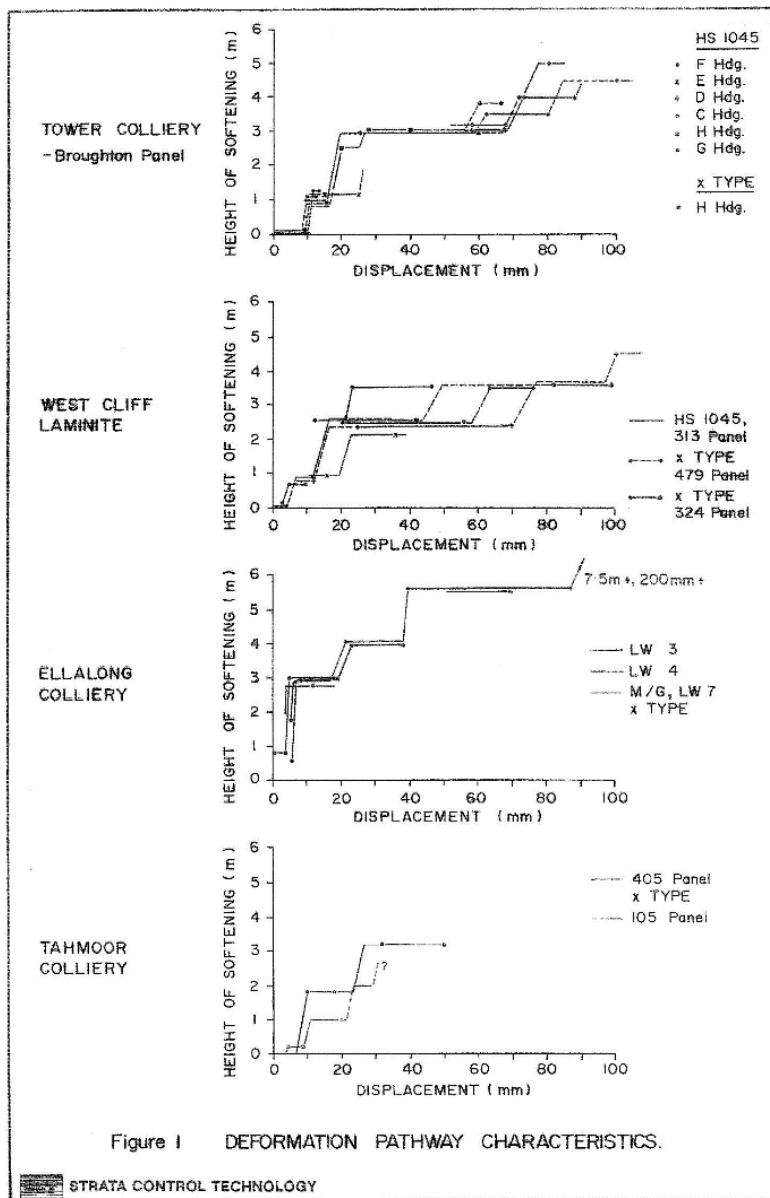
FIG 6 – Roof softening progression with displacement (after Fabjanczyk, Tarrant and Guy, 1992).

The behavioural logic behind this is that roof buckling at any given horizon in the roof can only occur if there is an underlying void into which the strata can move. Therefore for buckling of higher roof measures to take place, the underlying strata must have displaced vertically by a certain amount (ie only 10 to 20 mm TRD is required), resulting in a void into which higher measures can move and this process is described as one of strata de-coupling.

The other significant point of note with respect to Figure 6 is that the Height of Softening (HOS, m) rapidly extends to around 2 to 3 m above the roofline for TRD's of 10 to 20 mm and then tend to flatten off. This suggests that roof softening to 3 m can occur quite rapidly (within which slender beams are formed) at relatively low roofline displacement levels providing the condition by which buckling of the roof layers (due to horizontal stress) within this zone can occur.

Typically with 10 to 20 mm TRD, the roof is still under reasonable control (ie the roof achieves a load-balance equilibrium), such that further vertical displacement is controlled. The slender beams formed may have buckled and (if so) to a degree are 'behaving like a spring' as shear/tensile failure has yet to occur. However, it is once these levels of TRD are exceeded that there is a far greater likelihood of shear/tensile failure as illustrated by Figures 5 and 7 (a photo from a US coalmine; ARBS, version 2, by NIOSH) occurring and loss of control leading to a roof fall.

FIG 7 – Coalmine roadway roof displaying buckling and shear/tensile failure due to horizontal stress.

Furthermore, if one assumes that the shear stress distribution and deformation is parabolic in the roof, then the maximum HOS should be approximately 2/3 of the span (ie approximately 3 m for a 5 m span) with higher softening only then occurring if the immediate 3 m roof section is allowed to displace excessively.

Figure 8 is a sonic probe roof extensometer plot (with anchors at approximately 0.3 m intervals), which illustrates the behaviour (or response) of a section of maingate roof during adjacent longwall retreat and further demonstrates that softening to 3 m occurs rapidly for relatively low TRD values, while becoming increasingly more difficult to propagate higher, as disproportionately higher levels of roof displacement in the lower roof are required. Similar roof behaviour to that displayed in Figure 8 is found routinely where significant roof displacement has occurred, all of which is consistent with Figure 6.
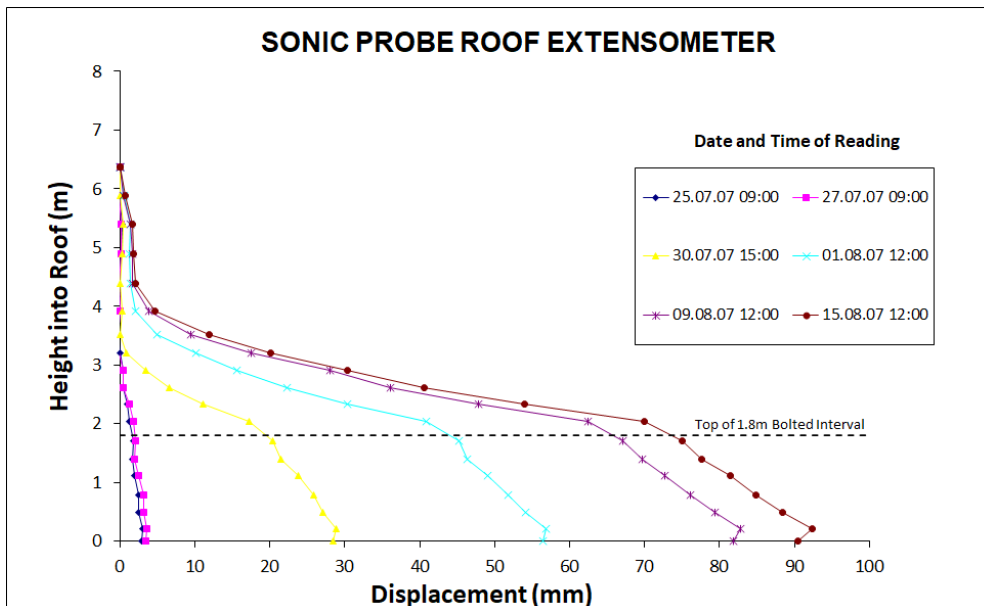
FIG 8 – Roof behaviour adjacent to longwall extraction.

Figure 8 further illustrates how the roof delaminates into thinner beams and how the 1.8 m bolts (that were utilised to reinforce the immediate roof) modify the beam behaviour via the roof reinforcement mechanism/concept of 'beam building' or as Oliveira and Pells (2014) explain in discussing the design of semi flat-roofed tunnels in Sydney using voussoir beam theory:

> *...rock bolts are typically used to stitch together near horizontal beds of limited and variable thickness, to 'trick' the rock mass into behaving as an appropriately thick linear arch, robust against the uncertainties in joint directions that may be expected in strata such as the Hawkesbury Sandstone of Sydney.*

The concept being that the bolts/cables create 'thicker' beams within the reinforced section (or the primary bolted interval) and that a thicker beam will have a greater axial load-bearing capacity than a thinner beam, this being consistent with the statement of Hoek and Brown (1980):

> *...thin plates will buckle more easily than thick plates. This suggests that an effective method for reinforcing an underground excavation in which slab buckling is considered to be a problem is to pin the slabs together by means of short rockbolts.*

Roof reinforcement mechanisms

In terms of roof reinforcement, bolts and longer pre-tensioned cables are fundamentally different for a variety of technical reasons. The way in which longer cables reinforce or 'suspend' the roof and where they are positioned across the roof will depend on several factors (including but not limited to), whether the cables are post-grouted or simply point-anchored, the level of pre-load applied and most importantly whether the geotechnical engineer (and the methodology used) views the role of the cables as one of roof reinforcement or suspension.

Irrespective of what model/design approach to the cables is used, it can only be effectively employed if in fact there is 'beam behaviour' associated with the primary bolted interval and to form a beam within a coalmine roof (so that it can behave as a beam across the full width of the roadway) will only come about through 'pattern bolting' and this is the role of the bolts installed off the continuous miner.

A reasonable spread of bolts is required at a regular spacing to assist in building a reinforced beam; that is the bolts are close enough to each other and the riblines to effectively interact to form such a beam. However, the questions are; how do the bolts reinforce the roof mass and how is the beam formed?
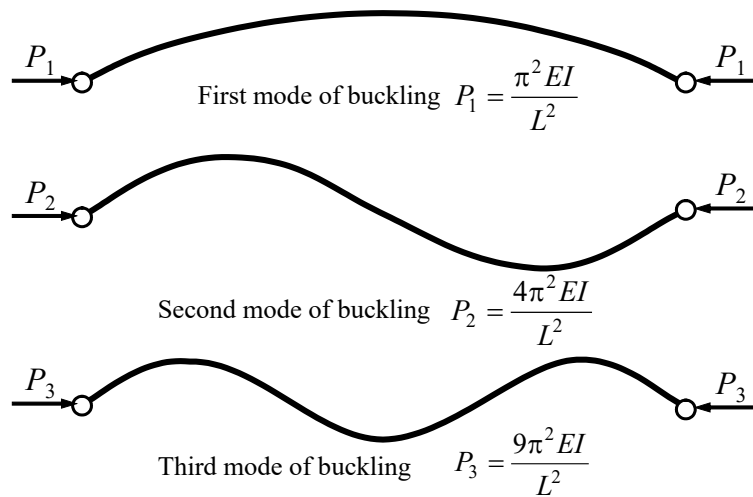
Figure 7 visibly demonstrates that immediately about the bolt a thicker beam can be created by pinning 'the slabs together by means of short rock bolts' as suggested by Hoek and Brown (1980). However, Figure 7 also clearly reveals that this effect does not radiate across the entire roadway, because if it did, only one bolt/m would be required to stabilise the roof and that is not a reality! Figure 7 also demonstrates why it is important to assess the potential for instability not simply across the entire roadway width, but also between bolts and in particular between the two centre bolts, which is generally the greatest 'unreinforced' span.

In examining the interaction of bolts with the rock mass and the role that they play in modifying rock mass behaviour about an opening, typically the rock mechanics researchers' concept is that the ground support reinforces the broken (ie post failure) rock by offering additional confinement and in so doing improves its residual strength (ie about the bolt) thereby minimising further stress redistribution and restricting the extent and severity of failure. Based on these concepts, the rock reinforcement or confinement provided by the bolts manifests itself in two ways; ie axial and shear restraint.

However, given that slender beam behaviour or buckling (due to axial loading) is typically the dominant behavioural mechanism occurring within the immediate coalmine roof and that 'nodes' along a beam are as important as the end-fixing condition in assessing its axial load-bearing capacity; there is another reinforcement mechanism whereby the bolts essentially act as 'moveable nodes' within a buckling beam system.

The critical load (referred to as the Euler Buckling Load) for a beam pinned at both ends at which buckling can occur is given by; $P_{crit} = n^2 \pi^2 E I/L^2$, where E is Young's modulus of the beam material, L the length and I is the least moment of inertia of the beam.

The values of n, define the buckling mode shapes, with the first three modes of buckling illustrated in Figure 9. However, since $P_1 < P_2 < P_3$ (for n = 1, 2 and 3), the beam buckles at P_1 and essentially never reaches P_2 or P_3, unless bracing or a fixed node is placed at points along the beam to prevent buckling at lower loads.

First mode of buckling $P_1 = \dfrac{\pi^2 EI}{L^2}$

Second mode of buckling $P_2 = \dfrac{4\pi^2 EI}{L^2}$

Third mode of buckling $P_3 = \dfrac{9\pi^2 EI}{L^2}$

FIG 9 – First three modes of buckling behaviour.

Unless the bolts are securely anchored into a 'fixed' rock layer (or strong bed) they will effectively 'float' with roof movement and become 'moveable nodes'. Even when anchored into a supposed stable rock layer there will inevitably be some vertical movement. The nature of the anchor, quality of installation, the stiffness of the bolt and the level of pre-load applied to the bolt will all affect the 'Theoretical K Value' as illustrated in Figure 10 (which is adapted from information contained in Standards Australia AS 3600–2001: Concrete Structures) and therefore the effective length (L_{eff}) of the beam (overall and between bolts/nodes); where $L_{eff} = K L$ and it is L_{eff}, which is substituted in all calculations to determine the critical buckling load.

FIG 10 – K values for buckling columns.

The ALTS research in conjunction with the development of the Analytical Model for Coal Mine Roof Reinforcement (AMCMRR, Colwell and Frith, 2010), demonstrated that for fully encapsulated bolts the significant predictors of the bolts' effectiveness in terms of roof reinforcement are individually 1) the length of the bolts, 2) the capacity of the bolts (ie Typical Ultimate Tensile Strength, kN), and 3) the bolting density as well as when these are combined into the Primary Roof Support (PRSUP) rating.

PRSUP is a roof reinforcement index, which 'captures' the mechanistic effects of axial/shear restraint provided by the tendons and their interaction in reinforcing the roof and is a measure of the tendon capacity (kN/m^2) along the roadway normalised to the primary bolted interval (ie over which the CMRR is calculated). PRSUP includes all bolt/cable roof support that is installed off the continuous miner in its calculation.

A suitably qualified/experienced geotechnical engineer is able to readily convert PRSUP into an appropriate balance of bolts and longer cables and where to position said tendons. For further information in calculating PRSUP, the interested reader is referred to Colwell and Frith (2012).

Therefore, anything that can be done to make the bolt/cable a more fixed or less moveable node in a buckling system will promote roof stability or at minimum, allow a unit achieve its maximum lateral load-bearing capacity, remembering that no matter how many bolts/cables are installed, one can't make the 'rock stronger than the rock'!

The 'moveable nodes' model does not rely on failure of the rock mass to trigger a response but simply 'turns up the volume' on the roof unit's own ability to resist buckling. It is considered that the 'moveable nodes' model provides a far more rational explanation as to how the bolts/cables interact across the roof and why pattern bolting proved to be a great success in terms of roadway roof reinforcement.

The reinforcement mechanism or concept of beam building associated with the installation of roof bolts has long been recognised in the underground coal mining industry. While numerous researchers have discussed the various mechanisms by which the bolts act to 'create thicker beams' (eg by maintaining friction on bedding planes), AMCMRR was the first such study/model that in a practical way attempted to quantify the beam building effect and then incorporate this effect within an analytical model.

However, as this discussion indicates, the introduction of roof bolts does not actually 'create thicker beams' across the entire roadway width as that is not likely with the typical Australian primary roof support pattern of six bolts/m and certainly not with four bolt/m patterns. Mechanistically what is occurring is that the bolts are modifying the effective length of the beam (overall and between bolts/nodes).

As illustrated by Figure 10, the end-fixing condition of the beam will have a significant impact on its load-bearing capacity. With respect to coalmine roof beams Galvin (2016) states, 'In most cases of practical interest, values of K of about 0.6–0.8 can be expected to apply'. However due to the possible/probable presence of subvertical jointing, Colwell and Frith (2010) suggest a K of 1 is more appropriate. Therefore the problem faced in the development of AMCMRR is that it is not possible to quantify the exact starting K value or end-fixing condition of the roof beams prior to or subsequent to the bolts being installed.

However, what is known is that the lateral load-bearing capacity of the roof beam(s) will be a function of: 1) its end-fixing condition, 2) the nodes along the beam, 3) its actual geometry (ie length – L and thickness – d) and 4) its modulus. While the effective length of the beam over which buckling occurs (ie L_{eff}) is affected by the end-fixing condition and the nodes along the beam, **its thickness is not!** In relation to the average beam thickness within a rock unit, there is a reasonable starting point and that is FS_{eff}, being derived from the UR calculation.

Utilising the concept of beam building, one can use FS_{eff} and PRSUP to evaluate the 'effective' Reinforced Beam Thickness (RBT, mm) and thereby the increased lateral load-bearing capacity of the reinforced roof unit. Colwell and Frith (2010) explain this process, which resulted in the relationship detailed in Figure 11. While recognising that the concept of beam building (across the full roof span) is not entirely mechanistically correct, it can still be effectively utilised (via practical engineering simplification) to obtain the same end result being the lateral load-bearing capacity of the reinforced roof unit, thereby quantifying the 'trick' alluded to by Oliveira and Pells (2014).
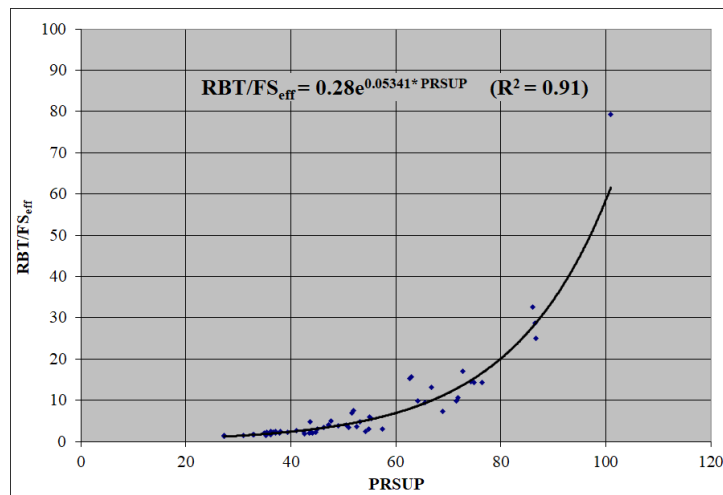
FIG 11 – Relationship between RBT/FS$_{eff}$ and PRSUP.

The process by which the RBT/FS$_{eff}$ relationship to PRSUP was determined is in many ways similar to the process by which the empirically derived Hoek–Brown Failure Criterion for rock was developed (Hoek and Brown, 1980). However in using the RBT/FS$_{eff}$ relationship to PRSUP, it is important to note that irrespective of the resultant RBT, the beam's lateral load-bearing capacity will be limited by the material's strength and the unit's lithological thickness, ie one can't make the 'rock stronger than the rock' or the RBT greater than the unit's actual thickness.

In its adaptation from the RMR one of the most important concepts incorporated into the CMRR is that of the Strong Bed Adjustment (SBADJ). Many years of experience with roof bolting (in Australia and US) has found that the overall structural competence of coalmine roof is very often determined by the quality of the most competent unit within the bolted interval.

The original SBADJ concept was primarily to do with the reinforcement mechanism of 'suspension'. As Mark and Molinda (2007) explain,

> ...experience in many US coalfields has clearly established that roof stability is greatly enhanced when the roof bolts anchor in a strong layer. This effect is most evident in the Illinois Basin, where roof falls are almost unknown when the bolts anchor in a limestone that is at least 0.6 m thick. The strong bed effect has also been recognized in Alabama and central Appalachia. Indeed, even the Code of Federal Regulations implies a strong bed effect when it states at 30 CFR 75.204(f)(1) that roof bolts that provide support by suspending the roof from overlying stronger strata shall be long enough to anchor at least 12 inches into the stronger strata.

In Australia, (while fewer) there are also several examples and it was apparent from the analyses and field investigations; at those collieries where the SBADJ is a significant component of the CMRR, if for <u>any</u> reason anchorage within the strong bed is compromised (eg due to gloving, water, installation difficulties) or the strong bed is absent within the bolted interval (for example due to a thickening of weaker strata beneath the strong bed or the strong bed 'lenses out') then roof performance can be significantly and adversely effected particularly during longwall retreat. Conversely, where solid anchorage within the strong bed is maintained, then 'bagging' of the roof was not observed and significant deformation/delamination was not measured.

If the bolts are solidly anchored into a strong bed they essentially become 'less moveable' and 'more fixed' nodes within the weaker roof below the strong bed as illustrated by Figure 12, with the driving force being the resultant horizontal stress acting across the roof (σ_R, MPa) and the red dots representing the bolts as nodes in a buckling system. The relative decrease in the K value would result in greater stability for the weaker material beneath the strong bed as the effective beam lengths (ie across the roadway or between bolts) within the weaker units would be reduced. Mechanistically, this explains why the SBADJ reinforcement mechanism has such a significant impact on roof behaviour and therefore has very little to do (if at all) with suspension and furthermore is totally consistent with slender beam behaviour/reinforcement concepts.
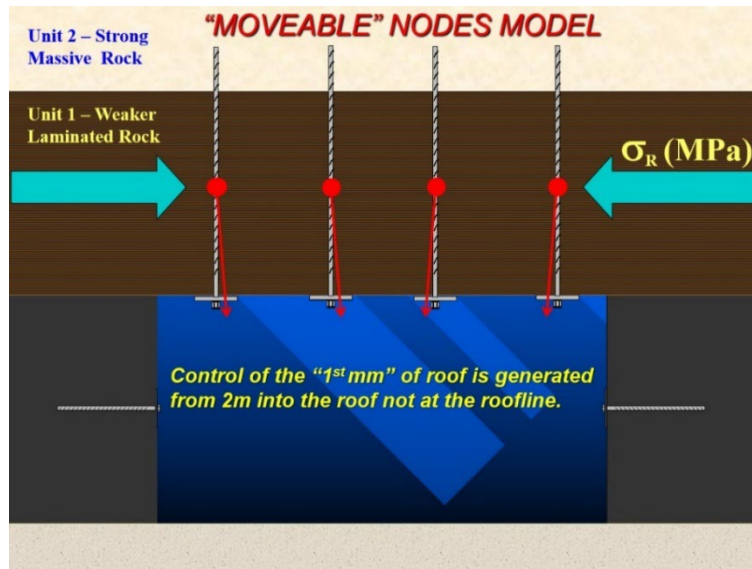
FIG 12 – Moveable nodes model and SBADJ reinforcement mechanism.

ASSESSING THE CMRR AND UR IN TERMS OF SLENDER BEAM BEHAVIOUR

Utilising multiple regression, the ALTS/ADFRS research found (with extraordinarily high correlations, ie R^2 values typically between 0.8 and 0.9) that the two dominant/significant predictors of the level of roof support required to maintain satisfactory roof stability during and subsequent to development as well as during longwall retreat or roadway widening are:

1. An index directly related to the lateral load-bearing capacity of the <u>unreinforced</u> structure being the CMRR for normal width roadways of 4.5 to 6 m wide and for wide-roadway formation (eg 7.5 to 14 m wide) the average UR over the first 5 m above the roofline, referred to as Average $UR_{5\,m}$ and;

2. The horizontal stress acting across the roof at each stage of development/longwall extraction cycle (σ_R, MPa).

For example; Figure 13 illustrates the required level of primary roof support installed off the continuous miner (designated as $PRSUP_{Dev}$) to maintain satisfactory roof stability subsequent to development, while prior to the roadway being subject to either 1) adjacent longwall extraction or 2) roadway widening; where $PRSUP_{Dev}$ is a function of the CMRR and the resultant horizontal stress acting normal to the development direction, designated as σ_R-Dev (MPa).
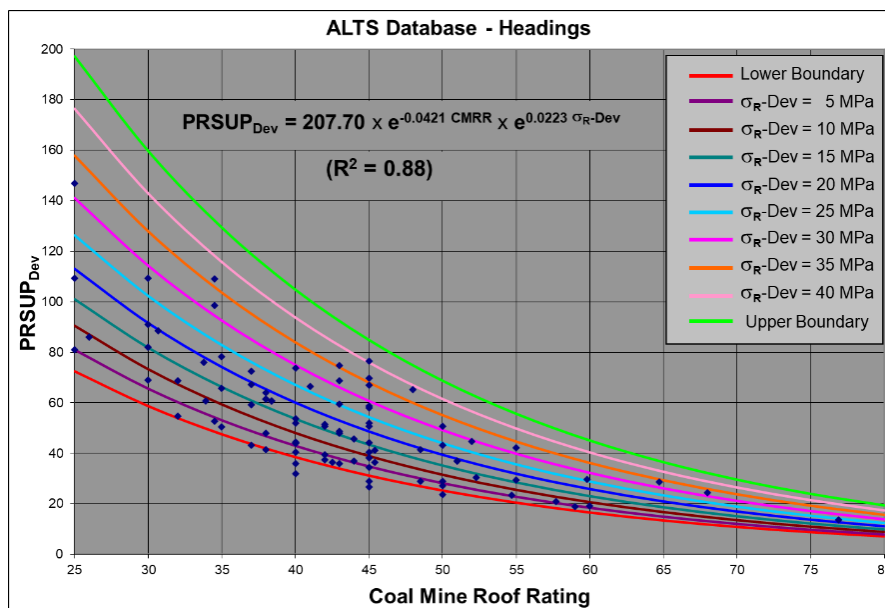

FIG 13 – $PRSUP_{Dev}$ versus CMRR and σ_R-Dev.

The relationship depicted in Figure 13 makes perfect mechanistic sense and also illustrates that the $PRSUP_{Dev}$ versus CMRR relationships for varying stress levels acting across the roof fit seamlessly within the upper and lower boundaries.

The extraordinarily high correlation (ie R^2 value) of 0.88 essentially means that 88 per cent of the reason(s) as to why Australian collieries select primary roof support levels to maintain satisfactory roadway conditions to an Australian 'standard', is a function of the CMRR and σ_R-Dev. In relation to the 12 per cent not accounted for directly by the relationship, this would include a number factors other than purely geotechnical considerations; a perfect example being the variability in the quality and timing of bolt/cable installation across the industry (ie operational/human factors).

In relation to these extraordinarily high roof support correlations associated with ALTS and ADFRS; why and how did this come about? It is either a statistical fluke that has 'accidently' worked for several independent databases in Australia and overseas (which is not credible reasoning), or the manner by which the key parameters (PRSUP, UR, CMRR, FS_{eff} and σ_R) have been calculated in those databases are a credible representation of the mechanistic aspects associated with the 'system'.

The weighting or relative impact of the two dominant factors (ie FS_{eff} and UCS) associated with the UR/CMRR is consistent with established beam theories; in that beam geometry (and its end-fixing conditions) dominate, as compared to the beam material's UCS, when calculating the beam's axial load-bearing capacity (MPa). Utilising information from the ADFRS database, the following example is provided to illustrate.

With respect to the 201 roof units associated with the ADFRS database, the average UCS, FS_{eff} and E (GPa):UCS (MPa) ratio are approximately 35 MPa, 164 mm and 0.26 and therefore for a UCS of 35 MPa an E of 9.1 GPa would be returned. The ADFRS database also revealed the average 1st pass roadway drivage width is 5.1 m, which would also represent the average roadway width for mains and gate road development.

Colwell and Frith (2010) detail the process by which the axial load-bearing capacity of a column/beam (length, L) with increasing thickness (d) is calculated moving from long (slender) columns/beams that fail due to buckling through intermediate to short (stumpy) beams which will fail by compression. Beams of intermediate slenderness exhibit a combined failure mode involving both yielding and large lateral deflections.

Utilising the average values previously detailed, K values of 0.7 and 1 and a beam width of 1 m (representing the typical bolt row spacing), Figure 14 is produced which displays both the axial load-bearing capacity and UR for a variable FS_{eff} up to 2000 mm. For simplicity the yield strength is taken to be equal to the UCS (being brittle failure). Utilising a constant UCS of 35 MPa; the UCS Rating is also a constant of 12.5 such that the variation in the UR is solely due to the variation in the Discontinuity Rating based on FS_{eff}.
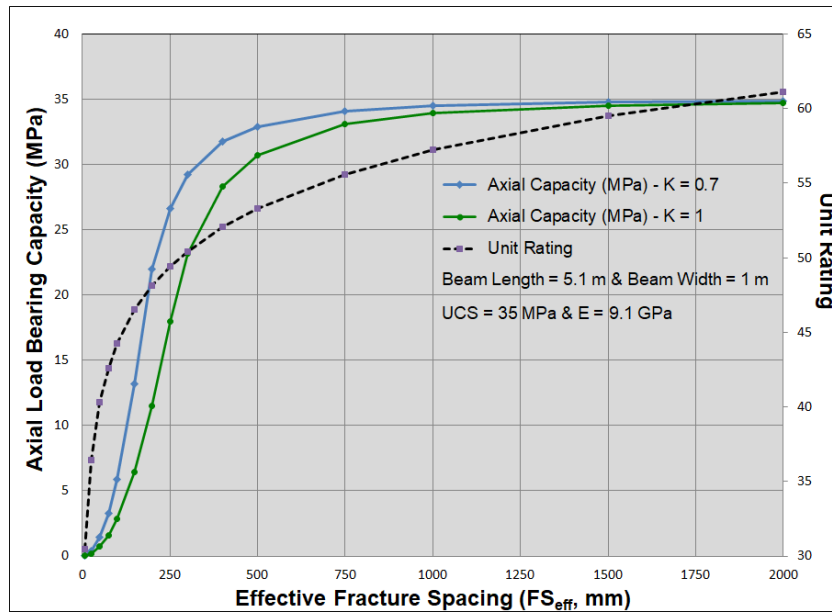
FIG 14 – Axial load-bearing capacity and UR vs FS_{eff}.

Figure 14 confirms that up to approximately 500 mm, it is the change in the beam thickness that dominates the axial load-bearing capacity of the beam and that the change in the UR (in this case solely due to the increase in the Discontinuity Rating) is consistent with the change in the beam's axial strength.

In an attempt to assess the impact of <u>both</u> a change in the UCS and beam thickness on the beam's axial load-bearing capacity, Figure 15 has been produced. In this instance the typical range of 5 to 80 MPa for coalmine roof strata has been utilised. A reasonable assumption has been made that as the FS_{eff} increases the more 'massive' the unit becomes and accordingly its UCS and E would typically increase.
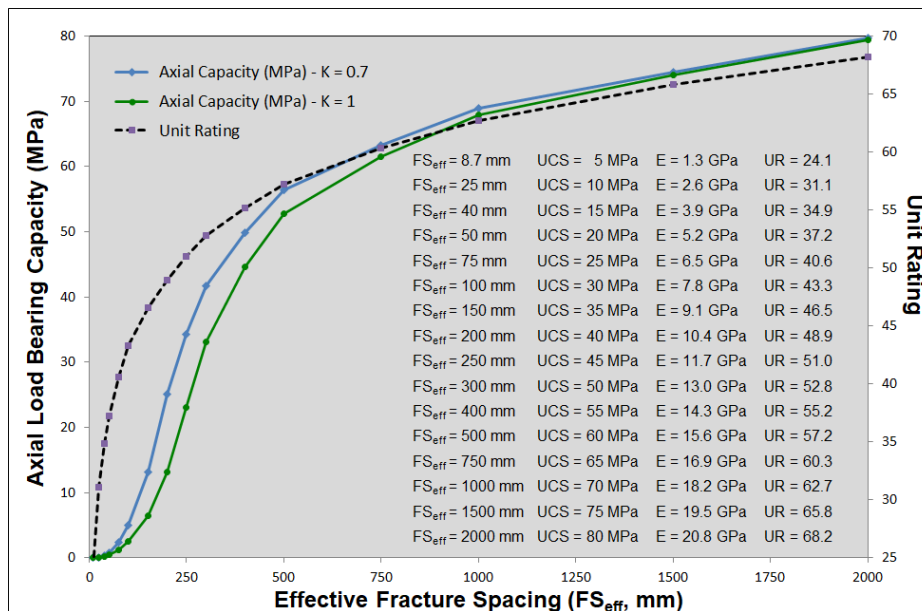

FIG 15 – Axial load-bearing capacity and UR versus FS_{eff} utilising E (GPa):UCS (MPa) ratio = 0.26.

It is <u>fully recognised</u> that there will be rock types, such as that depicted in Figure 2 (where the sonic-derived UCS ≈ 50 MPa and the FS_{eff} ≈ 25 mm) that are not consistent with the assumption made; however, the material properties listed on Figure 15 are considered to be a reasonable approximation so as to assess and simply <u>demonstrate</u> the relative impact of UCS and beam thickness on the beam's axial strength. The change in UR is now almost entirely consistent with the resultant axial load-bearing capacity of the beam.

Figure 14 (on its own) mechanistically explains why the extraordinarily high ground support correlations associated with ALTS and ADFRS are not a 'statistical fluke', with Figure 15 providing compelling confirmation.

Therefore the statement by Galvin (2016), '.. as with all rock mass classification systems, the CMRR does not take account of behaviour mechanisms' is incorrect and illustrates how a superficial review of a RMC system (or any engineering/scientific process/methodology) by simple comparison, can lead to 'misconceptions' that unfortunately influence others and require, as our esteemed colleagues Barton and Bieniawski (2008) state, 'Setting records straight' when addressing others' concerns with respect to the use of the RMR and Q indices.

Furthermore, it is logically concluded that the CMRR is not simply a numerical rock mass 'index', but a rock/roof mass classification system that is totally consistent with structural engineering principles and so can be used with a high degree of confidence by the underground coal industry in assessing the structural competence of the bolted mine roof interval for roof support design purposes.

Finally, remembering that the CMRR was developed to adequately provide for the layered roof geology and geologic structures typical of underground coalmines; as a 'model' the CMRR is totally consistent with the structural component of the ACIRL physical model (Figure 5); while the ALTS/ADFRS models are then consistent with the ACIRL physical model as a whole, simulating the typical structural/stress conditions associated with the vast bulk of Australian collieries.

CONCLUSIONS

The primary purpose of this paper is to explain mechanistically why the CMRR has been successfully/widely utilised for over 25 years by Australia collieries and demonstrate that in fact the CMRR **does** take account of roof behaviour mechanisms.

This paper is also intended to emphasise as Kleingeld (2010) advises:

> Engineers need to guard against focusing solely on the technical content of their work. They must simplify their processes, methodologies and products to ensure that their efforts contribute real value to society.

Or as Salamon (1989) states:

> I do not believe that the simplicity of the model is the problem. Measurements will soon support or reject an oversimplified attempt.

A clear example of the above is the contribution that ALTS, AMCMRR and ADFRS (and their use of the CMRR) has made to the Australian underground coal industry. For example, in relation to gate road design Emery, Canbulat and Zhang (2020) state:

> Worthy of special mention is the ALTS design methodology, which was initially provided to the Australian coal industry in early 1999 and over a 10 year period was continually refined and updated such the latest version, ALTS 2009 and associated software package, has grown to be the prevalent technique for chain pillar and gateroad ground (roof and rib) support design at most operating longwall mines in Australia.

> This is largely because the outputs from ALTS 2009 most accurately reflect the design requirements to provide serviceable gateroads associated with longwall extraction. In addition, ALTS 2009 is relatively quick and straightforward to use allowing typically time poor mine site geotechnical engineers to conduct in house design work with high levels of accuracy, improving both safety and productivity at those mine sites.

In his keynote address to the Eighth International Strata Control Conference Professor Salamon (1989) advises researchers:

> ...strata control must improve safety, efficiency and the economy of mining. However, it is not enough for us to do the research which potentially can achieve these goals, we must ensure also that the research results are also put into practice effectively. I feel that on occasions in the past we did not devote sufficient attention to this fundamental obligation.' and 'In the past those who were involved in research did not

> *devote sufficient attention and effort to make their results readily accessible and usable [Professor Salamon's emphasis] by the practicing engineers.*

Professor Salamon's advice is as relevant today as it was over 30 years ago. The use of the CMRR, related geotechnical research and resultant design tools/software packages provided to Australian collieries is totally consistent with his advice.

REFERENCES

Barton, N and Bieniawski, Z T, 2008. RMR and Q – setting records straight, *Tunnels and Tunnelling International*, *February 2008*:26–29.

Bieniawski, Z T, 1973. Engineering classification of jointed rock masses, *Transaction of the South African Institution of Civil Engineers 15:*335–344.

Colwell, M and Frith, R, 2009. ALTS 2009 – A ten year journey, in *Proceedings of the 2009 Underground Coal Operator's Conference*, (ed: N Aziz and J Nemcik), pp 37–53 (The Australasian Institute of Mining and Metallurgy: Illawarra Branch).

Colwell, M and Frith, R, 2010. AMCMRR – An analytical model for coal mine roof reinforcement, in *Proceedings of the 29th Conference on Ground Control in Mining*, pp 38–45 (West Virginia University).

Colwell, M and Frith, R, 2012. Analysis and Design of Faceroad Roof Support (ADFRS) – A roof support design methodology for longwall installation roadways, ACARP report C19008.

Colwell, M and Frith, R, 2021. Utilising the scientific method to demonstrate that slender beam/column behaviour is the dominant behavioural mechanism leading to roof/rib failure, *International Journal of Mining Science and Technology*, 2021;31(5):867–887.

Emery, J, Canbulat, I and Zhang, C G, 2020. Fundamentals of modern ground control management in Australian underground coal mines, *International Journal of Mining Science and Technology*, 2020;30(5):573–582.

Fabjanczyk, M W, Tarrant, G C and Guy, R J, 1992. Summary Report No.1 – Assessment and application of high capacity roof bolting systems, AMIRA report P207A.

Galvin, J M, 2016. *Ground Engineering – Principles and Practices for Underground Coal Mining*, 684 p (Springer International: Switzerland).

Hoek, E and Brown, E T, 1980. *Underground Excavations in Rock*, 527 p (The Institution of Mining and Metallurgy: London).

Kleingeld, M, 2010. Simplification in engineering: contributing real value. Inaugural Lectures – Potchefstroom Campus. Potchefstroom: Noordwes-Universiteit, Potchefstroomkampus (Suid-Afrika).

Mark, C, and Molinda, G M, 2007. Development and application of the coal mine roof rating (CMRR), in *Proceedings of the International Workshop on Rock Mass Classification in Underground Mining*, pp 95–109 (NIOSH Information Circular 9498).

Oliveira, D A F and Pells, P J N, 2014. Revisiting the applicability of voussoir beam theory for tunnel design in Sydney, *Australian Geomechanics Journal 49(3):29–44.*

Palmström, A and Broch, E, 2006. Use and misuse of Rock Mass Classification systems with particular reference to the Q-system, *Tunnelling and Underground Space Technology, 21(6):*575–593.

Salamon, M D G, 1989. Significance of strata control to the safety and efficiency in mining, in *Proceedings of the 8th International Strata Control Conference*, Düsseldorf, Germany pp1–9.

Standards Australia. Concrete Structures. AS 3600–2001.

Rock mechanics in mining, civil and petroleum engineering

Optimal slope profiles for maximum mine pit-wall steepness in banded iron formation rocks

A Agosti[1] and S Utili[2,3]

1. CTO, OptimalSlope, London, W1S 4BS. Email: andrea_agosti@optimalslope.com
2. CEO, OptimalSlope, London, W1S 4BS. Email: stefano_utili@optimalslope.com
3. Professor of Geotechnical Engineering, Newcastle University, Newcastle upon Tyne, NE1 7RU.

ABSTRACT

The Overall Slope Angle (OSA) of pitwalls plays a crucial role in the financial return of an open pit mine. In current practice, pitwall profiles are designed to be planar in cross-section within each rock layer, ie the profile inclination across each layer tends to be constant. A new slope design software, OptimalSlope, has been recently proposed to determine the geotechnically optimal profile shapes for the pitwalls of mines. OptimalSlope seeks the solution of a mathematical optimisation problem where the overall steepness of the pitwall to be designed is maximised for an assigned stratigraphy, rock properties (unit weight and strength) and Factor of Safety. The geometry of the benches is provided as input to OptimalSlope. The results obtained so far on three mine case studies in isotropic rock masses (Utili *et al*, 2022; Agosti *et al*, 2021a, 2021b) show that optimal profiles are up to 5° steeper than their planar counterparts – ie the planar profiles exhibiting the same FoS – leading to realising significant saving on waste rock and as a consequence Net Present Value increments and carbon footprint reductions. OptimalSlope algorithms have been modified to deal with anisotropic rock masses characterised by direction dependent shear strength.

In the paper, the case of rock masses in banded iron formations (BIF) is tackled. A data set of anisotropic rock shear strengths typical of Western Australia is considered. The Snowden modified nonlinear model was employed to characterise the anisotropy of the rock mass shear strength.

From the OptimalSlope simulations performed emerges that optimal pitwall profiles can increase significantly the Overall Slope Angle in comparison with planar profiles featured by the same Factor of Safety. LEM stability analyses of all the profiles were also performed by Rocscience Slide 2 to independently verify the FoSs of the optimal profiles obtained.

INTRODUCTION

Anecdotal evidence that slope profiles nonlinear in cross-section, ie a profile whose inclination varies with depth, are better than linear ones was first reported as far back as 1890 (Newman, 1890). Almost a century later, Hoek and Bray, in chapter 12 of the second edition of Rock slope engineering (Hoek and Bray, 1977), analysed the stability of some concave circular slopes in cross-section. After that, the first systematic theoretical study on the mechanical properties of concave slope profiles for geomaterials exhibiting some cohesion, so applicable to all rocks and clayey soils, appeared in Utili and Nova (2007). By employing the upper bound theorem of limit analysis, they proved that logspiral profiles exhibit higher FoS than their planar counterparts for any value of *c* and φ considered. A fundamental limitation of the studies listed above is the assumption that the shape claimed to be optimal is found as the shape associated among curves belonging to a very restricted family and the assumption of uniform slope and no consideration of benches. More recently, a new geotechnical software, OptimalSlope (Utili, 2016), has been introduced which calculates the slope optimal profile for any specified lithological sequence without unduly restricting the search to any predefined family of shapes. To be able to quantify the gains of Net Present Value (NPV) and carbon footprint reduction in a consistent way in (Utili *et al*, 2022; Agosti *et al*, 2021a, 2021b) the open pit mines considered were designed twice employing the same pit optimiser software, economic parameters and optimisation strategy, with the only difference between the two designs being the pitwall profiles adopted. NPV gains of up to 53 per cent and carbon reductions of 600 000 t CO_2 were obtained.

In all the previous works the rock mass strength is isotropic as prescribed in the Generalised Hoek–Brown rock model whereas in this paper rock mass anisotropy is considered. Although the G-H-B is routinely employed by practitioners to characterise the rock mass behaviour, there is an increasing interest in the geotechnical community to account for rock mass anisotropy in the design of pitwalls.

In Agosti *et al* (2022) OptimalSlope was applied for the first time to anisotropic rocks employing an anisotropic model where both the cohesion and internal friction angle were prescribed as a function of angle of anisotropy to characterise the anisotropic behaviour of bedded sedimentary rocks with nine joint-sets. The model is very general since it can account for the presence of any number of joint-sets. Here instead OptimalSlope is applied to banded ironstone formations (BIF) of the Pilbara region and therefore a different anisotropic model was employed.

ROCK MATERIALS AND GEOTECHNICAL MODEL

Anisotropic strength models are employed to capture the effect of discontinuities on the rock mass strength. Mercer (2012) defines:

> *'An anisotropic strength model a constitutive model that describes the shear strength of an anisotropic rock mass in relation to the change in the angle between the plane of shear, and either the predominant plane of weakness of the rock fabric or the predominant orientation of major structural weakness.'*

The so called Snowden models were formulated and calibrated to capture the anisotropic behaviour of the banded ironstone formations (BIF) of the Pilbara region in Western Australia (Mercer, 2012, 2013; Bar *et al*, 2016). Here we employed an experimentally derived model to characterise the anisotropic shear strength of four BIF units in the Pilbara region (see Figure 1). The shear strength parameters for four types of rock from the Hamersley Group of the Pilbara region (see Figure 1a) were determined by Mercer (2013) on the basis of virtual shear box tests with input parameters such as GSI, UCS, JRC. Also Mercer (2013) provides the normalised shear strength – angle of anisotropy relationships experimentally determined at a normal stress of 500 kPa (see Figure 1b). Because the normal stress applied may affect the relationships due to the pressure dependency exhibited by rock shear strength, assuming a unit weight of 26.2 kN/m³ we considered the design of a slope 195 m high so that the average confining stress in the slope is around 500 kPa. A typical bench height of 15 m was assumed so that 13 benches result.

To characterise the anisotropic rock strength for the simulations we performed in OptimalSlope and Slide 2 we calculated the cohesion and friction angle at every degree of the angle of anisotropy using the relationships provided in Figure 1b and assuming the same strength reduction with the angle of anisotropy for both cohesion and angle of internal friction, for instance for a normalised shear strength of 0.40 we calculated $c_{0.4} = (c_{max} - c_{min}) * 0.4 + c_{min}$ and likewise $tan\varphi_{0.4} = (tan\varphi_{max} - tan\varphi_{min}) * 0.4 + tan\varphi_{min}$.

(a)

Unit	Type	GSI	UCS (MPa)	m_i	JRC	JCS	Phi_b (°)	Cohesion (kPa)	Friction	Tau BB (kPa)	Tau HB (kPa)	Strength ratio
BIF Units												
Dales (DG)	Rock mass	50	33	10				385	53°		1037	0.20
Dales (DG)	Bedding				2.5	24	18	11	21°	204		
Newman (MN)	Rock mass	43	37	10				328	52°		981	0.25
Newman Shale Band	Bedding				3	4	23	14	25°	241		
Shales												
McRae (MCR)	Rock mass	44	15	7				223	41°		660	0.37
McRae (MCR)	Bedding				2.5	15	22	12	26°	241		
West Angela (WA)	Rock mass	26	12	6				140	30°		434	0.48
West Angela (WA)	Bedding				3	16	18	13	21°	207		
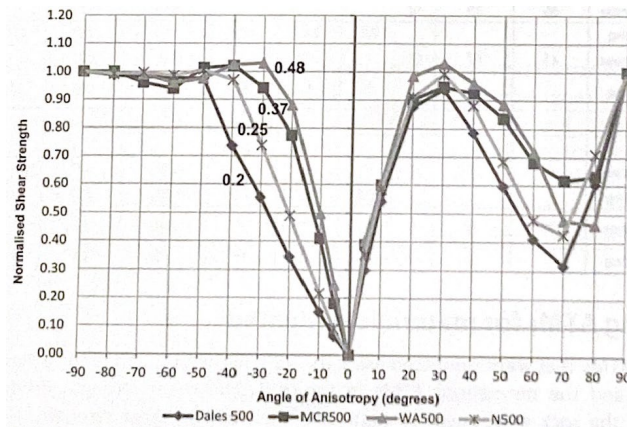
(b)

FIG 1 – (a) strength parameters for the rock mass and bedding of the four BIF units considered (after Mercer, 2013); (b) experimentally determined normalised shear strength versus angle of anisotropy of the BIF units (after Mercer, 2013).

RESULTS

Albeit OptimalSlope can be applied to any complex stratigraphy made of different rock layers (see for instance Agosti *et al*, 2021a), for sake of model simplicity we considered only uniform slopes in this exercise. We considered the two BIF units at the extreme of the spectrum in terms of the strength difference between rock mass and bedding, ie the Weathered Dale Gorge (Dales in Figure 1a) and the West Angela shale, exhibiting the highest and lowest difference respectively. A bedding orientation of 90 degree to the horizontal was chosen for the simulations so that slope stability is affected by both bedding and rock mass strength.

To quantify the benefit provided by the adoption of optimally shaped pitwalls, first we designed planar pitwalls by trial and error by changing the inclination of the slope until the target Factor of Safety of 1.3, calculated by performing Slide 2 simulations with the Morgenstein-Price method, was met (Figure 2a). Then we ran OptimalSlope to determine the optimally shaped pitwall for that same Factor of Safety (Figure 2b).

(a)   (b)
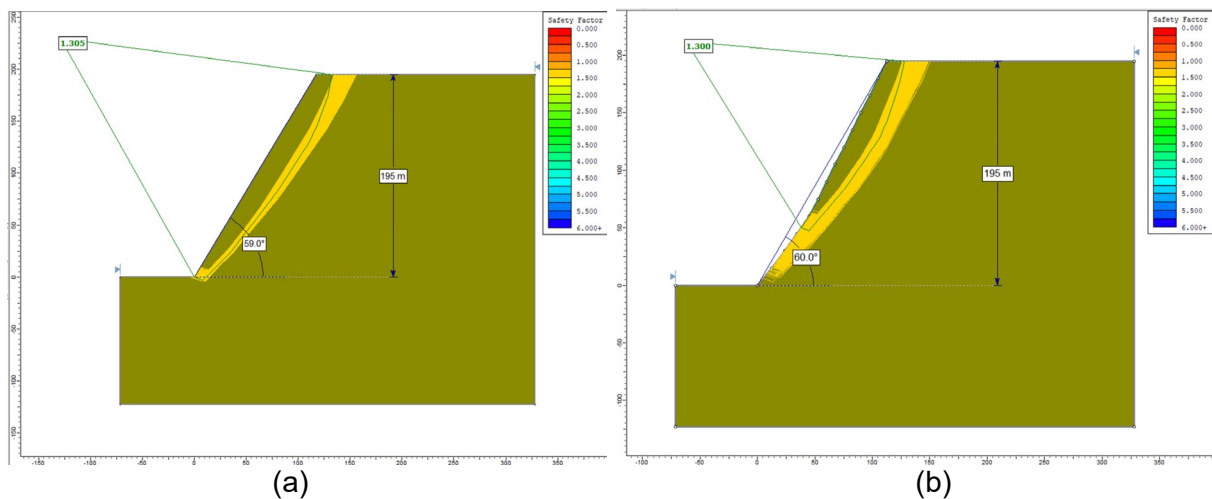
FIG 2 – Designed pitwalls for the Weather Dale Gorge with a target FoS of 1.30: (a) planar pitwall; (b) optimally shaped pitwall calculated by OptimalSlope. Note benches are not included in the image but their geometry has been accounted for in determining the optimally shaped pitwall.

In the case of Weathered Dale Gorge, the optimally shaped profile exhibited a gain of 1.0° steepness whilst in the case of West Angela shale, the gain was of 1.6° (31° inclination for the optimal profile instead of 29.4° for the planar one). In previously analysed case studies of open pit mines (Utili *et al*, 2022; Agosti *et al*, 2021a, 2021b), a one degree gain in steepness corresponds to a cost saving of USD15 million on average.

CONCLUSIONS

Pitwalls were designed for a data set of anisotropic banded iron formations (BIF) typical of Western Australia is considered whose anisotropic strength was characterised by an experimentally derived nonlinear model.

Optimally shaped pitwalls were calculated by the software OptimalSlope (Utili, 2016) for two BIF formations featured by the highest and lowest difference between rock mass and bedding strengths so at the ends of the spectrum of values presented in Mercer (2013), see Figure 1a. From the calculations it emerges that optimal pitwall profiles can meaningfully increase the Overall Slope Angle in comparison with planar profiles featured by the same Factor of Safety. LEM stability analyses of all the profiles were also performed by Rocscience Slide 2 to independently verify the FoSs of the optimal profiles obtained.

REFERENCES

Agosti, A, Cylwik, S and Utili, S, 2022. Geotechnically optimal profiles to maximise pit-wall steepness in anisotropic bedded sedimentary rocks, *Rock Mechanics and Rock Engineering,* under review.

Agosti, A, Utili, S, Gregory, D, Lapworth, A, Samardzic, J and Prawasono, A, 2021a. Design of an open pit goldmine by optimal pitwall profiles, *CIM Journal*, 12(4):149–168.

Agosti, A, Utili, S, Valderrama, C and Albornoz, G, 2021b. Optimal pitwall profiles to maximise the Overall Slope Angle of open pit mines: the McLaughlin mine, *Proceedings of the Slope Stability in Mining Conference 2021*, pp 69–82 (Australian Centre for Geomechanics, Perth).

Bar, N, Johnson, T and Weekes, G, 2016. Using directional shear stress models to predict slope stability in highly anisotropic rock masses, *Rock Mechanics and Rock Engineering: From the Past to the Future*, Cappadocia, Turkey, pp 595–600. https://doi.org/10.1201/9781315388502–103

Newman, J, 1890. *Earthwork slips and subsidences upon public works*, E & F N Spon, London.

Mercer, K G, 2012. The history and development of the anisotropic linear model: part 1, *Australian Centre for Geomechanics Newsletter*, July 2012.

Mercer, K G, 2013. Ongoing research into anisotropic rock masses using numerical modelling, P Dight (ed.) in *Proceedings of the Slope Stability in Mining Conference 2013*, pp 237–247 (Australian Centre for Geomechanics, Perth).

Hoek, E and Bray, J, 1977. *Rock Slope Engineering*, The Institution of Mining and Metallurgy, London.

Utili, S, 2016. OptimalSlope: Software for the determination of optimal profiles for slopes and pit-walls, US Copyright Registration TXu 2–254–159, https://www.optimalslope.com

Utili, S, Agosti, A, Morales, N, Valderrama, C, Pell, R and Albornoz, G, 2022. Optimal pitwall shapes to maximise financial return and decrease carbon footprint of open pit mines, Mining Metallurgy Exploration, 39:335–355. DOI 10.1007/s42461–022–00546–8

Utili, S and Nova, R, 2007. On the optimal profile of a slope, *Soils and Foundations,* 47:717–729. https://doi.org/10.3208/ sandf.47.717

An analysis of impact of weak rock formation on mining-induced deformation of rock slope

C A Amagu[1], C Zhang[2], J Kodama[3], K Shioya[4], T Yamaguchi[5], A Sainoki[6], D Fukuda[7], Y Fujii[8], M Sharifzadeh[9] and S Saydam[10]

1. PhD student, Rock Mechanics Laboratory, Graduate School of Engineering, Hokkaido University, N13 W8, Kita-Ku, Sapporo 060-8628, Japan. Email: amaguclementglk@gmail.com
2. MSc student, Rock Mechanics Laboratory, Graduate School of Engineering, Hokkaido University, N13 W8, Kita-Ku, Sapporo 060-8628, Japan.
    Email: zhangcheng1031@yahoo.co.jp
3. Associate Professor, Rock Mechanics Laboratory, Graduate School of Engineering, Hokkaido University, N13 W8, Kita-Ku, Sapporo 060-8628, Japan. Email: kodama@eng.hokudai.ac.jp
4. Nittetsu Mining Co. Ltd., Yusen Building, 3-2, Marunouchi 2-Chome, Chiyoda-Ku, Tokyo 100-8377, Japan. Email: k-sioya@nittetsukou.co.jp
5. Nittetsu Mining Co. Ltd., Yusen Building, 3-2, Marunouchi 2-Chome, Chiyoda-Ku, Tokyo 100-8377, Japan. Email: yamagutt@nittetsukou.co.jp
6. Associate Professor, International Research Organization for Advanced Science and Technology, Kumamoto University, Kumamoto 860-8555, Japan.
    Email: atsushi_sainoki@kumamoto-u.ac.jp
7. Assistant Professor, Rock Mechanics Laboratory, Graduate School of Engineering, Hokkaido University, N13 W8, Kita-Ku, Sapporo 060-8628, Japan.
    Email: d-fukuda@frontier.hokudai.ac.jp
8. Professor, Global Resources and Environmental Systems Laboratory, Graduate School of Engineering, Hokkaido University, N13 W8, Kita-Ku, Sapporo 060-8628, Japan.
    Email: fujii6299@frontier.hokudai.ac.jp
9. Associate Professor, Key Laboratory of Ministry of Education for Safe Mining of Deep Metal Mines, Northeastern University, Shenyang, 110819, China. Email: most.sharif@gmail.com
10. Professor, UNSW Sydney NSW 2052 Australia. Email: s.saydam@unsw.edu.au

ABSTRACT

In an open pit mining, ensuring stability of rock slope has been one of the major challenges. As the instability of rock slopes can results in slope failures; consequently, endanger the lives of workers, affect mining operations, and often lead to economic losses. Therefore, it is practical important to study the stability of rock slopes to ensure safe, smooth, and effective mining. The stability of rock slope of about 130 m height at Higashi-shikagoe limestone quarry, which has experienced slope failures four times since 1996, was assessed. The rock mass at the quarry is consists of mainly limestone, schalstein and slate rocks intersected by clay seams of about 70 m thick at footwall of the rock slope. Previously, the effects of limestone excavation at the foot of the rock slope and shear failure due to rainfall infiltration have been investigated. Although clay is widely known to plays a vital role in the stability of slopes in engineering projects including mines, but its impacts on slope deformation at the study quarry are not adequately examined. Therefore, the present study addressed the impact of presence of clay on slope deformation at Higashi-shikagoe limestone quarry by employing both field displacement measurements and numerical simulation. Firstly, surface displacements measured by automated polar system (APS) for over eight years were analysed to understand the overall characteristics of the slope deformation. The measured results show that the displacement gradually decreases with time. The maximum displacement of about 100 mm was observed at middle of the rock slope. Secondly, the effect of deterioration and plastic behaviour of the thick clay layer were simulated using two-dimensional finite element method (2D FEM). The simulated results reveal that the clay exhibited deterioration by water contact and plastic behaviour arising from mining activities at the footwall of the clay zone. Based on the characteristics of the measured and simulated results, it was found that the displacement induced by the effect of deterioration of clay is more noticeable at the north side of the quarry whereas displacement induced by excavation is quite significant at the south side of the quarry if clay behaves as an elasto-plastic material.

INTRODUCTION

Excavation activities at open pit mines; mostly during the operation stage often causes stress redistribution arising of release of gravity and horizontal rock stresses. Significantly, these affect the strength, failure mode and deformational behaviour of rock slope (He, Feng and Sun, 2008; Kodama, Nishiyama and Kaneko, 2009). In that light, ensuring stability of rock slopes during an operation stage has been a major challenge in an open pit mining, particularly when the rock mass included weak rock formation (clay seam). This is because stress redistribution near the working face in the mine often becomes complicated as the mining continues with excavation activities (He, Feng and Sun, 2008). Therefore, understanding behaviour of rock mass in the mine subjected to continuous excavation are of great significance to the safe and efficient development process of mining activities (Willie and Mah, 2004).

Till date, extensive studies have been done on the stability of rock slopes subjected to continuous excavation (He, Feng and Sun, 2008; Li *et al,* 2020). Kodama, Nishiyama and Kaneko (2009) used 3D mesh technique to evaluated long-term deformation of a rock slope at Ikura limestone quarry, which are significantly affected by excavation progresses. He, Feng and Sun (2008) conducted a 3D model to assess the impact of excavation and backfill process on the stability of rock slope at Antaibao open pit coalmine. Kaneko *et al* (1996) and Obara *et al* (2000) used a 2D boundary element method to calculate rock slope deformation resulting from floor excavation in an open pit mine. They established that the rock slope above the floor contracted upon excavation when the ratio of horizontal stress to vertical stress is small; and extension when the ratio is larger. Nilsen (2011) concluded that slope excavation within the presence of swelling clay plays key role in causing instability of rock slope over time. As matter of fact, clay rocks also exhibit plastic deformation and/or squeezing when it is overstress due to excavation (Zhang, Sun and Zhang, 2018). The studies above indicate that excavation significantly affect rock slope deformation, thus the rock slope at the studied quarry is expected to deform if the clay exhibit plastic behaviour due to excavation at the footwall of the clay zone.

At the studied quarry, the effects of limestone excavation at the foot of the rock slope, the deterioration of about 70-m-thick clay layer at the rock slope footwall and shear failure owing to rainfall infiltration on the rock slope deformation have been investigated (Amagu *et al,* 2021); but the impacts of clay deterioration by water contact and plastic behaviour of the clay due to excavation at the footwall of the clay zone on the slope deformation were not adequately examined. Therefore, this study aimed at clarifying the effects of deterioration and plastic behaviour of the clay layer on mining-induced deformation. To achieve these, the mechanism of the slope deformation was clarified by analysing surface displacements of the rock slope measured by automated polar system (APS) for over eight years. Afterward, the relationship between the characteristics of the slope deformation and elevation of the quarry was established. Subsequently, displacement induced by the effect of clay deterioration and the effect of plastic behaviour of the clay resulting from excavation at the foot of the clay zone were simulated by 2D finite element methods. Finally, the possible causes of the deformation were assessed by comparing the tendencies of the measured results with simulated results of the surface displacement along the rock slope.

GEOLOGICAL AND DISPLACEMENT CHARACTERISTICS OF THE ROCK SLOPE

Geological conditions of the rock slope

The Higashi-shikagoe limestone quarry is an open pit quarry with an annual production of 200 000 t located at Hokkaido prefecture, Japan. The rock mass at the quarry is characterised by complex geological formation, which consists of limestone, schalstein and slate rocks. The schalstein and slate rocks have weathered forming clay seams of about 70 m thick at footwall of the rock slope (elevations of 440–370 m), which likely affects the slope deformation. The limestone on the floor of the quarry has been excavated by bench cut method forming slope height of about 130 m. The quarry was designed with bench height of 10 m at an average slope angle of about 42°. The quarry has experienced slope failures four times from 1996 to 2017 as shown in Figure 1. At present, mining operation has been undertaken at 340 m and 400 m levels whereas backfilling has been done on the northern side of the quarry (Figure 1). The major geological structure in the quarry is

characterised as a right lateral fault, which strike and dip at N70° E-80° S and N70° E-75° N, respectively. Because of the discontinuous nature of the rock mass, pre-split blasting is used to cushion it from vibrations induced by the main blast.
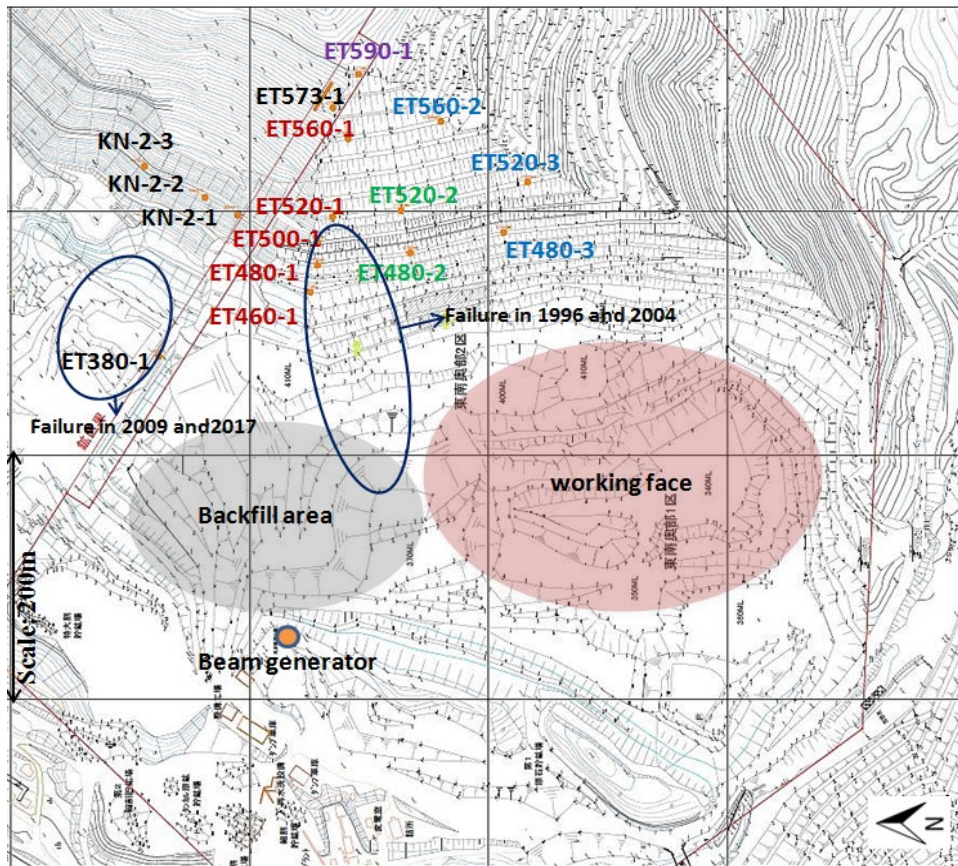
FIG 1 – Map showing the APS layout at the quarry. The ET represents the mirror point locations of automated polar system (APS) set on the rock slope. Each mirror point is represented with a number that indicates its level of elevation.

Measured results

The surface measurement between each of the mirror points and the beam generator point are shown in Figure 2. The APS measured travelling times of laser beam from a beam generator to each mirror (designated as ET) located at various elevation along the slope (Figure 1). Change in distances from 11 APS monitoring mirrors (see Figure 1), from January 1, 2014 to July 30, 2021 were analysed to understand the overall characteristics of slope deformation. As shown in Figure 2, there is a constant decrease in the distances with time. The change in distances trends with similar displacement rate at each mirror point. This implies that the rock slope shows no acceleration for the period of eight years, although it still exhibits continuous displacement. Hence, the assessed rock slope is expected to be stable. Figure 3 shows the relationship between the measured displacement and elevation of the quarry. The measured result was correlated with elevations of the quarry at north side of the quarry (ET460–1, ET480–1, ET500–1, ET520–1 and ET560–1) and south side of the quarry: ET480–3, ET520–3 and ET560–2) for comparison purpose with the simulated results. From Figure 3, the displacement is seen being greatest at middle of the slope (elevation 520 m) in the north side of quarry but greatest at the foot of the slope (elevation 460 m) in the south side of the quarry. Hence, this indicates that the probable causes of the slope deformation depend on the position of the quarry.
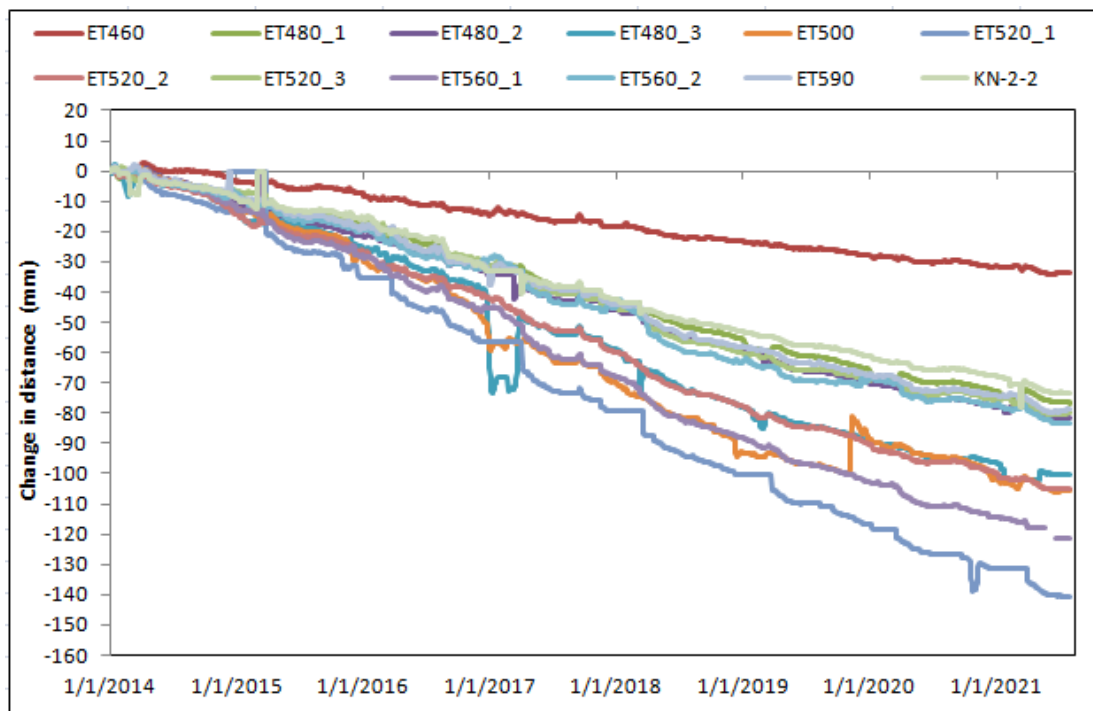
FIG 2 – Change in distance with time for eight years.
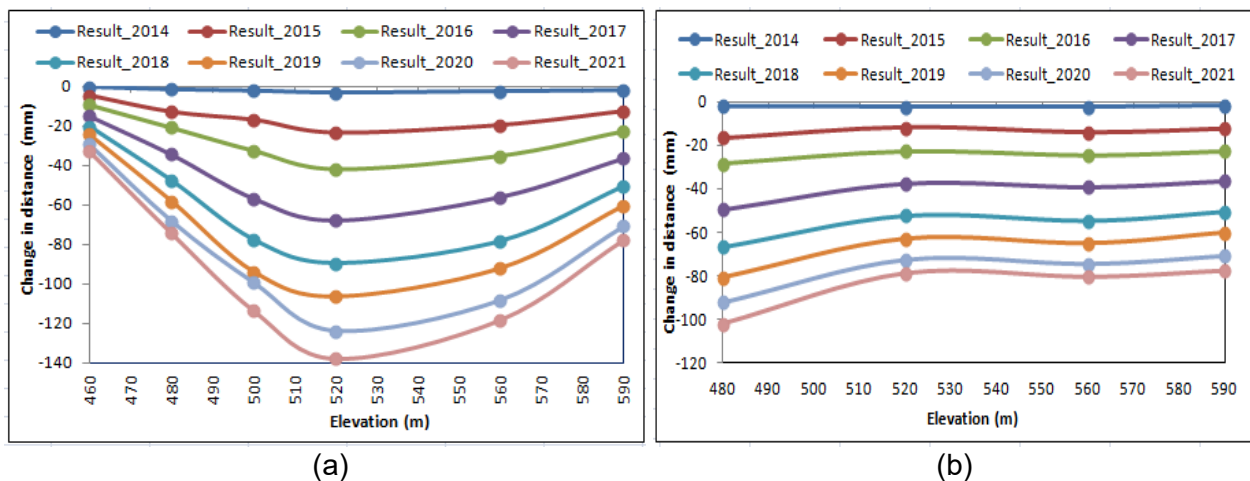

| (a) | (b) |

FIG 3 – Relationship between measured results and elevations at the north-side (a) and at the south-side (b) of the quarry.

ANALYTICAL METHOD AND RESULTS

Analytical method

In the model, the materials are grouped as hard rock mass and clay rock as shown in Table 1. The main rock types: the limestone, schalstein and slate rocks were modelled as homogeneous hard rock mass by using 2 Dimensional Finite element methods (2D FEM).

A finite element mesh (Figure 4a) was generated using six-node triangular elements based on the elevations read from the contour map of the cross-sectional areas as shown in Figure 4b, using commercial software, MIDAS GTS/NX 2014 (V2.1). The excavation model of the quarry in terms of excavation level progressing from 2015 to 2019 was also generated as shown in Figure 5. The model has a dimension of 830 m in vertical direction and 1489 m in horizontal direction. The total number of elements and nodes in the model are 24512 and 12488, respectively. The mechanical properties presented in Table 1, which were adopted from the previous studies (Obara *et al*, 2000; Chai and Miura, 1999) and triaxial laboratory tests were used. The analyses were carried out under a plane-strain condition. The nodal displacement perpendicular to the right, left and the bottom surface of

the model were fixed at zero. Afterwards, change in distance between several points along surface of the slope surface at different elevations and beam generator points were calculated. Also, the displacement vector along the slope surface and the beam generator point in the blue rectangle (Figure 4a) are shown.

TABLE 1
Mechanical properties of the rock materials.

Parameters	Hard rock mass	Clay
Material type	Isotropic	
Material model	Elastic/Mohr–Coulomb	
Unit weight, γ (kN/m³)	26.20 [a]	18.00 [b]
Young's modulus, E (GPa)	63.00	0.05 [c]
Poisson's ratio, v	0.20 [a]	0.30 [b]
Cohesion, c (MPa)	30 [c]	0.04 [b]
Friction angle, ϕ (°)	50.00 [c]	35.00 [b]

[a] Obara *et al* (2000); [b] Adopted from Chai and Miura (1999); [c] Estimated from laboratory test.

(a)   (b)
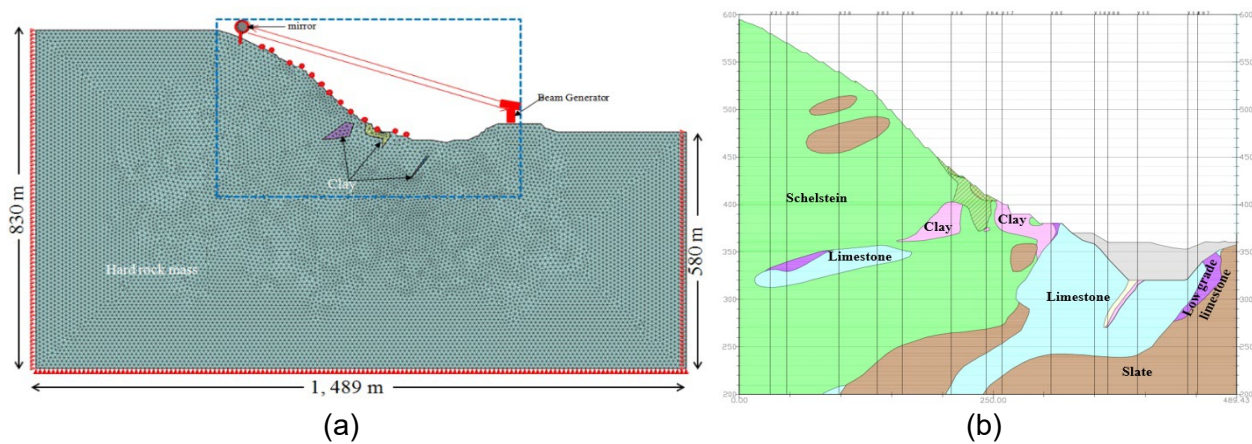
FIG 4 – Entire analytical model (a) and geological cross-section of the quarry (b). The change in distance between several red points along the slope surface at different elevations and beam generator point were analysed for comparison with the measured results.
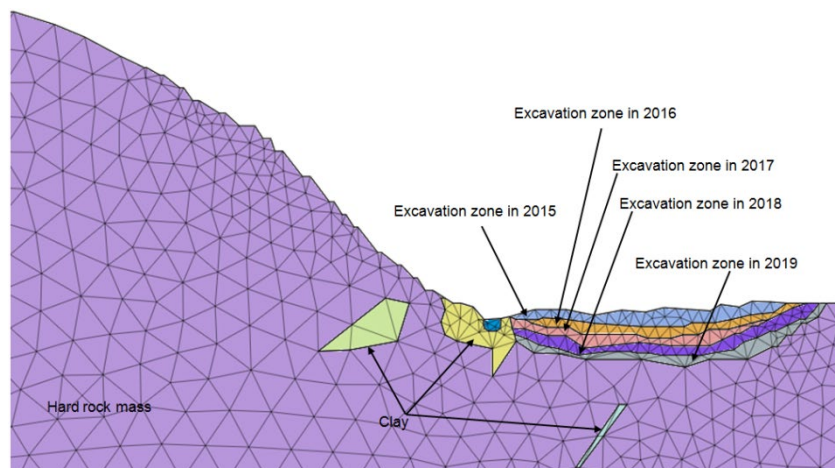

FIG 5 – FEM meshes in terms of excavation level progressing yearly, in blue dotted rectangle in Figure 4a.

Analytical results and discussion

Effect of deterioration of clay on slope deformation

Two basic cases (deterioration case and plastic case) were simulated following the model conditions as described in the *Analytical method* section. At first, effect of the deterioration of clay on the slope deformation was modelled in terms of reduction in Young's modulus of the clay from 50.0 to 20.0 MPa. Initially, the Young's modulus of clay was set to 50.0 MPa, and then assumed to deteriorate to 20.0 MPa by water contact, whereas the Young's modulus of the hard rock was set to 63.0 GPa (Table 1). The displacement induced by the reduction in Young's modulus of the clay was calculated as deterioration case. Afterward, the change in the state of clay from elastic to plastic was simulated by assuming clay as a perfect elasto-plastic material. Subsequently, relative displacement due to the change in state of clay from elastic to plastic was calculated as plastic case.

Figure 6 show the displacement vectors along the slope surface of both cases. Figure 7 show the change in distance along the slope (elevation of 460–590 m) calculated from the displacement vectors. As seen in Figure 6a, the displacement vectors shows that the rock mass slide downward from the top to the toe of the slope surface and within the clay zone. Conversely, the vector indicates yielding occurred only within clay zone as the rock mass moved downward with negligible magnitude of displacement as shown in Figure 6b. This suggests that yielding occurred only within clay zone. In Figure 7, the distance along the slope surface (elevations of 460–590 m) decreased due to clay deterioration but slightly increased when clay exhibits plastic behaviour; with the greatest rate seen at the middle of the rock slope. As seen in Figure 7, the magnitude of the simulated values was highly lower than that of measured results. Thus, the analytical results cannot quantitatively describe the measured results. In that regard, the slope deformation was described qualitatively by comparing the tendency of the simulated result with the measured results (Figure 3). The calculated results for deterioration case were in good agreement with the measure results (Figure 3a), suggesting that the clay deterioration has more significant effect on the slope deformation at the north side of the quarry than plastic behaviour of the clay. Thus, the rock slope at the quarry is expected to deform because of deterioration of thick clay layer distributed at the footwall of the rock slope as can be deduce from the comparison.

(a)   (b)
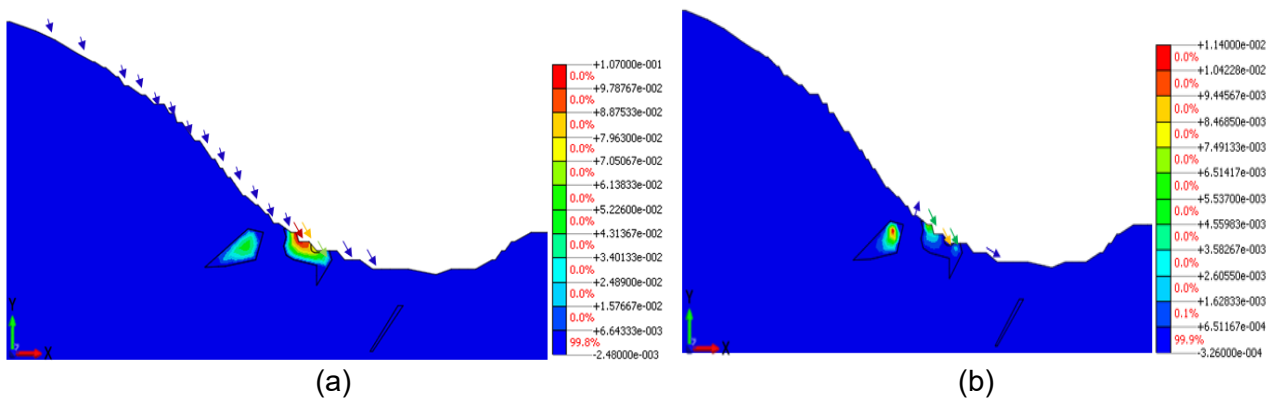
FIG 6 – Displacement (m) along the slope surface in the blue dotted rectangle in Figure 4a. (a) Displacement induced by deterioration of clay and (b) displacement induced by plastic behaviour of clay. The arrows indicate the direction of the displacement.
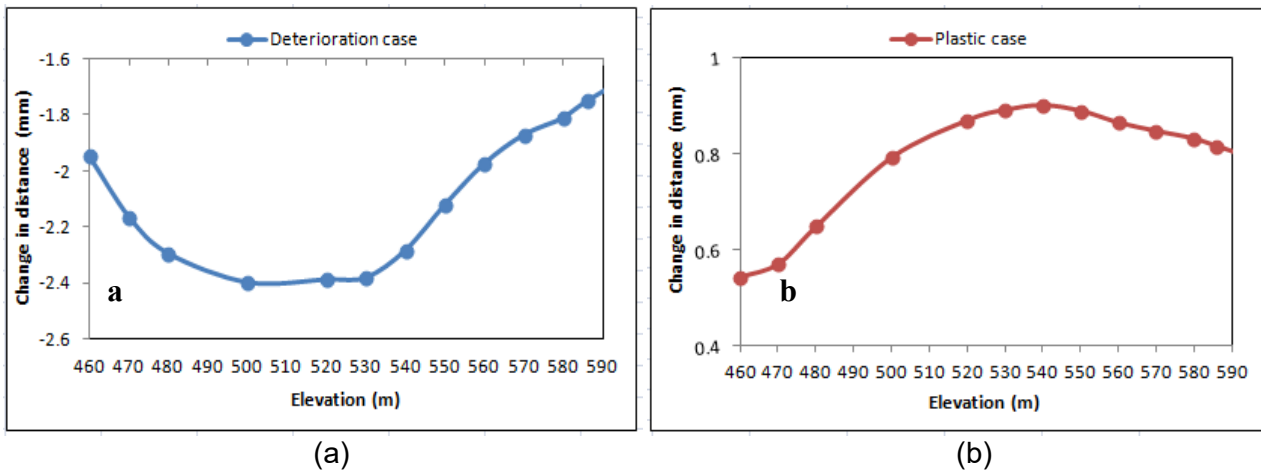
FIG 7 – Change in distance of the simulated results of displacement induced by deterioration of clay (a) and plastic behaviour of the clay (b).

Effect of mining-induced plastic behaviour of clay on the slope deformation

It is expected that the rock slope can be deformed by plastic behaviour of clay resulting from stress state change due to excavation. To clarify the above factor, mining-induced plastic behaviour of clay simulated under elasto-plastic analysis was analysed. The excavation model shown in Figure 5, showing excavation at foot of clay zone progressing from 2015 to 2019 was used. The mechanical properties presented in Table 1, were used. Two stress conditions (displacement induced by release of horizontal rock stress and gravity) were applied. The analytic conditions of the model are the same with the conditions described in the *Analytical method* section except that horizontal rock stress (σxx) of 1 MPa was applied to the right-hand side of the model while simulating displacement induced by release of horizontal rock stress. In both two stress conditions, the hard rock mass and clay were assumed to be elastic and elasto-plastic materials, respectively. The displacement increment resulting from plastic behaviour of clay due to excavation was calculated.

Figure 8 shows example of surface displacement vector of the rock slope. The change in distance calculated from displacement along the slope surface at each elevation and beam generator point are shown in Figure 9. The calculated results of elastic analysis were included in Figure 9 for comparison with the results of elasto-plastic analyses. From Figure 8a, the vectors shows that the rock mass moved forward from the top to the middle of the slope but moved downward at the toe of the slope due to release of horizontal stress. In contrast, the rock mass moved upward-leftward at the top but moved upward at the toe of the slope due to release of gravity as seen in Figure 8b. The calculated distance decreases due to release of horizontal stress, but increases due to release of gravity, in both cases of elastic and elasto-plastic analysis as seen in Figure 9. Although, magnitude of displacement from elasto-plastic analysis is notably greater than that of elastic analysis.
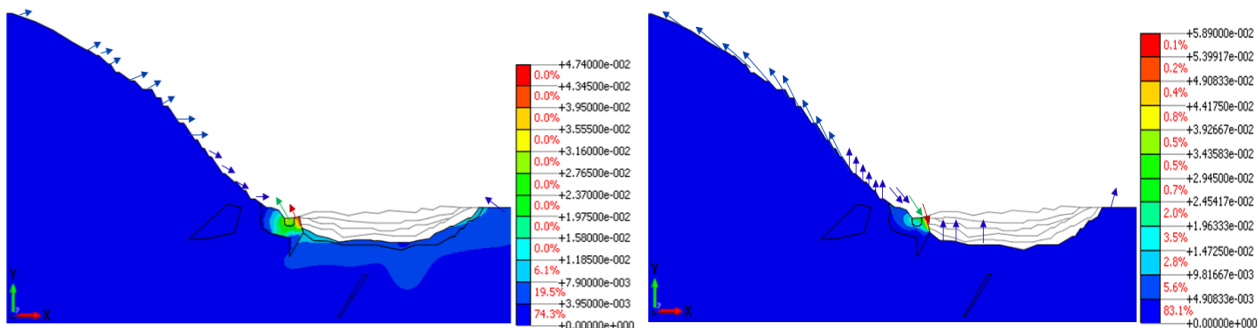
FIG 8 – Examples of surface displacement vector at along slope induced by excavation due to release of horizontal stress (a) and gravity (b) in 2019 at the blue dotted rectangle in Figure 4a. The arrows indicate the directions of the displacement.
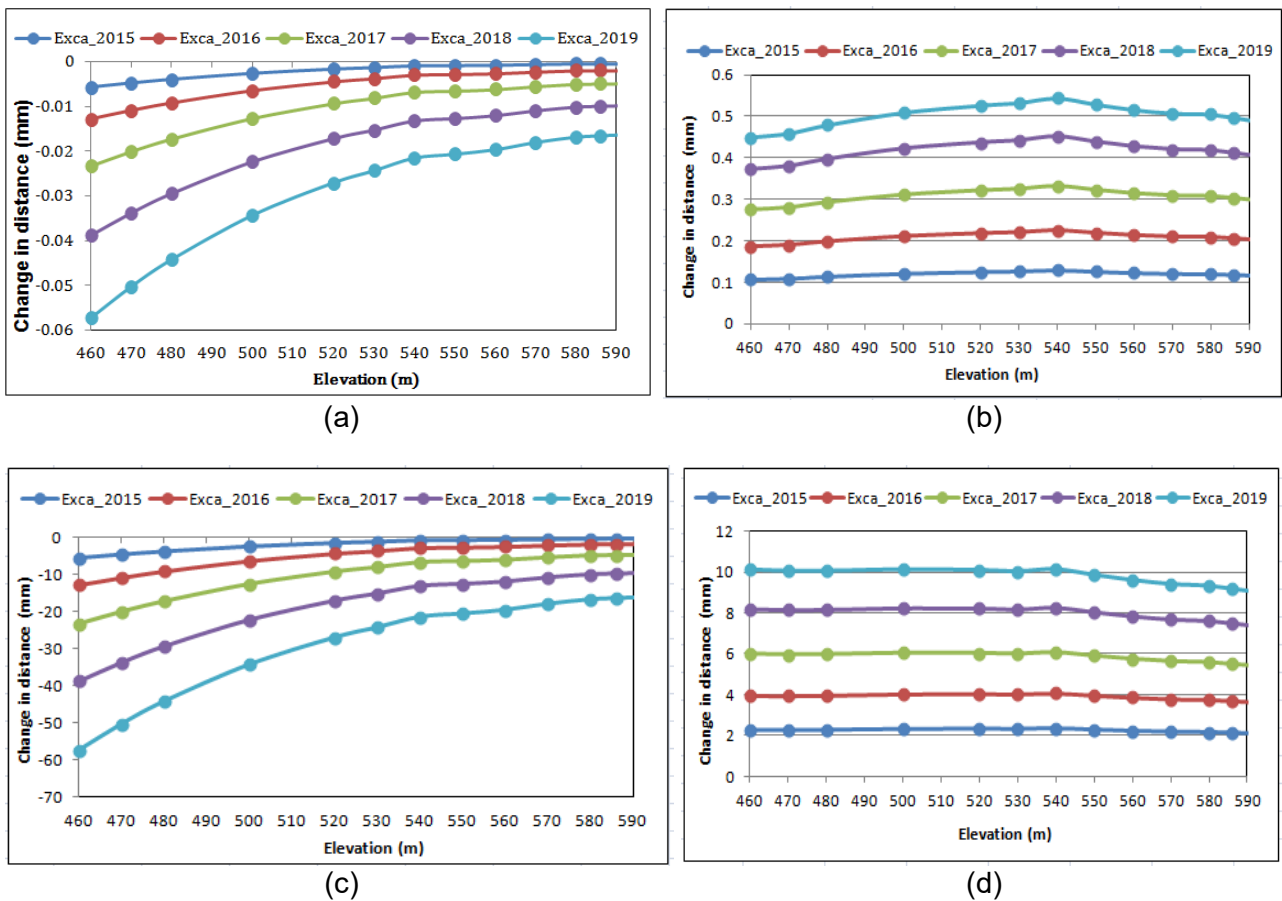
FIG 9 – Calculated change in distance from surface displacement induced by excavation due to release of horizontal stress (a) and gravity (b) under elastic analysis, and excavation due to release of horizontal stress (c) and gravity (d) under elasto-plastic analysis.

The calculated results also reveal that the decreasing and increasing rate of distance due to release of horizontal stress and gravity, respectively, were seen being greatest at the foot of the slope. The calculated results using tendency of displacement were in good agreement with measured results (Figure 3b), mostly the result of Figure 9a, Figure 9c. This implies that the release of horizontal rock stress arising from excavation strongly affected the slope deformation at south side of the limestone open pit quarry than that of gravity. It can be seen from Figure 9c, that the calculated values of displacement induced by the release of horizontal stress were somewhat closer to the measured results (Figure 3b). From the above, it is apparent that the elasto-plastic analysis can qualitatively and quantitatively describe the mining-induced deformation if clay behaves as an elasto-plastic material and horizontal rock stress is large enough with a smaller Young's modulus of rock mass.

CONCLUSIONS

Rock slope deformation arising from the presence of weak rock in Higashi-shikagoe limestone quarry was assessed using 2D finite element analysis. The comparison of the calculated results with the measured results provided a unique understanding of the impacts of the presence of clay on the rock slope deformation at the quarry.

The results of measured surface displacement showed that distance between the beam generator and mirrors at all elevations constantly decreased for over eight years. The decreasing rate of the distance differs at the north – and south-hand side of the quarry, suggesting different probable factors triggers the deformation at each side of the quarry.

To identify these causes, effect of deterioration of clay on the slope deformation was predicated by using the 2D meshes to model deterioration of clay in term of reduction in the Young's modulus of clay by water contact. Secondly, rock slope deformation induced by plastic behaviour of clay resulting from excavation was also analysed using model of excavation at foot of clay zone

progressing from 2015 to 2019. Based on the characteristics of the measured and simulated results, it can be deduced that the effect of deterioration of clay on the slope deformation is noticeable at the north side of the quarry whereas mining-induced deformation has significant effect on the slope deformation at south side of the quarry if clay exhibit elasto-plastic behaviour.

REFERENCES

Amagu, A C, Zhang, C, Kodama, J, Shioya, K, Yamaguchi, T, Sainoki, A, Fukuda, D, Fujii, Y and Sharifzadeh, M, 2021. Displacement measurements and numerical analysis of long-term rock slope deformation at higashi-shikagoe limestone quarry, Japan, *Advances in Civil Engineering*, 1316402, 15 p.

Chai, J C and Miura, N, 1999. Investigation on some factors affecting vertical drain behavior, *Journal of Geotechnical and Geoenvironmental Engineering*, 125(3):216–222.

He, M C, Feng, J L and Sun, X M, 2008. Stability evaluation and optimal excavated design of rock slope at Antaibao open pit coal mine, China, *International Journal of Rock Mechanics and Mining Science*, 45:289–302.

Kaneko, K, Noguchi, Y, Soda, K and Hazuku, M, 1996. Stability assessment of rock slope by displacement measurement, *Resources and Materials*, 112:915–920.

Kodama, J, Nishiyama, E and Kaneko, K, 2009. Measurement and interpretation of long-term deformation of a rock slope at the Ikura limestone quarry, *International Journal of Rock Mechanics and Mining Science*, 46:148–158.

Li, Q, Wang, Y M, Zhang, K B, Yu, H and Tao, Y Z, 2020. Field investigation and numerical study of a siltstone slope instability induced by excavation and rainfall, *Landslides*, 17:1485–1499.

Nilsen, B, 2011. Case of instability caused by weakness zones in Norwegian tunnels, *Bulletin Engineering Geology and Environment*, 70:7–13.

Obara, Y, Nakamura, N, Kang, S S and Kaneko, K, 2000. Measurement of local stress and estimation of regional stress associated with stability assessment of an open-pit rock slope, *International Journal of Rock Mechanics and Mining Science*, 37:1211–1221.

Willie, D C and Mah, C W, 2004. *Rock Slope Engineering*, 4th edition, Spon Press, New York, pp 320–327.

Zhang, W, Sun, Q and Zhang, Y, 2018. Correlation analyses of effects of temperature on physical and mechanical properties of clay, *Environmental Earth Sciences*, 77(17):614.

Data mining in rock mining – predicting mechanical properties of carbonate rocks using hyperspectral remote sensing

D Bakun-Mazor[1], Y Ben-Ari[2] and E Ben-Dor[3]

1. Department of Civil Engineering, Shamoon College of Engineering, Beer-Sheva 8410802, Israel. Email: daganba@sce.ac.il
2. Department of Geophysics, Tel Aviv University, Tel-Aviv 6997801, Israel. Email: yoavbenari@mail.tau.ac.il
3. Department of Geography and Human Environment, Tel Aviv University, Tel-Aviv 6997801, Israel. Email: bendor@tauex.tau.ac.il

ABSTRACT

Determining the mechanical properties of rocks is important for various civil engineering fields, including the mining of raw materials for aggregates used in the construction and paving industries. Traditionally, the mechanical properties of rocks are obtained through *in situ* and laboratory tests during geotechnical surveys. However, these time-consuming surveys involve many resources. In contrast, hyperspectral remote sensing methods make it possible to identify the mineralogical composition and crystallographic structure of the rock; properties that control the mechanical properties of the rocks. In this work, we characterise the mechanical properties of carbonate rocks by using a hyperspectral sensor in laboratory conditions.

We collected about 150 cylindrical samples of carbonate rock, with a wide range of strength values from several rock outcrops in Israel. We used a point spectrometer in the range of 0.4–2.5 μm and a spectral image sensor in the range of 3.0–12.0 μm, scanning the samples to obtain the signature of their light reflections and spectral emissivity. We then measured the samples' density, porosity, water absorption, and uniaxial compressive strength (UCS). We used sophisticated data mining to find statistical relationships between the hyperspectral signatures of the samples and their mechanical properties. We used this data to identify the most dominant wavelengths for predicting mechanical properties. We found that the density, porosity, and water absorption of carbonate rocks could be confidently predicted based on spectroscopy data, while the UCS of the rock could also be predicted, but less significantly.

The results of the study pave the way for the development of measuring tools for the mechanical properties of rock, based on non-destructive tests of quarrying materials.

INTRODUCTION

The Israeli construction and paving industries use natural aggregates for substrates for roads and concrete mixtures. The main source of aggregates is stiff limestone and dolomite from quarries in Canoman Torun rock formations (The Standards Institution of Israel, 1998), but reserves of these raw materials are limited. Hence, we need to optimise the use of natural quarrying materials while searching for recycled sources for alternatives. The optimisation process requires a tool that enables quick identification of the material reserves in the quarry walls while supervising the quality of the quarried material.

Geotechnical characterisation of quarrying materials includes measuring rock properties such as density, porosity, water absorption, and uniaxial compression strength UCS of rock samples. Traditional methods for the geotechnical characterisation of quarrying materials are based on laboratory tests. These tests are time-consuming and are performed on relatively small samples from the quarried material, which does not always represent the entire material. In contrast, hyperspectral remote sensing methods make it possible to identify the mineralogical composition and crystallographic structure of the rock.

Passive remote sensing is generally described as the measurement of reflected or emitted electromagnetic radiation (EMR). The visible to near-infrared (VNIR) range of reflected EMR is dominated by electronic processes that produce broad absorptions in wavelengths of 0.4–1.0 μm. The short wave infrared (SWIR) range of reflected EMR is dominated by overtone and the combination modes of fundamental molecular vibration processes that produce sharp absorptions

in wavelengths of 1.0–2.5 μm. The thermal infrared (TIR) range is emitted (with some reflected EMR that is also dominated by molecular vibration processes) and produces both sharp and broad absorptions in wavelengths of 3.0–12.0 μm. This absorption enables mineral recognition and geology mapping by hyperspectral remote sensing (eg Kruse, 2012; van der Meer *et al*, 2012; Notesco *et al*, 2015). In this study, we seek to examine the use of hyperspectral remote sensing methods to identify the mechanical properties of carbonate rocks.

DATA COLLECTION

To establish empirical models between the hyperspectral signature of the surface of carbonate rocks and their mechanical properties, we collected about 150 samples of carbonate rock from several outcrops in Israel (Figure 1a). Rock blocks were drilled in the workshop to prepare cylindrical rock samples 54 mm in diameter and 110 mm long (Figure 1b, Figure 1c). Specimen ends were ground to a flatness of 0.02 mm to minimise end effects during pressing (Figure 1d, Figure 1e). We measure the surface reflectance spectra in the VNIR-SWIR range with the Analytical Spectral Devices (ASD®) spectroradiometer covering 2151 spectral bands with using a high-intensity contact probe (Figure 1f). We also measure the emissivity spectra of rock samples in the TIR range with a Telops Hyper-Cam hyperspectral sensor with 120 spectral bands (Figure 1g). We determine the UCS of the rock samples using a large hydraulic compression frame, manufactured by ELE, with an axial compressive loading capacity of 3000 kN (Figure 1h). We determine the remaining physical properties of the rock samples (Density, Porosity, Water absorption) in the laboratory, according to ISRM methods (Figure 1i).

FIG 1 – Data collection process (see text for details).

EMPIRICAL MODELS

We use PARACUDA-II® (Carmon and Ben-Dor, 2017), an automatic data-mining machine that searches for the best spectral combinations, to form a reliable spectral-based model for predicting the mechanical attribute in question. This engine has three major modules, each with a specific purpose in the modelling process: (1) outlier detection and elimination; (2) preprocessing and transformations, based on the 'all-possibilities-approach' in which all possible combinations are evaluated in the preprocessing implementation; and (3) model development and validation, based on partial least squares regression and a conditional Latin hypercube sampling algorithm (Carmon and Ben-Dor, 2017).

Figure 2a shows the empirical models obtained using the PARACUDA-II® data-mining machine. The best model was obtained after performing a first derivation on the spectral data during the preprocessing stage. The Root Mean Square (RMS) errors of the models are 34, 0.13, 0.05, 2.3, for UCS, density, water absorption, and porosity, respectively. Figure 2b shows the most indicative wavelengths used to perform the prediction on the tested population.
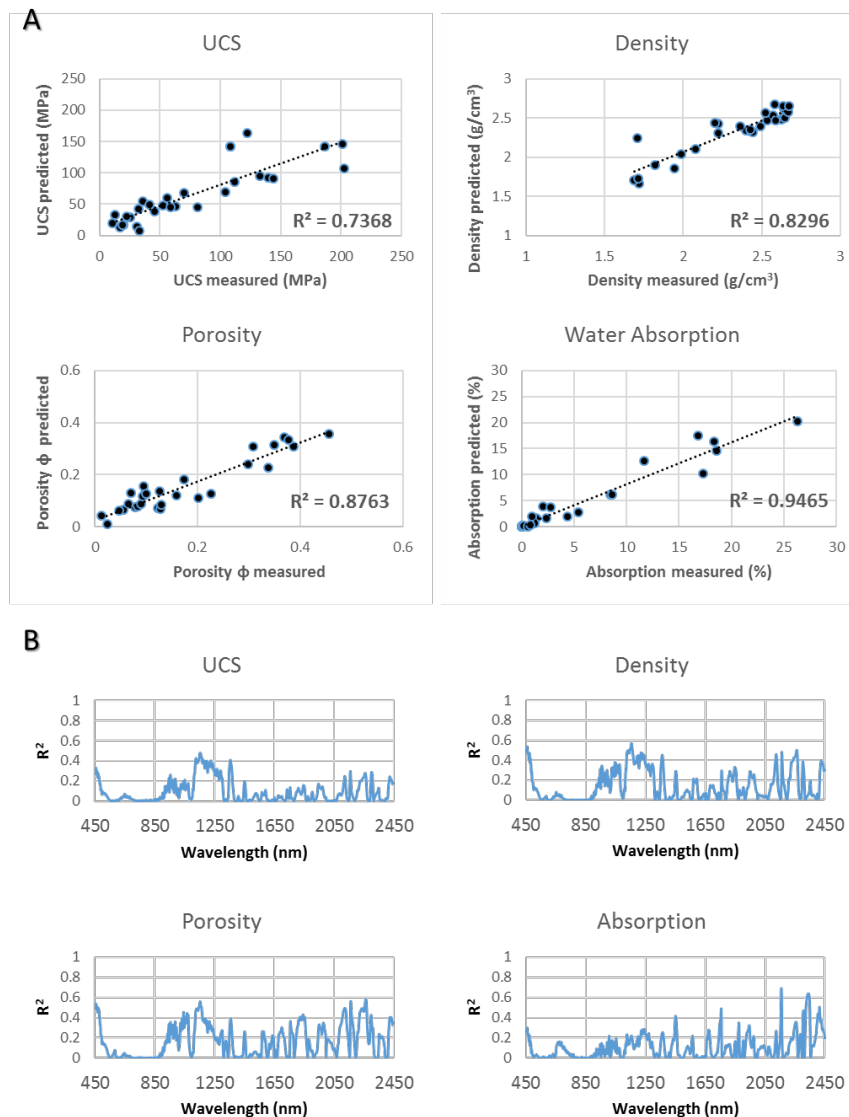
FIG 2 – (a) Prediction models, (b) Correlograms.

The results from the analyses performed on the emissivity spectra along the TIR spectral region are presented in Table 1. The correlations between the measured and the predicted values for the tested and the calibration sets are given by R-square coefficients (R^2_{Test}, and $R^2_{Calibration}$). The RMS is for the tested sets.

TABLE 1

Results of the models performed on the emissivity spectra (TIR range).

	R^2_{Test}	$R^2_{Calibration}$	RMS_{Test}	No. of Samples
UCS	0.75	0.59	33.94	134
Density	0.84	0.72	0.18	132
Absorption	0.82	0.57	5.30	137
Porosity	0.81	0.69	0.07	132

DISCUSSION

The validation models presented in Figure 2 are based on data obtained from 150 samples of carbonate rocks. The sample collection consists of rocks with a wide range of mechanical properties: from soft chalk to stiff limestone and dolomite. The models presented in Figure 2 were performed on

the entire sample collection, without distinguishing between dominant types of minerals. When performing the analysis on the sample population dominated by the calcite mineral only (Table 2), the model results indicate an even better correlation than the analysis of the entire sample collection before. The analysis performed on the emissivity spectra obtained along the TIR spectral region also yielded very encouraging results (Table 1).

TABLE 2

Results of the models performed on calcite samples only.

	R^2 Test	R^2 Calibration	RMS Test	No. of Samples
UCS	0.91	0.71	18	87
Density	0.96	0.95	0.09	93
Absorption	0.98	0.96	1.58	93
Porosity	0.98	0.95	0.03	93

CONCLUSIONS

For the first time, by using empirical research, it has been shown that the mechanical properties of carbonate rocks can be predicted by hyperspectral remote sensing. The results of the study pave the way for the development of measuring tools for the mechanical properties of rock, based on non-destructive tests on quarrying materials.

ACKNOWLEDGEMENTS

REFERENCES

Carmon, N and Ben-Dor, E, 2017. An advanced analytical approach for spectral-based modelling of soil properties, *IEEE Geosci Int J Emerg Technol Adv Eng,* 7:90–97.

Kruse, F A, 2012. Mapping surface mineralogy using imaging spectrometry, *Geomorphology,* 137:41–56.

Notesco, G, Ogen, Y and Ben-Dor, E, 2015. Mineral classification of Makhtesh Ramon in Israel using hyperspectral longwave infrared (LWIR) remote-sensing data, *Remote Sensing,* 7:12282–12296.

The Standards Institution of Israel, 1998. *Mineral aggregates from natural sources*.

Van Der Meer, F D, Van Der Werff, H M, Van Ruitenbeek, F J, Hecker, C A, Bakker, W H, Noomen, M F, Van Der Meijde, M, Carranza, E J M, De Smeth, J B and Woldai, T, 2012. Multi-and hyperspectral geologic remote sensing: A review, *International Journal of Applied Earth Observation and Geoinformation,* 14:112–128.

Using a Schmidt hammer to estimate geotechnical properties of carbonate rocks in Israel

D Bakun-Mazor[1], Y Ben-Ari[2] and N Trabelsi[3]

1. Department of Civil Engineering, Shamoon College of Engineering, Beer-Sheva 8410802, Israel. Email: daganba@sce.ac.il
2. Department of Geophysics, Tel Aviv University, Tel-Aviv 6997801, Israel. Email: yoavbenari@mail.tau.ac.il
3. Department of Mechanical Engineering, Shamoon College of Engineering, Beer-Sheva 8410802, Israel. Email: nirtr@sce.ac.il

ABSTRACT

As part of a comprehensive project to develop a remote sensing tool for evaluating the mechanical properties of rocks, one must obtain a rapid indication of these properties using conventional field methods. A common method for evaluating the mechanical properties of rocks in the field is to use a Schmidt hammer, a portable device that measures the rebound (R) of a spring-loaded mass impacting against the rock surface. Since the 1960s many studies have been made to find empirical correlations between the R value measured by the Schmidt hammer and mechanical and physical properties such as uniaxial compressive strength (UCS), elastic modulus, density, and porosity. Despite the existing correlations in the literature, this work is required to establish detailed empirical relationships for the carbonate rock units in Israel. To do so, 150 rock samples were collected from 38 different outcrops of carbonate rock units. In each outcrop, 20 impacts were made using a Schmidt hammer at different but adjacent points. The impacts were done horizontally perpendicular to the vertical rock walls. In the laboratory, we measured the density, effective porosity, water absorption, UCS, and elastic modulus. The rock samples we selected contained a wide range of UCS: from 7 to 270 MPa. Our empirical correlations indicate an exponential relationship between R and UCS and the elastic modulus, and linear relationships between R and density, porosity, and water absorbance. The most reliable index is the average of the five maximum impacts out of the 20 made in each rock outcrop. The correlation equations obtained from this work will make it possible to effectively evaluate the mechanical properties of the intact rock in the field, thereby aiding development of advanced tools for rock mass characterisation by means of remote sensing.

INTRODUCTION

In the 1960s, the Schmidt hammer was adopted for use in rock mechanics. The Schmidt hammer consists of a metal rod tensioned by a spring, released at constant energy to impact on the tested material's surface. The return displacement, referred to as rebound value (R-value), is recorded on the device and indicates the stiffness of the tested material's surface. Over the years, many works have focused on relating the R-value to the mechanical properties of rocks, particularly the uniaxial compressive strength (UCS).

Although the Schmidt hammer has found wide application, a generally accepted testing procedure is still not well-established, particularly for field applications. Different authors have proposed various procedures for recording R-values. These procedures are based on either' single impacts' or' continuous impacts' at one point. The most frequently adopted procedures in common engineering practice are those suggested by ISRM (1977) and ASTM (2014) and based on single impacts at one point. However, it has been shown that test procedures based on continuous impacts at one point provide a more reliable and accurate estimation of UCS than single impacts tests (eg Buyuksagis and Goktan, 2007; Goktan and Gunes, 2005). Moreover, there is no accepted indication in the literature for determining the reference R-value to calculate the intact rock strength. Some works suggest excluding outliers from 20 continuous impacts at one point by Chauvenet's criterion and averaging the remaining readings (eg Goktan and Gunes, 2005). ISRM recommends selecting the average upper ten readings from 20 single impacts. In contrast, ASTM suggests discarding readings differing from the average of ten readings by more than seven units and determining the average of the remaining readings.

As part of a study that seeks to develop a tool for evaluating the mechanical properties of rocks through remote sensing, it is required to use conventional methods for determining these properties in the field by rapid means. Therefore, the Schmidt hammer is used intensively in the study for evaluating the mechanical properties of rocks in the outcrops of carbonate rock units in Israel. During the study, extensive work was done to establish empirical relationships between R-values and the mechanical properties of the rock: UCS, dry density, and water absorption.

METHODS

During the data collection process, rebound tests were carried out with a Proceq N-type Schmidt hammer on 38 different rock units throughout Israel. In each rock unit, a series of 20 continuous impacts was performed in situ. The representative R-value was calculated using three methods:

1. The mean value over the full 20 impacts (referred to as 'mean all').

2. The mean value for the ten highest impacts (referred to as 'mean 10').

3. The mean value for the five highest impacts (referred to as 'mean 5').

At the same time, blocks of rock were collected from the same outcrops to determine the laboratory's mechanical properties. The blocks were drilled to prepare 79 cylinders with a diameter of 54 mm and a length of 110 mm. Some rock units produced a single sample, while other rock units were able to produce more than one sample.

We determine the UCS of the rock samples using a large hydraulic compression frame manufactured by ELE International, with an axial compressive loading capacity of 3000 kN. We placed the rock samples in water at room temperature for 48 hours to measure water absorption. The samples removed from the water were weighed on a 0.01 g precision scale. We dried the samples in the oven for 24 hours at 105°C and weighed them again. We calculated the water absorption capacities of the samples using the following equation:

$$\omega_{wet} = \frac{M_{wet} - M_{dry}}{M_{dry}} 100\%$$

Where ω_{wet} is the percent water by weight (refer to as 'absorption'), M_{wet} is the saturated weight and M_{dry} is the dry weight of the sample.

RESULTS

The represented R-value is calculated using three different methods, as described above. Figure 1 shows the empirical relationships between R-values and the mechanical properties of UCS (top row), rock dry density (middle row), and water absorption (bottom row). In each row of Figure 1, the left graph shows the relations obtained for 'mean all', the middle graph for 'mean 10' and the right graph for 'mean 5'. Error bars represent the range of the values where there is more than one rock sample for a single rock unit.

A linear relationship describes the best fit for dry density and water absorption. For UCS, an exponential relation is adjusted. The grey area (Figure 1, top row) represents the 95 per cent confidence band.

DISCUSSION

The results obtained indicate the degree of heterogeneity of the rock samples. In rock units where we have collected more than one sample, quite a large scatter in the values of the mechanical properties, as reflected in the error bar, can sometimes be seen, especially for UCS. It is therefore not surprising that the degree of correlation of R-values is not high. Yet, we found that the average use of the five highest values ('mean 5') yielded slightly better correlations than the other methods.

It is interesting to see the suitability of other empirical relations from existing literature. For example, the relationship developed by Katz, Reches and Roegiers (2000) for UCS is shown as a dashed red line in the top row of Figure 1.
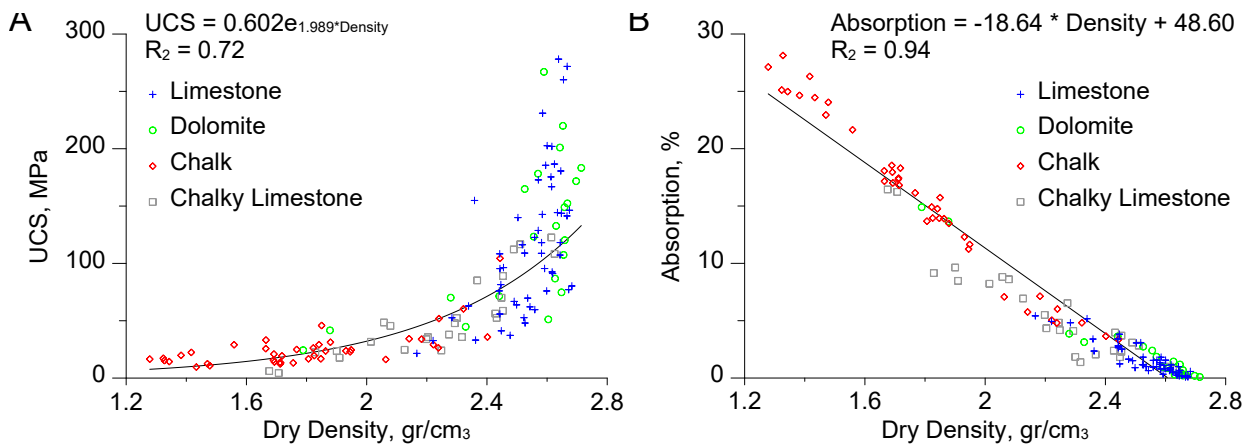
The mechanical properties' relationship has also been examined (Figure 2). We found a substantial linear relationship between the degree of absorption and the rock dry density (Figure 2a). This

connection is well-known in the literature and is explained by the fact that the dense rock samples contain fewer pores into which the water is absorbed. We found an exponential relationship between UCS and rock dry density (Figure 2b).
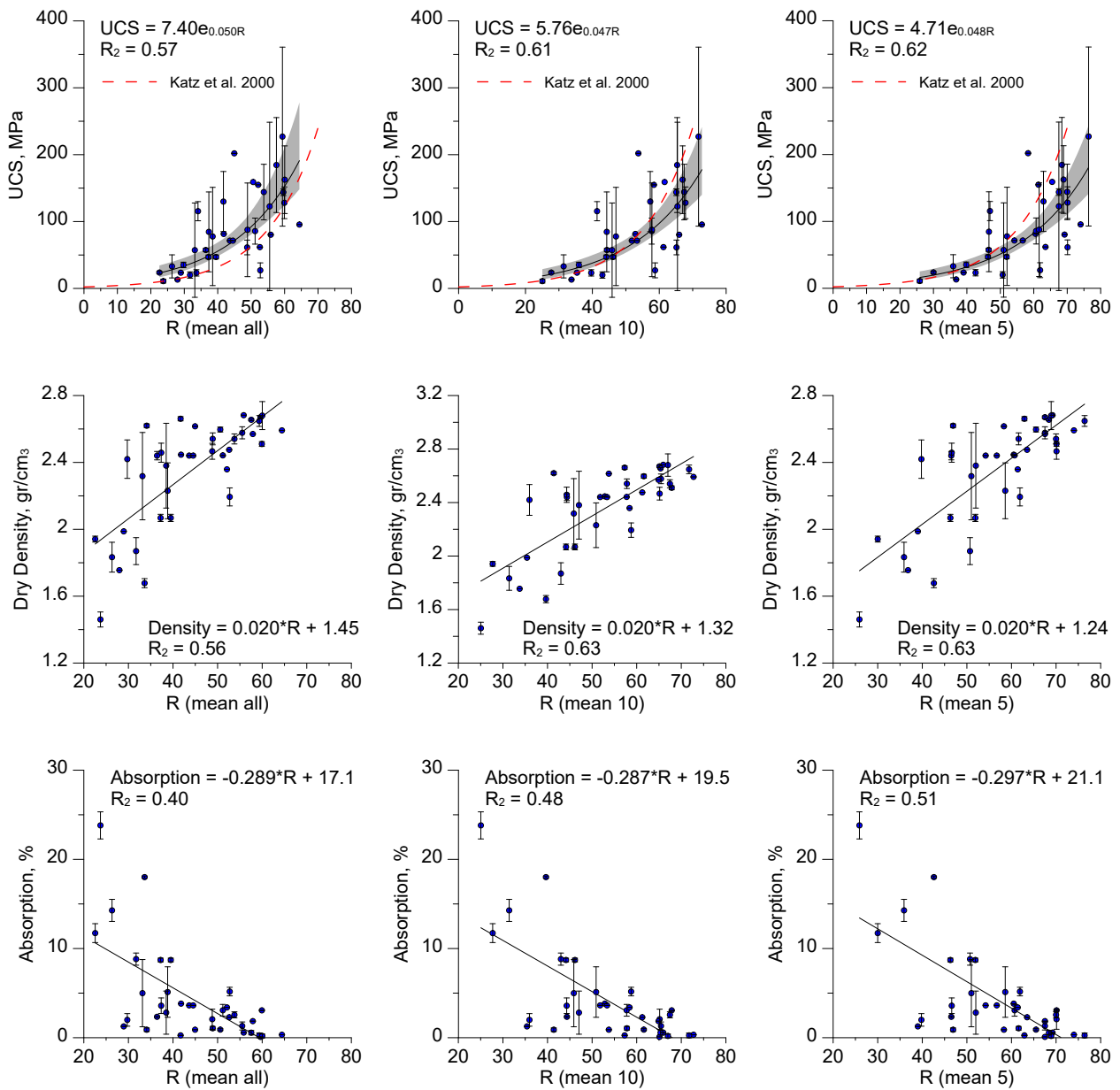
FIG 1 – Correlations between R-values and UCS (top row), dry density (middle row), and water absorption (low row).

FIG 2 – Correlation between mechanical properties of rock samples.

CONCLUSIONS

During this study, dozens of rock samples were used to establish an empirical relationship between the R values from the Schmidt hammer in situ and the mechanical properties of the intact rock. These empirical relationships will serve us later as a reference when we seek to measure these properties by remote sensing.

ACKNOWLEDGEMENTS

REFERENCES

ASTM, 2014. *Standard test method for determination of rock hardness by rebound hammer method*. West Conshohocken, PA: ASTM International Designation: D5873–14.

Buyuksagis, I and Goktan, R, 2007. The effect of Schmidt hammer type on uniaxial compressive strength prediction of rock, *International Journal of Rock Mechanics and Mining Sciences*, 44:299–307.

Goktan, R and Gunes, N, 2005. A comparative study of Schmidt hammer testing procedures with reference to rock cutting machine performance prediction, *International Journal of Rock Mechanics and Mining Sciences*, 42:466–472.

ISRM, 1977. Suggested methods for determining hardness and abrasiveness of rocks, *International Society for Rock Mechanics,* Commission on Standardization of Laboratory, Field Tests.

Katz, O, Reches, Z and Roegiers, J-C, 2000. Evaluation of mechanical rock properties using a Schmidt Hammer, *International Journal of Rock Mechanics and Mining Sciences*, 37:723–728.

The risks and challenges of using Earth rock mass classification systems on the Moon

R deMoraes[1] and A Bobet[2]

1. Director of Tunnels, AECOM, Barnaby, BC V5A 4R4, Canada, roberto.demoraes@aecom.com
2. Professor of Civil Engineering, Purdue U., West Lafayette, IN, 47905, USA, bobet@purdue.edu

ABSTRACT

The last decade has seen a resurgence of interest in lunar exploration and the emergence of countries like China and India as space fairing nations. In 2004, the US announced a new Vision for Space Exploration, whose objectives focused on human missions to the Moon and then Mars. The near future is likely to see the emergence of a worldwide drive to revisit the Moon as the first step in investigating the Solar System. To date, the Apollo missions provide our only experience of human operations on the Moon or anywhere else beyond Low Earth Orbit. Much was learned from these missions. However, their short duration means that many of the environmental effects that will be important for longer-duration missions could not be quantified. In addition, long-duration missions and infrastructure on the Moon require new technologies and capabilities, which must operate successfully and reliably in this lunar environment. Developing these technologies poses significant challenges for the exploration program. The paper discusses the risks associated with the construction of lunar surface and underground structures and the challenges to adopting the standards and rock mass classification systems developed on Earth and their applicability to the Moon. Moreover, an exchange of views to explore near-surface geologic and geotechnical profiles of the Moon is emphasized and implications of the lack of knowledge on rock mass characterisation of the Moonrock mass, the lack of theoretical/empirical experience on the use of rock mass systems outside Earth, and uncertainties.

INTRODUCTION

After 50 years since the last Apollo astronauts left the surface of the Moon, and for most of that time, the lunar surface has been left undisturbed. However, continued analysis of the Apollo samples, and more recent measurements made by lunar orbiting spacecraft, have confirmed that the lunar geological record still has much to tell us about the earliest history of the Solar System, the origin of the Earth and Moon, and the geological evolution of rocky planets. There is broad agreement that further advances in these areas will require an end to the 50-year hiatus of lunar surface exploration and the placing of new scientific instruments on, and the return of additional samples from, the surface of the Moon. For these reasons, several space agencies around the world are actively planning a return to the lunar surface. Initially, some of the scientific objectives may be met by robotic exploration but eventually with astronauts. In addition to these government-led activities, there is also increasing interest in non-governmental projects to land spacecraft on the Moon, plans for permanent habitats, exploration of In-Situ Resource Utilization (ISRU), shallow and deep excavations, and the foundation for launching and landing pads, infrastructure for power generation, communication, etc.

The exploration of the lunar surface may require the use of novel geotechnical and geomechanical engineering methods, techniques and procedures, or at least available geotechnical engineering methodologies for the Earth environment need to be adjusted to take into account the special requirements of the lunar environment (Ettouney and Benaroya, 1990). This paper examines and brings light to some of the possible differences in practices when characterising soils and rocks on the Moon, their stiffness, and performance under different stress conditions. Proper analysis and design of regolith configurations such as slopes and embankments, shallow and deep foundations under low gravity conditions, tunnels, footings, and other geotechnical devices such as, eg rock anchors will require an accurate estimate of the properties of regolith and lunar rocks. This is so because the practice of soil and rock mechanics on Earth is rooted in decades of observations of soil and rock behaviour under a variety of work conditions, but all under gravity that is six times larger than that of the Moon. Such a large difference may challenge concepts as fundamental as how soils

may be classified on the Moon, given that the distinction we have on Earth between fine- and coarse-grained materials may not hold on the Moon.

GEOTECHNICAL AND GEOMECHANICAL EXPLORATION ON THE MOON

The extreme ultrahigh-vacuum, extreme temperature ranges, dust micrometeorites, landing-craft generated projectiles, sunlight, and radiation conditions in the lunar environment will deepen known mining exploration (Heiken, Vaniman and French, 1991) and excavation problems, and demand more specialised equipment and structures than those needed at even the harshest locations on Earth. Particular aspects of the lunar environment such as gravity, tectonics, topography, lunar rocks, and regolith could potentially have a large impact on the design of above- and below-ground structures, mines, pipelines, etc.

The Moon's gravity, one-sixth that of Earth, would on the one hand reduce the load on any structure. On the other hand, however, it would also affect materials handling operations, decrease lateral stability of equipment, and increase the danger of fly-rock if blasting were to be used. The absence of atmosphere on the Moon requires that any human habitat be pressurised at the non-negligible pressure of one atmosphere (about 100 KPa). In other words, most structures built on the Moon will work mostly in tension, and their foundations may have to be designed to resist large tensile loads. These are not the usual working conditions of buildings on Earth. Because of the ubiquitous atmospheric pressure on Earth, the structures work in compression, subjected to their weight and so the foundations work under compression. Such radically different working conditions on the Moon will pose a challenge to those structures built with regolith, eg 3D printed structures. The challenges are many and mostly not well understood. Even though tectonic events are not active on the Moon, Moonquakes, mostly with magnitudes of 1 to 2 on the Richter scale, but occasionally up to magnitude 5, (Taylor, 1986) have a very different frequency content than Earthquakes, of the order of tens of Hz, and may last about an hour because of the low damping of the Moon rocks. Also, meteoroid collisions with the surface of the Moon may induce large seismic/dynamic loading, again due to the low damping on the Moon. Wasting processes are also very different. For example, rock surfaces have been weathered and eroded by micrometeorites, thermal cycles, and gravity since no geomorphic process resulting from Earth-type weather has occurred (Siekmeier, 1992).

Rock properties, such as compressive strength, elastic modulus, surface friction, and abrasiveness are needed for the design of any geostructure and foundation in rock or soil. Unfortunately, very few mechanical property tests have been conducted on actual lunar rocks because large samples are required. During the Apollo Program, several laboratory tests were conducted, but on Earth rocks. For instance, the point-load strength of a basalt increased by 52 per cent, and the modulus of rupture increased by 49 per cent as the temperature decreased from 24°C to -196°C (Heins and Friz, 1967). Additional tests performed in other laboratories showed that the unconfined compressive strength of rock was greater in ultra-high vacuum. Similar conditions were found for the elastic modulus of some limestones. The limestone samples were 2.3 times stiffer at the lower temperature (Atkins and Peng, 1974). These results indicate that the lunar rocks would be stiffer than their similar terrestrial rocks. Surface friction increased by a factor of 2 to 3 for the rock materials studied in ultra-high vacuum (Roepke and Peng, 1975). Increased friction between rock blocks would increase the stability of rock excavations, but it would also increase the energy requirements and wear of the excavators or mining equipment.

Rock mass formation may also show large differences. Volcanic activity on the Moon, 3 to 4 billion years ago, was more intense on the Moon than on Earth and the volume of lava flows was much larger (Melosh, 2011). Yet, cooling processes were much different due to the absence of an atmosphere and, most importantly, due to the lack of water. Thus, it should be expected that the formation of joints and discontinuities on the Moon would be very different than on Earth, pointing towards a more massive rock mass on the Moon, with joints less weathered and thus with higher frictional strength and stiffness. The absence of tectonic activity on the Moon and low gravity may also bring into question our understanding and expectations for the selenostatic (ie *in situ*) stress profile with depth. Those are a significant issues that may put into question well-established tools such as the rock mass classification systems (eg RMR, Q, or GSI systems), widely used by engineers on Earth to design rock excavations, slope stability and support, tunnelling, and mining.

DISCUSSION

The fundamental laws of physics, mechanics, Newton's laws etc still apply to the lunar environment. There are three issues however that need to be considered:

1. Hazards that exist in an extraterrestrial environment do not occur on Earth, we have no experience with them and yet they must be accounted for in the design.

2. What is the probability of failure (ie factor of safety) that should be used on the Moon? On Earth, we accept a level of risk/uncertainty for design (eg we, as a society, accept using a factor of safety of three for a foundation design), but would the accepted consequences of (building) failure be the same on Earth than on the Moon? Probably not.

3. We need to realise that many tools, techniques, and methods we use for geotechnical exploration, ground characterisation, and design that we take for granted on Earth are rooted in observations and so they have an important empirical component. Fundamental issues such as how we define a fine-grained soil on the Moon, correlations between SPT and CPT tests with soil properties, and the design of tunnel support based on rock mass classification systems, need to be brought into question.

We certainly need to build on the experience and knowledge that we have gained on Earth, but an effort must be made to make a distinction between the knowledge that comes from fundamentals and that from empiricism. Here, we should recall the concept of the 'Observational Method' put forward by Terzaghi that now may be very relevant to our future endeavours on geotechnical (selenotechnical?) engineering on the Moon. Terzaghi (1961) states:

> *The case records presented under the heading 'Foundation Design' showed that many problems of earthwork engineering can be solved without a detailed and accurate forecast of performance. Satisfactory solutions to such problems can be obtained based on our knowledge of the fundamental principles of soil mechanics supplemented by a moderate amount of boring and testing. However, there are others in which the geological conditions preclude the possibility of securing in advance of construction all the essential information required for adequate design. If this condition prevails, sound engineering calls for design based on the most unfavourable assumptions compatible with the results of the subsoil explorations. This rather uneconomical procedure can be avoided only on the condition that the project permits modifications in the design during or after construction following the results of significant observational data which are secured after construction is started.*

REFERENCES

Atkins, J and Peng, S, 1974. *Compression Testing of Rock in Simulated Lunar Environment,* USBM-RI-7983, USBM, Washington DC, 21 p.

Ettouney, M and Benaroya, H, 1990. Regolith Mechanics, Dynamics, and Foundation, *Journal of Aerospace Engineering*, 5(2):214–229.

Heiken, G, Vaniman, D and French, B, 1991. *Lunar Sourcebook,* Cambridge University Press, New York, 736 p.

Heins, R and Friz, T, 1967. *The Effect of Low Temperature on Some Physical Properties of Rock,* SPE-1714, Preprint, American Institute of Mining, Metallurgical, and Petroleum Engineering, Inc., 8 p.

Melosh, J, 2011. *Planetary Surface Processes*, Cambridge University Press, Cambridge.

Roepke, W and Peng, S, 1975. *Surface Friction of Rock in Terrestrial and Simulated Lunar Environments,* NASA-CR-146359, NASA, Washington DC, 34 p.

Seikmeier, J, 1992. *Design Criteria for an Underground Lunar Mine,* MSc Thesis, University of Minnesota, Minneapolis.

Taylor, S, 1986. Geologic Considerations for Lunar Telescopes, *Proceedings of the Workshop on Astronautical Observations from a Lunar Base*, N89–15813, NASA, Houston, pp 189–197.

Terzaghi, K, 1961. Past and Future of Applied Soil Mechanics, *Journal of the Boston Society of Civil Engineers*, 68:110–139.

Development of a visual measurement system of geomaterials under triaxial compression

T Endo[1], D Asahina[2], H Hosono[3] and T Takemura[4]

1. Master's student, Nihon University, Tokyo 156–8550 Japan. Email: chtk22001@gmail.com
2. Senior Scientist, Geological Survey of Japan, AIST, Ibaraki 305–8567 Japan.
   Email: d-asahina@aist.go.jp
3. Master's student, Nihon University, Tokyo 156–8550 Japan. Email: hosono.h175@gmail.com
4. Professor, Nihon University, Tokyo 156–8550 Japan. Email: takemura.takato@nihon-u.ac.jp

INTRODUCTION

Changes in the stress field around faults due to the excavation of underground space or the extraction of underground resources induce fault reactivation. To understand the mechanism of fault reactivation, it is important to observe the deformation and sliding processes of the asperities, which is regionally contacted areas at the fault planes. In the laboratory, triaxial compression tests are commonly conducted to reproduce the stress conditions around faults and study their mechanical behaviours. The conventional measurement devices for triaxial compression testing (eg load cells, local deformation transducers, and piezoelectric sensors) uses sensors to measure changes in the physical properties of rocks, but the direct visual information for the sample condition inside the pressure vessel is limited and can only be estimated from the sample after the experiment.

We recently developed a direct visual measurement system to observe the slip behaviour of rocks from the inside of the pressure vessel of a triaxial test apparatus. This paper introduces this visual measurement system and presents some preliminary experimental results. The visual measurement system consists of a steel housing with a built-in commercially available digital camera. The triaxial compression tests were conducted to visually observe the sliding behaviour of the pre-cut specimens and to measure its behaviour through the digital image correlation (DIC) method.

The captured images and the DIC results show the displacement field of the specimens for different confining pressure. We verified the sliding behaviour and the failure at/around the triangular asperity under at different confining pressure.

EXPERIMENTAL PROCEDURE

Dental plaster was used as a rock-like cylinder specimen with dimensions of φ30 × 60 mm (Figure 1a). The specimen has a smooth joint inclined at 30° to the specimen axis and a triangular asperity with a height of 2 mm and a base of 10 mm (Figure 1a).

The triaxial test apparatus at the Geological Survey of Japan, Ibaraki, Japan, was used to conduct the triaxial compression tests of the rock-like specimens. Various studies on the mechanical and hydraulic behaviour of rock samples have been conducted with this apparatus, and additional details can be found elsewhere (Asahina *et al*, 2019). The experiments of this study followed the procedure for a conventional triaxial test but with the addition of the proposed measurement system. The specimen is jacketed in transparent heat-shrinkable tube and placed inside the apparatus. Specimens were loaded axially at a rate of 0.04 mm/min after the confining pressure was applied in the pressure vessel (Figure 1b).

DIC obtains displacement and strain by comparing a reference image with the current image. The specimen surface was sprayed with random patterns necessary for DIC analysis of the captured images.

Figure 1c shows the visual measurement system consisting of a pressure tight steel housing (47 mm × 82 mm × 143 mm) with built-in camera. A commercial digital camera was used for visual observation. The front of the steel housing has a hole at the centre, which was covered with a polycarbonate plate as a viewing window. During the tests, the steel housing device, containing a digital camera, was placed inside the pressure vessel for visual observation (Figure 1d).
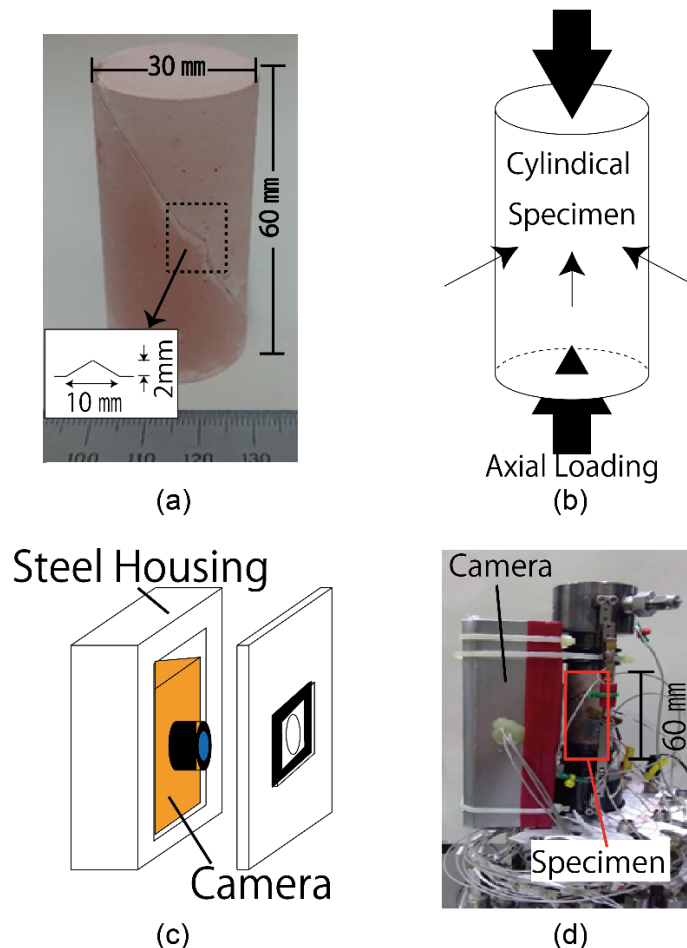
FIG 1 – Rock-like specimens and steel housing. (a) The cylindrical specimen (φ = 30 mm, h = 60 mm) with a pre-cut joint inclined 30° to the specimen axis with a triangular asperity (height of 2 mm, base of 10 mm) at the centre of the joint. (b) The triaxial loading condition. (c) The digital camera inside the steel housing. (d) Photo image of the specimen assembly with the steel housing.

RESULTS

Figure 2a shows the evolution of the differential stress and lateral displacement for the two specimens under different confining pressures, Pc (Specimen 1 for 1 MPa and Specimen 2 for 6 MPa). The results clearly show the effect of Pc on the sliding behaviour, such as the stress grows and the post-peak trends. Figure 2b shows the captured images near the triangular asperities at the post-peak of two specimens. We have observed two different sliding modes: sliding over asperity and shear through asperity. For Specimen 1 in Figure 2b shows the mode of the sliding over the asperity. Upper half of the specimen rides up without a large damage of the asperity. For Specimen 2 in Figure 2b shows the mode of shearing through asperity, which the triangular asperity was cut-off by shearing. For Specimen 1, the upper half of the specimen shows a large amount of displacement, while the lower half shows little. It indicates that the upper half of the specimen slides along the triangular asperity. Figure 2c shows the displacement fields calculated by the DIC method for each specimen. The right figure of Figure 2c shows the displacement fields of Specimen 2 before the peak stress. It shows the amount of displacement is different between the asperities and the surroundings. Such differences in the local displacement cannot be seen from the captured images. These results confirm the sliding mode of the triangular asperity varies at different Pc.
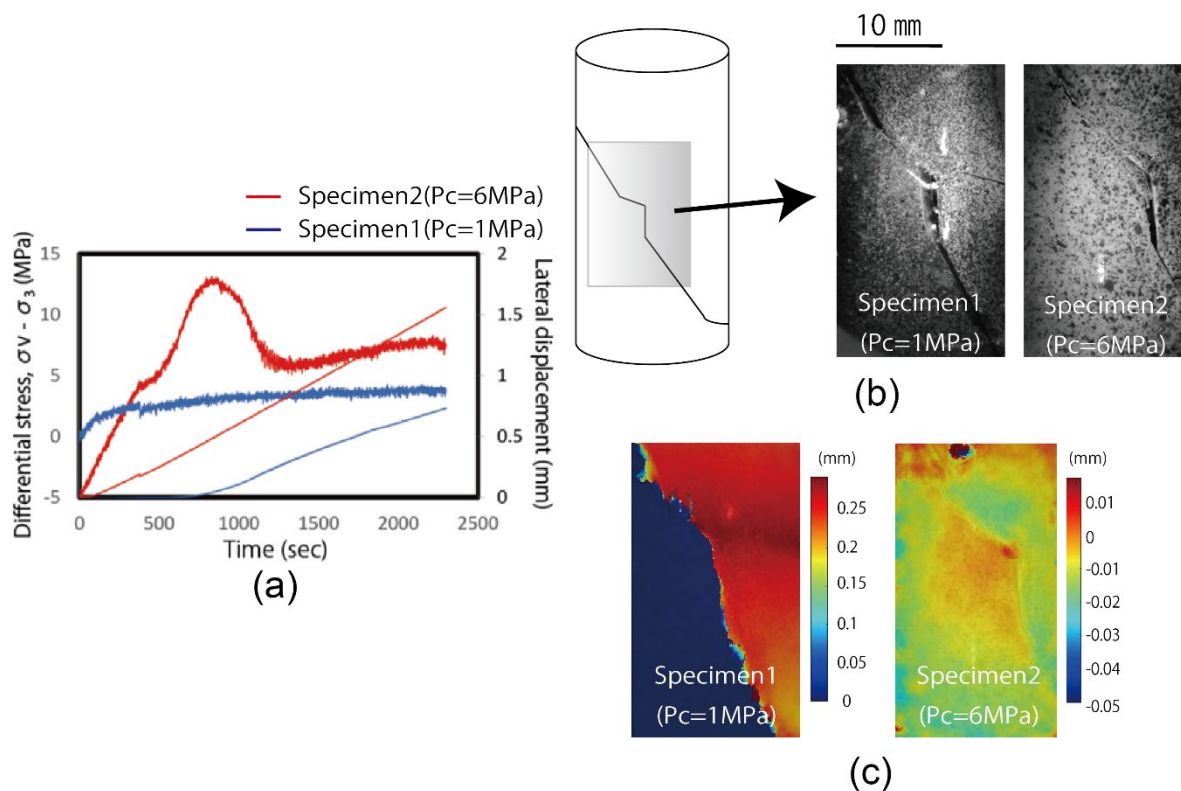
FIG 2 – (a) Triaxial compression test results for different confining pressures. (b) the images of the triangular asperities at the post-peak of specimen. (c) the DIC results of specimen (lateral displacement).

CONCLUSION

A novel measurement system using a digital camera developed in this study was successfully observed and measured the sliding behaviours of the rock-like specimens. The effect of the confining pressure on the sliding behaviour of pre-cut joint with the triangle asperities was confirmed. With further development, it is envisaged that the proposed measurement system will be an effective means for observing and measuring a variety of experimental applications.

REFERENCE

Asahina, D, Pan, P-Z, Sato, M, Takeda, M and Takahashi, M, 2019. Hydraulic and Mechanical Responses of Porous Sandstone During Pore Pressure-Induced Reactivation of Fracture Planes: An Experimental Study, *Rock Mechanics and Rock Engineering*, 52:1645–1656.

Evaluation of rock joint on construction tunnel face using convolutional neural network

K D Halim[1], Y Yun[2], H Kusumi[3] and A Nishio[4]

1. Graduate Student, Kansai University Graduate School of Science and Engineering, Suita, Osaka 564–8680. Email: k696905@kansai-u.ac.jp
2. Professor, Kansai University, Suita, Osaka 564–8680. Email: yeboon@kansai-u.ac.jp
3. Professor, Kansai University, Suita, Osaka 564–8680. Email: kusumi@kansai-u.ac.jp
4. Construction Services in Kinki Region, Kinki Regional Development Bureau, Osaka 540–6591. Email: nishio-akinobu@kyoukai-kinki.or.jp

ABSTRACT

In Japan, evaluation of rock mass is crucial in mountain tunnels that are constructed using the NATM (New Austrian Tunneling Method) to determine the support pattern that in turns determine the final support structure of the tunnel. The current evaluation method is highly dependent on the observations of on-site expert engineers that grades the rock mass in four levels across nine criteria:

 A. Condition of tunnel face.

 B. Condition of excavated surface.

 C. Compressive rock strength.

 D. Weathering.

 E. Spacing of discontinuity.

 F. Condition of discontinuity.

 G. Orientation of discontinuity.

 H. Spring water.

 I. Water degradation.

However, in recent years, the number of said experts are decreasing rapidly due to labour shortage caused mainly by an aging population and declining birth rates. This is one of the biggest challenges that the construction sector currently faces, and this may affect the efficiency of tunnel construction projects in the future. Thus, this study proposes the implementation of a deep learning tool called the convolutional neural network (CNN) to quantitatively evaluate rock fractures on tunnel face. In addition, Gradient-weighted Class Activation Mapping (Grad-CAM) is applied to visualise CNN, as well as verify the applicability of CNN to the evaluation of rock fractures. In other words, by creating heat maps of tunnel face images, CNN is utilised to evaluate rock mass in categories that are associated with discontinuities. The CNN model is most accurate when six convolution layers, four pooling layers, and three dense layers are used. This yields an accuracy of 75.0~88.0 per cent. Thus, the CNN model is verified to be feasible method to evaluate rock fractures.

INTRODUCTION

In Japan, the New Austrian Tunneling Method (NATM) is a very popular tunnel construction method because it can adapt to the complex geological formation of Japan. This construction method relies on the surrounding rock mass to ensure the stability of the structure. To maximise safety and minimise costs, support structure (determined through support patterns) could be change from the original design based on the observed rock mass as stated in the Index for Road Tunnels Observation and Measurement (Japan Road Association, 2009). Rock mass on tunnel face are evaluated and graded based on a set of criteria, and labelled with a support pattern. Rock mass evaluation are typically done by on-site engineers, but since these decisions are based on their individual experiences, there is a discrepancy in judgement resulting in differing evaluations. This study will apply a type of deep learning, the Convolutional Neural Network (CNN), to the process of rock mass evaluation. This study will focus on evaluating the observable feature of rock mass,

namely the rock fractures. Gradient-weighted Class Activation Map (Grad-CAM) is implemented to visualise CNN.

ROCK MASS EVALUATION

In tunnel construction, the foremost rock surface of the excavated tunnel is called the tunnel face. The rock mass of the tunnel face is divided into three sections (left shoulder, crest, right shoulder) and each section is scored in four levels across nine criteria:

A. Condition of tunnel face.

B. Condition of excavated surface.

C. Compressive rock strength.

D. Weathering.

E. Spacing of discontinuity.

F. Condition of discontinuity.

G. Orientation of discontinuity.

H. Spring water.

I. Water degradation.

These are regulated by the Ministry of Land, Infrastructure, Transport and Tourism (MLIT, 2016) as shown in Table 1. This score is called an evaluation point.

TABLE 1

Criteria of rock mass evaluation.

	Criteria	Description
A	Condition of tunnel cutting face	State of rock mass at tunnel face
B	Condition of excavated surface	State of rockfall at tunnel face
C	Compressive rock strength	Hardness of rock
D	Weathering	Degradation by weathering
E	Discontinuity spacing	Interval of discontinuity
F	Condition of discontinuity	State of discontinuity
G	Discontinuity orientation	Shape and direction of discontinuity
H	Spring water	Wetness of rock mass
I	Water degradation	Degradation caused by spring water

In this study, analysis through deep learning will implement the criteria regarding rock fractures: (E) spacing of discontinuity, (F) condition of discontinuity, and (G) orientation of discontinuity.

CNN AND GRAD-CAM

CNN is a type of deep learning method widely used in image recognition in recent years. By inputting images into several featured layers, CNN is able to analyse the images. A CNN is typically made up of a convolutional layer, a pooling layer, and a fully connected layer. Firstly, features of the image is being selected and recognised in the convolutional layer through several filters. Next, the image goes through the pooling layer from the convolutional layer and gets spatially reduced to decrease calculation time. This process is repeated and the features selected from the layers so far are combined in the fully connected layer to predict outputs. Finally, the margin of error from the forward propagation (from the first layer to the final layer) output and the prepared supervised data is calculated. This is then processed through back propagation (from the final layer to the first layer) and by implementing the stochastic gradient descent, the bias and weight values of each layer is regulated, minimising the error and optimising the model.

Grad-CAM is a visualisation technique for CNN output and was proposed by Selvaraju *et al* (2017). The feature map and output results are extracted during forward propagation, and these results are then used in backward propagation to calculate the gradient of each attribute map. The bigger the pixel, the bigger the influence of the gradient on the prediction results. Therefore, by heatmapping the calculated gradient, which part of the image did the CNN observe to make the predictions can be visualised.

EVALUATION OF ROCK JOINT USING CNN

From the nine criteria of rock mass evaluation, this study uses images of criteria that can be observed visually for the input and output. These criteria are (E) spacing of discontinuity, (F) condition of discontinuity, and (G) orientation of discontinuity. Evaluation points from these three criteria are used to train and build the CNN model, analyse the results, and evaluate rock joints.

The input image is pre-processed as shown in Figure 1. Pictures of tunnel faces photographed at construction sites was trimmed to remove the surrounding rock mass, and segmented into 1 m^2 (400 px × 400 px) images. Thus, the crest is divided into 14 images and the left and right shoulder are divided into ten images respectively. Images without sprayed concrete and bolts are selected to be the input data. The labelled data for the input images are evaluation points used at the actual construction site, and revised evaluation points based on each divided image.
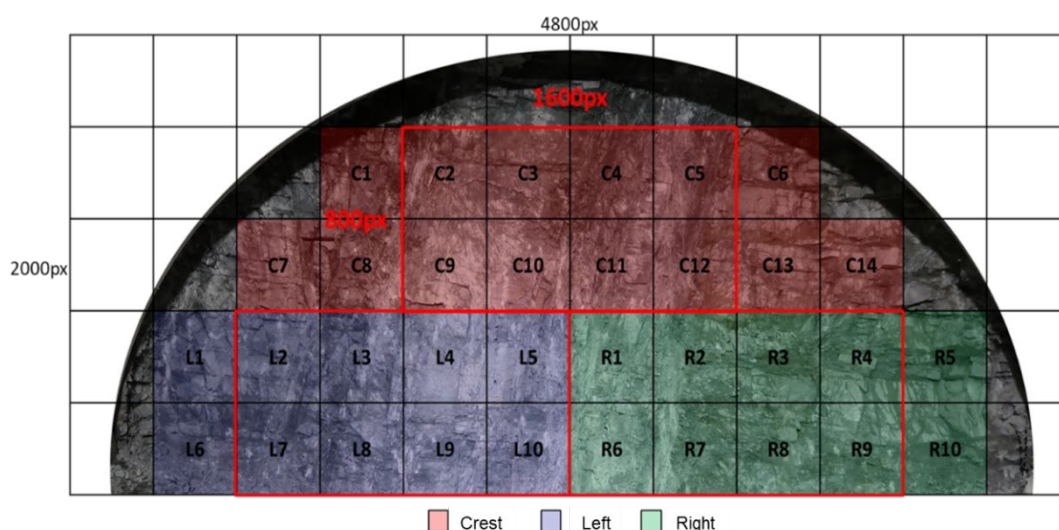
FIG 1 – Tunnel face mesh segmentation mapping.

The CNN model is made up of six convolutional layers, four pooling layers and three fully connected layers. The pooling layers are Max Pooling, the activation function uses ReLU function at the CNN and NN components, the output function uses Softmax function, and Dropout layer is added to the NN component to prevent overfitting. Furthermore, k-fold cross validation (k=5) is applied to improve the accuracy of the CNN model. As shown in Figure 2, the data set is split into five groups and four of the groups are used as to train the CNN model while the remaining group is used for validation. Two sets of such groups are created and the training and validation process is repeated five times, before selecting ten models where the validation loss value is the smallest.

Moreover, the number of epoch is 300, batchsize is 16, loss function uses categorical cross-entropy, and the stochastic gradient descent algorithm to search for weight and bias values uses Adagrad.
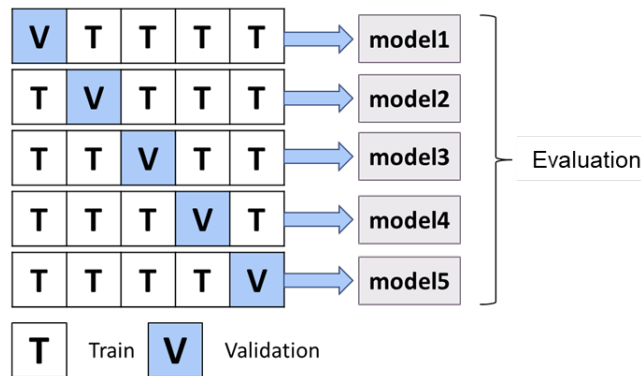
FIG 2 – K-fold cross validation (k=5).

## Case 1 – Revision to evaluation points in relevance on segmented image

First, 307–476 images are used to analyse the data using the CNN model as shown in Table 2. The training data in Table 2 are tunnel faces which evaluation points have been revised by expert engineers. In this case, the ratio of training data to test data is 8:2. The rock mass in these images are mainly made up of igneous rocks (granodiorite) and sedimentary rocks (sandstone, mudstone).
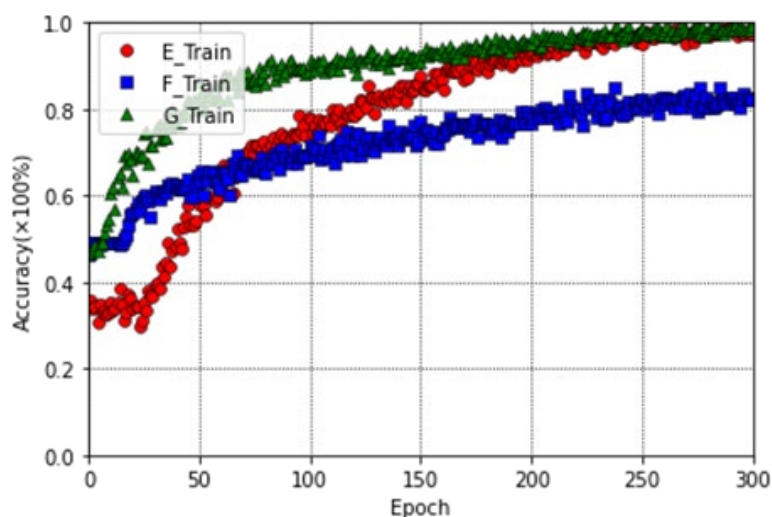
TABLE 2

(Case 1) Number of data for each evaluation criteria and scores.

Criteria	# of images	Score	Score 2	Score 3	Score 4
(E)	476	69	159	139	109
(F)	460	69	214	96	81
(G)	307	71	10	150	76

Figures 3 and 4 are the CNN-predicted results using data from Table 2 to train and test the model. The accuracy for each evaluation point of each criteria is shown. The overall accuracy for criteria (E) is 75.3 per cent, (F) is 69.1 per cent, and G is 88.6 per cent, while the accuracy depending on the model is 80.0 per cent for (E), and over 90.0 per cent for (G). On the other hand, all the models for criteria (F) shows low accuracy. However, prediction accuracy draws close to 100 per cent as the epoch number reaches 300 for criteria (E) and (G), but stops at 80 per cent for criteria (F). Thus, it can be said that criteria (F) can't be analysed with the current model. The reason for this is that compared to criteria (E) and (G), the standard of scoring for (F) is ambiguous and there is a tendency for engineers to score this criterion as 2. For that reason, the CNN model misclassifies evaluation point 3 as 2.
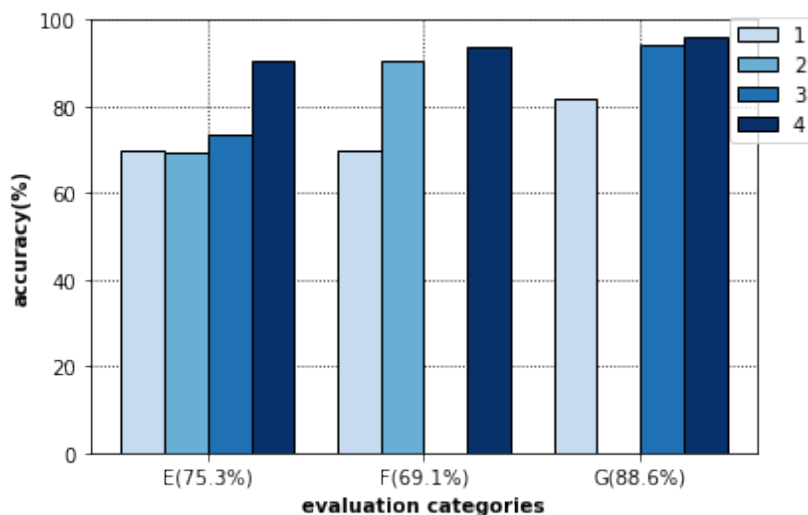
FIG 3 – (Case 1) Accuracy for each evaluation criteria by score.

FIG 4 – (Case 1) Progress of accuracy for each evaluation criteria.

Case 2 – Evaluation points used in actual construction sites

Next, Table 3 shows an additional 2307 images to train the CNN model. The training data in Table 3 are evaluation points used in actual construction sites. Similar to the data in Table 2, the rock mass in these images are mainly made up of igneous rocks (granodiorite) and sedimentary rocks (sandstone, mudstone). Figure 5 shows the results for the CNN-predicted results using data from Table 3 to train and test the model. The accuracy for each evaluation point of each criteria is shown. The overall accuracy for criteria (E) is 66.1 per cent, (F) is 66.9 per cent, and (G) is 64.3 per cent. All the accuracy is lower than the results shown in Figure 3. From this, it can be said that revising the evaluation points is a more effective method. To improve the model, the following Case 3 and Case 4 method is proposed.

TABLE 3

(Case 2) Number of data for each evaluation criteria and scores.

Criteria	# of Images	Score 1	Score 2	Score 3	Score 4
(E)		33	788	1327	159
(F)	2307	408	1469	324	106
(G)		891	26	1273	117
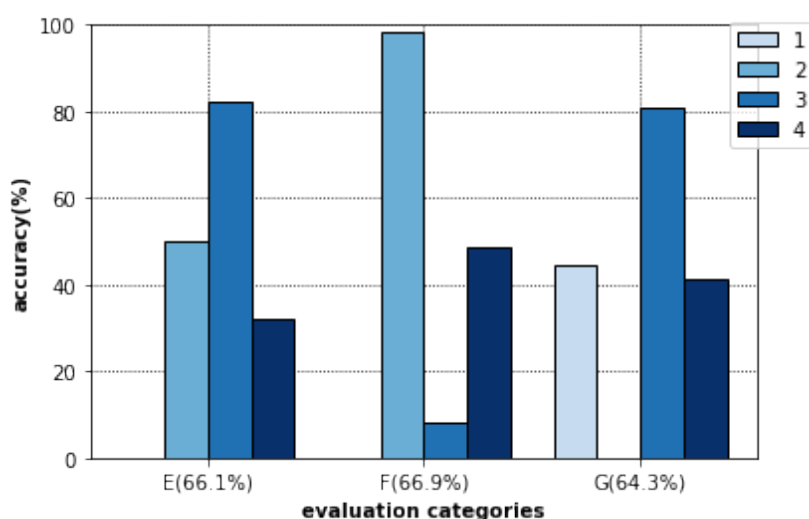
FIG 5 – (Case 2) Accuracy for each evaluation criteria by score.

Case 3 – Grading evaluation points after revision to segment size

To first improvement to the model is to expand the segment size. Originally, the tunnel face is segmented into 400 px × 400 px images, with the crest divided in 14 images, the left and right shoulders into ten images respectively. However, as shown in Figure 6, the crest is segmented into a single 1600 px × 800 px image and this is used as the input image. Similarly, the left shoulder is made up of images L2-L10, and the right shoulder is made up of images R1-R9.
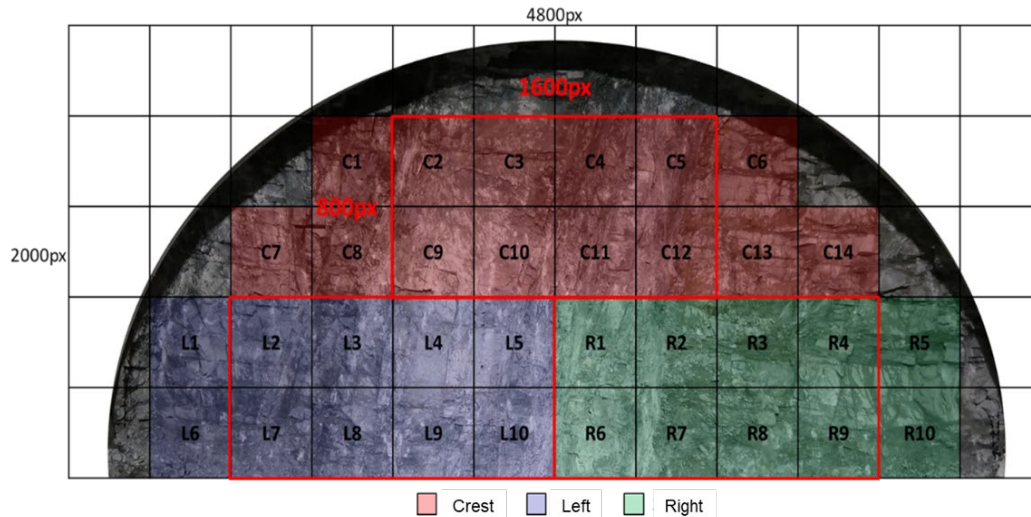
FIG 6 – Revision to tunnel face segmentation size.

Table 4 shows the detail breakdown of the image data, with each criteria having a total of the same 315 images. Figure 7 shows the results for the CNN-predicted results using data from Table 4 to train and test the model. The accuracy for each evaluation point of each criteria is shown. The overall accuracy for criteria (E) is 65.1 per cent, (F) is 75.0 per cent, and (G) is 72.6 per cent. From Table 4, it can be seen that the CNN model tends to predict (F) as a score of 2, and (G) tends to be scored 3 due to the training data having the most images for those scores and causing an imbalance in training data. Moreover, the reason for the accuracy of (E) and (G) being lower than the results in Case 1 is that the image data is too large for the rock joints to be properly observed by the CNN model. Therefore, it can be thought that the smaller the image the easier it is for CNN to analyse rock joints.

**TABLE 4**

(Case 3) Number of data for each evaluation criteria and scores.

Criteria	# of images	Score 1	Score 2	Score 3	Score 4
(E)		2	122	181	10
(F)	315	35	233	40	7
(G)		81	3	223	8
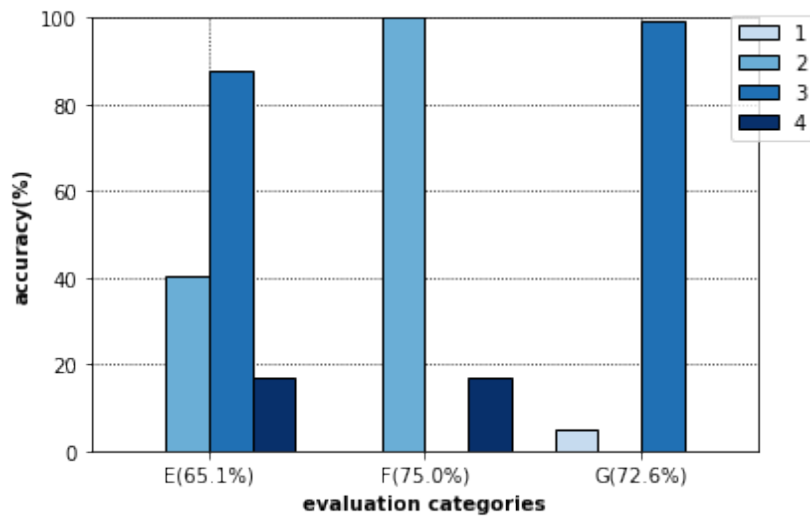
FIG 7 – (Case 3) Accuracy for each evaluation criteria by score.

Case 4 – Evaluation of rock joints using revised evaluation points model

The second improvement is by using the revised evaluation points from the data shown in Table 3. Ten models as shown in Figure 8 is trained using the data shown in Table 2. This is because the data in Table 2 is revised by an expert engineer and is considered as the correct evaluation point. The images with the highest probability value from the results of all ten models is chosen as the new evaluation point. After revision, the new evaluation points are shown in Table 5.
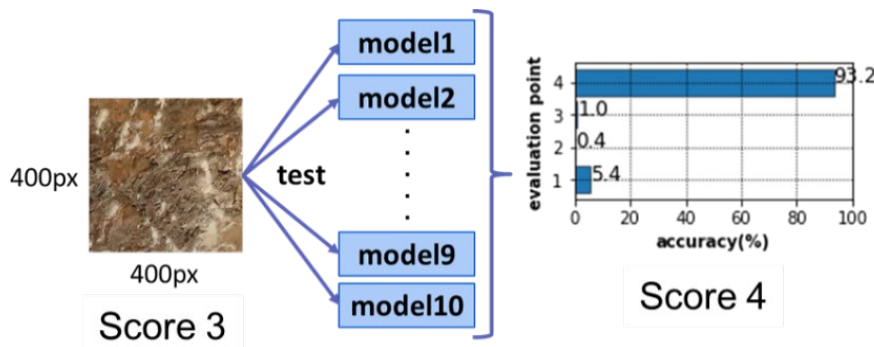
FIG 8 – Method of evaluation point revision.

TABLE 5

(Case 4) Number of data for each evaluation criteria and scores.

Criteria	# of images	Score 1	Score 2	Score 3	Score 4
(E)		239	1241	447	380
(F)	2307	203	1773	0	331
(G)		376	0	1596	335

The number of images for criteria (F) score 3 and criteria (G) score 2 are 0. The reason for this is that the result of the training data shown in Figure 3 misclassifies these images. Thus, criteria (F) and (G) becomes a 3 class multiclass problem instead of 4.

Figure 9 shows the results for the CNN-predicted results using data from Table 5 to train and test the model. The accuracy for each evaluation point of each criteria is shown. The overall accuracy for criteria (E) is 93.4 per cent, (F) is 97.9 per cent, and (G) is 96.6 per cent. One of the reasons that can be thought of as to why criteria (F) and (G) shows high accuracy is because there are less classes to classify data into.
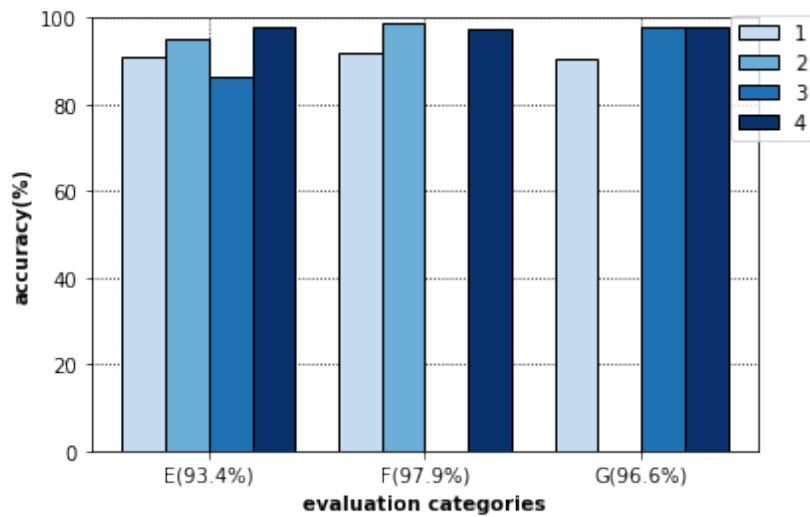
FIG 9 – (Case 4) Accuracy for each evaluation criteria by score.

Therefore, by revising the evaluation points of segmented images data, the CNN model is able to evaluate rock mass with the same standard as those evaluated with human judgement.

ANALYSIS OF ROCK JOINTS RECOGNITION BY GRAD-CAM

In this study, Grad-CAM is used to analyse criteria (G) orientation of discontinuity. Figures 10 to 13 are heatmaps produced by Grad-CAM. The range in heatmaps are shown from the colour blue to red, and CNN focuses more on the objects indicated by the colour red. This means that the closer the object is to the colour red, the more sensitive the CNN model is to that object.

Figure 10 shows a portion of a tunnel face when evaluation point is a score of 3. From this, it can be seen that images that show rock mass such as stratified rock, schistose rock, and sheet rock where rock joints are objects of analysis shows rock joints coloured yellow-red. Figure 11 shows a portion of a tunnel face when evaluation point is a score of 4. In this case, in images that show rock mass such as sedimentary rock and fragmented rock where rock joints are not objects of analysis, the CNN model focuses on the surrounding. Figures 12 and 13 shows a portion of a tunnel face when evaluation point is a score of 1. When there is a fracture on the rock mass, the fracture is coloured red; when there is no fracture on the rock mass, the whole image is coloured red. From this, it can be confirmed that the CNN model is able to analyse criteria (G) orientation of discontinuity.
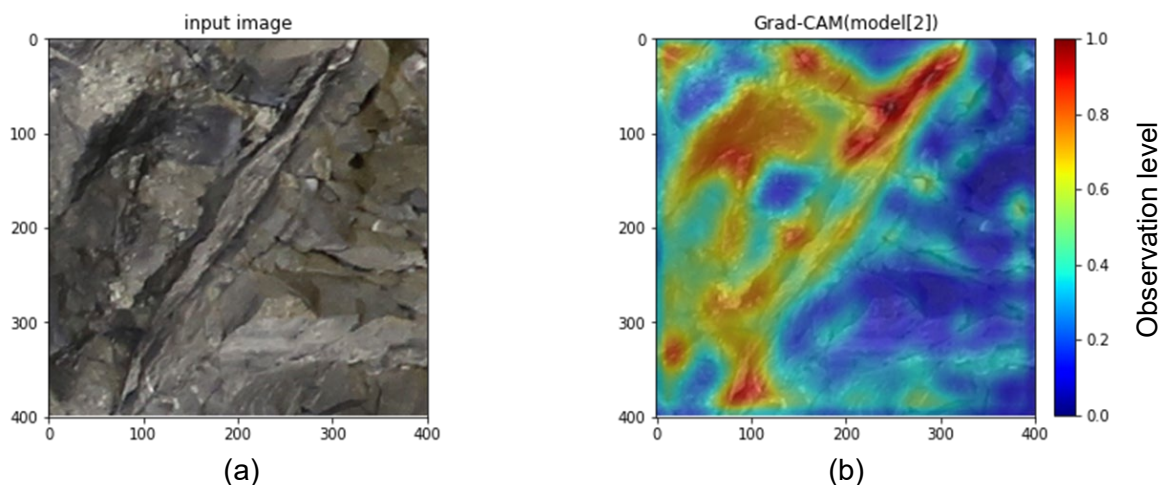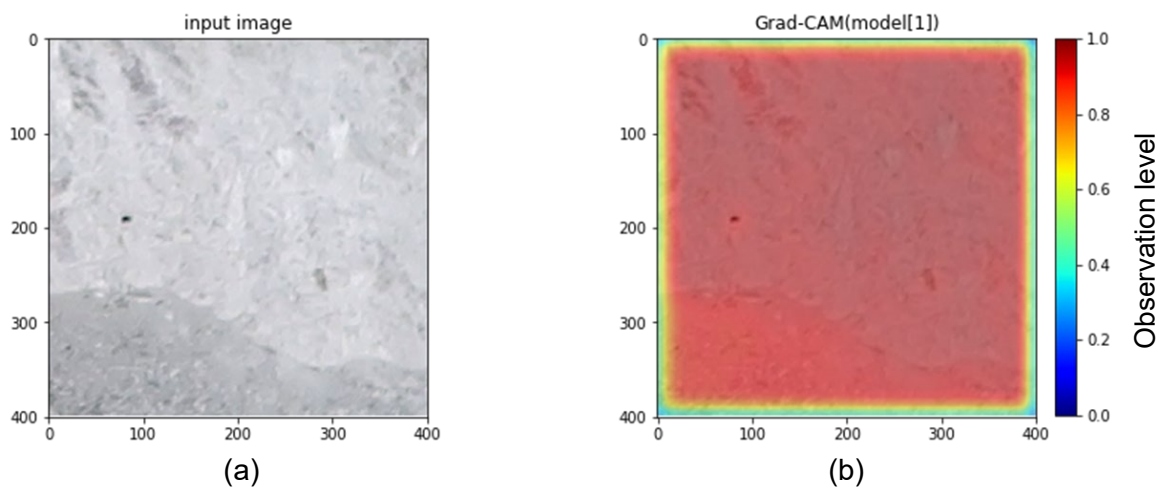

FIG 10 – (a) Image of rock mass; (b) Heatmap of rock mass image by Grad-CAM (Score 3).

(a)   (b)
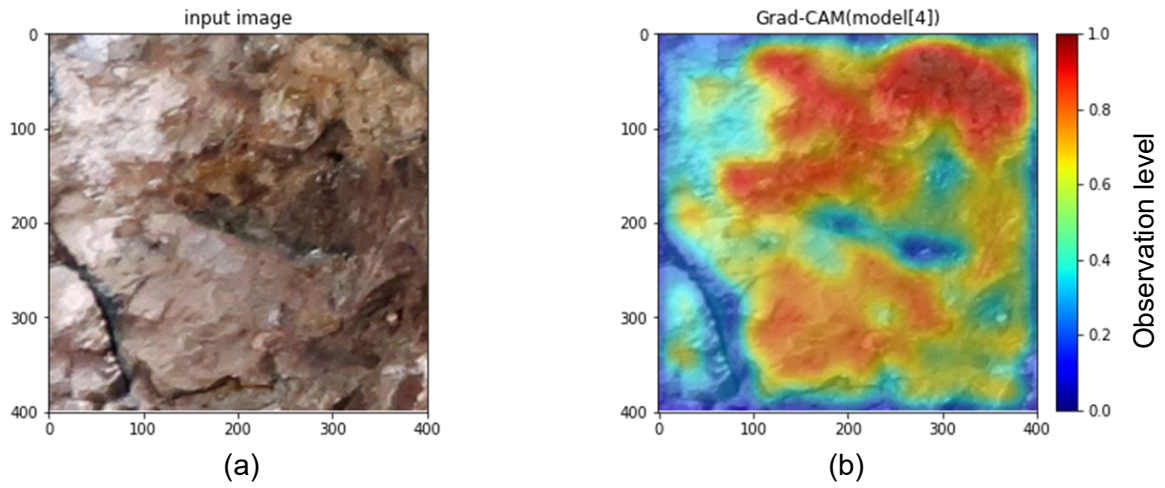
FIG 11 – (a) Image of rock mass; (b) Heatmap of rock mass image by Grad-CAM (Score 4).

(a)   (b)
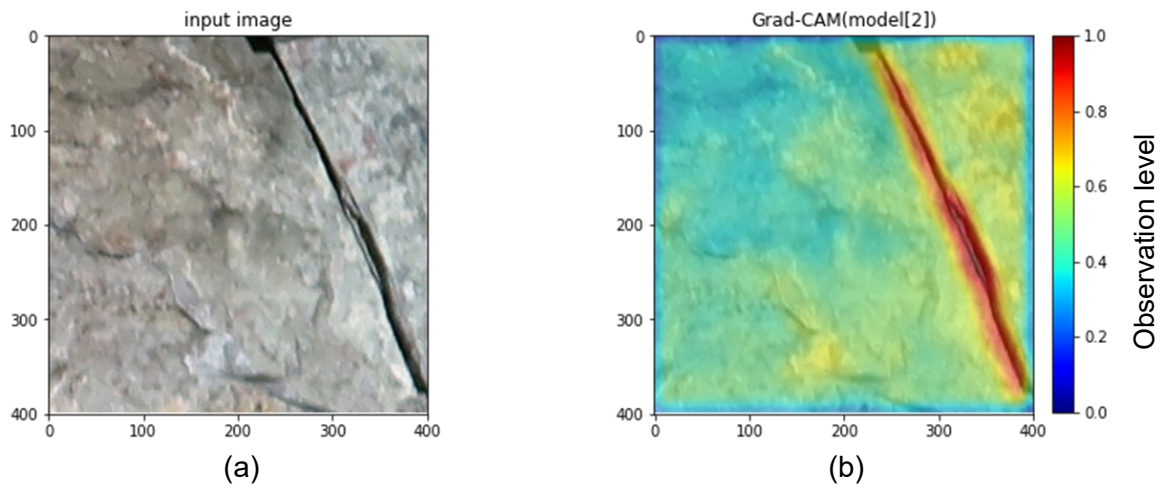
FIG 12 – (a) Image of rock mass; (b) Heatmap of rock mass image by Grad-CAM (Score 1, Fractured).

(a)   (b)

FIG 13 – (a) Image of rock mass; (b) Heatmap of rock mass image by Grad-CAM (Score 1, Non-fractured).

CONCLUSION

In this study, one of the deep learning methods, CNN and its mapping method, Grad-CAM, is applied to the analysis of rock joints in tunnel faces. This study can be concluded as the following.

- The accuracy for the CNN model when the tunnel face image is mesh segmented, and analysis of evaluation points is done on each individual image is higher compared to when the tunnel face is evaluated by section.

- According to analysis by Grad-CAM, CNN is able to evaluate rock joints based on criteria (G) orientation of discontinuity.

Based on the results above, it can be concluded that CNN is able to evaluate and analyse rock joints in tunnel faces with the exception of several images due to the way the photographs were taken at the construction site.

ACKNOWLEDGEMENTS

REFERENCES

Japan Road Association, 2009. Index for Road Tunnels Observation and Measurement (in Japanese).

Ministry of Land, Infrastructure, Transport and Tourism (MLIT), 2016. Manual for Rock Mass Evaluation during Tunnel Construction, Kinki Regional Development Bureau (in Japanese).

Selvaraju, R R, Cogswell, M, Das, A, Vedantam, R, Parikh, D and Batra, D, 2017. Grad-CAM: Visual Explanations from Deep Networks via Gradient-Based Localization, *2017 IEEE International Conference on Computer Vision (ICCV),* pp 618–626.

Estimation of rock brittleness for jointed specimens under cyclic triaxial loading

P Khalkho[1] and M Singh[2]

1. Research Scholar, Civil Engineering Department, IIT Roorkee, Roorkee India 247667.
   Email: pkhalkho@ce.iiitr.ac.in
2. Professor, Civil Engineering Department, IIT Roorkee, Roorkee India 247667.
   Email: msinghfce@iitr.ac.in

ABSTRACT

Rock masses when subjected to uniaxial or triaxial cyclic loading (eg in hydraulic running tunnels, during retrieval and injection of oil and gas from storage underground caverns and haulage roads), the material has a tendency to fail in fatigue. In order to design safe and reliable underground structures, the determination of brittleness under such loading conditions becomes a pre-requisite. Brittleness influences strongly the failure process and makes the rock mass behaviour complex under different tunnelling and mining activities. Brittleness Index is a term to quantify the brittleness feature of a specimen. In the present study, an attempt has been made to quantify the brittleness of jointed specimens using different brittleness criteria. The joints of the model jointed specimens were oriented at an angle of $\theta=15°$ normal to the loading direction, each having three different JRC's=2–4, 12–14 and 14–16. The specimens were tested under triaxial conditions in incremental complete cyclic test scheme performed at displacement-controlled mode. Different brittleness criteria were used ie stress-strain dependent brittleness index, Young Modulus approach and energy-balance based mechanism. It was observed that energy-balance based mechanism which consider the post failure behaviour is more descriptive to reflect the whole variation of brittleness from sheer brittleness to ductility.

INTRODUCTION

Brittleness of the rock is an important parameter as an indicator for rock burst precursor. In order to break, drill or core the rock, tunnel boring machines are used. Less energy is required to bore brittle rocks as compared to non-brittle rocks of comparable strength (Gong and Zhao, 2007). The efficiency of hydraulic fracturing also depends on whether the shale reservoir is brittle or ductile. Brittleness is more favourable for hydraulic fracturing (Meng *et al,* 2015). In various mining, tunnelling and drilling operations, rock brittleness is an important parameter shaping the failure characteristics of rock upon external loading conditions. For design and selection of mining machineries, stability assessment of hard rock tunnels, precise determination of brittleness of rock is a prerequisite. In the present study, laboratory tests were performed on jointed specimens and brittleness was examined. Various brittleness indices have been used to check which reflects the whole variation of brittleness with confinement.

METHODOLOGY

Methodology comprised of laboratory tests performed on model rock. Tests were performed for monotonic and cyclic loading conditions.

Model material

Model materials are used to simulate the rock as it is easy to reproduce results unlike extracted specimens from natural rocks. In the present study, a model material named Ultrarock, has been used as a model rock. The joint was oriented at $\theta=15°$ and three roughness's have been incorporated according to Barton's standards, ie JRC=2–4,12–14 and 14–16 as shown in Figure 1. The mechanical properties of the model rock are shown in Table 1. The material has a uniaxial compressive strength (UCS) of 45.62 MPa and tangent modulus (E_{t50}) of 8.80 GPa respectively. The model rock is classified as 'DL' (low strength and low modulus ratio) group, according to the Deere-Miller Classification Chart (Deere and Miller, 1966). On testing the specimens for a range of confining pressure of 0–10 MPa, Mohr–Coulomb shear strength parameters, c and ϕ values were observed to be 11.83 MPa and 31.33°, respectively.

TABLE 1

Mechanical properties of model rock.

Properties	Symbol	Value	Unit
Unit Weight	γ	21.3	kN/m^3
Cohesion (For $\sigma_3 = 0 - 10\ MPa$)	c	11.83	MPa
Angle of internal friction	ϕ	31.33	°
UCS of intact rock	σ_{ci}	45.62	MPa
Tangent modulus	E_{t50}	8.80	GPa
Brazilian tensile strength	σ_t	3.14	MPa
Deere-Miller classification (Deere and Miller, 1966)	-	DL	-
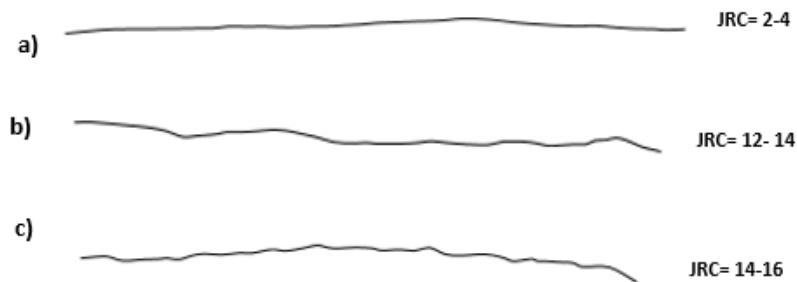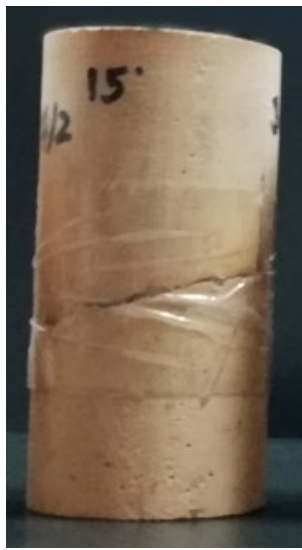
FIG 1 – Prepared specimen and three different roughness profiles used for the joint wall surface.

Test scheme

The triaxial tests were conducted at confining pressure of 0, 1, 2 and 3 MPa under both monotonic loading and cyclic loading. The confining pressure was kept in the low range in order to mainly study the attributes of joints, ie effect of orientation of joint and joint roughness. The tests were conducted at the displacement-controlled mode at the rate of 0.002 mm/s. Tests per confinement level for each roughness, four levels of confining pressures were used for both monotonic and cyclic loading. The cyclic loading was applied monotonically at the same former rate of displacement with an amplitude of 0. 1 mm. The incremental complete cyclic loading was applied by loading the specimen initially from 0 mm to 0.1 mm and then unloading it to 0.05 mm. For the next consecutive cycle to continue, the specimen was again loaded till 0.2 mm from 0.05 mm and then unloaded from 0.2 mm till 0. 005 mm. This procedure is continued till post failure where the residual state of the specimen is reached. Various brittleness indices have been defined in the past on the basis of angle of internal friction, strength parameters, elastic parameters, mineral composition, shape of stress-strain curves, Young's modulus – Poisson's ratio, penetration-impact and hardness test approaches. In the present study, some of the approaches have been applied for the generated triaxial test data under both monotonic and cyclic loading. The effort has been made to annotate which index better reflects the brittleness.

A strain-based quantification for rock brittleness was proposed by Hajiabdolmajid and Kaiser (2003):

$$BI_1 = \frac{\varepsilon_f^p - \varepsilon_c^p}{\varepsilon_c^p} \tag{1}$$

Where ε_f^p is the plastic strain at which the friction is fully mobilised and ε_c^p is the plastic strain at which cohesive strength reduces to residual point. The values of ε_f^p and ε_c^p have been obtained as shown in Figure 2 for all the jointed specimens. The obtained brittleness index has been plotted with confining pressure (Figure 3).
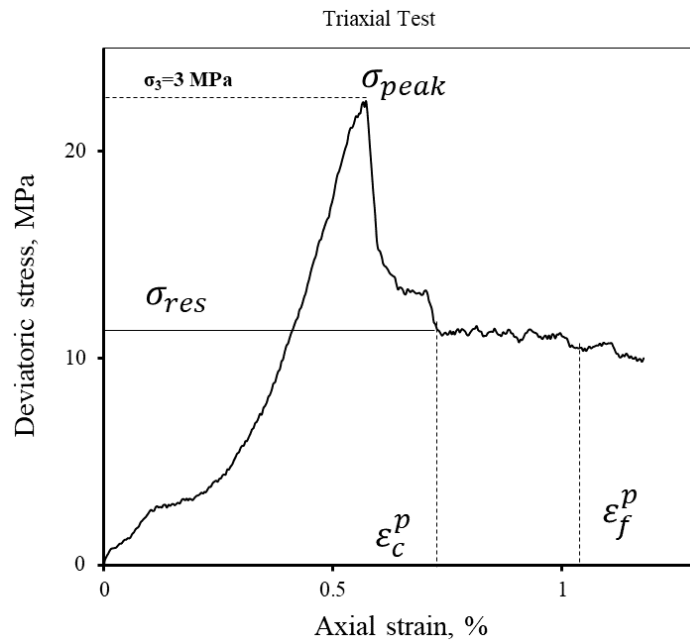
**FIG 2** – Typical stress-strain plot of triaxial tests under monotonic loading.
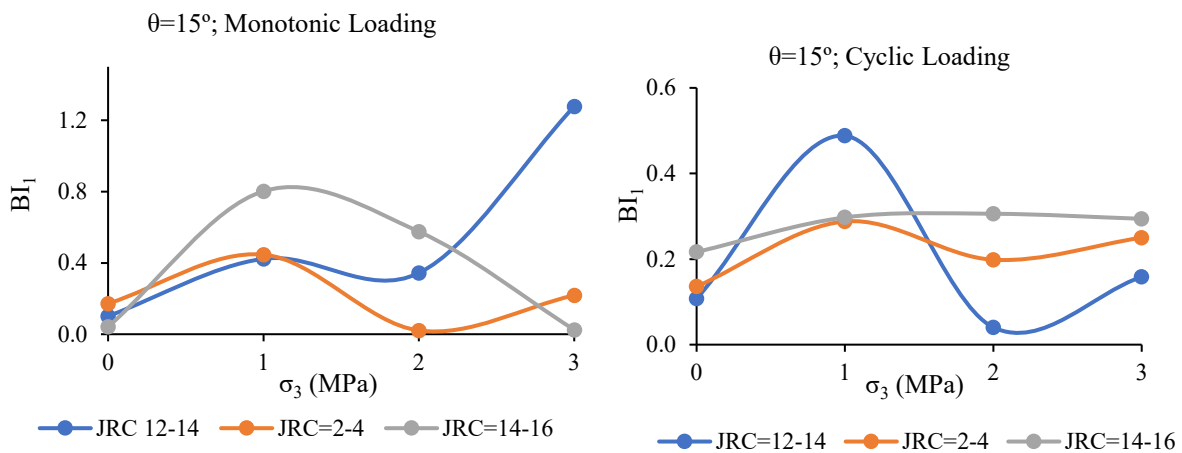
FIG 3 – Plot of Brittleness index (BI$_1$) with confinement for jointed specimens under monotonic loading and cyclic loading.

It was observed that BI$_1$ values were higher for jointed specimens under monotonic loading. For the same configuration of jointed specimens under cyclic loading, the BI$_1$ values were low. The BI$_1$ values varies with JRC but no distinct pattern has been observed for the relationship of BI$_1$ with JRC for both monotonic and cyclic loading. In general, under cyclic loading, the BI$_1$ values are low when the confinement increases to 3 MPa. It might be due to ε_c^p (high cohesive strength loss rate) and ε_f^p (small frictional strengthening rate) in the case of monotonic loading. This indicates more brittleness and thus is a reason for creation of microcracks and propagation of macrocracks. It was also observed that under the cyclic loading, there is more internal deterioration as compared to more visible tensile cracks under monotonic loading. This index is used for short and long-term stability of underground excavation (Hajiabdolmajid and Kaiser, 2003) but does not precisely reflect the brittleness under monotonic loading.

BI$_2$ is defined as the crack initiation stress to the UCS of the rock given by following expression:

$$BI_2 = \frac{\sigma_{ci}}{\sigma_c} \tag{2}$$

σ_{ci} is the crack initiation stress and is obtained by plotting the failure envelope for stress-strain curve under cyclic loading. It is the point at the stress-strain curve where the lateral strain curve starts to deviate from linear trend. This index was primarily used for UCS tests. For the present study, the crack initiation stress was estimated for the stress-strain curves obtained for triaxial tests also. It was observed from Figure 4 that BI_2 for cyclic loading, does decreases with increase in confinement and is more or less has similar values irrespective of JRC's. It shows that BI_2 does not reflect the effect of JRC.
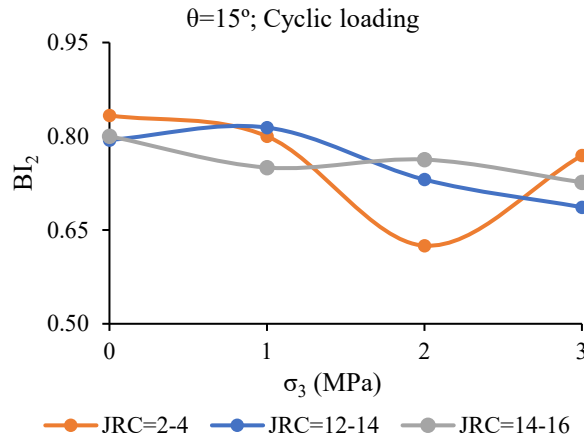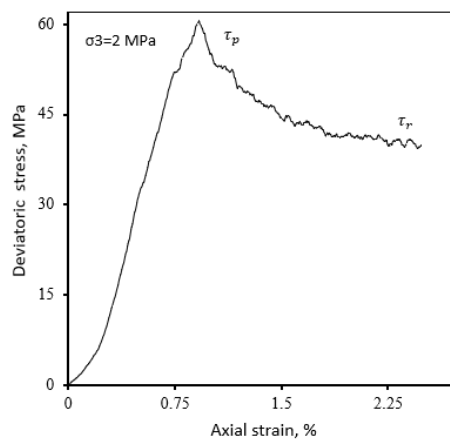

θ=15°; Cyclic loading

FIG 4 – BI₂ for jointed specimens with confining pressure under cyclic loading.

Bishop (1967) proposed rock brittleness using post-peak stress-strain curve and is given by following expression:

$$BI_3 = \frac{\tau_p - \tau_r}{\tau_p} \tag{3}$$

where τ_p and τ_r are the peak and residual strengths, respectively, in the compression test. Figure 5 shows the typical plot of deviatoric stress and axial strain indicating τ_p and τ_r. The values of BI_3 have been obtained and plotted with confining pressure as shown in Figure 6.

**FIG 5** – Stress-strain curves showing peak and residual strengths.
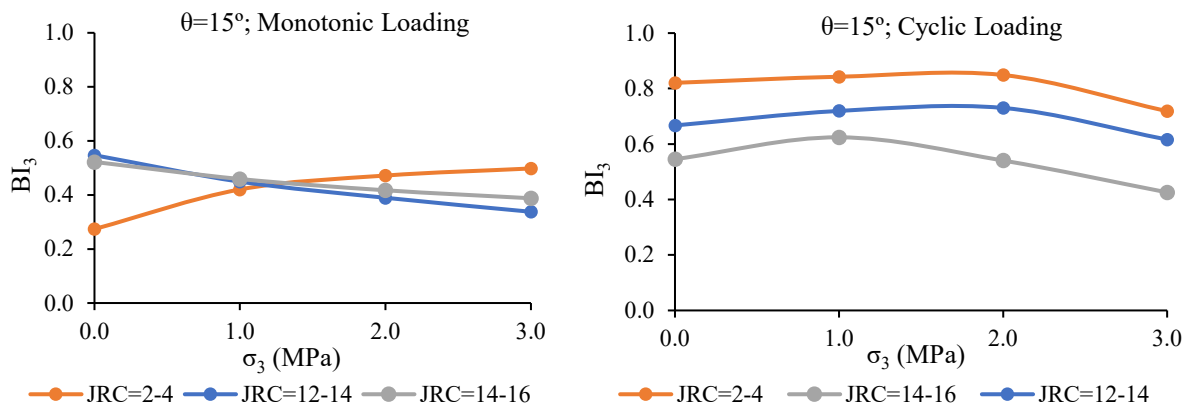
FIG 6 – BI3 values for jointed specimens under monotonic and cyclic loading.

It was observed that under monotonic loading, the BI_3 values decreased with increase in confining pressure except for JRC=2–4 where the BI_3 increased at σ_3=3 MPa. For cyclic loading, BI_3 values initially show no effect of σ_3. However, at higher σ_3 there is trend of decreasing BI_3 with increase in σ_3. BI_3 only takes the strength values into account not the rate at which strength is dropped (Meng *et al*, 2021). For the case of monotonic loading, the BI_3 values for different JRC's were obtained to be similar. The effect of JRC was quite visible for the case of cyclic loading.

BI_4 is the brittleness index which considers post-peak behaviour rate also and is given by expression:

$$BI_4 = (\sigma_p - \sigma_r)\frac{\log_{10}|k_{AD(GF)}|}{10} \tag{4}$$

Schematic diagram to obtain the required parameters to calculate BI_4 is shown in Figure 7. Variation of BI_4 with σ_3 is shown in Figure 8 It was observed that BI_4 for cyclic loading for all the jointed specimens decreases at σ_3=3 MPa. The trend in general is similar for monotonic loading also, except for JRC=12–14. There are some outliers also. The pattern of effect of JRC was found to be quite similar for both the cases of monotonic and cyclic loading. The values of BI_4 for JRC=2–4 were higher followed by JRC=14–16 and JRC=12–14 for both the monotonic and cyclic loading.
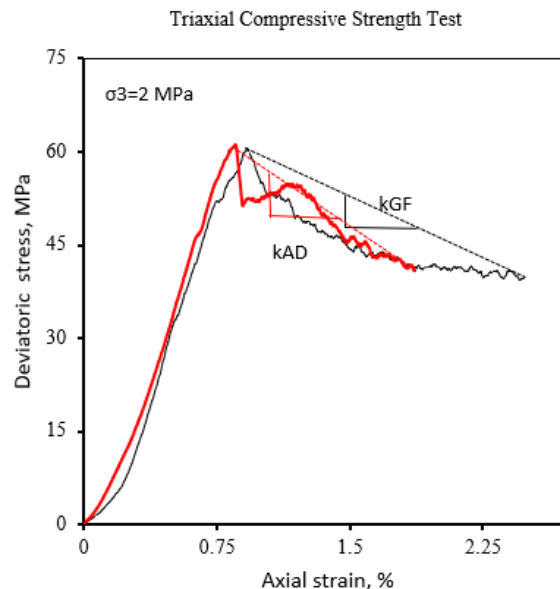
FIG 7 – Schematic diagram for obtaining the parameters for BI4.
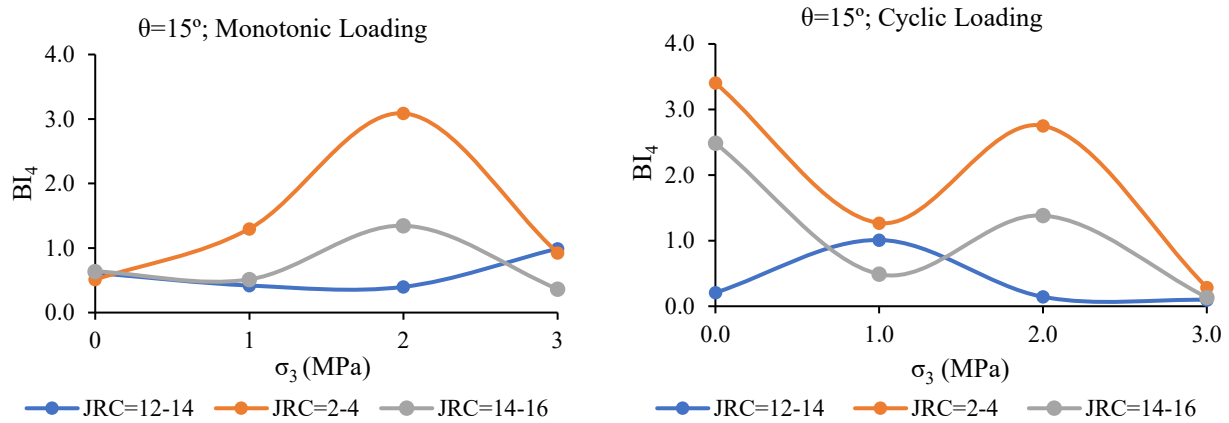
FIG 8 – BI$_4$ values obtained for jointed specimens under monotonic loading and cyclic loading.

Wang *et al* (2016) introduced the Brittleness value BI$_5$ as homogeneity parameter (m) given by expression as follows:

$$BI_5 = m = \frac{1}{\log_{10} E - \log_{10} E_s}$$ (5)

Where E is the elastic modulus obtained by drawing tangent at 50 percent of the peak stress of the linear curve of stress-strain curve. E$_s$ is the secant modulus obtained by getting the slope drawing from the origin to the peak of the stress-strain curve. It can be seen from Figure 9 that this brittleness index gives very high values for specimens tested under cyclic loading. BI_5 values increase with increase in confining pressure except for JRC=12–14 for both the loading conditions. Whereas, for the specimens tested under monotonic loading, with confinement, BI_5 in general has a trend to go down with confinement. There was slight difference of BI_5 values for different JRC's for monotonic loading. The lowest values were observed for JRC=14–16 and the highest values for JRC=12–14 were obtained. For JRC=2–4, the BI_5 values lied somewhere in the mid of JRC=12–14 and 14–16. No definite pattern was observed of BI_5 with JRC under cyclic loading.

Tarasov and Potvin (2013) proposed the following equation for evaluation of brittleness in terms of rupture energy and elastic energy. The equation was further simplified in terms of post peak modulus (M) and elastic modulus (E) and is given as follows:

$$BI_6 = \frac{dW_r}{dW_e} = \frac{M-E}{M}$$ (6)

Figure 10 shows that for both the cases of monotonic and cyclic loading, the BI$_6$ values increases with increase in confining pressure. This index does not reflect the effect of confining pressure (ductility) as BI$_6$ increases with increases with increase in confining pressure. Under monotonic loading, effect of JRC on BI$_6$ was not noticeable. For the case of cyclic loading, BI$_6$ values were higher for JRC=12–14 followed by JRC=2–4 and JRC=14–16. The above index can be used as a precursor for rock burst potential.
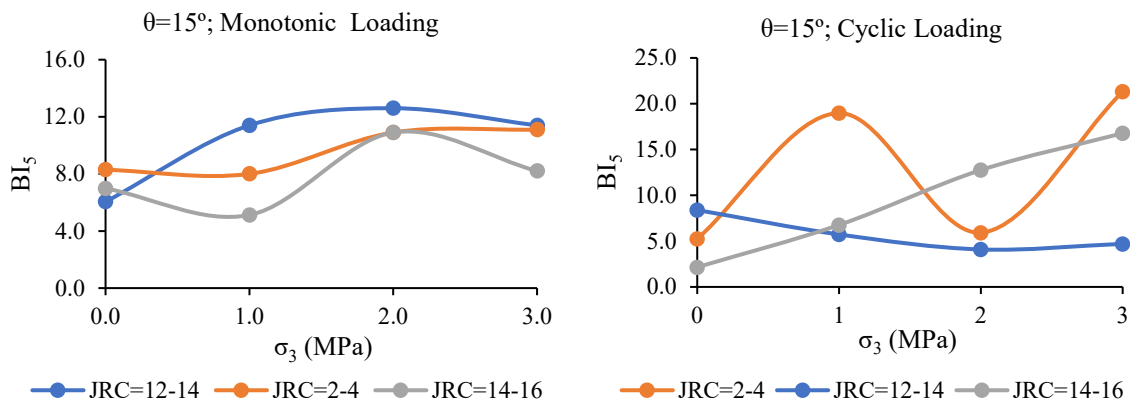
FIG 9 – BI$_5$ values obtained for jointed specimens under monotonic loading and cyclic loading.
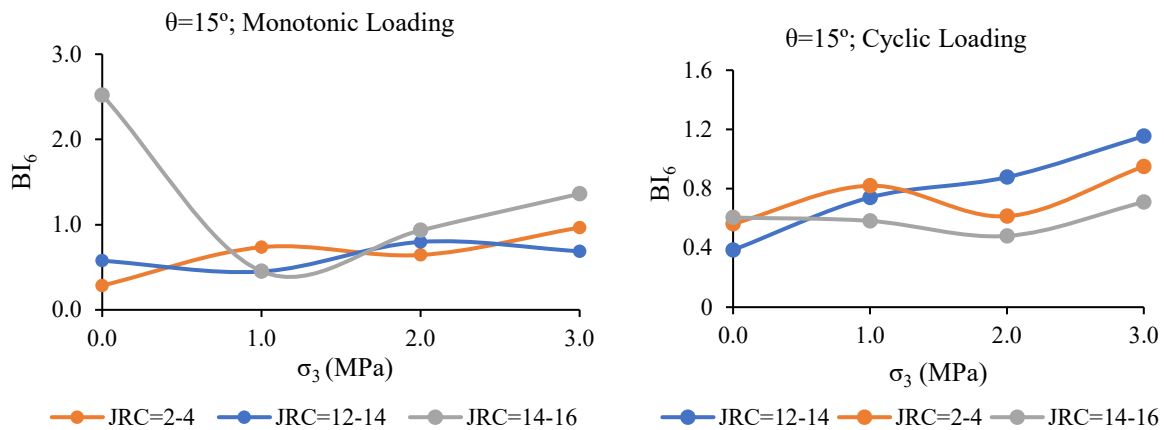
FIG 10 – BI$_6$ values obtained for jointed specimens under monotonic loading and cyclic loading.

DISCUSSION

The engineering behaviour of jointed specimens is governed by the attributes of joint, ie orientation and roughness of the joint. Very small information is available taking into account the attributes of joint for quantification of brittleness index which becomes essential as the rock encounters anisotropy in the realistic field situations. Zhou *et al* (2018) stated that for higher internal friction angle, higher BI values were observed for different types of rock. The friction angle of the joint increased with increase in JRC for the present case. It was observed that with increase in JRC, BI_4 values decreased in general. Single data was available for each confinement level per JRC. It is encouraged to use more sets of data to check the applicability of different brittleness index. It would be subjective to just accept one BI and apply it universally.

CONCLUSION

For the present study, it was observed that the BI_4 brittleness index was able to reflect the brittleness comparatively well for both monotonic and cyclic loading. There were some outliers also. BI_4 is associated with the energy release rate at the onset of failure. It was noticed that BI_4 values were higher for JRC=2–4 and low for JRC=14–16. BI$_4$ considers the combined effect of stress-strain and post failure behaviour. It was observed from the present study that for the same rock material and jointed configuration, using different brittleness indices, different values were obtained. It is then suggested that the index should be so that it takes into account the anisotropy of the rock and the combined stress-strain effects.

REFERENCES

Bishop, A W, 1967. Progressive failure with special reference to the mechanism causing it, *Proceedings of the Geotechnical Conference*, pp 142–50, Oslo.

Deere, D U and Miller, R P, 1966. Engineering classification and index properties for intact rock, *Technical Report No. AFNL-TR-65- 116*, Air Force Weapons Laboratory, New Mexico.

Hajiabdolmajid, V and Kaiser, P, 2003. Brittleness of rock and stability assessment in hard rock tunnelling, *Tunnelling and Underground Space Technology,*18:35–48.

Gong, Q M and Zhao, J, 2007. Rock brittleness indices and their applications to different fields of rock engineering: A review, *Tunnelling and Underground Space Technology,* 22:317–324.

Meng, F Z, Zhou, H, Zhang, C, Xu, R and Lu, J, 2015. Evaluation methodology of brittleness of rock based on post-peak stress-strain curves, *Rock Mechanics and Rock Engineering,* 48(5):1787–1805.

Meng, F Z, Wong, L N Y and Zhou, H, 2021. Influence of brittleness on TBM penetration rate in Singapore granite, *Journal of Rock Mechanics and Geotechnical Engineering,* 13:221–247.

Tarasov, B G and Potvin, Y, 2013. Universal criteria for rock brittleness estimation under triaxial compression, *International Journal of Rock Mechanics and Mining Sciences*, 59:57–69.

Wang, M M, Li, P, Wu, X W and Chen, H R, 2016. A study on the brittleness and progressive failure process of anisotropic shale, *Environmental Earth Sciences*, 75(10):1–8.

Zhou, H, Chen, J, Lu, J, Jiang, Y and Meng, F, 2018. A New Rock Brittleness Evaluation Index Based on the Internal Friction Angle and Class I Stress–Strain Curve, *Rock Mech. Rock Eng,* 51:2309–2316.

Evaluation of smartphone photogrammetry for 3D surface roughness computation

K Li[1], H L Ramandi[2], C Zhang[3], J Oh[4] and S Saydam[5]

1. PhD candidate, Minerals and Energy Resources Engineering, UNSW Sydney NSW 2052.
   Email: kunze.li@student.unsw.edu.au
2. Senior Lecturer, Minerals and Energy Resources Engineering, UNSW Sydney NSW 2052.
   Email: h.lameiramandi@unsw.edu.au
3. Senior Lecturer, Minerals and Energy Resources Engineering, UNSW Sydney NSW 2052.
   Email: chengguo.zhang@unsw.edu.au
4. Associate Professor, Minerals and Energy Resources Engineering, UNSW Sydney NSW 2052.
   Email: joung.oh@unsw.edu.au
5. Professor, Minerals and Energy Resources Engineering, UNSW Sydney NSW 2052.
   Email: s.saydam@unsw.edu.au

INTRODUCTION

Rock surface roughness plays an important role in excavation engineering projects and applications related to surface support structures, such as shotcrete and thin-sprayed liner (TSL). The morphology of the substrate affects the mechanical behaviour at the interface significantly. Therefore, it is necessary to quantify the roughness to investigate the relationship between roughness and mechanical properties. The joint roughness coefficient (JRC) proposed by Barton and Choubey (1977) is widely used in practice. It initially estimated the roughness by comparing it to 10 standard profiles visually. However, this method has lots of limitations, it is not only subjective but also a two-dimensional parameter with a small lab scale (Beer, 2002).

The subsequent research on JRC, from visual comparison with Barton's standard profiles to measuring the roughness with a profilometer (Weissbach, 1978; Alameda-Hernández *et al*, 2014). Then, 2D profiles or 3D surfaces by different technologies with higher resolution and accuracy, such as 3D laser or optical scanners (Fardin, 2004; Jiang, 2020, 2021). These 3D scanners are expensive and only suitable for laboratory scales. LiDAR scanners (Lato, 2009; Aubertin, 2022) have been applied in industrial size, but it is difficult to achieve a millimetre-level accuracy, which is mostly used to detect the thickness of shotcrete in practice. Thus, finding a cost-effective surface roughness measurement method with high accuracy is necessary.

Photogrammetry is another method to digitalise the roughness of the surface. Similar to 3D scanners, photogrammetry also generates the point cloud of the objective surface and then reconstructs the 3D model of the objects. 3D reconstruction technology is a trendy technology in recent years. The structure from motion (SfM) algorithm (Westoby, 2012) to rebuild the 3D model with a flexible workflow, aligning photos, building dense point cloud, mesh and texture, which has been proved that can rebuild an accurate model in variable fields.

METHODOLOGY

Surface roughness design

Three 100 mm × 100 mm surfaces with different roughness, smooth, intermediate, and rough are used in this research. These surfaces are designed based on natural rock profiles that are scanned by a 3D structured light scanner, whose scan accuracy reaches 0.04 mm. It can generate a set of point cloud data of the original rock surface, which is then subjected to some artificial adjustments to remove the noise point and generate a new 3D mesh file.

Sample preparation

These surfaces can be reproducible and can be measured physically. 3D printed moulds are used to cast these surfaces by grout. To make the loss of profile accuracy during the casting process as less as possible, flexible polyurethane resin material rather than PLA material is used to cast the

surfaces. After each specimen is made, the resin mould should be carefully cleaned to brush off the residual grout particles to reduce the loss of accuracy of the profile next time.

Point cloud acquisition

Although flexible materials are used to reduce the loss of profile accuracy during the inversion process, it is inevitable that the surface roughness of the produced specimens will still have errors with the original point cloud model. Therefore, it is necessary to scan the produced specimens accurately again.
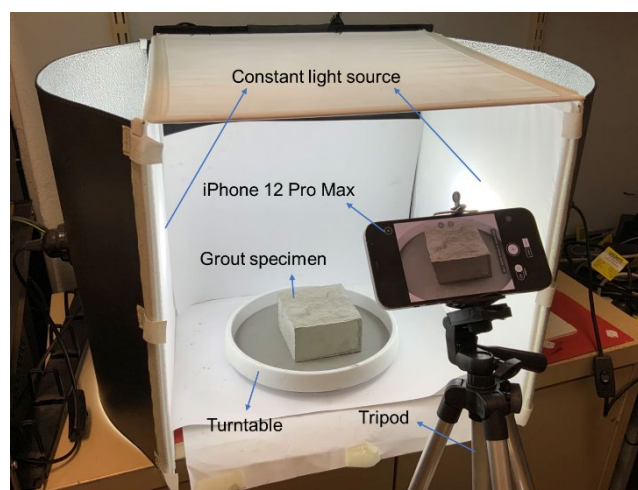
3D structured light scanner

A handheld 3D structured light scanner was used in this research. The accuracy and resolution can reach 0.04 mm with fixed scan mode. The object (casted sample) is placed on an automatic turntable. The angle of each rotation depends on how many pictures the user wants to take of the object per circle. The scanner is standing next to the turntable and uses LED as the light source to take photos of the object, as shown in Figure 1a.

Smartphone photogrammetry

Smartphones equipped with high-resolution camera have the potential to generate an accurate point cloud set. iPhone 12 Pro Max with a 12 megapixels camera was used to take a series of photos for the samples from 360 degrees, as shown in Figure 1b. A mobile application, Polycam, could regenerate a 3D model in 20 minutes and export the point cloud and mesh file directly.
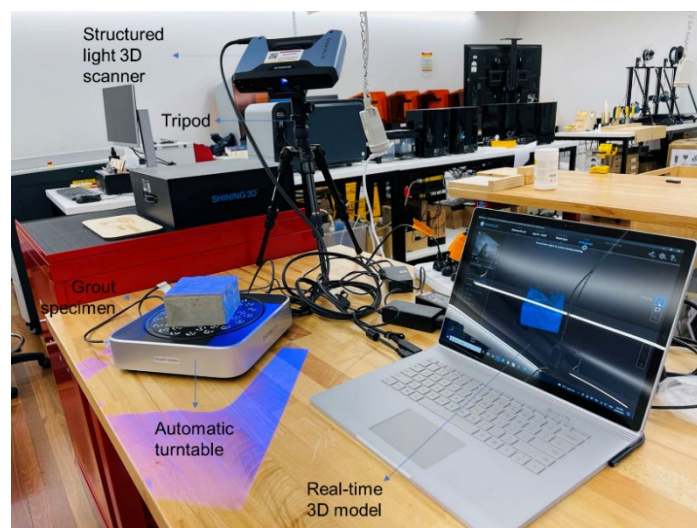
(a)

(b)

FIG 1 – EinScan Pro 2X 3D structured light scanner and smartphone photogrammetry.

Quantify surface roughness

JRC

JRC is a 2D parameter to describe the profile roughness initially. Some researchers have applied JRC to the 3D surface by taking several equally spaced lines along a certain direction of the surface, then calculating the JRC of each line and using the average value to represent the JRC of the surface. A limitation of this method is that the JRC value can only represent the roughness of a specific direction of the surface instead of the whole area. Therefore, other scholars pick profiles at certain degree intervals using the centre of the surface as circle centre, then calculating the average value as the JRC of the whole surface. In this research, a MATLAB code was developed to calculate the JRC for X, Y directions and the whole surface, as well as the Grasselli's parameter. Because the analysed 3D surfaces are composed of points, the statistical parameter Z_2 is very suitable in these cases.

Physical measurement (shear test)

Make grout samples followed by AS 1012. Samples are mixed with water and cement with a ratio of 0.2 and cured at room temperature for 28 days. The UCS of the cement samples is 42.7 MPa, the basic friction angle φ_r = 34.35°.

RESULTS AND DISCUSSION

Reconstructed 3D surface models

The 3D surfaces reconstructed by 3D structured light scanner and smartphone photogrammetry are illustrated in Figure 2.
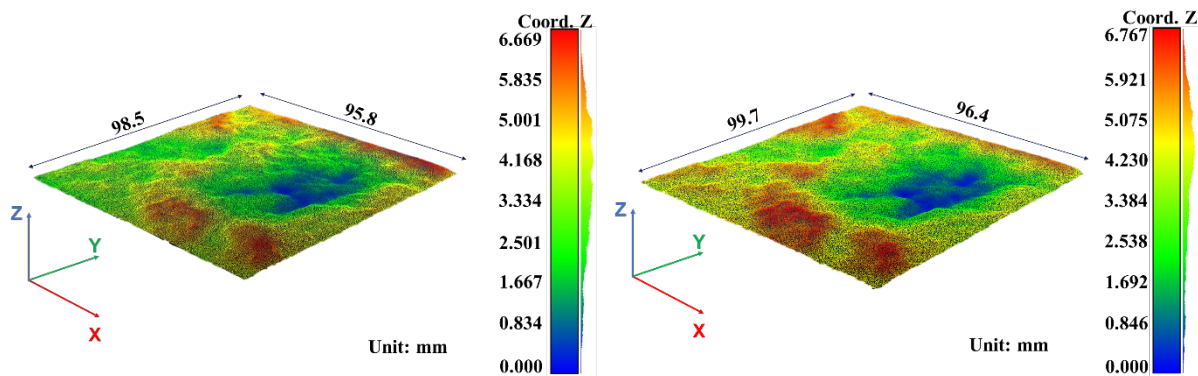

FIG 2 – Reconstructed 3D surface model by 3D structured light scanner and smartphone photogrammetry.

Quantify roughness

JRC is a 2D parameter to illustrate the profile waviness. Grasselli's parameter is a 3D parameter to describe the topography of surface whose shear direction also needs to be determined in advance.

The empirical relationship between peak shear strength and JRC was described by:

$$\tau = \sigma_n \cdot \tan[JRC \cdot \log_{10}(JCS/\sigma_n) + \varphi_b] \tag{1}$$

Hence the JRC can be back calculated by:

$$JRC = \frac{\arctan\left(\frac{\tau}{\sigma_n}\right) - \varphi_b}{\log_{10}(JCS/\sigma_n)} \tag{2}$$

where τ is peak shear strength, σ_n is effective normal stress, JCS is joint wall compressive strength that can be considered as UCS.

A maximum apparent dip θ^*_{max} can be found from all triangles on the surface. The triangles facing to the shear direction can be filtered out by the requirement $\tan \theta^*_i > 0$. The maximum possible

contact area A_0 and potential contact area A_{θ^*} for threshold inclination θ^* have the empirical relationship expressed as:

$$A_{\theta^*} = A_0 \left(\frac{\theta^*_{max} - \theta^*}{\theta^*_{max}} \right)^C \qquad (3)$$

where C is the empirical roughness coefficient. The 3D roughness parameter $\frac{\theta^*_{max}}{C+1}$ revised by has been widely accepted.

Discussion

The shot angle and the light source may lead to appear in shadow in some areas. Moreover, optical scanners are not sensitive to black that result in errors. During the surface digitalisation process, the extraction of the analysed surface from intact model results in differences in the dimensions of the cut due to the large amount of noise point at the edge of the surface.

CONCLUSION

- Surface profile accuracy will be lost during the casting samples. Because soft resin material is used to make surface mould, some grout will be left on the mould.

- A smartphone for \$1000–\$2000 is more economical than conventional 3D scanners and LiDAR scanners that cost over \$10 000.

- The smartphone application (Polycam) can generate high-quality point clouds and mesh in 20 minutes, which is faster than most computer programs and eliminates time-consuming steps such as transferring images.

- Compare the 3D structured light scanner and smartphone photogrammetry (Polycam), the smartphone photogrammetry can provide reliable results.

ACKNOWLEDGEMENTS

REFERENCES

Alameda-Hernández, P, Jiménez-Perálvarez, J, Palenzuela, J A, El Hamdouni, R, Irigaray, C, Cabrerizo, M A and Chacón, J, 2014. Improvement of the JRC calculation using different parameters obtained through a new survey method applied to rock discontinuities, *Rock Mechanics and Rock Engineering*, 47(6):2047–2060.

Aubertin, J D and Hutchinson, D J, 2022. Scale-dependent rock surface characterization using LiDAR surveys, *Engineering Geology*, 301:106614.

Barton, N and Choubey, V, 1977. The shear strength of rock joints in theory and practice, *Rock Mechanics*, 10(1):1–54.

Beer, A J, Stead, D and Coggan, J S, 2002. Technical note estimation of the joint roughness coefficient (JRC) by visual comparison.

Fardin, N, Feng, Q and Stephansson, O, 2004. Application of a new in situ 3D laser scanner to study the scale effect on the rock joint surface roughness, *International Journal of Rock Mechanics and Mining Sciences*, 41(2):329–335.

Lato, M, Diederichs, M S, Hutchinson, D J and Harrap, R, 2009. Optimization of LiDAR scanning and processing for automated structural evaluation of discontinuities in rockmasses, *International Journal of Rock Mechanics and Mining Sciences*, 46(1):194–199.

Jiang, Q, Yang, B, Yan, F, Liu, C, Shi, Y and Li, L, 2020. New method for characterizing the shear damage of natural rock joint based on 3D engraving and 3D scanning, *International Journal of Geomechanics*, 20(2):06019022.

Jiang, Q, Yang, Y, Yan, F, Zhou, J, Li, S, Yang, B and Zheng, H, 2021. Deformation and failure behaviours of rock-concrete interfaces with natural morphology under shear testing, *Construction and Building Materials*, 293:123468.

Weissbach, G, 1978. A new method for the determination of the roughness of rock joints in the laboratory, *International Journal of Rock Mechanics and Mining Science*, 15(3).

Westoby, M J, Brasington, J, Glasser, N F, Hambrey, M J and Reynolds, J M, 2012. Structure-from-Motion photogrammetry: A low-cost, effective tool for geoscience applications, *Geomorphology*, 179:300–314.

Effect of horizontal stress on shallow coalmine slopes

A McQuillan[1] and I Canbulat[2]

1. Director, Rocscience, Inc., Southport Qld 4215. Email: alison.mcquillan@rocscience.com
2. Professor and Head of School, Kenneth Finlay Chair of Rock Mechanics, UNSW Sydney, Kensington NSW 2052. Email: i.canbulat@unsw.edu.au

INTRODUCTION

This paper presents a parametric analysis showing the impact of virgin in situ stresses on a shallow (less than 100 to 150 m) high slope in a jointed sedimentary rock environment. Slope stability is assessed at varying ratios of slope orientation and horizontal stresses. The results of this study indicate stress conditions should be included in stability assessments of excavated slopes, particularly where structure is orientated perpendicular to the direction of horizontal stress.

Some consideration of stress state is applied in deep open cut pits (eg those with planned excavations of 400–1200 m) (Myrvang *et al*, 1993; Stacey *et al*, 2003; de Bruyn *et al*, 2014; Kozyrev *et al*, 2015). Dodd and Anderson (1972), Kalkani and Piteau (1976), Lee (1978), Coulthard *et al* (1992), Noorani *et al* (2011) have studied the effect or horizontal stress and its impact on slope stability, showing that tensile stresses tend to develop at the crest of the slope, with larger tensile zones for higher horizonal stresses and steeper slope angles (Stacey, 1970, 1973; Sjoberg, 2013). However, the consideration of virgin stresses on shallow slope stability is less frequent (Lynch *et al*, 2005; Dight, 2006; Lucas, 2006; Sjoberg, 2013). This has led many geotechnical engineers to believe the impact of virgin in situ stresses on open cut slope stability is minimal and not worth time or consideration in modelling, or their effects on slope stability are still poorly understood (Stacey *et al*, 2003; Sjoberg, 2013).

PARAMETRIC STUDY

The effect of horizontal stress on a shallow jointed coalmine slope was assessed using 3D finite element modelling (FEM), using RS3 code (Rocscience, Inc., 2021). Elastic analyses were run to determine the distribution of stresses at varying horizontal stresses. Jointed rock mass was simulated by applying anisotropy through ubiquitous joints. A consistent slope configuration of 75° slope batter and 100 m slope height was modelled, in a 90° highwall-endwall configuration, to show the stress distribution around the corners of typical open pit design configurations, Figure 1. A parametric study was then completed varying horizontal stress (K1) orientations, relative to the highwall orientation, to show the variance in tensile stress behind the excavated face. Horizontal stresses of K1 = 2 and K2 = 0.8 were applied to the models (after Mark and Gadde, 2010). Modelled scenarios are summarised in Table 1. A graded mesh (minimum mesh size of 5 m, maximum mesh size of 50 m) was applied to the model.
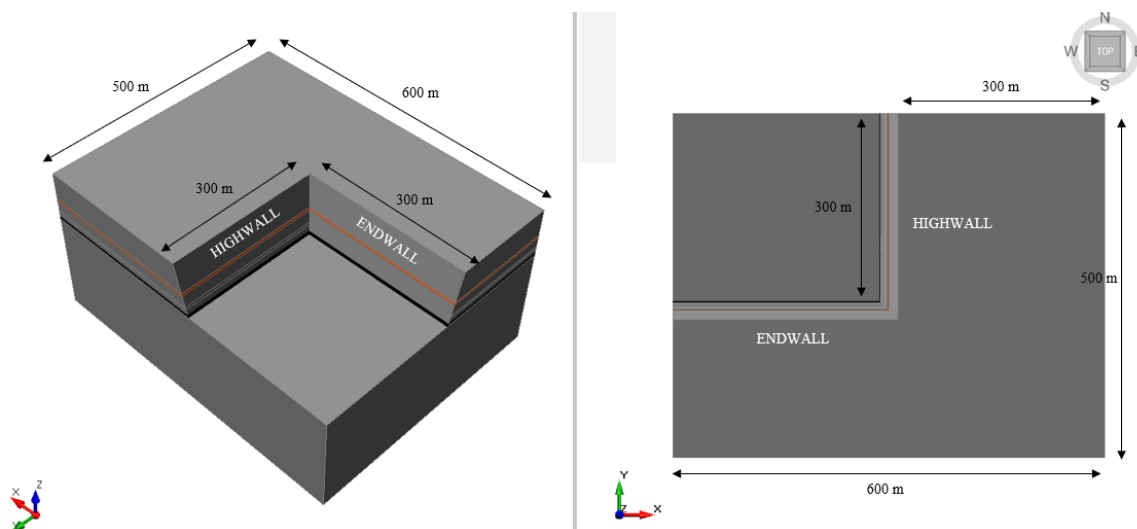

FIG 1 – Model dimensions. Oblique view (left); Plan view (right).

TABLE 1

Modelled scenarios.

| Scenario	HW orientation (DDNº)	Joint condition	K1	K2	K1 Trend (°)
1	270º	Ubiquitous	2	0.8	90
2	270º	Ubiquitous	2	0.8	75
3	270º	Ubiquitous	2	0.8	60
4	270º	Ubiquitous	2	0.8	45
5	270º	Ubiquitous	2	0.8	30
6	270º	Ubiquitous	2	0.8	15

Material parameters applied to 3D models are summarised in Table 2. Ubiquitous joints were modelled with a trend of 0° and plunge of 90°. Applied Joint normal stiffness = 100 000 kPa, shear stiffness = 10 000 kPa.

TABLE 2

Material parameters.

Material	Unit Weight (kN/m³)	Cohesion (kPa)	Friction Angle (º)	Peak Tensile Strength (kPa)	Poisson's ratio	Young's modulus (MPa)
Jointed Fresh coal measure rock	24	200	35	0	0.4	4 000 000
Joints	24	2	12	0	-	-
Coal	15	35	30	1	0.25	3 500 000
Competent Sandstone	26	300	38	1	0.4	4 500 000

RESULTS

The parametric study shows that tensile stress is highest behind the highwall face when horizontal stress is perpendicular to joint orientation and highwall orientation; and tensile stresses are lowest when horizontal stress is nearing parallel to joint orientation, Figure 2.
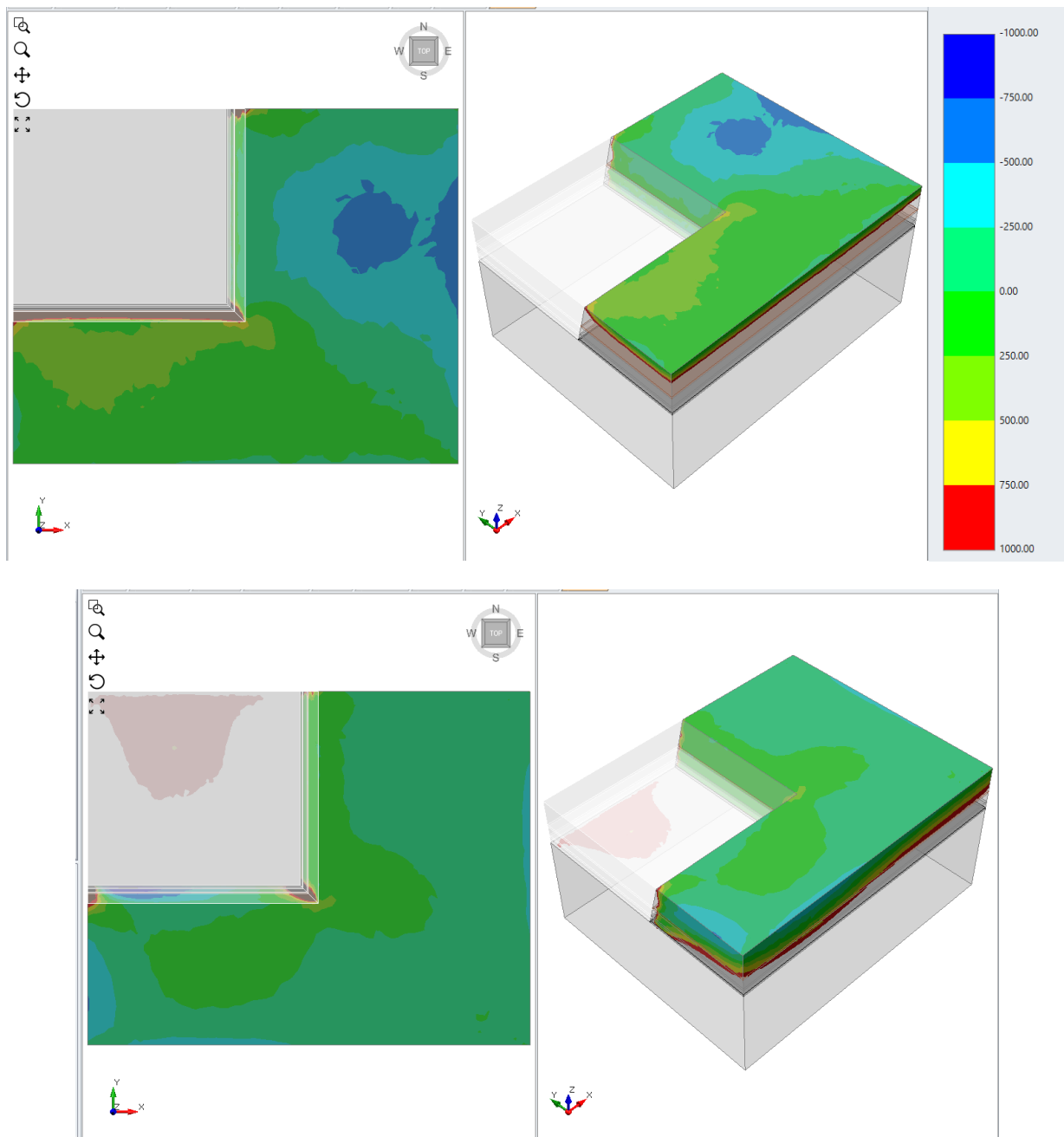
FIG 2 – Contours of SigmaXX Effective, showing modelled tensile stress. Top: K1 = 90°
(ie horizontal stress is perpendicular to slope orientation). Plan view (top left), Oblique view (top right). Bottom: K1 = 15° (ie horizontal stress is near parallel to slope orientation). Plan view (bottom left), Oblique view (bottom right).

In all modelled K1 orientations, compressive stresses are higher at the toe of the slope compared to at the crest in both the highwall and endwall.

Results also indicate a compression zone in all scenarios at the intersection of the highwall and endwall. This stretch notch is observed to decrease as horizontal stress orientation nears parallel to joint orientation.

DISCUSSION

The results of this parametric study are in agreeance with other publications that analysed the effect of horizontal stresses on pit wall stability.

Kozyrev *et al* (2015) found that induced fracturing and dynamic rock pressure events in-pit slopes were governed by the slope orientation relative to the maximum compression orientation and that high compressive stresses heightened rock burst hazards.

Stacey *et al* (2003) reported that stresses at the toe of slopes were found to be concentrated and compressive. And for higher K ratios tensile stress zones develop in the crest of the slope. Stacey *et al* (2003) remarked that this tensile stress zone can be significant, and often tension cracks will develop behind the slope crest.

Resultant tension cracks forming in the extension zone may not only lead to an increase in susceptibility for toppling failure depending on joint orientations, but will also likely create zones of preferential groundwater pooling and surface water drainage that will be detrimental to slope stability.

CONCLUSIONS

This paper has provided several case studies to show that horizontal stresses can affect the stability of shallow (less than 100 to 150 m) coalmine slopes.

Cases show that tensile stress is highest behind the highwall face when horizontal stress is perpendicular to joint orientation and highwall orientation. High tensile stresses behind an excavated slope crest can accentuate the likelihood of slope failure along joints near parallel to the slope face.

Cases also show that compressive stresses are higher at the toe of the slope at varying K1 orientations. High compressive stresses may lead to floor heaving which may then trigger instability in the surrounding slopes.

Although difficult to modify slope designs once mining commences (eg due to economics of mining down dip), this study shows the importance of considering horizontal stresses on slope stability for shallow pit configurations traditionally not considered susceptible to failure by *in situ* stresses.

To adequately assess the impact of horizontal stresses 3D numerical analysis methods should be utilised in slope stability assessments.

REFERENCES

Coulthard, M, Journet, N and Swindells, C, 1992. Integration of stress analysis into mine excavation design, rock mechanics, In *Proceedings: 33rd US Symposium on Rock Mechanics*, New Mexico, pp. 451–460.

de Bruyn, I, Baczynski, N, Lee, M, Mills, K, Mylvaganam, J and Prado, D, 2014. The Application of Rock Stress Inputs to Stability Assessments at Ok Tedi Mine, Papua New Guinea, In *Proceedings: AusRock 2014: Third Australasian Ground Control in Mining Conference*, Melbourne.

Dight, P, 2006. Pit wall failures on 'unknown structures, *J Sth Afr Inst Min Metall*, 106:451–458.

Dodd, J and Anderson, H, 1972. Tectonic stresses and rock slope stability, In *Proceedings: Thirteenth Symposium on Rock Mechanics*, New York, pp. 171–182.

Kalkani, E and Piteau, D, 1976. Finite element analysis of topping failure at Hell's Gate Bluffs, British Columbia, *Bull Ass Engineering Geology*, 13(4):315–327.

Kozyrev, A, Semenova, I, Rybin, V and Avetisyan, M, 2015. Stress redistribution in deep open pit mine Zhelezny at Kovdor iron ore deposit, *Journal of Mining Science*, 51(4):659–665.

Lee, C, 1978. Stress relief and cliff stability at a power station near Niagara Falls, *Engineering Geology*, 12:193–204.

Lucas, D, 2006. Stress failure of a shallow open cut mine, Australian Centre for Geomechanics, December Newsletter, pp. 4–6.

Lynch, R, Wuite, R, Smith, B and Cichowicz, A, 2005. Microseismic Monitoring of Open Pit Slopes, In: *Proceedings of the Sixth International Symposium on Rockburst and Seismicity in Mines*, Australian Centre for Geomechanics, Perth, pp. 581–592.

Mark, C and Gadde, M, 2010. Global trends in coal mine horizontal stress measurements, In *Proceedings: Coal Operators' Conference*, Wollongong, pp. 21–39.

Myrvang, A, Handsen, S and Sörensen, T, 1993. Rock stress redistribution around an open pit mine in hardrock, *Int J Rock Mech Min Sci & Geomech Abstr*, 30(7):1001–1004.

Noorani, R, Ahangari, K and Aloodari, S, 2011. The influence of horizontal stress on the failure mechanism and slope stability in Chador-Malu Iron Open Pit Mine, In *Proceedings: International Symposium on Rock Slope Stability in Open Pit Mining and Civil Engineering (Slope Stability 2011)*, Vancouver.

Rocscience, Inc., 2021. https://www.rocscience.com/support/rs3/release-notes

Sjoberg, J, 2013. Numerical analysis, slope design and in situ stress, In *Proceedings: Slope Stability 2013*, Perth, pp. 29–42.

Stacey, T, 1970. The stresses surrounding open pit mine slopes, In *Planning Open Pit Mines*, P W J van Rensburg (ed), A.A. Balkema, pp. 199–207.

Stacey, T, 1973. A three-dimensional consideration of the stresses surrounding open pit mine slopes, *International Journal of Rock Mechanics and Mining Sciences*, 10:523–533.

Stacey, T, Xianbin, Y, Armstrong, R and Keyter, G, 2003. New slope stability considerations for deep open pit mines*, The Journal of The South African Institute of Mining and Metallurgy*, 103(6):373–390.

Ore recovery on a room and pillar zinc mine

J Santana[1], G Cruzado[2], G Pinto[3] and V Ferraz[4]

1. Geotechnical Engineer, Nexa Resources, Vazante/MG 38780–000.
   Email: jessica.santana@nexaresources.com
2. Geotechnical Coordinator, Nexa Resources, Vazante/MG 38780–000.
   Email: gustavo.cruzado@nexaresources.com
3. Geotechnical Engineer, Nexa Resources, Vazante/MG 38780–000.
   Email: gabriel.pinto@nexaresources.com.
4. Technical Services Manager, Nexa Resources, Vazante/MG 38780–000.
   Email: vitor.ferraz@nexaresources.com

ABSTRACT

Morro Agudo is an underground zinc and lead mine owned by Nexa Resources. The mine uses room and pillar as the main mining method. The recovery of pillars as well as the opening of new excavations using sublevel stoping as mining method has been studied. On some occasions, the need to recover pillars and open a stope by using the sublevel method happens in a region that is already excavated or in deeper areas than those mined so far. These changes represent a major geotechnical challenge due to the complex openings of the mine and interaction between two different mining methods. Historically, geotechnical mapping, kinematic analysis and a 2D numerical model were used to evaluate the new mine openings, and in 2021, 3D numerical model was introduced, which enabled global and local assessment of new excavations impact and the stability of openings after recoveries. The 3D model, made with MAP3D, is used to evaluate each pillar to be recovered, considering the spans of the resulting openings, the ideal sequencing of removal to maintain stability, in addition to the impact and geometry of the pillars left in the chambers. Pillar recoveries done in 2021 and the impact of it on the pillars left were the sources of the back analysis to calibrate parameters inputted on numerical model to assess recovery on new chambers and Phyllite has been considered into the model and it has been a source of instability due to its parallel position to roof of room and pillars and stope hanging walls.

Elastoplastic parameter change at claystone rock mass during sliding failure at Warukin Formation, Indonesia

G W Swana[1]

1. Geotechnical Engineer, Arutmin Indonesia Ltd., 40291, Indonesia.
   Email: galihwiriaswana@gmail.com; galih.swana@arutmin.com

ABSTRACT

Elastoplastic parameter is a parameter that describe how much materials behave elastically up to certain stress states and plastically thereafter (Hudson and Harrison, 1997). In the continuum analysis, two main parameters of the elastoplastic parameter are modulus elasticity and Poisson's ratio. In the slope, elastoplastic parameter holds the main role for stability related to deformation in ductile type of rock. There's a limitation to determine elastic or plastic deformation at the field for ductile rock type. Field manifestation commonly showed that there was no accumulation zone during and after the sliding failure mechanism, in other hand, at the research area, manifestation of deformation at the toe of slope only indicated by bulging shape. This paper will focus at the sliding failure occurred at Coal mining Pit Y owned by Arutmin Indonesia, which according to failure investigation report similar with the condition described above. This paper also will be based on two hypotheses, first hypothesis is claystone rock mass has not been reached plastic deformation yet and the second hypothesis is there is a chance that elastoplastic parameter of the rock mass has been changed during the deformation/sliding failure process. Research method of this paper are back analysis using probabilistic analysis in Finite Element Method (FEM), which conducted before and after failure. Then, the result of the displacement or deformation of the analysis will be checked with the actual deformation shape. Meanwhile, the change of the elastoplastic parameter will be analysed and interpreted. This paper hopefully able to be developed to study about elastoplastic behaviour of rock mass in actual condition and the influence of another uncertainty factor which determine the slope stability.

INTRODUCTION

In Indonesia, claystone massively spread out all along the archipelago within the formation. One of the Formations that contain the claystone is Warukin Formation (Figure 1). Warukin Formation located at South Kalimantan Province, Indonesia, formed at late Miocene-Middle Miocene Age. This Formation regionally contain alternating of fine to coarse grained quartz sandstone with local conglomeratic (5–30 cm) and claystone (3–100 cm) with interbeds of sandy claystone and coal (20–50 cm) this formation deposited in a paralic depositional environment with the thickness of about 1250 m (Sikumbang and Heryanto, 1994). Coal resources commodities brought by Warukin Formation, and become main commodities to be mined. Coal mining itself is owned by Arutmin Indonesia Ltd., at Satui District, Tanah Bumbu City (red square in Figure 1).
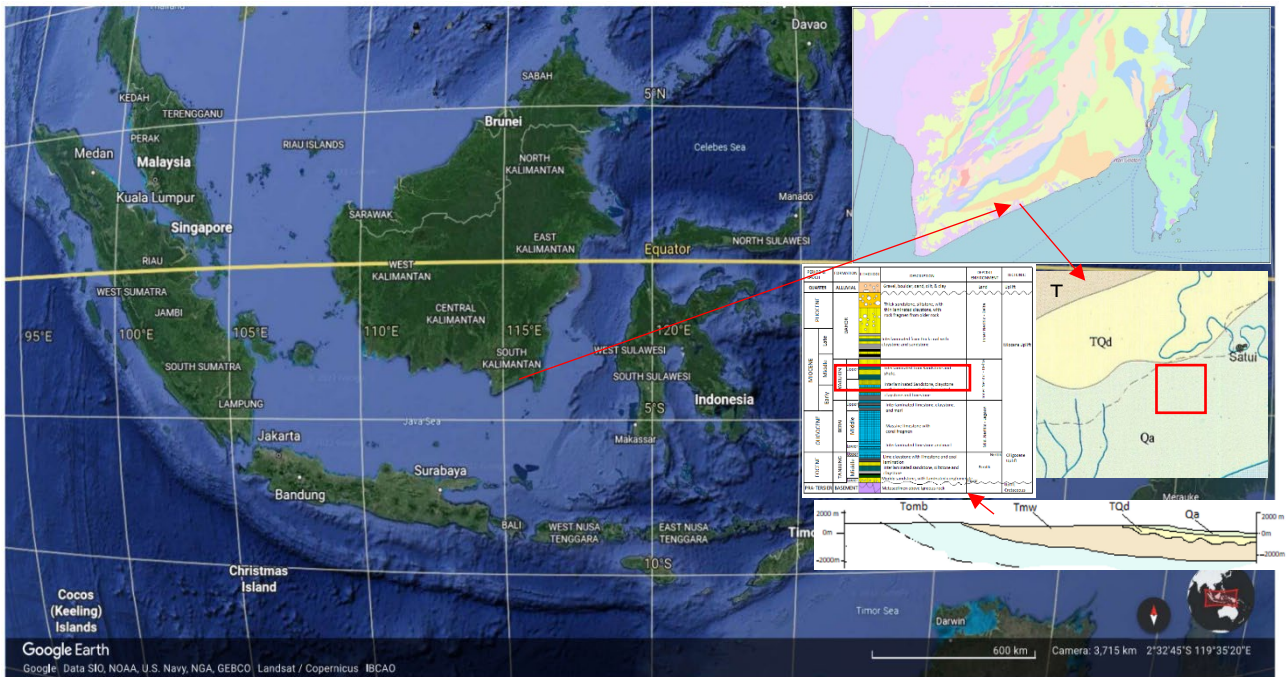
FIG 1 – Location and geological formation of the research area.

Regional geomorphology condition of the area is dominated by gently sloping hills morphography and gentle slopes morphometry (van Zuidam, 1985). Highest elevation of research area is 85 m above sea level, and lowest is 5 m above sea level. In nature, claystone is one of the ductile types of rock. Ductile type of rock characterises by a deformation under influence of stress without macroscopic fracturing (Fossen, 2010). According to the rheological principle, that condition highly related to the elastoplastic deformation. Ductile type of rock also showed the behaviour of low strain during the high temperature and high confining compressive stress, in other hand, brittle material showed the behaviour of high strain rate in low temperature and low confining pressure (Figure 2). Minerals like quartz, olivine, and feldspars are very brittle. Others, like clay minerals, micas, and calcite are more ductile due to the chemical bond types that hold them together (Nelson, 2015).
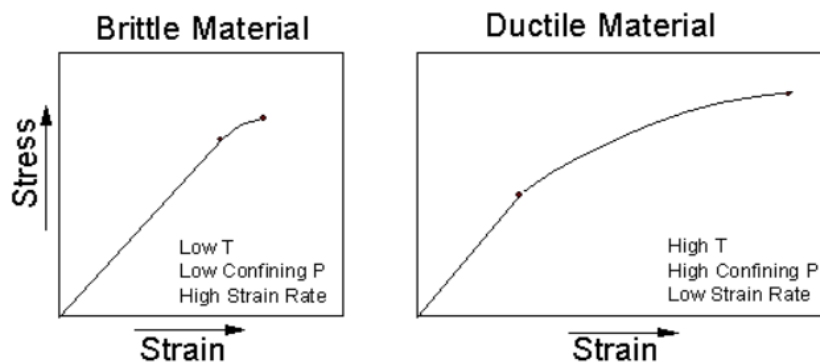
FIG 2 – Brittle and ductile material behaviour (Nelson, 2015).

Elastoplastic parameter is a parameter that describe how much materials behave elastically up to certain stress states and plastically thereafter (Hudson and Harrison, 1997). Elastoplastic described by two parameters which are Elastic modulus and Poisson's ratio. Elastic modulus (E) is a ratio between stress (σ) and strain (ε), while Poisson's ratio (v) is a ratio between transversal strain (ε_{trans}) and axial strain (ε_{axial}).

This research will be focusing on elastoplastic parameter of the claystone at Warukin Formation, which has been suffered by a Planar-Circular Sliding failure. Interestingly, the behaviour of the ductile rock mass retains the deformation shape quite a while, while being affected by constant stress. elastoplastic parameter will be observed during the failure by conducting back analysis.

DATA AND METHOD

The research method in this research is to perform a back analysis of each failure event. The back analysis in this study is to use the Finite Element Method (FEM), which will see the total displacement and its Strength Reduction Factor (SRF). These two parameters will be considered to represent the geometry of the displacement that occur in every failure phase. Because the deformation geometry has been collected previously, each analysis in the probabilistic analysis will be compared to the total displacement against the actual deformation geometry in every failure phase, then the elastoplastic parameter of the total displacement corresponding to the actual deformation geometry will be selected for back analysis in the subsequent landslide stages.

This research will focus on the elastoplastic parameter in claystone rock mass that included in FEM analysis those are peak and residual elastic modulus, and Poisson's ratio. SRF value bigger closer to the 1 will represent the stable condition and SRF less and near to 1 will represent unstable condition. Other parameters that will be included and supported in this research are:

1. Topography of the slope before and after failure of the Coal Mining Area.

2. Intact rock and rock mass engineering properties (Shear strength, Elastoplastic, and index properties).

3. Field evidence and special feature of the failure.

4. Additional slope monitoring result.

Flow chart of this research can be seen in Figure 3.
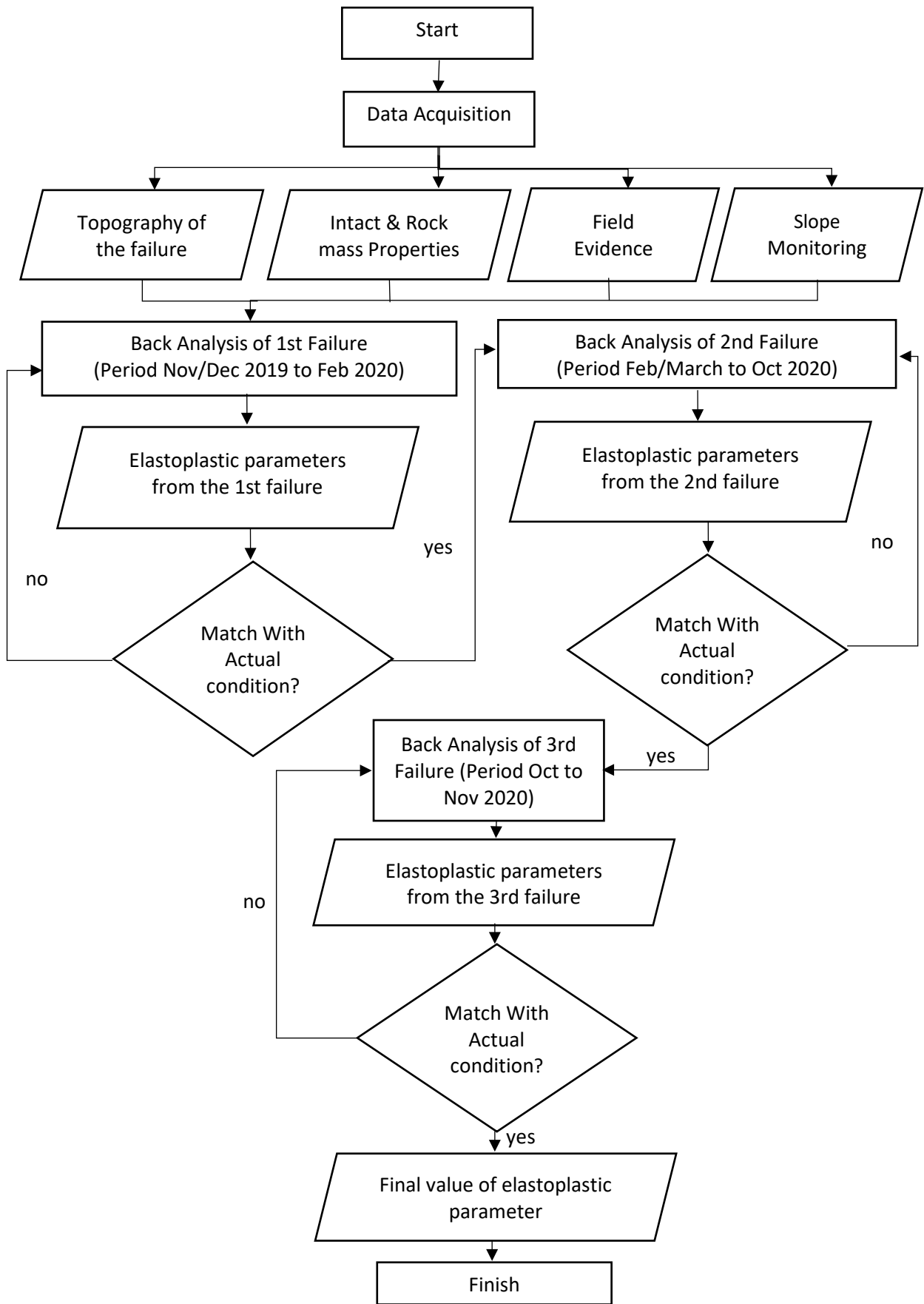
FIG 3 – Flow chart of research method.

Coal mining area

Main commodity of Arutmin Indonesia Ltd. in Pit Y area is coal. Naturally, the Warukin Formation is formed in deep neritic sedimentary basins to swamp areas. The sedimentation process continues to form stratification conditions. After the sediment undergoes a lithification process, tectonic processes play a role in the formation of the slope of the bedding plane. Based on local geological mapping, the orientation of the bedding plane is N123°E/12°.

Economically, total reserve of the coal is mineable by excavating from Low wall to highwall area. Low wall slope is a slope that has a lower overall and single slope angle, and Highwall slope is a slope with steeper overall and single slope angle (Figure 4). Low wall slope angle, has the same value as the dip of major discontinuity plane (bedding plane) which is 12°, then for Highwall, single slope angle is 55° with overall slope angle is 26°.
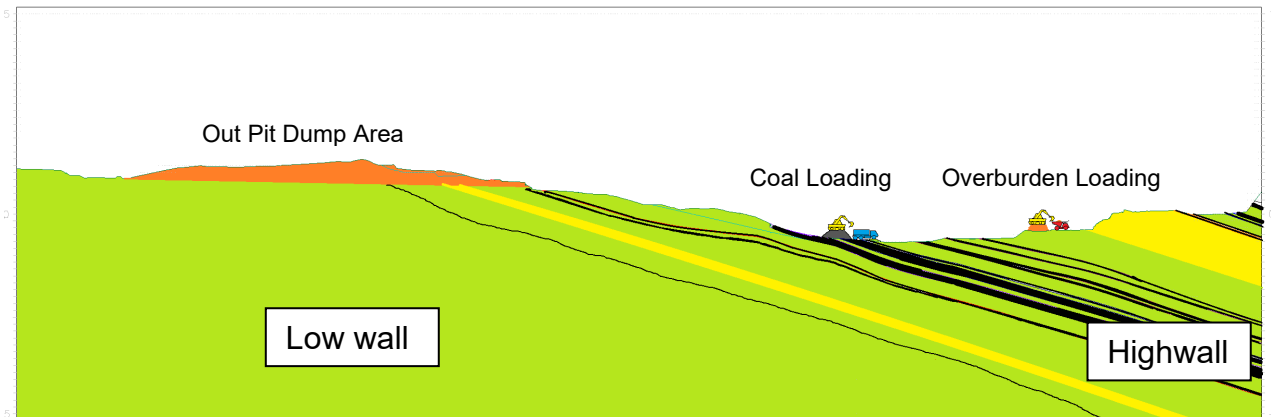
FIG 4 – Illustration of coal mining procedure of Pit Y Arutmin Indonesia Ltd.

The research area will focus on the Low wall slopes which have been displaced in the last quarter of 2019. The low wall slopes that have displaced are in Block 18–19–20 or Western part of Pit Y (Figure 5). The topographic Map itself is an updated version after the last failure event (November 2020). On the lower part is the Low wall slope and the steeper is the Highwall slope.
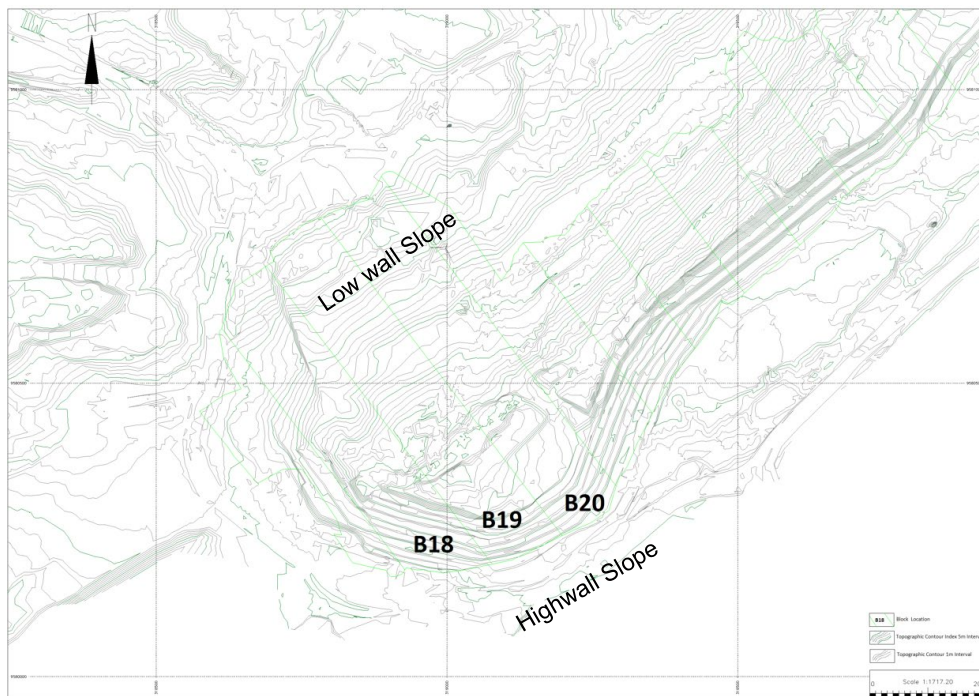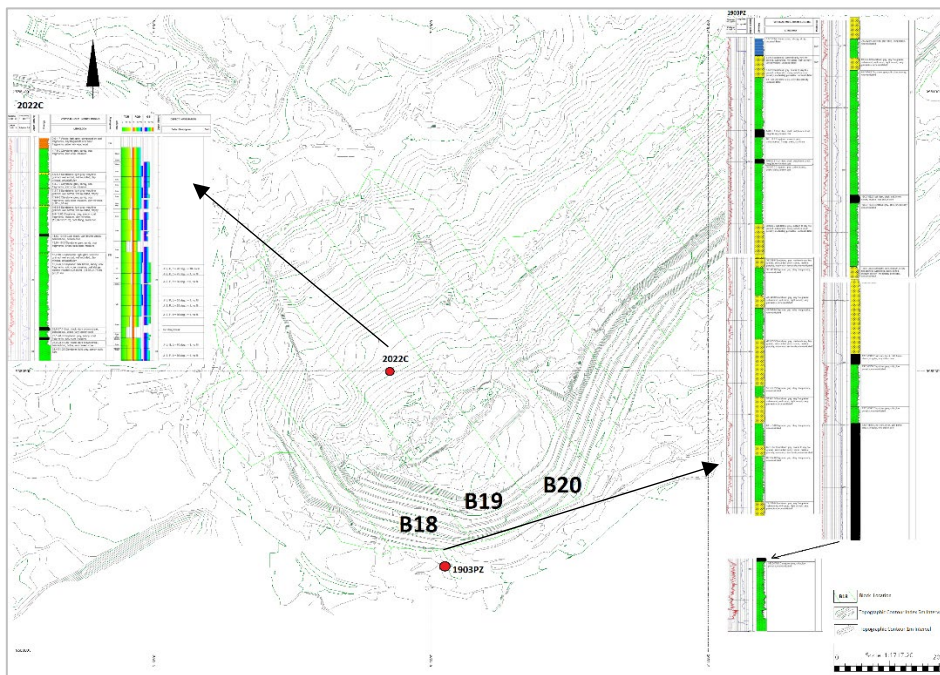

FIG 5 – Location of the slope failure of Pit Y.

Engineering geology

According to the geotechnical drilling and local engineering geological mapping, lithostratigraphy consist of massive claystone, Carbonaceous claystone, Sub-Bituminous Coal, Sandstone, and Interlaminated Claystone-Sandstone as shown at bore log below (Figure 6).

FIG 6 – Geotechnical drilling log and their location of the research area.

Claystone rock mass of research area characterise by massive form, grey to dark grey colour, earthy lustre, there is local lenticular structure filled with coal, moderately to poor permeability, sideritic mineral found as a nodule at some place, compressive strength of the intact claystone rock is classified as a weak to very weak rock (1–25 MPa), Geological Strength Index (GSI) ranged from 50 to 45, Average thickness of the massive claystone is 5 to 10 m, massive claystone is a major lithology that makes up most of the lithology of the Low wall Area. Carbonaceous claystone commonly found as a sediment floor at the bottom of coal bedding, has a dark grey colour, and shaly structure, thickness of the carbonaceous claystone is about 5–10 cm.

Meanwhile Sandstone of the research area are light grey to yellowish in colour, fine–very fine grained, well sorted, lithic and coal fragment occurred in some place, intercalated to gradational contact with the underlying base, compressive strength of intact rock as a weak to very weak rock and easily crumbled by hand, GSI ranged from 30 to 40 average thickness is about 10 m. Interlaminated Sandstone and claystone is a lamination of a very fine sandstone and carbonaceous claystone with total thickness is about 5 m, compressive strength ranged from 1 to 5 MPa (Very weak rock), has a GSI value 25 to 30.

Coal of the research area characterise as a sub bituminous coal, has a black colour, with waxy lustre, highly cleated, intact compressive strength ranging from 5 to 25 MPa characterise as a weak rock, intercalated contact with the claystone, GSI value is ranging from 30 to 40, thickness of the coal is about 0.2 m to 5 m thick.

According to the observation well, elevation head occurred at Elevation 30 near crest of Low wall slope and Elevation 18 near the crest of Highwall. The groundwater table is also represented by the discharge point that occurs at the bottom of the pit on both the Low wall and Highwall slopes. The aquifer in the study area is sandstone and classified as a confined aquifer.
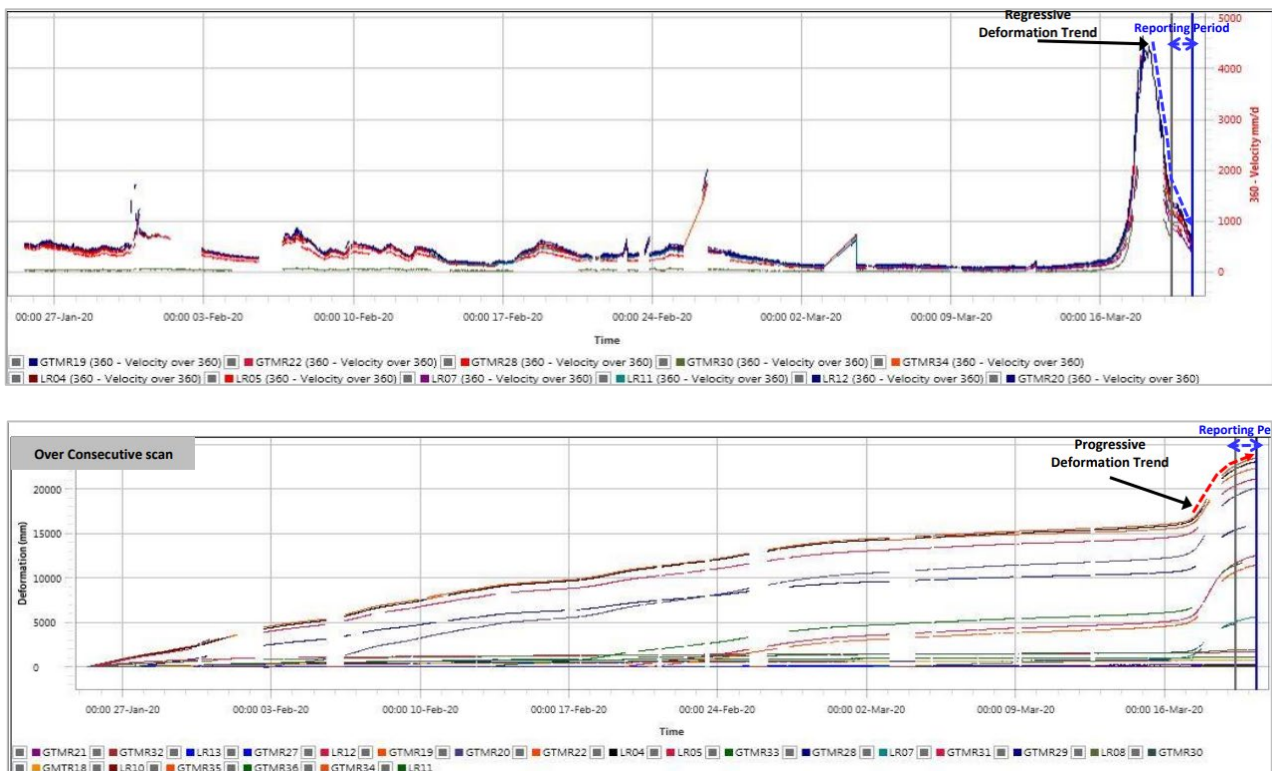
Sliding failure event

Based on the collected data, slope failure occurred three times from November 2019 to November 2020. The failure itself, described as a circular-planar sliding failure. Reactivation of the failure

occurred twice at the period above, namely in March 2020 and November 2020 due to the coal mining process at the toe of the Low wall slope. Main scarp in the study area has an orientation of N35°E/80°. Displaced material is a massive claystone rock mass with thin coal and sandstone. Accumulation zone has not occurred during the first failure and reactivation phase. Thus, the result of the deformation is a bulging deformation that is formed at the toe of the slope. The bulging deformation also results in a steeper slope in the bedding plane (Figure 7) from 14° to 40°.
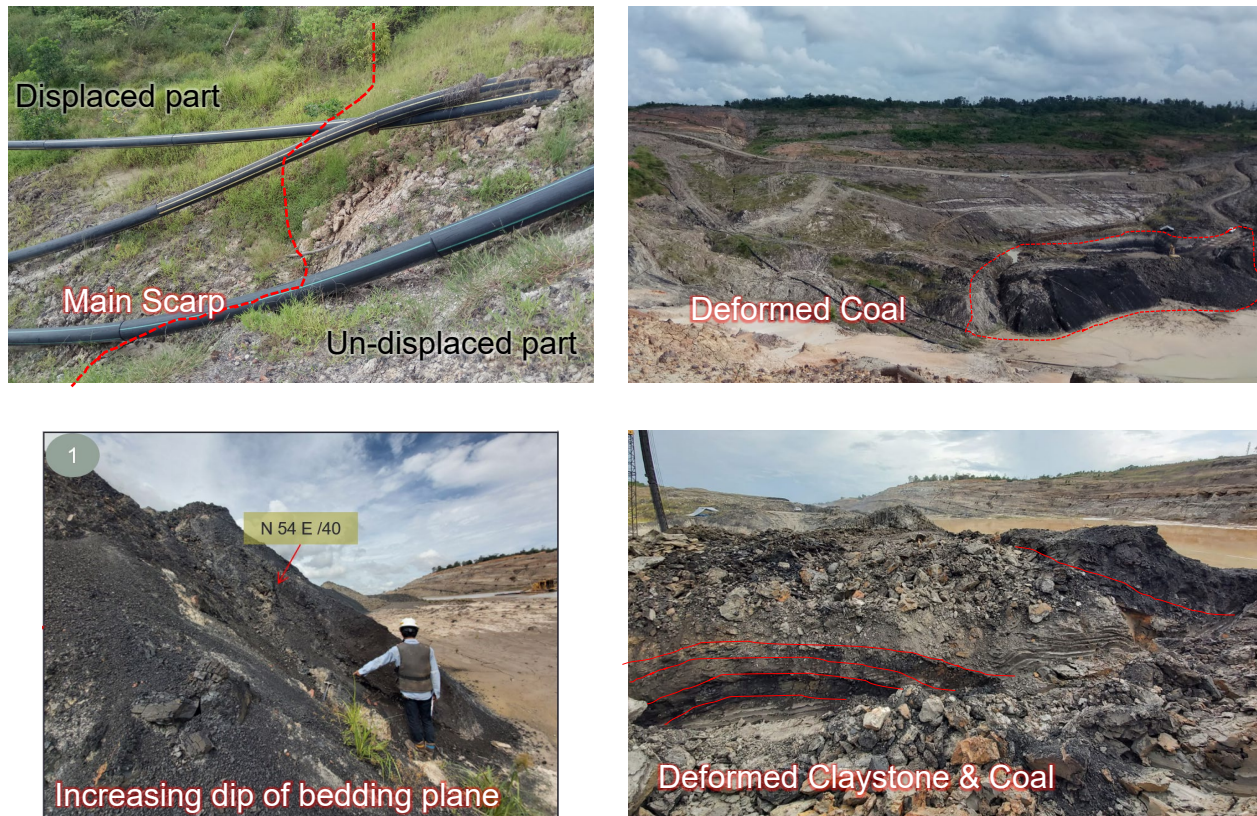
FIG 7 – Main scarp and bulging deformation of the last failure event.

According to the Geotechnical Monitoring System (GMS), displacement of the slope has reach 28 000 mm with the fastest velocity is about 4500 mm/day (Figure 8). Cruden and Varnes (1996, in Transportation Research Board, 1996) described the velocity as a low velocity failure or creeping mechanism.

FIG 8 – Velocity and displacement graph of the failure (February 2020 – March 2020).

Sliding failure was controlled by the thin carbonaceous claystone formed at the intercalation contact between coal and claystone, in this case is sediment roof of coal seam CU. In other hand, this failure also triggered by coal excavation process at the toe of the slope. The stages of sliding failure in the study area can be seen in Figure 9.
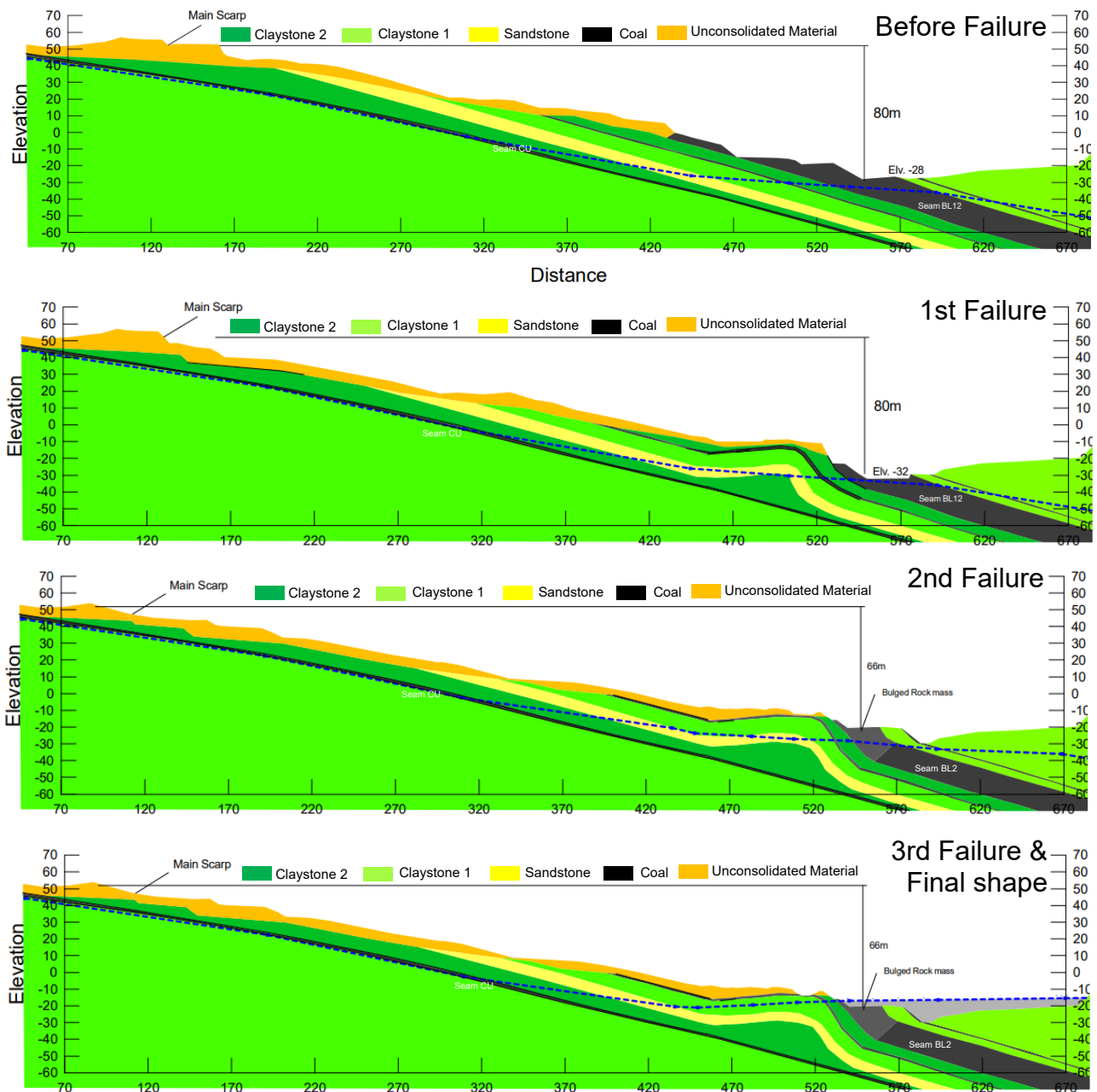
FIG 9 – Cross-section of the failure event time by time.

Geotechnical engineering

Geotechnical engineering drilling was carried out before and after the failure. However, these engineering properties are tested before failure. Since the intact rock compressive strength is concluded as a very weak rock, so the results of rock mass properties are very similar to the properties of intact rock that will be used in this study. Engineering properties of intact and rock mass can be seen at the table below (Table 1). This engineering property will also be used as the basis for the back analysis in first failure phase.

TABLE 1
Engineering properties of the material.

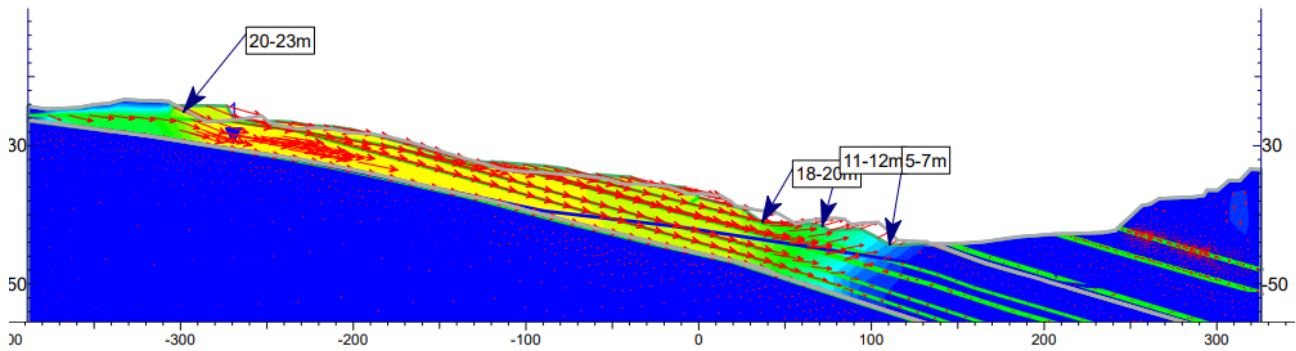| Lithology	γ (kN/m³)	C (kPa)	Φ (°)	C' (kPa)	Φ' (°)	σ_t (kg/cm²)	σ_t' (kg/cm²)	E (kPa)	E' (kPa)	v
Waste Material	20.3	40	16	23.6	13.5	0.048	0.0437	333.33	326.11	0.4
Claystone 1	20.4	136	27.51	71	14.9	3.9	0.128	45500	955.22	0.26
Claystone 2	20.4	100	24.48	61	13.86	2.75	0.11	28370	595.77	0.27
Sandstone	23	74	26.5	10	19.9	0.9	0.036	2066100	43388.31	0.24
Siltstone	21.7	84.9	56.6	75	19.6	3.4	0.136	1514100	31796.1	0.27
Coal	13.1	183	46.8	107	25.46	1.07	0.0428	420000	8820	0.27

RESULT AND DISCUSSION

First failure event

Back analysis of the first geometry (November 2019) was carried out before the first failure occurred. First failure phase will use the engineering properties value of the material at Table 1. The purpose of the probabilistic analysis in the first failure phase is to determine the shear strength of the discontinuity of the CU coal seam layer, which is the rupture plane of the sliding failure. This analysis also to determine the most representative value and similar bulging deformation of the first failure phase (Figure 9).

Since the rupture plane is a bedding plane, and sediment floor of coal seam CU has a planar waviness and smooth roughness with no infilling, file number 4 (Table 2) shows a suitable value based on the actual discontinuity plane condition above based on the shear strength classification of the discontinuity plane by Barton and Choubey (1974). In addition, the results of the analysis also show the results of the total displacement and deformation geometry that match the actual conditions (Figure 10). So, file number 4's shear strength of discontinuity will be used during the assessment.

TABLE 2
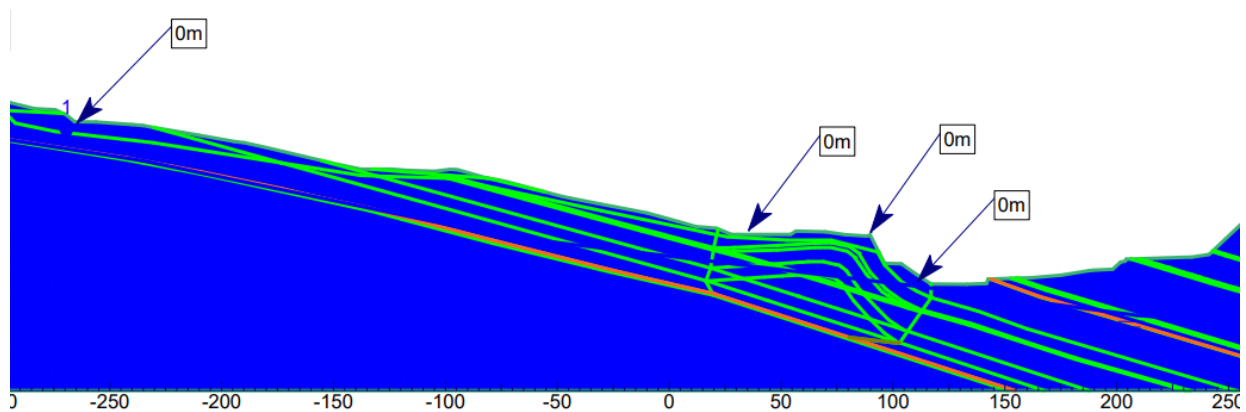Probabilistic parameter value of discontinuity shear strength of rupture plane.

File #	Tensile strength (kPa)	Cohesion (kPa)	Friction Angle (°)	Critical SRF
1	20	50	20	1.55
2	0	50	20	1.55
3	20	0	20	0.92
4	0	0	20	0.92
5	20	50	0	0.72
6	0	50	0	0.72
7	20	0	0	0.71
8	0	0	0	0.71

FIG 10 – FEM analysis of the first failure unstable condition.

Result of the first failure is a bulging shape and total displacement that shown in Figure 9 and Figure 10. Before entering second failure phase, first failure reached a stable (dormat) state after the final form was reached (February 2020) and showed no displacement (Figure 11). At that time the elastoplastic material had undergone a change in value, the change can be seen in Table 3. Based on the series of values indicating the critical SRF, the value that is greater and closest to 1 is file number 17.

FIG 11 – FEM analysis of the first failure at stable/dormant condition.

TABLE 3

Probabilistic parameter value of deformed claystone of first failure.

| File #	Deformed Claystone 2			Deformed Claystone 1			Critical SRF
	Young's modulus	Residual Young's modulus	Poisson's ratio	Young's modulus	Residual Young's modulus	Poisson's ratio	
14	14370	890.77	0.15	20500	1405.22	0.46	0.99
15	42370	300.77	0.15	20500	1405.22	0.46	0.91
16	14370	300.77	0.15	20500	1405.22	0.46	0.99
17	42370	890.77	0.45	70500	505.224	0.46	1.03
18	14370	890.77	0.45	70500	505.224	0.46	0.91

Second failure event

The second failure occurred when there was a coal excavation in the deformed coal seam (Seam BL2). The excavation resulted in the second failure in March 2020. Based on the back analysis, the elastoplastic parameter value which has the most appropriate deformation shape and SRF value according to actual conditions is file number 47 (Table 4).

TABLE 4

Probabilistic parameter value of deformed claystone of second failure.
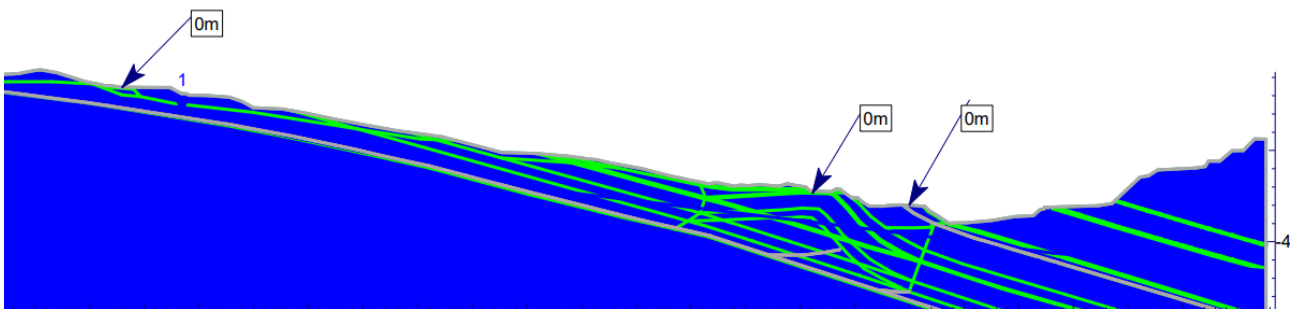
File #	Deformed Claystone 2			Deformed Claystone 1			Critical SRF
	Young's modulus	Residual Young's modulus	Poisson's ratio	Young's modulus	Residual Young's modulus	Poisson's ratio	
51	42370.5	150.77	0.49	105750	0.224	0.43	0.95
47	42370.5	150.77	0.41	35250	1010.22	0.43	0.94
62	42369.5	1630.77	0.41	35250	0.224	0.43	1
63	42370.5	150.77	0.41	35250	0.224	0.43	1
64	42369.5	150.77	0.41	35250	0.224	0.43	1

This failure event phase, resulted in more even displacement especially shows at the toe of the slope. Bulging deformation shows more advancing deformation to the toe of the slope (Figure 12).
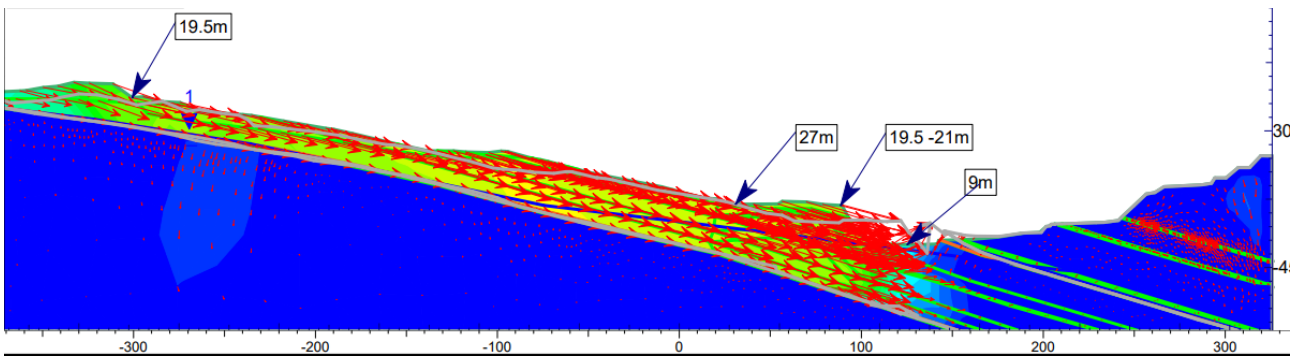
FIG 12 – FEM analysis of the second failure at Unstable condition.

Before entering the third failure phase, second failure reaches a stable status after the final form reached (October 2020), and shown no displacement (Figure 13). At that time elastoplastic material has changed to the value below (Table 5). Elastoplastic parameter which shows the SRF value is greater and closest to 1 is file number 55.

FIG 13 – FEM analysis of the second failure stable condition.

TABLE 5

Probabilistic parameter value of deformed claystone of second failure.

| File #	Deformed Claystone 2			Deformed Claystone 1			Critical SRF
	Young's modulus	Residual Young's modulus	Poisson's ratio	Young's modulus	Residual Young's modulus	Poisson's ratio	
51	55250	405.22	0.49	72370	75.77	0.33	1.3
52	15250	405.22	0.49	72370	75.77	0.33	1.57
53	55250	2405.22	0.37	72370	75.77	0.33	0.99
54	15250	2405.22	0.37	72370	75.77	0.33	1.55
55	55250	405.22	0.37	72370	75.77	0.33	1.19

Third failure event

third failure phase triggered by excavation progress at the bulging deformation area (October 2020) and finally reached the final form/dormant status on December 2020. According to the final deformation shape displacement value increased in a slight value. Based on the analysis, the value of the elastoplastic parameter shows a value below (Table 6). Slight displacement occurred at this failure especially at the toe of the slope (Figure 14).

TABLE 6

Probabilistic parameter value of deformed claystone of third failure.

| File #	Deformed Claystone 2			Deformed Claystone 1			Critical SRF
	Young's modulus	Residual Young's modulus	Poisson's ratio	Young's modulus	Residual Young's modulus	Poisson's ratio	
20	20500	505.224	0.46	42370	300.77	0.45	0.94
21	70500	1405.22	0.06	42370	300.77	0.45	0.55
22	20500	1405.22	0.06	42370	300.77	0.45	0.92
23	70500	505.224	0.06	42370	300.77	0.45	0.94
24	20500	505.224	0.06	42370	300.77	0.45	0.92
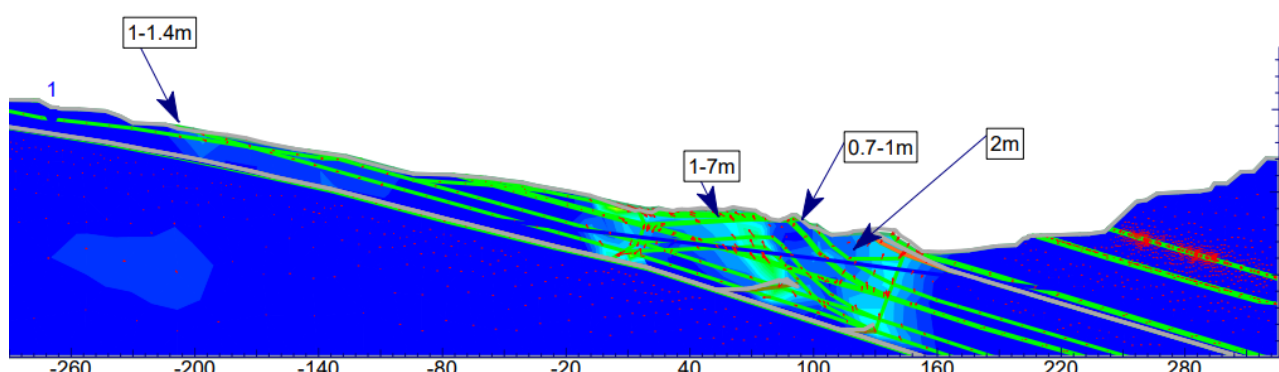
FIG 14 – FEM analysis of the third failure unstable condition.

CONCLUSIONS

Based on the analysis of every failure, shown that during the failure progress elastoplastic parameter has been changed. Elastic modulus shows an increasing trend for Claystone 2. After the first failure reach stable status, elastic modulus has increased about 33 per cent, then second failure appears

to be constant therefore increasing about 23 per cent in dormant status, and finally increasing again at the third failure phase for about 21 per cent. Claystone 1 shows a slight increasing trend generally. At the dormant status from first failure phase elastic modulus increased about 35 per cent, then decreased about 50 per cent at the second failure. Therefore, at the dormant status of second failure phase increased again for about 51 per cent, and finally decreased at the third failure phase for about 41 per cent (Figure 15).
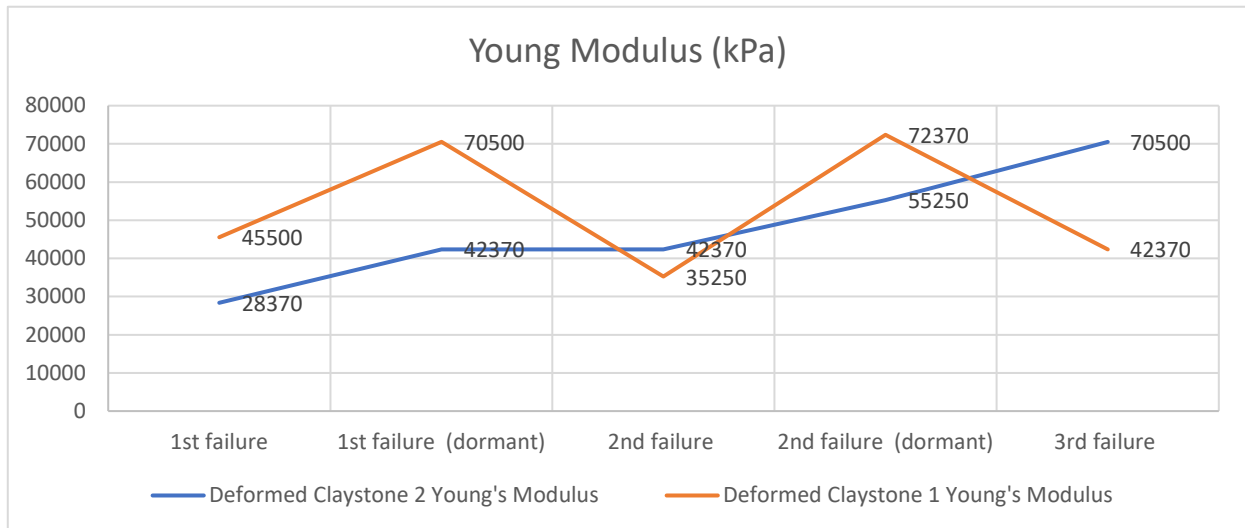
FIG 15 – Chart of elastic modulus during sliding failure.

Meanwhile, residual elastic modulus value gradually become lower in every failure progress (Figure 16). At the first failure phase to dormant status, Claystone 1 shows a decreased value for about 47 per cent, then increasing at second failure phase for about 49 per cent, then decreased significantly until the dormant status of second failure phase for about 92 per cent. Finally, At the third failure phase the value increased again for about 74 per cent.
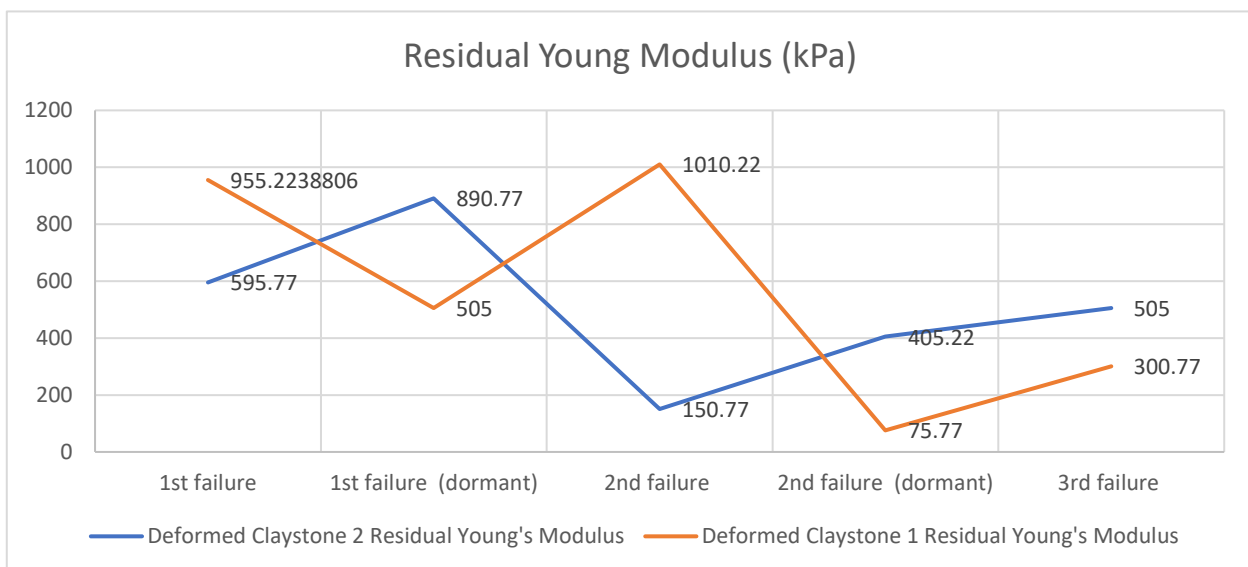

FIG 16 – Chart of residual elastic modulus during sliding failure.

At the first failure, Claystone 2 shows an increased value for about 33 per cent from the first failure phase to the dormant status, then decreased about 83 per cent at the second failure phase. Therefore, continue to increase about 62 per cent and 19 per cent at the dormant state of the second failure phase and third failure phase.

Poisson ratio in other hand become gradually increased for Claystone 2 and Claystone 1. Meanwhile there's a small decreased at the third failure phase at the Claystone 2 (Figure 17). At the Claystone 1 after the first failure phase reach dormant status, Poisson ratio increased for about 40 per cent. After

that decreased from second failure phase until reach dormant status for about 8 per cent and 9 per cent. at the third failure phase, Poisson ratio decreased significantly for about 83 per cent.
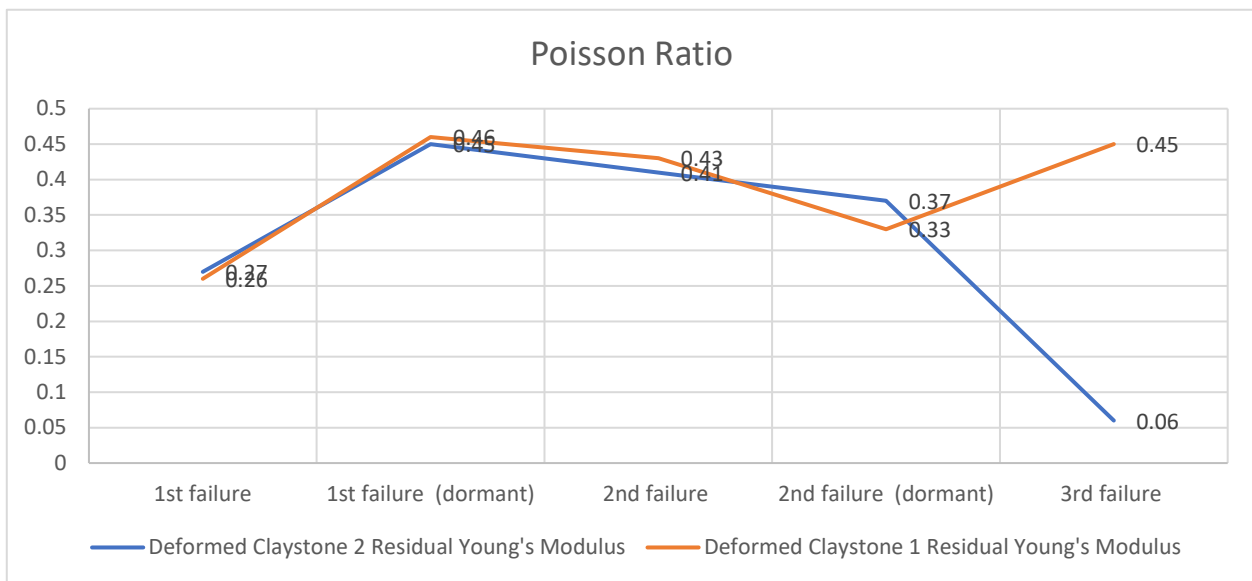

FIG 17 – Chart of Poisson ratio during sliding failure.

Claystone 2 shows similar value with Claystone 1, after the first failure phase reach dormant status, Poisson ratio increased for about 43 per cent. After that decreased from second failure phase until reach dormant status for about 6 per cent and 23 per cent. Finally at the third failure phase, Poisson ratio increased for about 26 per cent.

According to those value, elastoplastic parameter of claystone rock mass has been changed during the sliding failure mechanism. Peak elastic modulus of claystone slightly increased during the sliding failure mechanism, while the residual elastic modulus decreased. So, it can be concluded that, the strain of the claystone rock mass is slightly reduced in the same stress, according to the Hudson and Harrison (1997), a material that continues to strain when the applied stress is held constant is considered to be a creep. Meanwhile the decreased of residual elastic modulus means during the failure, strain value become larger after every failure process. Therefore, in every failure phase claystone rock mass become more fragile which will be more easily deformed after peak elastic modulus reached.

Poisson's ratio seemingly increased during the first failure phase and decreased gradually during the sliding failure. Generally, during the first failure phase Poisson's ratio value increased significantly since the first axial strain formed and manifested by bulging deformation shape. After first failure phase lateral strain gradually reduced and axial strain become slightly bigger until third failure phase.

This behaviour probably is a manifestation of true strain. The different between engineering strain is engineering strain generate by engineering stress simplifies by neglecting cross-sectional change. True strain which also generate by true strain correctly accounts for the changing cross-sectional area (Gedeon, 2013). Therefore, true stress-strain curve never decreases (Çapar, 2020) (Figure 18). Mineral and grain of claystone presumably hold an important role which will behave differently during high and constant stress.
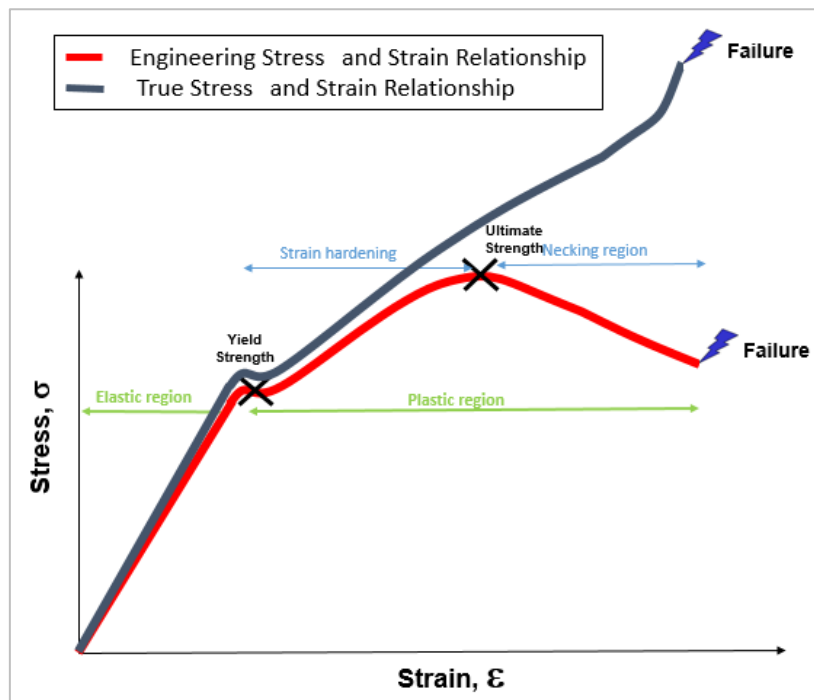
FIG 18 – Chart of Stress versus Strain between Engineering strain and True strain (Çapar, 2020).

However, there's still need further research especially for collecting intact rock samples to obtain the elastoplastic parameter along the slope after the failure event to compare the result computationally and actually. Besides that, need to considerate the relation to another parameter (shear strength, compressive strength, plasticity index etc) and another rock mass condition (sandstone, siltstone, and coal).

ACKNOWLEDGEMENTS

REFERENCES

Barton, N and Choubey, V, 1974, Shear Strength of Rock Joints in Theory and Practice *Rock mechanics*, 10:1–65, Norway.

Çapar, Y, 2020. Engineering Stress Strain VS True Stress Strain [online], Available from: <http://yasincapar.com/engineering-stress-strain-vs-true-stress-strain/> [Accessed: 5 September 2022].

Fossen, H, 2010. *Structural Geology*, p 17, ch 6, Cambridge University Press: Cambridge, UK.

Gedeon, M, 2013. The hard work of work hardening an in-depth discussion of strain hardening in metals, *Technical Tidbits, Materion Brush Performance Alloys*, issue 50, US.

Hudson, J A and Harrison, J P, 1997. *Engineering Rock Mechanics*,, first edition, p 215, ch 13, Elsevier Science Ltd, Pergamon: Oxford, UK.

Nelson, S A, 2015. Mineralogy Lectures, Tulane University, New Orleans, US.

Sikumbang, N and Heryanto, R, 1994. Geological Map of The Banjarmasin, Kalimantan, Geological Agency (PPPG) Ministry of Energy and Mineral Resources Indonesia, Indonesia.

Transportation Research Board (TRB), 1996. Landslides: investigation and mitigation, A K Turner and R L Schuster (eds), US National Academy Press.

Van Zuidam, R A, 1985. Aerial Photo – Interpretation in Terrain Analysis and Geomorphologic Mapping, Smith Publisher, The Hague, ITC.

Integration of Geoblast and D&B Engineering as an engineering tool in PT. Indo Muro Kencana

H Utama[1] and A Suwandhi[2]

1. Junior Manager Mining, PT. Indo Muro Kencana, Central Kalimantan, Indonesia, 73911.
   Email: heru.utama@imkgold.co.id
2. Vice Chairman of Academic and Research, Mining Engineering Department, Indonesian College of Mineral Technology, Bandung, West Java, Indonesia 40274.
   Email: awang.suwandhi@gmail.com

ABSTRACT

PT. Indo Muro Kencana (PT.IMK) is gold and silver mine located in Central Kalimantan province, Indonesia. Mining activities in PT.IMK is conducted in Bantian pit area by applying surface mining method and using combination of excavator and hauler (articulated dump truck and rigid haul truck) as the transportation for ore to the crushing plant and waste material to the waste dump. Current blasting practice is ore-waste blasting. Ore-waste blasting is the term where the ore and waste rock are blasted in the same blasting process. Blasting is conducted by using nonel initiation system. By multiple pits operation, monthly powder factor is varied from 0.23 kg/t to 0.27 kg/t. Emulsion blend with density 1.15 g/cc is used as bulk explosive. At this stage, the concept of geoblast is proposed as an engineering tool for Drill and Blast engineering practice in PT.IMK. In addition, there is a need to maintain rock fragmentation by blasting, to maintain monthly powder factor, and to maintain excavator's productivity. Next, the concept of scaled depth of burial (Chiappetta and Treleven, 1997) and the concept of blastability index (Lilly, 1986) are proposed as geoblast's tools to improve blasting practice in PT.IMK. It is expected that rock fragmentation by blasting, explosive consumption and excavator's productivity will be maintained by integration of geoblast and drill and blast engineering. Furthermore, the objective of this paper is to integrate geoblast and drill and blast engineering in order to create an engineering guideline in PT.IMK. Additionally, blasting trials with air decking application is proposed in order to support the geoblast's improvement. It is planned that these blasting trials will be conducted in 2022. In conclusion, it can be seen that integration of geoblast and D&B engineering in PT.IMK is relevant to improve current drill and blast current practice and applicable to maintain rock fragmentation by blasting.

INTRODUCTION

First of all, PT. Indo Muro Kencana (PT.IMK) is a gold mine that is located in Murung Raya region, Central Kalimantan province, Indonesia. This mining area (Muro Gold mine) can be reached by using land transport at approximately seven hours by land transport from city of Palangka Raya, the capital city of Central Kalimantan province. Alternatively, it can be reached by using air transport, approximately one hour flight from Tjilik Riwut airport, airport of Palangka Raya.

Secondly, the mining operation is operated in multiple open pits using the surface mining method (combination excavator and haul truck). The daily mining operation is performed in two shifts. In addition, the heights of mining benches are 15 m and 18 m. Moreover, blasting of ore and waste rock is applied in PT.IMK to fulfil the mining production target. At this point, conventional drilling and blasting with nonel initiation system is applied in order to support mining production.

Next, waste fragmentation resulted from blasting is hauled and dumped to waste dump area. Later, ore fragmentation resulted from blasting is hauled to mineral processing plant.

Then, the concept of geoblast is proposed as an engineering tool for Drill and Blast engineering practice in PT.IMK. Current practice of D&B engineering will be combined with the concept of scaled depth of burial (Chiappetta and Treleven, 1997) and the concept of blastability index (Lilly, 1986) as geoblast's engineering tools. Initially, the concept of scaled depth of burial is used as geoblast engineering tool to design stemming height in explosive charging sheet. Also, the concept of blastability index is used as an engineering tool to design initial blast geometry, such as burden and spacing. Furthermore, it seems that blastability index is an effective engineering tool to

propose technical adjustments of blast design based on current rock mass condition. It is important to note that this technical adjustment is made by D&B Engineer in order to achieve optimum blasting condition. Then, it is expected that rock fragmentation by blasting will be optimum and excavator's productivity will be maintained.

Afterwards, the main objective of this paper is to integrate geoblast (rock mechanics and explosive engineering) and drill and blast engineering practice in order to improve current blasting's practices in PT.IMK. It is expected that this integration will improve existing blasting practice (blast design and blast engineering) in order to maintain rock fragmentation by blasting, to maintain bulk explosives consumption (powder factor) and also to maintain excavator's productivity. Then, it is expected that this integration of geoblast and D&B engineering is applicable for blasting improvement (project improvement) in PT.IMK.

Additionally, the purpose of this paper is to promote integration of geoblast in drill and blast engineering practice in Indonesia. It is essential for D&B engineer in Indonesia to gain knowledge in geoblast, especially during blast design and blast planning activity. At this stage, the writers will only evaluate the integration of geoblast aspects and D&B engineering in PT.IMK in order to achieve optimum blasting condition and to maintain rock fragmentation by blasting. Furthermore, blasting trials with air decking application is proposed for this improvement in order to maintain bulk explosive consumption and to maintain excavator's productivity. During these blasting's trial, integration of geoblast (rock mechanics and explosive engineering) in drill and blast engineering practice will be applied in order to design initial blast design (blast geometry selection, stemming height) and blast planning. It is planned that these blasting trials will be conducted in 2022.

MINING ACTIVITY IN PT.IMK

Currently, mining activities in PT.IMK is conducted by applying surface mining method and using combination of excavator and haul trucks (articulated dump truck and rigid haul truck). Haul truck (hauler) is as the transportation for ore to the crushing plant and waste material to the waste dump. At this point, there are several excavators with various capacities used to achieve the production target. There also several dump trucks with the capacity of 40 t to 60 t used for the transportation of the ore to the crushing plant and overburden material to the waste dump. The list of mining equipment in PT.IMK is shown in Table 1.

TABLE 1

Mining equipment.

Unit	Type	Average capacities (payload)
Excavator	Excavator Volvo 750BL	4.5 bcm
Excavator	Excavator Caterpillar Cat 349	3.6 bcm
Excavator	Excavator Volvo 480D	3.5 bcm
Excavator	Excavator PC 400	2.6 bcm
HD Hauler	HD (Rigid Dump Truck) Caterpillar 773E	55.5 t
ADT Hauler	ADT Volvo A40G/F	40 t
ADT Hauler	ADT Volvo A60H	60 t

In simple terms, a diagrammatic in Figure 1 is illustrating the typical transportation system in the mine area to the crushing plant (ore) and waste dump (waste). Currently, ADT is the acronym for Articulated Dump Truck (Volvo A40G/F, with capacity of 40 t and A60H, with capacity of 60 t). In addition, HD is acronym for Rigid Dump Truck (HD Caterpillar 773, with capacity of 55 t). Next, waste dump is acronym to describe area to dump waste material (barren rock). On the other hand, rom pad stockpile is acronym to define ore stockpile at processing plant area. It is located at crusher area (mineral processing plant). There is nothing special in the transportation system except a requirement that the ore production must be met to the target of the crushed rock for the next step of mineral processing.
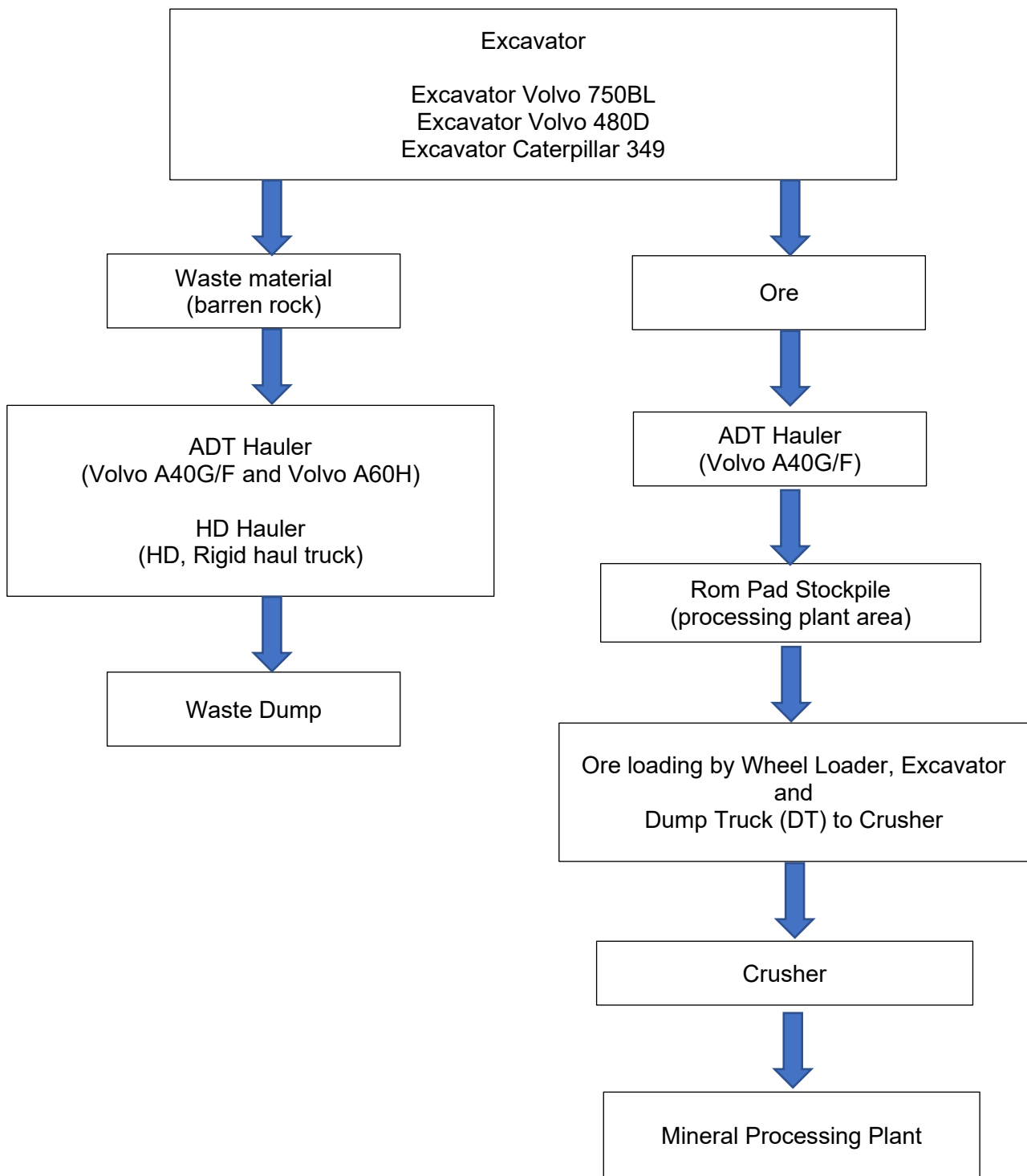
FIG 1 – Mining processes and system in PT. Indo Muro Kencana.

DRILLING AND BLASTING PRACTICE IN PT. INDO MURO KENCANA

First of all, drilling and blasting or process of breakage it the only first step in the production process for mines and quarries and the cost of this first step is normally only 8 per cent to 12 per cent of total production cost (Suwandhi, 2012). Next, drilling and blasting is applied in order to support mining production. Then, in blasting activity in a mine, the total costs are composed of drilling, blasting, secondary blasting, digging (loading), hauling and crushing. Furthermore, distribution of fragmentation by blasting will affect each step in production cycle. If a blasting cost reduced will had a chance to raise drilling cost per ton, secondary blasting costs, loading costs, hauling costs and crushing costs. Otherwise, if explosive cost would increase but produce optimum

rock fragmentation, then reduction for other production costs will happen and production cost total be optimum (Suwandhi, 2012).

Next, current blasting practice in PT.IMK is ore-waste blasting. In addition, ore-waste blasting is the term where the ore and waste rock are blasted in the same blasting process. Then, blasting of ore and waste rock is applied in PT.IMK to fulfil the mining production target and ore fragmentation resulted from blasting is hauled to mineral processing plant.

In general, these are overview of drilling and blasting practices in PT.IMK. Initially, ore and waste blasting is conducted by using conventional blasting method (with Nonel initiation system) and also sleep blasting method (with Nonel initiation system). Then, D&B Engineers design blast geometry on the basic of blasthole diameter of 127 mm. Average blasthole depth 5.5 m to 9.0 m. Average rock density is 2.5 ton/bcm.

Then, mining bench height in PT.IMK are 15 m and 18 m. In addition, blastholes are drilled as per design and instruction from PT.IMK D&B engineer and drilled by an on-site drilling contractor. At this time, various drill units (type: top hammer) are used in IMK site to drill blastholes (Furukawa HCR 1500, Sandvik Pantera 1100 and Atlas Copco T45). Next, emulsion blend with density 1.15 g/cc is used as bulk explosive. Loading density of explosive of that diameter is 14.57 kg/m.

Afterward, daily production blasting in PT.IMK is conducted at 12.30 pm (rest time for day shift). Afterward, on the blast locations, explosive charging practice is conducted by refer to explosive charging sheet. Explosive charging practice for waste area and ore area are identified and divided by the ore line. At this stage, these ore line guidelines are provided by grade control geologist (Grade control section from Mine Geology services department). At this moment, in term of blastholes, 127 mm diameter is used in PT.IMK.

Next, explosives supply, explosives transport and explosive storage are managed by PT.IMK and explosives supplier (on-site blasting services company). Additionally, daily blasting activity, mobilisation of explosives from magazine to bench location, priming explosives, charging explosives, stemming, and tie in surface detonator, then firing (blasting) are conducted by blasting contractor. Securing blasting area (area demarcation), blasting coordinator, blasting clearance (sweeper), road blocker are conducted by PT.IMK Drill and Blast team.

Subsequently, by multiple pits operation, monthly powder factor (production holes, trim blasting and secondary blasting/boulder blasting) is varied from 0.23 kg/t to 0.27 kg/t. As a result, there is a need to maintain monthly powder factor (PF), to maintain rock fragmentation and to maintain excavator's productivity. Other parameter of blast geometry with variation of bench height is shown at Table 2. Table 2 also shows the powder factor (PF) that is the ratio of explosive to tonnage of ore or waste rock for each bench height, where the density of rock is 2.5 t/bcm. If burden and spacing are always the same for any different bench height, it can be found that the higher the bench height, than the lower PF will be obtained. The same thing will happen when burden and spacing are increased.

TABLE 2

Blast geometry with variation of bench height (H).

Blast geometry		Waste H=5.0 m	Ore H=5.0 m	Waste H=6.0 m	Ore H=6.0 m
Blasthole diameter, d	(mm)	127	127	127	127
Burden, B	(m)	3.5	3.5	4.0	4.0
Spacing, S	(m)	4.0	4.0	4.5	4.5
Stemming, T	(m)	2.5	3.1	2.5	3.2
Bench Height, H	(m)	5.0	5.0	6.0	6.0
Hole depth, L	(m)	5.5	5.5	6.5	6.5
Sub drill, J	(m)	0.5	0.5	0.5	0.5
Powder Column, PC	(m)	3.0	2.4	4.0	3.3
Explosive density, ∂_E	(g/cc)	1.15	1.15	1.15	1.15
Explosive Loading Density, L_d	(kg/m)	14.57	14.57	14.57	14.57
Explosive weight, W_E	kg/hole)	43.7	35.0	58.3	48.1
Powder Factor, PF	(kg/tonne)	0.25	0.20	0.22	0.18
Scaled Depth of Burial, SDoB	$(kg/m^{1/3})$	1.19	1.41	1.19	1.45
Scaled Depth of Burial, SDoB		Controlled energy, good fragmentation	Very Controlled energy, larger fragmentation	Controlled energy, good fragmentation	Very Controlled energy, larger fragmentation
Blast geometry		**Waste H=7.5 m**	**Ore H=7.5 m**	**Waste H=9.0 m**	**Ore H=9.0 m**
Blasthole diameter, d	(mm)	127	127	127	127
Burden, B	(m)	4.0	4.0	5.0	5.0
Spacing, S	(m)	5.0	5.0	6.0	6.0
Stemming, T	(m)	2.5	3.1	2.5	3.2
Bench Height, H	(m)	7.5	7.5	9.0	9.0
Hole depth, L	(m)	8.0	8.0	9.5	9.5
Sub drill, J	(m)	0.5	0.5	0.5	0.5
Powder Column, PC	(m)	5.5	4.9	7.0	6.3
Explosive density, ∂_E	(g/cc)	1.15	1.15	1.15	1.15
Explosive Loading Density, L_d	(kg/m)	14.57	14.57	14.57	14.57
Explosive weight, W_E	kg/hole)	80.1	71.4	102.0	91.8
Powder Factor, PF	(kg/tonne)	0.21	0.19	0.15	0.14
Scaled Depth of Burial, SDoB	$(kg/m^{1/3})$	1.19	1.41	1.19	1.45
Scaled Depth of Burial, SDoB		Controlled energy, good fragmentation	Very Controlled energy, larger fragmentation	Controlled energy, good fragmentation	Very Controlled energy, larger fragmentation

TABLE 3

Types of explosives in use at PT.IMK.

Explosives	Type	Notes
Bulk Explosives	Emulsion blend, 70 per cent emulsion matrix and 30 per cent ANFO	Explosive diameter 5 inches (127 mm)
		Density 1.15 g/cc
		Explosive loading density 14.57 kg/m
	Dabex FRG series	Emulsion explosives have high water resistance in order to anticipation of wet holes
Cast Booster	Dayaprime 200 g	200 g booster for trim blasting and secondary blasting (boulder blasting)
Cast Booster	Dayaprime 400 g booster	400 g booster (for production holes blasting; ore and waste blasting)
Package Booster	Dayagel Magnum 1000 g	1000 g package booster (for trim blasting, secondary and production blasting)
In hole detonator	Dayadet in-hole delay	6.0 m; 9.0 m; 12.0 m
	Dayadet in-hole delay	500 ms; 3000 ms
Surface detonator	Dayadet surface delay	6.0 m
	Dayadet surface delay	17 ms; 25 ms; 42 ms; 67 ms; 109 ms
Lead-in Line	Dayadet Lead-in Line	500 m

THE CONCEPT OF GEOBLAST

Initially, the concept of geoblast is proposed as an engineering tool for Drill and Blast engineering practice in PT.IMK. It is expected that optimum blast operation and blast efficiency can be achieved by the application of the concept of geoblast as an engineering tool in daily blasting practice. At this stage, the concept of scaled depth of burial and the concept of blastability index are proposed to implement as geoblast engineering tools.

Additionally, for the purpose of this paper, the term of geoblast can be defined as rock mass properties, explosives properties and interaction between rock mass and explosives in blasting activity. Next, the term of drill and blast engineering can be defined as all engineering activities (planning and design) that are conducted by Drill and Blast Engineers, such as:

1. blast planning

2. blast geometry selection (burden selection, the concept of blastability index)

3. drill and blast proposal based on mine planning

4. drill design (drilling plan)

5. explosive charging sheet (explosive loading sheet)

6. stemming design based on the concept of scaled depth of burial.

7. blasting design (tie up design)

8. explosives planning (blasting accessories and bulk explosives requirements)

9. blast prediction (blast fragmentation prediction)

10. ground vibration prediction and air blast prediction.

11. blast monitoring.

12. blast reporting (blasting economics and blasting report).

At this stage, initial blast pattern selection can be proposed based on rock mass condition and blastability index (BI). Also, the concept of scaled depth burial will be used an engineering tool to design stemming height. Then, it is expected that the concept of geoblast will be implemented by D&B Engineer as drill and blast engineering standard. As mentioned earlier, in term of integration of geoblast and drill and blast engineering, these geoblast's parameters will be discussed.

Rock characteristic

First of all, rock strength, rock density, geological structure, rock blastability are classified as rock characteristic in term of geoblast. Regarding this, engineering tool that can be used by D&B engineer to create initial blast geometry and design is the concept of blastability index (Lilly, 1986). In addition, the concept of blastability index (Lilly, 1986) is proposed as geoblast's engineering tools to classify of rock mass condition, especially to propose initial blast design, such as burden and spacing.

In general, several basic blasting parameters of rock can be obtained by current geotechnical data (geotechnical engineering database), such as rock strength and rock density. With regards to these geotechnical data is based on laboratorial database, as a result these rock data is needed to be adjusted based on current rock mass condition. At this point, it is possible that this engineering adjustment can be made by using the concept of blastability index (Lilly, 1986). Furthermore, based on current practice of drill and blast engineering in PT.IMK, it seems that the concept of blastability index can be used to design initial blast geometry (adjusted blast geometry based on the actual rock mass condition on blast location. At this point, it can be said that rock blastability index, rock characteristic and explosive properties are important parameters for engineering consideration in order to create initial blast design in PT. Indo Muro Kencana.

Explosives properties

Secondly, it is important to note that explosives properties is also an essential geoblast's parameter. These explosives properties that are classified as geoblast parameters are explosives strength, explosive density, velocity of detonation (VOD explosives), borehole pressure, detonation pressure and explosive weight (explosive charge per hole). In PT.IMK, emulsion blend with density 1.15 g/cc is used as bulk explosive. Velocity of detonation of this bulk explosive is around 4500–4900 m/s. Next, explosive loading density of this bulk explosive of that diameter is 14.57 kg/m. Consequently, monthly powder factor (production holes, trim blasting and secondary blasting/boulder blasting) is varied from 0.23 to 0.27 kg/t. It is clear that there is a concern for D&B Engineer to maintain monthly powder factor (PF) and bulk explosives consumption in order to maintain rock fragmentation and to maintain excavator's productivity.

Blast geometry (initial blast geometry)

Next, blast geometry. Generally, initial blast geometry in surface mine is consist of blasthole diameter, burden, spacing, bench height, stemming height, hole depth and length of explosive charge. In addition, in daily practice of drill and blast engineering in Indonesia, it seems that blasthole diameter is the key of others blasting geometry, such as burden and spacing.

In addition, initial blast geometry, such as blasthole diameter, burden, spacing, stemming and explosive charge, can be defined by using basic formulas and basic calculation that are common for drill and blast engineering practice and blasting application.

Stemming and scaled depth of burial

To begin with, stemming is act as the energy confinement. Moreover, blasting performance will be influenced by correctly stemming practice and confined stemming practice. Moreover, it is recommended that crushed rock (gravel/aggregate) to be used as stemming material in order to create optimum energy confinement. On the other hand, drill cutting is not recommended to be used as stemming material.

Next, for surface mine's blasting practice, it is important to note that stemming is the key on blasting. Stemming is important part of blasting in order to minimise excessive fly rock due to blasting and also to maintain rock fragmentation by blasting. In addition, excessive fly rock can be created by blastholes with unconfined stemming condition and overcharged (over explosives charge). Later, it is expected that optimum blasting will be achieved by applied a confined stemming practice for production blasting in a mineral mine.

Then, in order to manage and to improve stemming practice in PT.IMK, the concept of scaled depth of burial can be used as an engineering tool to determine stemming height. In addition, the concept of scaled depth of burial (Chiappetta and Treleven, 1997) is a geoblast engineering tool to

design stemming height above explosive charge in order to prevent over energy and to maintain potential excessive fly rock.

Next, the concept of scaled depth of burial is applied by D&B Engineer in PT.IMK to create explosive charging sheet for daily blasting. Furthermore, it is important to note that the concept of scaled depth of burial is consistently applied and implemented by D&B Engineer at PT.IMK as an engineering tool to design stemming height in explosive charging sheet.

Additionally, the concept of scaled depth of burial is also used by D&B Engineer for fly rock prediction (estimated maximum rock projection and estimated blast clearance radius). Then, it is clear that this concept is applicable as a geoblast tool (engineering tool) to maintain over energy (that can cause excessive fly rock), to maintain rock fragmentation and digger's productivity, and to increase blast efficiency.

Rock and explosives interaction, detonation pressure, borehole pressure and impedance factor

Next, in term of rock and explosives interaction, these following geoblast parameters will be discussed. These geoblast's parameters are consist of rock mass information (rock density, rock velocity), explosive properties (explosive density, velocity of detonation), detonation pressure (PD), borehole pressure (PB) and impedance factor.

In addition, rock and explosives interaction will be involved in blasting activity in mine. Also, blasting in mine is consisting of rock types, explosives and blast geometry that will create rock and explosives interaction. Then, these rock and explosive interaction will produce explosives detonation and also produce blast energy.

Next, this detonation pressure and borehole pressure (PB) will be produced by explosives detonation during blasting process. Normally, the value of borehole pressure (PB) is approximately 50 per cent of detonation pressure (PD). Then, a common practice to assess explosive energy is enough to break the rock mass is the value of borehole pressure (PB) versus the value of rock strength. At this time, the value of borehole pressure (PB in MPa) that produced by explosives detonation (rock explosives interaction) is compared with the value of intact rock strength (MPa).

Next, the concept of impedance factor is another parameter of geoblast in term of rock and explosives interaction. In general, the concept of impedance factor is used to calculate the value (percentage) of waste energy that is produced by blasting in a mine. Correspondingly, impedance factor consist of rock impedance and explosive impedance. Later, the concept of impedance factor can be applied to measure the value (percentage) of waste energy and work energy that are produced during blasting in mine (rock and explosive interaction). Additionally, the term of work energy is an energy (explosive energy) that is produced during blasting process to create rock fragmentation by blasting. In addition, work energy is consisting of shock energy and gases energy that are produced during explosives detonation. Shock energy and gases energy will produce rock fragmentation by blasting. Later, this rock fragmentation by blasting will be used as blasting material to be mined. In general, it can be said that work energy is a productive and useful explosive energy that is produced during explosive detonation and rock explosive interaction. On the other hand, waste energy is an energy that is created during blasting process and this energy is not use to create rock fragmentation by blasting. Heat energy, light energy, shock energy (ground vibration) and sound energy (noise) are produced by waste energy during explosive detonation and during rock and explosive detonation process during blasting in mine. At this stage, it seems that waste energy that is consist of heat energy, light energy, seismic energy, sound energy will cause negative impact to the environment due to blasting, such as ground vibration, air blast and fly rock. Currently, it important to note that ground vibration due to blasting, air blast and excessive fly rock are results of rock and explosive interaction during blasting process in a mine. For that reason, there is a need for D&B Engineer to consider several geoblast aspects, such as impedance factor, during blast planning in order to achieve optimum blasting condition. It can be seen that geoblast engineering tool (detonation pressure, borehole pressure, rock impedance, explosive impedance and impedance factor) can be applied in order to maintain waste energy that caused by blasting.

Rock breakage and fragmentation by blasting

Essentially, rock fragmentation by blasting is the result of blasting activity. Then, it is expected that rock fragmentation by blasting will be used for further process, such as ore fragmentation by blasting will be transported to crusher at mineral processing plant for further process. On the other hand, waste fragmentation (barren rock) that is produced by blasting is transported and dumped to waste dump area. Afterward, it is expected that the size of rock fragmentation by blasting is smaller than size of excavator's bucket and also smaller that crusher's opening size. Presently, it is claimed that blasting practices, rock fragmentation by blasting and excavator's productivity will be maintained by integration of geoblast and drill and blast engineering.

ROCK MASS CONDITION IN PT. INDO MURO KENCANA

Currently, it can be seen that there are several active pits at PT.IMK with the routine activities of drilling, blasting, loading and hauling. In addition, for the multiple pits operation, the company has a blasting target of around 2000 kilotonne (kt) per month of both ore and waste rock. In general, the rock mass is classified as hard rock with unconfined compressive strength (UCS) varying from 40–195 MPa and consists of small portion of transition soft rock material of oxide and alluvial.

Current rock mass condition in PT.IMK is shown in Table 4.

TABLE 4

Rock condition in PT. Indo Muro Kencana.

Lithology	Test type	Dry density (t/m³)	Wet density (t/m³)	Natural density (t/m³)	UCS (Mpa)	Young's modulus (Gpa)	Poisson Ratio	Project Information
Lithic tuff	UCS	2.00	2.24	2.03	22.36	4.87	0.13	Bantian
Andesite tuff	UCS	2.26	2.36	2.31	78.74	8.40	0.19	Serujan 7
Andesite tuff	UCS	2.26	2.37	2.33	85.4	8.89	0.18	Serujan 7
Andesite tuff	UCS	2.01	2.21	2.08	15.58	3.29	0.23	Bantian 3
Andesite tuff	UCS	2.03	2.23	2.1	22.5	4.51	0.22	Bantian 5–2
Andesite tuff	UCS	2.11	2.27	2.16	27.94	3.70	0.21	Bantian 5–2
Andesite tuff	UCS	2.14	2.29	2.17	28.07	3.51	0.2	Bantian 5–2
Andesite tuff	UCS	1.96	2.17	2.07	9.29	1.25	0.23	Bantian 5–2
Andesite tuff	UCS	2.37	2.46	2.4	98.38	11.21	0.18	Bantian 6
Transition rock	UCS	0.81	1.47	0.86	0.98	0.15	0.21	Bantian 6
Andesite	UCS	2.33	2.42	2.36	76.52	10.34	0.18	Bantian 6

DRILL and BLAST ENGINEERING PRACTICE AND GEOBLAST

Drill and Blast Engineering practice in PT.IMK

For the purpose of this paper, drill and blast engineering practice can be defined as activities (daily practice) that are conducted by Drill and Blast engineer to design blasting in order to achieve optimum blasting condition. In addition, the term of optimum blasting can be defined as a condition where the fragmentation of the blasting results can be utilised for further processes with guaranteed safely, controlled blast negative impact to surrounding area and blasting cost-effective. Furthermore, it can be seen that these activities are also included as drill and blast engineering practices in PT.IMK:

1. Weekly Blast planning (drill and blast planning, explosive planning and explosive engineering).

2. Drill and Blast proposal.

3. Drill design.

4. Explosive loading sheet (Charging sheet).

5. Blast design (Tie up design).

6. Engineering review of blasthole drilling.

7. Prediction of size of rock fragmentation by blasting (fragmentation distribution).

8. D&B Engineer as a blast controller during blasting.

9. Prediction of blasting impact to the environment.

10. Blast monitoring (ground vibration monitoring and air blast monitoring).

11. Blasting economics calculation (drilling and blasting cost) and reporting.

To begin with, the planning for drilling and blasting (such as: drill and blast proposal, drill design, blast design and explosive charging sheet) is conducted by its D&B engineers. Current practice of D&B engineering in PT.IMK.

Next, blast pattern selection for 127 mm blasthole is contained of burden, spacing, bench height and sub drill. In general, 3.5 m–4.0 m burden is used and 4.5–5.0 m spacing is applied for 5.0 m, 6.0 m, 7.5 m and 9.0 m bench height.

Then, the D&B proposal is created by D&B Engineer as a detailed plan of weekly mine planning (production schedule). Information in D&B proposal is a polygon of the blast area, blast geometry, recommendation (from mine planning engineer, geotechnical engineer, grade control geologist, and mine survey), drilled metre required, explosives requirement, blast volume, blast tonnage and powder factor. Next, it is reviewed and then approved by D&B superintendent.

Subsequent, a drill design is created by D&B Engineer as a detailed version of the drill and blast proposal and as per mine plan schedule. The information in the drill design is a polygon of the blasting area, blasting geometry (burden, spacing, drill depth), and recommendation/instruction from D&B Engineer. Later, this drill design will be used as a design guide for drill foreman/supervisor and drill operator to drill blastholes on bench location.

Next, after blastholes are drilled, the explosive charging sheet is created by D&B Engineer. In addition, the explosive charging sheet is a charging standard (guide) for blaster and blast crew for loading explosives on bench. At this stage, it is clear that scaled depth of burial is consistently applied and implemented as an engineering tool to design stemming height in explosive charging sheet. Additionally, the concept of scaled depth of burial is a geoblast tool (an engineering tool) to determine stemming height in explosive charging sheet. At this stage, it is clear that the concept of scaled depth of burial is applied by D&B Engineer in order to reduce over energy, to reduce excessive fly rock, to maintain rock fragmentation (digger's productivity) and to increase blast efficiency. On the other hand, for trim blasting and secondary blasting (boulder blasting), it is clear that technical adjustments based on actual rock conditions must be made by D&B engineer. This adjustment is applied for trim blasting application and secondary blasting (boulder blasting) in order to control and to anticipate the over energy condition that can caused excessive fly rock.

Then, a blast design (tie up design) is made by D&B Engineer for daily production blasting. This blasting design is created by the D&B engineer using blast design software. It is used as a guide for blaster and blasting coordinator. Furthermore, the main purpose of this blasting design is to achieve optimum blasting condition.

Afterward, in term of explosives engineering, the rock mass conditions in PT.IMK has the potential for reactive ground, therefore to bulk explosive is added with inhibitors in order to anticipate the presence of reactive ground. The type of explosive used is an emulsion blend, normally blended 70 per cent emulsion matrix and 30 per cent ANFO, called Dabex FRG produced by PT. Dahana, Indonesia, and initiated by conventional Nonel system. This type of explosive has enough power to break rock mass of ore and waste rock when having a density of 1.15 g/cc.

As a final point, drill and blast engineering practice in PT IMK is blast reporting. Generally, blast reporting is consisting of blast prediction and blasting economics. In addition, blast prediction is consisting of ground vibration prediction and air blast prediction (scaled distance, maximum

instantaneous charge and holes blasted in same delay), estimated blast volume, blast tonnage, explosive consumption (powder factor). Furthermore, blasting economics aspects are also calculated and reported by D&B engineer. At this point, blasting economics is consisting of prediction of drilling cost, the cost of blasthole drilling (meter drilled), cost of bulk explosives usage, and cost of blasting accessories (surface detonator, in hole detonator, booster, Lead in Line), blasting cost and finally, drill and blast cost.

Geoblast

At the moment, it is not a common practice for drill and blast engineering practice in Indonesia to incorporate geoblast parameters in their blasting practices (drill and blast engineering daily practice). Then, there is an idea from writers in order to increase awareness about geoblast consciousness for drill and blast engineering practice in Indonesia. Next, it is expected that all Drill and Blast engineer in PT.IMK is aware about the role of geoblast (rock mechanics and explosive engineering) in drill and blast engineering practice and design activity.

Also, it is expected that the concept of geoblast will be integrated with Drill and Blast engineering practice in PT.IMK as engineering tool. In addition, it is said that the concept of geoblast will be implemented as drill and blast engineering guidelines in order to improve blasting practice in PT.IMK. Drill pattern selection in PT.IMK is designed by using concept for 127 mm blasthole, average rock density is 2.5 ton/bcm and explosive density 1.15 gr/c. Next, engineering adjustment can be made to initial drill pattern (burden and spacing) in blasting practices in PT.IMK. Then, in order to incorporate geoblast and drill and blast engineering practice in PT.IMK, it is proposed that the concept of blastability index (Lilly, 1986) is used as a geoblast's engineering tool to propose initial blasting pattern based on rock mass condition. This technical adjustment (for example is expanding drill pattern) is made and proposed by Drill and Blast Engineer and later validated by Drill and Blast Superintendent. Also, it seems that blastability index can be used as a guide for initial blast design, pattern selection, to design stemming height and powder factor. Next, the value of rock factor based on blastability index (BI) is used as a parameter for prediction of blast fragmentation distribution. Then, it is expected that the concept of geoblast that is proposed by the writers will improve drill and blast engineering practice in PT.IMK in order to achieve optimum blasting condition. At this point, it is clear that the concept of geoblast can be used to design initial design guide for drill and blast engineer in term of rock and explosive interaction.

Next, in order to integrate geoblast and drill and blast engineering in PT.IMK, it is proposed that the concept of scaled depth of burial (Chiappetta and Treleven, 1997) is used as another geoblast tool to improve drill and blast current practice in PT.IMK. At this stage, the concept of scaled depth of burial is use for stemming design and to reduce over energy due to blasting activity. In addition, it is claimed that the concept of scaled depth of burial is applicable as an engineering tool to design stemming height for explosive charging sheet in daily blasting practice. Moreover, it seems that stemming height is designed by using the concept of scaled depth of burial in order to prevent over energy, to maintain rock fragmentation by blasting and to increase blast efficiency.

Then, it is clear that stemming is an important concern in blast design of ore and waste blasting in PT.IMK. In addition, stemming acts as an energy confinement and stemming is the key to an optimum blasting in surface mine blasting. At this point, it is clear that crushed rock (gravel) is recommended to be used for stemming material at PT.IMK in order to increase blasting performance. On the other hand, drill cuttings are not recommended as stemming material for ore and waste blasting in PT.IMK. At present, the concept of scaled depth of burial is applied by Drill and Blast engineer in PT.IMK for daily practice in order to design stemming height for explosive charging sheet (loading sheet). This concept is used by D&B Engineer to design and to maintain stemming height in order to prevent over energy and to reduce excessive fly rock than can cause property damage to mine equipment. Also, this concept can be applied to maintain rock fragmentation and also to increase blast efficiency.

Furthermore, explosive charging sheet for daily blasting practice is created by D&B Engineer and use as charging sheet for loading explosives for blaster and blasting crew on bench.

However, it is important to note that the concept of scaled depth of burial cannot be fully utilised as an engineering tool to determine stemming height in trim blastholes (blasting near final wall) and

secondary blasting area (boulder blasting). As a result, blast re-design and engineering adjustment need to be made by D&B Engineer for charging explosives practices in trim blasting holes and secondary blasting (boulder blasting).

INTEGRATION OF GEOBLAST AND D&B ENGINEERING

First of all, the main objective of this paper is to integrate geoblast and D&B engineering as an engineering tool in order to improve current blasting practice in PT.IMK. Additionally, it is expected that this improvement will improved blasting performance and blast design practices in PT.IMK. Also, it is expected that rock fragmentation by blasting and excavator's productivity are maintained by using integration of the concept of geoblast in drill and blast engineering practice.

Then, in order to integrate geoblast aspect with drill and blast engineering practice, the concept of blastability index (Lilly, 1986) is proposed as a geoblast's engineering tool. In PT.IMK, it can be seen that the concept of blastability index (Lilly, 1986) can be applied as one of geoblast's engineering tool to classify rock mass condition in order to propose initial blast design. At present, it seems that this concept is applicable as an engineering tool to propose initial blasting pattern in PT.IMK. Also, it is important to note that blastability index was initially developed to assist with blast design in the rock masses found in the iron ore mines of the Pilbara (Lilly, 1986). Next, initial blast geometry (burden and spacing) can be designed by using the concept of blastability index (BI). This concept can be used as a guide for Drill and Blast Engineer to classify the rock mass that need to be blasted and also to design initial blast geometry (burden and spacing).

Furthermore, these following parameters in Table 5 are used to calculate blastability index.

TABLE 5

Parameters for calculation of the blastability index.

	Parameter	Rating
1	Rock mass description (RMD)	Powdery or friable (rating 10) Blocky (rating 20) Massive (rating 50)
2	Joint plane spacing (JPS)	Close (<0.1 m), (rating 10) Intermediate (0.1 m to 1.0 m), (rating 20) Wide (>1.0 m), (rating 50)
3	Joint plane orientation (JPO)	Horizontal (rating 10) Dip out of face (rating 20) Strike normal to face (rating 30) Dip into face (rating 40)
4	Rock density influence (RDI)	RDI = 25 (D) – 50. D is the rock mass density given in tonnes per cubic metre (t/bcm)
5	Rock strength influence (S)	The rock strength influence (S) is estimated as follows: S = 0.05 (UCS). Where UCS is the uniaxial compressive strength of rock material given in megapascals (MPa)
	Then, the blastability index (BI) is calculated as follows:	BI = 0.5 (RMD + JPS + JPO + RDI + S) BI = Blastability Index

Next, the value of blastability index that is obtained based on current rock mass condition will be used to design initial blast geometry, such as burden, spacing, stemming height and also to estimate the powder factor. Afterwards, the value of rock factor based on blastability index can be used as an input for prediction of fragmentation distribution. At this stage, rock factor value that defined by using blastability index (0.12 times blastability index). Furthermore, it is important to note that this value is used as an input for blast fragmentation distribution.

$$BI = 0.5 \ (RMD + JPS + JPO + SGI + H)$$

Table 1

Ratings for Blastability Index Parameters

Parameter	Rating
1. Rock mass description (RMD)	
1.1 Powdery/Friable	10
1.2 Blocky	20
1.3 Totally massive	50
2. Joint Plane Spacing (JPS)	
2.1 Close (<0.1m)	10
2.2 Intermediate (0.1 to 1m)	20
2.3 Wise (>1m)	50
3. Joint Plane Orientation (JPO)	
3.1 Horizontal	10
3.2 Dip out of face	20
3.3 Strike normal to face	30
3.4 Dip into face	40
4. Specific Gravity Influence (SGI)	
SGI = 25 SG − 50 (where SG is in tonnes/cu metre)	
5. Hardness (H)	1 to 10
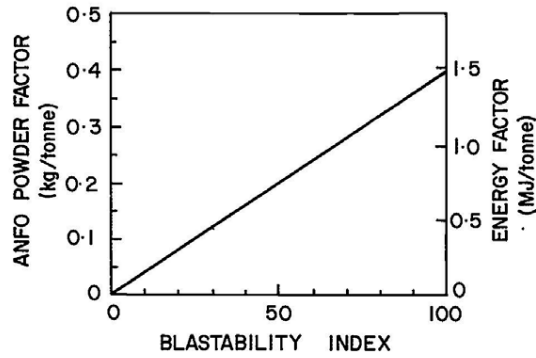
Figure 1 : Blastability Index Versus powder/energy factor

FIG 2 – Blastability Index (Lilly, 1986).

The concept of scaled depth of burial is applied by D&B Engineer in daily practice to maintain stemming height in order to prevent over energy and to maintain rock fragmentation by blasting. Next, the implementation of scaled depth of burial as an engineering tool to design stemming height has been consistently applied by PT.IMK's D&B Engineer. In addition, excess blast energy sometimes occurs due to poor of the amount of stemming material and the overcharging of explosives. The result of 'over energy' is uncontrolled energy that can lead to violent fly rock, excessive air blast noise and dust. In addition, good crater and oversized material can be produced. Furthermore, it is clear that oversize will negatively influence excavator productivity. It is expected that rock fragmentation by blasting that is blasted with scaled depth of burial application will increase blast efficiency.
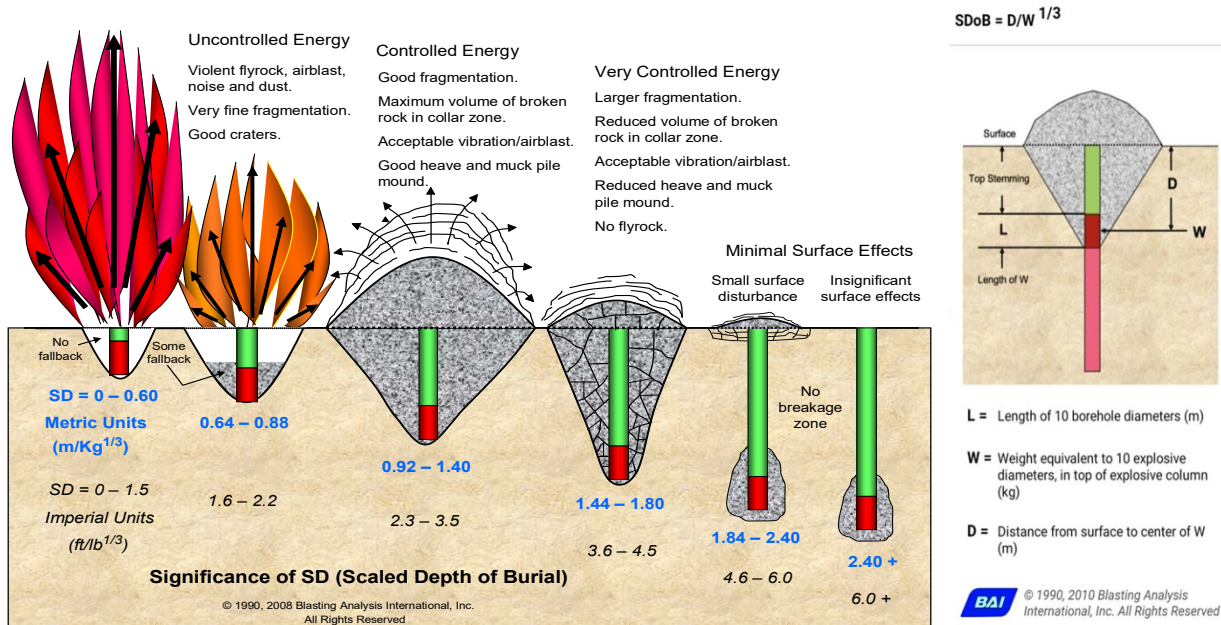
FIG 3 – Scaled depth of burial (Chiappetta and Treleven, 1997).

Stemming height (m) and scaled depth of burial are used in explosive charging sheet for waste blasting is stemming height$_{waste}$ = 2.5–3.0 m, SDoB$_{waste}$ = 0.92–1.4 kg/m$^{1/3}$ (controlled energy). The value for scaled depth of burial is 1.2–1.3 kg/m$^{1/3}$ for waste blast design at PT.IMK. Stemming height (m) and scaled depth of burial are used in explosive charging sheet for ore blasting is stemming height $_{ore}$ = 3.2–4.0 m, SDoB$_{ore}$ = 1.44–1.68 kg/m$^{1/3}$ (very controlled energy). The value for scaled depth of burial is 1.44–1.5 kg/m$^{1/3}$ for ore blasting at PT.IMK. However, the scaled depth of burial cannot apply as engineering tool to design stemming height for trim blasting holes (final

wall), shallow blastholes and secondary blasting (boulder blasting). Furthermore, the concept of scaled depth of burial also can be used as an engineering tool for estimated max rock projection and estimated blast clearance radius. The formula for estimated maximum rock projection is:

$$\text{Range Max} = 11 \times \text{SDoB}^{-2.167} \times D^{0.667}$$

The formula for estimated blast clearance radius is:

$$\text{BCR or Blast Clearance Radius} = \text{FoS} \times 11 \times \text{SDoB}^{-2.167} \times D^{0.667}$$

Details are listed in Tables 6 and 7.

Table 7 shows the Maximum Rock Projection and the Blast Clearance Radius calculation.

TABLE 6

Scaled depth of burial application in PT.IMK.

Blast design parameter	Waste blasting	Ore blasting
Hole diameter (mm)	127	127
Stemming rule of thumb	20–24 × hole diameter	25–30 × hole diameter
Stemming (m)	2.54	3.18
Explosive Density (g/cc)	1.15	1.15
Explosive Loading density (kg/m)	14.57	14.57
L (Length of 10 × Borehole diameter) in m	1.27	1.27
D (Distance from surface to centre of W) (m)	3.18	3.82
W (Weight equivalent to 10 × Borehole diameter) (kg)	18.5	18.5
Scaled Depth of Burial (m/kg$^{1/3}$)	1.2	1.44
Scaled Depth of Burial (m/kg$^{1/3}$)	Controlled energy, good fragmentation	Very controlled energy, larger fragmentation

TABLE 7

Scaled depth of burial application in PT.IMK.

Blast design parameter	Estimated max rock projection (Range Max)	Estimated blast clearance radius (BCR = Blast Clearance Radius)
Hole diameter (mm)	127	127
Formula	Range max = $11 \times SDoB^{-2.167} \times D^{0.667}$	Blast clearance radius = $FoS \times 11 \times SDoB^{-2.167} \times D^{0.667}$
Scaled Depth of Burial (m/kg$^{1/3}$)	1.2 Controlled Energy	1.2 Controlled Energy
Range max	$11 \times SDoB^{-2.167} \times D^{0.667}$ $11 \times (1.2)^{-2.167} \times (127)^{0.667} = 187.5$ m Blast radius for mining equipment (m) = 300 m	$FoS \times 11 \times SDoB^{-2.167} \times D^{0.667}$ Blast clearance radius = $(2) \times 11 \times (1.2)^{-2.167} \times (127)^{0.667} = 375$ m Blast radius for human (m) = 500 m

Furthermore, it is projected that rock fragmentation by blasting with integration of geoblast and drill and blast engineering is smaller than the size of the excavator's bucket and also smaller than the crusher's opening size in process plant area. Moreover, it is expected that this improvement will reduce monthly powder factor and also will maintain excavator's productivity. At this point, it is recommended that integration of geoblast in drill and blast engineering will give good contribution to drill and blast engineering practice and rock fragmentation by blasting (optimum blasting).

PROJECT IMPROVEMENT (BLASTING WITH AIR DECKING APPLICATION)

Blasting trials with air decking application is proposed to reduce bulk explosive consumption and to maintain excavator's productivity. In addition, the concept of geoblast can be used as an initial design guide for drill and blast engineer to create initial blast design for blasting with air decking application. At this stage, pattern selection in PT.IMK is designed by using concept for 127 mm blasthole, average rock density is 2.5 ton/bcm and explosive density 1.15 gr/c. Next, it is expected that the concept of geoblast is applied as an engineering tool for drill and blast engineering standard (guidelines and procedures) for blasting with air decking application. Next, blasting trials with air decking application is proposed for improvement to incorporate geoblast aspect with drill and blast engineering practice, to reduce bulk explosive consumption and to maintain excavator's productivity. It is planned that these blasting trials will be conducted in 2022.

It is planned that top air deck method will be applied on these blasting trials in PT.IMK. For purpose of this project improvement, three blasting scenarios will be conducted:

Scenario 1: Top air deck method, 0.5 m air deck, stemming height 2.3 m.

Scenario 2: Top air deck method, 1.0 m air deck, stemming height 2.3 m.

Scenario 3: Top air deck method, 1.5 m air deck, stemming height 2.3 m.

TABLE 8

Blast geometry for air deck blasting trial.

Blast geometry		Waste H=6.0 m	Ore H=6.0 m	Waste H=6.0 m	Ore H=6.0 m	Waste H=6.0 m	Ore H=6.0 m	Waste H=6.0 m	Ore H=6.0 m
Blasthole diameter, d	(mm)	127	127	127	127	127	127	127	127
Burden, B	(m)	4.0	4.0	4.0	4.0	4.0	4.0	4.0	4.0
Spacing, S	(m)	4.5	4.5	4.5	4.5	4.5	4.5	4.5	4.5
Stemming, T	(m)	2.3	2.3	2.3	2.3	2.3	2.3	2.3	2.3
Bench Height, H	(m)	6	6	6	6	6	6	6	6
Hole depth, L	(m)	6.5	6.5	6.5	6.5	6.5	6.5	6.5	6.5
Sub drill, J	(m)	0.5	0.5	0.5	0.5	0.5	0.5	0.5	0.5
Air Deck	(m)	0.0	0.0	0.5	0.5	1.0	1.0	1.5	1.5
Average rock density	(tonne/bcm)	2.5	2.5	2.5	2.5	2.5	2.5	2.5	2.5
Powder Column, PC	(m)	4.2	4.2	3.7	3.7	3.2	3.2	2.7	2.7
Explosive density, ∂_E	(g/cc)	1.15	1.15	1.15	1.15	1.15	1.15	1.15	1.15
Explosive Loading Density, L_d	(kg/m)	14.57	14.57	14.57	14.57	14.57	14.57	14.57	14.57
Explosive weight, W_E	(kg/hole)	61.2	61.2	53.9	53.9	46.6	46.6	39.3	39.3
Reduction in Explosive weight	(kg/hole)	0.0	0.0	7.3	7.3	14.6	14.6	21.9	21.9
Powder Factor, PF	(kg/tonne)	0.23	0.23	0.20	0.20	0.17	0.17	0.15	0.15
Scaled Depth of Burial, SDoB	(kg/m$^{1/3}$)	1.1	1.1	1.1	1.1	1.1	1.1	1.1	1.1
Reduction in Powder Factor, PF	(kg/tonne)	0.0	0.0	-0.03	-0.03	-0.05	-0.05	-0.08	-0.08
% Reduction in Powder Factor, PF	(%)	0.0	0.0	-12%	-12%	-24%	-24%	-36%	-36%

CONCLUSIONS

To begin with, there is awareness from writers in order to campaign about geoblast (rock mechanics and explosive engineering) for drill and blast engineering practice in Indonesia. In the future, it is expected that Drill and Blast engineers in Indonesia are alert about the role of geoblast (rock mechanics and explosive engineering) in their drill and blast engineering practice.

At this point, the concept of geoblast is proposed by the writers in order to improve drill and blast engineering practice in PT.IMK. In order to incorporate geoblast and drill and blast engineering practice, it is proposed that the concept of blastability index (Lilly, 1986) and the concept of scaled depth burial are used as a geoblast's engineering tool. These engineering tools are can be used to design initial blast pattern and to design stemming height.

Next, the concept of blastability index (Lilly, 1986) will be used as one of geoblast's engineering tool to classify rock mass condition on the field (rock mass classification). It seems that this rock mass classification is an essential engineering tool in order to propose initial blast design, burden selection, stemming height and to estimate powder factor required to break the rock mass. Afterward, the concept of scaled depth of burial is also proposed as a geoblast tool for drill and blast engineering practice, especially for stemming design (stemming height). It is applied as an engineering tool to design stemming height in explosive charging sheet application in order to prevent over energy (to reduce excessive fly rock). It is clear that excessive fly rock can cause

property damage to mine equipment. Also, the concept of scaled depth of burial is applicable to maintain rock fragmentation and to increase blast efficiency.

However, the concept of scaled depth of burial cannot be utilised as an engineering tool to determine stemming height in trim blastholes (blasting near final wall) and secondary blasting area (boulder blasting). As a result, engineering adjustment need to be made by D&B Engineer for charging explosives in trim blasting holes and secondary blasting (boulder blasting). In conclusion, it can be seen that integration of geoblast and D&B engineering in PT.IMK is relevant to improve current drill and blast practice and also applicable to maintain rock fragmentation by blasting.

Finally, it can be seen that the concept of geoblast is proposed by the writers in order to improve current drill and blast engineering practice in PT.IMK. This concept can be used as an initial design guide for drill and blast engineer in order to create a blast design by using rock mass information, explosives properties and also rock and explosive interaction. It is expected that drill and blast engineers in PT.IMK will aware about the role of geoblast (rock mechanics and explosive engineering) in order to improve their drill and blast engineering practice.

ACKNOWLEDGEMENTS

REFERENCES

Chiappetta, R F and Treleven, T, 1997. Expansion of the Panama Canal, in *ISEE Blasters' handbook* (ed: J F Stiehr), 18th Edition, pp 389–392 (International Society of Explosives Engineers: Cleveland).

Lilly, P A, 1986. An empirical method of assessing rock mass blastability, in the *AusIMM/IE Aust Newman Combined Group Large Open Pit Mining Conference 1986*, pp 89–92 (The Australasian Institute of Mining and Metallurgy: Melbourne).

Suwandhi, A, 2012. Mengoptimasi pengeboran dan fragmentasi batuan oleh peledakan, in *Proceeding of Rock Breakage and Fragmentation Workshop 2012* (Balinga Utama, Yogyakarta, Indonesia).

Implementation on stability of rock slope in abandoned quarry wall – Singapore case study

K Winn[1], C W Lee[2] and H A Linn[3]

1. Sessional Lecturer, Newcastle Australia Institute of Higher Education, Singapore. Email: winn.kar@newcastle.edu.au
2. Sterling C&S Consulting Engineer Pte Ltd.
3. Senior Manager, Monolithic Pte Ltd, S596692. Email: al@monolithicsg.com

ABSTRACT

The Q-slope method for rock slope engineering was developed to enable engineering geologists and rock engineers to rapidly assess the stability of excavated rock slopes in the field and make optimal adjustments to slope angles as rock mass conditions become apparent during construction of road cuts or benches. An empirical relationship between Q-slope and long-term stable slope angle is now supported through over 500 cases studies from Asia, Australia, the Americas and Europe. This paper presents about the stability analysis by first-ever applying Q-slope method on abandoned quarry wall in Singapore. The 30 m high rock slope which is composed of monzogranite rock was severely damaged by blasting operation. As the rock slope is intended for public view the objective was to retain the natural outlook and without any artificial support application thus manual scaling was carried out to clear the loosed rock blocks. In the end stable slope angle of clean rock face is determined once again by Q-slope method.

INTRODUCTION

In both civil and mining engineering projects, it is practically impossible to assess the stability of rock slope cuttings and benches in real time, using approaches such as kinematics, limit equilibrium or numerical modelling. Excavation is usually too fast for this. The same limitation usually applies to tunnelling: however, rock caverns of larger span are sufficiently 'stationary' for thorough and more necessary analysis, and the same applies to higher rock slopes.

The Q-slope method for rock slope engineering (Barton and Bar, 2015; Bar and Barton, 2016, 2017) is based on the Q-system for characterising rock exposure, drill core and tunnels under construction. This was developed from rock tunnelling and rock cavern related case records that has been used by engineering across the world for almost 45 years (Barton, Lien and Lunde, 1974; Grimstad and Barton, 1993; Barton and Grimstad, 2014).

The purpose of Q-slope is to allow engineering geologists and rock engineers to assess the stability of excavated rock slopes in the field and make potential adjustments to slope angles as rock mass conditions become visible during construction. Prime areas of application are 'from-surface-and-downwards' bench angle decisions in open pits and for the numerous slope cuttings needed to reach remote hydropower projects, tunnel, bridge and dam sites, often through strongly varying structural geologists. In rock masses where very few joints and no faults or fault zone exist, very steep slopes including cliffs can form (Bar and Barton, 2018; Barton and Shen, 2018; Barton, Shen and Bar, 2018). On the other side of the spectrum, in faulted rocks and fault zones, slope angles are significantly shallow and more variable.

In this case study project in Singapore, a monzogranitic rock slope about 30 m high in an abandoned quarry which was severely damaged by drill-blast operation was assessed. The rock slope is intended to support a public viewing deck on top of the cliff and to allow the public to view and appreciate the natural features of the rock cliff. As such, visible artificial support application was not preferred. Thus, an assessment on the required rock slope angle that can provide long-term stability was determined by the Q-slope method. The application of the methodology on this rock slope is presented in the following sections.

GEOLOGY OF THE CASE STUDY AREA

Geologically speaking, the study area belongs to Dairy Farm Granite-Microgranite pluton of Bukit Timah Centre (Building and Construction Authority Singapore (BCA), 2021) as depicted in Figure 1.

They are monzogranitic composition with equigranular texture. The monzonite yielded a zircon population with a U-Pb age of 244 ± 2 Ma (Triassic Period). The rock is observed as slightly weathered condition with highly jointed (Figure 2).
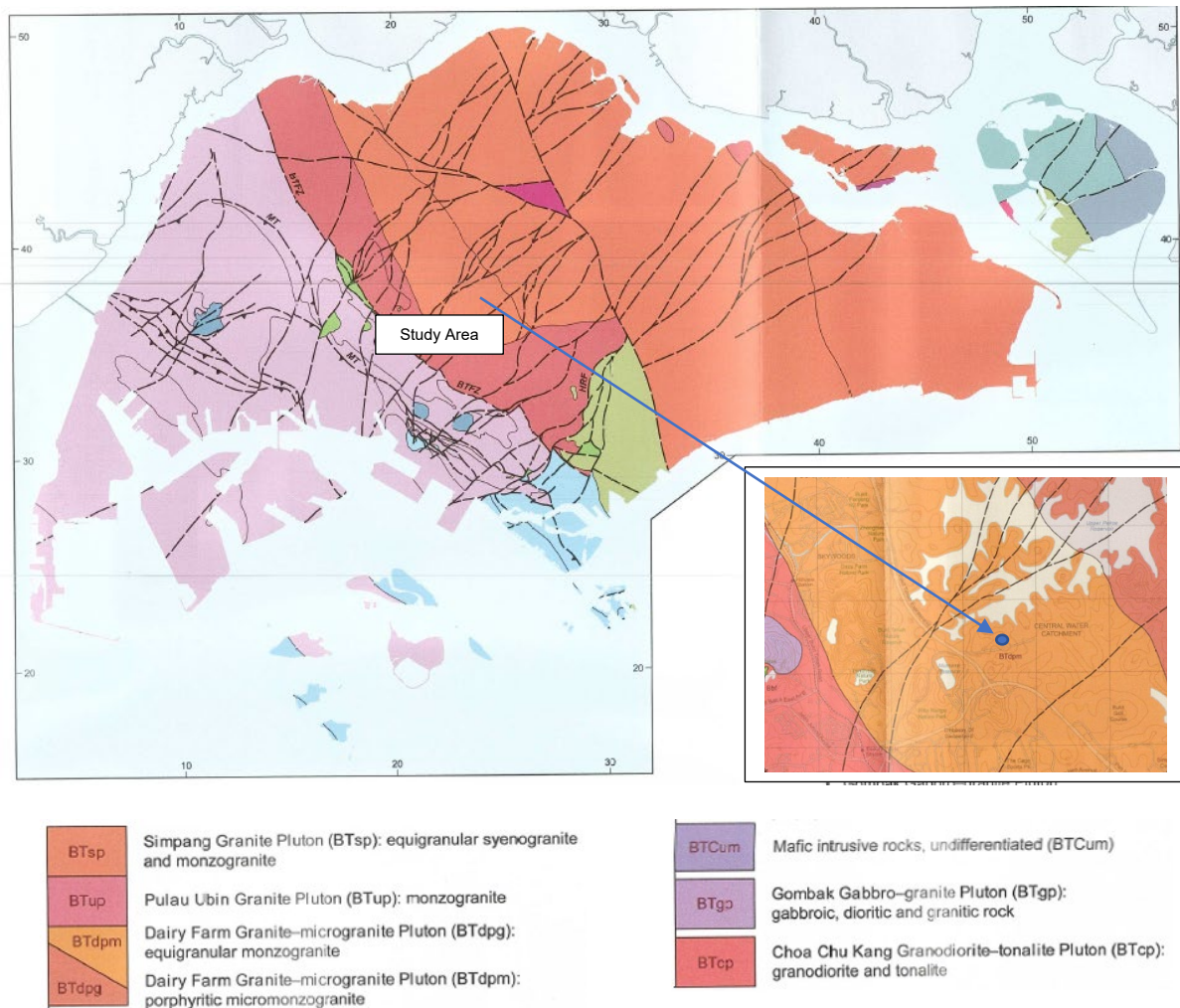
FIG 1 – Geology map of the study area (BCA, 2021).

The rock slope under stability study is the abandoned quarry wall where rocks were mined by drill and blast method for construction usage. By the aid of boom lift, the whole surface condition of the rock slope was evaluated, the geological structures (discontinuities of rock mass) were measured and required engineering geological parameters of rock mass were recorded for further analysis. The current rock slope is facing towards SW direction with angle of around 70° (070/240–250) with 30 m in height (Figure 2).

FIG 2 – The old quarry wall slope.

Joint (discontinuity) systems of the rock mass

The lithology of quarry wall is monzogranite igneous rock with common porphyritic texture. The dip amount/direction of joint planes was measured using Geological Compass by sighting method during field work. The major three sets with a few minor sets of joint system is observed as shown in Table 1 and the stereographic projection of the joint systems by applying dips program was shown in Figure 3.

TABLE 1

Joint system of the rock mass.

Joint set	Dip amount/dip direction
1	70/320–330
2	35/240–255
3	50/60–75

(a)   (b)
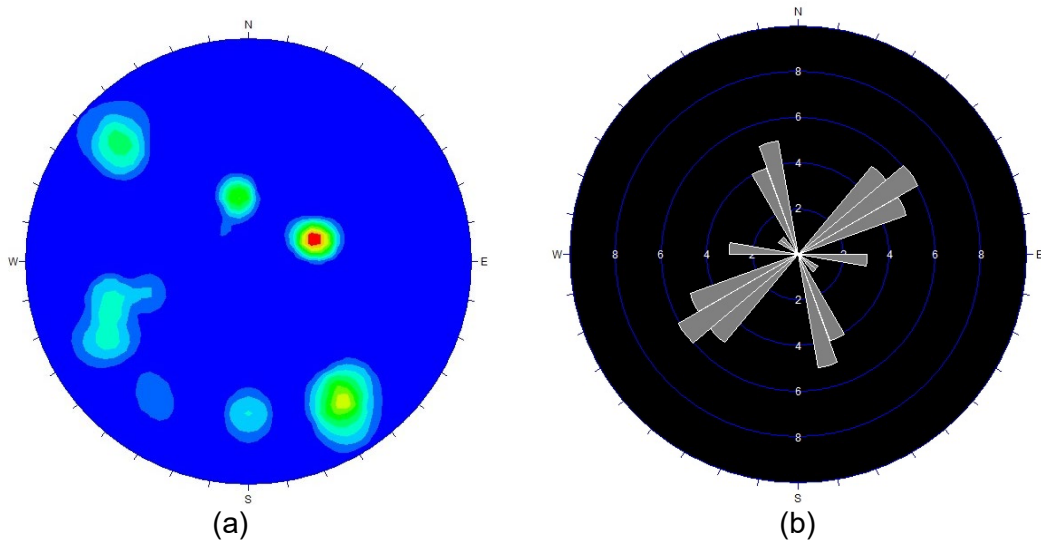
FIG 3 – (a) Contour diagram of joint system of the rock mass; (b) Rose Net diagram of joint system (three major joint sets with a few minor set).

Among the above joint sets, the following types are noticed:

1. Day lighting joint – it inclines outwards of the slope face (Figure 4a, 4b).

2. Inclined inwards of the slope face (Figure 4c, 4d).

(a)   (b)

Day lighting joints

(c)   (d)

Inclined joints inwards slope
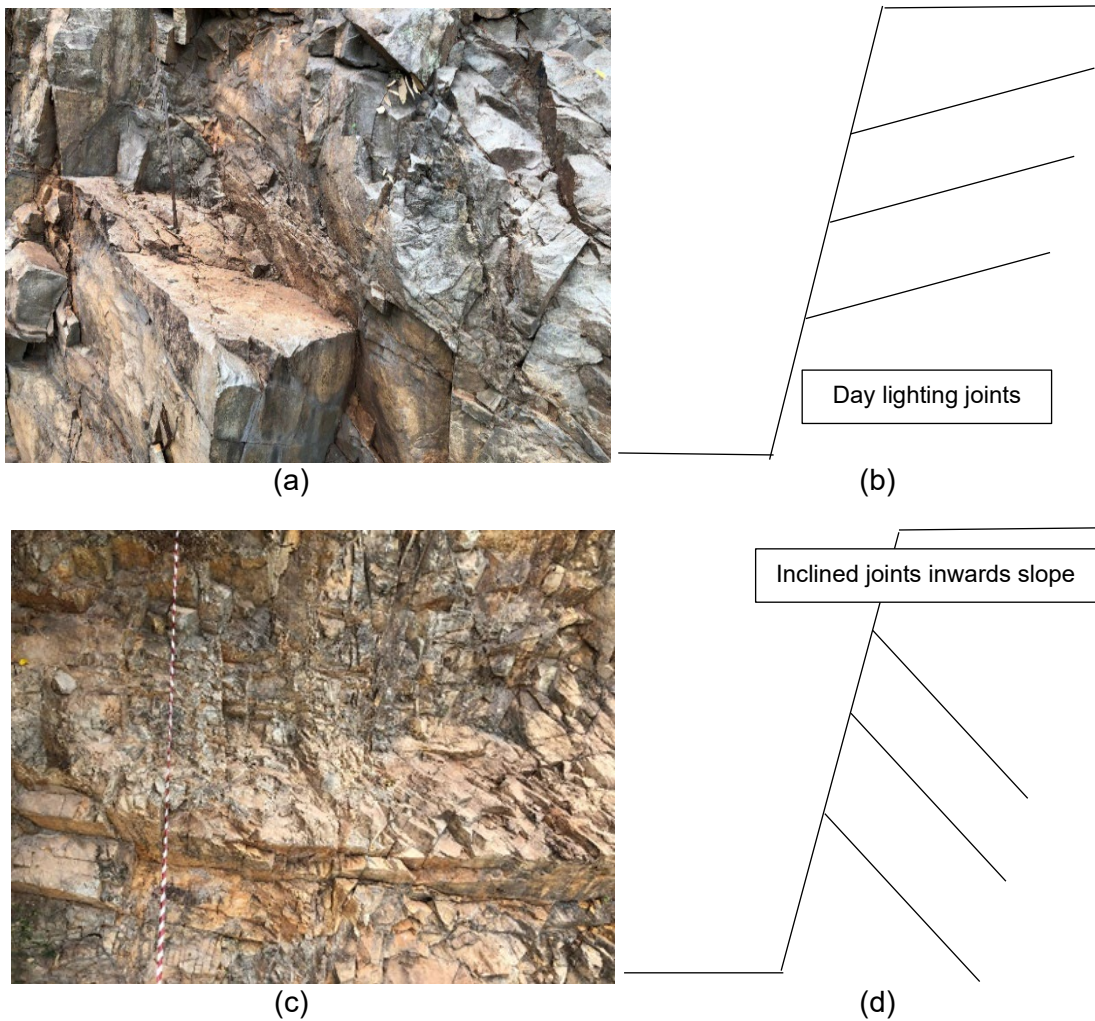
FIG 4 – Some noticeable joint system of rock mass.

STABILITY ANALYSIS OF QUARRY WALL SLOPE BY EMPIRICAL Q-SLOPE

Barton and Bar introduced Q-slope at Eurock 2015 (European Rock Mechanics) Conference and presented additional notes at ARMA2016 symposium. Q-slope enables geotechnical engineers and engineering geologists to quickly and effectively assess the stability of slope in the field, both during and post-excavation works.

For Q-system users, the formula for estimating Q-slope is mostly familiar (Barton and Bar, 2015).

$$Q\text{-slope}= \frac{RQD}{J_n} \times \left(\frac{J_r}{J_a}\right)_O \times \frac{J_{wice}}{SRF_{slope}} \tag{1}$$

The rating system of each parameter (RQD, J_n, J_r, J_a, J_{wice} and SRF_{slope}) in Equation 1 is given in the Appendix Section of paper by Barton and Bar (2015).

Barton and Bar (2015) derived a simple formula for the steepest angle (β) not requiring reinforcement or support for slope height less than 30 m:

$$\beta=20 \ \log_{10} Q\text{-slope}+65° \tag{2}$$

The recorded and calculated Q-slope with maximum stable steepest slope angle on two different scenarios in this study area are presented in Table 2. It is to note that the Engineering Judgement is used in the empirical approaches based on engineer's experience and local condition.

TABLE 2
Q-slope and β determination of quarry wall rock mass (Singapore case study).

	Case 1 (Area free of loose rock pieces)	Case 2 (Area with loosely attached rock pieces)
RQD	90	90
J_n	12	12
J_r	2	2
J_a	1	1
O factor	1	0.75
J_{wice}	0.7	0.7
SRF_a	2.5	2.5
SRF_b	1	2.5
SRF_c	1	2
Q-slope	4.2	0.63
β (Slope angle)	77	61

In case 1 for the area free of loosely attached rock pieces, the calculated steepest angle (β) is 77° which shows the current slope of 70° is in stable condition. However, case 2 for the area with loosely attached rock pieces is not safe for long-term condition after the calculated steepest angle (β) is lower than the current slope.

Recommended scaling of loosely attached rock

The loosely attached rock pieces in various sizes (Figure 5) are observed at different locations on rock slope. They are formed by the drill and blasting in previous quarry mining works and left on the slope after incomplete scaling.

FIG 5 – Observed loosely attached rock pieces on different locations on rock slope (case 2 area).

As the natural rock slope face is planned for public view, the slope protection works such as applying shotcrete, rock bolts and slope protection steel mesh were not feasible.

Hence, for long-term stability of slope and safety of the workers in future maintenance works, it is recommended to scale down of those pieces in case 2 area (Table 2) by manually or mechanically. It is advised to pay more attention of joint types (Figure 4a, 4b) during scaling works as they are prone to fall outwards.

MANUAL SCALING WORKS

Scaling was done by rope access specialist for current project. Key objectives were to remove loose rocks/daylighting joints/potential debris to make safe and prevent injuries/damage in the future works below rock cliff as recommended after previous field assessment. Rock face was throughly scanned through various time from top to bottom and left to right by the specialist via rope access. Key areas which were hightlighted before project was proritised (Figure 6). Such areas were throughly checked and scaled down.

FIG 6 – Area of focus for scaling work.

Empirical Q-slope stability analysis of quarry wall slope after scaling work

The rock slope face is later divided into four zones for final assessment after manual scaling work as shown in Figure 7. The recorded and calculated Q-slope with maximum stable steepest slope angle for four different zones after scaling work are presented in Table 3. It is to note that the Engineering Judgement is used in the empirical approaches based on engineer's experience and local condition.
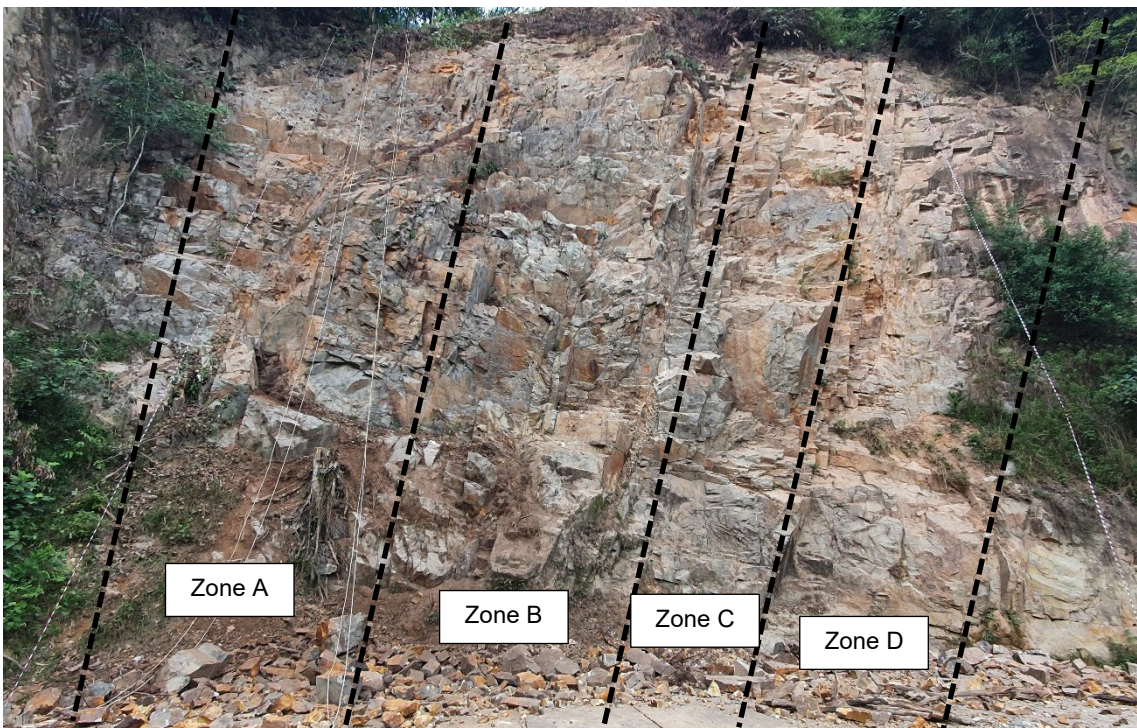
FIG 7 – Four zonal division on rock slope face for final assessment.

TABLE 3

Q-slope and β determination of four zones in Figure 7 after manual scaling.

	Slope face after free of loose rock pieces			
	Zone A	**Zone B**	**Zone C**	**Zone D**
RQD	85	85	95	85
J_n	12	12	12	12
J_r	2	2	2	2
J_a	1	1	1	1
O factor	1	1	2	1
J_{wice}	0.7	0.7	0.7	0.7
SRF_a	2.5	2.5	2.5	2.5
SRF_b	1	1	1	1
SRF_c	1	1.25	1	1.25
Q-slope	3.97	3.2	8.87	3.2
Steepest angle (β) not requiring reinforcement or support	77	75	84	75

As in Table 3, the slope face area free of loosely attached rock pieces after scaling work, the calculated steepest angle (β) which do not require reinforcement or support is in the range of 75–84°. It shows that the current slope of 70° is in stable condition.

Some of the rock slope face photos which compare before and after scaling works are depicted in Figure 8. The Overall rock slope condition after scaling work with colugo deck structure on top which is used for public viewing is shown in Figure 9.

Before scaling work   After scaling work

FIG 8 – Comparison of rock slope condition before scaling work (left photo) versus after scaling work (right photo) at some selected locations.

FIG 9 – Overall rock slope condition after scaling work with colugo deck structure on top.

CONCLUSION

For long-term stability assessment of one of the old quarry walls in Singapore is successfully conducted by applying Q-slope method. It is observed that the slope faces with loosely attached rock blocks were unstable after the calculated steepest angle (β) is lower than the current condition.

The need for rock support measures was eliminated by the judicious removal of all loose rock pieces and unfavourable rock orientation by carrying out the manual scaling work. With the application of the Q-slope methodology and implementation of rock scaling works carried out to meet the maximum allowable rock slope angle, it was able to reduce risk of major rock failure on the rock cliff.

ACKNOWLEDGEMENT

REFERENCES

Bar, N and Barton, N, 2017. The Q-Slope Method for Rock Slope Engineering, *Rock Mechanics and Rock Engineering,* 50(12):3307–3322.

Bar, N and Barton, N, 2018. Q-Slope: An Empirical Rock Slope Engineering Approach in Australia, *Australian Geomechanics Journal,* 53(4):73–86.

Bar, N and Barton, N R, 2016. Empirical slope design for hard and soft rocks using Q-slope, *Symposium of American Rock Mechanics Society*, ARMA 16–384.

Barton, N and Grimstad, E, 2014. Forty years with the Q-system in Norway and abroad, *Fjellsprengningsteknikk, Bergmekanikk, Geoteknikk,* 4.1–4.25:25.

Barton, N and Shen, B, 2018. Extension Strain and Rock Strength Limits for Deep Tunnels, Cliffs, Mountain Walls and the Highest Mountains, *Rock Mechanics and Rock Engineering,* 51(12):3945–3962.

Barton, N, Lien, R and Lunde, J, 1974. Engineering classification of rock masses for the design of tunnel support, *Rock Mechanics,* 6:189–236.

Barton, N, Shen, B and Bar, N, 2018. Limited heights of vertical cliffs and mountain walls linked to fracturing in deep tunnels – Q-slope application if jointed slopes, *Proceedings XIX Congresso Brasileiro de Mecânica dos Solos e Engenharia Geotécnica Geotecnia e Desenvolvimento Urbano: COBRAMSEG 2018*, 13 p (ABMS).

Barton, N R and Bar, N, 2015. Introducing the Q-slope method and its intended use within civil and mining engineering projects, in Schubert and Kluckner (eds.), *Future Development of Rock Mechanics, Proceedings ISRM reg Symposium Eurock 2016 and 64th Geomechanics Colloquim,* pp 157–162 (Salzburg: OGG).

Building and Construction Authority Singapore (BCA), 2021. Singapore Geology, 173 p, ISBN 978–0-85272–791–1.

Grimstad, E and Barton, N, 1993. Updating of the Q-system for NMT, in *Proceedings International Symposium on Sprayed Concrete,* pp 46–66 (Norwegian Concrete Association).

An improved hydro-mechanical model for 3D rough-walled rock joints considering contact area during shearing

X Zhu[1], J Oh[2], G Si[3] and C Zhang[4]

1. PhD Candidate, Minerals and Energy Resources Engineering, UNSW, Sydney NSW 2052. Email: xu.zhu1@unsw.edu.au
2. Associate Professor, Minerals and Energy Resources Engineering, UNSW, Sydney NSW 2052. Email: joung.oh@unsw.edu.au
3. Senior Lecturer, Minerals and Energy Resources Engineering, UNSW, Sydney NSW 2052. Email: g.si@unsw.edu.au
4. Senior Lecturer, Minerals and Energy Resources Engineering, UNSW, Sydney NSW 2052. Email: chengguo.zhang@unsw.edu.au

INTRODUCTION

The presence of rock joints has a huge impact on the strength, deformability, and permeability of fractured rock masses by providing surfaces of weakness on which further deformation are more prone to occur, and by serving as the major channels of water flow due to low matrix permeability. In earlier studies, water flow-through rock joints is often assumed as laminar flow between two ideal smooth parallel plates, and the well-known cubic law was derived and widely used to characterise the hydraulic behaviour of rock joints. However, natural rock fractures are irregular and of spatially varied aperture. Thus, the concept of equivalent hydraulic aperture was introduced to modify the cubic law. Numerous works have been conducted on the relation between hydraulic aperture and mechanical aperture incorporating various geometrical parameters.

The surface roughness is one of the most sensitive factors for water flow-through rock joints. The aperture distributions are irregular in natural roughed fractures relative to the parallel plates. Barton *et al* (1985) and Olsson and Barton (2001) incorporated the joint roughness coefficient JRC in evaluating hydraulic aperture and proposed an empirical equation based on fluid flow tests. However, their equations do not conform to the dimensional consistency. Many other researchers (Zimmerman and Bodvarsson, 1996; Xiong *et al*, 2011; Li *et al*, 2019) considered aperture distributions in their equations. But the aperture distributions change during shear was always neglected. The contact of rock joints also has a significant impact on the hydro-mechanical behaviour of rock joint, since fluid tends to flow-through a rough joint along connected channels while bypassing the contact obstacles with tortuosity. Nonetheless, previous research mostly considered joint roughness or aperture changes based on 2D joint profiles, while the contact and tortuosity based on 3D surfaces were often overlooked. Only a few works have been made on quantifying the effect of contact area on flow behaviour (Walsh, 1981; Zimmerman *et al*, 1992; Zimmerman and Bodvarsson, 1996; Yeo, 2001), and mostly ignored contact area change induced by shearing and the associated impact on flow behaviour.

Summarily, the quantification of fracture geometry effects on water flow in single rock joints still needs further investigation, especially when considering coupled shear-flow processes. This paper, therefore, aims to study the impacts of contact area and aperture distributions of the single rock joint on the flow behaviour. The evolutions of contact area and aperture distributions induced by shear are considered. Then, an improved model for estimating the hydraulic aperture with the mechanical aperture incorporating the above factors is developed. Finally, a series of shear and shear-flow tests are conducted on artificial joint samples and the model performance is verified by comparing against the results of experimental tests.

MECHANICAL BEHAVIOUR DURING SHEAR

In this paper, the commonly used joint constitutive model – Barton's model (Barton and Choubey, 1977; Barton, 1982) is adopted for mechanical behaviour analysis, since it is simple and can be easily upscaled to field scale.

Asperity degradation and dilation

After peak shear strength, a mobilised JRC is used to describe the asperity degradation. The joint model is expressed as:

$$\tau = \sigma_n \tan\left[\phi_r + JRC_{mob} \cdot \log\left(\frac{JCS}{\sigma_n}\right)\right]$$

(1)

The dilation can be calculated by:

$$\Delta\delta_n = \Delta\delta_s \tan\left(\frac{1}{M}JRC_{mob} \cdot \log\left(\frac{JCS}{\sigma_n}\right)\right)$$

(2)

where M is a damage coefficient, the value of which for this study is determined by direct shear tests.

Evolution of contact area

The evolution of contact area during shearing is considered based on Grasselli's criterion (Grasselli *et al*, 2002), which proposed a three-dimensional morphology characterisation approach and expressed the variation of the actual contact area A_{θ^*} as a function of the apparent dip angle θ^* of the surface along the shear direction. The equation is expressed as:

$$A_{\theta^*} = A_0 \left(\frac{\theta^*_{max} - \theta^*}{\theta^*_{max}}\right)^C$$

(3)

where A_0 and θ^*_{max} are the maximum possible contact area and the maximum apparent dip angle in the shear direction, respectively. C is a fitting parameter.

The concept of the threshold inclination angle is introduced, which equivalent to threshold apparent dip angle θ^*_{cr} for Grasselli's criterion. Based on Barton's model, the threshold inclination angle, which mobilised during shear, is defined as:

$$i_{mob} = JRC_{mob} \cdot \log\left(\frac{JCS}{\sigma_n}\right)$$

(4)

Thus, the relation between mobilised threshold inclination angle i_{mob} and mobilised contact area ratio c_{mob} is calculated as:

$$c_{mob} = A_0 \left(\frac{\theta^*_{max} - i_{mob}}{\theta^*_{max}}\right)^C$$

(5)

AN EQUATION FOR EVALUATING FLOW BEHAVIOUR DURING SHEAR

When water flow-through rock joints, the complexity mainly comes from the irregularity of aperture distributions and the tortuosity of the flow path caused by contact areas, as illustrated in Figure 1.
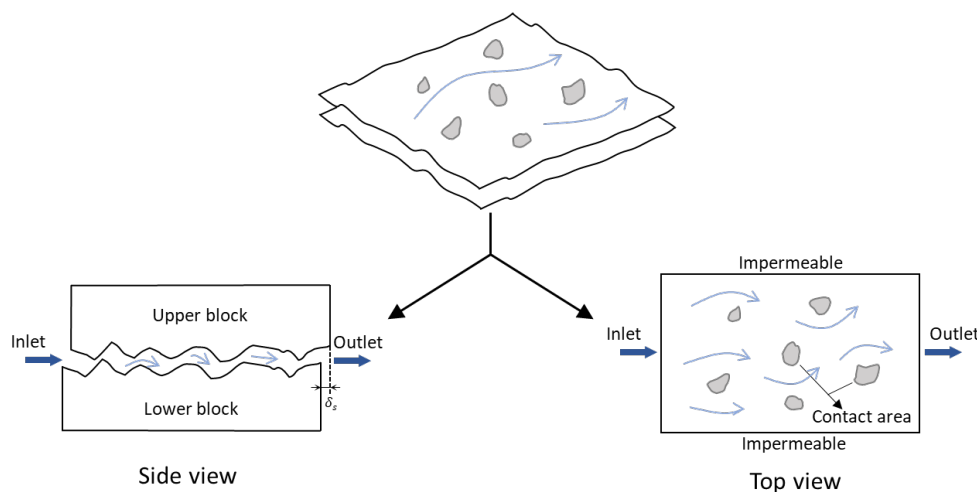
FIG 1 – Schematic representation of water flow-through a natural rough rock joint.

Two correction terms, aperture correction term and contact correction term, that explain the reduction of flow rate by aperture irregularities and contact obstacles are incorporated. The proposed equation is in the form of:

$$e_h^3 = e_m^3 \left[1 - 1.5 \frac{\sigma_{e\_mob}^2}{e_m^2} \right] (1 - \frac{1}{A_0} c_{mob})$$ (6)

The proposed equation conforms to the dimensional consistency and possesses a clear physical significance.

EXPERIMENTS AND CORRELATION

The proposed model is implemented and correlated with experimental results.

Shear model calibration

The direct shear tests are conducted for calibrating the adopted shear model, to make sure the accuracy of mechanical behaviour analysis before considering shear-flow coupling.

The Barton's model is incorporated into 3DEC and numerical simulations are performed. Simulation results show a good agreement with experimental data. The damage coefficient M is obtained from test results.

Shear-flow model verification

The shear-flow tests are conducted under constant normal load (CNL) conditions and low inlet pressure. At sufficiently low flow rates, the cubic law is applicable to describe fluid flow-through a single rock fracture, as:

$$Q = \frac{w e_h^3}{12\mu} \nabla P$$ (7)

Both normal and shear stresses change the fracture void geometry that serve as the spaces for water flow. The mechanical aperture of a rock joint, e_m, can be calculated from:

$$e_m = e_0 - \Delta e_n + \Delta e_s$$ (8)

where e_0 represents the initial aperture. Δe_n is the aperture variation induced by normal load, which is equal to 0 under CNL conditions. Δe_s is the variation of aperture due to shearing.

The joint surface is scanned by the 3D optical scanner system, as illustrated in Figure 2. A matlab code is then developed for processing the scanning point cloud data and obtaining the three Grasselli's parameters A_0, θ_{max}^* and C in the specified shear direction. Thus, the equation for this joint is:

$$e_h^3 = e_m^3 \left[1 - 1.5 \frac{\sigma_{e_{mob}}^2}{e_m^2} \right] (1 - 2.29 c_{mob})$$ (9)
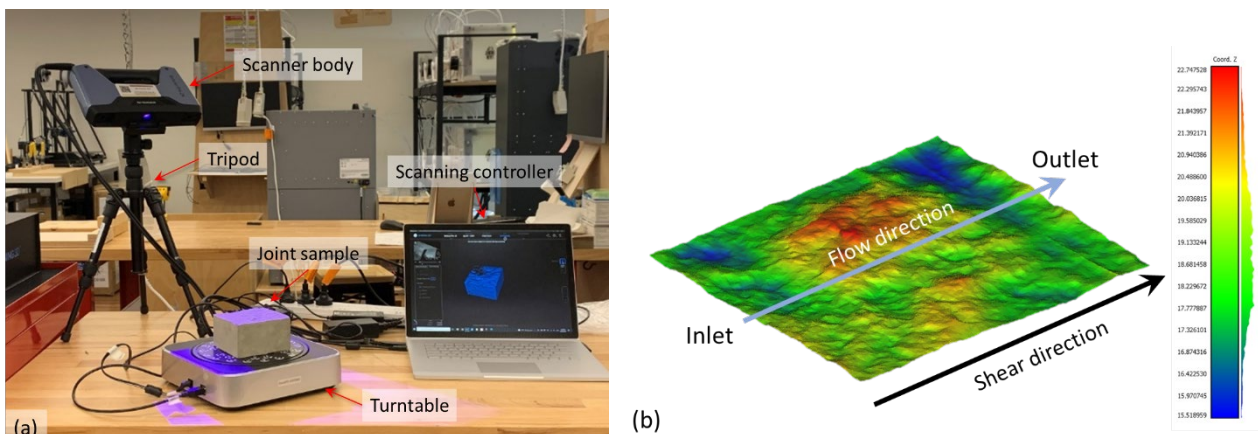
FIG 2 – (a) the 3D optical scanner system and (b) the scanned rock joint surface.

The measured e_h and e_m at different shear displacements are calculated with Equations 7 and 8. The calculated e_h is obtained from Equation 9. Comparisons between the calculated e_h with proposed equation and the measured e_h are being processed and the preliminary result is promising.

To further verify the proposed model quantitatively, the estimations from Equation 9 are compared with the results from the model proposed by Olsson and Barton (2001), which also considered the hydromechanical coupling during shear and expressed as follow:

$$\begin{cases} e_h = \dfrac{e_m^2}{JRC_0^{2.5}}, \delta_s \leq 0.75\delta_{sp} \\ e_h = \sqrt{e_m} \cdot JRC_{mob}, \delta_s \geq \delta_{sp} \end{cases} \tag{10}$$

The comparison between the calculated results with different equations and the measured hydraulic apertures from experiments are presented in Figure 3. It can be seen that the old model shows a signficant underestimation whereas the proposed equation has better accuracy.
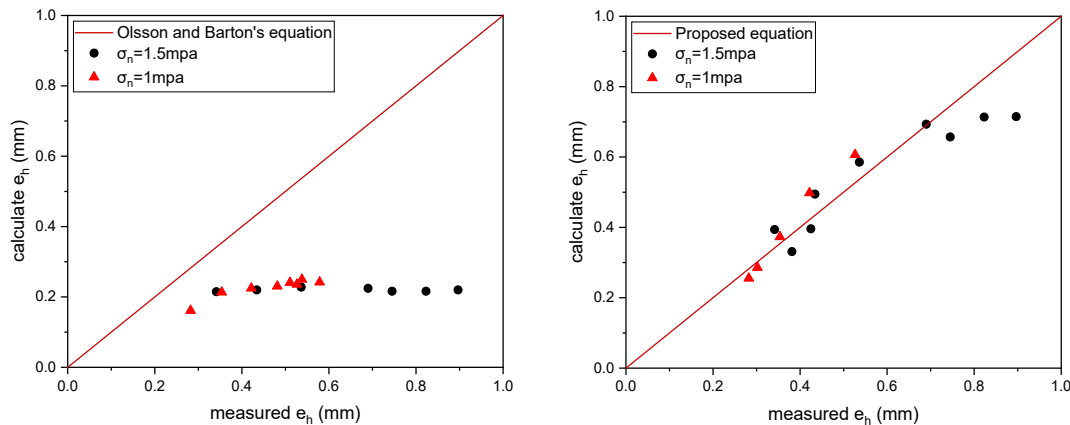
FIG 3 – Comparison between measured hydraulic apertures and calculated results with (a) Olsson and Barton (2001)'s equation and (b) proposed equation.

CONCLUSIONS

In this work, a new model for estimating the hydro-mechanical behaviour of rock joint is proposed. The evolutions of aperture distributions and contact area ratio during shearing are considered and incorporated. The direct shear tests and shear-flow tests on artificial joint samples under constant normal load are conducted to calibrate the adopted shear model and verify the proposed model. A comparison between the new model and the previous model is also conducted based on the test results, and the previous one shows a signficant underestimation. The results show that the proposed model has the potential to accurately evaluate the shear-flow coupled behaviour of rock joints. The developed model can then be implemented in finite or discrete element code to perform hydraulic analysis in many practical cases, thereby improving the reliability of stability and safety predictions for rock masses in engineering applications.

ACKNOWLEDGEMENTS

REFERENCES

Barton, N, 1982. Modelling rock joint behavior from in situ block tests: implications for nuclear waste repository design, Office of Nuclear Waste Isolation, Battelle Project Management Division.

Barton, N, Bandis, S and Bakhtar, K, 1985. Strength, deformation and conductivity coupling of rock joints, *International Journal of Rock Mechanics and Mining Sciences & Geomechanics Abstracts*, 22:121–140.

Barton, N and Choubey, V, 1977. The shear strength of rock joints in theory and practice, *Rock Mechanics Felsmechanik Mécanique des Roches*, 10:1–54.

Grasselli, G, Wirth, J and Egger, P, 2002. Quantitative three-dimensional description of a rough surface and parameter evolution with shearing, *International Journal of Rock Mechanics and Mining Sciences*, 39:789–800.

Olsson, R and Barton, N, 2001. An improved model for hydromechanical coupling during shearing of rock joints, *International Journal of Rock Mechanics and Mining Sciences*, 38:317–329.

Renshaw, C E, 1995. On the relationship between mechanical and hydraulic apertures in rough-walled fractures, *Journal of Geophysical Research: Solid Earth*, 100:24629–24636.

Walsh, J B, 1981. Effect of pore pressure and confining pressure on fracture permeability, *International Journal of Rock Mechanics and Mining Sciences & Geomechanics Abstracts*, 18:429–435.

Xiong, X, Li, B, Jiang, Y, Koyama, T and Zhang, C, 2011. Experimental and numerical study of the geometrical and hydraulic characteristics of a single rock fracture during shear, *International Journal of Rock Mechanics and Mining Sciences*, 48:1292–1302.

Yeo, W, 2001. Effect of contact obstacles on fluid flow in rock fractures, *Geosciences Journal*, 5:139–143.

Zimmerman, R and Bodvarsson, G, 1996. Hydraulic conductivity of rock fractures, *Transport in Porous Media*, 23:1–30.

Zimmerman, R W, Chen, D-W and Cook, N G W, 1992. The effect of contact area on the permeability of fractures, *Journal of Hydrology*, 139:79–96.

Slope stability

The risk management and cost benefits of using a total monitoring approach to managing slope instability hazards in open pit mines

N Harries[1] and C Jacobsen[2]

1. Director APAC, Hexagon Mine Monitoring, Brisbane Qld 4000.
   Email: neal.harries@hexagon.com
2. Senior Monitoring Surveyor, Hexagon Mine Monitoring, Brisbane Qld 4000.
   Email: Christian.jacobsen@idsgeoradar.com

ABSTRACT

Assessing and managing instability hazards is an essential activity when working with unstable natural slopes and excavated open pit mining slopes. Slope monitoring has become the standard technique for the management of geotechnical risks associated with mine slope instability hazards. In recent decades, a proliferation of new monitoring techniques such as terrestrial radar, satellite InSAR and LIDAR have become standard operational tools, complementing conventional survey-based monitoring solutions. A reliable monitoring system should identify and record incipient anomalous slope movement. Although the most obvious purpose of a monitoring system is safety related, slope deformation and performance monitoring also enhance the understanding of slope behaviour and assists in improving system design and implementation. For a monitoring system to be considered an effective early warning tool, it needs to operate in real-time and should be linked to the mine's emergency communication systems. Terrestrial radar systems have been developed that can provide near real-time measurements, at a high level of precision and covering broad areas in all weather conditions. This has had a positive impact on the management of geotechnical risks in operational conditions.

The technology adoption of RADAR in mine monitoring has significantly progressed in the last 20 years from technology enthusiasts, to visionaries, to pragmatists to conservative users. However, the increasing adoption of RADAR cannot reduce or remove other monitoring techniques that often have important benefits; even if these technologies cannot be used as a real-time operational tool. An increasing awareness on the importance of combining data from different monitoring techniques to develop a holistic picture of all possible geotechnical hazards is a current industry trend. This is proving to be an excellent foundation for managing hazards associated with slope instability in open pit mines, and is only expected to improve with time with the adoption of new technologies based on big data and Artificial Intelligence (AI).

INTRODUCTION

The management of risks associated with slope instability is an essential process in the safe and economic operation of open cut mines (Bar and Dixon, 2021). Geotechnical monitoring programs of open pit slopes have been developed to better manage those risks (Bar *et al*, 2020). In the last two decades, large-scale transformational changes have occurred in these programs as specialist tools and techniques (eg Terrestrial radar, Satellite InSAR, Lidar etc) have been added to traditional survey-based information and observations. Whilst this has added to the repertoire of site-based geotechnical engineers, it has also added to the workload of site-based engineers; both, in relation to the upkeep of systems and managing the data produced.

A reliable monitoring system should record and identify incipient anomalous slope movement. Although the most obvious purpose of a monitoring system is safety related, slope deformation and performance monitoring also enhance the understanding of slope behaviour and assist in improving system design and implementation. In order for a monitoring system to be considered an effective early warning alarm, it needs to operate in real-time and should be linked to the mine's emergency communication system (Sharon, 2020). Terrestrial radar systems have been developed that are capable of providing near real-time measures at a high level of precision and covering broad areas in all weather conditions (Bar *et al*, 2020). This has had a particular impact on the management of geotechnical risks in operational conditions, without precluding the use of other essential technologies. In the authors' opinion, a balanced monitoring strategy using multiple technologies

remains the most appropriate solution for almost all open pit settings. In the remainder of this paper, this approach is referred to as a 'Total Monitoring (TM) approach'.

TOTAL MONITORING (TM) APPROACH

It is widely accepted that the collection of data from different sources is essential to understanding geotechnical risk on-site (Zevgolis *et al*, 2019). GB-InSar radar is the industry standard to measure rapid deformations of open pit mining walls. However, it cannot be used to measure subsidence, pore pressures and many other important determinants of slope stability. Being able to overlay multiple data sources to derive a holistic picture of all possible geotechnical risks is what the total monitoring approach stands for.

In recent years, technology companies have been working at automating the mining environment at a fast pace and the telemetry of mesh systems, automating entire new and old sensor installations has become highly sophisticated. Similar advancements have been achieved in the geotechnical and survey domains, where, for instance, data fusion and system synergies have been implemented. Such solutions run on software that can read multiple sources of data, therefore evading dependency on a single data source. Moreover, they can effectively visualise the data and automatically alarm on trigger action response plan (TARP) thresholds. The TM approach combines assurance, convenience and safety benefits on a macro (eg pit closure due to TARP activation by radar) and micro level (eg lower risk of injury due to reduced time spent in the field).

Individual monitoring technologies

Terrestrial radar (GB-InSar)

Ground-based or terrestrial radar (Figure 1) has become the industry standard to manage geotechnical risk in open pit mining operations. Fast acquisition times (<1 min) and very high accuracies (<1 mm) have contributed to the success of terrestrial radar. In addition to overcoming atmospherics (eg humidity, temperature) and long distances (up to 5 km in range), their ability to automatically report and alarm on areas of concern has presented a technological leap.
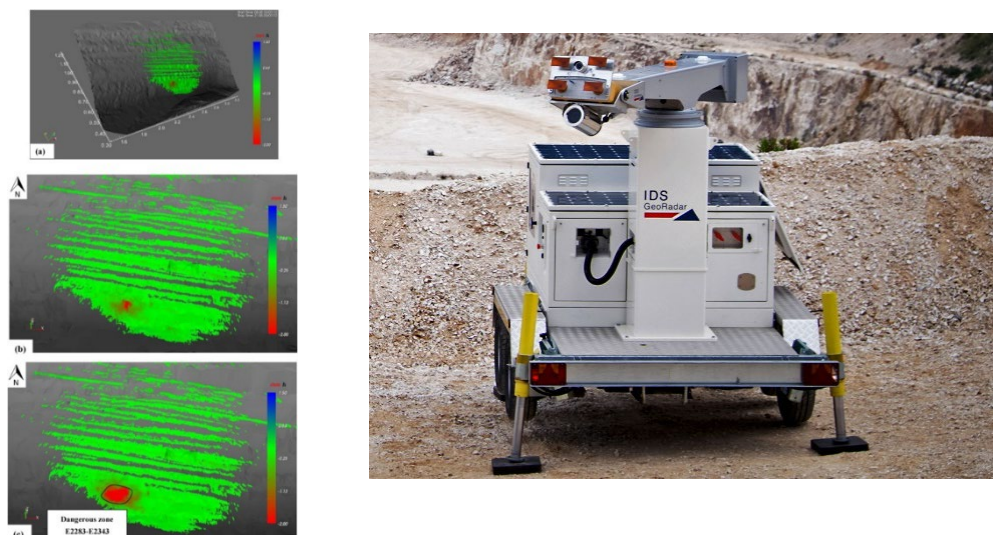
FIG 1 – Active slope failure detected and alarmed by IDS GB InSAR (Li *et al,* 2015) and next gen ArcSAR.

Satellite InSAR (Interferometric synthetic aperture radar) analysis

Satellite interferometric synthetic aperture radar (InSAR) monitoring is widely used in open pit mining operations around the world, including spoil heaps and tailings storage facilities (TSF). Sampling frequency using TSF usually ranges from 11 to 22 days, depending on satellite availability and commercial offering. Satellite InSAR monitoring is suitable for use across large areas, that have either previously not been monitored or are inaccessible for ground-based sensor deployment.

The long timespans between acquisitions make InSAR not suitable for critical monitoring. It is also important to note that north–south movement is not easily derived from satellite InSAR acquisitions as east–west and vertical displacement, due to the ascending and descending satellite orbits measuring perpendicular to the east and west only (Bar and Dixon, 2021).

LIDAR

LIDAR monitoring uses a laser measurement component (laser scanner) for monitoring the rock face. The principle behind the software is to establish a grid of measurement points and to re-measure the grid periodically to look for differences in the position of the grid nodes. This allows displacement to be measured without use of prisms or access to the wall. While it is not real-time or all-weather like RADAR, it has some advantages in that accurate up to date DTMs are created and the data can sometimes be used for rock mass characterisation.

Geodetic monitoring – total stations

Together with ground-based radar, prism monitoring by means of automated total stations (ATS) remains the backbone of most open pit hard rock mining operations. Depending on the pit-geometry, a number of ATS are carefully placed around the pit crest to measure prisms placed around the mine at set intervals (several times a day as a minimum). A prism monitoring system can comprise of hundreds to thousands of prisms. High accuracy instruments, such as the Leica TM60 0.5" can measure accurately over several kilometres. Atmospherics, weather events and dust can impact the accuracy and reliability of such systems. However, due to the affordability of survey prisms, large areas can be monitored cost-effectively using 3D vectors, or (adjusted) slope-distance. Prism monitoring cannot be classed as critical (ie near-real time) monitoring but serves as the single most important validation tool for ground-based radar and is important for long-term, lower risk monitoring as I can be used in an episodic fashion.

Geodetic monitoring – GNSS

GNSS monitoring has extensively been used in the civil construction industry as well as in land-slide monitoring. It can serve as a validation tool to ground truth line of sight sensors (LOS) data, such as Satellite InSAR acquisitions (Carlà *et al*, 2019). Horizontal accuracies are in the sub decimetre range. Whereas vertical accuracies range between 10–15 mm depending on baseline length. Sampling frequency can be up to 50 Hz for sophisticated receivers, making them suitable to track seismic activity (Kudłacik *et al*, 2021). GNSS sensors are single point acquisitions and are hence less suitable to monitor larger areas compared with remote sensing instrumentation.

Geotechnical sensors

There is a vast array of sensors available to measure deformation or change in a mining environment. However, cost prohibitive telemetry results in many mines still manually collecting data. A leap in technology over the last few years has seen many cost-effective wireless mesh systems enter the market, mainly operating via 900 Mhz radios and hence enabling the sensors to talk over long distances coherent with mining environment. The telemetry for piezometers, tilt and other sensors can now incorporated into an automated data collection process. Data is automatically collected (Figures 2 and 3) by the node from the sensor, then uploaded to a gateway either via direct communication or a mesh algorithm, finding the easiest path to relay the information back to the gateway. The gateway then typically uploads the data into an online portal where alarming and thresholds can be configured. While this allows for a lower degree of human error, it is also worth mentioning that it reduces the risk of injury to personnel as the physical presence (manual field data collection procedure) is no longer required as the sensors convert the physical field parameters into the virtual, cloud or on-premises hosted environment automatically (Dener, 2017).

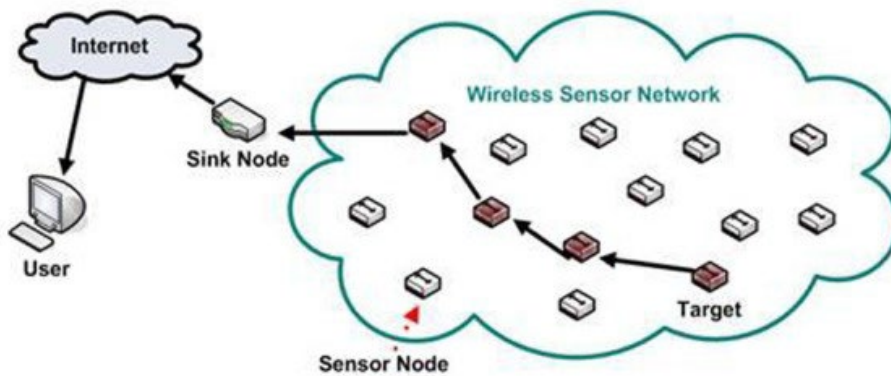**FIG 2** – WiSen principle (Dener, 2017).

FIG 3 – Wisen MeshWan wireless mesh four channel VW interface node.

Example use

A medium sized gold mine in Queensland uses a total monitoring approach by acquiring and combining several sources of data a holistic view of geotechnical hazards can be established, including: Terrestrial Radar, Satellite InSAR, ATS (Prism) Monitoring, Photogrammetry, Tilt and Distance Sensors, Piezometers, GNSS and HxGn GeoMonitoring Hub (Figure 4). While radar is used to monitor rapid brittle failures in the pit, GNSS and tiltmeters support monitoring of the TSF.

FIG 4 – Hexagon GeoMonitoring Hub sensor aggregation software.

Lower cost sensors like tiltmeters and distos are used to augment the real time radar systems and prisms remain the background reference for long-term movement analysis, verification of trends and determining vectors of movement.

RISK MANAGEMENT

The term 'risk' denotes exposure to the possibility of such things as economic or financial loss or gain, physical damage, injury or delay, as a consequence of pursuing or not pursuing a particular course of action. It is described and evaluated in terms of likelihood and consequences; with the likelihood a rating of the probability of an event occurring and the consequence related to the outcome of this event, which may be given as the consequence to people (eg a single fatality) or a dollar value attached to property damage. Risk management is the process by which informed decisions are made to accept known levels of risk or to implement a set of actions to reduce unacceptable risks to acceptable levels (Figure 5). A risk management framework from the Australian Risk Management Standard (Australian Standard ISO3100.2018) is used to discuss slop monitoring applications in this paper.
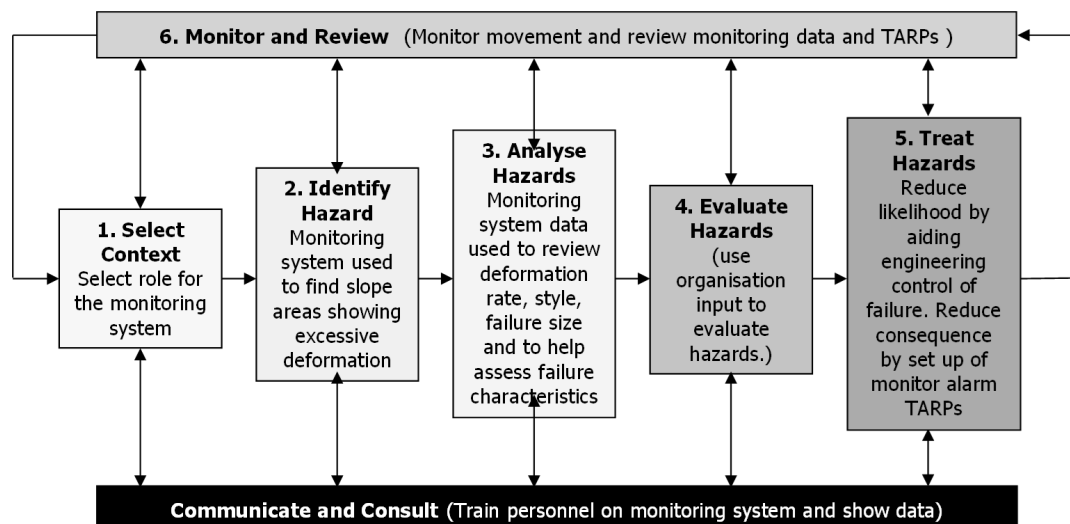
FIG 5 – Risk management process.

Before detailing specifics associated with use of the framework for managing the risk related to slope instability using the monitoring data, an overview of the main components of risk management is warranted. The activities that are required to manage risks effectively in this framework include:

- Establishing the strategic, organisational, and risk management context in which the rest of the process will take place. This involves identifying criteria against which the risk will be evaluated. The structure of the risk analysis should be de-fined at this stage.

- Identification of all risks whether they are under the control of the organisation. What can happen? How and why can it happen.

- Analysing risks to separate the minor acceptable risks from the major risks, and to provide data to assist in the evaluation and treatment of risks. This requires estimation of the consequence and likelihood, the product of which is the risk.

- Risk evaluation involving comparing the level of risk found during the analysis with previously established risk criteria. The output is often a prioritised list of risks.

- Risk treatment involving identifying the range of options for treating risk, assessing these options, preparing risk treatment plans and implementing them. Options can include avoid, reduce likelihood, reduce consequence, transfer the risk and retain the risk (Residual Risk).

It is also essential to remember to communicate/consult and monitor/review processes at all levels. Effective communication is important to ensure that those responsible for implementing risk management, and those with a vested interest understand the basis on which decisions are made and why particular actions are taken. Risks and the effectiveness of control measures need to be monitored to ensure that changing circumstances do not alter risk priorities (few risks remain static). Review and regular repeat of the risk management cycle is an integral part of the process.

Example 1 – Identification of slope hazards

One of the primary roles of the slope monitoring is identifying areas of potential slope failures. Terrestrial radar offers broad area coverage and almost real time scanning means that large expanses of pit slope (eg >1 000 000 m^2) can be scanned and results obtained in less than 2 minutes (see Figure 6).
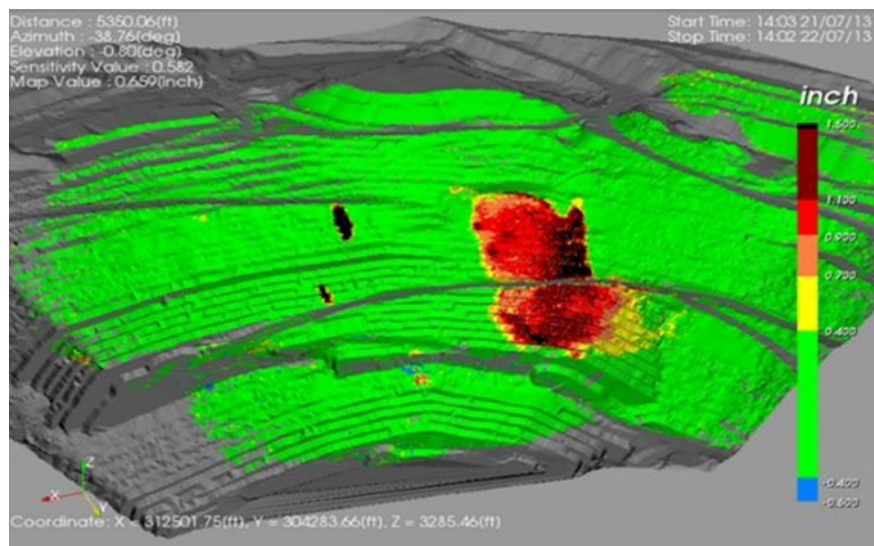
FIG 6 – IDS Georadar Guardian.

After a relatively short time, areas of stable slope can be quickly identified, as well as those areas that are showing greater surface deformation than expected (providing show >0.1 mm deformation). This increased deformation may represent areas of slope instability, which can be investigated. It can be seen in Figure 5 how terrestrial radar can quickly identify potential slope instability hazards. In this case in a copper mine in North America a number of slope failures can be identified in red/black where excess surface displacement can be clearly identified.

Example 2 – Analysis of slope hazards (consequence)

Slope monitoring can help contribute to the determination of the consequences of failure by providing information relating to four major factors size of failure, mode of failure, evacuation response and post failure behaviour.

The size of failure can be critical (eg is it small enough to be caught by the catch bench, will it cut access to the pit production areas) and the scanning technologies (LIDAR and RADAR) can be ideal to determine the areal size of the failure. RADAR is particularly useful that it can obtain more precise data after a very short monitoring time (less than 20 minutes) in all-weather conditions. In the authors experience with a number of synthetic and real aperture radar systems; some operations have been unpleasantly surprised by the size of a failure developing that had been missed between existing survey prisms. Mode of failure is an important characteristic for geotechnical engineers to understand. While newer radar systems all multiple systems to be used to determine vectors of movements, a well implemented and maintained prism monitoring system will allow best quality vector information to be produced on slope movements which should be reviewed with rock mass characterisation results to help identify failure mode.

Whether an area is evacuated in time prior to ultimate collapse obviously has major implications to the resulting consequence of that failure. Although loss of access and productivity may be minimised, an effective evacuation should mean a slope failure without damage to equipment or endangering workers. A fourth major factor also significantly impacts consequence, *post failure behaviour,* and it is in the authors experience the most poorly understood and least considered by operators. There have been numerous cases where the size of failures have been known prior to collapse, the failure mode known and the approximate time of failure predicted prior to collapse. However, poor risk outcomes resulted because the post failure behaviour was not predicted or clearly communicated to the operations.

Example 3 – Analysis of slope hazards (likelihood)

In determining the likelihood of slope failure, the slope monitoring record provides a particularly useful measure of deformation rate and trend which can be used in the analysis. While the rate of deformation is a clear indicator of potential failure, the trend is an even clearer measure. Idealised rates are shown in Figure 7.
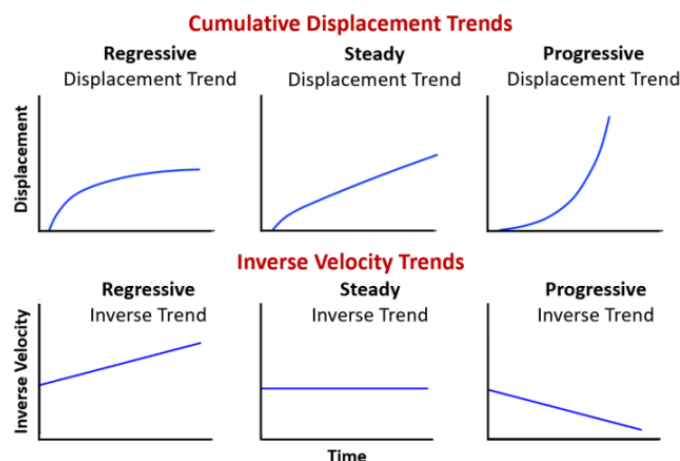

FIG 7 – Cumulative and Inverse Velocity Trends (Borron and Derby, 2019).

In environments such as open pit mining where blasting/excavation can occur at regular cycles, it is quite common to see a regressive rate of movement in the displacement of pit slopes following change in loading conditions. These are characterised by initially a high velocity caused by some trigger event (usually blasting, excavation or rainfall) which reduces with time to a lower background level (often zero velocity). Stress relief of excavations can lead to such a trend. This contrasts with a progressive rate of movement that has initial lower velocity but the velocity increases with time (see Figure 8). The likelihood of a failure event occurring is far greater when a progressive failure

curve is measured. When analysing a slope hazard, it is important to identify the scale and characteristics of the system being analysed, which supports selecting the best monitoring technique, ideally using a total monitoring strategy. This selection can primarily be focused on monitoring data characteristics needed, as well as cost which typically needs to be considered.
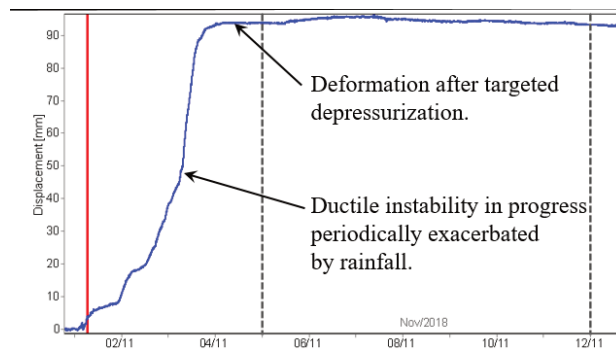
FIG 8 – Horizontal drain location to depressurise and stabilise slope.

Example 4 – Treatment of slope hazards

The example below on hazard treatment, refers to an open pit gold mine in Papua New Guinea, where comprehensive geotechnical modelling and monitoring was performed leading to successful a risk treatment discussed in McQuillan *et al* (2020). Initial slope deformation was identified by an IBIS-FM radar monitoring with deformation initiated by several days of heavy rainfall, and levels of movement recorded periodically increased with high intensity and prolonged rainfall events, and subsequently decreased when rain subsided. Visual inspections by UAV revealed the backscarp of the slope failure, where wide cracks were observed at the crest of the failure zone and further investigation established the failure mechanism related to a low-angle, in-pit dipping relic fault. Pore pressures recorded in a nearby vibrating wireline piezometer indicated that the slope was likely to be fully saturated. Slope stability models were subsequently updated to reflect these conditions, and a reduced FS of 1.03 was calculated with a good correlation observed between predicted slip surface locations and actual slope movement.

Remediation options were then determined by running a series of additional slope stability models that assessed various unloading, buttressing and depressurisation options. Models simulating deep horizontal drains and unloading indicated the FS could be significantly improved. Following execution of depressurisation and unloading program, significant improvements in the slope was achieved. Figure 8 plots displacement against time with the surface displacement recorded by IDS terrestrial radar. It can be seen that the curve flattens off (the slope movements) almost immediately after the slope depressurisation commences and driving forces (pore pressures) are reduced.

One of the advantages of radars is being near real-time with rapid scanning, the effects of active slope engineering like depressurisation, buttressing or unloading can often be seen very quickly. An iron ore miner made significant cost savings in their slope buttress program as they could use the observational method to back analyse some of their input assumptions used in the initial buttress design.

Discussion on residual risk and monitoring trends

Following identification of risks and mitigation of risks you find unacceptable (ie treating them), you won't completely eliminate all the risks because it is simply not possible – therefore, some risks will remain at a certain level, and this is called residual risk (Borron and Derby, 2019). The concept of residual risk is extremely important for geotechnical engineers to understand, and to be able to effectively consult and communicate to other stakeholders in the mining operation. Even with significant investment in slope monitoring systems, residual risk will likely remain. It is also essential not to underestimate the human factors in risk management. We can make increasing investments in multiple technologies, to improve resolution and redundancy in a slope monitoring program, but if we don't make similar investments in people, processes and systems; we can risk overwhelming site-based engineers who can be increasingly burdened in data collection and low level system

management. This is a necessary task, but if it removes a geotechnical engineer from analysing the data and working with operation teams to actively manage the geotechnical risks, the mine site will not be getting the benefit from the investments made.

One of the monitoring trends evident in recent years is the use of vendors or third-party service providers to support analysis of slope monitoring data, particularly RADAR and prism monitoring. This has been seen to be a useful service in the industry and allows on-site geotechnical engineers to relinquish some data gathering and reporting activities to focus more on geotechnical engineering and working with stakeholders on treating risks. Use of 24/7 monitoring centres has also been proven useful in support operations in identifying false alarms associated with weather events, machine interference or data loss. It is important that a structured and rigorous framework is put in place for these services, and a clear understanding of input requirements, communication protocols and risks is discussed and documented.

CONCLUSION

Whilst ground based RADAR monitoring has enabled a radical change in the management of risks in open cut mining operations; assessing and managing instability hazards in open pit mining slopes requires an approach that adopts multiple technologies and requires geotechnical engineers to understand limitations and strengths of all these techniques. The practical benefits of using a total monitoring approach based on using multiple technologies, is improved risk management outcomes and reduced cost to operations over the life-of-mine.

The Australian Standard on risk management provides a useful framework to frame these different technologies and should highlight the need to effectively communicate and consult these risks to other stakeholders in the mining operation. It is important with increasing data and systems available that a clear unambiguous status of geotechnical hazards can be presented to the stakeholders so they can work with the geotechnical engineers to effectively manage the risks associated.

REFERENCES

Bar, N and Dixon, R, 2021. Unveiling unknowns: Practical application of InSAR for slope performance monitoring and risk management across multiple surface mines, *Engineering Geology,* 293:106326. doi:https://doi.org/10.1016/j.enggeo.2021.106326

Bar, N, Kostadinovski, M, Tucker, M, Byng, G, Rachmatullah, R, Maldonado, A, ... Yacoub, T, 2020. Rapid and robust slope failure appraisal using aerial photogrammetry and 3D slope stability models, *International Journal of Mining Science and Technology,* 30(5):651–658. doi:https://doi.org/10.1016/j.ijmst.2020.05.013

Borron, S and Derby, M, 2019. *Ground Based Interferometric Synthetic Aperture Radar Combined With a Critical Slope Monitoring Program Will Provide Early Detection of Slope Movement Along Pipeline Corridors*.

Carlà, T, Tofani, V, Lombardi, L, Raspini, F, Bianchini, S, Bertolo, D, ... Casagli, N, 2019. Combination of GNSS, satellite InSAR and GBInSAR remote sensing monitoring to improve the understanding of a large landslide in high alpine environment, *Geomorphology,* 335:62–75. doi:https://doi.org/10.1016/j.geomorph.2019.03.014

Dener, M, 2017. WiSeN: A new sensor node for smart applications with wireless sensor networks, *Computers and Electrical Engineering,* 64:380–394. doi:https://doi.org/10.1016/j.compeleceng.2017.06.027

Kudłacik, I, Kapłon, J, Lizurek, G, Crespi, M and Kurpiński, G, 2021. High-rate GPS positioning for tracing anthropogenic seismic activity: The 29 January 2019 mining tremor in Legnica – Głogów Copper District, Poland, *Measurement,* 168:108396. doi:https://doi.org/10.1016/j.measurement.2020.108396

Li, Z, Wang, J-A, Li, L, Wang, L and Liang, R Y, 2015. A case study integrating numerical simulation and GB-InSAR monitoring to analyze flexural toppling of an anti-dip slope in Fushun open pit, *Engineering Geology,* 197:20–32. doi:https://doi.org/10.1016/j.enggeo.2015.08.012

McQuillan, A, Yacoub, T, Bar, N, Coli, N, Leoni, L, Rea, S and Bu, J, 2020. Three-dimensional slope stability modelling and its interoperability with interferometric radar data to improve geotechnical design, *Slope Stability 2020: 2020 International Symposium on Slope Stability in Open Pit Mining and Civil Engineering* (Australian Centre for Geomechanics: Perth), https://papers.acg.uwa.edu.au/p/2025_92_McQuillan/

Sharon, R, 2020. Slope performance monitoring: system design, implementation and quality assurance, in PM Dight (ed.), *Slope Stability 2020: Proceedings of the 2020 International Symposium on Slope Stability in Open Pit Mining and Civil Engineering* (Australian Centre for Geomechanics: Perth), pp. 17–38, https://doi.org/10.36487/ACG_repo/2025_0.02 (https://papers.acg.uwa.edu.au/p/2025_0.02_Sharon/)

Zevgolis, I E, Deliveris, A V and Koukouzas, N C, 2019. Slope failure incidents and other stability concerns in surface lignite mines in Greece, *Journal of Sustainable Mining,* 18(4):182–197. doi:https://doi.org/10.1016/j.jsm.2019.07.001

Structure stability

Three-dimensional modelling and analysis of high-speed train-induced building vibration considering different soil types

A A Faizan[1] and O Kirtel[2]

1. PhD student, Sakarya University of Applied Sciences, Sakarya, Turkey, 54050.
   Email: ahad.faizan@ogr.sakarya.edu.tr
2. Assistant Professor, Sakarya University of Applied Sciences, Sakarya 54050.
   Email: okirtel@subu.edu.tr

ABSTRACT

With the rapid increase and development of high-speed trains (HSTs), the problems such as train-induced ground vibration and its dynamic effects on nearby structures have become a major environmental concern in urban areas. Ground-born vibrations produced by high-speed trains pose a great challenge for engineers to build structures in such areas that is applicable for residents. In order to study the effect of train-induced ground vibration on nearby buildings, an advanced three-dimensional finite element model for train-induced ground vibrations has been developed using PLAXIS 3D Ultimate. The results of the *in situ* measurements which was previously carried out by the authors were used to validate the numerical model. The field test for ground vibration due to the passage of a high-speed train was carried out on the Istanbul-Ankara high-speed railway in Turkey with a train speed of 250 km/h. An in-depth analysis was achieved to investigate the effect of different soil properties on the train-induced ground vibrations by using the verified model. According to the result of the vibration analysis, the relative vibration response curves in all directions (x, y, z) for different soil conditions were obtained comparatively. The obtained results of the vibration analysis are discussed in order to figure out some useful conclusions.

INTRODUCTION

In the past few years, the problems such as train-induced ground-borne vibration and its dynamic effects on nearby structures have become a major environmental concern in urban areas with the rapid increase and development of high-speed trains (HSTs). With the rise of railway networks for HSTs, train-induced ground-born vibrations posing a great challenge for engineers to build structures in such area that are applicable for residents. The propagation of the High-speed train-induced vibrations through the surrounding soil layers cause damage to the nearby structures and may affect the people living near the railway.

Recently, many research works have been done on the ground-borne vibrations excited by high-speed trains. These studies can be categorised as numerical and analytical works. Lombaert and Degrande (2009) investigated the excitations of train-induced ground vibration to quasi-static and dynamic and suggested a numerical model. Faizan *et al* (2020) carried out a 2D finite element model for the purpose of studying train-induced ground-borne vibrations under different soil conditions and validating experimental results. Ribes *et al* (2017) developed a 3D finite element model to analyse the propagation of train-induced vibrations to a building close to the railway line. Zou *et al* (2020) proposed a prediction method to evaluate the train-induced vibration transmission from the ground up into the nearby building.

This paper intends to study the influence of train induced building vibrations for different soil conditions. For this purpose, a verified three-dimensional finite element model based on *in situ* measurements was developed to obtain the velocity spectra of the train-induced vibration records at the selected points.

RESEARCH MATERIALS AND METHODS

A field test and ground-borne vibration experiment due to the passage of high-speed train with speed of 250 km/h were performed by the authors on Istanbul-Ankara high-speed railway in Turkey. The place of the field measurement selected for this work was Kirkpinar which is located at the western end of the place in the Sapanca district. This place was chosen for experimental measurements because of its weak soil condition (V_S = 200 m/s), being close to the train line and away from other environmental vibrations. The measurement campaign was carried out in order to determine the free

field ground motion produced by repeated train passes. The obtained results of the field measurements are presently used to validate the prediction numerical model. The railway line selected for this purpose is the line L1 which stretches from Istanbul to Ankara. The field measurements have been performed in 4 measuring points in three directions during the passage of high-speed train. The directions are determined as perpendicular to the track (N-S), parallel to the track (E-W) and vertical downward (U-D). The accelerometers were placed at distances 7 m, 14 m, 21 m and 28 m from the railway Line 1 (Figure 1).
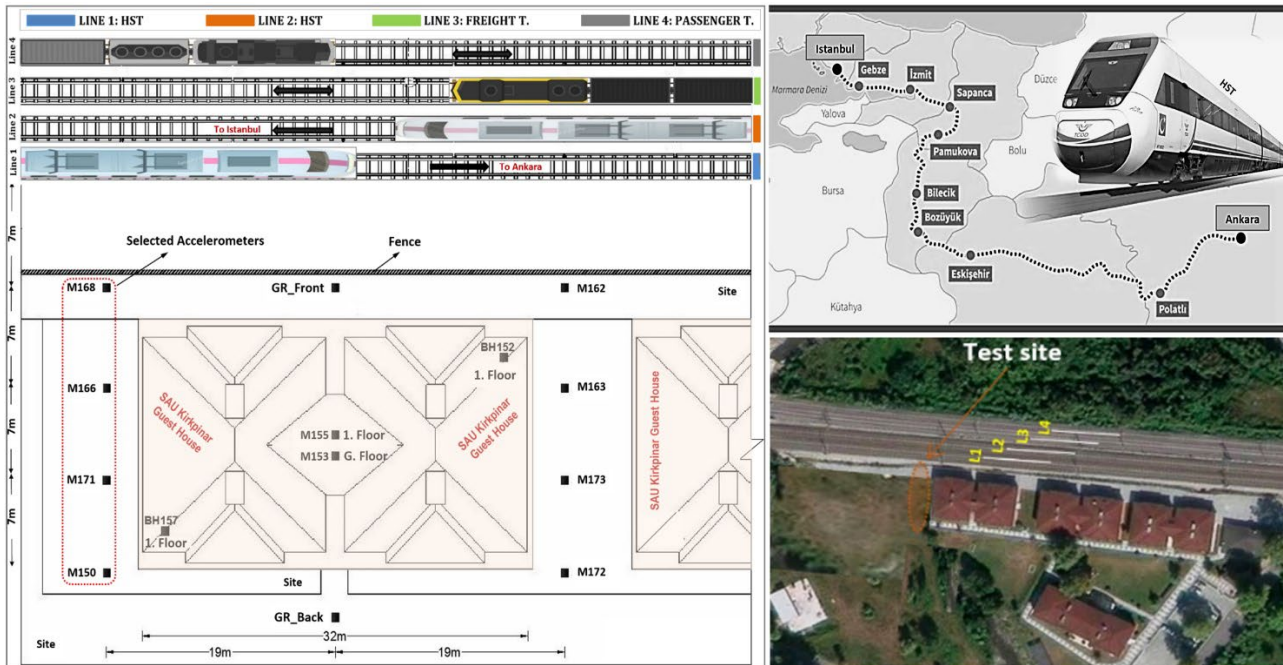
FIG 1 – The characteristics of the test site and investigated parameters for all selected points.

In this study, recorded ground vibration during the passage of the high-speed train is prepared in terms of acceleration. The extracted peak ground accelerations are given in Table 1.

TABLE 1

Summary of PGA values for parallel and perpendicular directions (cm/s^2).

Device No	Distance from track (m)	N-S	E-W	U-D
M168	7	11.971	16.332	28.856
M166	14	8.116	4.262	17.428
M171	21	4.966	4.366	9.595
M150	28	4.416	3.838	8.793

NUMERICAL PREDICTION MODEL

Finite element modelling

In this study, an advanced three-dimensional finite element model was developed in PLAXIS 3D Ultimate using 10-noded triangular elements (Plaxis, 2011). The finite element size (Δh) and time step integration (Δt) have been chosen properly for the finite element model simulations by considering the Courant condition. The FE model element size estimated according to the smallest wavelength that allows the high frequency motion to be simulated accurately. Standard fixities and absorbent boundaries were assigned along the model to reduce the wave reflections at the boundaries. The FE model developed in the current study is shown in Figure 2.
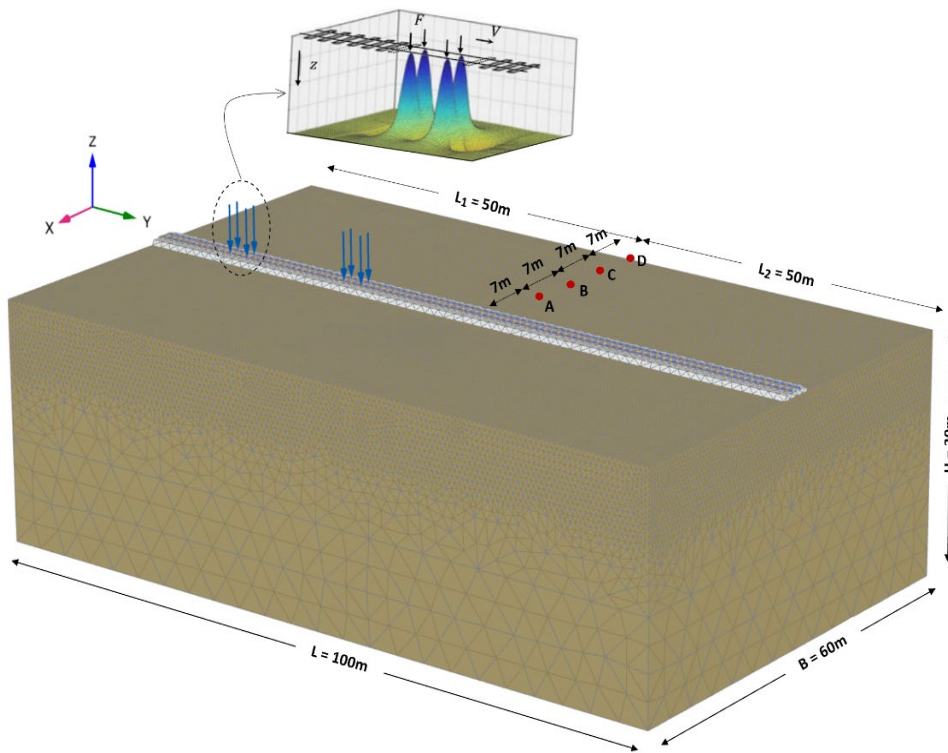
FIG 2 – Typical 3D FE model of track-ground system developed in PLAXIS.

Numerical results

The numerical analysis of the finite element model for different points has been performed in the time domain under plain-strain condition. In this study, a 3D linear elastic analysis was performed and the relative horizontal and vertical accelerations for point A, B, C and D were obtained. The peak ground accelerations (PGAs) of the finite element analysis for different points are given in Table 2.

TABLE 2

PGA values in horizontal and vertical directions (cm/s^2).

Measurement points	Distance from track (m)	a_x	a_y	a_z
A	7	15.204	17.790	25.379
B	14	8.787	5.235	14.643
C	21	5.590	5.168	12.583
D	28	4.440	5.183	11.247

Validation of FE model

The validation of the present numerical model was performed using field measurement data. The measured and calculations results were compared for validation by using peak ground acceleration (PGA) values. Figure 3 shows a comparison between measured and calculated peak ground accelerations on the ground at distances 7 m, 14 m, 21 m and 28 m from the track. The vertical and horizontal PGAs for selected points are presented and summarised in Table 3. A comparison between the measured and calculated accelerations on the ground shows a good agreement and the compatibility of the results proves that the verified FE model can be applied in the analysis of vibrations.
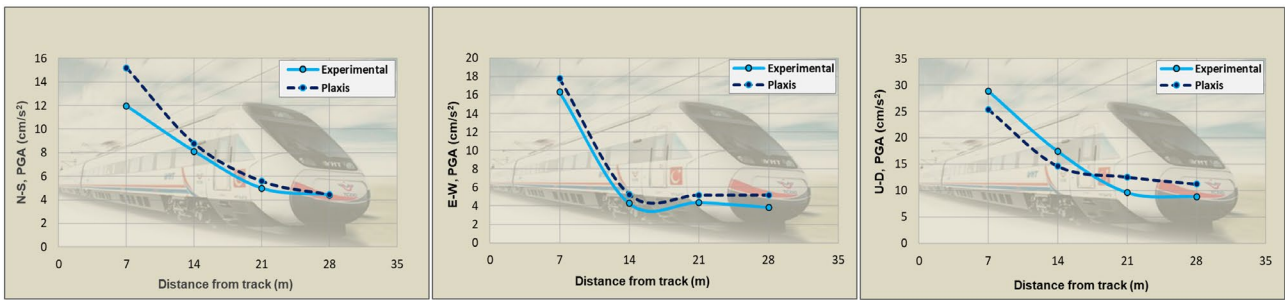
FIG 3 – Comparison of measured and calculated peak ground accelerations in horizontal and vertical directions.

TABLE 3

Comparing PGA of the measured and calculated accelerations (cm/s^2).

Device/ Point	Distance from track (m)	Exper. $a_{(N-S)}$	Plaxis a_x	Exper. $a_{(E-W)}$	Plaxis a_y	Exper. $a_{(U-D)}$	Plaxis a_z
M168/A	7	11.971	15.204	16.332	17.790	28.856	25.379
M166/B	14	8.116	8.787	4.262	5.235	17.428	14.643
M171/C	21	4.966	5.590	4.366	5.168	9.595	12.583
M150/D	28	4.416	4.440	3.838	5.183	8.793	11.247

IMPACT OF DIFFERNET SOIL PROPERTIES ON THE TRAIN-INDUCED BUILDING VIBRATIONS

To investigate the effect of soil properties on the train-induced building vibrations, analysis was performed for three types of soil. The soils were specified as hard rock, medium and soft soil. In the present study, a 3D linear elastic analysis was performed and the relative horizontal and vertical velocities for the top of the building (P1) were obtained by considering different soil conditions (Figure 4). The mechanical properties of different soil types are shown in Table 4.

(a)
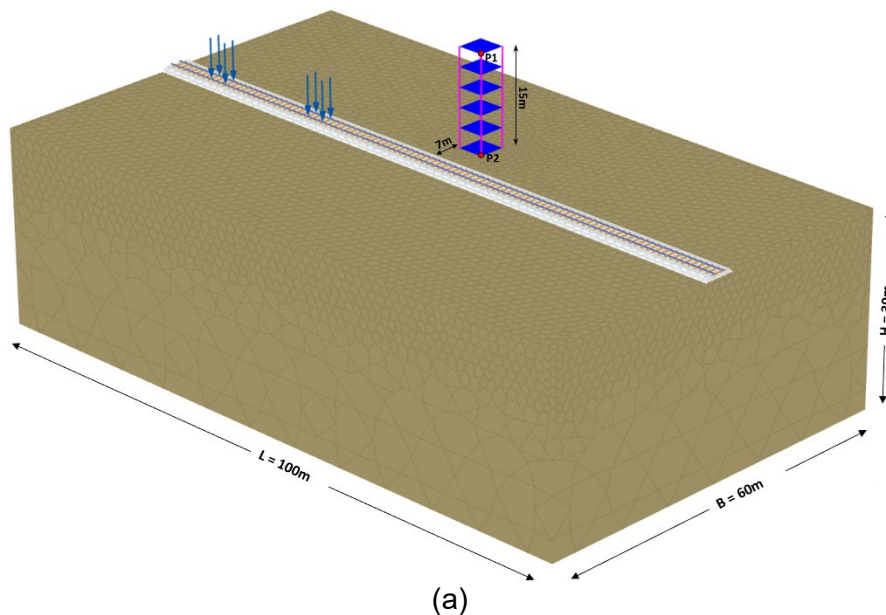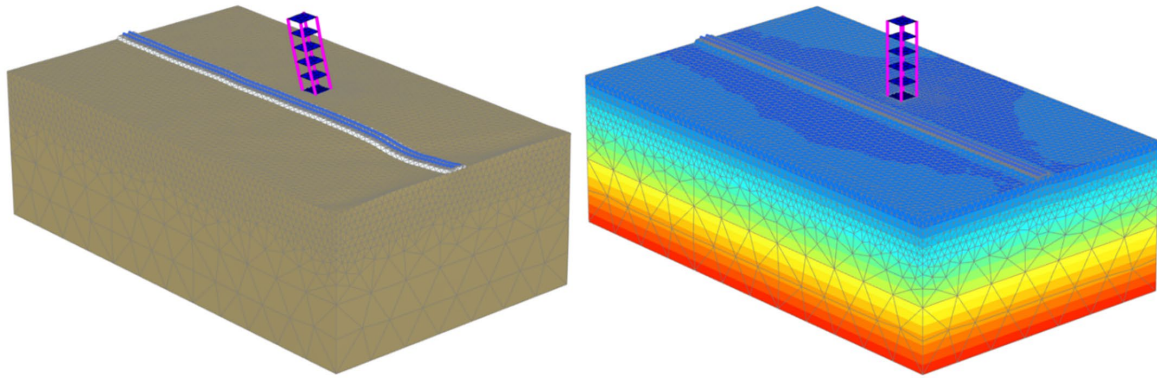
(b)

FIG 4 – Railway-soil-structure model (a) 3D FE model (before analysis) and (b) deformed shape and stress (after analysis).

TABLE 4

Mechanical properties of different soil types.

Soil types	Parameters			
	γ (kN/m³)	E (kN/m²)	υ (-)	V_S (m/s)
Hard rock (ZA)	27.45	$5.10×10^7$	0.25	2700
Medium (ZC)	17.65	$3.15×10^5$	0.4	250
Soft (ZE)	16.67	$4.93×10^4$	0.45	100

Based on the established FE model and numerical analysis, the resulting time-history spectra and peak ground velocity (PGV) of the vertical and horizontal vibrations on the top of the building are carried out and shown in Figures 5 and 6.
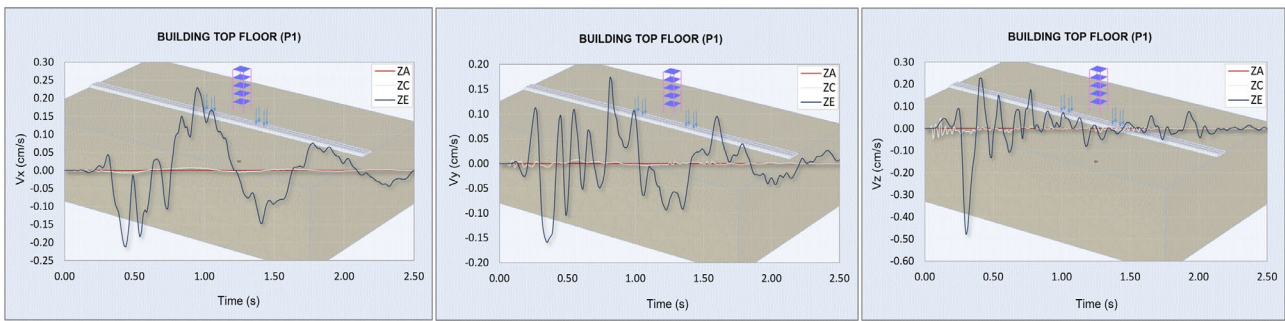
(a)
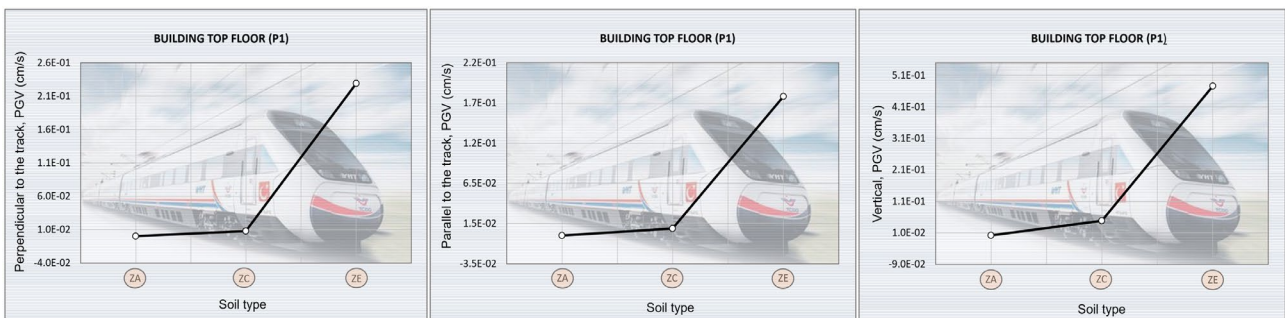
(b)

FIG 5 – Time history and peak ground velocity of the horizontal and vertical building vibrations for different soil types.
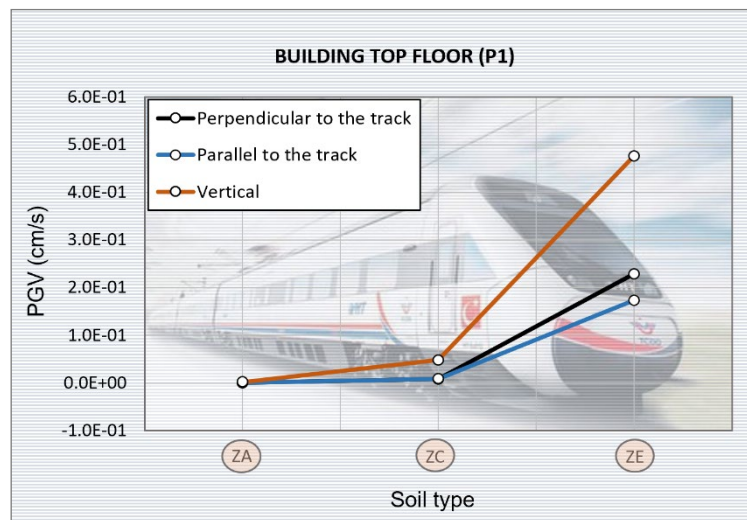
FIG 6 – Comparison of calculated peak ground velocities for different soil types in horizontal and vertical directions.

CONCLUSIONS

An *in situ* measurement due to the passage of high-speed train with speed of 250 km/h were performed by the authors on Istanbul-Ankara high-speed railway in Turkey. During the test, the resulting time histories of the vertical and horizontal accelerations on the ground are obtained. In order to investigate the train-induced vibrations, an advanced three-dimensional finite element model has been developed using PLAXIS 3D. The results of free field measurements used to validate the numerical model. Lastly, to investigate the effect of soil properties on the train-induced building vibrations, analysis was performed for three soil types with different stiffnesses by using verified model. The relative horizontal and vertical velocities for different soil conditions were obtained comparatively.

The field and numerical results presented in this study revealed that:

- The vibration levels on free field and top of the building are decreased with distance from the track. According to the results, the distance of railway lines and PGAs and PGVs values are directly proportional.

- The vibration results for both directions show that, the downward direction of train vibrations has more impact than the horizontal directions.

- The vibration analysis under different soil conditions demonstrated that, the train-induced ground vibrations for each soil type change according to its mechanical properties. It is observed that the PGV values on the top of the building are increasing from hard rock to soft soil because of stiffness of soils.

The established finite element model can be considered as a useful prediction tool and easily implemented by researchers and engineers to study the effect of high-speed train-induced vibrations in a fast and effective way. The verified computational FE model may help researchers determine further investigation strategies to develop cost-effective mitigation measures for structures near the railway track and significantly contribute to understanding complex wave propagation problems. Vibration measurement data collected from parametric analysis with numerical model for various soil characteristics can be particularly useful when planning residential and industrial facilities at new locations near railroads, to avoid the adverse effects of train-induced environmental vibrations.

ACKNOWLEDGEMENTS

REFERENCES

Faizan, A A, Kirtel, O, Celebi, E, Zulfikar, A C and Goktepe, F, 2020. Experimental and numerical study on free field motion due to passage of high-speed train considering different types of soil, *International Conference on Noise and Vibration Engineering, ISMA2020*, pp 2585–2597.

Lombaert, G and Degrande, G, 2009. Ground-borne vibration due to static and dynamic axle loads of InterCity and high-speed trains, *Journal of Sound and Vibration*, 319(3–5)1036–1066.

Plaxis, 2011. PLAXIS 3D 2011 – Reference vol 2, Netherlands: PLAXIS.

Ribes, L F, Marzal, S, Zamorano, C and Real, J, 2017. Numerical modelling of building vibrations due to railway traffic: analysis of the mitigation capacity of a wave barrier, *Shock Vib,* (4):1–11.

Zou, C, Wang, Y and Tao, Z, 2020. Train-induced building vibration and radiated noise by considering soil properties, *Sustainability*, 12(3):1–17.

Managing steep seam dips and floor shears related dragline bench and lowwall instabilities

J Li[1], D Payne[2] and J Regan[3]

1. Principal Engineer Geotechnical, BHP, Moranbah, Queensland 4744.
    Email: jianping.li@bhp.com
2. Manager Geotechnical Services, BHP, Brisbane, Queensland 4000.
    Email: dan.payne@bhp.com
3. Manager Mine Scheduling, BMA, Moranbah, Queensland 4744.
    Email: jonathan.regan@bhp.com

ABSTRACT

The Caval Ridge Mine is an open cut coalmine and located within the Bowen Basin region in Central Queensland, and commenced mining and processing operations in 2014. A number of geotechnical challenges for managing dragline bench and lowwall stabilities have been encountered in both southern and northern pits over the years. Southern Pits contain steep seam dips of up to 15° (27 per cent) whilst the northern pits also have shears below pit floors. Geotechnical guidelines to manage the risk of dragline bench failure and lowwall instability have been developed and improved since these geotechnical challenges were identified. The dragline guidelines include dragline tub offset distances from the 60° Line (SDL) or buttressing thickness for different seam dips greater than or equal to 8°. The low wall stabilisation guideline established floor disruption widths and depths depending on seam dips and presence of floor shears to known depths of up to 3 m.

As mining operations advance, lowwalls have remained stable until floor disruptions were fired, then returned to stable soon after the shot. The maximum distance of lowwall cracking with blasting has been as far back as the second spoil peak (the prestrip truck dumps construction limit). These failures need to be eliminated to allow the operational flexibility and haulage benefit of constructing the prestrip truck dumps behind the first spoil peak, while maintaining no risk to personnel or equipment. The floor shear depth was verified by collaborating with the exploration teams and taking advantage of the already planned 8-inch coal quality core holes, drilling them an extra 5–10 m past the coal seam floor and locating the shear presence. With this continuous improvement effort, no lowwall failures have occurred during floor disruption firing from the second strip after the new floor disruption depth guidance have been applied.

This paper documents the processes for developing these geotechnical guidelines, operational implementation, and outcomes. Operational applications over the years confirmed that these guidelines have effectively managed the dragline bench and lowwall failure risks related with the steep seam dips and floor shears in this open cut coalmine.

INTRODUCTION

The major geotechnical risks for an open cut coalmine having tailings disposed in tailings storage facilities are the failures of highwall, low wall and dragline bench. For open cut coalmines with tailings mechanically dewatered and co-disposed together with rejects in spoil dumps, end dumping active tip head instabilities are more prominent for dump stability, in addition of highwall, low wall, and dragline bench failures. Some of the challenges associated with highwall and mixed plant rejects spoil dump co-disposal at the Caval Ridge Mine (the subject mine) were addressed over the years since commenced operation in 2014 (Tucker, Li and Todd, 2015; Li, Tucker and Todd, 2016; Li, Payne and Hooi, 2018; Li, 2020; Li *et al*, 2021).

Whilst for the geotechnical challenges related to dragline bench and low wall, the subject mine has been confronting them since the start of operation. Geotechnical controls for dragline bench and lowwall stability have gone through a number of Plan-Do-Check-Act (PDCA) cycles, which included existing instability assessment and proposing controls, operational implementation of the controls, closely monitoring their effectiveness, and re-assessing and updating geotechnical controls when new geological conditions are encountered. The latest updated geotechnical controls have been implemented successfully for nearly three years.

There are a number of factors impacting on dragline bench and lowwall instabilities:

- Steep coal seam or floor dips.

- Weak contact between the blasted overburden (spoil) and coal seam roof prior to being stripped.

- Water building up in-pit to cause reduced strength of spoil and coal roof contact and thin interburden within the coal seam.

- Coal remnant and silty or muddy materials left on pit floor after coal mining.

- Low strengths of the pit floor rock masses.

- Shears present in-pit floor at various depths.

Dragline bench instabilities are related to the first three factors, while the lowwall instabilities would be caused by the first and last three factors. Spoil categories also impact on dragline bench and lowwall stability, however, the overburden stripped by draglines is consistently composed of fresh Permian rock masses, and thus the impact of spoil categories can be discounted.

For lowwall stability management, depth where the shears present below the pit floor are the most challenging to define. Pit 6–8 lowwall instability at Dawson Mine (Tsang *et al,* 2022) is a typical example to show how challenging it is to allocate a floor shear to a geotechnical model. They utilised through-spoil drilling, surface and subsurface monitoring techniques and then allocated the shear, a tuffaceous claystone unit, at 11–12 m below pit floor. To allocate floor shears at the subject mine two 8-inch cored holes for coal quality assessments were extended to ~10 m below the lowest mineable coal seam floor (ie pit floor), to define the depth of floor shear.

Rock mass mechanical properties for Bowen Basin coal measures were established in 1997 and formally published by Simmons (2018). These strength values have been confirmed as realistic from applications to Bowen Basin coalmines over the years, and confirmed by a different rock mass strength estimation approach (Li, 2020). Shear strength framework for spoil dump design was published in 2004 also for Bowen Basin open cut coalmines (Simmons and McManus, 2004). However, there are no strengths for contact of dragline spoil with coal roof for Bowen Basin coal measures and the existing basal strengths for lowwall from Simmons and McManus (2004) need further review.

Therefore, this paper presents details of how the geotechnical aspects of dragline bench and lowwall instabilities are managed, including:

- A coal contact and basal strength review.

- Dragline bench and lowwall stability assessments with and without floor shears using limit equilibrium methods.

- Geotechnical controls including buttressing or standoff from the 60° Line (SDL) for dragline bench.

- Floor disruption requirements for lowwall stabilisation.

MANAGING DRAGLINE BENCH INSTABILITIES

### Raise of concern from dragline bench instabilities

The first dragline bench instability occurred in front of the SDL in mid-2015 at R12N pit, one of the southern pits of the subject mine. As shown in Figure 1 the failure occurred within a section with no buttress and coal seam dips ranging from 8.1° to 10.4°, ie no failure was experienced within areas either having coal seam dips less than 8° or being buttressed. Water in-pit along highwall might be a contributing factor for weakening the spoil and coal roof contact, in addition to a reasonably narrow Key of 25 m wide. No coal heave was observed. An 8 m standoff from dragline tub to the SDL was conservatively proposed to keep the dragline safe.
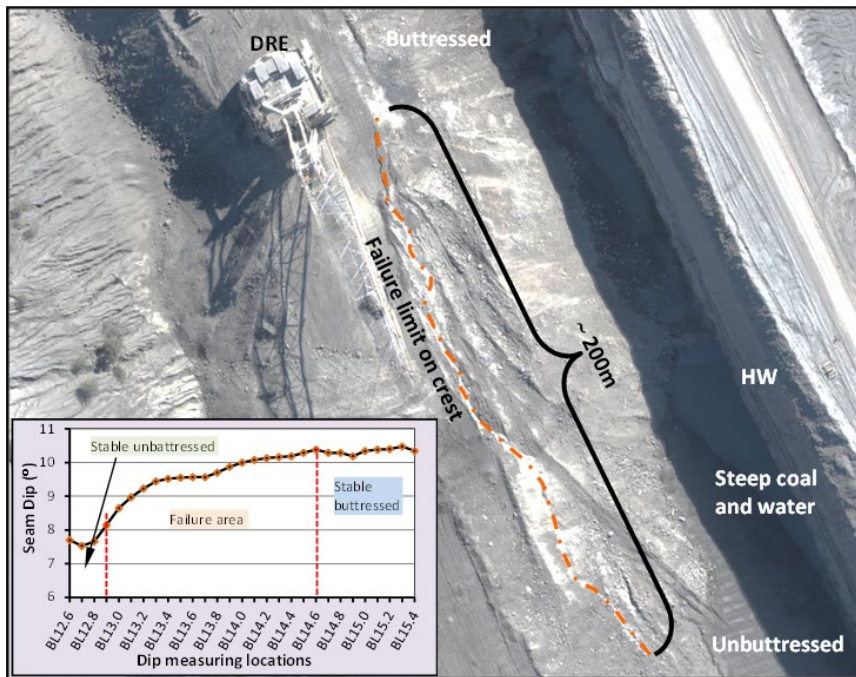
FIG 1 – The first dragline bench failure at southern pits of the subject mine in mid-2015.

In late 2016 another dragline in-pit bench failure, also close to the SDL, occurred in R30S (Figure 2), which was located in one of the northern pits. Contributing factors were steep coal seam, water pooled in-pit, reasonably narrow key width of 25 m and Category 2 spoil (Simmons and McManus, 2004), composed of Tertiary, weathered and fresh Permian materials. The 8 m standoff of dragline tub to the SDL on the elevated bench was recommended again as a risk control measure.
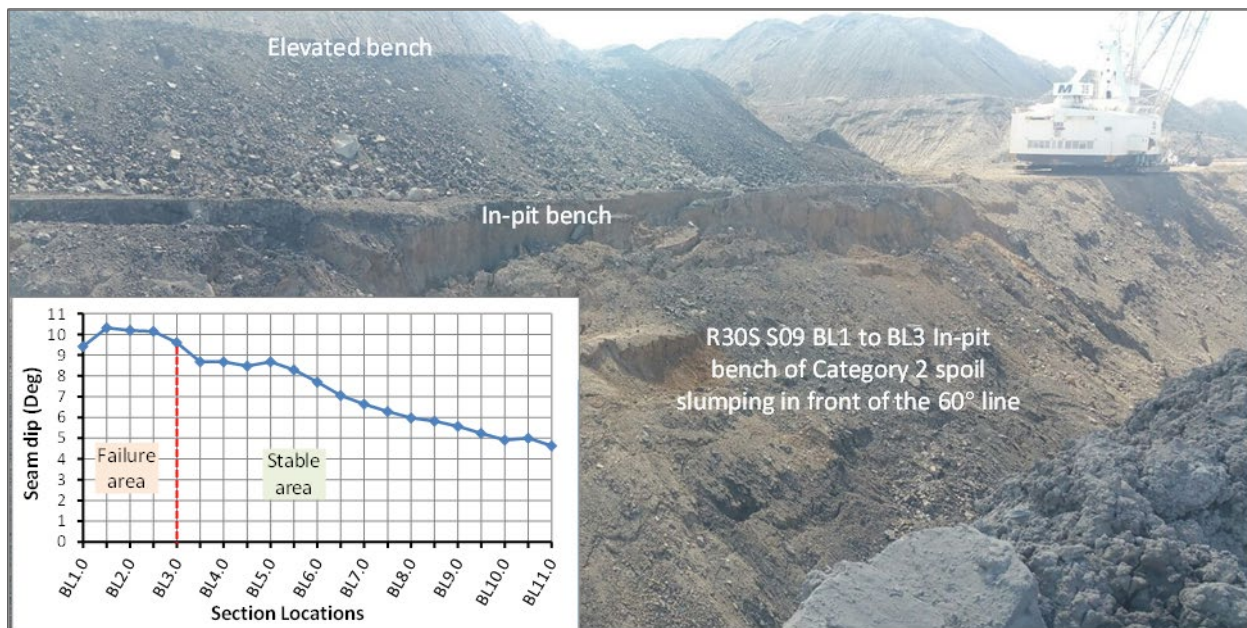
FIG 2 – First dragline bench failure in Northern pits of the subject mine in late 2016.

No direct risk was presented to draglines from these cases, as the failures occurred in front of the SDL, and the draglines were either kept behind the 60° line or stayed on buttressed benches at the time of dragline bench failure. However, these scenarios triggered a requirement for thorough geotechnical investigation, so that a geotechnical guideline could be established to manage the risks relating to the steep coal seam conditions for the future dragline operations. Approaches applied to this investigation were:

- Estimate shear strengths of the contact between top of coal and the blasted spoil above.

- Estimate strengths of shear planes within coal seams resulting from water induced thin interburden weakening.

- Conduct two-dimensional limit equilibrium (2D LE) analyses on dragline benches having different coal seam dips.

- Provide guidelines based on the stability assessment results, and validate the guidelines through operational applications.

Strength estimations for spoil and coal contact and coal seam shears

A number of ways exist to estimate shear strengths of the contact between blasted spoil and coal roof, including laboratory testing of core samples taken from exploration drilling, back analysis, or through reviewing of core photos of the contact. The first approach would be significantly challenging, as difficulties exist for collecting and testing the samples with rock and coal in either side of the contact are weak and broken. Therefore, the other two approaches were applied. The back analysis of the above two failure case histories gave the contact shear strengths of from 5–10 kPa cohesion and a 20–25° friction angle.

Core photos from a total of 62 exploration and geotechnical holes, crossing a number of strips, were reviewed. Quality of the contacts can be classified into three groups of weak, moderate and good (Figure 3). It was found that 32 coal roof and overburden contacts were weak with potential shear or broken and clayey rocks.
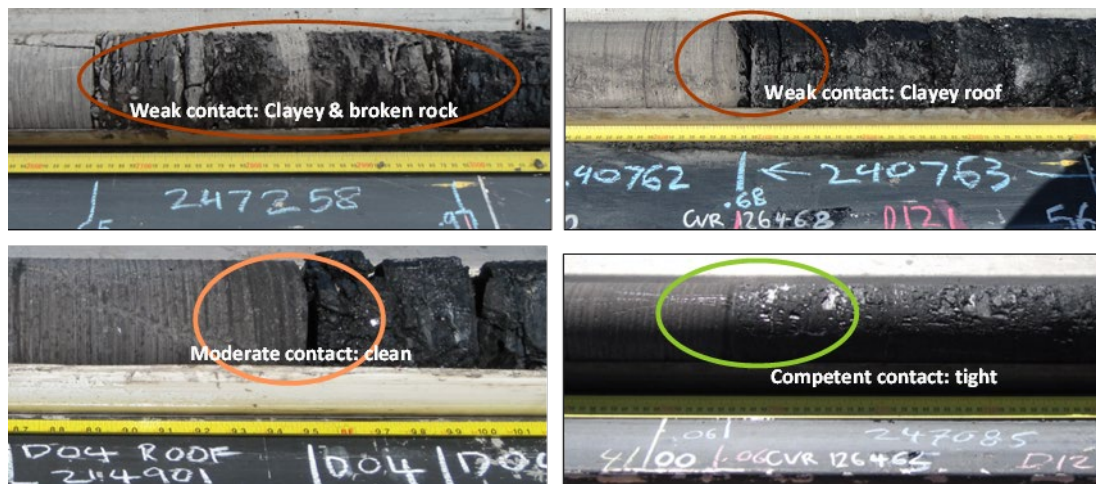
FIG 3 – Examples of core photos with different coal roof and overburden contact qualities.

For the weak contacts, shear strengths could be 0–5 kPa for cohesion and 15–20° for friction angle. Whilst for the moderate and good contacts, the shear strengths would be higher, the cohesion and friction angle could be as high as up to 25 kPa and 30°, respectively. For the safety of dragline, conservative strength values are applied to the spoil and coal contact in 2D LE dragline bench stability assessments, which are zero cohesion and 18° friction angle.

During this investigation another mechanism of dragline bench failure became evident. Failure through a weak plane within the coal seam, instead of along the roof contact, causing coal seam heave during dragline bench failure. In addition, this resulted in failure limit further behind the SDL than those dragline benches that failed through top of coal contact. Field inspections from highwall (Figure 4) and coal mining faces found that the only possible surface to fail through was the mudstone or claystone band in coal seam. This band is prone to slaking when saturated with water, particularly in wet seasons. Back analysis confirmed that this weak band had similar strength values as floor shears, which are 0 cohesion and 15° friction angle as given in Simmons and McManus (2004).
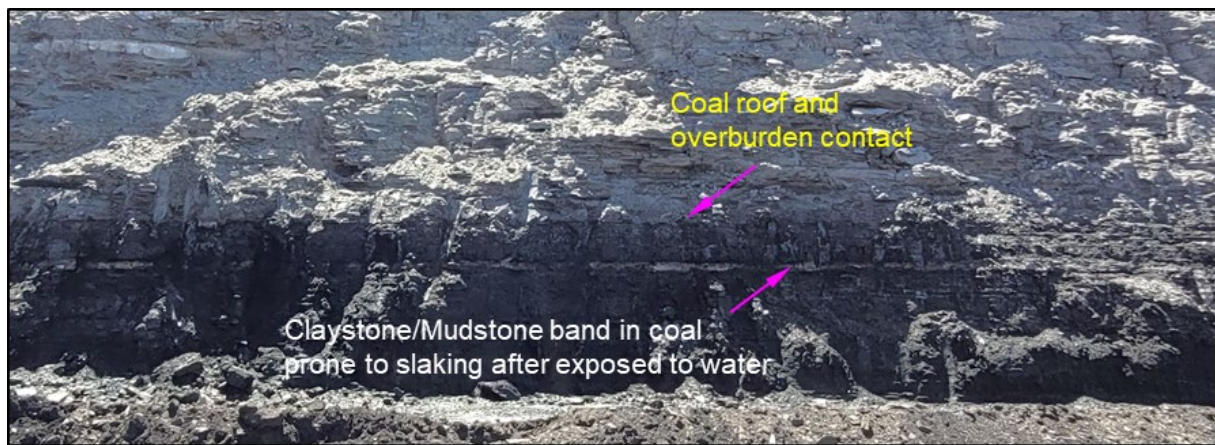
FIG 4 – Thin claystone or mudstone band within coal seam and weak contact along coal roof.

## Dragline bench stability analyses and risk control measures

The coal seam dips at the subject mine range from 3° to 15°. The stability analyses needed to determine the minimum seam dip that would require additional dragline risk controls, eg offset distance from the SDL but allowing the dragline bench to fail, or buttress thickness if no failure is allowed. The Key block is another operational factor impacting dragline bench stability, the narrower the Key, the longer the spoil and coal contact, the more unstable the dragline bench. Base case used for stability analysis was the dragline tub stays on and behind the SDL. There are 108 base cases with nine seam dips of 1° intervals from 7° to 15°, five Key widths in 5 m intervals from 25 m to 45 m (60 m wide strips) and two failure surfaces of through coal roof contact and coal seam shear. A total of ~300 stability assessments for dragline bench risk management were conducted using different SDL offset distances and buttress thicknesses for each base case being modelled, to optimise the outcomes. Other details for the dragline stability analyses are:

- Dragline bench is 50 m high, the maximum digging height of dragline, and measured from toe on coal roof. The batter angle is 45°.

- The SDL is projected up from floor of 4 m thick coal, representative of coal seams in northern pits. The outcomes would be more conservative for the 6 m thick coal seam in southern pits.

- Draglines only uncover coal below base horizon of weathering, thus, Category 3 spoil composed of blasted fresh Permian is considered.

- Material properties given in Simmons and McManus (2004) are applied, except for the spoil and coal roof contact, which are provided in the previous section.

- No pore pressure or water table is included, as the impact of water has been considered when determining the strengths for coal roof contact and coal seam shear.

- GLE/Morgenstern-Price and Spencer methods built-in the Rocscience Slide2 software are used for the 2D LE analysis.

- General active-passive wedge failure mechanism (Simmons and McManus, 2004) is used for searching the minimum factor of safety (Min FS) surfaces.

- Static design criterion is the Min FS = 1.2.

Figures 5 and 6 give examples of the 2D LE analysing results, where the coal seam dips 10°, Key widths of 25 m and 35 m, either with or with no offset from the SDL. We can see that the Min FS values are the same whether the SDL is offset or not. Min FS values are higher for the 35 m wide Key than the dragline bench with 25 m Key, as expected due to decreased weak contact with the increased Key width. We also can see from Figures 5 and 6 Min FS values for sliding along coal seam shear are slightly lower than the Min FS values along coal roof contact. A 4 m offset is sufficient to protect dragline where seam dips are less than or equal to 10°, however, dragline bench failures is expected to occur in front to the SDL with the offset.
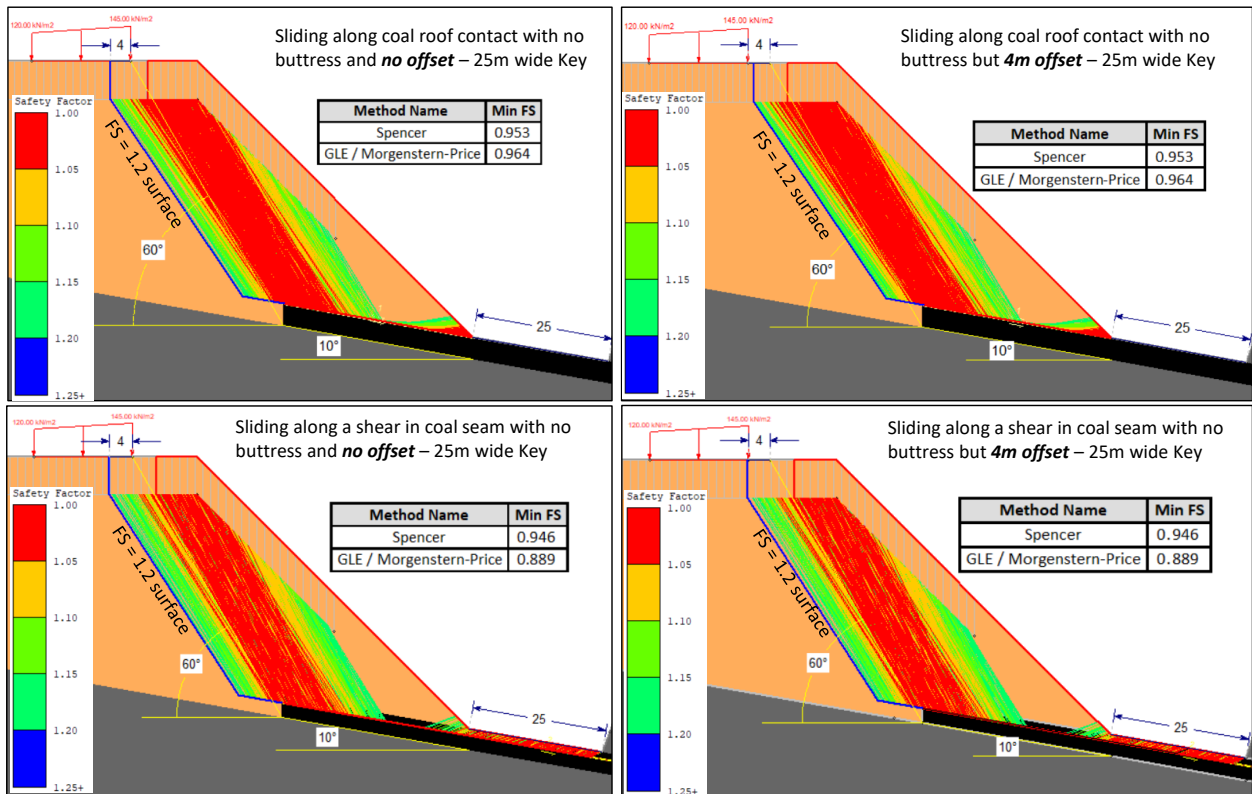
FIG 5 – Results for 10° seam, 25 m Key, sliding along coal roof or shear with or without SDL offset.
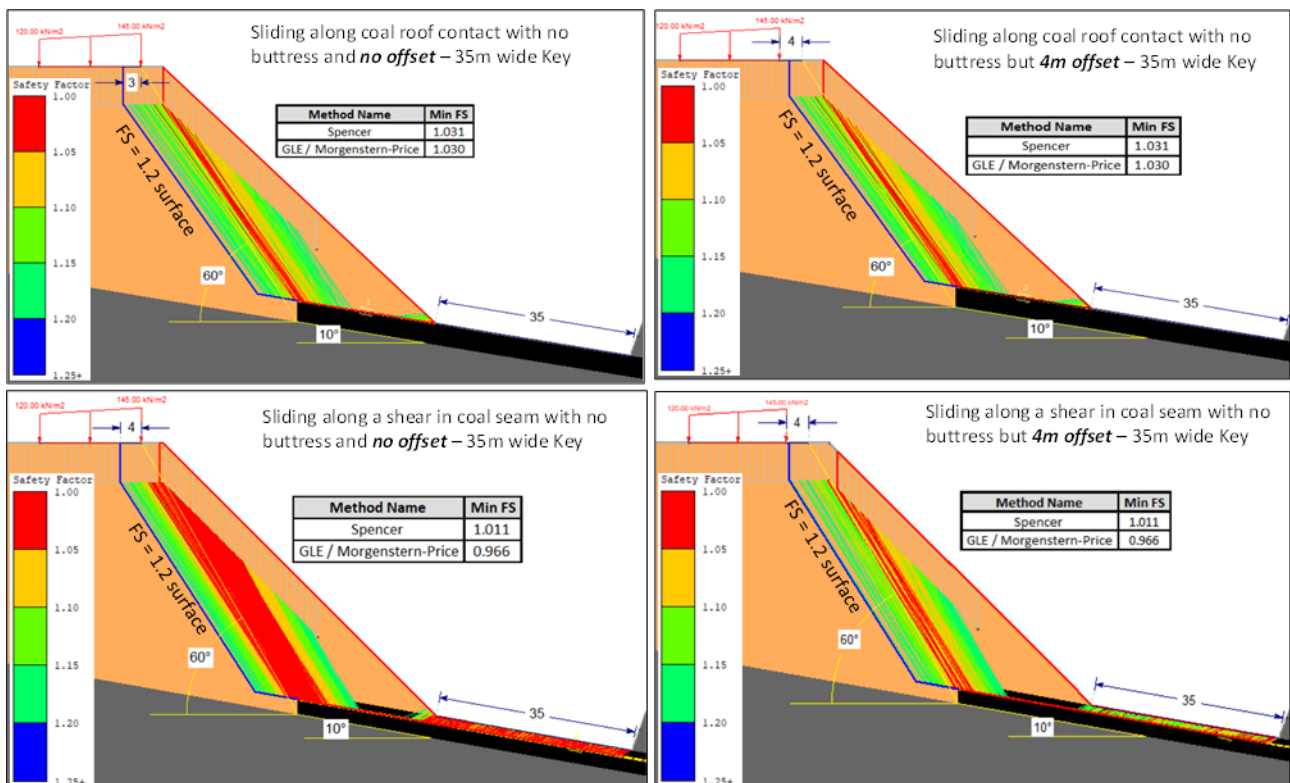
FIG 6 – Modelling results for 10° seam, 35 m Key, sliding along coal roof and coal shear with or without offsetting SDL.

Figure 7 shows the stability modelling results for the 10° seam dip and sliding along a coal shear with 4 m thick buttress above the 25 m wide Key, whether the dragline is kept behind or in front of the SDL. The top surface of the buttress is parallel to coal seam so that the thickness is the same across a section. It is safe to keep the dragline in front of the SDL with the 4 m thick buttress, even

though Min FS values from GLE/Morgenstern-Price are less than (but close to) 1.2, however, the Min FS values from Spencer method are much greater than the design Min FS = 1.2.
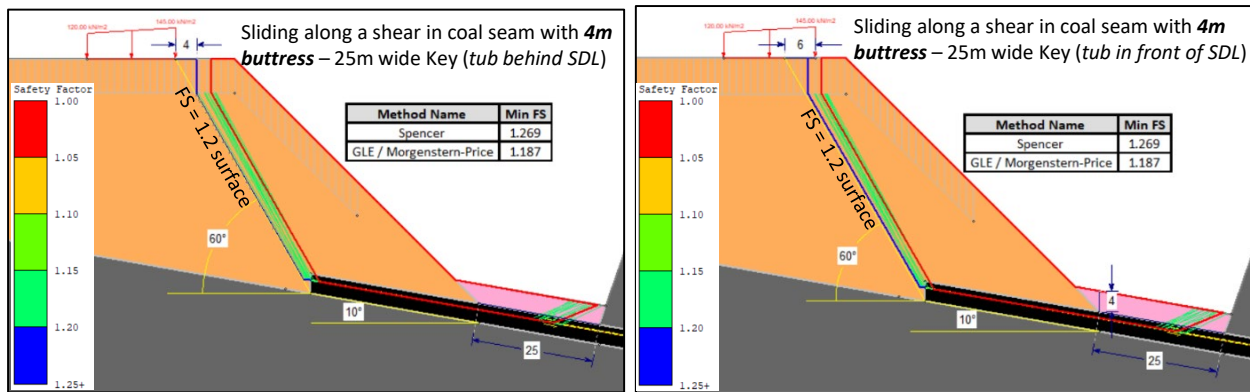
FIG 7 – Modelling results for 10° seam, 25 m Key and 4 m thick buttress either dragline staying behind or in front of the SDL.

Using the stability analysis results for approximately 300 models, geotechnical controls for managing the dragline bench failure risks due to the steep seam and coal seam shears are summarised in Tables 1 and 2. No additional geotechnical control, either offset or buttressing, is required where seam dips less than 8° (14 per cent), except keeping the dragline behind the SDL. The steeper the coal seam, the greater the SDL offset or thicker the buttress that is required.

TABLE 1

Dragline tub offset distance (m) from the SDL if the bench is not buttressed.

Seam dips	Key ≤ 35 m	Key ≤ 40 m	Key ≤ 45 m	Key > 45 m
< 8° (14%)	Not required (N/R)			
8° (14%) ≤ Dip ≤ 10° (18%)	4	2	N/R	
10° (18%) < Dip ≤ 12° (21%)	6	4	2	N/R
12° (21%) < Dip ≤ 14° (25%)	9	7	4	N/R
14° (25%) < Dip ≤ 15° (27%)	11	10	6	N/R

TABLE 2

Dragline bench buttress thickness (m) in the Key.

Seam dips	Key ≤ 35 m	Key ≤ 40 m	Key ≤ 45 m	Key > 45 m
< 8° (14%)	Not required (N/R)			
8° (14%) ≤ Dip ≤ 10° (18%)	4	3	N/R	
10° (18%) < Dip ≤ 12° (21%)	5	4	2	N/R
12° (21%) < Dip ≤ 14° (25%)	6	5	4	N/R
14° (25%) < Dip ≤ 15° (27%)	7	6	5	N/R

Where the SDL offset is applied, dragline bench failure is likely to happen, therefore, using a dozer to assist dragline clean up coal roof or hard dig along highwall can only work within 15 m of the completed Key from the dragline stripping front. The dragline stays behind the dragline bench crest if the SDL with offset is located in front of the crest. When the dragline is on the block of offline, the dozer is allowed to work within the pit to clean up the coal roof until approximately 60 per cent of spoil is in front of the SDL with offset is removed by the dragline.

Where the buttressing in Key is applied, not only is no SDL offset required, but also the dragline can stay in front of the SDL if needed. The Not Required (N/R) in Table 2 means that the dragline can remove the buttress as long as it stays behind the SDL. No post strip is required for the buttressing approach, as all the buttressing can be removed as soon as the Key has reached a width which allows no buttressing and with a dozer or an excavator feeding up to dragline and then cast to the lowwall. The controls given in Tables 1 and 2 can be applied together to maintain safety and optimise productivity.

The dragline bench instability control measures given in above two tables have been successfully implemented at the subject mine since they were established, after having gone through the PDCA processes. Mine planning and operational teams seemed to be more interested in the SDL offset strategy shown in Table 1 in past years, while the buttressing strategy was only implemented to where coal seam in-pit was fully submerged below water.

MANAGING DRAGLINE SPOIL LOWWALL INSTABILITIES

Controls for lowwall instability related to steep floor dips

Dragline lowwall instability control was reviewed soon after the first dragline bench failure occurred in R12N pit of the subject mine. Before commencing lowwall stability assessments, shear strengths of the contact between Category 3 spoil and the pit floor (ie spoil-floor contact), was reviewed, and the presence of shear plane below pit floor was also investigated.

According to Simmons and McManus (2004) the basal shear strengths are 0 cohesion and 18° friction angle for all three spoil categories. The weak Category 1 spoil consists of Tertiary, the moderately competent Category 2 spoil is composed of weathered Permian, and the more competent Category 3 spoil composed of fresh Permian. One may argue that the basal strengths, or the spoil-floor contact strengths, are residual values and exceeded peak strengths and failure occurred. However, the question becomes what the strengths of floor contact are prior to a failure being mobilised, particularly where the lowwall is constructed with Category 3 spoil. Rosengren *et al* (2010) state that stability of a standard dragline lowwall becomes questionable with floor dips greater than 7°. Stability analyses by the author found that a Category 3 dragline lowwall would not be stable even where floor dips are lower than 5° when using the basal strengths given by Simmons and McManus (2004), which contradict actual stable lowwall conditions in Bowen Basin coalmines.

Through detailed review of pit floor conditions, dragline spoil lithological proportions, particularly the percentage and composition of sandstones, as well as back analysis of stable lowwalls, the spoil-pit contact strengths are 5–10 kPa cohesion and 20–25° friction angle. Application at this subject mine and other BHP sites over the years confirmed the validity of this set of strength parameters.

Presence of bedding plane shear in the pit floor, or floor shear, was investigated by using the information from core photos of exploration and geotechnical diamond drill holes, downhole geophysical surveys and ATV/OTV data. No bedding plane shear (Shear) was identified below pit floors in either southern or northern pits.

Stability assessment for different floor dips from 7° to 15° were carried out to consider the maximum coal seam dip in the subject mine. Floor blasting is the preferred option for floor disruption over dozer ripping, as the steeply dipping bedding may still be the potential weak planes for lowwall instability after being dozer ripped. Floor blasting widths in metres could be provided for different floor dips, however, it would be more practical to give drill patterns and number of rows required, as well as disruption depth, to drill and blast engineers for floor disruption design. Holes close to the highwall are kept a minimum 10 m away from highwall for safety and floor disruption effectiveness reasons.

The GLE-Morgenstern/Price and Spencer methods built-in the Rocscience Slide2 software are utilised for stability analyses of lowwall with a standard profile: 45 m high and 42° batter for the lower batter, followed by a 10 m wide bench and then a 40 m high and 37° cast batter. Except the spoil-floor contact, properties for other materials are the same as those given in Simmons and McManus (2004)and Simmons (2018). In addition, the passive-active wedge failure mechanism is also applied to the lowwall stability assessments. As an example, Figure 8 shows stability analysis results for

standard lowwall on 11° dip floor, which is stable with a floor shot of three rows of 8 m × 8 m pattern holes.
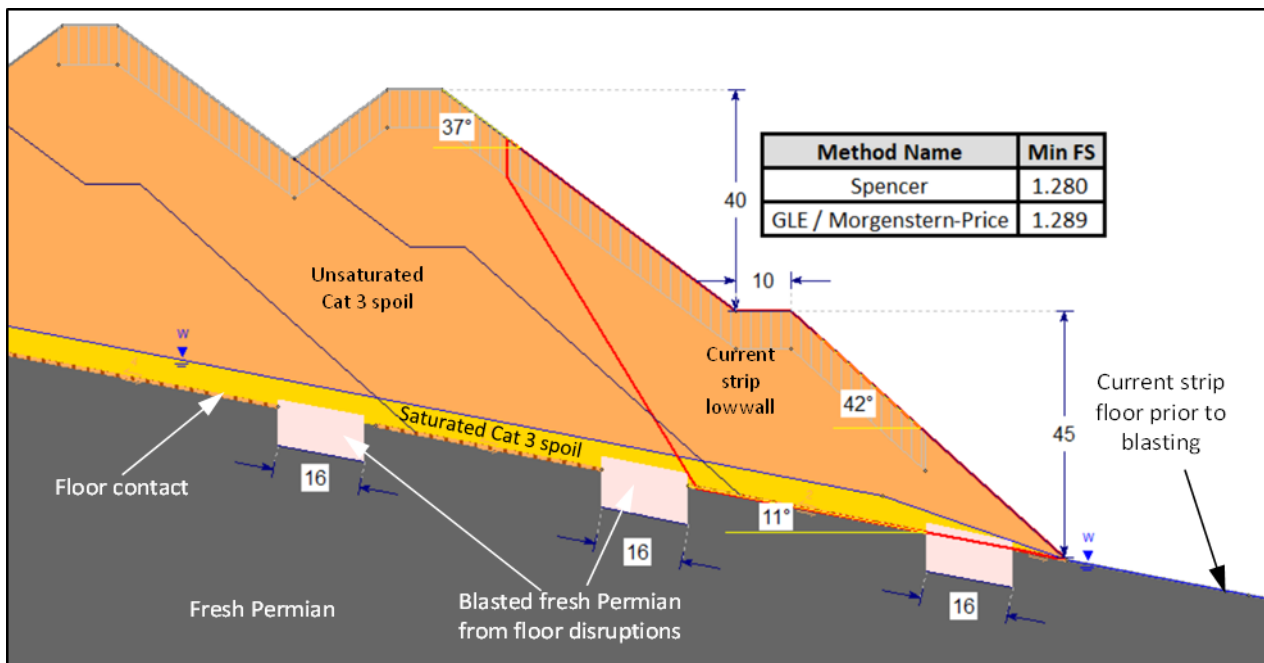
FIG 8 – 2D LE stability analysis results for a standard lowwall on 11° dip floor with three rows of 8 m × 8 m pattern floor shot disruption.

Geotechnical controls concluded from the lowwall stability assessments, as well as other operational considerations are that:

- The minimum floor dips requiring floor disruption is 8° or 14 per cent, ie no floor disruption is required if a pit floor is flatter than 8°.

- The floor disruption with three rows of 8 m × 8 m pattern blastholes are sufficient for all floor dips up to 15° or 27 per cent.

- Floor disruption depth is 7 m from pit floor after coal mining is complete, which suggests that each hole may be drilled deeper to account for collar collapsing etc.

- Cast the floor blasting for maximising disruption of the floor, particularly if a shear plane presents in the floor.

The successful implementation of the above controls confirm that the estimated shear strengths for the Category 3 spoil and pit floor contact, as well as the stability analysing results were valid or realistic.

Managing of lowwall instability related to floor shear and steep floor dips

As stated in previous section, no shear or shear plane was identified below the pit floor in both southern and northern pits of the mine. It is still true for the southern pits so far, however, this was true in northern pits until a lowwall failure occurred during floor shot blasting. A section view of the lowwall failure (Figure 9) shows that the floor disruption shots in all past strips to S10 did not induce any instability until the S11 floor disruption shot being fired, and caused a lowwall failure back to S10 dragline spoil peak. Total horizontal movement of the lowwall failure was less than 10 m until the lowwall stabilised in a few days. Even though there was no safety risk from the lowwall failure, a thorough geotechnical review was carried out to eliminate this kind of lowwall failure in the future.
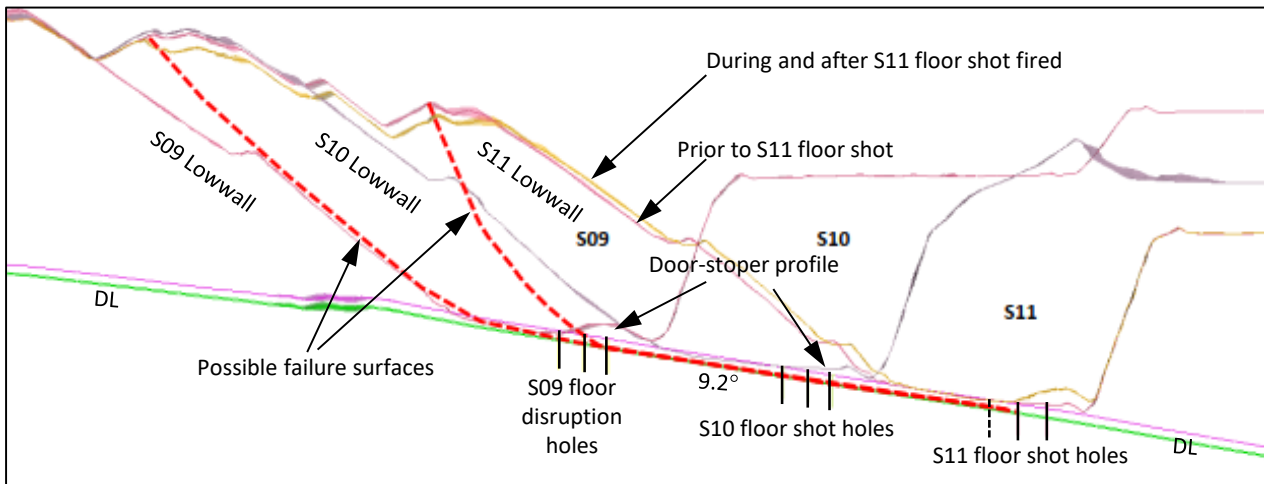
FIG 9 – Section view to show details of a floor disruption blast induced lowwall failure and floor disruption history.

The root causes of the lowwall failure were the presence of a floor shear and steep seam dip. Blasting vibration activated the shear, and allowed the lowwall to fail towards the pit due to free face produced from floor shot blasting. Therefore, it was critical to locate the floor shear and then disrupt it effectively to a sufficient width. Either centre lift or casting towards the highwall would have the same effect,, as both approaches create free face for the lowwall to move. However, the casting blast is expected to provide more effective disruption of the floor and the floor shear if it exists. In addition, the door-stopper profile from the casting blast allows the floor and spoil to interlock with each other and improve lowwall stability.

Investigation from the blast induced failures in northern pits found that the shear would be located within the first non-mineable coal seams, DL, DLL or DLLL, which are located from 0.5 m to 3 m below pit floor. Figure 10 shows a floor shear observed from another floor shot blasting induced lowwall failure, where the shear was ~1 m below the pit floor, and expected to have a friction angle of higher than 15°. Competent and massive floor rock shown in Figure 10 also suggests that the higher than Category 3 spoil properties can be applied to the blasted fresh Permian disrupted floor than given in Simmons and McManus (2004).

FIG 10 – Shear below floor observed from a floor disruption blasting induced dragline lowwall failure in one of the northern pits.

Back analysis of the floor disrupting blast induced lowwall failures suggests that the seismic load coefficient was 0.06 in the horizontal direction, and strengths of the floor shear are 0 cohesion and 18° friction angle. The vertical seismic loading coefficient was ignored, as the vertical component induces neither negative nor positive impact on slope stability.

Therefore, detailed lowwall stability analyses were carried out for pit floor dips ranging from 3° to 15° and depths of floor shear ranging from 0.5 m to 3 m below pit floor in 0.5 m intervals, as well as different floor disruption widths. Standard dragline lowwall profile and material properties given in Simmons and McManus (2004) were applied. An example shown in Figure 11 presents the general layout for floor shear related lowwall stabilisation through floor shot blasting.
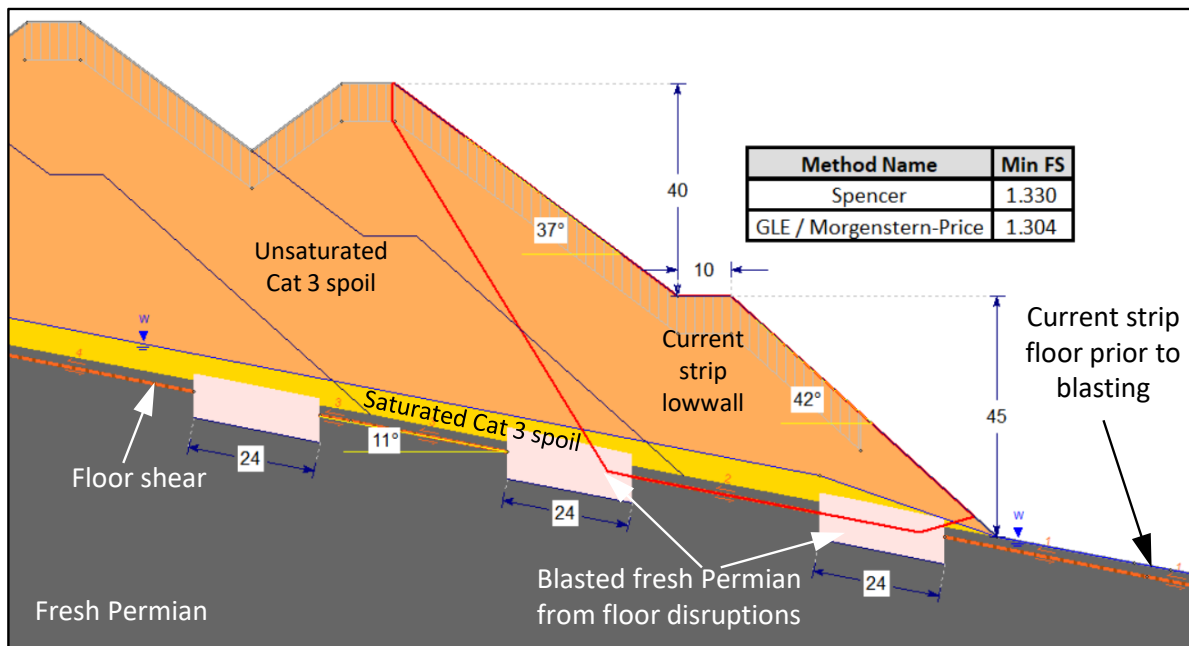
FIG 11 – Floor disruption details and stability analysis results for 11° floor with a shear 2 m below.

The 11° dip floor is disrupted by four rows of 8 m × 8 m pattern drill holes. The floor disruption depth, rather than drilling depth, is 7 m deep. Minimum FS values are much greater than 1.2, in order to account for impact of the dynamic loading from floor disruption blasting.

Seismic impact from blasting was also investigated to compare lowwall stability conditions with and without a floor shear, with the same floor disruption width. As shown in Figure 12, the free face from floor disruption blasting does not impact the lowwall where no floor shear exists, thus, the minimum pseudo-static factor of safety is ~1.15. However, where floor shear exists, the free face from floor disruption blasting allows the lowwall to fail and resulted in Min FS lower than 1.0, which is the minimum pseudo-static FS design criterion (Wesseloo and Read, 2009) for low consequence slope failures (Brown and Booth, 2009). The minimum pseudo-static FS is 1.08 for the lowwall shown in Figure 11. Therefore, the lowwall sitting on 11° dip floor disrupted by four rows of 8 m × 8 m pattern holes can withstand the blasting impact.
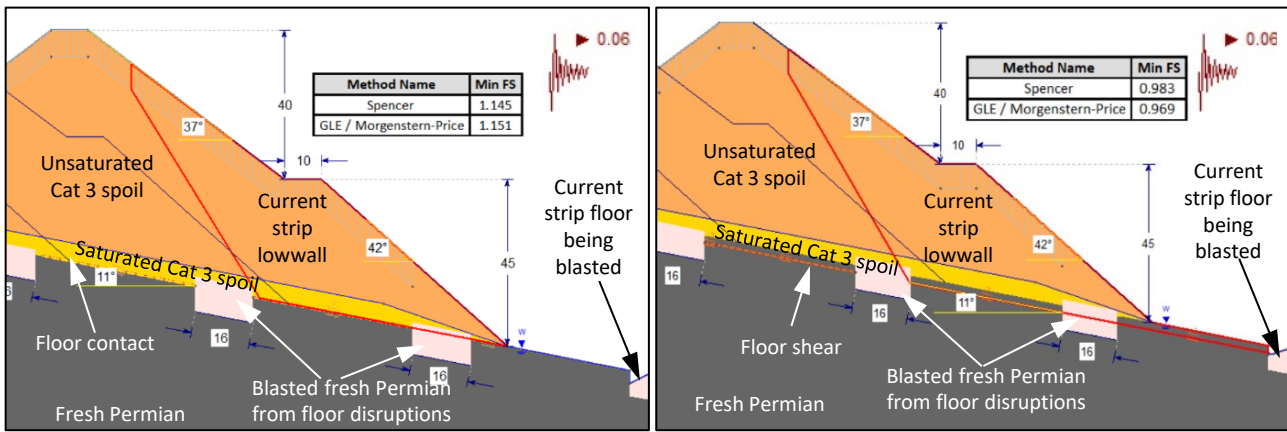
FIG 12 – Comparison of blast impact on stability of lowwall with or with no shear in-pit floor.

Table 3 presents the details of the floor disruption requirement based on different floor dips. A 7 m floor disruption depth is proposed, as at the time it was known that the floor shears were located within 3 m below pit floor. The floor disruption width increases as the floor dips increase.

TABLE 3

Floor disruption requirements where presence of shear in floor.

Floor dips	Floor disruption requirements
< 4° (7%)	Not required if ≥ 2 m below floor, otherwise, 3 rows of 8 m × 8 m holes
4° (7%) ≤ Dip ≤ 8° (14%)	3 rows of 8 m × 8 m pattern holes
8° (14%) < Dip ≤ 12° (21%)	4 rows of 8 m × 8 m pattern holes
12° (21%) < Dip ≤ 15° (27%)	5 rows of 8 m × 8 m pattern holes

The effect of the floor disruption recommendations given in Table 3 can only be seen from the second strip of their applications. Take the section view shown in Figure 9 as an example. The S12 lowwall is expected to fail during S12 floor disruption blasting, as the S11 floor disruption is insufficient to maintain stability of S12 lowwall when S12 floor disruption is fired as per Table 3. However, S13 lowwall would be stable during the S13 floor disruption blasting.

Three of northern pits experienced lowwall failures due to floor disruption blasting. Since the floor disruption requirements with floor shear was established in late 2019, blasting induced lowwall failures stopped in two out of three pits by early 2021. The third pit still waits for the second pit floor disruption to validate the recommendations. Nevertheless, the floor disrupting depth was increased from late 2020 after the shear depth was investigated through two 8-in core holes.

Floor shear allocation and floor disruption depth update

Taking advantages of coal quality exploration using the 8-inch core drilling in September and October 2020, the geotechnical team requested the exploration team to extend the core drilling deeper up to 10 m below pit floor. The two planned 8-inch cored holes were located on natural ground surface and around eight strips from the highwall crest at the time. Floor shears were only observed from one of the two holes. Figure 13 shows the core photos around DLL seam from both holes. It can be seen that only the # 201849 drill hole shows clay bands, the shears, above and below DLL seam. The shears are as thin as around 10 mm thick. The deepest shear was approximately 0.3 m below DLL. This finding suggests that the shear is located around the second non-mineable coal seam below floor in some pits, and deeper than the previous assumption, which is located along the first uneconomical coal seam. The absence of the floor shear in the #201850 hole could suggest that the floor shear may not be a continuous plane. This type of condition have been observed from localised shallow floor heaves within a pit.
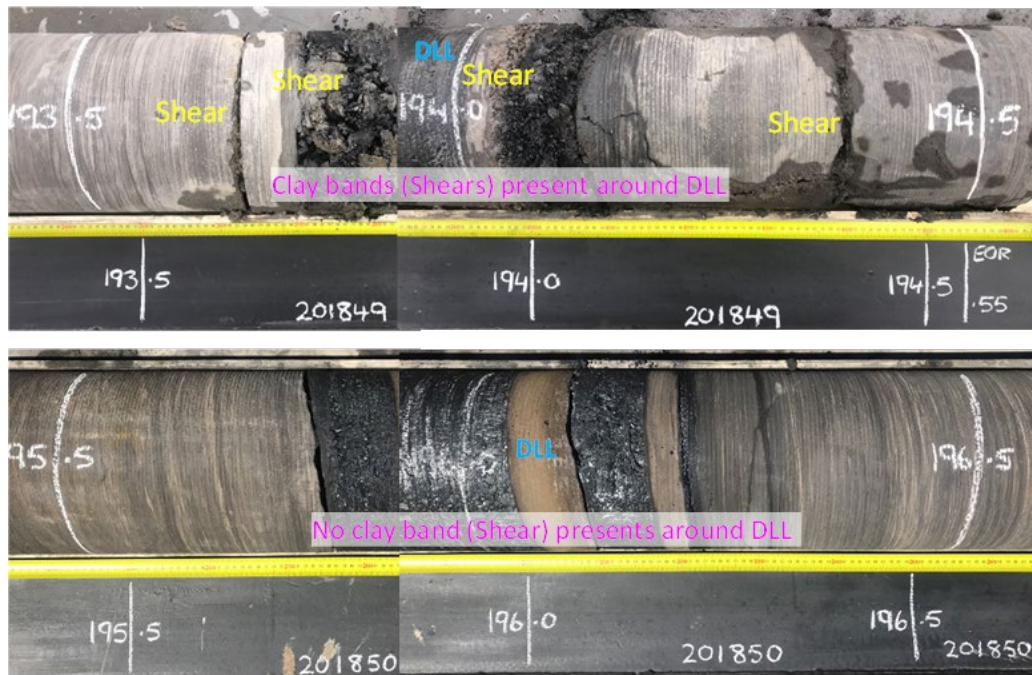
FIG 13 – 8-inch core photos from two holes. A number of clay bands or shears present in #201849 core, but no shear intersected in #201850 core.

Effectiveness of floor disruption is associated with both disruption width and depth. The width does not need to change with an increased depth of the floor shear. Therefore, the blasting depth becomes critical for effectively disrupting the floor. Research work from Onederra, Chacon and Kanchibotla (2020) and Onederra, Chacon and Kanchibolta (2021) provided guidance for improving floor disruption performance and then reducing lowwall failure risk through numerical modelling. One of the key points drawn from their work was that the floor disruption depth should be at least 4 m below the bottom weak layer, or the floor shear. Now that it is known that the floor shear is up to 0.5 m below DLL floor, the minimum floor disruption depth should be at least 4 m below DLL floor, but minimum 7 m, ie:

- Disrupt floor to 7 m below pit floor if the vertical distance from pit floor to DLL floor plus 4.5 m is less than or equal to 7 m.

- Disrupt floor to 4.5 m below DLL floor if the vertical distance from pit floor to DLL floor plus 4.5 m is greater than 7 m.

- Additional subdrilling is required to ensure that the floor is disrupted to the required depths.

Application of the updated floor disruption depths was commenced in December 2020. Lowwall stability improvement is seen from all three pits with low wall failures, particularly in the third pit, the failure limit is reduced from two spoil peaks behind to the first spoil peak only, as well as much less horizontal movement. Low wall of the next strip is expected to be stabilised by the floor disruption blasting.

CONCLUSIONS

Geotechnical work on managing the risk of dragline bench and low wall instability due to steep coal seams and shears within coal seam and below pit floor has been continued and evolved from commencement of operations at this subject mine. Outcomes from geotechnical investigations and assessments ensured the safety of the personnel and equipment, and also maintained and improved productivity.

Even though the geological conditions are more complex in the northern pits, the risk controls for dragline bench instability are the same for all northern and southern pits. Neither the 60° line offset nor dragline bench buttressing is required as long as the coal seam dips below 8°, but a minimum of 4 m offset or buttressing is required for coal seams which dip 8° or steeper and having a key width of 35 m or less.

Floor disruption requirements are easily determined if the stability is only associated with the steep floor dips, and simply three rows of 8 m × 8 m drill pattern can be applied to all floor dips up to 15° or 27 per cent. However, where dragline lowwall stabilities are associated with **both** steep floor dip and floor shear, the disruption width should be increased to account for blasting vibration impact from floor disruption shot firing. The floor shear location and disruption depth are the most critical factors for effectively disrupting the pit floor. It is significantly challenging to locate and apply the shear planes below floor, particularly for the <20 mm thick clay bands. It is more straightforward to assess the core photos than downhole survey data.

The new strength parameters for dragline spoil and coal roof contact, Category 3 spoil and pit floor contact, as well as for the floor shears are realistic, as they are validated by the dragline and low wall performance from the successful implementation of the newly established geotechnical controls.

The processes and strategies for establishing the dragline bench and lowwall instability risk controls can be applied to other open cut coalmines, and the controls outlined in this paper can be directly applied to other coalmines having similar geological conditions, especially to those mines located within the Bowen Basin region in Central Queensland.

ACKNOWLEDGEMENTS

The authors are grateful to BHP and BHP Mitsubishi Alliance for permission to publish the paper in this conference; the Geoscience teams for extending the 8-inch core holes to allocate the floor shear, and the mine scheduling and operational teams for implementing the geotechnical risk controls as outlined for dragline bench and lowwall stability.

REFERENCES

Brown, T and Booth A, 2009. Chapter 13 – Risk Management, in *Guidelines for Open Pit Slope Design* (eds: J Read and P Stacey), CSIRO Publishing, Australia, pp 381–400.

Li, J, 2020. Elimination of structure controlled highwall failures at an open cut coal mine, in *Proceedings of Slope Stability 2020* (ed: PM Dight), pp 1373–1382 (Australian Centre for Geomechanics: Perth).

Li, J, Fityus, S, Payne, D, Vaughan, S and Burton G, 2021. Full PSD rejects shear strength testing for co-disposal and assisted tailings dewatering technique selection, in *Proceedings of Mine Waste and Tailings 2021 Conference*, pp 471–484 (The Australasian Institute of Mining and Metallurgy: Melbourne).

Li, J, Payne, D and Hooi, H, 2018. Plant rejects disposal strategies applied at Caval Ridge open cut coal mine, in *Proceedings of the Mine Waste and Tailings Conference* (The Australasian Institute of Mining and Metallurgy: Melbourne).

Li, J, Tucker, N and Todd, J K, 2016. Impact of rock mass strength parameters on lowwall stability assessment outcomes in open-cut coal mines, in *Proceedings of the Fifth International Conference on Geotechnical & Geophysical Site Characterisation* (eds: A McConnell, R Kelly and B Lehane), Australian Geomechanics Society.

Onederra, I, Chacon, F and Kanchibolta, S, 2020. ACARP Project C28041: Improving blasting outcomes and reducing geotechnical risks, BOHOG ACARP Project Webinar presentation, October 2020.

Onederra, I, Chacon, F and Kanchibolta, S, 2021. Improving blasting outcomes and reducing geotechnical risks, Australian Coal Association Research Program (ACARP) Project C28041 final report, University of Queensland, 73 p.

Rosengren, K, Simmons, J, Maconochie, A P and Sullivan, T, 2010. Geotechnical investigation for open pit mines – 250 m and beyond, in *Proceedings of Bowen Basin Symposium 2010,* pp 169–179.

Simmons, J V and McManus, D A, 2004. Shear strength framework for design of dumped spoil slopes for open pit coal mines, in *Proceedings of Advances in Geotechnical Engineering, The Skempton Conference* (eds: RJ Jardine, D M Potts and K G Higgins), Thomas Telford Limited, Vol 2, pp 981–991.

Simmons, J V, 2018. Weak coal measures, in *Guidelines for Open Pit Slope Design in Weak Rocks* (eds: D Martin and P Stacey), CSIRO Publishing, pp 205–223.

Tsang, M, Bradfield, L, Muhsin, J, Colbourne, I, Bun-Seisay, S, Kelly, H and Makusha, G, 2022. Modelling and operational management of the Dawson Pit 6–8 lowwall instability, in *Proceedings of 2022 Coal Operators Conference*, Wollongong, Australia.

Tucker, N, Li, J and Todd, T K, 2015. Application of laboratory testing to approximate the behaviour of mixed plant rejects, in *Bowen Basin Symposium 2015* (ed: J W Beeston), pp 453–461 (The Geological Society of Australia Incorporated Coal Geology Group: Brisbane).

Wesseloo, J and Read, J, 2009. Chapter 9 – Acceptance Criteria, in *Guidelines for Open Pit Slope Design* (eds: J Read and P Stacey), CSIRO Publishing, pp 221–236.

Poster submissions

A new test method for directional propagation of type-I rock cracks

L X Chen[1], W Y Guo[2] and D X Zhang[3]

1. College of Energy and Mining Engineering, Shandong University of Science and Technology, Qingdao 266590, China. Email: 1159682957@qq.com
2. College of Energy and Mining Engineering, Shandong University of Science and Technology, Qingdao 266590, China. Email: 363216782@qq.com
3. College of Energy and Mining Engineering, Shandong University of Science and Technology, Qingdao 266590, China. Email: 1290763952@qq.com

ABSTRACT

To obtain the rock type-I crack propagation process accurately, a novel fixture is used to make the prefabricated crack of rock propagation along the predetermined direction. In this study, the crack propagation process of rock is monitored with the digital image correlation method (DICM), and a mechanical model of crack directional propagation was established. The results show that the simple crack directional propagation device can effectively realise the stable propagation of type-I crack along the predetermined direction, the crack initiation angle is less than 10°, and the deviation between the peak strength of crack propagation calculated by a simplified mechanical model and the tensile strength of Brazilian splitting is 22.76 per cent and 7.53 per cent, respectively. According to the deformation field evolution law, crack propagation can be divided into three stages: microcrack development, main crack propagation, and main crack propagation. As for the rock type-I crack initiation and propagation mechanism, before reaching the peak strength, the prefabricated crack tip is subjected to maximum tensile stress; the elastic energy increases rapidly, and the dissipation energy increases slowly; after the peak strength, elastic energy exceeds its energy storage limit and released rapidly, and most of the input energy is converted into dissipation energy, which makes the crack propagation rapidly. The crack directional propagation device will be further optimised and improved, and it is expected to provide a new method for the study of crack propagation mechanism, rock failure precursor information and crack arrest principle, etc. It will also provide theoretical references for the optimisation of coal strata directional blasting, fracturing, fracture arrest, and other related technologies in geotechnical engineering.

Deformation failure characteristics of rock-coal composites with different height ratios

S J Chen[1], D W Yin[2], F X Li[3], Y S Ding[4], F Wang[5] and N Jiang[6]

1. College of Energy and Mining Engineering, Shandong University of Science and Technology, Qingdao 266590, China. Email: csjwyb@163.com
2. College of Energy and Mining Engineering, Shandong University of Science and Technology, Qingdao 266590, China. Email: yindawei@sdust.edu.cn
3. College of Energy and Mining Engineering, Shandong University of Science and Technology, Qingdao 266590, China. Email: lifaxin@sdust.edu.cn
4. College of Energy and Mining Engineering, Shandong University of Science and Technology, Qingdao 266590, China. Email: 565197106@qq.com
5. College of Energy and Mining Engineering, Shandong University of Science and Technology, Qingdao 266590, China. Email: wangfeng@sdust.edu.cn
6. College of Energy and Mining Engineering, Shandong University of Science and Technology, Qingdao 266590, China. Email: jiangning@sdust.edu.cn

ABSTRACT

This study assessed the deformation failure characteristics of rock-coal composites with different height ratios. Uniaxial compression tests were conducted using an acoustic emission monitoring system and XTDIC three-dimensional full-field strain measurement system. The results showed that with the increase in rock-coal height ratios, the uniaxial compressive strength of composite samples increased from 5.26 MPa to 14.61 MPa. The evolution of the deformation localisation zone of the composite samples is closely related to the initiation and propagation of the primary cracks in the coal samples. At the moment when the main fracture of the coal samples occurs, there is a large drop after the peak of the stress-strain curve of the composite samples, and the height of the rock samples increased to varying degrees, which indicated that the failure of the coal samples induced the rebound deformation of the rock samples. With the increase in rock-coal height ratios, the rebound deformation amount of the rock samples decreased from 0.042 mm to 0.008 mm, and the rebound deformation rate decreased from 0.210 per cent to 0.010 per cent. Meanwhile, the rock samples' rebound deformation releases part of the elastic energy to act on the coal sample, further contributing to the destruction of the coal samples. Compared with single composite coal samples, the coal samples of the composite samples have much more failures. In addition, with the increase in rock-coal height ratio, the input energy density, elastic energy density, post-peak release energy density, and residual elastic energy density of the composite samples increased, the dissipation energy density decreased, and the percentage of pre-peak elastic energy density increased from 98.56 per cent to 99.86 per cent. These results revealed the deformation failure characteristics of rock-coal composite with different height ratios and provided a theoretical reference for understanding the underground dynamic rock failures.

Use of fly-ash slurry in backfill grouting in coalmines

N Jiang[1], J H Zhao[2], X Z Sun[3], L Y Bai[4] and C X Wang[5]

1. College of Energy and Mining Engineering, Shandong University of Science and Technology, Qingdao 266590, China. Email: jiangning198961@163.com
2. College of Mining and Safety Engineering, Shandong University of Science and Technology, Qingdao 266590, China. Email: jinhai.zhao@sdust.edu.cn
3. College of Mining and Safety Engineering, Shandong University of Science and Technology, Qingdao 266590, China. Email: 496661950@qq.com
4. College of Mining and Safety Engineering, Shandong University of Science and Technology, Qingdao 266590, China. Email: 786661009@qq.com
5. College of Mining and Safety Engineering, Shandong University of Science and Technology, Qingdao 266590, China. Email: 1554624100@qq.com

ABSTRACT

In backfill grouting for underground coalmines, the filling materials strengthen the caving rock and support the overlying strata to reduce surface subsidence. The broken roof strata fail and collapse during mining operations without appropriate supporting measures being taken. It is difficult to perform continuous backfill mining on the working face of such roofs using the existing mining technology. Therefore, in order to solve the above problems, fly ash and mine water are considered as filling materials, and flow characteristics of fly-ash slurry are investigated through laboratory experiments and theoretical analyses. Laws governing the diffusion of fly-ash slurry in the void of caving rock masses and in the void between a caving rock mass and a basic roof are obtained and verified. Based on the results obtained from the above analyses and field conditions at the Zhaoguan coalmine, Shandong Province, China, a cave backfill grouting system of the hauling pipeline is developed and successfully tested at the 1703 working face. The results demonstrate that a filling rate of 43.46 per cent is achieved, and the surface subsidence coefficient of the grouting process is found to be 0.475. Compared to the total caving method, the proposed system is found to achieve a reduction rate of 40.63 per cent. This effectively helps in lowering the value of the surface subsidence coefficient. Fly ash and mine water, considered as primary materials in this study, also play a significant role in improving the air quality and water environment.

The influence of the strain rate and pre-static stress on the dynamic mechanical properties of medium sandstone

J Wang[1], S Yang[2] and J G Ning[3]

1. College of Energy and Mining Engineering, Shandong University of Science and Technology, Qingdao 266590, China. Email: wangjunsdkjd@126.com
2. College of Energy and Mining Engineering, Shandong University of Science and Technology, Qingdao 266590, China. Email: yangshang0214@126.com
3. College of Energy and Mining Engineering, Shandong University of Science and Technology, Qingdao 266590, China. Email: njglxh@126.com

ABSTRACT

A series of conventional dynamic uniaxial compression (CDUC) tests and coupled static-dynamic loading (CSDL) tests were conducted using a split Hopkinson pressure bar (SHPB) system to explore the dynamic mechanical behaviour and fracture characteristics of medium sandstone on a microscale in the laboratory. In the CDUC tests, the dynamic uniaxial compressive strength of the medium sandstone was rate-dependent, while the dynamic elastic modulus was not dependent on the strain rate. Then, we proposed a generalised model to characterise the rate-dependent strength from 17.5 s-1 to 96.8 s-1. In the CSDL tests, with increasing initial pre-static stress, the dynamic elastic modulus and dynamic strength increased nonlinearly at first and then decreased. The results show that two classical mechanical types (ie Class I and Class II) are observed from the dynamic stress-strain responses of the CDUC and CSDL tests. By means of scanning electron microscopy (SEM), the micro difference of post-loading microfracture characteristics in Class I and Class II behaviour was identified. In Class I behaviour, intergranular fracture (IF) usually initiates at or near the grains, most cracks deflected along the grain boundaries, resulting in a sharp angular edge, then coalesces to the main fracture surface that splits the specimen along the direction of stress wave propagation. In contrast, Class II behaviour results from the combined IF and transgranular fracture (TF).

Multi-physical field coupling model development and parameter analysis of natural gas hydrate considering mechanical damage

X F Wang[1], Y Qiu[2] and Z R Guo[3]

1. College of Energy and Mining Engineering, Shandong University of Science and Technology, Qingdao 266590, China. Email: 1261996024@qq.com
2. College of Energy and Mining Engineering, Shandong University of Science and Technology, Qingdao 266590, China. Email: 412011152@qq.com
3. College of Energy and Mining Engineering, Shandong University of Science and Technology, Qingdao 266590, China. Email: 997465545@qq.com

ABSTRACT

Mechanical damage leads to the increase of effective stress of sediments, and pore closure hinders the discharge of methane gas. Ignoring the influence of mechanical damage leads to an excessive prediction of hydrate gas production. Therefore, a fully coupled model considering mechanical damage-chemical decomposition-gas-water two-phase seepage-temperature was developed in this study, and the model was verified by Masuda experiment. Based on the fully coupled model, the temporal and spatial evolution of the whole process of hydrate decomposition under the influence of three initial absolute permeabilities, three pressure drops and three water saturations were considered. The results showed that:

- The gas production rate reached the peak value in a short time after depressurisation, and the peak value increased with the increase of the absolute initial permeability. The larger the initial absolute permeability was, the faster the damage variable reached the peak value. The porosity increased gradually before the damage variable reached its peak, and the gas flowed more easily.

- When the pressure drop was low, the hydrate remained stable in solid form. As the pressure drop increased, the hydrate gradually began to decompose. The greater the pressure drop was, the faster the initial decomposition rate of the hydrate was. So the damage variable increased rapidly and the porosity increased continuously, resulting in a large gas production rate at the initial stage of decomposition.

- The larger the initial water saturation was, the smaller the effective stress wss, resulting in the slow growth of the damage variable and the small change of porosity.While the gas relative permeability was small, it resulted in a smaller gas production rate, and hydrate decomposition was slower.

- The damage variable showed a process of rapid growth first, then slowly increased to the peak, and then gradually decreased to a stable state. When the damage was considered, the hydrate decomposition time to the steady state was longer, and the gas production was about 80.68 per cent of that without considering the damage.

Creep properties and energy evolution characteristics of weakly cemented rock under step loading

C X Zhang[1], S C Hu[2] and W K Ru[3]

1. College of Energy and Mining Engineering, Shandong University of Science and Technology, Qingdao 266590, China. Email: 657487662@qq.com
2. College of Energy and Mining Engineering, Shandong University of Science and Technology, Qingdao 266590, China. Email: mining2@126.com
3. College of Energy and Mining Engineering, Shandong University of Science and Technology, Qingdao 266590, China. Email: 791637062@qq.com

ABSTRACT

To study the creep properties and the energy evolution characteristics of the weakly cemented rock (WCR) in western China, the creep deformation damage law of weakly cemented mudstone (WCM) under graded loading and the energy evolution characteristics of each creep stage were analysed based on the triaxial graded loading creep test of WCR. The results showed that as the confining pressure increased, the creep failure strength of the WCM increased from 9.5 to 24.8 MPa, and the relative displacement of the mineral particles in the mudstone increased gradually, resulting in a reduction in the fracture angle from 79.7° to 58.3°. At the same stress level, the strain energy U_e, the total energy U, and the dissipation energy U_d all increased as the confining pressure increased, but the growth rates of U and U_d decreased gradually, while the growth rate of U_e remained high. At the end of the stable creep stage, U_e increased slowly with the confining pressure, while U and U_d increased rapidly with the confining pressure, and their growth rates were basically the same. At the end of the accelerated creep stage, the growth trends of these three energies were all positively correlated with the confining pressure, U_e was significantly lower than that at the end of the stable creep stage, and U_d and U were further increased. These results revealed the unique creep properties and energy evolution characteristics of the WCR, providing a theoretical basis for long-term stability control of roadways that are built with WCR.

Analysis on crack distribution and evolution characteristics of gangue backfilled working face roof

P F Zhang[1], T B Zhao[2], X Y Ma[3], Z Y Fu[4], X G Tian[5] and Z H Li[6]

1. College of Energy and Mining Engineering, Shandong University of Science and Technology, Qingdao Shandong 266590, China. Email: 15064221133@163.com
2. College of Energy and Mining Engineering, Shandong University of Science and Technology, Qingdao Shandong 266590, China. Email: ztbwh2001@163.com
3. College of Energy and Mining Engineering, Shandong University of Science and Technology, Qingdao Shandong 266590, China. Email: 1365796096@qq.com
4. College of Energy and Mining Engineering, Shandong University of Science and Technology, Qingdao Shandong 266590, China. Email: fuzhiyonghappy@163.com
5. Kailuan (Group) Co., Ltd., Tangshan Hebei 063000, China. Email: xiuguotian@163.com
6. College of Energy and Mining Engineering, Shandong University of Science and Technology, Qingdao Shandong 266590, China. Email: l_zh2008@163.com

ABSTRACT

This study analysed the fracture characteristics and movement process of goaf roofs under the condition of gangue backfilled mining, based on the engineering conditions of Tangshan Mine F5001 gangue backfilled working face. The inclined borehole detection method is adopted to conduct long-term and fixed-point detection of the roof stability. The distribution characteristics of mining-induced cracks in the roof are described quantitatively based on the crack density, and a similar model test method is used to assist the analysis of the roof movement under the control of gangue backfilled mining using stress sensors and digital speckle deformation field monitoring. The results show that under the condition of gangue backfilled mining, structural cracks in the roof typically appear at the boundary of rock strata. The appearance of cracks is related to the rock strata where they are located. Structural cracks appear in the form of single cracks ahead of the working face and develop into structural cracks in the goaf. The roof movement of the coal seam develops in five stages: fracture incubation, crack extension in advance, dense fracture development, steady fracture expansion, and roof stability. Separation forms the primary component of the roof subsidence, accounting for more than half of the subsidence value. The separation generally extends over a long distance along the strike, and vertical crack-intensive areas appear in the roof above the cut-off and stop line. The findings of this study provide a theoretical basis to support designs of backfilled mining and upgrading of hydraulic supports in working faces.

Mechanism analysis and particle flow simulation of water-sand inrush in thin bedrock working face

W Q Zhang[1], X Wu[2], Y Lei[3], S Li[4] and C Ma[5]

1. College of Energy and Mining Engineering, Shandong University of Science and Technology, Qingdao 266590. Email: wenquanzhang@163.com
2. College of Energy and Mining Engineering, Shandong University of Science and Technology, Qingdao 266590. Email: xunanwu@126.com
3. College of Energy and Mining Engineering, Shandong University of Science and Technology, Qingdao 266590. Email: ly1440194949@126.com
4. College of Energy and Mining Engineering, Shandong University of Science and Technology, Qingdao 266590. Email: lisong575757@163.com
5. College of Energy and Mining Engineering, Shandong University of Science and Technology, Qingdao 266590. Email: m1422549368@126.com

ABSTRACT

The failure of roof of thin bedrock working face under loose aquifer in a coalmine can lead to water-sand inrush disaster. Based on the accident of water-sand inrush in 30108 working face of a mine in Shaanxi province, China, the mechanism of water-sand inrush is theoretically analysed. The process and critical conditions of water-sand inrush in working face are reproduced by numerical simulation where the bedrock thickness is 20 m, the clay layer thickness is 40 m and the mining height is 6.5 m. The study found that under the condition of thin bedrock and thick clay layer, the characteristics of the clay layer have a significant inhibitory effect on the development of the fractured zone, and the development of the water-conducting fractured zone is incomplete and insufficient. However, in the process of continuous mining of multiple adjacent working faces, the strength of the clay is gradually reduced by the influence of mining and the erosion of water, and the height of the fractured zone is gradually increased. In the subsequent mining process of the working face, the roof is more likely to be cut-off and lead to water-sand inrush. From the initial failure of the clay to the final crack directly through the surface, the shear strength of the clay is reduced by about 52 per cent. Further simulation found that in addition to the characteristics of the clay layer itself, the main factors affecting the water-sand inrush in the working face caused by overburden failure also include the difference in bedrock thickness and strength, and the difference in coal seam mining height. With the increase of bedrock thickness, the development height of the fractured zone increases gradually with increases of bedrock thickness when the cutting failure of overburden rock no longer occurs. With the increase of mining height, the height of water flowing fractured zone also increases, but the cracking ratio gradually decreases. Therefore, it's of great practical significance to systematically study the mechanism and critical conditions of water and sand inrush in mines and the main influencing factors for preventing similar accidents in mines with similar conditions.

Application of rock mass index in the prediction of mine water inrush and grouting quantity

W Zhu[1], J H Zhao[2] and H Ma[3]

1. College of Energy and Mining Engineering, Shandong University of Science and Technology, Qingdao, 266590, China. Email: 2639984564@qq.com
2. College of Energy and Mining Engineering, Shandong University of Science and Technology, Qingdao, 266590, China. Email: jinhai.zhao@sdust.edu.cn
3. College of Energy and Mining Engineering, Shandong University of Science and Technology, Qingdao, 266590, China. Email: 1766124758@qq.com

ABSTRACT

The permeability coefficient is an essential parameter for the study of seepage flow in fractured rock mass. This paper discusses the feasibility and application value of using readily available RQD (rock quality index) data to estimate mine water inflow and grouting quantity. Firstly, the influence of different fracture frequencies on permeability in a unit area was explored by combining numerical simulation and experiment, and the relationship between fracture frequencies and pressure and flow velocity at the monitoring point in fractured rock mass was obtained. Then, the stochastic function generation program was used to establish the flow analysis model in fractured rock mass to explore the relationship between flow velocity, pressure and analyse the universal law between fracture frequency and permeability. The concepts of fracture width and connectivity are introduced to modify the permeability calculation formula and grouting formula. Finally, based on the on-site grouting water control case study, the rock mass quality index is used to estimate the mine water inflow and the grouting quantity. The results show that it is feasible to estimate the fracture frequency and then calculate the permeability coefficient by RQD. The relationship between fracture frequency and RQD and the relationship between structure surface frequency and permeability follow an exponential function. The calculation results are in good agreement with the field monitoring results, which verifies the rationality of the calculation method. The relationship between the rock mass RQD index and the rock mass permeability established in this paper can be used to invert the mechanical parameters of the rock mass or to evaluate the permeability and safety of the rock mass, which is of great significance to the prediction of mine water inflow and the safety evaluation of water inrush disaster management.

Development of rock testing system with changeable stiffness and test research on failure characteristics of rock

Y H Zhu[1], Y C Yin[2], X X Tang[3] and M L Xing[4]

1. College of Energy and Mining Engineering, Shandong University of Science and Technology, Qingdao 266590, China. Email: 3158522427@qq.com
2. College of Energy and Mining Engineering, Shandong University of Science and Technology, Qingdao 266590, China. Email: yycrsd@163.com
3. College of Energy and Mining Engineering, Shandong University of Science and Technology, Qingdao 266590, China. Email: 1159347942@qq.com
4. College of Energy and Mining Engineering, Shandong University of Science and Technology, Qingdao 266590, China. Email: sixingziwei@163.com

ABSTRACT

Based on the stiffness theory, the stiffness difference and energy supply of surrounding rocks are important inducing factors for strain burst. However, due to the lack of multi-level low stiffness testing machine, there are few experimental studies on rock failure mechanisms under the influence of loading stiffness. This paper introduced a self-developed rock testing system with changeable stiffness. The main testing machine of this system is a combined structure of inner and outer frame. The change in the loading stiffness is achieved by using a stiffness servo control system to control the energy accumulation in the inner frame. The tests of the sandstone specimens under three different loading stiffnesses in the testing system showed that the loading stiffness did not significantly affect either the uniaxial compressive strength or the Young's modulus of the rock. However, the post-peak stress-strain curve of the rock became smoother and steeper when the loading stiffness was decreased, and the stress drop rate increased. It is shown that the stress drop rate had a power function correlation with the loading stiffness. After the peak load, the inner frame of the testing system rebounded several times at high speeds. The magnitude of the instantaneous rebound speed and the rebound duration increased with the decrease of loading stiffness. Both the mean rebound velocity and the total rebound deformation had power function correlations with the loading stiffness. The loading stiffness has limited effect on the energy storage and energy dissipation characteristics of the specimen, while the released energy of the testing machine increases as the loading stiffness decreases, which is the key factor affecting the failure mode of the specimen. According to the test results, a rock burst mechanical model considering the stiffness is established, and the energy supply mechanism of rock burst is quantitatively explained.

AUTHOR INDEX